eman ta zabal zazu

Universidad del País Vasco
Euskal Herriko Unibertsitatea

Kimika Aplikatua Saila/Departamento de Química Aplicada

Transition metal, lanthanide and mixed 3d-4f based compounds based on Mannich base ligands: a progressive magnetic study towards improved materials

Thesis presented by

Andoni Zabala Lekuona

To qualify for the degree of

Doctor from Universidad del País Vasco/Euskal Herriko Unibertsitatea

Supervisors: José Manuel Seco and Enrique Colacio

Donostia, May 2021

TABLE OF CONTENTS

ABBREVIATIONS and ACRONYMS

Abbrev. / Acronyms	Meaning
υ	Frequency
χ_M	Molar Magnetic Susceptibility
χ_M'	In-phase Magnetic Molar Susceptibility
χ_M''	Out-of-Phase Magnetic Molar Susceptibility
A	Direct relaxation parameter
Ac	Alternating current
Acac	Acetylacetonate
AF	Antiferromagnetic
AFM	Atomic Force Microscopy
B	Raman relaxation Parameter
CASSCF	Complete Active Space Self-Consistent Field
CF	Crystal Field
CPL	Circularly Polarized Luminescence
CShM	Continuous Shape Measurements
D	Zero Field Splitting Parameter
Dbm	1,3-diphenyl-1,3-propanedione
Dc	Direct current
E	Energy
EA	Elemental Analysis
EO	End-on
E_T	Thermal energy
EtOH	Ethanol
F	Ferromagnetic
FC/ZFC	Field Cooled/Zero Field Cooled
G	Graphene
g_{lum}	Dissymmetry factor
GO	Graphene Oxide
H	Magnetic field
H	Magnetic field
H_2L^1	N,N',N''-trimethyl-N,N''-bis(2-hydroxy-3-formyl-5-bromobenzyl) diethylenetriamine
H_2L^2	N,N'-dimethyl-N,N'-bis(2-hydroxy-3-formyl-5-bromobenzyl) ethylenediamine
H_2L^3	N,N′-dimethyl-N,N′-bis(2-hydroxy-3-methoxy-5-methylbenzyl)

	ethylenediamine
H_3L^5	1,1,1-tris[(salicylideneamino)methyl]ethane
H_4L^4	1, 4, 8, 11-tetraaza-1, 4, 8, 11-tetrakis(2-hydroxy-3-methoxy-5-methylbenzyl) cyclotetradecane
H_A	Axial ZFS Hamiltonian
Hfac	Hexafluoroacetylacetonate
H_T	Transversal ZFS Hamiltonian
I	Nuclear spin
IR	Infrared
J	Coupling Constant
K	Anisotropy
KD	Kramers Doublet
L	Angular Orbital Momentum
M	Magnetization
MeCN	Acetonitrile
MeOH	Methanol
MOF	Metal-Organic-Framework
M_S	Magnetic moment
n	Raman Relaxation Exponential Parameter
NMR	Nuclear Magnetic Resonance
OTf	Triflate
PXRD	Powder X ray diffraction
QTM	Quantum Tunneling of the Magnetization
RASSI	Restricted Active Space State Interaction
S	Spin
SC-XRD	Single Crystal X-ray Diffraction
SEM/EDX	Scanning Electron Microscopy/Energy Dispersive X-ray spectroscopy
SIM	Single Ion Magnet
SMM	Single Molecule Magnet
SOC	Spin Orbit Coupling
TA-QTM	Thermally Assisted Quantum Tunneling of the Magnetization
T_B	Blocking temperature
T_C	Curie temperature
TG	Thermogravimetry
TGA	Thermogravimetric Analysis

TM	Transition metal
U	Energy barrier
U_{cal}	Calculated energy barrier
U_{eff}	Effective energy barrier
V	Volume
XRPD	X-Ray Powder Diffraction
ZFS	Zero Field Splitting
ΔE	Activation barrier
τ	Relaxation Time
τ_0	Flipping Rate
τ_{QTM}	Flipping rate due to QTM

SUMMARY

The work presented in this Ph.D. dissertation falls fundamentally in the research area of *Molecular Magnetism*, but it also deals with *Photoluminescence*. The aim of this work was to synthesize transition metal, lanthanide or mixed 3d-4f ion based coordination compounds with Single Molecule Magnet (SMM) behaviour and, in some cases, with interesting photoluminescent properties.

The **Introduction** covers the basic topics of the research area. Specifically, it collects some of the most relevant research works published from the first reported SMM, Mn12-ac, to the current state of the art based on dysprosium metallocenes. Additionally, some interesting features are also described for multifunctional systems, hybrid materials (supported-SMMs), *ab initio* calculations and so on. The chapter concludes with the main objectives of this Ph.D. thesis. It is worth noting that this introduction has been accepted as a review in *Coordination Chemistry Reviews*.

Chapter 1 concerns the synthesis and characterization of three novel pairs of mononuclear complexes based on Dy^{III} and Er^{III}, and the Mannich base ligands N,N',N''-trimethyl-N,N''-bis(2-hydroxy-3-formyl-5-bromo-benzyl) diethylenetriamine (H_2L^1) and N,N'-dimethyl-N,N'-bis(2-hydroxy-3-formyl-5-bromo-benzyl) ethylenediamine (H_2L^2). Even though they all display a LnO_9 coordination sphere, the distribution and nature of the oxygen donor atoms differ from one pair to another due to (i) length differences in the side di- or triamine chain and (ii) coordination of a third (but monodentate) nitrate or a water molecule. Consequently, the dynamic magnetic properties change from one pair to another allowing us to postulate some magneto-structural correlations.

Chapter 2 is a direct continuation of our previously reported work (*CrystEngComm*, 2017, **19**, 256). The chapter reports on the synthesis, characterization and magnetic study of nine novel $Zn^{II}Dy^{III}$ based polynuclear systems with the Mannich base N,N′-dimethyl-N,N′-bis(2-hydroxy-3-methoxy-5-methylbenzyl) ethylenediamine (H_2L^3). We have been able to replace the bridging acetate group by a wide variety of di- and tricarboxylate groups maintaining the core structure of the system. We have carried out a complete magnetic study in both pure and magnetically diluted (in a diamagnetic Y^{III} matrix) materials in order to evaluate the influence of intra- and intermolecular interactions in the dynamic magnetic properties.

Chapter 3 focuses on the magnetic properties of three homopolynuclear Co^{II} based compounds and seven mixed 3d-4f-3d heterotrinuclear compounds with H_2L^3 as main ligand. In two of the homopolynuclear Co^{II} complexes we have been able to replace the

bridging chloride groups by azides, so that the nature of the magnetic coupling between Co^{II} centers has been completely changed from antiferromagnetic to ferromagnetic. Additionally, this change gave rise to a modest slow relaxation of the magnetization under an external magnetic field. The magnetic properties of a peculiar pentanuclear Co^{II} based compound are also reported, which behaves as a zero field SMM due to strong enough magnetic exchange interactions between Co^{II} centers that quenches QTM and/or to a negative anisotropy (*D*) value most likely provided by the Co^{II} ion with trigonal bipyramid geometry. Regarding heterotrinuclear compounds, we have combined the anisotropic Co^{II} with diamagnetic (Y^{III}), isotropic (Gd^{III}) and anisotropic (oblate type: Tb^{III} and Dy^{III}; prolate type: Er^{III} and Yb^{III}) metal centers according to different strategies previously studied in the literature. Interestingly, the combinations containing paramagnetic oblate ions displayed zero field SMM behaviour. With the aim of evaluating the influence of the exchange interactions, we also studied the $Zn^{II}Dy^{III}Zn^{II}$ analogue, which did not display slow relaxation of the magnetization in the absence of an external magnetic field.

Chapter 4 was also planned as a continuation of our above cited work. Thus, with the aim of extending the $Zn^{II}Ln^{III}$ entities along 1D, we synthesized a previously reported CYCLAM based H_4L^4 ligand (1, 4, 8, 11-tetraaza-1, 4, 8, 11-tetrakis(2-hydroxy-3-methoxy-5-methylbenzyl) cyclotetradecane). We rationally planned the synthetic steps, obtaining firstly a dinuclear Cu^{II} based compound, with which we concluded that the ligand adopts a suitable conformation for our 1D network extension purposes. Subsequently, a tetranuclear $Zn^{II}_2Dy^{III}_2$ compound with *syn-syn*-acetate groups bridging Zn^{II} and Dy^{III} ions was obtained, which was shown to be very similar to the reference compound in the above cited paper. As final step, when we tried to replace the acetate bridges by succinates, we serendipitously obtained an ionic tetranuclear $Zn^{II}_2Dy^{III}_2$ compound, $[Zn_2(\mu\text{-}H_2L^4)_2(\mu\text{-succinate})Dy_2(NO_3)_2](NO_3)_2\cdot 2H_2O\cdot 4MeOH$, behaving as zero field SMM as a consequence of the suitable ligand field. In fact, three oppositely coordinated (two in one side and one in another) short $Dy\text{-}O_{phenoxido}$ bonds with an additional relatively weak equatorial ligand field stabilizes the oblate electron density of the Dy^{III} ions giving rise to a U_{eff} of up to 260 K considering an Orbach relaxation process. In view of the interesting results, we also studied some other isostructural compounds containing a wide variety of 4f ions and Co^{II} instead of Zn^{II}. Noteworthy, diluted systems were also studied providing an exhaustive magnetic study of all the compounds.

Chapter 5 originates from the interesting results obtained in **Chapter 4**. More specifically, derived from the serendipitous preparation of $[Zn_2(\mu\text{-}H_2L^4)_2(\mu\text{-succinate})Dy_2(NO_3)_2](NO_3)_2\cdot 2H_2O\cdot 4MeOH$. Such complex is a racemate of two enantiomers, which emerge from the formation of quaternary zwitterionic amines. In this chapter, we have been able to stereospecifically control the formation of one enantiomer or the other by using enantiopure methylsuccinates, which act as directing agents. Considering an almost identical coordination sphere around the Ln^{III} ions, the zero field SMM behaviour of the Dy^{III} based counterpart was expected. Additionally, we have synthesized isostructural compounds based on Sm^{III}, Eu^{III}, Tb^{III}, Er^{III} and Yb^{III}, and studied their emissive properties. As highlighting features, the Tb^{III} counterparts display Circularly Polarized Luminescence, while the Eu^{III} based systems have been proposed as potential contactless thermometers due to the strongly temperature-dependent emission.

Chapter 6 also has its origin in the results of **Chapter 4**. In it, we have been able to rationally modify the equatorial ligand field of the ionic tetranuclear $Zn^{II}_2Dy^{III}_2$ compound. Based on previously reported works, we have mostly employed electron-withdrawing fluorides, but also phenyl groups as substituents within the equatorial ligand field to alter the electron density distribution around the Dy^{III} ion, consequently modulating the dynamic magnetic properties. Additionally, the structure allowed us to introduce modifications in two different positions, which at the same time presents the possibility of doing them individually or simultaneously. Finally, we have suggested some magneto-structural correlations based on the experimental results and supported by *ab initio* calculations.

***mini*-Chapter I** also arises from an idea of modifying the tetranuclear compound obtained in **Chapter 4**. Initially, we wanted to change the diamagnetic Zn^{II} ion by the bigger Cd^{II}. From this change, we expected to observe notable differences in both bond lengths and angles that would modify the magnetic properties. Unexpectedly, we obtained a dinuclear $Cd^{II}Dy^{III}$ compound behaving as field induced SMM. With the aim of exploring how the diamagnetic ion affects the magnetic relaxation dynamics, we also synthesized the isostructural $Hg^{II}Dy^{III}$ compound, which also behaves as field induced SMM. Some preliminar results are shown in this chapter.

***mini*-Chapter II** is the last research work based on **Chapter 4**. In it, we show our first attempts in trying to anchor our tetranuclear system to a surface, which is the next step towards the design of future devices. In order to do that, we were able to change the counterion of the tetranuclear system from nitrate to tetraphenylborate. We made

this with the aim of substantially enhancing our possibilities to anchor the compound to graphene or graphene oxide sheets. Some preliminar results are shown in this chapter.

***mini*-Chapter III** reports on the synthesis and magnetic properties of an unintentionally synthesized diamagnetic mononuclear Co^{III} based compound (the target was the mononuclear Co^{II} counterpart) and another Co^{II} based trinuclear complex. These two systems were obtained using the tripodal ligand 1,1,1-tris[(salicylideneamino)methyl]ethane, H_3L^5. Interestingly, the trinuclear compound behaves as zero field SMM with butterfly shaped hysteresis loops at 2 K. Moreover, in this work we suggest a new application for pulse magnetization measurements.

To end up, ***mini*-Chapter IV** collects few more results obtained during the Ph.D. thesis that have not been included within any other chapter. Furthermore, some other future perspectives are suggested which have derived from these results. Finally, collaborations that have been done with some other researchers are mentioned in this final section.

INTRODUCTION

SINGLE-MOLECULE MAGNETS: FROM Mn12-ac TO DYSPROSIUM METALLOCENES, A TRAVEL IN TIME

i. INTRODUCTION

We currently live in an era where mostly all of the information is electronically stored. Relatively few years ago books, notes, documents, photos, newspapers and so on where typically printed and paper based. Nowadays, however, all these data could be digitally found. It is worth mentioning, though, that this new technology has evolved along few decades involving huge and fast changes. Indeed, the first data storage devices were launched during the 70s, which were known as floppy disks. Despite their big dimensions, around 8 inch, they could barely store the information corresponding to a simple pdf. Around five decades later, USB flash drives no bigger than our thumbs are able to accumulate films, thousands of photographs and millions of documents. The evolution has been colossal.

In order to be able to save all these data, the devices employ the binary language: combinations of 1 and 0, which represent the bit information unit. For instance, the nuclei of hard drives are constituted by nanoscopic (few tens of nanometers) ferro- or ferrimagnetic (they behave as magnets below the Cure temperature, TC) alloy particles that form individual magnetic domains, where each of them contains a significant number of magnetic moments. Below the Curie temperature, TC, all the magnetic moments inside a nanoparticle are aligned giving rise to a resultant magnetic moment, MS. Similarly to common paramagnets, all the MS are randomly oriented due to the thermal energy, but since magnetic moments are much higher than for a single atom, this phenomenon is named superparamagnetism (Figure i.1).

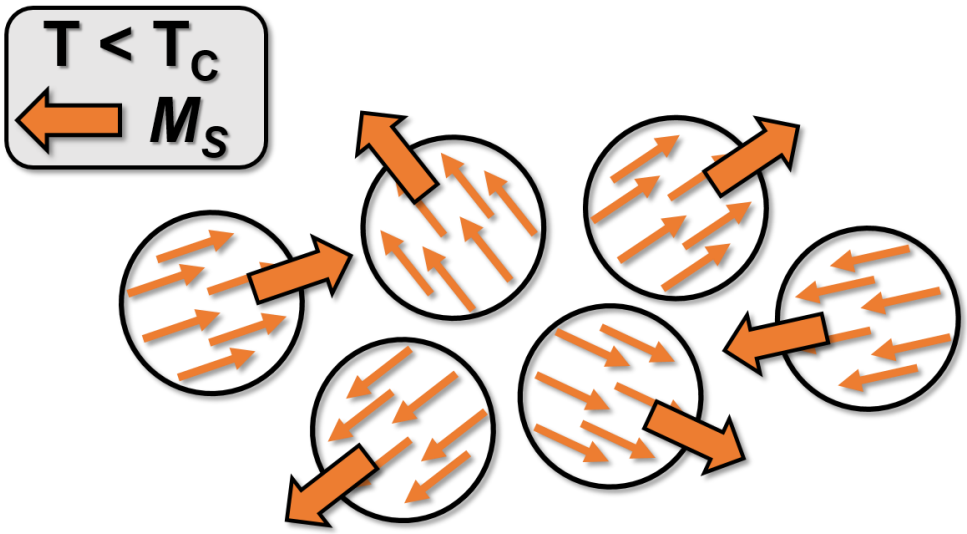

Figure i.1.- Superparamagnetic material.

In the presence of a magnetic field, these nanoparticles could be easily magnetized in a determined direction (easy axis of magnetization) due to the presence of an axial anisotropy, which depends on intrinsic factors, such as the type of metallic ions and the shape of the nanoparticles. When a magnetic field is applied, the nanoparticles tend to point out their magnetic moments collinear to the field, obtaining the highest magnetic moment (M_S). If the magnetic field is removed (H = 0) and the temperature of the system is below a certain temperature, known as blocking temperature T_B, the magnetic moment remains blocked in the same direction. Hence, the system behaves as a magnet, a hysteresis loop could be observed and, therefore, it has memory effect. This occurs due to the existence of an activation barrier, ΔE that prevents the reorientation of the magnetization, which depends on the anisotropy, K, and the volume of the nanoparticle, V (Figure i.2). Below T_B, the thermal energy, E_T, is not big enough to overcome the energy barrier ($E_T < \Delta E$) and thus the magnetic moment becomes blocked. Above T_B, in contrast, the system possesses enough energy to surpass the barrier ($E_T > \Delta E$) and an equilibrium between the two orientations (positive and negative) is obtained, where the material shows a superparamagnetic behavior and no hysteresis could be observed. Thus, if the system is maintained below T_B, the orientation of the magnetization in one direction will represent the information corresponding to 1, while in the opposite direction will represent 0. In consequence, the lower the dimensions of the nanoparticle, the higher the information density within the device.

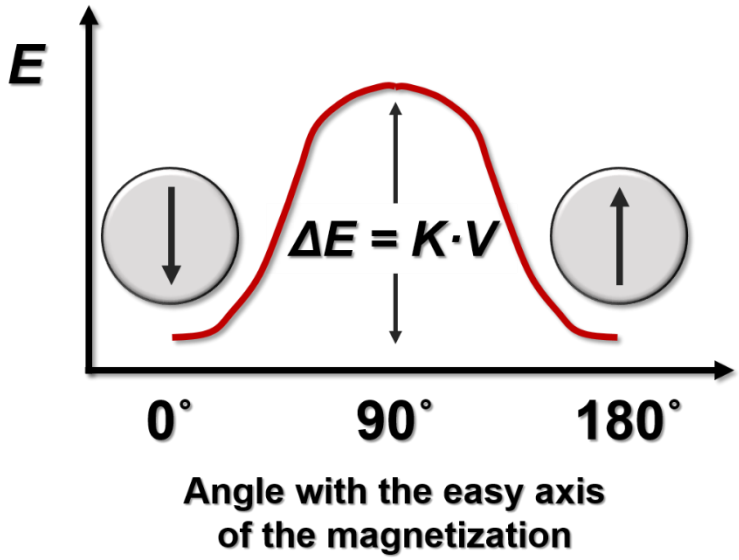

Figure i.2.- Energy of the orientation of the magnetization considering the easy axis of magnetization.

Nonetheless, this “up-down” strategy towards information storage devices presents some limitations. As an example, it is not possible to reduce the size of the nanoparticle as much as desired, since this inherently reduces the anisotropy value and hence the thermal activation barrier. Indeed, the critical size of the nanoparticle is known to be around 10 nm, and below it the hysteretic behavior disappears and therefore is not possible to store information (Figure i.3). Moreover, it is a hard task to obtain monodisperse particles and normally nanoparticles that differ in size and shape are obtained, which means that the anisotropy values will be different, as well as their activation barriers.

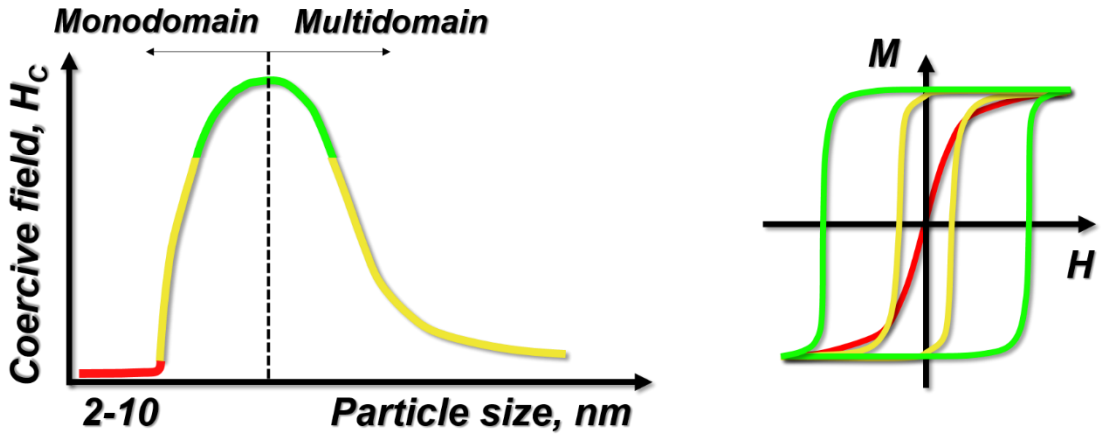

Figure i.3.- Evolution of the hysteresis loops considering the particle size.

In this context, Single Molecule Magnets, SMMs, emerged in 1993 when Sessoli and coworkers observed that the coordination compound named as Mn12-ac (compound **i1**, Figure i.4) was able to store information at a molecular level [1]. Thus, the smallest material unit with memory effect was heavily reduced in size from few hundreds of nanometers to few angstroms.

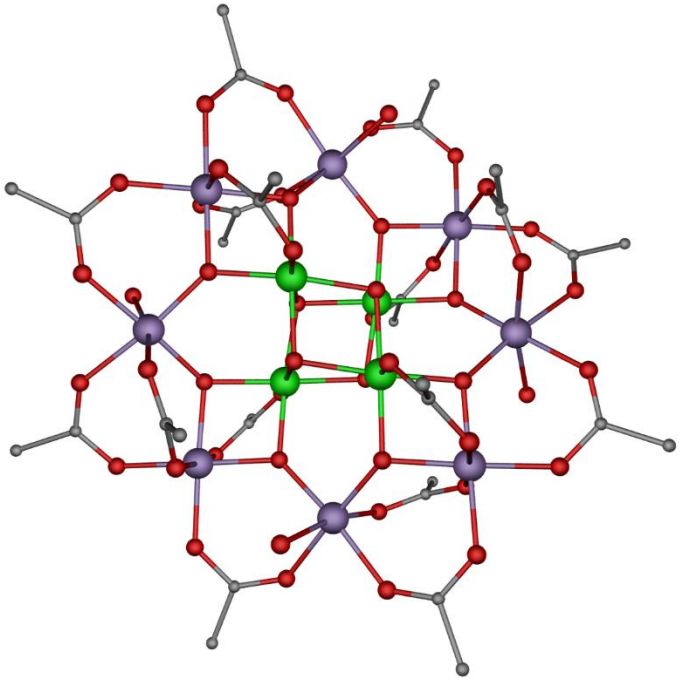

Figure i.4.- Structure of Mn12-ac (**i1**). Color code: Mn^{III}, Mn^{IV}, carbon and oxygen in purple, green, grey and red, respectively. Hydrogen atoms have been omitted for the sake of clarity. Reproduced from reference [2]. Creative Commons license.

i.i. How do Single Molecule Magnets work?

As it can be deducted from the name, Mn12-ac is a coordination compound containing 12 metallic centers, four Mn^{IV} and eight Mn^{III} ions. The antiferromagnetic interaction between metallic centers that possess different oxidation state gives rise to a ground state with a spin value of $S = 10$, which is 21-fold degenerate ($M_S = 2S + 1$). However, due to the zero field splitting (ZFS), which fundamentally depends on the axial anisotropy of the ground state, the 21 sublevels are separated by the energy that follows the expression: $E(M_S) = M_S^2 \cdot D$ (where D is the axial anisotropy parameter, see Figure i.5).

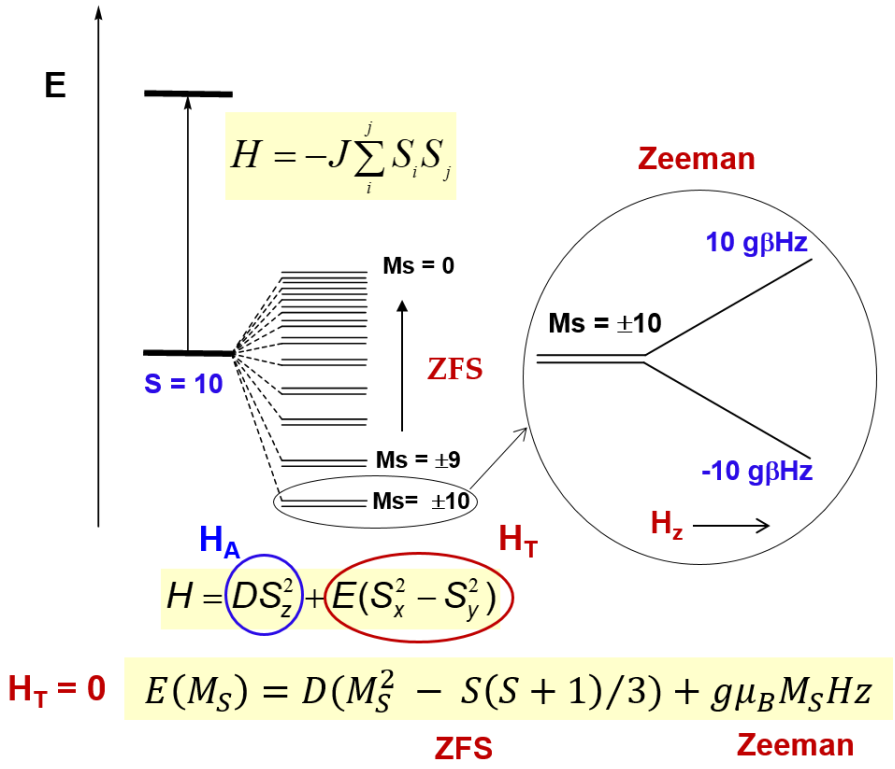

Figure i.5.- Qualitative energy diagram of Mn12-ac displaying the splitting of the ground spin state (*S* =10) by an axial zero-field splitting (ZFS) Hamiltonian (H_A), with a transversal Hamiltonian, H_T = 0. The splitting of the ground doublet M_S = ±10 by Zeeman interactions is highlighted in the figure.

When *D* < 0, the low lying energy levels are the ones with highest |M_S| value, in this case M_S = ±10. The magnetization associated to each of the M_S = ±10 sublevels has its particular orientation along the axial anisotropy axis (as it occurs for superparamagnetic nanoparticles, Figure i.6), thus M_S = +10 stands for spin up (or 1 in binary language), whereas M_S = -10 stands for spin down (or 0). However, when *D* > 0 the opposite and non-desired situation is given. The sublevels would be inversely oriented so that the ground state would be M_S = 0. In this particular situation, there is not any possibility for a bistable ground state and, hence, the system is not valid for information storage. Coming back to the first situation, in order to switch or have an inversion of the magnetization from M_S = +10 to M_S = -10 (or the other way round), the system needs to overcome an energy barrier, *U*, as it occurs for superparamagnetic materials (Figure i.6). The value of the barrier is the difference between the highest excited state and the ground state. For systems with integer and non-integer spin

values it is defined as $U = S^2|D|$ and $U = S^2 - 1/4|D|$, respectively (S being the spin value of the ground state).

Following with the example of compound **i1**, in the absence of an external magnetic field the $M_S = \pm 10$ sublevels own the same energy, are equally populated and thus the system does not present any magnetization (Figure i.6, left). When an external polarizing magnetic field of enough intensity is applied in a determined direction, one of the M_S sublevels is stabilized in comparison to the other. Therefore, the material suffers a magnetization, since the spin of all the molecules point out in the same direction (Figure i.6, center). When the polarizing magnetic field is removed, the ground state reaches again a doubly degenerate state and if $E_T > U$, the material will tend to achieve the equilibrium between the two orientations (positive and negative) losing magnetization. Nonetheless, if $E_T < U$, which is the situation that occurs when $T < T_B$ (T_B is the blocking temperature), the magnetization will be blocked and that is why SMMs are able to store information (Figure i.6, right). From this fact it is easy to conclude that the larger the energy barrier, the larger will be the temperature at which the magnetization can be retained. However, this is not always (or rather rarely) that way.

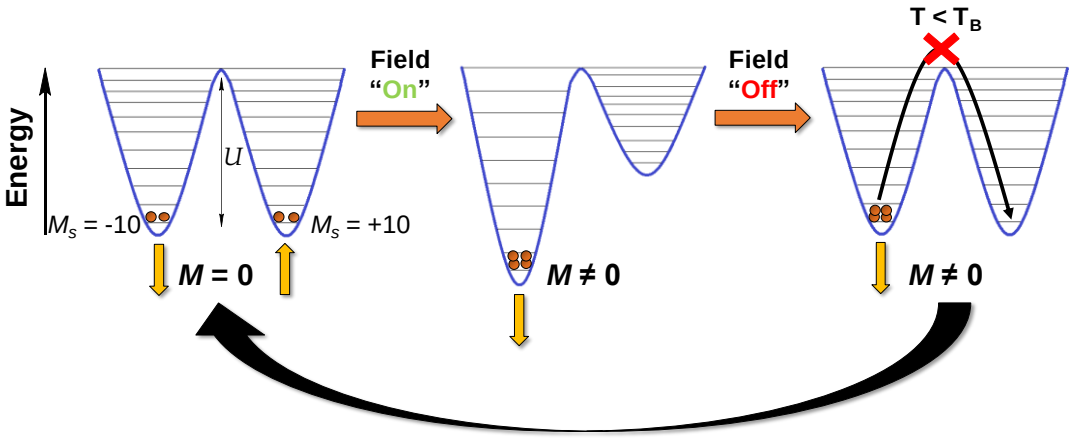

Figure i.6.- Magnetization projections (yellow arrows) in equilibrium in absence of external magnetic field (left), magnetization of the material due to the presence of an external field and subsequent stabilization of $M_S < 0$ sublevels (center) and blocking of the magnetization in absence of magnetic field for $T < T_B$ (right). Modified from reference [2]. Creative Commons license.

i.ii. Relaxation processes

If the reorientation or relaxation of the magnetization could occur only by overcoming the energy barrier through all the excited states, any material displaying a $U \sim 298$ K (~ 207 cm^{-1}) would be valid to implement it in an information storage device. Maintaining the temperature of the mentioned device below 298 K would assure not losing magnetization and thus, would have memory effect. Nevertheless, due to the quantic nature of these materials, the relaxation mechanisms are diverse, complex and extremely sensitive to numerous factors such as temperature, magnetic field, hyperfine (interactions between the electronic and nuclear spins) and intermolecular interactions.

The most common relaxation processes operating in SMMs are the ones that occur through spin-phonon coupling (Orbach, Raman and direct processes) or the ones that occur due to the quantic nature of the materials (Quantum Tunneling of the Magnetization, QTM, and Thermally Assisted QTM, TA-QTM) [3]. Orbach and Raman involve two phonons while a single one assists the direct process.

An ideal Orbach relaxation would be the one in which the system overcomes the entire barrier. The system would absorb phonons from the crystal network containing the exact energy ($(h/2\pi)\cdot\omega_1$) to jump from one of the ground sublevels ($M_S = \pm S$) to the highest excited sublevel ($M_S = 0$). From this excited state the system would relax to either of the ground $M_S = \pm S$ state emitting new phonons ($(h/2\pi)\cdot\omega_2$, Figure i.7, top left). Noteworthy, in the Figure the energies of the initial and final states are splitted by internal fields caused by dipolar or hyperfine interactions. Thus, the energy difference between the absorbed and emitted phonon corresponds to the energy difference between the $\pm M_S$ sublevels in the ground state. In any case, the Orbach process usually does not happen through the highest excited state and, instead, occurs through the first or second excited state (depending on the axiality of the system, Figure i.7, bottom right). The large phonon energy required for this process to occur is the main reason why it usually operates at highest temperatures.

The energy restrictions related to the Orbach process are not present for Raman, since this mechanism is driven by inelastic dispersion of phonons. The molecule absorbs a phonon $(h/2\pi)\cdot\omega_3$, reaches a virtual excited state and emits another phonon $(h/2\pi)\cdot\omega_4$ (Figure i.7, top right). Again, the energy difference between the two phonons corresponds to the energy difference between the $\pm M_S$ sublevels in the ground state. Meanwhile, the direct process is a single phonon magnetization relaxation process that

directly emits a phonon ($(h/2\pi)\cdot\omega_5$) corresponding to the energy difference of the $\pm M_S$ sublevels in the ground state (Figure i.7, bottom left).

All these mechanisms occurring due to spin-phonon interactions require of energy (thermal assistance), but for QTM is different. This process occurs between the $\pm M_S$ sublevels of the doubly degenerate ground state and it is often the primary pathway at low temperatures, where mainly the ground state is populated (Figure i.7, bottom right). However, the relaxation pathway could be a combination of processes, where the excited states are populated by absorbing phonons and then QTM might occur between M_S states of the same energy (but different sign) followed by relaxation to the ground sublevel. This combined mechanism is known as Thermally Assisted Quantum Tunneling of the Magnetization, TA-QTM (Figure i.7, bottom right). It is noteworthy that processes such as QTM and direct normally operate at low temperatures, Orbach at the highest temperatures and TA-QTM at intermediate ones. Raman, in contrast, could appear in the whole temperature range. Among all of them, QTM and TA-QTM are considered as through barrier shortcuts, since the system relax without overcoming it. Therefore, this causes a diminution on the value of the barrier U giving rise to an effective energy barrier, U_{eff}. This, at the same time, influences the value of the blocking temperature and the relaxation time.

The most common strategies in order to suppress the undesired QTM are: (i*)* diluting the samples by co-crystallizing the SMM with diamagnetic analogues (usually with Zn^{II} when working with transition metals and Y^{III} or La^{III} when using lanthanides) to avoid intermolecular interactions that enhance QTM, or (ii*)* applying an external magnetic field that breaks the degeneracy between $M_S = \pm S$ sublevels (or $M_J = \pm J$ usually when referring to lanthanides). Noteworthy, QTM is normally more noticeable for systems with an integer number of S than for non-integer ones (Kramers ions) due to cancellation principle of van Vleck [4]. It indicates that the phonons arising from the network could not induce QTM and direct relaxation processes in Kramers ions in the absence of a magnetic field. Unfortunately, hyperfine interactions, as well as transverse magnetic fields (created by intermolecular interactions) split the Kramers doublets giving rise to new magnetization relaxation channels for QTM and direct mechanisms. Hence, as it will be below discussed, when employing lanthanides, Dy^{III} is used more often than Tb^{III}, which are Kramers and non-Kramers ions, respectively. Moreover, compounds that are based on non-Kramers ions display an intrinsic tunneling gap in the absence of applied field that favors QTM. In summary, the transverse magnetic

fields and the intrinsic tunneling gaps determine the basic relaxation mechanism in metal complexes with SMM properties.

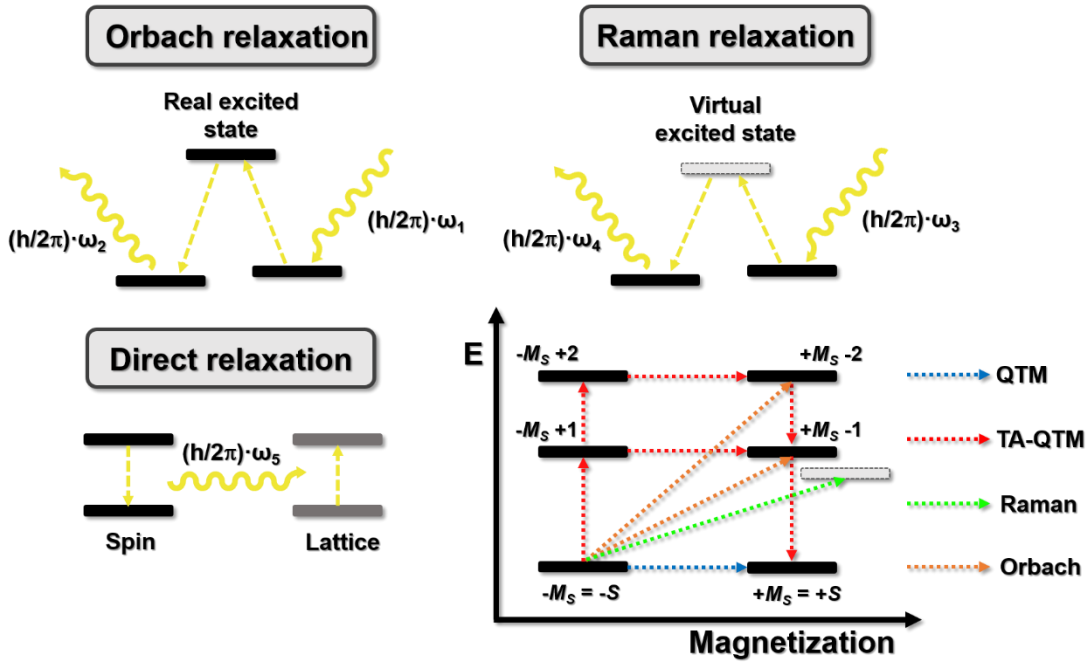

Figure i.7.- Schematic representation of Orbach (top left), Raman (top right) and Direct (bottom left) magnetization relaxation mechanisms. A combination of several relaxation mechanisms, including QTM and TA-QTM, for a part of double-well energy potential (bottom right).

i.iii. Detecting SMM behavior

Commonly, two techniques are used to determine whether a material displays slow relaxation of the magnetization or not. The first and the most used one involves carrying out in phase (χ_M') and out-of-phase (χ_M'') magnetic susceptibility measurements with an alternating magnetic field (*ac*). These kind of measurements are usually performed above 2 K until 300 K varying the frequency of the alternating current (Figure i.8a). In the example shown in this Figure i.8a, at 20 K and at a frequency of 60 Hz the material does not show any $\chi_M''(T)$ signal. This means that, at this temperature, the material has enough energy to follow the variations of the alternating magnetic field and, thus, the magnetic moment easily follows the change of direction of the magnetic field being in phase (χ_M') all the time. When diminishing the temperature and below 12 K, the out-of-phase signal starts to increase. At this

moment, the material possesses lower energy and the magnetic moment of some of the molecules are not able (due to their axial anisotropy and, therefore, to U_{eff}) to follow the flip of the alternating current. In other words, some of the spins are out-of-phase and, hence, an out-of-phase signal appears. When augmenting the frequency of the alternating current, for instance to 10,000 Hz, the reversal of the magnetic field becomes much faster and the signal is detected at higher temperature. In conclusion, detecting frequency dependent peaks in the $\chi_M''(T)$ plots means that the system shows slow relaxation of the magnetization and SMM behavior. Noteworthy, the non-zero going signals, or tails, below the peaks are indicative of QTM. This could also be detected in the $\chi_M''(\upsilon)$ plots when the position of the maxima, which is related to relaxation time, do not shift when increasing temperature (this is in agreement with the temperature independent behavior of this process).

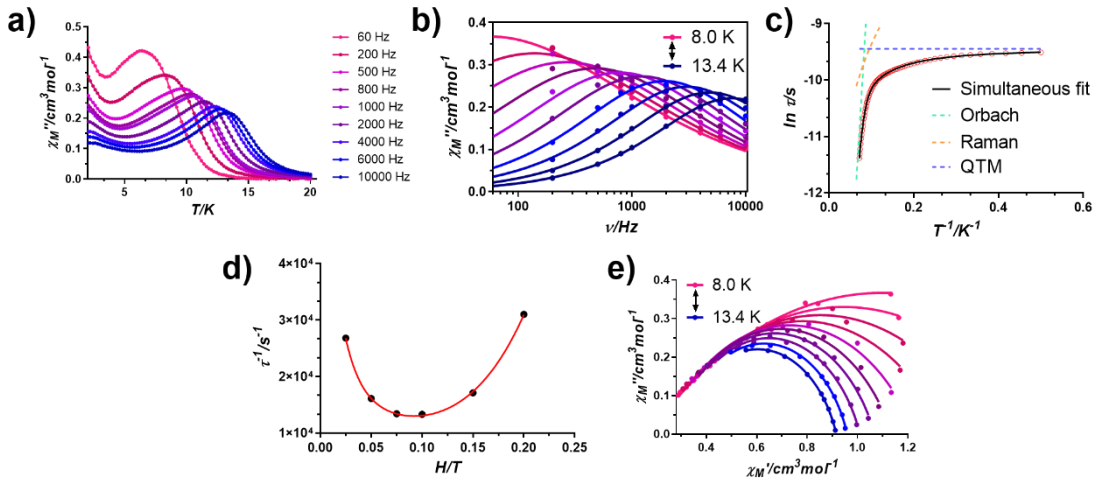

Figure i.8.- For a random Dy^{III} based SMM a) temperature dependence of the out-of-phase magnetic susceptibility (χ_M'') at different frequencies; b) frequency dependence of χ_M'' at different temperatures; c) fitting of the relaxation times to simultaneous Orbach, Raman and QTM processes; d) the inverse of the relaxation times obtained at different magnetic fields at a fixed temperature; e) Cole-Cole plot.

The fact that the magnetization of the molecule is not able to follow the flip of the magnetic field is related to magnetic anisotropy, since every spin projection has its own different energy. When the relaxation time and the period of the alternating current coincide, a maximum appears in both the $\chi_M''(T)$ plot at different frequencies and in the $\chi_M''(\upsilon)$ at different temperatures (Figures i.8a and i.8b). Among both types of graphs, $\chi_M''(\upsilon)$ plots can be fitted to the Debye model with the equation of Casimir-Du Pre [5].

The curves at different temperatures that show a maximum in the studied frequency range (8.0-13.4 K in Figure i.8b) are fitted to the mentioned model, which allows extracting relaxation times, τ, for each temperature. When the relaxation pathway is purely of Orbach type, the relaxation times follow the linear Arrhenius law (equation i.1) and the fitting directly provides the value of the effective energy barrier (U_{eff}). However, this rarely happens and the relaxation of the magnetization usually takes place through diverse mechanisms. In these cases, the equation needs to be completed with new fitting parameters referring to other pathways as exemplified in equation i.2 (τ_{QTM}^{-1} = QTM; BT^n = Raman and AT = direct). Figure i.8c displays a fitting of the relaxation times considering the simultaneous presence of Orbach, Raman and QTM processes. The dashed lines corroborate the previous statement, which indicates that these processes usually operate at low (QTM), intermediate (Raman) and high (Orbach) temperatures.

$$\tau^{-1} = \tau_0^{-1} exp(-U_{eff}/k_B T) \quad \text{(i.1)}$$

$$\tau^{-1} = \tau_{QTM}^{-1} + AT + BT^n + \tau_0^{-1} exp(-U_{eff}/k_B T) \quad \text{(i.2)}$$

Although relaxation times are commonly fitted to several mechanisms as in the example shown above, sometimes, when too many processes are included in the equation, this might be considered as an overparameterized situation. Including several mechanisms within the model could give us a better fit, but the obtained values for each mechanism will probably lose the physical meaning. In order to overcome this situation, additional experiments can be carried out. By studying the field-dependence of the relaxation times at a fixed temperature, a similar plot to what is shown in Figure i.8d can be obtained. As it can be observed, relaxation times become larger and the relaxation processes slower as the value of the external magnetic field is increased. This occurs up to 0.1 T, the value of the external magnetic field in which the relaxation process becomes the slowest, probably due to the quenching of QTM. Above it, relaxation times start to become faster again, which is probably originated by the enhancement of a direct process. Thus, this curve can be fitted to the following equation i.3, which accounts for the field-dependency of QTM and direct processes:

$$\tau^{-1} = AH^4T + B_1/(1+B_2H^2) + C \quad \text{(i.3)}$$

The first term corresponds to the direct process, which explains why at high fields becomes predominant (depends on H^4). The second term accounts for QTM and the constant term C accounts for field-independent relaxation processes. Hence, studying the field-dependence of the relaxation times could provide us additional information of the relaxation mechanisms. Once the parameters corresponding to direct and QTM mechanisms are obtained from this fit, they can be fixed in equation i.2 avoiding overparameterization. This will allow us to obtain more reliable parameters for each relaxation mechanism.

Even though the lack of linearity in the Arrhenius plot (Figure i.8c) already indicates that numerous processes are operating, this could be indeed proved by the Cole-Cole plots (Figure i.8e). In these plots, χ_M'' vs χ_M' curves display semicircles for each temperature and can be fitted to the generalized Debye model [6]. The fit provides α values between 1 and 0, where $\alpha = 0$ stands for a single relaxation mechanism, whereas for values nearer 1, the higher is the number of relaxation pathways operating simultaneously. Noteworthy, it is somehow common to find in the literature materials that display two sets of maxima in the $\chi_M''(T)$ plots instead of one (this, at the same time, provokes the presence of two sets of maxima in the $\chi_M''(\upsilon)$ plots and the sum of two semicircles in the Cole-Cole plots) [7–9]. This is associated to the presence of two thermally activated Orbach processes. The origin of this it is not always clear, but several reasons have been postulated and it can differ from one case to another. The presence of two crystallographycally independent compounds in the same structure could be a reason [10], although several compounds have been reported displaying two sets of maxima and with a single paramagnetic ion within the crystal structure [11]. In such cases, the presence of two thermally activated processes has been attributed to direct processes arising from the multi-level system (originated by the presence of an external magnetic field) or intermolecular interactions [12,13]. Anyway, in this special cases the data can be treated by using a sum of two modified Debye functions obtaining relaxation times for each single process. This can be easily done with the software CCFIT that Chilton *et al*. recently developed [14].

The second technique to determine whether a system behaves as SMM or not is the field dependence of the magnetization at different temperatures. When the compound is an SMM, the hysteresis cycles are often open (Figure i.9). Strictly speaking, this is the most relevant feature of an SMM to evaluate its potential. As it will be described during the following sections, even though a considerably large amount of SMMs have been described in the literature with high U_{eff}'s (> 500 K), most of them do

not display clear open hysteresis loops or these appear at very low temperatures, around 2 K (Figure i.9a). Ideally, the hysteresis loop displayed in Figure i.9b would be the desired one, which even at zero field would maintain all of the magnetization and at room temperature. Nowadays, open hysteresis loops have been reported at up to 80 K (see below) and this has been considered a huge step in the field, because this temperature is higher than the liquid nitrogen temperature.

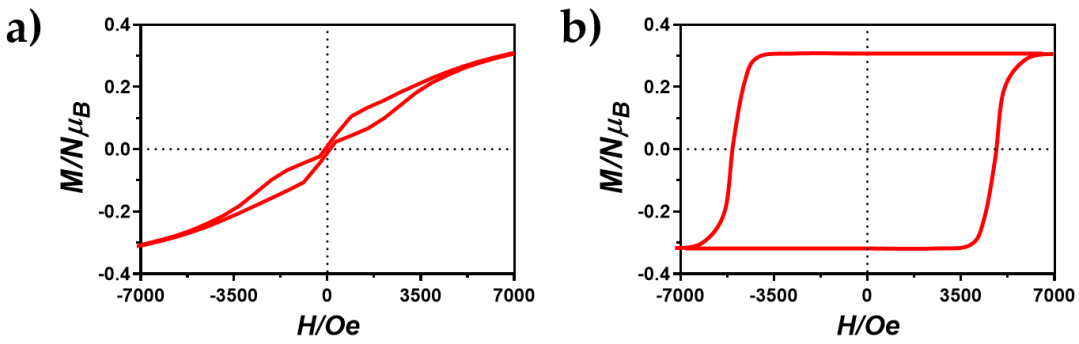

Figure i.9.- a) Common hysteresis cycle highly influenced by QTM at 2 K. b) Desired hysteresis loop at room temperature.

In contrast to *ac* measurements, this technique allows us to define a very important parameter characterizing SMMs, the blocking temperature (T_B). The most common definition of it stands for the highest temperature at which an open hysteresis cycle can be observed. However, this temperature is largely depending on the magnetic field sweeping rate and, therefore, when comparing different SMMs using blocking temperature, it is mandatory to be sure that the hysteresis loops were recorded under the same experimental conditions. Noteworthy, there exist some other criteria to determine the T_B: (i) temperature at which $\tau = 100$ s or (ii) temperature at which the FC (Field Cooled) and ZFC (Zero-Field Cooled) magnetic susceptibility curves differ.

ii. THE BEGINNING: THE AGE OF METAL CLUSTERS

The discovery of Mn12-ac was a milestone in materials science, specifically in the field of molecular magnetism. Indeed, if the temperature at which the SMMs based on transition metal clusters operate (typically below 5 K) was raised over the liquid nitrogen temperature, their application in data storage devices would be really

promising. To try to overcome the handicap of the very low working temperature of these systems, it should be kept in mind that the effective energy barrier that prevents the reorientation of the magnetization depends simultaneously on the total value of the spin and anisotropy:

$$U = S^2 \cdot |D|;\ S = integer \quad \text{(i.4)}$$

$$U = (S^2 - ¼) \cdot |D|;\ S = non\text{-}integer \quad \text{(i.5)}$$

Regarding the quadratic spin dependence of the energy barrier, the most logic and simple way to enhance the energy barrier, and therefore the blocking temperature, would be that of increasing the spin of the ground state. For it, ferromagnetically coupled high nuclearity systems were synthesized. Among them, those containing the Mn^{III} ion were appropriate candidates for exhibiting SMM behavior because twofold: (i) in the high spin configuration possesses up to 4 unpaired electrons, which is positive in terms of enhancing the total value of *S* and (ii) in an octahedral crystal field (the most common for this metal ion), the Mn^{III} is subjected to Jahn-Teller distortion, leading to zero-field splitting (ZFS) of the ground state and to axial anisotropy, characterized by the *D* parameter. In addition, numerous theoretical and experimental studies were carried out during these years with the aim of finding out new magneto-structural correlations that enable chemists to deliberately design and synthesize novel transition metal clusters displaying ferromagnetic interactions between metal ions [15–20]. It is worth mentioning that in some cases azide was used as auxiliary ligand because in its end-on bridging mode could lead to ferromagnetic interactions [21,22]. Moreover, apart from the conventional synthetic routes (reactions under atmospheric pressure and at temperatures that were limited to the solvent boiling point), some research groups started to exploit solvothermal techniques, which afforded polynuclear complexes [23]. Synthetic strategies based on all this previous information allowed the successful preparation of a large number of high nuclearity systems with high spin ground state containing not only Mn^{III} ions, but also other transition metal ions. Examples of these type of polynuclear complexes are Mn_9Mo_6 (**i2**), Fe_{19} (**i3**), Mn_{19} (**i4**) and Mn_{25} (**i5**) [24–27]. It is worth highlighting that **i4**, which really is a $Mn^{II}_7Mn^{III}_{12}$ complex, exhibited the record spin value of *S* = 83/2 (Figure i.10). In spite of the large ground state *S* value found for all these coordination compounds, they exhibited unexpectedly poorer magnetic properties than Mn12-ac in terms of U_{eff} and T_B. Specifically, compound **i4** presents a negligible anisotropy and a U_{eff} = 5.8 K (4 cm^{-1}).

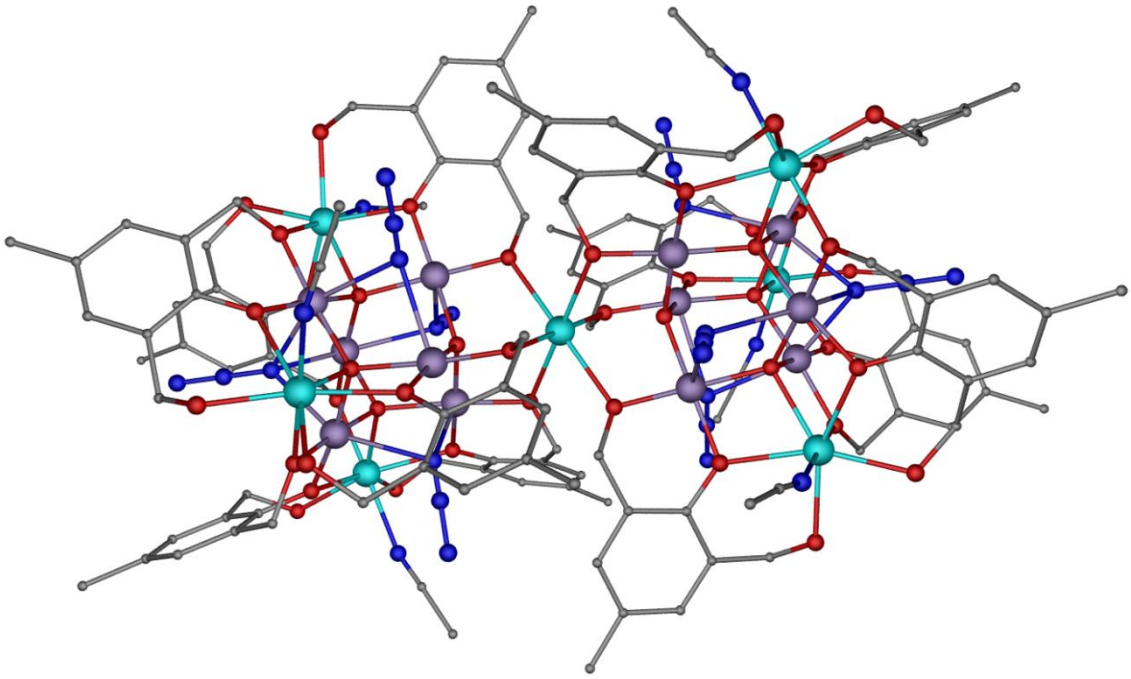

Figure i.10.- Perspective view of compound **i4** (Mn_{19}). Color code: Mn^{II}, Mn^{III}, carbon, nitrogen and oxygen in light blue, purple, grey, dark blue and red, respectively. Hydrogen atoms have been omitted for the sake of clarity. Generated from the crystal structure in reference [26].

Over the course of the time, the problem was more and more evident. Introducing a great number of paramagnetic ions within the system inherently reduced drastically the value of anisotropy. Several studies have proved that the overall anisotropy value is sensitive to the orientation of the Jahn-Teller axis of each single metallic center, diminishing the total anisotropy value when the Jahn-Teller axes are not collinear. Therefore, when including a huge number of metal ions into the cluster it is normal to have a smaller final *D* value [28]. Indeed, some mathematical expressions have been proposed to calculate the total anisotropy of a cluster considering *D* and the angle of the Jahn-Teller axis respect to the total anisotropy axis (α) for each ion [29]. In addition, theoretical studies carried out by Neese and coauthors demonstrated that $D \propto 1/S^2$ and, therefore, $U_{eff} = DS^2$ is, in a good approximation, independent of *S* [30].

All these results lately propitiate a new era for SMMs, in which the coordination compounds with lower nuclearity, but higher magnetic anisotropy became more important.

In order to get very high values of magnetic anisotropy, mainly two options exist: (i) transition metal mononuclear coordination compounds with very high single-ion magnetic anisotropy and (ii) coordination compounds containing lanthanide ions, which have exceptionally high single-ion anisotropy (with the exception of the Gd^{III} ion that is isotropic). In the former case, low-coordination complexes lead to weak crystal fields, which favor the presence of orbital angular momentum, spin-orbit coupling and then to high magnetic anisotropy. In the latter case, the inherent large magnetic anisotropy is the result of the combined actions of strong spin-orbit coupling and crystal effects. In addition to this, the geometry plays an essential role in influencing the SMM behavior.

iii. TRANSITION-METAL BASED LOW-COORDINATED SINGLE ION MAGNETS (SIMs)

The idea of substantially enhancing the total *S* value of the compounds was then somehow set aside and the strategy of increasing the anisotropy value became more prominent. In contrast to the valence electrons in lanthanides, where 4f orbitals are spatially 'buried' inside the atom and are shielded from the ligand field (*vide infra*), in first row transition metals the 3d orbitals, even though they are very contracted, are much more exposed to the ligand field. Therefore, the ligand-field splitting can in some cases, depending on the metal ion and symmetry, readily quench the orbital angular momentum, consequently quenching the first order spin-orbit coupling (SOC) [31]. This statement means that the SOC causing magnetic anisotropy often arises from second order SOC derived from the mixing between the excited states with the ground state through the spin-orbit operator [32,33]. However, the first order spin-orbit coupling could be preserved by a rational design of the ligand field, which involves low coordination numbers. Although numerous examples of transition metal complexes with low-coordination number and SIM behavior have been reported to date [34–38], we are going to present here only those having the best SIM properties, which possess linear geometry and contain Kramers metal ions.

Based on these considerations and after the intriguing results observed for linear Fe^{II} systems with $S = 2$ displaying field-induced SMM behavior [39–43], Long and co-workers decided to explore the possibility of achieving large energy barriers for the reversal of the magnetization in the absence of a magnetic field. So as to do that, they smartly took advantage of the Kramers theorem studying a linear Fe^{I} based coordination compound with $S = 3/2$ shown in Figure i.11 and with the general formula

[K(crypt-222)][Fe(C(SiMe$_3$)$_3$)$_2$] (**i6**) [44]. Based on the *ab initio* calculations, they demonstrated that the combination of a low coordination number together with the low oxidation state gives rise to a remarkably weak ligand field unable to quench the orbital angular momentum, thus enhancing the total anisotropy of the compound. This leads to a splitting of the ^{4}E ground state into four Kramers doublets (KD) better determined by M_J quantum numbers with M_J = ±7/2, ±5/2, ±3/2 and ±1/2. Besides, the energy difference calculated between the ground and first excited state was large, indicative of potential SMM behavior.

Indeed, *ac* measurements carried out at zero *dc* field showed SMM behavior for this compound with an experimentally calculated U_{eff} of 325 K (226(4) cm^{-1}). This value of the effective energy barrier is close to the calculated energy gap between the ground (M_J = ±7/2) and first excited state (M_J = ±5/2), indicating that the relaxation most likely occurs through this first excited state. Even though the relaxation times follow the Arrhenius law in the 20-29 K temperature range, giving rise to the mentioned U_{eff}, the τ values notably deviate from linearity below 20 K indicating that at the lower temperatures a tunneling relaxation that shortcuts the barrier is operative.

As mentioned in the general introduction, another way of determining the blocking temperature (T_B) is performing FC/ZFC measurements. This is because when magnetic blocking is present in a compound, χ_M *vs* T curves must be different when the measurement is accomplished in the presence or absence of a magnetic field. In fact, for compound **i6** the divergence of both curves was observed at 4.5 K. Since this suggests that hysteresis loops may be observable, they were measured in the 1.8-6.5 K temperature range. The loops showed butterfly shaped or waist-restricted features due to tunneling effect already observed in the *ac* measurements. With the aim of knowing the origin of QTM, they carried out the same magnetic measurements for frozen solutions of **i6**, since it is well known that dipolar intermolecular interactions could provoke transverse fields inducing QTM. The data, however, was overall comparable to the one collected for microcrystalline material confirming the molecular origin of such tunneling shortcut. Thus, they attributed this effect to geometric distortions that the C-Fe-C bond could suffer in both solution and solid state (of course, less in the latter) enhancing transverse components that facilitate the shortcut and to vibronic Renner-Teller activity [43].

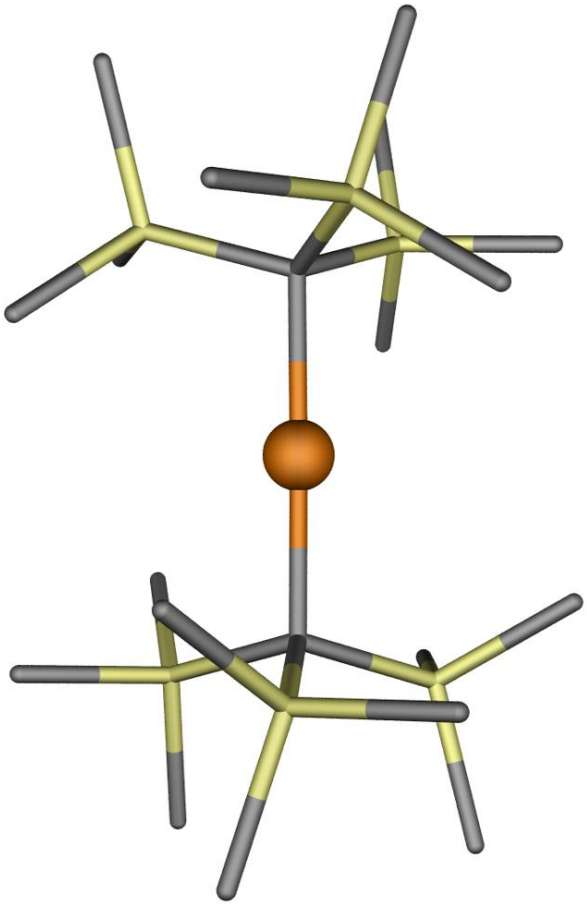

Figure i.11.- Perspective view of the anionic structure of compound **i6**. Color code: Fe^{I}, carbon and silicon in orange, yellow and grey, respectively. Hydrogen atoms have been omitted for the sake of clarity. Generated from the crystal structure in reference [44].

Apart from the showed example, other researchers also reported on two-coordinated homoleptic compounds based on iron, cobalt or nickel, though not all of them displayed such a good performance due probably to stronger QTM [35,38,45–47]. As abovementioned, the vibronic couplings could lead to fast tunneling and this is a clear consequence of the dynamic distortion of the long metal-ligand bonds present in the previous cited examples. To overcome these problems, Atanasov, Neese and co-workers provided a theoretical study analyzing the role of chemical bonding, vibronic coupling and magnetic anisotropy in linear Fe^{II} complexes showing SMM behavior [43]. As a general conclusion, they suggested that metal-ligand bonds with an increased

covalency may be the objective towards reducing vibronic coupling and, at the same time, increase magnetic anisotropy.

In the pursuit of obtaining coordination compounds with enhanced covalency, Gao *et al.*, reported on the synthesis and magnetic properties of three Co^{II} based compounds with the general formula [(NHC)CoNDmp] where Dmp = 2,6-dimesitylphenyl and NHC are different N-heterocyclic carbene ligands as depicted in Figure i.12 (**i7- i9**) [48]. Note that the synthesis, structure and reactivity of compound **i7** was previously reported [49]. These two-coordinate cobalt imido compounds showed an almost linear arrangement of the ligands with very short $Co\text{-}N_{imido}$ bond distances (1.691(6) Å) in agreement with a formal bond order of two.

The first clear evidence of the retention of first order SOC was already identified from *dc* data (Figure i.12c, left). The very large $\chi_M T$ values (3.86, 3.72 and 3.74 $emu \cdot K \cdot mol^{-1}$ for **i7**, **i8** and **i9**, respectively) at room temperature confirmed the unquenched orbital angular momentum provoked by the weak ligand field. Moreover, for compound **i9** an abrupt drop was identified at 3.5 K indicative of a blocking of the magnetic moments, which was then further verified by measuring hysteresis loops. *ac* measurements showed that the three complexes were single molecule magnets under a zero applied *dc* field. Noteworthy, the maxima within the $\chi_M''(\upsilon)$ plots for **i9** were found at up to 50 K at the frequency limit of 10,000 Hz (Figure i.12c, right), which gave rise to an effective energy barrier of 594.2 K (413 cm^{-1}), the highest reported until that moment for a 3d based SMM.

With the purpose of shedding some light to explain this extraordinary behavior and make magneto-structural correlations, they performed exhaustive theoretical studies. As expected from the short Co=N bond distance, the simulated variations in terms of this bond length provoked remarkable consequences. In fact, the energy gaps between the ground and excited states, as well as the axiality of the system were dramatically modulated by simply slightly lengthening or shortening the bond, which confirmed its role in determining the total magnetic anisotropy of the complexes. Finally, even though they did not exclude the possibility of considering the simple Co^{II} based mononuclear SMM model, they proposed that the large magnetic anisotropy of the systems arises from the $[CoN]^+$ core featuring a $M_J = \pm 7/2$ ground Kramers doublet with a large Co-N exchange coupling. This model could somehow explain the significant diminution of undesired QTM.

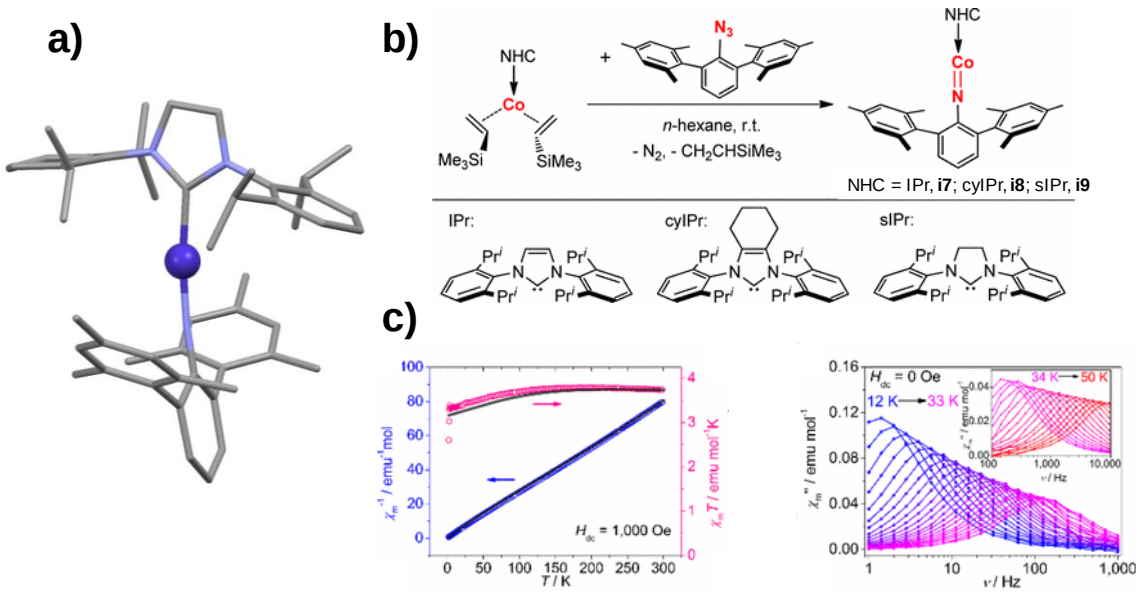

Figure i.12.- a) Perspective view of compound **i7**. Color code: Co^{II}, carbon and nitrogen in purple, grey and blue, respectively. Hydrogen atoms have been omitted for the sake of clarity. b) Synthetic route to the two-coordinate cobalt imido complexes and the designations for the NHC ligands. c) Temperature dependence of $\chi_M T$ (pink) and χ_M^{-1} (blue) values in the 2-300 K temperature range (left) and frequency dependence of the χ_M'' under zero applied *dc* field for **i9**. The perspective view of **i7** has been generated from the crystal structure in reference [49]. The scheme of the synthetic route and plots of the magnetic properties have been adapted with permission from [48]. Copyright 2017 American Chemical Society.

Finally, Long *et al*. recently reported compound **i10** (Figure i.13) with general formula $[Co(C(SiMe_2ONaph)_3)_2]$ being Naph = naphthyl [50]. They were motivated by the fact that calculations on the hypothetical $[Co(C(SiMe_3)_3)_2]$ predicted a ground state with L = 3 arising from a non-Aufbau 3d-orbital filling [51]. This would somehow mimic what is seen for lanthanides obtaining maximal orbital angular momentum and, thus, very large magnetic anisotropy. However, obtaining the targeted compound was expected to be arduous from the very beginning, since two-coordinate transition metal complexes involving alkyl ligands were only found as $[M(C(SiMe_3)_3)_2]^{0/1-}$, being M = Fe^{II} [52], Fe^{I} [53], Mn^{II} [54] and Mn^{I} [55]. For Co^{II}, instead, other systems such as the above cited ones, as well as $[OCoO]^-$ anions inserted into an apatite's channel [56] and single Co^{II} atoms on MgO surfaces have been described [57].

Prior to obtain the desired linear two-coordinate Co^{II} compound, they had a lot of synthetic challenges such as the strongly reducing nature of the carbanions, bent C-Co-C angles when trying with some other substituents within the ligands and formation of undesired dinuclear systems, among others. Lastly, however, by including –ONaph groups within the structure they crystallized the desired linear compound. Single crystal structure analysis suggested that –C-H···π interactions may be of relevance in the stabilization of the compound.

As expected from calculations that were previously made, theoretical analysis that was carried out for **i10** revealed that the $^4\Phi$ ground state follows a non-Aufbau filling of the d orbitals with a resulting $(d_{x^2-y^2}, d_{xy})^3(d_{xz}, d_{yz})^3(d_{z^2})^1$. The ligand field was so small that a high spin state with a maximized angular momentum was obtained. As a result, a 3d ion based SIM with a record U_{eff} value of 647.5 K (450 cm^{-1}) was obtained, the largest reported so far for a transition metal based SMM. The value of the effective energy barrier represents the energy separation between the ground M_J = ±9/2 and the first excited M_J = ±7/2 states, which was deducted from theoretical calculations, far-infrared (FIR) spectroscopy and *ac* measurements.

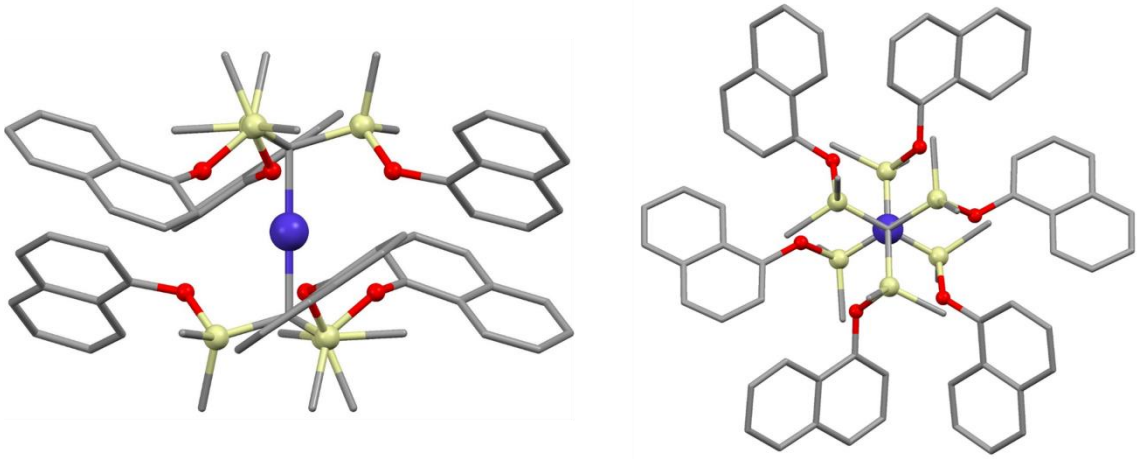

Figure i.13.- Perspective view of compound **i10** (left). Molecular structure of **i10** viewed along the *c* axis (right). Color code: Co^{II}, carbon, oxygen and silicon in purple, grey, red and pale yellow, respectively. Generated from the crystal structure in reference [50].

iv. THE AGE OF LANTHANIDES

The first examples of rare-earth or lanthanide based SMMs were reported by Ishikawa and coworkers in the year 2003 [58]. These were sandwich type coordination

compounds previously described by Koike *et al*., in which two phthalocyanine ligands surround the Ln^{III} ions forming double-deckers (**i11**, Figure i.14) [59]. Within the lanthanide series, the Tb^{III} (**i12**) and Dy^{III} (**i13**) counterparts displayed effective energy barriers of 330.9 and 40.3 K (or 230 and 28 cm^{-1}), respectively. This fact confirmed that a single metal center could be enough for the design of high U_{eff} owning SMM behavior.

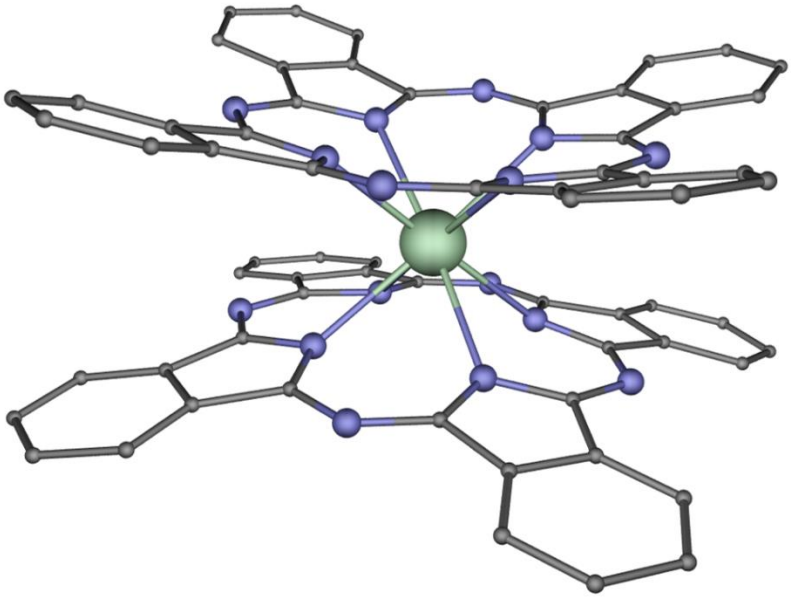

Figure i.14.- Perspective view of the cationic sandwich type double-decker described by Koike *et al*. Color code: Nd^{III}, carbon and nitrogen in green, blue and grey, respectively. Hydrogen atoms have been omitted for the sake of clarity. Reproduced from reference [2]. Creative Commons license.

In contrast to transition metals, the advantage for lanthanides is that, as indicated above, the 4f orbitals are spatially 'buried' inside the atom and are shielded from the ligand field by the fully occupied $5s^2$ and $5p^6$ orbitals. This implies an almost purely electrostatic interaction between the donor atoms of the ligands and the lanthanide ion and, consequently, the spin-orbit coupling (main cause of the magnetic anisotropy) cannot be quenched so easily as for transition metals. This means that, in principle, the anisotropy value will usually be higher for lanthanides than for transition metal complexes, so that, in theory, one could expect the achievement of SMMs with improved properties. However, as further discussed below, they also exhibit some disadvantages that are not so common for transition metals.

Due to the strong spin-orbit coupling, for most of the lanthanide ions, the spin is not the unique source of the angular momentum. Therefore, when describing their magnetic properties, it is necessary to consider spin-orbit coupling terms (characterized by the quantum number *J*) and their splitting by the ligand field, leading to the sublevels that are described by M_J instead of M_S quantum numbers. Even though the meaning differs from one to another, the interpretation is still similar. Indeed, when designing SMMs, the ground state should possess a well-defined ground state with the highest possible absolute value of M_J, which could be accomplished when the anisotropy of the ground state is axial. Moreover, the energetic separation between M_J and $M_J \pm 1$ states needs to be as high as possible to obtain high U_{eff} values and this implies a rational design of the ligand field.

For the mentioned rational design, Rinehart and Long proposed some very useful guidelines that were conceptually easy to understand [60]. Within the lanthanide series, each of them contains its own characteristics. For instance, although most of them have considerable spin-orbit coupling, the Gd^{III} ion is completely isotropic. Hence, in spite of the fact that it possesses the greatest number of unpaired electron spins possible for a lanthanide ion (which, in principle, would favor a high *S* value in the ground state), its potential for the design of SMMs is null. Among the ions with anisotropic electron density, two main groups may be distinguished (Figure i.15): oblate type ions (Tb^{III} and Dy^{III}, among others) and prolate type ones (Er^{III} and Yb^{III}, among others).

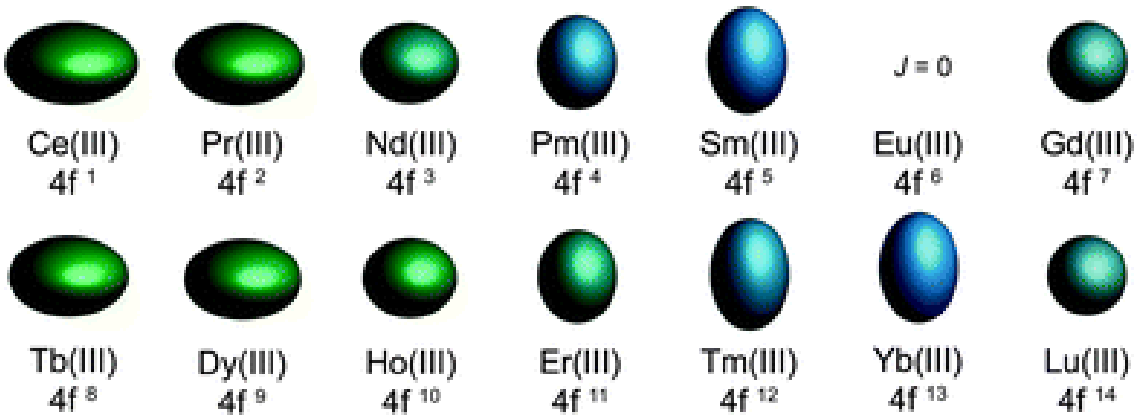

Figure i.15.- 4f shell electron distribution shapes for trivalent Ln^{III} ions. Reprinted with permission from [60]. Copyright 2011 The Royal Society of Chemistry.

The mere fact of knowing how the shape of the electron density looks like for each rare-earth ion enables a more effective rational design of the specific ligand field with the purpose of achieving large axial magnetic anisotropy (the ground state has the largest M_J value). Thus, for oblate type of ions, the ligand donor atoms with greatest electron density should coordinate at axial positions (Figure i.16, top). This disposition will cause less electronic repulsion between the oblate electronic density of the lanthanide ion and the ligands donor atoms with greatest electron density, stabilizing the ground state with higher M_J values). In this situation, the anisotropy axis, which is perpendicular to the oblate shaped electron density, points to the donor atoms with greater electron density and shorter Ln–X (X being the donor atom) distances. It is worth noting that if no donor ligands are coordinated in the equatorial positions, the electron density will expand along the plane enhancing the axial anisotropy. In contrast, if the donor atoms coordinate within the equatorial plane, the electron distribution will become more isotropic losing the potential to behave as SMM (Figure i.16, bottom).

Regarding the prolate type ions, the ligand donor atoms with greatest electron density should coordinate at equatorial positions for achieving axial anisotropy. In this disposition, the electronic repulsion between the prolate electronic density of the lanthanide ion and the ligands donor atoms with greatest electron density is smaller and the anisotropic axis, which is parallel to the prolate electron density, lies perpendicular to the plane where are located the ligands donor atoms with greatest electron density. If there are no donor ligands in axial positions, the electron density of the lanthanide metal ion can be expanded along the axial direction leading to a larger axial anisotropy. Conversely, the coordination in axial positions induced a more isotropic electron distribution, so that the anisotropy decreases (Figure i.16, bottom).

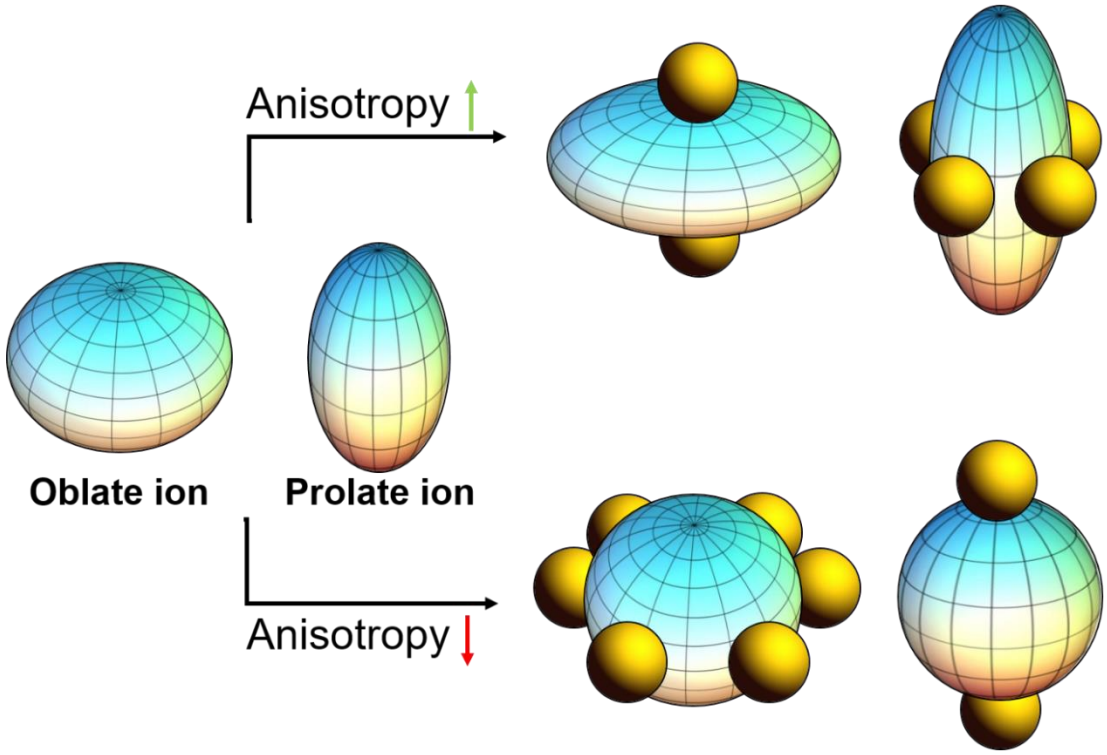

Figure i.16.- How to enhance or quench the anisotropy for oblate and prolate type of ions. Modified figure under Creative Commons license.

Even though the approach looks simple, the great ionic radii of lanthanides becomes a huge obstacle. Indeed, when the ligands are not specifically designed to obtain a certain geometry, it is very common to obtain high coordination numbers (> 8). However, here are shown two great impact studies that prove that the guidelines proposed by Rinehart and Long show the way towards the enhancement of the magnetic anisotropy.

In 2013, the group of Murugesu studied the magnetic properties of six very similar Dy^{III} based dinuclear systems, whose main difference resides in the electron donating character of the ancillary bidentate ligands (in the present work only three of them are described) [61]. In order to do that, they were based on their previously studied dinuclear compound **i14** (Figure i.17, left) [62,63]. Maintaining the core structure, they were able to substitute the nitrates in the equatorial plane (a phenoxido group provides axiality to the system) by other auxiliary ligands such as acetylacetonate, acac, (**i15**, Figure i.17, top) or hexafluoroacetylacetonate, hfac (**i16**, Figure i.17, bottom), which are more and less electron-donating groups than nitrate, respectively.

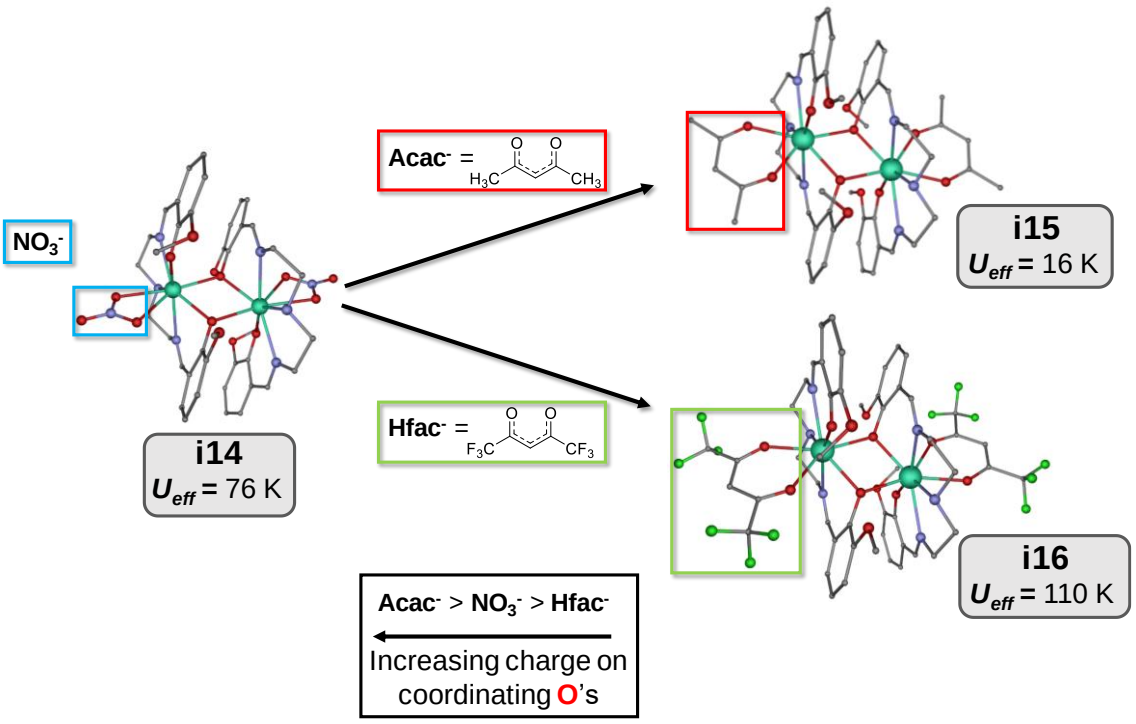

Figure i.17.- Compound of reference **i14** (left), compound with acac chelates **i15** (top right) and compound with hfac chelates **i16** (bottom right). Black inset: order of the chelates depending on the charge they provide to the lanthanide ion; based on *ab initio* calculations. Color code: Dy^{III}, carbon, nitrogen, oxygen and fluorine in turquoise, grey, blue, red and green, respectively. Hydrogen atoms have been omitted for the sake of clarity. Generated from the crystal structures in references [61,62].

For compound **i15**, the switching from nitrates to acetylacetonates provokes a shortening of the Dy-O_{chel} distances due to the greater charge of the donor atoms. Thus, the ligand field in the equatorial plane becomes more prominent. This was proven by measuring the *ac* dynamic magnetic properties and fitting the relaxation times to the Arrhenius law. The fit provided U_{eff} values of 76 and 16 K (or 52.8 and 11.1 cm^{-1}) for **i14** and **i15**, respectively. When replacing the acac ligands by the hfac counterparts to afford **i16**, the oxygen atoms become less donating, even less than the nitrate oxygen atoms (this was proven by *ab initio* calculations). Thereby, Dy-O_{chel} bond distances become larger, the electron density within the equatorial plane diminishes and the U_{eff} value increases up to 110 K (76.4 cm^{-1}).

Among the SMMs containing prolate lanthanide ions, those based on Er^{III} are the most common ones. In a research published by the group of Tang [64], they compared

two systems with the general formula $Ln[N(SiMe_3)_2]_3$, where Ln^{III} = Dy^{III} (**i17**) and Er^{III} (**i18**). Because of the opposite electron cloud distribution for these two lanthanide ions, the crystal field causes reversed effects. As it is shown in Figure i.18, the order of the Kramers doublets (KD) is exactly the opposite for both compounds. The ground state KD is M_J = ±1/2 for **i17**, whereas for **i18** M_J = ±15/2 KD is the most stable one. These results agree with the model proposed by Rinehart and Long. A strong equatorial ligand field diminishes the electronic repulsions for prolate ions such as Er^{III}, thus stabilizing the KD with the highest M_J value as ground state (axially anisotropic ground state). As aforementioned, one of the most important prerequisites to observe SMM behavior is to stabilize the M_J states with highest absolute values as ground KDs (axially anisotropic ground KD). Hence, it looks reasonable that compound **i18** displays an energy barrier for the reversal of the magnetization of 122 K (84.8 cm^{-1}), while compound **i17** does not show slow relaxation of the magnetization.

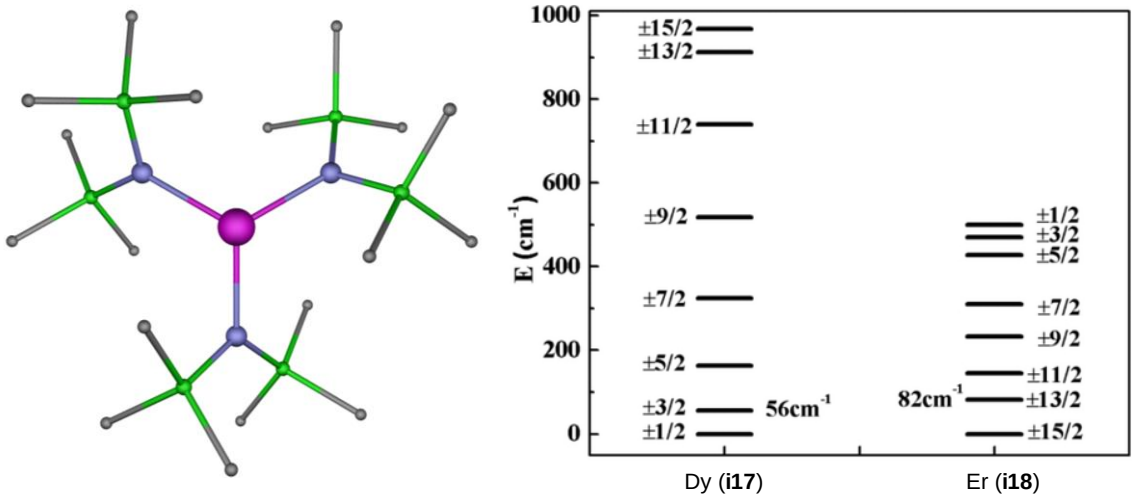

Figure i.18.- Structure of **i18** (left) and energy diagram of the eight Kramers doublets for **i17** and **i18** (right). Color code: Er^{III}, carbon, nitrogen and silicon in pink, grey, blue and green, respectively. Hydrogen atoms have been omitted for the sake of clarity. The perspective view of **i18** has been generated from the crystal structure downloaded from CCDC (YIBRUW). The energy diagram has been adapted with permission from [64]. Copyright 2014 American Chemical Society.

Based on the described oblate-prolate model, our research group made important contributions to the field of SMMs. For instance, the trinuclear $Zn^{II}Dy^{III}Zn^{II}$ system, **i19**, was prepared using a compartmental Mannich base ligand containing bridging phenoxido groups [65]. This kind of assembly was proven to be effective in order to

stabilize a ground state with highest M_J state (axial ground state), because the four phenoxido oxygen atoms (those having the highest electron density) are placed by couples in opposite sides of the Dy^{III} ion (Figure i.19). Besides, the incorporation of diamagnetic Zn^{II} ions within the structure may have several benefits. On the one hand, in contrast to diamagnetic Zn^{II}, paramagnetic metal centers are known to create transversal magnetic fields that enable fast relaxation of the magnetization through QTM [66]. On the other hand, Rajaraman *et al.* reported that, for phenoxido containing systems, the inclusion of diamagnetic ions can provoke greater charge polarization for the bridging phenoxido groups, thus creating a bigger energy splitting between the ground and excited states [67].

Compound **i19** exhibits a DyO_8 coordination environment that fits best to a square antiprism geometry (calculated by the SHAPE software [68]). Even though the presence of QTM is noticeable in the $\chi_M''(T)$ plots (Figure i.19c), it displays zero field SMM behavior. This is in fact due to an almost pure $M_J = \pm 15/2$ ground state with a marked axiality and with negligible transverse components calculated from CASSCF + RASSI methods. As expected for an oblate type of ion with well-defined axiality, the magnetic moment points to the stronger electron donating phenoxido oxygen atoms, so that it is oriented roughly collinear with the two shortest Dy-O distances and perpendicular to the oblate electron density.

For further confirming the appropriateness of the ligand field in **i19**, electrostatic potential maps caused by the ligands and projected into the Dy^{III} ion were calculated. It was proven that the beta electron density of the oblate ground state was accommodated in the region where the electronic repulsion was less important, whereas in the perpendicular direction the magnetic moment points to the more electron density donating phenoxido oxygen atoms. Finally, as a proof of concept, the isostructural analogue of Er^{III} (**i20**) was also studied. As expected, the ligand field was shown to be suitable for stabilizing high magnetic M_J states for oblate ions, but not for prolate ones. The latter ions require strong ligand fields in the equatorial plane. Thus, compound **i20** exhibited a field induced SMM with a very modest energy barrier for the reorientation of the magnetization.

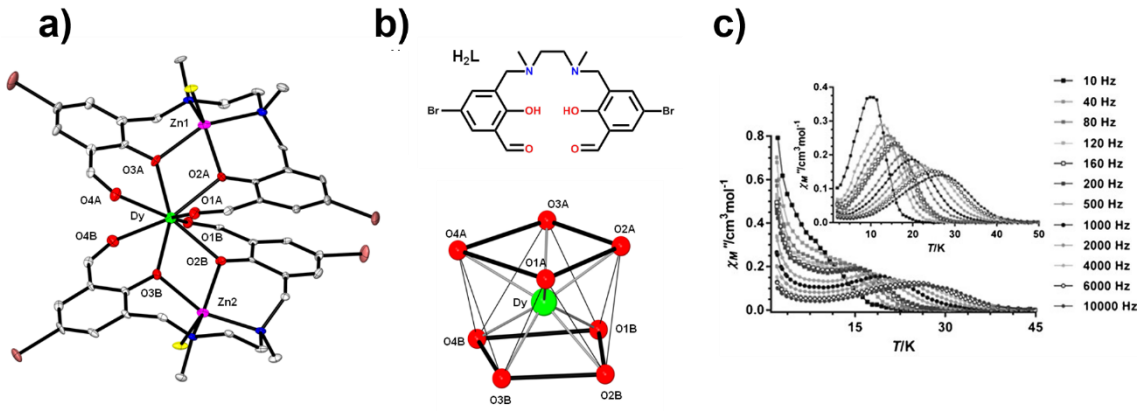

Figure i.19.- a) Perspective view of the cationic structure of **i19**. b) The Mannich base ligand used in this research (top) and DyO_8 coordination environment of the complex (bottom). c) Temperature dependence of χ_M'' under zero *dc* applied field and at H_{dc} = 1000 Oe (inset) for **i19**. Color code: Dy^{III}, Zn^{II}, carbon, oxygen, nitrogen, bromide and chloride in green, pink, grey, red, blue, brown and yellow, respectively. Hydrogen atoms and counterions have been omitted for the sake of clarity. Generated from the crystal structure in reference [65]. Magnetic data reprinted with permission from [65]. Copyright 2014 John Wiley and Sons.

As discussed, great efforts were done in synthesizing lanthanide based SMMs and understanding their magnetic properties. Indeed, the rational strategy following the oblate-prolate model allowed the researches to make magneto-structural correlations and be able to modify the ligand fields on demand. Some clear examples of it are the pentagonal-bipyramidal (PB) compounds. Overall, these systems contain strong oxygen donor atoms in the apical positions, for instance: phenoxido groups, phosphine oxides or siloxides. In contrast, the equatorial pentagonal positions are usually occupied by neutral atoms arising from solvents (tetrahydrofuran or pyridine, for example) or weakly coordinating macrocyclic and non-macrocyclic ligands. Within this family, some of the most cutting edge examples are $[Dy(O^tBu)_2(py)_5][BPh]_4$ (**i21**, OtBu = tert-butoxide, py = pyridine) [69] [Dy(bbpen)Br] (**i22**, H_2bbpen = N,N′-bis(2-hydroxybenzyl)-N,N′-bis(2-methylpyridyl)ethylenediamine) [70] and $[Dy(Cy_3PO)_2(H_2O)_5]Br_3\cdot2(Cy_3PO)\cdot2H_2O\cdot2EtOH$ (**i23**, Cy_3PO = tricyclohexyl phosphine oxide) [71]. In all these systems, the axiality is provided by strong oxygen donor atoms in the apical positions while the equatorial planes are occupied by less electron donating atoms with subsequent longer bond distances. The effective energy barriers were experimentally estimated to be of 1815 K, 1025 K and 543 K for **i21**, **i22** and **i23**,

respectively. Moreover, even though usually Orbach relaxation pathways occur through the first excited state (which could be better described as TA-QTM), the proper ligand field in those compounds provokes relaxation pathways involving higher excited states achieving high effective energy barriers. Lastly, it is worth mentioning the importance of designing and synthesizing compounds with improved properties, but being air stable. From the last three cited compounds, the one with the highest effective energy barrier (**i21**) is air sensitive, a fact that complicates its implementation in future devices. In this sense, some other compounds with high effective energy barriers have been reported, either with PB geometry or by using very electron-donating groups such as F^- to provide an axial ground state very well isolated from excited states [72–75].

One could think about these latter systems as ideal candidates for implementing them in information storage devices. However, the vast majority of lanthanide based SMMs face a common and important handicap: low blocking temperatures. Compound **i21**, for example, displays a T_B of "only" 14 K (defined by FC/ZFC experiments), which is mainly due to fast QTM at zero field. This is one of the biggest problems that researchers are nowadays facing in the way to achieve high blocking temperature SMMs.

v. QTM: THE UNDESIRED PHENOMENON

As previously discussed, it must be said that, in general, it is easier to synthesize a coordination compound with SMM properties when lanthanides are used. Besides, the effective energy barriers that they show are often greater than those found for SMMs based on transition metal ions. However, the QTM is, most of the times, very strong when the external magnetic field is removed and this means that there is not remnant magnetization at zero field. This is a huge problem for using these materials in a future device. Therefore, the QTM effect has been widely studied in the past few years and little by little we are learning how to quench it.

Tong's group, for instance, studied the effect of geometry of the coordination sphere on the QTM [76]. In order to do that, they investigated two very similar trinuclear $Zn^{II}Dy^{III}Zn^{II}$ systems, where the main difference between them consisted in the presence/absence of a methanol molecule within the equatorial plane (Figure i.20). Compound **i24**, with methanol, displays a pentagonal bipyramid geometry around the lanthanide ion, whereas **i25**, without methanol, shows an octahedral coordination

environment. Even though with the exception of the methanol oxygen atom in **i24** all the oxygen donor atoms around the Dy^{III} ion belong to phenoxido groups, the ligand field could be considered as optimum in reference to the model suggested by Rinehart and Long. This is because the oxygen atoms in the apical positions of the PB geometry show considerably shorter bond distances than those in the equatorial plane. Being so similar compounds and with a well-defined axial ligand field, it is interesting to remark that compound **i24** shows a U_{eff} = 438.8 ± 4.3 K (305 ± 3 cm^{-1}), whereas compound **i25** barely displays out-of-phase signals in the $\chi_M''(T)$ plots due to fast QTM (they manage to suppress it with an optimum external magnetic field). With the aim of rationalizing this behavior, they used *ab initio* calculations. They concluded that, as aforementioned, the PB geometry is an ideal candidate to observe SMM behavior, while octahedral ligand fields are prone to present tunneling. It is worth mentioning that the geometries are never ideal, which leads to adverse effects for the SMM behavior (in fact favors QTM). In connection with this, in compound **i24** the SMM behavior is not as good as expected, whereas QTM could be suppressed for **i25** by applying an external magnetic field, thus emerging slow magnetic relaxation.

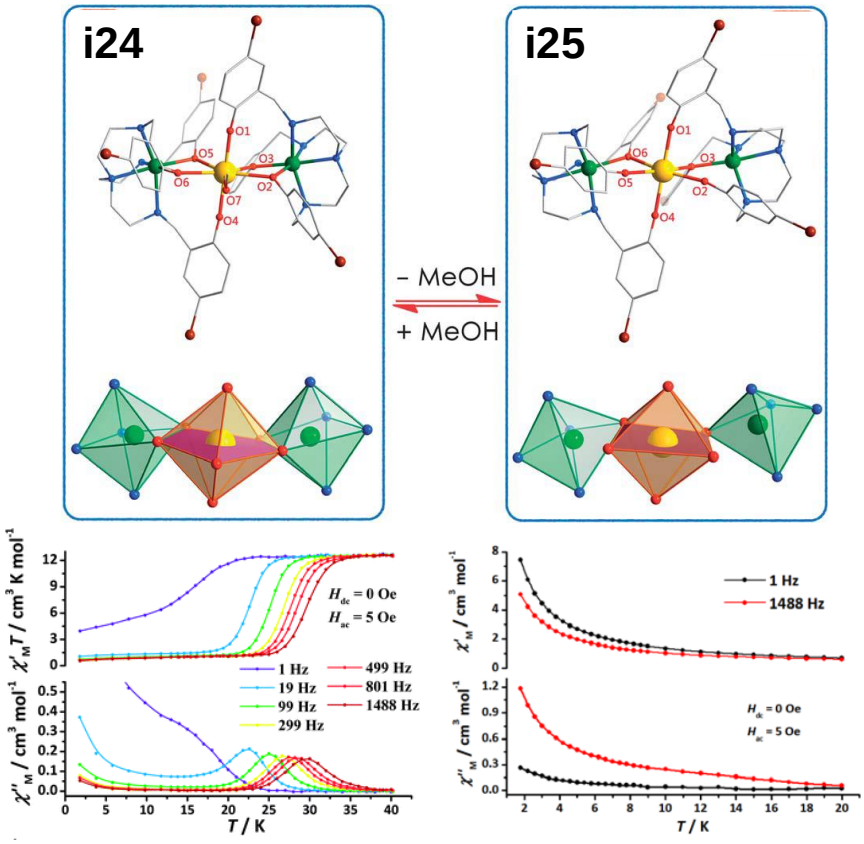

Figure i.20.- Structure of the complexes **i24** and **i25** with their respective coordination polyhedra for Zn^{II} and Dy^{III} (blue insets). Temperature dependence of χ_M'' under zero *dc* applied field for **i24** and **i25** (bottom). Color code: Zn^{II}, Dy^{III}, carbon, nitrogen, oxygen and bromine in green, yellow, grey, blue, red and brown, respectively. Hydrogen atoms have been omitted for the sake of clarity. Adapted with permission from [76]. Copyright 2013 The Royal Society of Chemistry.

In view of the essential role that plays symmetry for achieving high performance lanthanide-based single-molecule magnets, Tong and col. recently carried out a qualitative study, based on an effective charge model, which showed that certain symmetry groups, such as Cn (n ≥ 7), S_8/D_{4d}, C_{5h}/D_{5h} and S_{12}/D_{6d} could minimize transverse crystal field parameters (CFs) and then the QTM [77]. It is worth noting that none of these symmetries exists in all the 32 crystallographic point groups and, therefore, it would be impossible to reach such perfect geometries in crystalline complexes. In spite of this, one can attempt to achieve a symmetry as close as possible to the above-indicated symmetries. Experimental results, like those indicated above for compounds **i21**- **i23**, among others, support these qualitative expectations. It is worth mentioning that, to minimize the transverse CFs and then the QTM, the

magnetic anisotropy axis for the $\pm M_J$ ground doublet state should coincide with the principal symmetry axis. When this occurs, the anisotropy axes of the low-lying excited states and the ground state are parallel and the magnetization relaxation does not take place through the first excited state, but through higher excited states, thus leading to higher U_{eff} values. This is the case generally occurring for Dy^{III} complexes with high-performance SMM behavior. For instance, in compound **i21**, the anisotropy axes for the three low-lying excited states are almost collinear with that of the ground state, so that the magnetic relaxation occurs via the highly bunched set of states close in energy to the four excited state. It is also worth remarking that the change of charge density distribution around the trivalent lanthanide ion is more essential for determining the symmetry than the molecular geometry.

Another fundamental aspect to quench QTM is to prevent, as much as possible, weak intermolecular interactions. It is of vital importance to have single molecules well isolated within the crystal structure, so that there are not magnetic interactions between adjacent paramagnetic ions. This is because these interactions could provoke transversal magnetic fields favoring QTM. A widely used strategy is that of designing ligands that are not able to form intermolecular hydrogen bonds and thus the molecules should be isolated within the bulk structure [78]. However, this method is not always effective and even though, at first glance, the single molecules might be separated by a considerable distance they could show weak dipolar interactions. Another synthetic strategy could be that of diluting the paramagnetic centers within a diamagnetic matrix. In order to do that, the target compound needs to have isostructural counterparts that crystallize with diamagnetic ions. For instance, when using lanthanides, Y^{III} is usually employed since it contains a similar ionic radii compared to Dy^{III} and Er^{III} (La^{III} is also diamagnetic, but its ionic radii is larger and could not give rise to the same compound). Thus, both paramagnetic and diamagnetic compounds are co-crystallized in different ratios eliminating, at least partly, the undesired intermolecular dipolar interactions. This strategy was already employed by Ishikawa and col. when they discovered the first lanthanide based SMM, and it has been profusely used by other research groups during the last years [79–82].

Probably not at the same level as intermolecular dipolar interactions, the removal of hyperfine interactions between electrons and active nuclei has been proven to be another effective strategy towards diminishing the tunneling effect. In this regard, Cador and co-workers applied this approach firstly in the mononuclear $[Dy(tta)_3(L)]\cdot C_6H_{14}$ (**i26**, Figure i.21) compound (tta^- = 2-thenoyltrifluoroacetonate and L

= 4,5-bis(propylthio)-tetrathiafulvalene-2-(2-pyridyl)-benzimidazole methyl-2-pyridine) [83]. This study aimed to intrinsically improve the magnetic behavior of single molecules, since magnetic dilution strategies are a way to optimize the effect of the environments and not of the molecule itself. For this purpose, they synthesized first **i26** with natural Dy^{III} ion, which is mainly a mixing of the four out of seven different isotopes: ^{161}Dy (18.9%) and ^{163}Dy (24.9%) with I = 5/2 and ^{162}Dy (25.5%) and ^{164}Dy (28.2%) without nuclear spin. Then, natural Dy^{III} ions are replaced by ^{161}Dy (I = 5/2) or ^{164}Dy (I = 0) to isotopically enrich them, named **i^{161}26** and **i^{164}26** from now on. Both isotopically enriched compounds display frequency dependent out-of-phase susceptibility signals below 14 K at zero applied *dc* field, although they show notable differences. The maxima of the $\chi_M''(\upsilon)$ curves are much more shifted to lower frequencies for **i^{164}26**. Indeed, even though the thermally activated regime coincides for both compounds regarding τ_0 and U_{eff} values, the relaxation times in the temperature independent regime are increased around an order of magnitude for the compound with a non-active nucleus. To verify that the increment in relaxation times corresponds to the quenching of the hyperfine interactions, they repeated the measurements under an optimum external magnetic field suppressing the residual QTM. The extracted relaxation times coincide for all the derivatives, which clearly indicates that the isotopic enrichment only influences the temperature-independent regime.

This slowing down of the relaxation times in the temperature-independent regime was further confirmed by hysteresis loop measurements (Figure i.21, right). Compound **i26** displays the typical butterfly shape losing the vast majority of the magnetization at low fields. However, for isotopically enriched **i^{164}26**, the opening at zero field is more pronounced, which demonstrates that suppressing hyperfine couplings somehow enhances the SMM properties. Nonetheless, this finding might be cautiously taken, since even combining different strategies including the isotopic enrichment the QTM persists. Related to this work, Chilton and co-workers made an exhaustive field- and temperature-dependent study in a high effective barrier SMM [84]. In that work, although they confirm that magnetic dilution and isotopic enrichment strategies are effective to modify the magnetic behavior at low temperatures, they remark that probably the way forward still resides in the engineering of the molecular structure to avoid tunneling through crystal field effects.

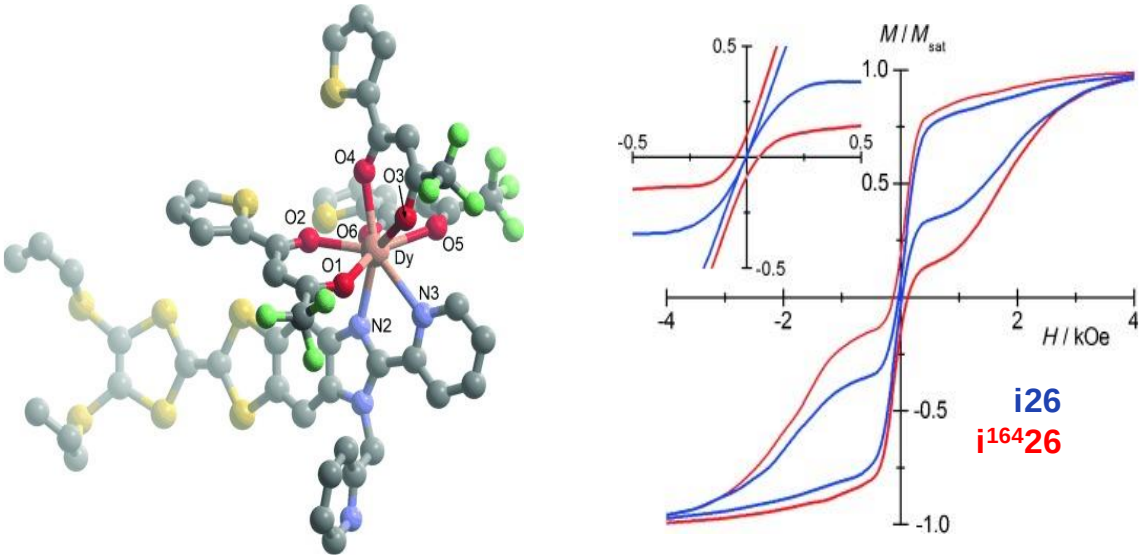

Figure i.21.- Structure of the complex **i26** (left). Hysteresis loops at 0.46 K for **i26** and **i^{164}26** (right). Color code: Dy^{III}, carbon, nitrogen, oxygen, sulfur and fluorine in pink, grey, blue, red, yellow and green, respectively. Hydrogen atoms and solvent molecules have been omitted for the sake of clarity. Reproduced with permission from [83]. Copyright 2015 John Wiley and Sons.

Completely opposite towards the previous strategy of eliminating any possible magnetic interactions of the paramagnetic centers with nuclei or other neighboring ions that could cause transverse magnetic fields, is to look for strong enough metal-metal interactions that might cause the contrary effect. Langley and co-authors reported the comparison between two butterfly type of complexes, namely $Co_2^{III}Dy_2^{III}$ (**i27**) and $Cr_2^{III}Dy_2^{III}$ (**i28**) systems (Figure i.22, top) [85]. For the former, taking into account that Co^{III} ions are in the diamagnetic low-spin state, the magnetic properties only arise from Dy^{III} ions. For the latter, the exchange interactions between both Cr^{III} and Dy^{III} paramagnetic ions are important. Even though the height of the energy barrier for both compounds is comparable, compound **i27** crosses to a pure quantum regime below 2.5 K. In contrast, compound **i28** displays open hysteresis loops up to 3.5 K with coercive fields as large as 2.8 T at 1.8 K (Figure i.22, middle). They carried out *ab initio* calculations to explain this huge difference in magnetic behavior. According to them, for the exchange coupled system the ground-state and thermally-assisted QTM are efficiently quenched and, thus, open loops are observable (Figure i.22, bottom). This research reveals the impact of magnetic exchange interactions within relaxation pathways.

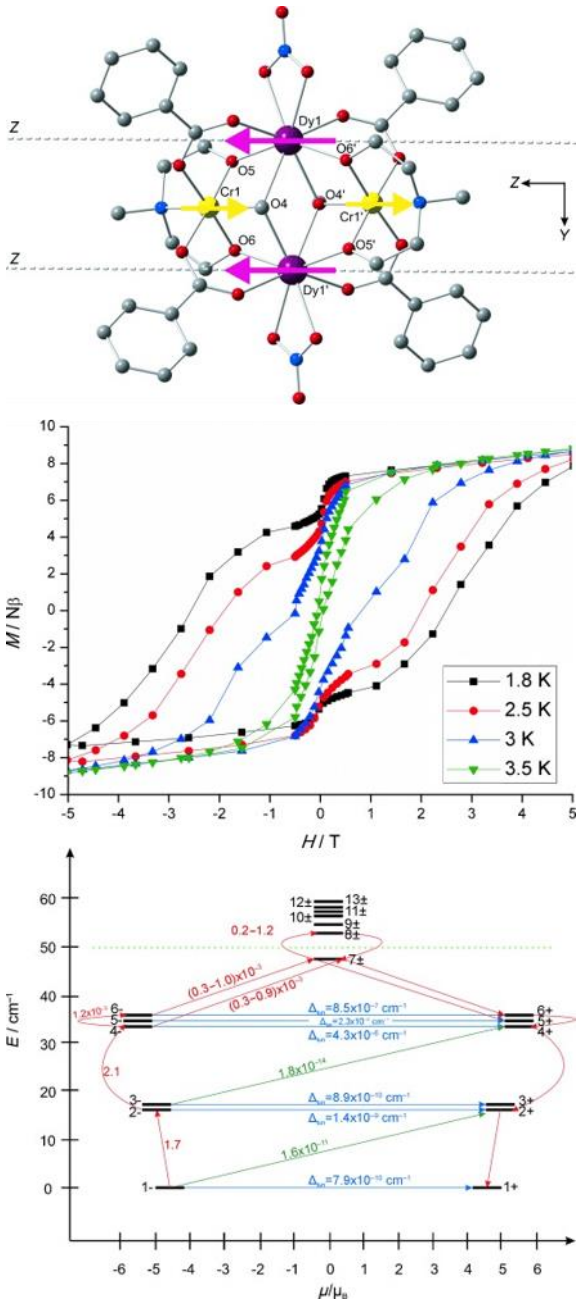

Figure i.22.- Structure of the complex **i28**. The dashed lines correspond to the main magnetic axes of the Dy^{III} ions. The arrows show the orientation of local magnetic moments in the ground exchange doublet state (top). Hysteresis loops measured with an average sweep rate of 0.003 T/s (middle). Low-lying exchange spectrum with the magnetization blocking barrier indicated by dashed green lines. The numbers for the horizontal blue arrows (Δ_{tun}) indicate an effective quenching of QTM (bottom). Color code: Cr^{III}, Dy^{III}, carbon, nitrogen and oxygen in yellow, purple, grey, blue and red, respectively. Hydrogen atoms have been omitted for the sake of clarity. Reproduced with permission from [85]. Copyright 2013 John Wiley and Sons.

Rajaraman *et al*. also made exhaustive studies regarding 3d-4f mixed systems. In a paper published in 2017, they compared four related octanuclear systems, in which they maintained their core structure, but modified either metal-metal bridging ligands and/or 3d metal ions [86]. The compounds **i29** and **i30** contained $Co_4^{III}Dy_4^{III}$ cores mainly differentiated by bridging OH^- (**i29**) or F^- (**i30**) groups, whereas **i31** and **i32** display two types of paramagnetic ions, $Cr_4^{III}Dy_4^{III}$, with bridging F^- (**i31**) or N_3^- (**i32**) groups (Figure i.23). Noteworthy, compounds **i31** and **i32** were previously reported [87,88]. Initially, leaving aside the effect of the 3d metal ion, they discovered that F^- bridges provide a bigger splitting between the ground and first excited states. Even though they both (**i29** and **i30**) have an $M_J = \pm 15/2$ as ground state and $M_J = \pm 1/2$ as first excited state, the higher electron density in fluoride ensures a better separation between both states. Hence, compound **i29** is not an SMM, but **i30** it is with a still marked QTM. When switching to structures containing a second type of paramagnetic ion, compound **i32** displays two improved features in comparison to **i30**. The height of the barrier was increased and QTM was effectively quenched. Moreover, when combining both strategies of implementing Cr^{III} ions and F^- bridges, the resultant compound **i31** displayed the best results with the highest U_{eff} and suppression of QTM. This fact was then clearly proved by *ab initio* calculations. Without considering intramolecular exchange interactions, **i31** should have even a more marked ground-state tunneling than **i30**, which is contrary to what experiments showed. Therefore, Cr···Dy and Dy···Dy exchange pathways should have been included in the calculations. In such case, considering the polynuclear framework for relaxation mechanisms, they verified that the presence of paramagnetic Cr^{III} ions were responsible of quenching the low temperature relaxation channels present in compound **i30**.

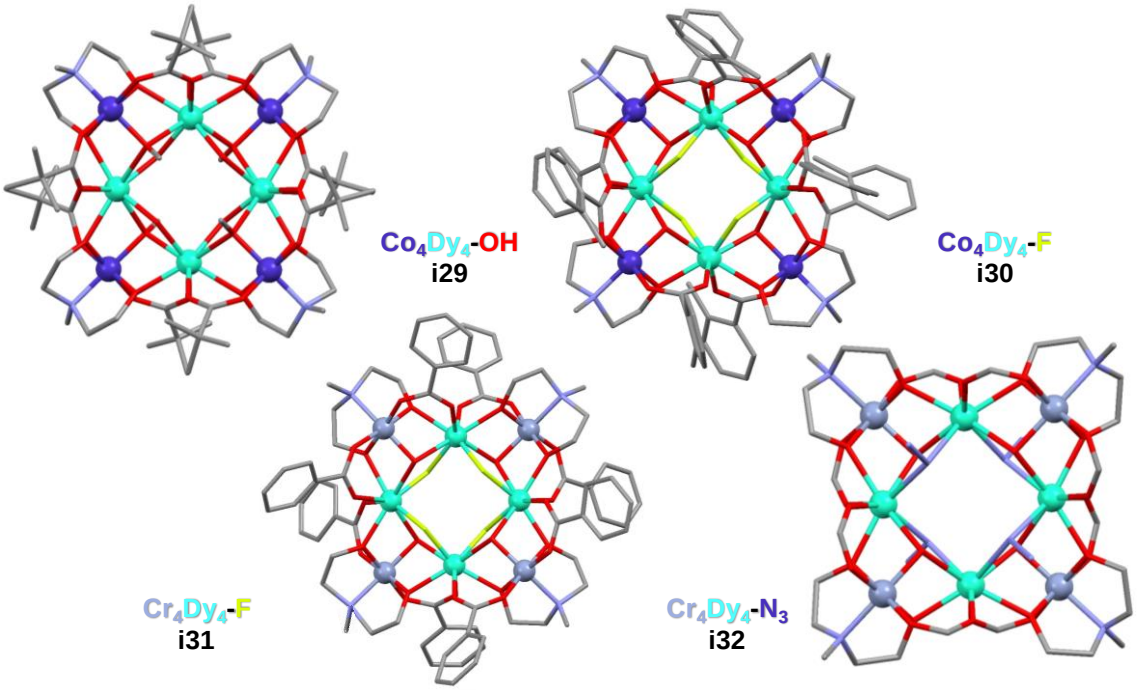

Figure i.23.- Structure of the complexes i**29-i32**. Color code: Co^{III}, Cr^{III}, Dy^{III}, carbon, nitrogen, oxygen and fluoride in purple, light grey, turquoise, grey, blue, red and green. Hydrogen atoms, solvent molecules as well as disordered fragments have been omitted for the sake of clarity. Generated from the crystal structures in references [86–88].

Even though the mentioned examples imply the presence of Cr^{III} ions, more examples including other 3d metals such as Mn^{II}, Fe^{II} and Co^{II} have been also reported [89–92]. Apart from them, the exchange coupled relaxation mechanisms were also investigated by Rajaraman *et al*. [93] for a previously reported Ni_3Dy (**i33**) tetranuclear compound (Figure i.24, top) [94]. Although weak, the compound displays zero field SMM behavior. As shown for compound **i25**, the octahedral coordination environments are not the most suitable in order to design high performance SMMs. Thus, it is not surprising that the distorted octahedral environment around the Dy^{III} ion in **i33** is not able neither to stabilize M_J = ±15/2 states as ground state nor to create huge splitting between the ground and first excited state. In fact, the ground state in this compound is far from being of pure Ising-type with a mixed wavefunction mainly composed of M_J = ±13/2. In addition, even though the *g*-tensor values indicate that the ground-state is axial, the transverse components are not negligible. All in all, the calculations suggest that the compound will show QTM and that is not a potential candidate to be an SMM. However, once again the calculations based on the exchange-coupled system suggest

that QTM is partially suppressed due to strong Ni···Dy interactions enabling zero-field SMM behavior (Figure i.24, bottom). Nonetheless, including paramagnetic 3d ions in 3d-4f mixed compounds is not always positive. The relaxation pathways in these complexes are not trivial and slight structural differences might be the line separating systems in which paramagnetic or diamagnetic 3d ions improve or deteriorate the SMM properties [95].

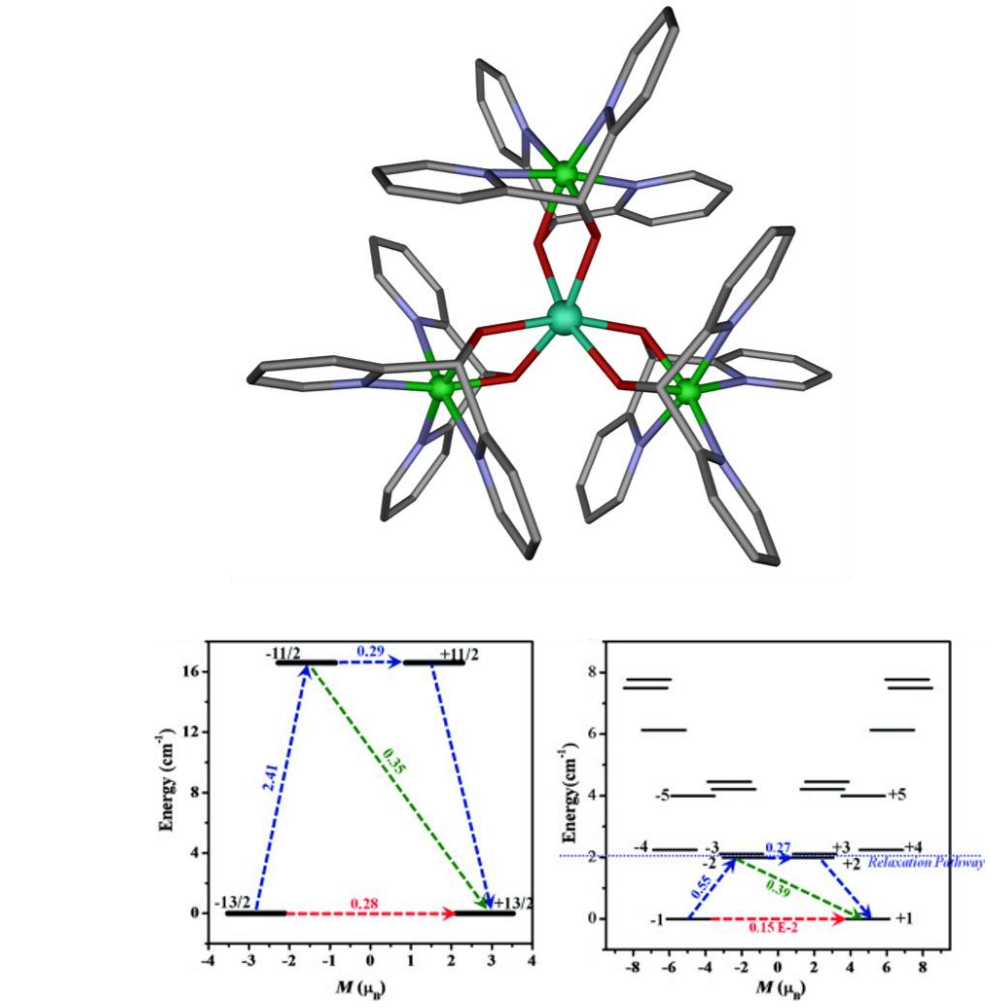

Figure i.24.- Structure of the complex **i33** (top). *Ab initio* computed magnetization blocking barriers for single ion (bottom left) and exchange-coupled system (bottom right) displaying a major contribution of QTM (dashed red arrow) for the former. Color code: Ni^{II}, Dy^{III}, carbon, nitrogen and oxygen in green, turquoise, grey, blue and red, respectively. Hydrogen atoms and counterions have been omitted for the sake of clarity. Generated from the crystal structure in reference [94]. *Ab initio* plots have been reproduced with permission from [93]. Copyright 2016 John Wiley and Sons.

Different bridging groups or heteroatoms could give rise to different exchange, either in nature (ferro- or antiferromagnetic) and strength. However, because the 4f valence electrons are deeply buried below $5s^2$ and $5p^6$ electrons, the metal-ligand interactions are usually purely electrostatic in nature and, thus, when a heteroatom acts as bridging group between two Ln^{III} ions weakly interacting exchange coupled systems are observed. Therefore, for polynuclear Ln^{III} systems the SMM behavior could be directly associated to single ion behavior and, often, the weak interactions may be an unfavorable factor provoking transverse fields. A very promising strategy towards obtaining stronger metal-ligand interactions is to use paramagnetic ligands or, in other words, radicals. Their diffuse feature has been proved to be very effective to penetrate through the lanthanides orbitals and provide strong metal-ligand interactions that cannot be obtained thorough diamagnetic ligands. Clear examples of it are the N_2^{3-} bridged dinuclear compounds of formula $[K(18\text{-crown-}6)][\{[(Me_3Si)_2N]_2(THF)Ln\}_2(\mu\text{-}\eta^2\text{:}\eta^2\text{-}N_2)]$, where Ln = Gd^{III} (**i34**) and Dy^{III} (**i35**) compounds (Figure i25) [96]. The very strong metal-radical interaction was proven by the noticeable rise in $\chi_M T$ observed in the $\chi_M T$ vs T curve below room temperature due to strong antiferromagnetic interactions. In fact, the value at 300 K for **i34** was already lower than that expected for two non-interacting S = 7/2 Gd^{III} ions and a single radical S = 1/2 N_2^{3-} unit in agreement with the mentioned antiferromagnetic interactions. The fitting of the data afforded a strong J = -27 cm^{-1} exchange constant, notably higher than those usually found for Gd^{III} systems usually below 3 cm^{-1} [97]. To verify that the strong interaction arises from the diffuse nature of the N_2^{3-} radical, the non-radical N_2^{2-} bridged analogues were also studied (Gd^{III} (**i36**) and Dy^{III} (**i37**)). Although it was already evident from $\chi_M T$ curves, the fitting of the data for **i36** supported a weak antiferromagnetic exchange interaction with J = -0.49 cm^{-1} constant. Noteworthy, the non-radical counterparts displayed some differences regarding structural parameters, but they were the best models to compare it to the data obtained for **i34** and **i35**.

The lack of spin-orbit coupling in Gd^{III} ion is a good feature in order to evaluate the *dc* data and somehow easily obtain exchange coupling constant values. However, its isotropic character prevents it to be a potential candidate for the design of SMMs. The Dy^{III} based compound **i35**, instead, displays zero-field SMM behavior due to its anisotropic nature. The calculated U_{eff} of 177 K (123 cm^{-1}) is comparable to other Dy^{III} based SMMs, whereas the low temperature regime differs from usual. Some other compounds with similar effective energy barriers [98] display deviations in the Arrhenius plots that are clearly related to under barrier shortcuts. Compound **i35** displays a clear linear dependence in the whole studied temperature range related to a

pure Orbach mechanism. Moreover, N_2^{2-} bridged **i37** displays a modest barrier of 25.9 K (18 cm^{-1}) with nearly constant relaxation times in the low temperature regime indicative of fast tunneling. Differently to **i35**, weakly coupled SMMs usually behave as single ion magnets instead of single molecule magnets highlighting the importance of strong exchange coupling constants. Finally, SMM behavior was verified by measuring hysteresis loops up to 8.3 K with large coercive fields.

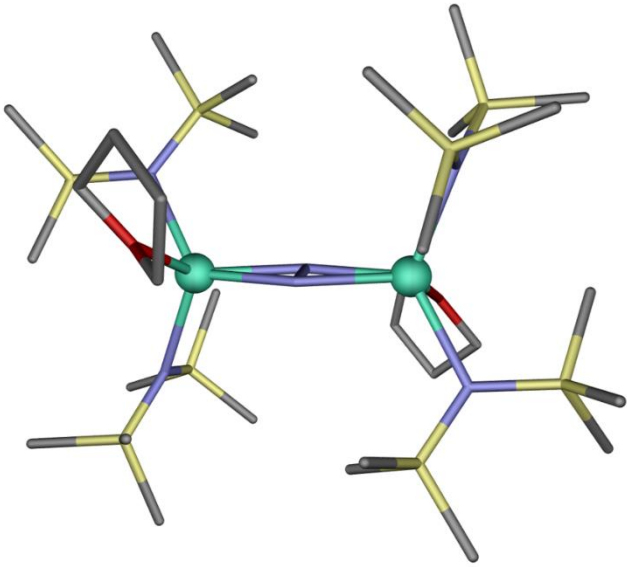

Figure i.25.- Structure of the $[\{[(Me_3Si)_2N]_2(THF)Gd\}_2(\mu\text{-}\eta^2\text{: }\eta^2\text{-}N_2)]$ anion in **i34** Color code: Gd^{III}, carbon, nitrogen, silicon and oxygen in turquoise, grey, blue, yellow and red, respectively. Hydrogen atoms and counterions have been omitted for the sake of clarity. Generated from the crystal structure in reference [96].

After the research related to Gd^{III} and Dy^{III} ions, the Long's group continued exploring N_2^{3-} bridged systems. Firstly, maintaining the structure, but switching to Tb^{III} (**i38**) they obtained even better results since it showed a blocking temperature as high as 14 K [99]. After that, and in view of the great results obtained for sandwich type of complexes (later discussed) with cyclopentadienide derivatives, they managed to introduce again the N_2^{3-} radical to bridge Dy^{III} and Tb^{III} ions [100]. Among other compounds, they reported on the synthesis, characterization and magnetic properties of four novel compounds with general formula [K(crypt-222)(THF)][$(Cp^{Me4H}{}_2Ln(THF))_2(\mu{-}N_2)$] for Tb^{III} (**i39**) and Dy^{III} (**i40**) and [K(crypt-222)][$(Cp^{Me4H}{}_2Ln)_2(\mu{-}N^{\cdot}{}_2)$] for Tb^{III} (**i41**) and Dy^{III} (**i42**) where crypt-222 = 2.2.2-cryptand and Cp^{Me4H} = tetramethylcyclopentadienyl (Figure i.26). Structurally speaking, the main

difference between both structures is the presence/absence of a THF molecule coordinated to the lanthanide ions. This was then easily removed by dissolution in 2-methyltetrahydrofuran. Even though compounds **i39**- **i42** are all zero field SMMs, there are some remarkable differences among them. Relaxation times extracted from *ac* measurements follow the Arrhenius law in the whole temperature range except for **i40**, which crosses to a pure QTM regime at the lowest temperatures. This was then verified by variable-field magnetization measurements; in which it did not show any remnant magnetization even at 2 K. However, the removal of the THF molecules from the coordination environment substantially improved the magnetic behavior for **i40** and open hysteresis loops were observed up to 8 K for **i42**. Considering that Tb^{III} based compound **i39** was already displaying open loops up to 15 K, great improvements were also predicted for **i41** after THF removal. Indeed, open hysteresis loops were measured up to 30 K with a 100 s-magnetic blocking temperature of 20 K. Therefore, these research works regarding radical bridged coordination compounds exhibited great potential in terms of future design of high performance SMMs.

Figure i.26.- Structure of the anionic complexes **i39** and **i41**. Color code: Tb^{III}, carbon, nitrogen and oxygen in turquoise, grey, blue and red, respectively. Hydrogen atoms and counterions have been omitted for the sake of clarity. Generated from the crystal structures in reference [100].

As it will be further discussed in the next section, compounds with a single paramagnetic ion (SIMs) compose the state of the art for SMMs, since so far they have shown the greatest properties. However, it is still necessary and challenging to study polynuclear systems that maintain the high anisotropy. The group of Rinehart employed the $[Er(COT)]^{+}$ (COT^{2-} = cyclooctatetraenide anion) as building block to construct four novel compounds; a mononuclear one (**i43**) and three dinuclear systems (**i44**- **i46**) [101]. This fragment was selected because it is well known that it is suitable

to stabilize the states with highest magnetic moment (M_J = ±15/2) for the Er^{III} ion and the anisotropy axis is known to point along the Er-$COT_{centroid}$ axis. The coordination spheres were completed by I^- ions and weakly coordinating phosphines (Figure i.27). Within the dinuclear systems, the former ones act as magnetic coupling bridges, while the latter non-coupling ligands were introduced to modulate the angles between the magnetic anisotropy axes. Noteworthy, phosphine ligands were selected based on their weakly coordinating character, which was not expected to alter the Er-$COT_{centroid}$ based anisotropy axis. Several interesting conclusions were obtained from the study of these four compounds. On the one hand, the effective energy barriers for **i44**- **i46** were around 150 K higher than for **i43**, and very similar between them. However, the hysteretic behavior at 2 K did not follow the same trend (Figure i.27). Compounds **i43** and **i44** displayed waist-restricted butterfly-shaped hysteresis loops in agreement with a large influence of QTM. In contrast, compounds **i45** and **i46**, which show greater angles between Er-COT centroids, displayed open hysteresis loops without clear QTM contribution at zero field. Thus, this study emphasizes the importance of aligning the anisotropy axes in polynuclear systems (as it was previously demonstrated for transition metal clusters). In addition, relaxation times at 2 K were enhanced around six orders of magnitude from **i43** to **i46**, hence reaffirming the relevance of nuclearity and orientation of the axes in terms of slow relaxation of the magnetization.

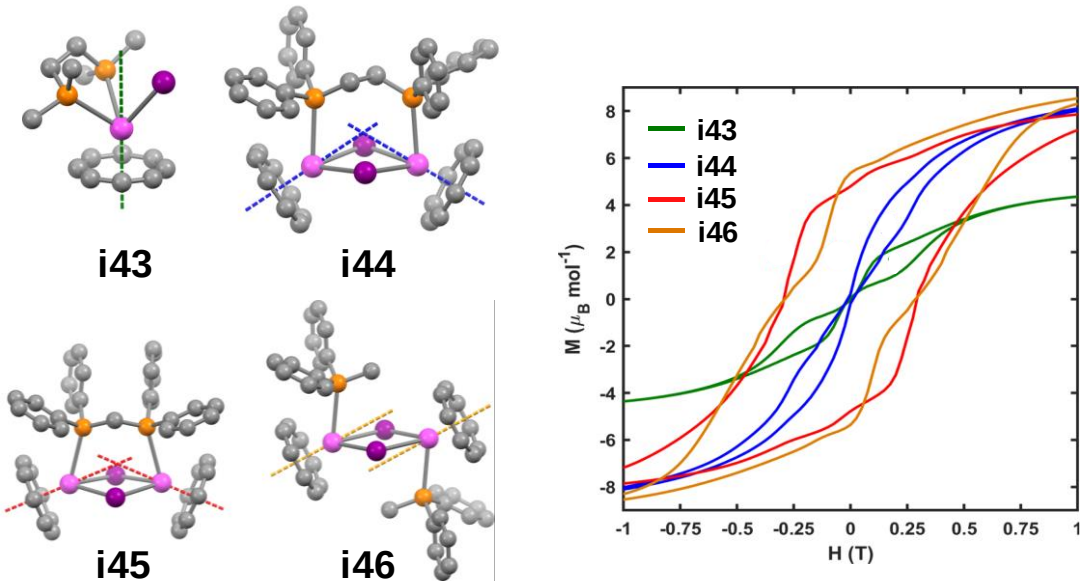

Figure i.27.- Structure of the complexes i**43-i46** along with Er-$COT_{centroid}$ vector directions (left). Hysteresis loops at 2 K with a sweep-rate of 10.1 Oe/s (right). Color code: Er^{III}, carbon, phosphor and iodide in pink, grey, orange and purple, respectively. Hydrogen atoms have been omitted for the sake of clarity. Adapted with permission from [101]. Copyright 2019 American Chemical Society.

vi. STATE OF THE ART: DYSPROSIUM METALLOCENES

As discussed along the paper, during the last decades several SMMs have been reported displaying large effective energy barriers to prevent the reorientation of the magnetization. Blocking temperatures, in contrast, have not been enhanced at the same pace due to the additional relaxation pathways that shortcut the energy barrier. Designated as outliers in this trend, trivalent dysprosium based metallocenes are the current state of the art of SMMs displaying magnetic blocking temperatures already above the liquid nitrogen. In the same way that COT ligands are appropriate for the design of Er^{III} based SMMs, Cp derivatives (Cp = cyclopentadienyl anion) have provoked a revolution among Dy^{III} based systems. Already from Rinehart and Long's design principles Cp sandwiched Dy^{III} compounds (without ligands in the equatorial plane) were envisioned as potential candidates, although the large ionic radii of Ln ions hindered or complicated their synthesis. However, Mills *et al*. and Layfield *et al*. almost simultaneously reported on a sandwiched dysprosocenium compound with Cp^{ttt} ligands (Cp^{ttt} = {$C_5H_2{}^tBu_3$-1,2,4} and ^tBu = $C(CH_3)_3$) (**i47**, Figure i.28, top left) [102,103]. Compound **i47**, with general formula $[Dy(Cp^{ttt})_2][B(C_6F_5)_4]$, shows a wide bent Cp-Dy-Cp angle of 152.56(7)˚ with relatively short Dy-$Cp_{centroid}$ distances of 2.316(3) Å [102]. Already from this structural features, it was evident that the slow relaxation dynamics were going to be really promising. Indeed, open hysteresis loops were observed below 60 K (measured with a sweep rate of 22 Oe/s), although a zero-field step was already observable at 2 K attributed to QTM. FC/ZFC measurements confirmed the value of T_B displaying a bifurcation of both curves at 61 K.

In order to study the mechanism of magnetic relaxation, *ab initio* calculations were performed. Interestingly, the spin-phonon coupling arising from C-H vibrational mode in the Cp^{ttt} ligands was found to be of relevance promoting the first transition from the ground ±15/2 state to the excited ±13/2 one. Thus, pointing out that the substitution of such groups should potentially enhance the hysteretic behavior of dysprosium metallocenes. Furthermore, the outlier character of this compound was attributed to the particular ligand field around the ion, since the rigid Cp^{ttt} ligands constrain metal-ligand vibrational modes that could enhance the through barrier shortcuts. In fact, the obtained energy barrier of 1760 K (1223 cm^{-1}) was found in the range of other previously reported SMMs such as $[Dy(O^tBu)_2(py)_5][BPh]_4$ (**i21**) [69], the blocking temperature, however, is far greater for **i47**. When comparing both systems, the former one contains single donor atoms in the first coordination sphere displaying a more

pronounced metal-ligand flexibility, which might provide detrimental vibrational modes accelerating relaxation times through barrier shortcuts.

In light of these outstanding results, in 2018 again Layfield and co-workers went further and synthesized another dysprosocenium compound with enhanced performance [104]. By studying compound **i47** the design principles for an improved ligand field were clearer: (i) shorter Dy-Cp bond distances, (ii) wider Cp-Dy-Cp angles and (iii) absence of C-H bonds were targeted. However, in order to fulfil these purposes a compromise needed to be taken, since bulky ligands could provide wide angles (and absence of equatorially coordinated ligands), but too bulky ones favor longer bond distances. All in all, they managed to synthesize the targeted compound **i48** (Figure i.28) with general formula $[(\eta^5\text{-Cp*})\text{Dy}(\eta^5\text{-Cp}^{i\text{Pr5}})][\text{B}(\text{C}_6\text{F}_5)_4)]$ where Cp* = pentamethylcyclopentadienyl and $\text{Cp}^{i\text{Pr5}}$ = pentaisopropylcyclopentadienyl (Figure i.28, top right). As a result of the appropriate ligand design, from the crystal structure analysis they concluded that the Dy-Cp* and Dy-$\text{Cp}^{i\text{Pr5}}$ distances were on average 0.026 Å shorter compared to **i47**. Moreover, the Cp*-Dy-$\text{Cp}^{i\text{Pr5}}$ angle showed a notably wider value of 162.507(1)˚, almost 10˚ nearer from the perfectly lineal value of 180˚. Thus, already from these considerations, a stronger crystal field effect along with an enhanced magnetic behavior was expected.

Certainly, at a sweep rate of 25 Oe/s the hysteresis loops remained open up to 80 K, a temperature that is already above the liquid nitrogen (Figure i.28, bottom right). This blocking temperature was also certified by FC/ZFC measurements, in which a divergence of both curves was observed at 78 K (Figure i.28, bottom left). The axiality of the system was further confirmed by *ab initio* calculations suggesting a perfectly axial ground state. This was in fair agreement with the hysteresis loops at 2 K. In contrast to what observed for **i47**, there was no sign of any zero-field step suggesting a total blocking of QTM (Figure i.28, bottom middle). Finally, taking into account that C-H bonds within the ring were replaced by either isopropyl groups or methyl groups, the vibrational mode initiating the first transition from the ground to the first excited state was found to be the out-of-plane vibration of the Cp* ligand.

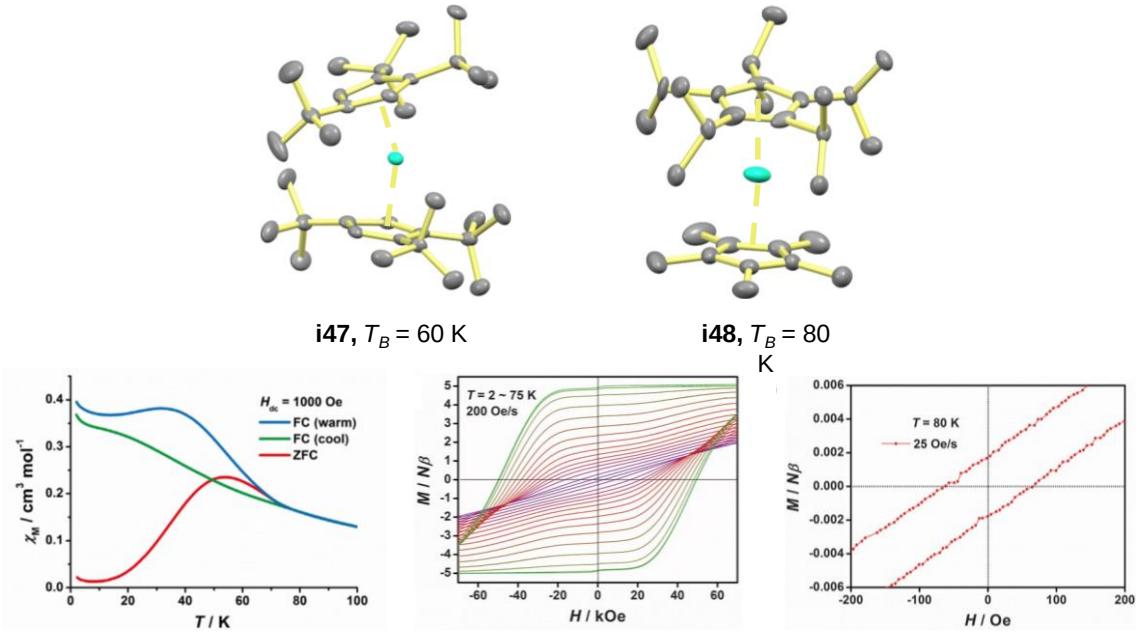

Figure i.28.- Cationic structures of complexes **i47** and **i48** (top). FC/ZFC variable-temperature magnetic susceptibility under 1000 Oe (bottom left), hysteresis loops in the 2-75 K temperature range using a sweep rate of 200 Oe/s (bottom middle) and hysteresis loops at 80 K using a sweep rate of 25 Oe/s for **i48** (bottom right). Color code: Dy^{III} and carbon in turquoise and grey, respectively. Hydrogen atoms and counterions have been omitted for the sake of clarity. Generated from the crystal structures in references [102,104]. Magnetic data reproduced with permission from [104]. Copyright 2018 The American Association for the Advancement of Science.

Parallel to the discovery of this last metallocene, Harvey and co-authors reported on four other related Dy^{III} sandwich compounds (Figure i.29) with general formula $[Dy(Cp^{iPr4R})_2][B(C_6F_5)_4]$ (R = H (**i49**), Me (**i50**), Et (**i51**), iPr (**i52**)) [105]. They were also inspired by compound **i47**, so they employed four different Cp ligands to mainly modify the Dy-Cp distance, Cp-Dy-Cp angle and vibrational modes around the metal ion. The structural parameters that they found were coherent with the substituents they employed. The more sterically demanding cyclopentadienyl ligands provoked longer bond distances, but wider angles (see Figure i.29). This confirmed the validity of the approach showing that a single modification within the Cp ring modifies the ligand field around the metal ion, possibly modulating magnetization relaxation dynamics. The first evidence of it was observed by FC/ZFC measurements detecting divergences in the wide range of 28-65 K. From *ac* measurements they obtained U_{eff} values of 1849, 2112, 1986 and 1919 K (1285, 1468, 1380 and 1334 cm^{-1}) for **i49**, **i50**, **i51** and **i52**,

respectively. They were able to rationalize this trend based on magneto-structural correlations. Between the four compounds, **i49** displays the most bent angle and, thus, the lowest effective energy barrier. Linearity increases upon introducing bulkier substituents to the fifth position of the Cp ligand. However, they theorize that among them the bond angle is no longer the determinant factor and that the Dy-Cp bond distance comes into play. Therefore, the value of U_{eff} increases from **i52** to **i50** as the Dy-Cp bond distance decreases. Following the observed trend, compound **i50** exhibited open hysteresis loops at the highest temperatures. As a general conclusion, they suggest that the ligands that are able to find a compromise between wide Cp-Dy-Cp angles and short Dy-Cp bond distances are the next target, though an exhaustive knowledge in terms of spin-phonon coupling is also fundamental as 100 s blocking temperatures are found in the regime where Raman pathway dominates. Although the effect of molecular vibrations in terms of Orbach relaxation could be evaluated, models are needed for other under-barrier mechanisms.

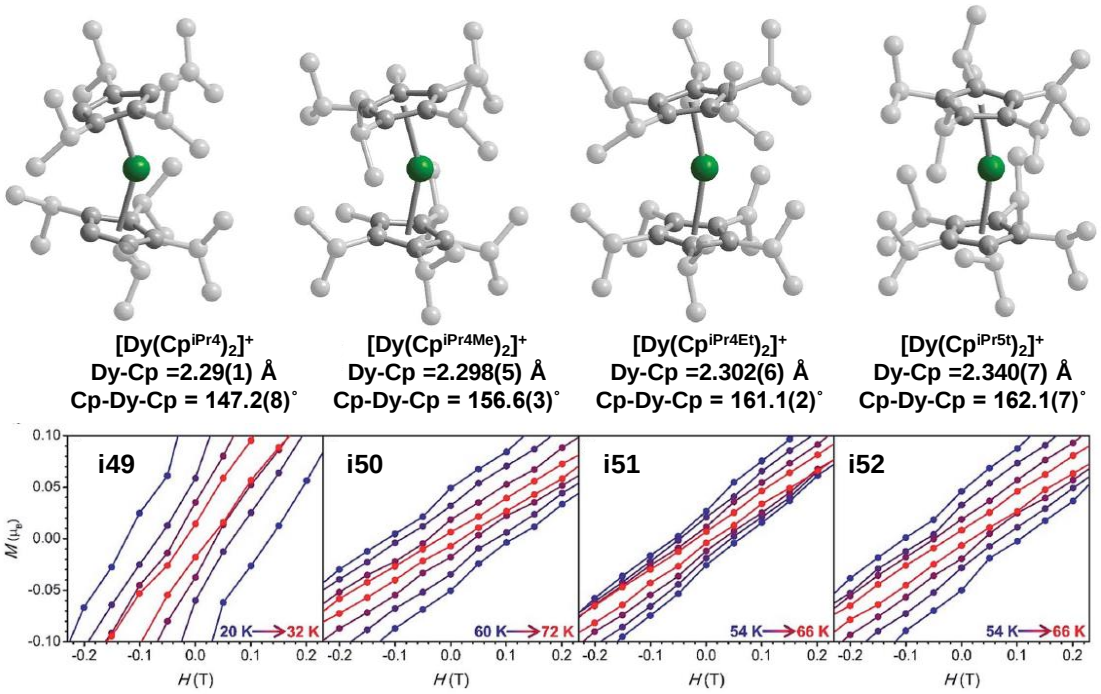

Figure i.29.- Cationic structures of complexes **i49- i52** (top). Expanded view of the hysteresis loops near zero field and at high temperatures (sweep rate of 31(4) Oe/s for H < 2 T) (bottom). Color code: Dy^{III} and carbon in green and grey, respectively. Hydrogen atoms, counterions and positional disorder have been omitted for the sake of clarity. [105] – Published by The Royal Society of Chemistry.

In view of the exceptional results obtained for all these Dy^{III} metallocenes, in the last few years several new structures have been reported. For instance, Evans *et al*. recently reported a sandwich structure in which the chemical nature of the ligands was modified by changing one carbon atom by a phosphor one in a bis-monophospholyl dysprosium compound [106]. This new system displayed magnetic hysteresis at 48 K. Meng and co-authors studied exchange coupled dinuclear systems varying the bridging ligands (CH_3^-, Cl^-, Br^- and I^-) [107]. Furthermore, isocarbonyl-ligated metallocene coordination polymers have also been studied [108], as well as dinuclear systems in which fulvalene has been used as platform instead of Cp rings [109]. All this research evidences that these systems have revolutionized the field of SMMs and the interested reader is addressed to read further cited literature [110–113].

vii. *AB INITIO* METHODS: VALUABLE TOOLS FOR A BETTER UNDERSTANDING AND IMPROVED DESIGN PRINCIPLES

Ab initio methods have emerged during the last years enabling a better interpretation, or even prediction, of the experimental magnetic properties, which at the same time facilitates developing improved ligand field design principles. The work of some specific authors in this field is remarkable as they were pioneers setting the basis of the extensively used softwares ORCA [114] and MOLCAS [115]. On the one hand, Frank Neese developed the former one and it has shown its validity for the calculation of *g* values and zero field splitting (ZFS) parameters, as well as the splitting of the d orbitals in transition metal complexes by using the *ab initio* ligand field theory (AILF, [51]). On the other hand, striking efforts of Liviu F. Chibotaru and Liviu Ungur have contributed in a decisive way to the development of the theoretical study of the electronic structure and the magnetic properties of lanthanide based SMMs with the MOLCAS software. In fact, they have built two programs, SINGLE_ANISO and POLY_ANISO for calculating local magnetic properties and the exchange energy spectrum and magnetic properties in polynuclear complexes, respectively, which were implemented in MOLCAS improving its functionality. Interestingly, this program can be used not only for calculating the electronic structure, magnetic properties and the effectiveness of the spin relaxation pathways in lanthanide based SMMs, but also in transition metal based SMMs. Apart from the above cited authors, numerous researchers working in the field of SMMs are notably contributing to the area of theoretical calculations. For instance, the results obtained by Gopalan Rajaraman

[116], Eliseo Ruiz [117], Nicholas F. Chilton [118], Roberta Sessoli [119], and Alessandro Soncini [120], among many others, have played an important role in developing and improving this research field. Note that, for example, Soncini and coauthors recently developed a novel *ab initio* code called CERES (Computational Emulator of Rare Earth Systems), which is able to efficiently calculate the electronic structure and magnetic properties in lanthanide complexes [120]. In this section, we have tried to briefly remark some of the cutting-edge studies that have been carried out in the last years in the field of theory.

Chilton and coworkers have very recently reported a theoretical study for the prediction of relaxation rates based on *ab initio* methods [118]. Within this work, they have implemented a refined *ab initio* method to theoretically calculate the relaxation dynamics of several dysprosium based metallocenes including compounds **i47**, **i48** and **i49**, which are intermediate, best and worst performing SMMs, respectively, among the compounds they consideredin the cited paper. Between the latter two, they have concluded that the most influencing factor regarding relaxation dynamics is the crystal field splitting related to the static crystal structure. Namely, the larger energy gaps between ground and excited states for **i48** in comparison to **i49** are the reason for a better performance. When considering **i47** and **i48**, the initial prediction was related to an improved spin-phonon engineering; in other words, the substitution of C-H bonds was expected to be discriminant factor for the enhanced magnetic properties. In this work, however, they found out that both a larger CF splitting and a reduced spin-phonon coupling were responsible of slowing down relaxation rates, but being the former one the prevailing reason. More interestingly, they also studied some other model compounds with general formula $[Dy(C_5R_5)_2]^+$ and $[Dy(C_4R_4)_2]^-$. From it, they concluded that organometallic sandwich compounds have probably reached their limit in terms of U_{eff} with a value of around 2100 K. Nevertheless, based on their study, the mentioned spin-phonon engineering may be now crucial to develop SMMs with improved properties. In fact, some of the studied model compounds displayed theoretical U_{eff} values that were similar to that of **i48**, but relaxation rates were expected to be orders of magnitude slower. As they state, this can be explained by the presence of far fewer available vibrational modes that are not, at the same time, so frequently on-resonance with electronic transitions. Hence, they finally remark the relevance of removing detrimental vibrational modes that provoke faster relaxation times.

Theoretical studies have shown to be important to figure out some other issues that are not obvious based on experimental data. The qualitative crystal field design principles proposed by Rinehart and Long have given rise to a large amount of SMMs with huge U_{eff} values and blocking temperatures. However, the results that have been obtained based on these principles are not always easy to understand. For instance, why Er^{III} based SMMs have not shown such a good performance as Dy^{III} based ones? Switching the chemical design from an axial ligand field to an equatorial one is not enough? Theoretical studies based on *ab initio* calculations are very useful to understand the reasons behind.

For this purpose, Lu *et al.*[121] selected the equatorially three coordinated compounds **i18** ($Er[N(SiMe_3)_2]_3$), **i53** ($Er(dbpc)_3$; dbpc = tris(2,6-di-*tert*-butyl-*p*-cresol)) and **i54** ($Er(btmsm)_3$; btmsm = tris(bis(trimethylsilyl)methyl)), being the latter two previously reported by Yamashita and coauthors [122]. For the three compounds shown in Figure i.30, they observed by theoretical calculations that the axiality of the systems was quite modest in contrast to what was expected by crystal field considerations. Indeed, the $g_{x,y}$ values that they obtained for the first excited Kramers doublets were no longer close to zero. Thus, these transverse components would be the reason for a fast QTM in the first excited state limiting the value of U_{eff} to the energy difference between the ground and first excited state. Additionally, they also studied theoretically the influence that would have the modulation of θ angles (angle between the vector connecting Er^{III} and L ligands and the anisotropy axis, see Figure i.30) and Er-L distances in the height of the energy barrier. The calculations were partially in agreement with the design principles proposed by Long *et al*. On the one hand, the highest U_{eff}'s were calculated for $\theta = 90^{o}$ angles and, in the other hand, a lengthening of Er-L bond distances would give rise to a smaller energy splitting between the ground and first excited states. In contrast, a shortening of Er-L bond distances would lead to an undesired competing effect, since the equatorially coordinated ligands would produce larger transverse components (higher $g_{x,y}$) in the ground and first excited states allowing fast QTM. Therefore, they conclude that for equatorially coordinated Er^{III} mononuclear compounds will be difficult to obtain energy barriers as high as for Dy^{III} compounds.

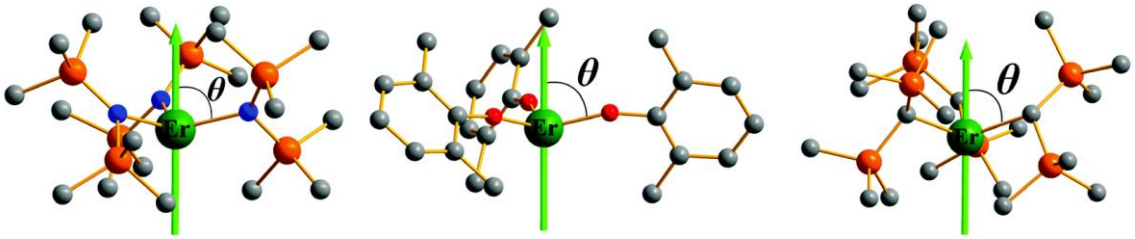

i18 **i53** **i54**

Figure i.30.- Structural view of complexes **i18**, **i53** and **i54**. The green axes show the orientations of the local main magnetic axes on Er^{III} in the ground KDs. Color code: Er^{III}, carbon, nitrogen, silicon and oxygen in green, grey, orange and red, respectively. Hydrogen atoms and tert-butyl groups in **i53** have been omitted for the sake of clarity. Adapted with permission from [121]. Copyright 2020 The Royal Society of Chemistry.

Another very interesting theoretical work was recently reported by Zhang and coworkers [123]. They made an *ab initio* study on robust divalent [LnO] units for enhanced SMM properties. Note that previously was done for the $[DyO]^+$ unit [124]. Furthermore, being aware of the importance of depositing SMMs on surfaces (see next section) for future devices, they also studied a model [DyO] unit deposited on the hexagonal boron nitride (h-BN) surface. As they state, the findings they made are important for two main reason. Firstly, as it has been shown for several recently reported Dy^{III} metallocenes, the limit of the blocking barrier seems to be enhanced to the maximum and to be hardly surpassable. This is directly related to the extreme difficulty of synthesizing low coordinated lanthanide based compounds. For this reason, switching to [LnO] units is presented as an attractive alternative towards SMMs with an improved efficiency. The energy splitting of the eight Ising doublets and a singlet for J = 8 in [DyO] spreads over 2500 cm^{-1} due to the strong covalent contribution and short Dy-O distance. Therefore, this system could be a potential candidate for future experimental studies. Finally, even though the model [DyO] system deposited on h-BN would theoretically be in a horizontal fashion (parallel to the surface), it is expected to preserve intrinsic axiality over the possible low-symmetric contributions from the surface. Consequently, this system is supposed to have a blocking barrier still exceeding 2000 cm^{-1} and to preserve excellent magnetic blocking properties even after depositing it into a surface.

During last years, there has been a more exhaustive study in order to try to understand how molecular or lattice vibrations affect the demagnetization process. As another recent example, Irländer and Schnack showed how phonon could open tunneling gaps between otherwise degenerate ground states in SMMs [125]. They believe that these kind of studies are very useful for future rational designs, since it enables identifying vibrations that are detrimental and facilitate demagnetization processes.

As a last example in this section, we would also like to remark an interesting recent paper by Aravena [126]. As it states, *ab initio* calculations have been and are very useful to rationalize the observed experimental magnetic properties. However, these are often case specific and approaches that could be generalized to bigger families of compounds are lacking. Fascinatingly, in this work a new method was proposed for the prediction of tunneling demagnetization times (named as τ_{QTM} in the present work) and effective energy barriers (U_{eff}). This method could be used by introducing the orientation of the molecule in the crystal structure, the ground and excited states energies and *g* factors to give rise to an *ab initio* prediction. To prove the validity of it, it was evaluated by considering 18 previously reported Ln^{III} based compounds (15 Dy^{III} based and 3 Er^{III} based) and comparing the obtained results with the experimental ones. As mentioned, we also consider this approach a valuable tool for evaluating a bigger family of SMMs by the same method.

viii. HYBRID MATERIALS BASED ON SMMs FOR FUTURE APPLICATIONS

During the last decades an enormous amount of SMMs have been reported in the literature. For the vast majority of them, the magnetic properties were studied in the bulk. However, with the aim of developing a future device and for reading/writting purposes, incorporating these systems in surfaces is imperative while preserving their magnetic properties, which could be a handicap due to potential surface-molecule interactions [127–130]. Moreover, a long range ordering, as well as high density of molecules is desirable for these hybrid systems. Although numerous examples of hybrid materials have been reported so far, here we will only describe a few selected examples of them.

Among different options [131,132], the use of three dimensional metal-organic frameworks (MOFs) could be an attractive one. Indeed, some of these systems

possess pores that could be suitable to load guest molecules. Even though few of these hybrid systems have been previously reported [133,134], the problem usually arises when designing specific pore sizes and functional groups that point towards the pore stabilizing the guests and providing great loading capacities. In a recently reported research by Chen and coworkers, they synthesized a La based mesoporous MOF based on short and rigid ligands showing 2 nm long pore diameter [135], suitable for incorporating Mn12-ac molecules inside (Figure i.31). By dipping samples of the MOF into saturated solutions of Mn12-ac, the colorless crystals turned from colorless to brown already indicating that the guest molecules were loaded. PXRD experiments showed that the 3D network remained intact after the process and N_2 adsorption isotherms as well as BET surface measurements were used to prove that the target molecules were encapsulated within the pores. They concluded that the designed system had special features that allowed a large loading. On the one hand, the hydrogen bonds between the –OH groups pointing to the center of the pores and acetate oxygen atoms (see red dashed lines in Figure i.31) stabilize the guests and, on the other hand, the flexibility of the material was essential since the interactions between the MOF and SMMs provoked a shrinking of the pores improving the loading capacity. Based on EDX, ICP-MS and ^{1}H-NMR techniques, they calculated a record-breaking loading capacity of 40.15 mol%. Finally, by measuring the magnetic properties of the hybrid system, they proved that the SMM properties were well preserved since maxima were visible in the $\chi_M''(T)$ and open hysteresis loops were observed at 2 K.

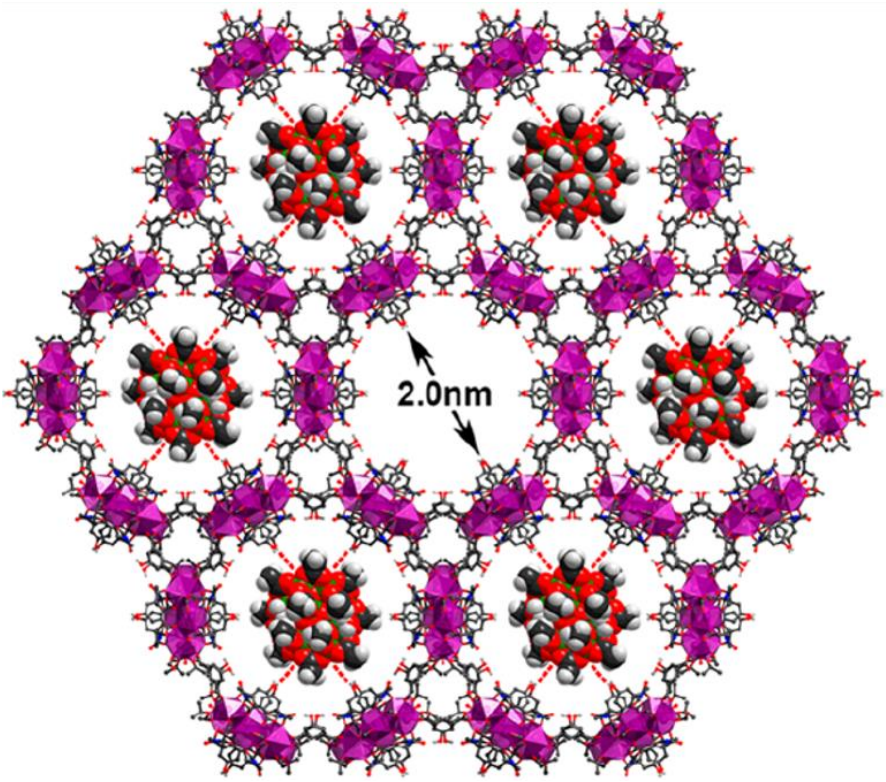

Figure i.31.- Crystal structure of the MOF reported by Chen and co-workers with a loading suggestion of Mn12-ac. Reproduced with permission from [135]. Copyright 2019 American Chemical Society.

As seen in the previous example and also in previous reported studies, indirect methods to prove the loading of the SMMs into the channels of the MOFs are well stablished. However, it was not until a couple of years that a direct method was employed in order to visualize guest molecules inside the pores. More specifically, Aulakh *et al*. synthesized a SMM@MOF composite using Mn12-ac as the guest molecule and the Zr^{IV} based MOF NU-1000 [136], named **Mn12-ac@NU-1000** [137]. By using a low-dose High-Resolution Transmission Electron Microscopy (HRTEM) technique they were able to unequivocally probe the incorporation of the SMMs into the channels of the MOF. As depicted in Figure i.32, the image that was acquired along the [001] direction displayed discrete particles of a ~2 nm size in the hexagonal channels. This particle size was in fair agreement with the expected size of 1.6 nm for Mn12-ac. In order to discard the possibility of these particles arising from the decomposition of the MOF due to prolonged exposure times, several other images were taken and compared to unmodified NU-1000, demonstrating that the observed particles were corresponding to Mn12-ac.

They finally studied the magnetic properties of the hybrid composite showing that the nanoconfinement of the SMM within the pores of NU-1000 only slightly modified the SMM properties that are observed for bulk samples of Mn12-ac, thus maintaining the slow relaxation of the magnetization. Interestingly, the authors extended their work to the synthesis and characterization of a thin film of the composite, which would be the next step to implementing them in future devices.

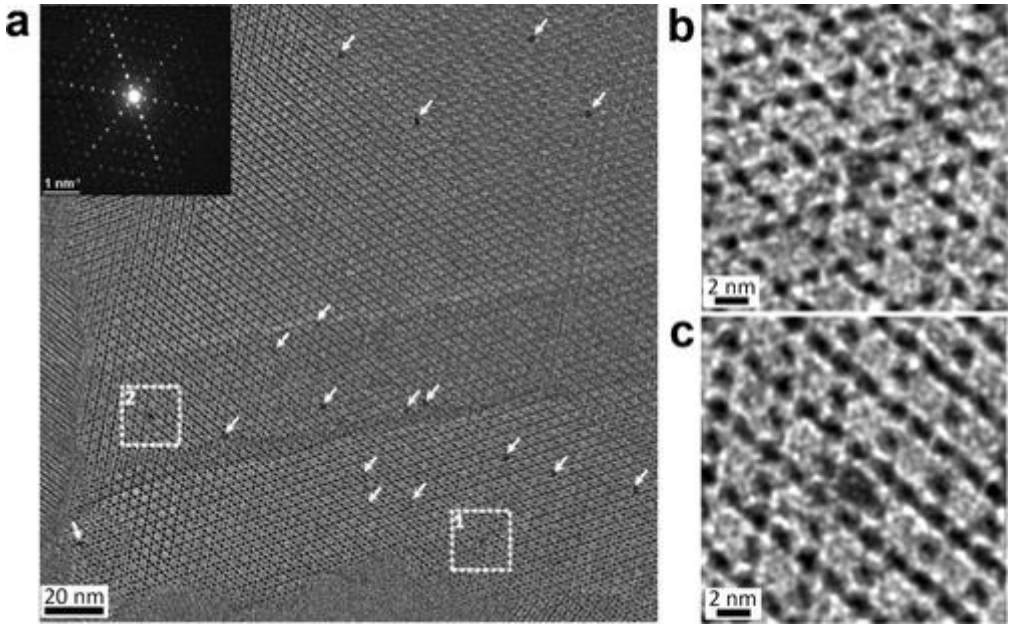

Figure i.32.- Structural characterization by HRTEM of **Mn12-ac@NU-1000**. a) HRTEM image and electron diffraction pattern (inset) of **Mn12-ac@ NU-1000** acquired along the [001] zone axis of NU-1000. Arrows indicate the observed particles that correspond to Mn12Ac. b) and c) Enlarged images of the highlighted areas in areas 1 and 2, respectively, showing that the clusters of Mn12-ac are precisely encapsulated and perfectly fitted in the hexagonal channels of NU-1000. Images were processed by using a Gaussian filter to enhance the signal-to-noise ratio. Reproduced with permission from [137]. Copyright 2019 American Chemical Society.

In those previous two examples, the SMMs were successfully introduced in diamagnetic MOFs. Therefore, the metal-organic architectures acted only as scaffolds to organize the systems without influencing the magnetic properties. Another intriguing approach could be to combine magnetically active MOFs with SMMs. Mon and co-authors [138] reported on hybrid systems combining the field-induced SMM $[Mn^{III}(TPP)(H_2O)_2]ClO_4$ (TPP = 5,10,15,20-tetraphenylporphyrin) [139,140] with the Mn^{II}

and Cu^{II} based 3D MOF $Na_4\{Mn_4[Cu_2(Me_3mpba)_2]_3\}\cdot 60H_2O$ (Me_3mpba^{4-} = N,N'-2,4,6-trimethyl-1,3-phenylenebis(oxamate)) [141], which shows long-range magnetic ordering below 15 K. The SMM was introduced within the MOF by a single-crystal to single-crystal post-synthetic procedure obtaining the hybrid **MnTPP@1**. Interestingly, the magnetic properties of both the MOF and SMM were modulated. On the one hand, measurements that were carried out with an alternating current displayed frequency independent χ_M'' signals below 20 K, indicating a long range magnetic ordering 5 K above respect to the 3D system without any incorporated SMM. Regarding slow magnetic relaxation, the hybrid system displayed frequency dependent χ_M'' signal in the absence of any external field. This unequivocally showed that the internal magnetic field provided by the ferrimagnetic MOF was able to somehow quench the fast QTM present in the unsupported compound. Moreover, an isostructural 3D compound was also synthesized by changing Mn^{II} with Mg^{II} ($Mg_2\{Mg_4[Cu_2(Me_3mpba)_2]_3\}\cdot 45H_2O$ [142]), a compound that does not show any long range magnetic ordering. By post-synthetically modifying it, they obtained another hybrid system **MnTPP@2**. Confirming the previously suggested hypothesis, no χ_M'' signal was observed in the absence of an external magnetic field, pointing out the importance of the intrinsic magnetic field in quenching the fast QTM.

Another essential feature for reading/writing processes is to orient the magnetic easy axis of the molecules perpendicular to the surface, so that many other systems have been reported which were anchored to two-dimensional layers. For example, Dreiser *et al*. reported on Er(trensal) molecules (H_3trensal = 2,2′,2″-tris-(salicylideneimino)-triethylamine) anchored to graphene (G) decoupling layers that were grown on Ru(0001) and Ir(111) single crystal surfaces [143]. For comparative purposes, they also studied Er(trensal) molecules grown in bare Ru(0001). Thus, three hybrid systems were targeted and named as **Er(trensal)/G/Ru(0001)**, **Er(trensal)/G/Ir(111)** and **Er(trensal)/Ru(0001)**. For the two former ones, scanning tunneling microscopy (STM) images showed that the lateral size of the unit cell of Er(trensal) molecules anchored to the surface was comparable to the unit cell of the model system, suggesting a similar molecular packing on the hybrid materials. In contrast, the molecules that were grown in bare Ru(0001) did not display any long-range ordering revealing the importance of implementing a decoupling graphene layer between the molecules and the metallic surfaces.

This different packing behavior was then noticeable in the *M(H)* curves obtained from low-temperature X-ray magnetic circular dichroism (XMCD) data. This technique

is capable of measuring the projection of the magnetic moment onto the beam direction. Thus, if in a certain surface all the molecules have the same orientation, the magnetic anisotropy axes of all these systems will also have the same direction. Therefore, normal and grazing incidences of the beam will show different magnetization data. When the molecules are not properly ordered within the mentioned surface, the response to the magnetic field will be the same for normal or grazing incidence. In the present case, the difference between the hybrid systems containing a decoupling G layer respect to the bare Ru(0001) was remarkable (Figure i.33). For both hybrid systems with G, the Er^{III} magnetic moment projected onto the surface normal (black data) is notably stronger than the one measured in grazing geometry (red data). Which means that the magnetic easy axes of the molecules are oriented perpendicular to the G surface, consistent with the STM data. In contrast, for Er(trensal) on bare Ru(0001), there was not any angular dependence, confirming the different adsorption conformations to the surface with random directions for the magnetic anisotropy axes. In addition to this work, other research papers such as the one reported by Marocchi and co-workers points out the importance of implementing a decoupling graphene monolayer between the SMMs and the metallic surface [144]. Besides the influence that it can have regarding the orientation and long-range ordering of the molecules, in this latter research work the graphene layer was of vital importance to maintain the nature of the target molecule. They anchored the so well-known $TbPc_2$ sandwich compounds to G/Ni(111) substrate, but when G was not used, the radical character of the phthalocyanine was lost.

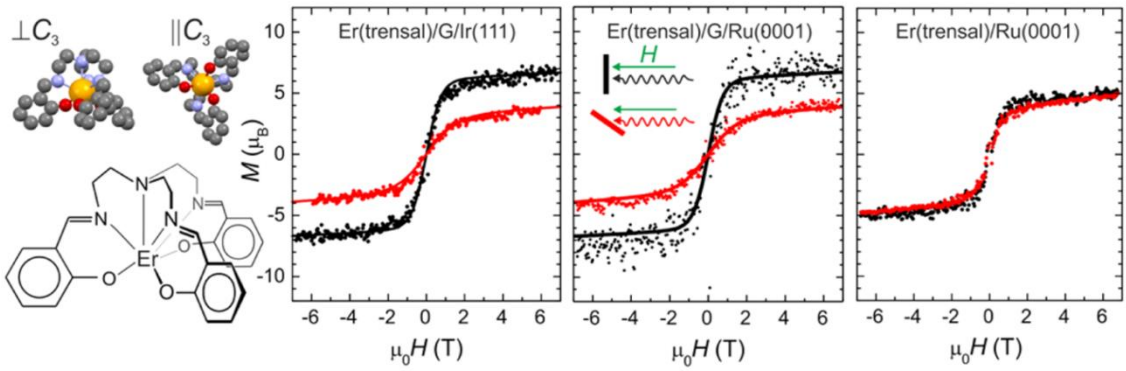

Figure i.33.- Structural views and scheme for Er(trensal) (left). Er *M(H)* from XMCD at 3 K in normal ($\theta = 0^{\circ}$) and grazing ($\theta = 65^{\circ}$) geometry for **Er(trensal)/G/Ru(0001)**, **Er(trensal)/G/Ir(111)** and **Er(trensal)/Ru(0001)**, respectively. Reproduced from [143] with *ACS Author Choice*.

Another interesting material for anchoring SMMs is a carbon nanotube (CNT). For data storage, spintronics or quantum information processing purposes, an electrical control of the material is fundamental [145,146], and since CNTs are excellent electrical conductors [147], CNT-SMM hybrids are of great interest. Moreover, due to their chemical and thermal stability, they are great candidates for fabrication [148]. CNT hybrid materials have been previously studied with gold or magnetic nanoparticles, proteins, enzymes or luminescent molecules [149–154]. These materials, however, usually display large amounts of anchored molecules per carbon nanotube, while CNT-SMM hybrids should display a very controlled amount of magnets within the nanotube.

With this purpose, Bogani *et al*. designed and synthesized the compound **i55** with general formula $[Fe_4(L)_2(dpm)_6]$ where Hdpm = dipivaloylmethane and H_3L = 2-hydroxymethyl-2-(4-(pyren-1-yl)butoxy)methylpropane-1,3-diol [155]. Noteworthy, other derivatives of this tetranuclear Fe^{III} based structures have also been extensively studied for their implementation in gold or graphene based surfaces [156–158]. For the present case, H_3L was rationally designed containing pyrene groups in the side chains, which are suitable for $\pi\cdots\pi$ interactions. Compound **i55** was proven to be an SMM displaying open hysteresis loops below 1 K. By immersion of the CNTs into solutions containing complex **i55**, they managed to synthesize the hybrid systems. AFM techniques were then used to prove the link between **i55** and CNTs. However, this strategy allowed developing systems in which the SMM is anchored in the outer surface of the CNT, thus being exposed to the outside world. Perhaps, a more interesting approach would be encapsulating the guest SMM within the carbon nanotube protecting it from the surrounding and preventing an undesired decoherence, which is fundamental for information processing purposes [159].

A clear example of this approach is the research carried out by Khlobystov and co-workers, who encapsulated Mn12-ac molecules within CNTs [160]. Firstly, considering the size of Mn12-ac, and taking into account a minimum van der Waals gap of 0.3 nm necessary between the molecules and CNTs [148], multiwalled carbon nanotubes (MWNT) were employed, whose internal diameters are found in the range of 5-50 nm (for this specific case, graphitized MWNTs, GMWNT, with internal diameter of 6.5±1.8 nm were used). Hybrid **Mn12-ac@GMWNT** (Figure i.34) were characterized by TEM showing that the SMMs were inside the nanotubes and not in the outer surface of the tubes as reported in other works where single-walled carbon nanotubes were used [155,161,162]. In addition, PXRD and TG experiments were carried out to prove that the molecules were interacting more strongly with the interior than with the exterior.

The $\chi_M''(T)$ plots for the hybrid material confirmed the retention of original SMM properties for **Mn12-ac@GMWNT**. However, the fact that two different sets of maxima appeared in this plot was justified by a tilt in a Jahn-Teller axis for a Mn^{III} species allowing an additional faster relaxation process. Hysteresis loops were found to be more influenced by QTM in the hybrid material due to larger transverse anisotropy, in fair agreement with the lower calculated energy barrier. All in all, though, these hybrid materials where the molecules were encapsulated within the nanotubes showed their great potential retaining the original SMM behavior.

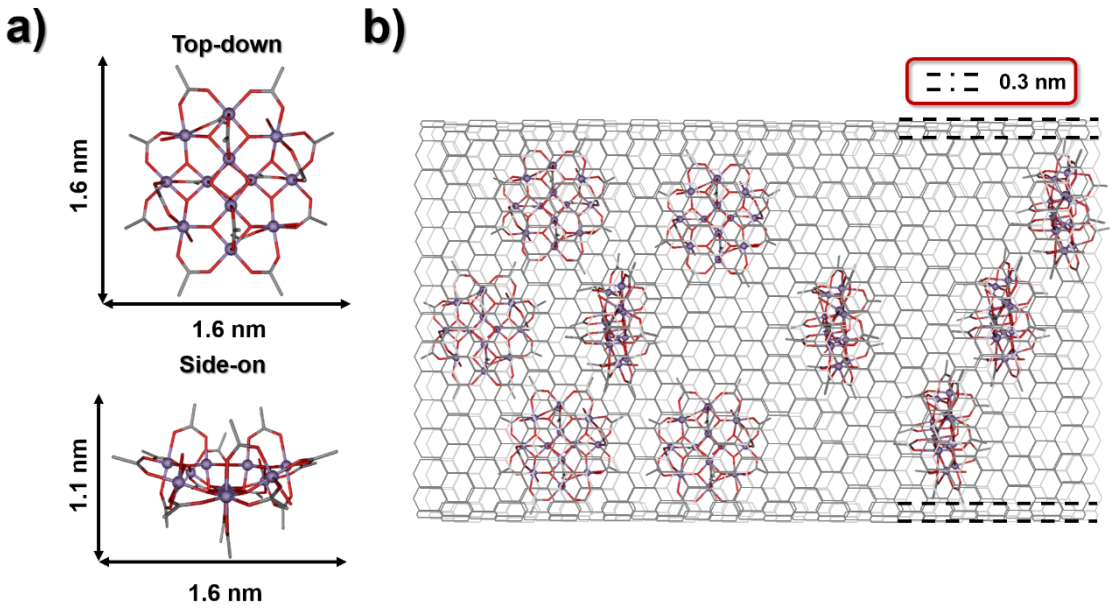

Figure i.34.- a) Structure of Mn12-ac with its dimensions. b) Schematic representation of the innermost layer of a GMWNT hosting Mn12-ac molecules. The representation is based on the original work [160].

To end this section, we would like to emphasize the relevance of implementing theory upon hybrid systems. The main handicap in these cases is that (normally) there is not a crystal structure that defines the explicit position of every single atom when the SMM is adsorbed or anchored to a surface. Therefore, this makes much harder to unequivocally define magneto-structural correlations. In this context, in 2015 Sessoli, Totti and coworkers [119] used *ab initio* molecular dynamics (AIMD) for the first time to examine the structural evolution of a previously reported SMM once adsorbed in a gold surface and, thus, they were able to predict changes in magnetic properties when going from the bulk to the anchored systems. Interestingly, they found out that

structural rearrangements induced by the surface were more relevant than electronic coupling (with gold) in the final magnetic properties of the system, which highlights the role of an appropriate ligand design.

ix. MULTIFUNCTIONAL SMMs

It is very common to find in the literature SMMs that display different functionalities and this is very interesting when the sum of them is synergistic in nature. In words of the philosopher Aristotle, multiple functionalities for a single system are justified as long as the *"whole is greater than the sum of its parts"*. The most common synergy for Ln-SMMs occurs when magnetic and luminescent properties are combined. As mentioned above, the unquenched spin-orbit coupling in Ln^{III} ions arises from the deeply buried 4f valence electrons. At the same time, the low sensitivity of these 4f electrons towards the coordination environment causes minor variations in the energy level spectrum of each Ln^{III} and, thus absorption and emission bands are very narrow giving rise to extremely pure colors. Each emission band, therefore, is a fingerprint of the ion. Along the lanthanide series, emission bands are found either in the visible (Tm^{III}, Tb^{III}, Dy^{III}, Eu^{III} and Sm^{III}; Figure i.35a) or near infrared range (Yb^{III}, Nd^{III} and Er^{III}; Figure i.35a).

The main problem to overcome arises from the fact that 4f-4f electronic transitions are parity-forbidden by the Laporte rule, which causes low brightness emissions. In addition, direct Ln^{III} excitation is not an effective strategy due to low absorption coefficients (ε). Hence, an effective way to overcome this problem is introducing the emissive ion within an organic matrix in order to sensitize the photoluminescent properties. With this purpose, organic ligands that contain wide absorption bands (ligands containing aromatic or conjugated unsaturated groups, for instance) are selected to achieve a good sensitization by the so-called *antenna-effect*. Such effect, among other factors, depends on the position of the lowest ligand triplet state (T_1, Figure i.35b) respect to the excited emissive state of the Ln^{III}. By use of the excitation light, the ligand is excited to a singlet state (S_n) from where can relax giving rise to fluorescence or it could relax to the triplet T_1 state. At the same time, from this level two things could happen: (i) the ligand can relax to the initial state emitting phosphorescence or (ii) if the energy difference between the ligand T_1 and emitting level of the Ln^{III} is in the optimal range, an energy transfer may occur sensitizing the emission of the Ln^{III} (Figure i.35b). For each trivalent lanthanide, the optimum energy difference range between these two states has been previously reported [163]. After

the sensitization process, though, the deactivation can occur through non-radiative pathways diminishing the quantum yield (Φ) of the emission. Even though we are not going to explain deep inside, these non-radiative processes, on the one hand, occur more or less depending on the Ln^{III} ion (intrinsic to the nature of the metal ion), but, on the other hand, could be enhanced by external factors. The smaller the energy gap between the emitting state and the first lower-lying energy level, the bigger the probability to observe non-radiative deactivating processes (this is one of the reasons why usually Tb^{III} based compounds display brighter emission than Dy^{III} ones, for example). Moreover, among the external luminescence quenchers, oscillators such as O-H, N-H and C-H groups are known to enhance the undesired non-radiative deactivation pathways. Thus, it is of vital importance to avoid these functional groups in close approximation of the luminophores [164,165]. Since only some of the most important features are going to be discussed along this section, the reader interested in luminescent Ln-SMMs is encouraged to read the cited literature [166–169].

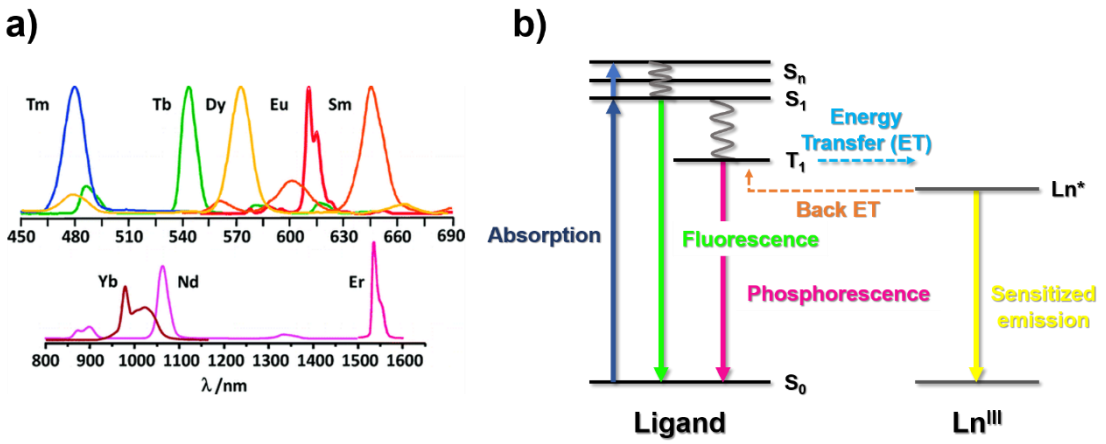

Figure i.35.- a) Emission spectra of tris-β-diketonate compounds. b) Simplified Jablonsky diagram. Reproduced with permission from [170]. Copyright 2010 American Chemical Society. Original data can be found in [171].

One of the exciting benefits of combining both magnetic and photoluminescent properties is the fact that once the molecules are anchored or attached to a surface, their emission could be used to verify the position and quantify the concentration of them in the material. Noteworthy, in order to develop bright emissions, asymmetric environments are beneficial in comparison to highly symmetric ones. This is somehow incompatible for enhanced magnetic properties, since as it has been discussed,

asymmetric features could provide the systems with transverse magnetic fields that provoke faster relaxation times and through barrier shortcuts. Therefore, when designing these bifunctional materials a compromise should be targeted.

Another interesting aspect of studying the luminescent properties is to obtain information about the crystal-field energy splitting of the ground multiplet. Usually, SMMs relax through the first excited state (or higher excited states when a strong axiality is provided to the system) and the energy splitting between the ground and this excited state is often calculated by *ab initio* computational methods. However, the narrow emission “lines” are in reality multiplets that could give us the energy splitting of the M_J sublevels [172–175]. When the excited emitting state of the Ln^{III} ion relaxes, the relaxation occurs to every M_J sublevels giving rise to the mentioned multiplet. Therefore, according to the position of each peak, the energy distribution of the states could be calculated (Figure i.36). Nevertheless, this process is not trivial. The emission multiplets are not composed only by transitions between the lowest emitting M_J and the different M_J in the ground state (these transitions are called zero-phonon bands), hot-bands and vibronic sidebands are usually present within the multiplet complicating its interpretation. Hot-bands correspond to transitions between higher M_J states of the emitting level and the ground M_J sublevels, while vibronic sidebands are a consequence of the electron-phonon coupling. Despite these drawbacks, the “quality” of the spectra could be improved by carrying out the measurements at low temperatures diminishing the contribution of the non-desired bands.

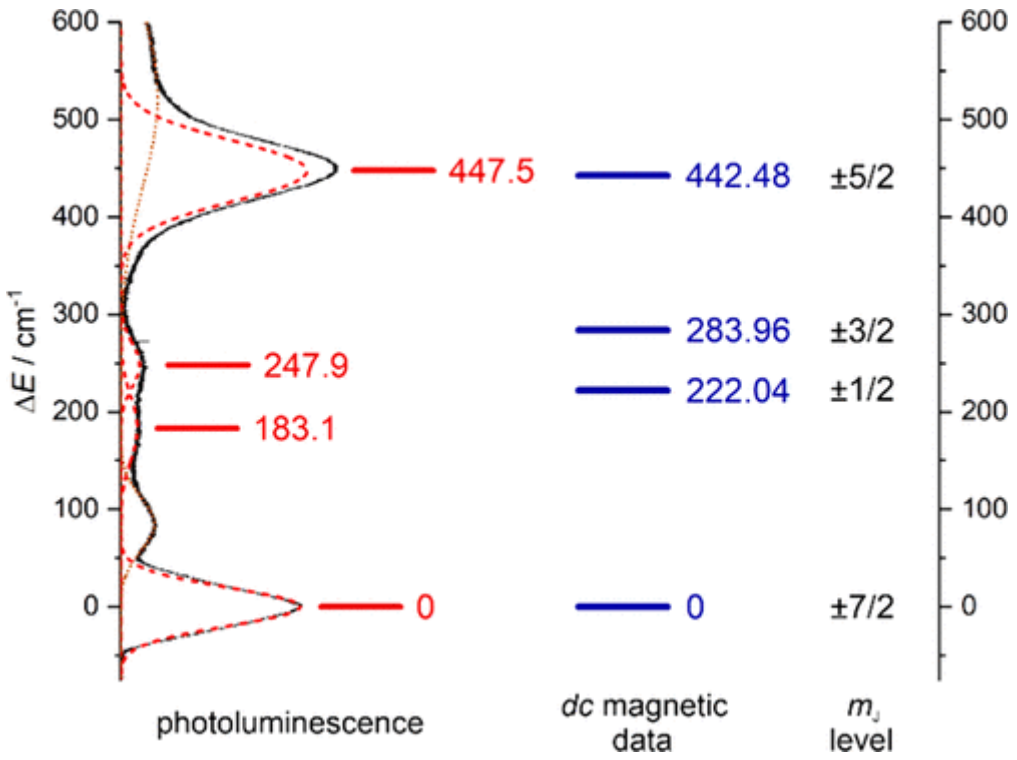

Figure i.36.- The energy level diagram of a Yb^{III} compound is shown as an example. The crystal field splitting of the ground $^2F_{7/2}$ multiplet was constructed based on the emission spectrum at 6 K (left) and based on the fitting of the *dc* magnetic data starting from *ab initio* studies (right). The presented M_J levels in the right side represent the components with the highest contribution. Reproduced with permission from [176]. Copyright 2020 American Chemical Society.

Another emerging and interesting synergy between magnetic and luminescent properties is related to SMM luminescence thermometry. As it has been shown along the entire review, temperature is a pivotal factor in determining the magnetic behavior of the systems. Below certain temperature SMMs are able to store information, while above it, the magnetization is lost at zero field and, thus there is not memory effect. Therefore, the control of the temperature within the system is essential, and taking into account that we are talking about the temperature of single molecules, conventional contact thermometers are no longer a valid alternative. An attractive opportunity to substitute these thermometers is to take advantage of the thermal variations that could be seen in the emission spectra of Ln^{III} ions. According to the temperature, the profile of the spectra may notably change and, hence, this thermal dependence of the emission signal can be used as a contactless and precise thermometer [176–180]. Anyway, the key point in combining these two features for a single system lies on the

fact that the working temperature related to magnetic memory and thermal dependence of the emission signal should overlap, which would allow to determine the temperature while the system works.

Related to photoluminescence, another emerging field is the one of circularly polarized luminescence (CPL), which could be detected when left/right circularly polarized emitted light is more intense than right/left one. Combining SMM and CPL features is captivating due to the fact that, just like SMMs (see next section), systems showing this chiroptical property are potential candidates for spintronic devices [181] and information storage [182] among other applications [183,184]. CPL is induced by chiral compounds, though the influence of achiral components such as solvent [185] or counterions [186] may play an essential role in the final result [187]. In order to quantify the effect, the luminescence dissymmetry factor g_{lum} is calculated by the following equation (the value ranges between -2 and +2):

$$g_{lum} = \frac{I_L - I_R}{1/2\,(I_L + I_R)} = \frac{\Delta I}{I} \qquad \text{(i.6)}$$

I_L and I_R stand for left and right circularly polarized emission intensity, respectively. Whereas for organic molecules or transition metal based coordination compounds small g_{lum} values (≤0.2) are usually found [188–193], the nature of the f-f transitions in Ln^{III} ions makes them potential candidates for this effect showing g_{lum} values as high as 1.45 [194]. As an example, the results of two chiral $Zn^{II}Dy^{III}$ (**i56-Λ** and **i56-Δ**) based coordination compounds are shown in Figure i.37, which have been recently reported by Sutter *et al*. [195]. These compounds exhibited slow magnetic relaxation below 12 K while g_{lum} values ranging between 0.04 and 0.18 for **i56-Λ** and between -0.04 and -0.16 for **i56-Δ** were observed vanishing at 25 K. Since CPL can be induced by magnetic fields (whether applied or intrinsic to the material) and not only by chiral environments [196], the CPL of $Zn^{II}Eu^{III}$ analogues was also studied in order to determine the nature of the optical property. Interestingly, the emission of the two circular polarizations remained exactly the same down to 5 K obtaining g_{lum} values near to zero and confirming that the structure originated CPL in those compounds was very low.

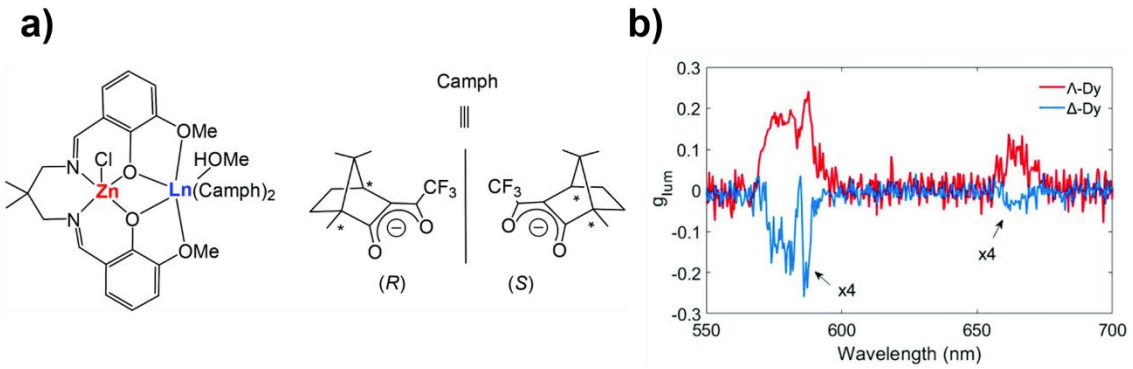

Figure i.37.- a) Scheme of the $Zn^{II}Ln^{III}$ based compounds. b) CPL dissymmetry factor glum as a function of the wavelength for **i56-Λ** and **i56-Δ** at 5 K. Reproduced with permission from [195]. Copyright 2020 the Partner Organisations.

When chirality is introduced within the molecular structure, this may give rise to a non-centrosymmetric crystal structure adopting a space group associated with one of the ten polar point groups: C_1, C_S, C_2, C_{2V}, C_3, C_{3V}, C_4, C_{4V}, C_6 and C_{6V}. These materials are potential candidates to display ferroelectricity [197]. Ferroelectrics are materials that display a spontaneous electric polarization that can be reversed by the application of an electric field. In synergy with magnetic and luminescent properties, materials with all these functionalities are considered very attractive target compounds due to their potential applicability as four-level density data storage or multifunctional sensors [198,199]. However, the many requirements (appropriate ligand fields to enhance anisotropy, good sensitization of the ion for a good emission and concrete crystallization in a space group, among others) that are needed to incorporate all these functionalities leads to a rather scarce group of materials found in the literature [200–203]. Moreover, in terms of potential applications, all the ferroelectric materials are at the same time piezoelectric, pyroelectric and they also exhibit second-harmonic generation (SHG). In contrast to perovskites, molecular materials display a much higher grade of tunability due to the flexibility of the ligands and besides they display lower density. Hence, they are an attractive alternative to them.

As last remarks for this section, SMMs with additional electrical properties have also been studied. For instance, when protic polar solvents such as alcohols or water are used, as well as counterions like sulfate, perchlorate or nitrate, it is possible to obtain hydrogen bonding networks that lie along an axis. In such cases, the materials are potential candidates to show proton conductivity [176,204]. Additionally, the idea of

combining single-molecule magnetism with electrical conductivity is also promising. In this sense, a bi-component approach has been usually employed in which the cationic or anionic extended π-structures act as electrical conductors, while the counterions contain paramagnetic ions that provide slow relaxation of the magnetization [205,206].

x. OTHER POTENTIAL APPLICATIONS FOR SMMs

In general, the introduction of this review paper has been focused on implementing SMMs in information storage devices. However, nowadays society needs more effective technologies either for information storage or information processing. For the first approach SMMs are potential candidates due to the fact that a molecule with a diameter in the 1-2 nm range would represent an information storage density of about ~30 Tbit/cm^2. For comparative purposes, in 2015 Seagate launched a hard drive with a density of 0.21 Tbit/cm^2, which is more than two orders of magnitude below the capacity of SMMs. The second approach related to a faster information processing drives us to quantum computing [207]. The traditional bit can “only” store binary information, while the qubits (quantum bits) can have both values at the same time due to their quantum nature. Since SMMs are within the interphase of classical and quantum nature, they are potential candidates for quantum computing. Shor and Grover showed that quantum computers can surpass the performance of any classical computers in terms of factoring numbers and in searching a database [208,209]. Interestingly, Grover’s algorithm was successfully implemented for molecular magnets proving their candidature for this purpose [210].

Moreover, the general necessity of miniaturizing magnetic devices leads to the possibility of studying SMMs for other emerging applications such as molecular spintronics [145], electronics [211] or magneto-optics [212]. The physics behind these other applications have been widely studied during the last years and even it is not within the scope of this research work, the interested reader is addressed to the cited literature for more details.

xi. OUTLOOK AND FUTURE PERSPECTIVES

The global trend of miniaturizing devices, including information storage devices, led to scientists to the discovery of the first SMM, Mn12-ac, a milestone in the area of

molecular materials. Along this entire review paper, we have shown that the trends towards synthesizing these materials have completely changed: starting from high spin and high nuclearity metal clusters to highly anisotropic low nuclearity systems. The last cutting edge discoveries of Dy metallocenes have somehow showed the way to follow, since one of the biggest handicaps towards incorporating them in future devices has been overcome; surpassing the temperature limit of liquid nitrogen. The unique coordination environment around the Dy^{III} ion constrains unfavorable vibrational modes that provoke QTM, an under-barrier shortcut that eclipsed the outstanding performance of several SMMs in terms of U_{eff}. Definitely, the discovery of these new systems has allowed the scientific community to create new magneto-structural correlations that facilitate novel ligand designs. In this direction, Zheng and coworkers [213] recently reported a research paper in which they improved the performance, in terms of magnetic blocking temperature, of the previously cited compound **i21** ($[Dy(O^tBu)_2(py)_5][BPh]_4$). They rationally selected another alkoxide containing a phenyl group and prepared compound **i57** with general formula $[Dy(L)_2(py)_5][BPh_4]$ (HL = (S)-(-)-1-phenylethanol). The aim of including a phenyl substituent was to provoke intra- or intermolecular interactions to stiffen the molecule and suppress QTM. As targeted, the metric parameters (bond distances and angles) for **i21** and **i57** were found to be comparable. But, additionally, **i57** displayed the expected C-H$\cdots\pi$ intramolecular interactions between hydrogen atoms belonging to equatorial pyridines and the aromatic rings in the apical chiral ligands (Figure i.38a). Moreover, intermolecular C-H$\cdots\pi$ and $\pi\cdots\pi$ interactions were also observed (Figure i.38b). According to density functional theory (DFT) calculations, the observed interactions must be strong enough to enhance the stiffness of the structure. When measuring the hysteresis loops, they found out that complex **i57** showed open hysteresis loops at considerably higher temperatures compared to **i21** and the step at zero field was less pronounced indicative of a quenching of QTM. Considering that the electronic structure calculated by *ab initio* calculations was found to be very similar for both of the compounds, the authors suggested that the alterations in the ligand periphery and modulation of vibrational modes must be the reasons of the observed magnetic properties. This work is also in agreement with a previously reported study in which Ortu and coauthors empirically proved that the molecular flexibility is related to QTM efficiency [214].

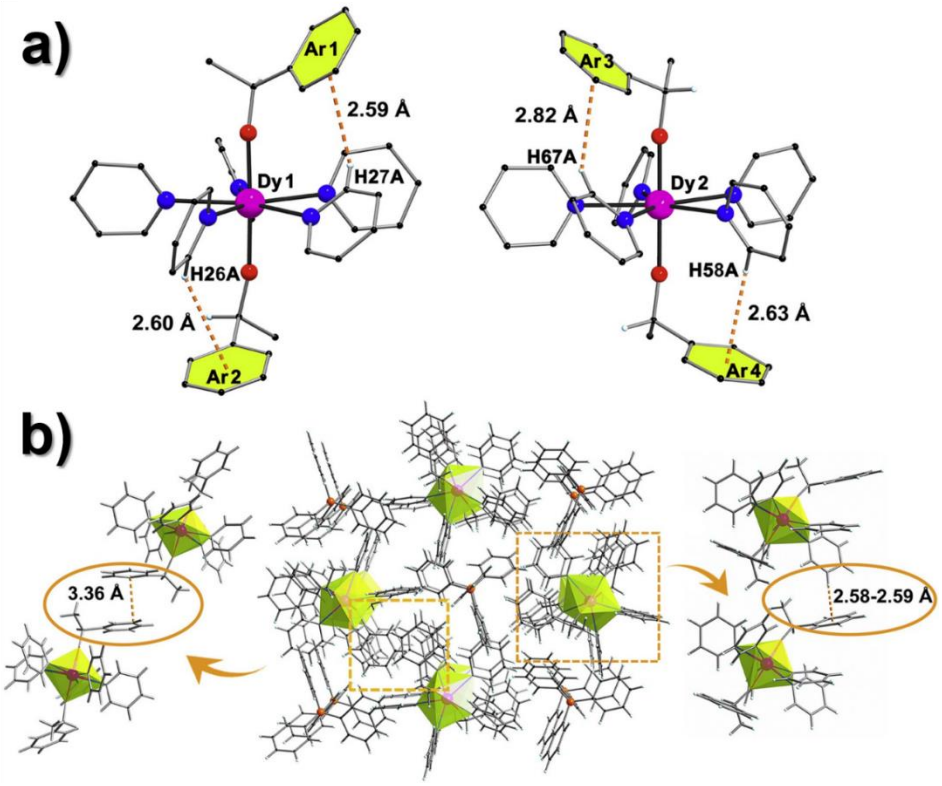

Figure i.38.- a) Structural view of compound **i57** along with intramolecular C-H···π interactions. b) Intermolecular π···π and C-H···π interactions. Color code: Dy^{III}, nitrogen, oxygen, carbon and hydrogen in fuchsia, blue, red, black and white, respectively. Reproduced from [213].

However, as discussed, new theoretical basis is of vital importance in order to deeply understand spin-phonon interactions and under-barrier shortcuts that determine the T_B. In fact, even though we are able to evaluate the effect of these interactions in terms of Orbach process, it has been seen that the blocking temperatures are highly influenced by Raman mechanism [215]. Chilton *et al*. made a study selecting some of the reported high performing SMMs (U_{eff} > 600 K) and concluded that there could be a correlation between T_B and the point at which Raman relaxation starts to operate [216]. Note that the T_B values that we mention in this work are referred to the ones obtained by FC/ZFC measurements. This specific relaxation time at which Raman starts to operate was named as τ_{switch}. By plotting $log_{10}(T_B)$ *vs* $log_{10}(\tau_{switch})$ they found a clear linear correlation. Thus, as mentioned, there might be a strong link between T_B and the relaxation time at the point at which Raman mechanism operates over the Orbach. Hence, the authors emphasize that further studies are of vital importance in order to

better understand this mechanism and to be able to improve chemical design principles for improved SMMs.

A last worth mentioning branch related to lanthanides is the field of clusterfullerenes. Very promising research works have been reported encapsulating Ln^{III} ions inside fullerenes [217–219]. These kind of materials show favorable properties such as thermal and chemical stability in contrast to the air sensitivity of the record breaking metallocenes. Moreover, the particularly short Ln-X (X = N^{3-}, S^{2-} or O^{2-}) bonds that can be obtained inside the fullerenes provide strong magnetic anisotropy as well as strong exchange interactions. The interested reader is encouraged to read the cited papers as well as the research progress that has been done implementing these materials into surfaces [220–222] and theoretical calculations [116] that have been carried out for a deeper understanding of these systems.

In general, it seems that the employment of lanthanides is a very promising way to follow. Indeed, they have opened a wide variety of possibilities to combine multiple functionalities in a single system breaking new ground with synergistic applications. However, this does not mean that transition metals are discarded for future devices. In fact, very recently some researchers have successfully combined large magnetic anisotropy along with strong ferromagnetic interactions for high spin ground states in transition metal clusters. Nevertheless, this was done in a novel way, since direct metal-metal orbital overlap was involved opening a new variant in the design of SMMs.

Long and co-workers synthesized the isostructural tetranuclear $M_4(NP^tBu_3)_4 \cdot n\text{-}C_6H_{14}$ (M^I = Ni^I (**i58**) or Cu^I (**i59**); ^{t}Bu = tert-butyl) compounds [223] following a modified previously reported procedure [224] and by protonolysis of mesitylcopper(I), respectively (Figure i.39, left). Furthermore, the oxidized $[M_4(NP^tBu_3)_4][B(C_6F_5)_4]$ ($M^{I/II}$ = $Ni^{I/II}$ (**i60**) or $Cu^{I/II}$ (**i61**) were also studied. In **i58**, the two coordinate Ni^I ions lie in the same plane displaying almost linear N-Ni-N angles (174.4(6)˚ in average), which has been shown to be effective in order to enhance magnetic anisotropy. Moreover, the average Ni-Ni distances are of 2.3631(1) Å falling in the range of metal-metal interactions [225]. After one electron oxidation in **i60**, the fact that all bond distances decrease precludes identifying a localized oxidized site within the structure confirming the delocalized character of the electrons in the metal-metal bonded cluster (further electrochemical experiments, as well as *dc* magnetic measurements were carried out to confirm this fact).

Easy axis and easy plane types of magnetic anisotropy were calculated for **i58** and **i60**, respectively with relatively high values of *D* (*D* = -1.93 and -1.74 cm^{-1} for **i58** calculated from magnetic and EPR measurements, respectively and *D* = +7.95 and +9.2 cm^{-1} for **i60**). However, the easy axis type compound **i58** did not displayed any slow magnetic relaxation probably due to a small energy separation between the ground and first excited state. As shown in the literature [226,227], Kramers ions with *D* > 0 can show SMM behavior under an external magnetic field and thus, **i60** was also a potential candidate. At zero field, no out-of-phase signal was detected, but under a small external field of 400 Oe χ_M'' peaks were observed in the 1.85-2.05 K temperature range with a calculated U_{eff} of 23.78 K (16.53 cm^{-1}). Furthermore, the fit of the relaxation times suggested that only Orbach mechanism was operative within the examined temperature range in contrast to other reported easy plane SMMs [228]. More interestingly, *ac* measurements carried out in frozen solution of **i60** showed slow magnetic relaxation under zero applied *dc* field confirming that dipolar interactions were at least partially responsible of originating zero field QTM. As far as we know, this is the first reported example of a zero field SMM with *D* > 0. Finally, compound **i61** displayed field induced SMM behavior relaxing through Raman and direct processes, since there is no magnetic excited state for a *S* = 1/2 system. Unequivocally, these new type of clusters with direct metal-metal orbital overlap open a new route for the design of SMMs. In fact, very recently some other systems have been reported for Co^{II} [229] or $Fe^{I/II}$ systems [230], for example (see Figure i.39).

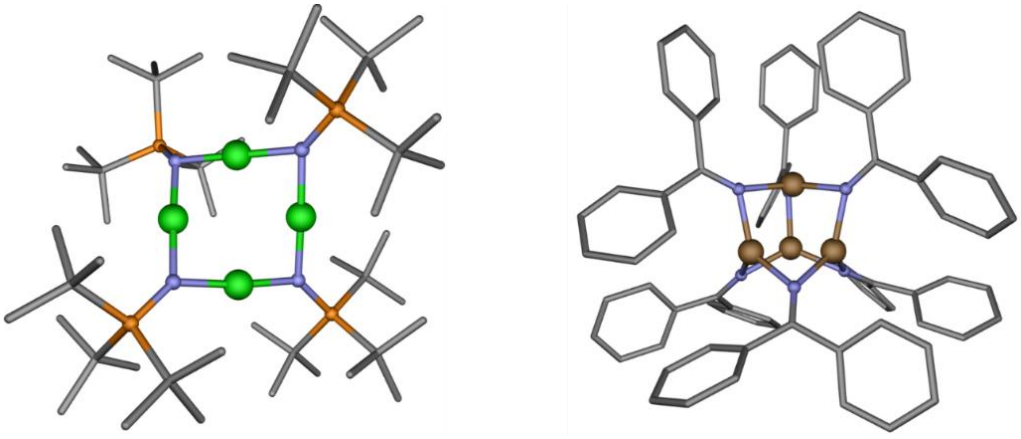

Figure i.38.- Perspective view of compounds **i58** (left) and a Fe based compound (right). Color code: Ni^{I}, Fe^{I}/Fe^{II}, carbon, nitrogen and phosphor in green, brown, grey, blue and orange, respectively. Hydrogen atoms, counterions and solvent molecules have been omitted for the sake of clarity. Generated from the crystal structures in references [223] and [230].

The interest regarding high nuclearity metal clusters remains also intact. For instance, Abbasi and co-authors recently published a novel mixed valence Mn_{31} structure with the general formula $[Mn_{31}O_{24}(OH)_2(OMe)_{24}(O_2CPh)_{16}(rac\text{-mpm})_2]$ (**i62**), where mpmH = *α*-methyl-2-pyridine-methanol [231]. Within the structure, $\{Mn^{II}_2Mn^{III}_{28}Mn^{IV}\}$ ions were found, where most of the Mn^{III} ions displayed Jahn-Teller axes parallel to each other indicative of a possible $D \neq 0$. Consequently, slow magnetic relaxation was observed for **i62** with a calculated U_{eff} of 58 K and hysteresis loops below 5 K. This value of the effective energy barrier is large when talking about 3d based SMMs [232,233]. But more interestingly, although **i62** is comparable in size to other magnetic nanoparticles, below 0.5 K displays quantum phenomena. Therefore, these kind of compounds could be very interesting to investigate the limit between SMMs and magnetic nanoparticles.

Even though their impact or future perspectives are not potentially so promising, field induced SMMs based on isotropic metal ions also have their own place in this field. More specifically, complexes containing almost isotropic Mn^{II} [234], Fe^{III} [235] or Gd^{III} [236–240] ions have been reported showing slow magnetic relaxation under the presence of an external magnetic field. Moreover, the use of actinides is also being studied [241,242]. They show stronger spin-orbit coupling and, in consequence, they may show enhanced magnetic anisotropy. Within the series, particularly U^{III} based compounds have been reported [243–245], though uranium compounds in other oxidation states or SMMs with other actinides such as Np have also been studied [246].

All in all, the field of SMMs can be considered as a young field barely reaching three decades of life since the discovery of Mn12-ac. In all these years synthetic and computational chemists, as well as physicists, have coexisted combining new synthetic strategies and theoretical knowledge, fundamental to understand quantum physics determining the slow relaxation of the magnetization. Thus, we would like to remark the importance of combining these two fields. Synthetic chemists have shown the ability to design and synthesize compounds almost *à la carte*, but theoretical chemists and physics have a pivotal role in explaining the quantum phenomena behind SMMs.

xii. OBJECTIVES

Basically, the initial objectives to fulfill within this work are the following ones:

1. Prepare mononuclear Dy^{III} and Er^{III} based compounds with novel and already known (but similar between them) compartmental Mannich base ligands and study their dynamic magnetic properties. This study will allow us to provide interesting magneto-structural correlations to better understand the factors governing the slow relaxation of the magnetization.

2. As a continuation of our previously reported research (*CrystEngComm*, 2017, **19**, 256), replace the bridging acetate group in the $Zn^{II}Dy^{III}$ system by a wide range of di- and tricarboxylate groups in order to exted the dinuclear entities obtaining polynuclear systems. By maintaining the same core structure, see how subtle modifications in the coordination sphere (which could be related to the stiffness of the bridging group) tune the dynamic magnetic properties. Additionally, study the photoluminescent properties of the polynuclear compounds in which the bridging group (aliphatic or aromatic) may play an essential role sensitizing the emission of the Dy^{III} ion.

3. Prepare homopolynuclear Co^{II} based compounds varying the bridging ligands in order to see which kind of groups could give rise to either ferro- or antiferromagnetic exchange couples sysems.

4. Combine paramagnetic 3d and 4f systems within the same structure and study their magnetic properties. As it has been seen in the literature, exchange coupled systems could show an enhanced SMM behavior due to a more effective suppression of the ground QTM, or even TA-QTM. Prepare isostructural compounds with a single paramagnetic ion replacing the other one by a diamagnetic ion. Evaluate the differences between two types of systems.

5. Prepare novel Mannich base ligands and synthesize lanthanide based compounds with enhanced effective energy barriers. Try to find magneto-structural correlations that allow an improved ligand field design.

6. Evaluate the photoluminescent properties of other lathanide based compounds such as Sm^{III}, Eu^{III}, Tb^{III} or Yb^{III}, which could give rise to emissive properties in the visible or in the near infrared region.

7. Try to anchor SMMs with interesting magnetic properties to a surface as a first step towards future devices. Evaluate the magnetic properties of the hybrid system.

xiii. REFERENCES

[1] R. Sessoli, D. Gatteschi, A. Caneschi, M.A. Novak, Magnetic bistability in a metal-ion cluster, Nature. 365 (1993) 141–143. https://doi.org/10.1038/365141a0.

[2] A. Zabala-Lekuona, Iman Molekularrak: Informazio unitate txikienaren bila, Ekaia. 35 (2019) 85–99. https://doi.org/0.1387/ekaia.19692.

[3] A. Abragam, B. Bleaney, Electron Paramagnetic Resonance of Transition Ions, Clarendon Press Oxford, UK,. (1970) 925.

[4] J.H. Van Vleck, Paramagnetic relaxation times for titanium and chrome alum, Phys. Rev. 57 (1940) 426–447. https://doi.org/10.1103/PhysRev.57.426.

[5] H.B.G. Casimir, D. Bijl, F.K. Du Pré, Measurememts on paramagnetic relaxation in chromium potassium alum, Physica. 8 (1941) 449–460. https://doi.org/10.1016/S0031-8914(41)90066-6.

[6] K.S. Cole, R.H. Cole, Dispersion and absorption in dielectrics I. Alternating current characteristics, J. Chem. Phys. 9 (1941) 341–351. https://doi.org/10.1063/1.1750906.

[7] I.F. Díaz-Ortega, J.M. Herrera, D. Aravena, E. Ruiz, T. Gupta, G. Rajaraman, H. Nojiri, E. Colacio, Designing a Dy2 Single-Molecule Magnet with Two Well-Differentiated Relaxation Processes by Using a Nonsymmetric Bis-bidentate Bipyrimidine- N-Oxide Ligand: A Comparison with Mononuclear Counterparts, Inorg. Chem. 57 (2018) 6362–6375. https://doi.org/10.1021/acs.inorgchem.8b00427.

[8] L. Zhang , J. Jung, P. Zhang, M. Guo, L. Zhao, J. Tang, B. Le Guennic, Site-Resolved Two-Step Relaxation Process in an Asymmetric Dy $_2$ Single-Molecule Magnet, Chem. - A Eur. J. 22 (2016) 1392–1398. https://doi.org/10.1002/chem.201503422.

[9] E. Echenique-Errandonea, A. Zabala-Lekuona, J. Cepeda, A. Rodríguez-Diéguez, J.M. Seco, I. Oyarzabal, E. Colacio, Effect of the change of the ancillary carboxylate bridging ligand on the SMM and luminescence properties of a series of carboxylate-diphenoxido triply bridged dinuclear ZnLn and tetranuclear Zn 2 Ln 2 complexes (Ln = Dy, Er), Dalton Trans. 48 (2019) 190–201. https://doi.org/10.1039/c8dt03800g.

[10] C. Shi, R. Nie, X. Yao, S. Fan, G. An, Y. Dong, G. Li, Asymmetry-unit-dominated double slow-relaxation modes of 2,6-dimethyl-3,5-heptanedione dysprosium SMMs, RSC Adv. 7 (2017) 49701–49709. https://doi.org/10.1039/c7ra09711e.

[11] J. Ruiz, A.J. Mota, A. Rodríguez-Diéguez, S. Titos, J.M. Herrera, E. Ruiz, E. Cremades, J.P. Costes, E. Colacio, Field and dilution effects on the slow relaxation of a luminescent DyO9 low-symmetry single-ion magnet, Chem. Commun. 48 (2012) 7916–7918. https://doi.org/10.1039/c2cc32518g.

[12] B. Liu, B. Wang, Z. Wang, S. Gao, Static field induced magnetic relaxations in dinuclear lanthanide compounds of [phen 2Ln 2(HCOO) 4(HCOO) 2-2x (NO 3) 2x] (1, Ln = Gd and x = 0.52; 2, Ln = Er and x = 0.90; Phen = 1,10-phenanthroline), Sci. China Chem. 55 (2012) 926–933. https://doi.org/10.1007/s11426-012-4599-5.

[13] A. Arauzo, A. Lazarescu, S. Shova, E. Bartolomé, R. Cases, J. Luzón, J. Bartolomé, C. Turta, Structural and magnetic properties of some lanthanide (Ln = Eu(iii), Gd(iii) and Nd(iii)) cyanoacetate polymers: Field-induced slow magnetic relaxation in the Gd and Nd substitutions, Dalton Trans. 43 (2014) 12342–12356. https://doi.org/10.1039/c4dt01104j.

[14] D. Reta, N.F. Chilton, Uncertainty estimates for magnetic relaxation times and magnetic relaxation parameters, Phys. Chem. Chem. Phys. 21 (2019) 23567–23575. https://doi.org/10.1039/c9cp04301b.

[15] O. Kahn, Molecular magnetism, VCH, Weinheim, Germany, 1993.

[16] T. Glaser, H. Theil, I. Liratzis, T. Weyhermüller, E. Bill, Ferromagnetic coupling by orthogonal magnetic orbitals in a heterodinuclear CuIIVIV=O complex and in a homodinuclear Cu IICuII complex, Inorg. Chem. 45 (2006) 4889–4891. https://doi.org/10.1021/ic0606328.

[17] T. Glaser, M. Gerenkamp, R. Fröhlich, Targeted Synthesis of Ferromagnetically Coupled

Complexes with Modified 1,3,5-Trihydroxybenzene Ligands, Angew. Chem. Int. Ed. 41 (2002) 3823–3825. https://doi.org/10.1002/1521-3773(20021018)41:20<3823::AID-ANIE3823>3.0.CO;2-I.

[18] T. Glaser, T. Beissel, E. Bill, T. Weyhermüller, V. Schünemann, W. Meyer-Klaucke, A.X. Trautwein, K. Wieghardt, Electronic structure of linear thiophenolate-bridged heterotrinuclear complexes [LFeMFeL](n+) (M = Cr, Co, Fe; n = 1-3): Localized vs delocalized models, J. Am. Chem. Soc. 121 (1999) 2193–2208. https://doi.org/10.1021/ja982898m.

[19] C. Beghidja, G. Rogez, J. Kortus, M. Wesolek, R. Welter, Very strong ferromagnetic interaction in a new binuclear μ-methoxo-bridged Mn(III) complex: Synthesis, crystal structure, magnetic properties, and DFT calculations, J. Am. Chem. Soc. 128 (2006) 3140–3141. https://doi.org/10.1021/ja0575023.

[20] A. Ferguson, J. Lawrence, A. Parkin, J. Sanchez-Benitez, K. V. Kamenev, E.K. Brechin, W. Wernsdorfer, S. Hill, M. Murrie, Synthesis and characterisation of a Ni4 single-molecule magnet with S4 symmetry, J. Chem. Soc. Dalt. Trans. (2008) 6409–6414. https://doi.org/10.1039/b807447j.

[21] G.S. Papaefstathiou, A. Escuer, C.P. Raptopoulou, A. Terzis, S.P. Perlepes, R. Vicente, Defective Double-Cubane, Tetranuclear Manganese(II) and Cobalt(II) Complexes with Simultaneous μ1,1-Azido and μ-O Bridges, Eur. J. Inorg. Chem. 2001 (2001) 1567–1574. https://doi.org/10.1002/1099-0682(200106)2001:6<1567::aid-ejic1567>3.0.co;2-7.

[22] G.S. Papaefstathiou, A. Escuer, R. Vicente, M. Font-Bardia, X. Solans, S.P. Perlepes, Reactivity in polynuclear transition metal chemistry as a means to obtain high-spin molecules: Substitution of μ4-OH− by η1,μ4-N3− increases nine times the ground-state S value of a nonanuclear nickel(II) cage, Chem. Commun. 1 (2001) 2414–2415. https://doi.org/10.1039/b106472j.

[23] D.M. Low, L.F. Jones, A. Bell, E.K. Brechin, T. Mallah, E. Rivière, S.J. Teat, E.J.L. McInnes, Solvothermal synthesis of a tetradecametallic FeIII cluster, Angew. Chem. Int. Ed. 42 (2003) 3781–3784. https://doi.org/10.1002/anie.200351865.

[24] J. Larionova, M. Gross, M. Pilkington, H. Andres, H. Stoeckli-Evans, H.U. Güdel, S. Decurtins, High-spin molecules: A novel cyano-bridged Mn9/(II)Mo6/(V) molecular cluster with a S = 51/2 ground state and ferromagnetic intercluster ordering at low temperatures, Angew. Chem. Int. Ed. 39 (2000) 1605–1609. https://doi.org/10.1002/(SICI)1521-3773(20000502)39:9<1605::AID-ANIE1605>3.0.CO;2-5.

[25] M. Affronte, J.C. Lasjaunias, W. Wernsdorfer, R. Sessoli, D. Gatteschi, S.L. Heath, A. Fort, A. Rettori, Magnetic ordering in a high-spin Fe19 molecular nanomagnet, Phys. Rev. B. 66 (2002) 644081–644087. https://doi.org/10.1103/PhysRevB.66.064408.

[26] A.M. Ako, I.J. Hewitt, V. Mereacre, R. Clérac, W. Wernsdorfer, C.E. Anson, A.K. Powell, A ferromagnetically coupled Mn19 aggregate with a record S = 83/2 ground spin state, Angew. Chem. Int. Ed. 45 (2006) 4926–4929. https://doi.org/10.1002/anie.200601467.

[27] M. Murugesu, M. Habrych, W. Wernsdorfer, K.A. Abboud, G. Christou, Single-Molecule Magnets: A Mn25 Complex with a Record S = 51/2 Spin for a Molecular Species, J. Am. Chem. Soc. 126 (2004) 4766–4767. https://doi.org/10.1021/ja0316824.

[28] J. Cirera, E. Ruiz, S. Alvarez, F. Neese, J. Kortus, How to build molecules with large magnetic anisotropy, Chem. - A Eur. J. 15 (2009) 4078–4087. https://doi.org/10.1002/chem.200801608.

[29] A. Sieber, R. Bircher, O. Waldmann, G. Carver, G. Chaboussant, H. Mutka, H.-U. Güdel, Effect of Pressure on the Magnetic Anisotropy in the Single-Molecule Magnet Mn12-Acetate: An Inelastic Neutron Scattering Study, Angew. Chem. Int. Ed. 44 (2005) 4239–4242. https://doi.org/10.1002/anie.200500171.

[30] F. Neese, D. a Pantazis, What is not required to make a single molecule magnet., Faraday Discuss. 148 (2011) 229–238; discussion 299-314. https://doi.org/10.1039/c005256f.

[31] P.P. Power, Stable two-coordinate, open-shell (d 1-d 9) transition metal complexes, Chem. Rev. 112 (2012) 3482–3507. https://doi.org/10.1021/cr2004647.

[32] R. Ruamps, L.J. Batchelor, R. Maurice, N. Gogoi, P. Jiménez-Lozano, N. Guihéry, C. Degraaf, A.L. Barra, J.P. Sutter, T. Mallah, Origin of the magnetic anisotropy in heptacoordinate NiII and CoII complexes, Chem. - A Eur. J. 19 (2013) 950–956. https://doi.org/10.1002/chem.201202492.

[33] Y. Rechkemmer, F.D. Breitgoff, M. Van Der Meer, M. Atanasov, M. Hakl, M. Orlita, P. Neugebauer, F. Neese, B. Sarkar, J. Van Slageren, A four-coordinate cobalt(II) single-ion magnet with coercivity and a very high energy barrier, Nat. Commun. 7 (2016) 10467. https://doi.org/10.1038/ncomms10467.

[34] J.M. Frost, K.L.M. Harriman, M. Murugesu, The rise of 3-d single-ion magnets in molecular magnetism: Towards materials from molecules?, Chem. Sci. 7 (2016) 2470–2491.

https://doi.org/10.1039/c5sc03224e.
[35] S. Gómez-Coca, D. Aravena, R. Morales, E. Ruiz, Large magnetic anisotropy in mononuclear metal complexes, Coord. Chem. Rev. 289–290 (2015) 379–392. https://doi.org/10.1016/j.ccr.2015.01.021.
[36] M. Feng, M.L. Tong, Single Ion Magnets from 3d to 5f: Developments and Strategies, Chem. - A Eur. J. 24 (2018) 7574–7594. https://doi.org/10.1002/chem.201705761.
[37] S. Tripathi, A. Dey, M. Shanmugam, R.S. Narayanan, V. Chandrasekhar, Cobalt(II) complexes as single-ion magnets, in: Top. Organomet. Chem., Springer, 2019: pp. 35–75. https://doi.org/10.1007/3418_2018_8.
[38] G.A. Craig, M. Murrie, 3d single-ion magnets, Chem. Soc. Rev. 44 (2015) 2135–2147. https://doi.org/10.1039/c4cs00439f.
[39] W.M. Reiff, A.M. LaPointe, E.H. Witten, Virtual free ion magnetism and the absence of Jahn-Teller distortion in a linear two-coordinate complex of high-spin iron(II), J. Am. Chem. Soc. 126 (2004) 10206–10207. https://doi.org/10.1021/ja030632w.
[40] W.M. Reiff, C.E. Schulz, M.H. Whangbo, J.I. Seo, Y.S. Lee, G.R. Potratz, C.W. Spicer, G.S. Girolami, Consequences of a linear two-coordinate geometry for the orbital magnetism and Jahn-Teller distortion behavior of the high spin iron(II) complex Fe[N(t-Bu)2]2, J. Am. Chem. Soc. 131 (2009) 404–405. https://doi.org/10.1021/ja806660f.
[41] W.A. Merrill, T.A. Stich, M. Brynda, G.J. Yeagle, J.C. Fettinger, R. De Hont, W.M. Reiff, C.E. Schulz, R.D. Britt, P.P. Power, Direct spectroscopic observation of large quenching of first-order orbital angular momentum with bending in monomeric, two-coordinate Fe(II) primary amido complexes and the profound magnetic effects of the absence of Jahnand- and Renner-Teller distortions in rigorously linear coordination, J. Am. Chem. Soc. 131 (2009) 12693–12702. https://doi.org/10.1021/ja903439t.
[42] J.M. Zadrozny, M. Atanasov, A.M. Bryan, C.Y. Lin, B.D. Rekken, P.P. Power, F. Neese, J.R. Long, Slow magnetization dynamics in a series of two-coordinate iron(ii) complexes, Chem. Sci. 4 (2013) 125–138. https://doi.org/10.1039/c2sc20801f.
[43] M. Atanasov, J.M. Zadrozny, J.R. Long, F. Neese, A theoretical analysis of chemical bonding, vibronic coupling, and magnetic anisotropy in linear iron(ii) complexes with single-molecule magnet behavior, Chem. Sci. 4 (2013) 139–156. https://doi.org/10.1039/c2sc21394j.
[44] J.M. Zadrozny, D.J. Xiao, M. Atanasov, G.J. Long, F. Grandjean, F. Neese, J.R. Long, Magnetic blocking in a linear iron(I) complex, Nat. Chem. 5 (2013) 577–581. https://doi.org/10.1038/nchem.1630.
[45] M. Dey, N. Gogoi, Geometry-mediated enhancement of single-ion anisotropy: A route to single-molecule magnets with a high blocking temperature, Angew. Chem. Int. Ed. 52 (2013) 12780–12782. https://doi.org/10.1002/anie.201304982.
[46] J.M. Frost, K.L.M. Harriman, M. Murugesu, The rise of 3-d single-ion magnets in molecular magnetism: towards materials from molecules?, Chem. Sci. 7 (2016) 2470–2491. https://doi.org/10.1039/C5SC03224E.
[47] Y.S. Meng, Z. Mo, B.W. Wang, Y.Q. Zhang, L. Deng, S. Gao, Observation of the single-ion magnet behavior of d8 ions on two-coordinate Co(i)-NHC complexes, Chem. Sci. 6 (2015) 7156–7162. https://doi.org/10.1039/c5sc02611c.
[48] X.N. Yao, J.Z. Du, Y.Q. Zhang, X.B. Leng, M.W. Yang, S. Da Jiang, Z.X. Wang, Z.W. Ouyang, L. Deng, B.W. Wang, S. Gao, Two-coordinate Co(II) imido complexes as outstanding single-molecule magnets, J. Am. Chem. Soc. 139 (2017) 373–380. https://doi.org/10.1021/jacs.6b11043.
[49] J. Du, L. Wang, M. Xie, L. Deng, A Two-Coordinate Cobalt(II) Imido Complex with NHC Ligation: Synthesis, Structure, and Reactivity, Angew. Chem. Int. Ed. 54 (2015) 12640–12644. https://doi.org/10.1002/anie.201505937.
[50] P.C. Bunting, M. Atanasov, E. Damgaard-Møller, M. Perfetti, I. Crassee, M. Orlita, J. Overgaard, J. Van Slageren, F. Neese, J.R. Long, A linear cobalt(II) complex with maximal orbital angular momentum from a non-Aufbau ground state, Science. 362 (2018) 3719. https://doi.org/10.1126/science.aat7319.
[51] M. Atanasov, D. Aravena, E. Suturina, E. Bill, D. Maganas, F. Neese, First principles approach to the electronic structure, magnetic anisotropy and spin relaxation in mononuclear 3d-transition metal single molecule magnets, Coord. Chem. Rev. 289–290 (2015) 177–214. https://doi.org/10.1016/j.ccr.2014.10.015.
[52] T. Viefhaus, W. Schwarz, K. Hübler, K. Locke, J. Weidlein, Das unterschiedliche Reaktionsverhalten von basefreiem Tris(trimethylsilyl)methyl-Lithium gegenüber den

Trihalogeniden der Erdmetalle und des Eisens, Zeitschrift Fur Anorg. Und Allg. Chemie. 627 (2001) 715–725. https://doi.org/10.1002/1521-3749(200104)627:4<715::aid-zaac715>3.0.co;2-0.

[53] J.M. Zadrozny, D.J. Xiao, M. Atanasov, G.J. Long, F. Grandjean, F. Neese, J.R. Long, Magnetic blocking in a linear iron(I) complex, Nat. Chem. 5 (2013) 577–581. https://doi.org/10.1038/nchem.1630.

[54] N.H. Buttrus, C. Eaborn, P.B. Hitchcock, J.D. Smith, A.C. Sullivan, Preparation and crystal structure of a two-co-ordinate manganese compound, bis[tris(trimethyl)silylmethyl]manganese, J. Chem. Soc. Chem. Commun. (1985) 1380–1381. https://doi.org/10.1039/c39850001380.

[55] C.Y. Lin, J.C. Fettinger, N.F. Chilton, A. Formanuik, F. Grandjean, G.J. Long, P.P. Power, Salts of the two-coordinate homoleptic manganese(i) dialkyl anion [Mn{C(SiMe3)3}2]- with quenched orbital magnetism, Chem. Commun. 51 (2015) 13275–13278. https://doi.org/10.1039/c5cc05166e.

[56] P.E. Kazin, M.A. Zykin, L.A. Trusov, A.A. Eliseev, O. V. Magdysyuk, R.E. Dinnebier, R.K. Kremer, C. Felser, M. Jansen, A Co-based single-molecule magnet confined in a barium phosphate apatite matrix with a high energy barrier for magnetization relaxation, Chem. Commun. 53 (2017) 5416–5419. https://doi.org/10.1039/c7cc02453c.

[57] I.G. Rau, S. Baumann, S. Rusponi, F. Donati, S. Stepanow, L. Gragnaniello, J. Dreiser, C. Piamonteze, F. Nolting, S. Gangopadhyay, O.R. Albertini, R.M. Macfarlane, C.P. Lutz, B.A. Jones, P. Gambardella, A.J. Heinrich, H. Brune, Reaching the magnetic anisotropy limit of a 3d metal atom, Science. 344 (2014) 988–992. https://doi.org/10.1126/science.1252841.

[58] N. Ishikawa, M. Sugita, T. Ishikawa, S.Y. Koshihara, Y. Kaizu, Lanthanide double-decker complexes functioning as magnets at the single-molecular level, J. Am. Chem. Soc. 125 (2003) 8694–8695. https://doi.org/10.1021/ja029629n.

[59] N. Koike, H. Uekusa, Y. Ohashi, C. Harnoode, F. Kitamura, T. Ohsaka, K. Tokuda, Relationship between the Skew Angle and Interplanar Distance in Four Bis(phthalocyaninato)lanthanide(III) Tetrabutylammonium Salts ([NBu4n][LnIIIPc2]; Ln = Nd, Gd, Ho, Lu), Inorg. Chem. 35 (1996) 5798–5804. https://doi.org/10.1021/ic960158d.

[60] J. Rinehart, J. Long, Exploiting single-ion anisotropy in the design of f-element single-molecule magnets, Chem. Sci. 2 (2011) 2078–2085. https://doi.org/10.1039/c1sc00513h.

[61] F. Habib, G. Brunet, V. Vieru, I. Korobkov, L.F. Chibotaru, M. Murugesu, Significant enhancement of energy barriers in dinuclear dysprosium single-molecule magnets through electron-withdrawing effects, J. Am. Chem. Soc. 135 (2013) 13242–13245. https://doi.org/10.1021/ja404846s.

[62] J. Long, F. Habib, P.H. Lin, I. Korobkov, G. Enright, L. Ungur, W. Wernsdorfer, L.F. Chibotaru, M. Murugesu, Single-molecule magnet behavior for an antiferromagnetically superexchange-coupled dinuclear dysprosium(III) complex, J. Am. Chem. Soc. 133 (2011) 5319–5328. https://doi.org/10.1021/ja109706y.

[63] F. Habib, P.H. Lin, J. Long, I. Korobkov, W. Wernsdorfer, M. Murugesu, The use of magnetic dilution to elucidate the slow magnetic relaxation effects of a Dy2 single-molecule magnet, J. Am. Chem. Soc. 133 (2011) 8830–8833. https://doi.org/10.1021/ja2017009.

[64] P. Zhang, L. Zhang, C. Wang, S. Xue, S.Y. Lin, J. Tang, Equatorially coordinated lanthanide single ion magnets, J. Am. Chem. Soc. 136 (2014) 4484–4487. https://doi.org/10.1021/ja500793x.

[65] I. Oyarzabal, J. Ruiz, J.M. Seco, M. Evangelisti, A. Cam??n, E. Ruiz, D. Aravena, E. Colacio, Rational electrostatic design of easy-axis magnetic anisotropy in a ZnII-DyIII-ZnII single-molecule magnet with a high energy barrier, Chem. - A Eur. J. 20 (2014) 14262–14269. https://doi.org/10.1002/chem.201403670.

[66] L. Ungur, M. Thewissen, J.P. Costes, W. Wernsdorfer, L.F. Chibotaru, Interplay of strongly anisotropic metal ions in magnetic blocking of complexes, Inorg. Chem. 52 (2013) 6328–6337. https://doi.org/10.1021/ic302568x.

[67] A. Upadhyay, S.K. Singh, C. Das, R. Mondol, S.K. Langley, K.S. Murray, G. Rajaraman, M. Shanmugam, Enhancing the effective energy barrier of a Dy(iii) SMM using a bridged diamagnetic Zn(ii) ion., Chem. Commun. 50 (2014) 8838–41. https://doi.org/10.1039/c4cc02094d.

[68] M. Llunell, D. Casanova, J. Cirera, J.M. Bofill, P. Alemany, S. Alvarez, M. Pinsky, D. Avnir, SHAPE, (2005).

[69] Y.S. Ding, N.F. Chilton, R.E.P. Winpenny, Y.Z. Zheng, On Approaching the Limit of Molecular Magnetic Anisotropy: A Near-Perfect Pentagonal Bipyramidal Dysprosium(III) Single-Molecule Magnet, Angew. Chem. Int. Ed. 55 (2016) 16071–16074. https://doi.org/10.1002/anie.201609685.

[70] J. Liu, Y.C. Chen, J.L. Liu, V. Vieru, L. Ungur, J.H. Jia, L.F. Chibotaru, Y. Lan, W. Wernsdorfer, S. Gao, X.M. Chen, M.L. Tong, A Stable Pentagonal Bipyramidal Dy(III) Single-Ion Magnet with a Record Magnetization Reversal Barrier over 1000 K, J. Am. Chem. Soc. 138 (2016) 5441–5450.

https://doi.org/10.1021/jacs.6b02638.

[71] Y.C. Chen, J.L. Liu, L. Ungur, J. Liu, Q.W. Li, L.F. Wang, Z.P. Ni, L.F. Chibotaru, X.M. Chen, M.L. Tong, Symmetry-Supported Magnetic Blocking at 20 K in Pentagonal Bipyramidal Dy(III) Single-Ion Magnets, J. Am. Chem. Soc. 138 (2016) 2829–2837. https://doi.org/10.1021/jacs.5b13584.

[72] S.K. Gupta, T. Rajeshkumar, G. Rajaraman, R. Murugavel, An air-stable Dy(III) single-ion magnet with high anisotropy barrier and blocking temperature, Chem. Sci. 7 (2016) 5181–5191. https://doi.org/10.1039/c6sc00279j.

[73] Z. Jiang, L. Sun, Q. Yang, B. Yin, H. Ke, J. Han, Q. Wei, G. Xie, S. Chen, Excess axial electrostatic repulsion as a criterion for pentagonal bipyramidal DyIII single-ion magnets with high: U eff and T B, J. Mater. Chem. C. 6 (2018) 4273–4280. https://doi.org/10.1039/c8tc00353j.

[74] A.B. Canaj, S. Dey, C. Wilson, O. Céspedes, G. Rajaraman, M. Murrie, Engineering macrocyclic high performance pentagonal bipyramidal Dy(iii) single-ion magnets, Chem. Commun. 56 (2020) 12037–12040. https://doi.org/10.1039/d0cc04559d.

[75] L. Norel, L.E. Darago, B. Le Guennic, K. Chakarawet, M.I. Gonzalez, J.H. Olshansky, S. Rigaut, J.R. Long, A Terminal Fluoride Ligand Generates Axial Magnetic Anisotropy in Dysprosium Complexes, Angew. Chem. Int. Ed. 57 (2018) 1933–1938. https://doi.org/10.1002/anie.201712139.

[76] J. Liu, Y. Chen, Y. Zheng, W. Lin, L. Ungur, W. Wernsdorfer, L. Chibotaru, M. Tong, Switching the anisotropy barrier of a single-ion magnet by symmetry change from quasi-D5h to quasi-Oh, Chem. Sci. 4 (2013) 3310. https://doi.org/10.1039/c3sc50843a.

[77] J.L. Liu, Y.C. Chen, M.L. Tong, Symmetry strategies for high performance lanthanide-based single-molecule magnets, Chem. Soc. Rev. 47 (2018) 2431–2453. https://doi.org/10.1039/c7cs00266a.

[78] E. Colacio, J. Ruiz-Sanchez, F.J. White, E.K. Brechin, Strategy for the rational design of asymmetric triply bridged dinuclear 3d-4f single-molecule magnets, Inorg. Chem. 50 (2011) 7268–7273. https://doi.org/10.1021/ic2008599.

[79] S. Titos-Padilla, J. Ruiz, J.M. Herrera, E.K. Brechin, W. Wersndorfer, F. Lloret, E. Colacio, Dilution-triggered SMM behavior under zero field in a luminescent Zn 2Dy2 tetranuclear complex incorporating carbonato-bridging ligands derived from atmospheric CO2 fixation, Inorg. Chem. 52 (2013) 9620–9626. https://doi.org/10.1021/ic401378k.

[80] T. Han, M.J. Giansiracusa, Z. Li, Y. Ding, N.F. Chilton, R.E.P. Winpenny, Y. Zheng, Exchange-Biasing in a Dinuclear Dysprosium(III) Single-Molecule Magnet with a Large Energy Barrier for Magnetisation Reversal, Chem. – A Eur. J. 26 (2020) 6773–6777. https://doi.org/10.1002/chem.202000719.

[81] R.J. Blagg, L. Ungur, F. Tuna, J. Speak, P. Comar, D. Collison, W. Wernsdorfer, E.J.L. McInnes, L.F. Chibotaru, R.E.P. Winpenny, Magnetic relaxation pathways in lanthanide single-molecule magnets., Nat. Chem. 5 (2013) 673–678. https://doi.org/10.1038/nchem.1707.

[82] K.R. Meihaus, J.D. Rinehart, J.R. Long, Dilution-Induced Slow Magnetic Relaxation and Anomalous Hysteresis in Trigonal Prismatic Dysprosium(III) and Uranium(III) Complexes, Inorg. Chem. 50 (2011) 8484–8489. https://doi.org/10.1021/ic201078r.

[83] F. Pointillart, K. Bernot, S. Golhen, B. Le Guennic, T. Guizouarn, L. Ouahab, O. Cador, Magnetic memory in an isotopically enriched and magnetically isolated mononuclear dysprosium complex, Angew. Chem. Int. Ed. 54 (2015) 1504–1507. https://doi.org/10.1002/anie.201409887.

[84] Y.S. Ding, K.X. Yu, D. Reta, F. Ortu, R.E.P. Winpenny, Y.Z. Zheng, N.F. Chilton, Field- and temperature-dependent quantum tunnelling of the magnetisation in a large barrier single-molecule magnet, Nat. Commun. 9 (2018) 3134. https://doi.org/10.1038/s41467-018-05587-6.

[85] S.K. Langley, D.P. Wielechowski, V. Vieru, N.F. Chilton, B. Moubaraki, B.F. Abrahams, L.F. Chibotaru, K.S. Murray, A {CrIII2DyIII2} single-molecule magnet: Enhancing the blocking temperature through 3d magnetic exchange, Angew. Chem. Int. Ed. 52 (2013) 12014–12019. https://doi.org/10.1002/anie.201306329.

[86] K.R. Vignesh, S.K. Langley, K.S. Murray, G. Rajaraman, Quenching the Quantum Tunneling of Magnetization in Heterometallic Octanuclear {TM $^{III}_{4}$ Dy $^{III}_{4}$} (TM=Co and Cr) Single-Molecule Magnets by Modification of the Bridging Ligands and Enhancing the Magnetic Exchange Coupling, Chem. - A Eur. J. 23 (2017) 1654–1666. https://doi.org/10.1002/chem.201604835.

[87] S.K. Langley, C.M. Forsyth, B. Moubaraki, K.S. Murray, A fluoride bridged {CrIII4DyIII4} single molecule magnet, Dalton Trans. 44 (2014) 912–915. https://doi.org/10.1039/c4dt03100h.

[88] J. Rinck, G. Novitchi, W. Van Den Heuvel, L. Ungur, Y. Lan, W. Wernsdorfer, C.E. Anson, L.F. Chibotaru, A.K. Powell, An octanuclear [Cr^{III}4DyIII4] 3d-4f single-molecule magnet, Angew. Chem. Int. Ed. 49 (2010) 7583–7587. https://doi.org/10.1002/anie.201002690.

[89] X.L. Li, F.Y. Min, C. Wang, S.Y. Lin, Z. Liu, J. Tang, Utilizing 3d-4f magnetic interaction to slow the magnetic relaxation of heterometallic complexes, Inorg. Chem. 54 (2015) 4337–4344. https://doi.org/10.1021/acs.inorgchem.5b00019.

[90] J.L. Liu, J.Y. Wu, Y.C. Chen, V. Mereacre, A.K. Powell, L. Ungur, L.F. Chibotaru, X.M. Chen, M.L. Tong, A Heterometallic FeII-DyIII Single-Molecule Magnet with a Record Anisotropy Barrier, Angew. Chem. Int. Ed. 53 (2014) 12966–12970. https://doi.org/10.1002/anie.201407799.

[91] M. Hołyńska, D. Premužić, I.R. Jeon, W. Wernsdorfer, R. Clérac, S. Dehnen, [MnIII6O3Ln2] single-molecule magnets: Increasing the energy barrier above 100 K, Chem. - A Eur. J. 17 (2011) 9605–9610. https://doi.org/10.1002/chem.201101807.

[92] K.C. Mondal, A. Sundt, Y. Lan, G.E. Kostakis, O. Waldmann, L. Ungur, L.F. Chibotaru, C.E. Anson, A.K. Powell, Coexistence of distinct single-ion and exchange-based mechanisms for blocking of magnetization in a Co II2Dy III2 single-molecule magnet, Angew. Chem. Int. Ed. 51 (2012) 7550–7554. https://doi.org/10.1002/anie.201201478.

[93] S.K. Singh, M.F. Beg, G. Rajaraman, Role of Magnetic Exchange Interactions in the Magnetization Relaxation of {3d-4f} Single-Molecule Magnets: A Theoretical Perspective, Chem. - A Eur. J. 22 (2016) 672–680. https://doi.org/10.1002/chem.201503102.

[94] C.G. Efthymiou, T.C. Stamatatos, C. Papatriantafyllopoulou, A.J. Tasiopoulos, W. Wernsdorfer, S.P. Perlepes, G. Christou, Nickel/lanthanide single-molecule magnets: {Ni3Ln} “stars” with a ligand derived from the metal-promoted reduction of di-2-pyridyl ketone under solvothermal conditions, Inorg. Chem. 49 (2010) 9737–9739. https://doi.org/10.1021/ic101504c.

[95] T. Gupta, M.F. Beg, G. Rajaraman, Role of Single-Ion Anisotropy and Magnetic Exchange Interactions in Suppressing Zero-Field Tunnelling in {3d-4f} Single Molecule Magnets, Inorg. Chem. 55 (2016) 11201–11215. https://doi.org/10.1021/acs.inorgchem.6b01831.

[96] J.D. Rinehart, M. Fang, W.J. Evans, J.R. Long, Strong exchange and magnetic blocking in N_2^{3-}-radical-bridged lanthanide complexes., Nat. Chem. 3 (2011) 538–42. https://doi.org/10.1038/nchem.1063.

[97] C. Benelli, D. Gatteschi, Magnetism of lanthanides in molecular materials with transition-metal ions and organic radicals, Chem. Rev. 102 (2002) 2369–2387. https://doi.org/10.1021/cr010303r.

[98] Y.N. Guo, G.F. Xu, P. Gamez, L. Zhao, S.Y. Lin, R. Deng, J. Tang, H.J. Zhang, Two-step relaxation in a linear tetranuclear dysprosium(III) aggregate showing single-molecule magnet behavior, J. Am. Chem. Soc. 132 (2010) 8538–8539. https://doi.org/10.1021/ja103018m.

[99] J.D. Rinehart, M. Fang, W.J. Evans, J.R. Long, A N23- radical-bridged terbium complex exhibiting magnetic hysteresis at 14 K, J. Am. Chem. Soc. 133 (2011) 14236–14239. https://doi.org/10.1021/ja206286h.

[100] S. Demir, M.I. Gonzalez, L.E. Darago, W.J. Evans, J.R. Long, Giant coercivity and high magnetic blocking temperatures for N23- radical-bridged dilanthanide complexes upon ligand dissociation, Nat. Commun. 8 (2017) 2144. https://doi.org/10.1038/s41467-017-01553-w.

[101] J.D. Hilgar, M.G. Bernbeck, J.D. Rinehart, Million-fold Relaxation Time Enhancement across a Series of Phosphino-Supported Erbium Single-Molecule Magnets, J. Am. Chem. Soc. 141 (2019) 1913–1917. https://doi.org/10.1021/jacs.8b13514.

[102] C.A.P. Goodwin, F. Ortu, D. Reta, N.F. Chilton, D.P. Mills, Molecular magnetic hysteresis at 60 kelvin in dysprosocenium, Nature. 548 (2017) 439–442. https://doi.org/10.1038/nature23447.

[103] F.S. Guo, B.M. Day, Y.C. Chen, M.L. Tong, A. Mansikkamäki, R.A. Layfield, A Dysprosium Metallocene Single-Molecule Magnet Functioning at the Axial Limit, Angew. Chem. Int. Ed. 56 (2017) 11445–11449. https://doi.org/10.1002/anie.201705426.

[104] F.S. Guo, B.M. Day, Y.C. Chen, M.L. Tong, A. Mansikkamäki, R.A. Layfield, Magnetic hysteresis up to 80 kelvin in a dysprosium metallocene single-molecule magnet, Science. 362 (2018) 1400–1403. https://doi.org/10.1126/science.aav0652.

[105] K.R. McClain, C.A. Gould, K. Chakarawet, S.J. Teat, T.J. Groshens, J.R. Long, B.G. Harvey, High-temperature magnetic blocking and magneto-structural correlations in a series of dysprosium(III) metallocenium single-molecule magnets, Chem. Sci. 9 (2018) 8492–8503. https://doi.org/10.1039/C8SC03907K.

[106] P. Evans, D. Reta, G.F.S. Whitehead, N.F. Chilton, D.P. Mills, Bis-monophospholyl dysprosium cation showing magnetic hysteresis at 48 K, J. Am. Chem. Soc. 141 (2020) 19935–19940. https://doi.org/10.1021/jacs.9b11515.

[107] Y. Meng, J. Xiong, M. Yang, Y. Qiao, Z. Zhong, H. Sun, J. Han, T. Liu, B. Wang, S. Gao, Experimental Determination of Magnetic Anisotropy in Exchange-Bias Dysprosium Metallocene Single-Molecule Magnets, Angew. Chem. Int. Ed. 59 (2020) 13037–13043.

https://doi.org/10.1002/anie.202004537.
[108] R. Collins, M.J. Heras Ojea, A. Mansikkamäki, J. Tang, R.A. Layfield, Carbonyl Back-Bonding Influencing the Rate of Quantum Tunnelling in a Dysprosium Metallocene Single-Molecule Magnet, Inorg. Chem. 59 (2020) 642–647. https://doi.org/10.1021/acs.inorgchem.9b02895.
[109] M. He, F.S. Guo, J. Tang, A. Mansikkamäki, R.A. Layfield, Fulvalene as a platform for the synthesis of a dimetallic dysprosocenium single-molecule magnet, Chem. Sci. 11 (2020) 5745–5752. https://doi.org/10.1039/d0sc02033h.
[110] B.M. Day, F.S. Guo, R.A. Layfield, Cyclopentadienyl Ligands in Lanthanide Single-Molecule Magnets: One Ring to Rule Them All?, Acc. Chem. Res. 51 (2018) 1880–1889. https://doi.org/10.1021/acs.accounts.8b00270.
[111] T. Pugh, N.F. Chilton, R.A. Layfield, A Low-Symmetry Dysprosium Metallocene Single-Molecule Magnet with a High Anisotropy Barrier, Angew. Chem. Int. Ed. 55 (2016) 11082–11085. https://doi.org/10.1002/anie.201604346.
[112] P. Evans, D. Reta, C.A.P. Goodwin, F. Ortu, N.F. Chilton, D.P. Mills, A double-dysprosocenium single-molecule magnet bound together with neutral ligands, Chem. Commun. 56 (2020) 5677–5680. https://doi.org/10.1039/c9cc08945d.
[113] D. Errulat, B. Gabidullin, A. Mansikkamäki, M. Murugesu, Two heads are better than one: Improving magnetic relaxation in the dysprosium metallocene DyCp2*BPh4 upon dimerization by use of an exceptionally weakly-coordinating anion, Chem. Commun. 56 (2020) 5937–5940. https://doi.org/10.1039/d0cc01980a.
[114] F. Neese, The ORCA program system, WIREs Comput. Mol. Sci. 2 (2012) 73–78. https://doi.org/10.1002/wcms.81.
[115] F. Aquilante, J. Autschbach, R.K. Carlson, L.F. Chibotaru, M.G. Delcey, L. De Vico, I. Fdez. Galván, N. Ferré, L.M. Frutos, L. Gagliardi, M. Garavelli, A. Giussani, C.E. Hoyer, G. Li Manni, H. Lischka, D. Ma, P.Å. Malmqvist, T. Müller, A. Nenov, M. Olivucci, T.B. Pedersen, D. Peng, F. Plasser, B. Pritchard, M. Reiher, I. Rivalta, I. Schapiro, J. Segarra-Martí, M. Stenrup, D.G. Truhlar, L. Ungur, A. Valentini, S. Vancoillie, V. Veryazov, V.P. Vysotskiy, O. Weingart, F. Zapata, R. Lindh, <scp>Molcas</scp> 8: New capabilities for multiconfigurational quantum chemical calculations across the periodic table, J. Comput. Chem. 37 (2016) 506–541. https://doi.org/10.1002/jcc.24221.
[116] A. Swain, A. Sarkar, G. Rajaraman, Role of Ab Initio Calculations in the Design and Development of Organometallic Lanthanide-Based Single-Molecule Magnets, Chem. – An Asian J. 14 (2019) 4056–4073. https://doi.org/10.1002/asia.201900828.
[117] D. Aravena, E. Ruiz, Shedding light on the single-molecule magnet behavior of mononuclear DyIII complexes, Inorg. Chem. 52 (2013) 13770–13778. https://doi.org/10.1021/ic402367c.
[118] D. Reta, J.G.C. Kragskow, N.F. Chilton, Ab Initio Prediction of High-Temperature Magnetic Relaxation Rates in Single-Molecule Magnets, J. Am. Chem. Soc. (2021) jacs.1c01410. https://doi.org/10.1021/jacs.1c01410.
[119] A. Lunghi, M. Iannuzzi, R. Sessoli, F. Totti, Single molecule magnets grafted on gold: magnetic properties from ab initio molecular dynamics †, J. Mater. Chem. C. 7294 (2015) 7294. https://doi.org/10.1039/c5tc00394f.
[120] S. Calvello, M. Piccardo, S.V. Rao, A. Soncini, CERES: An ab initio code dedicated to the calculation of the electronic structure and magnetic properties of lanthanide complexes, J. Comput. Chem. 39 (2018) 328–337. https://doi.org/10.1002/jcc.25113.
[121] F. Lu, M.M. Ding, J.X. Li, B.L. Wang, Y.Q. Zhang, Why lanthanide ErIIISIMs cannot possess huge energy barriers: A theoretical investigation, Dalton Trans. 49 (2020) 14576–14583. https://doi.org/10.1039/d0dt02868a.
[122] H. Zhang, R. Nakanishi, K. Katoh, B.K. Breedlove, Y. Kitagawa, M. Yamashita, Low coordinated mononuclear erbium(III) single-molecule magnets with C3v symmetry: A method for altering single-molecule magnet properties by incorporating hard and soft donors, Dalton Trans. 47 (2018) 302–305. https://doi.org/10.1039/c7dt04053a.
[123] W. Zhang, A. Muhtadi, N. Iwahara, L. Ungur, L.F. Chibotaru, Magnetic Anisotropy in Divalent Lanthanide Compounds, Angew. Chem. Int. Ed. 59 (2020) 12720–12724. https://doi.org/10.1002/anie.202003399.
[124] L. Ungur, L.F. Chibotaru, Magnetic anisotropy in the excited states of low symmetry lanthanide complexes, Phys. Chem. Chem. Phys. 13 (2011) 20086–20090. https://doi.org/10.1039/c1cp22689d.
[125] K. Irländer, J. Schnack, Spin-phonon interaction induces tunnel splitting in single-molecule magnets, Phys. Rev. B. 102 (2020) 054407. https://doi.org/10.1103/PhysRevB.102.054407.

[126] D. Aravena, Ab Initio Prediction of Tunneling Relaxation Times and Effective Demagnetization Barriers in Kramers Lanthanide Single-Molecule Magnets, J. Phys. Chem. Lett. 9 (2018) 5327–5333. https://doi.org/10.1021/acs.jpclett.8b02359.

[127] L. Bogani, L. Cavigli, M. Gurioli, R.L. Novak, M. Mannini, A. Caneschi, F. Pineider, R. Sessoli, M. Clemente-León, E. Coronado, A. Cornia, D. Gatteschi, Magneto-Optical Investigations of Nanostructured Materials Based on Single-Molecule Magnets Monitor Strong Environmental Effects, Adv. Mater. 19 (2007) 3906–3911. https://doi.org/10.1002/adma.200700594.

[128] Z. Salman, K.H. Chow, R.I. Miller, A. Morello, T.J. Parolin, M.D. Hossain, T.A. Keeler, C.D.P. Levy, W.A. MacFarlane, G.D. Morris, H. Saadaoui, D. Wang, R. Sessoli, G.G. Condorelli, R.F. Kiefl, Local magnetic properties of a monolayer of Mn12 single molecule magnets, Nano Lett. 7 (2007) 1551–1555. https://doi.org/10.1021/nl070366a.

[129] F. Moro, R. Biagi, V. Corradini, M. Evangelisti, A. Gambardella, V. De Renzi, U. Del Pennino, E. Coronado, A. Forment-Aliaga, F.M. Romero, Electronic and magnetic properties of Mn 12 molecular magnets on sulfonate and carboxylic acid prefunctionalized gold surfaces, J. Phys. Chem. C. 116 (2012) 14936–14942. https://doi.org/10.1021/jp3031896.

[130] C. Wäckerlin, F. Donati, A. Singha, R. Baltic, S. Rusponi, K. Diller, F. Patthey, M. Pivetta, Y. Lan, S. Klyatskaya, M. Ruben, H. Brune, J. Dreiser, Giant Hysteresis of Single-Molecule Magnets Adsorbed on a Nonmagnetic Insulator, Adv. Mater. 28 (2016) 5195–5199. https://doi.org/10.1002/adma.201506305.

[131] D. Aulakh, H.K. Bilan, M. Wriedt, Porous substrates as platforms for the nanostructuring of molecular magnets, CrystEngComm. 20 (2018) 1011–1030. https://doi.org/10.1039/c7ce01978e.

[132] E. Coronado, Molecular magnetism: from chemical design to spin control in molecules, materials and devices, Nat. Rev. Mater. 5 (2020) 87–104. https://doi.org/10.1038/s41578-019-0146-8.

[133] D. Aulakh, J.B. Pyser, X. Zhang, A.A. Yakovenko, K.R. Dunbar, M. Wriedt, Metal-Organic Frameworks as Platforms for the Controlled Nanostructuring of Single-Molecule Magnets, J. Am. Chem. Soc. 137 (2015) 9254–9257. https://doi.org/10.1021/jacs.5b06002.

[134] D. Aulakh, H. Xie, Z. Shen, A. Harley, X. Zhang, A.A. Yakovenko, K.R. Dunbar, M. Wriedt, Systematic Investigation of Controlled Nanostructuring of Mn12 Single-Molecule Magnets Templated by Metal-Organic Frameworks, Inorg. Chem. 56 (2017) 6965–6972. https://doi.org/10.1021/acs.inorgchem.7b00514.

[135] H.-J. Chen, X.-Y. Zheng, Y.-R. Zhao, D.-Q. Yuan, X.-J. Kong, L.-S. Long, L.-S. Zheng, A Record-Breaking Loading Capacity for Single-Molecule Magnet Mn 12 Clusters Achieved in a Mesoporous Ln-MOF , ACS Appl. Electron. Mater. 1 (2019) 804–809. https://doi.org/10.1021/acsaelm.9b00088.

[136] T.C. Wang, N.A. Vermeulen, I.S. Kim, A.B.F. Martinson, J. Fraser Stoddart, J.T. Hupp, O.K. Farha, Scalable synthesis and post-modification of a mesoporous metal-organic framework called NU-1000, Nat. Protoc. 11 (2016) 149–162. https://doi.org/10.1038/nprot.2016.001.

[137] D. Aulakh, L. Liu, J.R. Varghese, H. Xie, T. Islamoglu, K. Duell, C.W. Kung, C.E. Hsiung, Y. Zhang, R.J. Drout, O.K. Farha, K.R. Dunbar, Y. Han, M. Wriedt, Direct Imaging of Isolated Single-Molecule Magnets in Metal-Organic Frameworks, J. Am. Chem. Soc. 141 (2019) 2997–3005. https://doi.org/10.1021/jacs.8b11374.

[138] M. Mon, A. Pascual-Álvarez, T. Grancha, J. Cano, J. Ferrando-Soria, F. Lloret, J. Gascon, J. Pasán, D. Armentano, E. Pardo, Solid-State Molecular Nanomagnet Inclusion into a Magnetic Metal-Organic Framework: Interplay of the Magnetic Properties, Chem. - A Eur. J. 22 (2016) 441–441. https://doi.org/10.1002/chem.201504827.

[139] B.J. Kennedy, K.S. Murray, Magnetic Properties and Zero-Field Splitting in High-Spin Manganese(III) Complexes. 2. Axially Ligated Manganese(HI) Porphyrin Complexes, Inorg. Chem. 24 (1985) 1557–1560. https://doi.org/10.1021/ic00204a030.

[140] M.M. Williamson, C.L. Hill, Molecular Stereochemistry of Aquamanganese(III) Porphyrins. Demonstrable Effect of π-Arene-Porphyrin Interaction on the Metal Coordination Environment in a Metalloporphyrin, Inorg. Chem. 26 (1987) 4155–4160. https://doi.org/10.1021/ic00272a005.

[141] J. Ferrando-Soria, P. Serra-Crespo, M. De Lange, J. Gascon, F. Kapteijn, M. Julve, J. Cano, F. Lloret, J. Pasán, C. Ruiz-Pérez, Y. Journaux, E. Pardo, Selective gas and vapor sorption and magnetic sensing by an isoreticular mixed-metal-organic framework, J. Am. Chem. Soc. 134 (2012) 15301–15304. https://doi.org/10.1021/ja3045822.

[142] T. Grancha, J. Ferrando-Soria, H.-C. Zhou, J. Gascon, B. Seoane, J. Pasán, O. Fabelo, M. Julve, E. Pardo, Postsynthetic Improvement of the Physical Properties in a Metal-Organic Framework through a Single Crystal to Single Crystal Transmetallation, Angew. Chem. Int. Ed. 54 (2015) 6521–6525. https://doi.org/10.1002/anie.201501691.

[143] J. Dreiser, G.E. Pacchioni, F. Donati, L. Gragnaniello, A. Cavallin, K.S. Pedersen, J. Bendix, B. Delley, M. Pivetta, S. Rusponi, H. Brune, Out-of-Plane Alignment of Er(trensal) Easy Magnetization Axes Using Graphene, ACS Nano. 10 (2016) 2887–2892. https://doi.org/10.1021/acsnano.5b08178.

[144] S. Marocchi, A. Candini, D. Klar, W. Van Den Heuvel, H. Huang, F. Troiani, V. Corradini, R. Biagi, V. De Renzi, S. Klyatskaya, K. Kummer, N.B. Brookes, M. Ruben, H. Wende, U. Del Pennino, A. Soncini, M. Affronte, V. Bellini, Relay-Like Exchange Mechanism through a Spin Radical between TbPc2 Molecules and Graphene/Ni(111) Substrates, ACS Nano. 10 (2016) 9353–9360. https://doi.org/10.1021/acsnano.6b04107.

[145] L. Bogani, W. Wernsdorfer, Molecular spintronics using single-molecule magnets, Nat. Mater. 7 (2008) 179–186. https://doi.org/10.1038/nmat2133.

[146] M. Trif, F. Troiani, D. Stepanenko, D. Loss, Spin-electric coupling in molecular magnets, Phys. Rev. Lett. 101 (2008) 217201. https://doi.org/10.1103/PhysRevLett.101.217201.

[147] A. Saywell, G. Magnano, C.J. Satterley, L.M.A. Perdigão, A.J. Britton, N. Taleb, M. Del Carmen Giménez-López, N.R. Champness, J.N. O'Shea, P.H. Beton, Self-assembled aggregates formed by single-molecule magnets on a gold surface, Nat. Commun. 1 (2010) 75. https://doi.org/10.1038/ncomms1075.

[148] T.W. Chamberlain, M.C. Giménez-López, A.N. Khlobystov, Carbon Nanotubes and Related Structures: Synthesis, Characterization, Functionalization, and Applications, Wiley-VCH, 2010. https://www.wiley.com/en-ar/Carbon+Nanotubes+and+Related+Structures%3A+Synthesis%2C+Characterization%2C+Functionalization%2C+and+Applications-p-9783527324064 (accessed January 28, 2021).

[149] K. Jiang, A. Eitan, L.S. Schadler, P.M. Ajayan, R.W. Siegel, N. Grobert, M. Mayne, M. Reyes-Reyes, H. Terrones, M. Terrones, Selective attachment of gold nanoparticles to nitrogen-doped carbon nanotubes, Nano Lett. 3 (2003) 275–277. https://doi.org/10.1021/nl025914t.

[150] V. Georgakilas, D. Gournis, V. Tzitzios, L. Pasquato, D.M. Guldi, M. Prato, Decorating carbon nanotubes with metal or semiconductor nanoparticles, J. Mater. Chem. 17 (2007) 2679–2694. https://doi.org/10.1039/b700857k.

[151] Y.B. Zhang, M. Kanungo, A.J. Ho, P. Freimuth, D. Van Der Lelie, M. Chen, S.M. Khamis, S.S. Datta, A.T.C. Johnson, J.A. Misewich, S.S. Wong, Functionalized carbon nanotubes for detecting viral proteins, Nano Lett. 7 (2007) 3086–3091. https://doi.org/10.1021/nl071572l.

[152] K. Besteman, J.O. Lee, F.G.M. Wiertz, H.A. Heering, C. Dekker, Enzyme-coated carbon nanotubes as single-molecule biosensors, Nano Lett. 3 (2003) 727–730. https://doi.org/10.1021/nl034139u.

[153] S. Banerjee, T. Hemraj-Benny, S.S. Wong, Covalent Surface Chemistry of Single-Walled Carbon Nanotubes, Adv. Mater. 17 (2005) 17–29. https://doi.org/10.1002/adma.200401340.

[154] J. Kong, N.R. Franklin, C. Zhou, M.G. Chapline, S. Peng, K. Cho, H. Dai, Nanotube molecular wires as chemical sensors, Science. 287 (2000) 622–625. https://doi.org/10.1126/science.287.5453.622.

[155] L. Bogani, C. Danieli, E. Biavardi, N. Bendiab, A.-L. Barra, E. Dalcanale, W. Wernsdorfer, A. Cornia, Single-Molecule-Magnet Carbon-Nanotube Hybrids, Angew. Chem. Int. Ed. 48 (2009) 746–750. https://doi.org/10.1002/anie.200804967.

[156] L. Malavolti, V. Lanzilotto, S. Ninova, L. Poggini, I. Cimatti, B. Cortigiani, L. Margheriti, D. Chiappe, E. Otero, P. Sainctavit, F. Totti, A. Cornia, M. Mannini, R. Sessoli, Magnetic bistability in a submonolayer of sublimated Fe4 single-molecule magnets, Nano Lett. 15 (2015) 535–541. https://doi.org/10.1021/nl503925h.

[157] L. Gragnaniello, F. Paschke, P. Erler, P. Schmitt, N. Barth, S. Simon, H. Brune, S. Rusponi, M. Fonin, Uniaxial 2D Superlattice of Fe4 Molecular Magnets on Graphene, Nano Lett. 17 (2017) 7177–7182. https://doi.org/10.1021/acs.nanolett.6b05105.

[158] C. Cervetti, A. Rettori, M.G. Pini, A. Cornia, A. Repollés, F. Luis, M. Dressel, S. Rauschenbach, K. Kern, M. Burghard, L. Bogani, The classical and quantum dynamics of molecular spins on graphene, Nat. Mater. 15 (2016) 164–168. https://doi.org/10.1038/nmat4490.

[159] S.C. Benjamin, A. Ardavan, G.A.D. Briggs, D.A. Britz, D. Gunlycke, J. Jefferson, M.A.G. Jones, D.F. Leigh, B.W. Lovett, A.N. Khlobystov, S.A. Lyon, J.J.L. Morton, K. Porfyrakis, M.R. Sambrook, A.M. Tyryshkin, Towards a fullerene-based quantum computer, J. Phys. Condens. Matter. 18 (2006) S867. https://doi.org/10.1088/0953-8984/18/21/S12.

[160] M. Del Carmen Giménez-López, F. Moro, A. La Torre, C.J. Gómez-García, P.D. Brown, J. Van Slageren, A.N. Khlobystov, Encapsulation of single-molecule magnets in carbon nanotubes, Nat.

Commun. 2 (2011) 407. https://doi.org/10.1038/ncomms1415.
[161] S. Kyatskaya, J.R.G. Mascarós, L. Bogani, F. Hennrich, M. Kappes, W. Wernsdorfer, M. Ruben, Anchoring of rare-earth-based single-molecule magnets on single-walled carbon nanotubes, J. Am. Chem. Soc. 131 (2009) 15143–15151. https://doi.org/10.1021/ja906165e.
[162] A. Giusti, G. Charron, S. Mazerat, J.-D. Compain, P. Mialane, A. Dolbecq, E. Rivière, W. Wernsdorfer, R. Ngo Biboum, B. Keita, L. Nadjo, A. Filoramo, J.-P. Bourgoin, T. Mallah, Magnetic Bistability of Individual Single-Molecule Magnets Grafted on Single-Wall Carbon Nanotubes, Angew. Chem. Int. Ed. 48 (2009) 4949–4952. https://doi.org/10.1002/anie.200901806.
[163] J.C.G. Bünzli, On the design of highly luminescent lanthanide complexes, Coord. Chem. Rev. 293–294 (2015) 19–47. https://doi.org/10.1016/j.ccr.2014.10.013.
[164] M.J. Weber, Radiative and multiphonon relaxation of rare-earth ions in Y2O3, Phys. Rev. 171 (1968) 283–291. https://doi.org/10.1103/PhysRev.171.283.
[165] C.P. Montgomery, D. Parker, L. Lamarque, Effective and efficient sensitisation of terbium luminescence at 355 nm with cell permeable pyrazoyl-1-azaxanthone macrocyclic complexes, Chem. Commun. (2007) 3841–3843. https://doi.org/10.1039/b709805g.
[166] J. Long, Y. Guari, R.A.S. Ferreira, L.D. Carlos, J. Larionova, Recent advances in luminescent lanthanide based Single-Molecule Magnets, Coord. Chem. Rev. 363 (2018) 57–70. https://doi.org/10.1016/j.ccr.2018.02.019.
[167] J.H. Jia, Q.W. Li, Y.C. Chen, J.L. Liu, M.L. Tong, Luminescent single-molecule magnets based on lanthanides: Design strategies, recent advances and magneto-luminescent studies, Coord. Chem. Rev. 378 (2019) 365–381. https://doi.org/10.1016/j.ccr.2017.11.012.
[168] J. Long, Luminescent Schiff-Base Lanthanide Single-Molecule Magnets: The Association Between Optical and Magnetic Properties, Front. Chem. 7 (2019) 63. https://doi.org/10.3389/fchem.2019.00063.
[169] F. Pointillart, O. Cador, B. Le Guennic, L. Ouahab, Uncommon lanthanide ions in purely 4f Single Molecule Magnets, Coord. Chem. Rev. 346 (2017) 150–175. https://doi.org/10.1016/j.ccr.2016.12.017.
[170] J.C.G. Bünzli, Lanthanide luminescence for biomedical analyses and imaging, Chem. Rev. 110 (2010) 2729–2755. https://doi.org/10.1021/cr900362e.
[171] S. V. Eliseeva, M. Ryazanov, F. Gumy, S.I. Troyanov, L.S. Lepnev, J.-C.G. Bünzli, N.P. Kuzmina, Dimeric Complexes of Lanthanide(III) Hexafluoroacetylacetonates with4-CyanopyridineN-Oxide: Synthesis, Crystal Structure, Magnetic and Photoluminescent Properties, Eur. J. Inorg. Chem. (2006) 4809–4820. https://doi.org/10.1002/ejic.200600673.
[172] D. Errulat, R. Marin, D.A. Gálico, K.L.M. Harriman, A. Pialat, B. Gabidullin, F. Iikawa, O.D.D. Couto, J.O. Moilanen, E. Hemmer, F.A. Sigoli, M. Murugesu, A Luminescent Thermometer Exhibiting Slow Relaxation of the Magnetization: Toward Self-Monitored Building Blocks for Next-Generation Optomagnetic Devices, ACS Cent. Sci. 5 (2019) 1187–1198. https://doi.org/10.1021/acscentsci.9b00288.
[173] F. Pointillart, J. Jung, R. Berraud-Pache, B. Le Guennic, V. Dorcet, S. Golhen, O. Cador, O. Maury, Y. Guyot, S. Decurtins, S.X. Liu, L. Ouahab, Luminescence and single-molecule magnet behavior in lanthanide complexes involving a tetrathiafulvalene-fused dipyridophenazine ligand, Inorg. Chem. 54 (2015) 5384–5397. https://doi.org/10.1021/acs.inorgchem.5b00441.
[174] F. Pointillart, B. Le Guennic, S. Golhen, O. Cador, O. Maury, L. Ouahab, A redox-active luminescent ytterbium based single molecule magnet, Chem. Commun. 49 (2013) 615–617. https://doi.org/10.1039/c2cc37635k.
[175] G. Brunet, R. Marin, M.J. Monk, U. Resch-Genger, D.A. Gálico, F.A. Sigoli, E.A. Suturina, E. Hemmer, M. Murugesu, Exploring the dual functionality of an ytterbium complex for luminescence thermometry and slow magnetic relaxation, Chem. Sci. 10 (2019) 6799–6808. https://doi.org/10.1039/c9sc00343f.
[176] J. Wang, J.J. Zakrzewski, M. Heczko, M. Zychowicz, K. Nakagawa, K. Nakabayashi, B. Sieklucka, S. Chorazy, S.I. Ohkoshi, Proton Conductive Luminescent Thermometer Based on Near-Infrared Emissive {YbCo2} Molecular Nanomagnets, J. Am. Chem. Soc. 142 (2020) 3970–3979. https://doi.org/10.1021/jacs.9b13147.
[177] J. Wang, J.J. Zakrzewski, M. Zychowicz, V. Vieru, L.F. Chibotaru, K. Nakabayashi, S. Chorazy, S. Ohkoshi, Holmium(iii) molecular nanomagnets for optical thermometry exploring the luminescence re-absorption effect , Chem. Sci. 12 (2021) 730–741. https://doi.org/10.1039/d0sc04871b.
[178] A.A. Kitos, D.A. Gálico, R. Castañeda, J.S. Ovens, M. Murugesu, J.L. Brusso, Stark Sublevel-

Based Thermometry with Tb(III) and Dy(III) Complexes Cosensitized via the 2-Amidinopyridine Ligand, Inorg. Chem. 59 (2020) 11061–11070. https://doi.org/10.1021/acs.inorgchem.0c01534.

[179] M. Fondo, J. Corredoira-Vázquez, A.M. García-Deibe, J. Sanmartín-Matalobos, M. Amoza, A.M.P. Botas, R.A.S. Ferreira, L.D. Carlos, E. Colacio, Field-induced slow magnetic relaxation and luminescence thermometry in a mononuclear ytterbium complex, Inorg. Chem. Front. 7 (2020) 3019–3029. https://doi.org/10.1039/d0qi00637h.

[180] R. Marin, G. Brunet, M. Murugesu, Shining New Light on Multifunctional Lanthanide Single-Molecule Magnets, Angew. Chem. Int. Ed. 60 (2021) 1728–1746. https://doi.org/10.1002/anie.201910299.

[181] R. Farshchi, M. Ramsteiner, J. Herfort, A. Tahraoui, H.T. Grahn, Optical communication of spin information between light emitting diodes, Appl. Phys. Lett. 98 (2011) 162508. https://doi.org/10.1063/1.3582917.

[182] J.F. Sherson, H. Krauter, R.K. Olsson, B. Julsgaard, K. Hammerer, I. Cirac, E.S. Polzik, Quantum teleportation between light and matter, Nature. 443 (2006) 557–560. https://doi.org/10.1038/nature05136.

[183] M.C. Heffern, L.M. Matosziuk, T.J. Meade, Lanthanide probes for bioresponsive imaging, Chem. Rev. 114 (2014) 4496–4539. https://doi.org/10.1021/cr400477t.

[184] M. Schadt, Liquid crystal materials and liquid crystal displays, Annu. Rev. Mater. Sci. 27 (1997) 305–379. https://doi.org/10.1146/annurev.matsci.27.1.305.

[185] M. Leonzio, M. Bettinelli, L. Arrico, M. Monari, L. Di Bari, F. Piccinelli, Circularly Polarized Luminescence from an Eu(III) Complex Based on 2-Thenoyltrifluoroacetyl-acetonate and a Tetradentate Chiral Ligand, Inorg. Chem. 57 (2018) 10257–10264. https://doi.org/10.1021/acs.inorgchem.8b01480.

[186] L. Arrico, C. De Rosa, L. Di Bari, A. Melchior, F. Piccinelli, Effect of the Counterion on Circularly Polarized Luminescence of Europium(III) and Samarium(III) Complexes, Inorg. Chem. 59 (2020) 5050–5062. https://doi.org/10.1021/acs.inorgchem.0c00280.

[187] S. Wada, Y. Kitagawa, T. Nakanishi, M. Gon, K. Tanaka, K. Fushimi, Y. Chujo, Y. Hasegawa, Electronic chirality inversion of lanthanide complex induced by achiral molecules, Sci. Rep. 8 (2018) 16395. https://doi.org/10.1038/s41598-018-34790-0.

[188] K. Dhbaibi, L. Favereau, J. Crassous, Enantioenriched Helicenes and Helicenoids Containing Main-Group Elements (B, Si, N, P), Chem. Rev. 119 (2019) 8846–8953. https://doi.org/10.1021/acs.chemrev.9b00033.

[189] Z.P. Yan, K. Liao, H.B. Han, J. Su, Y.X. Zheng, J.L. Zuo, Chiral iridium(III) complexes with four-membered Ir-S-P-S chelating rings for high-performance circularly polarized OLEDs, Chem. Commun. 55 (2019) 8215–8218. https://doi.org/10.1039/c9cc03915e.

[190] G. Park, H. Kim, H. Yang, K.R. Park, I. Song, J.H. Oh, C. Kim, Y. You, Amplified circularly polarized phosphorescence from co-assemblies of platinum(ii) complexes, Chem. Sci. 10 (2019) 1294–1301. https://doi.org/10.1039/c8sc04509g.

[191] R. Aoki, R. Toyoda, J.F. Kögel, R. Sakamoto, J. Kumar, Y. Kitagawa, K. Harano, T. Kawai, H. Nishihara, Bis(dipyrrinato)zinc(II) Complex Chiroptical Wires: Exfoliation into Single Strands and Intensification of Circularly Polarized Luminescence, J. Am. Chem. Soc. 139 (2017) 16024–16027. https://doi.org/10.1021/jacs.7b07077.

[192] J.R. Jiménez, B. Doistau, C.M. Cruz, C. Besnard, J.M. Cuerva, A.G. Campaña, C. Piguet, Chiral Molecular Ruby [Cr(dqp)2]3+ with Long-Lived Circularly Polarized Luminescence, J. Am. Chem. Soc. 141 (2019) 13244–13252. https://doi.org/10.1021/jacs.9b06524.

[193] M. Deng, N.F.M. Mukthar, N.D. Schley, G. Ung, Yellow Circularly Polarized Luminescence from C_1-Symmetrical Copper(I) Complexes, Angew. Chem. Int. Ed. 59 (2020) 1228–1231. https://doi.org/10.1002/anie.201913672.

[194] J. Kumar, B. Marydasan, T. Nakashima, T. Kawai, J. Yuasa, Chiral supramolecular polymerization leading to eye differentiable circular polarization in luminescence, Chem. Commun. 52 (2016) 9885–9888. https://doi.org/10.1039/c6cc05022k.

[195] B. El Rez, J. Liu, V. Béreau, C. Duhayon, Y. Horino, T. Suzuki, L. Coolen, J.P. Sutter, Concomitant emergence of circularly polarized luminescence and single-molecule magnet behavior in chiral-at-metal Dy complex, Inorg. Chem. Front. 7 (2020) 4527–4534. https://doi.org/10.1039/d0qi00919a.

[196] J.P. Riehl, F.S. Richardson, Circularly Polarized Luminescence Spectroscopy, Chem. Rev. 86 (1986) 1–16. https://doi.org/10.1021/cr00071a001.

[197] W. Zhang, H.Y. Ye, R.G. Xiong, Metal-organic coordination compounds for potential ferroelectrics, Coord. Chem. Rev. 253 (2009) 2980–2997. https://doi.org/10.1016/j.ccr.2009.02.028.

[198] M. Gajek, M. Bibes, S. Fusil, K. Bouzehouane, J. Fontcuberta, A. Barthélémy, A. Fert, Tunnel junctions with multiferroic barriers, Nat. Mater. 6 (2007) 296–302. https://doi.org/10.1038/nmat1860.

[199] J.F. Scott, Multiferroic memories, Nat. Mater. 6 (2007) 256–257. https://doi.org/10.1038/nmat1868.

[200] P.H. Guo, Y. Meng, Y.C. Chen, Q.W. Li, B.Y. Wang, J.D. Leng, D.H. Bao, J.H. Jia, M.L. Tong, A zigzag DyIII4 cluster exhibiting single-molecule magnet, ferroelectric and white-light emitting properties, J. Mater. Chem. C. 2 (2014) 8858–8864. https://doi.org/10.1039/c4tc01275e.

[201] X.L. Li, C.L. Chen, H.P. Xiao, A.L. Wang, C.M. Liu, X. Zheng, L.J. Gao, X.G. Yang, S.M. Fang, Luminescent, magnetic and ferroelectric properties of noncentrosymmetric chain-like complexes composed of nine-coordinate lanthanide ions, Dalton Trans. 42 (2013) 15317–15325. https://doi.org/10.1039/c3dt51743h.

[202] P.-H. Guo, J.-L. Liu, J.-H. Jia, J. Wang, F.-S. Guo, Y.-C. Chen, W.-Q. Lin, J.-D. Leng, D.-H. Bao, X.-D. Zhang, J.-H. Luo, M.-L. Tong, Multifunctional Dy $^{III}_{4}$ Cluster Exhibiting White-Emitting, Ferroelectric and Single-Molecule Magnet Behavior, Chem. - A Eur. J. 19 (2013) 8769–8773. https://doi.org/10.1002/chem.201300299.

[203] J. Long, J. Rouquette, J.-M. Thibaud, R.A.S. Ferreira, L.D. Carlos, B. Donnadieu, V. Vieru, L.F. Chibotaru, L. Konczewicz, J. Haines, Y. Guari, J. Larionova, A High-Temperature Molecular Ferroelectric Zn/Dy Complex Exhibiting Single-Ion-Magnet Behavior and Lanthanide Luminescence, Angew. Chemie. 127 (2015) 2264–2268. https://doi.org/10.1002/ange.201410523.

[204] S.D. Zhu, J.J. Hu, L. Dong, H.R. Wen, S.J. Liu, Y.B. Lu, C.M. Liu, Multifunctional Zn(ii)-Yb(iii) complex enantiomers showing second-harmonic generation, near-infrared luminescence, single-molecule magnet behaviour and proton conduction, J. Mater. Chem. C. 8 (2020) 16032–16041. https://doi.org/10.1039/d0tc03687k.

[205] G. Cosquer, Y. Shen, M. Almeida, M. Yamashita, Conducting single-molecule magnet materials, Dalton Trans. 47 (2018) 7616–7627. https://doi.org/10.1039/c8dt01015c.

[206] N.D. Kushch, L.I. Buravov, P.P. Kushch, G. V. Shilov, H. Yamochi, M. Ishikawa, A. Otsuka, A.A. Shakin, O. V. Maximova, O.S. Volkova, A.N. Vasiliev, E.B. Yagubskii, Multifunctional Compound Combining Conductivity and Single-Molecule Magnetism in the Same Temperature Range, Inorg. Chem. 57 (2018) 2386–2389. https://doi.org/10.1021/acs.inorgchem.7b03152.

[207] J.A. Jones, Fast Searches with Nuclear Magnetic Resonance Computers, Science. 280 (1998) 229–229. https://doi.org/10.1126/science.280.5361.229.

[208] P.W. Shor, Algorithms for quantum computation: discrete logarithms and factoring, in: Institute of Electrical and Electronics Engineers (IEEE), Santa Fe, NM, USA, 1994: pp. 124–134. https://doi.org/10.1109/sfcs.1994.365700.

[209] L.K. Grover, Quantum computers can search arbitrarily large databases by a single query, Phys. Rev. Lett. 79 (1997) 4709–4712. https://doi.org/10.1103/PhysRevLett.79.4709.

[210] M.N. Leuenberger, D. Loss, Quantum computing in molecular magnets, Nature. 410 (2001) 789–793. https://doi.org/10.1038/35071024.

[211] C. Joachim, J.K. Gimzewski, A. Aviram, Electronics using hybrid-molecular and mono-molecular devices, Nature. 408 (2000) 541–548. https://doi.org/10.1038/35046000.

[212] M. Affronte, Molecular nanomagnets for information technologies, J. Mater. Chem. 19 (2009) 1731–1737. https://doi.org/10.1039/b809251f.

[213] K.X. Yu, J.G.C. Kragskow, Y.S. Ding, Y.Q. Zhai, D. Reta, N.F. Chilton, Y.Z. Zheng, Enhancing Magnetic Hysteresis in Single-Molecule Magnets by Ligand Functionalization, Chem. 6 (2020) 1777–1793. https://doi.org/10.1016/j.chempr.2020.04.024.

[214] F. Ortu, D. Reta, Y.S. Ding, C.A.P. Goodwin, M.P. Gregson, E.J.L. McInnes, R.E.P. Winpenny, Y.Z. Zheng, S.T. Liddle, D.P. Mills, N.F. Chilton, Studies of hysteresis and quantum tunnelling of the magnetisation in dysprosium(iii) single molecule magnets, Dalton Trans. 48 (2019) 8541–8545. https://doi.org/10.1039/c9dt01655d.

[215] A. Chiesa, F. Cugini, R. Hussain, E. MacAluso, G. Allodi, E. Garlatti, M. Giansiracusa, C.A.P. Goodwin, F. Ortu, D. Reta, J.M. Skelton, T. Guidi, P. Santini, M. Solzi, R. De Renzi, D.P. Mills, N.F. Chilton, S. Carretta, Understanding magnetic relaxation in single-ion magnets with high blocking temperature, Phys. Rev. B. 101 (2020) 174402. https://doi.org/10.1103/PhysRevB.101.174402.

[216] R.E.P. Winpenny, N.F. Chilton, M. Giansiracusa, D. Collison, A. Kostopoulos, Correlating Blocking Temperatures with Relaxation Mechanisms in Monometallic Single-Molecule Magnets with High Energy Barriers (Ueff > 600 K), Chem. Commun. (2019). https://doi.org/10.1039/C9CC02421B.

[217] G. Velkos, W. Yang, Y.R. Yao, S.M. Sudarkova, X. Liu, B. Büchner, S.M. Avdoshenko, N. Chen,

A.A. Popov, Shape-adaptive single-molecule magnetism and hysteresis up to 14 K in oxide clusterfullerenes Dy2O@C72 and Dy2O@C74 with fused pentagon pairs and flexible Dy-(μ2-O)-Dy angle, Chem. Sci. 11 (2020) 4766–4772. https://doi.org/10.1039/d0sc00624f.

[218] F. Liu, S. Wang, C.-L. Gao, Q. Deng, X. Zhu, A. Kostanyan, R. Westerström, F. Jin, S.-Y. Xie, A.A. Popov, T. Greber, S. Yang, Mononuclear Clusterfullerene Single-Molecule Magnet Containing Strained Fused-Pentagons Stabilized by a Nearly Linear Metal Cyanide Cluster, Angew. Chem. Int. Ed. 56 (2017) 1830–1834. https://doi.org/10.1002/anie.201611345.

[219] F. Liu, C.L. Gao, Q. Deng, X. Zhu, A. Kostanyan, R. Westerström, S. Wang, Y.Z. Tan, J. Tao, S.Y. Xie, A.A. Popov, T. Greber, S. Yang, Triangular Monometallic Cyanide Cluster Entrapped in Carbon Cage with Geometry-Dependent Molecular Magnetism, J. Am. Chem. Soc. 138 (2016) 14764–14771. https://doi.org/10.1021/jacs.6b09329.

[220] L. Spree, A.A. Popov, Recent advances in single molecule magnetism of dysprosium-metallofullerenes, Dalton Trans. 48 (2019) 2861–2871. https://doi.org/10.1039/c8dt05153d.

[221] D.S. Krylov, F. Liu, A. Brandenburg, L. Spree, V. Bon, S. Kaskel, A.U.B. Wolter, B. Büchner, S.M. Avdoshenko, A.A. Popov, Magnetization relaxation in the single-ion magnet DySc2N@C80: Quantum tunneling, magnetic dilution, and unconventional temperature dependence, Phys. Chem. Chem. Phys. 20 (2018) 11656–11672. https://doi.org/10.1039/c8cp01608a.

[222] C.H. Chen, D.S. Krylov, S.M. Avdoshenko, F. Liu, L. Spree, R. Westerström, C. Bulbucan, M. Studniarek, J. Dreiser, A.U.B. Wolter, B. Büchner, A.A. Popov, Magnetic hysteresis in self-assembled monolayers of Dy-fullerene single molecule magnets on gold, Nanoscale. 10 (2018) 11287–11292. https://doi.org/10.1039/c8nr00511g.

[223] K. Chakarawet, M. Atanasov, J. Marbey, P.C. Bunting, F. Neese, S. Hill, J.R. Long, Strong electronic and magnetic coupling in M4(M = Ni, Cu) clusters via direct orbital interactions between low-coordinate metal centers, J. Am. Chem. Soc. 142 (2020) 19161–19169. https://doi.org/10.1021/jacs.0c08460.

[224] J. Camacho-Bunquin, M.J. Ferguson, J.M. Stryker, Hydrocarbon-soluble nanocatalysts with no bulk phase: Coplanar, two-coordinate arrays of the base metals, J. Am. Chem. Soc. 135 (2013) 5537–5540. https://doi.org/10.1021/ja401579x.

[225] P. Pyykkö, M. Atsumi, Molecular Single-Bond Covalent Radii for Elements 1-118, Chem. - A Eur. J. 15 (2009) 186–197. https://doi.org/10.1002/chem.200800987.

[226] M.A. Palacios, J. Nehrkorn, E.A. Suturina, E. Ruiz, S. Gómez-Coca, K. Holldack, A. Schnegg, J. Krzystek, J.M. Moreno, E. Colacio, Analysis of Magnetic Anisotropy and the Role of Magnetic Dilution in Triggering Single-Molecule Magnet (SMM) Behavior in a Family of $Co^{II}Y^{III}$ Dinuclear Complexes with Easy-Plane Anisotropy, Chem. - A Eur. J. 23 (2017) 11649–11661. https://doi.org/10.1002/chem.201702099.

[227] A.K. Mondal, A. Mondal, B. Dey, S. Konar, Influence of the Coordination Environment on Easy-Plane Magnetic Anisotropy of Pentagonal Bipyramidal Cobalt(II) Complexes, Inorg. Chem. 57 (2018) 9999–10008. https://doi.org/10.1021/acs.inorgchem.8b01162.

[228] J.M. Zadrozny, J. Liu, N.A. Piro, C.J. Chang, S. Hill, J.R. Long, Slow magnetic relaxation in a pseudotetrahedral cobalt(ii) complex with easy-plane anisotropy, Chem. Commun. 48 (2012) 3927–3929. https://doi.org/10.1039/c2cc16430b.

[229] K. Chakarawet, P.C. Bunting, J.R. Long, Large Anisotropy Barrier in a Tetranuclear Single-Molecule Magnet Featuring Low-Coordinate Cobalt Centers, J. Am. Chem. Soc. 140 (2018) 2058–2061. https://doi.org/10.1021/jacs.7b13394.

[230] A.W. Cook, J.D. Bocarsly, R.A. Lewis, A.J. Touchton, S. Morochnik, T.W. Hayton, An iron ketimide single-molecule magnet [Fe4(NCPh2)6] with suppressed through-barrier relaxation, Chem. Sci. 11 (2020) 4753–4757. https://doi.org/10.1039/d0sc01578d.

[231] P. Abbasi, K. Quinn, D.I. Alexandropoulos, M. Damjanović, W. Wernsdorfer, A. Escuer, J. Mayans, M. Pilkington, T.C. Stamatatos, Transition Metal Single-Molecule Magnets: A {Mn31} Nanosized Cluster with a Large Energy Barrier of ~60 K and Magnetic Hysteresis at ~5 K, J. Am. Chem. Soc. 139 (2017) 15644–15647. https://doi.org/10.1021/jacs.7b10130.

[232] N.E. Chakov, S.C. Lee, A.G. Harter, P.L. Kuhns, A.P. Reyes, S.O. Hill, N.S. Dalal, W. Wernsdorfer, K.A. Abboud, G. Christou, The properties of the [Mn12O12(O2CR) 16(H2O)4] single-molecule magnets in truly axial symmetry: [Mn12O12(O2CCH 2Br)16(H2O)4]·4CH 2Cl2, J. Am. Chem. Soc. 128 (2006) 6975–6989. https://doi.org/10.1021/ja060796n.

[233] C.J. Milios, A. Vinslava, W. Wernsdorfer, S. Moggach, S. Parsons, S.P. Perlepes, G. Christou, E.K. Brechin, A record anisotropy barrier for a single-molecule magnet, J. Am. Chem. Soc. 129 (2007) 2754–2755. https://doi.org/10.1021/ja068961m.

[234] K. Uchida, G. Cosquer, K. Sugisaki, H. Matsuoka, K. Sato, B.K. Breedlove, M. Yamashita, Isostructural M(II) complexes (M = Mn, Fe, Co) with field-induced slow magnetic relaxation for Mn and Co complexes, Dalton Trans. 48 (2019) 12023–12030. https://doi.org/10.1039/c8dt02150c.

[235] C. Rajnák, J. Titiš, J. Moncoľ, F. Renz, R. Boča, Slow magnetic relaxation in a high-spin pentacoordinate Fe(iii) complex, Chem. Commun. 55 (2019) 13868–13871. https://doi.org/10.1039/c9cc06610a.

[236] G. Handzlik, M. Magott, M. Arczyński, A.M. Sheveleva, F. Tuna, M. Sarewicz, A. Osyczka, M. Rams, V. Vieru, L.F. Chibotaru, D. Pinkowicz, Magnetization Dynamics and Coherent Spin Manipulation of a Propeller Gd(III) Complex with the Smallest Helicene Ligand, J. Phys. Chem. Lett. 11 (2020) 1508–1515. https://doi.org/10.1021/acs.jpclett.9b03275.

[237] M.J. Martínez-Pérez, S. Cardona-Serra, C. Schlegel, F. Moro, P.J. Alonso, H. Prima-García, J.M. Clemente-Juan, M. Evangelisti, A. Gaita-Ariño, J. Sesé, J. Van Slageren, E. Coronado, F. Luis, Gd-based single-ion magnets with tunable magnetic anisotropy: Molecular design of spin qubits, Phys. Rev. Lett. 108 (2012) 247213. https://doi.org/10.1103/PhysRevLett.108.247213.

[238] R.J. Holmberg, L.T.A. Ho, L. Ungur, I. Korobkov, L.F. Chibotaru, M. Murugesu, Observation of unusual slow-relaxation of the magnetisation in a Gd-EDTA chelate, Dalton Trans. 44 (2015) 20321–20325. https://doi.org/10.1039/c5dt04072h.

[239] D.C. Izuogu, T. Yoshida, H. Zhang, G. Cosquer, K. Katoh, S. Ogata, M. Hasegawa, H. Nojiri, M. Damjanović, W. Wernsdorfer, T. Uruga, T. Ina, B.K. Breedlove, M. Yamashita, Slow Magnetic Relaxation in a Palladium–Gadolinium Complex Induced by Electron Density Donation from the Palladium Ion, Chem. – A Eur. J. 24 (2018) 9285–9294. https://doi.org/10.1002/chem.201800699.

[240] J. Mayans, A. Escuer, Correlating the axial Zero Field Splitting with the slow magnetic relaxation in Gd III SIMs , Chem. Commun. 57 (2021) 721–724. https://doi.org/10.1039/d0cc07474h.

[241] S.T. Liddle, J. van Slageren, Actinide Single-Molecule Magnets, in: Lanthanides Actinides Mol. Magn., Wiley-VCH Verlag GmbH & Co. KGaA, Weinheim, Germany, 2015: pp. 315–340. https://doi.org/10.1002/9783527673476.ch10.

[242] S.K. Singh, C.J. Cramer, L. Gagliardi, Correlating Electronic Structure and Magnetic Anisotropy in Actinide Complexes [An(COT)2], AnIII/IV = U, Np, and Pu, Inorg. Chem. 59 (2020) 6815–6825. https://doi.org/10.1021/acs.inorgchem.0c00105.

[243] J.T. Coutinho, M. Perfetti, J.J. Baldoví, M.A. Antunes, P.P. Hallmen, H. Bamberger, I. Crassee, M. Orlita, M. Almeida, J. van Slageren, L.C.J. Pereira, Spectroscopic Determination of the Electronic Structure of a Uranium Single-Ion Magnet, Chem. - A Eur. J. 25 (2019) 1758–1766. https://doi.org/10.1002/chem.201805090.

[244] K.R. Meihaus, S.G. Minasian, W.W. Lukens, S.A. Kozimor, D.K. Shuh, T. Tyliszczak, J.R. Long, Influence of pyrazolate vs N -heterocyclic carbene ligands on the slow magnetic relaxation of homoleptic trischelate lanthanide(III) and uranium(III) complexes, J. Am. Chem. Soc. 136 (2014) 6056–6058. https://doi.org/10.1021/ja501569t.

[245] J.J. Le Roy, S.I. Gorelsky, I. Korobkov, M. Murugesu, Slow magnetic relaxation in uranium(III) and neodymium(III) cyclooctatetraenyl complexes, Organometallics. 34 (2015) 1415–1418. https://doi.org/10.1021/om501214c.

[246] N. Magnani, C. Apostolidis, A. Morgenstern, E. Colineau, J.-C. Griveau, H. Bolvin , O. Walter, R. Caciuffo, Magnetic Memory Effect in a Transuranic Mononuclear Complex, Angew. Chem. Int. Ed. 50 (2011) 1696–1698. https://doi.org/10.1002/anie.201006619.

CHAPTER 1

AN EXPERIMENTAL MAGNETO-STRUCTURAL STUDY OF THE SLOW RELAXATION IN Ln^{III} (Dy and Er) BASED MONONUCLEAR COMPLEXES WITH MANNICH COMPARTMENTAL LIGANDS DERIVED FROM LINEAR AMINES AND 5-BROMOSALICYLALDEHYDE

1.1. INTRODUCTION

As it has been discussed in the general introduction, the coordination environment around the lanthanide ion has a crucial effect on the final energy distribution of the Kramers doublets (when using Kramers ions) and relaxation mechanisms. Indeed, coordination compounds that possess the same geometry and donor atoms may show completely different dynamic magnetic properties when subtle modification involving bond distances, angles or variations in the charge of the donor atoms are introduced. This implies that magneto-structural correlations are of vital importance to rationally design SMMs with controlled magnetic properties.

Although great efforts have been done in this direction during the last years, only in a few cases clear and useful magneto-structural correlations have been obtained. This fact is mainly due to the wide range of coordination numbers and geometries that lanthanide coordination compounds can exhibit, as a consequence, among other reasons, of: (i) the large ionic radii and subsequent high coordination numbers of lanthanides ions and (ii) the non-directional nature of the electrostatic metal-ligand bonds, which favours the steoreochemical versatility. As mentioned before, especial work was made, for instance, for pentagonal bipyramidal systems, which allow to modify selectively the ligands in axial positions, as well as in the equatorial plane, and to extract enough accurate relaxation parameters for establishing a well-defined magneto-structural correlation [1]. However, when using compartmental ligands such as the ones employed in this chapter (Figure 1.1), it is hard to predict the final geometry of the compounds (generaly it is intermediate between different ideal coordination polyhedra) and then the magnetization relaxation parameters. Specifically, for this study, N,N',N''-trimethyl-N,N''-bis(2-hydroxy-3-formyl-5-bromo-benzyl) diethylenetriamine and N,N'-dimethyl-N,N'-bis(2-hydroxy-3-formyl-5-bromo-benzyl) ethylenediamine ligands have been used, H_2L^1 and H_2L^2 hereafter.

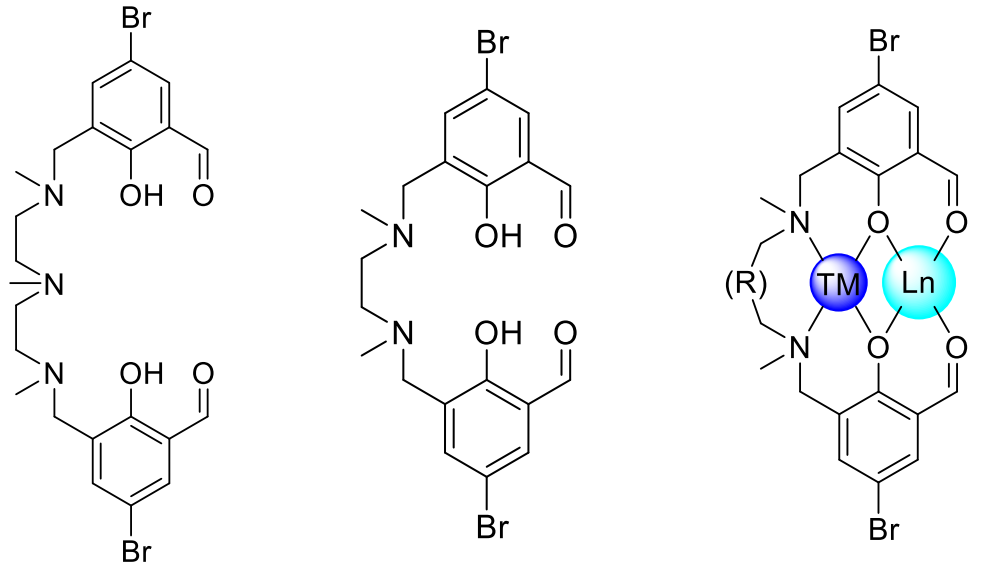

H_2L^1 H_2L^2

Figure 1.1.- Structure of the ligands H_2L^1 and H_2L^2 and representation of a transition metal (TM) and a lanthanide (Ln) ion in the inner and outer pocket, respectively. R = $(CH_2)_2NCH_3$ for H_2L^1 and R = nothing for H_2L^2.

These Mannich base kind of ligands are especially suitable to accommodate transition metals in the inner pocket (N_2O_2) and lanthanides in the outer one (O_4), though only the latter has been used for the compounds reported in this chapter. Moreover, the implementation of donor atoms of different nature enables to create anisotropic ligand fields that will define the resultant magnetic properties. In our case, the deprotonated oxygen atoms of the phenol groups will provide large electron density and short Ln-O bond distances to the system, so that, using a simple electrostatic model, they are going to determine the orientation of the anisotropy axis, whereas aldehydes, with much longer Ln-O distances, will not play an important role in the adoption of the anisotropy axis orientation. The fact of modifying the length of the side amine chain from a diamine to a triamine could also have an important effect in the adoption of the final lanthanide coordination sphere, since the size and donor atoms of the chain affords more or less flexibility to the ligand and thus the donor atoms will occupy different positions in the coordination sphere, giving rise to variable geometries.

This chapter has been proposed as a continuation of a previous work reported by some members of our group [2], where a mononuclear Dy^{III} based field induced SMM was studied with a similar ligand. In that case, instead of the aldehyde groups in H_2L^1,

methoxy groups were employed (Figure 1.2). Encouraged by the obtained interesting results, slightly modified ligands were targeted for this study.

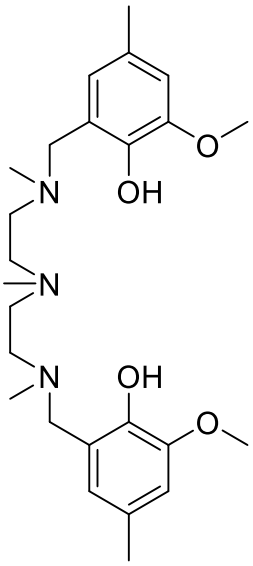

Figure 1.2.- Structure of the ligand employed in a previous study.

Furthermore, keeping in mind that for this kind of low-symmetry systems it is not easy to predict whether they will be suitable to stabilize high magnetic ground states for oblate or prolate type of ions, it is of great interest to compare isostructural systems containing both type of ions. Thus, this chapter collects the synthesis, structural characterization and magnetic properties of three pairs of Dy^{III} and Er^{III} complexes based on H_2L^1 and H_2L^2. These ions have been chosen for two reasons: (i) they both are Kramers type of ions and, therefore, show less probability to suffer undesired QTM phenomenon and (ii) they are opposite in electron density distribution, being oblate and prolate ions, respectively.

1.2. PREPARATION OF THE LIGANDS

1.2.1. H_2L^1: N,N',N''-trimethyl-N,N''-bis(2-hydroxy-3-formyl-5-bromobenzyl) diethylenetriamine

A mixture of N,N',N'''-trimethyldiethylenetriamine (1.45 g, 10 mmol), 5-bromosalicylaldehyde (4.02 g, 20 mmol) and 37% aqueous formaldehyde (1.62 g, 20 mmol) were stirred under reflux in ethanol for 48 h. After cooling the brown solution to

room temperature, the solvent was removed under reduced pressure obtaining a dark brown oil. In order to improve the handling of the ligand, the product was disolved in acetonitrile assuming a 100% yield to prepare a 0.072 M solution.

^{1}H-NMR (300 MHz, $CDCl_3$, ppm, Figure A1.55): 10.25 (s, 2H, formyl-*H*), 7.73 (d, 2H, aryl-*H*), 7.33 (d, 2H, aryl-*H*), 3.67 (s, 4H, aryl-CH_2N), 2.60 (m, 8H, NCH_2CH_2N), 2.30 (s, 6H, NCH_3), 2.26 (s, 3H, NCH_3).

1.2.2. H_2L^2: N,N'-dimethyl-N,N'-bis(2-hydroxy-3-formyl-5-bromobenzyl) ethylenediamine

The ligand was prepared by using a previously reported procedure [3].

1.3. PREPARATION OF THE COMPLEXES

1.3.1. $[Ln(H_2L^1)(NO_3)_3]$ (Ln^{III} = Dy (1), Er (2))

1.7 mL of the solution of H_2L^1 (0.125 mmol) were diluted in 7 mL of acetonitrile and the corresponding $Ln(NO_3)_3{\cdot}xH_2O$ (0.125 mmol) was then added. The resulting solution was stirred for 0.5 h and after filtering, it was allowed to stand at room temperature. After a few days X-ray quality crystals were formed, which were filtered, washed several times with acetonitrile and air-dried. Even though we managed to obtain these two products without any crystallization solvent molecules, they normally crystallize with two acetonitrile molecules (named as **8-MeCN** and **9-MeCN**), which were lost when grinding them for further experiments. See appendices for crystallographic tables. Yield and elemental analysis results in Table A1.1.

1.3.2. $[Ln(H_2L^1)(H_2O)(NO_3)_2]{\cdot}0.75Br{\cdot}0.25NO_3{\cdot}CH_3CN{\cdot}0.5CH_3OH$ (Ln^{III} = Dy (3), Er (4))

After diluting 1.7 mL of H_2L^1 (0.125 mmol) in a 7 mL mixture of acetonitrile and methanol (1:1 ratio), 14.9 mg of potassium bromide (0.125 mmol) and 0.125 mmol of the corresponding $Ln(NO_3)_3{\cdot}xH_2O$ were added subsequently. After stirring for 0.5 h the resultant yellow solution was kept undisturbed at room temperature. In few days, suitable crystals for X-ray diffraction were obtained. They were filtered, washed several times with acetonitrile and methanol and air-dried. Yield and elemental analysis results in Table A1.1.

1.3.3. $[Ln(H_2L^2)(NO_3)_3)]\cdot CH_3CN$ (Ln^{III} = Dy (5), Er (6))

Firstly, 0.125 mmol of $Ln(NO_3)_3\cdot xH_2O$ were dissolved in acetonitrile and then 62.5 mg of H_2L^2 (0.125 mmol) were added to obtain an initial yellow solution, from which, in a few seconds, a copious yellow precipitate started to appear. The precipitate was filtered, washed several times with acetonitrile and air-dried. The mother liquor kept at room temperature for a fews, afforded a small number of X-ray quality crystals. Yield and elemental analysis results in Table A1.1.

1.3.4. Magnetically diluted 1_Y-6_Y compounds

The magnetically diluted derivatives were synthesized following the same procedures as those above described for the the non-diluted compounds, but employing a Ln:Y ratio of 1:10.

1.4. EXPERIMENTAL RESULTS

The reaction between $Ln(NO_3)_3\cdot xH_2O$ and H_2L^1 using acetonitrile as solvent leads to the formation of well-shaped prismatic yellow crystals of $[Ln(H_2L^1)(NO_3)_3]$ (Ln^{III} = Dy (**1**)) or $[Ln(H_2L^1)(NO_3)_3]\cdot 2CH_3CN$ (Ln^{III} = Dy (**8-MeCN**), Er (**9-MeCN**)) (crystal structures are shown in the appendices). However, it is important to note that, probably, the former ones are formed in a notably lower amount. Indeed, even though we were able to collect the diffraction data for both **1** and **8-MeCN** for crystals in the same vial, all attempts to obtain crystallographic data for **2** were unsuccessful and only **9-MeCN** was found. In any case, elemental analyses and powder X-ray diffractograms undoubtedly show that the powdered products of **8-MeCN** and **9-MeCN** lose both solvent molecules and give rise to **1** and **2**. The reaction of $Ln(NO_3)_3\cdot xH_2O$ and KBr with H_2L^1 in a CH_3OH:CH_3CN 1:1 mixture gives rise to the ionic mononuclear complexes $[Ln(H_2L^1)(H_2O)(NO_3)_2]\cdot 0.75Br\cdot 0.25NO_3\cdot CH_3CN\cdot 0.5CH_3OH$ (Ln^{III} = Dy (**3**), Er (**4**)).

The reaction between $Ln(NO_3)_3\cdot xH_2O$ and H_2L^2 in acetonitrile gives rise to a yellow precipitate complex, with the general formula $[Ln(H_2L^2)(NO_3)_3)]\cdot CH_3CN$ (Ln^{III} = Dy (**5**), Er (**6**)). Few suitable crystals for X-ray diffraction are obtained allowing the mother liquors stand at room temperature. The results of the X-ray crystal studies reveal that **5** and **6** are structurally similar to complexes **1** and **2**.

1.4.1. Crystal structures of complexes 1, 3-6 and 1-MeCN to 10-MeCN

Due to the isostructural character of each pair of complexes (Dy^{III} and Er^{III} pair), only the structure of the Dy^{III} analogues is described as an example, though singularities of Er^{III} based compounds are also mentioned. Selected bond distances and angles, as well as the crystallographic data for all above mentioned structures are found in Tables A1.2-A1.8. The crystal structure of compound **1** is shown in the Figure 1.3. This compound crystallizes as a discrete monomer in the triclinic *P-1* space group. As it has been shown to occur in previously reported similar complexes [2], the coordination of the phenoxido groups of the neutral ligand to the Dy^{III} ion takes place with the simultaneous migration of the phenolic protons to the benzylamine groups, so that the ligand adopts a phenolate-ammonium zwitterionic form. The DyO_9 coordination environment of the lanthanide cation is completed by the coordination of the two aldehyde groups, two bidentate nitrates and a monodentate nitrate, thus exhibiting a distorted spherical tricapped trigonal prism geometry/muffin (calculations were performed by SHAPE software [4], Table A1.9). The shortest Dy-O bonds are those involving the phenoxido groups, showing bond distances of 2.234(5) Å and 2.310(5) Å for Dy-O2 and Dy-O3, respectively. Bond lengths involving the oxygen atoms of the aldehyde and nitrate groups are longer, appearing in the range of 2.401(5)-2.410(5) Å and 2.398(5)-2.519(5) Å ranges, respectively. Intramolecular hydrogen bonds stabilize the previously mentioned zwitterionic form with N1···O2, N3···O3 and N3···O7N distances of 2.828 Å, 2.742 Å and 2.977 Å. The shortest intermolecular Dy···Dy distance is of 8.448 Å.

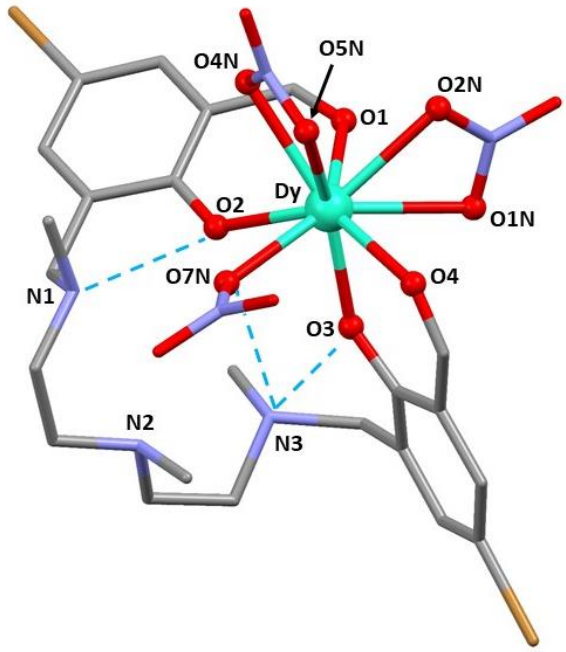

Figure 1.3.- Perspective view of complex **1**. Colour code: dysprosium, bromine, nitrogen, oxygen and carbon atoms are in turquoise, brown, light blue, red and grey, respectively. Hydrogen atoms are omitted for the sake of clarity.

As mentioned in the experimental section, mononuclear compounds **1** and **2** generally crystallize with two additional acetonitrile molecules, named as **8-MeCN** and **9-MeCN**. However, the powdered samples were isostructural to **1** and **2**, without any crystallization molecule. In order to study more deeply this behaviour, the X-ray structures of the family of complexes with the trivalent lanthanide ions of Ce, Pr, Nd, Sm, Eu, Gd, Tb, Dy, Er $Dy_{0.1}Y_{0.9}$ and Y (which are termed as **1-MeCN** (Ce) to **9-MeCN** (Er), **8$_Y$-MeCN** ($Dy_{0.1}Y_{0.9}$) and **10-MeCN** (Y) were solved. The results show that in all cases the compounds were solvated and that in mother liquor the most stable species were those with crystallization acetonitrile molecules. However, once the compounds were powdered the somehow volatile solvents were removed. This fact could be explained by the weak to negligible intermolecular interactions that the acetonitriles molecules present within the crystal structure. Indeed, only one of them displays short interactions with a bromine of the H_2L^1 ligand. The distance between the acetonitrile and the bromine becomes shorter as the cell volume of the compound decreases (Figure 1.4). Which is, at the same time, related the employed ion.

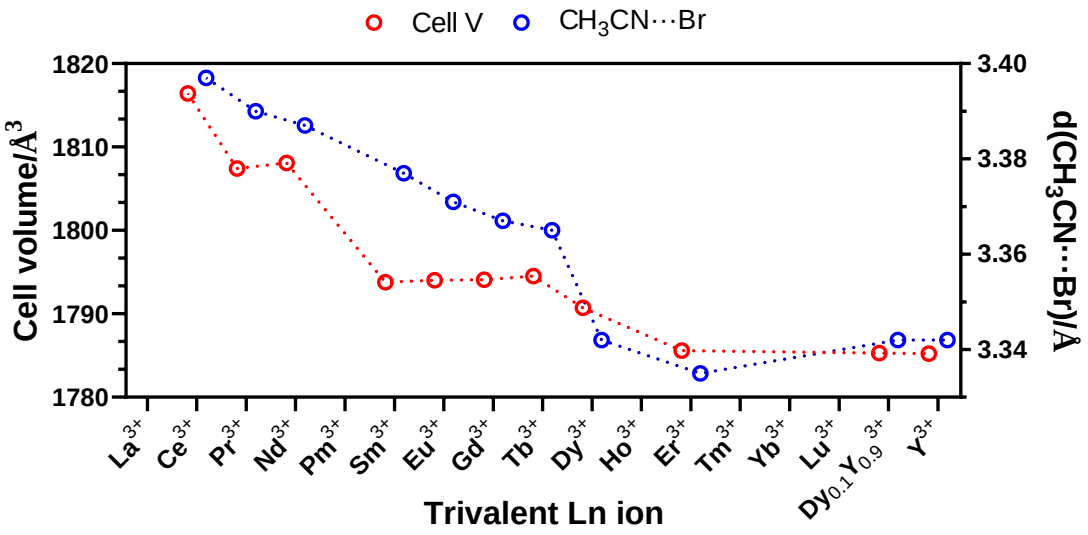

Figure 1.4.- Cell volume vs employed trivalent ion (left *y* axis, red coloured) and d($CH_3CN\cdots Br$) vs employed trivalent ion (right *y* axis, blue coloured).

Another crystallographycally interesting aspect of these compounds is the coordination behaviour of the nitrates (chelate versus monodentate) and consequently the coordination number of the metal ion. For the biggest studied ions, Ce^{III} and Nd^{III}, the coordination number is 10 and the three nitrate anions act as chelates. Sm^{III} and Eu^{III}, however, display an inexact coordination number. Indeed, for the former analogue one of the nitrates was refined with a 50% disorder, where half of the nitrate acts as chelate, whereas the other half acts as monodentate (Figure 1.5). In **5-MeCN**, instead, the same nitrate shows a marked monodentate character, since 85% was refined as monodentate and 15% as chelate. The **6-MeCN** and smaller counterparts show a coordination number of 9, with two chelate nitrates and a monodentate one.

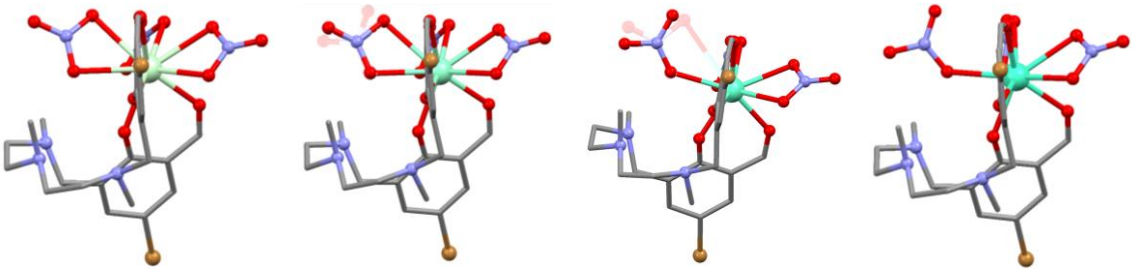

3-MeCN (Nd) **4-MeCN (Sm)** **5-MeCN (Eu)** **6-MeCN (Gd)**

Figure 1.5.- Change in coordination number around the lanthanide centres. The two limit cases (**3-MeCN** and **6-MeCN**) and the intermediates (**4-MeCN** and **5-MeCN**) are shown. Solvent crystallization molecules were omitted.

In terms of Ln-O distances, the tendency is the same as for compound **1** and **2**, where the shortest bond distances correspond to Ln-$O_{phenoxido}$, whereas Ln-$O_{carbonyl}$ and Ln-O_{NO3} were shown to be notably longer (Figure 1.6). As the ionic radii of the lanthanides decreases, the bond distances also become smaller, as expected. It is worth mentioning that the monodentate nitrate anions display notably shorter (in the range of Ln-$O_{carbonyl}$) bond distances in comparison to than the chelate ones, which was also predictable. However, it is interesting to remark the behaviour in the intermediate compounds. For **4-MeCN**, the monodentate nitrate exhibits a longer distance Dy-O distance than the Dy-$O_{carbonyl}$ one. This fact may be explained by the 50:50 monodentate/chelate ratio oobserved in this compound, which is responsible of lengthening somehow the bond distance and placing it in the middle position between monodentate/chelate. From **5-MeCN** on, however, the monodentate nitrates show always shorter Dy-O distances than the carbonyls groups. Finally, the Y^{III} counterpart **10-MeCN** displays similar structural parameters to those observed for the Dy^{III} and Er^{III} analogues, which makes of this metal ion an ideal candidate for further magnetic dilution studies.

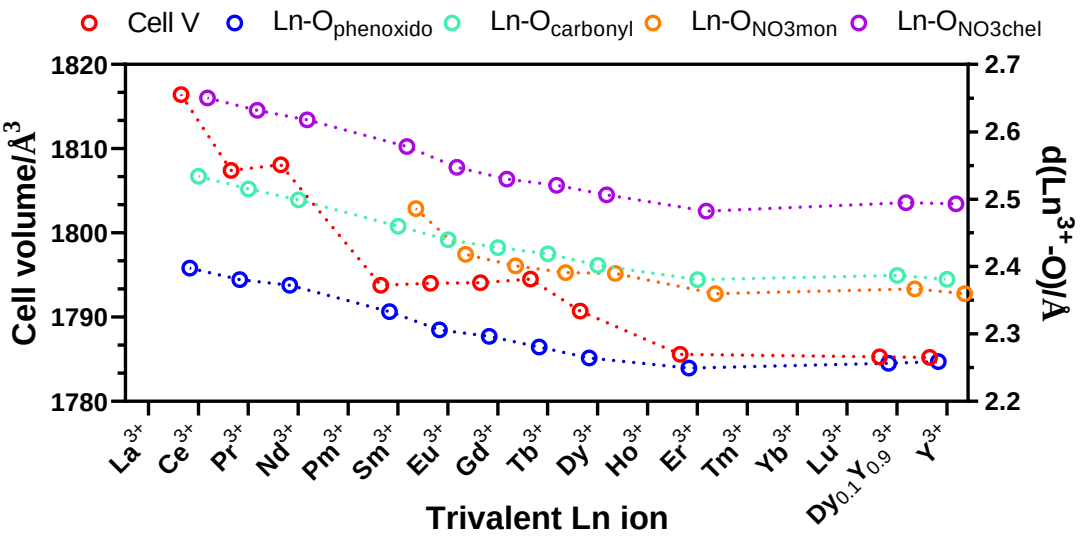

Figure 1.6.- Cell volume vs employed trivalent ion (left *y* axis, red coloured) and average d(Ln-O) vs employed trivalent ion (right *y* axis; blue, turquoise, orange and purple coloured).

Complex **3** also crystallizes in the triclinic *P-1* space group and the structure of its cationic unit $[Dy(H_2L^1)(H_2O)(NO_3)_2]^+$ is illustrated in Figure 1.7. Although the Dy^{III} is again nonacoordinated, the monodentate nitrate anion is replaced by a water molecule. The charge of the cationic unit is neutralized by a complex anionic structure. In fact, it was found a position for a half bromide ion, whereas the remnant half charge is balanced by a quarter of nitrate and another quarter of bromide sharing the same *xyz* coordinates (see Figure A1.1). The DyO_9 coordination sphere appears far from a well-defined geometry, being a spherical tricapped trigonal prism the ideal polyhedron to which it better fits to an ideal one (it shows continuous measure value of 2.008 for the indicated ideal polyhedron, Table A1.9). In the case of the Er^{III} analogue **4**, due to its slightly smaller ionic radio, one of the nitrates is monocoordinated giving rise to an ErO_8 coordination environment, which is more close to a triangular dodecahedron. The Dy-$O_{phenoxido}$ bonds are of 2.284(3) Å and 2.238(3) Å for Dy-O2 and Dy-O3, respectively. Again, distances from the metallic centre to the rest of oxygen atoms are longer, appearing in the 2.368(4)-2.746(5) Å range. Hydrogen bonds from N1 to O2 and O1N and from N3 to O3 are responsible of stabilizing the zwitterionic form with bond lengths of 2.733 Å, 2.947 Å and 2.777 Å, respectively. In addition, the coordinated water molecule gives rise to another two intermolecular hydrogen bonds. The first one with the half methanol solvent molecule (O1W···O1M) and the second one with the half independent bromide counteranion, which at the same time is connected with another

cationic unit (see Figure A1.2). The mononuclear cationic entities are isolated from each other displaying shortest intramolecular Dy···Dy distances of 9.324 Å.

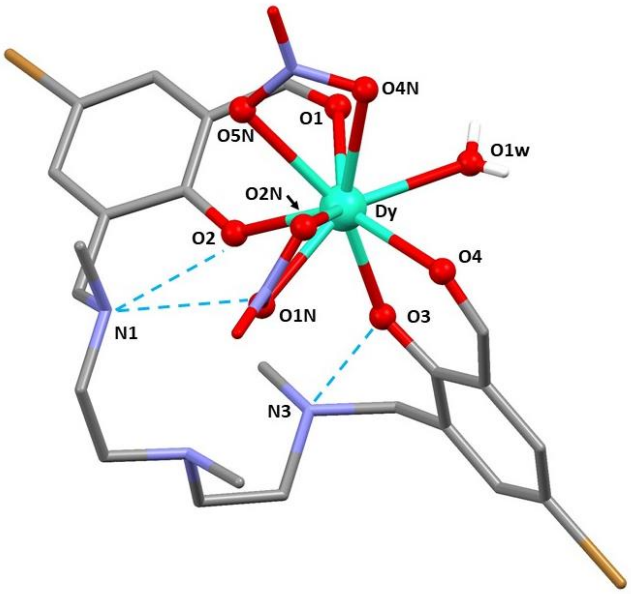

Figure 1.7.- Perspective view of complex **3**. Colour code: dysprosium, bromine, nitrogen, oxygen, carbon and hydrogen atoms are in turquoise, brown, light blue, red, grey and white, respectively. Hydrogen atoms from the ligand, solvent molecules and the counterions are omitted for the sake of clarity.

The mononuclear complex **5**, shown in Figure 1.8, crystallizes in the monoclinic *P* $2_1/c$ space group. As it was found for complex **1**, the distorted muffin shaped DyO_9 coordination environment is again completed by two phenoxido groups, two aldehydes, two bidentate nitrates and a monodentate nitrate anion. Dy-O2 and Dy-O3 bond lengths are of 2.2795(18) Å and 2.2459(17) Å, respectively, are shorter than the rest of Dy-O bonds, which are in the 2.3994(19)-2.5329(19) Å range. Each zwitterionic nitrogen presents two hydrogen bonds, one to the nearest phenoxido group and the other to O7N, displaying 2.755 Å, 2.955 Å, 2.759 Å and 3.041 Å distances for N1···O2, N1···O7N, N2···O3 and N2···O7N, respectively. The shortest intermolecular Dy···Dy distance is of 9.004 Å.

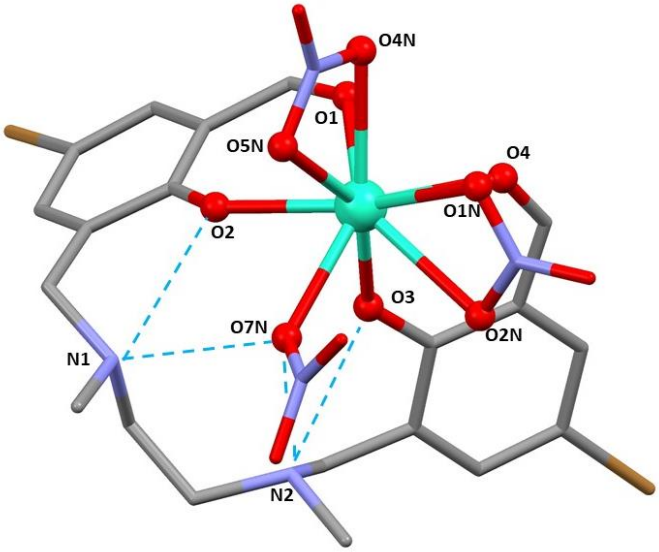

Figure 1.8.- Perspective view of complex **5**. Colour code: dysprosium, bromine, nitrogen, oxygen and carbon atoms are in turquoise, brown, light blue, red and grey, respectively. Hydrogen atoms and solvent molecules are omitted for the sake of clarity.

1.4.2. Static magnetic properties of complexes 1-6

The temperature dependence of the magnetic susceptibility was measured on polycrystalline samples for complexes **1-6** in the 2-300 K temperature range under an applied field of 0.1 T (Figure 1.9). The room temperature $\chi_M T$ values of 14.24 (**1**), 11.88 (**2**), 14.20 (**3**), 11.60 (**4**), 14.24 (**5**) and 11.65 (**6**) $cm^3 \cdot mol^{-1} \cdot K$ are in good agreement with the expected values for a Dy^{III} (14.17 $cm^3 \cdot mol^{-1} \cdot K$; $^6H_{15/2}$, and g = 4/3) or Er^{III} (11.48 $cm^3 \cdot mol^{-1} \cdot K$; $^4I_{15/2}$, and g = 6/5) ion. Generally, they all show a gradual decrease of the $\chi_M T$ on cooling down with sharper final drops at low temperatures. This behaviour is in agreement with the depopulation of the Stark sublevels and is rather common in Dy^{III} and Er^{III} based SMMs. Isothermal magnetization curves (insets) collected in the 2-7 K temperature range display both lack of saturation and non-superimposable features indicative of magnetic anisotropy.

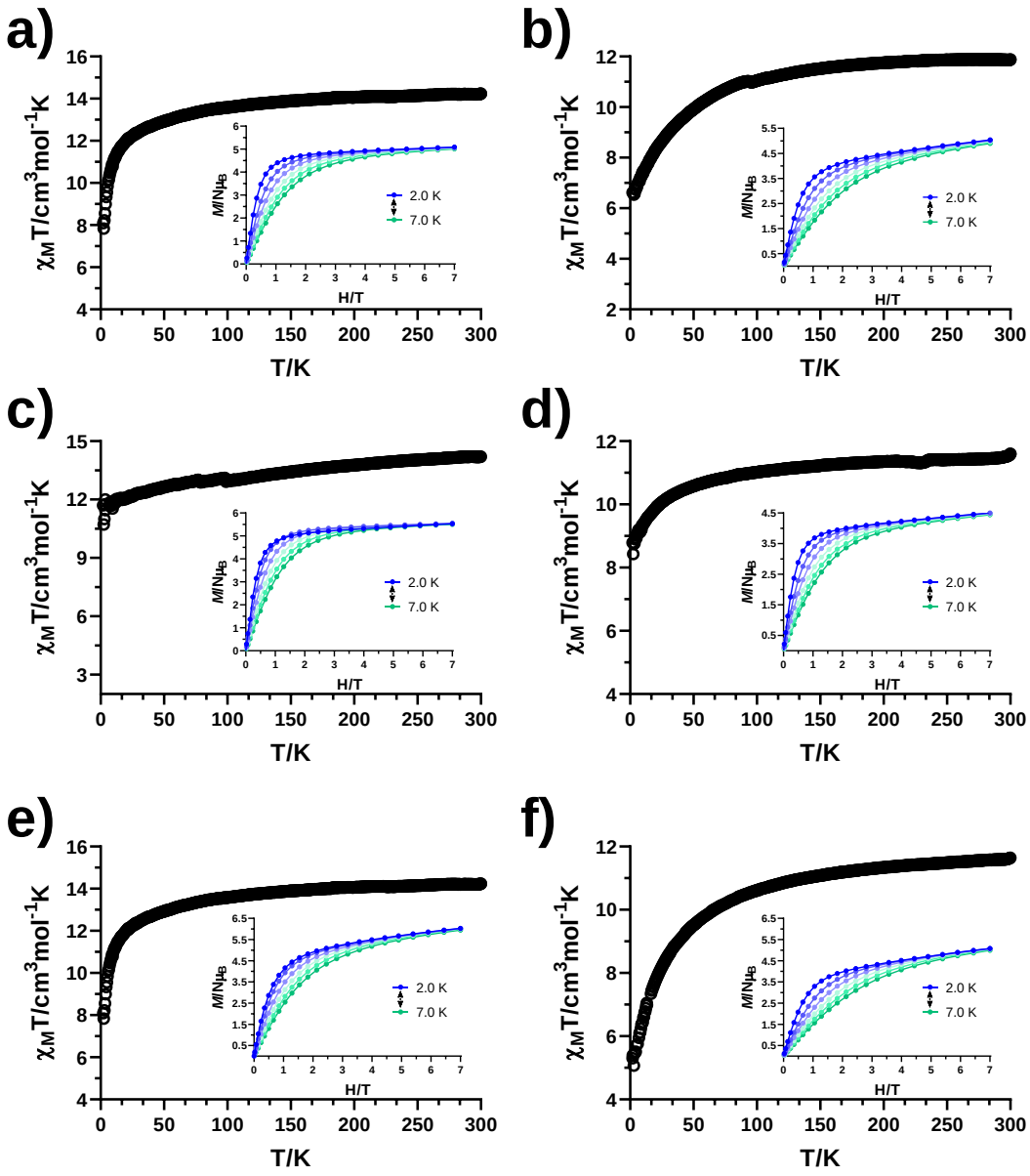

Figure 1.9.- Temperature dependence of the $\chi_M T$ product at 1000 Oe for complexes **1-6** (from a) to f), respectively). Insets: Field dependence of the magnetization in the 2-7 K temperature range. Dashed solid lines are a guide to the eye.

1.4.3. Dynamic magnetic properties of complexes 1-6

In order to determine whether the complexes behave as SMMs, dynamic alterning-current (*ac*) magnetic susceptibility measurements as a function of the temperature and frequency were performed for compounds **1-6** on polycrystalline samples with an oscillating field of 3.5 Oe. At zero applied *dc* field, only compound **1** displayed a

maximum in the out-of-phase susceptibility component (χ_M'') at the highest measured frequency (10000 Hz, Figures A1.9-A1.11). The other two dysprosium based compounds **3** and **5** displayed non-zero χ_M'' signals, but without any maxima above 2.0 K, the lower temperature limit of the instrument. Meanwhile, the Er^{III} counterparts did not display any signal in the out-of-phase region. The lack of any maximum or even signal could be due to either strong quantum tunnelling effects, which prevent us to observe any SMM behaviour, or the thermal energy barrier is too small as to show slow relaxation above 2 K. Therefore, as it will be discussed later in this section, the application of external magnetic fields and magnetic dilution effects to fully or partly eliminate QTM have also been studied. Note that a summary containing all the parameters related to different relaxation pathways is available at the end of this section in Table 1.1.

Although compound **1** presents SMM behaviour at zero field, the set of maxima at all the used frequencies in the $\chi_M''(T)$ curves shows a very low definition due to the strong overlapping with the intense tail of the signal due QTM at low temperature below the maxima (Figure 1.10, left). This is reflected also in the $\chi_M''(\upsilon)$ curves, where the position of the maxima remains unshifted in the lowest temperature region (Figure A1.16). Relaxation times were extracted from the fitting of these curves to the generalized Debye model. The Arrhenius plot built from the extracted relxation times in the form $\ln\tau$ vs T^{-1} is linear in the highest temperatures region followed by a curvature in the intermediate range and a clear temperature-independent relaxation regime at the lowest temperatures region indicative of QTM (Figure 1.10, inset). This result clearly suggests that various mechanisms are operating in the magnetic relaxation, in concordance with the high α values extracted from the Cole-Cole plots (0.33 (2.0 K)-0.11 (14.0 K)). Thus, the relaxation times were fitted to the equation that simultaneously considers QTM, Raman and Orbach processes:

$$\tau^{-1} = \tau_{QTM}^{-1} + BT^{n} + \tau_0^{-1}exp(-U_{eff}/k_BT) \qquad \textit{Equation 1.1}$$

The fit afforded the following set of parameters: τ_{QTM} = 7.9·10^{-5} s, B = 234.4 s^{-1}K$^{-1.696}$, n = 1.696, τ_0 = 2.4·10^{-9} s and U_{eff} = 125.2 K. For a Kramers ion a n value of 9 is expected [5], though values between 1-6 are also considered as reasonable when both optical and acoustic phonons participate in the magnetic relaxation [6].

With the aim of partially or totally suppressing QTM, *ac* susceptibility measurements were carried out with an optimum external magnetic field of 1 kOe (see Figures A1.18-A1.19 for field dependent measurements to optimize the field). In this

case, the maxima below 14.0 K are much better defined due to a considerable quenching of QTM (Figure 1.10, right). Nonetheless, the tails at the lowest temperatures remain appreciable, indicative of some residual QTM. The $\chi_M''(\upsilon)$ and Cole-Cole plots were studied in the 8.0-13.4 K temperature range, where a relatively high distribution of relaxation mechanisms is expected (α values in the range of 0.52(8.0 K)-0.22 (13.4 K)). The relaxation times, however, show a nearly perfect linear trend in the studied temperature region and, hence, they were fitted to the Arrhenius law providing τ_0 and U_{eff} values of $2.4 \cdot 10^{-8}$ s and 93.5 K. The high α value obtained at 8.0 K probably indicates that below this temperature several mechanisms must be cooperating, which is in fair agreement with the Raman predominance region for **1** under zero applied field. In this case, however, the maxima in the $\chi_M''(\upsilon)$ curves would appear below the frequency limit of the instrument (Figure A1.21), what prevents us from evaluating Raman's contribution through incorporating it into the equation.

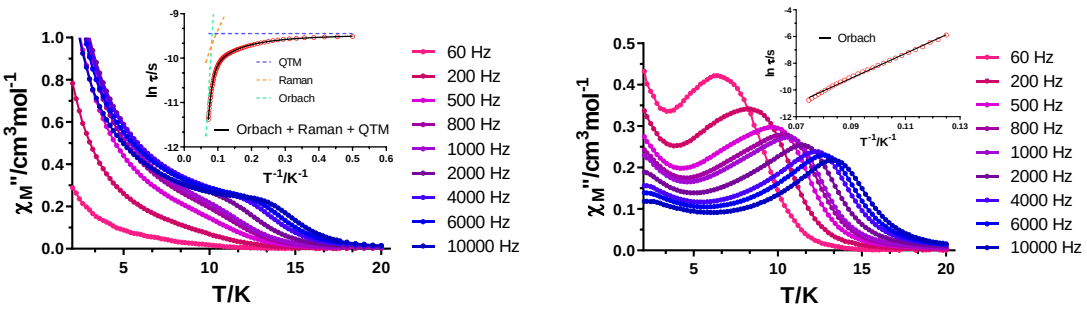

Figure 1.10.- Temperature dependence of the out-of-phase components of the *ac* susceptibility in a zero applied field (left) and under an external field of 1 kOe (right) for **1**. Inset: Arrhenius plot for the relaxation times extracted under zero applied *dc* field considering Orbach + Raman + QTM (left) and under 1 kOe *dc* field for an Orbach process (right). Dashed lines represent the contribution of each mechanism to the overall fit.

Compound **2** displayed an out-of-phase signal under an external magnetic field of 1 kOe and 500 Hz, but without any maximum (Figure A1.12). Thus, field dependent measurements were carried out at 2.0 K. As it can be seen in Figure A1.23, the relaxation becomes slower as the external field increases (maxima are moved towards lower freq.), but above 1000 Oe the relaxation accelerates as the maxima are shifted again towards higher frequencies, which could be indicative of the occurrence of a direct process [7]. The $\chi_M''(\upsilon)$ curves at different fields were fitted with the generalized

Debye mode obtaining the slowest relaxation times at 1000 Oe (Figure A1.24). Noteworthy, the curve at 2500 Oe was not fitted since a second maximum begins to appear at the lowest frequencies region. In view of the above considerations, the $\tau^{-1}(H)$ could be represented by the following equation, where the first two terms account for field dependent QTM and direct processes, respectively, and the latter for field independent mechanisms.

$$\tau^{-1} = \frac{B_1}{1+ B_2 \cdot H^2} + AH^4T + k \quad \textit{Equation 1.2}$$

The best fit afforded B_1 = 41990 s^{-1}, B_2 = 2436 T^{-2}, A = 6.36·10^6 $s^{-1}T^{-4}K^{-1}$ and k = 10146 s^{-1}. The high value of k must indicate that even at 2.0 K field independent relaxation mechanisms, such as Orbach and Raman, are operative. A complete temperature and frequency dependent measurement was then performed under an external optimum field of 1 kOe, which displayed a set of maxima in the out-of-phase region below 3.5 K (Figure 1.11). In order to obtain relaxation times and α values, the data were evaluated in 2.0-3.5 K range. The results suggest a quite narrow distribution of relaxation processes. Nevertheless, the smooth curvature in the low temperature region of the Arrhenius plot (Figure 1.11, inset) indicates that in addition to Orbach other mechanisms contribute to the relaxation process. Thus, we took advantage of the relaxation parameters obtained from the field dependent measurements and we fixed τ_{QTM}^{-1} and AH^4 to 1656 s^{-1} and 636.4 $s^{-1}K^{-1}$, respectively, in the following equation, which considers QTM, direct and Orbach mechanisms:

$$\tau^{-1} = \tau_{QTM}^{-1} + AH^4T + \tau_0^{-1}exp(-U_{eff}/k_BT) \quad \textit{Equation 1.3}$$

The fitting afforded τ_0 and U_{eff} values of 5.0·10^{-7} s and 12.8 K. This method allowed us to avoid overparametrization of the equation that describes the relaxation times. However, it is visible from the fitting that the predominant relaxation pathway is the Orbach one, while direct and QTM mechanisms slightly influence relaxation dynamics. This is in fair agreement with the α values, which indicate a predominant single process.

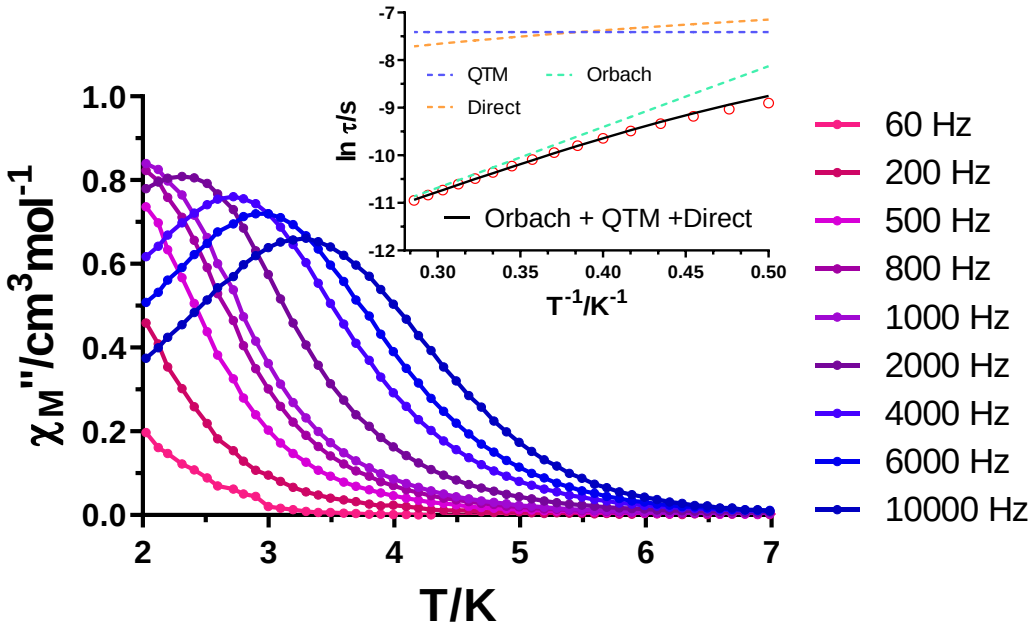

Figure 1.11.- Temperature dependence of the out-of-phase components of the *ac* susceptibility under an external field of 1 kOe for **2**. Inset: Arrhenius plot for the relaxation times considering Orbach + Direct + QTM processes. Dashed lines represent the contribution of each mechanism to the overall fit.

Dysprosium based compound **3** displayed a well-defined maximum around 6 K under an external magnetic field of 1 kOe at 500 Hz (Figure A1.13). Field dependent measurements carried out at 5.0 K showed that the optimum *dc* field is of 1.5 kOe (Figures A1.28-A1.29), thus a complete measurement was carried out in these conditions (Figure 1.12). The relaxation times display a linear trend at the highest temperatures followed by a curvature, which could be indicative of the presence of several relaxation mechanisms. Indeed, this is in agreement with the high α values in the whole studied temperature range (0.34 (5.0 K) – 0.32 (9.9 K)). However, we were not able obtain reasonable parameters considering simultaneous mechanisms. Hence, the data at the highest temperatures was fitted to a single Orbach process providing τ_0 and U_{eff} values of $1.4 \cdot 10^{-8}$ s and 68.8 K.

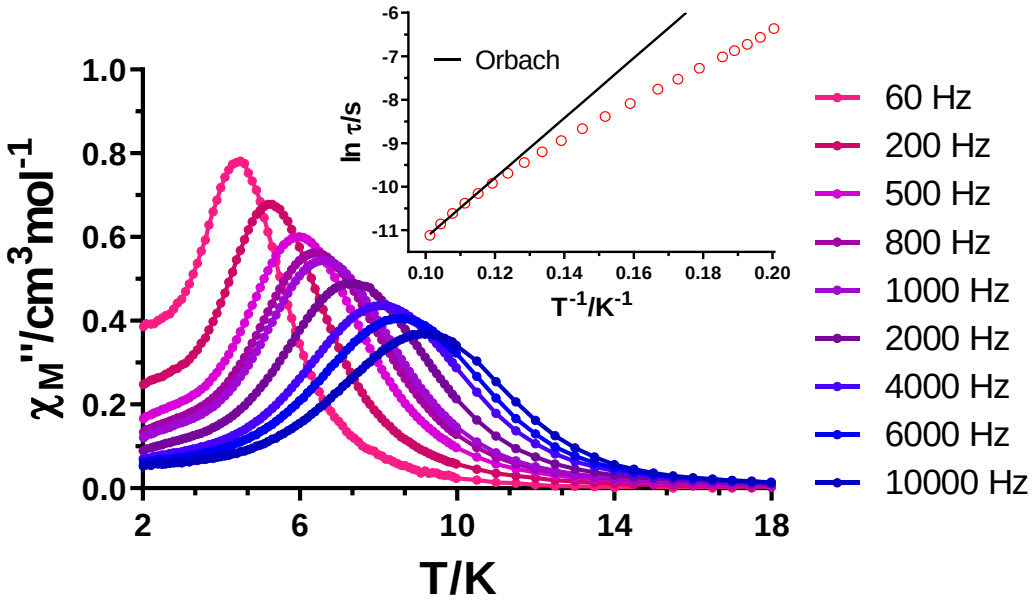

Figure 1.12.- Temperature dependence of the out-of-phase components of the *ac* susceptibility under an external field of 1.5 kOe for **3**. Inset: Arrhenius plot for the relaxation times fitted with an Orbach process.

Considering the poor SMM properties of complex **4**, which does not show any clear maximum at 500 Hz and with an external magnetic field of 1 kOe at 2.0 K (Figure A1.13), the temperature and frequency dependency was directly studied with the mentioned external field to make an estimation of the energy barrier. As depicted in Figure 1.13, the χ_M'' signals are strongly frequency dependant, however, the maxima are slightly below the limit of the instrument. This fact impedes the extraction of the relaxation times from the fitting of the $\chi_M''(\upsilon)$ plot (Figure A1.33), and therefore obtaining U_{eff} and τ_0 values through conventional Arrhenius method. To overcome this problem, we have applied an alternative approach to extract the relaxation parameters from the *ac* data. This approach consists in considering that the ratio between the out-of-phase and in-phase components of the *ac* susceptibility can be expressed in an approximate manner as $\chi''_M/\chi'_M = 2\pi\upsilon\tau$. Hence, assuming that there is a single Orbach relaxation process, the following equation can be obtained:

$$ln(\chi_M''/\chi_M') = ln(2\pi\upsilon\tau_0) + E_a/k_BT \qquad \textit{Equation 1.4}$$

The fitting of the data at several frequencies (Figure 1.13, inset) afforded $U_{eff} \approx 6.2$ K and $\tau_0 = 1.2 \cdot 10^{-6}$ s.

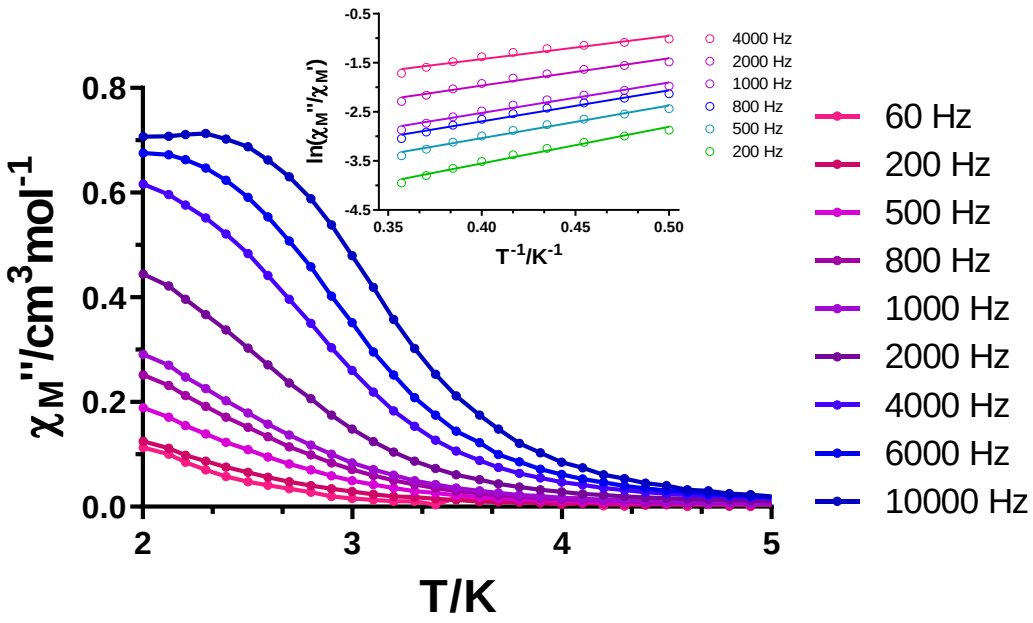

Figure 1.13.- Temperature dependence of the out-of-phase components of the *ac* susceptibility under an external field of 1 kOe for **4**. Inset: Fitting of the data to the Debye model with the equation $ln(\chi_M''/\chi_M') = ln(2\pi\upsilon\tau_0) + E_a/k_BT$.

The H_2L^2 based compound **5** displays the poorest SMM properties of the studied complexes. Although applying an external magnetic field of 1 kOe a frequency dependant signal can be observed, the maxima are outside the instrument limit, somewhat below the maxima of that **4** (Figure A1.14). This suggests a negligible value of the effective energy barrier and therefore no further analysis was done for this compound.

For **6**, field dependent measurements carried out at 2.0 K show a similar behaviour to **2** (Figures A1.37-A1.38). In this case, however, the second maximum at lowest frequencies starts to appear at lower fields (1000 Oe, see Figure A1.37). The optimum field was determined to be 500 Oe where a single maximum with the slowest relaxation time is obtained. The temperature dependence of the out-of-phase signal at different frequencies display maxima below 2.5 K only at the three highest frequencies, being below the instrument limit for the rest of the frequencies (Figure 1.14). Relaxation times

within the 2.0-2.5 K range display a linear tendency so they were fitted by the Arrhenius law obtaining an effective energy barrier of 14.6 K and τ_0 = 3.3·10^{-8} s. Moreover, the Cole-Cole plots provide low α values in the range of 0.15-0.13 (2.0-2.5 K), suggesting a narrow distribution of relaxation mechanisms.

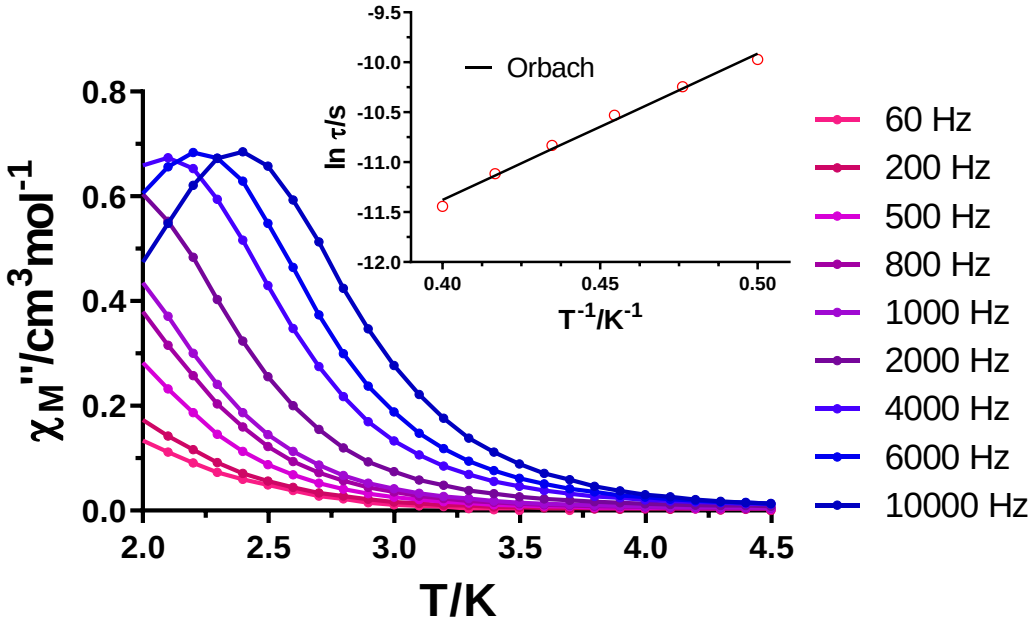

Figure 1.14.- Temperature dependence of the out-of-phase components of the *ac* susceptibility under an external field of 500 Oe for **6**. Inset: Arrhenius plot for the relaxation times fitted with an Orbach process.

Once studied the magnetic properties of the pure samples under zero and optimum applied fields, the diluted analogues of all compounds were synthesized in a Ln:Y 1:10 molar ratio for further quenching the non-desired QTM that might arise from intermolecular dipolar interactions. Under zero applied *dc* field, none of the Er^{III} analogues displayed maxima in the out-of-phase signal, though a weak response was observed for **2$_Y$** and **4$_Y$** (Figures A1.9-A1.10). In contrast, compound **1$_Y$** at a frequency of 10000 Hz, showed a better defined maximum due to a partial quenching of QTM and **3$_Y$** displayed a maximum below 10 K, suggesting that intermolecular interactions were hiding the zero field SMM character of this complex (Figures A1.9-A1.10). In both cases, however, the long tails below the maxima are indicative of residual QTM, which suggests that for these compounds the low symmetry coordination environments provide the systems with transverse components that favour this relaxing mechanism.

For the last Dy^{III} based compound $\mathbf{5_Y}$, no remarkable difference was observed upon dilution at zero applied *dc* field (Figure A1.11). When combining both QTM quencher techniques (diamagnetic dilution + external magnetic field, Figures A1.12-A1.14), the tail in $\mathbf{1_Y}$ was completely removed, whereas no remarkable difference was observed for the rest of the Dy^{III} based compounds. Note that for compound **3**, the QTM was effectively suppressed by the application of an external magnetic field, thus there was no difference between **3** and $\mathbf{3_Y}$ when performing the measurement with the external field. For Er^{III} counterparts, instead, the main remarkable difference was observed for $\mathbf{4_Y}$, where a clear peak shift towards a higher temperature can be observed (Figure A1.13).

For $\mathbf{1_Y}$, relaxation times at zero *dc* field display a linear tendency at the very highest temperatures, while in the rest of the temperature range a curved plot is observed (Figure 1.15, left inset). In contrast to **1**, we were not able to fit the data at the lowest temperatures due to the fact that no maxima are observed in the measured frequency range below 7.0 K (Figure A1.43). Thus, even though the curvature would probably reach a plateau at the lowest temperatures corresponding to QTM, in this case only Raman and Orbach processes were considered for the fitting:

$$\tau^{-1} = BT^{n} + \tau_0^{-1}exp(-U_{eff}/k_BT) \qquad \textit{Equation 1.5}$$

The best fit afforded the following set of parameters: $B = 0.19\ s^{-1}K^{-4.408}$, $n = 4.408$, $\tau_0 = 5.7 \cdot 10^{-10}$ s and $U_{eff} = 147.0$ K. Apart from the curvature of the data, the α values obtained from the Cole-Cole plots also indicate a quite wide distribution of relaxation pathways (0.54 (7.0 K)-0.15 (13.4 K)). When applying the optimum external magnetic field to $\mathbf{1_Y}$, the long tails below the maxima completely disappeared, indicating that the dilution and the application of a magnetic field are able to suppress efficiently the QTM (Figure 1.15, right). In this case, the relaxation times were fitted to a single Orbach process following the Arrhenius law. The obtained energy barrier and τ_0 values are 111.5 K and $6.7 \cdot 10^{-9}$ s.

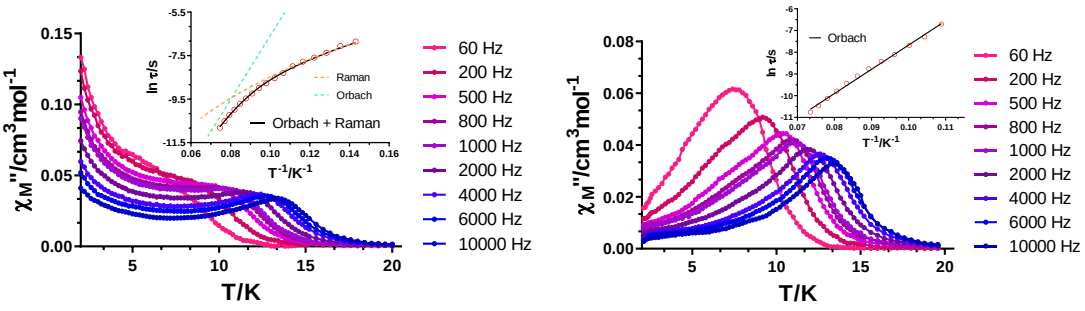

Figure 1.15.- Temperature dependence of the out-of-phase components of the *ac* susceptibility in a zero applied field (left) and under an external field of 1 kOe (right) for $\mathbf{1_Y}$. Inset: Arrhenius plot for the relaxation times considering Orbach + Raman (left) and Orbach (right) processes. Dashed lines represent the contribution of each mechanism to the overall fit.

Once intermolecular interactions partly eliminated in $\mathbf{3_Y}$, the compound displayed SMM behaviour at zero applied *dc* field (Figure 1.16). However, the distribution of the relaxation times in the 2.0-10.8 K temperature range display a linear fraction at the highest temperatures followed by a curvature that ends in a temperature independent regime at 2.0 K attributed to QTM. The contribution of several relaxation mechanisms is well reflected in the α values, which do not fall below 0.35. In order to obtain a reliable fit, the data was fitted to the sum of Orbach, Raman and QTM processes by Equation 1.1, but including a constrain of τ_{QTM}^{-1} = 992 s^{-1} which is obtained from the relaxation time at the lowest temperature (QTM must be the main relaxation pathway at this temperature). Otherwise, the fitting affords senseless values. The following set of parameters was obtained: B = 2.8 $s^{-1}K^{-3.743}$, n = 3.743, τ_0 =3.1·10^{-8} s and U_{eff} = 77.2 K. In view of the fact that **3** and $\mathbf{3_Y}$ displayed the same behaviour under an external magnetic field (see Figure A1.13), no further measurements were performed.

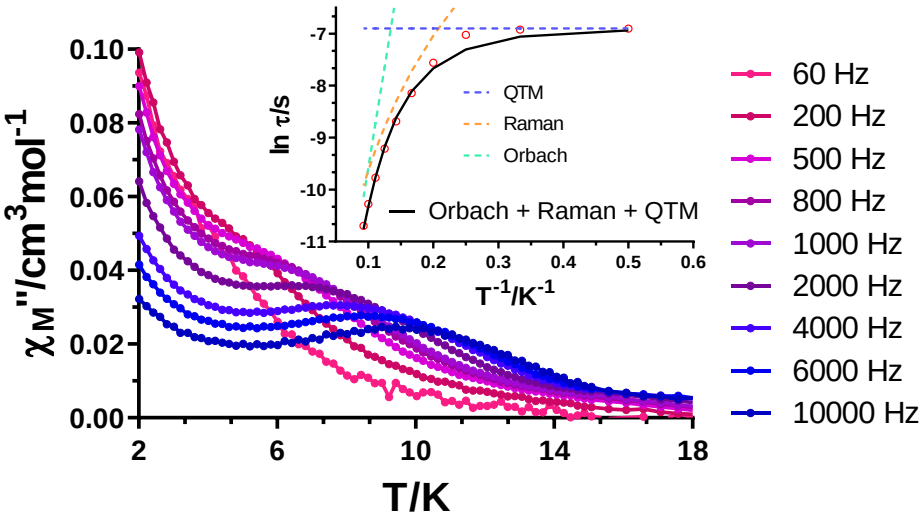

Figure 1.16.- Temperature dependence of the out-of-phase components of the *ac* susceptibility in a zero applied field for **3**$_{Y}$. Inset: Arrhenius plot for the relaxation times considering Orbach + Raman + QTM processes. Dashed lines represent the contribution of each mechanism to the overall fit.

Compound **4**$_{Y}$, in contrast to **4**, displays well defined maxima below 3 K in presence of an external magnetic field (Figure 1.17). Relaxation times were obtained by fitting the $\chi_M''(\upsilon)$ curves in the 2.0-3.2 K range. Their curved nature, as well as the relatively high α values (0.30 (2.0 K)-0.16 (3.2 K) indicate the presence of simultaneous relaxation mechanisms. The data was best described by fitting it to Equation 1.6, which considers Orbach and direct processes:

$$\tau^{-1} = AH^4T + \tau_0^{-1}exp(-U_{eff}/k_BT) \qquad \textit{Equation 1.6}$$

The following set of parameters was obtained: AH^4 = 1966 s^{-1}, τ_0 = 8.5·10^{-8} s and U_{eff} = 17.8 K.

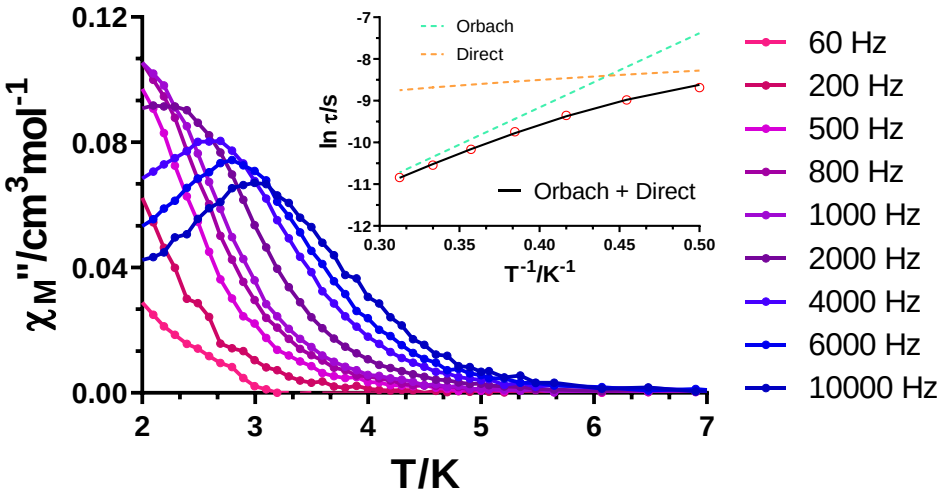

Figure 1.17.- Temperature dependence of the out-of-phase components of the *ac* susceptibility under an external field of 1 kOe for **4**$_{Y}$. Inset: Arrhenius plot for the relaxation times considering Orbach + Direct processes. Dashed lines represent the contribution of each mechanism to the overall fit.

Table 1.1.- U_{eff}, τ_0, B, n, τ_{QTM} and A parameters generated from the fit of the relaxation time-temperature dependence for **1**, **1**$_{Y}$, **2**, **3**, **3**$_{Y}$, **4**, **4**$_{Y}$ and **6**.

	***dc* field**	**Orbach**		**Raman**		**QTM**	**Direct**
Comp.	Oe	U_{eff} (K)	τ_0 (s)	B ($s^{-1}K^{-n}$)	n	τ_{QTM} (s)	A ($s^{-1}T^{-4}$ K^{-1})
1	0	125.2	$2.4\cdot10^{-9}$	234.4	1.7	$7.9\cdot10^{-5}$	
	1000	93.5	$2.4\cdot10^{-8}$				
1$_{Y}$	0	147.0	$5.7\cdot10^{-10}$	0.19	4.4		
	1000	111.5	$6.7\cdot10^{-9}$				
2	1000	12.8	$5.0\cdot10^{-7}$			$6.0\cdot10^{-4}$	$6.4\cdot10^{6}$
3	1500	68.8	$1.4\cdot10^{-8}$				
3$_{Y}$	0	77.2	$3.1\cdot10^{-8}$	2.8	3.7	$1.0\cdot10^{-3}$	
4	1000	6.2	$1.2\cdot10^{-6}$				
4$_{Y}$	1000	17.8	$8.5\cdot10^{-8}$				$2.0\cdot10^{7}$
6	500	14.6	$3.3\cdot10^{-8}$				

1.4.4. Magneto-structural correlations

It is of vital importance to obtain magneto-structural correlations with the aim of better understanding which are the parameters that mostly influence the dynamic magnetic properties and, thus to be able to further improve the crystal fields of the systems, thus leading to a slower magnetization relaxation. This has been recently done for high performance SMMs with quite rigorous linear and $D5_h$ symmetry [1,8,9]. In such systems where the geometry of the coordination environment is very defined, the effect that cause modifications in the ligand field are sometimes easier to detect. For instance, it is known that in a pentagonal bipyramidal system where the equatorial field is formed of THF molecules, as a general statement the more electronegative and short bond distances in the apical position will provide the system a higher axiality and, as a consequence, higher effective energy barriers. For low symmetry systems, however, this might be more challenging.

Based on the results obtained from the Magellan software [10], in three of the Dy^{III} compounds the anisotropic axis (An_{axis}) is mostly influenced by the shortest Dy-$O_{phenoxido}$ bond, named as Dy-O_{SP}; the longer Dy-$O_{phenoxido}$ is named as Dy-O_{LP} in Table 1.2 (see Figure 1.18 for anisotropic axis in **1** and Figure A1.54 for **3** and **5**). This was an expected feature, since between all donor atoms the phenoxido ones contain the highest negative net charge and they display the shortest bond distances. Taking into account that the anisotropy axes lie perpendicular towards the oblate like electron distribution of the Dy^{III} ion, we believe that the most critical parameters are the following ones: Dy-$O_{phenoxido}$ distances, Dy-O distance towards monodentate nitrate (or water molecule in **3**) and angles between the An_{axis}-Dy-O of the above mentioned donor atoms, which we named as α (involving Dy-O_{SP}), β (involving Dy-O_{LP}) and γ (involving the monodentate nitrate anion, see Table 1.2 and Figure 1.18). We have included the monodentate nitrate anion because it is the one showing the shortest bond distance within all nitrates (which can be explained by the lower denticity). On the one hand, **1** and **3** display the shortest Dy-O_{SP} bond distances, although **5** possess a slightly shorter for Dy-O_{LP} distance than the former ones. We therefore decided to analyse α and β angles. Ideally, in order to stabilize the highest magnetic M_J states, both most electronegative and shortest bonds should be in opposite positions. This is not the case in any of these compounds, indeed, they are nearer to be orthogonal to each other, which would be unfavourable to achieve an axial Kramers ground state (M_J = ±15/2). Hence, we believe that as α and β angles are smaller, the adoption of a M_J = ±15/2 ground Kramers doublet is more favoured, since this means that both phenoxido

groups are nearer to be in the same side of the spheroid (Figure 1.18c). Bearing this in mind, the smallest sum of α and β angles were calculated for **1**, which is the only compound showing zero field SMM behaviour and the highest effective energy barrier. On the other hand, compounds **3** and **5** show almost the same sum of α and β values, being α smaller for **5** and β for **3**. This is the reason why we considered studying the parameters related to the monodentate nitrate in **5** or a water molecule in **3**. The oxygen atoms belonging to these ligands (monodentate nitrate or water) show larger angles respect to the anisotropy axis, γ, and they can perturb the equatorial ligand field. The difference between **3** and **5** is that for the former this position is occupied by a neutral and less electron donating water molecule, whereas for the latter a negatively charged and shortly bonded (compared to the rest of nitrate oxygen atoms) atom is present. The effect of the difference in γ angles and Dy-O distance to the water or monodentate nitrate anion affecting the transverse anisotropy and dipolar interactions may lead to the different relaxation behaviour between **3** and **5**.

Table 1.2.- Relevant Dy-O bond distances and angles respect to the calculated anisotropy axis for **1**, **3** and **5**.

	Dy-O_{SP} (Å)	**Dy-O_{LP} (Å)**	**Dy-$O_{monNO3/1W}$ (Å)**	**α (º)**	**β (º)**	**γ (º)**
1	2.234(5)	2.310(5)	2.397(5)	18.32	56.92	77.04
3	2.238(3)	2.284(3)	2.368(4)	18.22	60.49	94.06
5	2.2459(17)	2.2795(18)	2.3994(19)	17.68	61.82	67.35

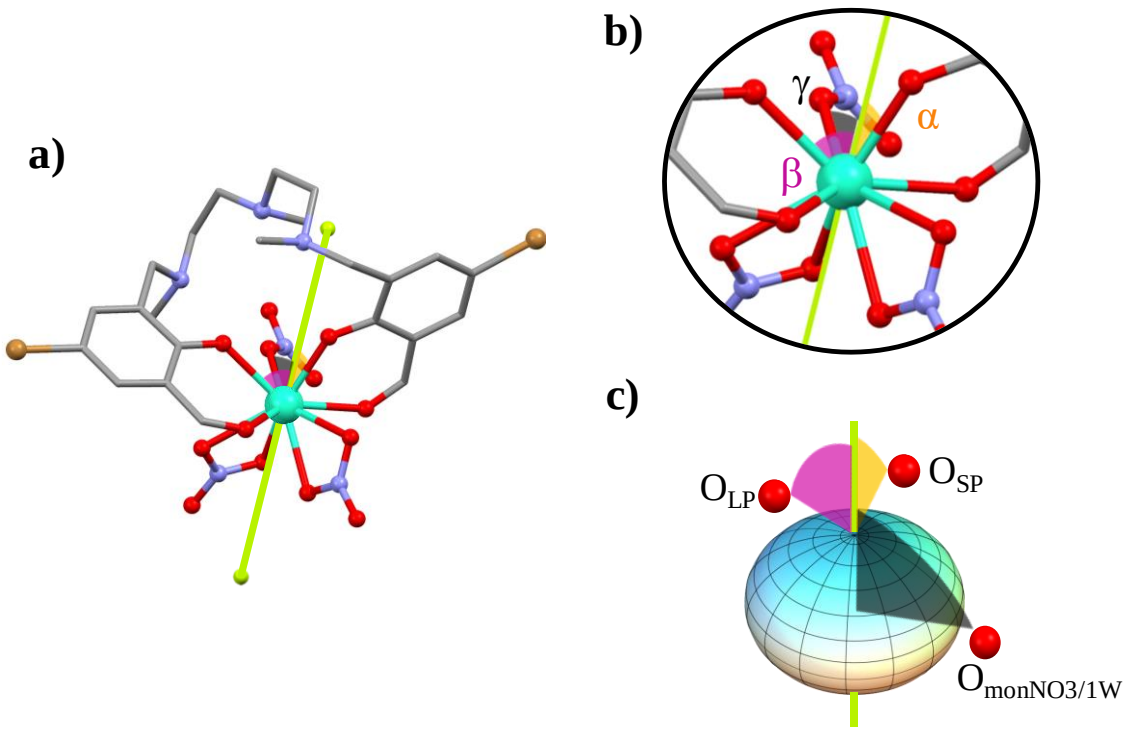

Figure 1.18.- a) Anisotropy axis for compound **1** obtained with Magellan software (green line); b) Angles that may mostly affect the dynamic magnetic properties of Dy^{III} based compounds: **α**: axis-Dy-O_{SP}; **β**: axis-Dy-O_{LP}; **γ**: axis-Dy-O_{monNO3}; c) Suggested electron distribution around Dy^{III} ion and position of most influencing donor atoms.

All in all, it is worth mentioning that these suggested correlations must be regarded with precaution. In systems with such a high coordination number the sum of variables and slight angular/distance alterations are numerous. All of them must have their own impact in the overall dynamic magnetic properties, but we have tried to evaluate the most influencing ones.

In the case of **2**, **4** and **6**, the Er^{III} ions possess exactly the opposite electron density distribution to the Dy^{III}, named as prolate. In such cases, for stabilizing the highest magnetic states as ground states, strong equatorial ligand fields are required. As it was shown for **1**, **3** and **5**, the ligand field is not either axial or equatorial. However, we might assume that what is somehow suitable for one, it has to be worse for the other. Therefore, the weaker SMM behaviour for **2** could be in agreement with the enhanced properties of **6**.

1.5. CONCLUSIONS

The compartmental ligands H_2L^1 and H_2L^2 allowed us to synthesize three novel pairs of mononuclear systems based on the oblate and prolate Dy^{III} and Er^{III} ions, respectively. The low symmetry coordination environments are very similar between the three pairs of systems. The dynamic magnetic properties, however, differ considerably being only compound **1** a zero field SMM. The poorly defined geometries might be a principle reason to enable fast tunnelling of the magnetization and external magnetic fields were required to emerge slow magnetic relaxation in the other compounds.

Although at first glance the mononuclear systems were well isolated within the crystal structure (over 8 Å between ions in all cases), the study of the magnetically diluted compounds was relevant, since it has been proven that intermolecular interactions were having an important role creating transverse magnetic fields responsible of QTM. In fact, tunnelling was partially reduced for $\mathbf{1_Y}$, $\mathbf{3_Y}$ displayed out-of-phase maxima at zero applied field and the peaks were shifted towards higher temperatures for $\mathbf{4_Y}$.

For the studied mononuclear systems, it is not easy to find magneto-structural correlations due to the fact that either axial or equatorial ligand fields are not well stablished. Nonetheless, in this chapter we have tried to indetify the main factors influencing magnetic properties. As expected, the shortest bond distances corresponding to phenoxido oxygen atoms define the magnetic anisotropy axes calculated for Dy^{III} compounds by Magellan software. Beyond that, we believe that the named α, β and γ angles, as well as the difference in Dy-O distances between phenoxido and nitrate (or water) atoms allow us to explain the experimental results. Finally, by considering the opposite electron density between Dy^{III} and Er^{III} ions, reversed dynamic magnetic properties might make sense.

1.6. REFERENCES

[1] Y. Ding, T. Han, Y. Zhai, D. Reta, N.F. Chilton, R.E.P. Winpenny, Y. Zheng, A Study of Magnetic Relaxation in Dysprosium(III) Single-Molecule Magnets, Chem. – A Eur. J. 26 (2020) 5893–5902. https://doi.org/10.1002/chem.202000646.

[2] J. Ruiz, A.J. Mota, A. Rodríguez-Diéguez, S. Titos, J.M. Herrera, E. Ruiz, E. Cremades, J.P. Costes, E. Colacio, Field and dilution effects on the slow relaxation of a luminescent DyO9 low-symmetry single-ion magnet., Chem. Commun. 48 (2012) 7916–8. https://doi.org/10.1039/c2cc32518g.

[3] M. Yonemura, Y. Matsumura, M. Ohba, H. Okawa, D.E. Fenton, Template synthesis of phenol-

based heterodinucleating macrocycles with dissimilar N(amine)2O2 and N(imine)2O2 metal-binding sites, Chem. Lett. (1996) 601–602. https://doi.org/10.1246/cl.1996.601.

[4] M. Llunell, D. Casanova, J. Cirera, J.M. Bofill, P. Alemany, S. Alvarez, M. Pinsky, D. Avnir, SHAPE, (2005).

[5] A. Abragam, B. Bleaney, Electron Paramagnetic Resonance of Transition Ions, Clarendon Press Oxford, UK,. (1970) 925.

[6] K.N. Shrivastava, Theory of Spin–Lattice Relaxation, Phys. Status Solidi. 117 (1983) 437–458. https://doi.org/10.1002/pssb.2221170202.

[7] S. Roy, I. Oyarzabal, J. Vallejo, J. Cano, E. Colacio, A. Bauza, A. Frontera, A.M. Kirillov, M.G.B. Drew, S. Das, Two Polymorphic Forms of a Six-Coordinate Mononuclear Cobalt(II) Complex with Easy-Plane Anisotropy: Structural Features, Theoretical Calculations, and Field-Induced Slow Relaxation of the Magnetization, Inorg. Chem. 55 (2016) 8502–8513. https://doi.org/10.1021/acs.inorgchem.6b01087.

[8] K.R. McClain, C.A. Gould, K. Chakarawet, S.J. Teat, T.J. Groshens, J.R. Long, B.G. Harvey, High-temperature magnetic blocking and magneto-structural correlations in a series of dysprosium(III) metallocenium single-molecule magnets, Chem. Sci. 9 (2018) 8492–8503. https://doi.org/10.1039/C8SC03907K.

[9] H. Wu, M. Li, B. Yin, Z. Xia, H. Ke, Q. Wei, G. Xie, S. Chen, S. Gao, Fine-Tuning the type of equatorial donor atom in pentagonal bipyramidal Dy(iii) complexes to enhance single-molecule magnet properties, Dalton Trans. 48 (2019) 16384–16394. https://doi.org/10.1039/c9dt03292d.

[10] N.F. Chilton, D. Collison, E.J.L. McInnes, R.E.P. Winpenny, A. Soncini, An electrostatic model for the determination of magnetic anisotropy in dysprosium complexes, Nat. Commun. 4 (2013) 1–7. https://doi.org/10.1038/ncomms3551.

CHAPTER 2

EXTENDING DINUCLEAR $Zn^{II}Dy^{III}$ ENTITIES THROUGH A VARIETY OF BRIDGING DI- AND TRICARBOXYLATE GROUPS: AN EXHAUSTIVE MAGNETIC STUDY

2.1. INTRODUCTION

The second chapter of this thesis is a direct continuation of our previously reported research [1], in which we studied the magnetic and luminescent properties of twelve diphenoxido and acetate triply-bridged dinuclear $Zn^{II}Ln^{III}$ systems. Among them, the $Zn^{II}Dy^{III}$ based counterpart displayed the most promising magnetic properties and, therefore, it was selected for the following study.

After the discovery of Mn12-ac, the initial trend towards enhancing the magnetic performance of the materials was focused on increasing the total spin of the molecules (as mentioned in the general introduction, *U* is defined as $S^2|D|$ and $(S^2-1/4)|D|$ for integer and non-integer spins, respectively). However, this approach did not succeed as expected, since even though high spin systems were discovered, it was a tough task to maintain the high anisotropy within the whole molecule. It has been observed for transition metals as well as for lanthanides that the alignment of the magnetic anisotropy axes can have positive effects in the overall relaxation properties [2,3]. Thus, by aligning the anisotropy axes of the paramagnetic metal centers within a molecule could have an additive effect, giving rise to larger *D* values and hence to enhanced energy barriers.

The group of Murugesu tried this approach for some quadruply-stranded dinuclear Dy^{III} based helicate/mesocate complexes [4]. Within their study, they employed three related Schiff base ligands in which they maintained the coordination sites, but they modulated the spacer groups to obtain three helicate/mesocate dinuclear compounds. The aim of this was to maintain as intact as possible the coordination environments of all the Dy^{III} sites to have the same energy splitting within the Kramers doublet and, at the same time, modulate the orientations of the anisotropy axes. This strategy could lead to very interesting magneto-structural correlations, since structural features related to modulations in the angles between anisotropy axes could be directly associated to differences in the magnetic properties. As mentioned, by varying the spacer ligand they managed to obtain three dinuclear systems in which the angles between anisotropic axes were modulated. However, they were not able to make clear magneto-strucural correlations between these differences in the angles and the magnetic properties. Indeed, they concluded that the observed relaxation dynamics were intrinsic to the coordination environment of each Dy^{III} site, since slight differences were found from one to another.

More recently, some other mononuclear and polynuclear compounds were studied based on tris(pyrazolyl) borate and oligo(β-diketonate) ligands [5]. Even though they point out that in contrast to mononuclear systems, polynuclear ones display zero-field SMM behaviour, once more, there is no a clear correlation between the orientations of the anisotropy axes and magnetic properties. Besides, luminescence properties were studied for other lanthanides such as Tb^{III} and Eu^{III}. Overall, they concluded that in order to combine and enhance both magnetic and luminescent properties, it is reasonable to focus on mononuclear systems or in dinuclear ones with long intramolecular Ln···Ln distances.

Zhao and co-authors have recently published a similar work for $Zn^{II}Dy^{III}$ based dinuclear systems in which they have succeed in extending dinuclear entities to tetranuclear systems [6]. The model compound, which contains a pyridine ligand coordinated to Zn^{II} in the axial vertex of the square pyramid, was modified by introducing other double bridging ligands (such as 4,4'-bipyridine) to obtain the targeted tetranuclear compounds. These modifications in the spacer ligands lead to the modulation of the coordination sphere in the Dy^{III} sites and, once again, these subtle modifications within the surrounding of the lanthanide ions are most likely responsible for the improved magnetic properties of the extended compounds.

Based on these previous works, we proposed a similar strategy to carry out in our model $Zn^{II}Dy^{III}$ complex (Figure 2.1). The aim of this was to replace the bridging acetate group by carbonate and other di- and tricarboxylates (Figure 2.1). We expect the carbonate bridge gives rise to the shortest Dy-Dy intramolecular distances as previously reported for other similar compounds [7]. Meanwhile, by employing aliphatic carboxylic acids differing in chain length we wanted to study systems in which extended dinuclear entities will have different folding and, hence, variations in the orientation of the anisotropy axes. Auxiliary ligands, such as terephthalic acid or biphenyl-4,4'-dicarboxylic acid are expected to give linear compounds, whereas trimesic acid could give rise to propeller like structures, such as the one previously published by Powell *et al* [8]. In addition, the use of different aliphatic or aromatic linkers allows us to study how these groups sensitize or not lanthanide centered emissions, giving rise to possible interesting luminescent properties. These measurements are planned as future work.

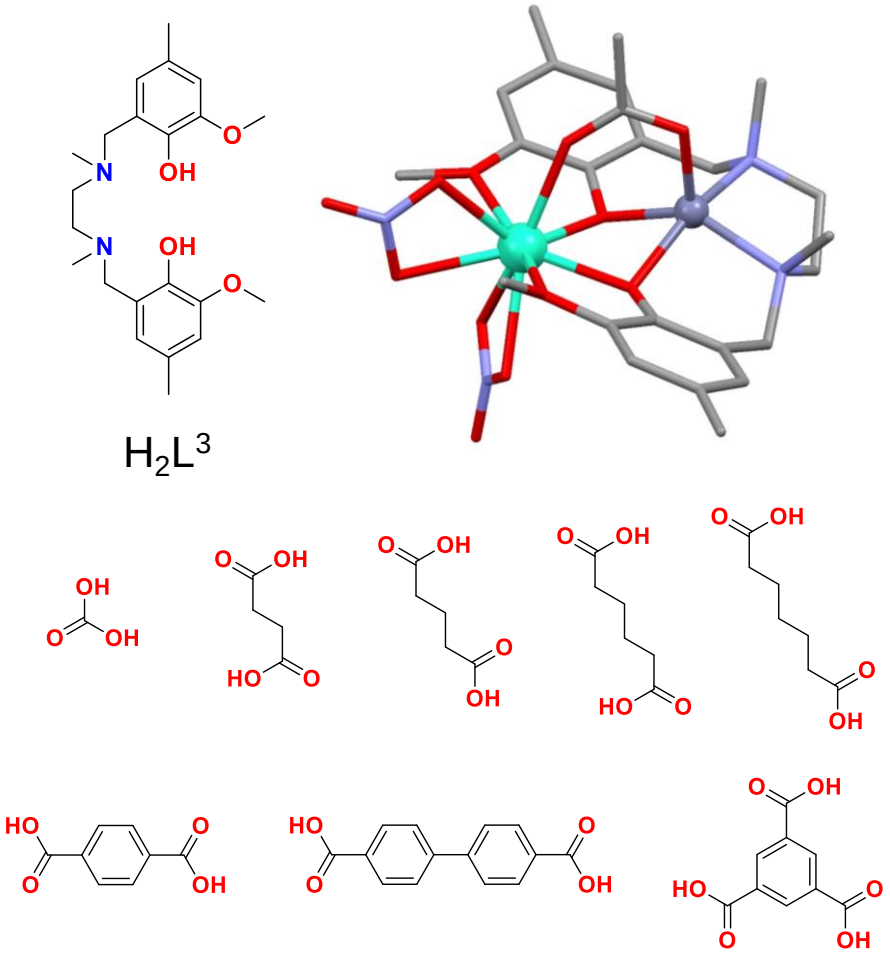

Figure 2.1.- Structure of the ligand employed in this study (top left), perspective view of our previously reported $Zn^{II}Dy^{III}$ based complex (top right) and bridging groups employed for this study. Colour code: dysprosium, zinc, nitrogen, oxygen and carbon atoms are in turquoise, dark grey, light blue, red and grey, respectively. Hydrogen atoms and solvent molecules are omitted for the sake of clarity.

Thus, this chapter covers the synthesis, characterization and study of magnetic properties of nine novel $Zn^{II}Dy^{III}$ based polynuclear compounds bridged by a wide variety of polycarboxylate groups. For all of them, the magnetically diluted counterparts were also studied. Moreover, some magneto-structural correlations have been proposed to better understand the observed experimental magnetic properties.

2.2. PREPARATION OF THE LIGAND

2.2.1. H_2L^3: N,N′-dimethyl-N,N′-bis(2-hydroxy-3-methoxy-5-methylbenzyl) ethylenediamine

The ligand was prepared by using a previously reported procedure [9].

2.3. PREPARATION OF COMPLEXES

2.3.1. {(μ-CO_3)$_2$[Zn(μ-L^3)Dy(NO_3)$_2$]$_2$} (7)

The ligand H_2L^3 (48.0 mg, 0.125 mmol), $Zn(NO_3)_2{\cdot}6H_2O$ (37.2 mg, 0.125 mmol) and $Dy(NO_3)_3{\cdot}5H_2O$ (54.8 mg, 0.125 mmol) were dissolved in 7 mL of absolute ethanol with continuous stirring. To this, triethylamine (0.034 mL, 0.250 mmol) and Na_2CO_3 (13.2 mg, 0.125 mmol) were successively added and the resulting mixture was stirred for 4 h at 70°C. The white powder was filtered, washed with absolute ethanol several times and dried. Mother liquor was allowed to stand at room temperature and in few days good quality crystals were obtained. Yield and elemental analysis results in Table A2.1.

2.3.2. {(μ-L')[Zn(μ-L^3)Dy(NO_3)$_2$]$_2$}·nMeCN (L' = succinate, n = 2 (8); L' = glutarate, n = 0 (9), L' = adipate, n = 0.5 (10); L' = pimelate, n = 0 (11))

The ligand H_2L^3 (48.0 mg, 0.125 mmol) and $Zn(NO_3)_2{\cdot}6H_2O$ (37.2 mg, 0.125 mmol) were dissolved in 8 mL of acetonitrile. Then, a solution of the corresponding dicarboxylic acid (0.0625 mmol) with triethylamine (0.051 mL, 0.375 mmol) in 2 mL of acetonitrile and $Dy(NO_3)_3{\cdot}5H_2O$ (54.8 mg, 0.125 mmol) were successively added with continuous stirring. The resultant solution was filtered to eliminate the possible undissolved particles and was allowed to stand at room temperature. In few days, suitable crystals for X-ray diffraction were obtained. Yield and elemental analysis results in Table A2.1.

2.3.3. {(μ-L')[Zn(μ-L^3)Dy(NO_3)$_2$]$_2$} (L' = terephthalate (12))

The ligand H_2L^3 (48.0 mg, 0.125 mmol) and $Zn(NO_3)_2{\cdot}6H_2O$ (37.2 mg, 0.125 mmol) were dissolved in 16 mL of acetonitrile and the solution was heated to 78ºC. Two solutions of terephthalic acid (10.4 mg, 0.0625 mmol) with triethylamine (0.051 mL, 0.375 mmol) in 2 mL of acetonitrile and $Dy(NO_3)_3{\cdot}5H_2O$ (54.8 mg, 0.125 mmol) in 2 mL of acetonitrile were successively added dropwise. When adding the dysprosium salt

solution, a white precipitate was formed. However, it instantly got dissolved. At this moment, the reaction was filtered to a vial that was at room temperature and due to this temperature difference, the product precipitated in crystal form in few seconds. Yield and elemental analysis results in Table A2.1.

2.3.4. {(μ-L')[Zn(μ-L^3)Dy(NO$_3$)$_2$]$_2$}·2MeCN (L' = biphenyl-4,4'-dicarboxylate (13))

This compound was prepared by following the same procedure as for compound **12** was, but using biphenyl-4,4'-dicarboxylic acid (15.1 mg, 0.0625 mmol) instead of terephthalic acid, and a mixture of acetonitrile:methanol (1:1) instead of acetonitrile as solvent. The first crystals started to appear in few minutes from the resulting filtered solution. Yield and elemental analysis results in Table A2.1.

2.3.5. {(μ-L')[Zn(μ-L^3)Dy(NO$_3$)$_2$]$_3$}·CHCl$_3$·1.5·MeOH (L' = trimesate (14))

In order to avoid the formation of compound **15** as by-product (see below), it is necessary to use sub-stoichiometric amounts of trimesic acid. The ligand H_2L^3 (48.0 mg, 0.125 mmol), $Zn(NO_3)_2{\cdot}6H_2O$ (37.2 mg, 0.125 mmol) and $Dy(NO_3)_3{\cdot}5H_2O$ (54.8 mg, 0.125 mmol) were dissolved in 9 mL of a 1:1:1 mixture of chloroform, acetonitrile and methanol. After 10 minutes of stirring, another solution of trimesic acid (2.63 mg, 0.0125 mmol) with triethylamine (0.039 mL, 0.288 mmol) in 2 mL of methanol was added to the former solution. The resulting solution was stirred for 15 minutes, filtered and allowed to stand at room temperature. In few days, good quality crystals were obtained. Yield and elemental analysis results in Table A2.1.

2.3.6. {(μ-L')$_2$[Zn(μ-L^3)Dy(NO$_3$)$_2$]$_2$[Zn(μ-L^3)Dy(NO$_3$)]$_2$} (L' = trimesate (15))

The ligand H_2L^3 (48.0 mg, 0.125 mmol), $Zn(NO_3)_2{\cdot}6H_2O$ (37.2 mg, 0.125 mmol) and $Dy(NO_3)_3{\cdot}5H_2O$ (54.8 mg, 0.125 mmol) were dissolved in 9 mL of a 1:1:1 mixture of chloroform, acetonitrile and methanol. After 10 minutes of stirring, another solution of trimesic acid (13.2 mg, 0.0625 mmol) with triethylamine (0.026 mL, 0.188 mmol) in 2 mL of methanol was added. When adding the carboxylate, a cloudy solution was obtained, which was instantly filtered and mother liquor was allowed to stand at room temperature affording suitable crystals for X-ray diffraction. Yield and elemental analysis results in Table A2.1.

2.3.7. Compounds 7_Y-15_Y, 7_{Gd}, 14_{Gd} and magnetically diluted 7_{DyY}-15_{DyY}

The diamagnetic **7_Y-15_Y**, isotropic **7_{Gd}** and **14_{Gd}** and magnetically diluted **7_{DyY}-15_{DyY}** derivatives were synthesized following the same procedure as described for complexes **7-15**. For complexes **7_{DyY}-13_{DyY}** the Dy:Y ratio was of 1:10, whereas for complexes **14_{DyY}-15_{DyY}** 1:15 and 1:20 were employed, respectively, to ensure an effective magnetic dilution.

2.4. EXPERIMENTAL RESULTS

The compartmental ligand H_2L^3 owns two coordination sites, a N_2O_2 inner site, which is more suitable for the coordination of transition metals, and an O_4 outer site that shows preference for harder metal ions, for instance lanthanides. In light of our previous research [1], where we managed to synthesize a family of triple-bridged dinuclear $Zn^{II}Ln^{III}$ based complexes, in this chapter we have succeed in extending the dinuclear entities by replacing the acetate bridge with a carbonate, a wide variety of dicarboxylates and a tricarboxylate bridge. In this way, we have obtained nine polynuclear complexes (seven tetranuclear compounds, one hexanuclear and one octanuclear).

In all the cases suitable crystals for X-ray diffraction analysis were obtained. However, the simulated powder X-ray diffractograms do not always fit to the obtained experimental result (Figures A2.2-A2.6). We believe that this is due to the loss of relatively volatile crystallization molecules within the structure, which give rise to a new reorganization of the crystal structure. This new arrangement occurs for compounds **8-12** and **15**. In order to verify our hypothesis, an alternative characterization of the materials was performed for all of the compounds (even though compounds **7** and **13-14** were proved pure by PXRD). First we verified that the reorganization occurs also for diamagnetic **7_Y-15_Y** analogues, so that they show the same modifications in their respective diagrams (Figures A2.2-A2.6). Secondly, thermogravimetric analyses were carried out for the Y^{III} counterparts in order to determine the initial molecular weight of the materials (Figures A2.16-A2.18). Thirdly, all the diamagnetic compounds (**7_Y-15_Y**) were characterized by NMR (Figures A2.111-A2.119). Therefore, knowing that **7_Y-15_Y** were the desired compounds, the fact that their PXRD were the same as for **7-15** confirmed our hypothesis. Lastly, X-ray powder diffractograms were recorded for the single crystals within the mother liquor (Figures A2.8-A2.10), which verified that

compounds suffer from transformations when dry, but perfectly match to simulated patterns when pristine. IR spectra were additionally measured for Dy^{III} based compounds and it could be seen that the bands are very similar to the previously reported acetate bridged dinuclear compound (named as **0**, Figures A2.12-A2.15). Results obtained from elemental analysis also supported our hypothesis. Therefore, it is important to remark that in some cases the formula in the crystal structure and the formula provided in the experimental section differ. As an example, the crystal structure of **9** contains two crystallization acetonitrile molecules, whereas the studied powdered samples does not contain any (as written in the formula). We decided not to use different names for the sake of clarity.

2.4.1. Powder X-ray diffraction analysis of complexes 7-15, 7_{Y}-15_{Y} and 7_{DyY}-15_{DyY}

The use of solvents such as acetonitrile, methanol or chloroform could cause some troubles as in this case. The fact that they have relatively low boiling points, as well as that they do not make strong interactions within the structure could be the reason why they evaporate and, therefore, the crystal structures undergo transformations (the lost of solvent molecules has already been seen in Chapter 1). The first evidence of this phenomenon could be the fact that some of the crystal structures (**7**, **8**, **12** and **15**) needed a squeeze routine since solvent molecules were showing disordered features and not well defined occupations. Thus, the alternative characterization began with the PXRD analysis of the diamagnetic **7_{Y}-15_{Y}** counterparts. Thus, even though at first we did not know what these new phases were corresponding to, if we were able to completely characterize the diamagnetic analogues, we were going to be able to say that Dy^{III} based materials were pure too and that the new powder X-ray diffractograms correspond to reorganized phases due to solvent lost.

As shown in Figures A2.2-A2.6, for compounds which phase transformations were detected (**8-12** and **15**), the diffractograms of the Dy^{III} and Y^{III} based compounds perfectly match to each other confirming the presence of the same crystal structure phase (compound **8_{Y}** is an exception, though **8** and **8_{DyY}** perfectly fit). Moreover, the diffractograms for magnetically diluted **7_{DyY}-15_{DyY}** are also shown in the same figures to prove the isostructural character.

Finally, diffraction was also collected for the crystals that were formed within mother liquor. This enabled us to study the materials prior to suffering loss of crystallization

molecules. As shown in Figures A2.8-A2.10, the diffractograms in these conditions fit well to the simulated patterns and the dried versions fit well to the previously indicated diffractograms.

2.4.2. Thermogravimetric analysis of complexes 7_Y-15_Y

Once confirmed the isostructural character of paramagnetic and diamagnetic analogues, thermal analysis was carried out for **7_Y-15_Y**. These experiments gave rise to the following valuable information: (i) when crystallization solvent molecules were present in the structure, their weight loss was perfectly seen below 200 ºC, and (ii) considering that in all cases (except for **8**, residual ZnO and Dy_2O_3 were obtained) the final residue obtained after combustion of the organic moieties corresponds to ZnO and Y_2O_3 (see Figure A2.11), the molecular weight of the initial product was calculated and it proved to correspond to the desired product.

Compounds **7_Y**, **13_Y** and **14_Y** display powder X-ray diffractograms that perfectly fit to the simulated patterns, from which we concluded that the thermogravimetric analysis should agree with that expected for the structure of the compounds. In fact, compound **7_Y** does not show any considerable solvent lost below 200 ºC, which is in agreement with the solvent free structure. Compounds **13_Y** and **14_Y**, in contrast, display clear steps below the mentioned temperature related to the loss of two acetonitrile molecules for the former and one molecule of chloroform and 1.5 molecules of methanol, for the latter. The single crystal structure of **8** was refined using the squeeze routine, which could be due to partially evaporated solvent molecules. Indeed, thermogravimetric analysis shows a clear step corresponding to the loss of two acetonitrile molecules. Compound **9** has two acetonitrile molecules within the structure, while the thermal behaviour of **9_Y** clearly indicates that no solvent molecule is present in it, which is in well agreement with the transformation. Compound **10** also contains two MeCN molecules, while only a small step related to 0.5 MeCN release could be identified for **10_Y**. The single acetonitrile molecule present in **11** is also absent for **11_Y**. Finally, the single crystal structures of **12** and **15** were refined by squeeze routines due to the impossibility to assign the residual peaks. Their low density could be somehow explained by the plateaus in the thermal behaviour for **12_Y** and **15_Y** indicating their desolvatated character.

For calculating and comparing the molecular weights of the compounds, two different approaches have been used. On the one hand, for the molecules that we

knew that they were pure (**7**$_Y$, **13**$_Y$ and **14**$_Y$), knowing that the residual percentage corresponds to the sum of ZnO and Y_2O_3 oxides, the molecular weight corresponding to the 100% of the material was calculated (see Table 2.1). For compounds suffering transformation, on the other hand, the molecular weight corresponding to the plateaus on the thermogravimetric data was compared to the desolvated molecular weights, since some of them showed solvent molecules in the crystal structure, but not in the TG analysis. Therefore, the values at 100% weight would not be comparable. Finally, the error between the experimentally calculated and theoretical values were calculated with the following equation:

$$Error\ (\%) = (mw_{theor.} - mw_{exp.}) \cdot 100 / mw_{exp.} \qquad Equation\ 2.1$$

Table 2.1.- Summary of molecular weights (mw), calculated error and comparison between solvent presence in single crystal (SC) and thermogravimetric analysis (TG).

	$mw_{theor.}$ (g/mol)	$mw_{exp.}$ (g/mol)	Error (%)	Solvent (SC)	Solvent (TG)
7$_Y$	1325.6	1260.4	5.2	-	-
8	1592.8	1572.5	1.2	-	2 MeCN
9$_Y$	1459.7	1418.1	2.9	2 MeCN	-
10$_Y$	1473.7	1390.1	6.0	2 MeCN	0.5 MeCN
11$_Y$	1487.7	1421.8	4.6	MeCN	-
12$_Y$	1493.7	1405.0	6.3	-	-
13$_Y$	1651.9	1538.3	7.2	2 MeCN	2 MeCN
14$_Y$	2368.9	2297.4	3.2	$CHCl_3$, 1.5 MeOH	$CHCl_3$, 1.5 MeOH
15$_Y$	2949.3	2899.8	1.7	-	-

Even though some of the errors could be considered somehow high (> 5%), the fact that in all the cases we have obtained systematically lower experimental values compared to theoretical molecular weights could mean that this negative error could be

intrinsic to the instrument. At the same time, this suggests that the real mw's are greater in value and, thus, the error would be smaller.

2.4.3. Nuclear Magnetic Resonance for complexes 7_Y-15_Y

Even though we believe that the study based on powder X-ray diffraction and thermogravimetric analysis certifies our hypothesis about reorganized crystal structures, diamagnetic Y^{III} compounds open the possibility to study these materials by NMR. All of the compounds are best solubilized in DMSO and, hence, the experiments were performed in DMSO-d^6.

In Figures A2.111-A2.118 all the ^{1}H-NMR spectra are shown, in which all the different protons corresponding to the main ligand and bridging di- or tricarboxylates are assigned by different colours. For some of the compounds (**12_Y**, **14_Y** and **15_Y**) additional COSY, $^{13}C\{^1H\}$ and ^1H-^{13}C-HSQC experiments were done due to more complicated signal assignation. Noteworthy, due to longer bond distances (see next section), we believe that the methoxy groups are somehow labile in solution. A single signal should be expected for it, but multiple signals are obtained for all of the compounds. The fact that they all belong to the same group and thus, same carbon atom, was certified by HSQC experiments.

Noteworthy, the geminal protons belonging to methylene groups (indicated with pink and yellow colors) appear at different ppm values. This fact indicates that the skeleton of the structures is preserved in solution. These are diastereotopic [10] protons and within the structure the electronic environment of each germinal proton differs. In fact, for the free ligand a single signal is observed for each pair of geminal proton (Figure A2.120), which is due to the possibility of interconversion.

2.4.4. Crystal structures of complexes 7-15

In all nine complexes the basic unit consists of a dinuclear $[ZnDyL(NO_3)]^{2+}$ entity. In compound **7**, two tetradentate carbonate anions are responsible of connecting two basic entities within a single molecule (Figure 2.2). Compounds **8-14** exhibit an additional bidentate nitrate anion in the fundamental entity (Figures 2.3-2.4), and a dicarboxylate (tricarboxylate in the case of **14**) acting as a bridging ligand to form tetranuclear (hexanuclear in the case of **14**) coordination compounds. Finally, complex

15 displays a combination of two basic $[ZnDyL(NO_3)]^{2+}$ and two $[ZnDyL(NO_3)_2]^{+}$ systems connected by two trimesate molecules (Figure 2.5). Relevant bond distances and angles, as well as the crystallographic data for complexes **7-15**, are shown in Tables A2.2-A2.7.

Single crystal X-ray analyses reveal that compounds **7**, **11** and **15** crystallize in the triclinic *P-1* space group; **8**, **10**, **12** and **13** in the monoclinic $P2_1/c$; **9** in the monoclinic *C2/c* and, lastly, **14** in the trigonal *R-3* space group. Within the asymmetric unit of **7**, **9**, **12**, **14** and **15** a single Zn^{II} and a single Dy^{III} are shown, whereas in **8**, **10**, **11**, **13** and **15** two pairs of crystallographycally independent Zn^{II} and Dy^{III} metal centers are found. Zn^{II} ions in the inner site display a well definite (CShM value lower than 1) ZnN_2O_3 square pyramid coordination sphere (Table A2.8) calculated by the SHAPE software [11]. In all cases, two nitrogen atoms belonging to the amine groups and two oxygen atoms pertaining to phenoxido groups of the dideprotonated L^{2-} ligand form the base of the pyramid. The remaining axial oxygen atom comes from the $Zn^{II}Dy^{III}$ bridging carbonate in **7** and bridging carboxylate in **8-15**.

The DyO_9 coordination environment of all complexes deviates much more from an ideal polyhedron. However, the main objective of preserving as most similar as possible ligand field for all Dy^{III} centers succeeded. In fact, they all oscillate between muffin, spherical capped square antiprism and spherical tricapped trigonal prism type of polyhedron. More specifically, between all fourteen DyO_9 environments (even though there are 9 complexes, 14 crystallographycally independent Dy^{III} centers are studied), eleven fit best to muffin type, three fit best to spherical capped square antiprism and one fits best to spherical tricapped trigonal prism type of polyhedron (see Table A2.9). However, for all of them these three types of polyhedrons show the lowest values.

As aforementioned, two dinuclear $[ZnDyL(NO_3)]^{2+}$ entities are connected by two carbonates in **7**. The DyO_9 is composed by four oxygen atoms belonging to L^{2-}, three to bridging carbonates and two to a terminal bidentate nitrate ligand. Dy-O bond distances can be grouped in three categories; short $Dy\text{-}O_{phenoxido}$ (2.288(9)-2.319(9) Å), intermediate $Dy\text{-}O_{carbonate}$ (2.347(9)-2.395(8) Å) and long $Dy\text{-}O_{methoxy}$ or $Dy\text{-}O_{NO3}$ (2.431(9)-2.555(9) Å). The intramolecular Dy1···Dy1(i: 1-x, -y, 2-z) distance is of 4.039(1) Å and the bridging $Dy1\text{-}O_{carbonate}\text{-}Dy1(i)$ angle is of 116.9(3)º.

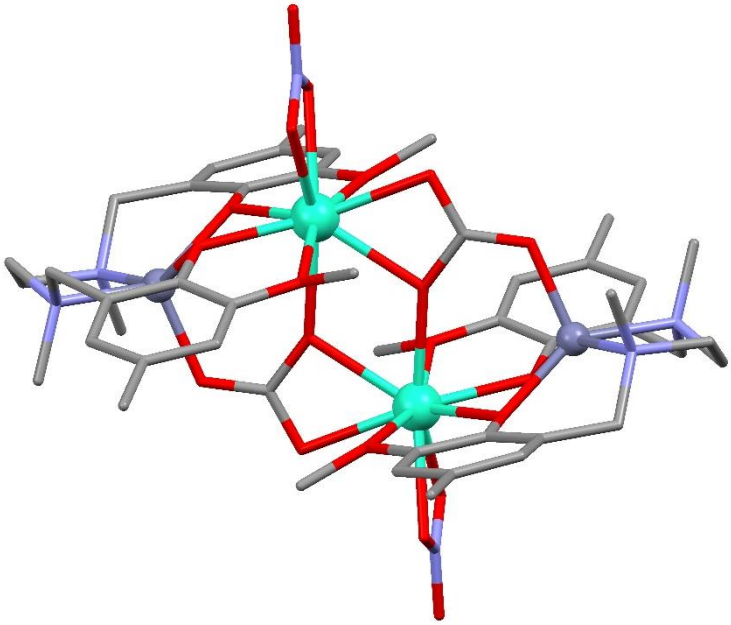

Figure 2.2.- Perspective view of complex **7**. Colour code: dysprosium, zinc, nitrogen, oxygen and carbon atoms are in turquoise, dark grey, light blue, red and grey, respectively. Hydrogen atoms are omitted for the sake of clarity.

Tetranuclear compounds **8-13** contain two basic $[ZnDyL(NO_3)_2]^+$ entities connected by succinate, glutarate, adipate, pimelate, terephthalate and biphenyl-4,4'-dicarboxylate bridges, respectively. Hence, the DyO_9 sphere is made of four oxygen atoms belonging to the deprotonated L^{2-} ligands, four oxygen atoms from two bidentate nitrate ligands and one oxygen atom from a *syn-syn* carboxylate group bridging Zn^{II} and Dy^{III} metal ions of the same dinuclear $Zn^{II}Dy^{III}$ unit. In each basic unit, a Dy-$O_{phenoxido}$ bond is always the shortest, but they can be grouped along with Dy-$O_{carboxylate}$ bonds as the shortest ones (in the range of 2.242(3)-2.3296(14) Å). Dy-O_{NO3} bond distances display intermediate values (2.417(5)-2.560(5) Å), whereas Dy-$O_{methoxy}$ bonds are the longest ones (2.5016(15)-2.612(3) Å). Intramolecular Dy···Dy distances do not follow a specific trend in the case of the aliphatic bridges as the chain length is increased because of the different folding possibilities that they have. Thus, these distances are of 9.377(2), 11.616(3), 9.5908(8) and 9.7774(8) Å for **8-11**, respectively. The longest intramolecular Dy···Dy distances appear in the case of **12** and **13**, 11.823(2) and 15.811(2) Å, respectively.

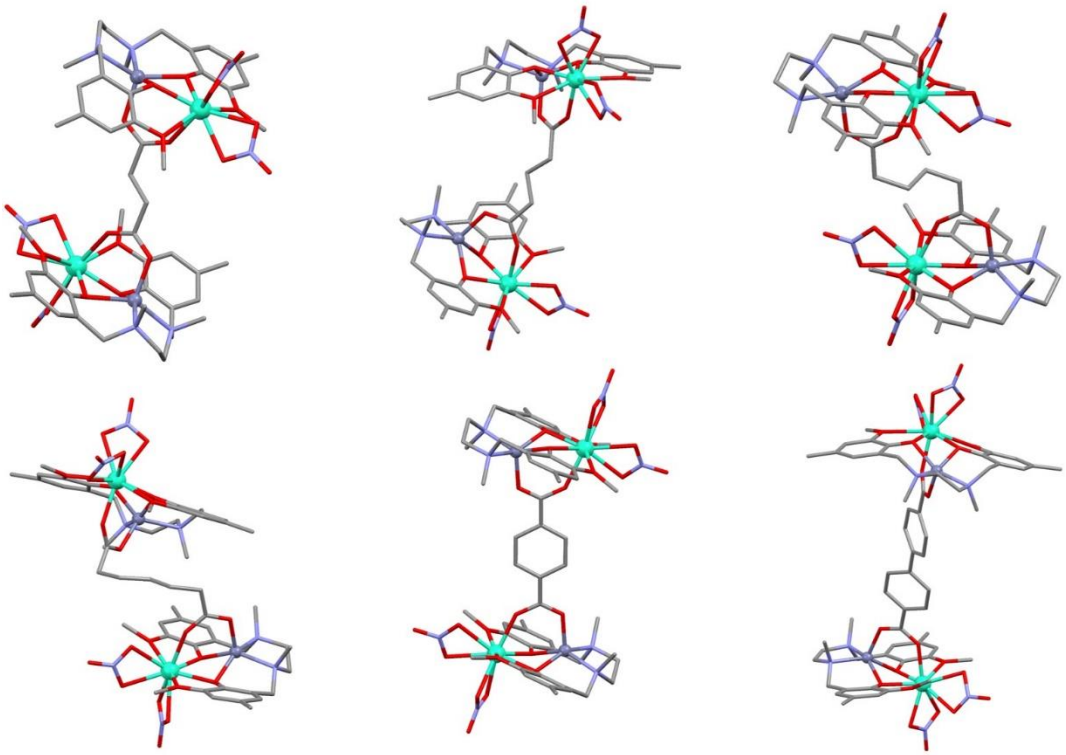

Figure 2.3.- Perspective view of complexes **8-13**. Colour code: dysprosium, zinc, nitrogen, oxygen and carbon atoms are in turquoise, dark grey, light blue, red and grey, respectively. Hydrogen atoms and solvent molecules are omitted for the sake of clarity.

When replacing dicarboxylate bridging groups by trimesate tricarboxylate bridging groups, hexanuclear **14** and octanuclear **15** are obtained changing the stoichiometry of the bridging molecule. Regarding to the coordination environment, the DyO_9 sphere (there is a single different Dy^{III}, as a C_3 axis goes through the $CHCl_3$ molecule) in compound **14** follows the same trend as in **8-13**, it contains short $Dy\text{-}O_{phenoxido/carboxylate}$ (2.2764(17)-2.3122(17) Å), intermediate $Dy\text{-}O_{NO3}$ (2.4372(19)-2.4858(19) Å) and long $Dy\text{-}O_{methoxy}$ (2.510(2)-2.5724(18) Å) bond distances. Within the structure, a crystallization chloroform molecule plays an essential role when folding the fundamental dinuclear entities (Figure A2.1). The solvent molecule is stabilized by intermolecular C-H···π interaction towards the aromatic ring of the trimesate (with a $H\cdots Ring_{centroid}$ distance of 2.401 Å), as well as Cl···π interactions towards the double bond between C14 and C15 (with a $Cl\cdots C14\text{-}C15_{centroid}$ distance of 3.249 Å). Thus, the cavities in both sites of the trimesate bridge own different size, being smaller the one that contains the chloroform molecule (Figure A2.1). The distance between centroids formed by C11-C16 and C11(ii or iii)-C16(ii or iii) (carbon atoms corresponding to the

aromatic rings of the main ligand in the $CHCl_3$ side) is of 8.726 Å, whereas the distance between C1-$C6_{centroid}$···C1(ii or iii)-$C6(ii\ or\ iii)_{centroid}$ is much longer (carbon atoms from the aromatic rings in the other side), 10.881 Å (ii: 1-y, x-y,z; iii: 1-x+y, 1-x, z). This confirms that the haloform folds the structure and forces the dinuclear entities not to be parallel between them. The intramolecular Dy···Dy distances are of 10.123 Å.

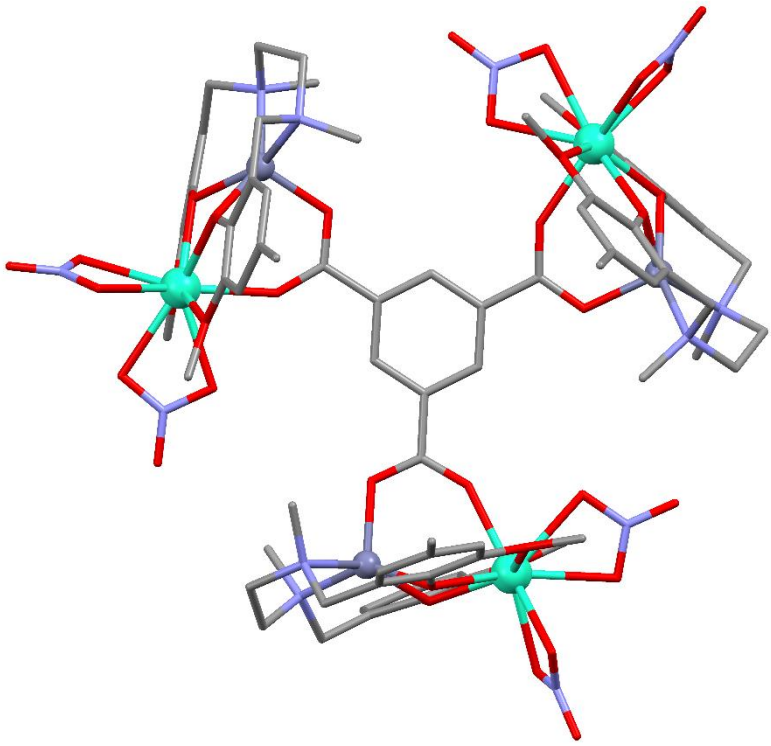

Figure 2.4.- Perspective view of complex **14**. Colour code: dysprosium, zinc, nitrogen, oxygen and carbon atoms are in turquoise, dark grey, light blue, red and grey, respectively. Hydrogen atoms and solvent molecules are omitted for the sake of clarity.

Compound **15** is obtained when increasing the concentration of trimesic acid in the reaction environment. As aforementioned, it contains two basic $[ZnDyL(NO_3)_2]^+$ and two $[ZnDyL(NO_3)]^{2+}$ units connected by two trimesate bridges, the former ones being the terminal systems and latter ones located in the inner site of the molecule. The dinuclear units in the terminal position show exactly the same disposition of the atoms as in **14**. In contrast, the ones in the inner site contain a chelating carboxylate group coordinated to the Dy^{III} center instead of a nitrate. Nevertheless, the disposition of the atoms is still the same. The trend of bond distances remains nearly constant, owning short Dy-$O_{phenoxido/carboxylate}$ (2.235(9)-2.302(8) Å), intermediate Dy-O_{NO3} (2.433(9)-2.496(9) Å) and long Dy-$O_{methoxy}$ (2.496(10)-2.644(10) Å) bonds. However, the bond distances of the

chelating carboxylate groups differ a little bit, since Dy1B-O6TR can be included as a short one (2.345(9) Å), while Dy1B-O5TR can be considered as a long one (2.612(8) Å). Within the molecule, the two trimesate bridges, the two terminal dinuclear entities and the inner dinuclear systems are parallel between them. Although minimum, there is a separation of 0.157 Å between the planes formed by aromatic trimesate rings, while the four Dy^{III} ions are coplanar as observed in Figure 2.5, right. Finally, intramolecular Dy1A···Dy1B, Dy1A···Dy1B(iv: 1-x, 1-y, -z) and Dy1A···Dy1A(iv) are of 9.968(1), 11.041(1), 8.218(1) and 19.364(2) Å, respectively.

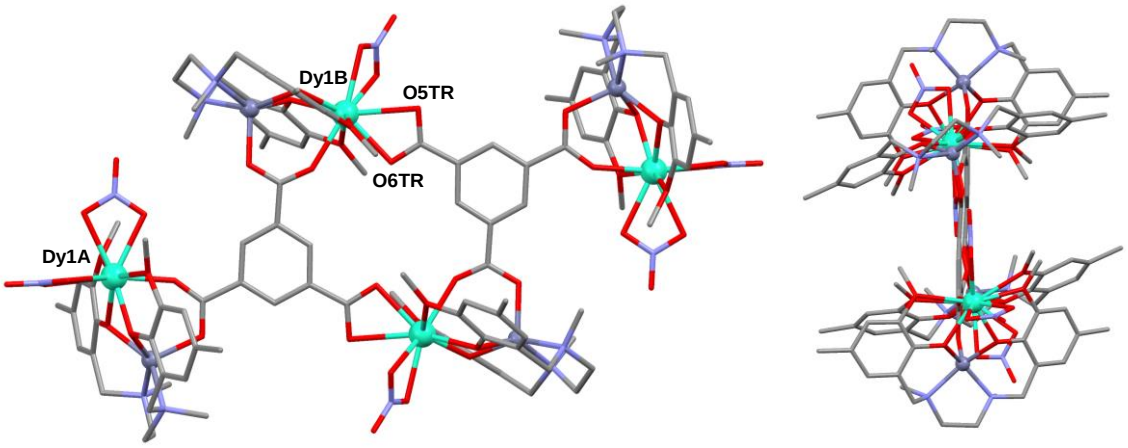

Figure 2.5.- Two perspective views of complex **15**. Colour code: dysprosium, zinc, nitrogen, oxygen and carbon atoms are in turquoise, dark grey, light blue, red and grey, respectively. Hydrogen atoms are omitted for the sake of clarity.

2.4.5. Static magnetic properties of complexes 7-15, 7_{Gd} and 14_{Gd}

The temperature dependence of the magnetic susceptibility was measured on polycrystalline samples for complexes **7-15**, $\mathbf{7_{Gd}}$ and $\mathbf{14_{Gd}}$ in the 2-300 K temperature range under an applied field of 0.1 T (Figures 2.6, 2.7 and A2.19). At room temperature, the $\chi_M T$ value of 28.54 $cm^3 \cdot mol^{-1} \cdot K$ for **7** is in agreement with the presence of two non-interacting Dy^{III} ions (14.17 $cm^3 \cdot mol^{-1} \cdot K$; $^6H_{15/2}$, and g = 4/3). On cooling down, the $\chi_M T$ product gradually decreases due to the depopulation of the Stark sublevels reaching a minimum value of 20.54 $cm^3 \cdot mol^{-1} \cdot K$ at 2.0 K. Isothermal magnetization curves in the 2-7 K temperature range (inset) reveal a non-superimposable character and lack of saturation in agreement with the presence of magnetic anisotropy.

Since, the gradual decay in $\chi_M T$ for **7** could be also influenced by intramolecular exchange interactions between Dy^{III} centers, with the aim of evaluating them, the static magnetic properties of the isotropic $\mathbf{7_{Gd}}$ counterpart were studied. The room temperature value of 15.68 $cm^3 \cdot mol^{-1} \cdot K$ is very close to the theoretical one for two non-interacting Gd^{III} ions (7.88 $cm^3 \cdot mol^{-1} \cdot K$; $^8S_{7/2}$, and g = 2). This value remains almost constant in the 300-10 K temperature range and then sharply increases to reach a maximum value of 18.55 $cm^3 \cdot mol^{-1} \cdot K$ at 2.0 K. This final increase is attributed to weak intramolecular ferromagnetic interactions. Indeed, the $\chi_M T(T)$ data was analysed by using a simple dimer mode for two interacting Gd^{III} certers with the isotropic spin Hamiltonian and PHI software [12]:

$$\hat{H} = -J\hat{S}1 \cdot \hat{S}2 \quad Equation\ 2.2$$

Which afforded J = 0.015 cm^{-1} and g = 1.99 confirming the presence of weak ferromagnetic interactions. The field dependence of the magnetization at 2.0 K shows a rapid increase up to 2 T followed by a linear increase reaching a maximum value of 13.63 μ_B at 7 T, which is close to the theoretical value of 14.0 μ_B for two individual Gd^{III} ions. In fact, the curve at 2.0 K is well reproduced by the Brillouin function for two magnetically isolated Gd^{III} ions with g = 2.0 confirming the weak nature of the interaction.

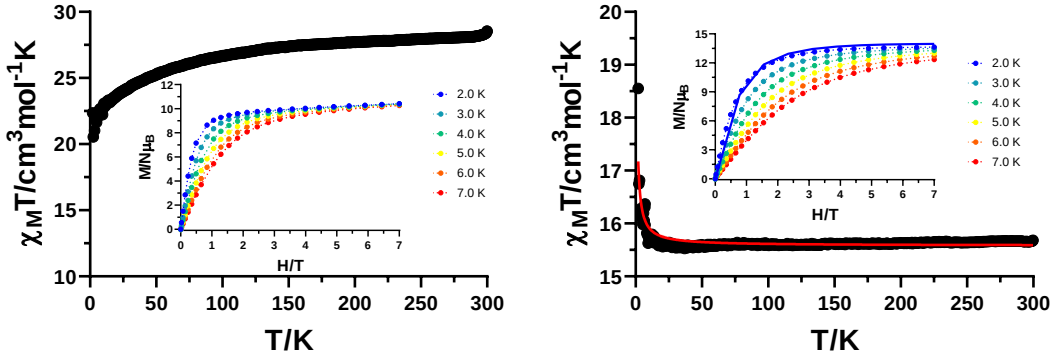

Figure 2.6.- Temperature dependence of the $\chi_M T$ product at 1000 Oe for complexes **7** (left) and $\mathbf{7_{Gd}}$ (right). Insets: Field dependence of the magnetization in the 2-7 K temperature range. The solid red line represent the best fit obtained with Equation 2.1, while the blue line shows the *M(H)* curve reproduced by the Brillouin function at 2.0 K. Dashed solid lines are a guide to the eye.

For compounds **8-15**, the room temperature $\chi_M T$ values of 28.47, 27.97, 28.53, 28.52, 28.20, 28.30, 42.66 and 57.29 $cm^3 \cdot mol^{-1} \cdot K$ are within the expected range for two (**8-13**), three (**14**) and four (**15**) non-interacting Dy^{III} ions (Figure 2.7). In comparison to **7**, the fact of not having direct short bridges between paramagnetic ions encourages us to indicate that the gradual decrease from room temperature to 2.0 K is mainly associated to the depopulation of the Stark sublevels. Isothermal magnetization curves collected for all the compounds show a non-superimposable feature and lack of saturation indicative of magnetic anisotropy. In any case, the static magnetic properties of $\mathbf{14_{Gd}}$ were also evaluated. The orientation of the magnetic anisotropy axes of the three Dy^{III} ions (see discussion below; Figure A2.110) in the triangular system could be suitable to observe toroidal moments [13–15], though strong enough interactions are needed to observe such an effect. As it is shown in Figure A2.19, the lanthanide ions barely interact in $\mathbf{14_{Gd}}$ as it was expected.

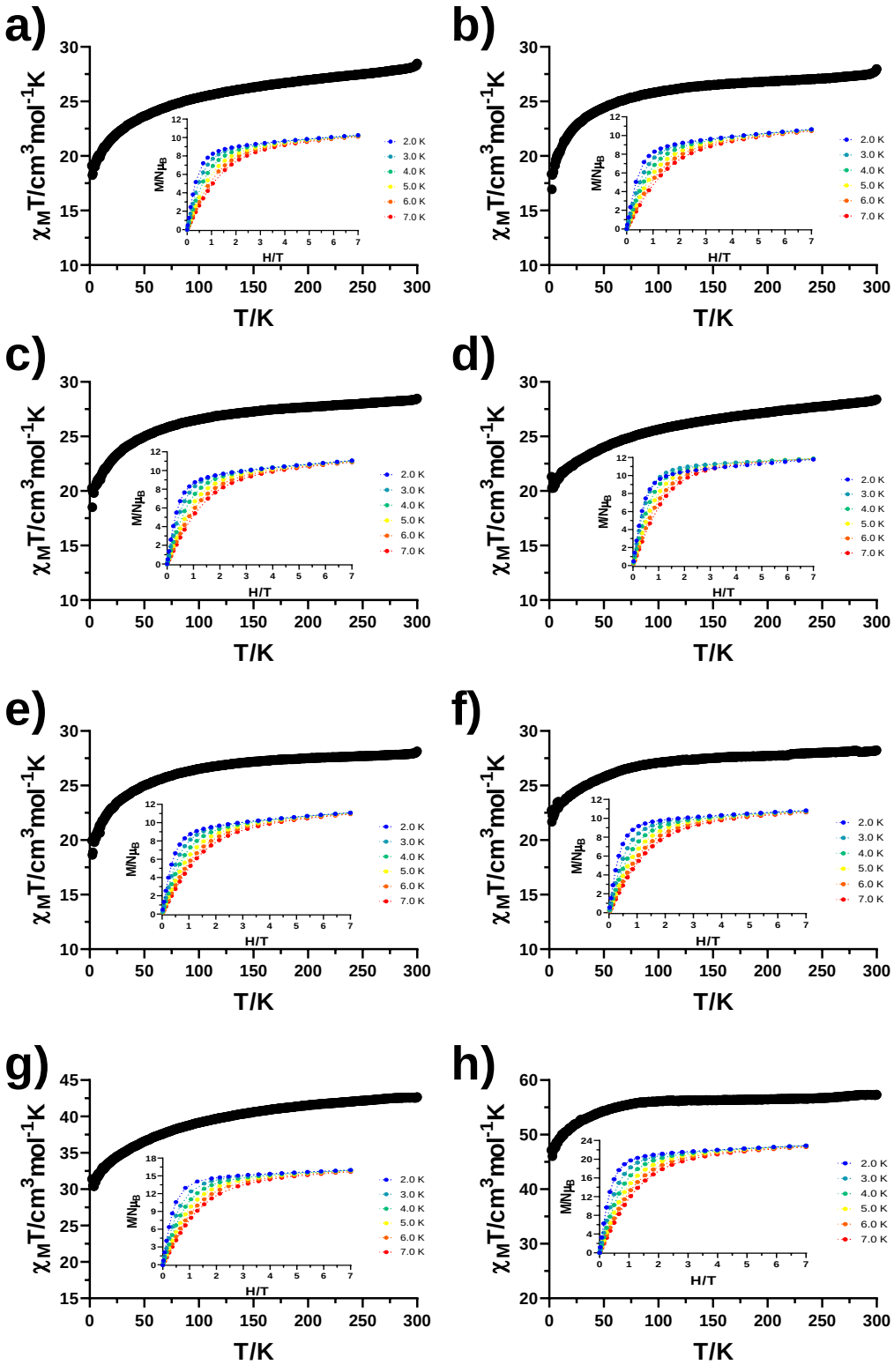

Figure 2.7.- Temperature dependence of the $\chi_M T$ product at 1000 Oe for complexes **8-15** (from a) to h), respectively). Insets: Field dependence of the magnetization in the 2-7 K temperature range. Dashed solid lines are a guide to the eye.

2.4.6. Dynamic magnetic properties of complexes 7-15

In order to prove the dynamic magnetic properties of all nine compounds, *ac* measurements were carried out under zero and under an applied *dc* field of 1 kOe with an oscillating field of 3.5 Oe. This was done for **7-15** and diluted $\mathbf{7_{DyY}}$-$\mathbf{15_{DyY}}$ samples at the highest frequency (10,000 Hz) in order to perform a preliminary evaluation of the SMM properties (Figures A2.21-A2.30). It is well known that Dy^{III} based compounds often do not display maxima in the out-of-phase susceptibility (χ''_M) component under zero *dc* field due to strong QTM. Moreover, either intra- or intermolecular interactions could give rise to transverse fields that enhance this tunnelling, hiding the slow magnetic relaxation. These both situations might be overcome either by using an external magnetic field that breaks the degeneracy of the M_J states partially or totally quenching QTM or by diluting the paramagnetic centres in a diamagnetic matrix (Y^{III} in this case). Thus, this preliminary analysis gives us a general overview of how these techniques improve or not the initial results prior to performing other measurements.

At zero applied *dc* field, none of the pure compounds displays a maximum in the out-of-phase component. However, on the one hand, diluted $\mathbf{7_{DyY}}$, $\mathbf{11_{DyY}}$ and $\mathbf{13_{DyY}}$ display quite well defined maxima below 9 K, 7.5 K and 11 K, respectively. In these compounds, the elimination of possible intra- or intermolecular dipolar interactions (remember that for $\mathbf{7_{Gd}}$ the calculated exchange coupling constant was almost negligible) has partially quenched QTM, leading, in the three cases, to the observation of zero field SMM behaviour. On the other hand, compounds $\mathbf{8_{DyY}}$ and $\mathbf{9_{DyY}}$ display shoulders below 5 K. In all these cases, the long tails below the maxima (or shoulder for the two latter cases) are indicative of unquenched QTM. When repeating the measurements under an arbitrary external magnetic field of 1 kOe, all of the compounds display at least one maximum in the $\chi''_M(T)$ plots, revealing field induced SMM behaviour. Some remarkable differences might be observed between the pure and diluted counterparts under these conditions. For **7**, the combination of the external magnetic field along with diamagnetic dilution totally suppresses the undesired QTM. In the case of **8**, although QTM was successfully eliminated by applying an external field, the diluted analogue displays a better defined maximum with a positive shift in the temperature from 4.5 K to 6.5 K. Complex **9** displays two maxima, which remain intact upon dilution. For **10** no substantial differences are observed from **10** to $\mathbf{10_{DyY}}$, although a slight positive temperature shift occurs for the maximum at low temperature and the shoulder at higher temperature. The QTM affected maximum at zero *dc* field for $\mathbf{11_{DyY}}$ is now well-defined for both **11** and $\mathbf{11_{DyY}}$ with a total quenching of the tunnelling. The

diluted analogue **12$_{DyY}$** shows intriguing results with an additional maximum/shoulder absent or almost undetectable in **12** below 9 K. In the case of **13$_{DyY}$**, apart from the not well-defined maxima present at zero field, an additional maximum is appreciable at low temperature, which is also present for the pure compound. Compound **14** exhibits nearly overlapping maxima around 5 K, while **14$_{DyY}$** displays a single broad maximum. Finally, both **15** and **15$_{DyY}$** show a similar behaviour with a well-defined maximum at the lowest temperatures and a shoulder like signal around 15 K. Bearing all this in mind, measurements for external field optimization were carried out for pure samples in **9**, **11** and **15**, whereas diluted analogues were used for **7$_{DyY}$**-**8$_{DyY}$**, **10$_{DyY}$** and **12$_{DyY}$**-**14$_{DyY}$**. In addition, frequency and temperature dependency was also studied at zero field for **7$_{DyY}$**, **11$_{DyY}$** and **13$_{DyY}$**.

Under an optimum external magnetic field of 1.5 kOe, compound **7** exhibits a set of well-defined maxima up to 10 K with an appreciable unquenched QTM below these peaks (Figure 2.8, top). Relaxation times and α values were extracted by fitting the $\chi''_M(\upsilon)$ and $\chi''_M(\chi'_M)$ curves, respectively, to the generalized Debye model in the 5.0-10.5 K temperature range (Figures A2.50-A2.51). The large α values (0.48(5.0 K)-0.29(10.5 K)) and the curvature of the relaxation times within the Arrhenius plot (Figure 2.8, top inset) indicate a wide distribution of relaxation pathways. The linear portion at the highest temperatures, where mainly Orbach mechanism contributes, was fitted to the Arrhenius law obtaining effective energy barrier and τ_0 values of 65.7 K and $2.9 \cdot 10^{-8}$ s (the values for all complexes are summarized in Table 2.2). However, the data in the whole temperature range could be also fitted by considering the simultaneous presence of Orbach and Raman mechanisms with the following equation, more in agreement with the large α values:

$$\tau^{-1} = BT^n + \tau_0^{-1}exp(-U_{eff}/k_BT) \qquad \textit{Equation 2.3}$$

The fit afforded the following set of parameters: B = 1.8 $s^{-1}K^{-4.192}$, n = 4.192, τ_0 = $3.1 \cdot 10^{-9}$ s and U_{eff} = 96.5 K. For a Kramers ion a n value of 9 is expected, though values between 1-6 are also considered as reasonable when both optical and acoustic phonons participate in the magnetic relaxation [16]. The diluted analogue **7$_{DyY}$** displays zero field SMM behaviour with maxima below 8.5 K. This fact, along with the *dc* magnetic properties, indicates that the weakly interacting carbonate bridged Dy^{III} ions display slow magnetic relaxation that has single ion origin. With a 1:10 magnetic dilution in **7$_{DyY}$**, the paramagnetic centers must be far enough from each other and the *ac* maxima shown in Figure 2.8 (bottom left) should mainly correspond to DyY based molecules. The fact that the diluted compound behaves as zero field SMM also points

out that either intra- or intermolecular interactions were favouring transverse components accelerating QTM. The poorly defined maxima and long tails at low temperature are indicative of unquenched tunnelling. The large α values (0.59(2.0 K)-0.28(9.2 K)) and the curvature of the relaxation times well represent the combination of several relaxation pathways, although the linear portion at the highest temperatures follows the Arrhenius law providing U_{eff} and τ_0 values of 43.0 K and $1.6 \cdot 10^{-7}$ s. The data in the whole temperature range was fitted by the following equation that considers simultaneous QTM and Orbach mechanisms:

$$\tau^{-1} = \tau_{QTM}^{-1} + \tau_0^{-1} exp(-U_{eff}/k_B T) \qquad \textit{Equation 2.4}$$

The best fit provided τ_{QTM}, τ_0 and U_{eff} values of $1.4 \cdot 10^{-4}$ s, $1.4 \cdot 10^{-7}$ s and 45.9 K, respectively. When performing the measurement under the optimum external field of 1.5 kOe, the residual QTM present in both previous cases disappears completely, which is in fair agreement with the lack of tails below the maxima. However, a second set of maxima could be appreciated at high frequencies. Relaxation times and α values were simultaneously extracted by fitting the $\chi''_M(\chi'_M)$ curves with the CCFIT software [17], which afforded linear portions for both fast relaxation (FR) and slow relaxation (SR) in the Arrhenius plot. The fit provided U_{eff} and τ_0 values of 52.3 K with $10.0 \cdot 10^{-8}$ s and 102.2 K with $4.7 \cdot 10^{-9}$ s for FR and SR, respectively. It is also worth mentioning that the suppression of QTM is also reflected in the smaller α parameters (0.29(7.8 K)-0.37 (11.8 K) for FR and 0.12(7.8 K)-0.08(11.8 K) for SR). The opposite trend in FR (values become bigger as temperature is increased) might be explained by the mixing of both processes, since at intermediate temperatures both mechanisms contribute to relax, whereas at lowest and highest temperatures only one of them mainly operates.

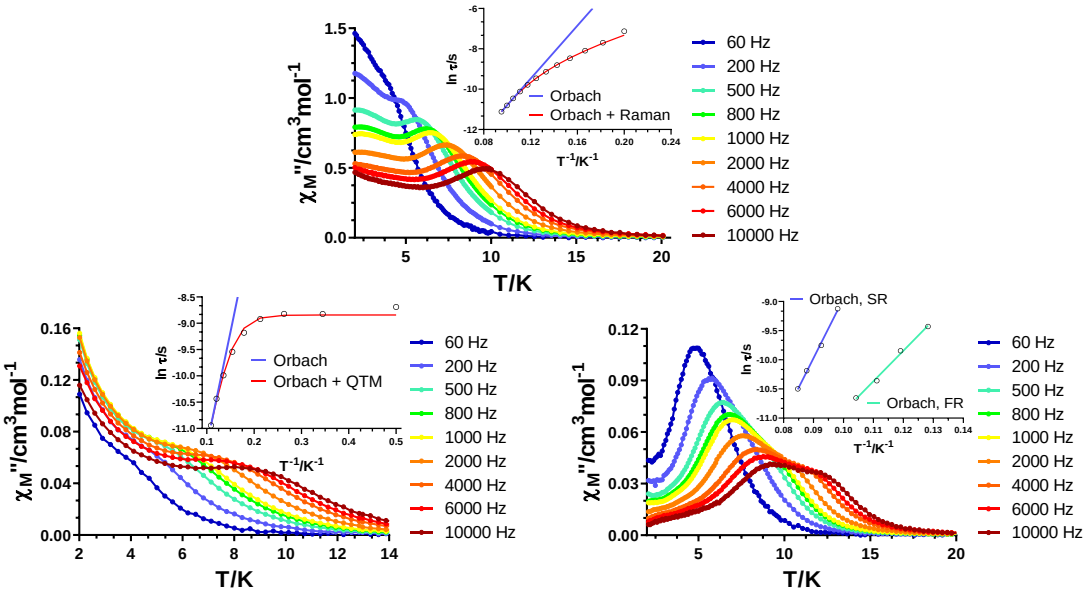

Figure 2.8.- Temperature dependence of the out-of-phase components of the *ac* susceptibility at different frequencies under an external field of 1.5 kOe for **7** (top) and under zero (bottom, left) and 1.5 Oe field (bottom, right) for $\mathbf{7_{DyY}}$. Insets: Arrhenius plot for the relaxation times considering an Orbach (blue or turquoise lines) or several simultaneous mechanisms (red line).

Measurements carried out under an optimum field of 750 Oe for **8** reveals broad signals in the out-of-phase component (Figure 2.9). Although this may be due to two overlapping maxima, the data was evaluated with a single Debye model, since it was not possible to distinguish them either in the $\chi''_M(\upsilon)$ or Cole-Cole plots (Figures A2.59-A2.60). The relaxation times at the highest temperatures were fitted to the Arrhenius law, providing U_{eff} = 35.5 K and $\tau_0 = 6.6 \cdot 10^{-8}$ s. When carrying out the same experiment to the diluted $\mathbf{8_{DyY}}$ counterpart, the maxima become much better defined, which indicates that intra- or intermolecular dipolar interactions influence the relaxation dynamics. The fit to the Arrhenius law provided a slightly bigger effective energy barrier with a value of 50.9 K with $\tau_0 = 3.3 \cdot 10^{-10}$ s. We attempted several other fittings considering various relaxation mechanisms, but we were not able to obtain reasonable parameters.

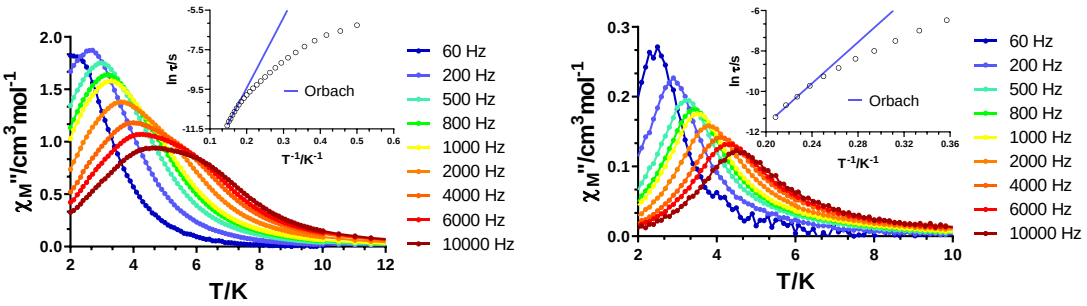

Figure 2.9.- Temperature dependence of the out-of-phase components of the *ac* susceptibility at different frequencies under an external field of 750 Oe for **8** (left) and $\mathbf{8_{DyY}}$ (right). Insets: Arrhenius plot for the relaxation times considering an Orbach mechanism.

In the case of complex **9**, only the pure sample was studied since no remarkable differences were observed for the diluted analogue. The $\chi''_M(T)$ curves under an external magnetic field of 1.5 kOe display two well separated sets, one related to FR in the 2.2-3.2 K range and a second one within 3.2-5.2 K attributed to SR (Figure 2.10). Hence, the data was analysed again with the CCFIT software, from where we obtained relaxation times for each process. The data between 2.3-2.9 K and 3.0-5.6 K for FR and SR, respectively, displayed a linear dependency, thus affording U_{eff} and τ_0 values of 15.9 K with $4.5\cdot10^{-7}$ s (FR) and 32.0 K with $8.0\cdot10^{-8}$ s (SR). To support these results, we also calculated indicative U_{eff} and τ_0 values by plotting $ln(1/(2\cdot\pi\cdot\upsilon))$ *vs* T^{-1} considering the positions of the maxima in the $\chi''_M(T)$ plots. From it, we obtained U_{eff} and τ_0 values of 19.5 K with $6.6\cdot10^{-8}$ s (FR) and 39.9 K with $7.7\cdot10^{-9}$ s (SR), similar to the results obtained with the CCFIT software.

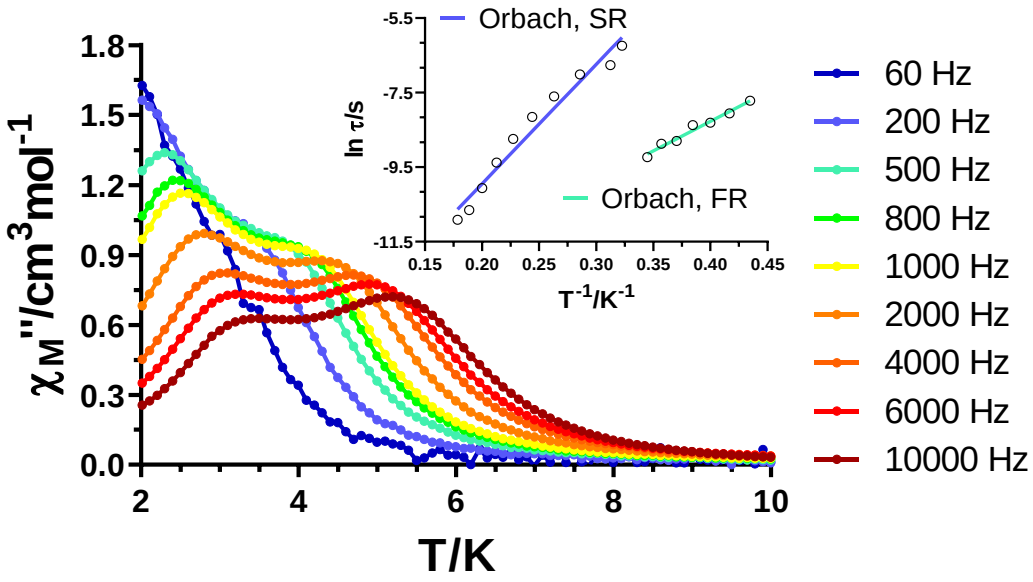

Figure 2.10.- Temperature dependence of the out-of-phase components of the *ac* susceptibility at different frequencies under an external field of 1.5 kOe for **9**. Inset: Arrhenius plot for the relaxation times considering an Orbach mechanism.

Compound **10** was also studied in the non-diluted form since no remarkable differences were observed upon dilution. Although not evident, two processes can be distinguished also for this system, the first one between 2.0-2.5 K and the second one below 5.0 K in the $\chi''_M(T)$ plots (Figure 2.11). However, in contrast to $\mathbf{7}_{DyY}$ and **9**, we employed a different approach in order to analyse the data. In the present case, $\chi''_M(\upsilon)$ plots in the 2.0-2.9 K and 3.8-5.2 K could be independently fitted so as to obtain relaxation times for FR and SR, respectively (Figures A2.68 and A2.70). For the former, all the curves display a clear frequency shift as the temperature is increased, in agreement with a temperature dependent Orbach mechanism. The latter, however, shows a negligible frequency shift for the lowest temperatures, which in common cases may be attributed to QTM, although at the highest temperatures this effect disappears (Figure A2.70). Thus, the shape of the distribution of relaxation times is not surprising. FR displays a completely linear portion in the whole temperature range, whereas SR exhibits a temperature independent regime at the lowest temperatures with a linear fraction at the higher ones. We believe that the temperature independent regime for SR appears due to the more intense signal of FR, which biases the data simulating a QTM

phenomenon. Fitting the linear portions to the Arrhenius law provided us with U_{eff} and τ_0 values of 15.6 K with $9.6 \cdot 10^{-8}$ s (FR) and 24.2 K with $1.8 \cdot 10^{-7}$ s (SR).

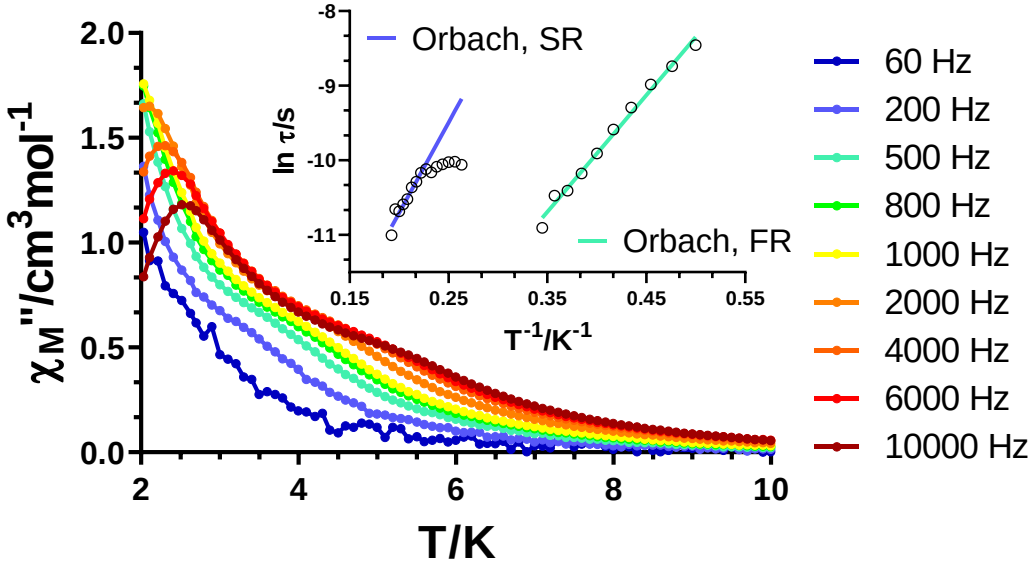

Figure 2.11.- Temperature dependence of the out-of-phase components of the *ac* susceptibility at different frequencies under an external field of 1 kOe for **10**. Inset: Arrhenius plots for the relaxation times considering an Orbach mechanism.

As aforementioned, the application of an optimum external magnetic field of 1.5 kOe was effective enough to suppress QTM and reveal field induced SMM behaviour for **11** (Figure 2.12, left). A well-defined set of maxima is appreciated in the 3.9-7.8 K range without any evidence of unquenched QTM. The Arrhenius plot for the relaxation times shows a linear trend in the whole temperature range suggesting a single Orbach mechanism in agreement with the relatively low α values (0.24(4.4 K)-0.15(8.8 K)). The fit provided U_{eff} = 42.3 K and $\tau_0 = 1.5 \cdot 10^{-7}$ s. The diluted $\mathbf{11_{DyY}}$ analogue behaves similar to $\mathbf{7_{DyY}}$. Although there is not any short bridge between paramagnetic Dy^{III} ions, eliminating intra- and intermolecular interactions thorough magnetic dilution endows $\mathbf{11_{DyY}}$ with zero field SMM behaviour (Figure 2.12, right). The peaking of the maxima remains in the same position, though unquenched QTM predominates at low temperatures. The linear fit of the relaxation times gives U_{eff} = 34.2 K and $\tau_0 = 2.1 \cdot 10^{-7}$ s, which are consistent with the thermally activated region of the pure sample. The α values extracted from the Cole-Cole plots and the distribution of the relaxation times

are consistent with several relaxation mechanisms including QTM. Thus, the data in the whole temperature range was fitted to Equation 2.4, providing τ_{QTM} = 1.4·10^{-4} s, τ_0 = 5.9·10^{-8} s and U_{eff} = 44.6 K. As observed, the application of an optimum external magnetic field is a more efficient strategy to suppress the undesired QTM. For **11$_{DyY}$**, the application of an external magnetic field did not improve the results observed for **11** and, therefore, no further study was done for it.

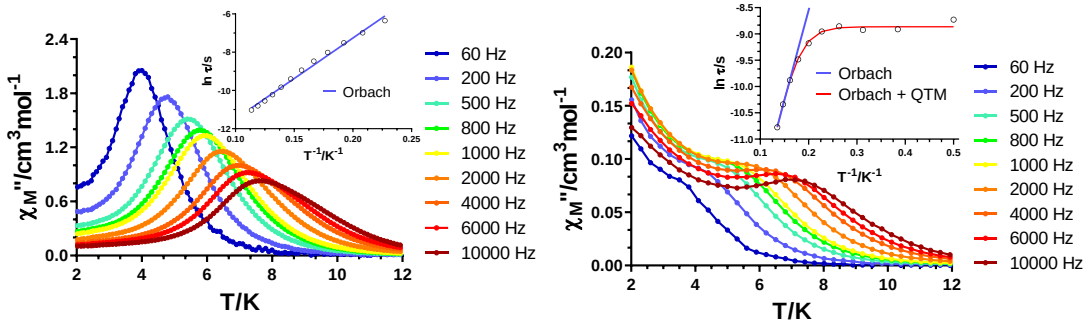

Figure 2.12.- Temperature dependence of the out-of-phase components of the *ac* susceptibility at different frequencies under an external field of 1.5 kOe for **11** (left) and under zero field for **11$_{DyY}$** (right). Insets: Arrhenius plot for the relaxation times considering an Orbach (blue line) or several simultaneous mechanisms (red line).

Under an optimum external magnetic field of 1.5 kOe, compound **12** displays clear maxima in the out-of-phase component below 2.5 K (FR) with an additional roughly undetectable shoulder at higher temperatures (SR, Figure 2.13, left). In the Cole-Cole and $\chi''_M(\upsilon)$ plot, however, the influence of the second set of maxima is clearly observable. In fact, in both cases the points corresponding the low frequency region (60-200 Hz), and therefore to SR, deviate from the calculated fit based on a single Debye function and they were, thus omitted in the calculation (Figures A2.79-A2.80). The α values increment from 2 K (0.30) to 2.8 K (0.48) in agreement with the appearance of a second relaxation process. The relaxation times, however, display linearity in the studied temperature range and were fitted to the Arrhenius law: U_{eff} = 9.6 K and τ_0 = 5.5·10^{-7} s.

Under the same conditions, the diluted counterpart **12$_{DyY}$** sample shows a first set of maxima nearly at the same position, but the shoulder present in **12** is now somehow better defined (Figure 2.13, right). According to the nature of the data at low temperatures, no reliable fitting of the $\chi''_M(\upsilon)$ curves was possible, but based on the

same positions of the maxima a similar effective energy barrier as extracted for **12** is expected (estimating $\tau = 1/2\pi\upsilon_{max}$ approximated U_{eff} and τ_0 values of 8 K and $1\cdot10^{-6}$ s were obtained). In contrast, the high temperature regime in the 6.8-8.8 K range related to SR was studied. The broad maxima in the lower temperature $\chi''_M(\upsilon)$ curves (Figure A2.82) might be indicative of the partial mixing of both processes, in agreement also with the high α values (0.36 at 6.8 K). The linear trend in the whole temperature range afforded U_{eff} and τ_0 parameters of 36.4 K and $4.6\cdot10^{-7}$ s. Even though a dilution of 1:10 should be enough to perfectly isolate paramagnetic Dy^{III} ions, a higher dilution with a 1:20 ratio was tried in order to see whether SR could be better defined or not. As displayed in Figure A2.84, no remarkable difference is observed between both dilutions.

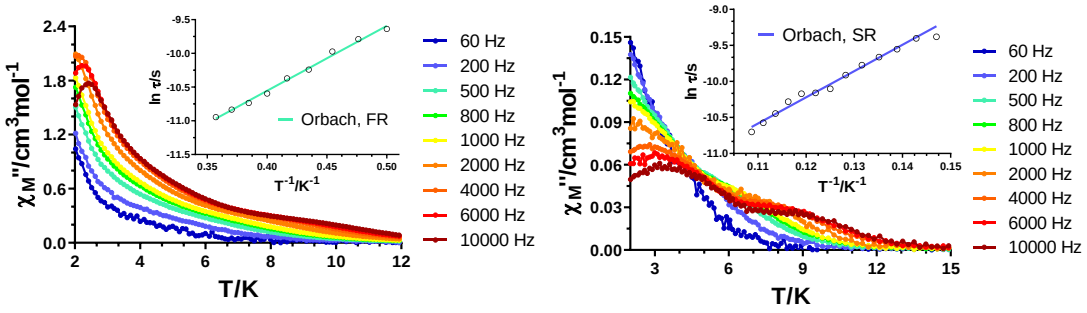

Figure 2.13.- Temperature dependence of the out-of-phase components of the *ac* susceptibility at different frequencies under an external field of 1.5 kOe for **12** (left) and **12**$_{DyY}$ (right). Insets: Arrhenius plot for the relaxation times considering an Orbach mechanism.

Measurements carried out under an optimum external magnetic field of 1 kOe revealed field induced SMM behaviour for **13**, displaying a broad set of maxima below 11 K and another narrower set below 2.4 K (Figure 2.14, top). Even though at first glance both groups are well separated in terms of temperature range, the $\chi''_M(\upsilon)$ plots at the lowest temperatures show the combination of both relaxation processes (Figure A2.86). The peak corresponding to the FR is around 1000 Hz, whereas the shape of the curvature suggests that the peak for SR is far below the low frequency limit of our instrument. Due to this fact, the approach used for the treatment of the data of **10** is no further viable for this case. Hence, the data was studied with the CCFIT software in the 2.0-11.2 K temperature range. The relaxation times corresponding to FR in the 2.0-2.4

K range were fitted to the Arrhenius law affording U_{eff} and τ_0 values of 4.4 K and $7.5 \cdot 10^{-6}$ s. For SR, the relaxation times at the highest temperatures display a clear linear portion, which is in fair agreement with the α values at those temperatures (≈ 0) for a single relaxation mechanism. The curvature at intermediate temperatures and the tendency towards a temperature independent regime is associated to the mixing with FR process. The Orbach parameters for SR are 51.0 K and $3.6 \cdot 10^{-7}$ s for U_{eff} and τ_0, respectively.

As previously discussed, the diluted compound **13$_{DyY}$** shows zero field SMM behaviour. Indeed, the maxima observed for **13** at high temperatures are clearly shown for the diluted analogue in absence of an external field (Figure 2.14, bottom left). Although the $\chi''_M(T)$ plots suggest a single set of maxima, the $\chi''_M(\upsilon)$ plots are very helpful for this case (Figure A2.89). At 2.0 K, the maximum clearly appears at 4,000 Hz and shows a very little temperature dependence, shifting to the highest frequency limit of the instrument (10,000 Hz) at 4.7 K (tenth curve, light turquoise colour in Figure A2.89). This is consistent with the faster relaxation times in the inset of Figure 2.14, bottom left. However, above this temperature, the maximum is shifted towards lower frequency ranges (below 4000 Hz) and displays a clear temperature dependency at the highest temperatures. We believe that this behaviour is associated to the presence of two relaxation pathways, as it occurs for the pure analogue in the presence of an external field. Thus, the relaxation times obtained in the whole temperature interval (2.0-11.0 K) were fitted to two Orbach processes. For FR and SR the Arrhenius fits provided U_{eff} and τ_0 values of 1.5 K with $1.9 \cdot 10^{-5}$ s and 43.8 K with $3.4 \cdot 10^{-7}$ s, respectively. Since all the $\chi''_M(\upsilon)$ curves display a maximum in the studied temperature range, all the relaxation times that are displayed in the inset have a physical meaning and are shown to make visible the transition from one process to another.

The application of the optimum external magnetic field has two effects on **13$_{DyY}$**. On the one hand, the maxima that were visible at low temperatures for **13** appear again and, on the other hand, the maxima at higher temperatures are much better defined due to the suppression of the undesired QTM (Figure 2.14, down right). Even though the position of the peaks related to low temperature relaxation remain nearly intact, the nature of them changes and it was not possible to fit the $\chi''_M(\upsilon)$ curves in order to obtain relaxation times. However, considering the approach employed for **12$_{DyY}$**, an approximation of the relaxation parameters was obtained: $U_{eff} \approx 19$ K and $\tau_0 \approx 6 \cdot 10^{-8}$ s, achieving a higher barrier in comparison to **13**. For the high temperature regime, relaxation times display a linear portion in the 6.2-11.2 K region, thus providing U_{eff}

and τ_0 values for an Orbach process of 60.2 K and $1.3 \cdot 10^{-7}$ s. The high α values at the lowest temperature (0.54 at 6.2 K) could be explained by the influence of the relaxation occurring at lower temperatures, whereas at high temperatures much lower values are obtained (0.16 at 11.2 K) in agreement with a single Orbach mechanism.

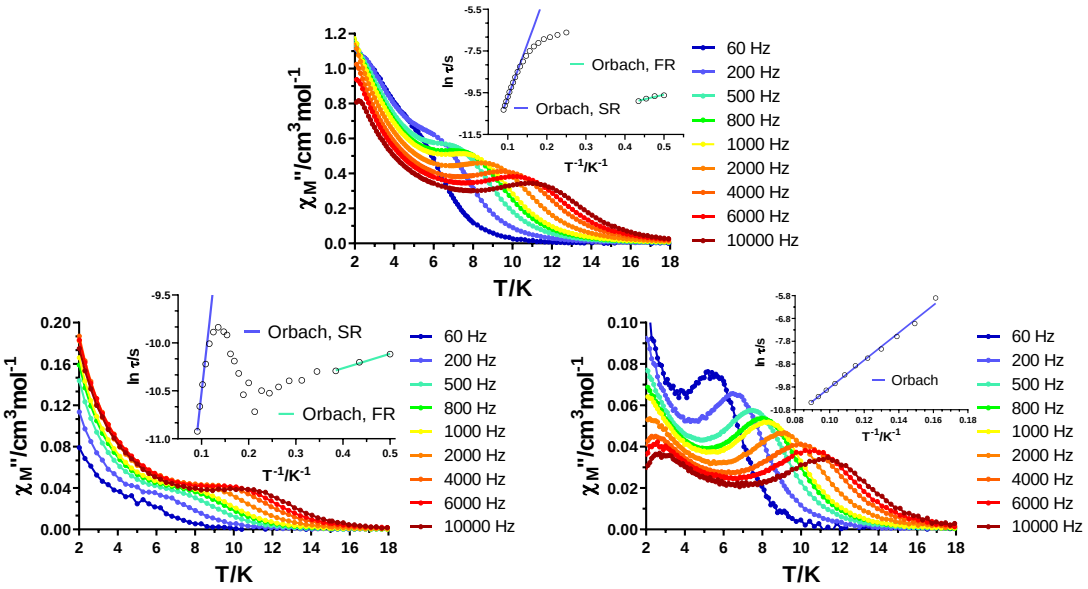

Figure 2.14.- Temperature dependence of the out-of-phase components of the *ac* susceptibility at different frequencies under an external field of 1 kOe for **13** (top) and under zero (bottom, left) and 1 Oe field (bottom, right) for $\mathbf{13_{DyY}}$. Insets: Arrhenius plot for the relaxation times considering an Orbach mechanism.

Compound **14** displays overlapping maxima in the in phase and out-of-phase susceptibility components under an external magnetic field of 1 kOe (Figure 2.15, left and A2.94). Thus, the $\chi''_M(\chi'_M)$ data was analysed by using the sum of two modified Debye models and the CCFIT software. The obtained relaxation times for both FR and SR processes follow the Arrhenius law providing U_{eff} and τ_0 values of 13.2 K with $1.9 \cdot 10^{-6}$ s for FR and 31.5 K with $2.3 \cdot 10^{-7}$ s for SR. The high α values in the fitted temperature range (0.36(2.5 K)-0.40(3.5 K) for FR and (0.23(4.0 K)-0.43 (7.0 K) for SR) are indicative of the high level of mixing of both relaxation pathways within the whole temperature range. The diluted compound $\mathbf{14_{DyY}}$ presents broad maxima in the same temperature region, which could be due to the mixing of the two relaxation mechanisms. The data, however, was analysed by a single Debye function, since there was not clear evidence of two peaks either in the $\chi''_M(\chi'_M)$ or $\chi''_M(\upsilon)$ plots. The *α*

parameters are high in the whole studied temperature range (0.51(3.6 K)-0.39(7.2 K)) in agreement with the possibility of two relaxation mechanisms that overlap. The relaxation times follow the Arrhenius law in the entire temperature range, providing an effective energy barrier of 23.9 K and τ_0 = 1.2·10^{-6} s. These values are almost the average of the parameters obtained for FR and SR in the undiluted sample.

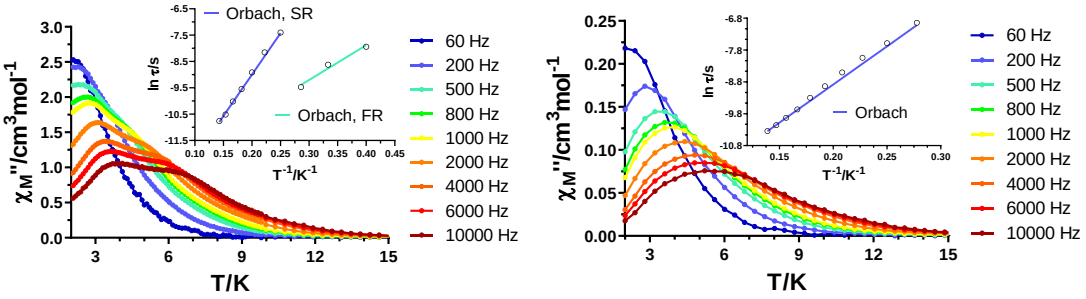

Figure 2.15.- Temperature dependence of the out-of-phase components of the *ac* susceptibility at different frequencies under an external field of 1 kOe for **14** (left) and **14$_{DyY}$** (right). Insets: Arrhenius plot for the relaxation times considering an Orbach mechanism.

Under the arbitrary external magnetic field of 1 kOe (Figure 2.16) two sets of maxima could be observed for **15** in the $\chi''_M(T)$ plots, the former one below 3.0 K and a second one below 16.0 K, which is less well-resolved. Relaxation times for FR (below 3.0 K) were obtained by fitting $\chi''_M(\upsilon)$ curves below this temperature and were fitted to an Orbach process providing τ_0 and U_{eff} values of 5.2·10^{-7} s and 13.6 K, respectively. The large α values (0.63 (2.0 K) - 0.69 (2.9 K)) are representative of a wide distribution of relaxation times. However, the linearity of the data, as well as the few amount of points in this temperature region prevents us from including additional mechanisms. SR was studied independently in the 11.6-15.8 K temperature range. The high temperature data for the relaxation times was also fitted to an Orbach process obtaining a notably higher effective energy barrier of 106.1 K with τ_0 = 2.5·10^{-8} s. With the aim of further studying the relaxation dynamics related to SR we carried out an optimization of the field by measuring field-dependent curves at a fixed temperature of 12.5 K (Figures A2.47-A2.48). From this study we concluded that an external magnetic field of 2.5 kOe would be appropriate to slow down the relaxation times. However, we performed the experiment under this theoretically ideal conditions and we did not obtain the expected results. As depicted in Figure A2.106, the maxima at lower temperatures is somehow

shifted towards higher temperatures, but there is not any considerable frequency dependence. Indeed, the maximum at the highest frequency appears lower in temperature than the maximum at 60 Hz, which is an unexpected feature. Furthermore, the set of maxima at the highest temperatures is even less defined and only a shoulder could be observed. We also tried the dilution strategy in this compound. Considering that it is an octanuclear system, we modified the Dy^{III}:Y^{III} ratio to 1:20 in order to try a more efficient dilution obtaining complex **15_{DyY}**. Nevertheless, once more the result was not the expected one. As it could be observed in Figure A2.108, now the maxima at low temperatures appear to be frequency-dependent, though due to their nature it is not possible to fit the $\chi''_M(\upsilon)$ curves. In addition, the expected set of maxima at higher temperatures has disappeared or is barely observable. We believe that the dilution strategy is not so efficient when working with polynuclear systems, since in this case the probability of having mixtures of Dy_4, Dy_3Y, Dy_2Y_2 or DyY_3 is higher and we cannot say that all the Dy^{III} centers are well isolated within the crystal structure. A fact that can bias the expected results.

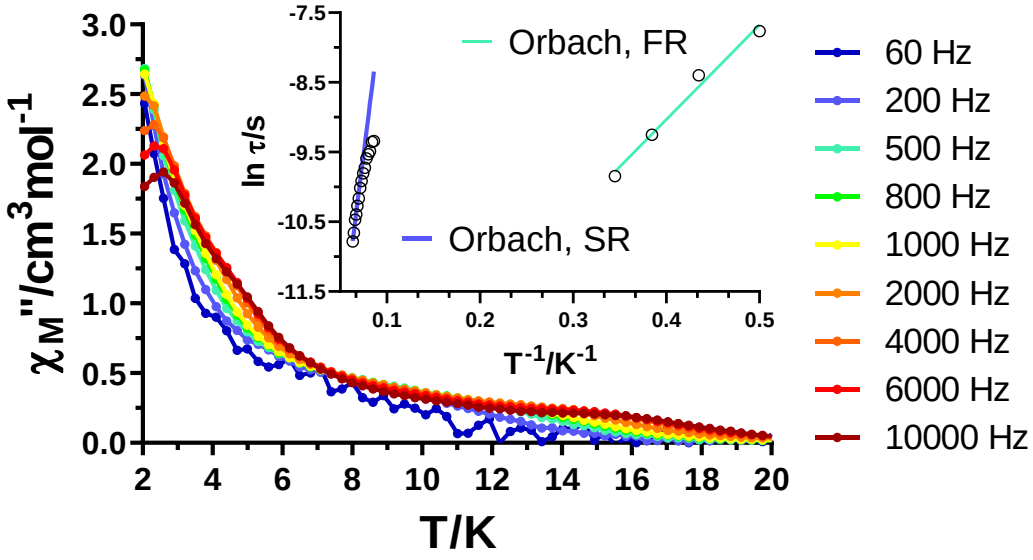

Figure 2.16.- Temperature dependence of the out-of-phase components of the *ac* susceptibility at different frequencies under an external field of 1 kOe for **15**. Inset: Arrhenius plots for the relaxation times considering an Orbach mechanism.

Table 2.2.- U_{eff}, τ_0, B, n, and τ_{QTM} parameters generated from the fit of the relaxation time-temperature dependence for **7-15** and diluted counterparts.

	dc **field**	**Orbach**		**Simultaneous relaxation mechanisms**				
				Orbach		**Raman**		**QTM**
Comp.	kOe	U_{eff} (K)	τ_0 (s)	U_{eff} (K)	τ_0 (s)	B ($s^{-1}K^{-n}$)	n	τ_{QTM} (s)
7	1.5	65.7	$2.9\cdot10^{-8}$	96.5	$3.1\cdot10^{-9}$	1.8	4.2	
7_{DyY}	0	43.0	$1.6\cdot10^{-7}$	45.9	$1.4\cdot10^{-7}$			$1.4\cdot10^{-4}$
7_{DyY}	1.5	52.3 (FR) 102.2 (SR)	$10.0\cdot10^{-8}$ $4.7\cdot10^{-9}$					
8	0.75	35.5	$6.6\cdot10^{-8}$					
8_{DyY}	0.75	50.9	$3.3\cdot10^{-10}$					
9	1.5	15.9 (FR) 32.0 (SR)	$4.5\cdot10^{-7}$ $8.0\cdot10^{-8}$					
10	1	15.6 24.2	$9.6\cdot10^{-8}$ $1.8\cdot10^{-7}$					
11	1.5	42.3	$1.5\cdot10^{-7}$					
11_{DyY}	0	34.2	$2.1\cdot10^{-7}$	44.6	$5.9\cdot10^{-8}$			$1.4\cdot10^{-4}$
12	1.5	9.6 (FR)	$5.5\cdot10^{-7}$					
12_{DyY}	1.5	~8 (FR) 36.4 (SR)	$\sim1\cdot10^{-6}$ $4.6\cdot10^{-7}$					
13	1	4.4 (FR) 51.0 (SR)	$7.5\cdot10^{-6}$ $3.6\cdot10^{-7}$					
13_{DyY}	0	1.5 (FR) 43.8 (SR)	$1.9\cdot10^{-5}$ $3.4\cdot10^{-7}$					
13_{DyY}	1	~19 (FR) 60.2 (SR)	$\sim6\cdot10^{-8}$ $1.3\cdot10^{-7}$					
14	1	13.2 (FR) 31.5 (SR)	$1.9\cdot10^{-6}$ $2.3\cdot10^{-7}$					
14_{DyY}	1	23.9	$1.2\cdot10^{-6}$					
15	1	13.6 (FR) 106.1 (SR)	$5.2\cdot10^{-7}$ $2.5\cdot10^{-8}$					

2.4.7. Magneto-structural correlations

The principal aim when developing this project was to maintain the coordination environment around the Dy^{III} ions (almost) unchanged in comparison to the previously studied dinuclear $Zn^{II}Dy^{III}$ system. We wanted to do this in order to change later the auxiliary ligands employing more or less rigid polycarboxylates. In recent years it has been reported that the different vibrations around the paramagnetic ion could be detrimental in terms of relaxation dynamics, pointing out that rigid systems could show reduced spin-phonon coupling and, thus, enhanced magnetic properties [18]. We believe that, to some extent, we have succeeded in fulfilling this first objective as was discussed in reference to the CShM values in the crystal structure descriptions. Furthermore, maintaining the core structure would also mean that the M_J states follow

a similar energy distribution and, at the same time, the anisotropy axes display similar orientations. Even though we are currently waiting for theoretical calculations, we carried out an indicative study by calculating the mentioned axes by Magellan software [19]. Three representative compounds, along with the anisotropy axes, are displayed in Figure 2.17 (the rest can be found in Figures A2.109-A2.110). We have chosen only these three compounds because (i) complex **7** is the only one containing CO_3^{2-} chelates, (ii) **8** is a representative example of the compounds with two nitrate chelates and (iii) **15** is the only example in which two of the Dy^{III} ions contain a chelating carboxylate. As it can be observed, the anisotropy axes of all the compounds are mostly influenced by the short Dy-$O_{phenoxido}$ bonds no matter what is occupying the rest of the positions. Thus, the axes go through the middle of the phenoxido groups and also through the middle of the groups that are in the opposite positions (CO_3^{2-} for **7**, NO_3^- for **8** and NO_3^-/carboxylate for **15**).

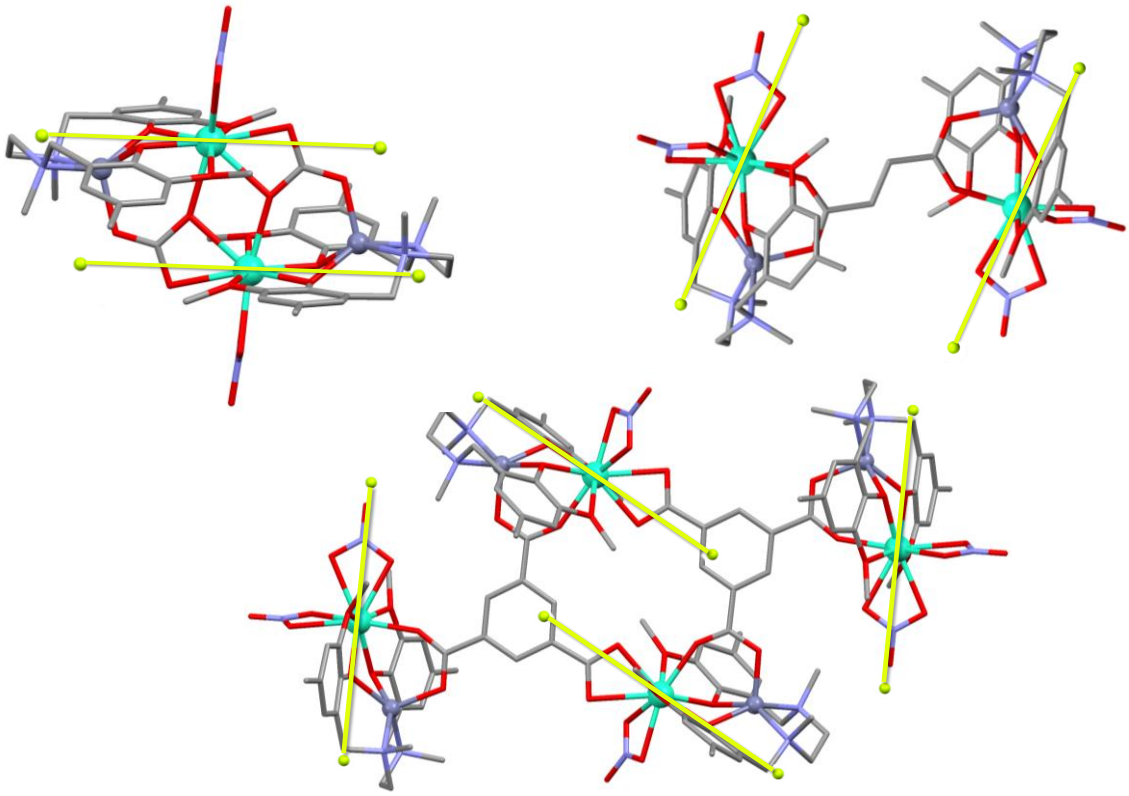

Figure 2.17.- Anisotropy axes for compounds **7** (top), **8** (middle) and **15** (bottom) obtained by Magellan software (green line).

Unfortunately, we think that we cannot make any correlation by considering the rigidity of the auxiliary ligands and the dynamic magnetic properties. It is true that

compounds **7**$_{DyY}$ and **13**$_{DyY}$, which could be considered as two rigid systems, display zero field SMM behaviour, but **12**$_{DyY}$, **14**$_{DyY}$ and **15**$_{DyY}$ can also be grouped within the rigid category and do not show such a good behaviour. Furthermore, compound **11**$_{DyY}$, with a very flexible pimelate bridge, also displays zero field SMM behaviour and, therefore, we are obliged to discard such a possibility.

Nevertheless, based on the results obtained in this chapter, the ones obtained for compound **30** (see Chapter 4) and literature [20,21], we think that we can rationally explain the improved magnetic properties of **7**$_{DyY}$ and **15**. In comparison to the rest of the compounds, they both display notably larger U_{eff} values in the presence of an external magnetic field surpassing the barrier of the 100 K. Based on the fact that the phenoxido groups are responsible of directing the anisotropy axes, the oblate shape electron cloud of the M_J = ±15/2 could be expected to be as depicted in Figure 2.18. Phenoxido oxygen atoms would be in one side of the cloud, whereas CO_3^{2-}, NO_3^- or RCO_2^- would be in the other. Hence, the higher electron density provided by either carbonate or carboxylate groups will probably further stabilize M_J = ±15/2 as ground state with a larger energy splitting towards the excited states, inherently yielding higher U_{eff}'s. Considering this approach, we could say that SR in **15** is most likely associated to Dy1B, which has the carboxylate group as a chelate instead of the nitrate.

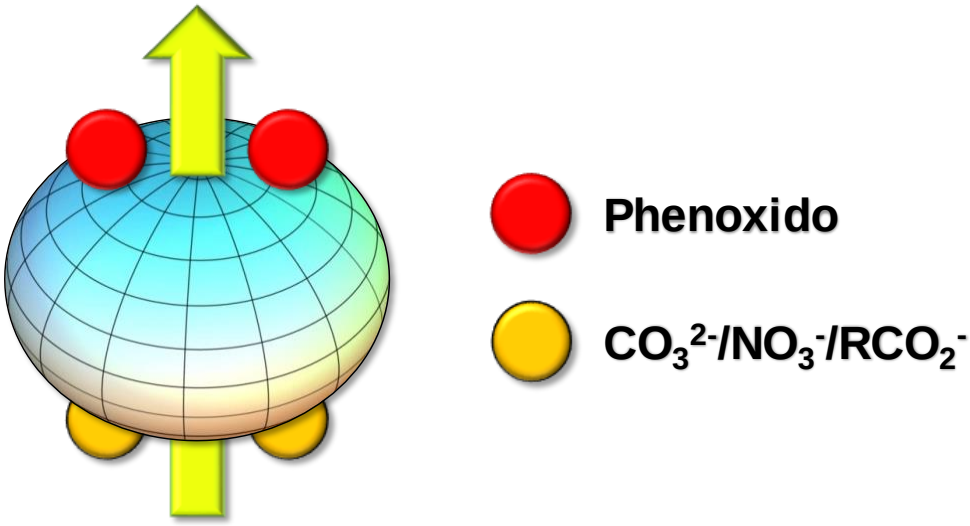

Figure 2.18.- Oblate electron sphere distribution of the M_J = ±15/2 state for the Dy^{III} ion. The anisotropy axis lies perpendicular to the spheroid. Red and orange balls simulate the positions corresponding to phenoxido and carbonate/nitrate/carboxylate, respectively.

Apart from what we have said, we think that it is difficult to make more correlations. In such systems where the coordination number is so high, slight modifications in bond distances and angles could have a significant effect and, at the same time, could be difficult to detect. Moreover, we believe that we cannot do such an exhaustive study based on the detailed structural parameters since most of the compounds suffer from transformations.

2.5. CONCLUSIONS

We have been able to successfully extend the previously reported acetate bridged dinuclear $Zn^{II}Dy^{III}$ system by employing carbonate and a wide variety of polycarboxylates giving rise to 9 novel polynuclear systems. Even though we managed to obtain the single crystal structures for all, some of the compounds suffer from transformations associated to the loss of crystallization solvent molecules. This fact was verified by carrying out an exhaustive alternative characterization study based on the diamagnetic $Zn^{II}Y^{III}$ based counterparts.

In their non-diluted form, none of the compounds displayed slow magnetic relaxation in the absence of an external magnetic field. When applying an optimum external *dc* field, all the compounds exhibited well defined sets of maxima in the out-of-phase susceptibility plots in agreement with a partial or total suppression of QTM. Regarding diluted systems, $\mathbf{7_{DyY}}$, $\mathbf{11_{DyY}}$ and $\mathbf{13_{DyY}}$ showed zero field SMM behaviour. From the *dc* magnetic data recorded for $\mathbf{7_{Gd}}$ we concluded that the magnetic exchanged interactions between Ln^{III} ions were very weak for this compound, a fact that explains why the dilution process improves the dynamic magnetic properties for $\mathbf{7_{DyY}}$. Most likely, the weak exchange interactions in **7** provide transverse components facilitating QTM. In the case of $\mathbf{11_{DyY}}$ and $\mathbf{13_{DyY}}$, avoiding weak dipolar interactions also quenched the undesired QTM.

Based on the results, we discarded rigidity driven magneto-structural correlations. In contrast, the larger U_{eff} values (above 100 K) found for $\mathbf{7_{DyY}}$ and **15** could be explained by a better ligand field design. Calculations made by Magellan software indicated that the anisotropy axes are mostly influenced by the short $Dy\text{-}O_{phenoxido}$ bond distances. Thus, the larger electron density in the opposite side of the ion, the larger energy splitting between the ground and first excited M_J states giving rise to enhanced U_{eff} values. Among our studied compounds, all the Dy^{III} centers except the ones in **7**

and Dy1B in **15** have a chelating nitrate opposite to the phenoxidos. In contrast, Dy^{III} ions in **7** and Dy1B in **15** contain a carbonate and a carboxylate, respectively. These groups are expected to provide larger electron density to the paramagnetic ions and, hence, the improved magnetic properties are explained by this fact.

2.6. REFERENCES

[1] A. Zabala-Lekuona, J. Cepeda, I. Oyarzabal, A. Rodríguez-Diéguez, J.A. García, J.M. Seco, E. Colacio, Rational design of triple-bridged dinuclear ZnIILnIII-based complexes: a structural, magnetic and luminescence study, CrystEngComm. 19 (2017) 256–264. https://doi.org/10.1039/c6ce02240e.

[2] R. Sessoli, D. Gatteschi, H.L. Tsai, D.N. Hendrickson, A.R. Schake, S. Wang, J.B. Vincent, G. Christou, K. Folting, High-Spin Molecules: [Mn12O12(O2CR)16(H2O)4], J. Am. Chem. Soc. 115 (1993) 1804–1816. https://doi.org/10.1021/ja00058a027.

[3] J.D. Hilgar, M.G. Bernbeck, J.D. Rinehart, Million-fold Relaxation Time Enhancement across a Series of Phosphino-Supported Erbium Single-Molecule Magnets, J. Am. Chem. Soc. 141 (2019) 1913–1917. https://doi.org/10.1021/jacs.8b13514.

[4] F. Habib, J. Long, P.H. Lin, I. Korobkov, L. Ungur, W. Wernsdorfer, L.F. Chibotaru, M. Murugesu, Supramolecular architectures for controlling slow magnetic relaxation in field-induced single-molecule magnets, Chem. Sci. 3 (2012) 2158–2164. https://doi.org/10.1039/c2sc01029a.

[5] E.A. Mikhalyova, M. Zeller, J.P. Jasinski, R.J. Butcher, L.M. Carrella, A.E. Sedykh, K.S. Gavrilenko, S.S. Smola, M. Frasso, S.C. Cazorla, K. Perera, A. Shi, H.G. Ranjbar, C. Smith, A. Deac, Y. Liu, S.M. McGee, V.P. Dotsenko, M.U. Kumke, K. Müller-Buschbaum, E. Rentschler, A.W. Addison, V. V. Pavlishchuk, Combination of single-molecule magnet behaviour and luminescence properties in a new series of lanthanide complexes with tris(pyrazolyl)borate and oligo(β-diketonate) ligands, Dalton Trans. 49 (2020) 7774–7789. https://doi.org/10.1039/d0dt00600a.

[6] Z.Y. Zhao, H.H. Xu, P. Chen, Y.X. Li, Y. Sui, W. Bin Sun, Optimization and expansion of the Schiff base [Zn-Dy] unit to enhance the performance of single molecule magnetic materials, J. Mater. Chem. C. 8 (2020) 4843–4850. https://doi.org/10.1039/d0tc00207k.

[7] S. Titos-Padilla, J. Ruiz, J.M. Herrera, E.K. Brechin, W. Wersndorfer, F. Lloret, E. Colacio, Dilution-triggered SMM behavior under zero field in a luminescent Zn 2Dy2 tetranuclear complex incorporating carbonato-bridging ligands derived from atmospheric CO2 fixation, Inorg. Chem. 52 (2013) 9620–9626. https://doi.org/10.1021/ic401378k.

[8] G. Novitchi, W. Wernsdorfer, L.F. Chibotaru, J.-P. Costes, C.E. Anson, A.K. Powell, Supramolecular “Double-Propeller” Dimers of Hexanuclear CuII/LnIII Complexes: A {Cu3Dy3}2 Single-Molecule Magnet, Angew. Chem. Int. Ed. 48 (2009) 1614–1619. https://doi.org/10.1002/anie.200805176.

[9] S.H. Kim, J. Lee, D.J. Kim, J.H. Moon, S. Yoon, H.J. Oh, Y. Do, Y.S. Ko, J.H. Yim, Y. Kim, Titanium complexes containing new dianionic tetradentate [ONNO]-type ligands with benzyl substituents on bridging nitrogen atoms: Syntheses, X-ray structures, and catalytic activities in ring opening polymerization of lactide, J. Organomet. Chem. 694 (2009) 3409–3417. https://doi.org/10.1016/j.jorganchem.2009.06.037.

[10] D. Brackemeyer, C. Schulte To Brinke, F. Roelfes, F.E. Hahn, Regioselective C8-metalation of N-phosphine tethered adenine derivatives via C8-H activation, Dalton Trans. 46 (2017) 4510–4513. https://doi.org/10.1039/c7dt00682a.

[11] M. Llunell, D. Casanova, J. Cirera, J.M. Bofill, P. Alemany, S. Alvarez, M. Pinsky, D. Avnir, SHAPE, (2005).

[12] N.F. Chilton, R.P. Anderson, L.D. Turner, A. Soncini, K.S. Murray, PHI: A powerful new program for the analysis of anisotropic monomeric and exchange-coupled polynuclear *d* - and *f* -block complexes, J. Comput. Chem. 34 (2013) 1164–1175. https://doi.org/10.1002/jcc.23234.

[13] X.L. Li, J. Tang, Recent developments in single-molecule toroics, Dalton Trans. 48 (2019) 15358–15370. https://doi.org/10.1039/c9dt02113b.

[14] Z.H. Zhu, X.F. Ma, H.L. Wang, H.H. Zou, K.Q. Mo, Y.Q. Zhang, Q.Z. Yang, B. Li, F.P. Liang, A triangular Dy3 single-molecule toroic with high inversion energy barrier: Magnetic properties and multiple-step assembly mechanism, Inorg. Chem. Front. 5 (2018) 3155–3162. https://doi.org/10.1039/c8qi01069b.

[15] S.K. Langley, K.R. Vignesh, B. Moubaraki, G. Rajaraman, K.S. Murray, Oblate versus Prolate Electron Density of Lanthanide Ions: A Design Criterion for Engineering Toroidal Moments? A

Case Study on {Ln^{III}_6} (Ln=Tb, Dy, Ho and Er) Wheels, Chem. – A Eur. J. 25 (2019) 4156–4165. https://doi.org/10.1002/chem.201805765.

[16] K.N. Shrivastava, Theory of Spin–Lattice Relaxation, Phys. Status Solidi. 117 (1983) 437–458. https://doi.org/10.1002/pssb.2221170202.

[17] D. Reta, N.F. Chilton, Uncertainty estimates for magnetic relaxation times and magnetic relaxation parameters, Phys. Chem. Chem. Phys. 21 (2019) 23567–23575. https://doi.org/10.1039/c9cp04301b.

[18] K.X. Yu, J.G.C. Kragskow, Y.S. Ding, Y.Q. Zhai, D. Reta, N.F. Chilton, Y.Z. Zheng, Enhancing Magnetic Hysteresis in Single-Molecule Magnets by Ligand Functionalization, Chem. 6 (2020) 1777–1793. https://doi.org/10.1016/j.chempr.2020.04.024.

[19] N.F. Chilton, D. Collison, E.J.L. McInnes, R.E.P. Winpenny, A. Soncini, An electrostatic model for the determination of magnetic anisotropy in dysprosium complexes, Nat. Commun. 4 (2013) 1–7. https://doi.org/10.1038/ncomms3551.

[20] F. Habib, G. Brunet, V. Vieru, I. Korobkov, L.F. Chibotaru, M. Murugesu, Significant enhancement of energy barriers in dinuclear dysprosium single-molecule magnets through electron-withdrawing effects, J. Am. Chem. Soc. 135 (2013) 13242–13245. https://doi.org/10.1021/ja404846s.

[21] J. Rinehart, J. Long, Exploiting single-ion anisotropy in the design of f-element single-molecule magnets, Chem. Sci. 2 (2011) 2078–2085. https://doi.org/10.1039/c1sc00513h.

CHAPTER 3

MAGNETIC STUDY OF MULTINUCLEAR Co^{II} BASED AND MIXED HETEROTRINUCLEAR $TM^{II}Ln^{III}TM^{II}$ COMPOUNDS: ROLE OF INTRAMOLECULAR INTERACTIONS TO OBTAIN ZERO FIELD SMMS

3.1. INTRODUCTION

As discussed in the general introduction, even though in the past years the tendency to design SMMs has been shifted towards low coordinated 4f based mononuclear complexes, the study of polynuclear magnetic clusters appears to be still of great interest. The first examples contained tetragonally distorted octahedral Mn^{III} ions due to its negative single-ion anisotropy provided by Jahn-Teller distortion, but the single ion anisotropy of Co^{II} makes it a potential candidate for the development of new high-nuclearity SMMs. When thinking about homometallic complexes, an option to achieve a resultant bistable high spin ground-state well isolated from excited states could be to employ ligands which impose metal bridging angles that are near to 90°. This favours ferromagnetic (F) interactions between metallic centers as it occurs in cubanes with $\{Ni_4O_4\}$ cores [1,2] or in face-sharing defective dicubanes with $\{Ni_4O_6\}$ cores [3]. In addition, this principle aimed to enhance the F interactions could be fulfilled combining the aforementioned structures with azido bridging ligands due to the tendency to transmit F coupling in its end-on (EO) mode [4–6].

However, when referring to 4f elements the strategy must be modified. The 4f electron shell is buried by the outer complete $5s^2$ and $5p^6$ orbitals, thus most of the polynuclear lanthanide compounds show very weak or no intramolecular magnetic exchange [7]. Therefore, even if it is possible to obtain large thermal energy barriers that prevent the reversal of the magnetization, in the low temperature regime the barrier is usually shortcut by the fast quantum tunnelling of the magnetization, inhibiting the presence of hysteresis at zero magnetic field or even hiding SMM phenomenon in *ac* measurements. As discussed, this can be successfully suppressed by applying a magnetic field, by diluting the sample with isostructural diamagnetic complexes to eliminate possible intermolecular interactions, replacing “innocent” ligands with radicals, etc. Although the latter alternative appears to be a successful approach, the manipulation and isolation of such species is more complicated.

Hence, another choice could be to introduce 3d elements into 4f systems so as to increase the magnetic exchange between metallic centers. For instance, K. S. Murray *et al.* published in 2014 a $[Co^{III}_2Dy^{III}_2]$ butterfly compound with SMM properties, however, this complex crossed to quantum regime below 2.2 K [8]. In contrast, one year before they had synthesized the analogue $[Cr^{III}_2Dy^{III}_2]$ compound, which contains paramagnetic Cr^{III} ions instead of diamagnetic Co^{III} ones, resulting in an improvement

in the magnetic properties. Even though the barrier was almost identical, magnetic hysteresis was observable at temperatures up to 3.5 K for the last one [9].

In this context, we have managed to combine some of the above mentioned strategies to synthesize ten novel complexes with the compartmental ligand *N,N'*-dimethyl-*N,N'*-bis(2-hydroxy-3-methoxy-5-methylbenzyl)ethylenediamine (H_2L^3). On the one hand, we have synthesized two defective dicubane Co^{II} based tetranuclear compounds by varying the bridging ligands that modulate the exchange coupling. Furthermore, we have serendipitously obtained a pentanuclear system that behaves as zero-field SMM. On the other hand, six heterotrinuclear mixed 3d-4f-3d systems have been studied to analyse the influence of exchange interactions in quenching or promoting zero-field QTM. For that purpose, in four out of six compounds we have combined two paramagnetic ions (Co^{II} and different Ln^{III} ions), whereas in other two only Co^{II} or Dy^{III} metal ions are paramagnetic (diamagnetic Y^{III} or Zn^{II} metal ions are used as 4f and 3d ions in those cases). Overall, we report the preparation, chemical characterization, X-ray structural description and magnetic properties of all the compounds.

3.2. PREPARATION OF COMPLEXES

3.2.1. $[Co_4(\mu\text{-}L^3)_2(\mu\text{-}Cl)_2Cl_2]\cdot 2H_2O$ (16)

To a solution of H_2L^3 (48 mg, 0.125 mmol) in 5 mL of MeCN, another solution of $CoCl_2\cdot 6H_2O$ (59.5 mg, 0.250 mmol) in 5 mL of MeCN was added dropwise and with continuous, but slow stirring. Once the addition was finished, the blue solution was allowed to stand at room temperature. In few days, well-formed prismatic light blue, purple/blue and purple (only few of them or none) coloured crystals were obtained. The former ones correspond to an ionic $H_4L^3[CoCl_4]$ monomer (compound **26**, Figure A3.1), the second to the desired product and the latter to an almost identical coordination compound (compound **27**, Figure A3.2). Nonetheless, it contains four crystallization acetonitrile molecules instead of two water molecules present in **16**. So as to separate the undesired monomer, the mother liquors were removed and water was added to dissolve the ionic product. The purple/blue solid was then filtered, washed with water several times and dried. Yield and elemental analysis results in Table A3.1.

3.2.2. $[Co_4(\mu\text{-}L)_2(\mu\text{-}N_3)_2(N_3)_2]\cdot 2H_2O$ (17)

To a purple solution containing H_2L^3 (69 mg, 0.18 mmol) and $Co(NO_3)_2\cdot 6H_2O$ (104.8 mg, 0.36 mmol) in 8 mL of MeCN, another solution of NaN_3 (23.4 mg, 0.36 mmol) in 2 mL of MeCN with three drops of H_2O was added dropwise. A blue precipitate was obtained immediately. The reaction was stirred for 10 minutes, the product was filtered, washed with MeCN and dried. From mother liquor purple crystals suitable for X-ray diffraction were achieved. Yield and elemental analysis results in Table A3.1.

3.2.3. $[Co_5(\mu\text{-}L^3)_2(\mu\text{-}OAc)_5(\mu\text{-}OH)]\cdot n$MeCN (n = 4 (18a); n = 3 (18b)

To a solution of H_2L^3 (48 mg, 0.125 mmol) in 5 mL of MeCN, a drop of distilled water was added followed by triethylamine (0.085 mL, 0.625 mmol). Subsequently, $Co(OAc)_2\cdot 4H_2O$ (78 mg, 0.312 mmol) was added with high stirring and assisted by ultrasound for few seconds obtaining a purple coloured solution. The reaction was stirred for 1.5 h and it was allowed to stand at room temperature. In few days, purple coloured crystals were achieved, which were filtered, washed several times with acetonitrile and dried. Yield and elemental analysis results in Table A3.1.

3.2.4. $[LnTM_2(\mu\text{-}L^3)_2(H_2O)_2Cl_2]Cl\cdot nH_2O\cdot$MeCN (TM = Co^{II}, Ln^{III} = Y (19), Gd (20), Tb (21), Dy (22), Er (23) and Yb (24); TM = Zn^{II}, Ln^{III} = Dy (25); n = 0 for 19 and 25 and n = 1 for 20-22 and 24; n = undefined for 23)

To a H_2L^3 (48 mg, 0.125 mmol) solution in 4 mL of MeCN, triethylamine (0.034 mL, 0.25 mmol) was added with continuous stirring followed by a drop of distilled water. Then, a solution containing both the corresponding $TMCl_2\cdot nH_2O$ (0.125 mmol) and $Ln(NO_3)_2\cdot nH_2O$ (0.0625 mmol) salts in 1 mL of MeCN was added dropwise obtaining a purple solution, which was immediately allowed to stand at room temperature to afford X-ray quality crystals. In some cases, the trinuclear complexes co-crystallized with compound **16** and then it was necessary to separate them. Yield and elemental analysis results in Table A3.1.

3.3. EXPERIMENTAL RESULTS

Despite the fact that at first sight H_2L^3 is similar to other reported Schiff bases [10], the lack of rigidity of Mannich bases allowed us to build up, apart from usual planar

systems [11], other less common compounds such as **18a** and **18b** (note that Schiff bases also form complexes with a rich variety of geometries [12]). Moreover, being aware of the possibility of coordinating transition metals in both sites [13], we were able to synthesize three novel Co^{II} based coordination compounds (**16**, **18a** and **18b**) and we reproduced a previously reported azide bridged compound (**17**) [14]. Apart from homonuclear cobalt based compounds, seven heterotrinuclear 3d-4f-3d mixed compounds were obtained. Crystallographic data and selected bond lengths and angles for compounds **16-22**, **24** and **25** are given in Tables A3.2-A3.7.

As indicated in the section devoted to the preparation of the complexes, the trinuclear compounds crystallize in two different phases, where one contains a water and an acetonitrile crystallization molecule and the other lacks of the water molecule. This is something that we recently found, since the first crystallized trinuclear **20-22** and **24** compounds displayed the same crystal structure. When carrying out powder X-ray diffraction experiments, however, we realized that for most of the compounds (**19**, **21**, **22**, **23** and **25**) were displaying extra diffraction peaks (Figures A3.9-A3.10). At first, these extra diffraction peaks were associated to a partial symmetry lost (perhaps due to partial solvent evaporation) since the peak positions coincide somehow with the systematic absences. The fact that **20** and **24** counterparts displayed diffraction patterns that perfectly matched with the simulated ones (Figure A3.11) made us discard the possibility of an ionic radius related effect (Gd^{III} and Yb^{III} ions have the biggest and the smallest ionic radius within the explored Ln^{III} ions). Hence, considering it a simple random effect, we decided to explore the thermal behaviour of all these trinuclear compounds.

By carrying out the experiments under synthetic air, the residues are expected to be metal oxides (CoO and Ln_2O_3 for **19-24** and ZnO and Dy_2O_3 for **25**). Thus, the technique allowed us to confirm that the initial products' molecular weights correspond to trinuclear systems (Figures A3.15-A3.17).

The fact that all the compounds displaying extra diffraction peaks were purely trinuclear TM_2Ln systems was confirmed when the crystal structures of **19** and **25** were measured. This new phase, which lacks of the crystallization water molecule, is responsible of the previously mentioned extra diffraction peaks. Figures A3.9-A3.10 are examples that perfectly prove that the majority of the studied compounds are mixtures of both crystallization phases.

3.3.1. Crystal structures of complexes 16-22, 24 and 25

The reaction between H_2L^3 and $CoCl_2{\cdot}6H_2O$ in a 1:1 molar ratio with acetonitrile as solvent afforded three different crystalline products (see preparation of the complexes and Figures A3.1-A3.2), but only complex **16** was studied. The crystal structure of the complex with the general formula $[Co_4(\mu\text{-}L^3)_2(\mu\text{-}Cl)_2Cl_2]{\cdot}2H_2O$ is shown in Figure 3.1, which crystallizes in the *R-3* space group. This centrosymmetric tetranuclear compound contains four Co^{II} ions, two deprotonated (L^{2-}) ligands, two triple bridging chloride anions, two terminal chloride anions, and two crystallization water molecules. In contrast to what occurred in the previous reported planar compounds, where the aromatic rings of L^{2-} are almost coplanar, the ligands are folded to give rise to an almost perpendicular angle (83.40°) between the planes formed by the aromatic rings. In this way, each ligand is coordinated to three metallic ions displaying a distorted face-sharing dicubane core with two missing vertices. The common face of the incomplete cubanes is composed by two centrosymetrically related Co1 and Co1(i) ions and two bridging chlorides (see crystallographic tables for symmetry operations).

The fully deprotonated ligand uses all its heteroatoms to coordinate the Co^{II} centers. The nitrogen and bridging chloride atoms are in *cis* position in the $CoN_2O_2Cl_2$ distorted octahedral environments of the related Co1 and Co1(i) ions, whereas the phenoxido bridging groups occupy *trans* positions. On the other hand, the CoO_4Cl_2 coordination environments of the Co2 and Co2(i) metal ions are between trigonal prism and octahedral polyhedra (calculated by SHAPE software [15], 5.565 and 6.845 values, respectively; Table A3.8,), where two oxygen atoms come from the phenoxido bridging groups, the other two correspond to methoxy groups (belonging to different ligands) and, finally, two chloride atoms (with terminal and triply bridging modes).

The Co-heteroatom distances vary in the range of 2.006(3)-2.515(13) Å, where the shortest distances correspond to $Co\text{-}O_{phenoxido}$ bonds and the longest to the $Co\text{-}Cl_{bridge}$ ones. Although all the bond lengths could be grouped based on their nature giving rise to similar distances, $Co\text{-}O_{methoxy}$ bonds can be shorter (2.218(3) Å) or longer (2.389(3) Å). The Co-X-Co (X = Cl or $O_{phenoxido}$) bridging angles are much smaller when the bridging atom is a chloride (83.66(4) to 89.40(4)°) instead of oxygen (111.67(13) to 115.76(15)°). Therefore, the shared face in the dicubane is almost a perfect square, but the other faces appear to be much more distorted. Although the Co1-(μ-Cl_2)-Co1(i) bridging fragment is coplanar, the other two Co1-μ-phenoxido/μ-chloride-Co2 bridging fragments slightly deviate from planarity with hinge angles of 3.47 and 10.78°. Co1···Co2 and Co1···Co2(i) distances are 3.447 and 3.365 Å, respectively.

Finally, it is worth mentioning that the crystal structure is largely stabilized by a supramolecular hydrogen bonding network. In particular, water molecules form a hexanuclear cluster (visible in the *c* axis), which describes an almost perfect hexagon owning O1W···O1W···O1W angles of 119.42° and O1W···O1W hydrogen bonds of 2.866 Å (Figure A3.3). This might be the reason why the main product contains water molecules and not acetonitrile, even though the reaction is carried out without adding extra water.

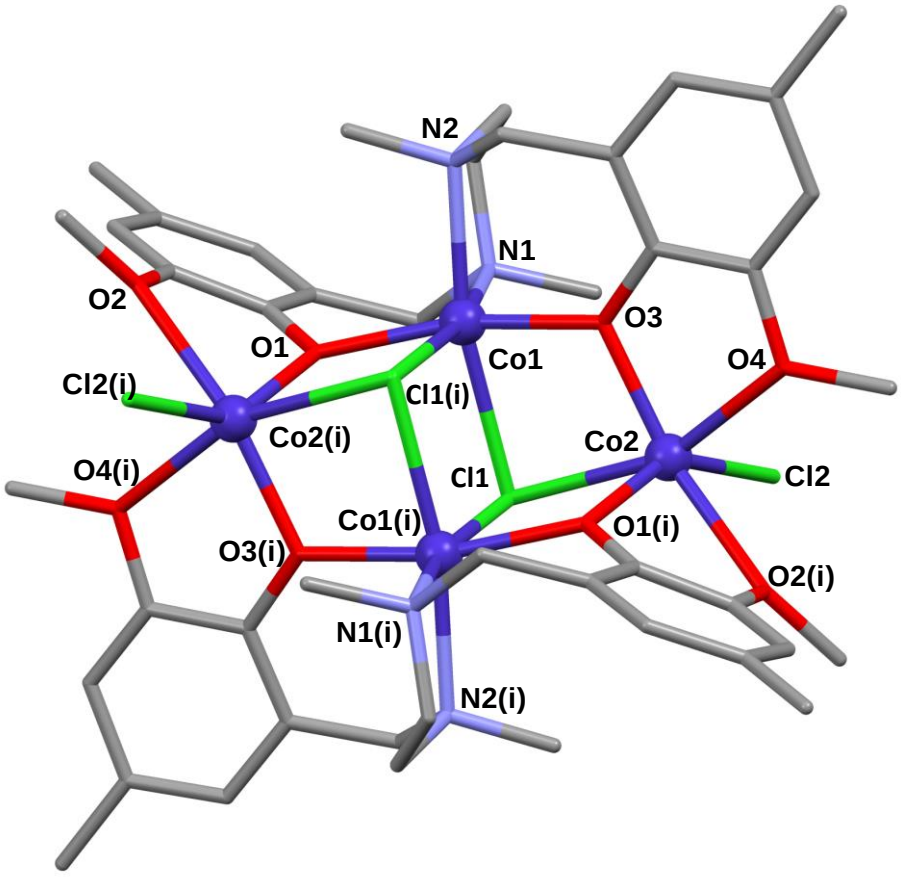

Figure 3.1.- Perspective view of complex **16**. Colour code: cobalt, chloride, nitrogen, oxygen and carbon atoms are in purple, green, light blue, red and grey, respectively. Hydrogen atoms and solvent molecules are omitted for the sake of clarity.

The reaction between H_2L^3, NaN_3 and $Co(NO_3)_2{\cdot}6H_2O$ in a 1:2:2 molar ratio with acetonitrile as solvent and with a couple of water drops instantly gave rise to a blue coloured precipitate complex **17** with general formula $[Co_4(\mu\text{-}L)_2(\mu\text{-}N_3)_2(N_3)_2]{\cdot}2H_2O$. This complex crystallizes in *R-3* space group and its crystal structure is shown in Figure 3.2. It shows a very similar structure to **16**, but containing $\mu_{1,1,1}$- triply bridging and terminal

azide ligands replacing chloride ligands. In this complex the crystallographycally related Co1 and Co1(ii) ions exhibit slightly distorted octahedral CoN_4O_2 environments, having the bridging phenoxido oxygen atoms in *trans* position (Table A3.9). On the other hand, Co2 and Co2(ii) are pentacoordinated with CoN_2O_3 coordination environments. In this case, the SHAPE measurements do not reveal a clear concordance with any particular polyhedron. The lower values are 2.895 and 3.903 for trigonal bipyramid and Johnson trigonal bipyramid, respectively (Table A3.10).

In contrast to the former tetranuclear complex **16**, Co-heteroatom distances are in a narrower range, where the shortest bonds are the Co-$O_{phenoxido}$ ones (1.984(3) to 2.046(3) Å) and Co2-$N_{terminalazide}$ one (1.993(5) Å). The rest of the Co-N_{amine} and Co-$N_{bridgeazide}$ are in a slightly longer range (2.173(4) to 2.252(4) Å). Similarly to what occurs in the previous complex, here Co1-X-Co2 (X = N_{azide} or $O_{phenoxido}$) bridging angles are smaller when bridged by the azide (92.95(16)-93.94(16)° in contrast to the range of 107.45(16)-108.70(16)° with phenoxido). Nevertheless, the shared face loses the square geometry with larger Co1-N_{azide}-Co1(ii) angles (100.41(17)°). The Co-(μ-azide)-Co(ii) bridging fragment is coplanar and the other two μ-phenoxido/μ-azide bridged Co1 and Co2 are near to it, since the hinge angles are of 3.90 and 1.97°. Lastly, within the molecule, intramolecular distances between Co centres are between 3.249 and 3.427 Å.

In terms of intermolecular arrangement, as it occurs with compound **16**, a supramolecular network can be observed. Differently, in this case the hexanuclear water cluster in compound **16** is replaced by a star shaped disposition, where six water molecules form hydrogen bonds towards terminal azides (Figure A3.4). It is noteworthy that in this case the water molecules are not in the same plane, but they are connected with the tetranuclear entities in *zig-zag* fashion as it is shown in the Figure A3.5 from the *b* axis.

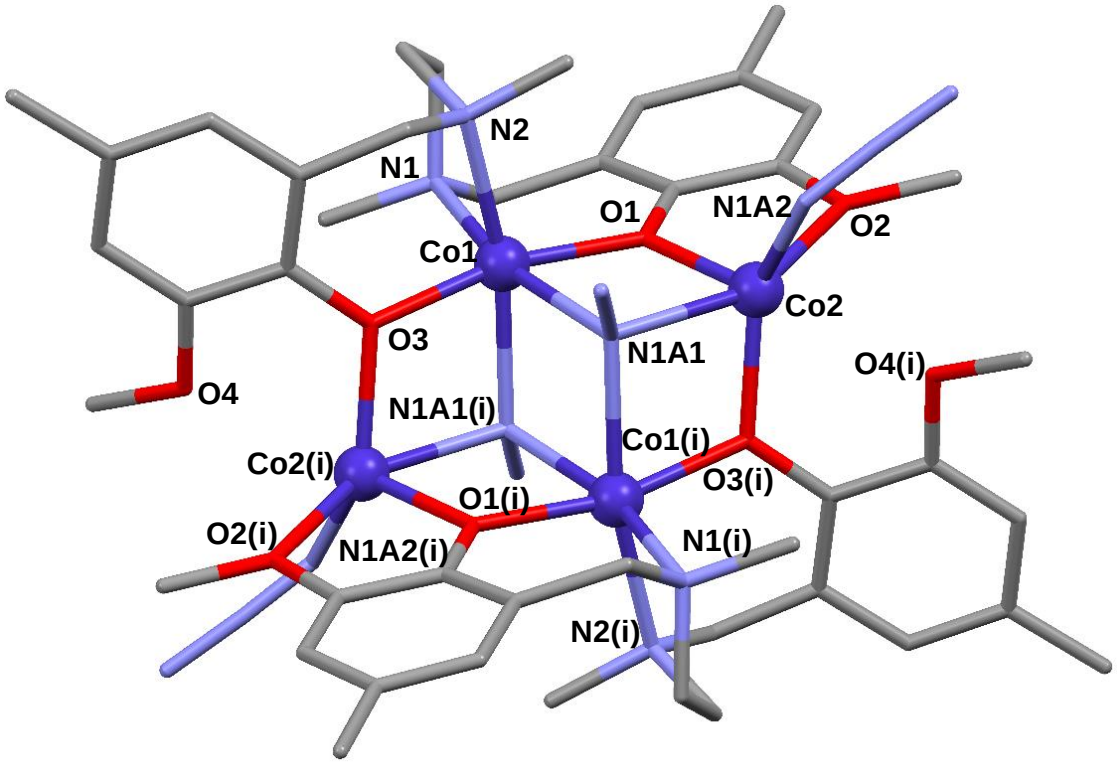

Figure 3.2.- Perspective view of complex **17**. Colour code: cobalt, nitrogen, oxygen and carbon atoms are in purple, light blue, red and grey, respectively. Hydrogen atoms and solvent molecules are omitted for the sake of clarity.

The reaction between H_2L^3, $Co(OAc)_2{\cdot}4H_2O$ and Et_3N in a 2:5:10 molar ratio with acetonitrile as solvent and a drop of water to ensure the presence of OH^- anions in the reaction environment afforded suitable crystals for X-ray diffraction analysis. Two different phases of the same pentanuclear compound were obtained, being the number of crystallization acetonitrile molecules the major significant difference (4 molecules for **18a** and 3 for **18b**). Hence, only crystal structure of **18a** will be described. This compound crystalizes in the *P-1* space group. Its crystal structure is presented in Figure 3.3 and consists of neutral molecules of formula $[Co_5(\mu\text{-}L)_2(\mu\text{-}OAc)_5(\mu\text{-}OH)]$ and four crystallization acetonitrile molecules. The complexity of the structure, as well as the diversity of coordination modes that are present for the same heteroatoms, proves the great versatility of the Mannich type H_2L^3 ligand to synthesize unusual compounds. The ten positive charges of five Co^{II} cations are balanced with two completely deprotonated ligand molecules (L^{2-}), four bidentate and one tridentate bridging acetates and a triple bridging OH^- in the centre of the structure. The similarities between Co^{II} center environments are not obvious, however, Co1 is the only one pentacoordinated,

while the rest have a coordination number of six. The SHAPE analysis of Co1 indicates that the cobalt ion acquires a trigonal bipyramid geometry (the SHAPE values for all Co^{II} centers are collected in Tables A3.11-A3.12). The base of the bipyramid is formed by a Co1-Co2 bridging (O1C) acetate oxygen atom, a Co1-Co2-Co4 bridging OH^- group in the centre of the structure and a Co1-Co5 bridging phenoxido (O1A) oxygen atom. The remaining two vertices belong to another Co1-Co2 bridging acetate (O1D) and a Co1-Co4-Co5 bridging phenoxido (O3A) oxygen atom. The CoO_6 coordination environment is of distorted octahedron type for Co2 (notably more distorted in **18a** than in **18b** and relatively near to a trigonal prism geometry). The octahedron of Co2 presents similarity respect to the environment of Co1, but is the coordinated methoxy O2B oxygen which completes the distorted octahedron (in Co1, the nearest methoxy O2A is too far and it is not bonded to the metal center). Five of the six oxygen atoms come from bridging groups, where two of them in *cis* position belong to Co2-Co1 bridging acetate groups (O2C and O2D), next two in *cis* position and completing the equatorial plane belong to Co2-Co3 bridging phenoxido atoms (O1B and O3B) and the last bridging oxygen, *trans* to the not bridging methoxy (O2B) oxygen, belongs to the triple Co1-Co2-Co4 bridging OH^- group (O1OH). The distorted octahedral CoN_2O_4 environment of Co3 and Co5 atoms differ slightly. In both cases, nitrogen atoms and bridging phenoxido oxygen atoms occupy *cis* positions between each of them. Nonetheless, for Co3 the remaining two positions are completed with a tridentate acetate group, which bridges Co3 and Co4. Instead, Co5 completes the coordination environment with two oxygen atoms belonging to two distinct Co5-Co4 bridging acetate groups (O2G and O2F). Noteworthy, the distortion degree for Co3 is notably larger and can be somehow described as trigonal prism. Lastly, Co4 is shifted towards Co5 since two acetate groups and a phenoxido oxygen atom are bridging both metallic ions (Co4···Co5 and Co4···Co3 distances of 3.304(1) and 4.113(1) Å, respectively). The last three positions are formed by a methoxy (O4A) oxygen atom *cis* to the phenoxido O3A, the triple bridging OH^- group and the oxygen atom of the tridentate acetate group (O2E).

The OH^- group is stabilized in the middle of the structure by a hydrogen bond pointing to a methoxy oxygen atom (O4B). The shortest Co-heteroatom distances are those where the coordinating atom is oxygen, but they appear in a wide range of values from 1.988(4) to 2.338(4) Å. Moreover, Co-N bond distances appear in the 2.146(4)-2.258(4) Å range. The Co-X-Co (X = $O_{phenoxido}$ or OH^-) bridging angles exhibit a wide range of values, from 94.87(13)° to 127.64(19)°. The Co1-(μ-O2)-Co5, Co2-(μ-O2)-Co3 and μ-phenoxido/μ-OH^- bridged Co1 and Co4 exhibit hinge angles with the

following values: 18.77°, 24.11° and 15.82°, respectively. Finally, the shortest distance between metallic ions is about 3.194 Å (Co2···Co3), while the largest one is about 7.216 Å (Co5···Co3).

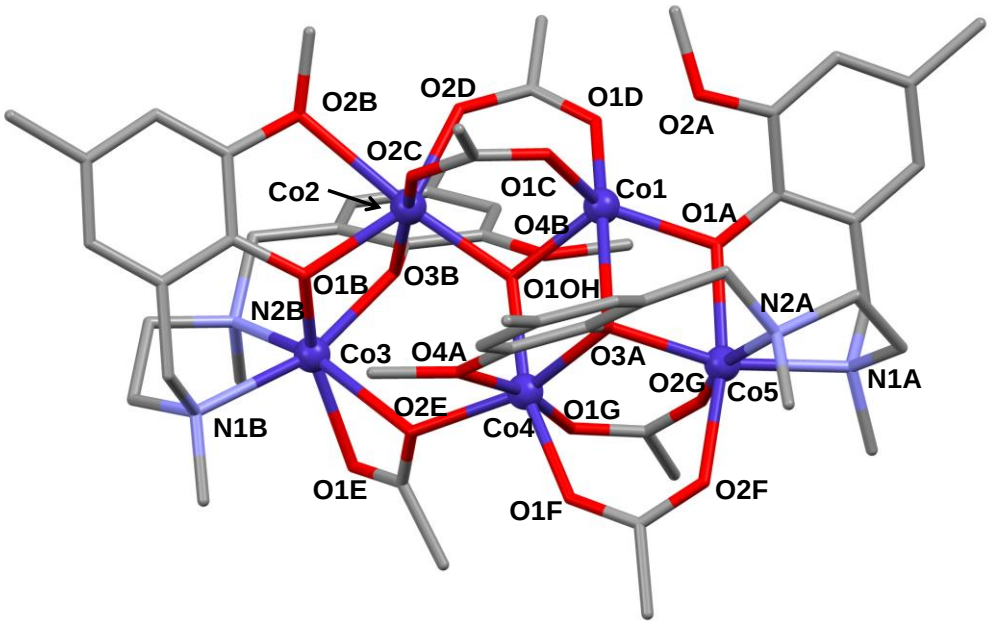

Figure 3.3.- Perspective view of complex **18a**. Colour code: cobalt, nitrogen, oxygen and carbon atoms are in purple, light blue, red and grey, respectively. Hydrogen atoms and solvent molecules are omitted for the sake of clarity.

Complexes **19-25**, synthesized by mixing H_2L^3, Et_3N, $TMCl_2{\cdot}nH_2O$ and $Ln(NO_3)_2{\cdot}nH_2O$ crystallize in two possible polymorphs: in the monoclinic $P2_1/c$ (**20-22** and **24**) or in the orthorhombic $C222_1$ space group (**19** and **25**). The former type contains an entire molecule within the asymmetric unit, whereas the latter displays half a molecule. The trinuclear core, though, remains unaltered being the presence/absence of a crystallization water molecule the main difference. As an example, the structure of **22** is given in Figure 3.4 with the general formula $[DyCo_2(\mu\text{-}L^3)_2(H_2O)_2Cl_2]Cl{\cdot}H_2O{\cdot}MeCN$, which consists of a cationic $[DyCo_2(\mu\text{-}L^3)_2(H_2O)_2Cl_2]^+$ unit, a Cl^- anion and a water and an acetonitrile crystallization molecules. Within the cationic trinuclear entity, two $[CoCl(L^3)]^-$ units are coordinated to the central $[Dy(H_2O)_2]^{3+}$ unit, each of them through two bridging phenoxido and a single methoxy group of the deprotonated compartmental ligand L^{2-}.

This way, four phenoxido, two methoxy groups and two water molecules complete the DyO_8 coordination polyhedron exhibited by the central metal ion. The shorter Dy-O1 and intermediate Dy-O3 or Dy-OW bond distances are in the range of 2.258(6)-2.354(7) Å, whereas the longer Dy-$O_{methoxy}$ are of about 2.585(6)-2.657(7) Å. The coordination sphere was analysed by the SHAPE software (Table A3.14), in order to see the degree of distortion with respect to an ideal eight-vertex polyhedron. The analysis indicates that the best fit is obtained by a square antiprism polyhedron with a SHAPE value of 1.847. In any case, square antiprism and triangular dodecahedron geometries show similar low SHAPE values in all the complexes. In contrast, Co^{II} ions show a CoO_2N_2Cl coordination environment where Co-$O_{phenoxido}$, Co-N and Co-Cl distances are in the ranges of 1.978(6)-2.150 (7) Å, 2.090(9)-2.271(9) Å and 2.290(3)-2.256(3) Å, respectively. SHAPE values suggest that the geometry is best described as distorted square pyramid in both Co^{II} ions (Table A3.13). The nitrogen and oxygen atoms are in the vertices of the square base and the apical position is occupied by the chloride atom. The intramolecular distances between the paramagnetic Co^{II} and Dy^{III} centers are 3.4859(15) and 3.4532(15) Å, which form an angle near to linearity, exhibiting a Co-Dy-Co angle of 163.02(3)°. The intramolecular Co···Co distance is of 6.863(2) Å. Bridging phenoxido groups form Co-O-Dy angles in the 100.9(2)-110.6(3)° range. The oppositely located water molecules in the $[Dy(H_2O)_2]^{3+}$ units are responsible for stablishing hydrogen bonds with the chloride counteranions (O1W···Cl2 and O2W···Cl2) in such a way that they form chains along the *b* axis (Figure A3.6). An additional intramolecular hydrogen bond appears between the non-coordinating methoxy groups and the coordinated water molecules (O1W···O4B and O2W···O4A). Furthermore, the crystallization water molecule is stabilized by additional hydrogen bonds, O1S···Cl1A and O1S···O2W. Note that this last pattern is absent in the second polymorph found for **19** and **25**. Finally, the shortest Co···Co and Dy···Dy distances between neighbouring $[DyCo_2(\mu\text{-}L^3)_2(H_2O)_2Cl_2]^+$ trinuclear units are 7.924 and 9.541 Å, respectively, so they can be considered as completely isolated.

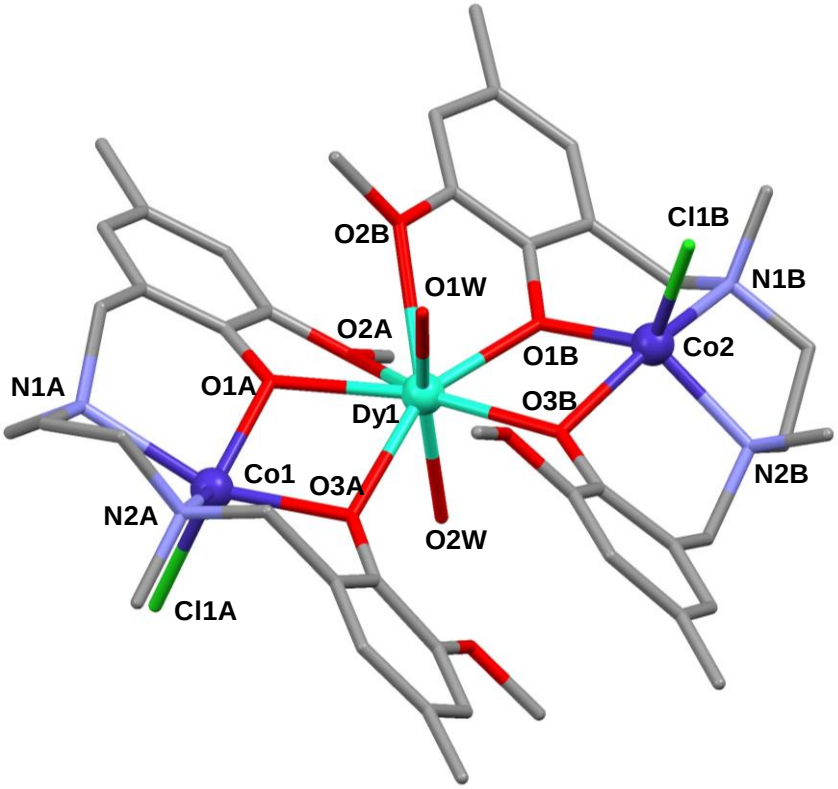

Figure 3.4.- Perspective view of complex **22**. Colour code: cobalt, dysprosium, nitrogen, oxygen and carbon atoms are in purple, turquoise, light blue, red and grey, respectively. Hydrogen atoms, counterions and solvent molecules are omitted for the sake of clarity.

3.3.2. Static magnetic properties of complexes 16-25

Magnetic susceptibility measurements in the temperature range of 2-300 K under a constant magnetic field of 0.1 T and variable field magnetization measurements were performed on polycrystalline samples of **16-25**.

At room temperature the $\chi_M T$ value of 12.56 $cm^3 \cdot mol^{-1} \cdot K$ in complex **16** is higher than the spin-only value (7.50 $cm3 \cdot mol^{-1} \cdot K$) for four isolated Co^{II} ions with $S = 3/2$ and $g = 2.0$ (Figure 3.5, left) indicative of the unquenched orbital angular momentum. Similarly, the room temperature value of 11.46 $cm^3 \cdot mol^{-1} \cdot K$ for **17** is also well above the spin-only value (Figure 3.5, right). However, when lowering the temperature, the behaviour drastically changes from **16** to **17**. For the former, the $\chi_M T$ value remains nearly constant from room temperature to 75 K, where it starts to fall more drastically reaching a minimum value of 5.97 $cm^3 \cdot mol^{-1} \cdot K$ at 2 K. This decrease could be attributed to both spin-orbit coupling effects and intramolecular antiferromagnetic

interactions. For the latter, as the temperature is lowered from room temperature to 26.0 K, the $\chi_M T$ value increases continuously to a value of 13.61 $cm^3 \cdot mol^{-1} \cdot K$. This is followed by a sharp increase up to 15.60 $cm^3 \cdot mol^{-1} \cdot K$ at 7.0 K and a sudden decrease to 14.41 $cm^3 \cdot mol^{-1} \cdot K$ at 2.5 K. The initial and final sharp increases suggest that the intramolecular interactions are ferromagnetic, while the final decrease may arise from intermolecular antiferromagnetic interactions and an anisotropic contribution (*D*) observed for similar clusters [16–18]. Considering that both complexes display a similar core structure with two possible exchange pathways (J_1 and J_2 in Figure 3.5), we attempted to fit the susceptibility data using the PHI [19] software and a simplified model that was previously used in the literature [14]. Unfortunately, we were not able to obtain reasonable fitting parameters. We associate the difficulty of fitting the data to several reasons: (i) presence of spin-orbit coupling, (ii) two different exchange pathways, (iii) two different coordination environments, (iv) possible intermolecular interactions and so on. In any case, it is worth remaking that the substitution of the bridging chlorides by azides provokes a global change in magnetic behavior from antiferromagnetic to ferromagnetic.

The *M(H)* plots at variable temperature (Figure 3.5, insets) display non-superimposable curves, which together with the absence of saturation at the maximum applied field of 7 T, indicates the presence of significant anisotropy in these compounds (or the presence of low-lying excited states very close in energy to the ground state, which can be field and thermally populated). It is worth mentioning that the magnetization for **16** increases slower that of **17** at low field, which match well with the global intramolecular antiferromagnetic interactions in the former and ferromagnetic in the latter. The magnetization values at 2 K and 7 T for **16** and **17** of 9.23 and 8.3 $N_{\mu B}$, respectively, are close for that expected for isolated Co^{II} ions (considering distorted octahedral geometries for all of them) with an $S_{effective}$ = 1/2 and g =4.3 of 8.6 $N_{\mu B}$.

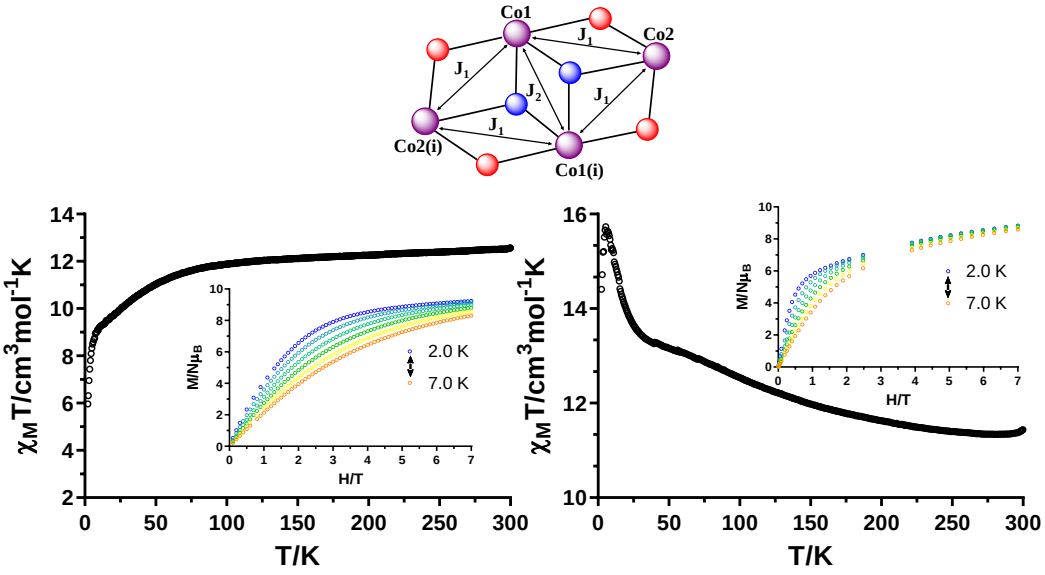

Figure 3.5.- Temperature dependence of the $\chi_M T$ product for **16** (left) and **17** (right) in the 2-300 K range. Insets: field dependence of the magnetization at different temperatures. Top: magnetic exchange pathways in compounds **16** and **17**, where red balls represent oxygen atoms and blue ones chlorides or azide N atoms.

At room temperature, the $\chi_M T$ value of 18.36 $cm^3 \cdot mol^{-1} \cdot K$ for **18** is higher than the spin only value due to unquenched orbital angular momentum. When lowering the temperature, the $\chi_M T$ product gradually decreases reaching a minimum value of 8.83 $cm^3 \cdot mol^{-1} \cdot K$ at 10 K. Then a sharp increase is observed reaching a maximum value of 13.24 $cm^3 \cdot mol^{-1} \cdot K$ at 4 K before the final decrease to 9.08 $cm^3 \cdot mol^{-1} \cdot K$ at 2 K. The gradual decrease below room temperature indicates the presence of magnetic anisotropy within the system, as well as the non-overlapping magnetization curves at different temperatures (Figure 3.6). The sharp increase evidences the intramolecular ferromagnetic interactions between cobalt centers, whereas the final decrease can be explained by the zero-field splitting and/or intermolecular antiferromagnetic interactions.

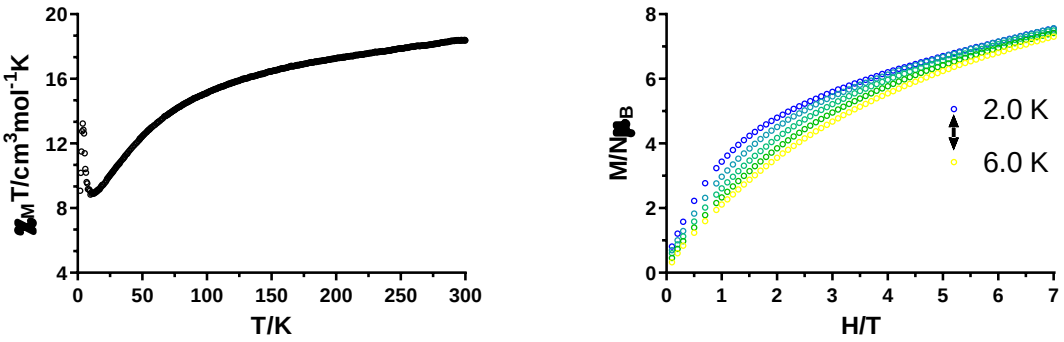

Figure 3.6.- Temperature dependence of the $\chi_M T$ product for **18** in the 2-300 K range (left) and field dependence of the magnetization at different temperatures (right).

For compounds **19-25**, the temperature-dependent susceptibility data is shown in Figure 3.7. At room temperature, the $\chi_M T$ values of 6.24, 14.24, 18.07, 20.33, 17.71 and 9.74 cm^3·mol^{-1}·K are all greater than the expected ones for two Co^{II} and one Ln^{III} non-interacting ions mainly due to the unquenched orbital angular momentum of the Co^{II} ions. In contrast, the value of 13.43 cm^3·mol^{-1}·K for **25** is slightly lower than the expected value of 14.17 cm^3·mol^{-1}·K for an isolated Dy^{III} ion ($^6H_{15/2}$, S = 5/2, L = 5, and g = 4/3), but falls within the expected range [20]. When lowering the temperature, different behaviors are detected for several of those complexes. For **19**, the $\chi_M T$ product slightly decreases upon cooling down, though a change in slope could be observed below 50 K reaching a minimum value of 3.80 cm^3·mol^{-1}·K at 2 K. This behaviour is mainly associated to spin-orbit coupling effects of the Co^{II} center, because trinuclear Co^{II}Y^{III}Co^{II} systems are theoretically well isolated from each other as discussed in the crystal structure description section. For **20-24**, additional effects can be observed originating either from lanthanide single-ions or due to exchange interactions between Co^{II} and Ln^{III} ions (we assume that intramolecular Co···Co distances are too large to detect any contribution of it). In the case of **20**, the 4f ion Gd^{III} with 4f^7 configuration is expected to be isotropic in nature, thus the gradual increase in the $\chi_M T$ product reaching a maximum value of 19.04 cm^3·mol^{-1}·K at 2.5 K is associated to overall intramolecular ferromagnetic interactions. Compounds **21-23** contain anisotropic Tb^{III}, Dy^{III} and Er^{III} ions, respectively. In such cases, the thermal dependence is more pronounced (not so evident in **21**) gradually decreasing from room temperature to around 50 K, 28 K and 9 K for **21**, **22** and **23** before reaching maximum values of 21.62, 18.74 and 13.64 cm^3·mol^{-1}·K at low temperatures. In these cases, the shape of the $\chi_M T$ vs T curves is dominated by the single ion effects of the Ln^{III} ions, the

gradual decrease arises from thermal depopulation of the M_J states belonging to the ground multiplet. The maxima at lowest temperatures, in contrast, appears due to the intramolecular ferromagnetic interactions that were already detected for the **20** counterpart. The fact of displaying maxima at similar temperatures is indicative of exchange coupling constants of similar magnitude. For **21** and **22**, a small decrease below the maxima is also observed, which can be indicative of weak intermolecular antiferromagnetic interactions. Compound **24**, in contrast, shows a gradual decrease over the whole temperature range reaching a minimum value of 5.28 $cm^3 \cdot mol^{-1} \cdot K$ at 2 K attributed to the depopulation of the Stark sublevels without any sign of intramolecular ferromagnetic interactions. Lastly, **25** displays a usual thermal dependence of the $\chi_M T$ product showing a gradual decrease over the whole temperature regime with a minimum value of 11.61 $cm^3 \cdot mol^{-1} \cdot K$ at 2 K.

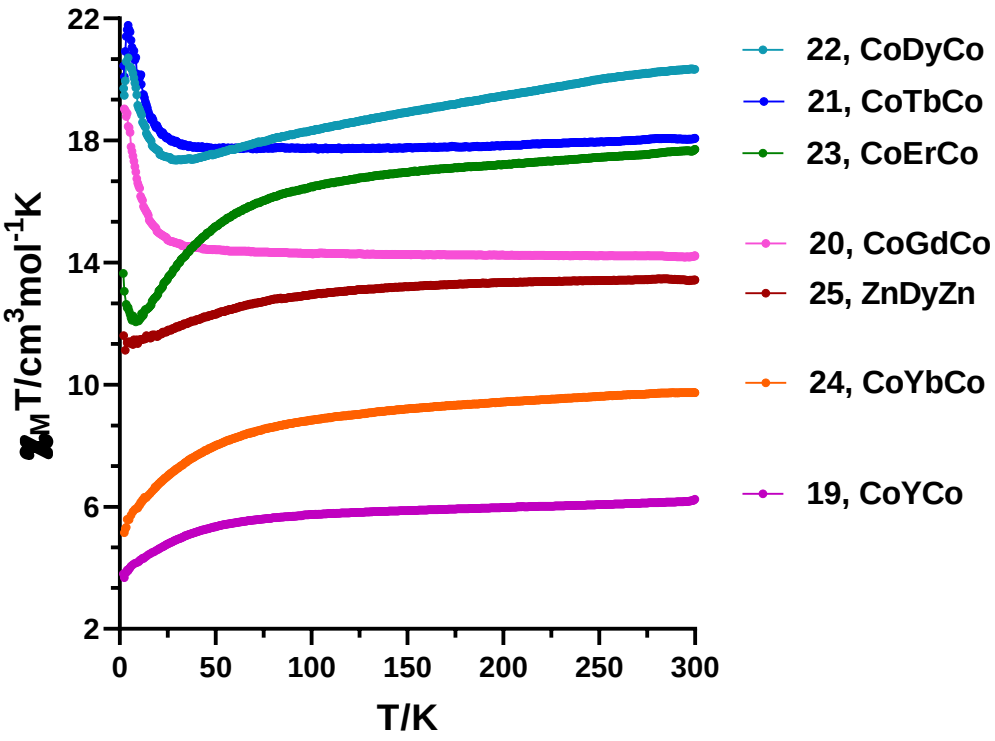

Figure 3.7.- Temperature dependence of the $\chi_M T$ product for **19-25** in the 2-300 K range.

The isothermal magnetization curves measured at 2 K and up to 7 T for compounds **19-25** do not display saturation even at the maximum applied magnetic field (Figure 3.8). The magnetization values at 7 T of values of 4.75, 11.59, 9.59, 8.52, 9.45, 7.32 and 5.23 $N_{\mu B}$, respectively, are far from the expected saturation values for the

combinations of two Co^{II} ions and a Ln^{III} for **19-24** and a single Dy^{III} for **25** without magnetic anisotropy of 6, 13, 15, 16, 15, 10 and 10 $N_{\mu B}$, respectively, with *g* = 2 and *S* = 3/2 for the Co^{II} ions and the corresponding *g* and *J* values for the lanthanides ions. This behavior is a clear indication of the presence of magnetic anisotropy in the Co^{II} ions as well as for the Ln^{III} ions. Thus, the magnetization value for compound **19** is very close to the value expected for two anisotropic Co^{II} ions of ~4.3 $N_{\mu B}$., whereas for compound **20** the magnetization value agrees well with that calculated for the contribution of the isotropic Gd^{III} ion (*S* = 7/2, *g* =2) and two anisotropic Co^{II} ions of 11.30 $N_{\mu B}$. In the rest of cases, the values corresponding to the sum of the contributions of two anisotropic Co^{II} ions and the value expected for magnetization of the multiplet ground state of the lanthanide ions (characterized by the corresponding *J* and *g* values) are rather larger than the experimental one, thus showing the anisotropy of the Ln^{III} ions arising form to the crystal field splitting of the multiplet ground state.

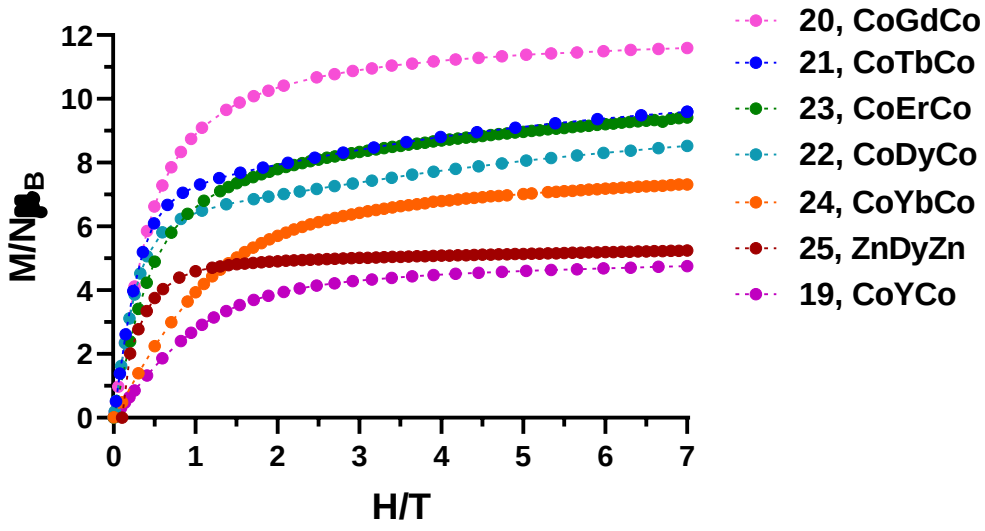

Figure 3.8.- Field dependence of the magnetization at 2 K for **19-25**. Dashed solid lines are a guide to the eye.

3.3.3. Dynamic magnetic properties of complexes 16-25

Regarding the dynamic magnetic properties, alternating current (*ac*) measurements were carried out for almost all the complexes under zero *dc* field (compounds **23** and **24** were discarded since **23** displayed only slightly frequency dependent out-of-phase signals with an external *dc* field, Figure A3.29, and **24** did not display any signal, Figure

A3.30). Only complexes **18** and **22** showed clear frequency dependent maxima in the χ_M'' signals below 5 K (Figures 3.9 and 3.12). Compound **21** exhibited a single maximum at 10,000 Hz at the lowest temperatures (Figure 3.12). Complexes **20** and **25** showed slightly frequency dependent signals, whereas **16**, **17** and **19** did not even display out-of-phase signal (Figures A3.21-A3.23). Nevertheless, as it is observed in the vast majority of the SMMs, the fast QTM is responsible for hiding the slow relaxation of the magnetization. It is worth mentioning that this effect is forbidden for Kramers doublets, but could act because of dipolar effects and coupling with the nuclear spin of the cobalt ion [21]. In order to suppress it, all the alternating current measurements were repeated with an arbitrary external *dc* field of 1000 Oe. This external magnetic field was selected as an intermidiate one in order to totally or at least partially quench the undesired QTM, but without enhancing the field dependent direct mechanism, which is quite common in Co^{II} based magnets [22,23]. In this case, while compounds **17**, **20** and **23** exhibited slightly frequency dependant signals (Figure A3.29); **18**, **19**, **21** and **22** showed clear frequency and temperature dependant maxima in the out-of-phase curves below 5 K (Figures 3.9, 3.11, 3.12), and complex **25** displayed the most remarkable difference showing maxima below 12 K (Figure 3.13). Therefore, it was proved that QTM operates at zero *dc* field but it was partially or effectively suppressed for most of the compounds by applying an external magnetic field.

In contrast to compound **16**, the combinative effect of ferromagnetic interactions promoted by the azido bridges, as well as the external magnetic field, were responsible for the appearance of slow magnetic relaxation in **17**. Nonetheless, QTM was shown to act due to its only partial suppression, which prevented the occurrence of maxima and, hence, the effective energy barrier (U_{eff}) and relaxation times (τ) could not be obtained by fitting the $\chi_M''(\upsilon)$ plots. However, assuming that there is only one relaxation process, the Debye model can be used with the equation:

$$ln(\chi_M''/\chi_M') = ln(2\pi\upsilon\tau_0) + E_a/k_BT \qquad \textit{Equation 3.1}$$

This approximation provided U_{eff} and τ_0 values of ≈ 7.8 K and ≈ $6.43 \cdot 10^{-8}$ s, respectively (Figure A3.42).

As mentioned in the crystal structure description, compound **18a**/**18b** contains four distorted octahedral centers and a trigonal bipyramid. For the former ones, a positive or easy plane anisotropy is usually expected ($D > 0$) [24–26], whereas for the latter type of geometry both easy plane and negative or easy axis anisotropy ($D < 0$) have been

previously reported [27]. In an overall $D > 0$ situation, in order to detect slow relaxation of the magnetization, one would expect that a static external magnetic field would be needed, since Kramers ions containing positive anisotropy require it. As far as we know, a $Ni^{I/II}$ based tetranuclear cluster is the only compound with $D > 0$ known to exhibit slow relaxation of the magnetization at zero applied *dc* field [28]. However, compound **18** exhibits broad maxima under zero *dc* field in the temperature range of 2.3–4 K in the $\chi_M''(T)$ plots (Figure 3.9, left). The broadness of the peaks could be explained by the sum of two sets of maxima, which is more noticeable at low frequencies (60-500 Hz). This slow relaxation of the magnetization in the absence of an exteral field could be explained by (a) a negative *D* value most likely provided by the trigonal bipyramid Co1 or the distorted Co2 and Co3 which can be also described as distorted trigonal prism geometry, by (b) the interactions between cobalt centers that are strong enough to suppress the quantum tunnelling of the magnetization at zero *dc* field or (c) the sum of both effects. In fact, there is another example of an heptanuclear cobalt based compound with two trigonal bipyramid and five octahedral centers that shows strong frequency-dependent χ_M'' signals below 4 K under zero *dc* field [29].

The presence of two almost overlapping sets of maxima can be due to the presence of two thermally assisted relaxation processes with similar effective energy barriers. In fact, α values accomplished from the Cole-Cole plots in the 2.3–3.8 K range (Figure A3.31) indicate a wide distribution of relaxation processes (0.30–0.50). However, it was not possible to distinguish independent semicircles corresponding to two different processes. The temperature dependence of the out-of-phase signals at each frequency were fitted to the generalized Debye model obtaining relaxation times at each temperature (Figure A3.37). The linear data was fitted to the Arrhenius equation affording an effective energy barrier (U_{eff}) and τ_0 values of 23.8 K and $6.52 \cdot 10^{-8}$ s.

The application of an arbitrary external magnetic field of 1000 Oe produces unexpected results. On the one hand, as seen in Figure 3.9 (right), the χ_M'' signal displays a remarkable tail below the maxima which is usually associated to the presence of QTM when the measurements are carried out in the absence of an external magnetic field. In this case, however, this is most likely associated to a direct process activated by the external field (see below). On the other hand, the two set of maxima are now better defined, where the first one appears below 4 K, while the second one arises below 5 K. However, the nature of them allows us to fit the $\chi_M''(\upsilon)$ curves only in the 3.2-4.4 K temperature range, covering the regime of the first set

(Figure A3.38). As seen in Figure A3.38, at higher temperatures the position of the maxima remains somehow unshifted and the relaxation times that were obtained are not consistent with SMM behaviour. We are not sure about the origin of this second set of maxima, but the noisy and not properly defined aspect of them complicates the interpretation of the data. We therefore studied the data in the 3.2-4.4 K temperature range and the linear fit of the relaxation times afforded U_{eff} and τ_0 values of 17.3 K and $2.92 \cdot 10^{-7}$ s. Cole-Cole plots afforded again large α values of 0.38 and 0.37 at 3.2 and 4.4 K, respectively in agreement with the appearance of a direct process at low temperatures and a second set of maxima at higher ones. We are currently planning to perform additional magnetic susceptibility measurements under different magnetic fields in order to discard a possible long range magnetic ordering.

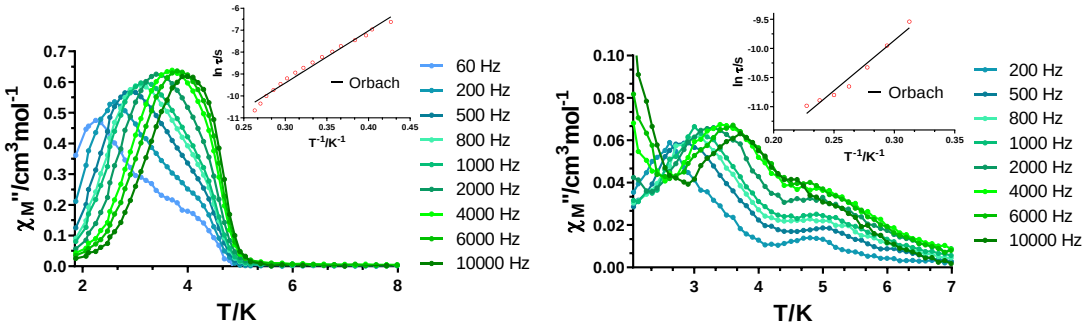

Figure 3.9.- Temperature dependence of the out-of-phase χ_M'' susceptibility signals under zero applied *dc* field (left) and under an applied field of 1000 Oe for **18**. Inset: Arrhenius plot for the relaxation times.

In view of the results obtained in the absence/presence of a magnetic field, we studied the field-dependence of the relaxation times at a fixed temperature of 3.2 K. As it is shown in Figure 3.10, the slowest relaxation times are obtained in the absence of any field. In addition, as the intensity of the external magnetic field is increased, the relaxation times become faster in agreement with the presence of a field induced direct process (note that for a direct process $\tau^{-1} = AH^4T$). With the aim of gathering more information about the origin of slow magnetic relaxation in the absence of an external magnetic field in **18**, a good approach would be to synthesize diluted samples in order to avoid intramolecular Co···Co interactions. This would clarify whether the SMM behaviour arises due to strong magnetic interactions or from negative *D* values of any

of the Co^{II} ions. Unfortunately, we were not able to crystallize the diamagnetic counterpart with Zn^{II}.

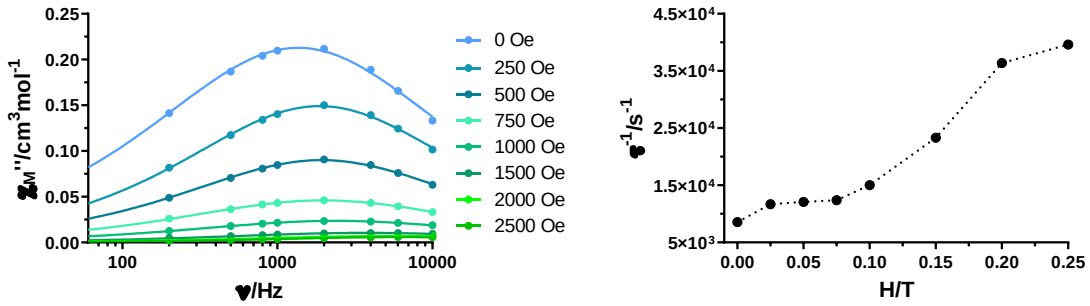

Figure 3.10.- Field dependence of the out-of-phase signal vs frequency at 3.2 K (left) and the inverse of the relaxation times obtained at different magnetic fields at for **18** (right).

Regarding heterotrinuclear compounds, we would like to emphasize first the rational design of the ligand. Colacio and co-workers previously reported on a $Co^{II}Y^{III}$ based compound with a similar ligand, but with a extended triamine side chain [25]. In that case, the ligand places the cobalt center in the inner site providing an octahedral coordination environment that is completed by a a Co-Y bridging acetate group. As above-mentioned, this normally generates positive *D* values as confirmed in the cited paper. In our case, our main purpose was to replace the triamine derived ligand by the diamine derived H_2L^3 in order to promote five coordinate cobalt centers. We were encouraged to make this study in light of the results previously obtained by members of our group regarding $Zn^{II}Dy^{III}Zn^{II}$ systems in which the transition metal ions display a distorted square pyramid geometry [30]. For five coordinate Co^{II} compounds, Cui and co-workers recently gathered most of the results concerning this type of compounds with trigonal bipyramid or square pyramid geometry [31]. As they showed, both positive or negative *D* values could be expected for these geometries, but even zero field SMMs can be obtained for trigonal bipyramid geometries [32]. In our case, the Co^{II} centers in **19** are best described by square pyramid geometry, but the Addison τ^5 parameter [33] with a value of 0.46 indicates a mixing of both possible geometries (τ^5 is zero for an ideal square pyramid, while a value of 1 accounts for an ideal trigonal bipyramidal configuration). Therefore, **19** was expected to be a potential SMM candidate.

However, the trinuclear compound **19** did not display χ_M'' signals under zero *dc* field, probably because of fast QTM (Figure A3.22). When applying an external magnetic field of 1000 Oe clear frequency dependent maxima appeared below 4 K indicating SMM behaviour (Figure 3.11). Even though the α values obtained from the Cole-Cole diagrams in the temperature range of 2.0–4.0 K indicate a quite narrow distribution of relaxation processes (0.24 and 0.08 at 2.0 and 4.0 K, respectively), the higher values at low temperatures, as well as the tails below the maxima in χ_M' (Figure A3.25), might be indicative of the still operative QTM or a field induced direct process. Hence, considering that we do not have further information about the sign and magnitude of the *D* value (we were not able to obtain reasonable fitting parameters from the *dc* data for compounds **19** and **20**, which should be the easiest models for fitting the data), relaxation times obtained from $\chi_M''(\upsilon)$ plots were fitted to the following equations:

$$\tau^{-1} = \tau_{QTM}^{-1} + \tau_0^{-1} \exp(-U_{eff}/k_BT) \qquad \text{Equation 3.2}$$

$$\tau^{-1} = AT + BT^n \qquad \text{Equation 3.3}$$

Equation 3.2 considers the simultaneous presence of QTM and Orbach relaxation modes (Figure 3.11, inset, grey line). The fit led to τ_{QTM}, effective energy barrier for the reversal of magnetization and τ_0 values of $1.42 \cdot 10^{-4}$ s, 12.7 K and $8.51 \cdot 10^{-7}$ s, respectively. Equation 3.3, in contrast, considers the simultaneous presence of direct and Raman mechanisms (inset, dark blue line) and the fitting afforded *A*, *B* and *n* values of 2319 $s^{-1}K^{-1}$, 322.3 $s^{-1}K^{-3.61}$ and 3.61. The parameters obtained for both fitting equations seem reasonable. We believe that *ab initio* calculations that are currently being performed will shed some light about the real origin of the slow magnetic relaxation in this compound.

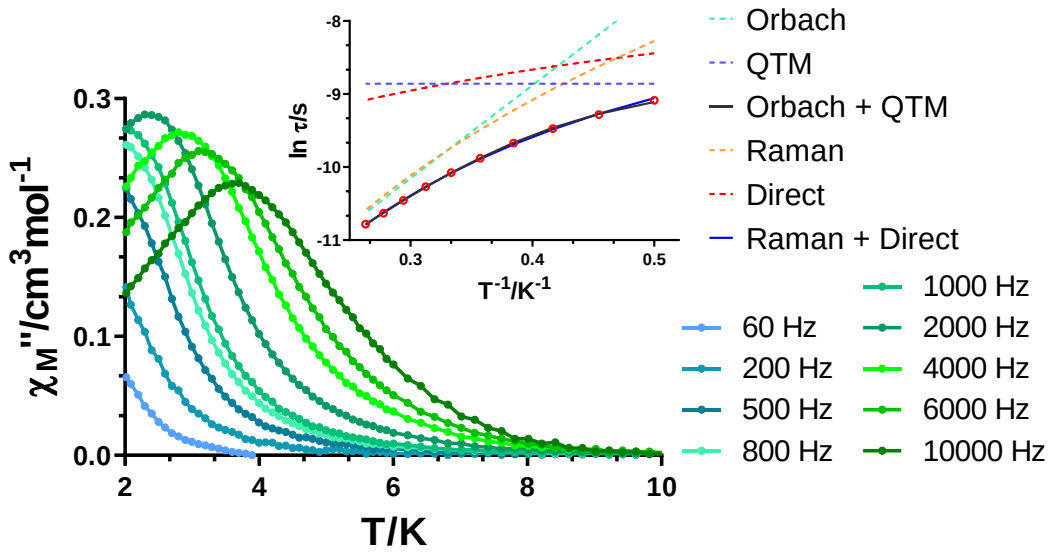

Figure 3.11.- Temperature dependence of the out-of-phase χ_M'' susceptibility signals for complex **19** under an applied field of 1000 Oe. Inset: Arrhenius plot for the relaxation times. The grey line corresponds to the best fit considering Orbach + QTM, whereas the dark blue considers Raman + Direct mechanisms. Dashed coloured lines account for the individual contribution of each process.

In regard to Co_2Ln based compounds (being Ln a paramagnetic ion), it is necessary to remark that even though several similar systems have been studied during the last years [34,35], it is still unclear which is the best strategy to enhance the SMM behaviour. In the research work by Ungur *et al*. [34], it was proven that the combination of anisotropic Co^{II} ions with the isotropic high spin Gd^{III} ion was the best method to synthesize zero field SMMs. However, other researches have shown that it is not possible to generalize this strategy to every $Co^{II}Ln^{III}$ system. As it occurs in several other systems, the $Co^{II}Dy^{III}$ (or even $Co^{II}Tb^{III}$) analogues turned out to be the ones with most interesting magnetic properties, showing that the anisotropic Dy^{III} can be successfully combined with 3d anisotropic ions [36–38].

Additionally, it is well known the importance that the coordination environment has around the 4f ion in terms of stabilizing the high magnitude $\pm M_J$ magnetic substates as ground state, which is fundamental when designing high performance SMMs. In our case, the square antiprism/triangular dodecahedron geometry around the lanthanide ion was expected to stabilize high magnitude $\pm M_J$ substates in oblate type of ions. This

is something we expected based on the results we previously mentioned for $Zn^{II}Dy^{III}Zn^{II}$ systems published by members of our group [30]. As it occurs in that case, in our trinuclear compounds the large negatively charged phenoxido groups are located in opposite sites displaying the shortest Dy-O bond distances, whereas the rest of the oxygen donors belong to neutral atoms. Thus, the ligand field is potentially suitable to stabilize the highest $\pm M_J$ states as ground state in oblate like ions. In order to prove the predicted hypothesis, two pairs of oblate like (**21**, Tb^{III} and **22**, Dy^{III}) and prolate like (**23**, Er^{III} and **24**, Yb^{III}) heterotrinuclear compounds were studied, as well as the $Co^{II}Gd^{III}Co^{II}$ (**20**) counterpart containing the isotropic Gd^{III} ion.

At zero applied *dc* field only compounds **21** and **22** displayed frequency and temperature dependant out-of-phase maxima below 5 K, behaving as zero field SMMs (Figure 3.12). For compound **21**, the α values obtained in the 2.0–2.7 K range indicate a relatively wide distribution of relaxation processes (0.22 (2.0 K) – 0.20 (2.7 k)). Nevertheless, the relaxation times obtained from the $\chi_M''(\upsilon)$ plots were fitted to the Arrhenius equation considering only an Orbach process due to the linearity shown in the whole temperature range (Figure 3.12, inset). The best fit was achieved with U_{eff} = 7.7 K and $\tau_0 = 8.27 \cdot 10^{-7}$ s parameters. For compound **22**, two maxima can be observed above 2000 Hz in the $\chi_M''(T)$ plots, but overall they overlap in the whole temperature range (Figure 3.12, top right). This effect suggests that two thermally activated processes compete in the magnetization relaxation with similar energy barriers. Therefore, in order to achieve independent parameters for the Fast and Slow relaxations (FR and SR), the $\chi_M''(\chi_M')$ data was fitted by using a sum of two modified Debye functions with the CCFIT software and two sets of relaxation times were extracted, one for each process [39]. Arrhenius plots were constructed for both processes affording similar effective energy barriers and τ_0 values of 13.0 K with $3.19 \cdot 10^{-7}$ s and 16.7 K with $1.08 \cdot 10^{-6}$ s for FR and SR, respectively. In any case, for this specific compound, even though two different maxima are more or less well resolved in the $\chi_M''(T)$ plots, if $\chi_M''(\upsilon)$ and Cole-Cole plots are considered solely, one would say that a single thermally activated process operated in this compound (see Figures A3.32 and A3.37). Thus, we also fit the data to the generalized Debye model in the 2.0-6.0 K temperature range to obtain α values and relaxation times considering a single process. On the one hand, the high α value of 0.35 at 2.0 K can be explained by the fact that the mentioned two processes almost overlap, while the much lower value of 0.06 at 6.0 K is in agreement with a single process, since FR does not operate at that high temperatures and only SR contributes. On the other hand, the Arrhenius plot constructed with the relaxation times displays two well resolved regimes (Figure

A3.41), one in the 2.0-3.2 K range and the other in the 3.6-6.0 K range compatible with what is seen in the $\chi_M''(T)$ plots. Fitting the data to Orbach mechanisms afforded U_{eff} and τ_0 values of 8.0 K with $1.08 \cdot 10^{-5}$ s and 15.5 K with $1.17 \cdot 10^{-6}$ s for FR and SR, respectively.

The presence of two maxima can be explained by the presence of two different anisotropic metal centers centers [40], but considering the above discussed *dc* magnetic properties, as well as the completely different behavior detected for **25** (see below), we believe that it is not the case. In some cases, a unique anisotropic Dy^{III} center can also display multiple relaxation processes [41]. When applying an external magnetic *dc* field of 1000 Oe to both **21** and **22**, the maxima clearly shifted to higher temperatures (Figure 3.12, bottom), indicating that the presence of QTM is at least partially quenched. In both cases, the values of the barrier experiment a slight improvement. Arrhenius fits gave rise to effective energy barriers and τ_0 values of 11.3 K with $3.50 \cdot 10^{-7}$ s, 13.6 K with $4.76 \cdot 10^{-7}$ s and 20.0 K with $6.72 \cdot 10^{-7}$ s for **21**, **22** FR and **22** SR, respectively. We tried to perform the same approach for **22** as done for the measurement in the absence of an external magnetic field, but the Arrhenius fit showed a single linear regime in the whole temperature range (Figures A3.43).

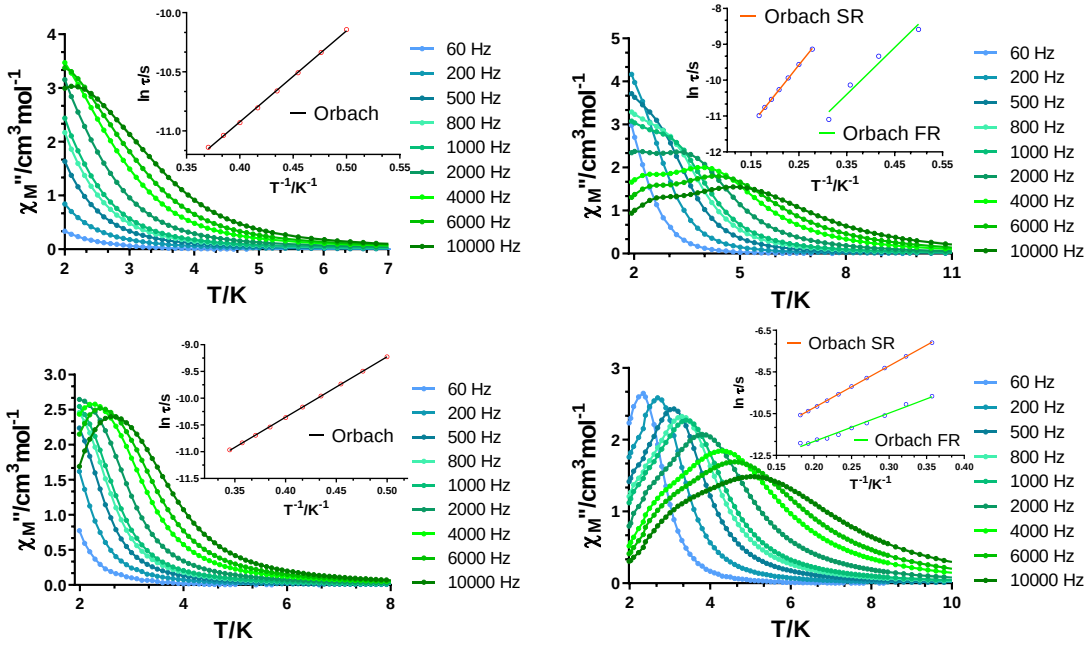

Figure 3.12.- Temperature dependence of the out-of-phase χ_M'' susceptibility signals for complexes **21** and **22** under zero applied *dc* field (top; left and right, respectively) and under an applied field of 1000 Oe (down; left and right, respectively). Insets: Arrhenius plots for the relaxation times.

Among the other heterotrinuclear $Co^{II}Ln^{III}Co^{II}$ compounds containing isotropic (Gd^{III}, **20**) and prolate type Ln^{III} ions (Er^{III}, **23** and Yb^{III}, **24**), only compound **20** displayed frequency and temperature dependant χ_M'' signals under zero applied external field, though no maxima were observed above the temperature limit of the instrument (Figure A3.22). To eliminate the possible effect of QTM, three of them were measured under an external *dc* field of 1000 Oe. The behaviour of **20** resulted to be similar, with slightly frequency and temperature dependant χ_M'' signals (Figure A3.29), as it occurred for compound **23** (Figure A3.29), but there was no out-of-phase signal for compound **24** (Figure A3.30). On the one hand, the results for **20** showed that in our case the combination of anisotropic 3d metal ions along with high spin isotropic 4f ions was not the most efficient model to synthesize SMMs. On the other hand, it seems that the square antiprism geometry around the lanthanide ion is suitable for stabilizing high M_J values for oblate like ions such as Tb^{III} and Dy^{III}, but not for prolate ions. As for compound **17**, the under zero and 1000 Oe applied external *dc* field data of compound **20** was fitted to the Debye model using the equation $ln(\chi_M''/\chi_M') = ln(2\pi\upsilon\tau_0) + E_a/k_BT$. The fit afforded effective energy barrier and τ_0 values under zero and 1 kOe field of 5.2 K with $6.34\cdot10^{-8}$ s and 5.8 K with $8.52\cdot10^{-8}$ s, respectively (Figures A3.40 and A3.42).

Finally, the dynamic magnetic properties of compound **25** were studied to analyse whether eliminating the intramolecular interactions between paramagnetic centers would enhance or worsen the SMM properties. When performing alternating current measurements at zero *dc* field, frequency and temperature dependant out-of-phase signals were visible in the $\chi_M''(T)$ plots but without any maximum (Figure A3.23). As in the previous cases, the sample was measured again with a 1000 Oe external field to remove the QTM. Clearly temperature and frequency dependant well defined maxima were obtained below 12.0 K for all frequency curves (Figure 3.13). Besides, the χ_M'' signals tend to zero below the maxima, confirming that QTM was successfully quenched. The Cole-Cole plots in the 5.5–11.9 K temperature range suggest a relatively narrow distribution of relaxation processes (0.10 (5.5 K) and 0.11 (11.9 K)). However, when fitting the relaxation times, it looks like two regimes are visible: a lineal portion in the high temperature range and a remarkable curvature is observed for the intermediate and low temperature regions, suggesting the presence of multiple relaxation processes. Therefore, the relaxation times were fitted to the following equation:

$$\tau^{-1} = BT^n + \tau_0^{-1}exp(-U_{eff}/k_BT) \qquad \textit{Equation 3.4}$$

This equation considers the simultaneous presence of Raman and Orbach relaxation modes, respectively. The best fit afforded the following values: B = 0.1 $s^{-1}K^{-5.23}$; n = 5.23; τ_0 = $5.14 \cdot 10^{-9}$ s and U_{eff} = 115.6 K. Regarding to the n parameter of the Raman process, a value of 9 is expected for Kramers ions [42], but depending on the structure of the levels values between 1 and 6 can be considered as reasonable [43]. As displayed in the inset of Figure 3.13, the value of U_{eff} could be an overestimation, since the Orbach contribution does not cover exactly the relaxation times at the highest temperatures and, instead, the Raman process almost perfectly describes the entire regime. Another fit was attempted considering only the Raman mechanism, but it does not fit so well the points at lowest temperatures. Thus, we are currently waiting for theoretical calculations to confirm that the energy barrier of 115.6 K corresponds to the energy difference between the ground and (most likely) the first excited state, or relaxation occurs through a virtual state.

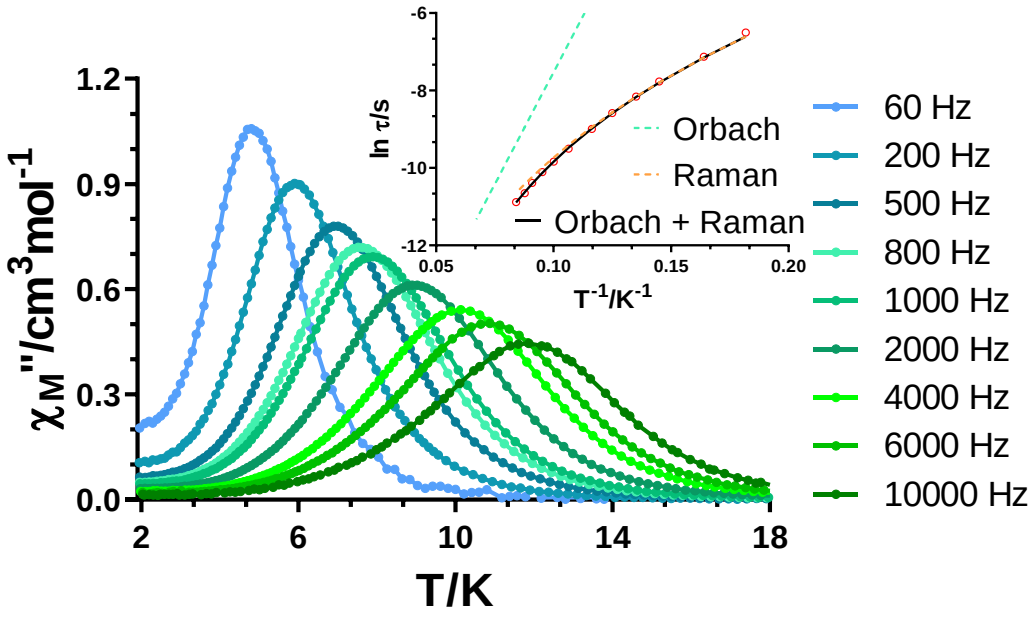

Figure 3.13.- Temperature dependence of the out-of-phase χ_M'' susceptibility signals for complex **25** under an applied field of 1000 Oe. Inset: Arrhenius plot for the relaxation times. Black line accounts for the best fit considering the simultaneous presence of Orbach + Raman relaxation.

This exhaustive study shows that, firstly, our ligand design stabilizes the high $\pm M_J$ magnetic substates for oblate type of ions, being suitable for Tb^{III} and Dy^{III} ions.

Secondly, that intramolecular magnetic interactions are responsible for quenching the fast tunnelling of the magnetization, thus showing SMM behaviour even at zero applied *dc* field for **21** and **22**. When these interactions are removed by replacing the paramagnetic Co^{II} ions with the diamagnetic Zn^{II}, a marked QTM operates hiding the SMM behaviour in compound **25**. This has been previously seen for other exchange coupled 3d-4f systems [9]. Many times, the buried 4f electrons in lanthanide ions interact very weakly with other metal ions and the SMM behaviour is usually associated to single ion in origin. Furthermore, when these interactions are weak they may create transverse magnetic fields and QTM can be even more pronounced. However, this is not always the case and many other systems have been previously reported in which the SMM behaviour arises from the exchange coupled system. Thirdly, in comparison to the mentioned $Zn^{II}Dy^{III}Zn^{II}$ systems reported by our group, the coordination environment around the Dy^{III} ion appears to be more distorted, a fact that explains the lack of slow magnetic relaxation in the absence of an external magnetic field. Anyway, we believe that the high U_{eff} of 115.6 K calculated for **25** is far greater in comparison to what observed for **22** and, thus, this corroborates the hypothesis of having an exchange coupled system for $Co^{II}Dy^{III}Co^{II}$ **22**.

3.4. CONCLUSIONS

In summary, two novel homonuclear Co^{II} based compounds, a previously reported tetranuclear compound and seven 3d-4f-3d mixed heterotrinuclear compounds have been synthesized based on *N,N′*-dimethyl-*N,N′*-bis(2-hydroxy-3-methoxy-5-methylbenzyl)-ethylendiamine (H_2L^3). On replacing the bridging chloride ions in **16** by end-on mode coordinating azide groups in **17**, intramolecular ferromagnetic interactions are induced, which are responsible of provoking slow relaxation of the magnetization under an external magnetic field with approximate U_{eff} and τ_0 values of 7.8 K and $6.43 \cdot 10^{-8}$ s. The case of compound **18** is not still clear. The fact of having a Co^{II} based zero field SMM is interesting, but due to the complexity of the structure, distorted geometries of all the metallic centers and the high nuclearity we are not able to firmly affirm where the slow relaxation of the magnetization arises from.

The first studied trinuclear compound **19** only contains one type of paramagnetic ion, Co^{II}. We targeted this compound due to the fact that pentacoordinated Co^{II} ions can display $D < 0$ being potential candidates for the design of zero field SMMs. However, it only displayed slow magnetic relaxation under an external magnetic field.

Regarding 3d-4f-3d compounds with paramagnetic 4f ions, only compounds **20-22** displayed zero field SMM behaviour. For compound **20** frequency dependent signals were obtained, but maxima were below the temperature limit of the instrument and only an approximation of the energy barrier could be obtained. By applying an external magnetic field no difference was found suggesting a very low value of the U_{eff}. Compounds **21** and **22** displayed maxima at 2 K and below 5 K, respectively, at zero field. The application of an external field of 1000 Oe showed a positive effect shifting the maxima at higher temperatures indicative of a partial/total quenching of QTM and increasing the U_{eff} values from 7.7 K to 11.3 K for **21** and from 13.0 K (FR) or 16.7 K (SR) to 13.6 K (FR) or 20.0 K (SR) for **22**. Compounds **23** and **24** did not displayed zero field SMM behaviour and only slightly frequency dependent signals were observed for **23** under an external magnetic field. This comparison between oblate and prolate type of ions let us conclude that our ligand design is more suitable for the former ones. Finally, compound **25** showed the highest effective energy barrier of 115.6 K in the presence of an external magnetic field. From this results we conclude that (i) intramolecular Co-Ln interactions are strong enough to suppress zero field QTM and (ii) slow magnetic relaxation in **22** arises from an exchange coupled system and not from single ion, since the difference in height of the barriers is too large.

3.5.- REFERENCES

[1] E.C. Yang, W. Wernsdorfer, L.N. Zakharov, Y. Karaki, A. Yamaguchi, R.M. Isidro, G. Di Lu, S.A. Wilson, A.L. Rheingold, H. Ishimoto, D.N. Hendrickson, Fast magnetization tunneling in tetranickel(II) single-molecule magnets, Inorg. Chem. 45 (2006) 529–546. https://doi.org/10.1021/ic050093r.

[2] A. Ferguson, J. Lawrence, A. Parkin, J. Sanchez-Benitez, K. V. Kamenev, E.K. Brechin, W. Wernsdorfer, S. Hill, M. Murrie, Synthesis and characterisation of a Ni4 single-molecule magnet with S4 symmetry, J. Chem. Soc. Dalt. Trans. (2008) 6409–6414. https://doi.org/10.1039/b807447j.

[3] I. Oyarzabal, J. Ruiz, A.J. Mota, A. Rodríguez-Diéguez, J.M. Seco, E. Colacio, An experimental and theoretical magneto-structural study of polynuclear NiII complexes assembled from a versatile bis(salicylaldehyde)diamine polytopic ligand, Dalton Trans. 44 (2015) 6825–6838. https://doi.org/10.1039/c5dt00356c.

[4] T.C. Stamatatos, K.A. Abboud, W. Wernsdorfer, G. Christou, {Mn 6} n single-chain magnet bearing azides and di-2-pyridylketone-derived ligands, Inorg. Chem. 48 (2009) 807–809. https://doi.org/10.1021/ic8020645.

[5] A. Escuer, G. Aromí, Azide as a Bridging Ligand and Magnetic Coupler in Transition Metal Clusters, Eur. J. Inorg. Chem. 2006 (2006) 4721–4736. https://doi.org/10.1002/ejic.200600552.

[6] S. Schmidt, D. Prodius, V. Mereacre, A.K. Powell, G.E. Kostakis, Unprecedented chemical transformation: Crystallographic evidence for 1,1,2,2-tetrahydroxyethane captured within an Fe6Dy3 single molecule magnet, Chem. Commun. 49 (2013) 1696–1698. https://doi.org/10.1039/c2cc38006d.

[7] J.D. Rinehart, M. Fang, W.J. Evans, J.R. Long, Strong exchange and magnetic blocking in N_2^{3-}-radical-bridged lanthanide complexes., Nat. Chem. 3 (2011) 538–42. https://doi.org/10.1038/nchem.1063.

[8] S.K. Langley, L. Ungur, N.F. Chilton, B. Moubaraki, L.F. Chibotaru, K.S. Murray, Single-molecule magnetism in a family of {CoIII2DyIII2} butterfly complexes: Effects of ligand replacement on the

dynamics of magnetic relaxation, Inorg. Chem. 53 (2014) 4303–4315. https://doi.org/10.1021/ic4029645.

[9] S.K. Langley, D.P. Wielechowski, V. Vieru, N.F. Chilton, B. Moubaraki, B.F. Abrahams, L.F. Chibotaru, K.S. Murray, A {CrIII2DyIII2} single-molecule magnet: Enhancing the blocking temperature through 3d magnetic exchange, Angew. Chem. Int. Ed. 52 (2013) 12014–12019. https://doi.org/10.1002/anie.201306329.

[10] A. Vráblová, M. Tomás, L.R. Falvello, Ľ. Dlháň, J. Titiš, J. Černák, R. Boča, Slow magnetic relaxation in Ni-Ln (Ln = Ce, Gd, Dy) dinuclear complexes, Dalton Trans. 48 (2019) 13943–13952. https://doi.org/10.1039/c9dt02122a.

[11] A. Zabala-Lekuona, J. Cepeda, I. Oyarzabal, A. Rodríguez-Diéguez, J.A. García, J.M. Seco, E. Colacio, Rational design of triple-bridged dinuclear ZnIILnIII-based complexes: a structural, magnetic and luminescence study, CrystEngComm. 19 (2017) 256–264. https://doi.org/10.1039/c6ce02240e.

[12] M. Andruh, The exceptionally rich coordination chemistry generated by Schiff-base ligands derived from o-vanillin, Dalton Trans. 44 (2015) 16633–16653. https://doi.org/10.1039/c5dt02661j.

[13] L. Botana, J. Ruiz, A.J. Mota, A. Rodríguez-Diéguez, J.M. Seco, I. Oyarzabal, E. Colacio, Anion controlled structural and magnetic diversity in unusual mixed-bridged polynuclear NiII complexes with a versatile bis(2-methoxy phenol)diamine hexadentate ligand. An experimental and theoretical magneto-structural study, Dalton Trans. 43 (2014) 13509–13524. https://doi.org/10.1039/c4dt01253d.

[14] A. Das, S. Goswami, A. Ghosh, Rare azido and hydroxido bridged tetranuclear Co(ii) complexes of a polynucleating Mannich base ligand with a defect dicubane core: structures, magnetism and phenoxazinone synthase like activity, New J. Chem. 42 (2018) 19377–19389. https://doi.org/10.1039/c8nj04750b.

[15] M. Llunell, D. Casanova, J. Cirera, J.M. Bofill, P. Alemany, S. Alvarez, M. Pinsky, D. Avnir, SHAPE, (2005).

[16] P. King, R. Clérac, W. Wernsdorfer, C.E. Anson, A.K. Powell, Synthesis and magnetism of oxygen-bridged tetranuclear defect dicubane Co(II) and Ni(II) clusters, Dalton Trans. (2004) 2670–2676. https://doi.org/10.1039/b405881j.

[17] J.M. Clemente-Juan, E. Coronado, Magnetic clusters from polyoxometalate complexes, Coord. Chem. Rev. 193–195 (1999) 361–394. https://doi.org/10.1016/S0010-8545(99)00170-8.

[18] H. Andres, J.M. Clemente-Juan, M. Aebersold, H.U. Güdel, E. Coronado, H. Büttner, G. Kearly, J. Melero, R. Burriel, Magnetic excitations in polyoxometalate clusters observed by inelastic neutron scattering: Evidence for anisotropic ferromagnetic exchange interactions in the tetrameric cobalt(II) cluster [Co4(H2O)2(PW9O34)2]10-. Comparison with the magnetic and specific heat properties, J. Am. Chem. Soc. 121 (1999) 10028–10034. https://doi.org/10.1021/ja990198r.

[19] N.F. Chilton, R.P. Anderson, L.D. Turner, A. Soncini, K.S. Murray, PHI: A powerful new program for the analysis of anisotropic monomeric and exchange-coupled polynuclear d- and f-block complexes, J. Comput. Chem. 34 (2013) 1164–1175. https://doi.org/10.1002/jcc.23234.

[20] L. Norel, L.E. Darago, B. Le Guennic, K. Chakarawet, M.I. Gonzalez, J.H. Olshansky, S. Rigaut, J.R. Long, A Terminal Fluoride Ligand Generates Axial Magnetic Anisotropy in Dysprosium Complexes, Angew. Chem. Int. Ed. 57 (2018) 1933–1938. https://doi.org/10.1002/anie.201712139.

[21] S. Vaidya, S. Tewary, S.K. Singh, S.K. Langley, K.S. Murray, Y. Lan, W. Wernsdorfer, G. Rajaraman, M. Shanmugam, What Controls the Sign and Magnitude of Magnetic Anisotropy in Tetrahedral Cobalt(II) Single-Ion Magnets?, Inorg. Chem. 55 (2016) 9564–9578. https://doi.org/10.1021/acs.inorgchem.6b01073.

[22] S. Roy, I. Oyarzabal, J. Vallejo, J. Cano, E. Colacio, A. Bauza, A. Frontera, A.M. Kirillov, M.G.B. Drew, S. Das, Two Polymorphic Forms of a Six-Coordinate Mononuclear Cobalt(II) Complex with Easy-Plane Anisotropy: Structural Features, Theoretical Calculations, and Field-Induced Slow Relaxation of the Magnetization, Inorg. Chem. 55 (2016) 8502–8513. https://doi.org/10.1021/acs.inorgchem.6b01087.

[23] O. Pajuelo-Corral, A. Zabala-Lekuona, E. San Sebastian, A. Rodríguez-Diéguez, J.A. García, L. Lezama, E. Colacio, J.M. Seco, J. Cepeda, Modulating Magnetic and Photoluminescence Properties in 2-Aminonicotinate-Based Bifunctional Coordination Polymers by Merging 3d Metal Ions, Chem. – A Eur. J. 26 (2020) 13484–13498. https://doi.org/10.1002/chem.202002755.

[24] R. Herchel, L. Váhovská, I. Potočňák, Z. Trávníček, Slow magnetic relaxation in octahedral cobalt(II) field-induced single-ion magnet with positive axial and large rhombic anisotropy, Inorg. Chem. 53 (2014) 5896–5898. https://doi.org/10.1021/ic500916u.

[25] E. Colacio, J. Ruiz, E. Ruiz, E. Cremades, J. Krzystek, S. Carretta, J. Cano, T. Guidi, W. Wernsdorfer, E.K. Brechin, Slow Magnetic Relaxation in a Co ^{II} -Y ^{III} Single-Ion Magnet with Positive Axial Zero-Field Splitting, Angew. Chem. Int. Ed. 52 (2013) 9130–9134. https://doi.org/10.1002/anie.201304386.

[26] Y.F. Deng, M.K. Singh, D. Gan, T. Xiao, Y. Wang, S. Liu, Z. Wang, Z. Ouyang, Y.Z. Zhang, K.R. Dunbar, Probing the Axial Distortion Effect on the Magnetic Anisotropy of Octahedral Co(II) Complexes, Inorg. Chem. 59 (2020) 7622–7630. https://doi.org/10.1021/acs.inorgchem.0c00531.

[27] A. Świtlicka, B. Machura, J. Cano, F. Lloret, M. Julve, A Study of the Lack of Slow Magnetic Relaxation in Mononuclear Trigonal Bipyramidal Cobalt(II) Complexes, ChemistrySelect. 6 (2021)

576–582. https://doi.org/10.1002/slct.202100061.
[28] K. Chakarawet, M. Atanasov, J. Marbey, P.C. Bunting, F. Neese, S. Hill, J.R. Long, Strong electronic and magnetic coupling in M4(M = Ni, Cu) clusters via direct orbital interactions between low-coordinate metal centers, J. Am. Chem. Soc. 142 (2020) 19161–19169. https://doi.org/10.1021/jacs.0c08460.
[29] E.C. Yang, Z.Y. Liu, L. Zhang, N. Yang, X.J. Zhao, Magnetism behaviours dominated by the interplay of magnetic anisotropy and exchange coupling in local Co II 7 discs, Dalton Trans. 45 (2016) 8134–8141. https://doi.org/10.1039/c6dt00010j.
[30] I. Oyarzabal, J. Ruiz, J.M. Seco, M. Evangelisti, A. Cam??n, E. Ruiz, D. Aravena, E. Colacio, Rational electrostatic design of easy-axis magnetic anisotropy in a ZnII-DyIII-ZnII single-molecule magnet with a high energy barrier, Chem. - A Eur. J. 20 (2014) 14262–14269. https://doi.org/10.1002/chem.201403670.
[31] H.H. Cui, M.M. Ding, X. Du Zhang, W. Lv, Y.Q. Zhang, X.T. Chen, Z. Wang, Z.W. Ouyang, Z.L. Xue, Magnetic anisotropy in square pyramidal cobalt(ii) complexes supported by a tetraazo macrocyclic ligand, Dalton Trans. 49 (2020) 14837–14846. https://doi.org/10.1039/d0dt01954b.
[32] A. Packová, J. Miklovič, R. Boča, Manifold relaxation processes in a mononuclear Co(II) single-molecule magnet, Polyhedron. 102 (2015) 88–93. https://doi.org/10.1016/j.poly.2015.08.002.
[33] A.W. Addison, T.N. Rao, J. Reedijk, J. Van Rijn, G.C. Verschoor, Synthesis, structure, and spectroscopic properties of copper(II) compounds containing nitrogen-sulphur donor ligands; the crystal and molecular structure of aqua[1,7-bis(N-methylbenzimidazol-2′;-yl)-2,6-dithiaheptane]copper(II) perchlorate, J. Chem. Soc. Dalt. Trans. (1984) 1349–1356. https://doi.org/10.1039/DT9840001349.
[34] L. Ungur, M. Thewissen, J.P. Costes, W. Wernsdorfer, L.F. Chibotaru, Interplay of strongly anisotropic metal ions in magnetic blocking of complexes, Inorg. Chem. 52 (2013) 6328–6337. https://doi.org/10.1021/ic302568x.
[35] Q.W. Xie, S.Q. Wu, W.B. Shi, C.M. Liu, A.L. Cui, H.Z. Kou, Heterodinuclear MII-LnIII single molecule magnets constructed from exchange-coupled single ion magnets, Dalton Trans. 43 (2014) 11309–11316. https://doi.org/10.1039/c4dt00740a.
[36] M. Towatari, K. Nishi, T. Fujinami, N. Matsumoto, Y. Sunatsuki, M. Kojima, N. Mochida, T. Ishida, N. Re, J. Mrozinski, Syntheses, structures, and magnetic properties of acetato- and diphenolato-bridged 3d-4f binuclear complexes [M(3-MeOsaltn)(MeOH) x(ac)Ln(hfac)2](M = ZnII, CuII,NiII,CoII;Ln = LaIII,GdIII, TbIII, DyIII; 3-MeOsaltn = N,N-Bis(3-methoxy-2-oxybenzylidene)-1,3-propanediaminato; Ac = Acetato; Hfac = Hexafluoroacetylacetonato; X = 0 or 1), Inorg. Chem. 52 (2013) 6160–6178. https://doi.org/10.1021/ic400594u.
[37] X.Q. Zhao, J. Wang, D.X. Bao, S. Xiang, Y.J. Liu, Y.C. Li, The ferromagnetic [Ln2Co6] heterometallic complexes, Dalton Trans. 46 (2017) 2196–2203. https://doi.org/10.1039/c6dt04375e.
[38] S. Chen, V. Mereacre, Z. Zhao, W. Zhang, Z. He, Synthesis, structures and magnetic properties of linear {Co II 2 Ln III 2 } coordination clusters, New J. Chem. 42 (2018) 1284–1289. https://doi.org/10.1039/c7nj04022a.
[39] D. Reta, N.F. Chilton, Uncertainty estimates for magnetic relaxation times and magnetic relaxation parameters, Phys. Chem. Chem. Phys. 21 (2019) 23567–23575. https://doi.org/10.1039/c9cp04301b.
[40] L. Zhang , J. Jung, P. Zhang, M. Guo, L. Zhao, J. Tang, B. Le Guennic, Site-Resolved Two-Step Relaxation Process in an Asymmetric Dy $_2$ Single-Molecule Magnet, Chem. - A Eur. J. 22 (2016) 1392–1398. https://doi.org/10.1002/chem.201503422.
[41] J. Ruiz, A.J. Mota, A. Rodríguez-Diéguez, S. Titos, J.M. Herrera, E. Ruiz, E. Cremades, J.P. Costes, E. Colacio, Field and dilution effects on the slow relaxation of a luminescent DyO9 low-symmetry single-ion magnet., Chem. Commun. 48 (2012) 7916–8. https://doi.org/10.1039/c2cc32518g.
[42] A. Abragam, B. Bleaney, Electron Paramagnetic Resonance of Transition Ions, Clarendon Press Oxford, UK,. (1970) 925.
[43] K.N. Shrivastava, Theory of Spin–Lattice Relaxation, Phys. Status Solidi. 117 (1983) 437–458. https://doi.org/10.1002/pssb.2221170202.

CHAPTER 4

ON THE WAY TOWARDS 1D EXTENDED MAGNETS: SERENDIPITOUS FORMATION OF A TETRANUCLEAR $Zn^{II}_2Dy^{III}_2$ ZERO FIELD SMM, AN EXHAUSTIVE MAGNETIC STUDY

4.1. INTRODUCTION

As a continuation of Chapter 2, we rationally designed another Mannich base type of ligand based on CYCLAM, namely 1,4,8,11-tetraazacyclotetradecane (H_4L^4, Scheme 4.1). The targeted ligand possesses the same coordination pockets as H_2L^3, but twice. Thus, in view of the successful extension of the dinuclear $Zn^{II}Dy^{III}$ entities with different di- or tricarboxylic acids to obtain polynuclear systems, this ligand was considered to be a potential candidate to extend these systems within 1D. Moreover, based also on the results obtained in Chapter 3 for trinuclear systems, the same synthetic route could possibly lead to formation of 1D systems. In that hypothetic situation each inner pocket would be occupied by a transition metal ion and the outer pocket by a lanthanide ion, which at the same time would be coordinated to the outer pocket of another ligand.

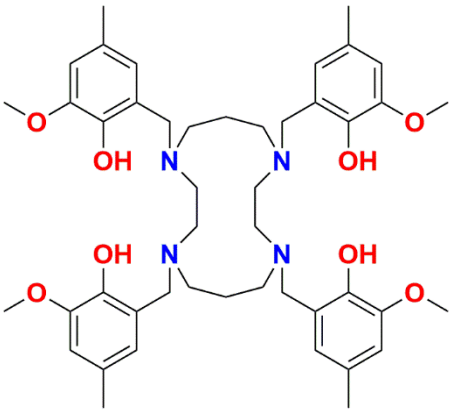

Scheme 4.1.- The compartmental ligand H_4L^4.

On the one hand, the idea of extending the structure in one dimension is appealing for two main reasons. Firstly, it would mean that all the paramagnetic ions are equally oriented in that dimension (and inherently the anisotropic axes) and, therefore, a fundamental prerequisite for the design of future devices would be fulfilled. Secondly, another exhaustive study could be done by varying the bridging dicarboxylate ligand, which would get closer or further away the paramagnetic centers. Note that the paramagnetic ions in the pockets of the same main ligand would be always separated by the same distance. On the other hand, in light of the interesting results obtained by exchange coupled systems in Chapter 3, we have considered that it would be interesting to combine both 3d and 4f paramagnetic ions to see whether these

exchange coupled systems display improved properties in comparison to systems in which a single type of paramagnetic ion is introduced.

In this chapter we report on the rational and gradual synthesis towards 1D systems, which though resulted unsuccessful, gave rise to very interesting compounds. Starting from a dinuclear Cu^{II} based compound, we went through an acetate bridged tetranuclear Zn_2Ln_2 complex to end up in a succinate bridged cationic tetranuclear Zn_2Ln_2 system. Based on the serendipitous preparation of the latter compound, we have synthesized seven novel coordination compounds varying both 3d and 4f type of ions and studied several different magnetic dilutions. Thus, we report on the synthesis, characterization and magnetic properties of the studied systems.

4.2. PREPARATION OF THE LIGAND

4.2.1. H_4L^4: 1, 4, 8, 11-tetraaza-1, 4, 8, 11-tetrakis(2-hydroxy-3-methoxy-5-methylbenzyl) cyclotetradecane

A mixture of 1, 4, 8, 11-tetraazacyclotetradecane (10 mmol, 2.00 g) and paraformaldehyde (44 mmol, 1.32 g) was refluxed in 15 mL of methanol for 1.5 h. At this time, 2-methoxy-4-methylphenol (44 mmol, 5.59 mL) was added to the solution and was refluxed for other 24 h. The white mixture was cooled to room temperature and the solid was filtered, washed with methanol and dried under vacuum yielding pure H_4L^4. Yield: 90%.

^{1}H-NMR (500 MHz, $CDCl_3$, ppm, Figure A4.86): 6.59 (s, 4H, aryl-*H*), 6.35 (s, 4H, aryl-*H*), 3.83 (s, 12H, OC*H*$_3$), 3.61 (s, 8H, aryl-C*H*$_2$N), 2.76 (s, 8H, NC*H*$_2$C*H*$_2$N), 2.60 (t, ^3J = 7.3 Hz, 8H, NC*H*$_2$CH$_2$C*H*$_2$N), 2.20 (s, 12H, aryl-C*H*$_3$), 1.81 (p, ^3J = 7.6 Hz, 4H, NCH$_2$C*H*$_2$CH$_2$N).

4.3. PREPARATION OF THE COMPLEXES

4.3.1. $[Cu_2L^4]\cdot 4H_2O$ (28)

To a solution of H_4L^4 (0.63 mmol, 0.5 g) and Et_3N (2.5 mmol, 0.35 mL) in 75 mL of chloroform was added a methanol solution (75 mL) of $Cu(OAc)_2\cdot 4H_2O$ (1 mmol, 0.20 g). The mixture immediately gave rise to a dark green coloured solution. In several

days good size and quality crystals were obtained by slow evaporation. Yield and elemental analysis results in Table A4.1.

4.3.2. $[Zn_2(\mu\text{-}L^4)(\mu\text{-}OAc)Ln_2(NO_3)_2]\cdot[Zn_2(\mu\text{-}L^4)(\mu\text{-}OAc)Ln_2(NO_3)(OAc)]\cdot 4CHCl_3\cdot 2MeOH$ (Ln^{III} = Y (29), Dy (30))

To a solution of H_4L^4 (0.04 mmol, 32.0 mg) and Et_3N (0.16 mmol, 0.02 mL) in 10 mL of chloroform was added a methanol solution (10 mL) containing $Zn(OAc)_2\cdot 2H_2O$ (0.08 mmol, 17.6 mg) and $Ln(NO_3)_3\cdot xH_2O$ (0.08 mmol). The resulting colourless solution was allowed to stand at room temperature and in few days, suitable crystals for X-ray diffraction were obtained. Note that two slightly different molecules cocrystallize within the crystal structure (see crystal structure description). Yield and elemental analysis results in Table A4.1.

4.3.3. $[TM_2(\mu\text{-}H_2L^4)_2(\mu\text{-succinate})Ln_2(NO_3)_2](NO_3)_2\cdot 2H_2O\cdot 6MeOH$ (TM^{II} = Co, Ln^{III} = Y (31), Gd (32), Dy (33); TM^{II} = Zn, Ln^{III} = Y (34), Tb (35), Dy(36), Er (37))

To a solution of H_4L^4 (0.04 mmol, 32.0 mg), $TM(NO_3)_2\cdot xH_2O$ and $Ln(NO_3)\cdot xH_2O$ in 20 mL of methanol was added dropwise another solution containing succinic acid (0.02 mmol, 2.4 mg) and Et_3N (0.12 mmol, 0.016 mL) in 1 mL of methanol. A thin powder was formed after the addition of each drop, but it easily got dissolved. The solution was stirred for few seconds, filtered in order to remove possible undissolved particles and allowed to stand at room temperature. In few days, suitable crystals for X-ray diffraction were obtained. Yield and elemental analysis results in Table A4.1.

4.3.4. Magnetically diluted $\mathbf{30_Y}$, $\mathbf{31_{Zn}}$, $\mathbf{33_{Zn}}$, $\mathbf{33_Y}$ and $\mathbf{35_Y}$-$\mathbf{37_Y}$

In the case of $\mathbf{30_Y}$ and $\mathbf{35_Y}$-$\mathbf{37_Y}$ the paramagnetic Ln^{III} ions were diluted by using the diamagnetic Y^{III} counterpart. For $\mathbf{31_{Zn}}$, the magnetic dilution was made by using Zn^{II}. In the case of **33**, however, both paramagnetic ions were diluted separately, Co^{II} with Zn^{II} and Dy^{III} with Y^{III} yielding $\mathbf{33_{Zn}}$ and $\mathbf{33_Y}$, respectively. In all the cases the diluted derivatives were synthesized following the same experimental procedure but using 1:10 Ln:Y and Co:Zn molar ratios.

4.4. EXPERIMENTAL RESULTS

The compartmental ligand H_4L^4 (Scheme 4.1) possesses two double pockets. Each pocket consists of an inner N_2O_2 site suitable for transition metals and another outer O_4 site, more suitable for harder oxophilic metal ions such as lanthanides.

With the aim of performing a further analysis related to the dinuclear $Zn^{II}Dy^{III}$ systems that we previously reported [1], we designed the H_4L^4 ligand in order to extend these $Zn^{II}Dy^{III}$ field induced SMMs in 1D (Scheme 4.2, top). In this sense, each main ligand would contain two dinuclear systems in one, which may be extended by replacing the original acetate bridges with dicarboxylate bridging ligands. Before doing this, the previous step has been to prove that the ligand displays a suitable conformation so as to synthesize one dimensional chains. Thus, the reaction of H_4L^4 with $Cu(OAc)_2{\cdot}4H_2O$ gives rise to the dinuclear compound $[Cu_2L^4]{\cdot}4H_2O$ (**28**), which shows the desired conformation. Secondly, the acetate bridged tetranuclear Zn_2Dy_2 (**30**) system was obtained by the reaction of H_4L^4 with $Zn(OAc)_2{\cdot}2H_2O$ and $Dy(NO_3)_3{\cdot}5H_2O$, which was shown to be very similar to our previously reported dinuclear compound in terms of coordination environment of the metal ions. Finally, when trying to extend these systems along one dimension by using nitrate salts of Zn^{II} and Dy^{III}, as well as succinic acid, an unexpected Zn_2Dy_2 tetranuclear (**36**) complex was obtained, which turned to be a high performance zero field SMM. In view of this, other lanthanide based analogues (Y (**34**), Tb (**35**), Er (**37**)), 3d-4f mixed systems (Co_2Y_2 (**31**), Co_2Gd_2 (**32**) and Co_2Dy_2 (**33**)) and diluted samples (**30$_Y$**, **31$_{Zn}$**, **33$_{Zn}$**, **33$_Y$** and **35$_Y$-37$_Y$**) were synthesized and their magnetic properties were studied. Note that we carried out some more experiments in order to try an extension along one dimension based on the trinuclear compounds described in Chapter 3 (Scheme 4.2, bottom). Unfortunately, we were not able to characterize any material with this strategy.

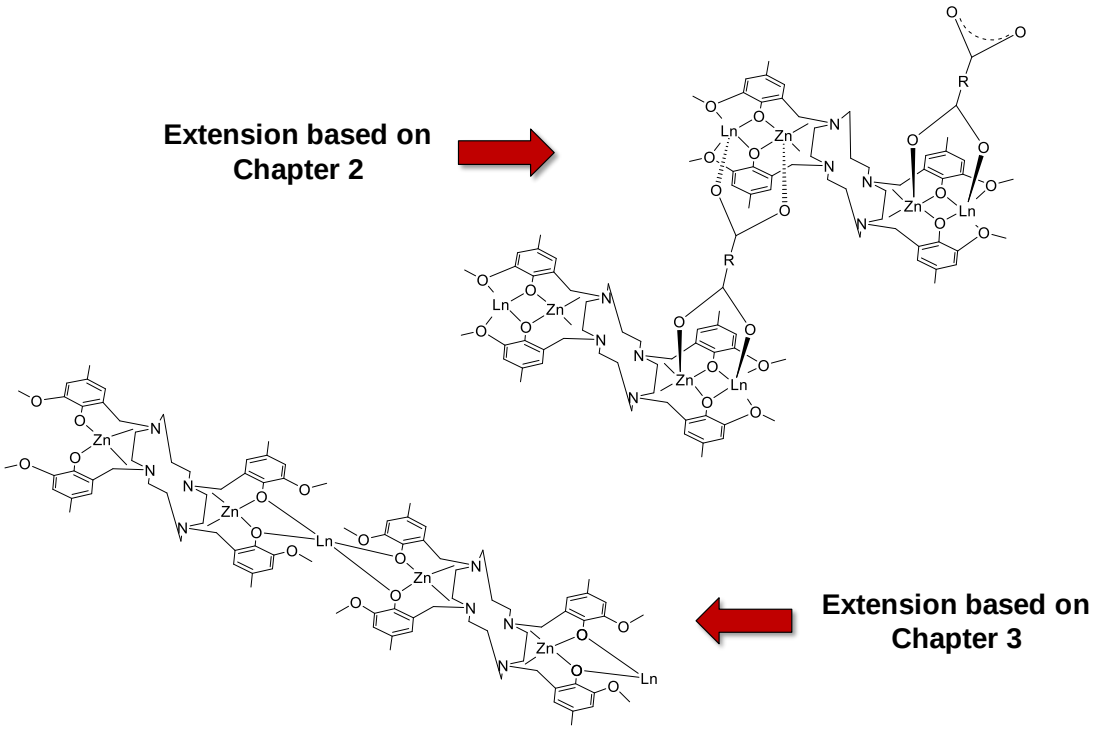

Scheme 4.2.- Proposed structure for the extended $Zn^{II}Ln^{III}$ one dimensional chains based on the results of Chapter 2 (top) and Chapter 3 (bottom).

4.4.1. Crystal Structures of the ligand H_4L^4 and the complexes 28, 30-31, 33 and 36

The compartmental ligand H_4L^4 crystallizes in the triclinic *P-1* space group. The asymmetric unit consists of half a ligand, where the phenol groups are stabilized by intramolecular hydrogen bonds towards the amines (crystallographic data is given in Table A4.2 and the structure is shown in Figure A4.1).

Regarding to coordination compounds, the dinuclear Cu^{II} complex **28** crystallizes in the monoclinic *P 21/c* space group and its structure is shown in Figure 4.1 (crystallographic data is given in Table A4.2). This centrosymmetric compound contains two Cu^{II} ions, a fully deprotonated L^{4-} ligand and four crystallization water molecules. As expected for a transition metal, the copper ions are located in the inner pockets of the ligand with a N_2O_2 coordination environment. The coordination environment was calculated by using the SHAPE software [2] obtaining the lowest value for the square geometry (Table A4.5). Indeed, when considering an average plane formed by the N_2O_2 donor atoms, the distance from the plane to the Cu^{II} ion appears to be minimum (0.090 Å), which corroborates the calculated geometry for Cu1.

Regarding to bond distances, the shortest bonds are the Cu1-O ones (1.9004(13) and 1.9263(13) Å), while Cu1-N are slightly longer (2.0156(15) and 2.0766 (15) Å). More importantly, **28** has proven that H_4L^4 is, *a priori*, a good candidate for synthesizing 1D chains as proposed in Scheme 4.2. Indeed, the inversion center located in the middle of the CYCLAM ring provides the structure to have a coplanar N_4 ring and two double pockets almost perpendicular to it. This is exactly the prerequisite we were looking for. Finally, the structure is stabilized and organized in 1D along the *b* axis by hydrogen bonds (Figure A4.2). On the one hand, O1W water molecules occupy somehow the O4 pockets directing their H atoms towards the phenoxido and methoxy oxygen atoms. On the other hand, O2W are responsible of bridging two different dinuclear systems by directing one of the hydrogen atoms towards O1 of a dinuclear complex and the other one towards one O1W located in an outer site of another adjacent dinuclear complex. Thus, this hydrogen bonding pattern forms six membered rings between dinuclear entities (O2W···O1W···O1/O3···O2W···O1W···O1/O3).

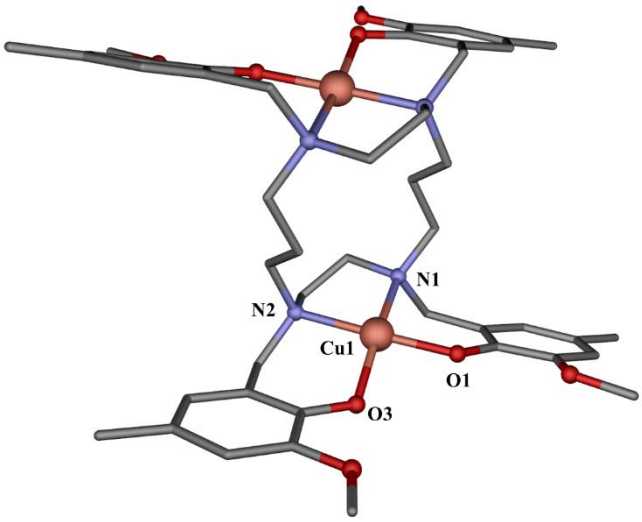

Figure 4.1.- Perspective view of the structure of **28**. Copper, oxygen, nitrogen and carbon atoms are in orange, red, blue and grey, respectively. Hydrogen atoms as well as crystallization water molecules have been omitted for the sake of clarity.

Once it was shown the adequateness of the chosen ligand, the next step was to obtain the tetranuclear Zn_2Dy_2 system **30**. Compound **30** crystallizes in the monoclinic *P 2/c* space group (Table A4.2 for crystallographic data). The asymmetric unit contains two half (but different) molecules and three crystallization solvent molecules: two of chloroform and one of methanol (Figure 4.3). Even though the solvents were clearly

visible during the refinement process, due to the large disorder, as well as their very volatile character, it was not possible to acquire a reasonable model and, hence, a squeeze routine was applied. Nevertheless, the chemical formula was then confirmed by additional elemental analysis (Table A4.1). As it has been said, two slightly different structures cocrystallize within the crystal structure, which will be referred as **30A** and **30B** hereinafter. In both cases, the fully deprotonated L^{4-} ligand encapsulates two pairs of $Zn^{II}Dy^{III}$ systems, which are triply bridged by two phenoxido groups of the main ligand and one *syn-syn* acetate group. As predicted, the softer Zn^{II} ions occupy the inner site of the pockets, whereas the harder Dy^{III} ions are in the outer site. In both **30A** and **30B** the transition metal possesses the same ZnN_2O_3 coordination environment, where two nitrogen and two oxygen atoms belong to L^{4-}, whereas the remaining oxygen atom belongs to the bridging acetate group. In contrast to Cu^{II} ions in **28**, in **30A** and **30B** the Zn^{II} ions are pentacoordinated, displaying a slightly distorted square pyramid geometry according to the SHAPE calculations (Table A4.6). Moreover, the bridging acetate forces the Zn^{II} ions to move out from the square bases formed by O1-O3-N1-N2. In fact, when considering average planes (since O1, O3, N1 and N2 are not strictly coplanar) the distances of Zn1A and Zn1B to these planes are of 0.595 Å and 0.626 Å, respectively. The shortest bond distances correspond to Zn-O (1.969(2)-2.064(2) Å), while Zn-N distances are somewhat longer (2.140(3)-2.221(3) Å).

The difference between **30A** and **30B** (bond distances and angles apart, Table A4.3) is found in the coordination environment of the Dy^{III} ions. They both exhibit DyO_9 coordination spheres and seven out of nine oxygen atoms belong to the same groups, namely: two phenoxido and two methoxy belonging to L^{4-}, two oxygen atoms coming from a bidentate nitrate and one oxygen pertaining to the bridging acetate. The last two oxygen atoms, however, belong to an additional bidentate nitrate in **30A** and to another additional chelating acetate in **30B**. In terms of bond distances, Dy-O bonds are divided in four different categories. The shortest $Dy\text{-}O_{phenoxido}$ in the range of 2.262(2)-2.285(2) Å, intermediates for $Dy\text{-}O_{\mu\text{-}acetate}$ with values of 2.329(3) Å and 2.346(3) Å, longer for $Dy\text{-}O_{nitrate}$ between 2.441(3) and 2.500(3) Å and the longest for $Dy\text{-}O_{methoxy}$ in the 2.515(2)-2.572(2) Å range. With regard to the chelating acetate, the $Dy\text{-}O_{acetate}$ bond distances are longer than for the bridging acetate, but shorter than $Dy\text{-}O_{nitrate}$ of 2.407(3) Å and 2.441(3) Å. Despite being a small difference, these variations might notably change the dynamic magnetic properties of the system. The SHAPE analysis indicates that the coordination polyhedra in both cases is far from an ideal symmetry, but in both cases it best fits to a capped square antiprism (Table A4.7).

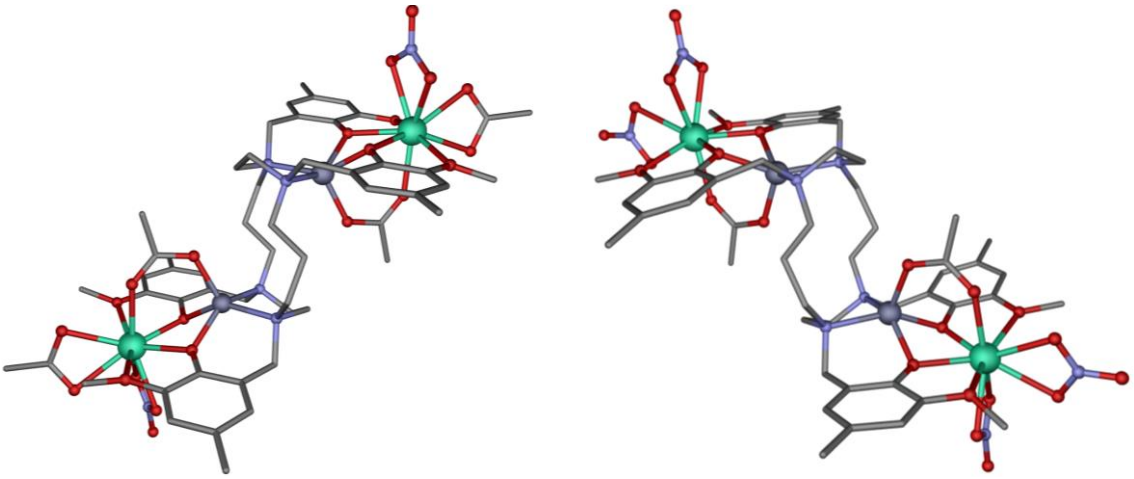

Figure 4.3.- Perspective view of the two different tetranuclear systems (left: **30B**; right: **30A**) within the crystal structure of **30**. Dysprosium, zinc, oxygen, nitrogen and carbon atoms are in turquoise, dark grey, red, blue and grey, respectively. Hydrogen atoms have been omitted for the sake of clarity.

Compounds **31**, **33** and **36** are isostructural and crystallize in the orthorhombic *Pba2* space group (crystallographic data in Table A4.2). Due to the isostructural character, hereinafter only compound **36** will be described. The X-ray crystal structure of **36** consists of $[Zn_2(\mu\text{-}H_2L^4)_2(\mu\text{-succinate})Dy_2(NO_3)_2]^{2+}$ cations, NO_3^- anions and six methanol and two water crystallization molecules (Figure 4.4). In the case of **36**, these solvent molecules were not assigned due to the large disorder and the structure was resolved with a squeeze routine. In **33,** however, a reasonable model was obtained with the mentioned crystallization molecules. Obviously, this is not the structure that was proposed in Scheme 4.2, since a molecular structure was obtained instead of an extended material.

Only one of the two double pockets in each ligand acts as predicted encapsulating a dinuclear $Zn^{II}Dy^{III}$ entity. Regarding to the other pocket, only one of the functionalized aromatic ring coordinates to a Dy^{III} ion (located in the pocket of the other H_2L^{2-}), whereas the other ring remains intact with the phenol group still protonated. Hence, three out of four phenol groups are deprotonated acting as $Zn^{II}Dy^{III}$ bridging phenoxido groups (O1 and O3 from the pocket) or monocoordinating phenoxido (O7). Nonetheless, the ligands show a H_2L^{2-} mode, since part of them displays a zwitterionic form. More specifically, the protons from O7 migrate to the nearest amine N4, forming one asymmetric center in each ligand, which are stabilized by hydrogen bonds between N4···O7. Taking into account that the asymmetric unit contains only half of a

molecule, both new centers in the molecule exhibit the same configuration (*R, R'* or *S, S'*). However, bearing in mind that there is not any chiral directing agent to force the structure to be one enantiomer or the other, both of them cocrystallize in the crystal structure (Figure A4.3). Although it is shown that the succinate has not been a good choice as a spacer for the initial purpose, it is essential in this structure acting as double bridging group. On the one hand, it forms a bridge between Zn^{II} and Dy^{III} ions identically as it does the acetate in **30**. On the other hand, it connects the two dinuclear entities located in a pocket of each ligand.

In terms of coordination environment, for the Zn^{II} ion there is not any notable difference in comparison to **30**. It possesses a ZnN_2O_3 coordination environment, where the oxygen atoms belong to two phenoxido groups and one succinate ligand and the nitrogen atoms to two amine groups of the CYCLAM ring. Zn-O distances range from 1.979(4) Å to 2.083(4) Å, while Zn-N have 2.101(5) Å and 2.190(5) Å bond distances. Once more, the polyhedron fits best to a square pyramid geometry according to the SHAPE values (Table A4.6). The case of the Dy^{III}, however, is completely different. Although it shows a DyO_9 coordination environment and seven out of nine oxygen atoms belong to the same groups as for **30**, the remaining two oxygen atoms will be then fundamental in order to explain its magnetic properties. The same DyO_7 sphere consists of two phenoxido, two methoxy, two nitrate and one carboxylate oxygen atoms. The difference, thus, corresponds to the replacement of an additional chelate nitrate (or acetate in **30B**) for another phenoxido and methoxy groups arising from the other main ligand. Regarding to bond distances, the Dy-$O_{phenoxido}$ ones are the shortest in the range of 2.227(4)-2.313(4) Å, the Dy-$O_{carboxylate}$ is slightly longer with a value of 2.320(4) Å, the Dy-$O_{nitrate}$ are of 2.456(5) Å and 2.519(4) Å and, finally, the non-charged methoxy groups display the longest Dy-O distances, in the range of 2.536(5)-2.708(5) Å. Noteworthy, between the wide variety of donor atoms in this system, the most negatively charged phenoxido groups are, somehow, providing the system with an appropriate crystal field as to lead to an axial ground state, which favours the SMM behaviour. Indeed, open angles are found between O1-Dy1-O7 and O3-Dy1-O7, with values of 137.32(16)º and 143.73(15)º, respectively. As it will be discussed in the following sections, this kind of ligand field will be fundamental when explaining the dynamic magnetic properties of this system. In contrast to **30A** and **30B**, the coordination sphere of the Dy^{III} ion in **36** fits best to a muffin conformation, although very distorted as in previous cases (Table A4.7).

Within the molecule, $Dy^{III}\cdots Dy^{III}$ and $Zn^{II}\cdots Zn^{II}$ distances are of 8.6991(6) Å and 7.6269(9) Å, respectively, while the shortest intermolecular $Dy^{III}\cdots Dy^{III}$ and $Zn^{II}\cdots Zn^{II}$ distances are of 10.8644(6) Å and 11.5391(9) Å, respectively. As aforementioned, solvent molecules could not be refined properly. However, in Figures A4.4-A4.5 is shown the supramolecular structure of **33** in order to clarify how these molecules grow in 3D. It is worth mentioning that the nitrate counterions, as well as the methanol and water molecules form a complex hydrogen bonding pattern along the entire *b* axis (Figure A4.4), while the cationic $[Co_2(\mu\text{-}H_2L)_2(\mu\text{-succinate})Dy_2(NO_3)_2]^{2+}$ units are linked by hydrogen bonds between O5···O3N. Thus, the cationic fragments grow in a 2D motion within the *ab* plane (Figure A4.5).

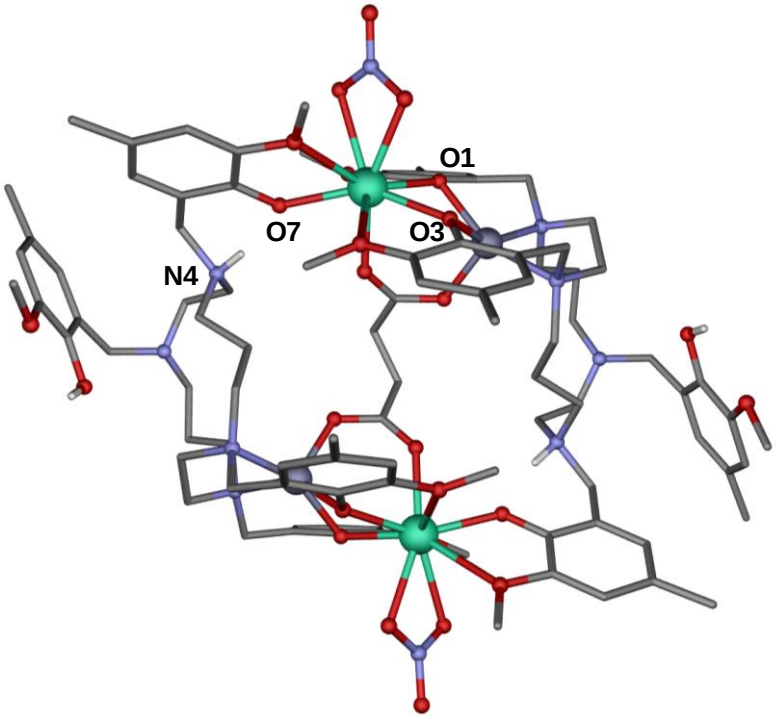

Figure 4.4.- Perspective view of the cationic structure of **36**. Dysprosium, zinc, oxygen, nitrogen, carbon and hydrogen atoms are in turquoise, dark grey, red, blue, grey and white, respectively. All hydrogen atoms except the phenolic and zwitterionic ones, as well as the counteranions, have been omitted for the sake of clarity.

4.4.2. Static magnetic properties of complexes 30-33 and 35-37

The temperature dependence of the magnetic susceptibility was measured on polycrystalline samples for complexes **30-33** and **35-37** in the 2-300 K temperature range under an applied field of 0.1 T (Figure 4.5). At room temperature, the $\chi_M T$ values of 57.90 (**30**), 23.42 (**35**), 28.26 (**36**) and 23.24 (**37**) $cm^3 \cdot mol^{-1} \cdot K$ are in the expected ranges for four non-interacting Dy^{III} ions (14.17 $cm^3 \cdot mol^{-1} \cdot K$; $^6H_{15/2}$, and g = 4/3), two non-interacting Tb^{III} ions (11.82 $cm^3 \cdot mol^{-1} \cdot K$; $^7F_6$, and g = 3/2), two non-interacting Dy^{III} ions and two non-interacting Er^{III} ions (11.48 $cm^3 \cdot mol^{-1} \cdot K$; $^4I_{15/2}$, and g = 6/5) in the free ion approximation. For compounds containing further anisotropic Co^{II} ions, the room temperature values of 6.05 (**31**), 21.72 (**32**) and 34.57 (**33**) $cm^3 \cdot mol^{-1} \cdot K$ are all greater than the expected ones for two Co^{II} and two Ln^{III} ions, mainly due to the unquenched orbital angular momentum of the former ones.

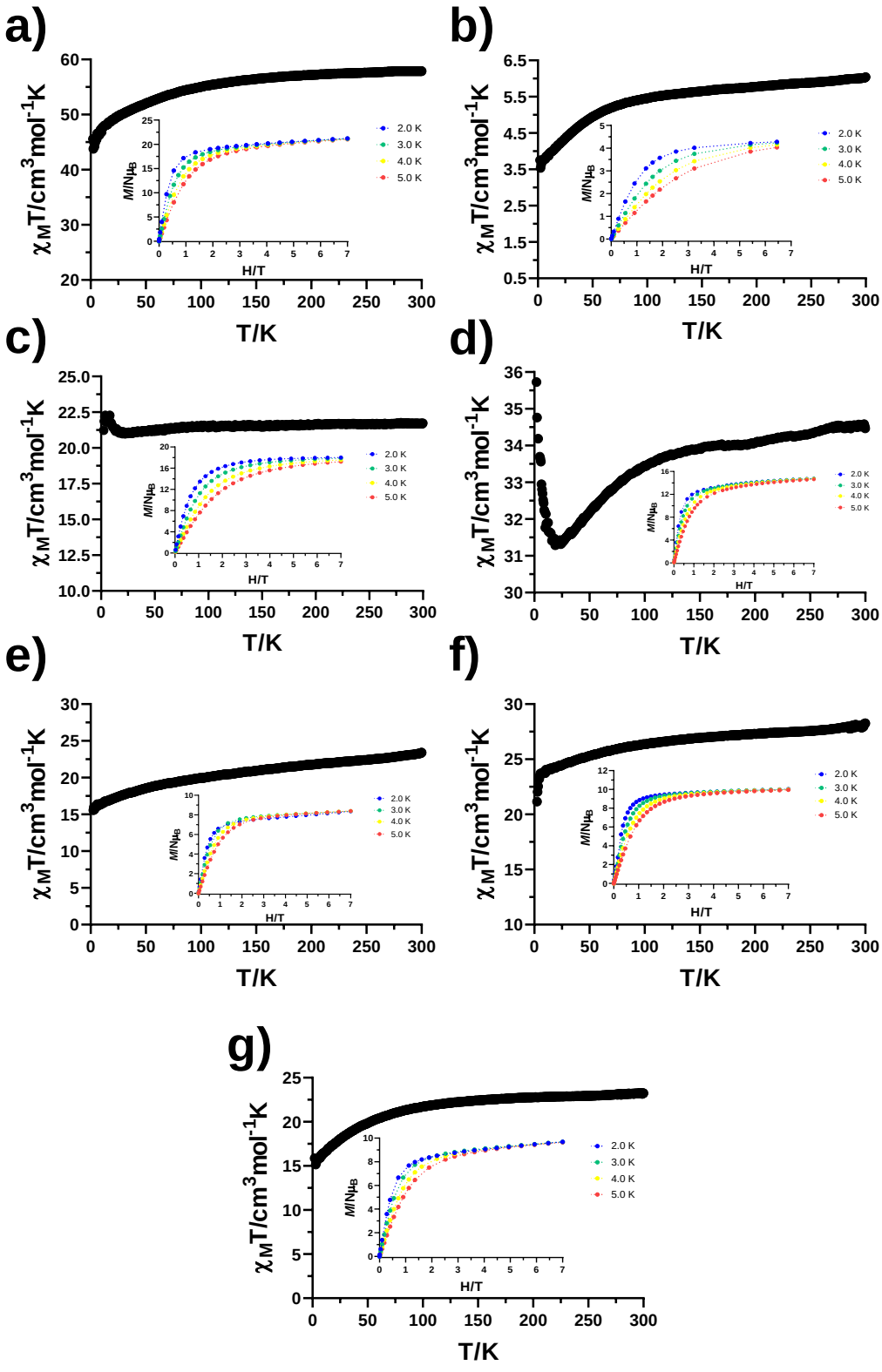

Figure 4.5.- Temperature dependence of the $\chi_M T$ product at 1000 Oe for complexes **30-33** and **35-37** (from a) to g), respectively). Insets: Field dependence of the magnetization in the 2-5 K temperature range. Dashed solid lines are a guide to the eye.

Complexes containing a single anisotropic ion (**30**, **31** and **35-37**) display the usual temperature dependence of the $\chi_M T$ product. Thus, $\chi_M T$ gradually decreases with decreasing temperature due to: (i) the depopulation of the M_J sublevels of the Ln^{III} ion arising from the splitting of the multiplets by the ligand field for complexes **30**, **35-37**, and (ii) the spin-orbit coupling of the Co^{II} ion for complex **31**. However, at the lowest temperatures the Zn_2Dy_2 based counterpart **36** (plot f)) shows a precipitous final drop, which could be indicative of magnetic blocking [3]. Compounds **32** and **33** display additional effects due to exchange interactions. On the one hand, the $\chi_M T$ value for **32** gradually decreases from room temperature to 22 K with a value of 20.99 $cm^3 \cdot mol^{-1} \cdot K$, then increases to a maximum value of 22.23 $cm^3 \cdot mol^{-1} \cdot K$ at 5.7 K to finally drop below this temperature. The initial decrease is associated to the spin-orbit coupling effects of the Co^{II} ion, whereas the subsequent increase and decrease could be explained by intramolecular ferromagnetic and intermolecular antiferromagnetic interactions, respectively. For **33**, the gradual decrease of $\chi_M T$ from room temperature to reach a minimum at 24 K (31.31 $cm^3 \cdot mol^{-1} \cdot K$) is more pronounced due to the depopulation of the M_J sublevels. Below 25 K, $\chi_M T$ also increases to a maximum value of 35.73 $cm^3 \cdot mol^{-1} \cdot K$ due to intramolecular ferromagnetic interactions. The non-superimposable reduced magnetization curves in the 2-5 K temperature range for all the compounds, as well as lack of saturation (in no case the magnetization at the maximum applied field reaches the value expected for the sum of the values corresponding to each of the metal ions) are indicative of magnetic anisotropy.

To confirm if whether or not there exists magnetic blocking in compound **36** we performed field-cooled (FC) and zero-field-cooled (ZFC) magnetic susceptibility experiments (Figure 4.6, right). As observed, both curves clearly bifurcate at a temperature of 5 K, which gives an idea of the blocking temperature. Additionally, we performed the same experiment for compound $\mathbf{33_{Zn}}$ (left). The curve suggests a similar blocking temperature for this compound.

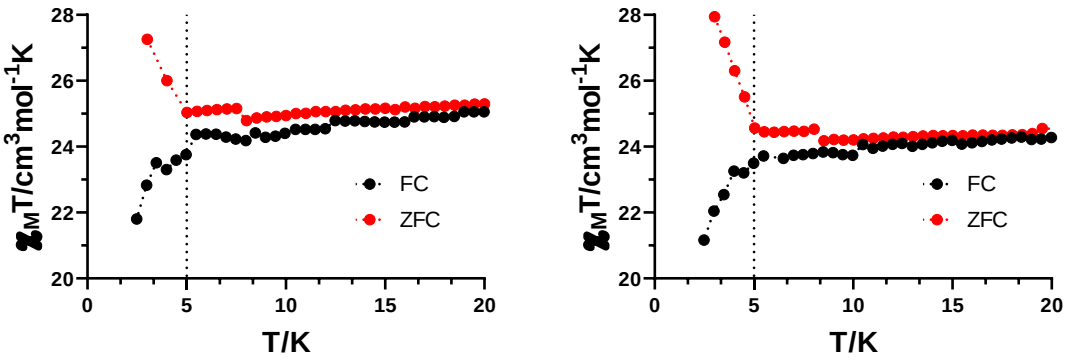

Figure 4.6.- Field-cooled (FC, black) and zero-field-cooled (ZFC, red) $\chi_M T$ product in the 2.5-20 K temperature range for **33$_{Zn}$** (left) and **36** (right). The dashed line at 5 K shows the temperature at which both curves bifurcate.

4.4.3. Dynamic magnetic properties of complexes 30-33, 35-37 and diluted samples

Except for **28**, **29** and **34**, *ac* magnetic measurements were carried out for the rest of the compounds as potential candidates for presenting SMM behaviour. At zero field, only compound **36** exhibits well defined maxima in the $\chi''_M(T)$ plot below 28 K. Compounds **30** and **33** display non zero signals, but without maxima and **31**, **32**, **35** and **37** do not have signal at all (Figures A4.10-A4.13). Considering the possibility of a fast QTM process hiding the desired SMM behaviour, the application of magnetic external fields and dilutions in diamagnetic matrices were also studied for each compound since they are well known techniques to avoid QTM [4–6].

When applying an external magnetic field of 1 kOe, **30** displayed two maxima at 10,000 Hz (Figure A4.10), a first well defined one at around 2.5 K (related to a fast relaxation, FR) and a shoulder like one at 9.0 K (related to a slow relaxation, SR). In view of that, the field dependence of the out-of-phase susceptibility at different frequencies was evaluated at a fixed temperature of 8.0 K, concluding that the optimum external field was of 2.5 kOe (Figures A4.14-A4.15). A complete measurement in these conditions was carried out obtaining two sets of maxima for two thermally activated relaxation processes (Figure 4.7). In an attempt to obtain the relaxation times for both of the processes, $\chi''_M(\upsilon)$ curves were fitted in the temperature range of 2.0-2.6 K for FR and in the range of 7.0-13.0 for SR (Figures A4.17-A4.18). The difference in operating temperature allowed us to do such a separation, however, it is worth mentioning that

for FR the fitted data was above 1000 Hz. Below this frequency, the influence of the SR is remarkable in the studied temperature range, hence, it should be removed. Despite the high α values obtained from the Cole-Cole plots in both regimes (FR: 0.37 (2.0 K) – 0.62 (2.6 K); SR: 0.52 (7.0 K) – 0.49 (13.0 K)), relaxation times in the Arrhenius plot (Figure 4.7, inset) could be fitted to an Orbach process leading to effective energy barriers (U_{eff}) and τ_0 values of 9.2 K and $8.31 \cdot 10^{-7}$ s for FR and 69.1 K and $1.12 \cdot 10^{-7}$ s for SR, respectively. We believe that the high α values in the low temperature range may arise from the mixing of both FR and SR processes, whereas in the higher temperature peaks are broad, which can be due to the existence of several very close relaxation processes. An additional analysis of the data was accomplished by using the CCFIT software [7] and fitting the $\chi''_M(\chi'_M)$ in the whole temperature range. This afforded comparable results to those obtained by separating the two temperature regimes (Figure A4.21).

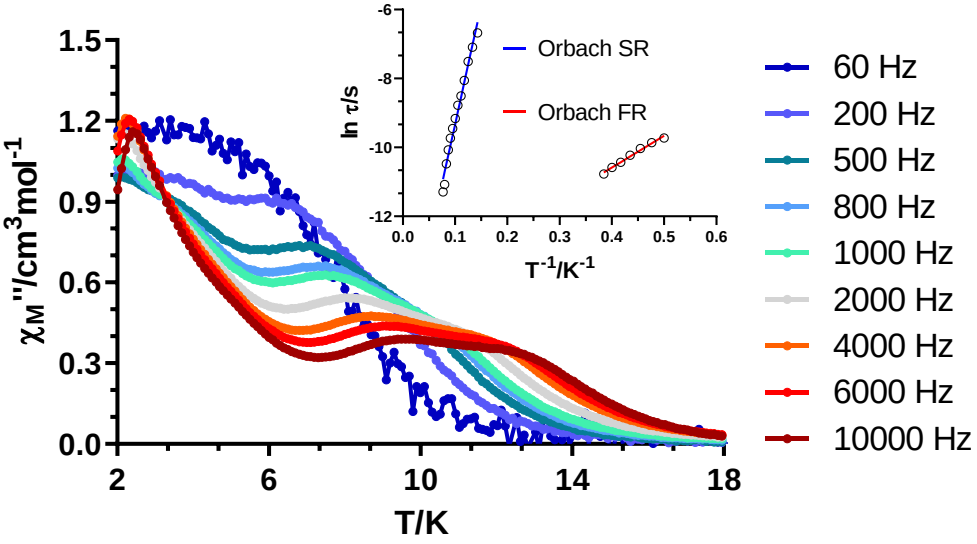

Figure 4.7.- Temperature dependence of the out-of-phase components of the *ac* susceptibility in a *dc* applied field of 2.5 kOe for **30**. Inset: Arrhenius plot for the relaxation times with Orbach fittings for FR and SR.

As mentioned, diluted samples were also studied in order to avoid the possible intra- or intermolecular Dy···Dy dipolar interactions that may contribute in the occurrence of QTM. At zero applied dc field, $\mathbf{30}_{\mathbf{Y}}$ behaves similar to **30** under an external field of 1 kOe (Figure A4.22) in terms of SR, whereas FR appears to be hidden by strong QTM. Thus, the experiment was repeated with a 2.5 kOe external field for

30$_Y$ obtaining the results depicted in Figure 4.8. At a first glance, it can be observed that there is a substantial positive temperature shift regarding to FR (from 2.3 K to 3.6 K at highest freq.) and that the peaks referring to SR are narrower and better defined. The same approach was used to evaluate both regions. Again, $\chi''_M(\upsilon)$ curves were carefully analysed in order to remove the biased data in the low temperature region (Figure A4.24). In the present case, relaxation times referring to FR were fitted to the equation that simultaneously considers Raman and Orbach processes:

$$\tau^{-1} = BT^n + \tau_0^{-1} exp(-U_{eff}/k_B T) \quad \textit{Equation 4.1}$$

which afforded the following set of parameters: B = 285.4 $s^{-1}K^{-2.042}$, n = 2.042, τ_0 = $2.6 \cdot 10^{-10}$ s and U_{eff} = 46.8 K. The high α values (0.42 (2.0 K) – 0.64 (4.0 K)) are justified by both the presence of simultaneous relaxation mechanisms and influence of the SR as the temperature increases. The relaxation times for SR were extracted from the 8.0-12.8 K data (Figure A4.25) and were fitted to a single Orbach process with U_{eff} and τ_0 values of 94.0 K and $1.6 \cdot 10^{-8}$ s. Noteworthy, the definition of the peaks is portrayed in the decrease of the α, which at the highest temperature shows a value of 0.30 in contrast to 0.49 in the non-diluted sample. Once more, the presence of two sets of maxima lead us to employ the CCFIT software. The results are in concordance with the mentioned ones (Figure A4.28). Nonetheless, it needs to be said that in this case the $\chi''_M(\chi'_M)$ plots are fitted above 3.2 K, which is the first temperature were two semicircles are appreciated. Therefore, the contribution of the FR is not so reliably considered.

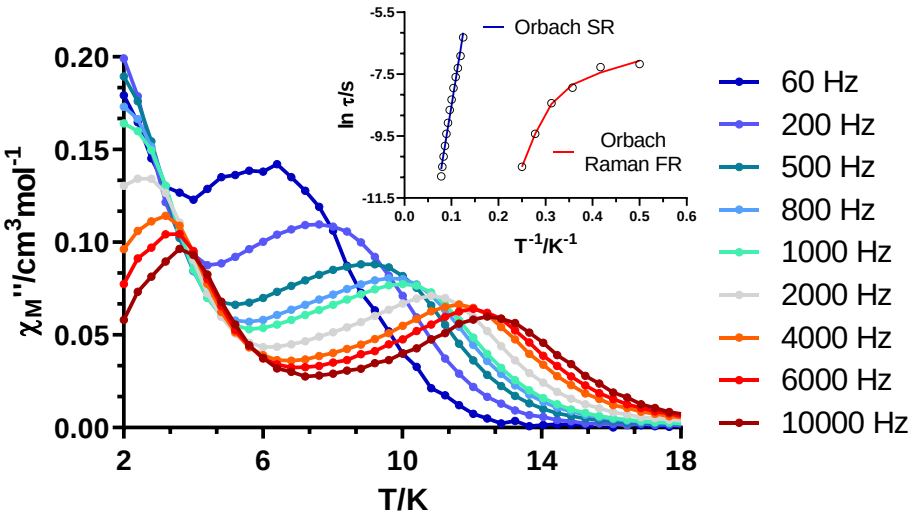

Figure 4.8.- Temperature dependence of the out-of-phase components of the *ac* susceptibility in a *dc* applied field of 2.5 kOe for **30**$_Y$. Inset: Arrhenius plot for the relaxation times with Orbach fitting for SR and Orbach + Raman for FR.

The simultaneous occurrence of two sets of maxima in the $\chi''_M(T)$ and $\chi'_M(T)$ plots could be justified by numerous reasons: (i) the presence of intra- or intermolecular interactions [8,9], (ii) occurrence of novel relaxation mechanisms due to the presence of an external magnetic field [10], (iii) the coexistence of two crystallographycally independent Dy^{III} ions [11] or (iv) even a single Dy^{III} ion is known to show two maxima [12]. In our case, the first hypothesis should be ruled out since **30**$_Y$ still shows two maxima. Moreover, we believe that the third hypothesis is the one that best describes the magnetic properties of this compound. Based on the strategical rules when designing ligand fields provided by Rinehart and Long [13], for oblate ions such as Dy^{III}, axial ligand fields are the optimum ones to stabilize the highest M_J states. Bearing in mind that the phenoxido groups are the ones mainly defining the crystal field, the greater electron density in the opposite position, the better the field to produce an axial ground state. Therefore, we conclude that the molecule that owns an acetate group as a chelate provides a better axiality to the Dy^{III} ion than the one that contains the second nitrate (acetates provide more electron density than nitrates [14]). Indeed, the orientation of the anisotropy axes, calculated by Magellan software [15] for both crystallographycally independent ions, point out that the easy axes are defined by the oxygen atoms of the phenoxido groups, which are expected to have more electronic charge (Figure A4.83). Thus, they pass through the middle of the phenoxido and nitrate or acetate groups depending on the molecule. Therefore, we associate the FR to the molecule possessing two chelate nitrates, whereas the SR can be attributed to the molecule with the acetate as a chelate.

In addition, this assumption is further consolidated by the following facts. The molecule displaying FR is comparable to the Dy^{III} based compound previously reported by us in terms of ligand field [1]. They both contain exactly the same donor atoms in the same positions and so comparable are the relaxation dynamics. For our previously reported compound the relaxation times were fitted to the simultaneous presence of Orbach and Raman mechanisms, obtaining the following set of parameters: $B = 10.2\ s^{-1}K^{-4.90}$, $n = 4.90$, $\tau_0 = 1.75 \cdot 10^{-9}$ s and $U_{eff} = 52.6$ K, which are in good agreement to the parameters obtained for **30**$_Y$ with respect to FR. Additionally, Murugesu *et al*. previously reported a family of complexes were the core of the compounds was maintained, but equatorial ligand field was modified [14]. In that case, the magnetic properties were enhanced when switching from acetate to nitrate. This can be explained by a weakening of the equatorial ligand field, which is positive for oblate ions. Thus, in our case the opposite effect could be expected by switching from acetate to nitrate, since what we weaken is the field created at both sides of the Dy^{III} ion. Finally,

this is further confirmed by looking to the bond distances referring to NO_3^- and OAc^- chelates. The acetates display shorter Dy-O distances than the nitrates, 2.407(3)-2.441(3) Å and 2.449(3)-2.486(3) Å, respectively. The influence of this shortening has also been previously reported in systems where two crystallographycally independent Dy^{III} ions were present [11].

The square pyramid geometry for Co^{II} in **31** is more defined than in the trinuclear **19**, with an Addison parameter τ^5 = 0.15. As mentioned, this could provide either positive or negative *D* values. In the present case, **31** behaves as field induced SMM showing a maximum around 7 K in the $\chi''_M(T)$ plot under an external magnetic field of 1000 Oe (Figure A4.10). In view of that, we performed field dependent measurements at 4 K to found the optimum external magnetic field. As shown in Figures A4.29-A4.30, the slowest relaxation times were obtained for an external magnetic field of 1.5 kOe. Moreover, the field dependent relaxation times were fitted to the following equation:

$$\tau^{-1} = \frac{B_1}{1 + B_2 \cdot H^2} + AH^4T + k \quad Equation\ 4.2$$

The first two terms account for field dependent QTM and direct processes, respectively, whereas the third term corresponds to field independent mechanisms, which could be Raman and/or Orbach. The best fit afforded the following set of parameters: B_1 = 9280 s^{-1}, B_2 = 489.1 T^{-2}, A = 60085 $s^{-1}T^{-4}K^{-1}$ and k = 9233 s^{-1}. The high value of *k* must indicate that at 4.0 K field independent relaxation mechanisms operate. A complete measurement was then carried out under the optimum external magnetic field of 1.5 kOe obtaining a set of maxima below 6 K (Figure 4.9, left). Cole-Cole plots, as well as $\chi''_M(\upsilon)$ curves were constructed and studied in the 2.0-6.0 K temperature range (Figures A4.32-A4.33). The obtained α values indicate a narrow distribution of the relaxation times (0.10 (2.0 K) – 0.02 (6.0 K)), but it was not possible to describe the curvature of the relaxation times with a single Raman process. Indeed, a nice fit was obtained by fixing the parameters corresponding to direct and QTM processes, which were obtained from the previous field dependent study. Thus, the data was fitted to the following Equation 4.3 that considers the simultaneous presence of QTM, direct and Raman processes:

$$\tau^{-1} = \tau_{QTM}^{-1} + AH^4T + BT^n \quad Equation\ 4.3$$

τ_{QTM}^{-1} and *A* were fixed to 773.0 s^{-1} and 60085 $s^{-1}T^{-4}K^{-1}$, respectively, obtaining *B* = 377.5 $s^{-1}K^{-2.66}$ and *n* = 2.66 for the Raman process. Note that we tried to combine QTM

and direct processes with an Orbach mechanism, but reasonable fitting parameters were not obtained.

The diluted **31**$_{Zn}$, which was measured under the same experimental conditions as the pure **31** (external field of 1.5 kOe), showed a clear positive temperature shift (Figure 4.9, right), what we associated to a further quenching of QTM by eliminating possible intra- or intermolecular $Co^{II}\cdots Co^{II}$ interactions (most likely intramolecular ones due to significantly shorter distances). The data was studied in the 3.2-7.8 K temperature range and, in this case, larger α values were obtained in agreement with several relaxation mechanisms (0.25 (3.2 K) – 0.06 (7.8 K)). We obtained the best fitting parameters considering direct and Raman mechanisms: A = 5.43·10^5 s^{-1}T^{-4}K^{-1}, B = 0.14 s^{-1}K$^{-6.18}$ and n = 6.18. The inclusion of QTM worsens the fitting in agreement with a more efficient quenching. An additional measurement under zero *dc* field is missing and it will be measured in a near future.

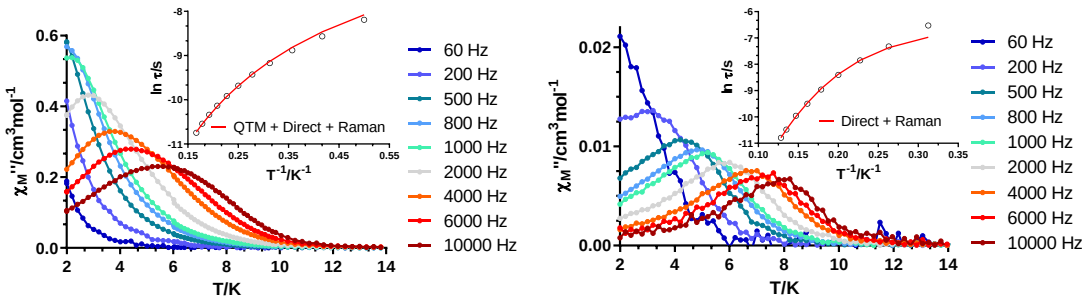

Figure 4.9.- Temperature dependence of the out-of-phase components of the *ac* susceptibility in a *dc* applied field of 1.5 kOe for **31** and **31**$_{Zn}$. Inset: Arrhenius plot for the relaxation times with QTM + direct + Raman and direct + Raman for **31** and **31**$_{Zn}$, respectively.

Compound **32** is the only compound that did not exhibit any out-of-phase signal even in the presence of an external magnetic field (Figure A4.11). Even though intramolecular ferromagnetic interactions were found similar to what we observed in the trinuclear compound **20** (see Chapter 3), it seems that the additional bridging carboxylate group modifies the relaxation dynamics for this system. We are currently waiting for theoretical calculations that may shed some light in this sense.

The heterometallic tetranuclear Co_2Dy_2 system **33** does not show any maxima in the $\chi'_M(T)$ and $\chi''_M(T)$ plots under zero *dc* field (Figure A4.11). The lack of SMM

behaviour in the absence of an external magnetic field could be attributed to weak exchange or dipolar Co-Dy interactions that may shortcut the relaxation processes by QTM. It has been seen in the literature that the combined 3d-4f systems where both of the metals are paramagnetic might have enhanced magnetic properties in comparison to 3d-4f systems where the 3d ion is diamagnetic [16]. In such systems, the collinear anisotropy axes of both ions and the relatively large exchange interactions are able to slow down the relaxation times and diminish the QTM regime. However, in many other combined systems the implementation of two paramagnetic ions may not be so fruitful [17]. The fast QTM was at least partially suppressed by applying an external magnetic field of 1 kOe (Figure A4.11). Moreover, the $\chi''_M(T)$ curve at 10,000 Hz displays two maxima, a former one at low temperatures (around 3 K) and a second one at high temperatures (around 25 K). According to the SMM behaviour observed for **36** (see later), the first maximum could be tentatively assigned to the relaxation related to the Co^{II} center, while the second one could be attributed to Dy^{III}.

With the aim of determining the optimum external magnetic field to maximally slow down the relaxation times for each process, two field dependent measurements were carried out at 2.0 K and 22.6 K. At 2.0 K and 250 Oe, the presence of two maxima indicates two relaxation processes (Figure A4.37). While augmenting the external magnetic field, it can be observed that the maximum at lower frequencies is moved towards even lower ones and besides covers the maximum at higher frequencies. We assume that the faster relaxation might be originated from Co^{II} centers, while the slower one may arise from a field induced direct relaxation, common feature in Co^{II} based magnets [18], or related to the relaxation of the Dy^{III} ion (see below the discussion for $\mathbf{33_Y}$). Unfortunately, the low frequency relaxation lies below the detection limit of the instrument, fact that prevents us of determining the optimum external field. At 22.6 K, maxima are shifted to lower frequencies indicating the slowing down of the relaxation times, fact that is clearly seen then in the $\tau^{-1}(H)$ plot (Figures A4.38-A4.39). Thus, the optimum external field was stablished at 2.5 kOe.

Measurements carried out at this external magnetic field revealed two set of well-defined maxima, the first one in the 2.0-3.0 K range and the second one between 12.0-27.0 K (Figure 4.10). However, the first set of maxima shows low frequency dependence with almost no shift in temperature from 60 to 10,000 Hz. To better estimate this effect, the ϕ parameter was calculated with the formula $\phi = \Delta T_p/[T_p\Delta(\log f)]$, where T_p is the peak temperature and f is the frequency. The frequency shifts from 200 to 10,000 Hz (we discarded the 60 Hz curve because of the evident

mixing of both maxima) gave a ϕ = 0.09 value, consistent with a glass-like behaviour [19]. The high temperature relaxation, in contrast, displays a noticeable frequency dependence, in agreement with SMM behaviour. Frequency dependent out-of-phase susceptibility curves were fitted in the 14.4-26.4 K temperature range obtaining relaxation times for each temperature (Figure A4.41). The curvature of the data in the Arrhenius plot, as well as the relatively large α values extracted from the Cole-Cole plots drove us to fit the relaxation times to a combined Orbach and Raman relaxation pathway (Equation 4.1), obtaining the following set of parameters: B = 9.8 $s^{-1}K^{-1.61}$, n = 1.61, τ_0 = $1.37 \cdot 10^{-8}$ s and U_{eff} = 203.0 K. As it is later discussed for compound **36**, the effective energy barrier for the magnetization reversal is notably lower than for **36** even measuring it at zero *dc* field. This suggests that the combination of two paramagnetic metal ions within this system causes faster relaxation times related to transverse fields that shortcut the mentioned barrier through QTM. However, it is worth mentioning that the height of it is still considered large, which can be explained by the suitable ligand field, later described for **36**.

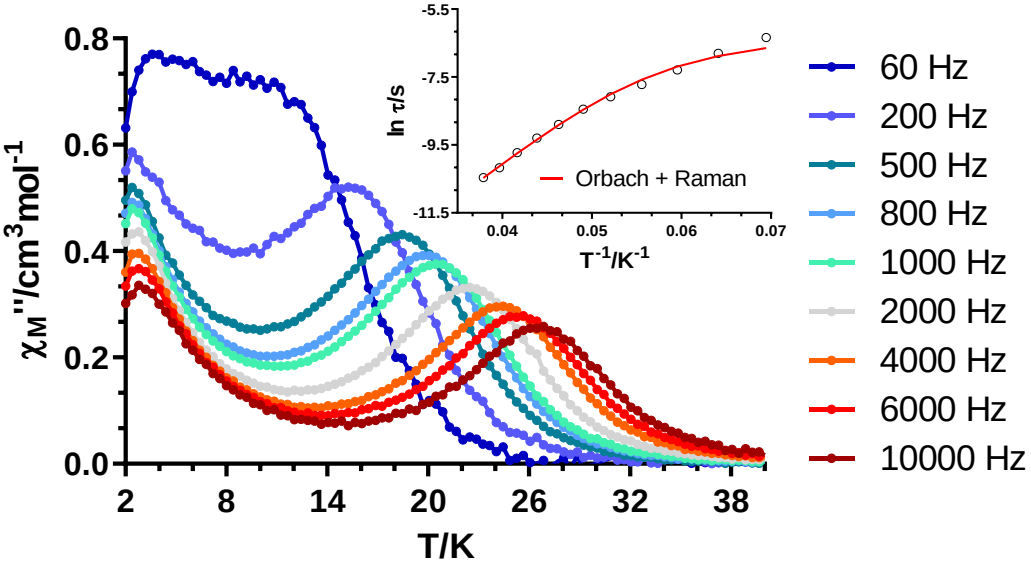

Figure 4.10.- Temperature dependence of the out-of-phase components of the *ac* susceptibility in a *dc* applied field of 2.5 kOe for **33**. Inset: Arrhenius plot for the relaxation times with simultaneous fitting considering Orbach + Raman.

As it has been done for compounds with a single type of paramagnetic center, the dilution effects on **33** were studied by individually diluting either the 3d ion with Zn^{II} or

the 4f ion with Y^{III}. Thus, another two derivatives of **33** were synthesized using 1:10 molar ratio of Co:Zn for $\mathbf{33_{Zn}}$ and 1:10 ratio of Dy:Y for $\mathbf{33_{Y}}$. By doing so, what we obtain in the crystal structure of $\mathbf{33_{Zn}}$ is the combination of a large amount of Zn_2Dy_2 (**36**), a considerably smaller part of the tetranuclear $ZnCoDy_2$ and, somewhat, few molecules of Co_2Dy_2 (**33**). Thus, it is not surprising that $\mathbf{33_{Zn}}$ behaves as a zero field SMM as it is shown in Figure 4.11. A thermally activated relaxation process is observed below 27.0 K, comparable to the relaxation that displays **36** in agreement with the greatest contribution of Zn_2Dy_2 system within the structure. At low temperatures, a pronounced contribution of QTM can be observed by the long tails below the maxima. In contrast to **36**, due to the nature of the data, $\chi''_M(\upsilon)$ curves allowed us to obtain the relaxation times for a wider temperature range (3.6-27.6, Figure A4.44), which at the same time provides us with a more extensive information according to relaxation dynamics, almost reaching temperatures where only QTM operates. In fact, relaxation times were fitted to the simultaneous presence of Orbach, Raman and QTM with Equation 4.4:

$$\tau^{-1} = \tau_{QTM}^{-1} + BT^n + \tau_0^{-1}exp(-U_{eff}/k_BT) \quad \textit{Equation 4.4}$$

The best fitting provide the following set of parameters: U_{eff} = 347.2 K, $\tau_0 = 9.0\cdot10^{-11}$ s, $B = 0.052$ $s^{-1}K^{-3.856}$, $n = 3.856$ and $\tau_{QTM} = 1.2\cdot10^{-3}$ s. The values related to Orbach and Raman are comparable to those obtained for **36** or $\mathbf{36_{Y}}$ under an external magnetic field. Regarding to the QTM mechanism, it is appreciable that its contribution is not perfectly portrayed in the fitting since even at 3.6 K the relaxation times still present a slight temperature dependence in contrast to the simulated fit (Figure 4.11 left, inset). We ascribe this to the fact that the QTM operates by itself at lower temperatures than 3.6 K as it can be observed in the remnant weak temperature dependence of the $\chi''_M(\upsilon)$ curves (Figure A4.44). Since we cannot achieve the relaxation times below this temperature, the fitting loses accuracy somehow. When the same measurements were repeated under an external magnetic field of 2.5 kOe (field selected according to the field dependent measurements carried out for **33** and **36**), QTM was successfully quenched and the contribution of Co^{II} centres came out at low temperatures (see Figure A4.46, $\chi'_M(T)$). However, no clear maximum was observed in the out-of-phase region even at the higher frequency (Figure 4.11, right). In this case, relaxation times were fitted to the combination of Orbach and Raman processes: U_{eff} = 334.8 K, $\tau_0 = 2.4\cdot10^{-10}$ s, $B = 1.0\cdot10^{-4}$ $s^{-1}K^{-5.648}$ and n = 5.648, almost identical values were obtained for **36** under an external magnetic field.

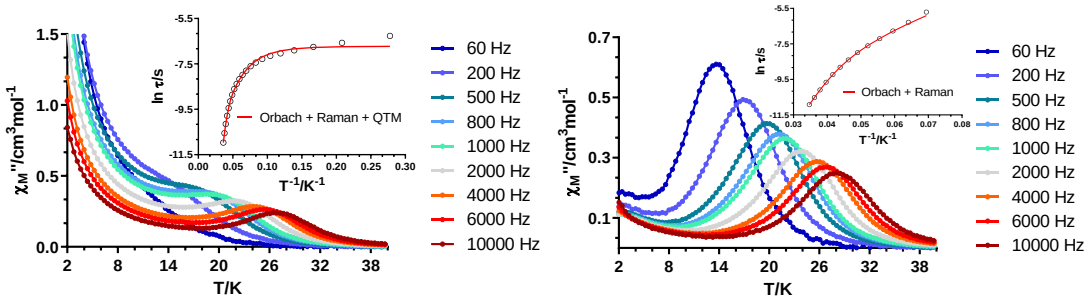

Figure 4.11.- Temperature dependence of the out-of-phase components of the *ac* susceptibility in a zero applied field (left) and under an external field of 2.5 kOe (right) for **33**$_{Zn}$. Inset: Arrhenius plot for the relaxation times with Orbach + Raman + QTM (left) and Orbach + Raman (right).

In the case of **33**$_{Y}$, the situation is reverted and the main system in the structure will be Co_2Y_2, followed by a substantially smaller amount of Co_2DyY and a vast minority of Co_2Dy_2. Thus, the lack of SMM behaviour at zero applied *dc* field was expected, since compounds **31** and **33** do not display slow relaxation of the magnetization in these conditions. When applying an external magnetic field of 1 kOe, two maxima are obtained, the first one below 4.0 K and a much less intense one below 26.0 K (Figure A4.49). We attribute the first one to the relaxation of Co^{II} ions, while the second corresponds to Dy^{III}. Field dependent measurements were carried out for the two individual processes. At 2.0 K, the $\chi''_M(\upsilon)$ curves shed some light to the behaviour observed for field dependent curves in **33**. Indeed, at 250 Oe a single maximum is observed at 2000 Hz (Figure A4.50, for **33** this same maximum is shifted towards higher frequencies). However, the data at all external fields were fitted for frequencies above 200 Hz, since below it the χ''_M value is clearly affected by the relaxation of the Dy^{III}, which in **33** was probably covering the relaxation related to Co^{II} due to the higher concentration (solid lines in Figure A4.50 represent the best fit, while dashed lines are a guide to the eye; no reasonable fitting was possible considering all points). For Dy^{III}, the field dependent measurements were performed at 22.6 K, concluding that an external magnetic field of 1.5 kOe was adequate for slowing down the relaxation times for both processes (Figures A4.51-A4.53).

When measuring *ac* dynamic magnetic properties for **33**$_{Y}$, the set of maxima at low temperature is not frequency independent anymore, the ϕ = 1.0 is consistent with a SMM behaviour, indeed (Figure 4.12). Although this system was measured under the

same external magnetic field as **33**, the maxima related to Co^{II} relaxation are moved towards lower temperatures, pointing out the influence of the Dy^{III} ions. The relaxation times were fitted by considering the simultaneous presence of Raman and QTM processes with Equation 4.5:

$$\tau^{-1} = BT^{n} + \tau_{QTM}^{-1} \qquad \textit{Equation 4.5}$$

The fitting afforded the following set of parameters: B = 128.4 $s^{-1}K^{-3.652}$, n = 3.652 and τ_{QTM} = $2.2 \cdot 10^{-4}$ s. Noteworthy, a reasonable fit could be also obtained by considering Raman and direct mechanisms with the following parameters: B = 23.9 $s^{-1}K^{-4.586}$, n = 4.586 and A = $5.34 \cdot 10^{6}$ $s^{-1}T^{-4}K^{-1}$. The inclusion of the three mechanisms, as in **33**, did not give any reasonable fit. The presence of multiple relaxation pathways is in agreement with the large α values (0.18 (2.0 K) – 0.36 (4.6 K)). In the case of the slower relaxation process related to Dy^{III}, the small proportion of the lanthanide within the structure leads to a weaker and noisier signal. Hence, the treatment of the data becomes slightly more complicated. In any case, in view of the results obtained for the rest of the compounds including Dy^{III}, we were forced to fix the parameter of U_{eff} with a value of 350.0 K to undertake good fit of the data. Otherwise, the fitting of the relaxation times considering the simultaneous presence of Orbach and Raman (α values of 0.46 and 0.12 at 13.6 and 25.6 K, respectively, suggest a wide distribution of mechanisms) afforded non-reasonable values. Thus, from the best fitting we obtained the following set of parameters: U_{eff} = 350.0 K, τ_0 = $3.7 \cdot 10^{-11}$ s, B = $8.7 \cdot 10^{-3}$ $s^{-1}K^{-4.476}$ and n = 4.476.

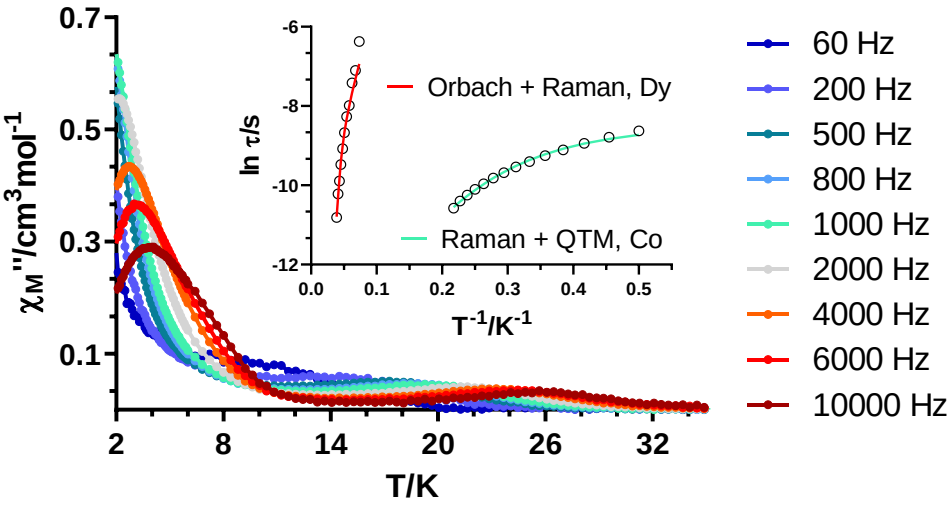

Figure 4.12.- Temperature dependence of the out-of-phase components of the *ac* susceptibility in a *dc* applied field of 1.5 kOe for $\mathbf{33_Y}$. Inset: Arrhenius plot for the relaxation times with simultaneous fitting considering Orbach + Raman for Dy^{III} and Raman + QTM for Co^{II}.

The oblate character of the trivalent terbium ion makes **35** to be a potential candidate for displaying SMM behaviour. However, *ac* measurements at zero *dc* field do not display any signal in the out-of-phase susceptibility (Figure A4.12). Although the fast QTM was partially suppressed when applying an external magnetic field of 1 kOe, still no clear maximum was observed at the highest measured frequency (Figure A4.12). This behaviour is not completely unexpected since for non-Kramers ions QTM is allowed and deviations from ideal symmetries enhance transverse components that at the same time intensify this relaxation mechanism [20]. As a final attempt, diamagnetically diluted **35$_Y$** was studied under an external magnetic field of 1 kOe, which showed a well-defined maximum below 4 K (Figure A4.12). Field dependent measurements revealed that this field was the optimum to suppress, at least partly, the QTM. Besides, above it, the presence of a field induced direct process is magnified (Figures A4.59-A4.60). The relaxation times at different external magnetic fields were fitted to the following equation:

$$\tau^{-1} = \frac{B_1}{1 + B_2 \cdot H^2} + AH^2T + k \quad Equation\ 4.6$$

In this case the direct process is described by AH^2, since Tb^{III} is a non-Kramers ion [21]. The fit afforded B_1 = 18096 s^{-1}, B_2 = 291.9 T^{-2}, A = 146744 $s^{-1}T^{-2}K^{-1}$ and k = 4193 s^{-1}. Afterwards, a complete measurement was performed for **35$_Y$** with an external *dc* field of 1 kOe (Figure 4.13). The $\chi''_M(\upsilon)$ curves were fitted in 2.0-3.8 K range obtaining relaxation times for each temperature (Figure A4.62). Relaxation times were fitted to Equation 4.3 (but considering a quadratic field dependence for the direct mechanism) considering simultaneous QTM, direct and Raman processes. A good fit was obtained by fixing τ_{QTM}^{-1} and A to 4618 s^{-1} and 146744 $s^{-1}T^{-2}K^{-1}$, which provided B = 913.4 $s^{-1}K^{-2.746}$ and n = 2.746. Even though we included the three mechanisms, the Raman process dominates the whole temperature range.

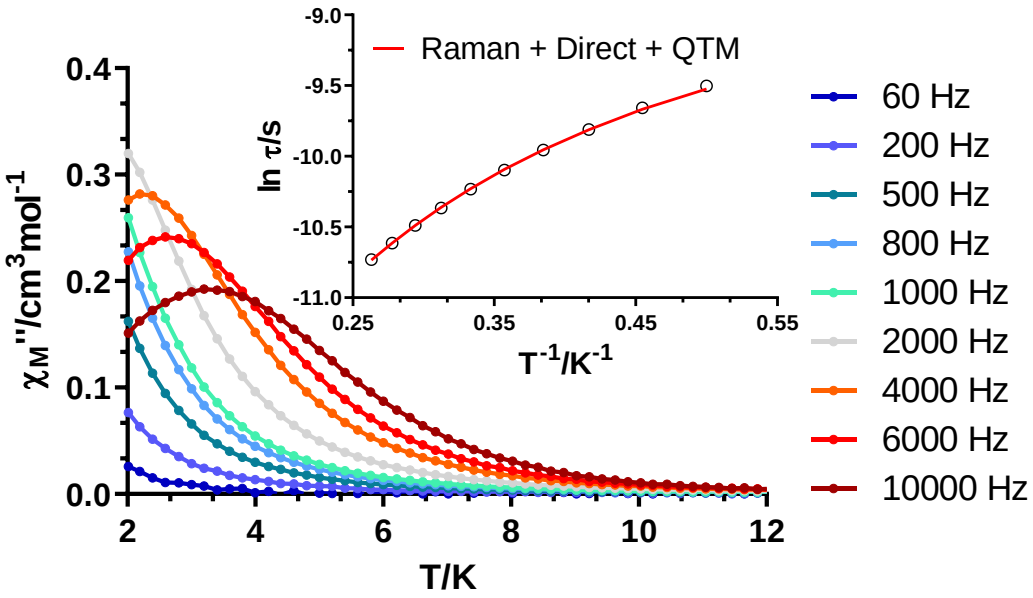

Figure 4.13.- Temperature dependence of the out-of-phase components of the *ac* susceptibility in a *dc* applied field of 1 kOe for **35**$_{Y}$. Inset: Arrhenius plot for the relaxation times with simultaneous fitting considering Raman + Direct + QTM.

As mentioned at the beginning of the section, compound **36** behaves as zero field SMM. In Figure 4.14 it can be seen that **36** displays maxima below 28 K, where temperature dependent relaxation mechanisms operate. In contrast, the long tails below the maxima and at low temperatures indicate the presence of quantum tunnelling of the magnetization. Relaxation times were obtained for the 17.2-27.6 K temperature range and the Arrhenius plot was constructed. Even though the curvature of the plot and the α values extracted from the Cole-Cole's (0.24(17.2 K)-0.23(27.6 K)) suggest a wide distribution of the relaxation processes, we were not able to obtain a reliable fitting of the data. Hence, from the linear portion of the high temperature regime we obtained U_{eff} and τ_0 values of 261.0 K and $2.1 \cdot 10^{-9}$ s. When considering the simultaneous presence of Raman and Orbach relaxation processes, the fitting provided non-reasonable *n* values that were out of the range related to Kramers ions (apart from an excessive U_{eff} value). The evidence of QTM provided by the long tails led us to consider implementing it within the equation. However, the $\chi''_M(\upsilon)$ curves and the Arrhenius plot do not show any temperature independent regime. This is due to the fact that the frequency range we employed to obtain relaxation times is over the QTM scope.

Anyway, with the aim of qualitatively investigating the field and dilution effects upon QTM, both quenching techniques were applied. Dynamic magnetic properties of **36** were firstly analysed under the optimum external magnetic field of 1 kOe (Figures A4.67-A4.68). As predicted, a huge part of QTM was quenched, tails below the maxima were not so prominent, and therefore all the maxima were better defined even at low frequencies (Figure 4.14, bottom left). In this occasion we were able to simultaneously fit the relaxation time data to Orbach and Raman processes. The best fit provided the subsequent set of parameters: U_{eff} = 342.4 K and τ_0 = $2.4 \cdot 10^{-10}$ s for Orbach and B = $4.9 \cdot 10^{-4}$ $s^{-1}K^{-5.112}$ and n = 5.112 for Raman. The diluted analogue **36$_Y$** was measured according to the same experimental conditions, which proved that avoiding intra- and intermolecular interactions and applying an external magnetic field contributes to a complete vanishing of QTM at low temperatures (Figure 4.14, bottom right). At high temperatures, in contrast, the relaxation dynamics are comparable to **36** under the external magnetic field. In fact, the fitting of the relaxation times to the same processes afforded similar parameters: U_{eff} = 326.7 K and τ_0 = $1.5 \cdot 10^{-10}$ s for Orbach and B = $1.0 \cdot 10^{-4}$ $s^{-1}K^{-5.640}$ and n = 5.640 for Raman.

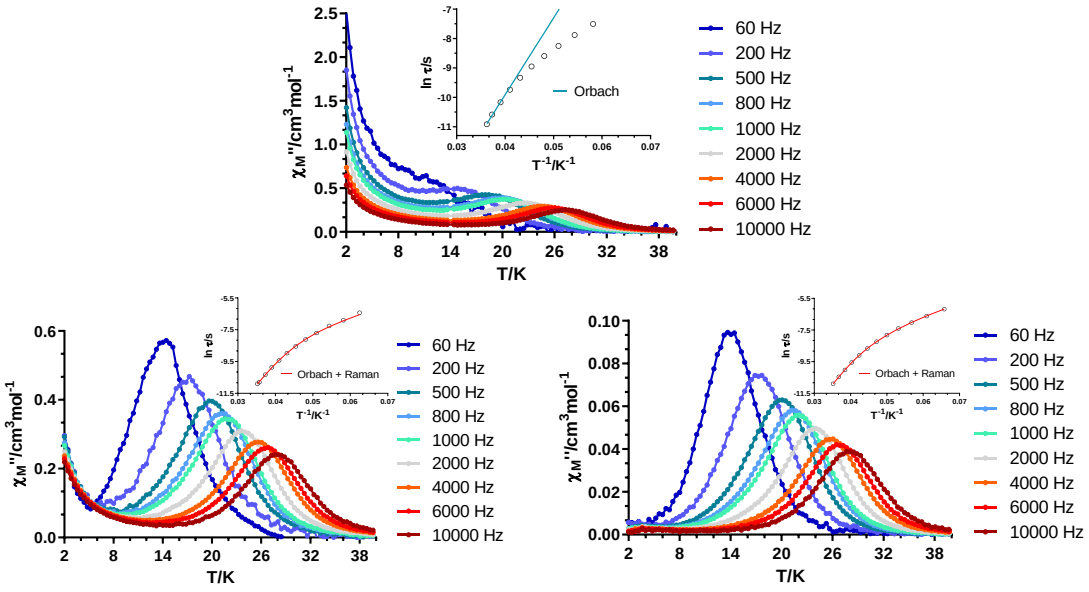

Figure 4.14.- Temperature dependence of the out-of-phase components of the *ac* susceptibility in a zero applied field (top) and under an external field of 1 kOe (bottom left) for **36** and under the same external field for **36$_Y$** (bottom right). Inset: Arrhenius plot for the relaxation times with Orbach (blue) and simultaneous fitting considering Orbach + Raman (red).

In spite of the fact that the coordination environment of **36** contains an important similarity to that of **30**, the replacement of the second nitrate (or chelating acetate) by other phenoxido and methoxy groups remarkably improves its SMM behaviour. Indeed, the Dy-O7 bond becomes the shortest between all Dy-O possible bonds and, inherently, this bond is now responsible of defining the orientation of the easy axis of magnetization according to Magellan software (Figure A4.84). The angle between the anisotropy axis and Dy-O7 bond is of 2.11º, from where we conclude that O7 is the heteroatom that provokes most of the axiality within the ground state. Moreover, as it was mentioned in the crystal structure description, the other two phenoxido groups that bridge Zn^{II} and Dy^{III} ions are located somehow in trans position, so that the angles between the anisotropy axis and Dy-O1 and Dy-O3 are relatively small, 42.41º and 34.62º, respectively. Furthermore, the strong axiality is accompanied by a weak equatorial ligand field, constituted of a nitrate, carboxylate and methoxy groups, which are known to generate softer fields, besides they are farer from the Dy^{III} ion. All in all, the serendipitous formation of such a coordination environment has been proven to be suitable to enhance the anisotropy of the trivalent dysprosium ion.

Once proved the suitability of the ligand when enhancing the magnetic anisotropy of the Dy^{III} ion, we moved to Er^{III}, which in terms of electron density distribution, the highest M_J = ±15/2 sublevels possess a prolate shape. It has been seen in the literature that in order to stabilize these sublevels as ground state and well separated from excited states, strong equatorial ligand fields should be surrounding the ion [22]. Thus, we did not expect significant SMM behaviour for **37**. Indeed, *ac* measurements under zero field revealed the lack of signal in the out-of-phase region (Figure A4.13). Subsequently, measurements were repeated under an optimum external *dc* field of 500 Oe (see next section for $\mathbf{37_Y}$) partially suppressing the QTM and uncovering field induced SMM behaviour (Figure 4.15). As it occurs with **30**, two relaxation processes are found, a FR occurring below 3.5 K and a SR below 7.0 K. In the present case, both sets of maxima are much closer than in **30**, which prevents us of fulfilling the same analysis of the data. Indeed, at low temperature the $\chi''_M(\upsilon)$ and $\chi''_M(\chi'_M)$ plots (Figures A4.76-A4.77) display broad maxima and semicircles, respectively, suggesting that both FR and SR are operative in that temperature range. Thus, due to the fact that they overlap, there is no way to select two temperature and frequency ranges to independently fit them.

Consequently, $\chi''_M(\chi'_M)$ plots were analysed in the 2.0-6.4 K temperature range using the CCFIT software obtaining relaxation times for each temperature. Arrhenius

plots for FR and SR are depicted in the inset of Figure 4.15. In the case of FR, α values suggest a wide distribution of relaxation mechanisms (0.10(2.0 K)-0.38(4.0 K)), but this could be justified by the mixing of both processes as the temperature is increased. Thus, in view of the linear tendency in the whole temperature range, relaxation times were fitted to a single Orbach process with U_{eff} = 5.0 K and $\tau_0 = 9.9 \cdot 10^{-6}$ s. In contrast, the relaxation times for SR where fitted in the 2.0-6.4 K range, since the maxima are visible in this region. The curvature of the relaxation times along with the large α values (0.40 (2.0 K)-~0(6.4 K)) suggest the presence of diverse mechanisms operating in SR. In addition, the tails around 2.0 K for the lowest frequencies might be due to the non-quenched QTM. Hence, relaxation times were fitted to Equation 4.4 that encompasses Orbach, Raman and QTM. The best fitting provide the following set of parameters: U_{eff} = 55.4 K, $\tau_0 = 7.7 \cdot 10^{-9}$ s, B = 5.538 $s^{-1}K^{-4.323}$, n = 4.323 and $\tau_{QTM} = 3.4 \cdot 10^{-3}$ s.

With the aim of further quenching the residual QTM and shedding some light related to the presence of two maxima, **37$_Y$** was synthesized and its dynamic magnetic properties were studied. At zero applied *dc* field, although no clear maximum is observed, a shoulder is visible both in the in phase and out-of-phase components indicating SMM behaviour (Figure A4.13). The field dependent measurements revealed an optimum external field of 500 Oe (Figures A4.78-A4.79). When accomplishing the temperature dependent measurements under this optimum *dc* field, we concluded that (i) the residual QTM was successfully supressed (maxima at low frequencies are better defined and do not display any tails) and (ii) the maxima related to FR disappeared. This latter fact clearly indicates that the SR has its origin in the single ion, whereas FR was originated from intra- or intermolecular interactions. Once fitted the $\chi''_M(\upsilon)$ data and plotting the relaxation times within the Arrhenius plot, our initial statements were proved. The relaxation times were fitted to the simultaneous presence of Orbach and Raman, pointing out that the remnant QTM in the non-diluted sample was successfully eliminated for **37$_Y$**. The fitting afforded B, n, U_{eff} and τ_0 values of 1.044 $s^{-1}K^{-5.583}$, 5.583, $7.2 \cdot 10^{-11}$ s^{-1} and 93.0 K, respectively, indicating a remarkable enhancement in the anisotropy barrier provided by the quenching of QTM.

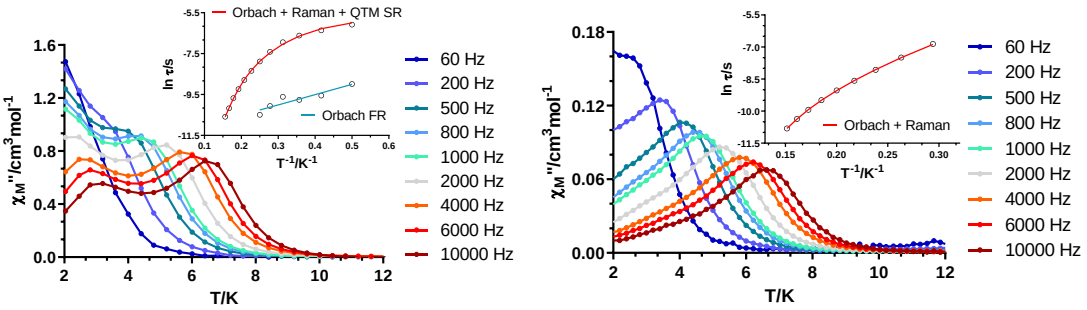

Figure 4.15.- Temperature dependence of the out-of-phase components of the *ac* susceptibility in a *dc* applied field of 500 Oe for **37** (left) and **37$_Y$** (right). Insets: Arrhenius plots for the relaxation times with Orbach (blue, FR) and Orbach + Raman + QTM (red, SR) for **37** and Orbach + Raman (red) for **37$_Y$**.

Although the results obtained for **36** confirmed our expectations regarding to the suitability of the ligand field when enhancing the SMM behaviour mostly for oblate ions, in view of the field induced slow relaxation of **37** (and remarkable shoulders in $\chi''_M(T)$ for **37$_Y$** at zero applied *dc* field), we wanted to find some magneto-structural correlation to explain such a behaviour. According to the prolate nature of Er^{III}, strong equatorial ligand fields are required to design zero field SMMs. Even though this is not the case, we think that in the same way that the ligands are not located in a strict axial fashion, an equatorial nature might be appreciated somehow. One of the most highly performing Er^{III} based SMM was studied by Tang *et al*. [22]. They described a three coordinated flat trigonal pyramid with an effective energy barrier of U_{eff} = 122 K at zero applied *dc* field, which besides displays a butterfly shaped hysteresis loop at 1.9 K. This coordination environment is responsible of stabilizing the M_J = ±15/2 doublet as ground state and well separated from excited states. In our case, the equatorial ligand field might be carefully assumed by the same heteroatoms we used to describe the axial ligand field for **36**. Although far from an ideal C_3 symmetry, where angles should be of 120º, the phenoxido groups form angles of 66.0(2), 137.3(1) and 143.7(1)º for O1-Dy-O3, O1-Dy-O7 and O3-Dy-O7, respectively. As mentioned, this ligand field has been proven to be more adequate for Dy^{III}, but it is also somehow able to provide an equatorial character.

Table 4.1.- U_{eff}, τ_0, B, n, τ_{QTM} and A parameters generated from the fit of the relaxation time-temperature dependence for **30**, **30$_Y$**, **31**, **33**, **33$_{Zn}$**, **33$_Y$**, **36**, **36$_Y$**, **37** and **37$_Y$**. (*) 4 and 2 for Kramers and non-Kramers ions, respectively.

	***dc* field**	**Orbach**		**Raman**		**QTM**	**Direct**
Comp.	kOe	U_{eff} (K)	τ_0 (s)	B ($s^{-1}K^{-n}$)	n	τ_{QTM} (s)	A ($s^{-1}T^{-*}K^{-1}$)
30	2.5	9.2 (FR) 69.1 (SR)	$8.3\cdot10^{-7}$ $1.1\cdot10^{-7}$				
30$_Y$	2.5	46.8 (FR) 94.0 (SR)	$2.6\cdot10^{-10}$ $1.6\cdot10^{-8}$	285.4	2.04		
31	1.5			377.5	2.66	$1.3\cdot10^{-3}$	$6.00\cdot10^{4}$
31$_Y$	1.5			0.14	6.18		$5.43\cdot10^{5}$
33	2.5	203.0	$1.4\cdot10^{-8}$	9.8	1.61		
33$_{Zn}$	0 2.5	347.2 334.8	$9.0\cdot10^{-11}$ $2.4\cdot10^{-10}$	0.052 $1.0\cdot10^{-4}$	3.86 5.65	$1.2\cdot10^{-3}$	
33$_Y$ Co	1.5			128.4	3.65	$2.2\cdot10^{-4}$	
33$_Y$ Dy		350.0	$3.7\cdot10^{-11}$	$8.7\cdot10^{-3}$	4.48		
35$_Y$	1			913.4	2.75	$2.2\cdot10^{-4}$	$1.45\cdot10^{5}$
36	0 1	261.0 342.4	$2.1\cdot10^{-9}$ $2.4\cdot10^{-10}$	$4.9\cdot10^{-4}$	5.11		
36$_Y$	1	326.7	$1.5\cdot10^{-10}$	$1.0\cdot10^{-4}$	5.64		
37	0.5	5.0 (FR) 55.4 (SR)	$9.9\cdot10^{-6}$ $7.7\cdot10^{-9}$	5.538	4.32	$3.4\cdot10^{-3}$	
37$_Y$	0.5	93.0	$7.2\cdot10^{-11}$	1.044	5.58		

4.4.4. Hysteretic behaviour of complexes 33$_{Zn}$ and 36

We performed magnetization hysteresis loop measurements on powdered samples of **33$_{Zn}$** and **36** at 2 K with the aim of confirming the SMM behaviour (Figure 4.16). Note that the employed sweep-rates were not constant over the entire field range, but were slower at low fields. For **33$_{Zn}$**, the average sweep-rate in the 0.55 to -0.55 T and -0.55 to 0.55 T was the same, 70 Oe/s (being slower at low fields and faster at high fields). In contrast, **36** was measured with a sweep-rate of 77 Oe/s in the 0.44 to -0.63 T range and 88 Oe/s in the -0.44 to 0.63 T range. Both compounds exhibited butterfly-shaped hysteresis loops without any remnant magnetization at zero field. This is consistent with the QTM regime also found in the $\chi''_M(T)$ plots by the long tails at lowest temperatures. The slightly larger opening of the loop in **36** might be explained by the faster sweep-rate employed in the experiment, but overall we believe that a similar behaviour is observed for both compounds.

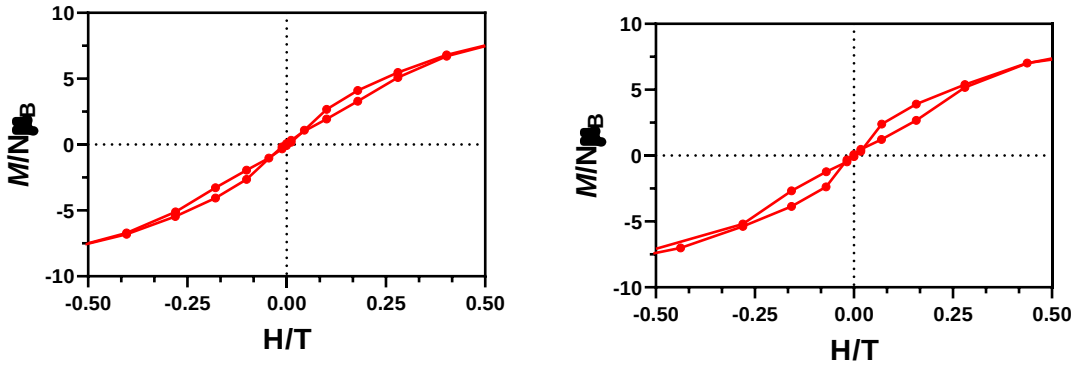

Figure 4.16.- Magnetic hysteresis loops for **33**$_{Zn}$ (left) and **36** (right) for *H* values between -0.5 T and 0.5 T at 2 K and at the indicated sweep rates.

4.4.5. Pulse magnetization measurements for 33, 33$_{Zn}$, 36 and 36$_{Y}$

To further study the magnetization dynamics of the most promising compounds, we measured the magnetization curves in a full cycle pulsed magnetic field for **33**, **33**$_{Zn}$, **36** and **36**$_{Y}$ (Figure 4.17) [23]. These experiments were performed during a one month stay in the Institue for Materials Research (Tohoku University, Sendai) under the supervision of Prof. Hiroyuki Nojiri.

These measurements were carried out at 0.4 K with a maximum field of 10.4 T. These measurements allow us to observe much larger hysteresis loops, since the sweep-rates are extremely fast compared to what we used in the previous section, specifically 4.2 T/ms. It is important to note that the strength is not symmetric between the positive and negative directions of the magnet during the pulsing (Figure A4.85).

First of all, we compared **33** and **36**. As deducted from the *ac* data, a large contribution of QTM was expected for the former one considering that it does not behave as zero field SMM. Indeed, even if an opening of the loop is observed at low fields, around zero field a sharp reversal is observed with a consequent negligible (in comparison to the others) coercive field of 0.14 T (Figure 4.17, inset). In contrast, the zero field SMM **36** displays a clear open loop even at zero field, in agreement to the *ac* data and butterfly shape hysteresis loops with slower sweep-rates. Besides, a larger coercive field of 0.75 T was measured for this compound. Surprisingly, the diamagnetically diluted **33**$_{Zn}$ (or in other words, compound **36** doped with Co^{II}) displayed a huge hysteresis loop compared to **36** with a notably lower contribution of QTM at zero field. In fact, the coercive field was calculated to be more than double, 2.0

T. In other words, the remnant magnetization at zero field is also higher for the diluted compound, having 57.5%, 63.5% and 67.6% of the saturation values for **33**, **36** and **33**$_{Zn}$, respectively at zero field. For some reason, a low concentration of Co^{II} replacing Zn^{II} ions favors the SMM behaviour quenching the undesired QTM. Currently, we are trying to better understand the obtained result, since it has been unexpected.

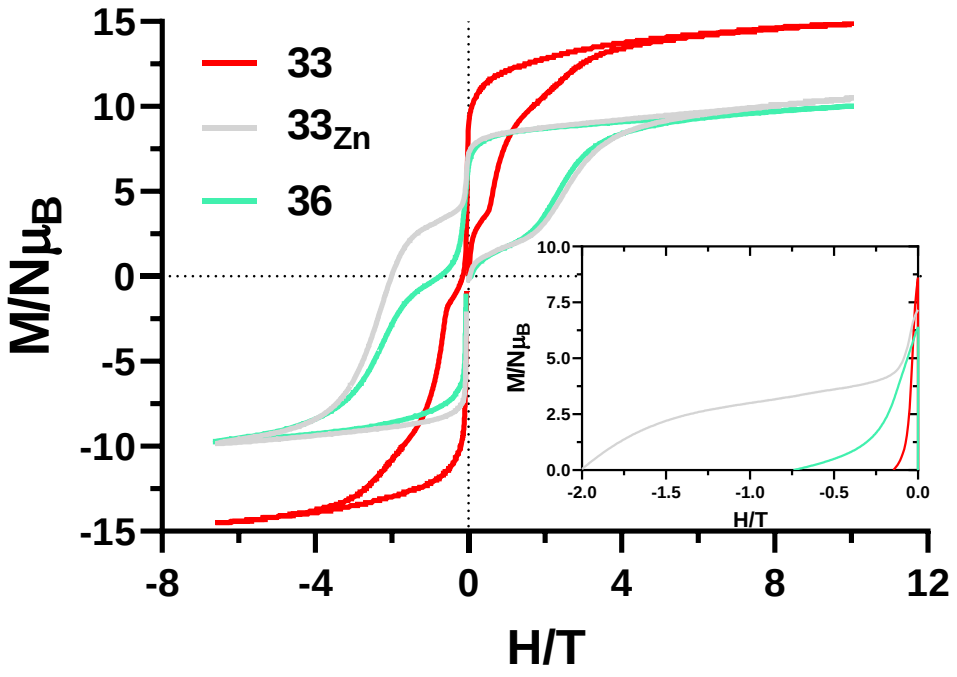

Figure 4.17.- Pulsed-field magnetization curves at maximum field of 10.4 T and 0.4 K for **33**, **33**$_{Zn}$ and **36**. Inset: Expansion of the loop to compare coercive fields.

Furthermore, we also studied compound **36**$_{Y}$, which was synthesized to avoid intra- and intermolecular Dy···Dy interactions that could facilitate QTM (Figure 4.18). Similarly to what we observed in *ac* measurements, QTM was at least partially quenched and the loops we observed for this diluted counterpart were even more pronounced than for **33**$_{Zn}$.

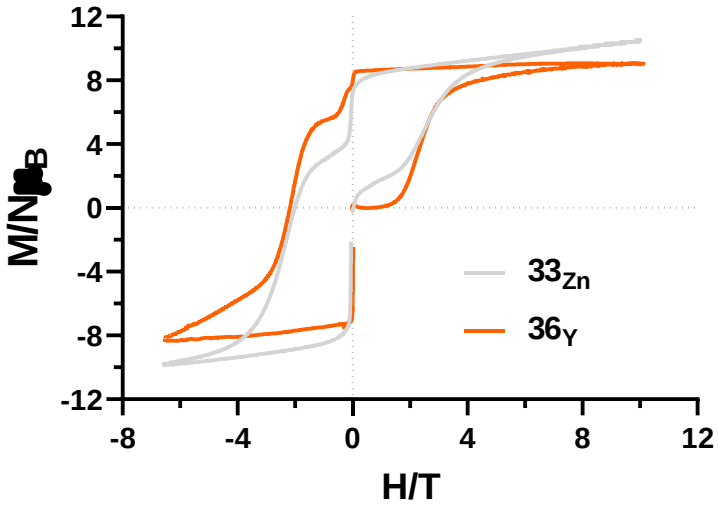

Figure 4.18.- Pulsed-field magnetization curves at maximum field of 10.4 T and 0.4 K for **33**$_{Zn}$ and **36**$_{Y}$. Note that the values of **36**$_{Y}$ have been normalized to obtain two comparable loops.

4.5. CONCLUSIONS

The initial results related to compounds **28** and **30** were found to be very promising. The disposition of the ligand in the dinuclear Cu^{II} based compound showed that H_4L^4 was probably a good candidate to synthesize one dimensional compounds. Furthermore, the acetate bridged Zn_2Dy_2 complex **30** displayed the expected arrangement of the metal ions, being a very similar structure in terms of coordination environments to the previously reported ZnLn dinuclear compounds and the polynuclear systems described in Chapter 2. More interestingly, two slightly different compounds cocyrstallized in **30**. Even though we are still waiting for theoretical calculations, we believe that each of the compounds displays an independent relaxation pathway, since the axiality of the Dy^{III} might be better defined in **30B** than in **30A**. Indeed, **30B** displays an acetate group trans to the phenoxido groups that provide the axiality to the system, whereas **30A** contains a less electron donating nitrate. Hence, a larger energy splitting between the ground and excited states is expected for **30B** showing enhanced magnetic properties.

When we incorporated the bridging succinate with the aim of extending the structure within 1D, a serendipitous formation of a cationic tetranuclear Zn_2Dy_2 system was observed. Luckily, the coordination environment around the Dy^{III} ion was improved

due to the presence of an additional phenoxido group somehow trans to the other two $Zn^{II}Dy^{III}$ bridging phenoxido groups. Consequently, compound **36** was determined to be a zero field SMM with a high U_{eff} of around 260 K. Additionally, several other isostructural compounds were studied based on different combinations of 3d-4f ions, as well as a wide variety of dilutions. In contrast to what we observed in Chapter 3, the incorporation of both 3d and 4f paramagnetic ions worsened the dynamic magnetic behaviour for **33**, being a field induced SMM. As a last concluding remark, even though in terms of blocking temperature (determined from FC/ZFC and hysteresis loops) $\mathbf{33_{Zn}}$ and **36** looked similar, pulse magnetization studies revealed a notably larger hysteresis loop for the former. A fact that we are still trying to comprehend.

4.6. REFERENCES

[1] A. Zabala-Lekuona, J. Cepeda, I. Oyarzabal, A. Rodríguez-Diéguez, J.A. García, J.M. Seco, E. Colacio, Rational design of triple-bridged dinuclear Zn ^{II} Ln ^{III} -based complexes: a structural, magnetic and luminescence study, CrystEngComm. 19 (2017) 256–264. https://doi.org/10.1039/C6CE02240E.

[2] M. Llunell, D. Casanova, J. Cirera, J.M. Bofill, P. Alemany, S. Alvarez, M. Pinsky, D. Avnir, SHAPE, (2005).

[3] K.R. Meihaus, J.R. Long, Magnetic blocking at 10 K and a Dipolar-mediated avalanche in salts of the bis(η8-cyclooctatetraenide) complex [Er(COT)2] -, J. Am. Chem. Soc. 135 (2013) 17952–17957. https://doi.org/10.1021/ja4094814.

[4] J. Luzon, K. Bernot, I.J. Hewitt, C.E. Anson, A.K. Powell, R. Sessoli, Spin chirality in a molecular dysprosium triangle: The archetype of the noncollinear ising model, Phys. Rev. Lett. 100 (2008) 247205. https://doi.org/10.1103/PhysRevLett.100.247205.

[5] K.R. Meihaus, J.D. Rinehart, J.R. Long, Dilution-Induced Slow Magnetic Relaxation and Anomalous Hysteresis in Trigonal Prismatic Dysprosium(III) and Uranium(III) Complexes, Inorg. Chem. 50 (2011) 8484–8489. https://doi.org/10.1021/ic201078r.

[6] R.J. Blagg, L. Ungur, F. Tuna, J. Speak, P. Comar, D. Collison, W. Wernsdorfer, E.J.L. McInnes, L.F. Chibotaru, R.E.P. Winpenny, Magnetic relaxation pathways in lanthanide single-molecule magnets., Nat. Chem. 5 (2013) 673–678. https://doi.org/10.1038/nchem.1707.

[7] D. Reta, N.F. Chilton, Uncertainty estimates for magnetic relaxation times and magnetic relaxation parameters, Phys. Chem. Chem. Phys. 21 (2019) 23567–23575. https://doi.org/10.1039/c9cp04301b.

[8] A. Arauzo, A. Lazarescu, S. Shova, E. Bartolomé, R. Cases, J. Luzón, J. Bartolomé, C. Turta, Structural and magnetic properties of some lanthanide (Ln = Eu(iii), Gd(iii) and Nd(iii)) cyanoacetate polymers: Field-induced slow magnetic relaxation in the Gd and Nd substitutions, Dalton Trans. 43 (2014) 12342–12356. https://doi.org/10.1039/c4dt01104j.

[9] A.A. García-Valdivia, A. Zabala-Lekuona, A. Goñi-Cárdenas, B. Fernández, J.A. García, J.F. Quílez del Moral, J. Cepeda, A. Rodríguez-Diéguez, Dilution effect on the slow relaxation of a luminescent dysprosium Metal-Organic Framework based on 2,5-dihydroxyterephthalic acid, Inorganica Chim. Acta. 509 (2020) 119687. https://doi.org/10.1016/j.ica.2020.119687.

[10] E. Echenique-Errandonea, A. Zabala-Lekuona, J. Cepeda, A. Rodríguez-Diéguez, J.M. Seco, I. Oyarzabal, E. Colacio, Effect of the change of the ancillary carboxylate bridging ligand on the SMM and luminescence properties of a series of carboxylate-diphenoxido triply bridged dinuclear ZnLn and tetranuclear Zn 2 Ln 2 complexes (Ln = Dy, Er), Dalton Trans. 48 (2019) 190–201. https://doi.org/10.1039/c8dt03800g.

[11] C. Shi, R. Nie, X. Yao, S. Fan, G. An, Y. Dong, G. Li, Asymmetry-unit-dominated double slow-relaxation modes of 2,6-dimethyl-3,5-heptanedione dysprosium SMMs, RSC Adv. 7 (2017) 49701–49709. https://doi.org/10.1039/c7ra09711e.

[12] J. Ruiz, A.J. Mota, A. Rodríguez-Diéguez, S. Titos, J.M. Herrera, E. Ruiz, E. Cremades, J.P. Costes, E. Colacio, Field and dilution effects on the slow relaxation of a luminescent DyO9 low-symmetry single-ion magnet, Chem. Commun. 48 (2012) 7916–7918. https://doi.org/10.1039/c2cc32518g.

[13] J. Rinehart, J. Long, Exploiting single-ion anisotropy in the design of f-element single-molecule

magnets, Chem. Sci. 2 (2011) 2078–2085. https://doi.org/10.1039/c1sc00513h.
[14] F. Habib, G. Brunet, V. Vieru, I. Korobkov, L.F. Chibotaru, M. Murugesu, Significant enhancement of energy barriers in dinuclear dysprosium single-molecule magnets through electron-withdrawing effects, J. Am. Chem. Soc. 135 (2013) 13242–13245. https://doi.org/10.1021/ja404846s.
[15] N.F. Chilton, D. Collison, E.J.L. McInnes, R.E.P. Winpenny, A. Soncini, An electrostatic model for the determination of magnetic anisotropy in dysprosium complexes, Nat. Commun. 4 (2013) 1–7. https://doi.org/10.1038/ncomms3551.
[16] S.K. Langley, D.P. Wielechowski, V. Vieru, N.F. Chilton, B. Moubaraki, B.F. Abrahams, L.F. Chibotaru, K.S. Murray, A {CrIII2DyIII2} single-molecule magnet: Enhancing the blocking temperature through 3d magnetic exchange, Angew. Chem. Int. Ed. 52 (2013) 12014–12019. https://doi.org/10.1002/anie.201306329.
[17] T. Gupta, M.F. Beg, G. Rajaraman, Role of Single-Ion Anisotropy and Magnetic Exchange Interactions in Suppressing Zero-Field Tunnelling in {3d-4f} Single Molecule Magnets, Inorg. Chem. 55 (2016) 11201–11215. https://doi.org/10.1021/acs.inorgchem.6b01831.
[18] O. Pajuelo-Corral, A. Zabala-Lekuona, E. San Sebastian, A. Rodríguez-Diéguez, J.A. García, L. Lezama, E. Colacio, J.M. Seco, J. Cepeda, Modulating Magnetic and Photoluminescence Properties in 2-Aminonicotinate-Based Bifunctional Coordination Polymers by Merging 3d Metal Ions, Chem. – A Eur. J. 26 (2020) 13484–13498. https://doi.org/10.1002/chem.202002755.
[19] J.A. Mydosh, Spin Glasses, Taylor & Francis: Washington, DC, 1993. https://doi.org/10.1201/9781482295191.
[20] J.H. Van Vleck, Paramagnetic relaxation times for titanium and chrome alum, Phys. Rev. 57 (1940) 426–447. https://doi.org/10.1103/PhysRev.57.426.
[21] A. Abragam, B. Bleaney, Electron Paramagnetic Resonance of Transition Ions, Clarendon Press Oxford, UK,. (1970) 925.
[22] P. Zhang, L. Zhang, C. Wang, S. Xue, S.Y. Lin, J. Tang, Equatorially coordinated lanthanide single ion magnets, J. Am. Chem. Soc. 136 (2014) 4484–4487. https://doi.org/10.1021/ja500793x.
[23] K. Saito, S. Miyashita, Magnetic Foehn Effect in Adiabatic Transition, J. Phys. Soc. Japan. 70 (2001) 3385–3390. https://doi.org/10.1143/JPSJ.70.3385.

CHAPTER 5

R- AND S-METHYLSUCCINATE INDUCED ENANTIOSPECIFIC FORMATION OF NOVEL $Zn^{II}_2Ln^{III}_2$ BASED TETRANUCLEAR COMPOUNDS: A STUDY OF THE MAGNETIC AND PHOTOLUMINESCENT PROPERTIES

5.1. INTRODUCTION

This chapter is a direct continuation of Chapter 4. In it, we have seen that within the tetranuclear systems (**31-37**) two enantiomers are formed due to the formation of two quaternary amines. The lack of any chiral inductor that could shift the equilibrium towards a certain enantiomer provokes that both cocrystallize within the same crystal structure giving rise to a racemate. However, considering the position of the bridging succinate we believed that, perhaps, a stereospecific formation of a specific enantiomer could be achieved.

Additionally, considering that we studied only the magnetic properties of those tetranuclear systems, we were also intrigued by the possibility of employing several other lanthanides that could give rise to other interesting properties such as photoluminescent ones. In order to do that, Sm^{III}, Eu^{III} or Tb^{III} could be considered as good candidates for bright luminescent emissive properties. Moreover, combining both chirality and luminescence could induce circularly polarized luminescence (CPL), another interesting property among lanthanide systems.

Thus, this chapter collects the synthesis, structural characterization and study of magnetic, luminescent and chiroptical properties of some novel tetranuclear systems that are very similar to the ones we studied in the previous chapter. However, for the present case, we have employed enantiopure R- and S-methylsuccinates as bridging ligands. Moreover, we have done a simple theoretical study in order to support the experimental results related to the chirality of the complexes.

5.2. PREPARATION OF COMPLEXES

5.2.1. $[Zn_2(\mu\text{-}H_2L^4)_2(\mu\text{-R/S-methylsuccinate})Ln_2(NO_3)_2](NO_3)_2\cdot 2H_2O\cdot 3MeOH$ (Ln^{III} = Sm (38-R/S), Eu (39-R/S), Tb (40-R/S), Dy (41-R/S), Er (42-R/S), Yb (43-R/S))

H_4L^4 (0.075 mmol, 60.1 mg), $Zn(NO_3)_2\cdot 6H_2O$ (0.075 mmol, 22.3 mg) and $Ln(NO_3)_3\cdot xH_2O$ were dissolved in 20 mL of methanol. To this, another solution containing the corresponding enantiopure R/S-methylsuccinic acid (0.0375 mmol, 4.9 mg) and Et_3N (0.225 mmol, 0.03 mL) in 1 mL of methanol was added dropwise. A fine powder was formed in each drop, but it easily got dissolved. The resulting solution was

stirred for few seconds, filtered in order to remove any possible undissolved material and allowed to stand at room temperature. In few days suitable crystals for X-ray diffraction were obtained. Yield and elemental analysis results in Table A5.1.

5.2.2. $[Zn_2(\mu\text{-}H_2L^4)_2(\mu\text{-methylsuccinate})Dy_2(NO_3)_2](NO_3)_2\cdot 2H_2O\cdot 6MeOH$ (44-rac)

The same procedure was employed, but using methylsuccinic acid as a racemate. In few days suitable crystals for X-ray diffraction were obtained. Yield and elemental analysis results in Table A5.1.

5.2.3. Magnetically diluted 41_Y-R/S, 43_Y-R and 44_Y-rac

The magnetically diluted derivatives were synthesized following the same procedures as those above described for the non-diluted compounds, but employing a Ln:Y molar ratio of 1:10.

5.3. EXPERIMENTAL RESULTS

As previously shown in Chapter 4, the compartmental ligand H_4L^4 is suitable for encapsulating either transition metal ions in the inner N_2O_2 site or lanthanides in the outer O_4 site. Moreover, as it was demonstrated for compound **36**, the axial ligand field provided by the three phenoxido groups in nearly opposite positions (two in one side and one in the other) has been proved to be adequate in order to synthesize Dy^{III} based zero field SMMs. In those systems, the partially deprotonated ligands show a zwitterionic form, inherently displaying two asymmetric centers in the tetrasubstituted amines. However, as there is not any external chiral inductor that breaks the equilibrium in the formation of the two possible enantiomers, they both crystallize as a racemate in the crystal structure. Anyway, this is not something unusual, since there are other examples in the literature (and the ones seen in Chapter 1) where the zwitterionic form provides asymmetric centers to the structure [1]. Nevertheless, the characteristics of the structure made us believe that the configuration of those quaternary amines could be controlled somehow.

In this sense, considering the aforementioned compound **36** as a reference, we decided to subtly modify the bridging succinate by incorporating enantiopure R- and S-methylsuccinates, respectively. Thus, the reaction between H_4L^4, $Zn(NO_3)_2\cdot 6H_2O$, $Ln(NO_3)\cdot xH_2O$ and R- or S-methylsuccinic acid, in presence of Et_3N, led to the

formation of six novel pairs of enantiomerically pure compounds, named as **38-R/S** to **43-R/S**. In these compounds, the chiral methylsuccinates act as directing agents, since the configuration of the quaternary amines is stereoespecifically controlled by them. In addition, as a prove of concept, racemic methylsuccinic acid was employed in an additional experiment obtaining the compound **44-rac**. As expected, this material shows both of the enantiomers (**44-R** and **44-S**) in the crystal structure.

5.3.1. Crystal Structures of Complexes 41-R/S and 44-rac

Compounds **41-R** and **41-S** both crystallize in the chiral *P* $2_12_12_1$ space group, where one is the specular image respect to the other. The phase purity and isostructural nature of the remaining pairs of enantiomers was confirmed by XRPD (Figures A5.2-A5.9). Taking into account that both compounds only differ in the configuration of the asymmetric centers (bond distances and angles are in the same ranges, see Tables A5.3-A5.4), only **41-R** will be described in this section (crystallographic data, as well as the most relevant bond distances and angles are presented in Tables A5.2-A5.4). However, both enantiomers are depicted in Figure 5.1, where the specular character is noticeable.

The X-ray crystal structure consist of tetranuclear $[Zn_2(\mu\text{-}H_2L^4)_2(\mu\text{-}R\text{-}methylsuccinate)Dy_2(NO_3)_2]^{2+}$ cations, NO_3^- anions and two water and three methanol solvent molecules. It is worth mentioning that we were not able to obtain a final crystal structure in which counterions and solvent molecules were localized, but considering previous results, elemental and thermogravimetric analysis and the fact that NO_3^- salts have been used, we conclude that nitrates act as counterions. Moreover, the amount of the solvent molecules was determined by elemental and thermogravimetric analysis (Table A5.1 and Figure A5.10). Even though H_4L^4 was initially designed to encapsulate two transition metals in the inner N_2O_2 sites and two lanthanides in the outer O_4 sites, in these specific systems only a pocket behaves as expected. Within this pocket, Zn^{II} and Dy^{III} ions are triply bridged by two phenoxido and a carboxylate group, the latter one arising from the chiral methylsuccinate. The functionalized aromatic groups in the other pocket behave differently. Phenoxido and methoxy groups in one are coordinated to another Dy^{III} ion located in the pocket of the other H_2L^{2-} ligand, whereas the other functionalized ring remains intact and still with the protonated phenol group. Thus, in each main ligand three out of four phenol groups are deprotonated and coordinated to either Dy^{III} or Dy^{III} and Zn^{II} ions, one acting as monodentate and two as bridging

groups. The overall charge of the ligand, though, is H_2L^{2-}, since one amine group in each ligand displays a zwitterionic form, as aforementioned. These zwitterions are stabilized by intramolecular hydrogen bonds involving the monocoordinating phenoxido groups with N4···O7 distances in the range of 2.62(1)-2.66(1) Å. Interestingly, the configuration of these amines is controlled by the configuration of the methylsuccinate. When R-methylsuccinic acid is used as bridging group, the amines are stereospecifically protonated exhibiting the S configuration (Figure 5.1). When S-methylsuccinic acid is used, in contrast, the opposite enantiomer is obtained and amines display the R configuration. Hence, the incorporation of a chiral methylsuccinic acid is responsible of the total configuration of the tetranuclear system. Noteworthy, the methyl groups in the succinate are disordered between the two possible positions with half occupation, even though only one is represented in Figure 5.1.

Regarding to the environment of the metal ions, the transition metals possess a ZnN_2O_3 coordination sphere. According to the SHAPE measurements [2], they can be considered as slightly distorted square pyramids (Table A5.6), where the square bases are formed by two nitrogen and two oxygen atoms corresponding to the main ligand. The remaining apical oxygen belongs to the *syn-syn* carboxylate bridging group of the bis(bidentate) methylsuccinate bridging ligand connecting the dinuclear Zn^{II}-Dy^{III} units. The shortest bond distances are Zn-O ones, in the range of 1.960(9)-2.111(8) Å, whereas Zn-N distance fall in the range of 2.123(10)-2.189(10) Å. The Dy^{III} ions display a DyO_9 coordination sphere, which is formed by the coordination of three phenoxido and three methoxy groups, one bidentate nitrate ion and one carboxylate oxygen atom belonging to the methylsuccinate bridging ligand. As it is expected for lanthanides with high coordination number, the spheres around them appear to be much distorted and far from an ideal polyhedron. In fact, SHAPE measurements indicate that they fit best to a muffin type geometry, but with a high level of distortion (Table A5.7). The shortest bond distances were found for Dy-$O_{phenoxido}$ in the range of 2.222(7)-2.337(8) Å, being especially short the ones corresponding to the monocoordinated phenoxido oxygen atoms. Dy-$O_{carboxylate}$ and Dy-O_{NO3} bond distances show intermediate distances of 2.340(8)-2.353(8) Å and 2.442(11)-2.478(9) Å, respectively, while Dy-$O_{methoxy}$ ones are notably longer in the range of 2.571(10)-2.737(10) Å. The axiality of the ligand field is preserved by the wide O1-Dy-O7 and O3-Dy-O7 angles in the range of 135.0(3)-144.0(3)º that were also observed for compound **36**. The shortest Dy···Dy distances are found between neighbouring molecules with a shortest 8.594(1) Å distance, whereas the intramolecular one is of 8.776(1) Å.

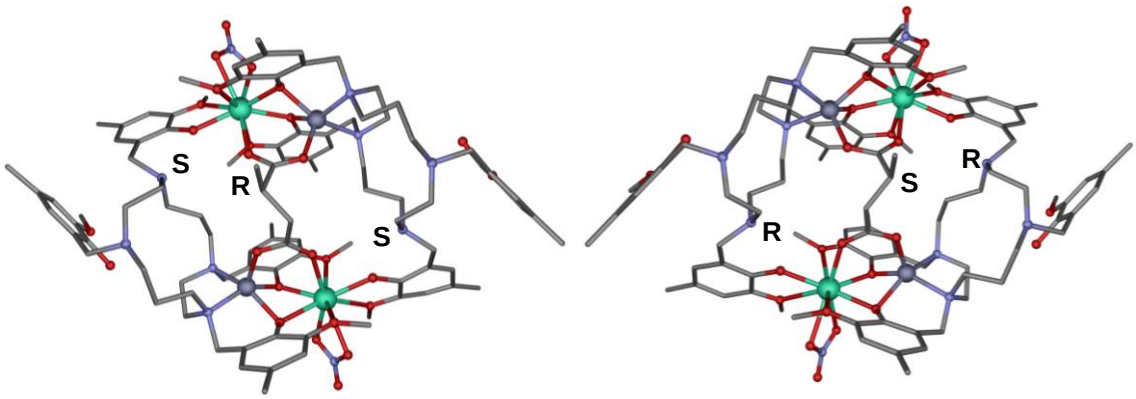

Figure 5.1.- Perspective view of the cationic structures of **41-R** (left) and **41-S** (right). Dysprosium, zinc, oxygen, nitrogen and carbon atoms are in turquoise, dark grey, red, blue, and grey, respectively. Hydrogen atoms have been omitted for the sake of clarity.

As mentioned, **44-rac** was also synthesized as a prove of concept. In this case, it crystallizes in the orthorhombic *Aba2* space group. The structure is comprised of $[Zn_2(\mu\text{-}H_2L)_2(\mu\text{-R/S-methylsuccinate})Dy_2(NO_3)_2]^{2+}$ cations, NO_3^- anions and crystallization solvent molecules (six methanol and two water molecules), which were firstly removed by a SQUEEZE routine, but then determined by other techniques such as EA and TGA (Table A5.1 and Figure A5.11). As expected, the coordination spheres of both ions, as well as bond distances and angles, are in the same ranges as the ones determined for **41-R** and **41-S** (Tables A5.4-A5.7).

What is more remarkable in **44-rac** is that when using the racemate methylsuccinic acid both enantiomers (R,S',S'' and S,R',R'') cocrystallize within the crystal structure (Figure 5.2). This proves again that the enantiopure R- or S-methylsuccinates determine the final configuration of the zwitterionic amines.

In the present case, intramolecular Dy···Dy distances are shorter than intermolecular ones, 8.8294(6) Å and 10.9544(6) Å, respectively. Finally, the cationic units are stabilized by intermolecular hydrogen bonds between the still protonated phenol groups and non-coordinated oxygen atoms from adjacent cationic structures. Thus, they grow in 2D within the *ab* plane (Figure A5.1).

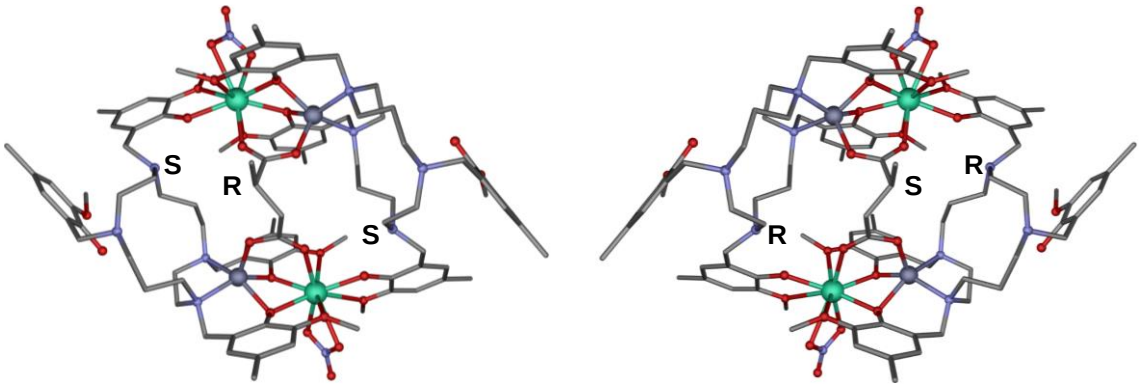

Figure 5.2.- Perspective view of the cationic structures of *R,S',S''* (left) and *S,R',R''* (right) enantiomers that cocrystallize within **44-rac**. Dysprosium, zinc, oxygen, nitrogen and carbon atoms are in turquoise, dark grey, red, blue, and grey, respectively. Hydrogen atoms and counteranions have been omitted for the sake of clarity.

5.3.2. Theoretical calculations for 41-R and 41-S

The crystallization of a single enantiomer (R,S',S'' or S,R',R'', where the first configuration corresponds to the methylsuccinate and second and third account for the amines), when either R- or S-methylsuccinate is present as bridging ligand, can be understood in terms of steric effects. This conclusion was easily drawn upon analysing the structures resulting from classical potential energy minimization protocols applied on the crystallized R,S',S'' enantiomer (**41-R**), as well as on the S,S',S'' diastereoisomer compound generated computationally by simple substitution of the position of the methyl group in the stereogenic carbon of the former (the same protocol was also carried out for **41-S**). As it could be observed in Figure 5.3 and in Movie A5.1, the close proximity between the mentioned methyl group (hydrogen atoms have been highlighted in yellow) in the bridging ligand and two methylene groups (highlighted in red) belonging to the H_4L^4 ligand in the R,R',R'' (bottom right) and S,S',S'' (top left) enantiomers provokes a complete structure rearrangement upon energy minimization, unravelling its thermodynamic instability. These rearrangement of the molecule could be observed in Movie A5.2, in which even after 100 steps the structure does not reach a minimum energy value in agreement with the steric hindrance between the mentioned groups. Equivalent results were obtained for the crystallized S,R',R'' enantiomer (**41-S**) and the computationally generated S,S',S'' diastereoisomer. Therefore, this is the reason why each specific methylsuccinate leads to a certain configuration of the amines and, thus, it could be considered as a directing agent.

The minimization of the structures was carried out with the Macromodel utility of the Schordinger software [3] using default settings. Only the atoms shown as capped sticks were allowed to move during the minimization process (100 steps). As abovementioned, the model compounds R,R',R'' and S,S',S'' did not reach the minimum energy after the process, while **41-R** and **41-S** did so in few steps as expected.

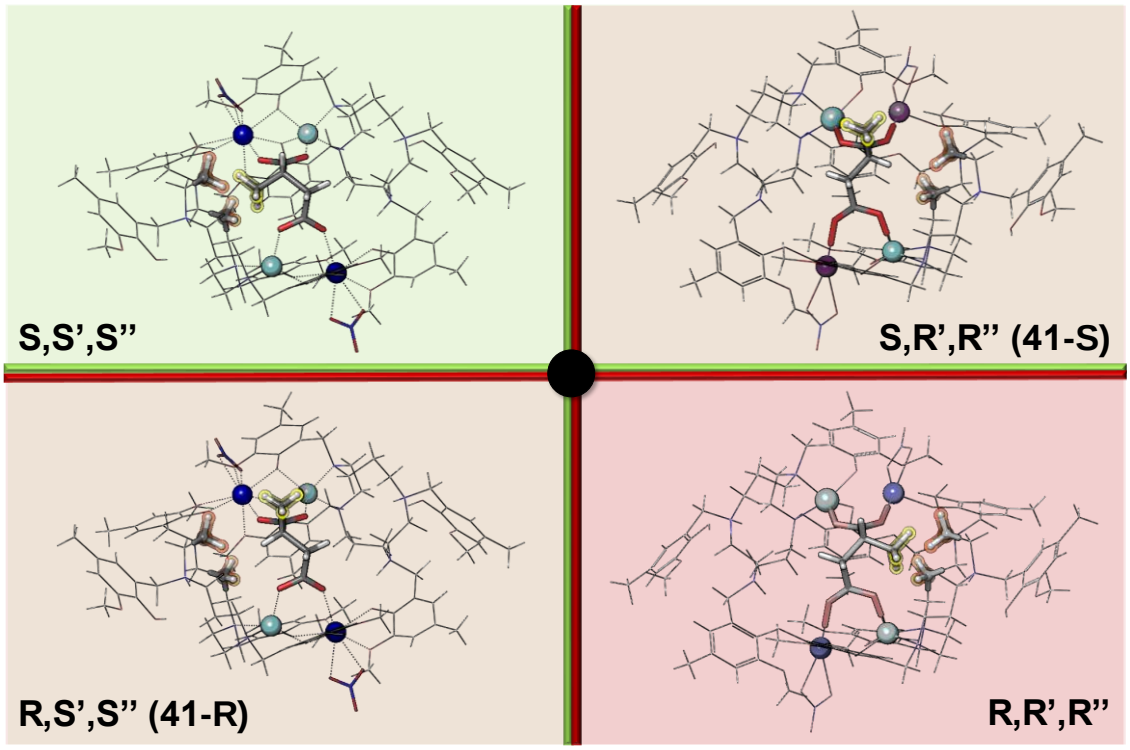

Figure 5.3.- Perspective view of the cationic structures of **41-R** (bottom left) and **41-S** (top right) enantiomers along with the model diastereoisomers R,R',R'' (bottom right) and S,S',S'' (top left). A red and a green background are used for the R and S configurations, respectively. Hydrogen atoms that are responsible of the steric hindrance are highlighted with red and yellow.

In view of these results, even though magnetically we would not expect to obtain a better SMM, it seems reasonable to carry out some experiments by using *meso*-2,3-dimethylsuccinic acid to obtain the 1D chain that was originally targeted in Chapter 4. This specific succinate derivative contains methyl groups in two positions with a different configuration (R and S). Therefore, we do not expect to obtain the tetranuclear systems that have been reported in this chapter. We are planning to perform these new experiments in the near future.

5.3.3. Dynamic magnetic properties of complexes 41-R/S, 43-R, 44-rac and diluted samples

Bearing in mind that compounds **41-R** and **41-S** contain nearly the same axial ligand field that **36**, they are both expected to be high performance zero field SMMs. Hence, alternating current (*ac*) magnetic measurements were carried out for both of them under zero applied *dc* field in the temperature range of 2.0-40.0 K at 10000 Hz. As it is depicted in Figure 5.4, both enantiomers display nearly the same behaviour as **36**, and exactly the same between them as predicted for enantiomeric compounds. The small positive temperature shift in the position of the maximum for **41-R/S** could be due to a slightly more appropriate ligand field. At low temperatures they all display long tails that are very representative of fast QTM, which may arise from dipolar or hyperfine interactions [4]. In contrast, around 30 K there are well defined maxima indicating the expecting SMM behaviour. It is well known that when the QTM arises from intra- or intermolecular interactions, a good method to quench it, at least partly, is that of diluting the paramagnetic centers in a diamagnetic matrix. Therefore, the diluted **41$_Y$-R** and **41$_Y$-S** analogues were synthesized in a 1:10 Dy:Y molar ratio (the phase purity was determined by XRPD, Figures A5.4 and A5.7). Once again, *ac* measurements were performed in these diluted samples in the same experimental conditions. It can be observed that the tails corresponding to QTM have almost disappeared for them, even though a tiny rise can be observed below the maxima at the lowest temperatures. This fact indicates that even though relatively long intra- and intermolecular distances were observed between Dy^{III} centers, significant interactions were taking place shortcutting the energy barrier. At the highest temperatures there is not any appreciable shift in the position of the maxima, indicating that the new matrix has little incidence in the Orbach process.

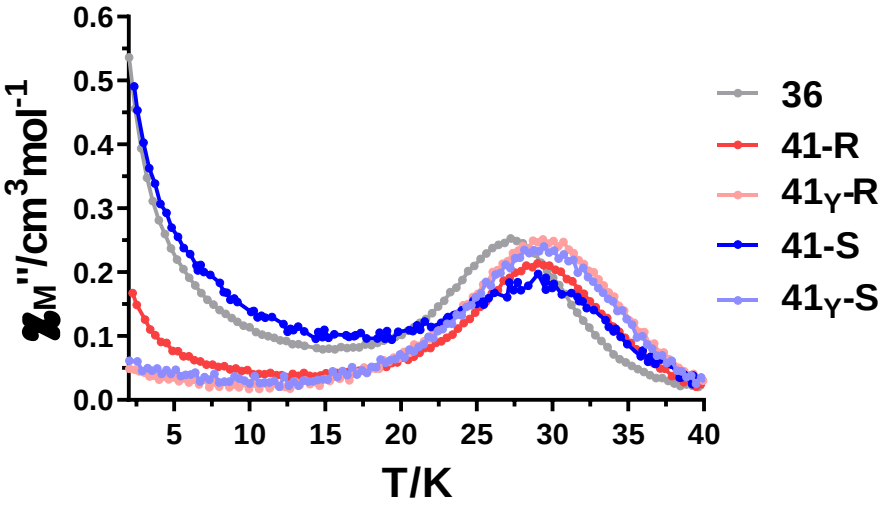

Figure 5.4.- Temperature dependence of the out-of-phase components of the *ac* susceptibility for complexes **36**, **41-R**, **41-S**, **41$_Y$-R** and **41$_Y$-S** under zero applied *dc* field and 10000 Hz. The χ_M'' values have been arbitrarily multiplied for the diluted samples for a more visual comparison.

In view of the positive effect of the magnetic dilution, we then proceed to optimize the external magnetic field for **41$_Y$-R** in order to completely remove the QTM. Alternating current measurements were carried out at a fixed temperature of 24.8 K and at diverse external magnetic fields, from where we determined the optimum field to be of 1000 Oe (Figures A5.12-A5.13). Hence, a complete measurement was carried out in the temperature range of 2.0-38.0 K under 1 kOe external *dc* field. In Figure 5.5 is shown that the tails associated to QTM have completely disappeared, corroborating that both the diamagnetic dilution and the external field are good techniques to remove it. The temperature dependence at each frequency (Figure A5.15) was fitted to the generalized Debye model in the temperature range of 18.0-30.0 K obtaining relaxation times. The Arrhenius plot of these data in Figure 5.5 (inset) shows a typical linear tendency at high temperatures associated to an Orbach process, but there is also a noticeable curvature at lower temperatures indicative of an additional Raman type relaxation. This was further confirmed by the fitting of the Cole-Cole plots in the same temperature range (Figure A5.16), from where the extracted α values reveal a quite narrow distribution of relaxation processes, but a possible mixing of Orbach and Raman mechanisms (0.15 (18.0 K) – 0.12 (30.0 K)). Thus, the relaxation times were fitted to the following Equation 5.1:

$$\tau^{-1} = BT^n + \tau_0^{-1} exp(-U_{eff}/k_B T) \quad Equation\ 5.1$$

Where the first term accounts for the Raman process and the second to Orbach. The best fitting of the data afforded the following set of parameters: B = 18.4 $s^{-1}K^{-1.28}$; n = 1.28; τ_0 = $3.80 \cdot 10^{-9}$ s and U_{eff} = 262.3 K. Even though a n = 9 value is expected for Kramers ions [5], values between 1 and 6 can be considered as reasonable when both optical and acoustic phonos participate in the magnetic relaxation [6]. Note that the value of U_{eff} is considerably lower (around 80 K) than the ones we obtained for **36** and **36$_Y$** under external magnetic fields when considering simultaneous presence of these two relaxation mechanisms. However, it is true that the value is in good agreement to the one we obtained for **36** under zero *dc* field with a single Orbach fit. We believe that the theoretical calculations that are currently in process will shed some light on this point.

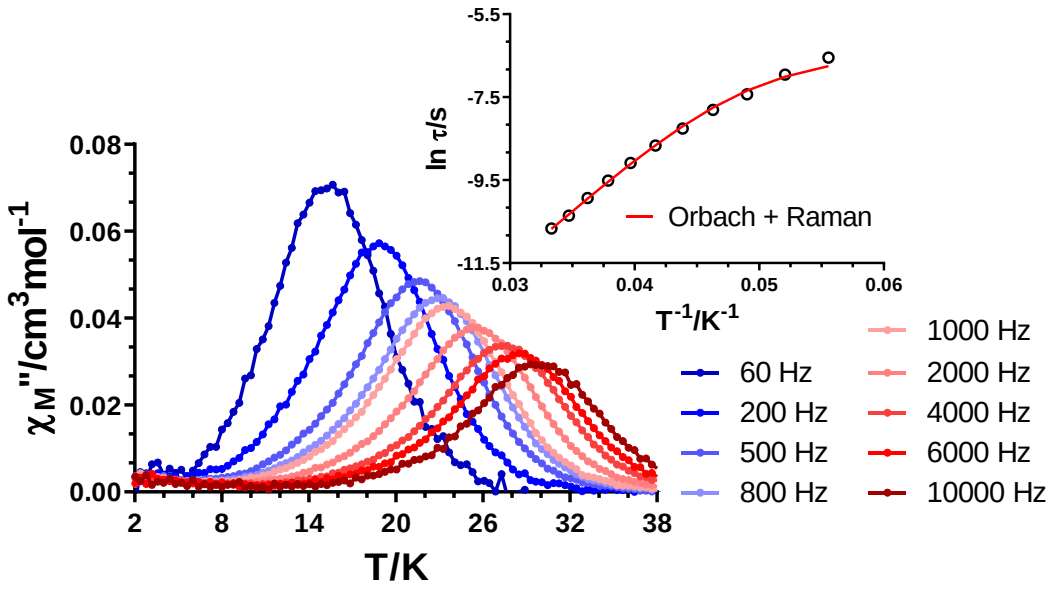

Figure 5.5.- Temperature dependence of the out-of-phase components of the *ac* susceptibility in a *dc* applied field of 1 kOe for **41$_Y$-R**. Inset: Arrhenius plot for the relaxation times with simultaneous fitting considering Orbach + Raman.

We studied the dynamic magnetic properties of **44-rac** under zero applied *dc* field (Figure 5.6). As expected, the curves at different frequencies showed a very similar behavior to the enantiopure compounds. The maxima were found slightly below 32 K and long tails were observed at the lowest temperatures due to QTM. The $\chi''_M(\upsilon)$

curves (Figure A5.18) and Cole-Cole plots (Figure A5.19) were constructed for the 13.2-31.6 K temperature range. The α values at the highest temperatures are relatively small (0.11 at 31.6 K) in agreement with a thermally activated Orbach process, while on lowering the temperature they increase up to 0.37 at 13.2 K. This could be explained by the mixing of several relaxation mechanisms including Raman and/or QTM processes. Relaxation times were fitted to equation 5.1 obtaining the following set of parameters: $B = 4.9 \cdot 10^{-2}$ $s^{-1}K^{-3.67}$; $n = 3.67$; $\tau_0 = 4.92 \cdot 10^{-9}$ s and $U_{eff} = 272.3$ K. Even though the presence of QTM is remarkable, we were not able to study the temperature range at which it operates due to the frequency limit of our instrument (note that relaxation times cannot be obtained below 13.2 K) and, therefore, it is not reasonable to include the presence of this mechanism in the fitting equation. The diluted **44$_Y$-rac** counterpart shows little difference in the same conditions and the tail at low temperatures remains almost unchanged, which indicates that intra- or intermolecular interactions were not the main reason for QTM to appear (Figure A5.20).

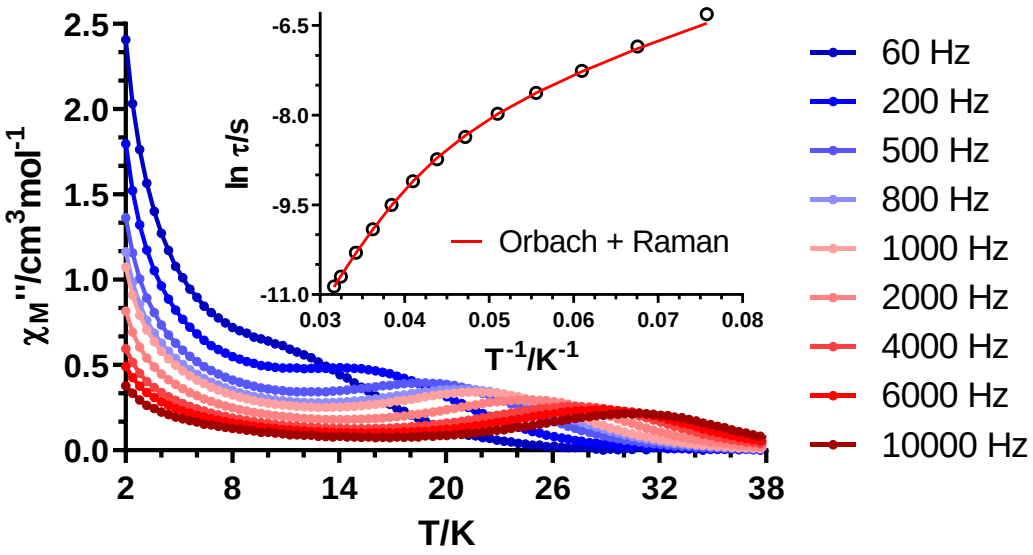

Figure 5.6.- Temperature dependence of the out-of-phase components of the *ac* susceptibility in a zero applied *dc* field for **44-rac**. Inset: Arrhenius plot for the relaxation times with simultaneous fitting considering Orbach + Raman.

In spite of the fact that the ligand field in **41-R** and **41-S** is suitable for stabilizing oblate type lanthanides such as Dy^{III}, it has been previously proved that prolate like Er^{III} analogues may also display field induced SMM behaviour (as shown in the previous

chapter). Hence, *ac* measurements were also carried out for another prolate ion based compound, **43-R**. At zero applied external field, this compound does not show any signal in the out-of-phase plots indicating the absence of slow relaxation of the magnetization (Figure A5.21). However, as usual, this might be attributed to strong QTM and the measurement was repeated under an external magnetic field of 1 kOe. In this case, a well-defined maximum appears in the out-of-phase region slightly below 5 K (Figure A5.21). In view of it, field-dependent *ac* measurements were carried out at 3.8 K in order to determine the optimum external magnetic field (Figures A5.22-A5.23). By fitting the data, we found that the optimum field was of 2 kOe. Below of it, **43-R** shows unquenched QTM, whereas above 2 kOe relaxation times are shortened by a field-induced direct process (Figure A5.23). In order to avoid the degrees of freedom and avoid overparametrization in the posterior Arrhenius fit, the $\tau^{-1}(H)$ data was fitted to the following equation:

$$\tau^{-1} = \frac{B_1}{1+ B_2 \cdot H^2} + AH^4T + k \qquad \textit{Equation 5.2}$$

Where the first term involving B_1 and B_2 describes QTM, the second one the direct process and k englobes field-independent processes. The best fit afforded the following set of parameters: B_1 = 4092 s^{-1}, B_2 = 32.34 Oe^{2-}, A = 115311 $s^{-1}K^{-1}Oe^{4-}$ and k = 24928 s^{-1}. The large value of k must indicate that at this temperature field-independent mechanisms such as Raman have a large influence in the relaxation process. Subsequently, *ac* measurements were completed in the 2.0-10.0 K temperature range at different frequencies (Figure 5.7), where a set of well-defined maxima is observed below 5.0 K. The $\chi_M''(\upsilon)$ curves were fitted to the generalized Debye model obtaining relaxation times at each temperature (Figure A5.24). As depicted in the inset of Figure 5.7, the relaxation times exhibit a curvature in the whole temperature regime, which could be associated to the sum of different relaxation processes. Nonetheless, an initial fit to a single Orbach process was done in the highest temperature regime, which afforded U_{eff} and τ_0 values of 14.1 K and $8.74 \cdot 10^{-7}$ s^{-1}. Even though at first glance these values may seem reasonable, the thermally activated Orbach mechanism has usually been inadequate to properly describe the relaxation dynamics of Yb^{III} based compounds [7–9].

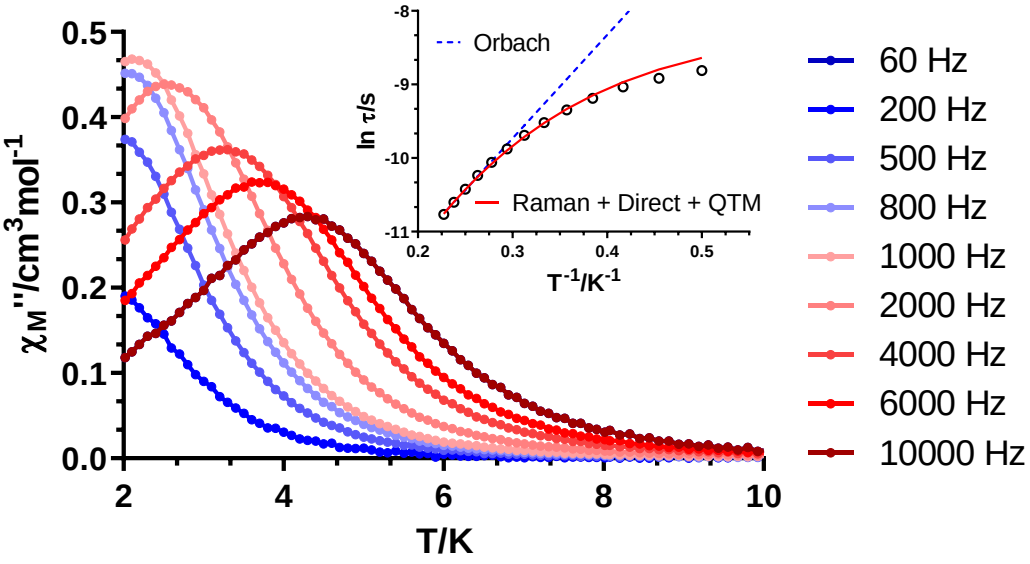

Figure 5.7.- Temperature dependence of the out-of-phase components of the *ac* susceptibility in a *dc* applied field of 2 kOe for **43-R**. Inset: Arrhenius plot for the relaxation times considering Orbach (dashed blue line) and simultaneous presence of Raman + QTM +Direct (red line).

Hence, relaxation times were fitted to the simultaneous presence of Raman, Direct and QTM processes according to equation 5.3:

$$\tau^{-1} = BT^{n} + AH^{4}T + \tau_{QTM}^{-1} \qquad \textit{Equation 5.3}$$

As previously mentioned, so as to avoid overparametrization, the values corresponding to direct and QTM processes (second and third term, respectively), were fixed by using the parameters obtained in the field-dependent measurements. Thus, being *B* and *n* parameters the unique variables to be fit. The best fitting was achieved with *B* and *n* values of 149.4 $s^{-1}K^{-3.822}$ and 3.822, respectively. The diluted **43_{Y}-R** counterpart did not show any remarkable difference respect to the non-diluted system under zero or under the optimum external magnetic field of 2 kOe (Figure A5.26).

5.3.4. Photoluminescent properties of complexes 38-R to 41-R

Solid state photoluminescence was studied for compounds **38-R** to **41-R**, since for them emissive properties are expected to be observed in the visible range. Compounds **42-R** and **43-R** may emit in the NIR region and are going to be studied in the near future. Note that we have only studied one enantiomer in each pair, because exactly the same properties are expected for the other enantiomer.

Low-temperature excitation spectra were recorded for **38-R**, **39-R**, **40-R** and **41-R** monitoring them in their more intense emission lines i.e., 646, 617, 548 and 578 nm (Figure A5.27). In most of them, a broad band could be observed in the 300-425 nm range, which is ascribed to n $\rightarrow \pi$ and $\pi \rightarrow \pi^*$ transitions of H_4L^4. In most of the cases, the broad bands are accompanied with some of the f-f transitions of the Ln^{III} ions. Except for **40-R**, the intensity of the f-f transitions is higher, signifying a not very efficient antenna effect occurring in the complexes. Conversely, the f-f transitions fall below the broad band of the ligand in compound **40-R**, which is indicative of an efficient luminescence sensitization *via* the ligand's excited states.

At low temperature, compounds **38-R** to **41-R** display their characteristic emission bands for f-f transitions under monochromatic laser excitation (λ_{ex} of 325 nm, Figure 5.8). Even though we studied the excitation spectra for all the compounds to evaluate the sensitization efficiency, no significant dependence was observed for the excitation wavelength, so all the emission spectra were then recorded at the fixed excitation wavelength (λ_{ex}) of 325 nm due to the stronger intensity provided by the laser in comparison to the lamp. The former is only available for 325 nm, while the second provides different wavelengths. Sm^{III} based **38-R** displays typical emission bands centered at 563, 600 and 646 nm corresponding to the $^4G_{5/2} \rightarrow {}^6H_J$ (J = 5/2, 7/2 and 9/2; Figure 5.8, top left). As observed in the temperature dependant spectra, the intensity of the signals decrease with increasing temperature (Figure A5.28), as expected for the increasing vibrational energy, despite of which the compound still shows the characteristic emission bands at room temperature (Figure A5.29). Compound **39-R** shows five characteristic groups of signals centered at 580, 592, 617, 652 and 700 nm, clearly dominated by the third one and responsible of the brilliant red emission (Figure 5.8, top right). This multiplet is attributed to the $^5D_0 \rightarrow {}^7F_2$ electron dipole transition, known as the hypersensitive transition. The signals centered at 580, 592, 652 and 700 nm are assigned to $^5D_0 \rightarrow {}^7F_0$, $^5D_0 \rightarrow {}^7F_1$, $^5D_0 \rightarrow {}^7F_3$ and $^5D_0 \rightarrow {}^7F_4$. The large difference in intensity of $^5D_0 \rightarrow {}^7F_2$ and $^5D_0 \rightarrow {}^7F_1$ transitions is in good

agreement with the low symmetry of the coordination environment of the metal center. At room temperature, the compound does not emit any characteristic Eu^{III} based light. The spectrum of **40-R** is comprised of four signal groups centered at 490, 543, 588 and 625 nm corresponding to $^5D_4 \rightarrow {}^7F_J$ (J = 6-3) transitions (Figure 5.8, bottom left). The $^5D_4 \rightarrow {}^7F_5$ transition dominates the spectrum in agreement with its largest probability for both electric-dipole- and magnetic-dipole-induced transitions [10]. As it is shown in Figure A5.30, the emissive capacity is maintained even at room temperature, in agreement with the aforementioned good sensitization by the ligand. We also studied if the excitation wavelength affects the emissive properties (Figure A5.31). As observed, the emission does not significantly change but for the signal intensity under λ_{ex} = 370 nm (maximum in the excitation spectra) compared to 308 nm. Moreover, it is important to notice that the much stronger emission recorded when using the monochromatic light of λ_{ex} = 325 nm is due to the high power of the laser source rather than being related to the optical features of the sample. Finally, the emission spectrum of **41-R** displays the characteristic emission bands of Dy^{III} (Figure 5.8, bottom right). The blue and yellow emission lines (centered at 482 and 579 nm, respectively) corresponding to $^4F_{9/2} \rightarrow {}^6H_{15/2}$ and $^4F_{9/2} \rightarrow {}^6H_{13/2}$ transitions dominate the spectrum, though other weaker emission bands as well as ligand fluorescence (350-440 nm range) could be observed. The latter one is in agreement with a less efficient energy transfer from the ligand to Dy^{III} ion, a feature previously anticipated in the excitation spectrum. As in the case of the Eu^{III} based compound, the fact of having a dominant $^4F_{9/2} \rightarrow {}^6H_{13/2}$ transition confirms the low symmetry environment of the metal ion, as expected from the isostructural nature of these compounds [11]. Even weak, compound **41-R** still displays Dy^{III} based emissive bands at room temperature (Figure 5.32).

The color of the emission for each compound could be observed in Figure A5.33, in which micro-photoluminescence images taken at room temperature in an optical microscope equipped with a Hg lamp. Compounds **38-R** and **40-R** display the expected red and green emission, respectively. The black image for **39-R** corroborates the lack of Eu^{III} based emission at room temperature (only observed at low temperature). Lastly, **41.-R** shows weak blue and yellow emission due to the poor sensitization by the ligand.

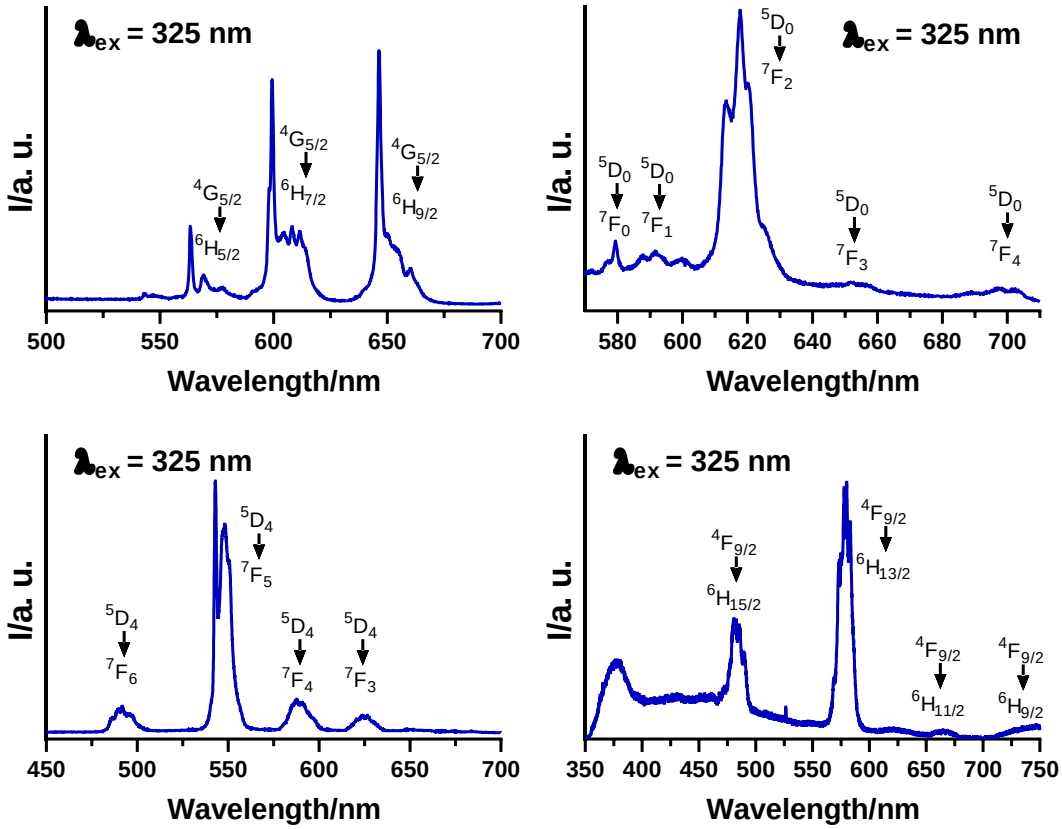

Figure 5.8.- Solid state photoluminescence emission spectra for compounds **38-R** (top left), **39-R** (top right), **40-R** (bottom left) and **41-R** (bottom right) recorded at 15, 10, 20 and 10 K, respectively, under excitation at 325 nm.

As we mentioned before, **39-R** does not show any Eu^{III} based emission at room temperature given the low antenna effect, whereas lowering the temperature promotes a significant enhancement of such energy transfer and, thus, a strong metal-centered emission capacity. In particular, there is a strong temperature dependence at low temperatures as shown in Figure 5.9, top left. Several spectra were measured in the 10-200 K temperature range with a 10 K step. More interestingly, this feature could be very valuable for a thermometer device, since the intensity ratio between some bands changes with the temperature. In our case, we have defined I_1 and I_2 as the total counts for the emission at 580 and 617 nm, respectively (Figure 5.9, top right). Then, we have defined a thermometric parameter (Δ) as:

$$\Delta = \frac{I_1}{I_2} \qquad \textit{Equation 5.4}$$

The Δ linearly increases as the temperature is increased in the 10-40 K temperature range following the empirical equation (Figure 5.9, bottom):

$$\Delta = 1.8 \cdot 10^{-3} T + 1.878 \cdot 10^{-1} \qquad \textit{Equation 5.5}$$

We have selected this temperature range considering that the Dy^{III} based counterpart shows out-of-phase susceptibility signals below 32 K. Therefore, the mixture of Dy^{III} ions with Eu^{III} ones in a heterometallic compound could allow us to obtain a device that might operate as a SMM and at the same time give information about the temperature in that operating range. Further details about this approach are explained in section 5.3.7.

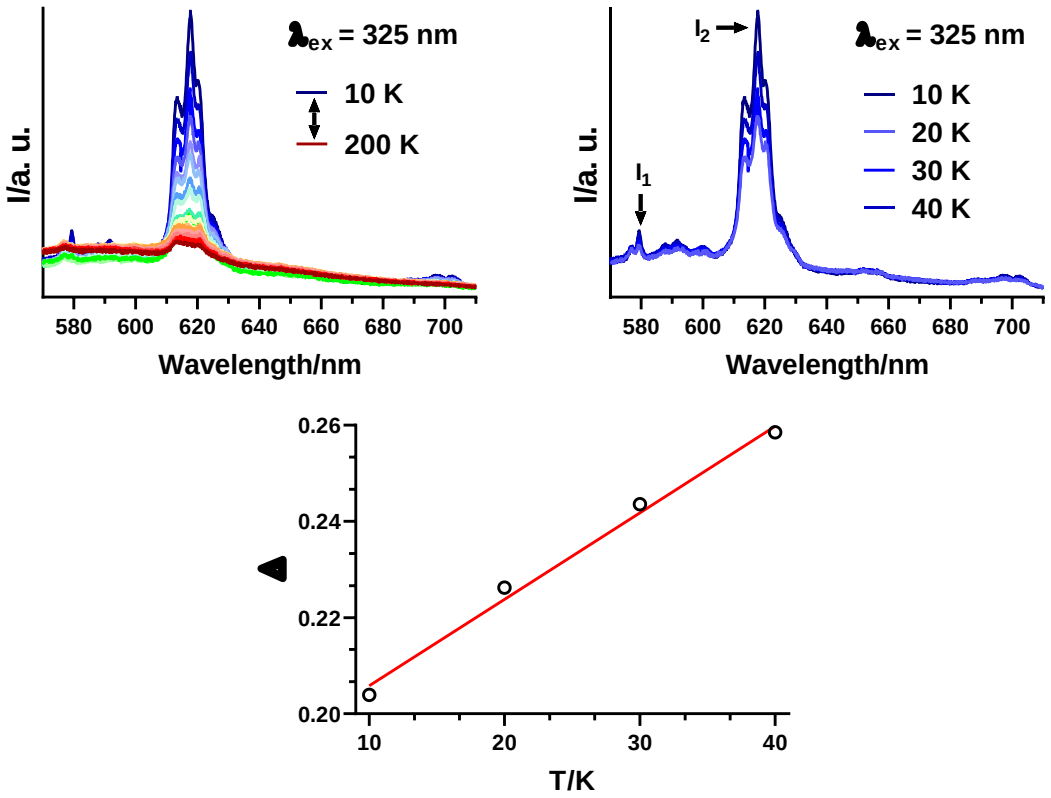

Figure 5.9.- Solid state photoluminescence emission spectra for compounds **39-R** recorded in the 10-200 K temperature range under excitation at 325 nm (top left). Signal and temperature range that we have selected for the thermometric device (top right). Thermometric parameter value as a function of the temperature.

The linear dependence observed for the relative intensity of the emission bands according to the temperature is, *a priori*, a good starting point for establishing the

temperature sensing capacity of the system, considering the large potential applicability of ratiomeric photoluminescent devices [12,13].

5.3.5. Circular dichroism (CD) experiments on R/S-methylsuccinic acid and 41-R/S

Due to the chirality of the prepared compounds, we decided to study their different absorption properties of circularly polarized light. The CD spectra were recorded in methanol solutions for the chiral free ligands (R- and S-methylsuccinic acid) and Dy^{III} based **41-R** and **41-S** compounds. As observed in Figure 5.10, the spectra of the free ligands are characterized by a broad band centered around 208 nm with opposite Cotton effects. Instead, the coordination compounds display several bands in the 200-320 nm region. Four small bands could be found with alternating Cotton effects peaking at 203, 212, 218 and 226 nm. This is followed by a large and most characteristic band at 245 nm with a subsequent broad, but less intense band centered around 290 nm. The spectra of the enantiomeric compounds are mirror images confirming the enantiopurity of the studied samples. We believe that the fact of having such different spectra for the free ligands and the compounds proves that the coordination complexes are stable in solution.

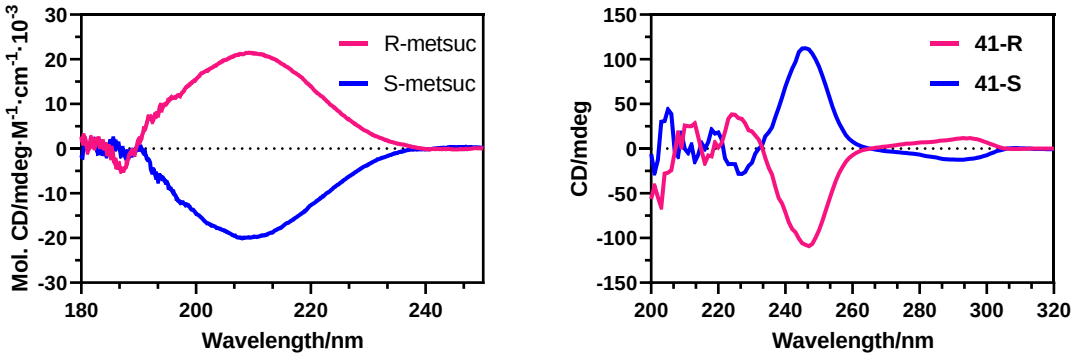

Figure 5.10.- Left: CD spectra recorded for the free chiral ligands. Right: CD spectra recorded for complexes **41-R** and **41-S**.

5.3.6. Circularly polarized luminescence (CPL) experiments for 40-R/S

As we discussed in the general introduction, lanthanide ions are potential candidates to show this property due to the dipole allowed Ln^{III} centered f-f transitions, which could give rise to large g_{lum} values. Among our studied compounds, we managed to measure this property to the Tb^{III} based **40-R** and **40-S** compounds in methanolic solution. As depicted in Figure 5.11, the CPL spectra were recorded for the emission centered at the $^7F_5 \leftarrow {}^5D_4$ transition multiplet. The spectra display the presence of two main bands at 541 and 553 nm, while a tiny third one centered at 531 nm could be also observed. As expected, both spectra display CPL bands with symmetrically opposed signs. We found dissymmetry factor g_{lum} values of around $4 \cdot 10^{-2}$, $7 \cdot 10^{-2}$ and $2 \cdot 10^{-2}$ for the bands at 531, 541 and 553 nm. Due to the weak chiroptical response of the rest of the emission bands, we were not able to obtain further reliable data. Similarly, the experiments carried out on the rest of the samples did not give measurable signals.

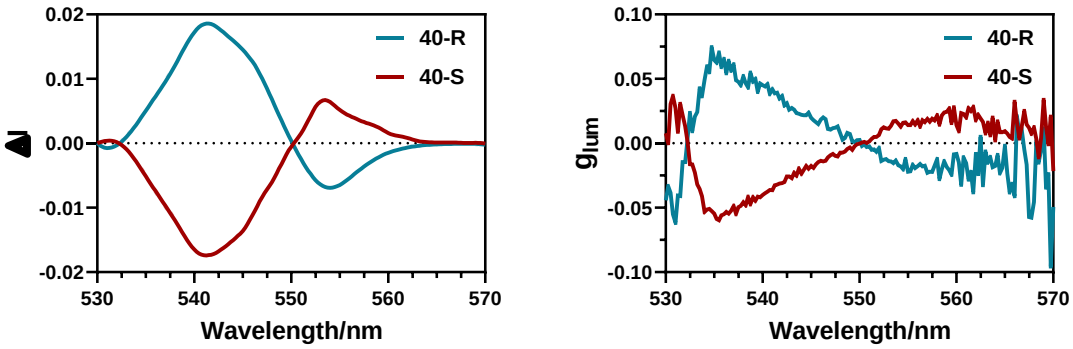

Figure 5.11.- Left: CPL spectra for the $^7F_5 \leftarrow {}^5D_4$ transition for complexes **40-R** and **40-S**. Right: g_{lum} values of the CPL bands found in the 530-570 nm range.

5.3.7. Preliminary results of the prototype thermometer/SMM Zn_2EuDy-R

We have found very interesting results for the tetranuclear systems studied in this chapter. More specifically, we were able to conclude that **41-R/S** behave as zero field SMMs with relatively high energy barriers and that **39-R/S** showed very interesting photoluminescent properties that strongly depend on temperature. In view of that, and considering what we said in the general introduction, it would be very interesting to combine both thermometry and SMM properties within the same system. This would allow us to determine the temperature of the system at operating temperatures and without the need of conventional contact thermometers. With this idea in mind, in this

dissertation we simply want to approach the concept of including both properties within the same system, because this goal presents a main drawback from the synthetic point of view. Even though our tetranuclear systems contain two outer pockets that are suitable for lanthanide ions, we believe that the target **Zn_2EuDy-R** compound would be difficult to isolate. Considering that both pockets are almost identical, when mixing both lanthanide precursors in the reaction vessel, the probability of obtaining our desired compound (containing 1 Eu^{III} and 1 Dy^{III} ion per molecule) is of 50% (Scheme 5.1).

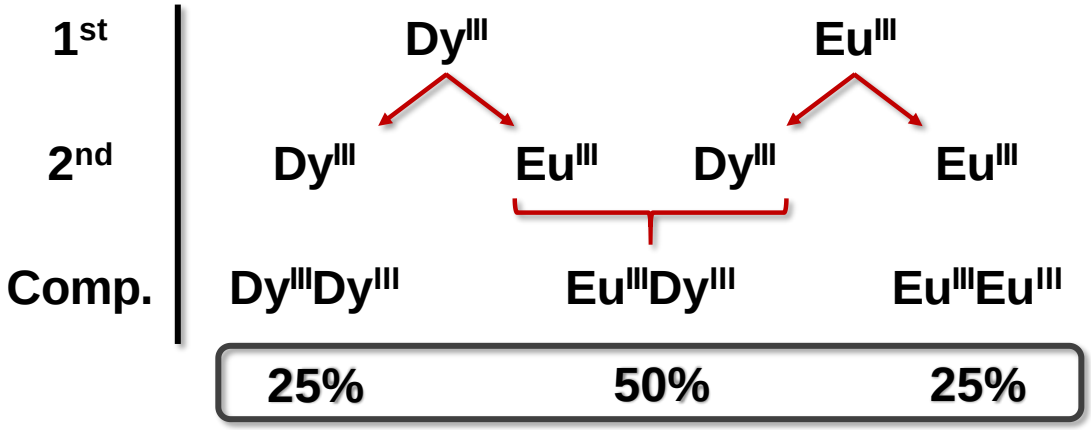

Scheme 5.1.- Compound formation probabilities when mixing both Eu^{III} and Dy^{III} precursors in the reaction.

Hence, when we study the magnetic and photoluminescent properties of our material, we are not going to be able to assure that the target **Zn_2EuDy-R** system retains the properties of the original Eu^{III} and Dy^{III} based compounds. Nevertheless, we decided to study first this material, which contains (most likely) 50% of the desired compound, 25% of **39-R** and 25% of **41-R**. Interestingly, the dynamic magnetic properties of **Zn_2EuDy-R** remained unchanged and it behaves as a zero field SMM (Figure 5.12).

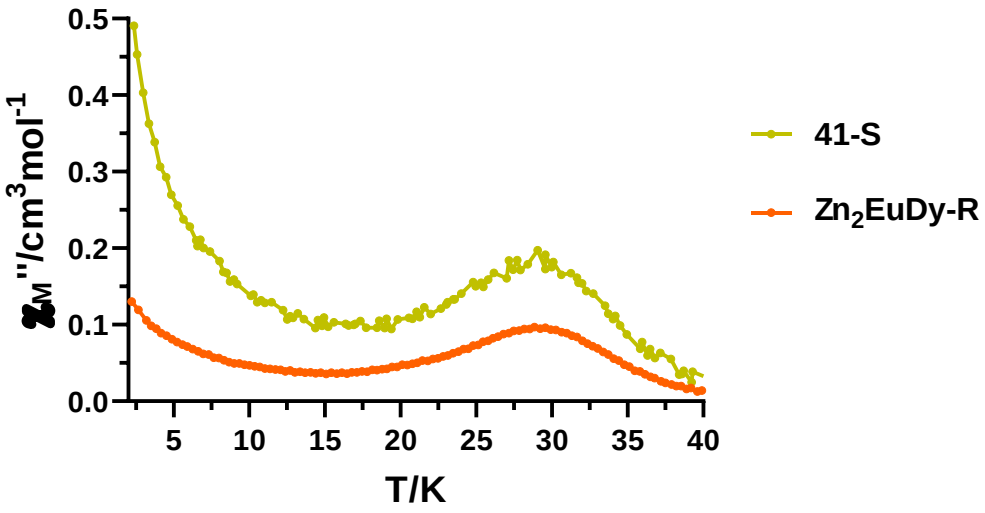

Figure 5.12.- Temperature dependence of the out-of-phase component of the *ac* susceptibility in a zero applied *dc* field for **41-S** and **Zn_2EuDy-R**.

The next step of this study will be to measure the photoluminescent properties of this mixed material to see that the interesting features that we observed for **39-R** are retained. If so, we will consider a second approach based on diamagnetic dilutions and we will synthesize doped **39_{Dy}-R** and **41_{Eu}-R**. By probability, the former one will contain a vast majority of **39-R**, but with a few amount of **Zn_2EuDy-R**, whereas the second one will have mainly **41-R** with less molecules of **Zn_2EuDy-R**. Therefore, if **39_{Dy}-R** still behaves as a zero field SMM and **41_{Eu}-R** shows temperature dependant photoluminescent properties, we will be able to state that the desired **Zn_2EuDy-R** compound is a dual thermometer/SMM.

5.4. CONCLUSIONS

In view of the position of the bridging succinate in compound **36** (described in Chapter 4), we believed that incorporating an enantiopure R- or S-methylsuccinate bridge would provoke the formation of a specific compound regarding the configuration of zwitterionic quaternary amines. Indeed, compounds **41-R/S** showed that when employing R-methylsuccinate amines acquire the S configuration and vice versa. By carrying out a simple theoretical study we have concluded that the methyl groups in the succinate are responsible for directing a stereospecific configuration of the compound.

Additionally, by measuring the single crystal structure of **44-rac**, we have seen that when the racemic precursor is employed, a mixture of both enantiomers is obtained.

Regarding magnetic properties, Dy^{III} based compounds revealed zero field SMM behaviour with effective energy barriers as high as 272 K. Moreover, the prolate like Yb^{III} based compound **43-R** exhibited field induced SMM behaviour relaxing via Raman, direct and QTM mechanisms.

In terms of luminescence, Sm^{III} and Tb^{III} based **38-R** and **40-R** displayed bright emissions even at room temperature due to a better sensitization by the ligand with a notable antenna effect. Dy^{III} and Eu^{III} based **41-R** and **39-R**, in contrast, displayed weak to none emissions at room temperature. However, an extremely temperature dependent behaviour was observed for **39-R**, which at low temperature presented the characteristic Eu^{III} based emissive bands. In fact, a preliminary study has been done to use this material as a contactless thermometer that, perhaps, could be combined with the magnetic **41-R** compound giving rise to a dual thermometer/SMM hybrid compound. Furthermore, based on the bright $^7F_5 \leftarrow {}^5D_4$ emission of **40-R/S**, circularly polarized luminescence was observed fot these complexes with g_{lum} values ranging in between $2 \cdot 10^{-2}$ and $7 \cdot 10^{-2}$.

5.5. REFERENCES

[1] J. Ruiz, A.J. Mota, A. Rodríguez-Diéguez, S. Titos, J.M. Herrera, E. Ruiz, E. Cremades, J.P. Costes, E. Colacio, Field and dilution effects on the slow relaxation of a luminescent DyO9 low-symmetry single-ion magnet, Chem. Commun. 48 (2012) 7916–7918. https://doi.org/10.1039/c2cc32518g.

[2] M. Llunell, D. Casanova, J. Cirera, J.M. Bofill, P. Alemany, S. Alvarez, M. Pinsky, D. Avnir, SHAPE, (2005).

[3] MacroModel, version 10.5, Schrödinger, LLC, New York, NY, 2014, (n.d.).

[4] F. Pointillart, K. Bernot, S. Golhen, B. Le Guennic, T. Guizouarn, L. Ouahab, O. Cador, Magnetic memory in an isotopically enriched and magnetically isolated mononuclear dysprosium complex, Angew. Chem. Int. Ed. 54 (2015) 1504–1507. https://doi.org/10.1002/anie.201409887.

[5] A. Abragam, B. Bleaney, Electron Paramagnetic Resonance of Transition Ions, Clarendon Press Oxford, UK,. (1970) 925.

[6] K.N. Shrivastava, Theory of Spin–Lattice Relaxation, Phys. Status Solidi. 117 (1983) 437–458. https://doi.org/10.1002/pssb.2221170202.

[7] J. Wang, J.J. Zakrzewski, M. Heczko, M. Zychowicz, K. Nakagawa, K. Nakabayashi, B. Sieklucka, S. Chorazy, S.I. Ohkoshi, Proton Conductive Luminescent Thermometer Based on Near-Infrared Emissive {YbCo2} Molecular Nanomagnets, J. Am. Chem. Soc. 142 (2020) 3970–3979. https://doi.org/10.1021/jacs.9b13147.

[8] K.S. Pedersen, J. Dreiser, H. Weihe, R. Sibille, H. V. Johannesen, M.A. Sørensen, B.E. Nielsen, M. Sigrist, H. Mutka, S. Rols, J. Bendix, S. Piligkos, Design of Single-Molecule Magnets: Insufficiency of the Anisotropy Barrier as the Sole Criterion, Inorg. Chem. 54 (2015) 7600–7606. https://doi.org/10.1021/acs.inorgchem.5b01209.

[9] F. Pointillart, O. Cador, B. Le Guennic, L. Ouahab, Uncommon lanthanide ions in purely 4f Single Molecule Magnets, Coord. Chem. Rev. 346 (2017) 150–175. https://doi.org/10.1016/j.ccr.2016.12.017.

[10] S. Shionoya, W.M. Yen, H. Yamamoto, eds., Phosphor Handbook, CRC Press, Boca Ranton,

2007. https://doi.org/10.1201/9781315222066.
[11] Y.H. Zhou, J. Lin, Luminescent properties of YVO4:Dy3+ phosphors prepared by spray pyrolysis, in: J. Alloys Compd., Elsevier, 2006: pp. 856–859. https://doi.org/10.1016/j.jallcom.2004.11.085.
[12] Y. Cui, F. Zhu, B. Chen, G. Qian, Metal-organic frameworks for luminescence thermometry, Chem. Commun. 51 (2015) 7420–7431. https://doi.org/10.1039/c5cc00718f.
[13] J. Rocha, C.D.S. Brites, L.D. Carlos, Lanthanide Organic Framework Luminescent Thermometers, Chem. - A Eur. J. 22 (2016) 14782–14795. https://doi.org/10.1002/chem.201600860.

CHAPTER 6

MODULATING THE SMM PROPERTIES OF A $Zn^{II}_2Dy^{III}_2$ BASED COMPOUND BY RATIONALLY REDUCING/INCREASING THE ELECTRON DENSITY IN THE EQUATORIAL PLANE PERPENDICULAR TO THE $O_{phenoxido}$-Dy-$O_{phenoxido\text{-}bridges}$ DIRECTION

6.1. INTRODUCTION

This chapter is based, to some extent, on a previous work carried out by Murugesu and coworkers [1], which has been discussed in the general introduction (compounds **i14-i16**). Based on a dinuclear Dy_2 system (**i14**), where a phenoxido is responsible for providing an appropriate ligand field to confer SMM behaviour to this system, they managed to modify the nitrate in the equatorial plane by other chelates providing the system with more or less electron density on it, and without altering the geometry around the lanthanide. As expected from the crystal field design principles provided by Rinehart and Long [2], the less electron density in this plane, the higher the effective energy barrier that prevents the reorientation of the magnetization.

Inspired by their work, we took into consideration our compound **36** (studied in Chapter 4). This particular system displays a ligand field defined by three short Dy-$O_{phenoxido}$ distances in opposite positions on the Dy^{III} coordination sphere, two in one side and one in the other side, which is appropriate to induce zero field SMM behaviour. Moreover, the charge of the two phenoxido groups that are located in the same side are polarized, since they both act as bridging groups to a Zn^{II} ion. This fact has been proved to effectively enhance SMM properties [3]. In the plane normal to the $O_{phenoxido}$-Dy-$(O_{phenoxido})_2$ direction (hereafter namely equatorial plane), apart from methoxy groups belonging to the main ligand, one nitrate and a carboxylate oxygen atom are coordinated to the Dy^{III} ion. It has been seen that when strongly electronegative atoms reside in the axial positions of the structure, the rest of the ligands occupying the equatorial plane favour transverse components that activate under-barrier relaxation processes [4–6].

Keeping this in mind, in this work we have been able to modify the equatorial ligand field of **36** by replacing the succinate and nitrate oxygen atoms by some other groups that are shown in Figure 6.1. In our case, the reference compound allows us to include individual (by replacing either the succinate or the nitrate ligands) or simultaneous (by replacing both nitrate and succinate legends) modifications, which could provide us a more valuable information regarding which positions contribute more to the modulation of the dynamic magnetic properties. Thus, in this chapter we report the synthesis, characterization and magnetic study of five novel complexes based on the H_4L^4 ligand. Additionally, we have carried out some preliminary theoretical studies to shed some light on the experimental results.

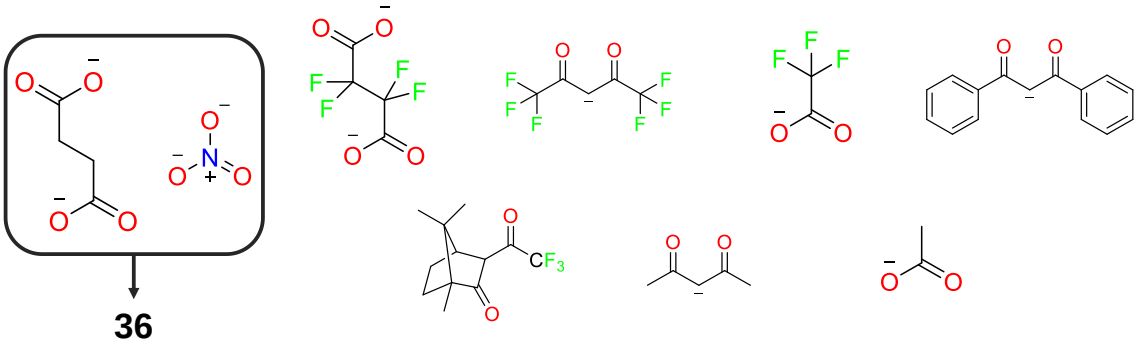

Figure 6.1.- Some of the oxygen donor atoms that are found in the equatorial plane of **36** (black box) and some other groups that have been used in this chapter to modify the electron density around the Dy^{III} ion.

6.2. PREPARATION OF COMPLEXES

6.2.1. $[Zn_2(\mu\text{-}H_2L^4)_2(\mu\text{-}F_4suc)Dy_2(NO_3)_2](NO_3)_2\cdot 9MeOH$ (45)

To a solution of H_4L^4 (0.05 mmol, 40.0 mg), $Zn(NO_3)_2\cdot 6H_2O$ (0.05 mmol, 14.9 mg) and $Dy(NO_3)\cdot 5H_2O$ (0.05 mmol, 21.9 mg) in 4 mL of methanol was added dropwise another solution containing tetrafluorosuccinic acid (F_4suc; 0.025 mmol, 4.8 mg) and NaOH (0.15 mmol from a methanolic 0.5 M solution) in 0.6 mL of methanol. A fine powder was formed after adding each drop, which it easily got dissolved. The solution was stirred for few seconds, filtered in order to remove possible undissolved particles and allowed to stand at room temperature. In few days suitable crystals for X-ray diffraction were obtained. Yield: 57%.

6.2.2. $[Zn_2(\mu\text{-}H_2L^4)_2(\mu\text{-}suc)Dy_2(hfac)_2](OTf)_2\cdot xH_2O\cdot yMeOH$ (46)

To a solution of H_4L^4 (0.05 mmol, 40.0 mg), $Zn(CF_3COCHCOCF_3)_2\cdot 2H_2O$ (hfac; 0.05 mmol, 25.8 mg) and $Dy(CF_3SO_3)_3$ (OTf; 0.05 mmol, 30.5 mg) in 10 mL of methanol was added dropwise another solution containing succinic acid (suc; 0.025 mmol, 3.0 mg) and NaOH (0.15 mmol from a methanolic 0.5 M solution) in 0.6 mL of methanol. A fine powder was formed in each drop, which it easily got dissolved. The pale yellow solution was stirred for few seconds, filtered in order to remove any possible insoluble material and allowed to stand at room temperature. In few days suitable yellow crystals for X-ray diffraction were obtained. Yield: 44%.

6.2.3. $[Zn_2(\mu\text{-}H_2L^4)_2(\mu\text{-}F_4suc)Dy_2(hfac)_2](OTf)_2 \cdot xH_2O \cdot yMeOH$ (47)

To a solution of H_4L^4 (0.05 mmol, 40.0 mg), $Zn(CF_3COCHCOCF_3)_2 \cdot 2H_2O$ (0.05 mmol, 25.8 mg) and $Dy(CF_3SO_3)_3$ (0.05 mmol, 30.5 mg) in 14 mL of ethanol was added dropwise another solution containing tetrafluorosuccinic acid (0.025 mmol, 4.8 mg) and Et_3N (0.15 mmol, 0.020 mL) in 1 mL of ethanol. A fine powder was formed in each drop, which it easily got dissolved. The pale yellow solution was stirred for few seconds, filtered in order to remove possible undissolved particles and allowed to stand at room temperature. In few days suitable yellow crystals for X-ray diffraction were obtained. Yield: 46%.

6.2.4. $[Zn_2(\mu\text{-}H_2L^4)_2(\mu\text{-}suc)Dy_2(CF_3CO_2)_2(MeOH)_2](OTf)_2 \cdot 3MeOH$ (48)

To a solution of H_4L^4 (0.075 mmol, 60.0 mg), $Zn(CF_3CO_2)_2 \cdot xH_2O$ (0.075 mmol, 21.9 mg) and $Dy(CF_3SO_3)_3$ (0.075 mmol, 45.7 mg) in 20 mL of methanol was added dropwise another solution containing succinic acid (0.0375 mmol, 4.4 mg) and Et_3N (0.225 mmol, 0.030 mL) in 1 mL of methanol. In view of the high solubility of the product, the solution was further concentrated by heating it at 75 ºC until a considerable amount of solid was obtained and then the solid was filtered while hot. Suitable crystals for X-ray diffraction were achieved from a diluted reaction. It is noteworthy that a second phase similar to this compound, **48b**, was also obtained in the same reaction, which contains a water molecule coordinated to the Dy^{III} ion instead of a methanol molecule (Figure A6.1). However, as it is shown in PXRD experiments, the phase that was studied corresponds to pure **48**. Yield: 38%.

6.2.5. $[Zn_2(\mu\text{-}H_2L^4)_2(\mu\text{-}suc)Dy_2(dbm)_2](OTf)_2 \cdot xH_2O \cdot xMeOH$ (49)

To a solution of H_4L^4 (0.02 mmol, 16.0 mg), $Zn(OTf)_2 \cdot$(0.02 mmol, 7.3 mg), $Dy(CF_3SO_3)_3$ (0.02 mmol, 12.2 mg) and 1,3-Diphenyl-1,3-propanedione (dbm; 0.02 mmol, 4.5 mg) in 20 mL of methanol was added dropwise another solution containing succinic acid (0.01 mmol, 1.2 mg) and Et_3N (0.08 mmol, 0.011 mL) in 1 mL of methanol. The colourless solution was stirred for few seconds, filtered in order to remove any possible insoluble material and allowed to stand at room temperature. In few days suitable crystals for X-ray diffraction were obtained. Yield: 30%.

6.3. EXPERIMENTAL RESULTS

As it has been shown in the previous two chapters, H_4L^4 is able to stabilize the highest Kramers doublet with the highest M_J value (± 15/2) as ground state and well separated from the excited states. As a result, compound **36** in Chapter 4, showed a high performance zero field SMM. In this project, we have maintained the core of the structure preserving the ligand field provided by the phenoxido groups, but subtly modifying the electron density in the equatorial plane. This led to the formation of five novel compounds with the general formula: $[Zn_2(\mu\text{-}H_2L^4)_2(\mu\text{-dicarb})Dy_2(L')_2]X_2{\cdot}xH_2O{\cdot}yMeOH$, where dicarb = succinate (**46**, **48** and **49**), tetrafluorosuccinate (**45** and **47**); L' = NO_3^- (**45**), hfac (**46** and **47**), $CF_3CO_2^-$ (**48**), dbm (**49**); X = NO_3^- (**45**), OTf (**46-48**) and x,y = 0,9 (**45**), undetermined (**46**, **47**, **49**), 0,3 (**48**). Powder X-ray diffractograms (Figures A6.2-A6.6) confirmed the phase purity of the samples.

6.3.1. Crystal structures of Complexes 45-49

The specific information relative to space groups, crystallographic data and a summary of the most relevant bond distances and angles is given in the appendices (Tables A6.1-A6.9). All the compounds display the same core structure as shown in Figure 6.2. Each double positive cationic fragment is constituted by two octadentate (N_2O_6) H_2L^{2-} ligands, two Zn^{II} and two Dy^{III} ions, a bridging succinate (or tetrafluorosuccinate) and two terminal chelates, each one coordinated to a Dy^{III} ion. Differently, compound **48** contains $CF_3CO_2^-$ molecules that are monocoordinated, so that methanol molecules complete the Dy^{III} coordination sphere. Regarding to the counterions, compound **45** contains nitrates to balance the charge, whereas compounds **46-49** contain triflates. Note that, as we discussed, some of the structures were refined with squeeze routines and we are still carrying out a more complete characterization to be sure of the counterions and crystallization solvent molecules present in the compounds. In **46-49**, nitrate salts were not used to avoid undesired mixture of anions in the in the final complexes. As in the previous similar structures reported in Chapters 4 and 5,[¡Error! Marcador no definido.] even though the ligand has three deprotonated phenol groups, the overall charge is H_2L^{2-}, since N4 is in the zwitterionic form (in Figure A6.1 the labelled compound **45** is displayed, the rest of the compounds follow the same pattern). It is worth mentioning that, in compounds **45**, **47**, **48** and **49** an entire molecule is within the asymmetric unit, whereas three of them are in **46**.

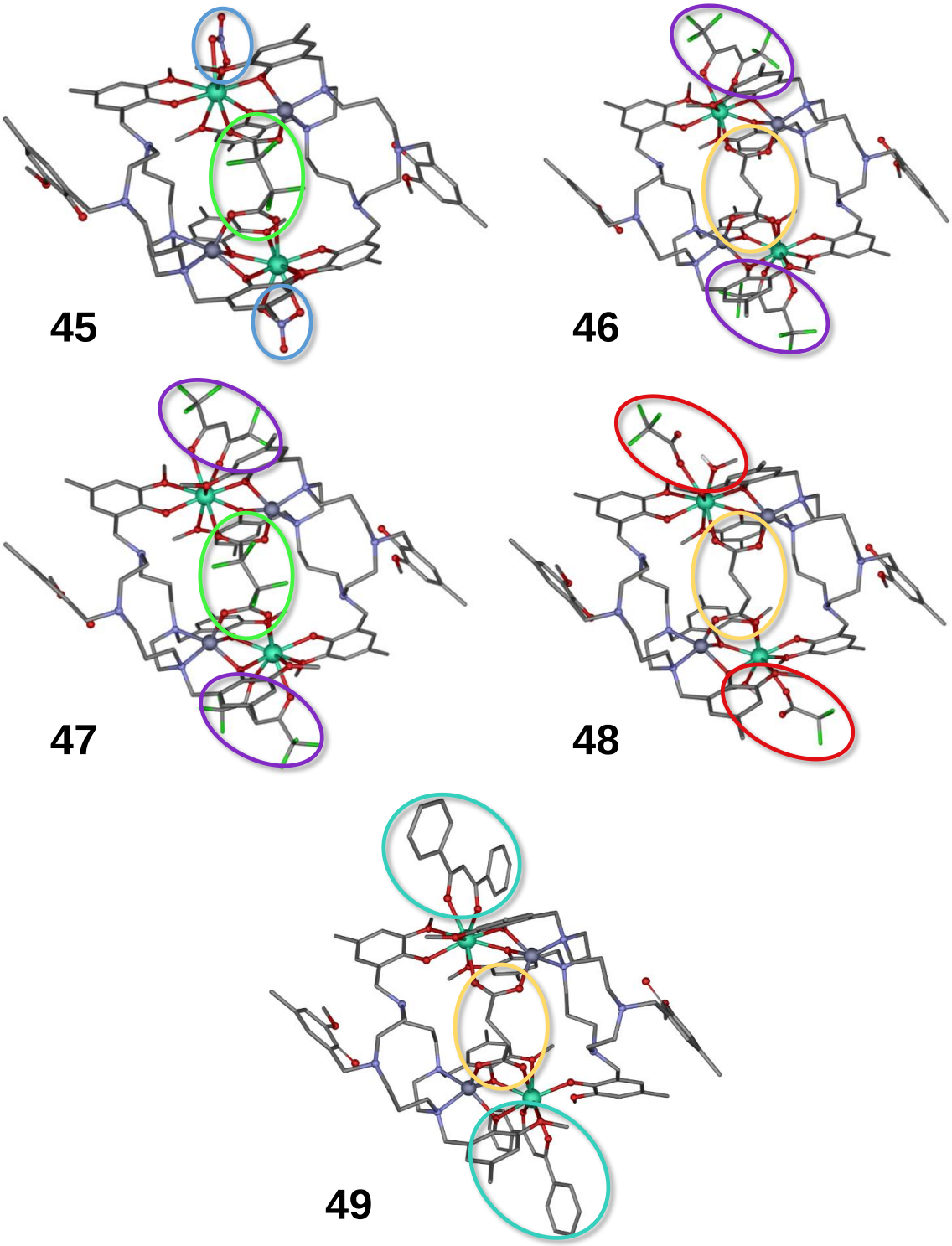

Figure 6.2.- Perspective view of the cationic structures of **45-49**. The modified parts are highlighted in ovals. Dysprosium, zinc, oxygen, nitrogen, carbon, fluoride and hydrogen atoms are in turquoise, dark grey, red, blue, grey, green and white, respectively. All hydrogen atoms except the methanolic OH atoms (**48**) and counteranions have been omitted for the sake of clarity.

One of the main objectives when synthesizing these tetranuclear derivatives was to minimally transform the coordination environment in terms of polyhedra, whereas the electronic distribution around Dy^{III} ions was significantly varied. The coordination environment geometries around metal ions were evaluated by the SHAPE software [7]. In the case of Zn^{II} ions, there is not any remarkable difference from one complex to another. In all compounds, the ZnN_2O_3 sphere fits best to a square pyramid, though they are all slightly distorted (Table A6.10). The case of Dy^{III} is not that simple and, as it might be expected for a DyO_9 sphere, there are much more possibilities. Indeed, among the thirteen different possibilities, there is not any single one which is adequate to describe correctly the polyhedra formed by the oxygen donor atoms. This corroborates the difficulty when designing a specific ligand field due to the high coordination numbers of lanthanide ions [8]. All CShM values are higher than 1.615 (value for Dy1A in **46** for spherical capped square antiprism, Table A6.11) for any of the possible ideal polyhedra, confirming the high grade of distortion. In general terms, however, it could be said that all Dy^{III} ions are between spherical capped square antiprism, tricapped trigonal prism, spherical tricapped trigonal prism and muffin type of polyhedra. Note that in **49** Dy1B can be considered intermediate between DyO_9 and DyO_8, and, therefore, both geometries were considered (Tables A6.11-A6.12)

Anyhow, we believe that the ligand field created the phenoxido groups is maintained in almost all the complexes. Figure 6.3 displays more clearly the aim of this research. It could be seen that the most electron-donating phenoxido groups are nearly in opposite positions. The equatorial plane, in contrast, is constituted of methoxy groups, a chelate (nitrate in Figure 6.3) and the succinate bridging ligand connecting two $Zn^{II}Dy^{III}$units. We have said that the ligand field created by the phenoxido groups is maintained, because for all the complexes the Dy-$O7_{phenoxido}$ bond is the shortest one, which is found in the range of 2.234(4)-2.279(4) Å. These bonds are followed, in almost all the cases, by Dy-$O1_{phenoxido}$ and Dy-$O3_{phenoxido}$ bonds falling in the range of 2.263(7)-2.358(4) Å. As an exception, in **49** the dbm chelates display shorter distances in the 2.275(4)-2.305(4) Å range. This will probably be detrimental for the SMM behaviour. For the rest of the compounds, chelates (or $CF_3CO_2^-$ and MeOH in **48**) in the equatorial plane display longer bond distances in the range of 2.358(3)-2.456(4) Å. It is interesting to note that, as a general trend, compounds containing tetraflurosuccinate instead of succinate display slightly longer Dy-$O_{carboxylate}$ bond distances (Tables A6.3-A6.9), which was the principal aim when including electron-withdrawing groups within the molecule.

Regarding to the most relevant angles, we can also say that the disposition of the core structure is maintained in all the complexes. Indeed, O1-Dy-O7, O3-Dy-O7, $O_{carboxylate}$-Dy-O7, O_{chel1}-Dy-O7 and O_{chel2}-Dy-O7 fall in relatively narrow angle ranges: 136.09(13)-141.1(2)º, 133.7(3)-144.16(14)º, 72.39(12)-77.94(13), 77.9(2)-90.72(8) and 126.19(13)-137.49(9), respectively.

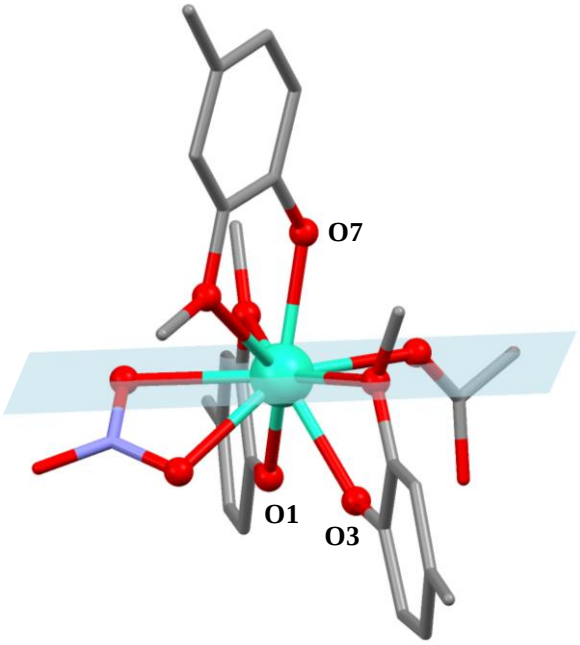

Figure 6.3.- Perspective view of a reduced fragment of **45**. O7, O1 and O3 provide axiality to the Dy^{III}. The blue plane represents an indicative equatorial ligand field.

6.3.2. Static magnetic properties of complexes 45-48

The temperature dependence of the magnetic susceptibility was measured on polycrystalline samples for complexes **45-48** in the 2-300 K temperature range under an applied field of 0.1 T (Figure 6.4). The same measurement will be carried out for **49** soon. At room temperature, the $\chi_M T$ values of 28.52 (**45**), 28.10 (**46**), 28.02 (**47**) and 28.75 (**48**) $cm^3 \cdot mol^{-1} \cdot K$ are in the expected ranges for two non-interacting Dy^{III} ions (14.17 $cm^3 \cdot mol^{-1} \cdot K$; $^6H_{15/2}$, and g = 4/3) in the free ion approximation. Noteworthy, the molecular weight values that we employed for the calculations of **46** and **47** are based on anhydrous compounds and, hence, they may slightly change afterwards. All the complexes display a similar behavior with a gradual decrease of the $\chi_M T$ product when lowering the temperature due to the depopulation of the M_J sublevels. At the lowest temperature region, all the compounds exhibit a more marked final drop, being

especially pronounced in the case of **45** which could be indicative of magnetic blocking. The fact that the reduced magnetization curves are not superimposable, as well as the low value of the magnetization at the highest applied magnetic field are indicative of magnetic anisotropy (Figure 6.4, insets).

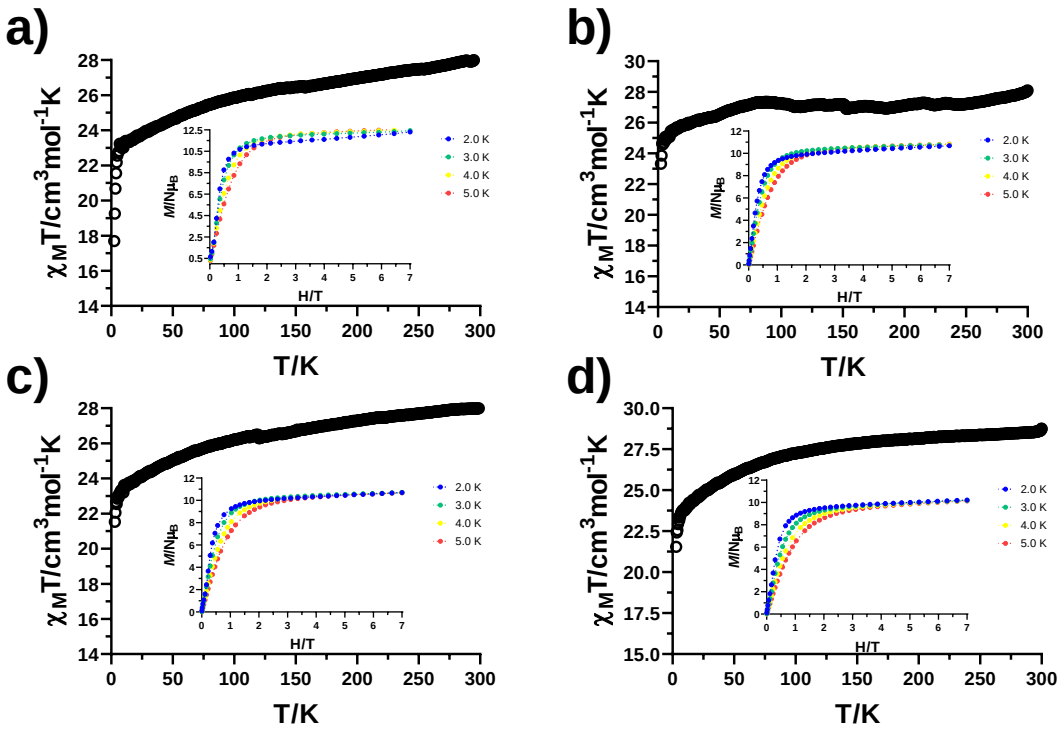

Figure 6.4.- Temperature dependence of the $\chi_M T$ product at 1000 Oe for complexes **45-48** (from a) to d), respectively). Insets: Field dependence of the magnetization in the 2-5 K temperature range. Dashed solid lines are a guide to the eye.

In order to confirm the possibility of magnetic blocking in all these compounds, we performed field-cooled (FC) and zero-field-cooled (ZFC) experiments (Figure 6.5). As it can be observer, in complexes **45** and **47** both curves bifurcate around 6 K, slightly at higher temperatures compared to compound **36**. In contrast, in **46** the curves are bifurcating at around 4 K, whereas in **48** they do it at 5 K. These values provide an idea of what we could expect to see in the dynamic magnetic properties.

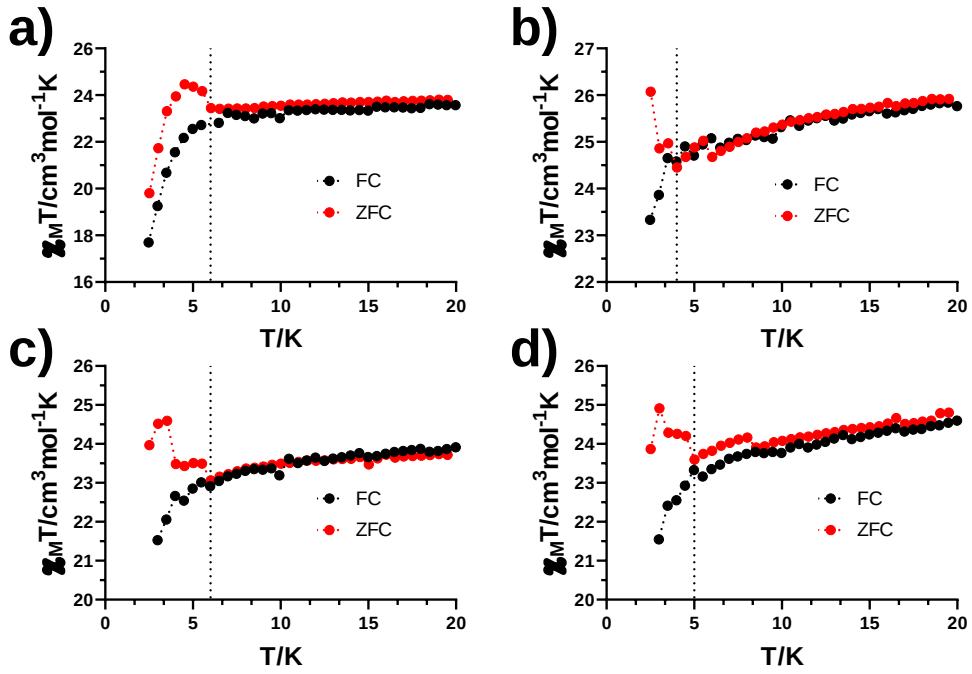

Figure 6.5.- Field-cooled (FC, black) and zero-field-cooled (ZFC, red) $\chi_M T$ product in the 2.5-20 K temperature range for **45-48** (from a) to d), respectively). The dashed lines show the temperature at which both curves bifurcate.

6.3.3. Dynamic magnetic properties of complexes 45-49

The introduced modifications around the Dy^{III} ion were expected to produce notable differences regarding dynamic magnetic properties. However, as the ligand field created by the phenoxido groups was maintained in almost all the compounds, a zero field SMM behaviour was expected for most of them. Indeed, *ac* measurements carried out under zero applied *dc* field and with an oscillating field of 3.5 Oe revealed out-of-phase maxima for all of the systems (Figures 6.6-6.9) except for **49** (Figure A6.19). Compounds **45-48** showed maxima below 33 K, 17 K, 26 K and 21 K, respectively, indicating that the different electronic distribution around the Dy^{III} ion led to a different energy distribution of the M_J states. As a general feature, all compounds displayed long tails below the maxima indicative of unquenched QTM.

For compound **45**, relaxation times were extracted from the fitting of the $\chi''_M(\upsilon)$ curves in the 15.8-32.6 K (Figure A6.8) temperature range. The $\ln\tau$ vs $1/T$ plot shows a clear curvature in the almost entire temperature range with a linear portion in the zone of highest temperatures, indicative of a combination of various relaxation mechanisms

operating simultaneously. A linear Arrhenius fit of the relaxation times at the highest temperatures afforded U_{eff} = 287.0 K and τ_0 = $3.0 \cdot 10^{-9}$ s. In addition, the data were fitted to a combination of Orbach and Raman relaxation pathways in the whole temperature range:

$$\tau^{-1} = BT^n + \tau_0^{-1} exp(-U_{eff}/k_BT) \qquad \textit{Equation 6.1}$$

The fit afforded the following set of parameters: U_{eff} = 369.2 K, τ_0 = $4.0 \cdot 10^{-10}$ s, B = $1.8 \cdot 10^{-3}$ $s^{-1}K^{-4.629}$ and n = 4.629. Within the inset of Figure 6.6 it can be observed marked by dashed lines the contribution of each relaxation mechanism respect to the overall relaxation process. This illustrates how the Raman process acts in a wide range, whereas the contribution of Orbach is limited to the highest temperatures. This is in good agreement with α values extracted from the Cole-Cole plots (Figure A6.9), which are abnormally high even at the highest temperatures (0.32(15.8 K)-0.23(32.6 K)), where normally slower values are expected due to a purer Orbach relaxation. The higher α values extracted in the low temperature region (below 20 K) are probably influenced by the incoming QTM. Nevertheless, these temperatures are still relatively high and, therefore, there is no sense in including QTM relaxation process into the equation. Besides, no temperature independent relaxation times were obtained in this regime, which would be indicative of QTM.

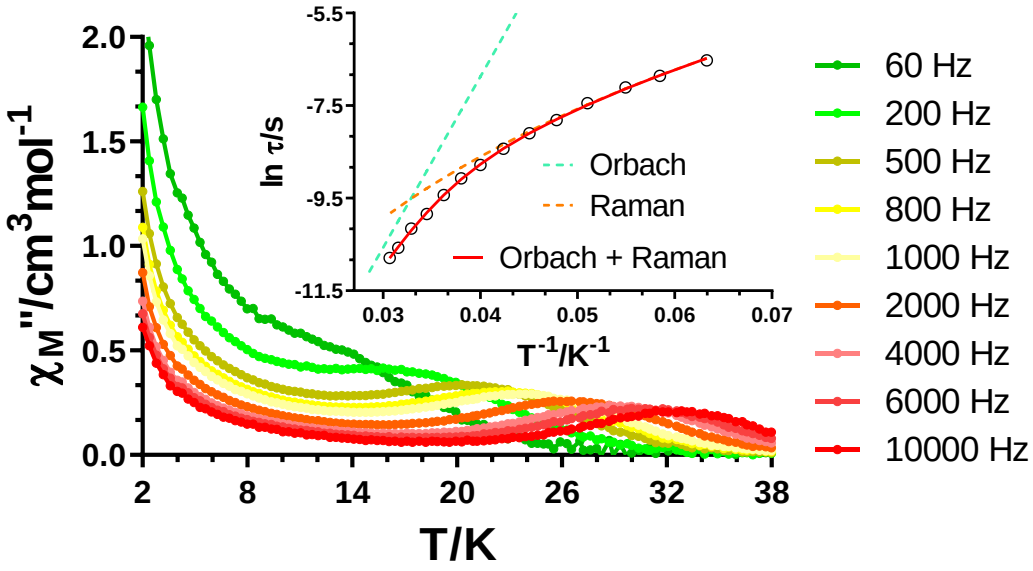

Figure 6.6.- Temperature dependence of the out-of-phase components of the *ac* susceptibility in a zero applied field for **45**. Inset: Arrhenius plot for the relaxation times considering a combination of Orbach and Raman relaxation processes. Dashed lines represent the individual contribution of each mechanism.

Compound **46** displays maxima at much lower temperatures compared to **45**. The temperature dependence of the relaxation times in the form lnτ vs 1/*T* plot shows, in this case, three different regimes. A clear linearity can be observed at the highest temperatures, a curvature in the intermediate range and an almost but not completely temperature independent range at the lowest temperatures, indicative of fast QTM. This is also detectable in the $\chi''_M(\upsilon)$ curves, where at the lowest temperature range a minor shift of the maxima is observed (Figure A6.11). The high α values also suggest the presence of simultaneous relaxation mechanisms (0.49(4.8 K)-0.17(17.6 K)). The linear Arrhenius fit at the highest temperatures gives rise to U_{eff} = 82.8 K and τ_0 = $2.0 \cdot 10^{-7}$ s. We attempted a simultaneous fit considering the three mentioned mechanisms, but we were not able to obtain a reasonable fit. We believe that this could be due to the fact that even though QTM is present, completely temperature-independent relaxation times are not still achieved. Thus, we fit the data with Equation 6.1 obtaining U_{eff} = 92.0 K, τ_0 = $1.4 \cdot 10^{-7}$ s, B = 70.6 $s^{-1}K^{-1.416}$ and n = 1.416.

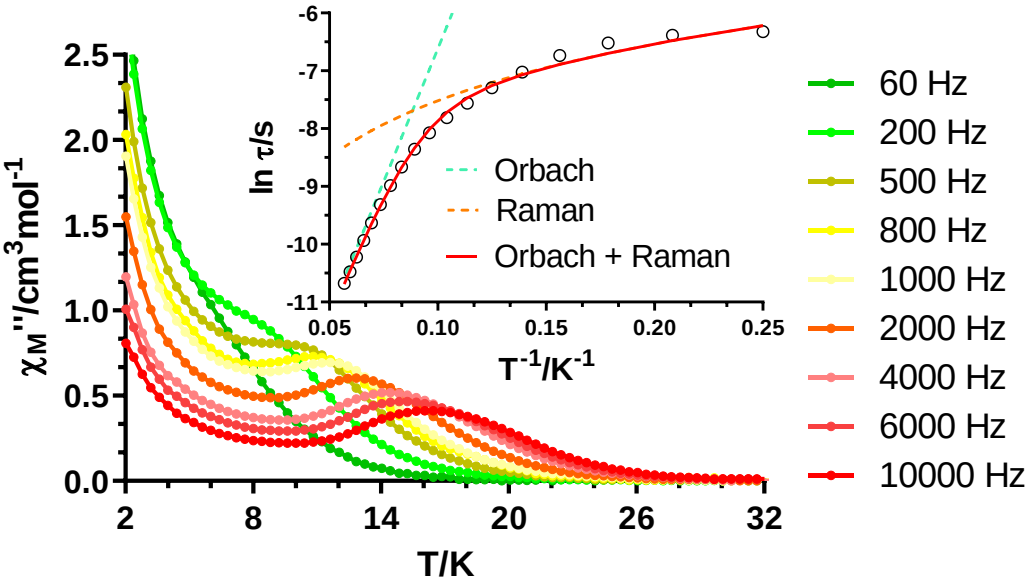

Figure 6.7.- Temperature dependence of the out-of-phase components of the *ac* susceptibility in a zero applied field for **46**. Inset: Arrhenius plot for the relaxation times considering a combination of Orbach and Raman relaxation processes. Dashed lines represent the individual contribution of each mechanism.

The two modifications implemented in **45** and **46** were combined in **47**, where the bridging succinate is changed to tetrafluorosuccinate and the chelating groups are hfac instead of bidentate nitrate ligands. Interestingly, this system shows a well-defined set of maxima below 26 K, a temperature value that is in between those observed for **45** and **46** and very similar to that of **36** (Figure 6.8). The relaxation times display a very similar trend to **45**, with a remarkable curvature in the whole temperature range and a linear portion at the highest temperatures. The fit of the later portion to the Arrhenius law provides U_{eff} and τ_0 values of 241.4 K and $2.1 \cdot 10^{-9}$ s, respectively. By considering the simultaneous presence of Raman and Orbach processes with Equation 6.1, the fit afforded the following values: U_{eff} = 403.8 K, $\tau_0 = 8.2 \cdot 10^{-12}$ s, $B = 2.2 \cdot 10^{-3}$ $s^{-1}K^{-4.965}$ and n = 4.965. As for **45**, the Raman process predominates in the widest range as seen in the inset of Figure 6.8.

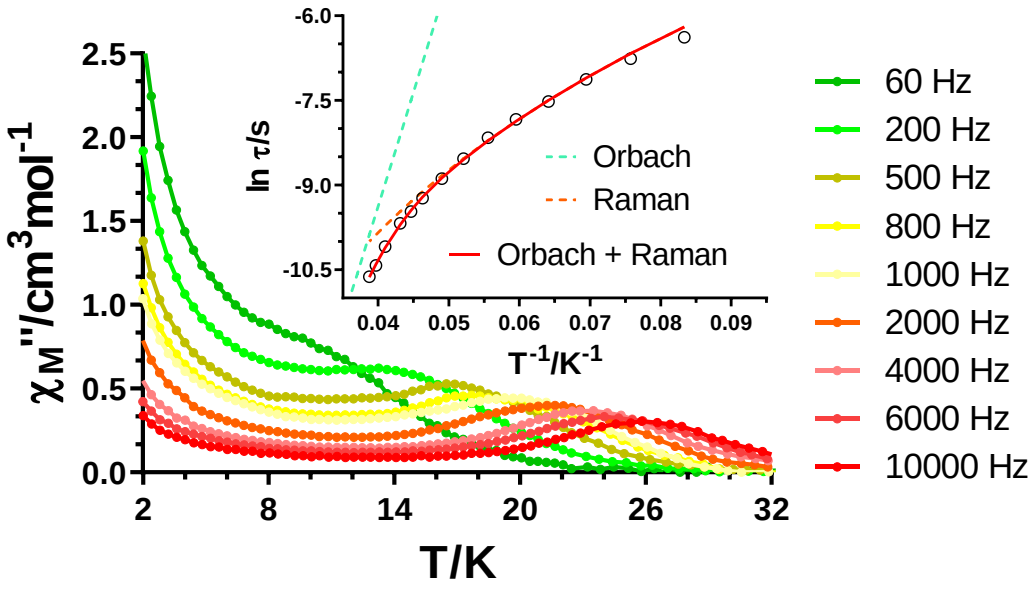

Figure 6.8.- Temperature dependence of the out-of-phase components of the *ac* susceptibility in a zero applied field for **47**. Inset: Arrhenius plot for the relaxation times considering a combination of Orbach and Raman relaxation processes. Dashed lines represent the individual contribution of each mechanism.

Compound **48** displays maxima below 21 K (Figure 6.9). In this case, due to the nature of the $\chi''_M(\upsilon)$ data, the curves could be fitted from the lowest measured temperature (2.0 K) until 21.2 K (Figure A6.17), a fact that allowed us to obtain more

information about the tunnelling regime. Indeed, the mentioned curves display no shift in the position of the maxima for the lowest temperatures, which is directly attributed to QTM. Similarly to **46**, the lnτ vs *T* distribution of the relaxation times displays a linear portion attributed to an Orbach process at the highest temperatures, a curvature related to a Raman in the mid-range and a temperature independent domain at the lowest temperatures. The linear fit of the data in the highest temperature region gave rise to U_{eff} = 132.4 K and $\tau_0 = 4.7 \cdot 10^{-8}$ s. The whole data was fitted to Equation 6.2 considering a sum of QTM, Raman and Orbach mechanisms:

$$\tau^{-1} = \tau_{QTM}^{-1} + BT^{n} + \tau_0^{-1} exp(-U_{eff}/k_B T) \qquad \textit{Equation 6.2}$$

The simultaneous presence of various mechanisms is reflected in the high α values obtained from the Cole-Cole plots (0.64(2.0 K)-0.20 (21.2 K)). The best fit of the data to the above equation led to the following set of parameters: U_{eff} = 214.8 K, $\tau_0 = 1.6 \cdot 10^{-9}$ s, $B = 4.7 \cdot 10^{-1}$ $s^{-1}K^{-3.420}$, n = 3.420 and $\tau_{QTM} = 2.4 \cdot 10^{-3}$ s.

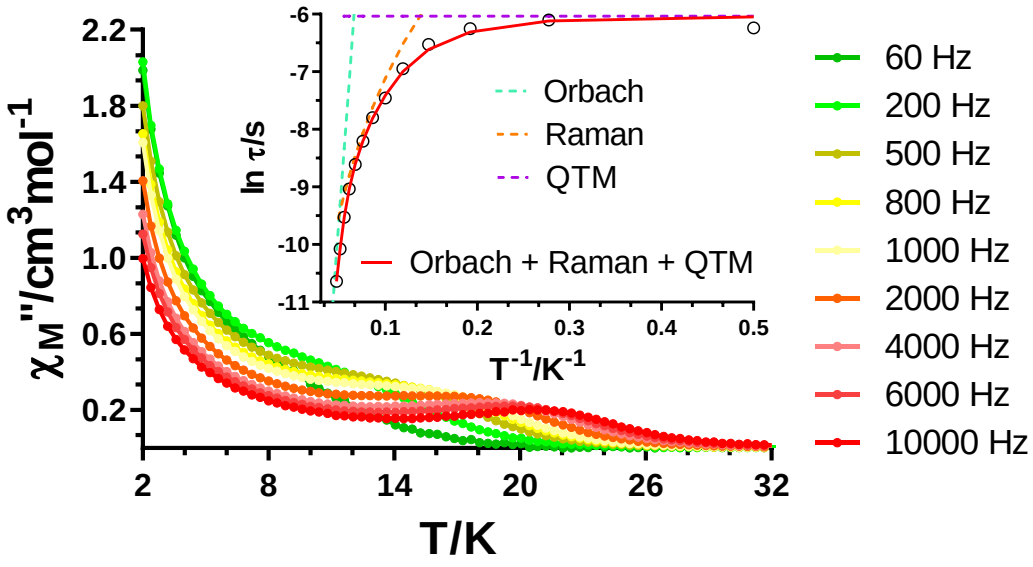

Figure 6.9.- Temperature dependence of the out-of-phase components of the *ac* susceptibility in a zero applied field for **48**. Inset: Arrhenius plot for the relaxation times considering a combination of Orbach, Raman and QTM relaxation processes. Dashed lines represent the individual contribution of each mechanism.

As abovementioned, compound **49** does not display any maximum in the out-of-phase region in the absence of an external magnetic field. Even though we did not know how the short dbm bonds in the equatorial plane would influence the magnetic properties, a poorer SMM behaviour would be expected for this compound. To at least partially suppress QTM we also carried out an additional measurement under an arbitrary external magnetic field of 1 kOe (Figure A6.19). A maximum could be seen in the temperature dependence of the in-phase component of the ac susceptibility around 2 K, whereas in the out-of-phase component it should be below the temperature limit of the instrument, thus indicating a negligible energy barrier.

The following Table 6.1 summarizes all the fitting parameters obtained by considering only Orbach or simultaneous presence of several mechanisms.

Table 6.1.- U_{eff}, τ_0, B, n and τ_{QTM} parameters generated from the fit of the relaxation time-temperature dependence for **45-48**.

	Orbach		**Simultaneous relaxation mechanisms**				
			Orbach		**Raman**		**QTM**
Comp.	U_{eff} (K)	τ_0 (s)	U_{eff} (K)	τ_0 (s)	B ($s^{-1}K^{-n}$)	n	τ_{QTM} (s)
45	287.0	$3.0 \cdot 10^{-9}$	369.2	$4.0 \cdot 10^{-10}$	$1.8 \cdot 10^{-3}$	4.6	
46	82.8	$2.0 \cdot 10^{-7}$	92.0	$1.4 \cdot 10^{-7}$	70.6	1.4	
47	241.4	$2.1 \cdot 10^{-9}$	403.8	$8.2 \cdot 10^{-12}$	$2.2 \cdot 10^{-3}$	5.0	
48	132.4	$4.7 \cdot 10^{-8}$	214.8	$1.6 \cdot 10^{-9}$	$4.7 \cdot 10^{-1}$	3.4	$2.4 \cdot 10^{-3}$

6.3.4. Hysteretic behaviour of complexes 45-48

In view of the zero field SMM behaviour compounds **45-48**, we performed magnetization hysteresis loop measurements on powdered samples at 2 K (Figure 6.10). Note that the employed sweep-rates were not constant over the entire field range, but were slower at low fields. For **45**, the average sweep-rate in the 0.63 T to -0.63 T and -0.63 T to 0.63 T range was 61 Oe/s; for **46** in the 0.57 T to -0.57 T and -0.57 T to 0.57 T range was 52 Oe/s; for **47** in the 0.57 T to -0.57 T and -0.57 T to 0.69 T range was 52 Oe/s and, lastly, for **48** in the 0.57 T to -0.57 T and -0.57 T to 0.57 T range was 51 Oe/s. Thus, we believe that overall the curves are comparable. All the

compounds exhibited butterfly-shaped hysteresis loops without any remnant magnetization at zero field. This is consistent with the QTM regime also found in the $\chi''_M(T)$ plots by the long tails at lowest temperatures. The opening of the loops is consistent with the U_{eff} values that we calculated only by considering an Orbach process, from which we can sort the compound in terms of performance as **45** > **47** > **48** > **46**. Note that the hysteresis loop is very similar to which we obtained for **36**, a compound that displays a very similar effective energy barrier considering an Orbach mechanism.

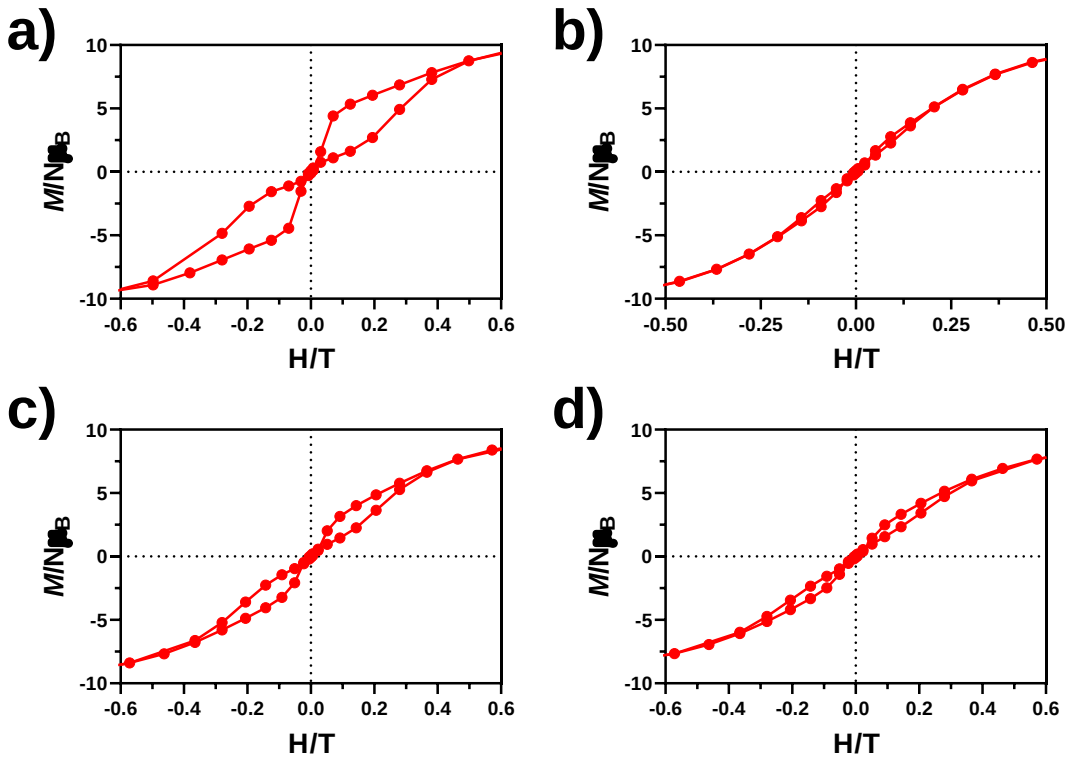

Figure 6.10.- Magnetic hysteresis loops for **45-48** (from a) to d), respectively) for *H* values between -0.6 T and 0.6 T at 2 K and at the indicated sweep rates.

6.3.5. *Ab initio* calculations on compounds 45-48

In collaboration with Prof. Nina P. Gritsan from the Russian Academy of Sciences (Institute of Chemical Kinetics and Combustion) we performed SA-CASSCF(9,7)/SO_RASSI/SINGLE_ANISO calculations [9] on compounds **45-48** with the aim of reaching a better understanding of the experimental results. Due to the large amount of atoms in each molecule, we had to cut the molecules trying to maintain the

core structure and the coordination environment of the Dy^{III} ion unchanged. In order to do that, as it is shown in Figures A6.20-A6.23, we took the following points into consideration: (i) a cationic fragment was selected for each compound (with one positive charge); (ii) a random $Zn^{II}Dy^{III}$ fragment was considered and (iii) half ligand from each fragment was chosen (one half acting with both inner and outer pockets and the other half in which one phenol derivative acts as monodentate and the other one is not coordinated). As it is shown in the mentioned figures, the main magnetic anisotropy axes are mostly influenced by the short Dy-O7 bonds.

Table 6.2 shows the results obtained for the first three (ground and first two excited states) Kramers' doublets (KD) of **45**, while the data corresponding to the eight doublets is shown in Table A6.13. As it can be observed in this table, the ground state is highly anisotropic with nearly perfect axiality (g_z = 19.9, g_x = 0.0004; g_y = 0.001) being almost pure M_J = ±15/2 (99%). The axial nature is also observed for the first excited state, whereas the second excited state displays non-negligible transverse components and a noticeable admixture of two different M_J states. Thus, this system would be expected to relax via the second excited state. Note that even though the first KDs are well defined the higher excited states show a high grade of mixing (Table A6.13), which is a common feature of systems without a strictly axial ligand field [10].

Table 6.2.- The energy splitting of the ground $^6H_{15}$ multiplet**,** principal values of the *g* tensor for each Kramers' doublet and decomposition of the wavefunctions of the components of each Kramers' doublet to the wavefunctions with definite J_z (z is the easy exes for the ground Kramers doublet).

Complex	KD	E, cm^{-1}	g_x	g_y	g_z	$\|J_z\|$ (contribution in %)
45	1	0	0.0004	0.001	19.9	15/2 (99)
	2	210	0.054	0.059	17.16	13/2 (94.4)
	3	345	0.37	0.9	13.6	11/2 (71.8), 9/2 (14.5)

Relaxation via the second excited state is also supported by the *ab initio* calculated relaxation dynamics for **45** (Figure 6.11). The matrix elements for ground state QTM, as well as for TA-QTM via the first excited state display low values ($2\cdot10^{-4}$ and $2\cdot10^{-2}$ μ_B, respectively; dashed black lines) in agreement with the observed zero field SMM

behavior. Therefore, a relaxation through the second excited state would be expected for this compound. The energy splitting between the ground and second excited state is of 496 K (345 cm^{-1}), which is well above the calculated U_{eff} of 369 K considering both Raman and Orbach relaxation mechanisms. However, in this case, the difference between the calculated and experimental one seems quite large. We are currently trying to better understand the relaxation of this system. Noteworthy, we do not think that this is a matter of choosing one or the other fragment of the molecule. Indeed, if there was such a difference between one and the other, this would probably be observable with two different sets of maxima in the $\chi''_M(T)$ plots

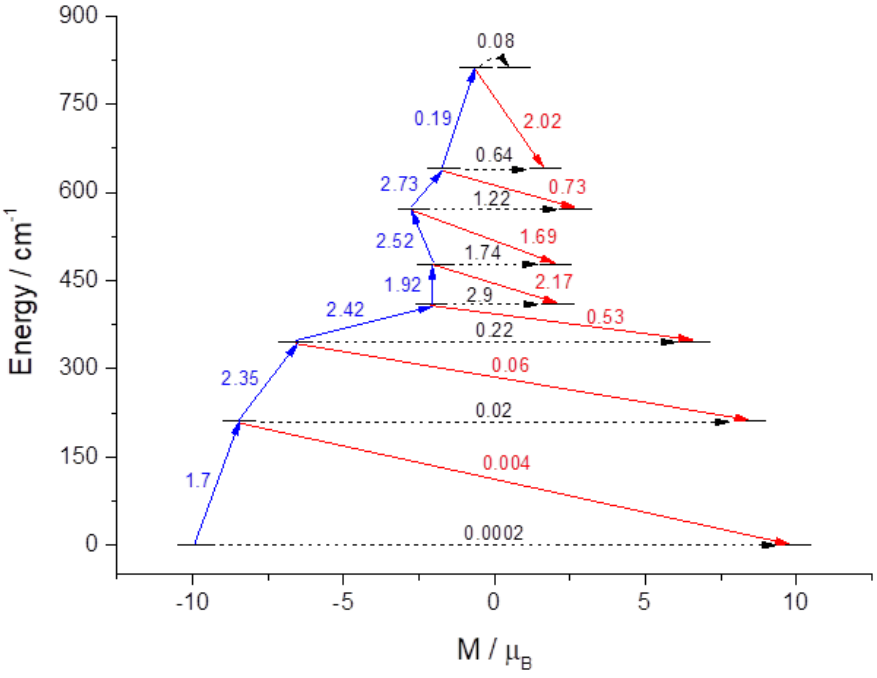

Figure 6.11.- *Ab initio* calculated relaxation dynamics for **45**. The exchange states are arranged according to the values of their magnetic moments. The arrows show the connected exchange states, and the numbers at each of them stand for the corresponding matrix element of the transversal magnetic moment.

Results for **46** are shown in Tables 6.3 and A6.14. Similar to **45**, the ground and first excited state are composed of almost pure M_J = ±15/2 and M_J = ±13/2, respectively. However, the first and specially the second excited state contain much larger transverse components that may facilitate tunneling gaps. The *ab initio* calculated relaxation dynamics (Figure 6.12) display a very low matrix element referring to ground state QTM ($2 \cdot 10^{-3}$ μ_B) in fair agreement with the zero field SMM behavior.

The TA-QTM through the first excited state, though, has a larger value of 0.11 indicating that relaxation may occur from it. Anyway, once more the calculated energy gap between these ground and first excited states appears to be overestimated, being 247 K (172 cm^{-1}) and 92 K the theoretically and experimentally determined ones, respectively.

Table 6.3.- The energy splitting of the ground $^6H_{15}$ multiplet**,** principal values of the *g* tensor for each Kramers' doublet and decomposition of the wavefunctions of the components of each Kramers' doublet to the wavefunctions with definite J_z (z is the easy exes for the ground Kramers doublet).

Complex	KD	E, cm^{-1}	g_x	g_y	g_z	$\|J_z\|$ (contribution in %)
46	1	0	0.008	0.012	19.85	15/2 (99.1)
	2	172	0.28	0.4	16.94	13/2 (92.7)
	3	247	2.67	5.6	13.38	11/2 (30.4), 5/2 (20), 9/2 (15.2), 7/2 (10)

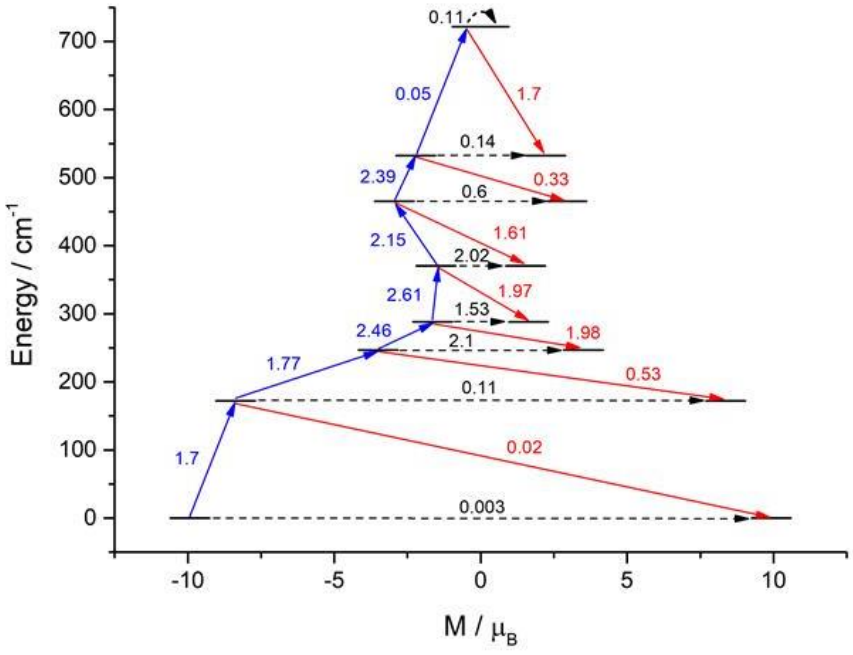

Figure 6.12.- *Ab initio* calculated relaxation dynamics for **46**. The exchange states are arranged according to the values of their magnetic moments. The arrows show the connected exchange states, and the numbers at each of them stand for the corresponding matrix element of the transversal magnetic moment.

Probably, the theoretical results that we obtained for **47** are the ones that better fit to the experimental ones (Table 6.4 and A6.15). As in **45**, the ground and first excited states are axial in nature with low transverse components and almost pure M_J = ±15/2 and M_J = ±13/2 wavefunctions. The g_x and g_y tensors in the second excited state have large values and the wavefunction is better described by a combination of different M_J sublevels, indicating a relaxation pathway through it. Moreover, the calculated relaxation dynamics (Figure 6.13) reveal low matrix elements in both ground and first excited states and, therefore, the larger value in the second excited state (0.7 μ_B) allows a TA-QTM process. In this case, the theoretically and experimentally calculated energy gaps are in closer agreement, 457 K (318 cm^{-1}) against 403 K. Still with a slight overestimation provided by theory.

Table 6.4.- The energy splitting of the ground $^6H_{15}$ multiplet**,** principal values of the *g* tensor for each Kramers' doublet and decomposition of the wavefunctions of the components of each Kramers' doublet to the wavefunctions with definite J_z (z is the easy exes for the ground Kramers doublet).

Complex	KD	E, cm^{-1}	g_x	g_y	g_z	$\|J_z\|$ (contribution in %)
47	1	0	0.005	0.007	19.8	15/2 (99.2)
	2	198	0.14	0.16	17.02	13/2 (96)
	3	318	1.32	2.76	13.44	11/2 (69.7), 9/2 (12)

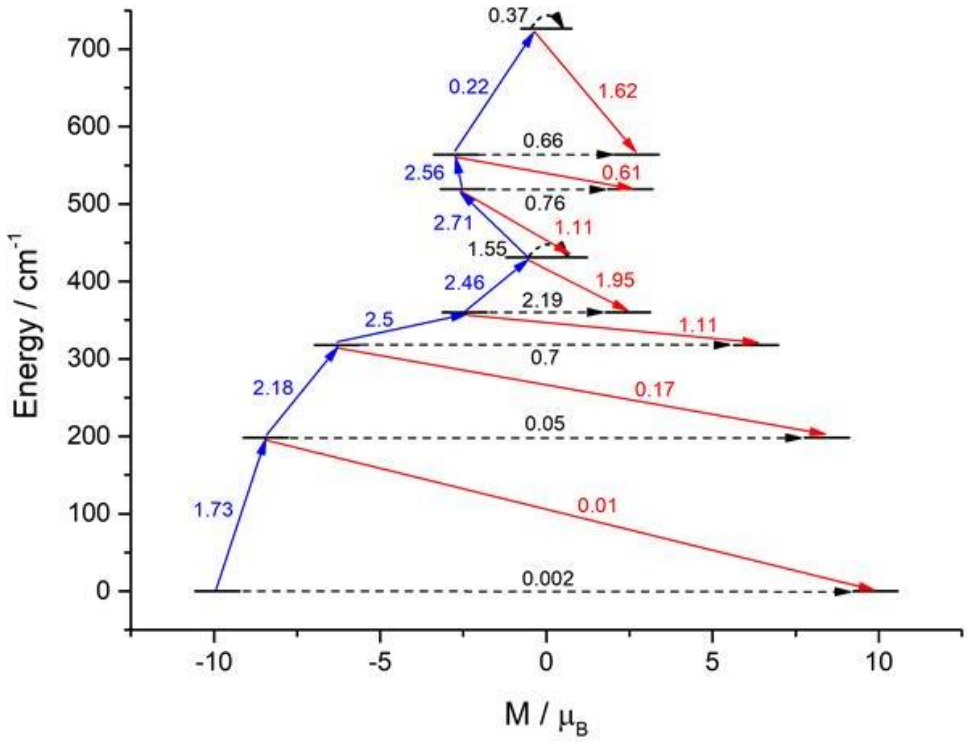

Figure 6.13.- *Ab initio* calculated relaxation dynamics for **47**. The exchange states are arranged according to the values of their magnetic moments. The arrows show the connected exchange states, and the numbers at each of them stand for the corresponding matrix element of the transversal magnetic moment.

Lastly, the results for compound **48** are shown in Tables 6.5 and A6.16. As in all the previous cases, the ground state is almost perfectly axial with negligible transverse components. Even the first excite state, although being better described by the sum of two wavefunctions, shows low g_x and g_y values. Relaxation most likely occurs through the second excited state as it is indicated by the larger *g* tensors and matrix element values in the calculated relaxation dynamics (Figure 6.14). Once again, the theoretically calculated energy gap of 300 K (209 cm^{-1}) is well above the experimentally calculated one.

Table 6.5.- The energy splitting of the ground $^6H_{15}$ multiplet**,** principal values of the *g* tensor for each Kramers' doublet and decomposition of the wavefunctions of the components of each Kramers' doublet to the wavefunctions with definite J_z (z is the easy exes for the ground Kramers doublet).

Complex	KD	E, cm^{-1}	g_x	g_y	g_z	$\|J_z\|$ (contribution in %)
48	1	0	0.002	0.003	19.75	15/2 (98.7)
	2	138	0.06	0.13	17.1	13/2 (85.3), 11/2 (10.6)
	3	209	1.62	2.74	13.52	11/2 (38.6), 9/2 (26.4), 5/2 (13.5)

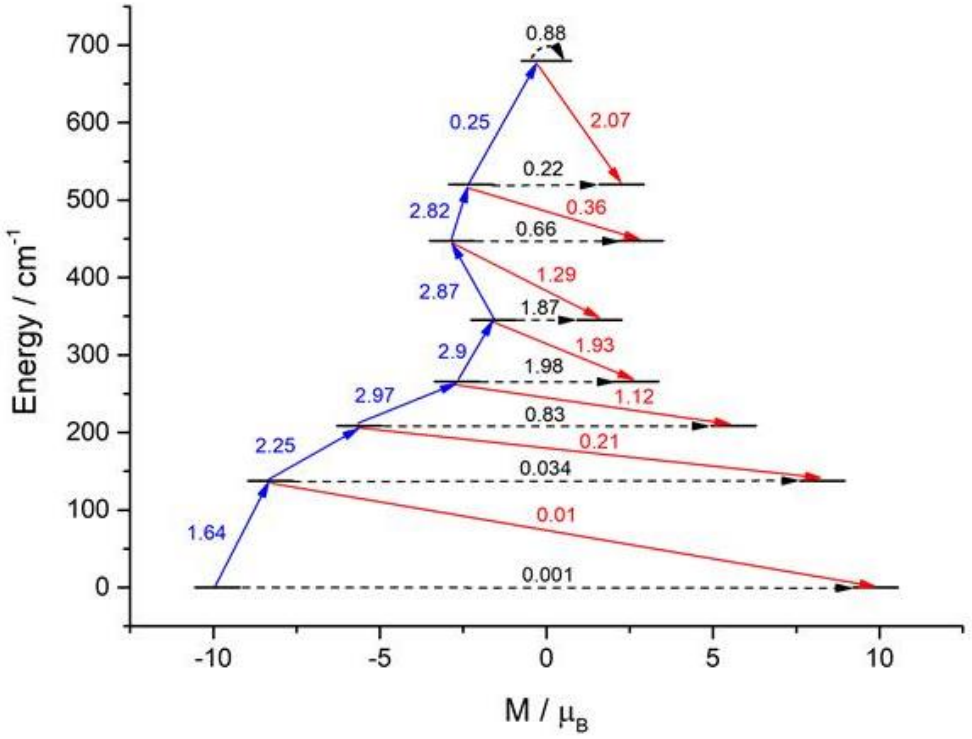

Figure 6.14.- *Ab initio* calculated relaxation dynamics for **48**. The exchange states are arranged according to the values of their magnetic moments. The arrows show the connected exchange states, and the numbers at each of them stand for the corresponding matrix element of the transversal magnetic moment.

Even though the results look more reliable when both theoretical and experimental perfectly coincide, we believe that the main objective of the calculations we have performed is to observe trends that can explain the experimental results. In our case,

we think that the objective has been fulfilled. We have notable differences between U_{eff} and U_{cal} (theoretically calculated energy barrier). Nevertheless, we believe that we have got signs of being in the good way. Indeed, if we compare, for example, the positions at which the maxima are visible in the $\chi''_M(T)$ plots and the aspect of the hysteresis loops, we could sort the SMMs in this order: **45** > **47** > **48** > **46**. This order is well reproduced by the theoretical results we have shown.

6.3.6. Magneto-structural correlations

With all these results in hand, we have been able to state some magneto-structural correlations that help us understand the differences in the dynamic magnetic behaviour.

First of all, let us compare compounds **36** (from Chapter 4) and **45**. The difference between these two compounds resides in the succinate/tetrafluorosuccinate bridging ligand. Already comparing the bond distances corresponding to Dy-OXS (OXS being the oxygen of the succinate/tetrafl.) we could say that our primitive aim of removing electron density from the equatorial plane was fulfilled. Indeed, for **36** the bond distance is of 2.320(4) Å, while for **45** the distance is 2.377(4)-2.432(4) Å. Consequently, the better performance of **45** could be understood by this change. Moreover, even though we do not have data for **36**, by comparing the results obtained for **45-48** we could see that oxygen atoms of compounds containing tetrafluorosuccinate provide less negative charge to the Dy^{III} ions based on the Mulliken charges (Table 6.6), which is what we aimed by incorporating electron-withdrawing fluorine atoms.

We should say that we were not expecting to see what we observed for **46**. Based on the previous work carried out by Murugesu and coworkers [1], we believed that the replacement of nitrate chelates by hfac groups would have a positive effect in the SMM behaviour. In fact, in the mentioned paper the authors state that the fluorinated chelate provides less electron density to the metal ion enhancing the axiality of it. In our case, however, regarding bond distances we noticed that **46** displays notably shorter Dy-$O_{chelate}$ bond distances in comparison to **36**: they range between 2.364(8)-2.432(7) Å and 2.456(5)-2.519(4) Å, respectively. Besides, the Mulliken charges that we calculated suggest a much larger negative charge for hfac than for nitrate. Hence, even though this was not initially predicted, these results help to understand why the SMM behaviour was worsened. We must indicate that, regarding bond distances, the

compounds containing nitrate and hfac show more similar bond distances in the cited paper. In our case, the difference is bigger (being remarkably shorter for hfac) and this could explain the contrasting effect observed in their and our work.

The properties observed for **47** could be understood by the sum of positive and negative effects we regarded for **45** and **46**. Indeed, its crystal structure displays long Dy-OXS bonds (2.437(2)-2.440(2) Å) and shorter Dy-Ochelate ones (2.358(3)-2.416(2) Å). Therefore, the position of the maxima in the $\chi''_M(T)$ plots looks reasonable being in between **45** and **46**, and in a similar position in comparison to **46**.

Compound **48** is not exactly the targeted one. We used trifluoroacetate aiming it to behave as a chelate, but it acts as monocoordinate and a methanol molecule occupies the other position. We believe that disparate effects act in this case. On the one hand, the bond distances related to Dy-O_{CF3CO2} are in a similar range to the ones we observed for hfac. However, in this case the negative charge is more concentrated in a single position due to the monocoordinated character of the trifluoroacetate ligand. In fact, the Mulliken charge value found for it is of -1.001, which is notably larger in comparison to the ones we found for hfac oxygen atoms. This would be detrimental for the magnetic properties. On the other hand, the neutral character of the methanol is evidenced by its lower value in terms of Mulliken charges, which would be positive for the magnetic properties. All in all, considering both effects we believe that having an intermediate SMM behaviour seems reasonable. We are currently working on the possibility of removing the coordinated methanol molecules to force the trifluoroacetate to work as bidentate. So far, we believe that the most plausible way goes through a thermal activation as we have done in previous reported works [11]. Another possibility could be to avoid using alcohols as solvent, but due to the hydrated character of the reagents, water molecules can also occupy the same position as we have observed for **48b**.

Finally, even though we do not still have *ab initio* calculations based on complex **49**, the results could be easily rationalized. On the one hand, as we have mentioned, in the crystal structure description, the chelating dbm groups display much shorter bond distances and, since they are located in the equatorial plane, this is detrimental for the axiality of the system. On the other hand, these diketones do not have such strong electron-withdrawing groups as the fluorines and, thus, larger Mulliken charges would be expected for them. Consequently, the lack of zero field SMM behaviour in this compound is comprehensible.

Table 6.6.- Results of calculations at the SA-CASSCF(9,7) level of the Mulliken atomic charges of atoms coordinated to Dy^{III} in complexes **45-48**.

Comp.	Mulliken charge								
	O7	**O1**	**O3**	**O1S**	**$O1_{chel}$**	**$O2_{chel}$**	**O2**	**O4**	**O8**
45	-1.145	-1.131	-1.131	-0.975	-0.692	-0.680	-0.812	-0.837	-0.827
46	-1.159	-1.138	-1.11	-1.0	-0.928	-0.917	-0.8	-0.84	-0.823
47	-1.16	-1.141	-1.109	-0.959	-0.926	-0.915	-0.8	-0.833	-0.813
48	-1.125	-1.147	-1.138	-0.99	-1.001	-0.898	-0.817	-0.827	-0.805

6.4. CONCLUSIONS

In this chapter we have been able to successfully modify the equatorial ligand field of compound **36** obtaining five novel compounds. More specifically, the model system allows as to modify single positions in an individual or simultaneous manner as it has been done, for instance, for compounds **45** and **47**, respectively.

In spite of the fact that this is an ongoing project (note that we suggested several more chelate possibilities in the introduction), we have been able to create some magneto-structural correlations that help us to understand the magnetic behaviour of these systems. For instance, we have clearly seen that the tetrafluorosuccinate is a more adequate ligand than the succinate to provide larger energy splitting between the ground and excited states. This is due to the longer bond distances that it creates, as well as the reduced electron density that transfers to the Dy^{III} ion. We have also noticed that, unexpectedly, nitrates are more suitable ligands in our system than the hfac chelates. Indeed, hfac ligands form shorter bond distances and the Mulliken charges have shown that they provide larger electron density. When combining both tetrafluorosuccinate and hfac chelates in **47**, a compound displaying a similar behaviour to **36** is obtained, which arises from the sum of the positive and negative effects of each individual modification.

Unfortunately, so far we have not been able create more systems including more modifications. For example, replacing the succinate bridge by tetrafluorosuccinate in **48** could be an interesting option to overcome the properties observed for **47** and, perhaps, obtain an SMM with similar properties to **45**. It could also be a very interesting option to do the same for **49**. We have seen that including dbm ligands has eradicated

the zero field SMM behaviour, but weakening the equatorial ligand field from the side of the succinate could somehow overcome this.

Another very interesting approach resides in including chiral chelates within the system as we proposed in the introduction with the camphor derivative. In view of the fact that we can have a stereospecific control over the quaternary amines (see Chapter 5), this would allow us to continue studying interesting magnetic and optical properties. Finally, in Chapter 4 we suggested that the ligand field in these systems could also be considered suitable for prolate ions. In that case, the interpretation completely changes. We would say that the three phenoxido groups are located in the equatorial ligand plane forming a very distorted triangle, whereas the succinate oxygen atoms and chelates would be in the axial positions. To prove that this is really like that, a similar behaviour to what observed for Dy^{III} counterparts must be expected for Er^{III} ones. For instance, tetrafluorosuccinate would move the oxygen away from the axial position and this must enhance the magnetic properties. In contrary, changing nitrate by hfac would worsen them.

6.5. REFERENCES

[1] F. Habib, G. Brunet, V. Vieru, I. Korobkov, L.F. Chibotaru, M. Murugesu, Significant enhancement of energy barriers in dinuclear dysprosium single-molecule magnets through electron-withdrawing effects, J. Am. Chem. Soc. 135 (2013) 13242–13245. https://doi.org/10.1021/ja404846s.

[2] J.D. Rinehart, J.R. Long, Exploiting single-ion anisotropy in the design of f-element single-molecule magnets, Chem. Sci. 2 (2011) 2078–2085. https://doi.org/10.1039/c1sc00513h.

[3] A. Upadhyay, S.K. Singh, C. Das, R. Mondol, S.K. Langley, K.S. Murray, G. Rajaraman, M. Shanmugam, Enhancing the effective energy barrier of a Dy(iii) SMM using a bridged diamagnetic Zn(ii) ion., Chem. Commun. 50 (2014) 8838–41. https://doi.org/10.1039/c4cc02094d.

[4] A.B. Canaj, M.K. Singh, C. Wilson, G. Rajaraman, M. Murrie, Chemical and in silico tuning of the magnetisation reversal barrier in pentagonal bipyramidal Dy(iii) single-ion magnets, Chem. Commun. 54 (2018) 8273–8276. https://doi.org/10.1039/c8cc03929a.

[5] L. Ungur, L.F. Chibotaru, Strategies toward High-Temperature Lanthanide-Based Single-Molecule Magnets, Inorg. Chem. 55 (2016) 10043–10056. https://doi.org/10.1021/acs.inorgchem.6b01353.

[6] Y.-S. Meng, Y.-Q. Zhang, Z.-M. Wang, B.-W. Wang, S. Gao, Weak Ligand-Field Effect from Ancillary Ligands on Enhancing Single-Ion Magnet Performance, Chem. - A Eur. J. 22 (2016) 12724–12731. https://doi.org/10.1002/chem.201601934.

[7] M. Llunell, D. Casanova, J. Cirera, J.M. Bofill, P. Alemany, S. Alvarez, M. Pinsky, D. Avnir, SHAPE, (2005).

[8] C. Huang, Rare Earth Coordination Chemistry: Fundamentals and Applications, John Wiley & Sons, Singapore, 2010.

[9] F. Aquilante, L. De Vico, N. FerrÃ©, G. Ghigo, P.-Ã. Malmqvist, P. NeograÃ¡dy, T.B. Pedersen, M. PitonÌŒÃ¡k, M. Reiher, B.O. Roos, L. Serrano-AndrÃ©s, M. Urban, V. Veryazov, R. Lindh, MOLCAS 7: The Next Generation, J. Comput. Chem. 31 (2010) 224–247. https://doi.org/10.1002/jcc.21318.

[10] N.F. Chilton, C.A.P. Goodwin, D.P. Mills, R.E.P. Winpenny, The first near-linear bis(amide) f-block complex: A blueprint for a high temperature single molecule magnet, Chem. Commun. 51 (2015) 101–103. https://doi.org/10.1039/c4cc08312a.

[11] U. Huizi-Rayo, A. Zabala-Lekuona, A. Terenzi, C.M. Cruz, J.M. Cuerva, A. Rodríguez-Diéguez, J.A. García, J.M. Seco, E. San Sebastian, J. Cepeda, Influence of thermally induced structural transformations on the magnetic and luminescence properties of tartrate-based chiral lanthanide organic-frameworks, J. Mater. Chem. C. 8 (2020) 8243–8256. https://doi.org/10.1039/d0tc00736f.

mini-CHAPTER I

HOW DOES THE DIAMAGNETIC ION INFLUENCE THE SMM BEHAVIOUR?

I.I. INTRODUCTION

In view of the excellent magnetic properties of the tetranuclear systems that we studied in the previous chapters, we thought that it could be a good idea to try to modify the diamagnetic Zn^{II} ion by a bigger one, Cd^{II} for example. We believed that if were able to obtain a similar tetranuclear system to **36**, the fact of having a bigger ion would also somehow modify the bond distances and angles corresponding to both Cd^{II} and Dy^{III}. This, at the same time, would be expected to modulate the magnetic properties.

In this *mini*-Chapter we report on the synthesis, characterization and study of the magnetic properties of two novel dinuclear $Cd^{II}Dy^{III}$ (**50**) and $Hg^{II}Dy^{III}$ (**51**) coordination compounds.

I.II. PREPARATION OF COMPLEXES

I.II.I. $[Cd(\mu\text{-}H_2L^4)_2Dy_2(NO_3)_3]\cdot 2MeOH$ (50)

This compound was serendipitously obtained by following the same synthetic methods as for **36**, but using $Cd(NO_3)_2\cdot 4H_2O$ instead of zinc(II) nitrate. Afterwards, the reaction procedure was optimized as follows. To a 10 mL ethanol suspension containing H_4L^4 (0.04 mmol, 32 mg) and Et_3N (0.08 mmol, 0.012 mL) were successively added $Cd(NO_3)_2\cdot 4H_2O$ (0.04 mmol, 12.3 mg) and $Dy(NO_3)_3\cdot 5H_2O$ (0.04 mmol, 17.5 mg). By stirring the reaction, a perfect solution is obtained, but in several minutes the product precipitates, which was washed with EtOH several times and air-dried. Yield: 45%.

I.II.II. $[Hg(\mu\text{-}H_2L^4)_2Dy_2(NO_3)_3]\cdot 2MeOH$ (51)

The same procedure was used, but $Hg(NO_3)_2$ was synthesized in the moment by reacting $HgCl_2$ and $AgNO_3$. The product was air-dried in the darkness due to the light sensitivity. Yield: 33%.

I.III. EXPERIMENTAL RESULTS

Even though our targeted compound was expected to be similar to **36**, it appears that the N_2O_3 cavity is not well suited for the Cd^{II} ion and therefore, even adding a bridging succinate to the reaction environment, the dinuclear $Cd^{II}Dy^{III}$ compound is obtained. Although this is not the expected product, it allowed us to start a new project.

In a research work reported by Rajaraman and coworkers [1], they compared a mononuclear Dy^{III} based complex and a dinuclear $Zn^{II}Dy^{III}$ based one. According to their work, the diamagnetic ion has a positive effect in the SMM behaviour. They state that it provides a greater charge polarization within the bridging phenoxido oxygen atoms giving rise to a larger energy splitting and, inherently, enhancing the magnetic properties. Based on that, the aim of our project was to synthesize compounds containing the exact same core structure, but modulating the diamagnetic ion. In order to do that, we have synthesized two novel $Cd^{II}Dy^{III}$ (**50**) and $Hg^{II}Dy^{III}$ (**51**) coordination compounds, from which we expected to see a different magnetic behaviour in agreement with a different charge polarization provided by each diamagnetic ion. We have not obtained the crystal structure of **51** yet, but we have proved its isostructural character by PXRD (Figure AI.II).

I.III.I. Crystal Structure of Complex 50

Two perspective views of complex **50** are shown in Figure I.I. As it could be observed, only two out of four functionalized aromatic rings are coordinated to metal ions, while the other two are stabilized by intermolecular hydrogen bonds (Figure AI.I). The Cd^{II} ions is located in the inner N_4O_2 pocket while the Dy^{III} ion is in the outer O_4 one. The coordination environment of the transition metal is completed by the atoms referring to the inner pocket, which belong to the ligand. However, the coordination environment of the lanthanide is completed by three nitrate chelates that, at the same time, balance the charge. As it is, it might not be the most promising SMM candidate, but we believe that this system is already opening a new gate to another system. Based on the perspective view of the compound shown in the right, one could think about replacing all the nitrates by another neutral and equal $[Cd(H_2L^4]$ fragment. In such hypothetical system the equatorial ligand field would be composed of just four long and neutral bonds corresponding to methoxy groups, while each axial position

would be occupied by two short phenoxido oxygen atoms. This is another project that we have got as future perspective.

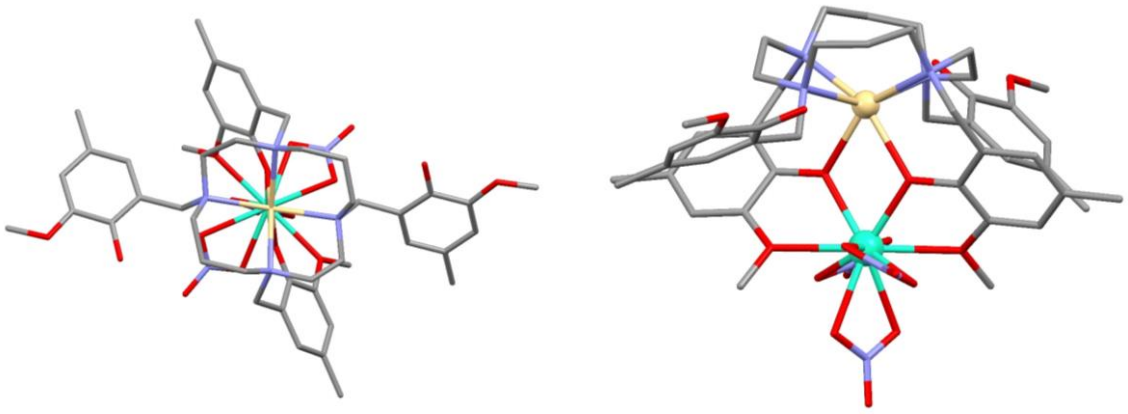

Figure I.I.- Two perspective views of **50**. Dysprosium, cadmium, oxygen, nitrogen and carbon atoms are in turquoise, yellow, red, blue and grey, respectively. Hydrogen atoms and solvent molecules have been omitted for the sake of clarity.

I.III.II. Dynamic magnetic properties of complexes 50 and 51

As we mentioned in the crystal structure description, probably at first glance compound **50** is not the most promising one to behave as a SMM. Indeed, when we carried out alternating current (*ac*) magnetic measurements on polycrystalline samples of **50** and **51**, neither of them displayed maxima in the out-of-phase susceptibility component (Figures AI.III-AI.IV). With the aim of (i) partially or totally suppressing QTM and (ii) for comparative purposes, we carried out the same experiments under an arbitrary external magnetic field of 1 kOe. Interestingly, both **50** and **51** displayed a clear set of maxima below 7.5 K and 6.5 K, respectively (Figures I.II-I.III). Although the temperature shift of 1 K maybe is not very significant, what we believe it is more attractive is the behaviour below the maxima. For **50**, it seems that there is not any residual QTM, since the χ''_M product goes to zero below the maxima. For **51**, in contrast, there is a clear appearance of the tails related to QTM, indicating that each diamagnetic ion contributes to a different relaxation mode.

For **50**, the $\chi''_M(\upsilon)$ curves were fitted in the 2.0-7.2 K temperature range obtaining relaxation times at each temperature (Figure AI.VI). In view of the linear and curved portions in the Arrhenius plot, as well as the relatively high α values (0.21(2.0 K)-0.10(7.2 K)) obtained from the Cole-Cole plots (Figure AI.VII), we fitted the data to

equation I.I considering the simultaneous presence of Orbach and Raman mechanisms:

$$\tau^{-1} = BT^{n} + \tau_0^{-1} exp(-U_{eff}/k_B T) \quad \textit{Equation I.I}$$

The fit provided B = 67.1 $s^{-1}K^{-2.68}$; n = 2.68; τ_0 = $2.12 \cdot 10^{-7}$ s and U_{eff} = 36.9 K. Even though the shape of the relaxation times may suggest that at slightly lower temperatures a temperature independent QTM regime could appear, considering the lack of any tails and temperature independent maxima in the $\chi''_M(\upsilon)$ plots, we did not include it.

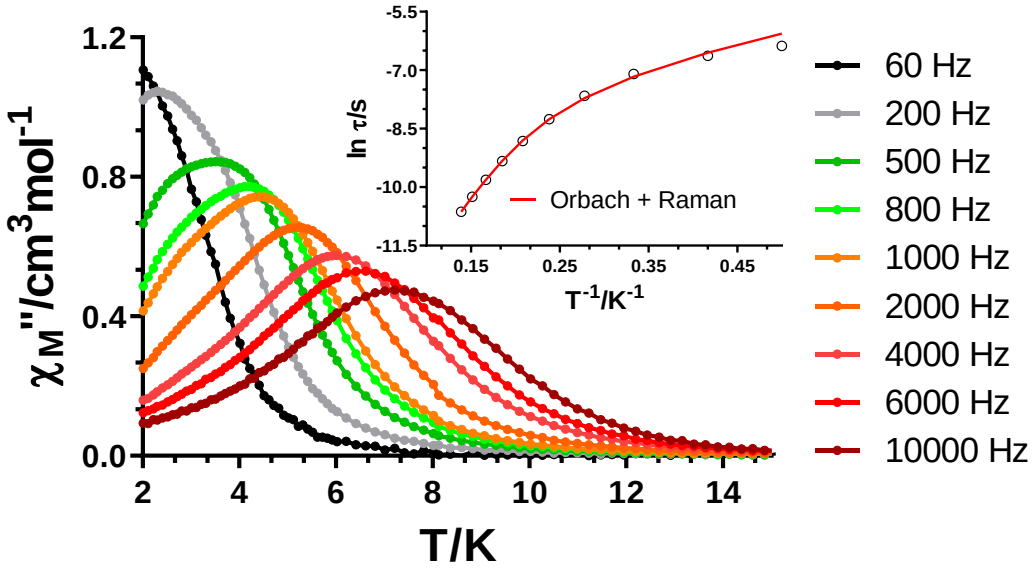

Figure I.II.- Temperature dependence of the out-of-phase components of the *ac* susceptibility in a *dc* applied field of 1 kOe for **50**. Inset: Arrhenius plot for the relaxation times considering a simultaneous presence of Orbach + Raman.

For compound **51**, instead, we fit the data in the 2.0-6.8 K temperature range to obtain relaxation times and α values (Figures AI.IX-AI.X). The curvature of the relaxation times in the Arrhenius plot is well accompanied with the large α values (0.38(2.0 K)-0.22(6.8 K)). Although in the $\chi''_M(T)$ plots we can clearly observe the presence of QTM, by looking at the $\chi''_M(\upsilon)$ curves (Figure AI.IX) we can see that in order to determine relaxation times related to it, we would need data at lower temperatures, which are below the instrument limit. Thus, we again fit the data to

equation I.I obtaining the following set of parameters: B = 246.4 $s^{-1}K^{-2.48}$; n = 2.48; τ_0 = $3.09 \cdot 10^{-8}$ s and U_{eff} = 46.1 K.

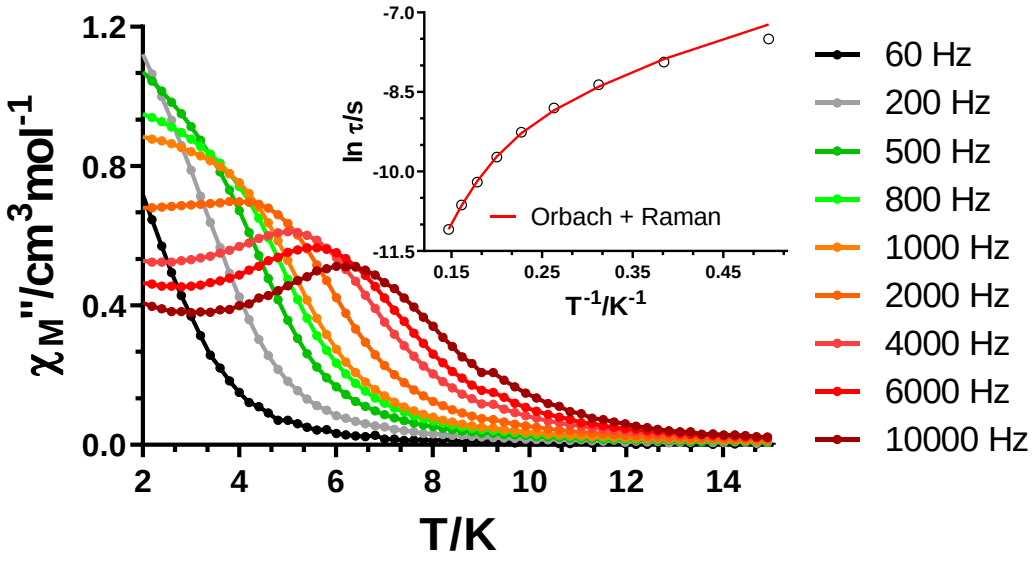

Figure I.III.- Temperature dependence of the out-of-phase components of the *ac* susceptibility in a *dc* applied field of 1 kOe for **51**. Inset: Arrhenius plot for the relaxation times considering a simultaneous presence of Orbach + Raman.

In spite of a higher effective energy barrier calculated for **51** in contrast to **50**, relaxation times at 2.0 K were found to be an order of magnitude slower for the latter: $1.7 \cdot 10^{-3}$ s *versus* $5.5 \cdot 10^{-4}$ s. Based on these preliminary results, we could say that we have been able to reinforce the theory suggested by Rajaraman *et al*. In their case, they compared a mononuclear Dy^{III} based magnet with a dinuclear $Zn^{II}Dy^{III}$ one, whereas in our case we have been able to modulate the diamagnetic ion. We are currently working on the crystallization of compound **51**. Afterwards, we would like to perform some *ab initio* calculations that help us to understand the different dynamic magnetic behaviour of these compounds.

I.IV. CONCLUSIONS

Even though our initial target tetranuclear compound was not formed by replacing the Zn^{II} precursor by Cd^{II} one in the same synthesis we employed for **36**, the formation of the dinuclear system **50** opened a new gate for an alternative study. In fact, we have been able to additionally synthesize the isostructural $Hg^{II}Dy^{III}$ counterpart.

Interestingly, they displayed field induced SMM behaviour with comparable energy barriers. However, we observed a different relaxing behaviour, especially in terms of QTM at the lowest temperatures. Additionally, relaxation times at 2.0 K were found to be one order of magnitude larger for **50** in comparison to **51**. Additional experiments are ongoing with the purpose of shedding some light on the differences in dynamic magnetic properties.

I.V. REFERENCES

[1] A. Upadhyay, S.K. Singh, C. Das, R. Mondol, S.K. Langley, K.S. Murray, G. Rajaraman, M. Shanmugam, Enhancing the effective energy barrier of a Dy(iii) SMM using a bridged diamagnetic Zn(ii) ion, Chem. Commun. 50 (2014) 8838–8841. https://doi.org/10.1039/c4cc02094d.

mini-CHAPTER II

ANCHORING A TETRANUCLEAR $Zn^{II}_2Dy^{III}_2$ BASED SMM TO GRAPHENE AND GRAPHENE OXIDE SURFACES

II.I. INTRODUCTION

As we have shown in the last chapters, based on the potential of compound **36** (Chapter 4), we have exploited it by working on chirality, luminescence, modulating the coordination environment and so on. Additionally, in this *mini*-Chapter II we show our first attempts trying to anchor a derivative of **36** to graphene (G) and graphene oxide (GO) surfaces.

As we discussed in the general introduction, normally SMMs are studied in bulk, but in order to design a future memory device, it is fundamental to know how these systems behave when they are deposited on a surface. We were encouraged to use a derivative of **36** and graphene (or graphene oxide) for two main reasons: (i) the compound displays two aromatic rings that are not coordinated to a metal, which could be useful to create some $\pi\cdots\pi$ stacking interactions with graphene and (ii) just considering the conformation of the molecule from the single crystal structure, the anisotropy axes would be orthogonal to the surface (see Figure II.I), a very interesting fact for memory effects and for possible future characterization by Synchrotron radiation [1]. We were aware of the difficulty of anchoring our target molecule to a graphene surface as suggested due to the large size of the molecule and a single anchoring point. In fact, larger anchoring groups such as pyrene are usually used for these purposes [2]. However, we decided that it was worth trying and we also considered graphene oxide to induce hydrogen bonds as well as $\pi\cdots\pi$ stacking interactions.

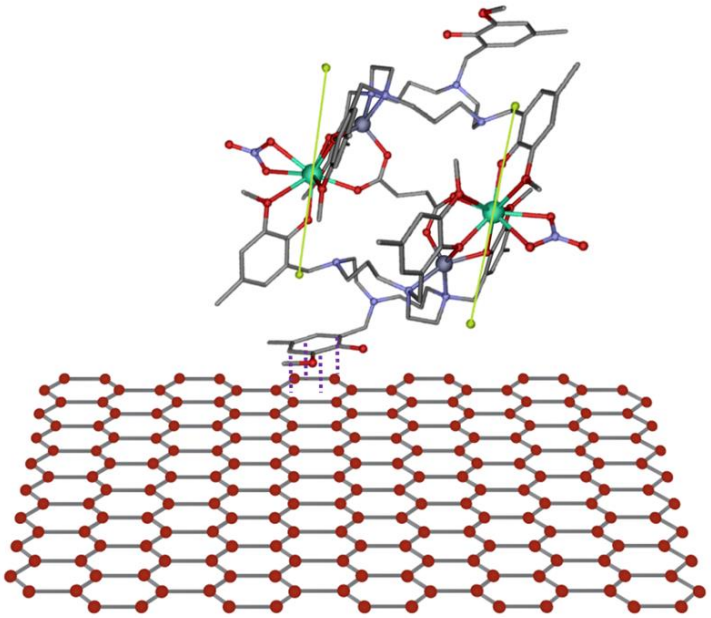

Figure I.I.- Proposed anchoring of our target molecule to a graphene surface by π···π stacking interactions. The green lines display the orientation the anisotropy axes based on Magellan software [3].

Thus, in this *mini*-Chapter II we report on the synthesis of the compound **52** (a derivative of **36**), bulk hybrid systems of **52@G** and **52@GO**, their characterization and magnetic properties. We also show the first results related to the synthesis and characterization of GO sheets deposited on silicon wafers (SW) to obtain flat surfaces This work has been done in collaboration with Ms. Iranzu Barbarin, Dr. Radmila Tomovska, Dr. Agnieszka Tercjak and Dr. Junkal Gutierrez. The former two collaborated with us in the synthesis and characterization, while the latter two did it in the characterization of the materials.

II.II. PREPARATION OF COMPLEX 52, HYBRID 52@G AND 52@GO AND SW-GO MONOLAYER

II.II.I. $[Zn_2(\mu\text{-}H_2L^4)_2(\mu\text{-succinate})Dy_2(NO_3)_2](BPh_4)_2$ (52)

To a 20 mL acetone solution of $NaBPh_4$ (0.10 mmol, 34.2 mg), another 20 mL methanolic solution containing H_4L^4 (0.10 mmol, 80.1 mg), $Zn(NO_3)_2{\cdot}6H_2O$ (0.10 mmol, 29.7 mg), $Dy(NO_3)_3{\cdot}5H_2O$ (0.10 mmol, 43.8 mg), succinic acid (0.05 mmol, 5.9 mg) and

Et_3N (0.30 mmol, 0.04 mL) were added dropwise. The solution was stirred for 30 minutes, filtered to remove possible undissolved particles and allowed to stand at room temperature. In few days good quality crystals were obtained. The product was collected when almost all the solvent was evaporated. Yield: 65%.

II.II.II. 52@G and 52@GO

We prepared bulk samples of **52@G** and **52@GO** following the same procedure for both. Powdered G (90 mg) and GO (90 mg) were suspended in 10 mL of DMF and CH_2Cl_2, respectively. The suspensions were sonicated for 30 minutes and **52** ($3.41 \cdot 10^{-3}$ mmol, 10 mg) was added. After 20 h stirring the suspensions were filtered and the products were washed with two fractions of 15 mL (DMF and CH_2Cl_2).

II.II.III. GO-SW

The commercially available aqueous dispersion of GO sheets was firstly diluted from 4 mg/mL to 10 mg/mL. This was then sonicated at room temperature for 1 h. Afterwards, the dispersion was cast in a silicon wafer (SW) substrate by spin-coating technique for 2 minutes and 2,000 rpm.

II.III. EXPERIMENTAL RESULTS

Considering that anchoring compound **36** to a graphene surface would probably be a challenge, in order to increase the probability, we thought that changing the counterion from nitrate to tetraphenylborate would be a good idea. This anion may create C-H$\cdots\pi$ interactions that stabilize the compound [4]facilitating the absorption. Thus, adding the corresponding equivalents of this anion to the reaction environment provokes the crystallization of compound **52**, even though an excess of nitrates is present in the reaction. Once confirmed that the SMM behaviour was maintained in the compound, we proceed to prepare the hybrid systems in bulk, before starting to prepare monolayers our material.

II.III.I. Crystal Structure of Complex 52

Compound **52** crystallizes in the monoclinic *I 2/a* space group. Crystallographic data and relevant bond distances and angles are collected in Tables AII.I-AII.II. As it is

shown in the left side of Figure II.II, the core structure is completely the same as in **36** (see Tables II.III-II.IV), in which the axiality is provided by the phenoxido oxygen atoms that are coordinated in almost opposite sides. In the right side, the asymmetric unit of the compound is shown in which a tetraphenylborate counterion is displayed.

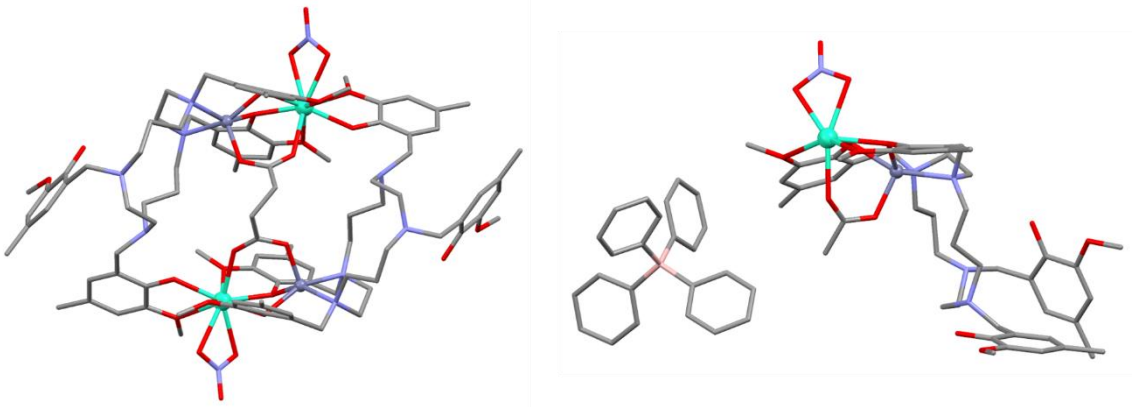

Figure II.II.- A perspective view of the cationic structure of **52** (left) and asymmetric unit of **52** (right) displaying the BPh4 anion. Dysprosium, zinc, oxygen, nitrogen, carbon and boron atoms are in turquoise, dark grey, red, blue, grey and pink, respectively. Hydrogen atoms have been omitted for the sake of clarity.

II.III.II. UV-Vis absorption spectra for 52, GO and 52@GO

In order to characterize the hybrid systems, we firstly studied the absorption spectra in the UV-Vis region. For that purpose, we prepared solution (**52**) and suspensions (GO and **52@GO**) in CH_2Cl_2 and collected their spectra in the 200-800 nm range. As it could be observed for compound **52**, it displays two very significant absorption bands at 242 and 292 nm (Figure II.III). For GO, a small bump is observed in the same region. Interestingly, the hybrid **52@GO** displays the two characteristic bands that were observed for **52** with a small peak shift. This has been the first evidence to prove that the compound may be absorbed within the surface.

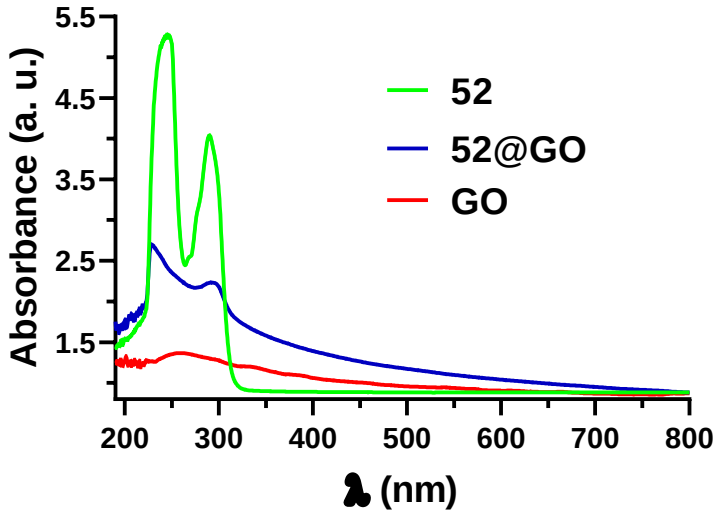

Figure II.III.- Absorption spectra in the UV-Vis range for **52**, GO and **52@GO**.

We tried to carry out the same characterization technique for **52@G** by preparing suspensions, but we obtained too cloudy suspensions that did not allowed to collect reliable spectra.

II.III.III. Scanning Electron Microscopy/Energy Dispersive X-ray spectroscopy (SEM-EDX)

We employed the SEM/EDX technique in order to identify characteristic elements of the samples, most importantly Zn^{II} and Dy^{III}. Figure II.III shows a pair of images collected for **52@GO** (up) and **52@G** (bottom). The technique allows us to carry out a fast elemental analysis of the surface. In the images we have highlighted the presence of Zn^{II} and Dy^{III} with blue and yellow colours, respectively, and at the bottom of each image we have written the atom percentage of each metal in the selected region. It is true that the amounts do not correspond exactly to a 1:1 ratio, but it is also true that the values differ by selecting one concrete region or another. In our opinion, the fact of being able to detect both metals within the samples is the best sign. Moreover, even though we were not able to characterize **52@G** with UV-Vis absorption, this technique has allowed us to see that we are probably on the good way.

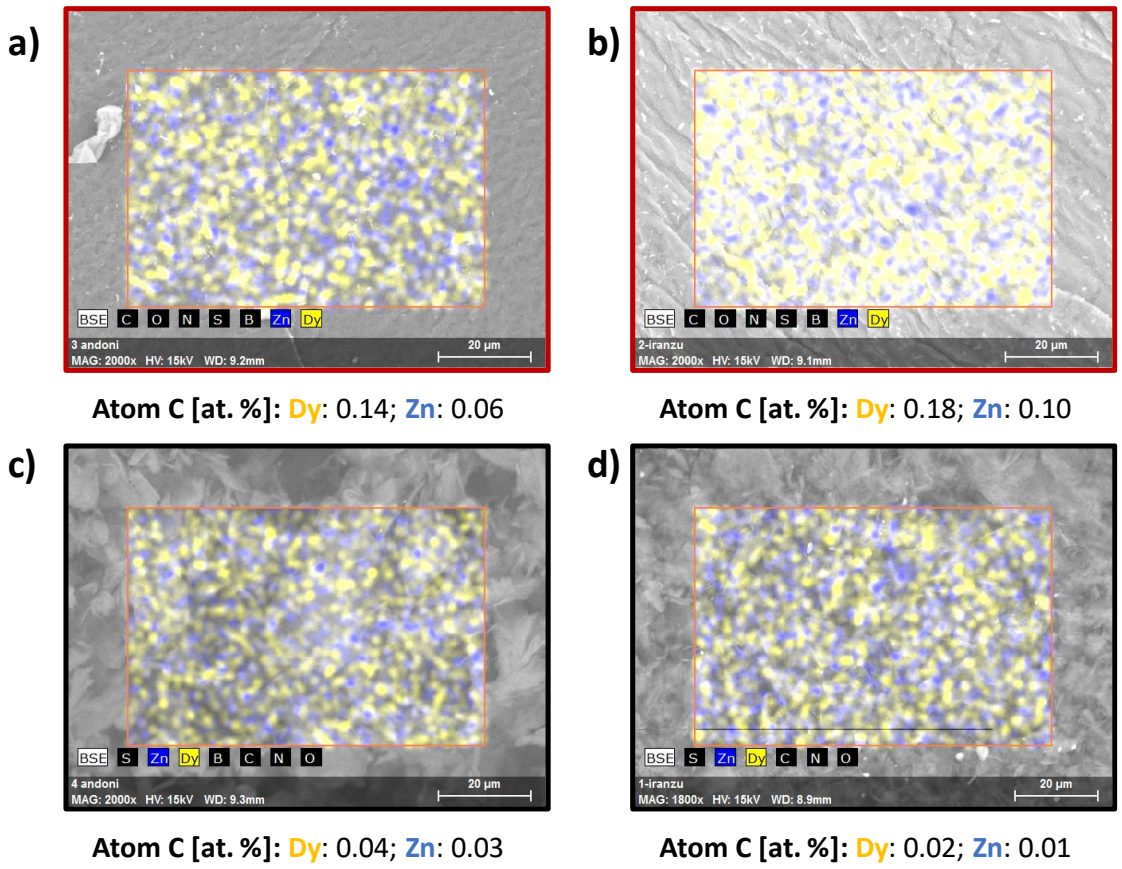

Atom C [at. %]: Dy: 0.14; Zn: 0.06

Atom C [at. %]: Dy: 0.18; Zn: 0.10

Atom C [at. %]: Dy: 0.04; Zn: 0.03

Atom C [at. %]: Dy: 0.02; Zn: 0.01

Figure II.III.- SEM/EDX images collected for **52@GO** (a) and b)) and **52@G** (c) and d)).

II.III.IV. Dynamic magnetic properties of complex 52 and hybrid 52@G and 52@GO

As we have said in the crystal structure description, in view of the very similar structure compared to **36**, we expected this compound to behave as a zero field SMM. Indeed, alternating current (*ac*) measurements carried out under zero applied *dc* field revealed a set of maxima below 32 K, slightly above **36**. The tails related to QTM are also present in this compound, but if we consider the intensity ratio between the maxima and the tails, we may conclude that QTM is somehow quenched in this compound in comparison to **36**. This fact would be in agreement with what they state Parmar and coworkers in a recently published work [5]. According to them, the use of bulky counterions may slow down the non-Orbach processes. We fitted the $\chi''_M(\upsilon)$ and $\chi''_M(\chi'_M)$ plots in the 17.2-30.4 K temperature range obtaining relaxation times and α values (Figure AII.III-AII.IV). The curvature of the relaxation times is in well agreement

with the relatively high α values that we found, especially at the lowest studied temperature (0.29(17.2 K)-0.05(30.4 K)). Thus, we fit the data to equation II.I considering a simultaneous presence of Orbach and Raman mechanisms:

$$\tau^{-1} = BT^{n} + \tau_0^{-1} exp(-U_{eff}/k_B T) \quad \textit{Equation II.I}$$

The fit provided: B = 3.9·10^{-5} s^{-1}K$^{-5.90}$; n = 5.90; τ_0 = 3.84·10^{-10} s and U_{eff} = 419.3 K. The value of the barrier is larger than the one we obtained for **36**, a fact that should have not been affected by the counterion according to the mentioned paper. This could be attributed to a slightly better defined axial ligand field, but just considering bond distances and angles (Table II.II) it is hard to say.

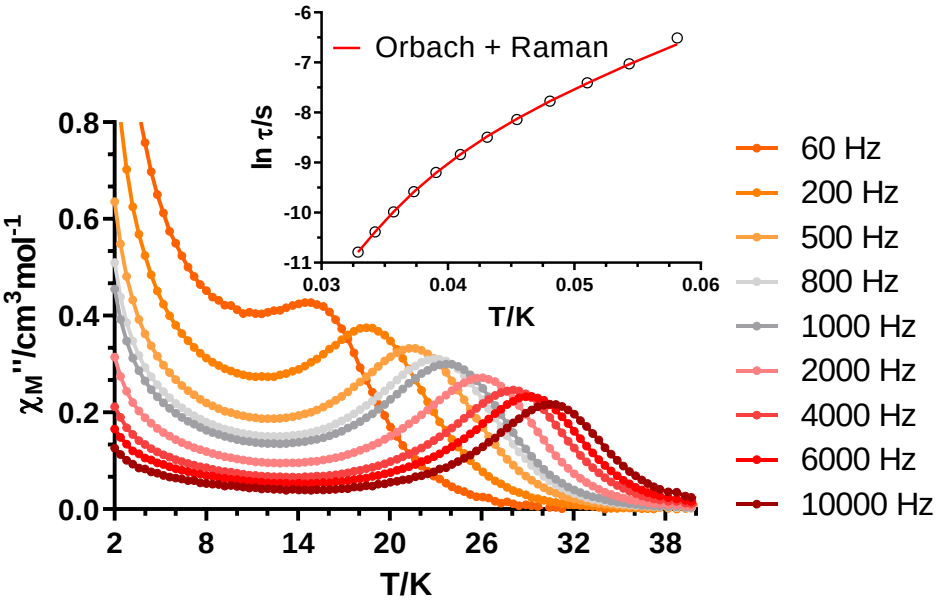

Figure II.IV.- Temperature dependence of the out-of-phase components of the *ac* susceptibility in a zero applied field for **52**. Inset: Arrhenius plot for the relaxation times considering Orbach + Raman relaxations.

The aim of preparing bulk hybrid **52@G** and **52@GO** was in part directed to have the possibility of measuring the dynamic magnetic properties of the samples. In fact, when the magnetic properties of hybrid systems are studied, usually these are monolayer samples and *ac* measurements are not carried out. Instead, XMCD (X-ray Magnetic Ciruclar Dichroism) experiments are more common as explained in the general introduction, which give specific information of the orientation of the molecules

and anisotropy axes. In our case, our first approach was addressed to an initial study in bulk as it had been done in a previous work [2]. Although **52** is a zero field SMM, we have seen that when compounds are anchored to a certain surface they might have a completely different relaxation behaviour [2,6,7]. Thus, in order to overcome a possible QTM shortcutting the effective energy barrier and hiding SMM behaviour, we directly carried out the measurements under the presence of an arbitrary external magnetic field of 1 kOe. Unfortunately, the maxima that were found for **52** were absent in both hybrid systems (Figure II.V). In any case, the presence of a non-zero signal even in the out of phase region confirms, once more, the presence of Dy^{III} in the material.

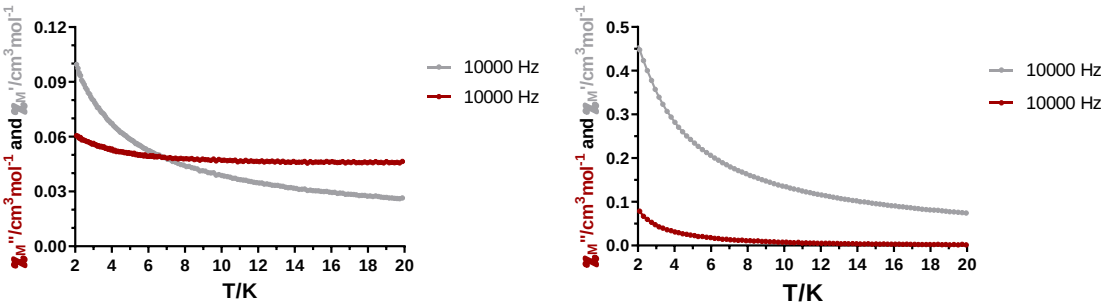

Figure II.V.- Temperature dependence of the in phase (grey) and out-of-phase (garnet) components of the *ac* susceptibility in a *dc* applied field of 1 kOe for **52@G** (left) and **52@GO** (right).

II.III.V. Atomic Force Microscopy (AFM)

In the previous section we have seen that the SMM behaviour was lost for the hybrid systems. Nevertheless, we are still encouraged to continue studying these systems. With this purpose, the following step would be to prepare a single layer of G or GO in which **52** is anchored. This is because the hybrid bulk samples are, to some extent, comparable to powdered samples of **52**. We have tried to show that in Figure II.VI. In **52@G** and **52@GO** the molecules might be oriented as we desire, but these layers will be then randomly oriented. Therefore, for practical purposes this is not an adequate situation. Additionally, an XMCD experiment would not give us any information about the orientation of the molecules, since an orthogonal or grazing incidence of the beam would give the same signal according to the random orientation. However, if we are able to prepare a monolayer of G or GO and then deposit our molecule in an ordered way, we will be able to see if all the molecules display the same orientation respect to the surface (see the section of hybrid materials in the general

introduction for further details), since the XMCD signal will be different depending on the incidence angle.

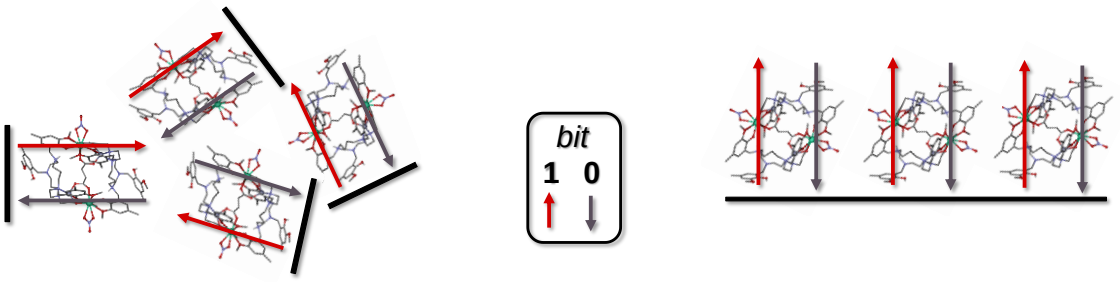

52@G and **52@GO** **52@G-SW** and **52@GO-SW**

Figure II.VI.- Schematic representation of the possible distribution of **52@G** and **52@GO** (left) and a single layer of **52@G-SW** and **52@GO-SW** (right). The black lines represent a G or GO layer, while the arrows are drown following the anisotropy axes. Each orientation represents either 1 or 0 in the binary language.

With all this in mind, we have done our first attempts to anchor GO layers within silicon wafers to obtain flat surfaces. The following images of Atomic Force Microscopy show a successful anchoring of GO layers within the surface by a spin-coating method. However, as it can be seen, the height distribution is quite large and we cannot say that we have obtained the desired flat surface. We are currently working on these results.

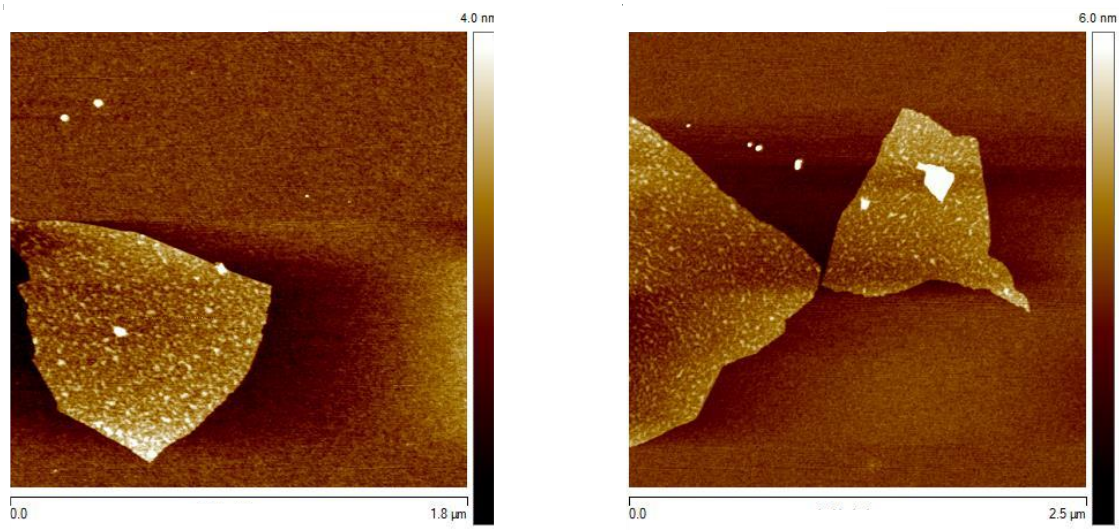

Figure II.VII.- AFM image of a **GO-SW**, GO deposited on a silicon wafer.

II.IV. CONCLUSIONS

In this *mini*-Chapter we have been able to step forward preparing some hybrid systems based on graphene/graphene oxide. For this purpose, we have successfully substituted the nitrate counterions in **36** by tetraphenylborates in **52**, which could give rise to interesting C-H$\cdots\pi$ interactions with the surface for a better deposition.

We have been able to make some initial characterization techniques for hybrid **52@G** and **52@GO** which suggest that our compound has been somehow anchored to the surface. Unfortunately, the zero field SMM behaviour found in **52** is lost in **52@G** and **52@GO**, which we associate to a complete modification of the phonon bath.

Finally, we have been able to incorporate GO into silicon wafers, which is the next step towards preparing a monolayer of our hybrid material.

II.V. REFERENCES

[1] J. Dreiser, G.E. Pacchioni, F. Donati, L. Gragnaniello, A. Cavallin, K.S. Pedersen, J. Bendix, B. Delley, M. Pivetta, S. Rusponi, H. Brune, Out-of-Plane Alignment of Er(trensal) Easy Magnetization Axes Using Graphene, ACS Nano. 10 (2016) 2887–2892. https://doi.org/10.1021/acsnano.5b08178.

[2] C. Cervetti, A. Rettori, M.G. Pini, A. Cornia, A. Repollés, F. Luis, M. Dressel, S. Rauschenbach, K. Kern, M. Burghard, L. Bogani, The classical and quantum dynamics of molecular spins on graphene, Nat. Mater. 15 (2016) 164–168. https://doi.org/10.1038/nmat4490.

[3] N.F. Chilton, D. Collison, E.J.L. McInnes, R.E.P. Winpenny, A. Soncini, An electrostatic model for the determination of magnetic anisotropy in dysprosium complexes, Nat. Commun. 4 (2013) 1–7. https://doi.org/10.1038/ncomms3551.

[4] B.R. Hall, L.E. Manck, I.S. Tidmarsh, A. Stephenson, B.F. Taylor, E.J. Blaikie, D.A.V. Griend, M.D. Ward, Structures, host-guest chemistry and mechanism of stepwise self-assembly of M4L6 tetrahedral cage complexes, Dalton Trans. 40 (2011) 12132–12145. https://doi.org/10.1039/c1dt10781j.

[5] V.S. Parmar, F. Ortu, X. Ma, N.F. Chilton, R. Clérac, D.P. Mills, R.E.P. Winpenny, Probing Relaxation Dynamics in Five-Coordinate Dysprosium Single-Molecule Magnets, Chem. – A Eur. J. 26 (2020) 7774–7778. https://doi.org/10.1002/chem.202001235.

[6] M. Mon, A. Pascual-Álvarez, T. Grancha, J. Cano, J. Ferrando-Soria, F. Lloret, J. Gascon, J. Pasán, D. Armentano, E. Pardo, Solid-State Molecular Nanomagnet Inclusion into a Magnetic Metal-Organic Framework: Interplay of the Magnetic Properties, Chem. - A Eur. J. 22 (2016) 441–441. https://doi.org/10.1002/chem.201504827.

[7] S. Marocchi, A. Candini, D. Klar, W. Van Den Heuvel, H. Huang, F. Troiani, V. Corradini, R. Biagi, V. De Renzi, S. Klyatskaya, K. Kummer, N.B. Brookes, M. Ruben, H. Wende, U. Del Pennino, A. Soncini, M. Affronte, V. Bellini, Relay-Like Exchange Mechanism through a Spin Radical between TbPc2 Molecules and Graphene/Ni(111) Substrates, ACS Nano. 10 (2016) 9353–9360. https://doi.org/10.1021/acsnano.6b04107.

mini-CHAPTER III

IN SEARCH OF Co^{II} BASED ZERO FIELD SMMs BASED ON TRIPODAL LIGANDS

III.I. INTRODUCTION

In view of some nice results that have been recently reported on Co^{II} based SMMs [1–3], we were encouraged to synthesize a previously reported ligand (Figure III.I) that has been already used for the synthesis of SMMs [4,5]. This ligand contains an inner N_3O_3 pocket that might be suitable to produce a trigonal prism coordination environment that can provide large and negative *D* values, ideal for the design of mononuclear Co^{II} based magnets [6,7].

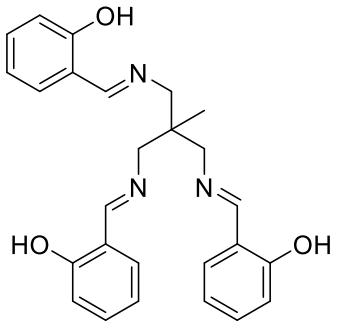

Figure III.I.- The tripodal H_3L^5 ligand employed in this *mini*-Chapter III.

Thus, in this *mini*-Chapter III we report on the synthesis, characterization and magnetic properties of the mononuclear diamagnetic compound **53** and the trinuclear zero field SMM **54**. Additionally, we suggest an alternative use for pulse magnetization measurements to obtain further information on the QTM regime.

III.II. PREPARATION OF THE LIGAND H_3L^5

The ligand was prepared by using previously reported procedures [8–10].

III.III. PREPARATION OF COMPLEXES 53 AND 54

III.III.I. [Co(μ-L^5)]·MeOH (53)

This diamagnetic (Co^{II} gets oxidized to Co^{III}) compound was not deliberately obtained. Several reactions were attempted by reacting H_3L^5 (0.03 mmol, 12.9 mg),

$Co(acac)_2$ (0.03 mmol, 7.71 mg), Et_3N (0.09 mmol, 0.013 mL) and large cations (NBu_4PF_6, NBu_4OH and NEt_4OH, for example) in MeOH:MeCN mixtures under atmospheric conditions. All of them gave rise to very dark brown solutions finally affording dark crystals of **53**. PXRD and ^{1}H-NMR of **53** in Figures AIII.I and AIII.IV.

III.III.II. $[Co_3(\mu\text{-}L^5)_2]$ (54)

In view of the results obtained for **53**, we attempted the same reactions under inert atmosphere and using deoxygenated MeOH and MeCN. **54** was obtained by adding a methanolic (5 mL) solution containing $Co(acac)_2$ (0.03 mmol, 7.71 mg) and NBu_4PF_6 (0.03 mmol, 11.6 mg) to another solution in MeCN (3 mL) of H_3L^5 (0.03 mmol, 12.9 mg) and Et_3N (0.09 mmol, 0.013 mL). The light orange solution afforded orange crystals of **54** in few hours. This reaction was carried out having a mononuclear compound as the target system, but afterwards was optimized by using H_3L^5 (0.03 mmol), $Co(acac)_2$ (0.045 mmol) and Et_3N (0.09 mmol). Yield: 68%. PXRD in Figure AIII.II.

III.IV. EXPERIMENTAL RESULTS

The first attempts towards synthesizing mononuclear Co^{II} based compounds under atmospheric conditions afforded a mononuclear diamagnetic Co^{III} based compound. In view of that, we repeated the same attempts under inert atmosphere. Even though we planned the reaction to obtain mononuclear compounds (regarding stoichiometry and addition of large counterions), we obtained the trinuclear compound **54**. We believe that this is due to the fact of not having an additional group in the *ortho*- position respect to the phenol that could create steric hindrance and avoid the inclusion of an additional metal. It is worth mentioning that the crystal structure of **54** was resolved by using a squeeze routine, which is probably associated to disordered solvent molecules. We, therefore, carried out a thermogravimetric analysis to determine the final molecular weight of the material (Figure AIII.III).

III.IV.I. Crystal Structure of Complexes 53 and 54

The diamagnetic compound **53** crystallizes in the monoclinic $P2_1/c$ space group along with a crystallization methanol molecule (crystallographic data and selected bond distances and angles are shown in Tables AIII.I-AIII.II). As it is shown in Figure III.II,

the Co^{III} ion is encapsulated in the N_3O_3 pocket coordinated to the three phenoxido and three imine groups. Although we selected this ligand to provide a trigonal prism geometry, in this case the coordination environment is almost a perfect octahedron (Table AIII.III).

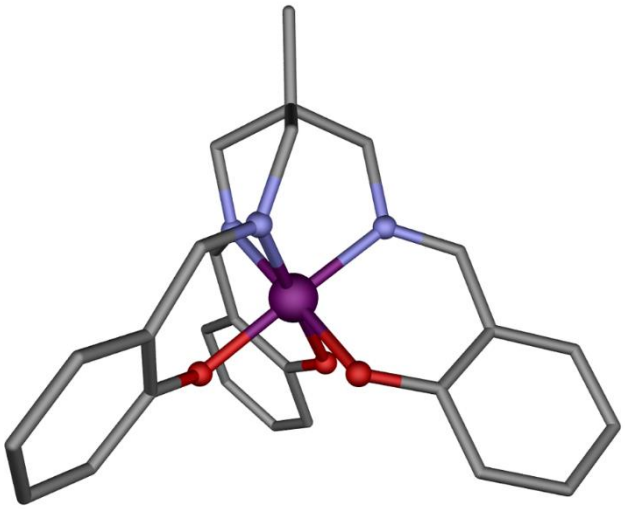

Figure III.II.- Perspective view of compound **53**. Co^{III}, oxygen, nitrogen and carbon atoms are in purple, red, blue and grey, respectively. Hydrogen atoms and solvent molecules have been omitted for the sake of clarity.

The trinuclear compound **54** crystallizes in the monoclinic *C2/c* space group (crystallographic data and selected bond distances and angles are shown in Tables AIII.I-AIII.II). The asymmetric unit contains one ligand and 1.5 Co^{II} ions. In this case, Co1, with the same coordination sphere of N_3O_3 as in **53**, displays a coordination polyhedron that better fits to a trigonal prism instead of an octahedron (Table AIII.III). Co2, instead, with a coordination sphere of O_6 is best described as a distorted octahedron (Table AIII.III). The three Co^{II} ions form a perfectly linear angle of 180º.

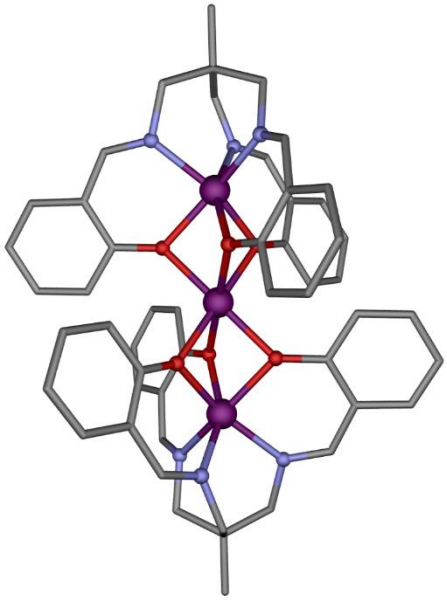

Figure III.III.- Perspective view of compound **54**. Co^{II}, oxygen, nitrogen and carbon atoms are in purple, red, blue and grey, respectively. Hydrogen atoms have been omitted for the sake of clarity.

III.IV.II. Dynamic magnetic properties of complex 54

Dynamic magnetic properties were studied for compound **54** carrying out alternating current (*ac*) measurements under zero applied *dc* field. Interestingly, a nice set of maxima was found below 8 K (Figure III.IV). Moreover, the maxima do not display any tails at low temperatures, a sign that suggests an absence of QTM. Even though these are still preliminary results, we attribute the presence of slow magnetic relaxation at zero applied *dc* field to (i) possible strong exchange interactions between metal ions that quench QTM (static magnetic properties are on progress) and (ii) large and negative magnetic anisotropy most likely arising from Co1, which displays a distorted trigonal prism geometry. Co2 has an octahedral environment, and as we previously discussed, this usually gives rise to positive *D* values.

The $\chi''_M(\upsilon)$ curves and Cole-Cole plots were constructed in the 4.4-7.6 K temperature range and fitted to the generalized Debye model obtaining relaxation times and α values at each temperature (Figures AIII.VI-AIII.VII). The α values found above 5.6 K suggest a very narrow distribution of relaxation times (values below 0.06), whereas at lower temperatures they suggest a simultaneous presence of relaxation mechanisms (0.22 at 4.4 K). However, the relaxation times display a completely linear

behaviour in the Arrhenius plot in the whole studied temperature. Therefore, we fitted the data to:

$$\tau^{-1} = \tau_0^{-1} exp(-U_{eff}/k_B T) \quad \textit{Equation III.I}$$

Obtaining a U_{eff} = 42.1 K and τ_0 = 6.9·10^{-8} s. We are currently waiting for additional experimental measurements, as well as theoretical calculations to shed some light in the dynamic magnetic behaviour of this compound. Additionally, we carried out another *ac* measurement by applying an external *dc* field of 1 kOe. As it is shown in Figure AIII.VIII, both curves (at zero applied *dc* field and under an applied field of 1 kOe) completely overlap suggesting that the external magnetic field has not any influence in the measurement.

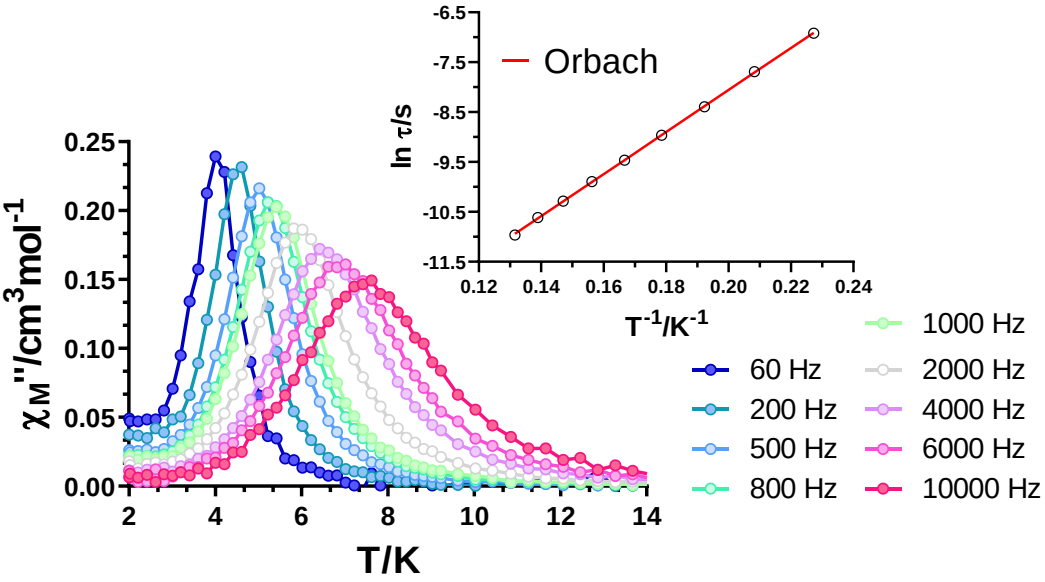

Figure III.IV.- Temperature dependence of the out-of-phase components of the *ac* susceptibility in a zero applied *dc* field for **54**. Inset: Arrhenius plot for the relaxation times.

III.IV.III. Hysteretic behaviour of complex 54

In view of the zero field SMM behaviour of **54**, we performed hysteresis loop measurements in a powdered sample at 2 and 3 K with a 50 Oe/s sweep rate. As it is shown in Figure III.V, at 2 K the compound shows a nice butterfly shaped loop strongly influenced by QTM, but with a noticeable coercive field of around 310 Oe (inset). At 3

K, there is not any appreciable hysteresis loop. Even though the system does not reach saturation, the maximum value of 1.98 μ_B at 2 T is remarkably low for three non-interacting Co^{II} ions. This has been previously seen in an antiferromagnetically coupled triangular Co^{II} compound [11]. In any case, further experiments are on process to better understand the behaviour of this compound.

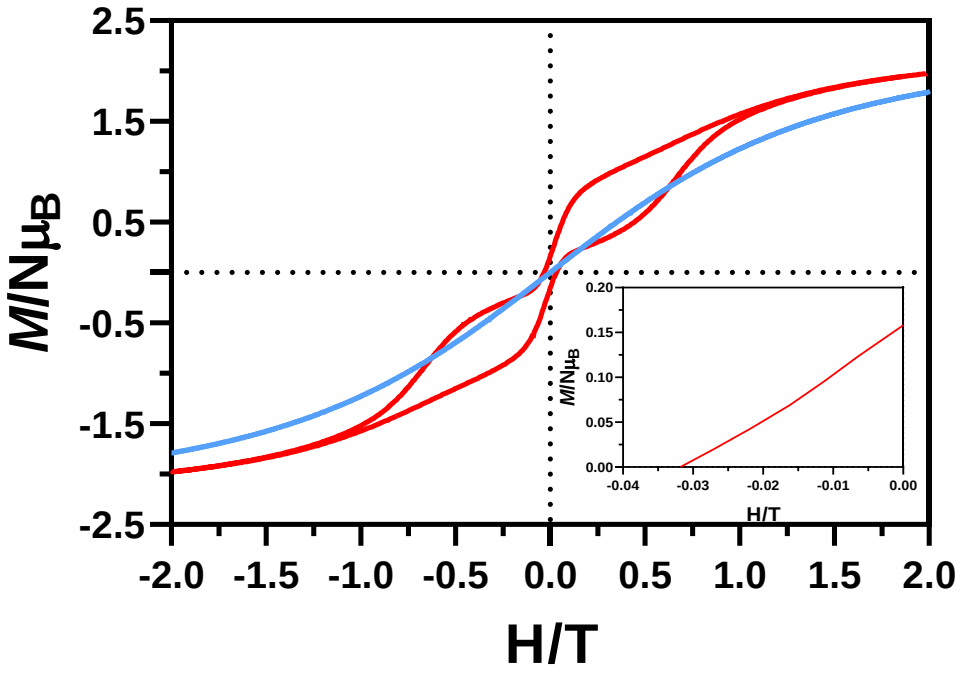

Figure III.V.- Magnetic hysteresis loops for **54** for *H* values between -2 T and 2 T at 2 K (red) and 3 K (blue) with a 50 Oe/s sweep rate. Inset: expansion of the loop to notice the coercive field.

III.IV.IV. Pulse magnetization measurements for 54

To further study the magnetization dynamics, we measured the magnetization curves in a full cycle pulsed magnetic field for **54** (Figure III.VI). These measurements were carried out at 0.4 and 1.6 K with a maximum field of 9.5 T. Due to the extremely fast sweep-rates (3.8 T/ms), larger hysteresis loops could be observed in comparison to conventional loop measurements. In fact, at 0.4 K a coercive field of 3.6 T was observed (Figure III.VI, inset).

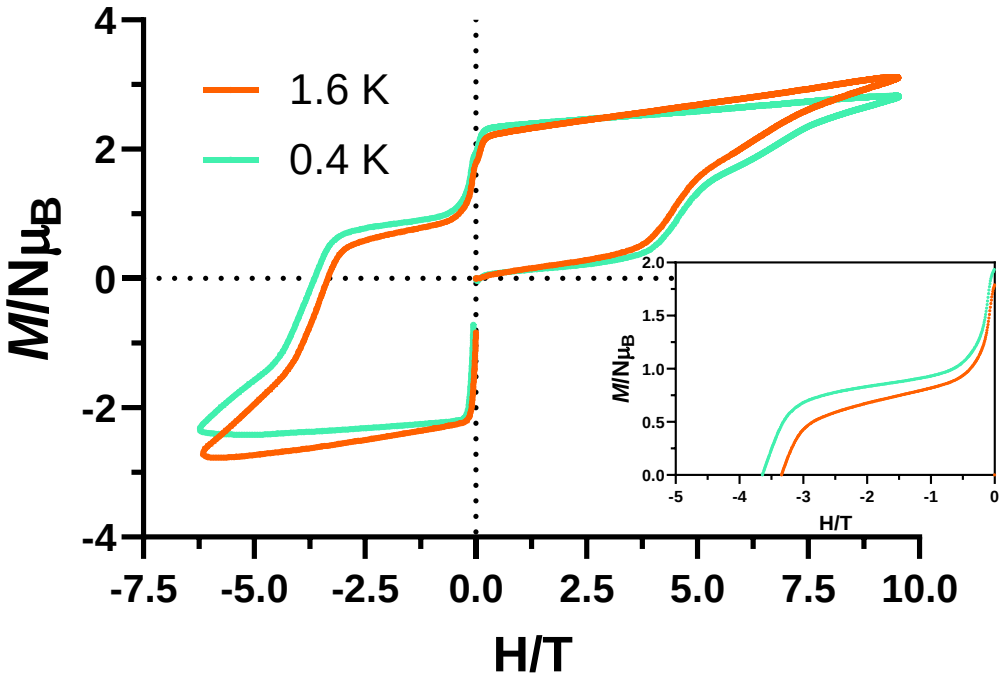

Figure III.VI.- Pulsed-field magnetization curves at maximum field of 9.5 T and at 0.4 K and 1.6 K for **54**. Inset: Expansion of the loop to compare coercive fields.

As we mentioned in the introduction, we believe that these kind of measurements could provide us some more valuable information. In fact, within these loops it is clearly observable that at zero field QTM operates losing a large amount of the magnetic moment, which could be due to hyperfine, intermolecular interactions or transverse components [12]. However, this was not possible to observe in the *ac* measurements and we were not able to obtain relaxation times below 4.4 K. Thus, we are losing information about the QTM regime, which clearly operates at the lowest temperatures as it is displayed in the pulse magnetization measurements. Regarding the loops, when the magnetic field is moved from negative values to zero, at very low fields (around 0.1 T) there is a strong slope change that we attribute to QTM losing completely the remnant magnetization. Therefore, as an approximation, we could say that the time that the system needs to lose the remnant magnetization below 0.1 T is equal to τ_{QTM}.

By considering this simple approach, we have extracted the value of τ_{QTM} at 1.6 and 0.4 K, which is the same value due to the temperature independent character, and we have included them in the Arrhenius fit. By considering the previously obtained U_{eff}

and τ_0 values, as well as a τ_{QTM} of 0.025 s, we obtain the following plot considering a simultaneous presence of Orbach and QTM (Figure III.VII). This is something similar to what is usually done by measuring decay curves [13]. When the maxima in the $\chi''_M(\upsilon)$ curves are out of the low frequency limit of the instrument, the mentioned decay curves are used to obtain relaxation times. In order to verify the effectivity of our approach, we are currently measuring additional $\chi''_M(T)$ curves below 60 Hz. By doing so, our aim is to obtain relaxation times in the 2.0-4.4 K temperature range and include them in the Arrhenius plot of the Figure III.VII, which must appear between the relaxation times that we have obtained from the pulse magnetization measurements and the ones we obtained by fitting the $\chi''_M(\upsilon)$ curves in the 4.4-7.6 K range.

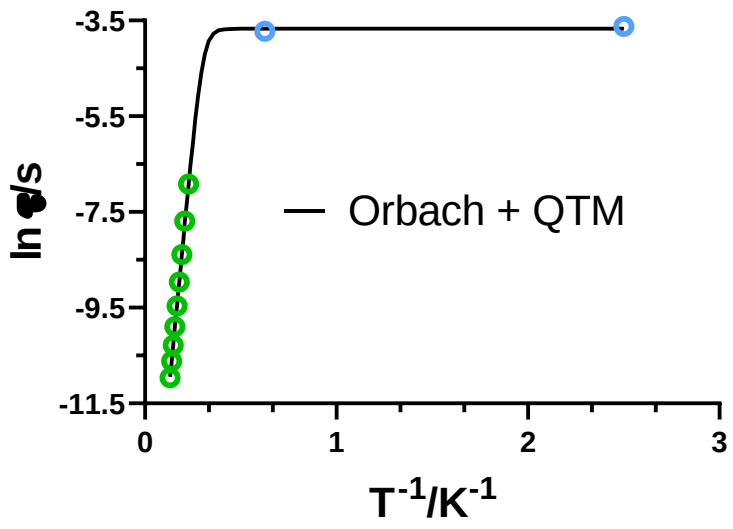

Figure II.IV.- Arrhenius plot for the relaxation times considering Orbach and QTM mechanisms. The relaxation times obtained from *ac* measurements and pulse magnetization measurements are displayed in green and blue, respectively.

III.V. CONCLUSIONS

By using the tripodal H_3L^5 ligand we have not been able to synthesize the initially targeted mononuclear Co^{II} based compound. Indeed, the reaction in atmospheric conditions afforded the diamagnetic mononuclear compound **53**.

We have been able to avoid having an oxidation by carrying out the same experiment under inert conditions, which afforded the trinuclear compound **54**.

Probably, the absence of any functional group in the other *ortho*- position of the phenol is the reason why we obtained the trinuclear compound even using sub-stoichiometric amounts of Co^{II}. In any case, the trigonal prism coordination environment around the Co1 ions or the strong enough exchange interactions allowed us to observe zero field SMM behaviour for this compound.

Finally, apart from observing large hysteresis loops in the pulse magnetization measurements, we have proposed another application for this technique, as we think it could be used to determine the parameter related to QTM, τ_{QTM}. We are currently performing more experiments in order to determine the origin of the slow relaxation of the magnetization in **54** and the validity of the proposed application for the determination of τ_{QTM}.

III.V. REFERENCES

[1] A.A. Pavlov, Y. V. Nelyubina, S. V. Kats, L. V. Penkova, N.N. Efimov, A.O. Dmitrienko, A. V. Vologzhanina, A.S. Belov, Y.Z. Voloshin, V. V. Novikov, Polymorphism in a Cobalt-Based Single-Ion Magnet Tuning Its Barrier to Magnetization Relaxation, J. Phys. Chem. Lett. 7 (2016) 4111–4116. https://doi.org/10.1021/acs.jpclett.6b02091.

[2] A.A. Pavlov, S.A. Savkina, A.S. Belov, Y. V. Nelyubina, N.N. Efimov, Y.Z. Voloshin, V. V. Novikov, Trigonal Prismatic Tris-pyridineoximate Transition Metal Complexes: A Cobalt(II) Compound with High Magnetic Anisotropy, Inorg. Chem. 56 (2017) 6943–6951. https://doi.org/10.1021/acs.inorgchem.7b00447.

[3] V. V. Novikov, A.A. Pavlov, Y. V. Nelyubina, M.E. Boulon, O.A. Varzatskii, Y.Z. Voloshin, R.E.P. Winpenny, A Trigonal Prismatic Mononuclear Cobalt(II) Complex Showing Single-Molecule Magnet Behavior, J. Am. Chem. Soc. 137 (2015) 9792–9795. https://doi.org/10.1021/jacs.5b05739.

[4] J.Y. Ge, J.Z. Xie, Z.Y. Zhao, J. Ru, Y. Song, J.L. Zuo, Thiacalix[4]arene-supported heterodinuclear NiII-LnIII complexes: Slow magnetic relaxation behavior in the dysprosium analogue, RSC Adv. 6 (2016) 1143–1150. https://doi.org/10.1039/c5ra23697e.

[5] T. Yamaguchi, Y. Sunatsuki, H. Ishida, M. Kojima, H. Akashi, N. Re, N. Matsumoto, A. Pochaba, J. Mroziński, Synthesis, structures, and magnetic properties of face-sharing heterodinuclear Ni(II)-Ln(III) (Ln = Eu, Gd, Tb, Dy) complexes, Inorg. Chem. 47 (2008) 5736–5745. https://doi.org/10.1021/ic8000575.

[6] V. V. Novikov, A.A. Pavlov, Y. V. Nelyubina, M.E. Boulon, O.A. Varzatskii, Y.Z. Voloshin, R.E.P. Winpenny, A Trigonal Prismatic Mononuclear Cobalt(II) Complex Showing Single-Molecule Magnet Behavior, J. Am. Chem. Soc. 137 (2015) 9792–9795. https://doi.org/10.1021/jacs.5b05739.

[7] Y.Y. Zhu, C. Cui, Y.Q. Zhang, J.H. Jia, X. Guo, C. Gao, K. Qian, S. Da Jiang, B.W. Wang, Z.M. Wang, S. Gao, Zero-field slow magnetic relaxation from single Co(ii) ion: A transition metal single-molecule magnet with high anisotropy barrier, Chem. Sci. 4 (2013) 1802–1806. https://doi.org/10.1039/c3sc21893g.

[8] L. Beaufort, L. Delaude, A.F. Noels, A new tripodal ligand system based on the iminophosphorane functional group. Part 1: Synthesis and characterization, Tetrahedron. 63 (2007) 7003–7008. https://doi.org/10.1016/j.tet.2007.05.022.

[9] R. Akbar, M. Baral, B.K. Kanungo, Design, synthesis and photophysical properties of 8-hydroxyquinoline-functionalized tripodal molecular switch as a highly selective sequential pH sensor in aqueous solution, RSC Adv. 5 (2015) 16207–16222. https://doi.org/10.1039/c4ra16345a.

[10] S. Katsuta, Y. Shimizu, R. Takahashi, N. Kanaya, T. Imoto, Y. Takeda, Metal complexes of tripodal ligands as ionophores for alkali metal ions, New J. Chem. 36 (2012) 1445–1448. https://doi.org/10.1039/c2nj40171a.

[11] D. Plaul, M. Böhme, S. Ostrovsky, Z. Tomkowicz, H. Görls, W. Haase, W. Plass, Modeling Spin Interactions in a Triangular Cobalt(II) Complex with Triaminoguanidine Ligand Framework:

Synthesis, Structure, and Magnetic Properties, Inorg. Chem. 57 (2018) 106–119. https://doi.org/10.1021/acs.inorgchem.7b02229.

[12] S. Vaidya, S. Tewary, S.K. Singh, S.K. Langley, K.S. Murray, Y. Lan, W. Wernsdorfer, G. Rajaraman, M. Shanmugam, What Controls the Sign and Magnitude of Magnetic Anisotropy in Tetrahedral Cobalt(II) Single-Ion Magnets?, Inorg. Chem. 55 (2016) 9564–9578. https://doi.org/10.1021/acs.inorgchem.6b01073.

[13] C.A.P. Goodwin, F. Ortu, D. Reta, N.F. Chilton, D.P. Mills, Molecular magnetic hysteresis at 60 kelvin in dysprosocenium, Nature. 548 (2017) 439–442. https://doi.org/10.1038/nature23447.

mini-Chapter IV

FUTURE PERSPECTIVES AND ADDITIONAL WORK

IV.I. FUTURE PERSPECTIVES

During the realization of this Ph.D. thesis, few more experimental results have been obtained, which are not included in detail in this work. As stated in some of the Chapters, new experiments are also planned for the near future to complete or even improve this work. All these considerations are compiled in this section.

Chapter 2

As seen in Chapter 2, we were able to extend the $Zn^{II}Dy^{III}$ dinuclear entities through a variety of di- and tricarboxylic acids. We are currently studying the photoluminescent properties of these compounds, but more interestingly, we were also able to introduce the pyrene derivative tetracarboxylic acid (which is used in the synthesis of the MOF NU-1000) as a linker obtaining the novel octanuclear compound **55** (Figure IV.I).

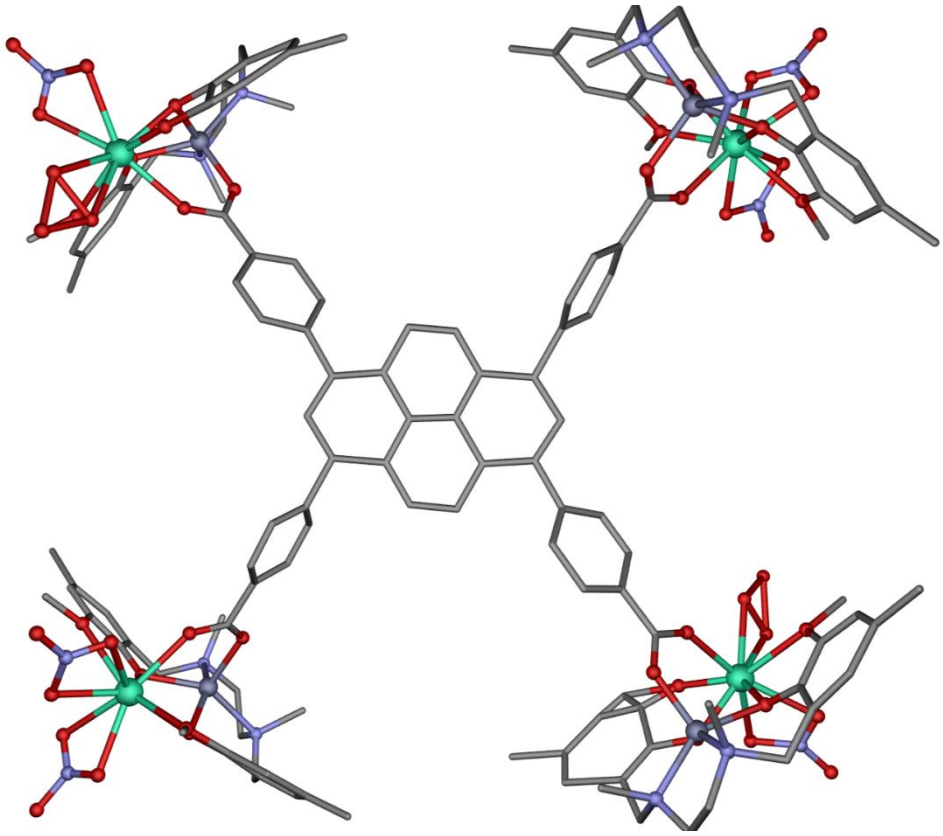

Figure IV.I.- Perspective view of compound **55**. Colour code: dysprosium, zinc, nitrogen, oxygen and carbon atoms are in turquoise, dark grey, light blue, red and grey, respectively. Hydrogen atoms are omitted for the sake of clarity.

As expected, this compound behaves as a field induced SMM, but we are more interested in luminescent properties, since the extensively conjugated linker could be effective to provide an *antenna effect*. We are planning to synthesize isostructural compounds with other Ln^{III} ions and study the emissive properties. Additionally, we started a collaboration with Dr. Joaquín C. García Martínez from Universidad de Castilla - La Mancha, who provided us with other extended and conjugated ligands depicted in Figure IV.II. We are currently working on the synthesis of novel compounds based on these linkers and H_2L^3.

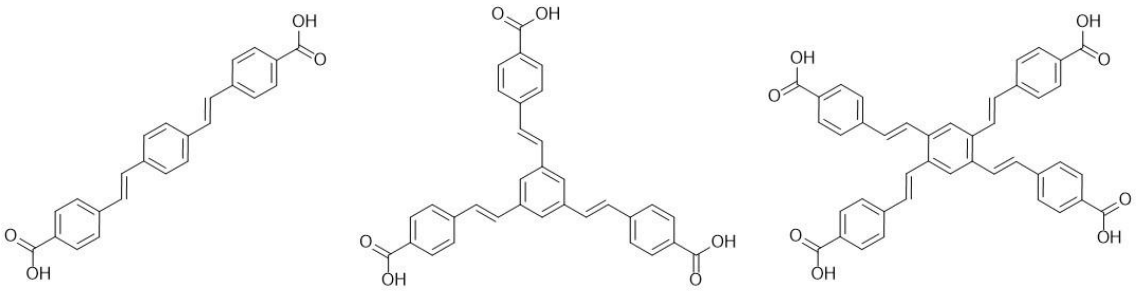

Figure IV.II- Additional conjugated ligands provided by J. C. García Martínez.

From this chapter we would also like to start a new research based on compound **14**. As discussed, the compound possesses two cavities, one in each side of the bridging trimesate group. One of the cavities stabilizes a $CHCl_3$ molecule forming intermolecular C-H$\cdots\pi$ and Cl$\cdots\pi$ interactions. This, at the same time, folds the structure making the second cavity slightly larger and showing, to some extenet, the adaptability of the structure. In spite of the fact that we would not expect great changes in the dynamic magnetic behaviour, from the structural point of view we would be interested in trying to introduce other haloforms in such cavities.

Chapters 4 and 5

In view of the results that we obtained in Chapters 4 and 5, we concluded that the succinate bridging ligand was not adequate to provide 1D extended networks. However, we have not given up towards this project. In the way towards the obtention of compound **36**, the first approach was to obtain compound **30**, an acetate bridged compound in analogy to the dinuclear compounds. After this, we changed the acetate

by succinate with the aim of extending the network, but we failed and serendipitously obtained **36**. Thus, continuing the stepwise process, a 1D extension based on Chapter 3 would be starting from the hexanuclear Zn_4Dy_2 compound depicted in Figure IV.III. To do so, we would combine both H_2L^3 and H_4L^4 ligands for the synthesis of an isolated molecule. If we are able to obtain this compound, we must be able to use just H_4L^4 ligands and obtain a 1D extended network.

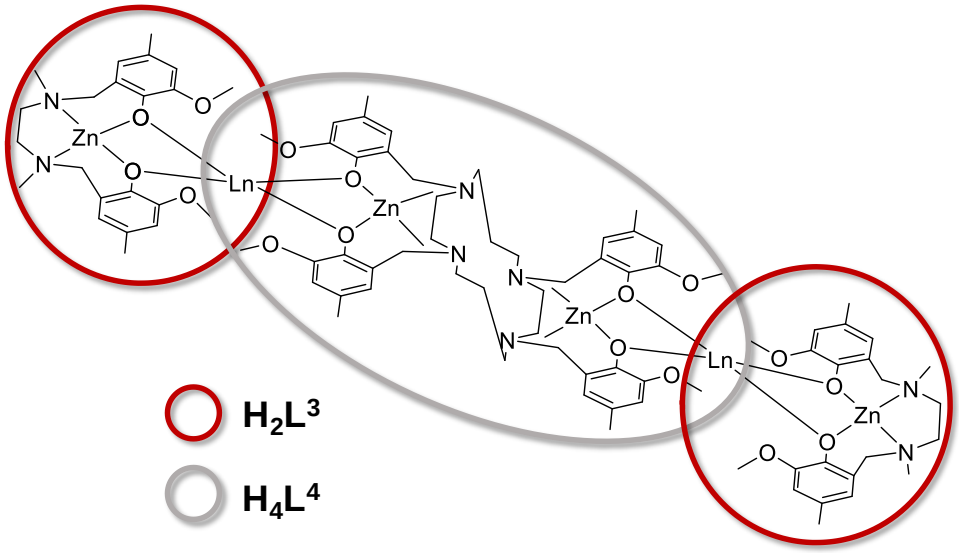

Figure IV.III.- The target hexanuclear Zn_4Ln_2 compound based on the coordination mode of the trinuclear systems we obtained in Chapter 3. Note that chloride atoms and water molecules that are supposed to coordinate to Zn^{II} and Ln^{III}, respectively, have been omitted.

Related to the pulse magnetization measurements, we would also like to study some other diluted samples of **33**. We have seen that in terms of coercive field Zn_2Dy_2 (**36**) behaves better than Co_2Dy_2 (**33**). However, $Zn_xCo_{2-x}Dy_2$ does not behave as something in between **33** and **36**, instead, $\mathbf{33_{Zn}}$ shows the largest coercive field. Therefore, it would be of great interest to study different systems varying the value of x in order to better understand the doping/diluting effect.

Finally, considering that these kind of tetranuclear compounds contain an extended hydrogen-bonded network based on protic solvents and nitrate counterions, we would like to study if these samples are good candidates to present proton conductivity.

Chapter 6

In Chapter 6 we have been able to modify the equatorial ligand field by using diverse chelates. We would like to continue enlarging this family by using some other chelated that were suggested in the introduction of such chapter. Additionally, Murrie and co-workers have recently reported a Dy^{III} based zero field SMM with sulfur ligands showing remarkably long Dy-S bond distances (Murrie *et al*., *Chem. Commun*., 2020, **56**, 1533-1536). It would be very interesting to be able to introduce the same ligands as chelates in our tetranuclear systems. We are aware of the difficulty of doing so due to the low affinity of Dy^{III} towards sulphur, but we do not discard carrying out some trials. Among other different chelates, we would like to emphasize the interest in the chiral camphor derivative (Figure 6.1, Chapter 6), which would allow us to obtain a wide variety of enantiomeric and diastereomeric compounds.

H_2L^6

Some other trials were carried out with the polytopic ligand H_2L^6 shown in Figure IV.IV. In a reactionin which we combined $Zn(acac)_2$, $Dy(acac)_3$ and H_2L^6 we obtained single crystals of compound **56**. However, due to the poor diffraction, we were not able to properly solve the structure. At first glance, the structure looks like a cage in which the main ligand and acac chelates could be observed. More attempts to obtain better data are planned for the near future.

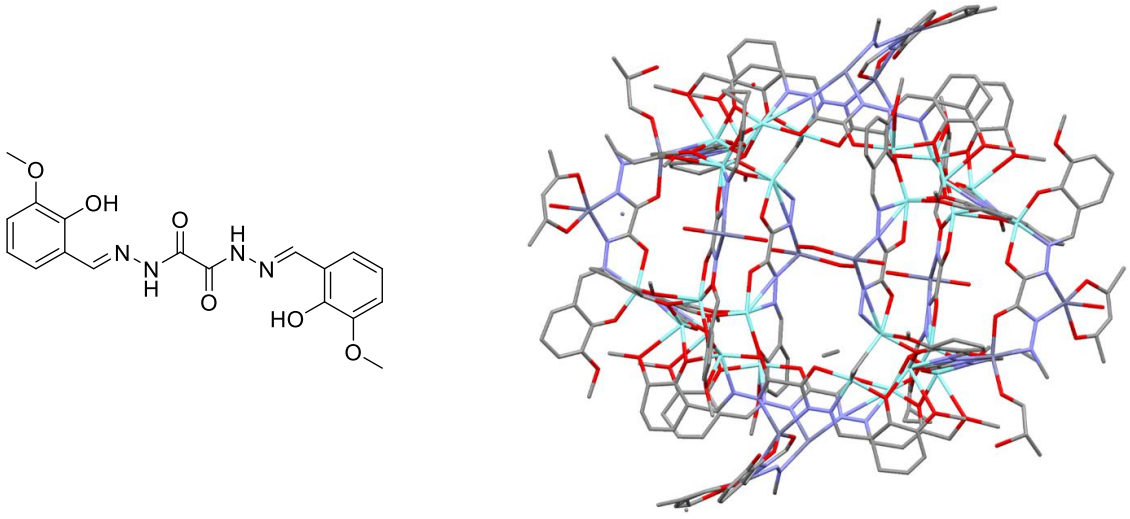

Figure IV.IV.- Ligand H_2L^6 (left) and perspective view of compound **56** (right).

IV.II. ADDITIONAL WORK

During the Ph.D. thesis, I have also had the pleasure of collaborating with some other researchers such as I. Oyarzabal, J. Cepeda and, especially, A. Rodríguez-Diéguez. In those works, we mostly studied transition metal and lanthanide based MOFs and I was particularly involved in the study of the magnetic properties. These collaborations have given rise to the following research papers:

- *Effect of the change of the ancillary carboxylate bridging ligand on the SMM and luminescence properties of a series of carboxylate-diphenoxido triply bridged dinuclear ZnLn and tetranuclear Zn_2Ln_2 complexes (Ln = Dy, Er).* E. Echenique-Errandonea, A. Zabala-Lekuona, J. Cepeda, A. Rodríguez-Diéguez, J.M. Seco, I. Oyarzabal, E. Colacio, *Dalton Trans.*, 2019, **48**, 190.

- *Dilution effect on the slow relaxation of a luminescent dysprosium Metal-Organic Framework based on 2,5-dihydroxyterephthalic acid.* A.A. García-Valdivia, A. Zabala-Lekuona, A. Goñi-Cárdenas, B. Fernández, J.A. García, J.F. Quílez del Moral, J. Cepeda, A. Rodríguez-Diéguez, *Inorganica Chim. Acta*, 2020, **509**, 119687.

- *Influence of thermally induced structural transformations on the magnetic and luminescence properties of tartrate-based chiral lanthanide organic-frameworks.* U. Huizi-Rayo, A. Zabala-Lekuona, A. Terenzi, C.M. Cruz, J.M. Cuerva, A. Rodríguez-Diéguez, J.A. García, J.M. Seco, E. San Sebastian, J. Cepeda, *J. Mater. Chem. C*., 2020, **8**, 8243.

- *Antiparasitic, anti-inflammatory and cytotoxic activities of 2D coordination polymers base don 1H-indazole-5-carboxylic acid.* A.A. García-Valdivia, A. García-García, F. Jannus, A. Zabala-Lekuona, J.M. Méndez-Arriaga, B. Fernández, M. Medina-O'donnell, G.B. Ramírez-Rodríguez, J.M. Delgado-López, L.M. Pastrana-Martínez, J. Cepeda, J.A. Lupiáñez, F.J. Reyes-Zurita, A. Rodríguez-Diéguez. *J. Inorg. Biochem*., 2020, **208**, 111098.

- *Magnetic and Luminescent Properties of Isostructural 2D Coordination Polymers Based on 2-Pyrimidinecarboxylate and Lanthanide Ions.* A. García-García, A. Zabala-Lekuona, A. Goñi-Cárdenas, J. Cepeda, J.M. Seco, A. Salinas-Castillo, D. Choquesillo-Lazarte, A. Rodríguez-Diéguez. *Crystals*, 2020, **10**, 571.

- *2D-Coordination polymers based on 1H-indazole-4-carboxylic acid and transition metal ions: magnetic, luminescence and biological properties.* A.A. García-

Valdivia, A. Zabala-Lekuona, G.B. Ramírez-Rodríguez, J.M. Delgado-López, B. Fernández, J. Cepeda, A. Rodríguez-Diéguez. *CrystEngComm*., 2020, **22**, 5086.

- *Modulating Magnetic and Photoluminescence Properties in 2-Aminonicotinate-Based Bifunctional Coordination Polymers by Merging 3d Metal Ions.* O. Pajuelo-Corral, A. Zabala-Lekuona, E. San Sebastian, A. Rodríguez-Diéguez, J.A. García, L. Lezama, E. Colacio, J.M. Seco, J. Cepeda. *Chem. Eur. J.*, 2020, **26**, 13484.

Additionally, some of the works carried out in this thesis have been presented in several meetings:

- Oral presentation at "IV Jornada de Promoción a la Investigación Básica para Estudiantes de Ciencias e Ingenierías" (Móstoles, **2019**). Title: *Nuevos factores determinantes en el comportamiento SMM de materiales basados en el Dy(III).*

- Poster presentation at "7th European Conference on Molecular Magnetism (ECMM2019)" (Florence, **2019**). Title: *Does the rigidity of the molecule influence the relaxation dynamics of SMMs based on Dy(III) ion?*

- Flash presentation at "4th Bordeaux Olivier Kahn Discussions (BOOK-D2019)" (Bordeaux, **2019**). Title: *Looking for other determinant factors influencing the SMM behavior in Dy(III) based compounds.*

- Flash presentation at "XXXVII Reunión Bienas de la Real Sociedad Española de Química" (Donostia, **2019**). Title: *En busca de factores determinantes en el comportamiento de SMMs basados en el ion Dy(III).*

- Poster presentation at "XV Simposio de Jóvenes Investigadores Químicos" (Toledo, **2018**). Title: *Diseño y síntesis progresiva desde compuestos 0D hasta 1D: influencia en las propiedades magnéticas.*

- Flash presentation at "XIV Simposio de Investigadores Jóvenes de la Real Sociedad Española de Química" (Badajoz, **2017**). Title: *Estudio magnético de compuestos de coordinación basados en el ion Dy^{III}: importancia del campo cristal.*

- Poster presentation at "17ª Reunión Científica Plenaria de Química Inorgánica y 11ª Reunión Científica Plenaria de Química del Estado Sólido (QIES2016)" (Málaga, 2016). Title: *Complejos dinucleares Zn^{II}-Ln^{III} con propiedades magneto-luminiscentes.*

- Poster presentation at “XIII Simposio de Investigadores Jóvenes de la Real Sociedad Española de Química” (Logroño, **2016**). Title: *Estudio magneto-luminiscente de materiales basados en complejos dinucleares $Zn^{II}Ln^{III}$.*

CONCLUSIONS

The main goal of the research work developed in this Ph.D was the design, synthesis and characterization of new materials based on either transition metal or lanthanide coordination complexes showing interesting magnetic (SMM behaviour) and/or luminescent properties. To achieve these objectives, four compartmental Mannich base ligands N,N',N''-trimethyl-N,N''-bis(2-hydroxy-3-formyl-5-bromo-benzyl) diethylenetriamine (H_2L^1), N,N'-dimethyl-N,N'-bis(2-hydroxy-3-formyl-5-bromo-benzyl) ethylenediamine (H_2L^2), N,N′-dimethyl-N,N′-bis(2-hydroxy-3-methoxy-5-methylbenzyl)-ethylenediamine (H_2L^3) and 1, 4, 8, 11-tetraaza-1, 4, 8, 11-tetrakis(2-hydroxy-3-methoxy-5-methylbenzyl) cyclotetradecane (H_4L^4) and a tripodal Schiff base ligand 1,1,1-tris[(salicylideneamino)methyl]ethane) (H_3L^5) were synthesized.

The results and discussions presented in this manuscript allow drawing the following conclusions:

Chapter 1

1) Three pairs of mononuclear Ln^{III} (Dy^{III} and Er^{III}) based compounds have been synthesized based on the compartmental H_2L^1 and H_2L^2 ligands. They all contain very similar coordination environments around the metal ions, but display different dynamic magnetic properties.

2) Interestingly, even though compounds **1** and **2** have been studied as desolvated compounds, the exhaustive study regarding other lanthanide ions (also including Dy^{III} and Er^{III}) has shown that they usually crystallize with additional crystallization acetonitrile molecules. However, the powdered samples suffer from solvent loss giving rise to **1** and **2**. The crystal structure analysis of these solvated compounds has let us observe the influence of the ionic radius acoording to the coordination number.

3) Among **1-6** studied compounds, only the Dy^{III} based compound **1** displays zero field SMM behaviour, while the rest display field induced slow magnetic relaxation.

4) From the crystal structure analysis, we concluded that the paramagnetic ions are well separated within the crystal structure with shortest intermolecular distances always above 8 Å. However, the magnetic study upon diluted counterparts has evidenced the role of dipolar intermolecular interacions in the slow relaxation of the magnetization. In fact, $\mathbf{3_Y}$ displayed zero field SMM behaviour.

5) Due to the low symmetrical coordination environment of these compounds, it has not been easy to postulate magneto-structural correlations that explain the

dynamic magnetic properties of these systems. However, calculating the magnetic anisotropy axes by the Magellan software has helped us suggesting some explanations. As it could be expected, the shortest Dy-$O_{phenoxido}$ bond distances determine the orientation of the axes. Considering that the Dy^{III} ion contains two phenoxido donor atoms in the three possible structures, ideally, the should both be oppositely coordinated. In our case, however, in the three cases they are nearer of being in the same side of the oblate electron sphere and, thus, the lowest angles between the anisotropy axis and phenoxido oxygen atoms give rise to enhanced magnetic properties for **1**.

6) Considering that the Er^{III} ion has an opposite electron cloud distribution, an inverse trend could be considered coherent.

Chapter 2

7) Based on H_2L^3, we have been able to extend dinuclear $Zn^{II}Dy^{III}$ units by using a wide variety of bridging groups such as carbonate, different dicarboxylates and trimesate giving rise to nine novel polynuclear compounds (**7-15**).

8) As it occurred in Chapter 1, even though we have been able to measure the crystal structure of the mentioned nine compounds, some of them suffer from reorganization due to solvent loss. In order to verify this hypothesis, we prepared isostructural and diamagnetic $Zn^{II}Y^{III}$ counterparts to perform an alternative study based on PXRD, TG analysis, NMR, IR and EA.

9) Under zero applied *dc* field, none of the compounds displays maxima in the out-of-phse susceptibility component. However, field optimization studies were carried out for all the compounds (in the diluted form for some of them) and once the measurements were performed under optmal conditions, they all displayed field induced SMM behaviour.

10) Interestingly, the diluted $\mathbf{7}_{DyY}$, $\mathbf{11}_{DyY}$ and $\mathbf{13}_{DyY}$ counterparts displayed zero field SMM behaviour, pointing out the relevance of quenching the weak intra- or intermolecular interactions that were favouring fast QTM. Indeed, in the case of **7**, which is the only compound with a direct bridge between paramagnetic ions, by evaluating the isotropic $\mathbf{7}_{Gd}$ counterpart we were able to calculate the exchange coupling constant being almost negligible. Therefore, these weak interactions in **7** might be the reason of causing transverse components facilitating under barrier shortcuts.

11) Unfortunatelly, we have not been able to correlate the stiffness of the structures with the dynamic magnetic properties. Even though **7$_{DyY}$** and **13$_{DyY}$** can be considered as rigid systems with improved magnetic properties, **11$_{DyY}$** contains the flexible pimelate bridge and, hence, zero field SMM behaviour cannot be related to the rigidity.

12) In contrast, the relatively high energy barriers found for **7$_{DyY}$** and **15** (over 100 K) under external magnetic fields, could be rationalized by an improved ligand field around the Dy^{III} ions. In fact, whereas almost all the compounds display nitrate chelates in the opposite side of the phenoxides (which display the shortest bond distances, thus defining the orientation of the anisotropy axes), **7$_{DyY}$** and Dy1B in **15** contain a carbonate and a carboxylate. These groups are supposed to provide larger electron density and, therefore, a larger energy gap could be expected between the ground and first excited Kramers doublet.

Chapter 3

13) Based on H_2L^3, we have been able to synthesize two novel homonuclear Co^{II} based compounds, a previously reported tetranuclear compound and seven mixed 3d-4f-3d mixed heterotrinuclear compounds (**16-25**).

14) By changing the bridging chloride atoms in **16** with end-on coordinating azides for **17**, we have been able to modulate the nature of the exchange interactions from antiferromagnetic to ferromagnetic. Additionally, the latter one displays weak field induced SMM behaviour wich may arise from a quenching of QTM.

15) The pentanuclear compound **18** displays an atypical structure with four distorted octahedral Co^{II} centers and a trigonal prism Co^{II}.Unexpectedly, this compound behaves as a zero field SMM and applying an external magnetic field accelerates the relaxation times, which is a rather strange behaviour. Based on the field-dependent measurements, we attribute this behaviour to the activation of a direct relaxation process.

16) Regarding the heterotrinuclear compounds, compounds **20**, **21** and **22** behave as zero field SMMs, which are copound containing anisotropic Co^{II} ions and isotropic Gd^{III} and oblate Tb^{III} and Dy^{III} ions, respectively. However, among these three compounds only **22** displays well defined maxima in the out-of-phase component.

17) Considering that compound **25** ($Zn^{II}Dy^{III}Zn^{II}$ counterpart) does not show SMM behaviour in the absence of a magnetic field, we believe that intramolecular exchange

interactions are important within **20**, **21** and **22** to quench QTM, a fact that has been previously seen in mixed 3d-4f compounds.

18) Since **23** and **24**, which contain prolate 4f ions apart from Co^{II}, do not display any SMM behaviour, we conclude that the ligand field is more suitable to stabilize high MJ states as ground state for oblate ions. This was expected considering the distribution of the donor atoms, being somehow similar to other compounds previously reported by our group.

Chapter 4

19) We designed the ligand H_4L^4 with the aim of extending $Zn^{II}Dy^{III}$ entities along 1D. The crystal structures found for the Cu^{II} based dinuclear compound (**28**) and tetranuclear $Zn^{II}Dy^{III}$ based (**30**) compound were promising towards the synthesis of 1D coordination polymers. Noteworthy, within compound **30** two similar, but different compounds cocrystallize (named as **30A** and **30B**).

20) Regarding its dynamic magnetic properties, we found field induced SMM behaviour with two relaxation pathways. Based on the magneto-structural correlations that we suggest, we think that each molecule (**30A** and **30B**) displays an independent relaxation mechanism. We associate FR to **30A** and SR to **30B** based on the same considerations that we have suggested in Chapter 2. Indeed, **30A** contains a nitrate opposite to the phenoxides, while **30B** dislays an acetate. Since the acetate must provide a larger electron density, a higher effective energy barrier is expected for it.

21) When introducing the dicarboxylate succinate to replace the acetate bridges in **30**, the ionic structure **36** was obtained, which turned to be a tetranuclear Zn_2Dy_2 compound. Luckily, the ligand field happened to be suitable for the oblate Dy^{III} ion, exhibiting zero field SMM behaviour with a U_{eff} of around 260 K. This good performance arises from the disposition of the phenoxide groups, being two of them in one side of the Dy^{III} ion and the other one in the opposite side.

22) Based on these interesting results, we have studied other isostructural compounds based on different combinations of 3d-4f ions, as well as a wide variety of dilutions. In contrast to what we observed in Chapter 3, in this occasion, the combination of two paramagnetic ions within the same structure has detrimental effects eliminating the zero field SMM behaviour.

23) As a last concluding remark, based on pulse magnetization measurements, we have seen that the hysteresis loops found for **33_{Zn}** (which could be considered as **36** doped with around 10% of Co^{II}) display notably larger hysteresis loops compared to **36**. Even though we do not know the reason, it seems that including a little amount of paramagnetic 3d ions within the system quenches more effectively the undesired QTM.

Chapter 5

24) By replacing the bridging succinate group in the tetranuclear systems reported in the previous Chapter 4, by enantiopure R-methylsuccinate or S-methylsuccinate, we have been able to stereospecifically control the configuration of the zwitterionic amines, thus obtaining R,S',S'' and S,R',R'' enantiopure compounds (where the first configuration corresponds to the methylsuccinate and the latter two to the amines).

25) Based on a simple theoretical study, we have concluded that the stereospecific contros arises from steric reasons. As a proof of concept, when using racemic methylsuccinate, both enantiomers cocrystallize within the crystal structure.

26) Regarding dynamic magnetic properties, due to the similar coordination environment around the 4f ions, Dy^{III} based **41-R** exhibits zero field SMM behaviour with an energy barrier as high as 272 K. Moreover, the Yb^{III} counterpart **43-R** shows field induced SMM behaviour.

27) In terms of luminescence, Sm^{III} and Tb^{III} counterparts (**38-R** and **40-R**) displayed bright emissive properties even at room temperature according to a better sensitization by the ligand. For **39-R** (Eu^{III} based), an extremely temperature dependent emission was found displaying the best emission performance at low temperatures. Based on that, we have suggested an approach by combining both Dy^{III} and Eu^{III} ions within the system with the aim of designing a bifunctional compound exhibiting SMM and thermometric properties.

28) Finally, based on the bright emission of the Tb^{III} based **40-R/S**, we have been able to measure circularly polarized luminescence with g_{lum} values ranging in between $2 \cdot 10^{-2}$ and $7 \cdot 10^{-2}$.

Chapter 6

29) In this chapter we have been able to modify the equatorial ligand field of compound **36** obtaining 5 novel compounds, from which four behave as zero field SMMs. More specifically, the model compound allows us to modify single positions

individually or simultaneously. The modified positions are the succinate and the nitrate chelate.

30) Among them, we have seen that changing the bridging succinate by tetrafluorosuccinate enhances the dynamic magnetic properties due to longer and less electron donating bonds.

31) In our case, in contrast to a previously reported research, the nitrate chelate is more appropriate than hfac. Indeed, the latter one provides shorter bond distances and, moreover, the Mulliken charges calculated from *ab initio* calculations suggest a greater electron density provided by hfac oxygen atoms.

32) As expected, dbm ligands create the shortes Dy-O bond distances among the used chelates and, hence, the equatorial ligand field becomes so strong that compound **49** does not display zero field SMM behaviour. Indeed, even under an external magnetic field, no maximum is observed in the out-of-phase component.

33) As we suggest, the synthesis and magnetic characterization of more compounds combining different chelates will shed more light about the most influencing factors in the dynamic magnetic properties of these kind of complexes.

***mini*-Chapter I**

34) Based on H_4L^4, we have been able to synthesize two novel $Cd^{II}Dy^{III}$ (**50**) and $Hg^{II}Dy^{III}$ (**51**) compounds. Even though they were not targeted compounds, these systems allow us to evaluate how the diamagnetic ion influences the dynamic magnetic properties.

35) Even though they both display field induced SMM behaviour, the QTM regime is not the same in both compounds. Additionally, relaxations times at 2.0 K were found to be one order of magnitude larger for **50** in comparison to **51**.

***mini*-Chapter II**

36) With the aim of anchoring the tetranuclear compound **36** to G and/or GO surfaces, we have been able to replace the nitrate counterions by tetraphenylborates to form compound **52**, which may create intermolecular C-H$\cdots\pi$ interactions enabling a better deposition on the surface.

37) We have prepared bulk samples of the hybrid **52@G** and **52@GO**. Based on absorption spectra in the UV-Vis range, as well as on SEM-EDX measurements, it looks that our target system has been successfully anchored to the surface.

38) Unfortunately, the zero field SMM behaviour found in **52** is lost for the hybrid systems.

***mini*-Chapter III**

39) Based on the tripodal ligand H_3L^5, we have been able to synthesize a trinuclear Co^{II} based compound behaving as zero field SMM. The trigonal prism coordination environment around Co1 or strong enough exchange interactions (or both effects) must be the reason of observing it.

40) We have proposed a new application for pulse magnetization measurements, since we believe that they could provide as more valuable information about the QTM regime. Note that large hysteresis loops were found for the trinuclear compound with this technique.

APPENDICES

Chapter 1: *An experimental magneto-structural study of the slow relaxation in Ln^{III} (Dy and Er) based mononuclear complexes with Mannich compartmental ligands derived from linear amines and 5-bromosalicylaldehyde*

Index:

1. Elemental Analyses and Crystallographic Tables.

Table A1.1.- Yields and elemental analyses for complexes **1**-**6**.

Complex	Yield (%)	Formula	% C calc./found	% H calc./found	% N calc./found
1	47	$C_{23}H_{29}Br_2N_6O_{13}Dy$	30.03/30.15	3.18/2.99	9.14/9.16
2	33	$C_{23}H_{29}Br_2N_6O_{13}Er$	29.88/30.22	3.16/3.27	9.09/8.95
3	31	$C_{25.5}H_{36}Br_{2.75}N_{6.25}O_{12.25}Dy$	30.37/30.25	3.60/3.76	8.68/8.82
4	56	$C_{25.5}H_{36}Br_{2.75}N_{6.25}O_{12.25}Er$	30.23/29.96	3.58/3.69	8.64/8.51
5	84	$C_{22}H_{25}Br_2N_6O_{13}Dy$	29.24/29.30	2.79/2.78	9.30/9.37
6	88	$C_{22}H_{25}Br_2N_6O_{13}Er$	29.08/28.93	2.77/2.75	9.25/9.20

Table A1.2.- Crystallographic data for compounds **1**, **3** and **4**.

Structure	**1**	**3**	**4**
Formula	$C_{23}H_{29}Br_2N_6O_{13}Dy$	$C_{25.5}H_{36}Br_{2.75}N_{6.25}O_{12.25}Dy$	$C_{25.5}H_{36}Br_{2.75}N_{6.25}O_{12.25}Er$
M_r	919.84	1008.36	1013.12
Crystal system	*triclinic*	*triclinic*	*triclinic*
Space group (no.)	*P -1* (2)	*P -1* (2)	*P -1* (2)
a (Å)	9.7409(7)	9.635(5)	9.684(5)
b (Å)	10.5058(7)	10.414(5)	10.453(5)
c (Å)	17.5110(12)	17.840(5)	17.862(5)
α (°)	82.198(2)	83.163(5)	83.034(5)
β (°)	75.792(2)	83.679(5)	83.424(5)
γ (°)	62.476(2)	77.318(5)	77.012(5)
V (Å^3)	1540.05(19)	1727.4(13)	1741.7(13)
Z	2	2	2
D_c (g cm^{-3})	1.984	1.939	1.932
μ(MoK$_\alpha$) (mm^{-1})[d]	5.094	15.893	5.631
*T (*K)	100(2)	100(2)	100(2)
Observed reflections	6125 (4670)	7331 (7127)	9020 (6701)
R_{int}	0.0661	0.0467	0.1385
Parameters	414	440	422
GOF	1.064	1.032	1.031
R_1[a,b]	0.0862 (0.0555)	0.0497 (0.0481)	0.0934 (0.0621)
wR_2[c]	0.1065 (0.0966)	0.1235 (0.1219)	0.1668 (0.1496)
Largest difference in peak and hole (e Å^{-3})	2.161 and -1.587	2.558 and -3.805	2.282 and -3.631

[a]$R_1 = \Sigma||F_o| - |F_c||/\Sigma|F_o|$. [b]Values in parentheses for reflections with $I > 2\sigma(I)$. [c]$wR_2 = \{\Sigma[w(F_o^2 - F_c^2)^2]/\Sigma[w(F_o^2)^2]\}^{½}$. [d] μ(CuK$_\alpha$) (mm^{-1}) in **3**.

Table A1.3.- Crystallographic data for compounds **5** and **6**.

Structure	**5**	**6**
Formula	$C_{22}H_{25}Br_2N_6O_{13}Dy$	$C_{22}H_{25}Br_2N_6O_{13}Er$
M_r	903.80	908.56
Crystal system	*monoclinic*	*monoclinic*
Space group (no.)	*P 21/c* (14)	*P 21/c* (14)
a (Å)	9.56720(10)	9.5259(9)
b (Å)	15.70050(10)	15.7465(14)
c (Å)	19.7956(2)	19.8277(18)
α (°)	90	90
β (°)	97.5930(10)	97.5760(10)
γ (°)	90	90
V (Å^3)	2947.42(5)	2948.2(5)
Z	4	4
D_c (g cm^{-3})	2.037	2.047
μ(MoK$_\alpha$) (mm^{-1})[d]	17.410	5.632
T (K)	100.00(10)	100(2)
Observed reflections	5931 (5696)	6833 (5382)
R_{int}	0.0340	0.0529
Parameters	400	408
GOF	1.044	1.030
R_1[a,b]	0.0246 (0.0233)	0.0629 (0.0458)
wR_2[c]	0.0578 (0.0570)	0.1188 (0.1040)
Largest difference in peak and hole (e Å^{-3})	1.953 and -0.905	1.941 and -1.661

[a]$R_1 = \Sigma||F_o| - |F_c||/\Sigma|F_o|$. [b]Values in parentheses for reflections with $I > 2\sigma(I)$. [c]$wR_2 = \{\Sigma[w(F_o^2 - F_c^2)^2]/\Sigma[w(F_o^2)^2]\}^{½}$. [d] μ(CuK$_\alpha$) (mm^{-1}) in **5**.

Table A1.4.- Crystallographic data for compounds **1-MeCN** to **5-MeCN**.

Structure	**1-MeCN**	**2-MeCN**	**3-MeCN**	**4-MeCN**	**5-MeCN**
Formula	$C_{27}H_{35}Br_2N_8O_{13}Ce$	$C_{27}H_{35}Br_2N_8O_{13}Pr$	$C_{27}H_{35}Br_2N_8O_{13}Nd$	$C_{27}H_{35}Br_2N_8O_{13}Sm$	$C_{27}H_{35}Br_2N_8O_{13}Eu$
M_r	979.59	980.36	983.69	989.80	991.41
Crystal system	*triclinic*	*triclinic*	*triclinic*	*triclinic*	*triclinic*
Space group (no.)	*P*-1 (2)	*P*-1 (2)	*P*-1 (2)	*P*-1 (2)	*P*-1 (2)
a (Å)	9.9047(4)	9.8928(11)	9.8938(5)	9.8721(4)	9.8905(4)
b (Å)	10.6938(5)	10.6725(12)	10.6837(5)	10.6837(5)	10.7451(5)
c (Å)	17.7205(8)	17.699(2)	17.6798(8)	17.6279(8)	17.5610(8)
α (°)	86.091(2)	85.9860(10)	85.970(2)	85.816(4)	85.448(4)
β (°)	79.1480(10)	79.1100(10)	79.178(2)	78.939(4)	78.774(3)
γ (°)	80.426(2)	80.3180(10)	80.343(2)	79.687(4)	78.791(4)
V (Å^3)	1816.38(14)	1807.4(4)	1808.10(15)	1793.77(14)	1793.99(14)
Z	2	2	2	2	2
D_c (g cm^{-3})	1.791	1.801	1.807	1.833	1.835
μ(MoK$_\alpha$) (mm^{-1})	3.525	3.631	3.718	3.937	4.048
T (K)	100(2)	100(2)	100(2)	100(2)	100(2)
Observed reflections	9394 (8159)	8263 (7436)	9336 (7994)	7880 (6937)	7870 (6874)
R_{int}	0.0462	0.0257	0.0649	0.0211	0.0288
Parameters	465	465	465	483	478
GOF	1.046	1.048	1.058	1.097	1.047
R_1[a,b]	0.0386 (0.0291)	0.0310 (0.0267)	0.0543 (0.0417)	0.0423 (0.0346)	0.0448 (0.0369)
wR_2[c]	0.0634 (0.0597)	0.0626 (0.0604)	0.0978 (0.0911)	0.0810 (0.0771)	0.0875 (0.0827)
Largest difference in peak and hole (e Å^{-3})	0.712 and -1.204	1.042 and -0.492	2.561 and -2.415	1.584 and -0.807	1.818 and -0.885

[a]$R_1 = \Sigma||F_o| - |F_c||/\Sigma|F_o|$. [b]Values in parentheses for reflections with $I > 2\sigma(I)$. [c]$wR_2 = \{\Sigma[w(F_o^2 - F_c^2)^2]/\Sigma[w(F_o^2)^2]\}^{½}$.

Table A1.5.- Crystallographic data for compounds **6-MeCN** to **10-MeCN**.

Structure	**6-MeCN**	**7-MeCN**	**8-MeCN**	**8_Y-MeCN**	**9-MeCN**	**10-MeCN**
Formula	$C_{27}H_{35}Br_2N_8O_{13}Gd$	$C_{27}H_{35}Br_2N_8O_{13}Tb$	$C_{27}H_{35}Br_2N_8O_{13}Dy$	$C_{27}H_{35}Br_2N_8O_{13}Dy_{0.1}Y_{0.9}$	$C_{27}H_{35}Br_2N_8O_{13}Er$	$C_{27}H_{35}Br_2N_8O_{13}Y$
M_r	996.70	998.37	1001.95	935.72	1006.71	928.36
Crystal system	*triclinic*	*triclinic*	*triclinic*	*triclinic*	*triclinic*	*triclinic*
Space group (no.)	*P*-1 (2)	*P*-1 (2)	*P*-1 (2)	*P*-1 (2)	*P*-1 (2)	*P*-1 (2)
a (Å)	9.885(5)	9.882(2)	9.8954(5)	9.8880(9)	9.893(5)	9.898(5)
b (Å)	10.785(5)	10.800(5)	10.7920(10)	10.8070(11)	10.814(5)	10.797(5)
c (Å)	17.518(5)	17.510(4)	17.4868(13)	17.4320(17)	17.417(5)	17.437(5)
α (°)	85.508(5)	85.590(6)	85.211(7)	85.416(4)	85.588(5)	85.384(5)
β (°)	78.630(5)	78.519(13)	78.323(5)	78.157(3)	77.976(5)	78.065(5)
γ (°)	78.726(5)	78.702(5)	78.565(6)	78.549(4)	78.667(5)	78.512(5)
V (Å^3)	1794.1(13)	1794.5(10)	1790.7(2)	1785.3(3)	1785.6(13)	1785.2(13)
Z	2	2	2	2	2	2
D_c (g cm^{-3})	1.845	1.848	1.858	1.741	1.872	1.727
μ(MoK$_\alpha$) (mm^{-1})[d]	4.148	4.270	14.418	3.990	4.661	3.945
T (K)	100(2)	100(2)	100(2)	100(2)	100(2)	100(2)
Observed reflections	8944 (5766)	7350 (5972)	7286 (6599)	5207 (4192)	7359 (6528)	8232 (6054)
R_{int}	0.1716	0.0688	0.0830	0.0491	0.0289	0.0380
Parameters	465	465	465	465	465	465
GOF	1.036	1.025	1.051	1.021	1.029	1.040
R_1[a,b]	0.1284 (0.0620)	0.0563 (0.0378)	0.0707 (0.0661)	0.0688 (0.0461)	0.0359 (0.0290)	0.0705 (0.0464)
wR_2[c]	0.0961 (0.0803)	0.0761 (0.0700)	0.1824 (0.1742)	0.1330 (0.1231)	0.0740 (0.0703)	0.1267 (0.1136)
Largest difference in peak and hole (e Å^{-3})	1.998 and -1.162	1.467 and -0.915	2.741 and -2.856	1.410 and -0.980	2.220 and -1.700	1.815 and -0.753

[a]$R_1 = \Sigma||F_o| - |F_c||/\Sigma|F_o|$. [b]Values in parentheses for reflections with $I > 2\sigma(I)$. [c]$wR_2 = \{\Sigma[w(F_o^2 - F_c^2)^2]/\Sigma[w(F_o^2)^2]\}^{½}$. [d] μ(CuK$_\alpha$) (mm^{-1}) in **8-MeCN**.

Table A1.6.- Bond lengths (Å) and angles (°) for compounds **1**, **3** and **5**.

Compound	**1**	**3**	**5**
Dy1-O1	2.401(5)	2.388(4)	2.4135(19)
Dy1-O2	2.234(5)	2.284(3)	2.2795(18)
Dy1-O3	2.310(5)	2.238(3)	2.2459(17)
Dy1-O4	2.410(5)	2.424(4)	2.4193(18)
Dy1-O1N	2.463(5)	2.406(4)	2.4610(19)
Dy1-O2N	2.518(5)	2.746(5)	2.5329(19)
Dy1-O4N	2.488(6)	2.436(4)	2.480(2)
Dy1-O5N	2.489(5)	2.499(4)	2.499(2)
Dy1-O7N/O1W	2.397(5)	2.368(4)	2.3994(19)
O2-Dy1-O3	75.21(18)	78.70(13)	79.40(6)
O2-Dy1-O1N	123.05(18)	71.54(13)	152.38(6)
O2-Dy1-O2N	72.54(18)	109.47(13)	138.77(6)
O2-Dy1-O4N	148.71(18)	126.48(12)	97.00(7)
O2-Dy1-O5N	151.93(19)	76.62(12)	78.83(6)
O2-Dy1-O7N/O1W	83.27(19)	128.05(14)	69.87(7)
O3-Dy1-O1N	140.63(18)	80.68(14)	124.08(6)
O3-Dy1-O2N	124.26(18)	116.37(13)	75.49(6)
O3-Dy1-O4N	116.42(18)	153.66(12)	153.42(7)
O3-Dy1-O5N	76.77(18)	154.44(12)	149.35(7)
O3-Dy1-O7N/O1W	70.04(18)	81.46(15)	73.99(7)

Table A1.7.- Bond lengths (Å) and angles (°) for compounds **4** and **6**.

Compound	**4**	**6**
Er1-O1	2.365(6)	2.394(4)
Er1-O2	2.257(5)	2.264(4)
Er1-O3	2.223(5)	2.230(4)
Er1-O4	2.385(5)	2.394(4)
Er1-O1N	2.404(5)	2.438(4)
Er1-O2N	2.489(5)	2.517(4)
Er1-O4N	2.344(6)	2.460(4)
Er1-O5N	-	2.488(4)
Er1-O7N/O1W	2.334(6)	2.377(4)
O2-Er1-O3	78.55(17)	80.08(14)
O2-Er1-O1N	128.43(17)	151.39(14)
O2-Er1-O2N	77.17(17)	139.14(14)
O2-Er1-O4N	72.21(18)	95.80(15)
O2-Er1-O5N	-	78.21(14)
O2-Er1-O7N/O1W	129.6(2)	70.55(14)
O3-Er1-O1N	152.93(18)	124.54(13)
O3-Er1-O2N	153.96(17)	75.38(13)
O3-Er1-O4N	83.4(2)	152.88(14)
O3-Er1-O5N	-	149.34(14)
O3-Er1-O7N/O1W	82.4(2)	75.07(14)

Table A1.8.- Bond lengths (Å) for compounds **1-MeCN** to **10-MeCN**.

Compound	**1-MeCN**	**2-MeCN**	**3-MeCN**
Ln1-O1	2.5241(18)	2.5056(18)	2.490(3)
Ln1-O2	2.4074(17)	2.3959(17)	2.387(3)
Ln1-O3	2.3883(17)	2.3656(17)	2.358(3)
Ln1-O4	2.5440(18)	2.5250(18)	2.508(3)
Ln1-O1N	2.5902(19)	2.5827(18)	2.562(3)
Ln1-O2N	2.715(2)	2.6820(18)	2.685(3)
Ln1-O4N	2.6972(18)	2.5842(17)	2.571(3)
Ln1-O5N	2.6066(18)	2.6794(18)	2.659(3)
Ln1-O7N	2.6257(19)	2.6009(18)	2.588(3)
Ln1-O8N	2.6668(19)	2.6630(19)	2.642(3)

Compound	**4-MeCN**	**5-MeCN**	**6-MeCN**
Ln1-O1	2.450(3)	2.435(3)	2.426(4)
Ln1-O2	2.347(2)	2.317(3)	2.311(4)
Ln1-O3	2.319(3)	2.295(3)	2.282(4)
Ln1-O4	2.470(3)	2.445(3)	2.430(4)
Ln1-O1N	2.486(3)	2.481(3)	2.461(5)
Ln1-O2N	2.737(5)[a]	2.606(3)	2.591(4)
Ln1-O4N	2.611(3)	2.527(3)	2.511(4)
Ln1-O5N	2.551(3)	2.576(3)	2.557(4)
Ln1-O7N	2.519(3)	2.418(3)	2.401(4)
Ln1-O8N	2.631(3)	2.92(3)[b]	-

Compound	**7-MeCN**	**8-MeCN**	**8_Y-MeCN**
Ln1-O1	2.418(3)	2.398(5)	2.392(4)
Ln1-O2	2.264(3)	2.247(5)	2.277(4)
Ln1-O3	2.297(3)	2.282(4)	2.236(4)
Ln1-O4	2.420(4)	2.406(5)	2.382(4)
Ln1-O1N	2.460(4)	2.434(5)	2.439(5)
Ln1-O2N	2.576(3)	2.563(5)	2.548(5)
Ln1-O4N	2.502(3)	2.496(5)	2.479(5)
Ln1-O5N	2.545(4)	2.533(5)	2.513(5)
Ln1-O7N	2.391(3)	2.390(5)	2.367(4)
Ln1-O8N	-	-	-

Compound	**9-MeCN**	**10-MeCN**
Ln1-O1	2.372(3)	2.376(3)
Ln1-O2	2.232(3)	2.241(3)
Ln1-O3	2.267(3)	2.277(3)
Ln1-O4	2.389(3)	2.386(3)
Ln1-O1N	2.428(3)	2.436(3)
Ln1-O2N	2.534(3)	2.546(3)
Ln1-O4N	2.468(3)	2.514(3)
Ln1-O5N	2.499(3)	2.477(3)
Ln1-O7N	2.360(3)	2.360(3)
Ln1-O8N	-	-

[a]O2N belongs to a disordered nitrate molecule, half of the nitrate acts as a chelate, whereas the other half is monocoordinated; [b]O8N belongs to a disordered nitrate molecule, 15% acts as a chelate, whereas the 85% is monocoordinated.

2. Continuous Shape Measurements.

The nearer the value to zero, the better fits to an ideal polyhedron.

Table A1.9.- Continuous Shape Measurements for the LnO_9 coordination environment in compounds **1-3** and **5-6**.

EP-9	1 D9h	Enneagon
OPY-9	2 C8v	Octagonal pyramid
HBPY-9	3 D7h	Heptagonal bipyramid
JTC-9	4 C3v	Johnson triangular cupola J3
JCCU-9	5 C4v	Capped cube J8
CCU-9	6 C4v	Spherical-relaxed capped cube
JCSAPR-9	7 C4v	Capped square antiprism J10
CSAPR-9	8 C4v	Spherical capped square antiprism
JTCTPR-9	9 D3h	Tricapped trigonal prism J51
TCTPR-9	10 D3h	Spherical tricapped trigonal prism
JTDIC-9	11 C3v	Tridiminished icosahedron J63
HH-9	12 C2v	Hula-hoop
MFF-9	13 Cs	Muffin

Structure [ML9]	EP-9	OPY-9	HBPY-9	JTC-9	JCCU-9	CCU-9	JCSAPR-9
Dy1 (1)	35.432	21.595	17.496	15.645	10.138	8.593	2.921
Dy1 (3)	36.698	20.793	18.750	16.267	9.513	7.531	2.793
Dy1 (5)	35.892	21.404	17.360	14.615	9.463	7.757	3.399
Er1 (6)	36.216	21.513	17.244	14.494	9.550	7.979	3.253

Structure [ML9]	CSAPR-9	JTCTPR-9	TCTPR-9	JTDIC-9	HH-9	MFF-9
Dy1 (1)	1.874	3.097	**1.637**	11.850	10.661	1.639
Dy1 (3)	2.638	3.608	**2.008**	12.833	8.201	2.415
Dy1 (5)	2.315	4.330	2.889	11.975	10.193	**1.572**
Er1 (6)	2.166	4.091	2.738	12.014	10.437	**1.444**

Table A1.10.- Continuous Shape Measurements for the LnO_8 coordination environment in compound **4**.

OP-8	1 D8h	Octagon
HPY-8	2 C7v	Heptagonal pyramid
HBPY-8	3 D6h	Hexagonal bipyramid
CU-8	4 Oh	Cube
SAPR-8	5 D4d	Square antiprism
TDD-8	6 D2d	Triangular dodecahedron
JGBF-8	7 D2d	Johnson gyrobifastigium J26
JETBPY-8	8 D3h	Johnson elongated triangular bipyramid J14
JBTPR-8	9 C2v	Biaugmented trigonal prism J50
BTPR-8	10 C2v	Biaugmented trigonal prism
JSD-8	11 D2d	Snub diphenoid J84
TT-8	12 Td	Triakis tetrahedron
ETBPY-8	13 D3h	Elongated trigonal bipyramid

Structure [ML8]	OP-8	HPY-8	HBPY-8	CU-8	SAPR-8	TDD-8	JGBF-8
Er1 (4)	29.261	23.545	16.764	11.043	1.975	**1.685**	14.454

Structure [ML8]	JETBPY-8	JBTPR-8	BTPR-8	JSD-8	TT-8	ETBPY-8
Er1 (4)	27.062	3.248	2.400	3.976	11.675	21.830

3. Additional Structural Figures.

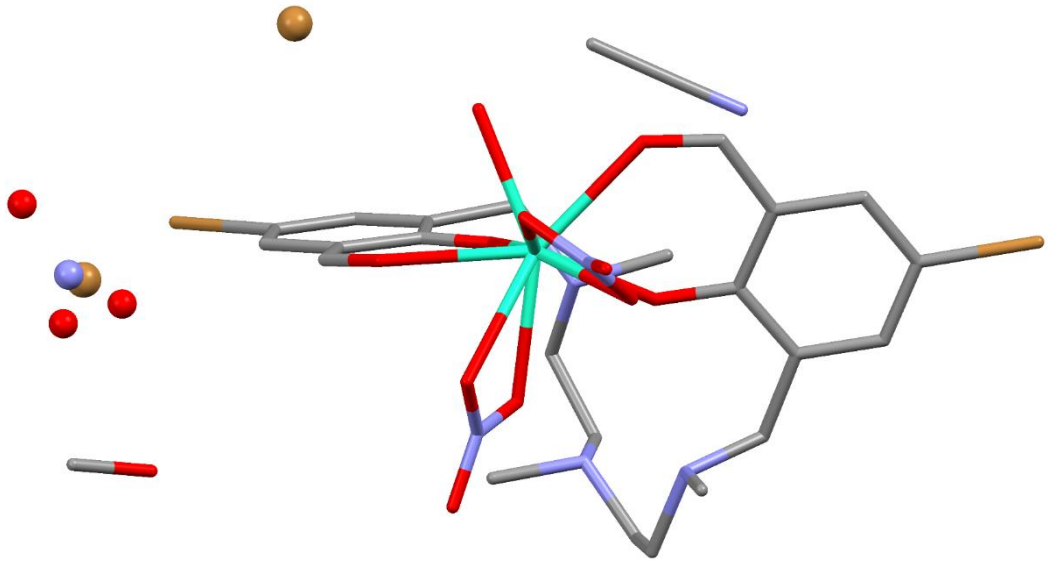

Figure A1.1.- Structural view of the asymmetric unit of **3**. Counterions are displayed as balls. Note these singular occupations: 50% for MeOH, 50% for Br^- and 25% for each *xyz* sharing Br^- and NO_3. Hydrogen atoms have been omitted for the sake of clarity.

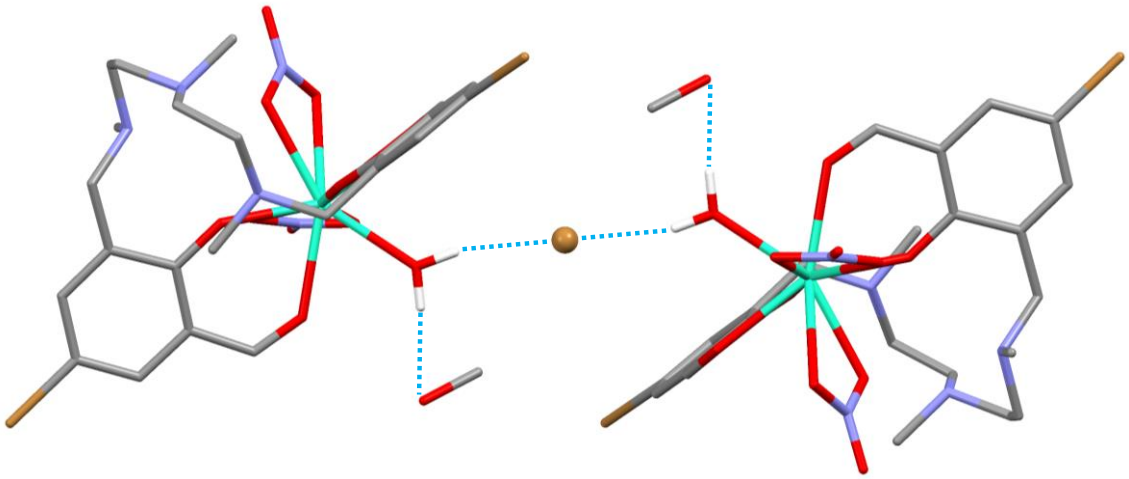

Figure A1.2.- Intermolecular hydrogen bonding pattern for **3**. Hydrogen atoms are shown for coordinated water molecules. The rest of counterions and acetonitrile molecules have been omitted for the sake of clarity.

4. Experimental XRPD.

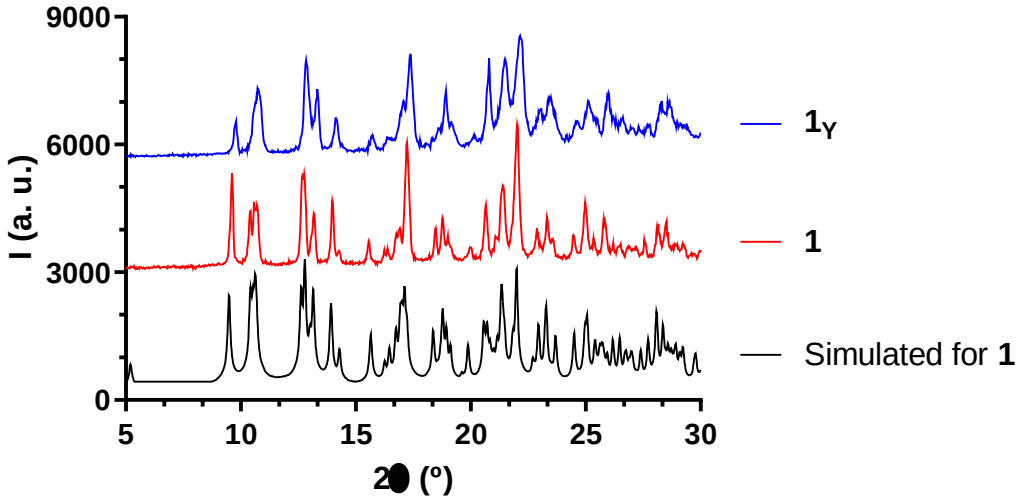

Figure A1.3.- For compounds **1** and $\mathbf{1_Y}$, simulated pattern from single-crystal X-ray diffraction of **1** (black line) and experimental XRPD for **1** (red) and $\mathbf{1_Y}$ (blue).

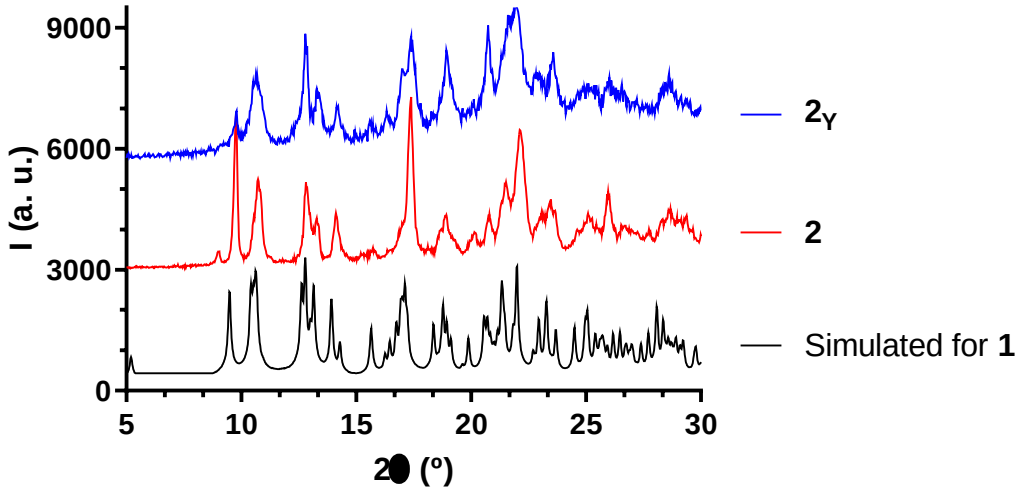

Figure A1.4.- For compounds **2** and $\mathbf{2_Y}$, simulated pattern from single-crystal X-ray diffraction of **1** (black line) and experimental XRPD for **2** (red) and $\mathbf{2_Y}$ (blue).

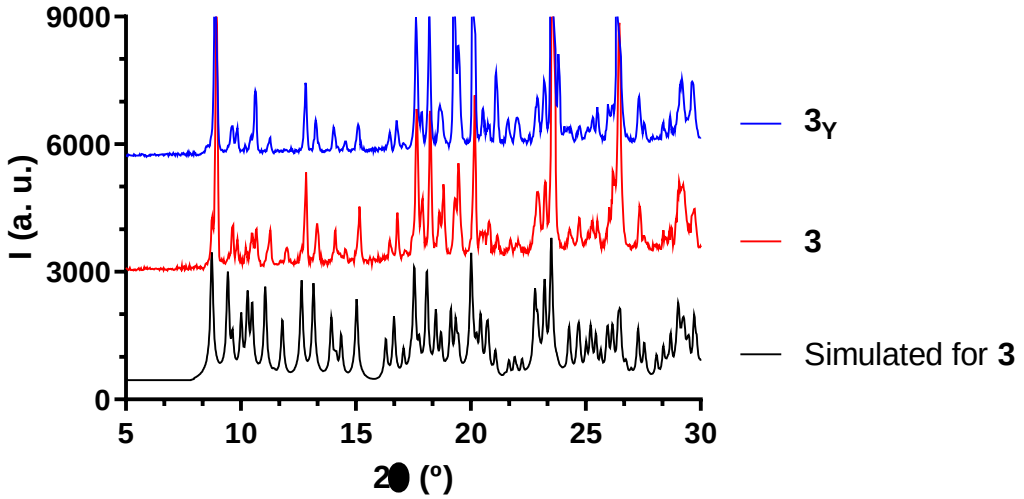

Figure A1.5.- For compounds **3** and $\mathbf{3_Y}$, simulated pattern from single-crystal X-ray diffraction of **3** (black line) and experimental XRPD for **3** (red) and $\mathbf{3_Y}$ (blue).

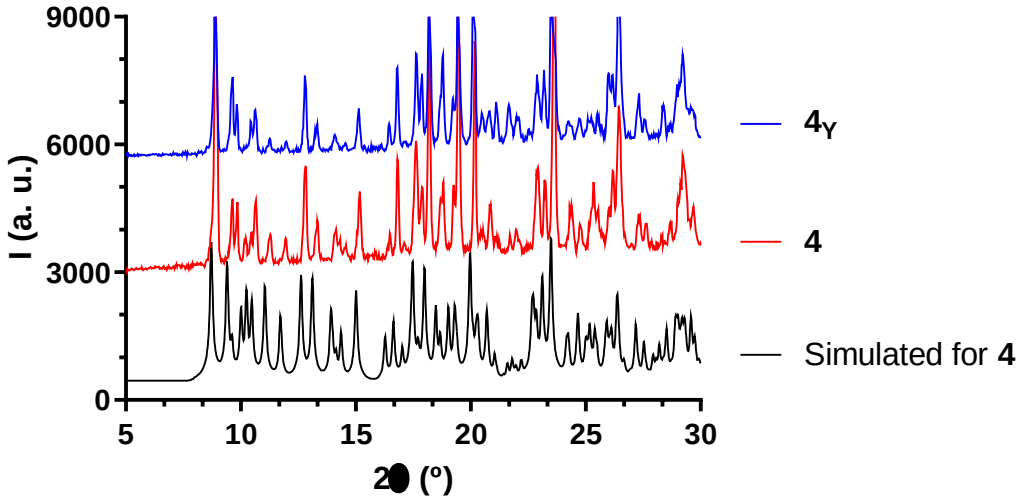

Figure A1.6.- For compounds **4** and $\mathbf{4_Y}$, simulated pattern from single-crystal X-ray diffraction of **4** (black line) and experimental XRPD for **4** (red) and $\mathbf{4_Y}$ (blue).

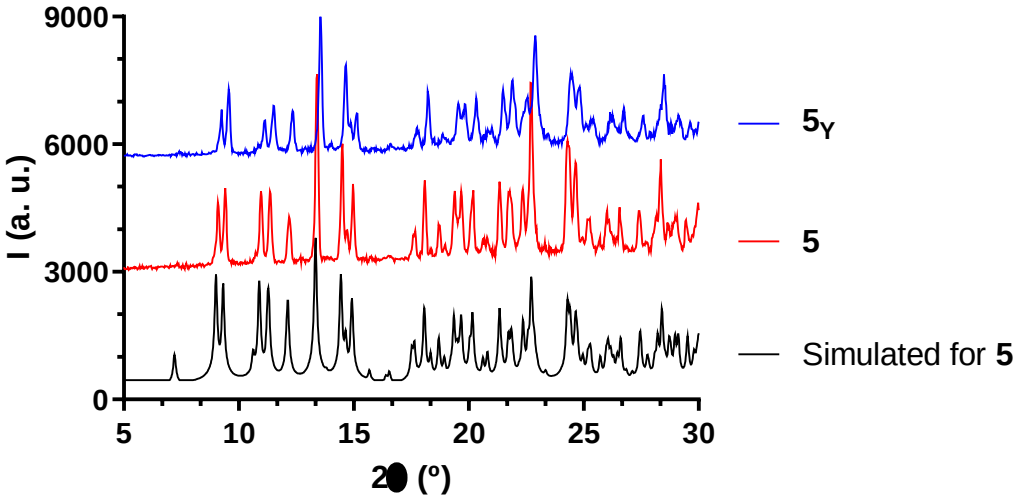

Figure A1.7.- For compounds **5** and **5**$_Y$, simulated pattern from single-crystal X-ray diffraction of **5** (black line) and experimental XRPD for **5** (red) and **5**$_Y$ (blue).

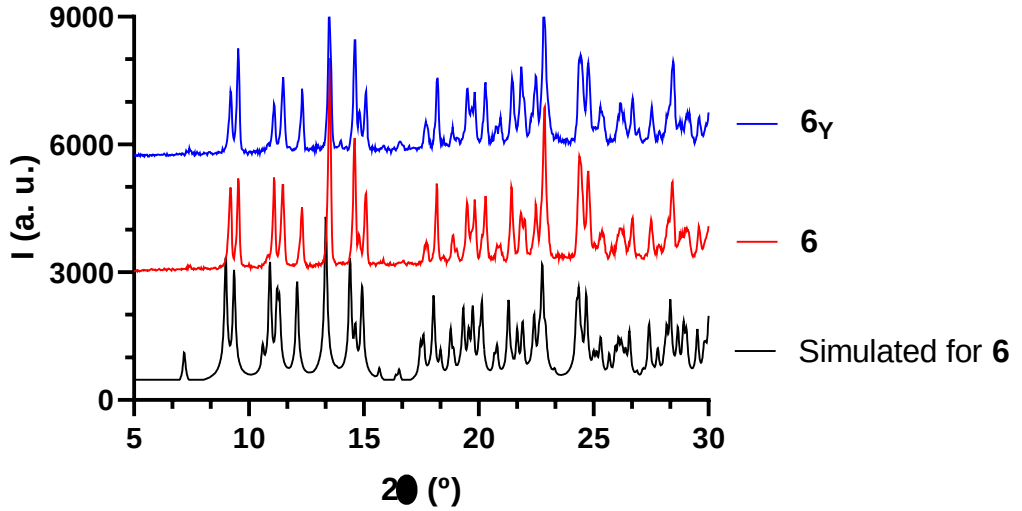

Figure A1.8.- For compounds **6** and **6**$_Y$, simulated pattern from single-crystal X-ray diffraction of **5** (black line) and experimental XRPD for **6** (red) and **6**$_Y$ (blue).

5. Magnetic Measurements.

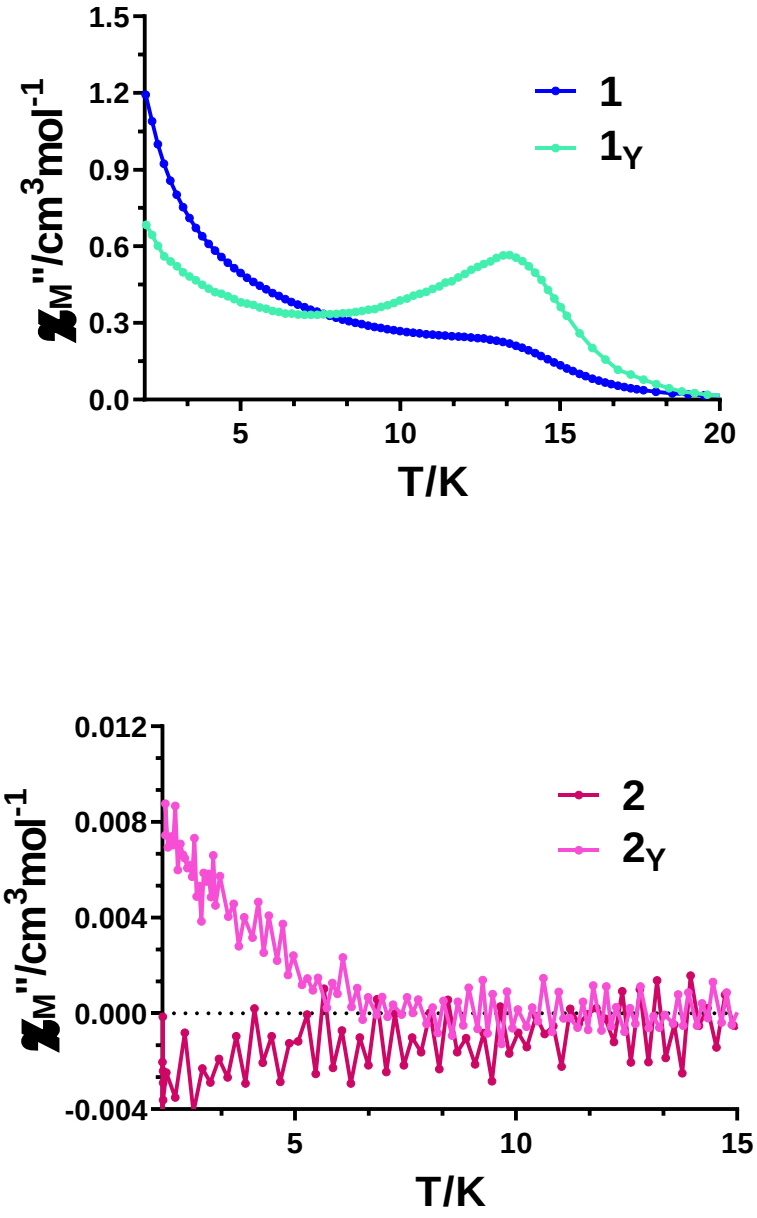

Figure A1.9.- Temperature dependence of the out-of phase χ_M" susceptibility signals at a frequency of 10000 Hz for complexes **1** and **1**$_Y$ (top) and **2** and **2**$_Y$ (bottom) under zero applied *dc* field. χ_M" values were arbitrarily multiplied for diluted analogues in order to provide a comparative illustration.

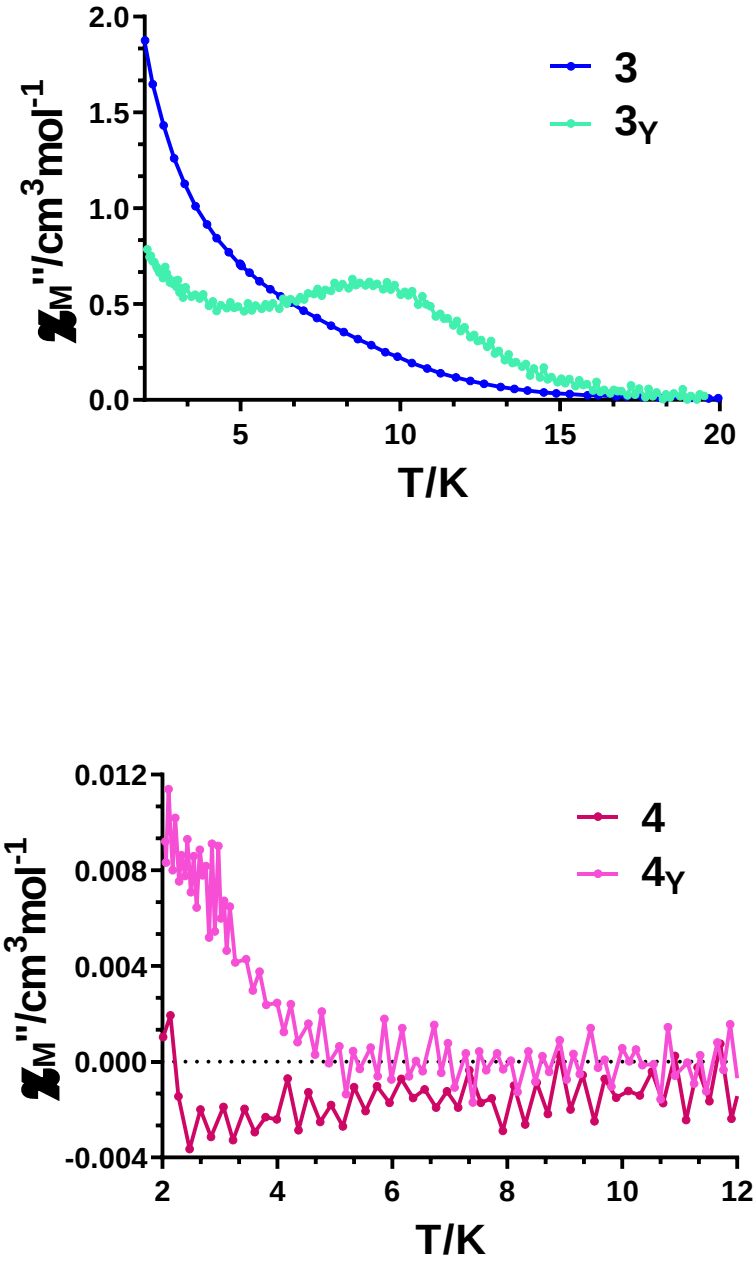

Figure A1.10.- Temperature dependence of the out-of phase χ_M'' susceptibility signals at a frequency of 10000 Hz for complexes **3** and **3$_Y$** (top) and **4** and **4$_Y$** (bottom) under zero applied *dc* field. χ_M'' values were arbitrarily multiplied for diluted analogues in order to provide a comparative illustration.

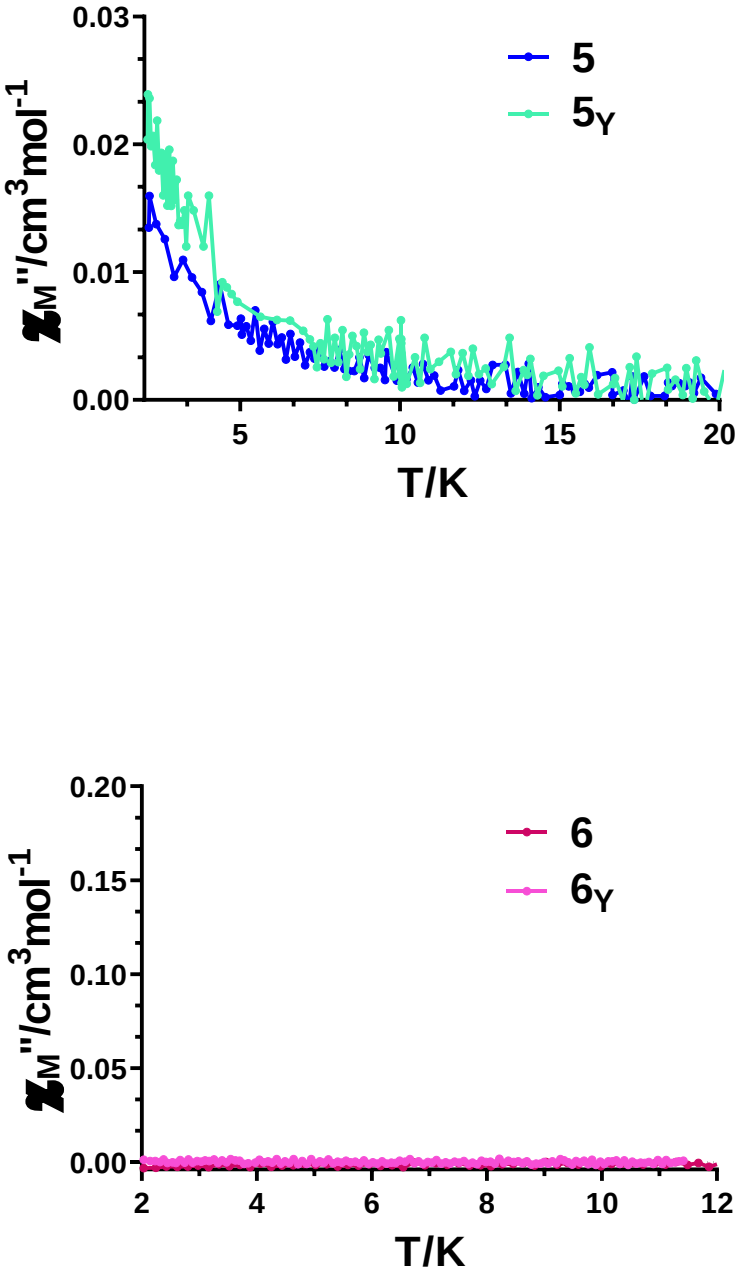

Figure A1.11.- Temperature dependence of the out-of phase χ_M'' susceptibility signals at a frequency of 10000 Hz for complexes **5** and **5$_Y$** (top) and **6** and **6$_Y$** (bottom) under zero applied *dc* field. χ_M'' values were arbitrarily multiplied for diluted analogues in order to provide a comparative illustration.

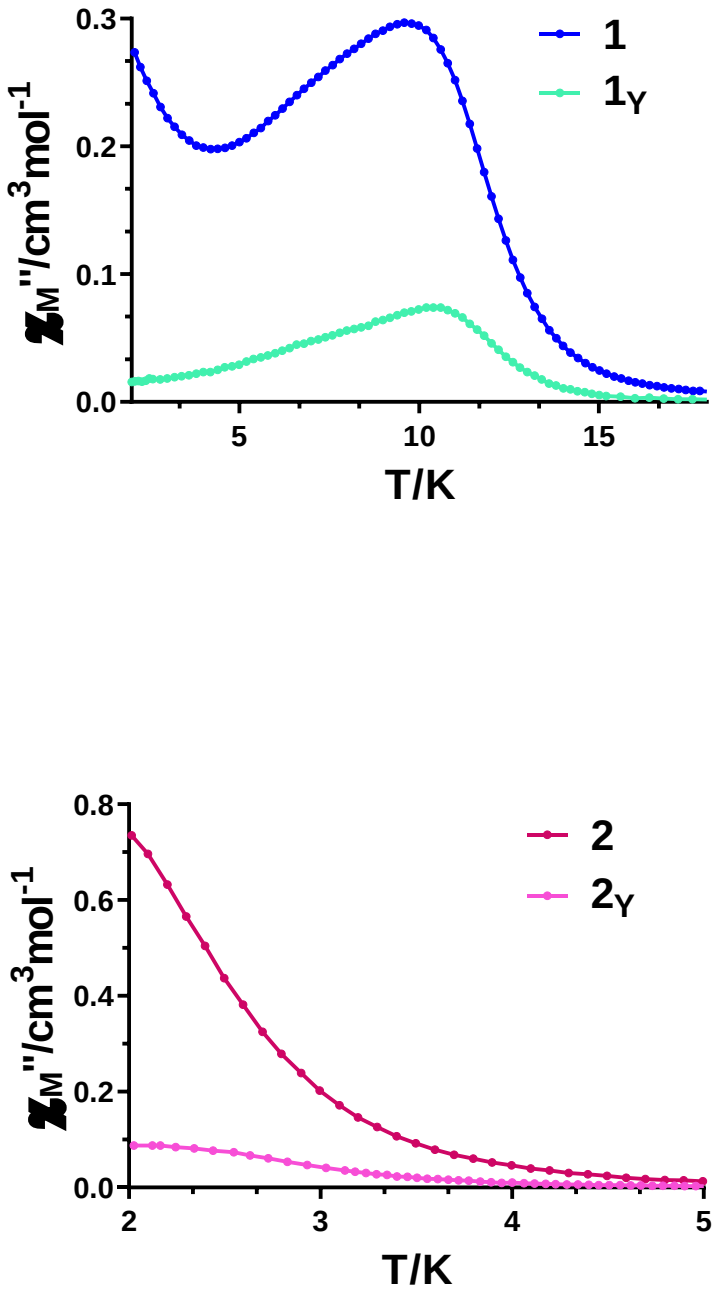

Figure A1.12.- Temperature dependence of the out-of phase χ_M'' susceptibility signals at a frequency of 500 Hz for complexes **1** and **1**$_Y$ (top) and **2** and **2**$_Y$ (bottom) under an external magnetic field of 1 kOe. χ_M'' values were arbitrarily multiplied for diluted analogues in order to provide a comparative illustration.

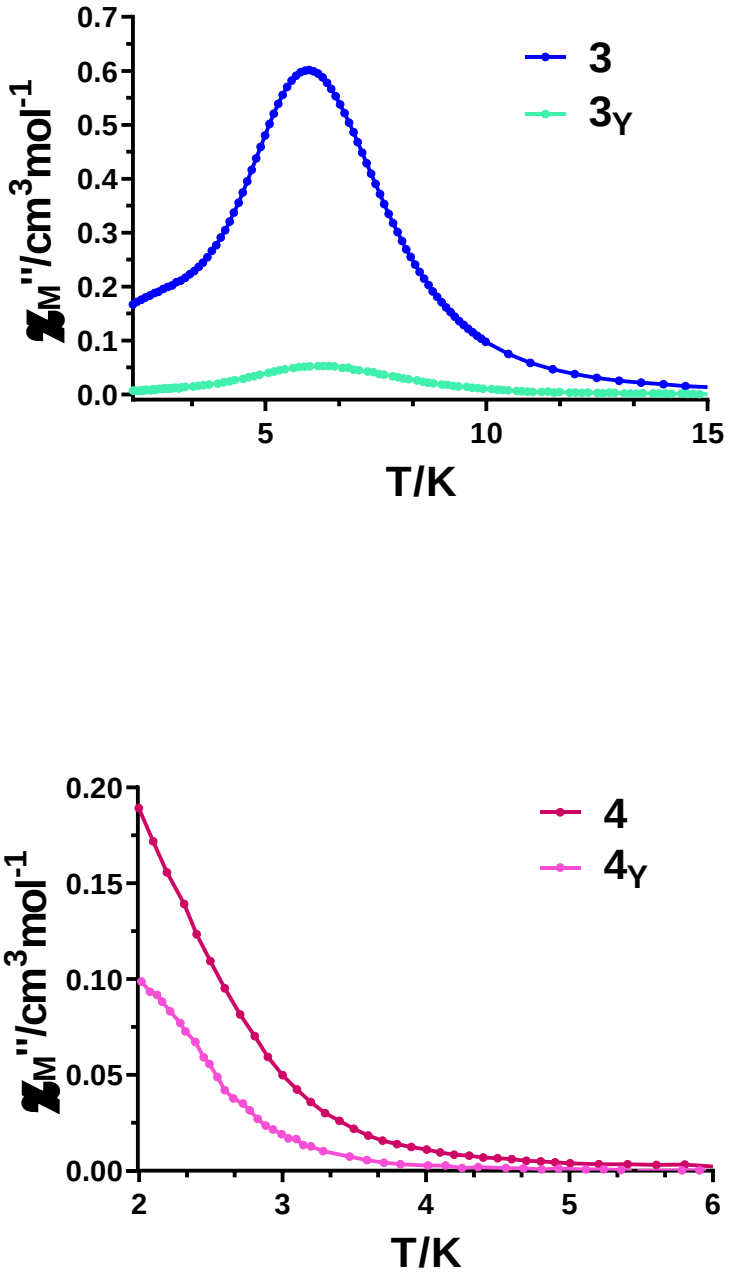

Figure A1.13.- Temperature dependence of the out-of phase χ_M'' susceptibility signals at a frequency of 500 Hz for complexes **3** and **3$_Y$** (top) and **4** and **4$_Y$** (bottom) under an external magnetic field of 1 kOe. χ_M'' values were arbitrarily multiplied for diluted analogues in order to provide a comparative illustration.

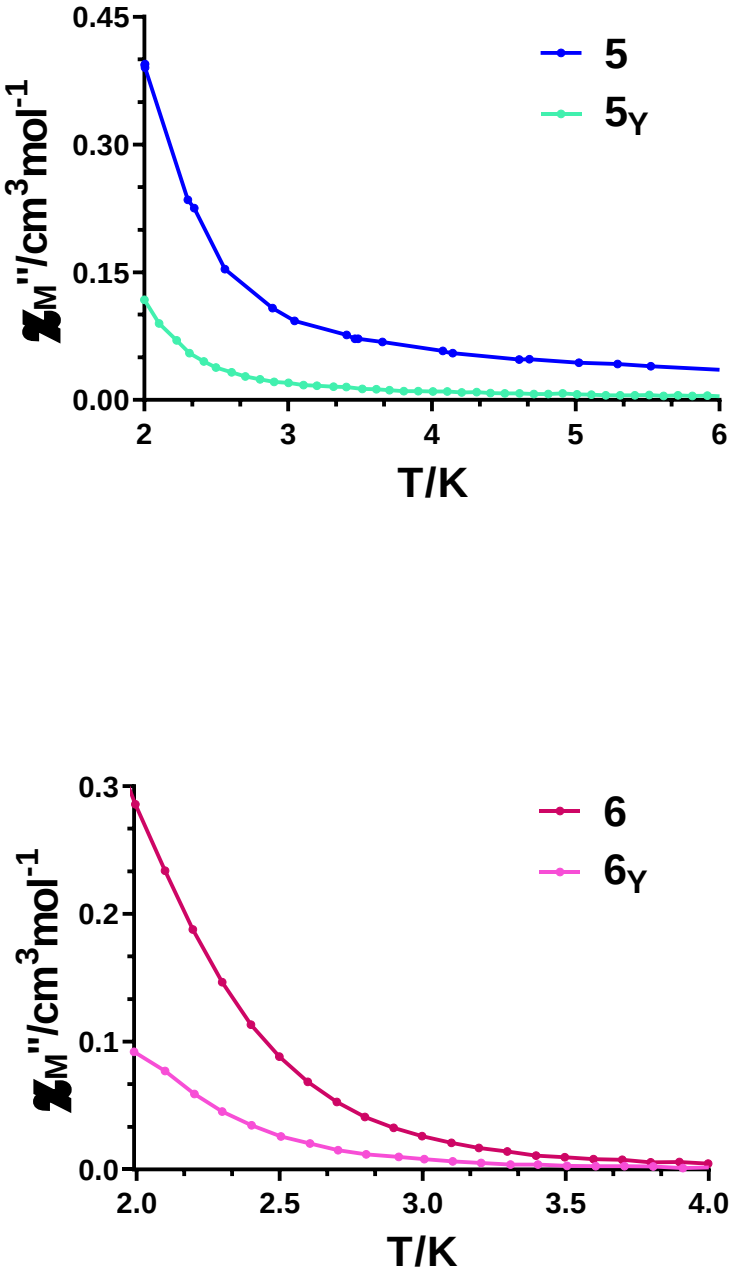

Figure A1.14.- Temperature dependence of the out-of phase χ_M'' susceptibility signals at a frequency of 1000 Hz for complexes **5** and **5$_Y$** (top) and at a frequency of 500 Hz for **6** and **6$_Y$** (bottom) under an external magnetic field of 1 kOe. χ_M'' values were arbitrarily multiplied for diluted analogues in order to provide a comparative illustration.

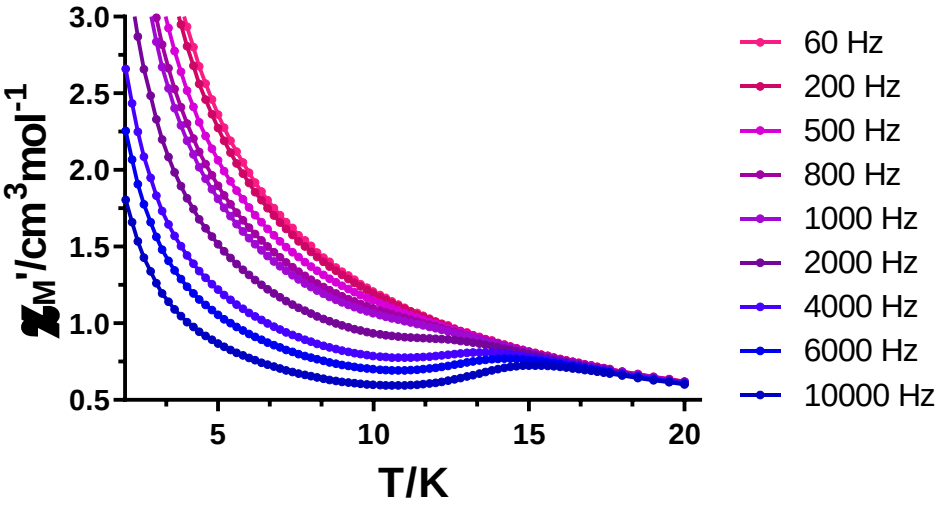

Figure A1.15.- Temperature dependence of the in phase χ_M' susceptibility signals for complex **1** under zero applied *dc* field.

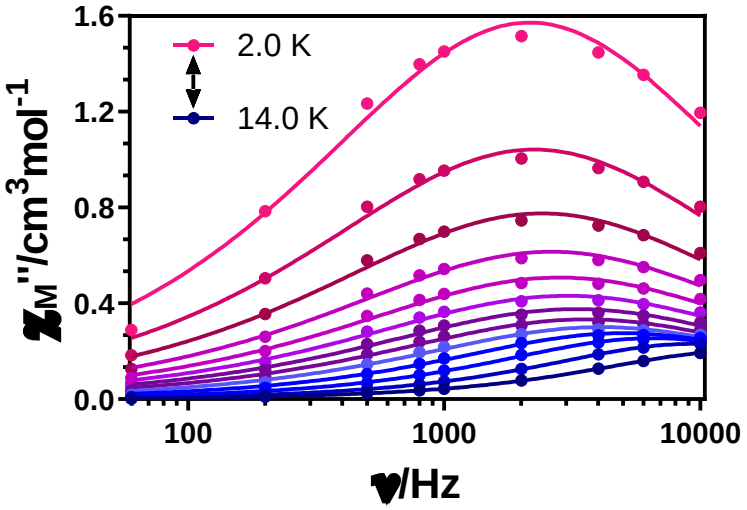

Figure A1.16.- Variable-temperature frequency dependence of the χ_M'' signal under zero applied *dc* field for **1**. Solid lines represent the best fitting of the experimental data to the Debye model.

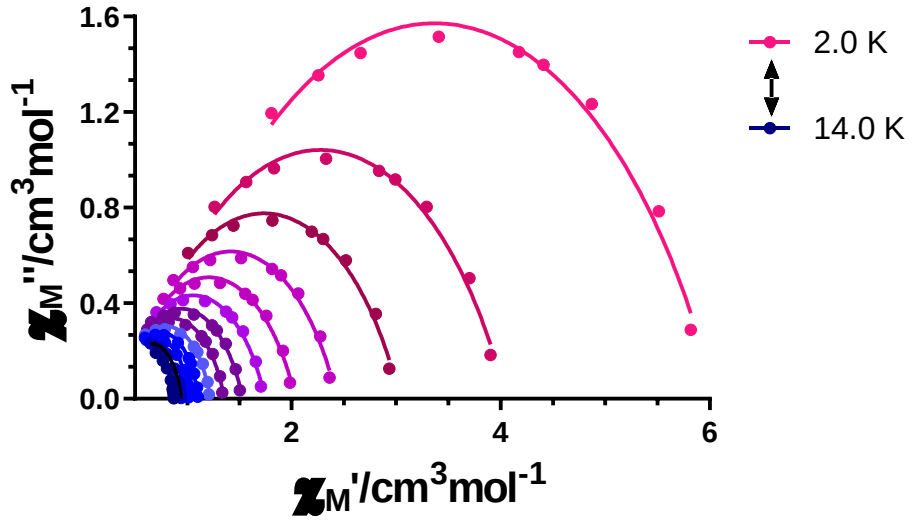

Figure A1.17.- Cole-Cole plots under zero *dc* field for **1**. Solid lines represent the best fits to the generalized Debye model.

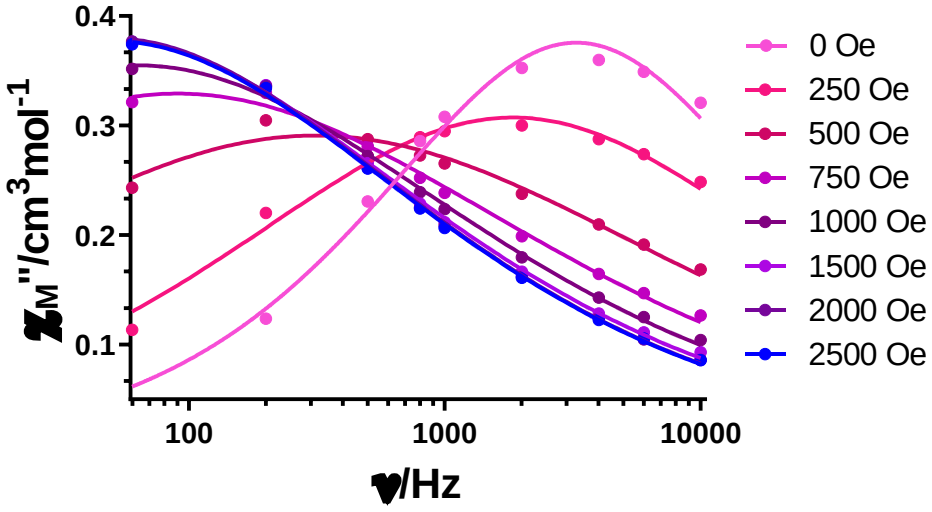

Figure A1.18- Field dependence of the out-of-phase signal *vs* frequency at 8.0 K for **1**.

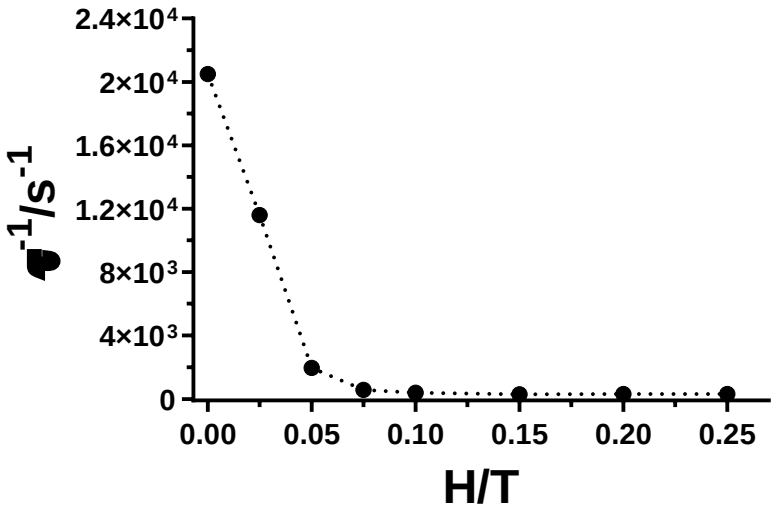

Figure A1.19.- The inverse of the relaxation times obtained at different magnetic fields at 8.0 K for **1**. The dashed lines are a guide to the eye.

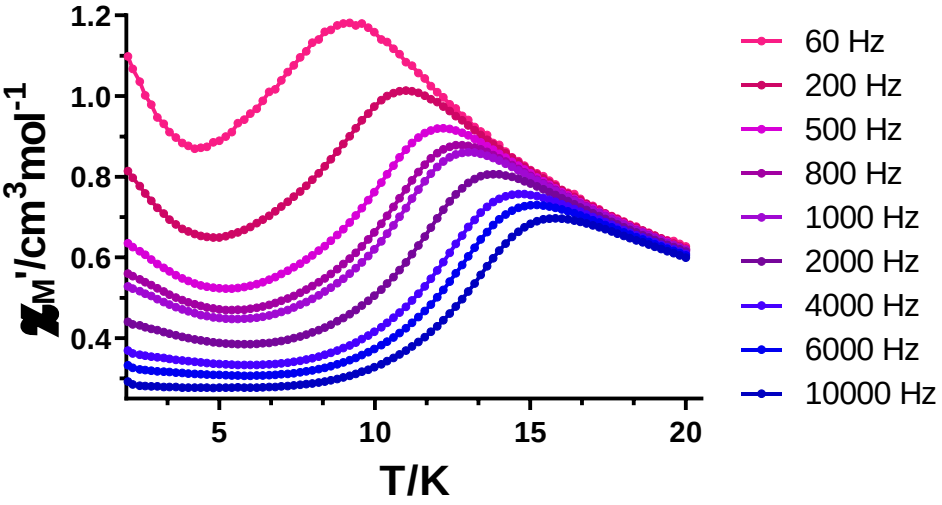

Figure A1.20.- Temperature dependence of the in phase χ_M' susceptibility signals for complex **1** under an applied field of 1000 Oe.

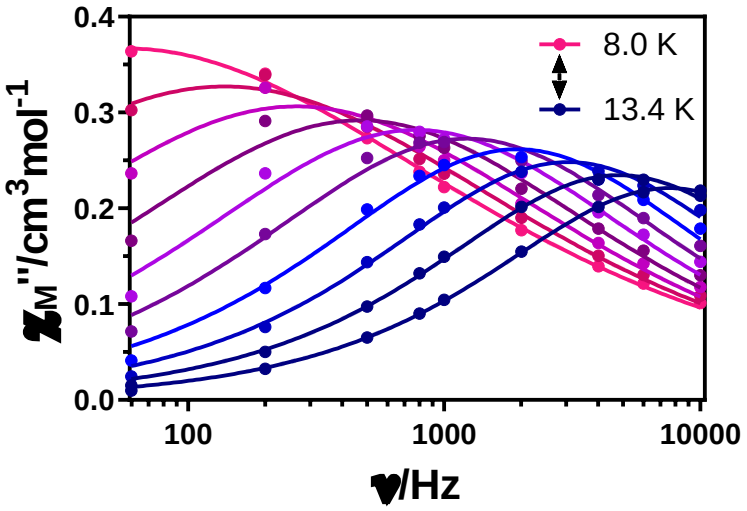

Figure A1.21.- Variable-temperature frequency dependence of the χ_M'' signal under 1000 Oe applied field for **1**. Solid lines represent the best fitting of the experimental data to the Debye model.

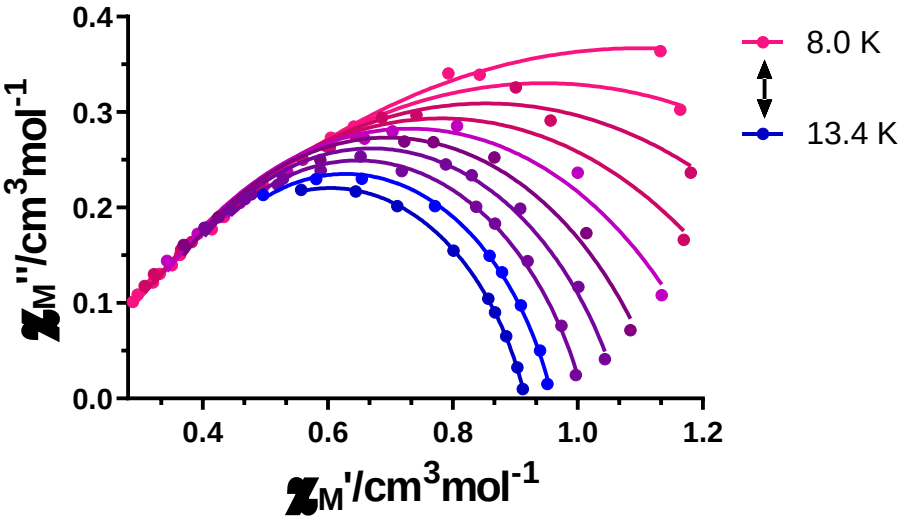

Figure A1.22.- Cole-Cole plots under 1000 Oe field for **1**. Solid lines represent the best fits to the generalized Debye model.

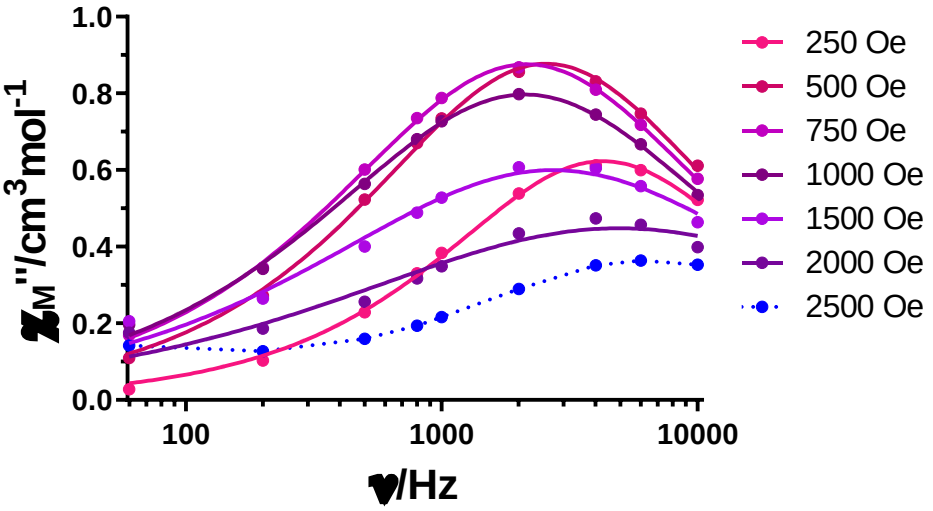

Figure A1.23.- Field dependence of the out-of-phase signal *vs* frequency at 2.0 K for **2**. The dashed line at 2500 Oe is a guide to the eye.

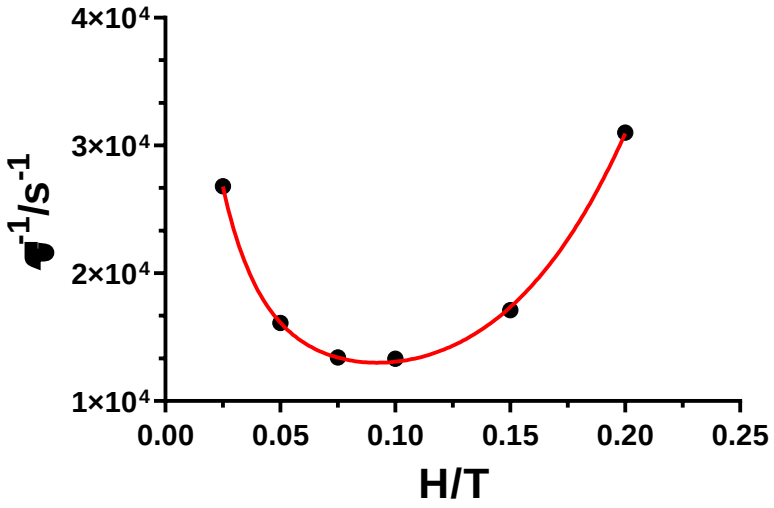

Figure A1.24.- The inverse of the relaxation times obtained at different magnetic fields at 2.0 K for **2**. The red line represents the best fit to the Equation 1.2 in the main text.

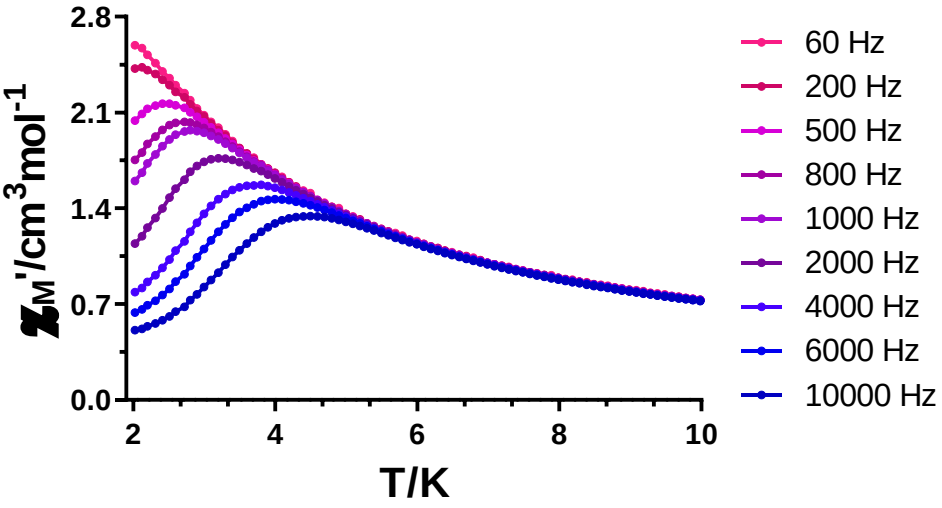

Figure A1.25.- Temperature dependence of the in phase χ_M' susceptibility signals for complex **2** under an applied field of 1000 Oe.

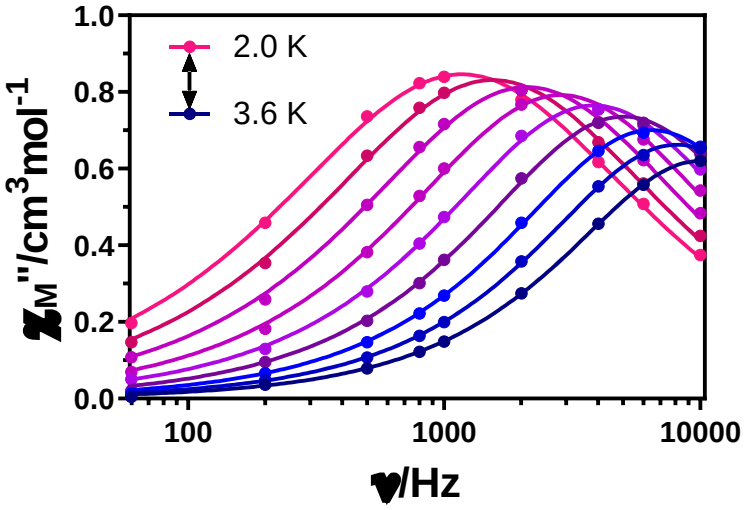

Figure A1.26.- Variable-temperature frequency dependence of the χ_M'' signal under 1000 Oe applied field for **2**. Solid lines represent the best fitting of the experimental data to the Debye model.

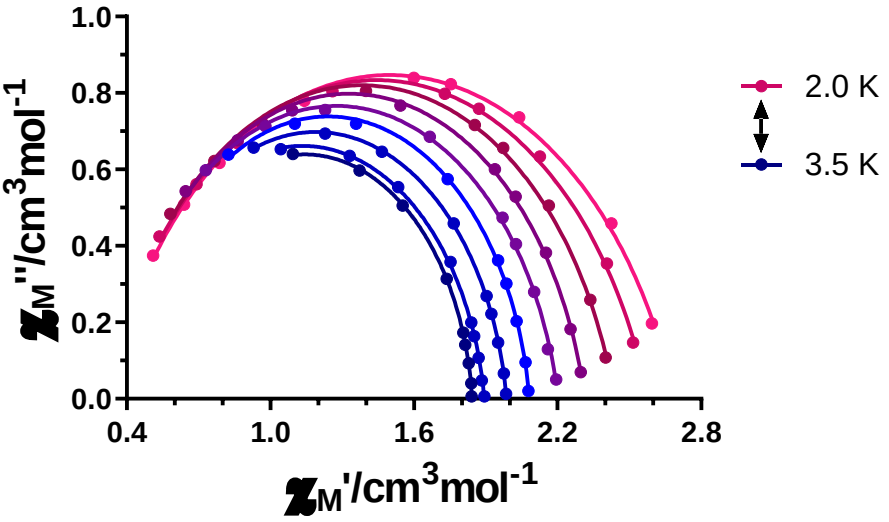

Figure A1.27.- Cole-Cole plots under 1000 Oe field for **2**. Solid lines represent the best fits to the generalized Debye model.

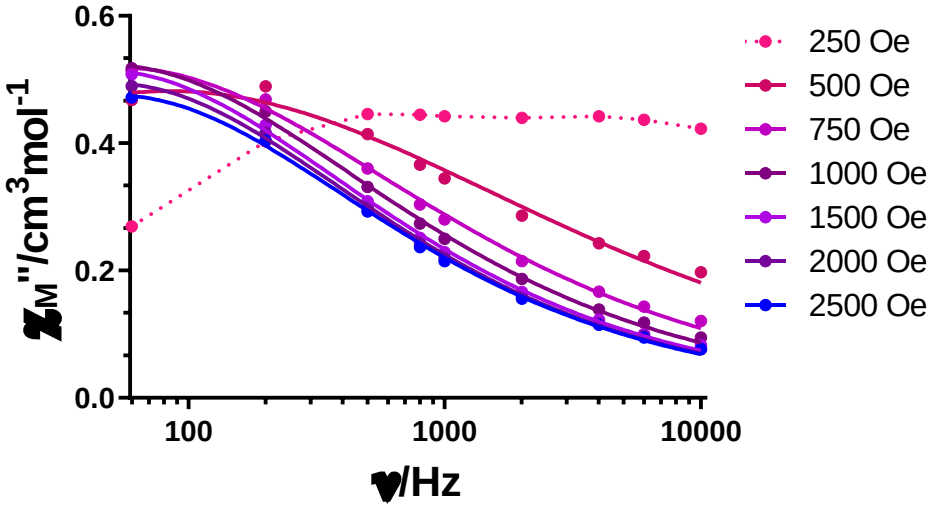

Figure A1.28.- Field dependence of the out-of-phase signal *vs* frequency at 5.0 K for **3**. The dashed line at 250 Oe is a guide to the eye.

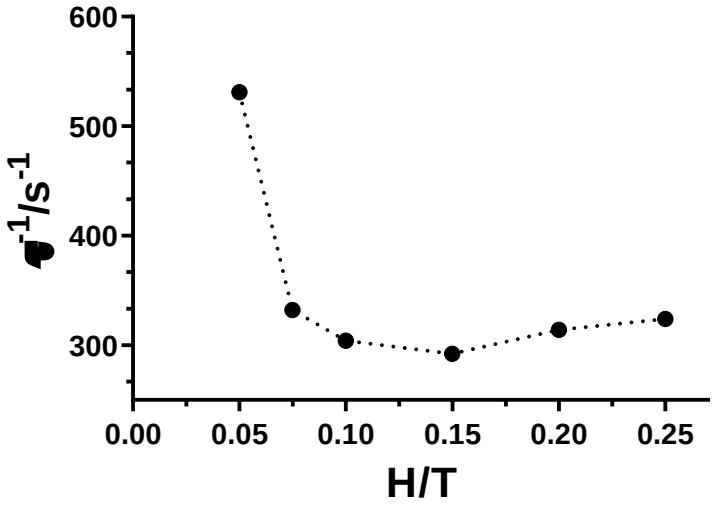

Figure A1.29.- The inverse of the relaxation times obtained at different magnetic fields at 5.0 K for **3**. The dashed line is a guide to the eye.

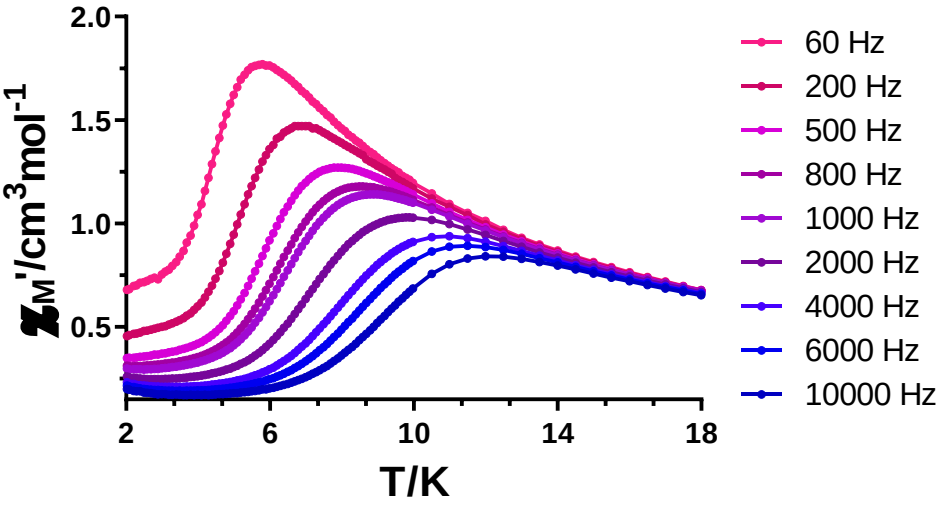

Figure A1.30.- Temperature dependence of the in phase χ_M' susceptibility signals for complex **3** under an applied field of 1500 Oe.

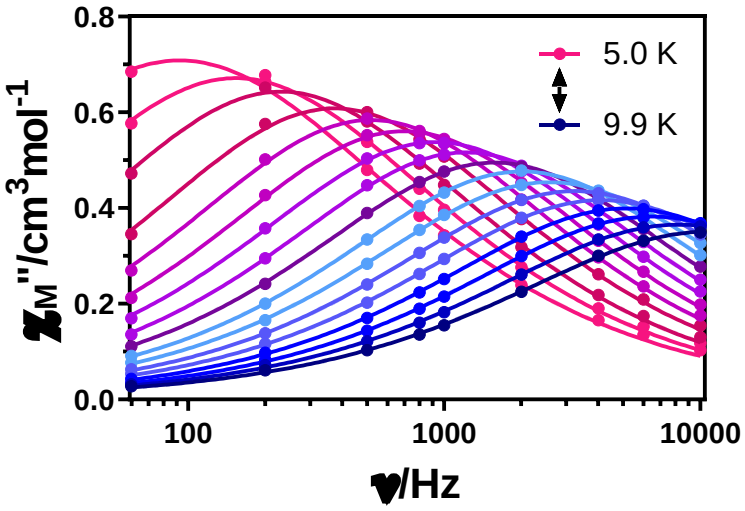

Figure A1.31.- Variable-temperature frequency dependence of the χ_M'' signal under 1500 Oe applied field for **3**. Solid lines represent the best fitting of the experimental data to the Debye model.

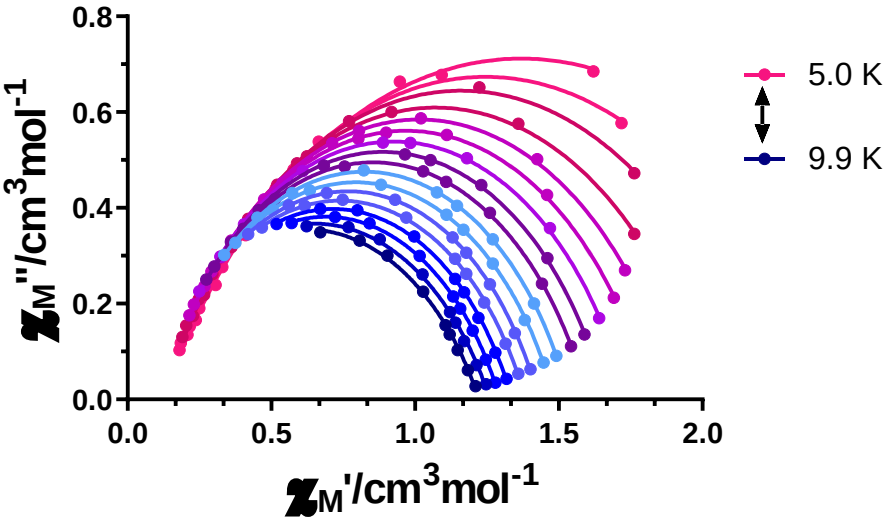

Figure A1.32.- Cole-Cole plots under 1500 Oe field for **3**. Solid lines represent the best fits to the generalized Debye model.

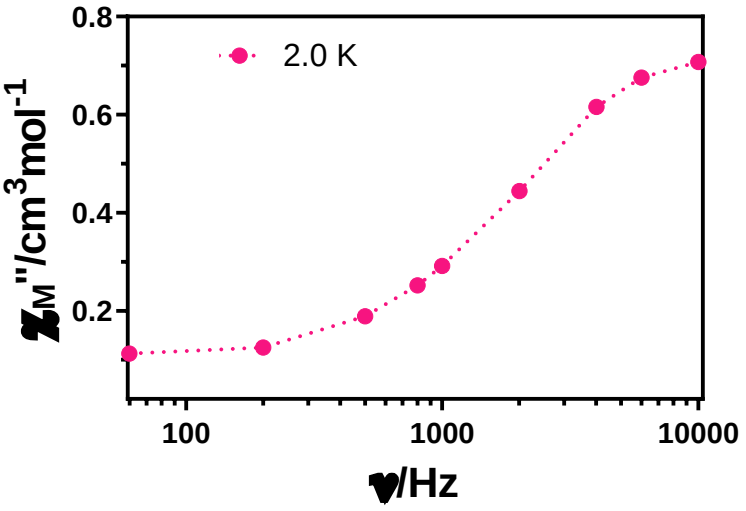

Figure A1.33.- Frequency dependence of the χ_M'' signal under 1000 Oe applied field for **4**. The dashed line is a guide to the eye.

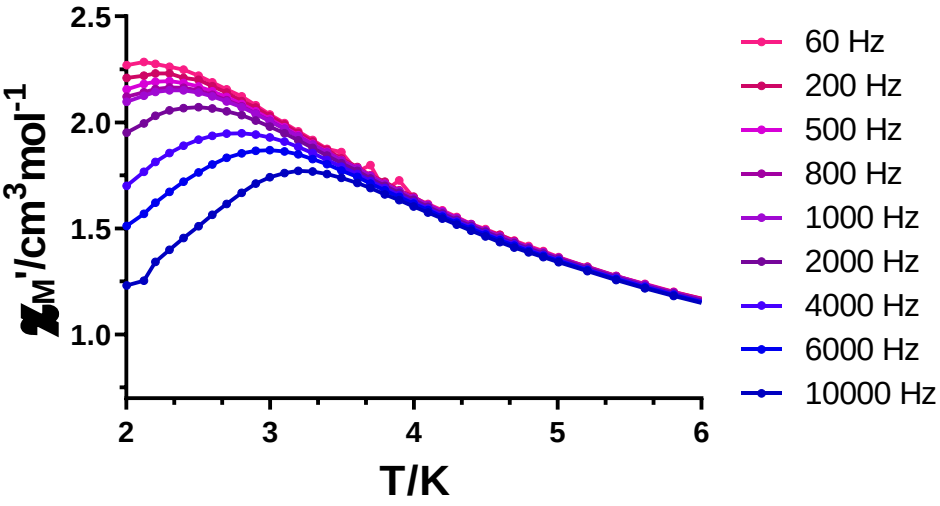

Figure A1.34.- Temperature dependence of the in phase χ_M' susceptibility signals for complex **4** under an applied field of 1000 Oe.

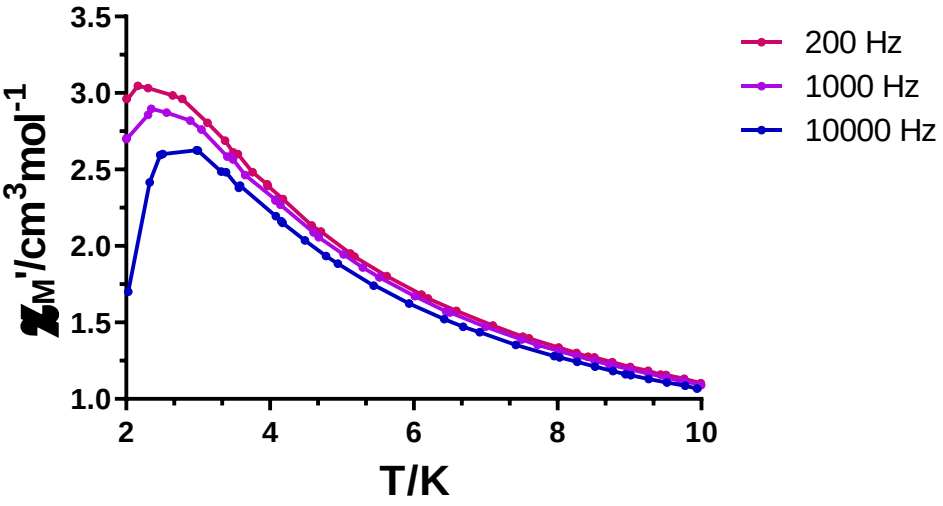

Figure A1.35.- Temperature dependence of the in phase χ_M' susceptibility signals for complex **5** under an applied field of 1000 Oe.

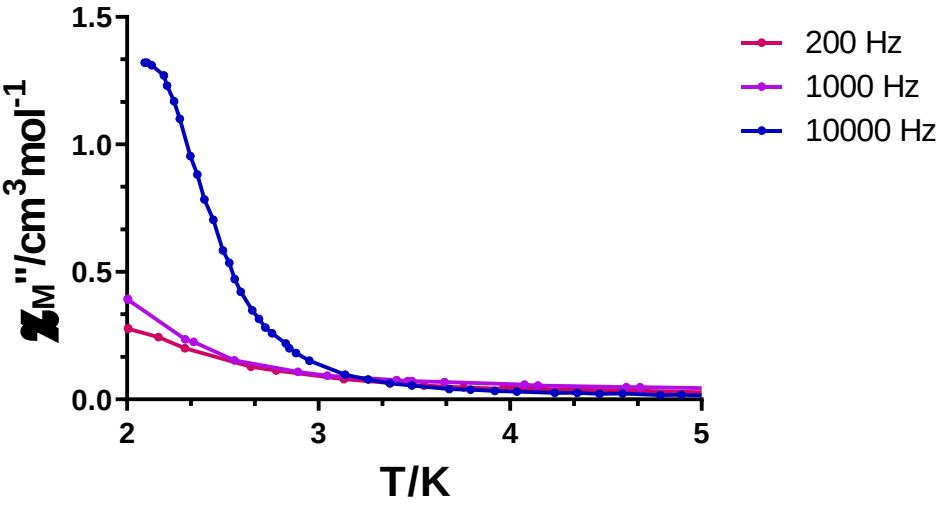

Figure A1.36.- Temperature dependence of the out-of-phase components of the *ac* susceptibility under an external field of 1000 Oe for **5**.

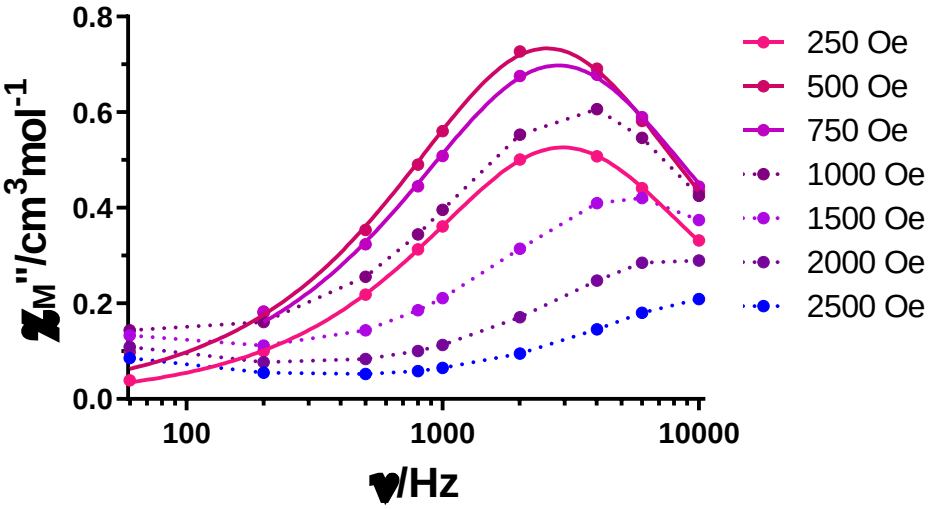

Figure A1.37.- Field dependence of the out-of-phase signal *vs* frequency at 2.0 K for **6**. The dashed lines at 1000 Oe and above are a guide to the eye.

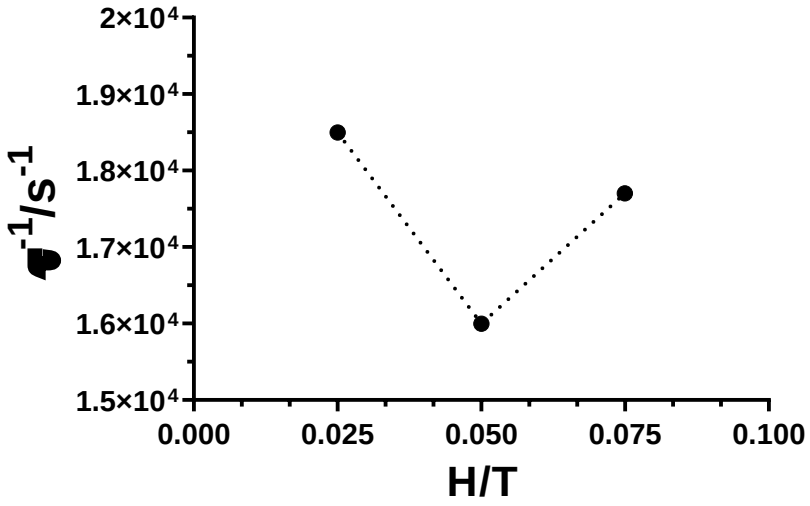

Figure A1.38.- The inverse of the relaxation times obtained at different magnetic fields at 2.0 K for **6**. The dashed line is a guide to the eye.

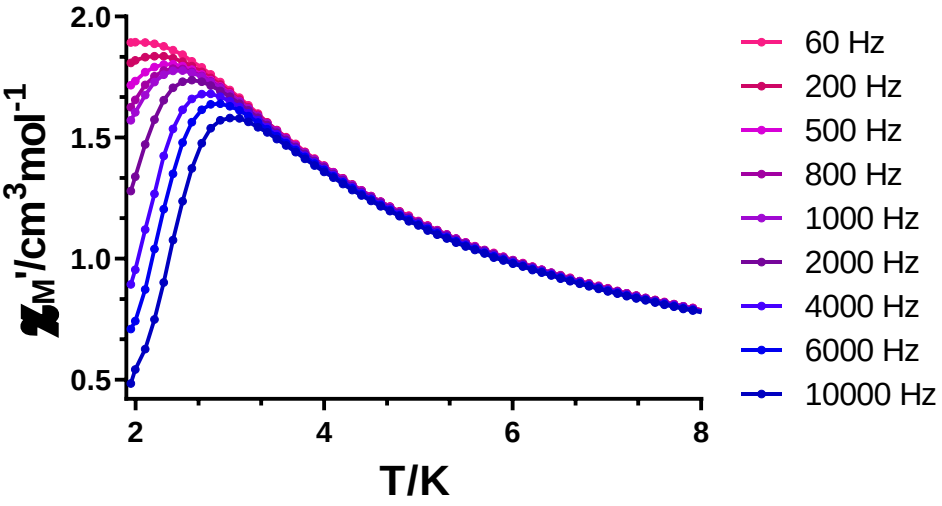

Figure A1.39.- Temperature dependence of the in phase χ_M' susceptibility signals for complex **6** under an applied field of 500 Oe.

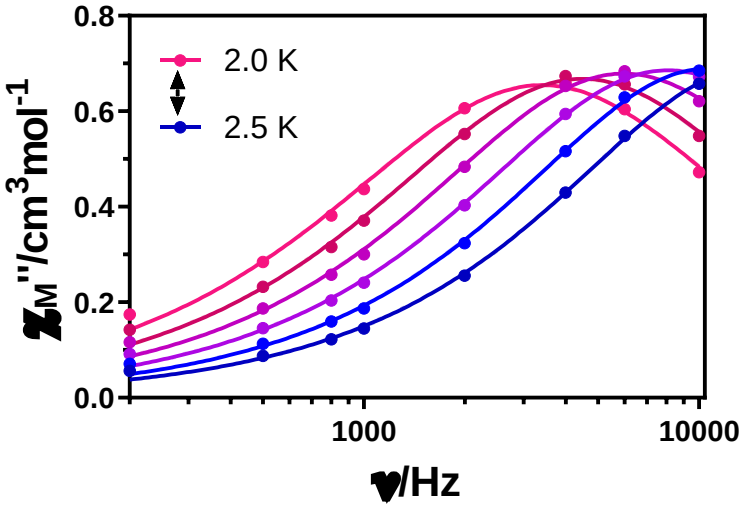

Figure A1.40.- Variable-temperature frequency dependence of the χ_M'' signal under 500 Oe applied field for **6**. Solid lines represent the best fitting of the experimental data to the Debye model.

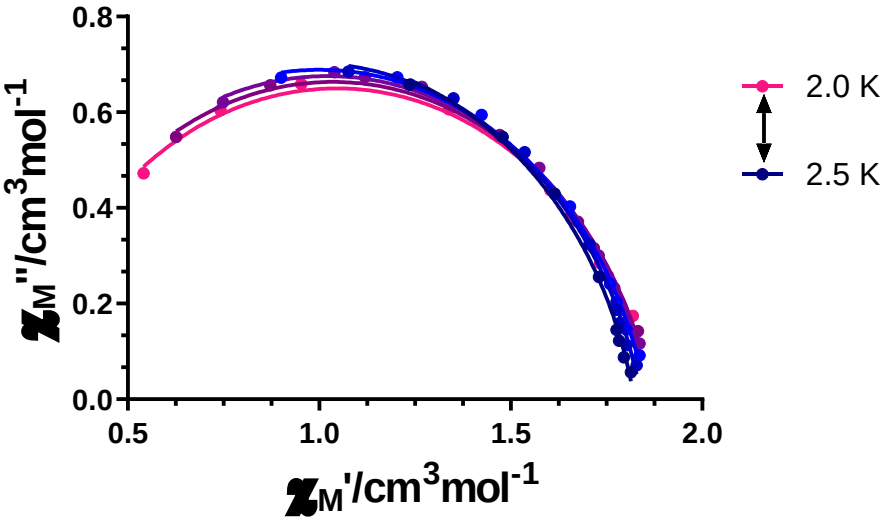

Figure A1.41.- Cole-Cole plots under 500 Oe field for **6**. Solid lines represent the best fits to the generalized Debye model.

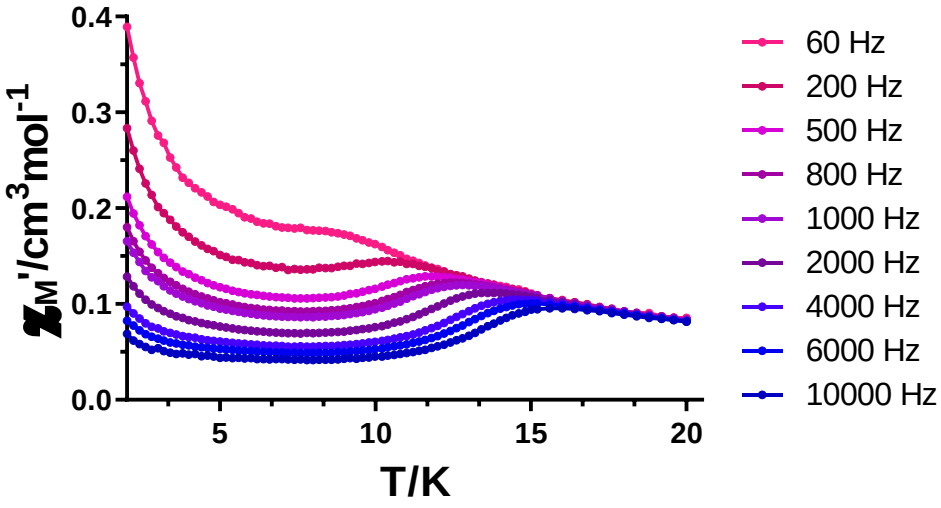

Figure A1.42.- Temperature dependence of the in phase χ_M' susceptibility signals for complex $\mathbf{1}_Y$ under zero applied *dc* field.

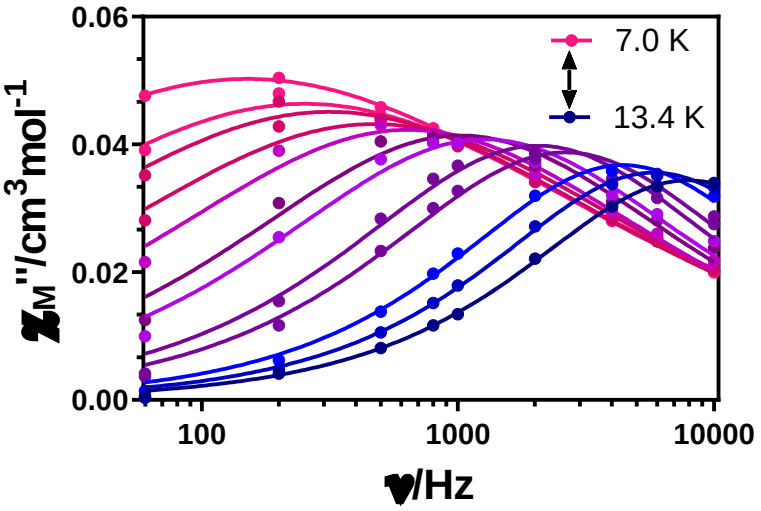

Figure A1.43.- Variable-temperature frequency dependence of the χ_M'' signal under zero applied *dc* field for **1**$_Y$. Solid lines represent the best fitting of the experimental data to the Debye model.

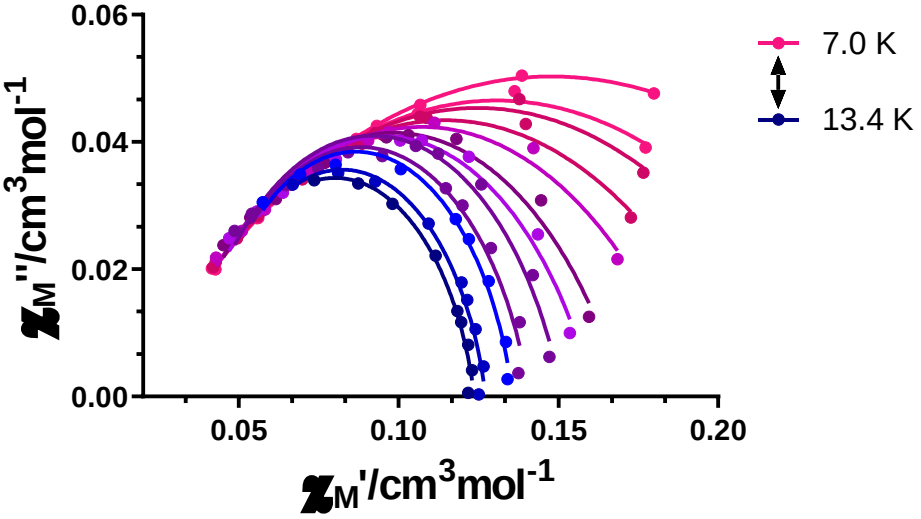

Figure A1.44.- Cole-Cole plots under zero *dc* field for **1**$_Y$. Solid lines represent the best fits to the generalized Debye model.

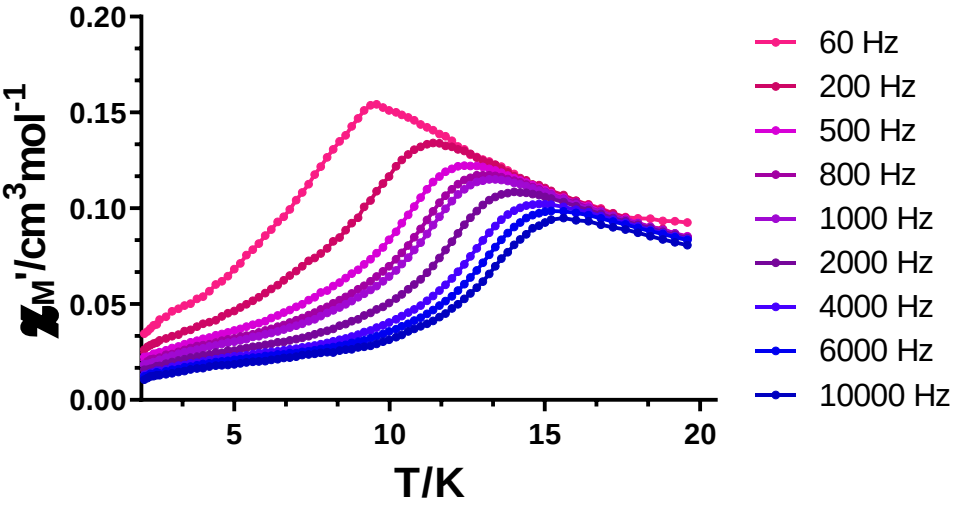

Figure A1.45.- Temperature dependence of the in phase χ_M' susceptibility signals for complex $\mathbf{1}_Y$ under an applied field of 1000 Oe.

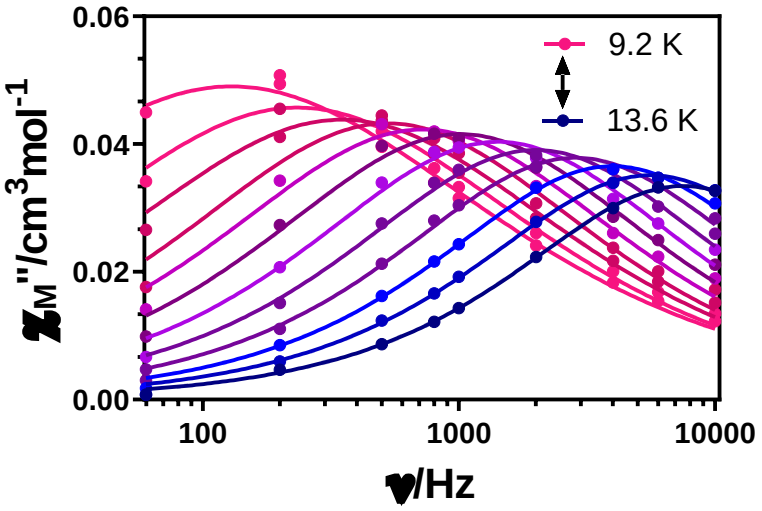

Figure A1.46.- Variable-temperature frequency dependence of the χ_M'' signal under 1000 Oe applied field for $\mathbf{1}_Y$. Solid lines represent the best fitting of the experimental data to the Debye model.

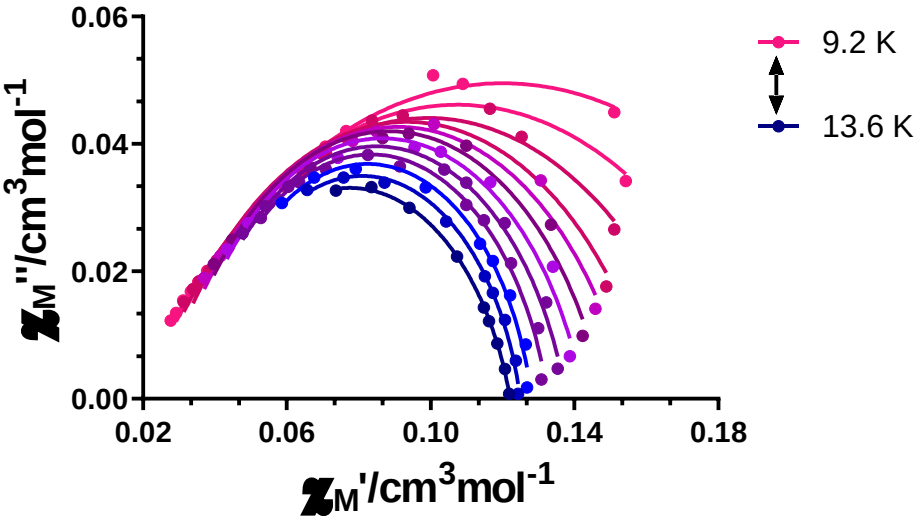

Figure A1.47.- Cole-Cole plots under under 1000 Oe applied field for **1**$_{Y}$. Solid lines represent the best fits to the generalized Debye model.

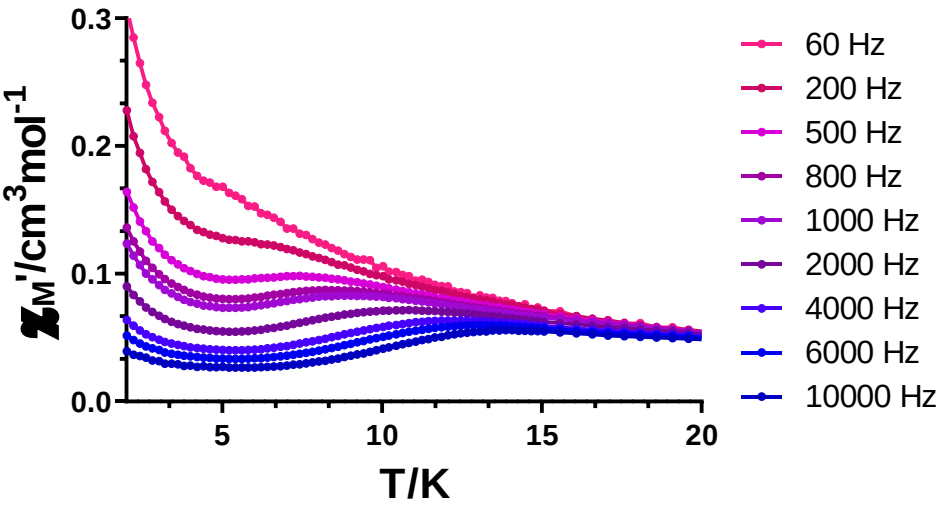

Figure A1.48.- Temperature dependence of the in phase χ_M' susceptibility signals for complex **3**$_{Y}$ under zero applied *dc* field.

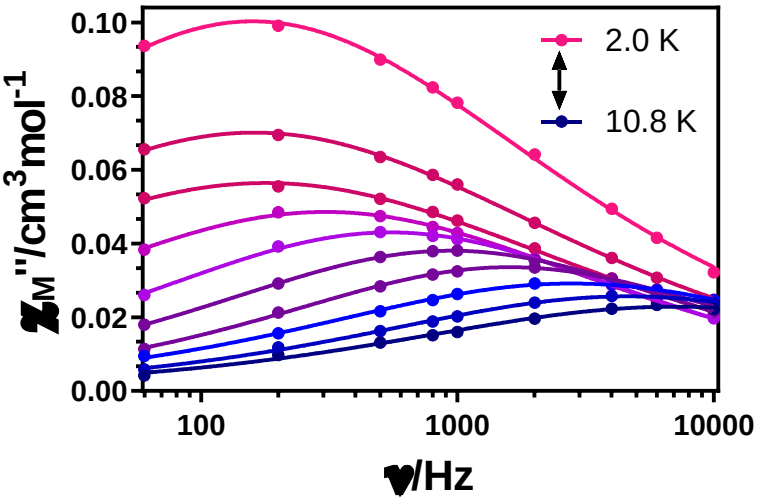

Figure A1.49.- Variable-temperature frequency dependence of the χ_M'' signal under zero applied *dc* field for **3**$_Y$. Solid lines represent the best fitting of the experimental data to the Debye model.

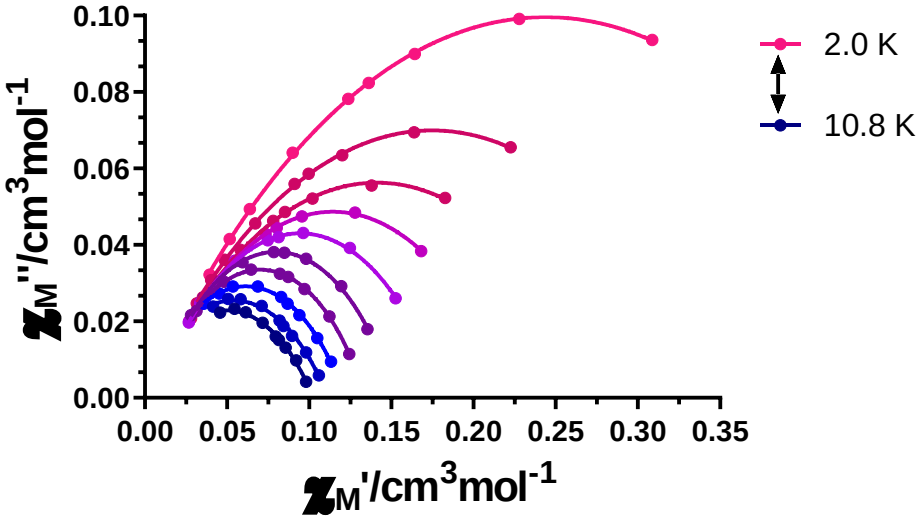

Figure A1.50.- Cole-Cole plots under zero *dc* field for **3**$_Y$. Solid lines represent the best fits to the generalized Debye model.

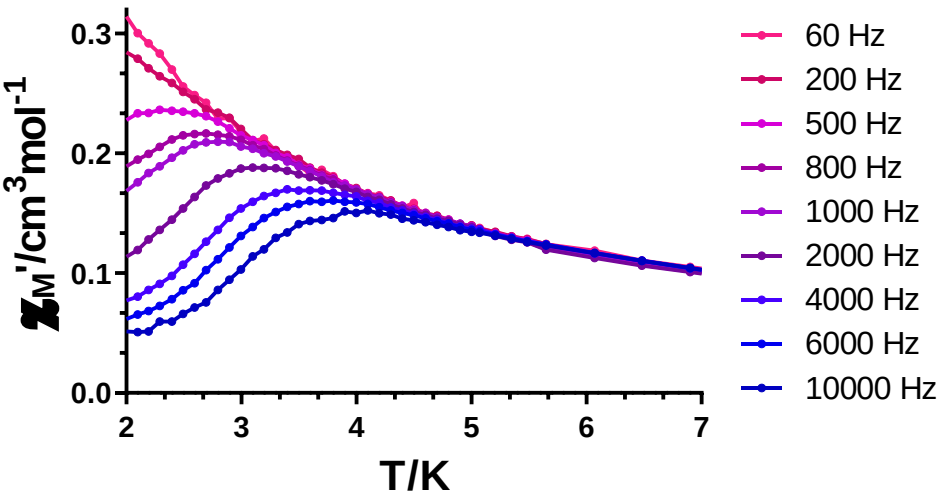

Figure A1.51.- Temperature dependence of the in phase χ_M' susceptibility signals for complex **4**$_Y$ under an applied field of 1000 Oe.

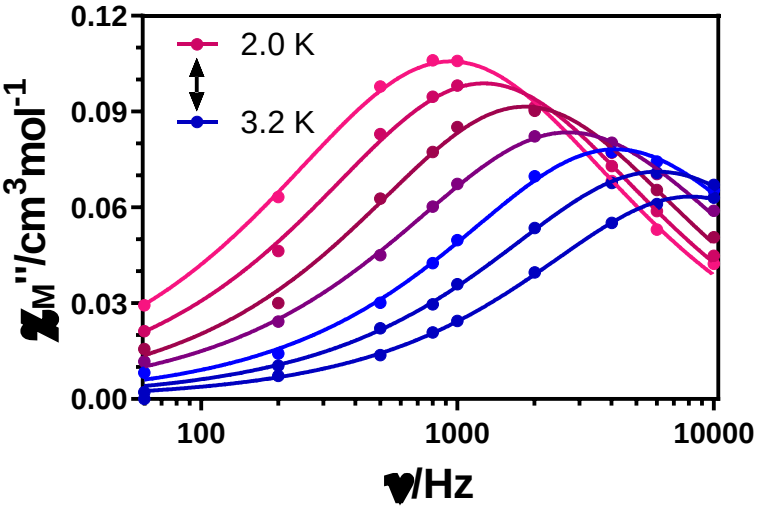

Figure A1.52.- Variable-temperature frequency dependence of the χ_M'' signal under 1000 Oe applied field for **4**$_Y$. Solid lines represent the best fitting of the experimental data to the Debye model.

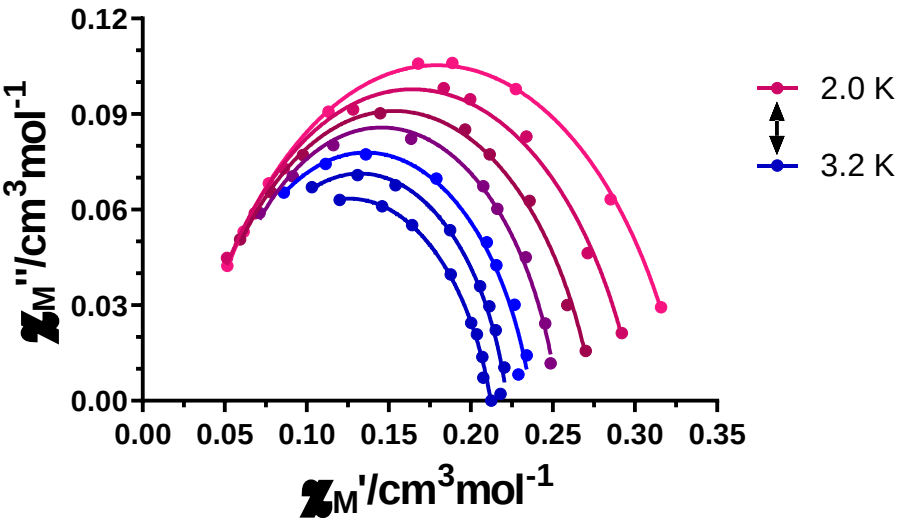

Figure A1.53.- Cole-Cole plots under under 1000 Oe applied field for $\mathbf{4_Y}$. Solid lines represent the best fits to the generalized Debye model.

6. Magellan Figures.

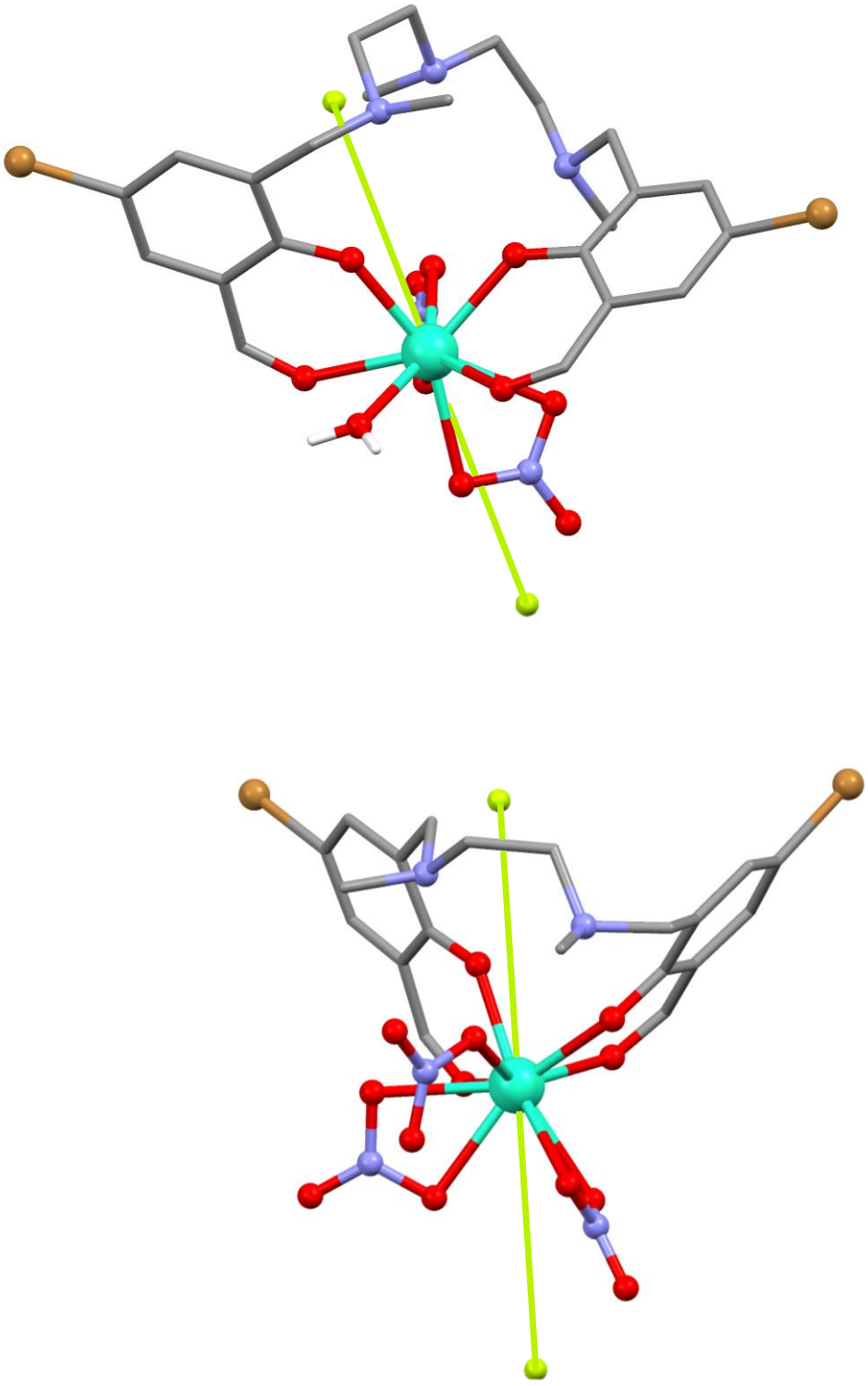

Figure A1.54.- Anisotropy axes for compounds **3** (top) and **5** (bottom) obtained by Magellan software (green line).

7. ^{1}H Nuclear Magnetic Resonance.

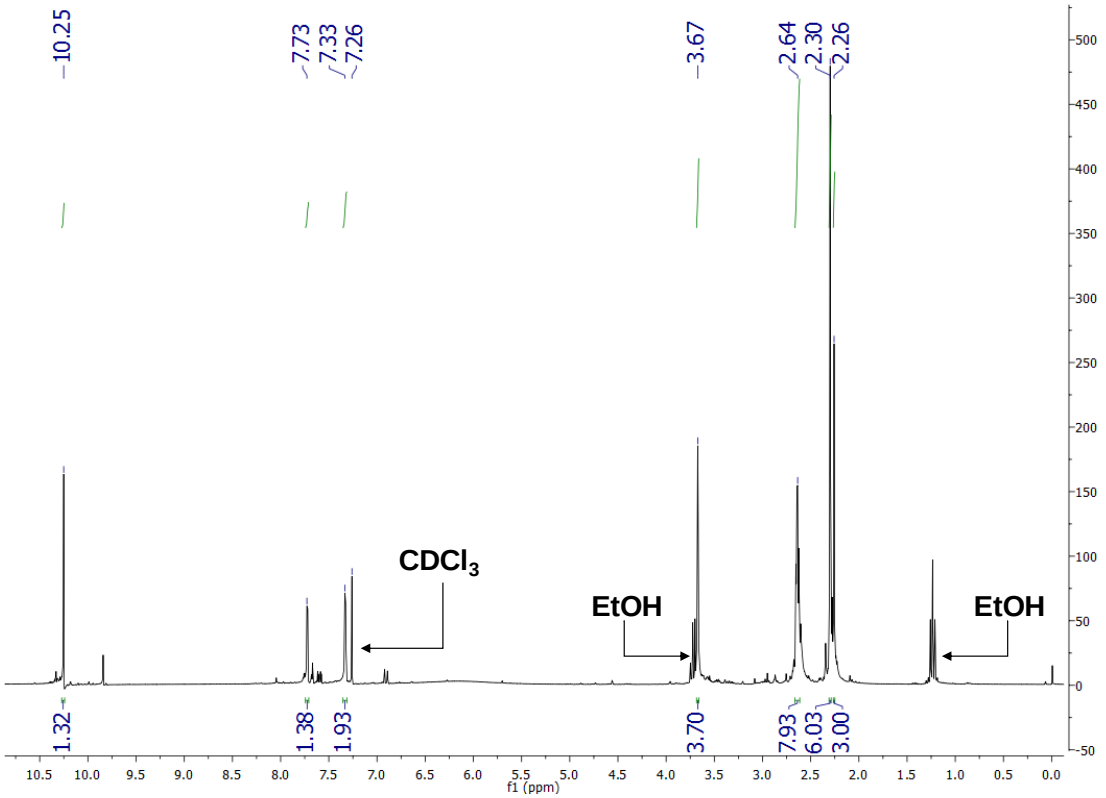

Figure A1.55.- ^{1}H NMR spectrum for H_2L^1 in $CDCl_3$.

APPENDICES

Chapter 2: *Extending dinuclear $Zn^{II}Dy^{III}$ entities through a variety of bridging di- and tricarboxylate groups: an exhaustive magnetic study*

Index:

1. Elemental Analyses and Crystallographic Tables.

Table A2.1.- Yields and elemental analyses for complexes **7**-**15**. The formulas have been suggested based on EA and TG results.

Complex	Yield (%)	Formula	% C calc./found	% H calc./found	% N calc./found
7	40	$C_{46}H_{60}Dy_2N_6O_{20}Zn_2$	37.51/37.55	4.11/4.17	5.71/5.66
8	73	$C_{50}H_{70}Dy_2N_{10}O_{24}Zn_2$	36.38/36.30	4.27/4.43	8.48/8.21
9	55	$C_{49}H_{66}Dy_2N_8O_{24}Zn_2$	36.63/36.44	4.14/4.23	6.97/7.11
10	60	$C_{51}H_{69.5}Dy_2N_{8.5}O_{24}Zn_2$	37.32/37.06	4.27/4.15	7.25/7.01
11	52	$C_{51}H_{70}Dy_2N_8O_{24}Zn_2$	37.47/37.26	4.32/4.08	6.85/6.97
12	75	$C_{52}H_{64}Dy_2N_8O_{24}Zn_2$	38.06/38.21	3.93/3.88	6.83/6.71
13	72	$C_{62}H_{74}Dy_2N_{10}O_{24}Zn_2$	41.39/41.02	4.14/4.29	7.78/7.59
14	60	$C_{77.5}H_{100}Cl_3Dy_3N_{12}O_{37.5}Zn_3$	35.94/36.11	3.89/4.16	6.49/6.50
15	25	$C_{106}H_{126}Dy_4N_{14}O_{46}Zn_4$	39.25/39.29	3.92/3.88	6.04/5.95

Table A2.2.- Crystallographic data for compounds **7-11**. The formulas correspond to what was found in the crystal structure.

Complex	**7**	**8**	**9**	**10**	**11**
Formula	$C_{46}H_{60}Dy_2N_6O_{20}Zn_2$	$C_{48}H_{64}Dy_2N_8O_{24}Zn_2$	$C_{53}H_{72}Dy_2N_{10}O_{24}Zn_2$	$C_{54}H_{74}Dy_2N_{10}O_{24}Zn_2$	$C_{53}H_{73}Dy_2N_9O_{24}Zn_2$
M_r	1472.78	1592.81	1688.94	1702.97	1675.94
Crystal system	*triclinic*	*monoclinic*	*monoclinic*	*monoclinic*	*triclinic*
Space group (no.)	*P*-1 (2)	$P2_1/c$ (14)	*C 2/c* (15)	$P2_1/c$ (14)	*P*-1 (2)
a (Å)	10.763(3)	17.183(5)	14.244(5)	21.8250(2)	10.6162(5)
b (Å)	12.060(3)	16.983(5)	16.852(5)	10.96480(10)	11.4909(7)
c (Å)	12.241(3)	20.680(5)	26.822(5)	28.2675(2)	28.7535(16)
α (°)	78.178(6)	90	90	90	87.797(2)
β (°)	81.044(7)	90.018(5)	92.887(5)	103.4710(10)	86.914(2)
γ (°)	64.531(6)	90	90	90	65.290(2)
V (Å^3)	1400.0(6)	6035(3)	6430(3)	6578.49(10)	3181.3(3)
Z	1	4	4	4	2
D_c (g cm^{-3})	1.856	1.753	1.745	1.719	1.750
μ(MoK$_\alpha$) (mm^{-1})[d]	3.570	3.317	3.120	13.493	3.152
T (K)	100(2)	100(2)	100(2)	150.00(10)	100(2)
Observed reflections	2926 (2051)	13981 (8996)	8319 (7537)	13259 (11807)	16477 (13433)
R_{int}	0.1349	0.0832	0.0329	0.0704	0.0798
Parameters	349	769	410	852	824
GOF	1.058	0.969	1.084	1.036	1.046
R_1[a,b]	0.0964 (0.0533)	0.0995 (0.0569)	0.0261 (0.0211)	0.0497 (0.0438)	0.0543 (0.0364)
wR_2[c]	0.1198 (0.1026)	0.1293 (0.1098)	0.0496 (0.0476)	0.1107 (0.1065)	0.0753 (0.0705)
Largest difference in peak and hole (e Å^{-3})	1.512 and -1.216	3.253 and -2.023	1.572 and -1.058	1.587 and -1.740	2.325 and -1.964

[a] $R_1 = \Sigma||F_o| - |F_c||/\Sigma|F_o|$. [b] Values in parentheses for reflections with $I > 2\sigma(I)$. [c] $wR_2 = \{\Sigma[w(F_o^2 - F_c^2)^2]/\Sigma[w(F_o^2)^2]\}^{½}$. [d] μ(CuK$_\alpha$) (mm^{-1}) in **10**.

Table A2.3.- Crystallographic data for compounds **12-15**. The formulas correspond to what was found in the crystal structure.

Complex	**12**	**13**	**14**	**15**
Formula	$C_{52}H_{64}Dy_2N_8O_{24}Zn_2$	$C_{62}H_{74}Dy_2N_{10}O_{24}Zn_2$	$C_{77.5}H_{100}Cl_3Dy_3N_{12}O_{37.5}Zn_3$	$C_{106}H_{126}Dy_4N_{14}O_{46}Zn_4$
M_r	1640.89	1799.05	2589.65	3243.78
Crystal system	*monoclinic*	*monoclinic*	*trigonal*	*triclinic*
Space group (no.)	*P*2$_1$/*c* (14)	*P*2$_1$/*c* (14)	*R-3* (148)	*P*-1 (2)
a (Å)	10.229(5)	19.8668(4)	26.6682(10)	10.1051(11)
b (Å)	34.381(5)	14.4958(2)	26.6682(10)	17.3240(9)
c (Å)	10.521(5)	24.0052(4)	26.0627(11)	21.8036(10)
α (°)	90	90	90	68.050(5)
β (°)	92.004(5)	103.851(2)	90	81.131(6)
γ (°)	90	90	120	86.652(6)
V (Å^3)	3698(3)	6712.1(2)	16052.3(14)	3497.9(5)
Z	2	4	6	1
D_c (g cm^{-3})	1.621	1.780	1.607	1.540
μ(MoK$_\alpha$) (mm^{-1})[d]	2.719	2.995	2.886	12.635
T (K)	100.01(10)	100.01(10)	100(2)	150.01(10)
Observed reflections	7667 (6746)	13957 (9210)	9097 (8506)	10699 (6484)
R_{int}	0.0787	0.0792	0.0152	0.1323
Parameters	403	915	425	783
GOF	1.196	1.043	1.080	1.031
R_1[a,b]	0.1016 (0.0928)	0.1005 (0.0556)	0.0264 (0.0240)	0.1189 (0.0725)
wR_2[c]	0.2043(0.2002)	0.1390 (0.1164)	0.0677 (0.0663)	0.2043 (0.1732)
Largest difference in peak and hole (e Å^{-3})	2.414 and -3.871	3.052 and -2.583	1.690 and -0.706	2.391 and -1.265

[a] $R_1 = \Sigma||F_o| - |F_c||/\Sigma|F_o|$. [b] Values in parentheses for reflections with $I > 2\sigma(I)$. [c] $wR_2 = \{\Sigma[w(F_o^2 - F_c^2)^2]/\Sigma[w(F_o^2)^2]\}^{½}$. [d] μ(CuK$_\alpha$) (mm^{-1}) in **15**.

Table A2.4.- Bond lengths (Å) and angles (°) for compounds **7**, **8** and **9**. O1X* and O2X* correspond to the bridging carboxylate oxygen atoms. Symmetry operations: (i) –x, -y, -z.

Compound	**7**	**8A**	**8B**	**9**
Dy1···Zn1	3.3745(18)	3.3370(11)	3.3465(11)	3.3296(8)
Dy1-O1	2.288(9)	2.245(4)	2.269(4)	2.2455(15)
Dy1-O2	2.544(9)	2.579(4)	2.584(4)	2.5292(15)
Dy1-O3	2.319(9)	2.279(4)	2.272(4)	2.3296(14)
Dy1-O4	2.555(9)	2.562(5)	2.582(5)	2.5016(15)
Dy1-O1X*	2.347(9)	2.281(5)	2.289(5)(O3BU)	2.2813(16)
Dy1-O5	2.431(9)	2.443(5)	2.417(5)	2.4394(16)
Dy1-O6	2.518(10)	2.446(5)	2.439(5)	2.4851(18)
Dy1-O8	2.392(9)(O1CA(i))	2.438(5)	2.428(5)	2.4825(17)
Dy1-O9	2.395(8)(O3CA)	2.555(5)	2.560(5)	2.4842(17)
Zn1-N1	2.097(11)	2.101(6)	2.131(5)	2.0925(18)
Zn1-N2	2.133(11)	2.142(5)	2.118(6)	2.1478(18)
Zn1-O1	2.071(9)	2.081(5)	2.054(5)	2.0675(16)
Zn1-O3	2.026(9)	2.033(5)	2.035(5)	2.0262(14)
Zn1-O2X*	1.950(9)	1.994(5)	2.017(5)(O4BU)	1.9843(15)
Dy1-O1-Zn1	101.3(4)	100.91(18)	101.36(18)	100.99(6)
Dy1-O3-Zn1	101.7(4)	101.27(19)	101.84(19)	99.48(6)
O1-Dy1-O3	65.1(3)	67.48(16)	66.76(16)	65.37(5)
O1-Dy1-O1X*	79.5(3)	85.21(17)	83.75(16)(O3BU)	81.74(5)
O3-Dy1-O1X*	77.9(3)	81.00(16)	80.68(17)(O3BU)	80.31(6)
O1-Zn1-O3	74.4(4)	75.30(18)	75.33(18)	74.28(6)
O1-Zn1-O2X*	105.9(4)	99.96(18)	99.04(19)(O4BU)	102.83(6)
O3-Zn1-O2X*	110.9(4)	104.57(19)	105.60(19)(O4BU)	113.01(6)
N1-Zn1-N2	84.2(4)	84.5(2)	84.8(2)	85.88(7)

Table A2.5.- Bond lengths (Å) and angles (°) for compounds **10** and **11**. O1X* and O2X* correspond to the bridging carboxylate oxygen atoms.

Compound	**10A**	**10B**	**11A**	**11B**
Dy1···Zn1	3.3427(5)	3.3365(5)	3.3419(5)	3.3233(4)
Dy1-O1	2.242(3)	2.249(3)	2.251(2)	2.252(3)
Dy1-O2	2.608(3)	2.612(3)	2.602(2)	2.604(3)
Dy1-O3	2.289(2)	2.292(2)	2.292(2)	2.288(2)
Dy1-O4	2.538(3)	2.543(3)	2.583(2)	2.517(3)
Dy1-O1X*	2.293(3)	2.299(3)(O3HX)	2.288(2)	2.277(3)(O3HP)
Dy1-O5	2.443(3)	2.436(3)	2.419(2)	2.440(3)
Dy1-O6	2.490(3)	2.481(3)	2.450(3)	2.472(3)
Dy1-O8	2.464(3)	2.454(3)	2.443(3)	2.441(4)
Dy1-O9	2.479(3)	2.480(3)	2.555(3)	2.460(3)
Zn1-N1	2.102(3)	2.103(3)	2.121(3)	2.124(3)
Zn1-N2	2.151(3)	2.145(3)	2.124(3)	2.119(3)
Zn1-O1	2.072(3)	2.060(3)	2.040(2)	2.037(3)
Zn1-O3	2.026(2)	2.022(2)	2.041(2)	2.059(2)
Zn1-O2X*	1.980(3)	1.977(3)(O4HX)	1.985(2)	1.974(3)(O4HP)
Dy1-O1-Zn1	101.52(12)	101.38(12)	102.20(10)	101.47(11)
Dy1-O3-Zn1	101.38(10)	101.15(10)	100.78(9)	99.59(10)
O1-Dy1-O3	65.56(9)	65.32(9)	66.02(8)	66.81(9)
O1-Dy1-O1X*	82.73(11)	83.33(11)(O3HX)	83.22(9)	81.08(10)(O3HP)
O3-Dy1-O1X*	79.77(10)	79.22(10)(O3HX)	82.74(8)	79.11(9)(O3HP)
O1-Zn1-O3	73.54(10)	73.77(10)	74.68(9)	75.19(10)
O1-Zn1-O2X*	102.67(11)	103.63(11)	101.68(10)	108.72(11)(O4HP)
O3-Zn1-O2X*	109.27(11)	109.35(11)(O4HX)	105.11(10)	104.84(10)(O4HP)
N1-Zn1-N2	86.38(12)	86.41(11)	85.88(11)	86.07(12)

Table A2.6.- Bond lengths (Å) and angles (°) for compounds **12**, **13** and **14**. O1X* and O2X* correspond to the bridging carboxylate oxygen atoms.

Compound	**12**	**13A**	**13B**	**14**
Dy1···Zn1	3.329(2)	3.3440(10)	3.3256(9)	3.3569(3)
Dy1-O1	2.245(7)	2.237(6)	2.276(5)	2.2763(16)
Dy1-O2	2.578(8)	2.523(6)	2.596(5)	2.5108(19)
Dy1-O3	2.285(7)	2.250(6)	2.283(5)	2.3121(16)
Dy1-O4	2.566(8)	2.585(6)	2.617(5)	2.5728(17)
Dy1-O1X*	2.280(8)	2.354(5)	2.323(5)(O3BI)	2.2779(18)
Dy1-O5	2.447(8)	2.429(6)	2.418(5)	2.4375(18)
Dy1-O6	2.458(9)	2.462(7)	2.436(5)	2.4695(18)
Dy1-O8	2.436(8)	2.436(6)	2.446(5)	2.4527(19)
Dy1-O9	2.508(8)	2.486(7)	2.456(5)	2.4863(18)
Zn1-N1	2.084(9)	2.104(7)	2.125(6)	2.088(2)
Zn1-N2	2.154(9)	2.104(8)	2.092(6)	2.145(2)
Zn1-O1	2.078(7)	2.042(6)	2.018(5)	2.0543(17)
Zn1-O3	2.014(7)	2.008(5)	2.039(5)	2.0368(17)
Zn1-O2X*	1.978(8)	1.986(5)	1.986(5)(O4BI)	1.9737(17)
Dy1-O1-Zn1	100.6(3)	102.7(2)	101.4(2)	101.51(7)
Dy1-O3-Zn1	101.3(3)	103.3(2)	100.5(2)	100.86(7)
O1-Dy1-O3	66.5(3)	66.1(2)	67.16(18)	65.18(6)
O1-Dy1-O1X*	82.9(3)	78.72(19)	80.77(18)(O3BI)	81.24(6)
O3-Dy1-O1X*	83.5(3)	84.7(2)	79.66(17)(O3BI)	79.63(6)
O1-Zn1-O3	74.7(3)	74.4(2)	76.8(2)	74.33(7)
O1-Zn1-O2X*	99.5(3)	99.6(2)	106.3(2)(O4BI)	105.22(7)
O3-Zn1-O2X*	107.9(3)	105.1(2)	103.4(2)(O4BI)	108.06(7)
N1-Zn1-N2	85.8(4)	86.2(3)	87.0(2)	86.29(8)

Table A2.7.- Bond lengths (Å) and angles (°) for compound **15**.

Compound	**15A**	**15B**
Dy1···Zn1	3.3364(18)	3.3516(17)
Dy1-O1	2.235(9)	2.261(9)
Dy1-O2	2.496(10)	2.644(10)
Dy1-O3	2.295(9)	2.302(8)
Dy1-O4	2.562(10)	2.575(10)
Dy1-O1TR	2.256(9)	-
Dy1-O3TR	-	2.285(6)
Dy1-O5	2.450(10)	2.433(9)
Dy1-O6	2.436(9)	2.482(11)
Dy1-O8	2.441(7)	-
Dy1-O9	2.496(9)	-
Dy1-O5TR	-	2.612(8)
Dy1-O6TR	-	2.345(9)
Zn1-N1	2.056(12)	2.077(12)
Zn1-N2	2.144(12)	2.137(11)
Zn1-O1	2.052(11)	2.076(8)
Zn1-O3	2.023(9)	2.025(9)
Zn1-O2TR	1.995(7)	-
Zn1-O4TR	-	1.977(7)
Dy1-O1-Zn1	102.1(5)	101.1(3)
Dy1-O3-Zn1	101.0(4)	101.3(3)
O1-Dy1-O3	64.7(4)	66.4(3)
O1-Dy1-O1TR	79.3(3)	-
O3-Dy1-O1TR	80.1(3)	-
O1-Dy1-O3TR	-	81.9(3)
O3-Dy1-O3TR	-	79.2(3)
O1-Zn1-O3	73.0(4)	75.0(3)
O1-Zn1-O2TR	101.6(3)	-
O3-Zn1-O2TR	113.8(3)	-
O1-Zn1-O4TR	-	107.5(3)
O3-Zn1-O4TR	-	101.9(3)
N1-Zn1-N2	86.8(5)	85.0(4)

2. Continuous Shape Measurements.

The nearer the value to zero, the better fits to an ideal polyhedron.

Table A2.8.- Continuous Shape Measurements for the ZnN_2O_3 coordination environment. Bold blue numbers indicate the nearer value to zero for each ZnN_2O_3.

PP-5 1 D5h Pentagon
vOC-5 2 C4v Vacant octahedron
TBPY-5 3 D3h Trigonal bipyramid
SPY-5 4 C4v Spherical square pyramid
JTBPY-5 5 D3h Johnson trigonal bipyramid J12

Structure [ML5]	PP-5	Voc-5	TBPY-5	SPY-5	JTBPY-5
Comp7 (Zn1)	31.431	2.430	4.241	**0.645**	6.687
Comp8 (Zn1A)	32.075	2.595	4.345	**0.606**	6.909
Comp8 (Zn1B)	31.489	2.420	4.384	**0.563**	7.192
Comp9 (Zn1)	31.686	2.704	3.561	**0.831**	6.022
Comp10 (Zn1A)	32.170	2.719	3.836	**0.731**	6.356
Comp10 (Zn1B)	32.114	2.750	3.825	**0.711**	6.425
Comp11 (Zn1A)	30.254	2.684	3.523	**0.838**	6.277
Comp11 (Zn1B)	31.019	2.171	5.330	**0.414**	7.997
Comp12 (Zn1)	30.233	2.357	4.687	**0.573**	7.023
Comp13 (Zn1A)	28.563	2.469	4.585	**0.761**	7.446
Comp13 (Zn1B)	30.732	2.049	5.003	**0.371**	7.940
Comp14 (Zn1)	31.141	2.175	4.328	**0.664**	6.738
Comp15 (Zn1A)	29.394	2.635	4.583	**0.815**	6.997
Comp15 (Zn1B)	27.841	2.552	4.337	**0.788**	6.716

Table A2.9.- Continuous Shape Measurements for the DyO_9 coordination environment. Green, orange and red colors indicate the three lowest values for each DyO_9.

EP-9	1 D9h	Enneagon
OPY-9	2 C8v	Octagonal pyramid
HBPY-9	3 D7h	Heptagonal bipyramid
JTC-9	4 C3v	Johnson triangular cupola J3
JCCU-9	5 C4v	Capped cube J8
CCU-9	6 C4v	Spherical-relaxed capped cube
JCSAPR-9	7 C4v	Capped square antiprism J10
CSAPR-9	8 C4v	Spherical capped square antiprism
JTCTPR-9	9 D3h	Tricapped trigonal prism J51
TCTPR-9	10 D3h	Spherical tricapped trigonal prism
JTDIC-9	11 C3v	Tridiminished icosahedron J63
HH-9	12 C2v	Hula-hoop
MFF-9	13 Cs	Muffin

Structure [ML9]	EP-9	OPY-9	HBPY-9	JTC-9	JCCU-9	CCU-9	JCSAPR-9
Comp7 (Dy1)	36.219	22.431	17.480	15.729	9.515	7.827	3.821
Comp8 (Dy1A)	36.081	22.042	18.198	15.779	7.445	6.309	3.472
Comp8 (Dy1B)	35.748	23.214	17.467	15.568	9.184	7.671	3.446
Comp9 (Dy1)	36.040	22.895	17.001	14.740	8.070	6.705	3.865
Comp10 (Dy1A)	35.418	23.299	17.893	15.207	9.147	7.612	3.873
Comp10 (Dy1B)	35.447	23.416	17.647	15.185	9.157	7.626	3.988
Comp11 (Dy1A)	34.896	23.143	16.295	16.550	7.094	5.790	4.355
Comp11 (Dy1B)	36.563	22.990	18.652	14.220	9.843	8.525	3.359
Comp12 (Dy1)	35.972	23.344	17.434	15.847	8.142	6.935	3.799
Comp13 (Dy1A)	35.914	22.530	16.983	14.366	8.066	6.826	4.261
Comp13 (Dy1B)	34.522	24.456	15.969	14.898	8.057	6.600	4.383
Comp14 (Dy1)	36.143	22.892	16.634	15.874	8.563	6.840	4.259
Comp15 (Dy1A)	36.175	23.460	17.209	15.067	8.975	7.409	3.860
Comp15 (Dy1B)	35.279	22.572	16.574	14.248	8.060	6.998	3.913

Structure [ML9]	CSAPR-9	JTCTPR-9	TCTPR-9	JTDIC-9	HH-9	MFF-9
Comp7 (Dy1)	2.541	4.789	2.843	8.720	9.788	2.856
Comp8 (Dy1A)	2.535	3.636	2.370	12.137	8.659	2.366
Comp8 (Dy1B)	2.117	4.170	2.968	10.313	8.498	2.290
Comp9 (Dy1)	2.707	5.279	3.642	9.872	8.248	2.344
Comp10 (Dy1A)	2.480	4.927	3.079	10.793	9.158	2.333
Comp10 (Dy1B)	2.554	4.956	2.954	10.674	9.040	2.411
Comp11 (Dy1A)	3.337	4.478	3.405	11.072	7.573	2.707
Comp11 (Dy1B)	2.069	4.691	2.805	10.388	10.417	2.383
Comp12 (Dy1)	2.477	4.355	3.059	10.463	8.085	2.211
Comp13 (Dy1A)	2.804	5.744	3.685	9.752	8.157	2.390
Comp13 (Dy1B)	3.875	4.613	3.399	11.117	6.330	2.947
Comp14 (Dy1)	2.996	5.601	3.489	9.355	7.818	2.542
Comp15 (Dy1A)	2.580	4.731	2.788	9.537	8.501	2.271
Comp15 (Dy1B)	2.548	4.516	3.102	10.843	9.380	2.291

3. Other Structural Figures.

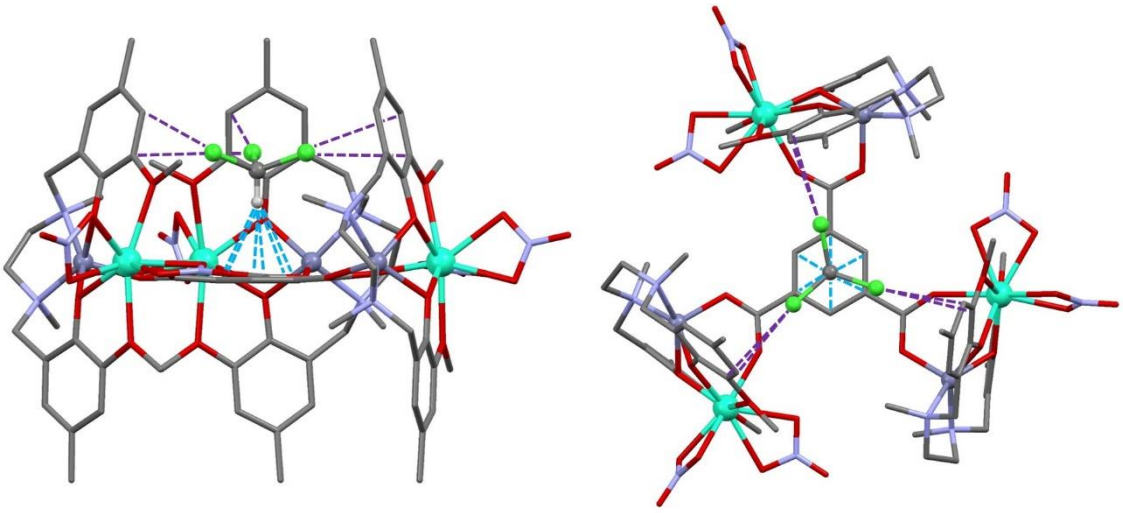

Figure A2.1.- Perspective view of compound **14** along *a* (left) and *c* (right) axes stabilizing a chloroform molecule. Dashed blue and purple lines represent C-H···π and Cl···π interactions, respectively. The rest of the solvent molecules, as well as hydrogen atoms belonging to L^{2-} and trimesate bridge were omitted for the sake of clarity.

4. Experimental XRPD.

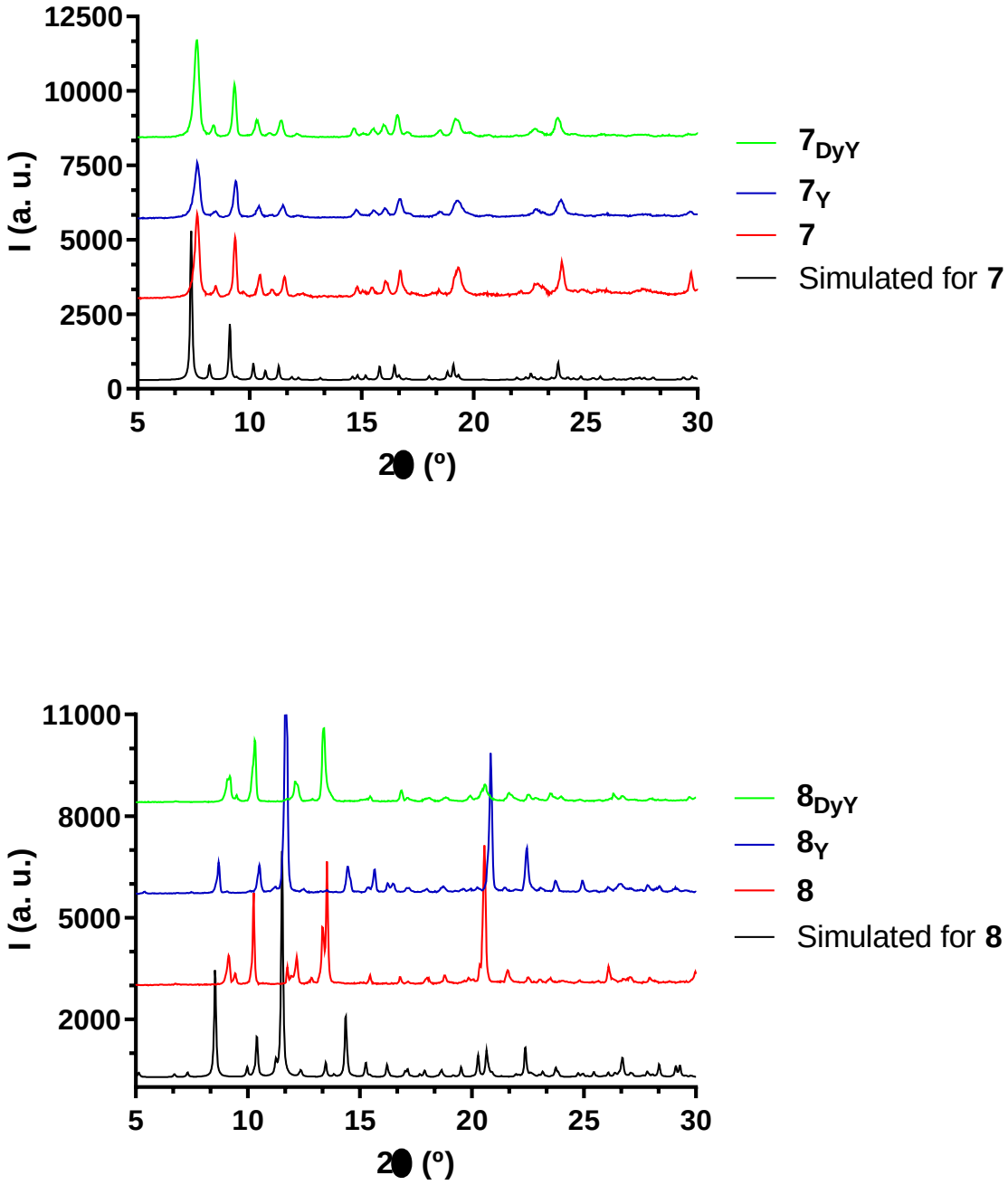

Figure A2.2.- For compounds **7** (top) and **8** (bottom), simulated pattern from single-crystal X-ray diffraction (black line) and experimental XRPD for Dy^{III} (red), Y^{III} (blue) and Dy^{III}:Y^{III} based (green) analogues.

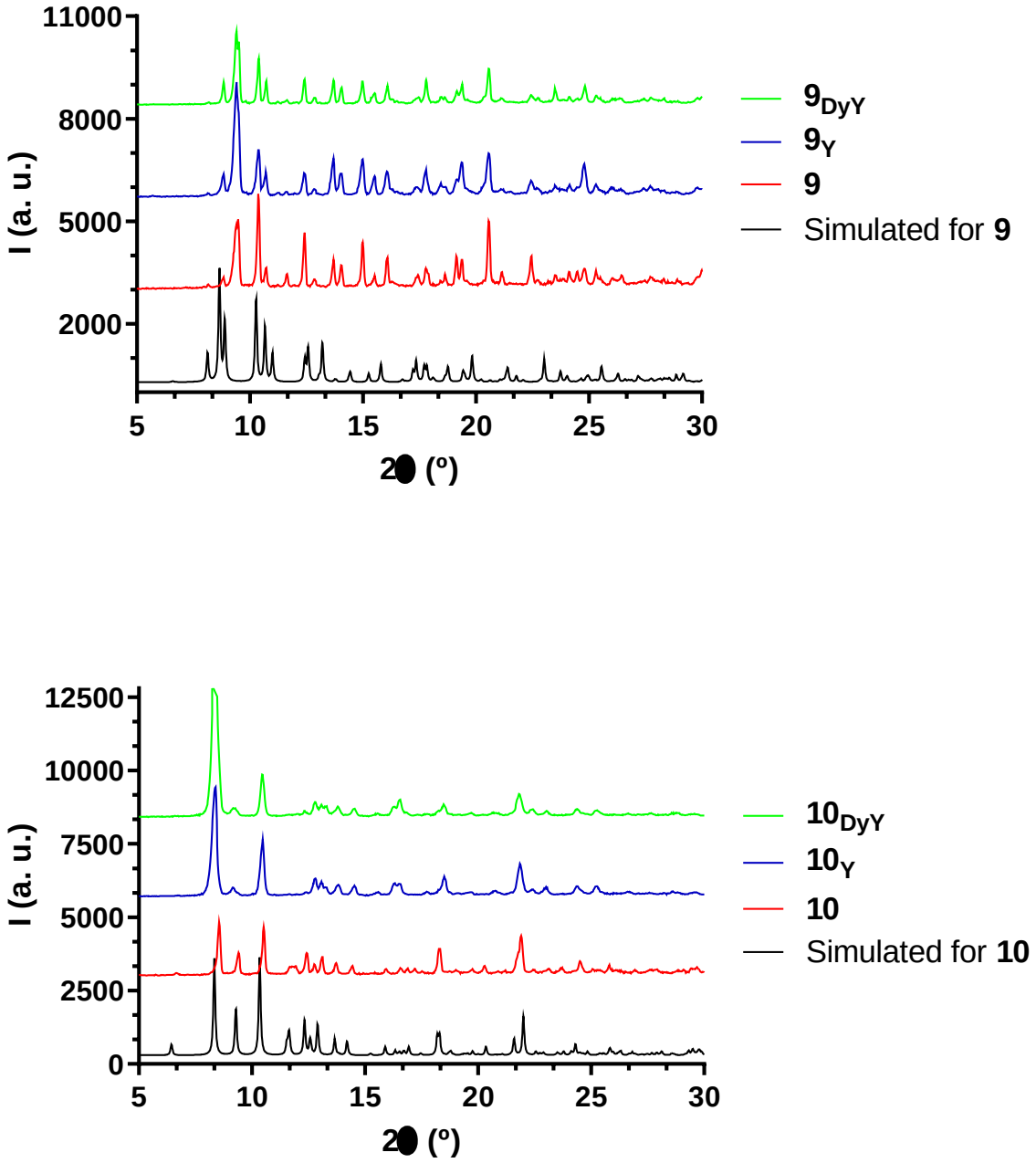

Figure A2.3.- For compounds **9** (top) and **10** (bottom), simulated pattern from single-crystal X-ray diffraction (black line) and experimental XRPD for Dy^{III} (red), Y^{III} (blue) and Dy^{III}:Y^{III} based (green) analogues.

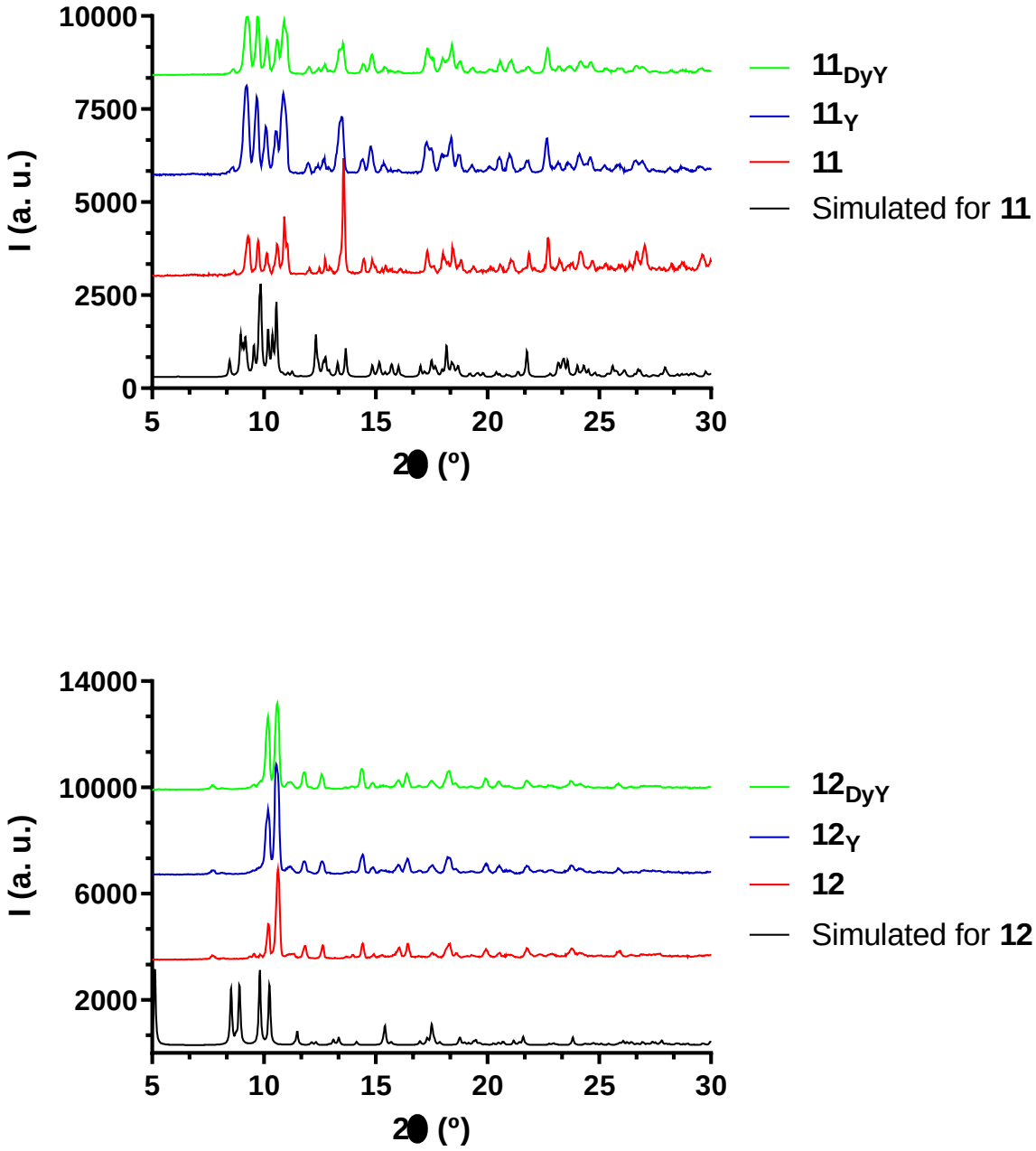

Figure A2.4.- For compounds **11** (top) and **12** (bottom), simulated pattern from single-crystal X-ray diffraction (black line) and experimental XRPD for Dy^{III} (red), Y^{III} (blue) and Dy^{III}:Y^{III} based (green) analogues.

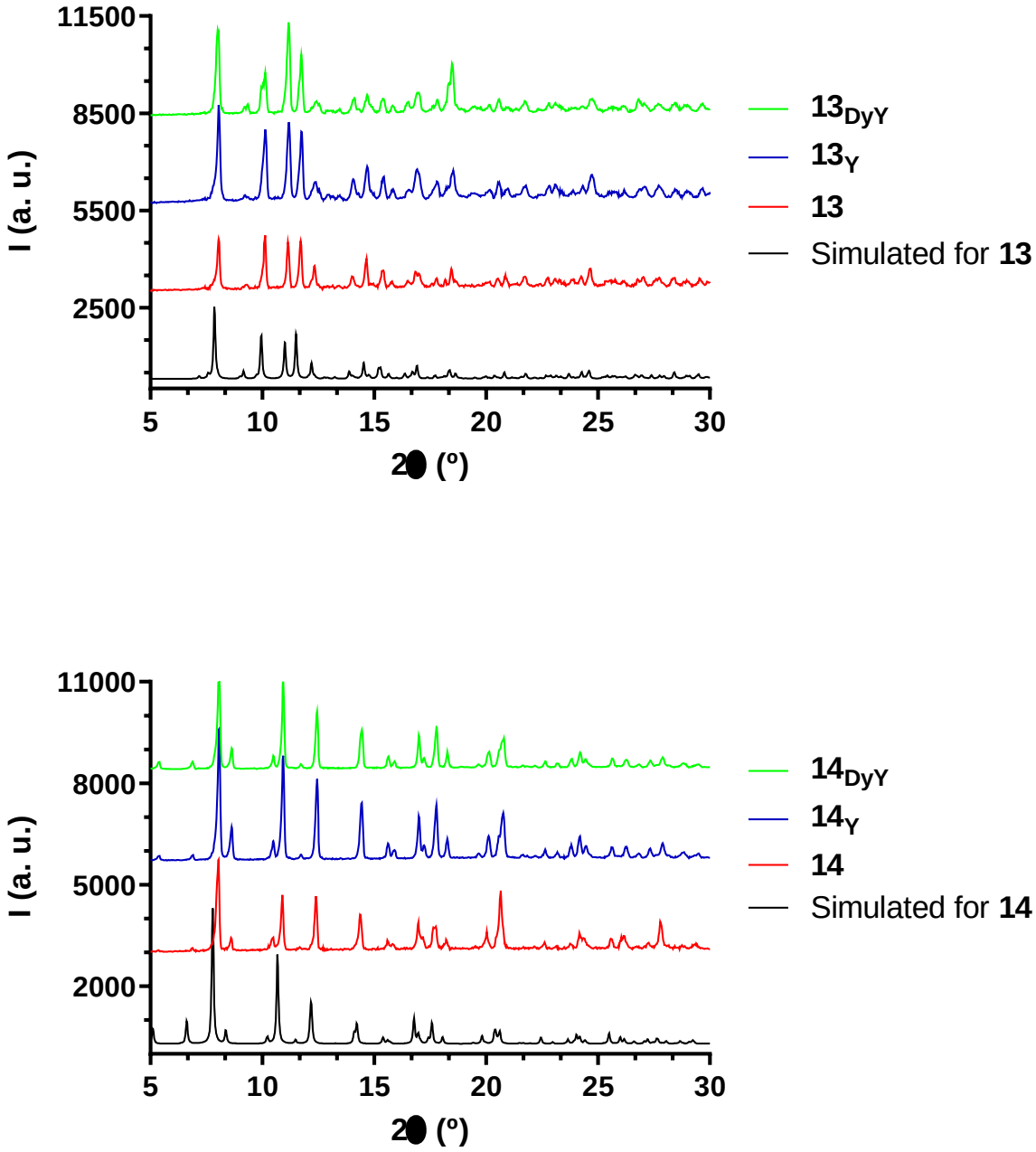

Figure A2.5.- For compounds **13** (top) and **14** (bottom), simulated pattern from single-crystal X-ray diffraction (black line) and experimental XRPD for Dy^{III} (red), Y^{III} (blue) and Dy^{III}:Y^{III} based (green) analogues.

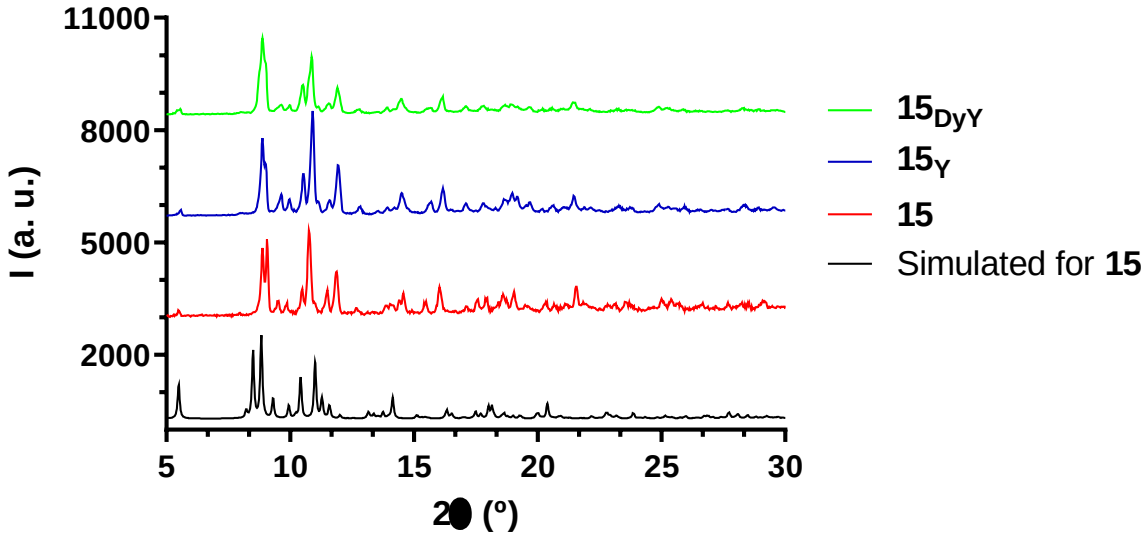

Figure A2.6.- For compound **15**, simulated pattern from single-crystal X-ray diffraction (black line) and experimental XRPD for Dy^{III} (red), Y^{III} (blue) and Dy^{III}:Y^{III} based (green) analogues.

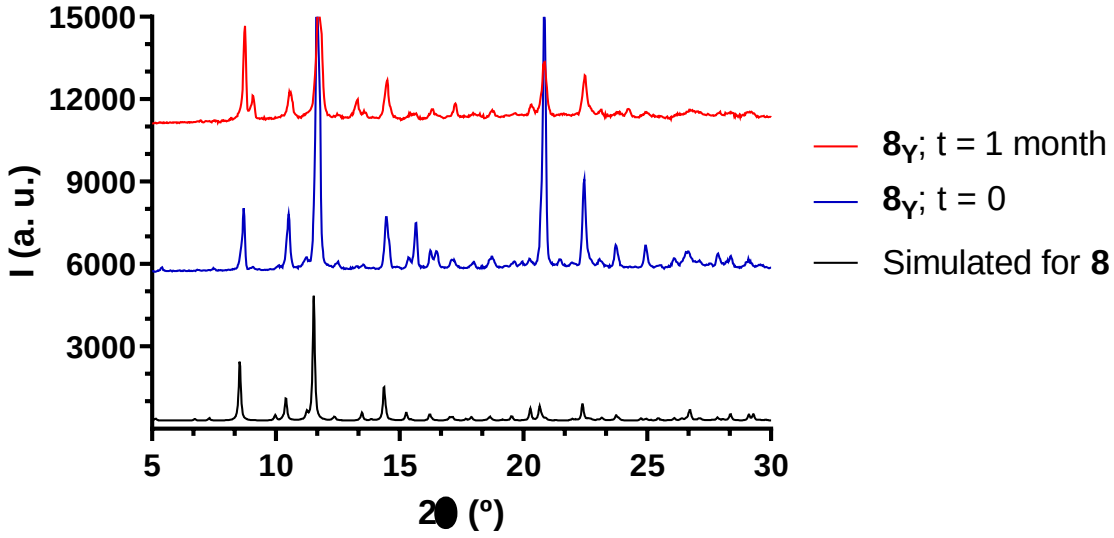

Figure A2.7.- For compound **8**, simulated pattern from single-crystal X-ray diffraction (black line) and experimental XRPD for $\mathbf{8_Y}$ once crystals were separated from mother liquor (blue) and the same sample of $\mathbf{8_Y}$ one month later (red).

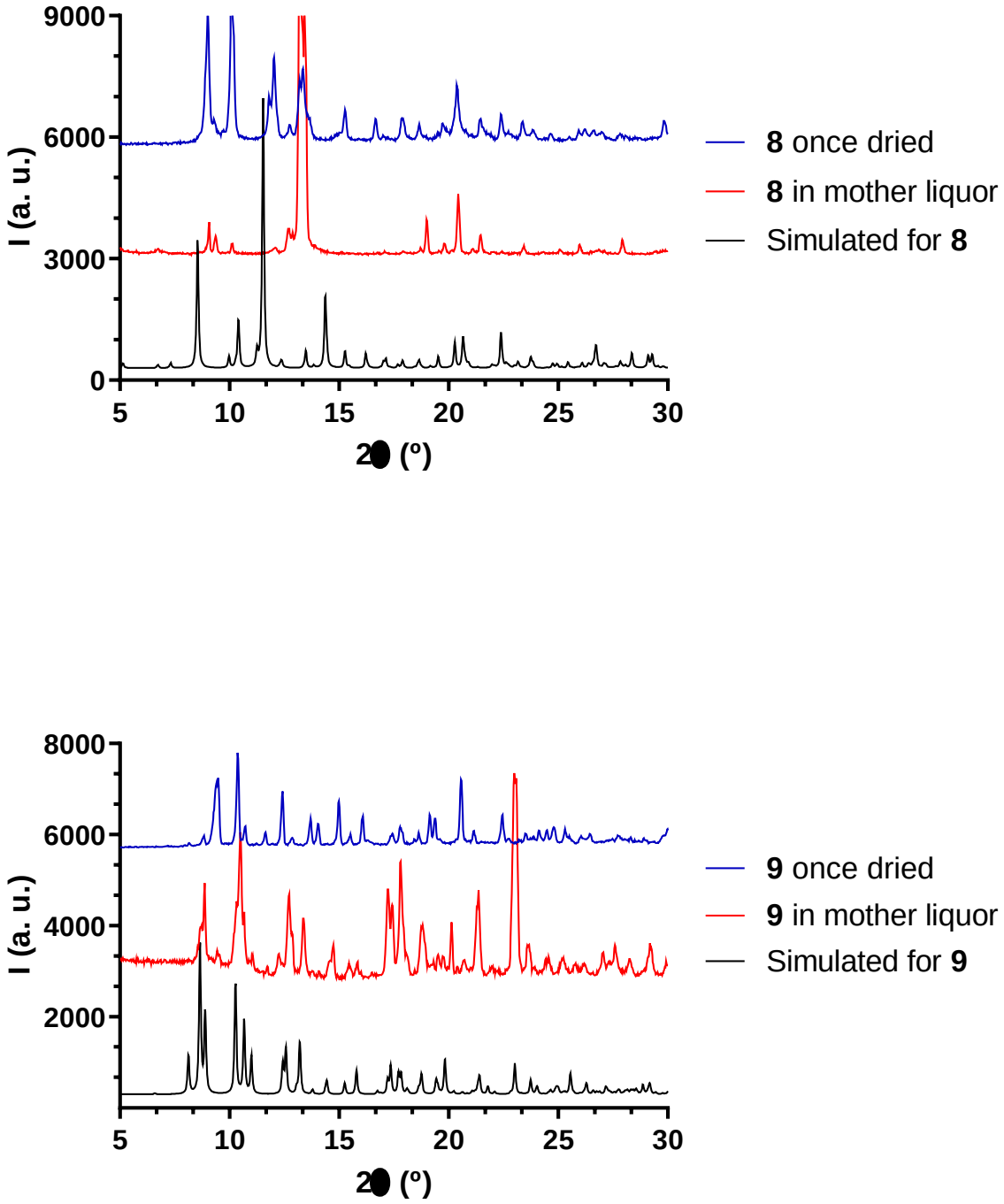

Figure A2.8.- Simulated pattern from single-crystal X-ray diffraction (black line), experimental XRPD in mother liquor (red line) and experimental XRPD once the product was dried (blue line) for **8** (top) and for **9** (bottom).

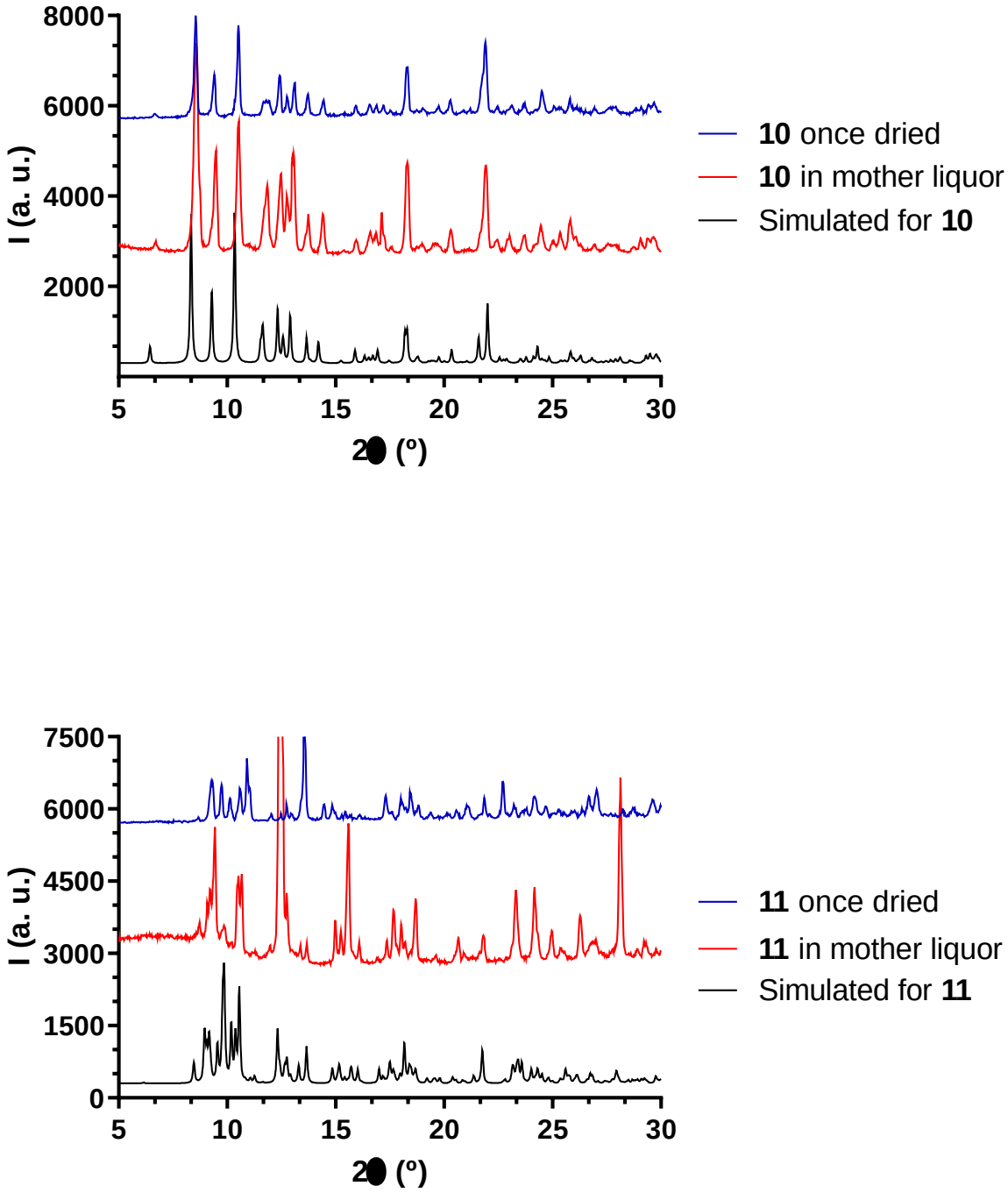

Figure A2.9.- Simulated pattern from single-crystal X-ray diffraction (black line), experimental XRPD in mother liquor (red line) and experimental XRPD once the product was dried (blue line) for **10** (top) and for **11** (bottom).

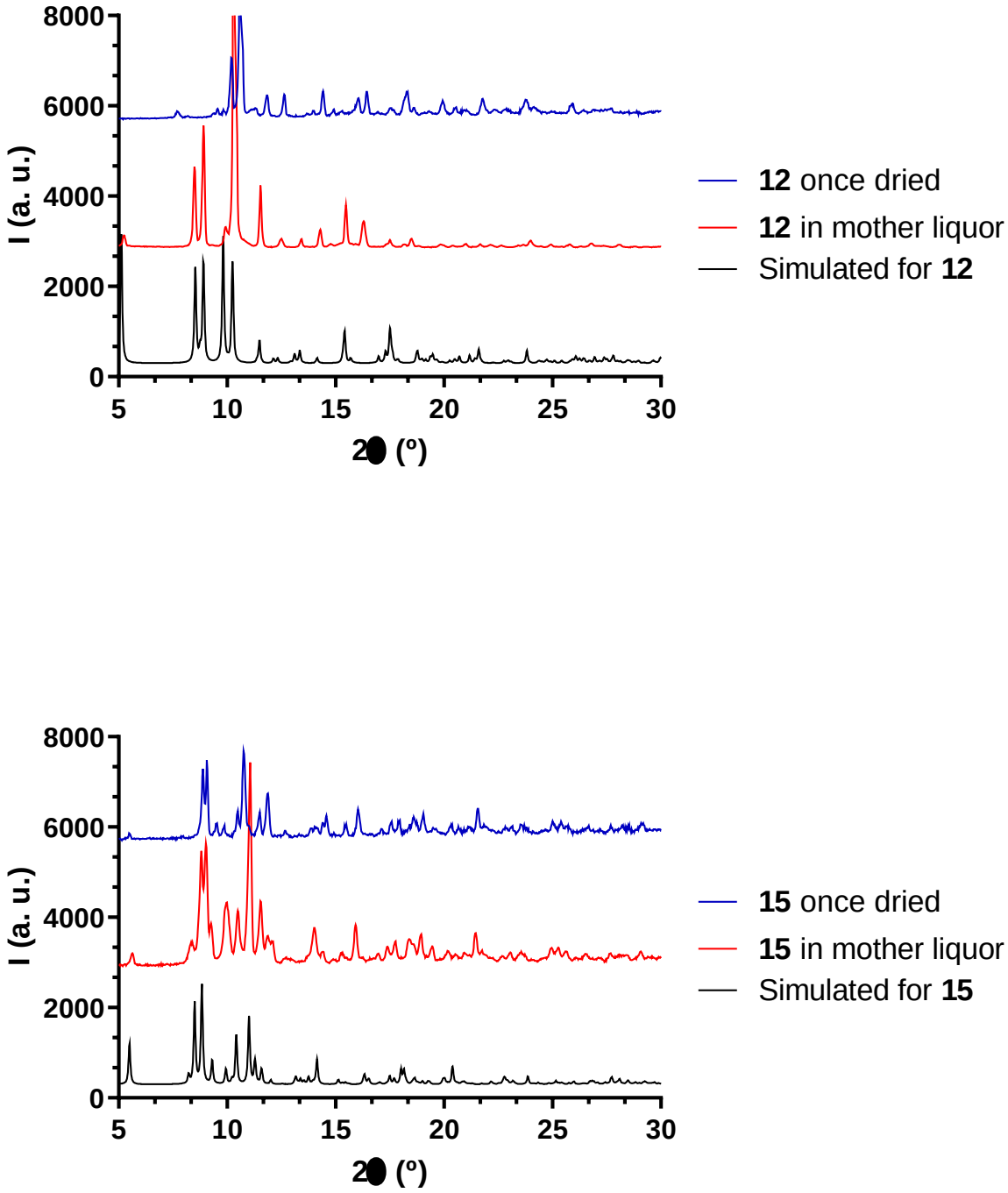

Figure A2.10.- Simulated pattern from single-crystal X-ray diffraction (black line), experimental XRPD in mother liquor (red line) and experimental XRPD once the product was dried (blue line) for **12** (top) and for **15** (bottom).

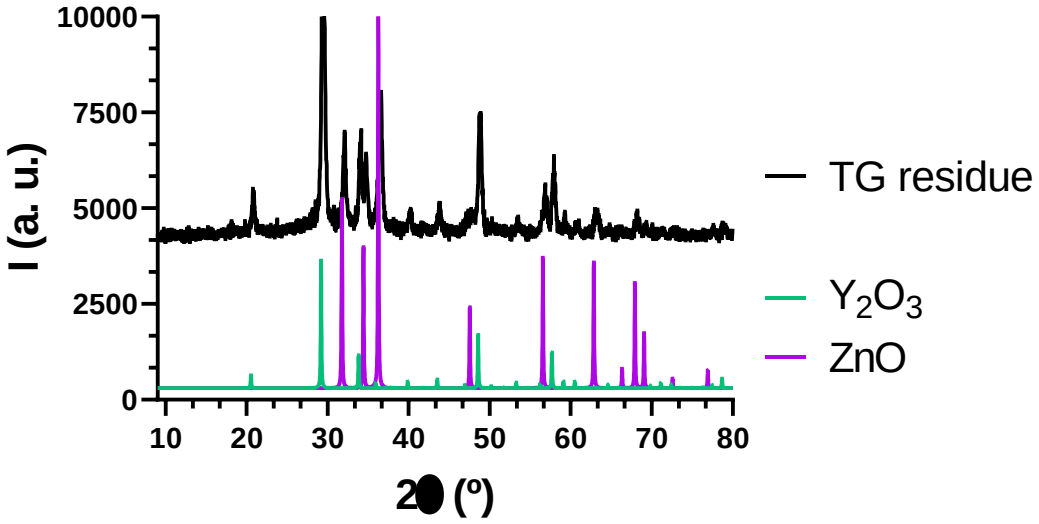

Figure A2.11.- Simulated patterns from single-crystal X-ray diffraction for ZnO (purple) and Y_2O_3 (turquoise) compared to the experimental XRPD of compound **9** after the thermogravimetric analysis (black line).

5. IR spectra.

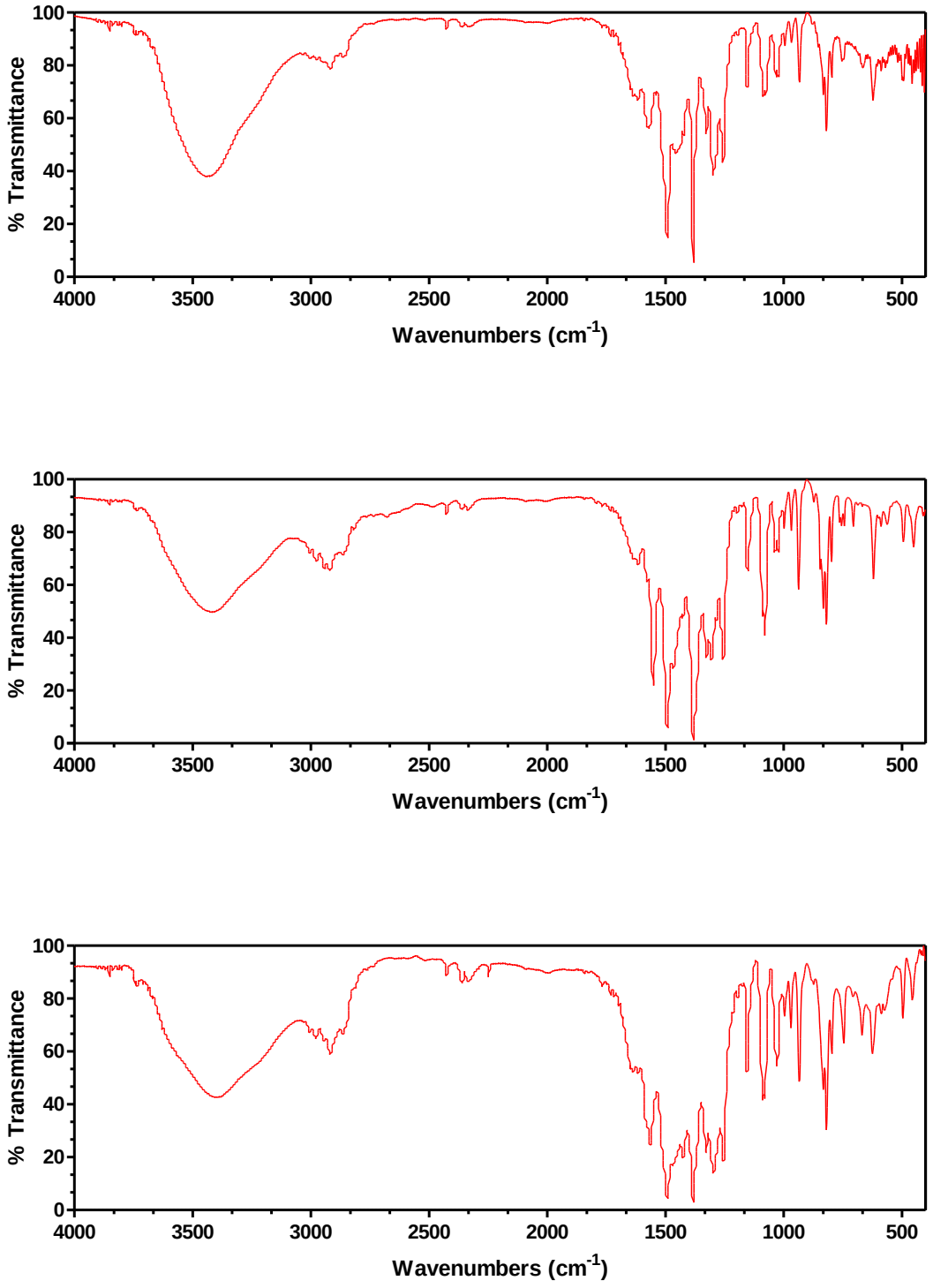

Figure A2.12.- IR spectra for compounds **0** (reference, top), **7** (middle) and **8** (bottom).

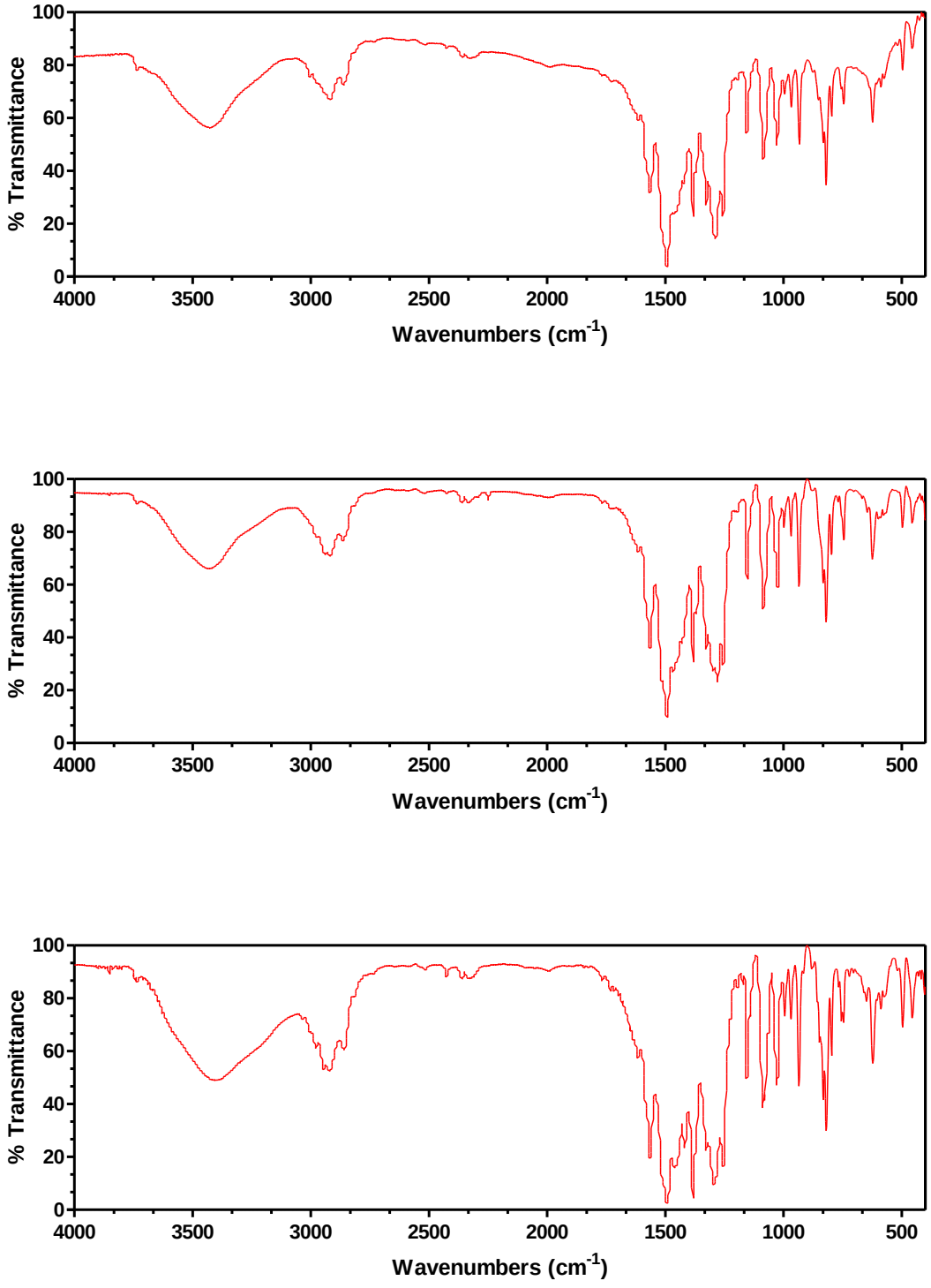

Figure A2.13.- IR spectra for compounds **9** (top), **10** (middle) and **11** (bottom).

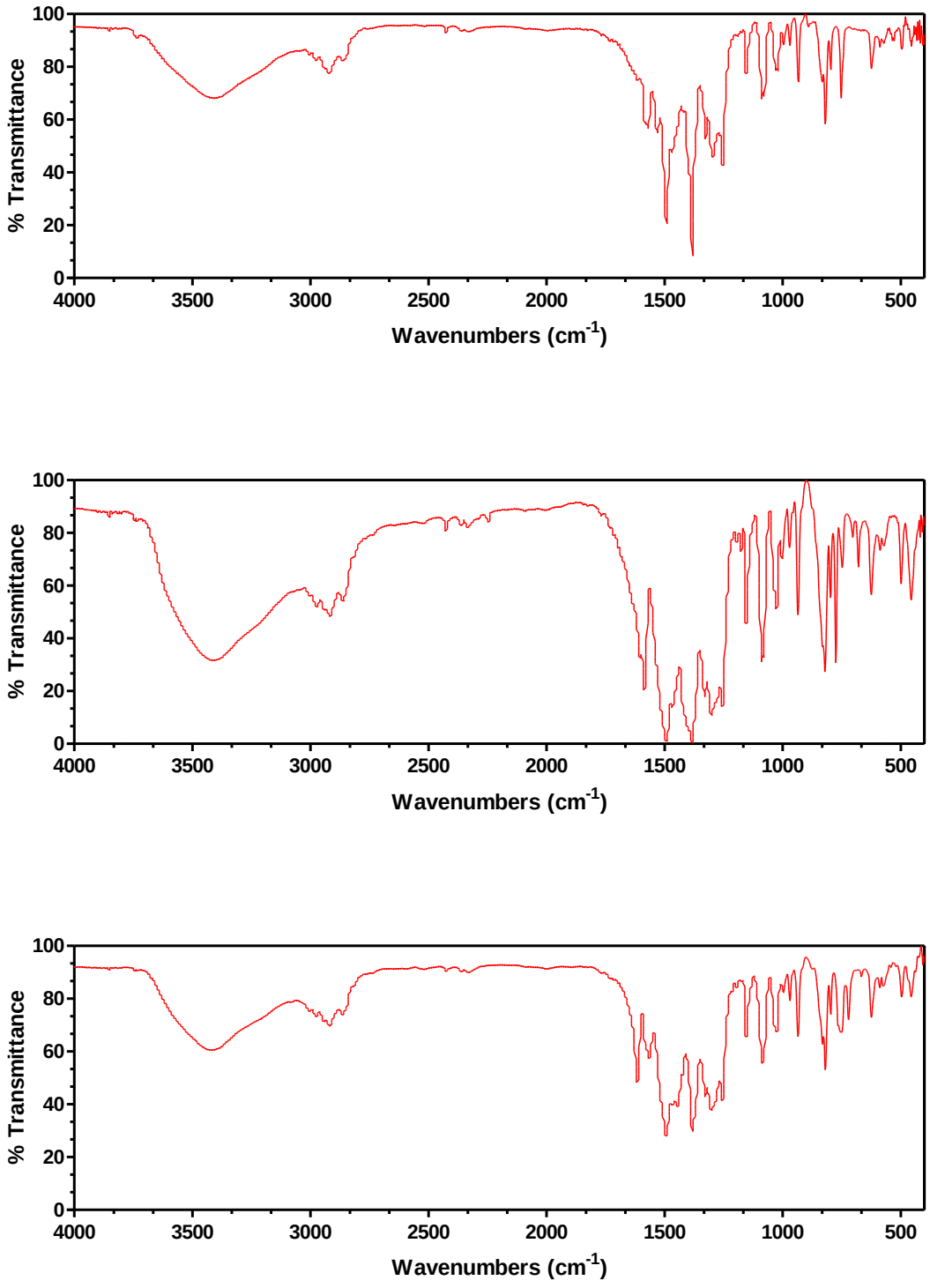

Figure A2.14.- IR spectra for compounds **12** (top), **13** (middle) and **14** (bottom).

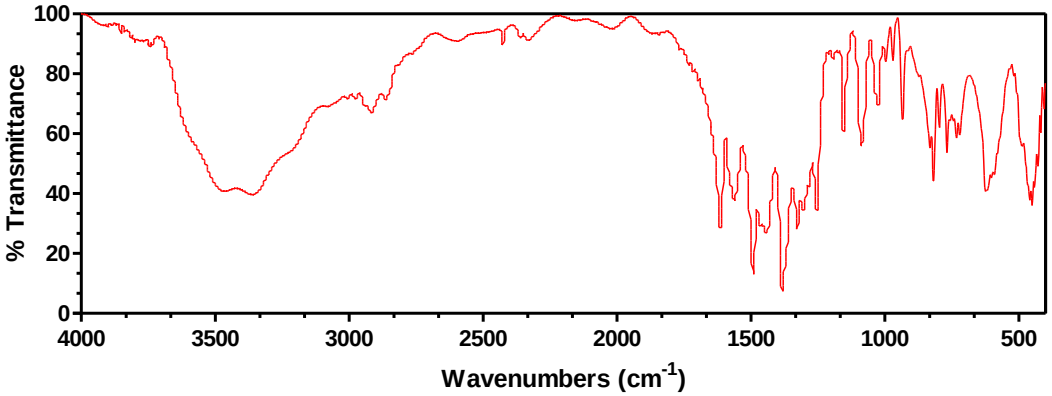

Figure A2.15.- IR spectra for compound **15**.

6. Thermogravimetric Analysis.

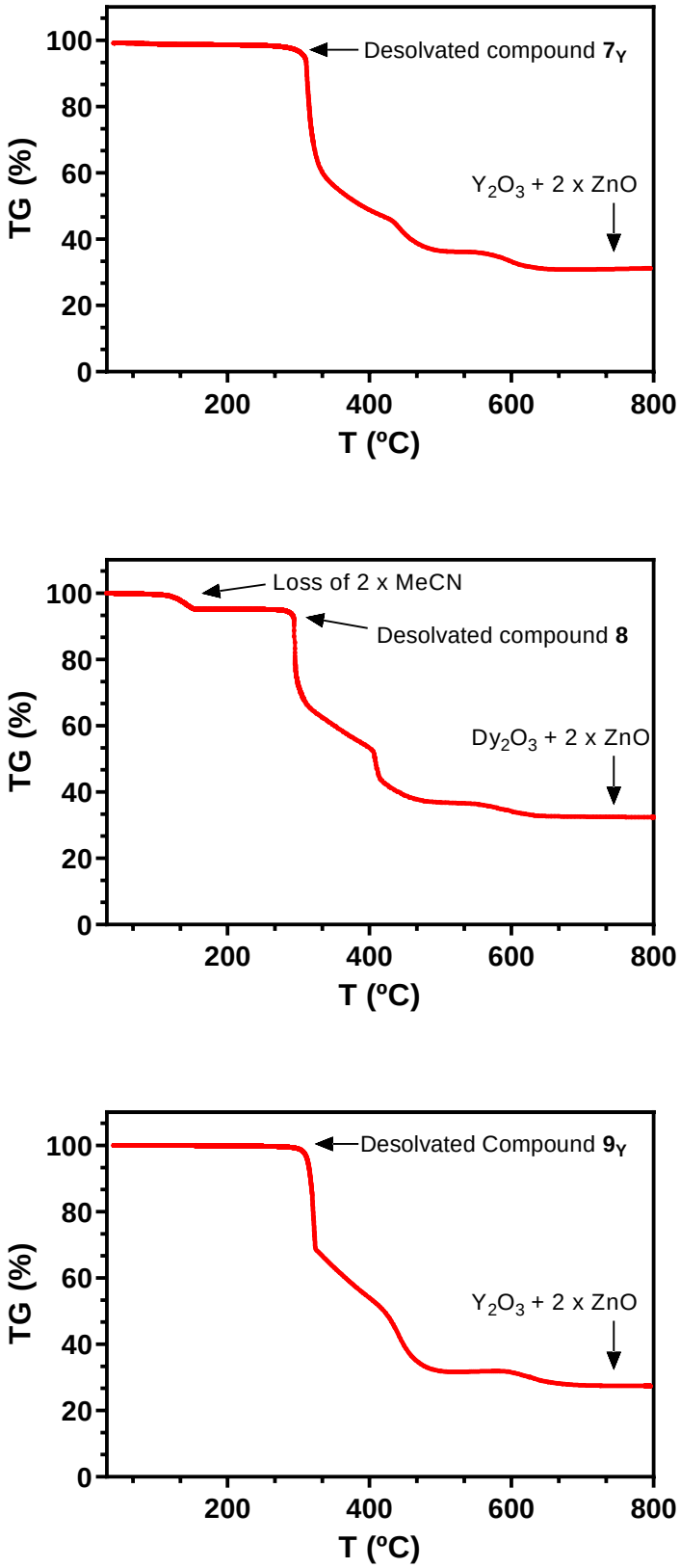

Figure A2.16.- Thermogravimetric analyses of compounds $\mathbf{7_Y}$ (top), **8** (middle) and $\mathbf{9_Y}$ (bottom).

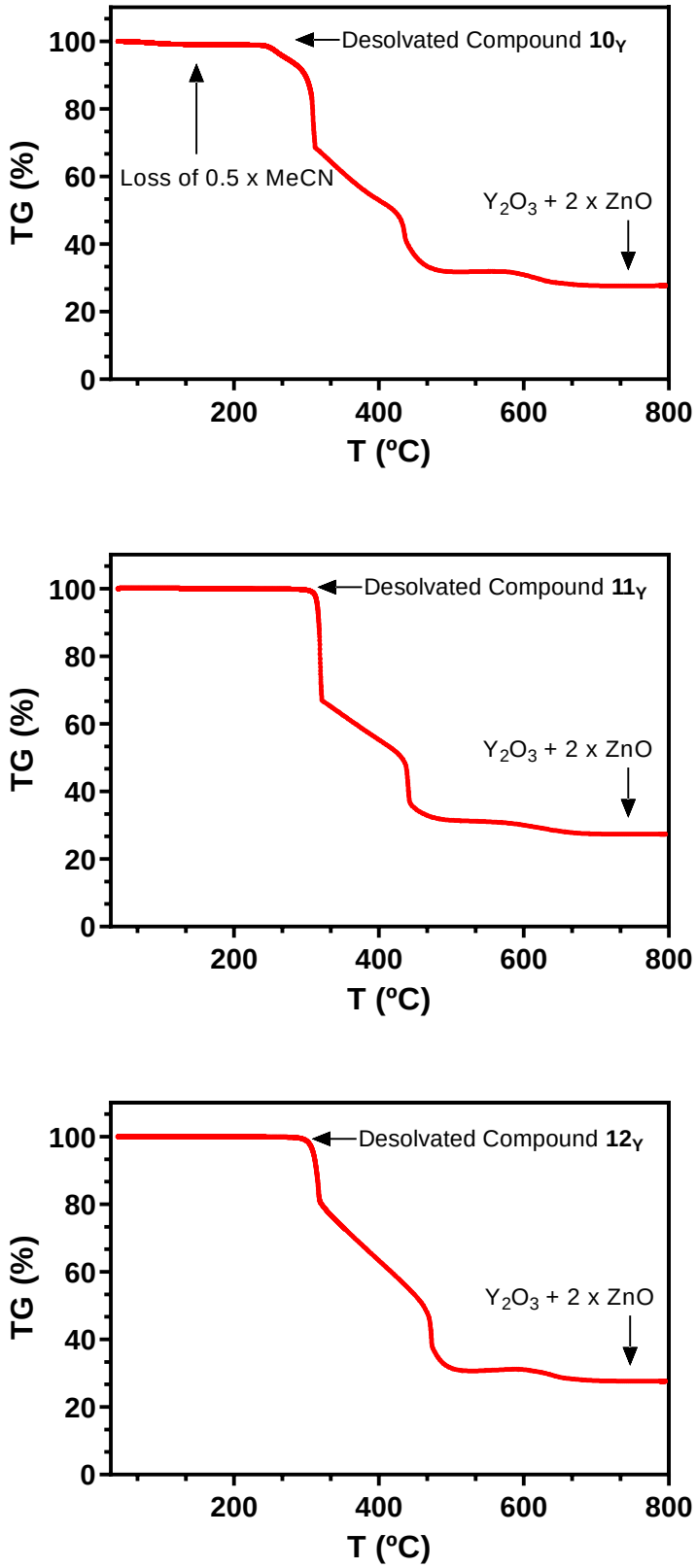

Figure A2.17.- Thermogravimetric analyses of compounds **10**$_{Y}$ (top), **11**$_{Y}$ (middle) and **12**$_{Y}$ (bottom).

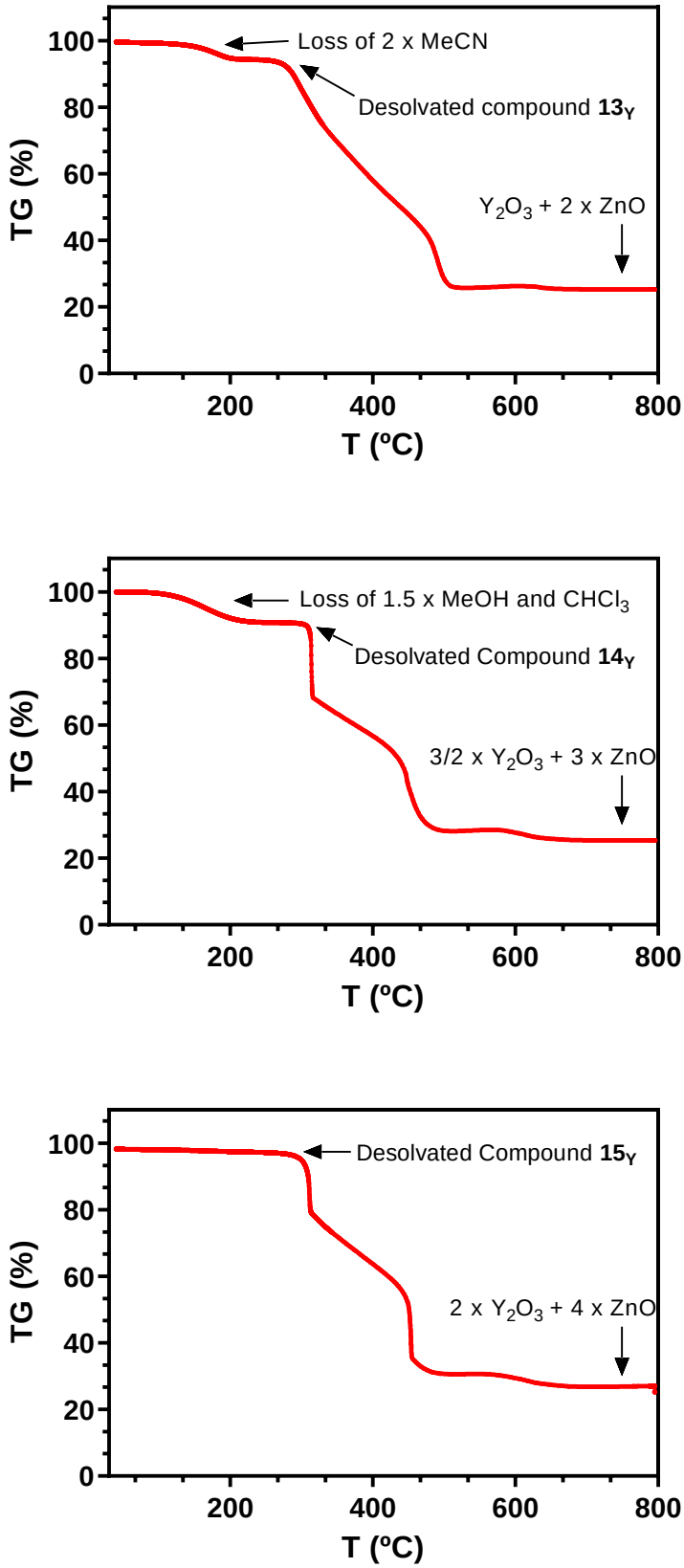

Figure A2.18.- Thermogravimetric analysis of compounds **13$_Y$** (top), **14$_Y$** (middle) and **15$_Y$** (bottom).

7. Magnetic Measurements

Static magnetic properties

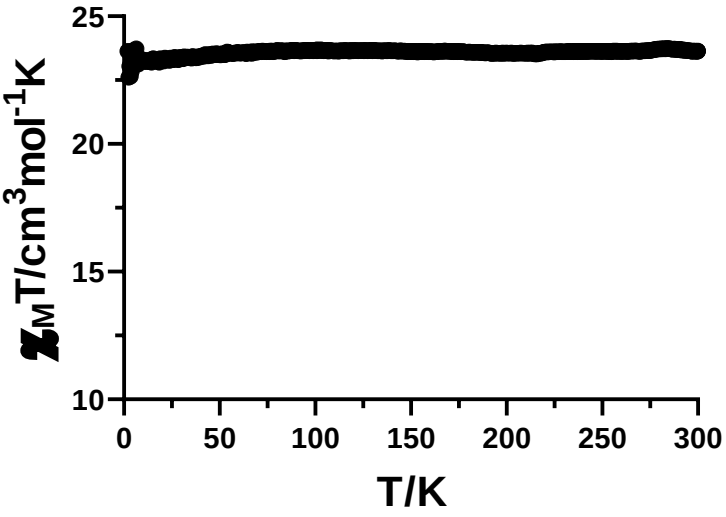

Figure A2.19.- Temperature dependence of the $\chi_M T$ product at 1000 Oe for complex **14**$_{Gd}$.

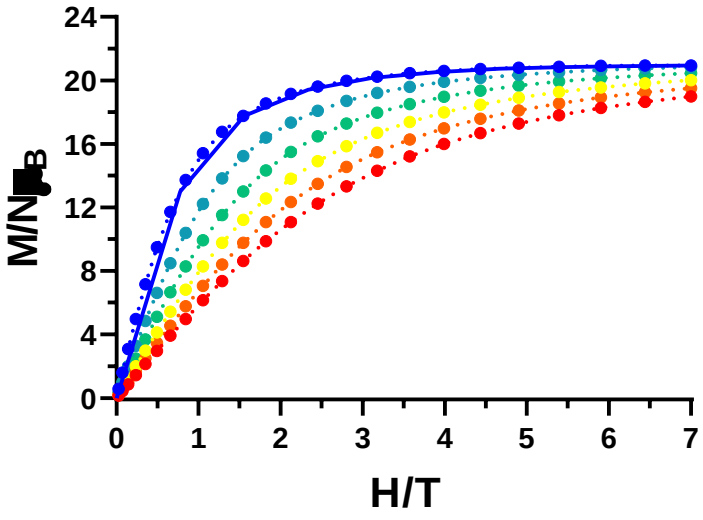

Figure A2.20.- Field dependence of the magnetization in the 2-7 K temperature range for complex **14**$_{Gd}$. The blue line shows the *M(H)* curve reproduced by the Brillouin function at 2.0 K. Dashed solid lines are a guide to the eye.

Dynamic magnetic properties

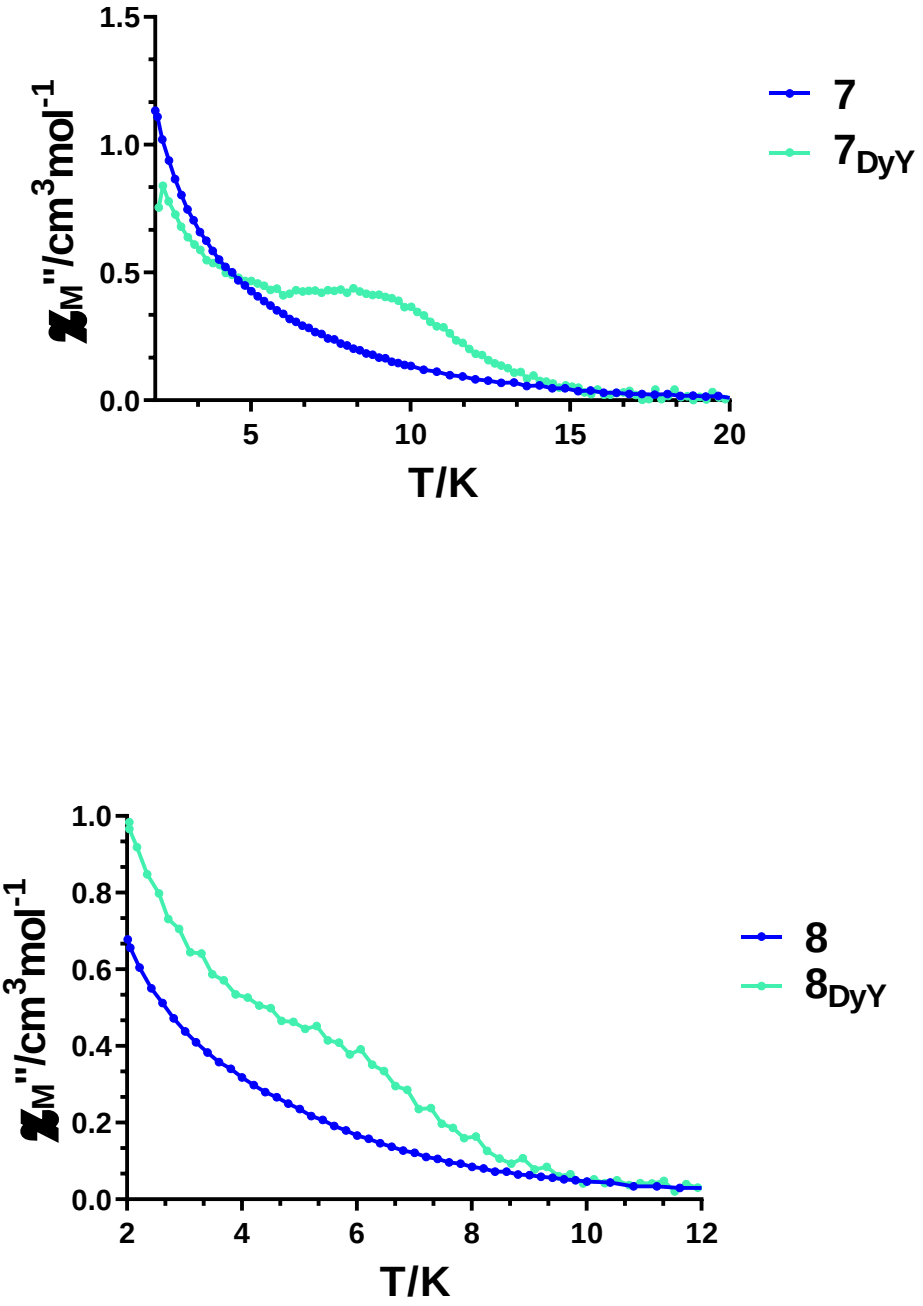

Figure A2.21.-Temperature dependence of the out-of-phase χ_M'' susceptibility signals for complexes **7-7$_{DyY}$** (top) and **8-8$_{DyY}$** (bottom) under zero applied *dc* field. An oscillating field of 3.5 Oe was used with a frequency of 10000 Hz. Noteworthy, the χ_M'' values of the diluted samples have been arbitrarily multiplied in order to be comparable.

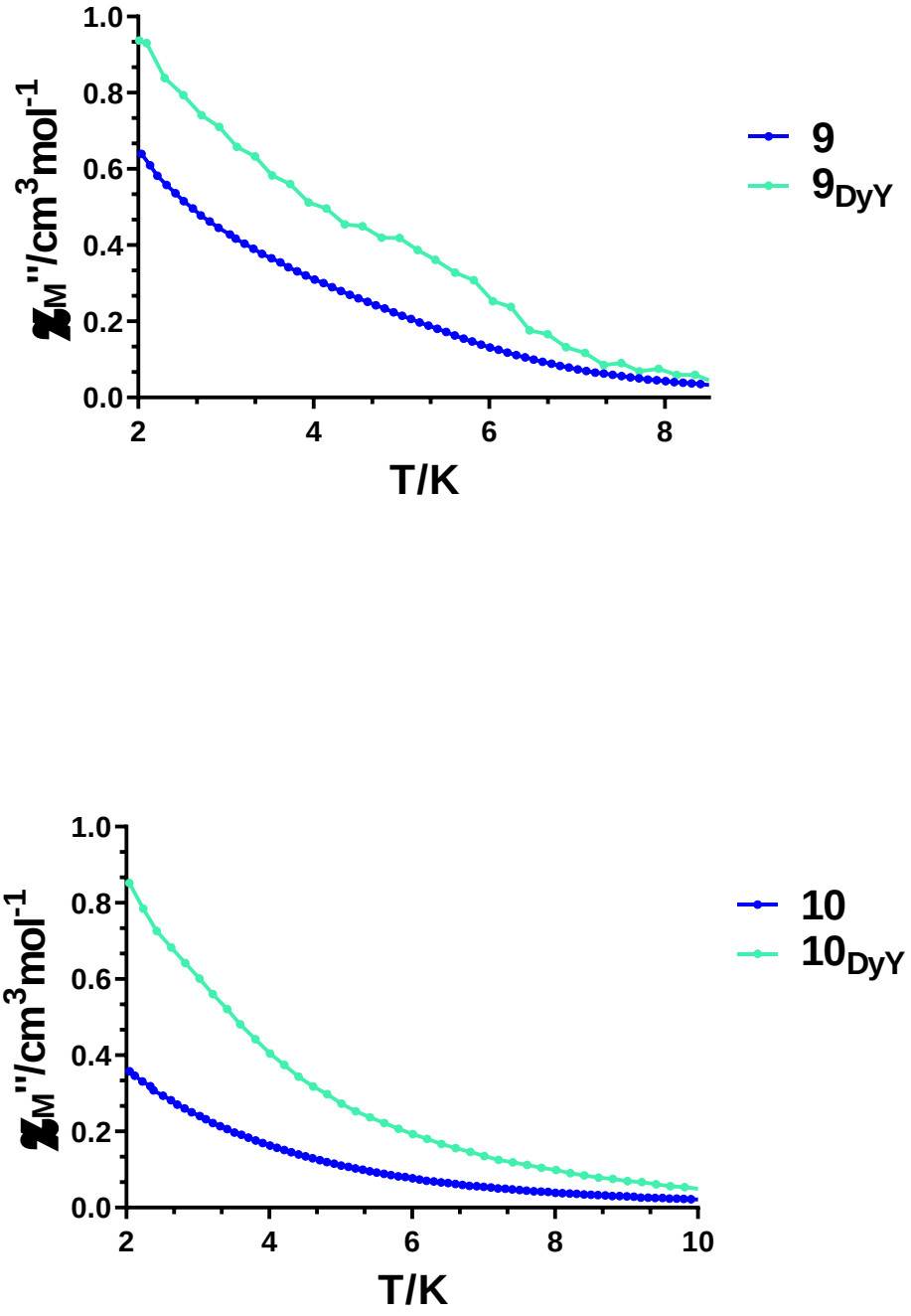

Figure A2.22.-Temperature dependence of the out-of-phase χ_M'' susceptibility signals for complexes **9-9$_{DyY}$** (top) and **10-10$_{DyY}$** (bottom) under zero applied *dc* field. An oscillating field of 3.5 Oe was used with a frequency of 10000 Hz. Noteworthy, the χ_M'' values of the diluted samples have been arbitrarily multiplied in order to be comparable.

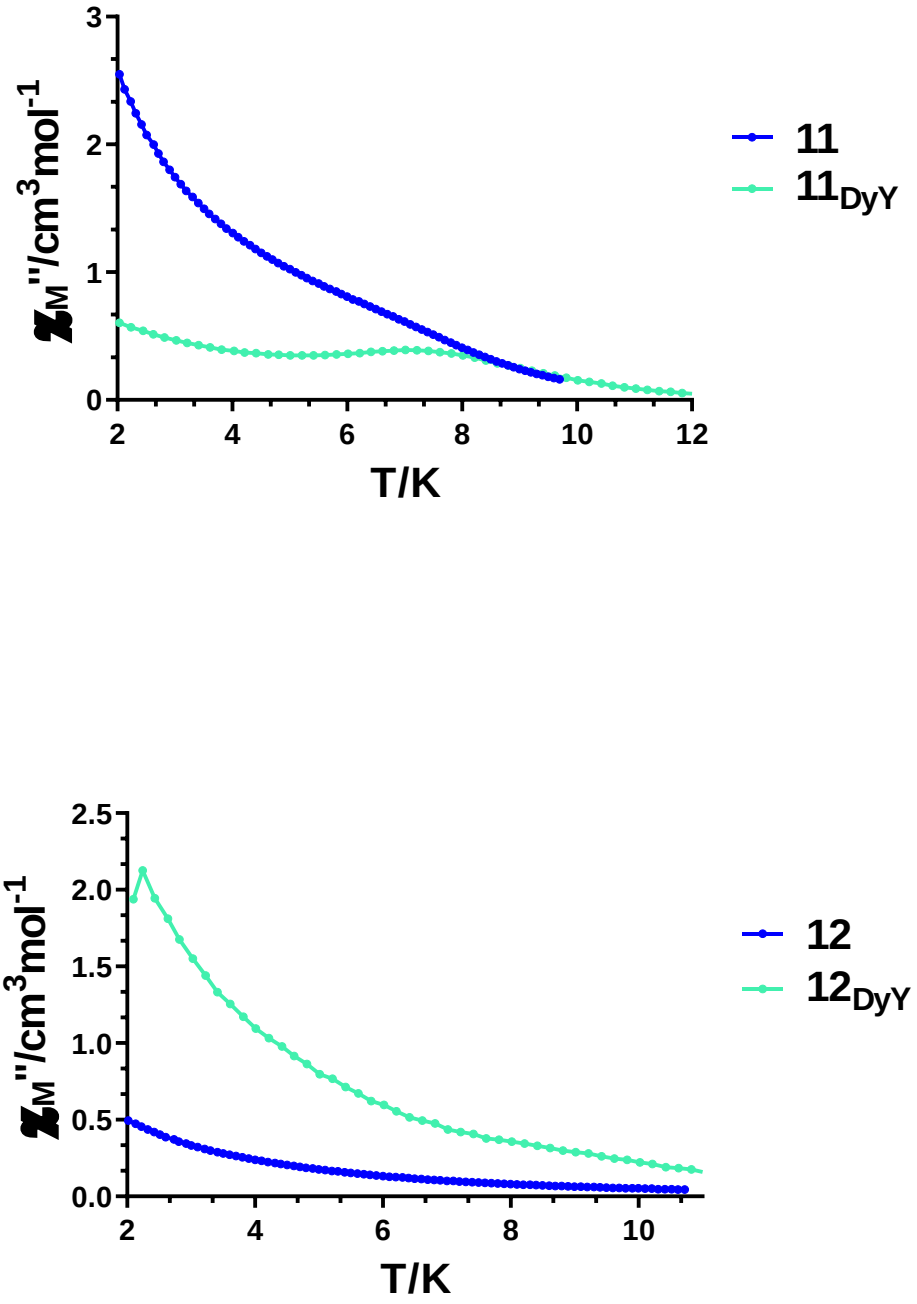

Figure A2.23.-Temperature dependence of the out-of-phase χ_M'' susceptibility signals for complexes **11-11$_{DyY}$** (top) and **12-12$_{DyY}$** (bottom) under zero applied *dc* field. An oscillating field of 3.5 Oe was used with a frequency of 10000 Hz. Noteworthy, the χ_M'' values of the diluted samples have been arbitrarily multiplied in order to be comparable.

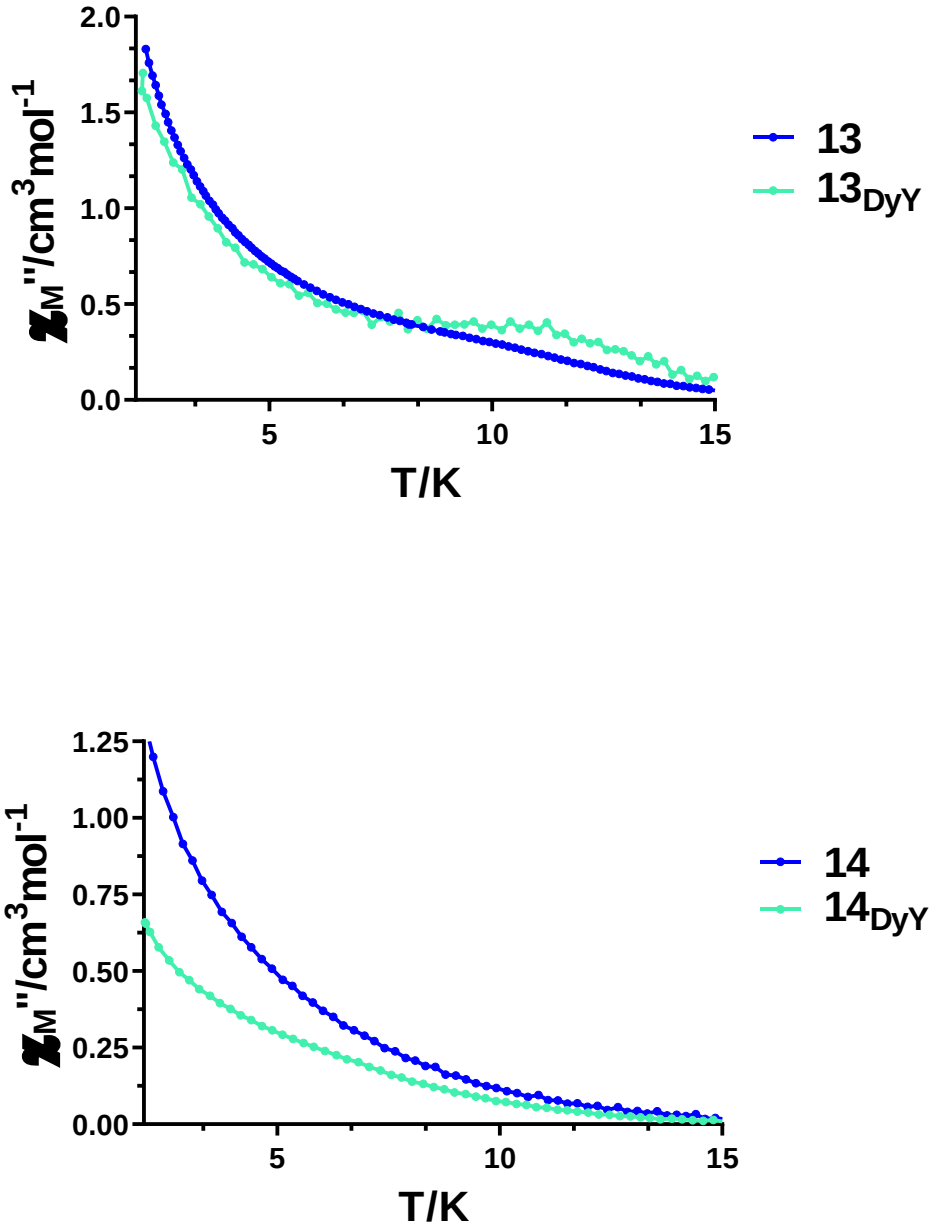

Figure A2.24.-Temperature dependence of the out-of-phase χ_M'' susceptibility signals for complexes **13-13$_{DyY}$** (top) and **14-14$_{DyY}$** (bottom) under zero applied *dc* field. An oscillating field of 3.5 Oe was used with a frequency of 10000 Hz. Noteworthy, the χ_M'' values of the diluted samples have been arbitrarily multiplied in order to be comparable.

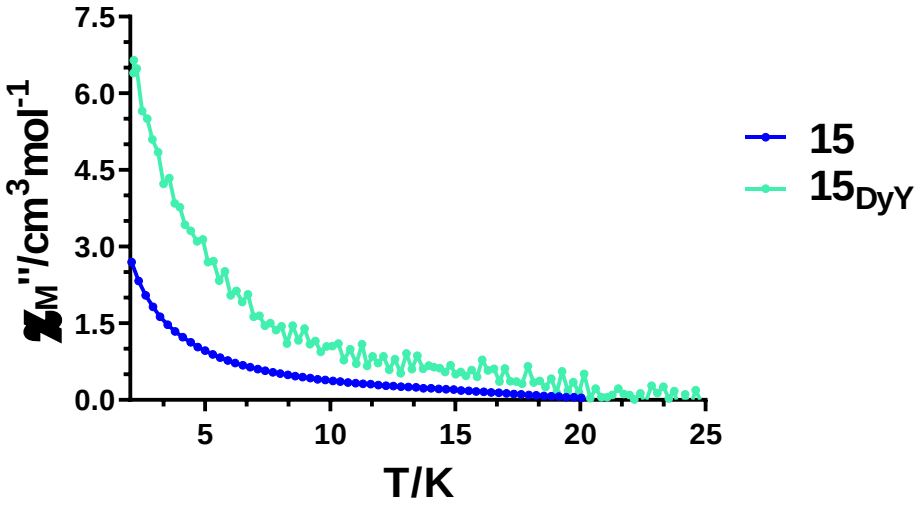

Figure A2.25.-Temperature dependence of the out-of-phase χ_M'' susceptibility signals for complexes **15-15$_{DyY}$** under zero applied *dc* field. An oscillating field of 3.5 Oe was used with a frequency of 10000 Hz. Noteworthy, the χ_M'' values of the diluted sample have been arbitrarily multiplied in order to be comparable.

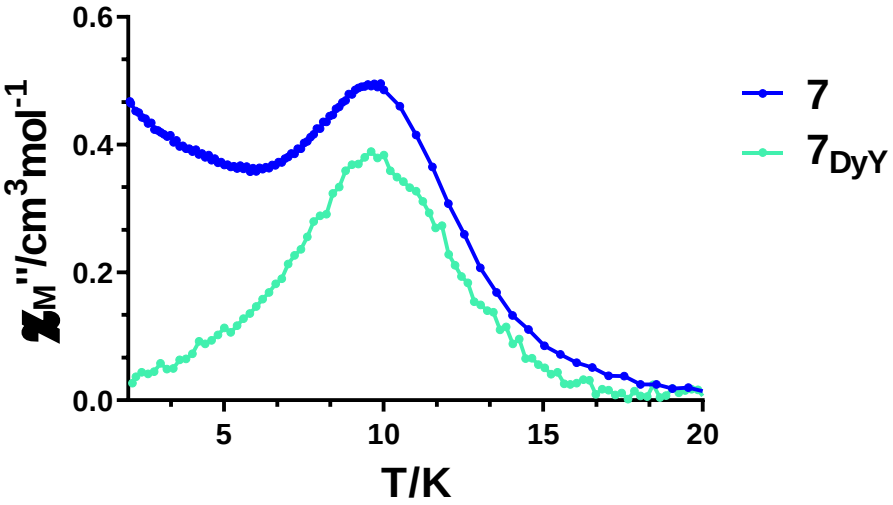

Figure A2.26.-Temperature dependence of the out-of-phase χ_M'' susceptibility signals for complexes **7-7$_{DyY}$** under an applied field of 1000 Oe. An oscillating field of 3.5 Oe was used with a frequency of 10000 Hz. Noteworthy, the χ_M'' values of the diluted sample have been arbitrarily multiplied in order to be comparable.

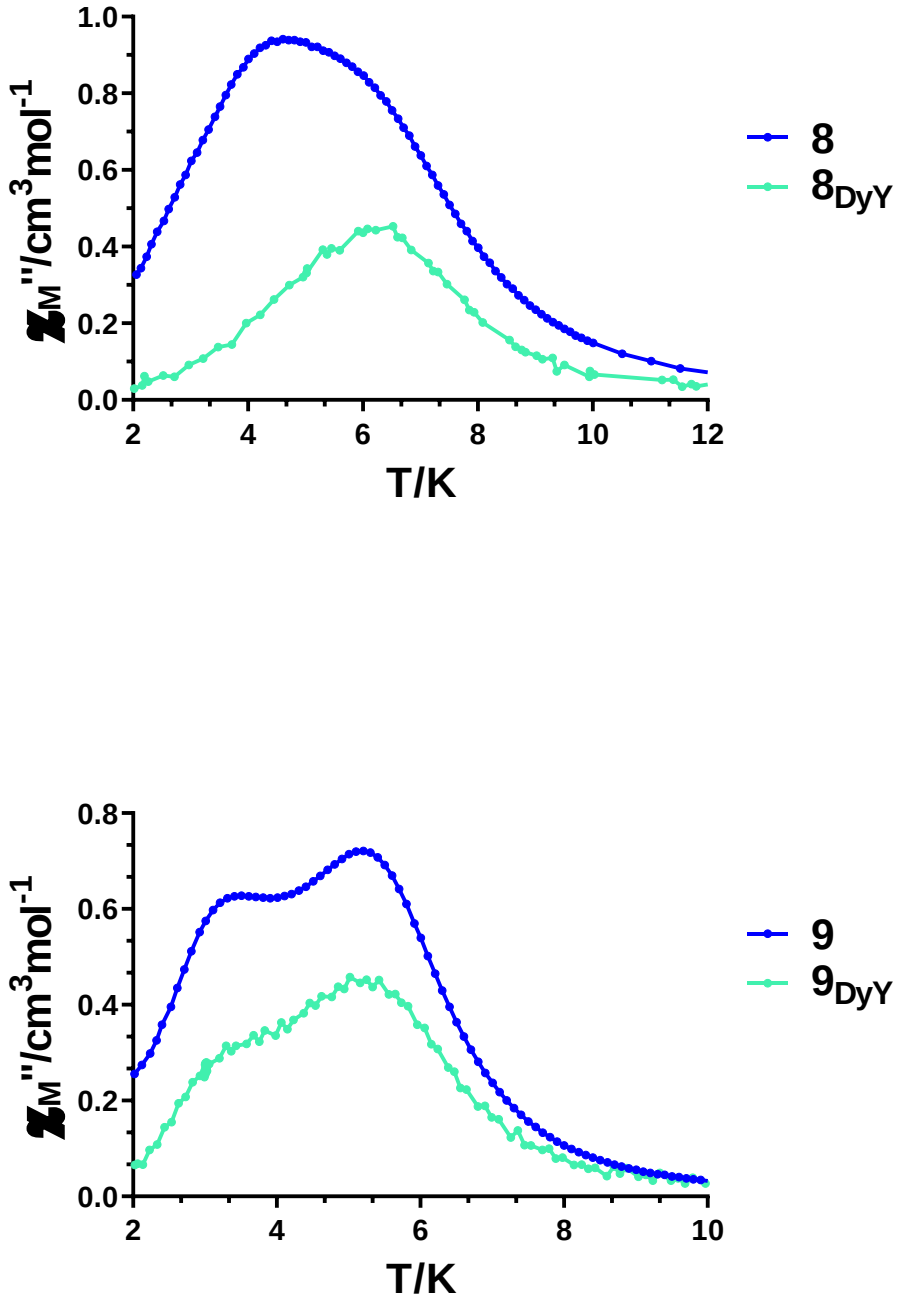

Figure A2.27.-Temperature dependence of the out-of-phase χ_M'' susceptibility signals for complexes **8-8$_{DyY}$** (top) and **9-9$_{DyY}$** (bottom) under an applied field of 1000 Oe. An oscillating field of 3.5 Oe was used with a frequency of 10000 Hz. Noteworthy, the χ_M'' values of the diluted samples have been arbitrarily multiplied in order to be comparable.

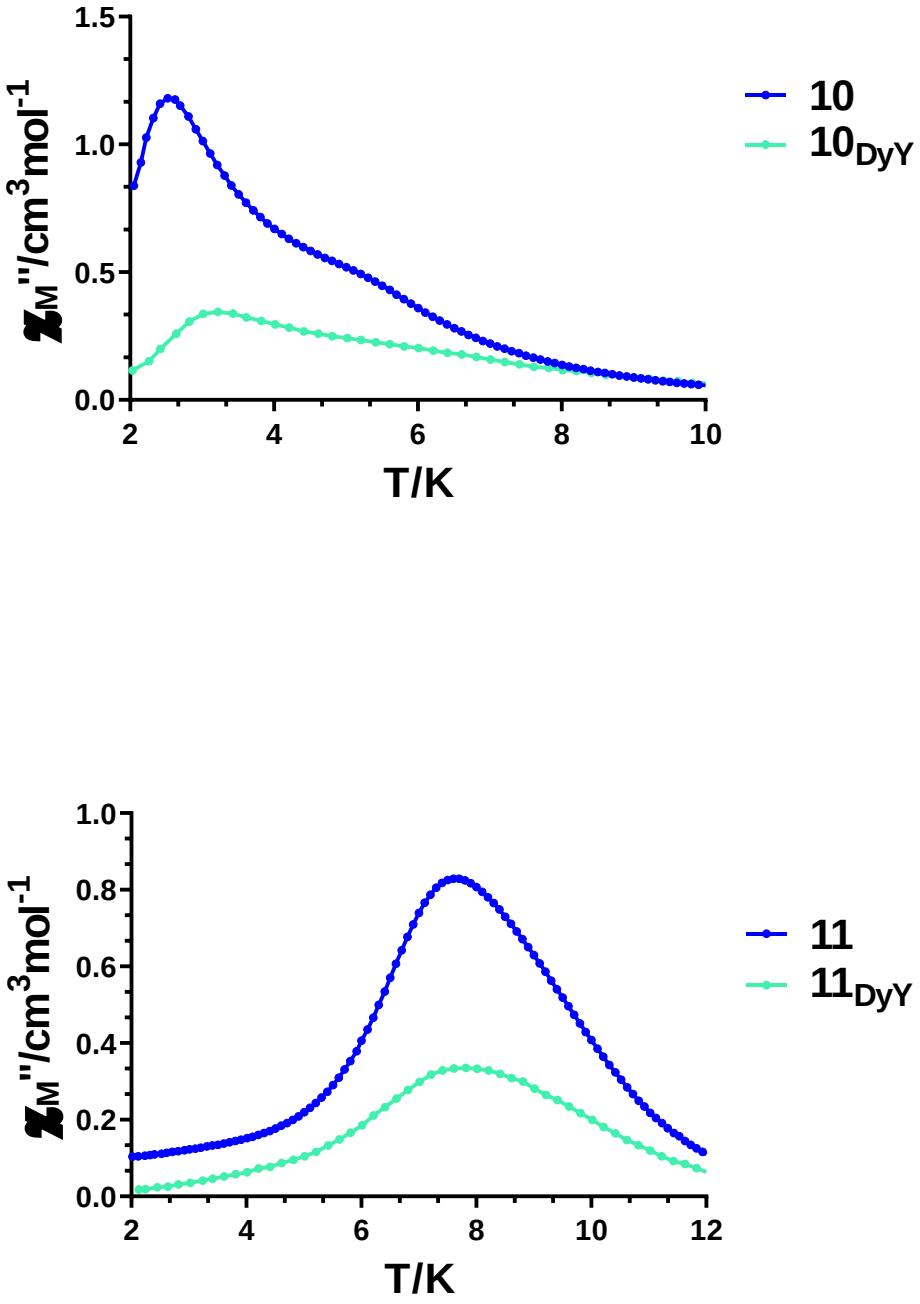

Figure A2.28.-Temperature dependence of the out-of-phase χ_M'' susceptibility signals for complexes **10-10$_{DyY}$** (top) and **11-11$_{DyY}$** (bottom) under an applied field of 1000 Oe. An oscillating field of 3.5 Oe was used with a frequency of 10000 Hz. Noteworthy, the χ_M'' values of the diluted samples have been arbitrarily multiplied in order to be comparable.

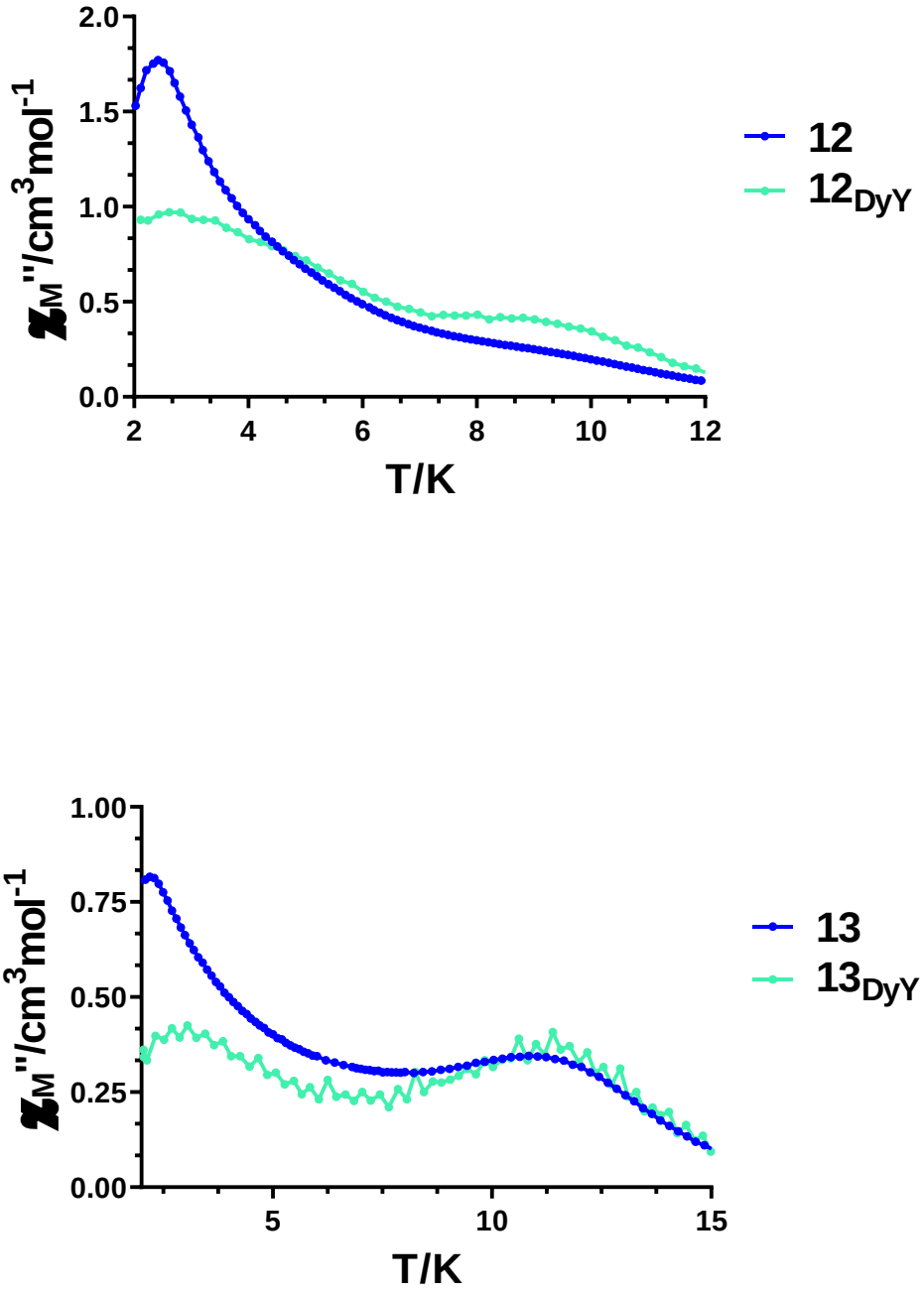

Figure A2.29.-Temperature dependence of the out-of-phase χ_M'' susceptibility signals for complexes **12-12$_{DyY}$** (top) and **13-13$_{DyY}$** (bottom) under an applied field of 1000 Oe. An oscillating field of 3.5 Oe was used with a frequency of 10000 Hz. Noteworthy, the χ_M'' values of the diluted samples have been arbitrarily multiplied in order to be comparable.

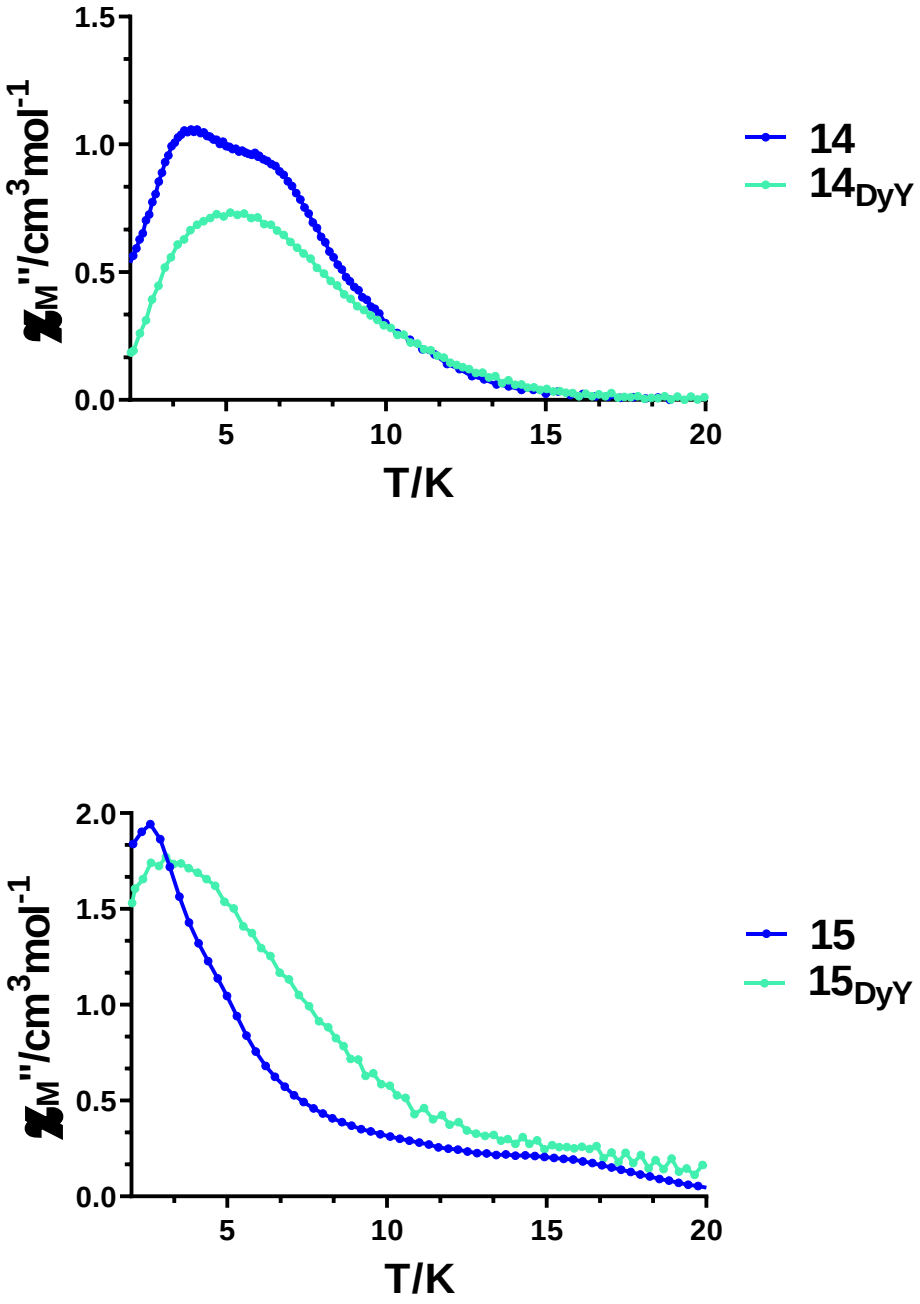

Figure A2.30.-Temperature dependence of the out-of-phase χ_M'' susceptibility signals for complexes **14-14$_{DyY}$** (top) and **15-15$_{DyY}$** (bottom) under an applied field of 1000 Oe. An oscillating field of 3.5 Oe was used with a frequency of 10000 Hz. Noteworthy, the χ_M'' values of the diluted samples have been arbitrarily multiplied in order to be comparable.

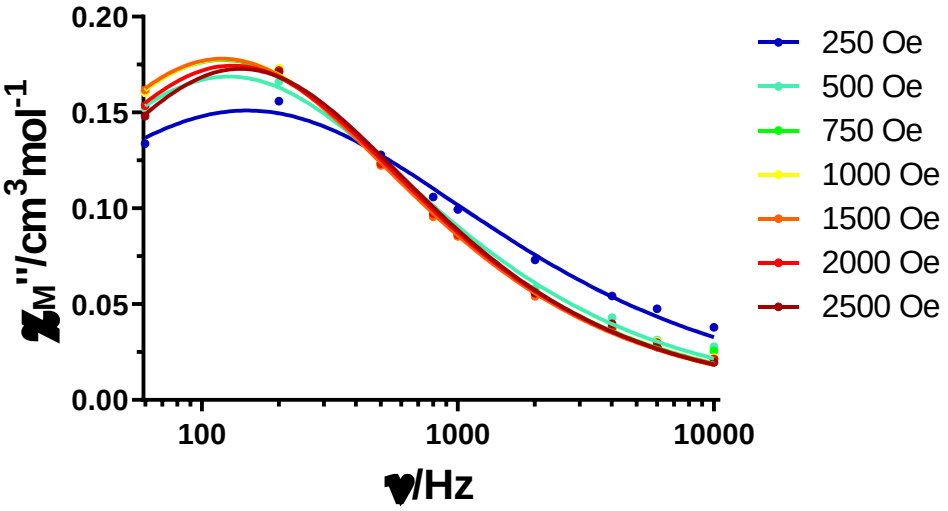

Figure A2.31.- Field dependence of the out-of-phase signal *vs* frequency at 5.2 K for **7**$_{DyY}$.

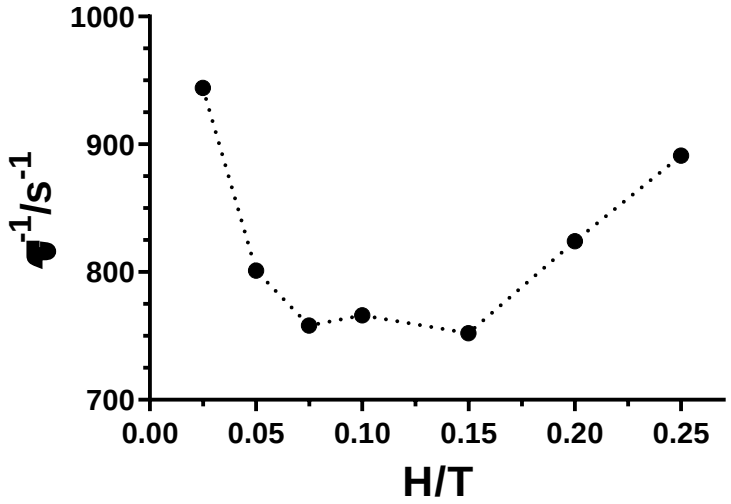

Figure A2.32.- The inverse of the relaxation times obtained at different magnetic fields at 5.2 K for **7**$_{DyY}$.

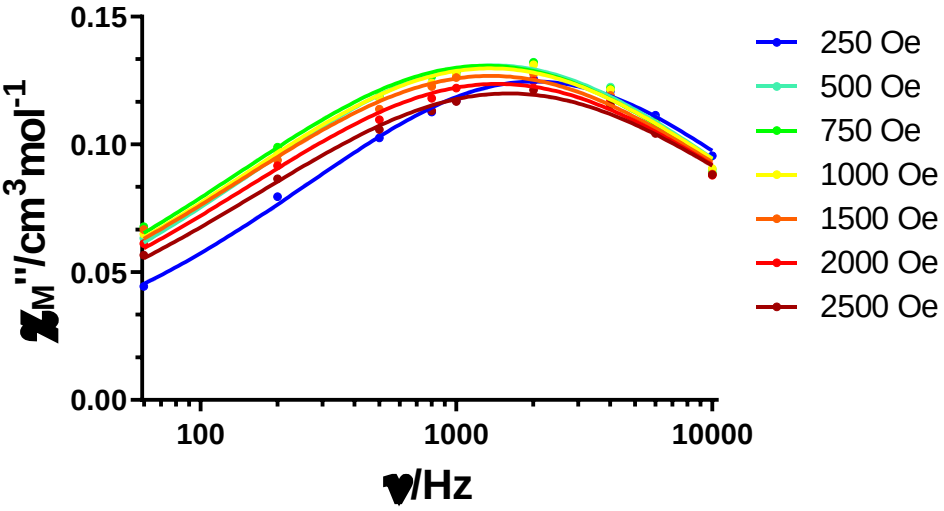

Figure A2.33.- Field dependence of the out-of-phase signal *vs* frequency at 4.0 K for $\mathbf{8_{DyY}}$.

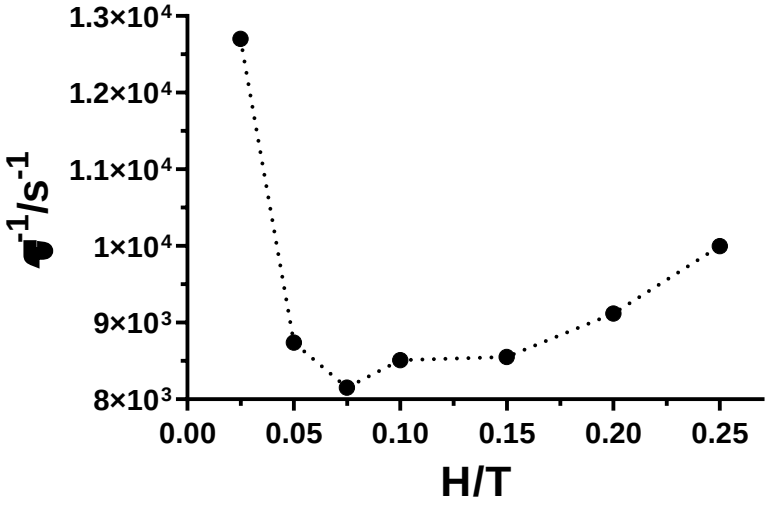

Figure A2.34.- The inverse of the relaxation times obtained at different magnetic fields at 4.0 K for $\mathbf{8_{DyY}}$.

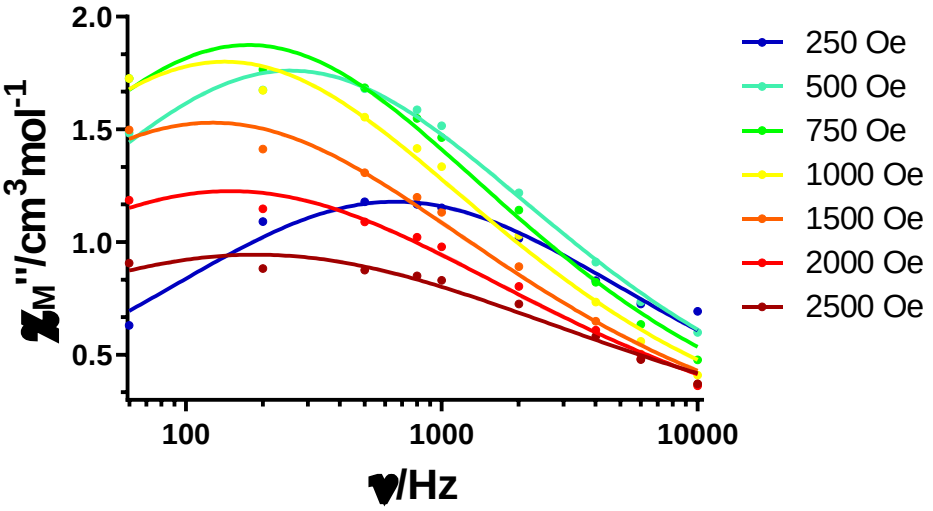

Figure A2.35.- Field dependence of the out-of-phase signal *vs* frequency at 2.5 K for **9**.

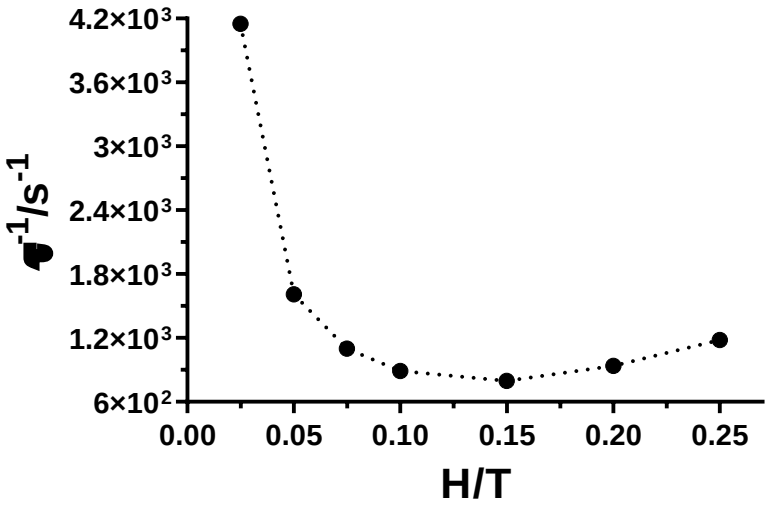

Figure A2.36.- The inverse of the relaxation times obtained at different magnetic fields at 2.5 K for **9**.

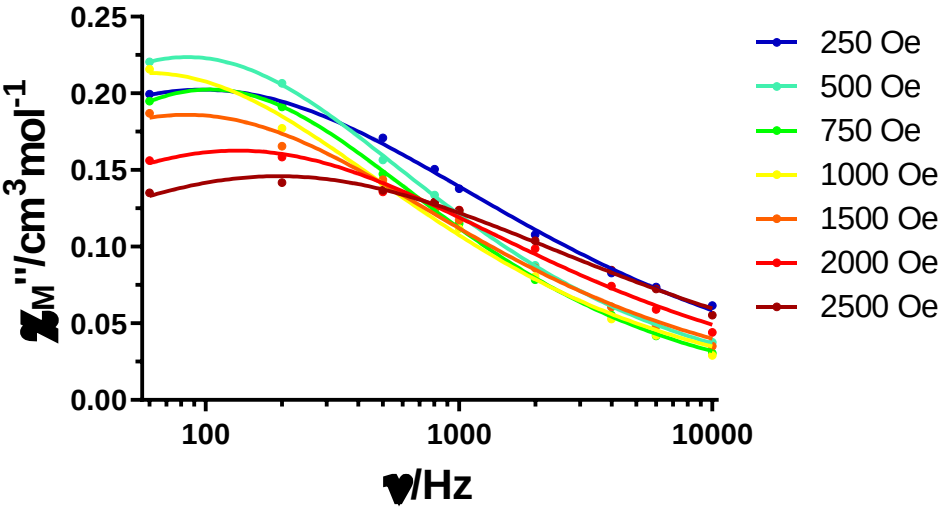

Figure A2.37.- Field dependence of the out-of-phase signal *vs* frequency at 2.2 K for **10**$_{DyY}$.

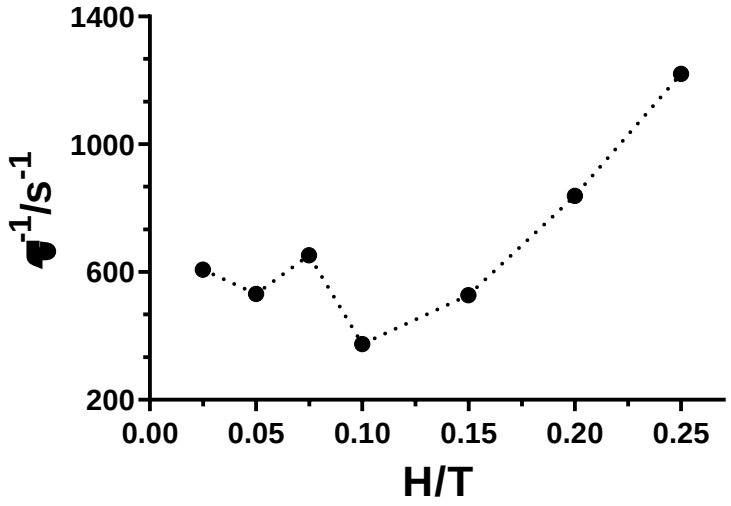

Figure A2.38.- The inverse of the relaxation times obtained at different magnetic fields at 2.2 K for **10**$_{DyY}$.

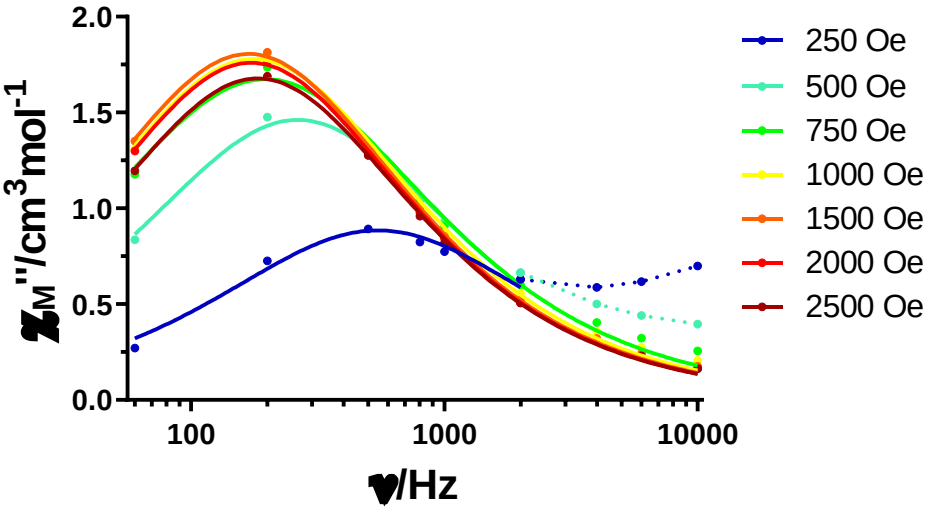

Figure A2.39.- Field dependence of the out-of-phase signal *vs* frequency at 4.8 K for **11**.

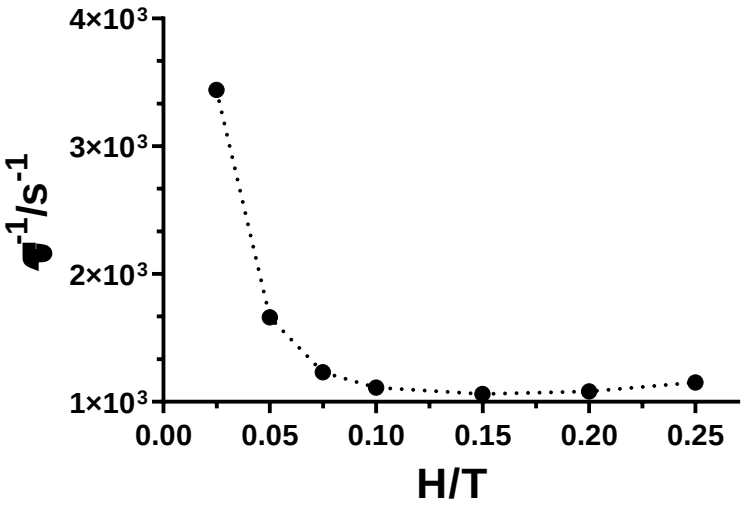

Figure A2.40.- The inverse of the relaxation times obtained at different magnetic fields at 4.8 K for **11**.

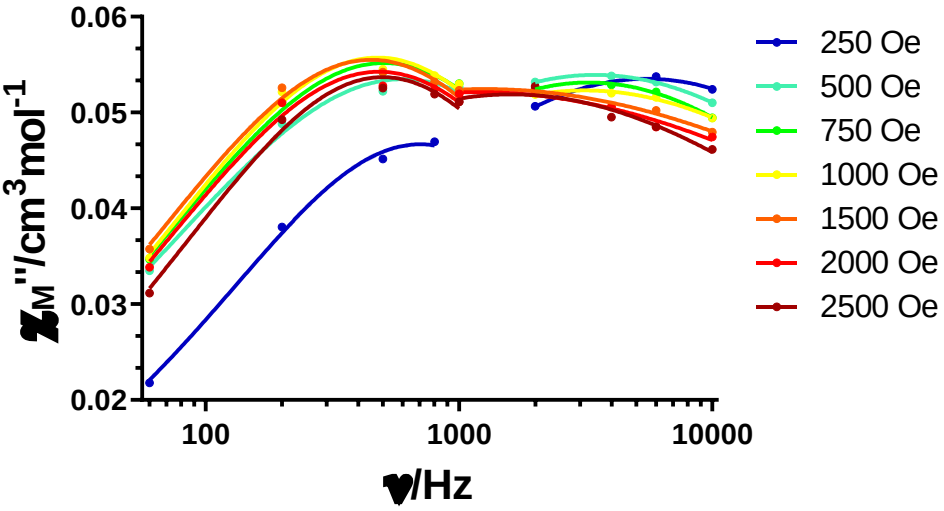

Figure A2.41.- Field dependence of the out-of-phase signal *vs* frequency at 5.0 K for **12**$_{DyY}$. Low frequency data was fitted for SR and high frequency data for FR.

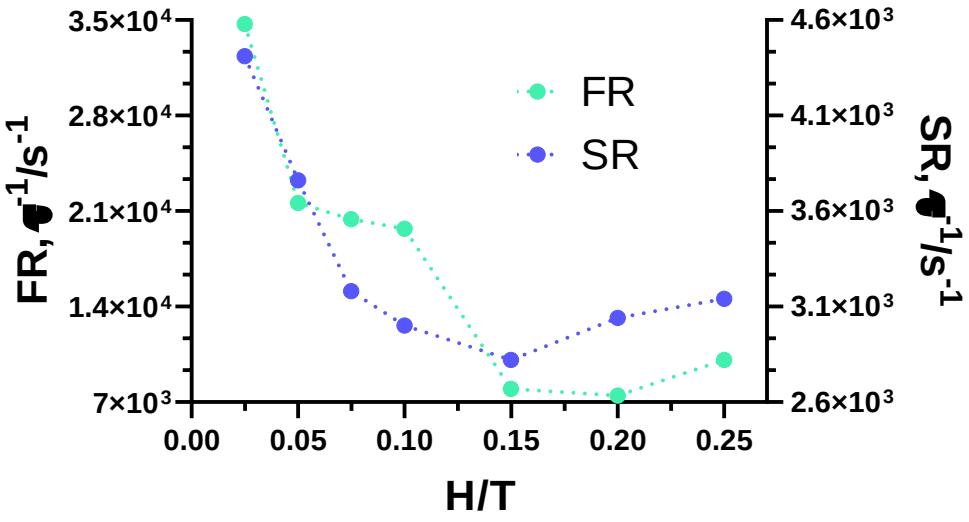

Figure A2.42.- The inverse of the relaxation times obtained at different magnetic fields at 5.0 K for **12**$_{DyY}$.

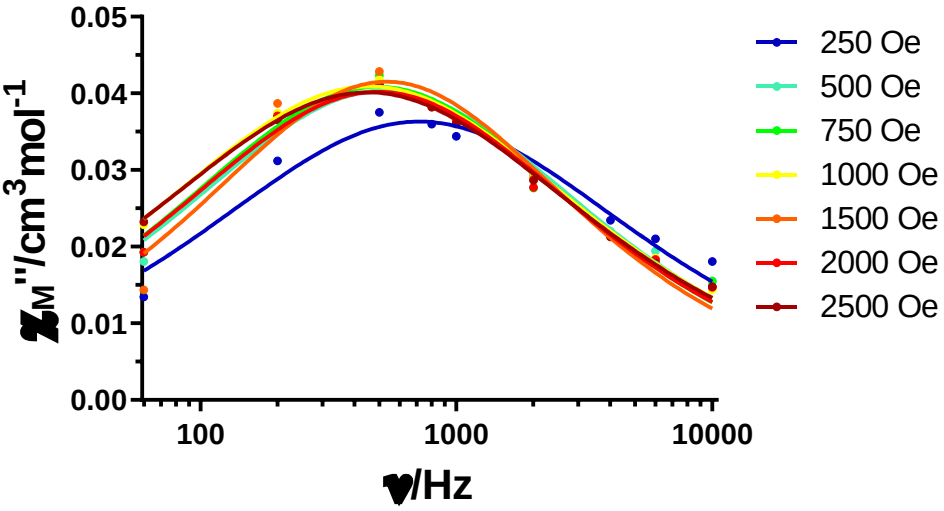

Figure A2.43.- Field dependence of the out-of-phase signal *vs* frequency at 7.6 K for **13**$_{DyY}$.

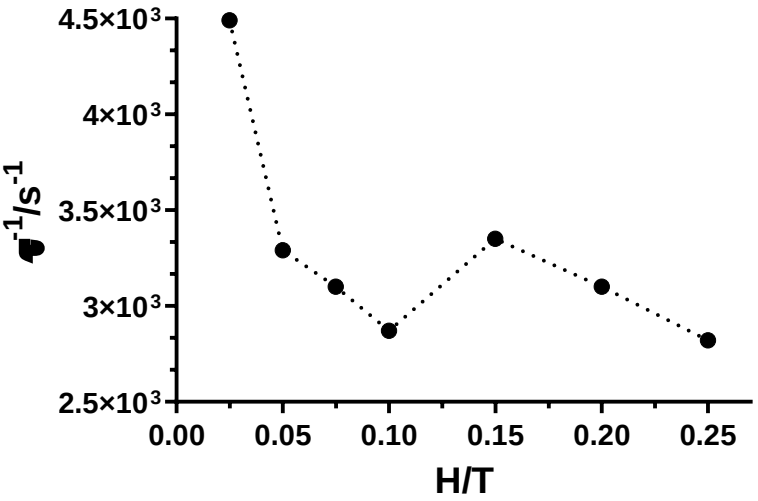

Figure A2.44.- The inverse of the relaxation times obtained at different magnetic fields at 7.6 K for **13**$_{DyY}$.

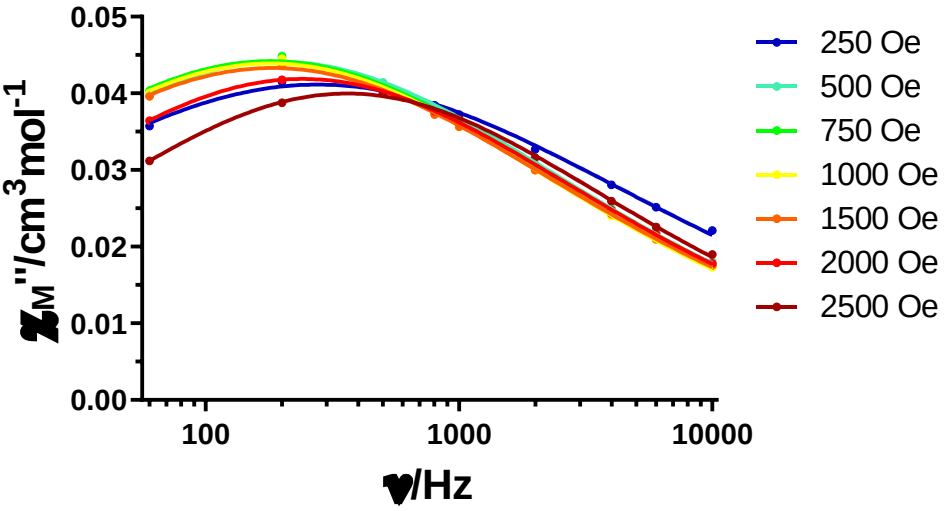

Figure A2.45.- Field dependence of the out-of-phase signal *vs* frequency at 3.6 K for **14**$_{DyY}$.

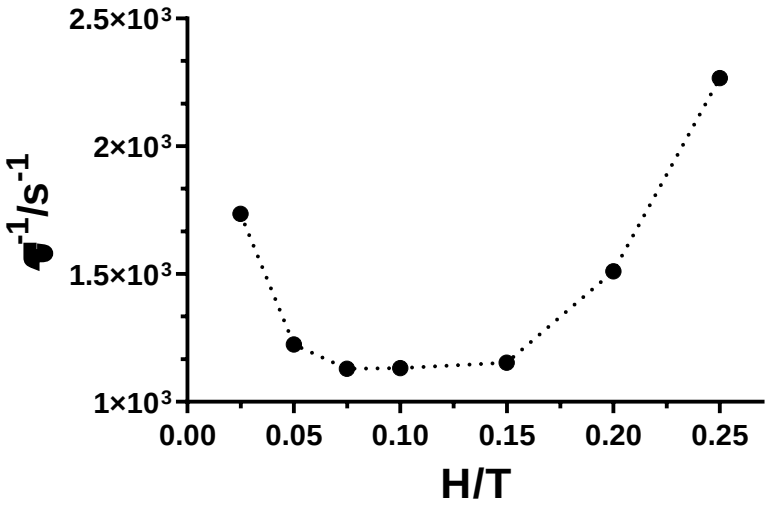

Figure A2.46.- The inverse of the relaxation times obtained at different magnetic fields at 3.6 K for **14**$_{DyY}$.

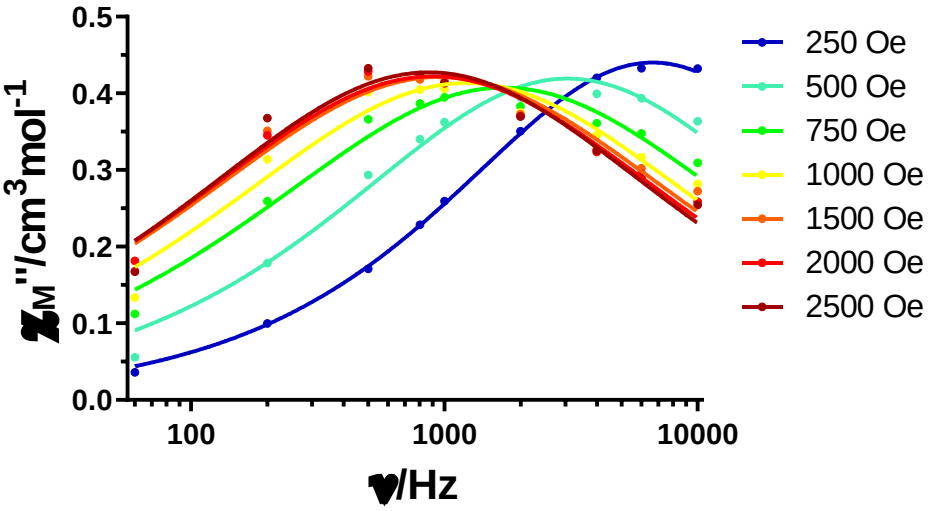

Figure A2.47.- Field dependence of the out-of-phase signal *vs* frequency at 12.5 K for **15**.

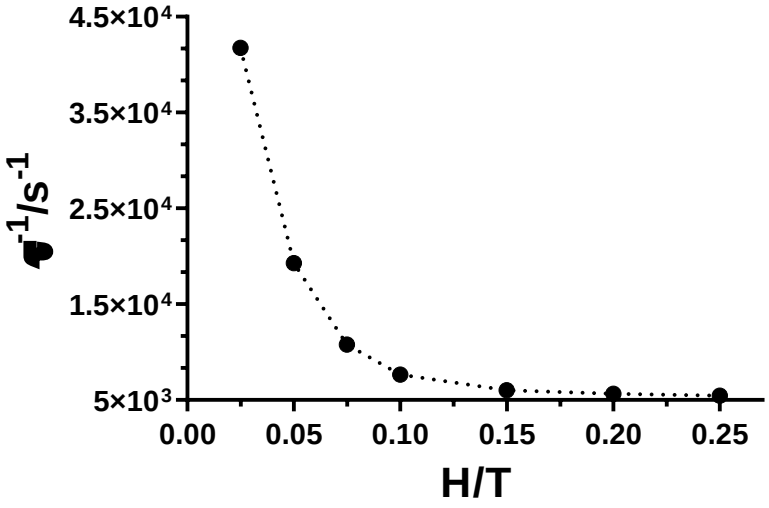

Figure A2.48.- The inverse of the relaxation times obtained at different magnetic fields at 12.5 K for **15**.

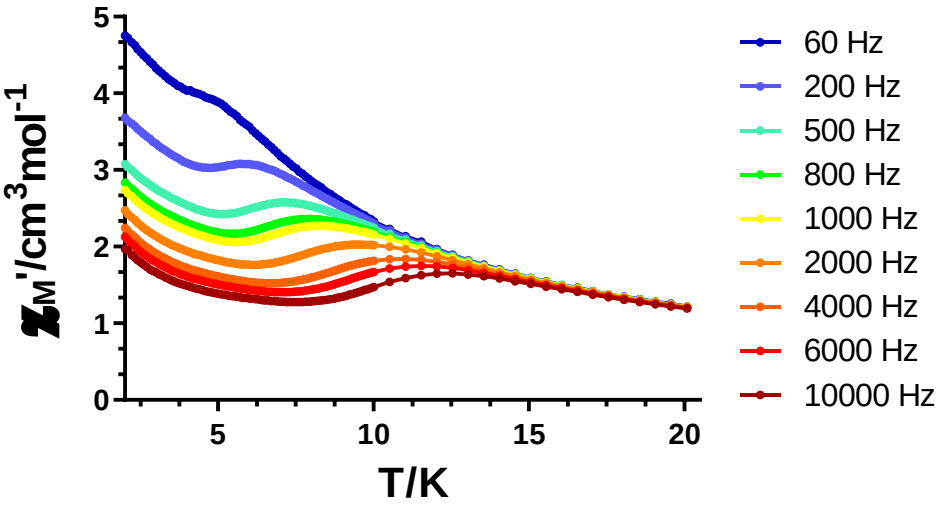

Figure A2.49.- Temperature dependence of the in phase components of the *ac* susceptibility in a *dc* applied field of 1.5 kOe for **7**.

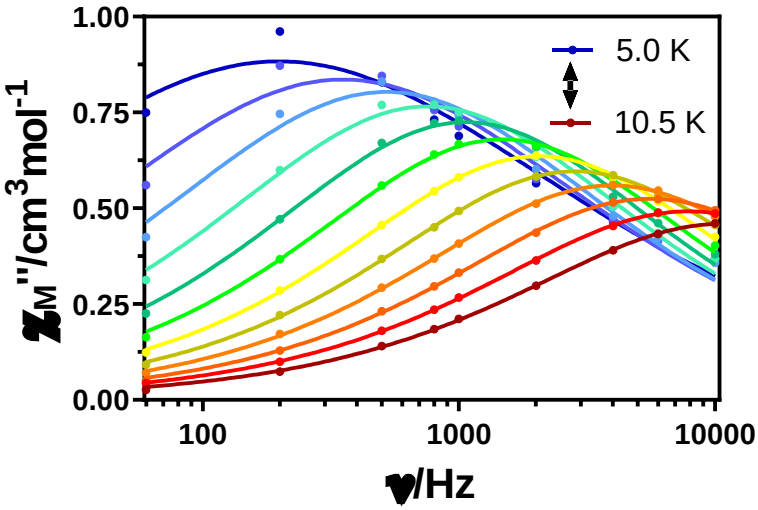

Figure A2.50.- Variable-temperature frequency dependence of the χ_M'' signal under 1.5 kOe applied field for **7**. Solid lines represent the best fitting of the experimental data to the Debye model.

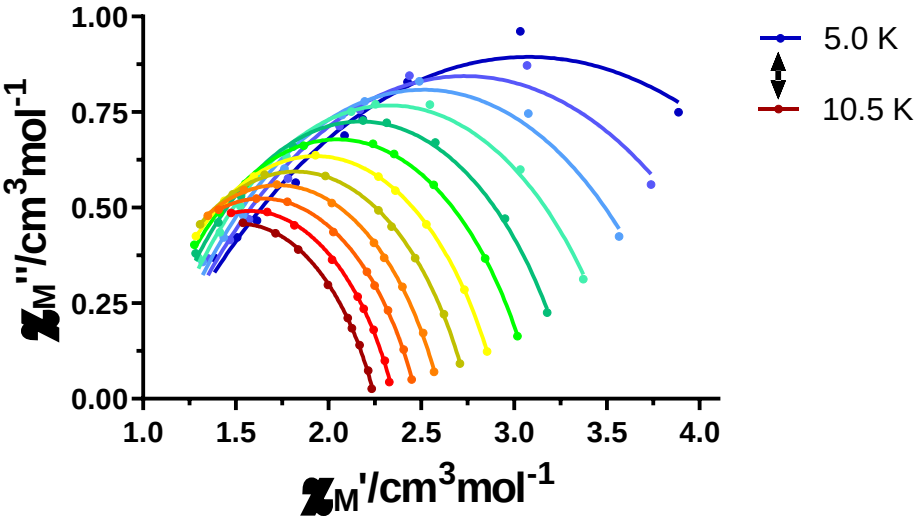

Figure A2.51.- Cole-Cole plots under 1.5 kOe field for **7**. Solid lines represent the best fit to the generalized Debye model.

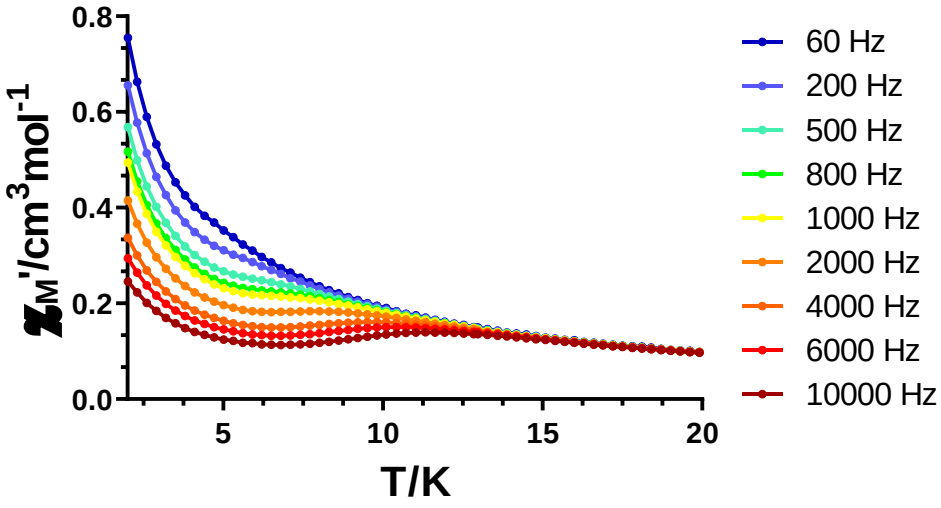

Figure A2.52.- Temperature dependence of the in phase components of the *ac* susceptibility in a zero applied *dc* field for $\mathbf{7}_{DyY}$.

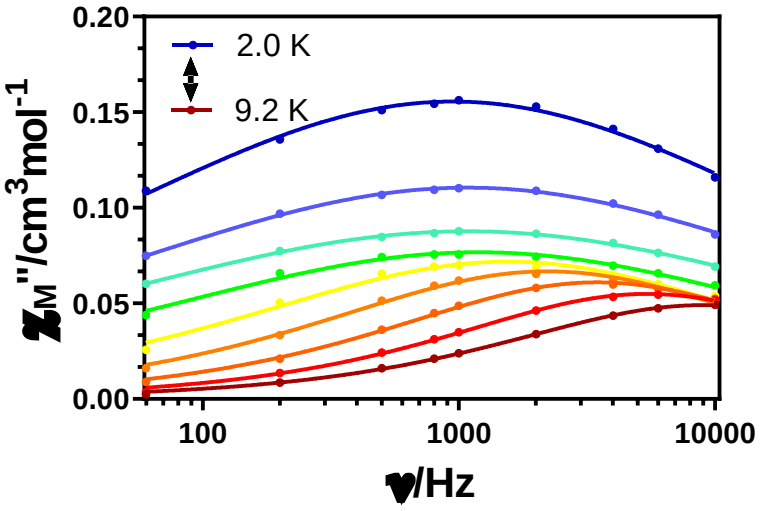

Figure A2.53.- Variable-temperature frequency dependence of the χ_M'' signal under zero applied *dc* field for **7**$_{DyY}$. Solid lines represent the best fitting of the experimental data to the Debye model.

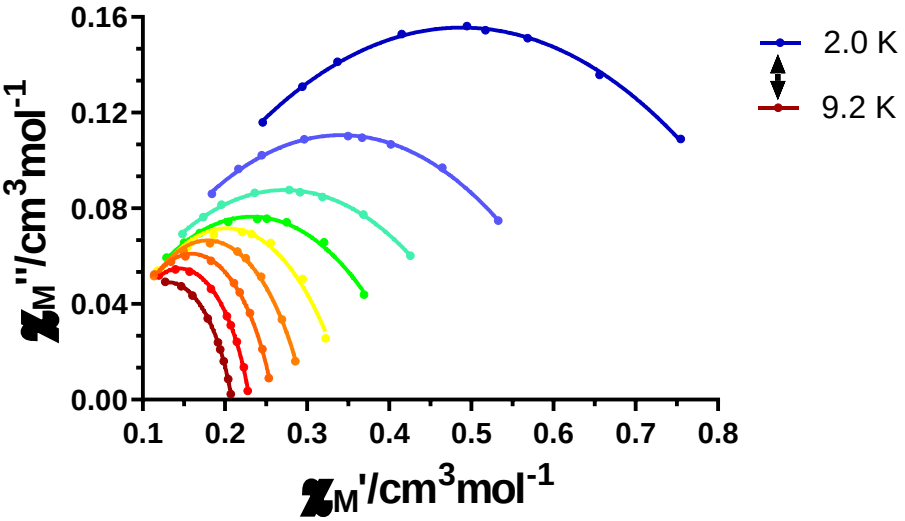

Figure A2.54.- Cole-Cole plots under zero applied *dc* field for **7**$_{DyY}$. Solid lines represent the best fit to the generalized Debye model.

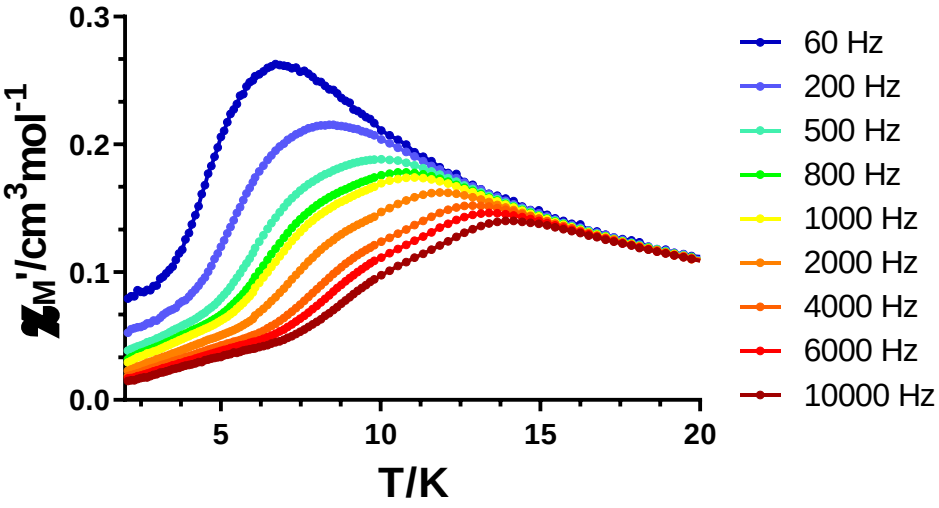

Figure A2.55.- Temperature dependence of the in phase components of the *ac* susceptibility in a *dc* applied field of 1.5 kOe for $\mathbf{7_{DyY}}$.

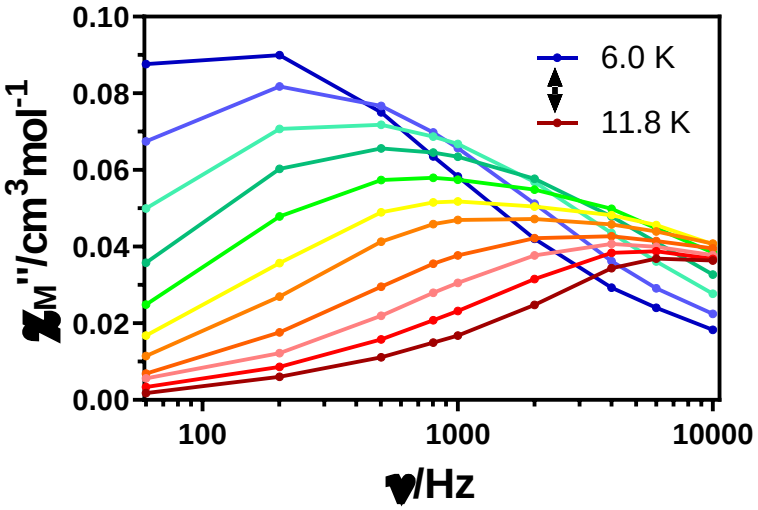

Figure A2.56.- Variable-temperature frequency dependence of the χ_M'' signal under 1.5 kOe applied field for $\mathbf{7_{DyY}}$. Solid lines are a guide to the eye.

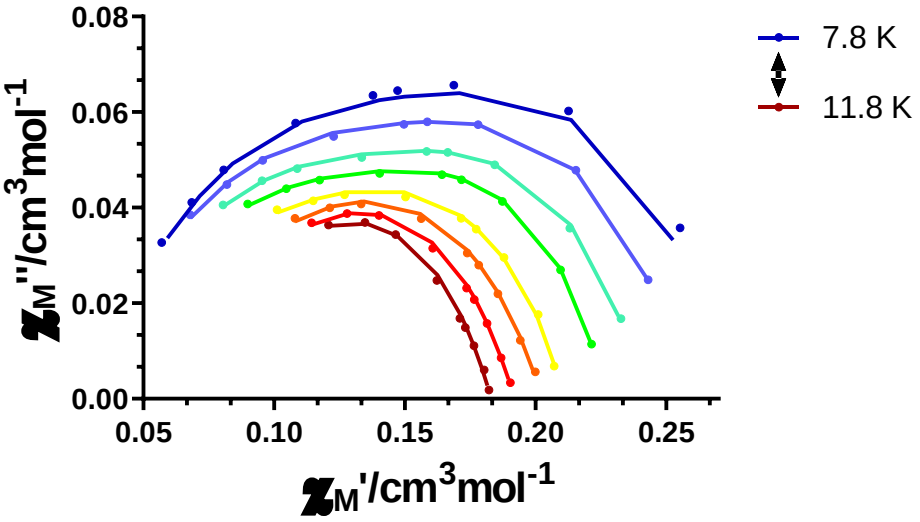

Figure A2.57.- Cole-Cole plots under 1.5 kOe field for $\mathbf{7}_{DyY}$. Solid lines represent the best fit using a sum of two modified Debye functions.

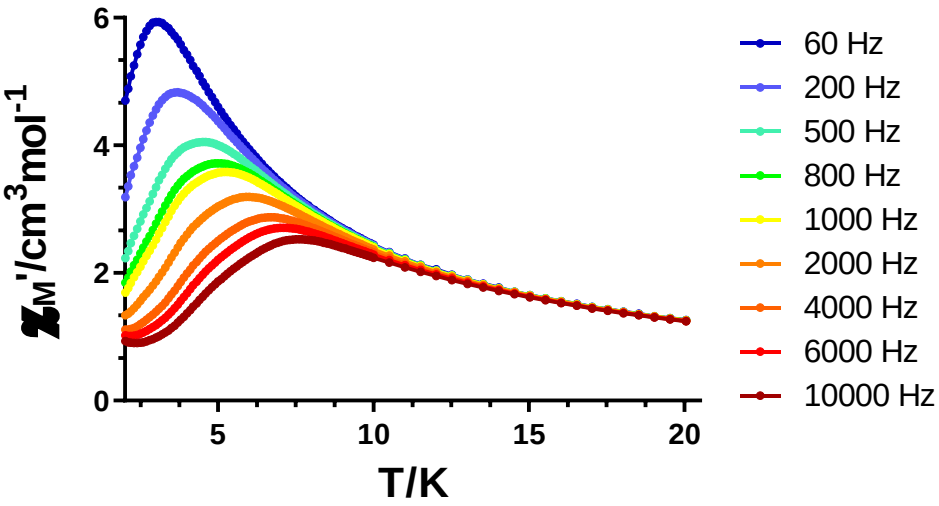

Figure A2.58.- Temperature dependence of the in phase components of the *ac* susceptibility in a *dc* applied field of 750 Oe for **8**.

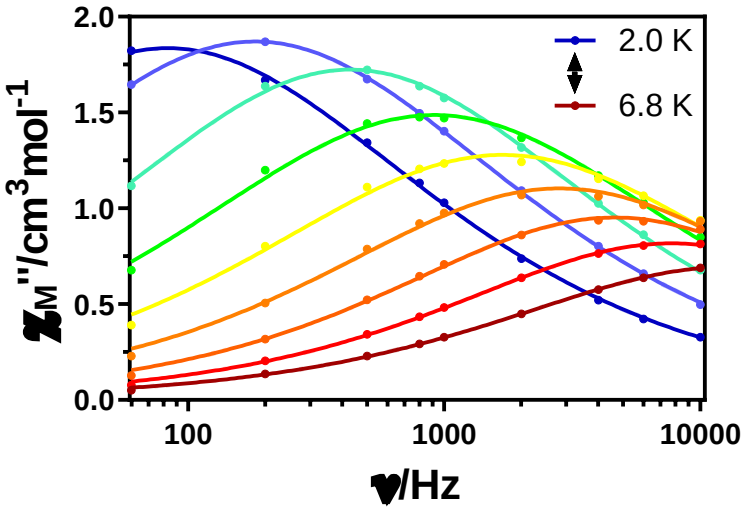

Figure A2.59.- Variable-temperature frequency dependence of the χ_M'' signal under 750 Oe applied field for **8**. Solid lines represent the best fitting of the experimental data to the Debye model.

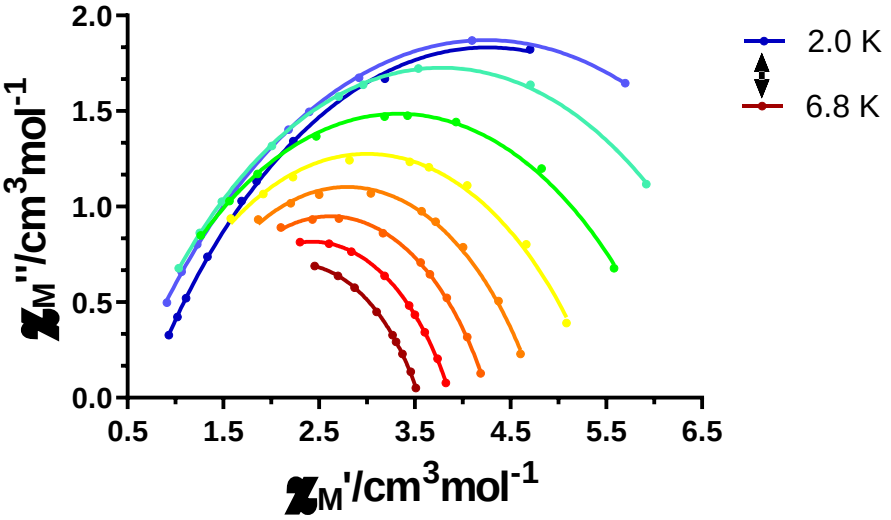

Figure A2.60.- Cole-Cole plots under 750 Oe field for **8**. Solid lines represent the best fit to the generalized Debye model.

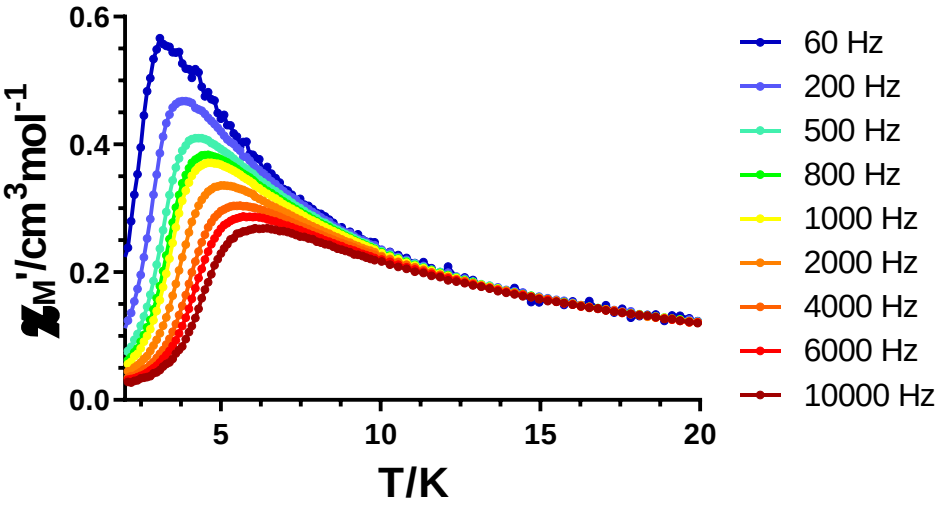

Figure A2.61.- Temperature dependence of the in phase components of the *ac* susceptibility in a *dc* applied field of 750 Oe for $\mathbf{8_{DyY}}$.

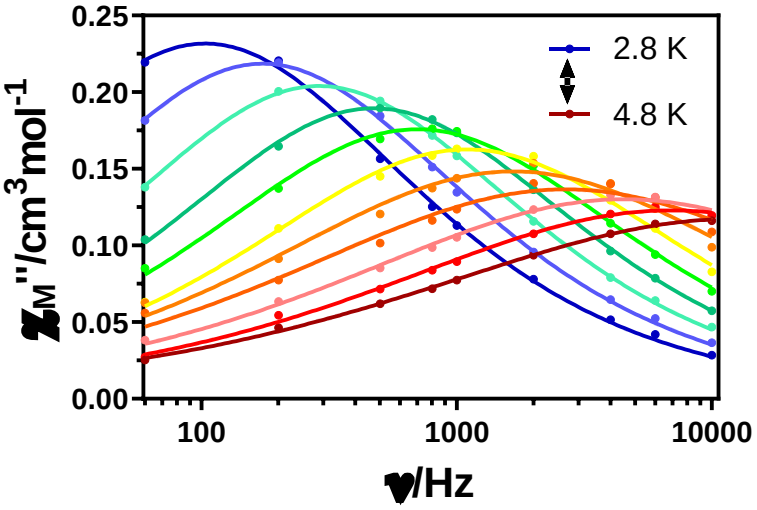

Figure A2.62.- Variable-temperature frequency dependence of the χ_M'' signal under 750 Oe applied field for $\mathbf{8_{DyY}}$. Solid lines represent the best fitting of the experimental data to the Debye model.

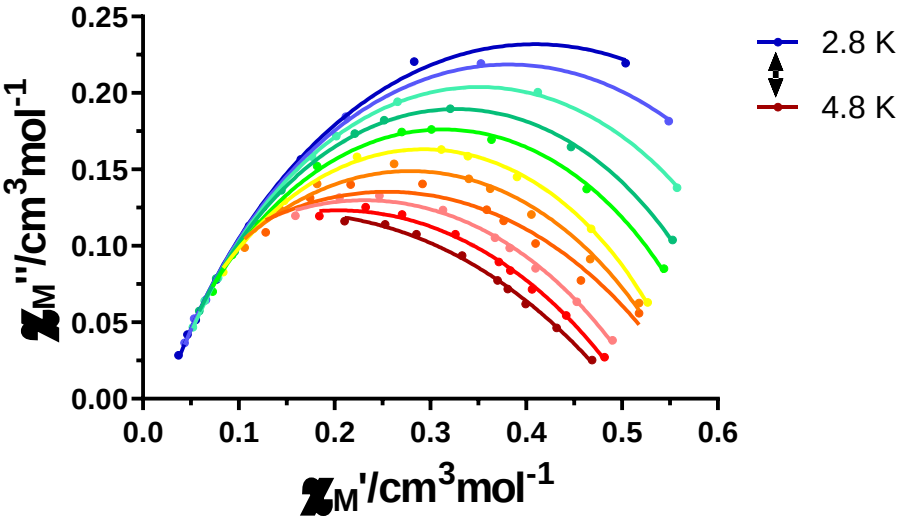

Figure A2.63.- Cole-Cole plots under 750 Oe field for **8**$_{DyY}$. Solid lines represent the best fit to the generalized Debye model.

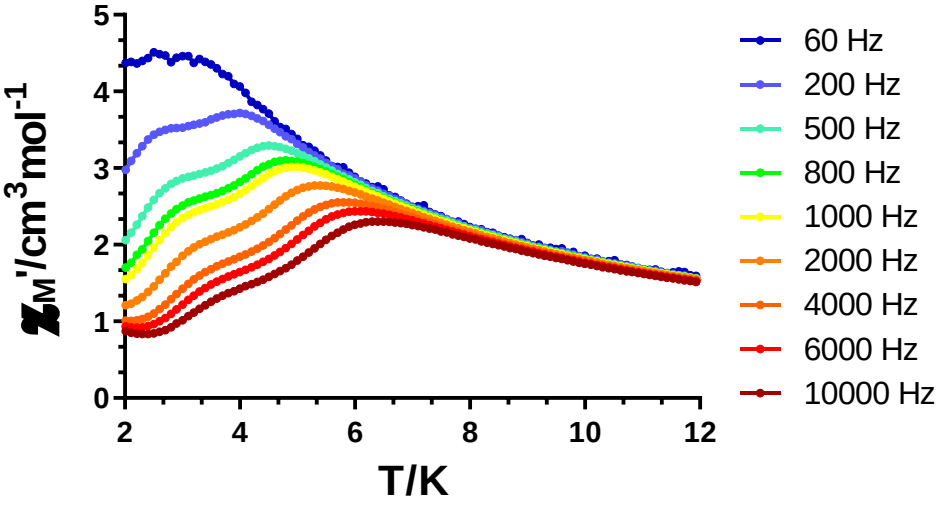

Figure A2.64.- Temperature dependence of the in phase components of the *ac* susceptibility in a *dc* applied field of 1.5 kOe for **9**.

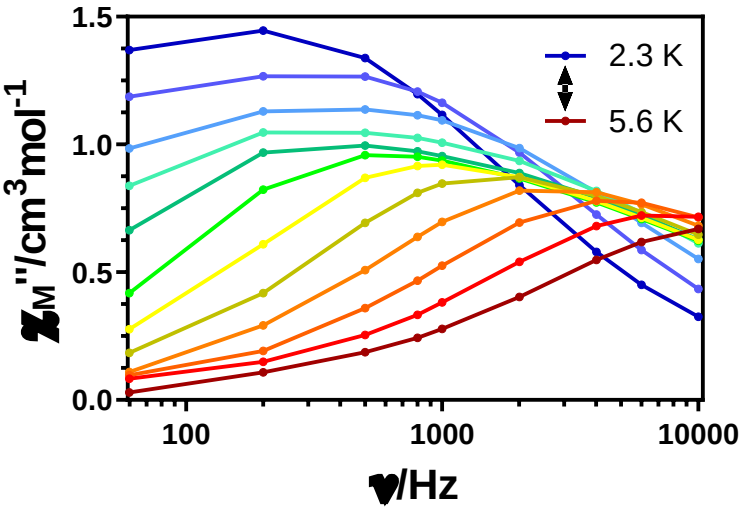

Figure A2.65.- Variable-temperature frequency dependence of the χ_M'' signal under 1.5 kOe applied field for **9**. Solid lines are a guide to the eye.

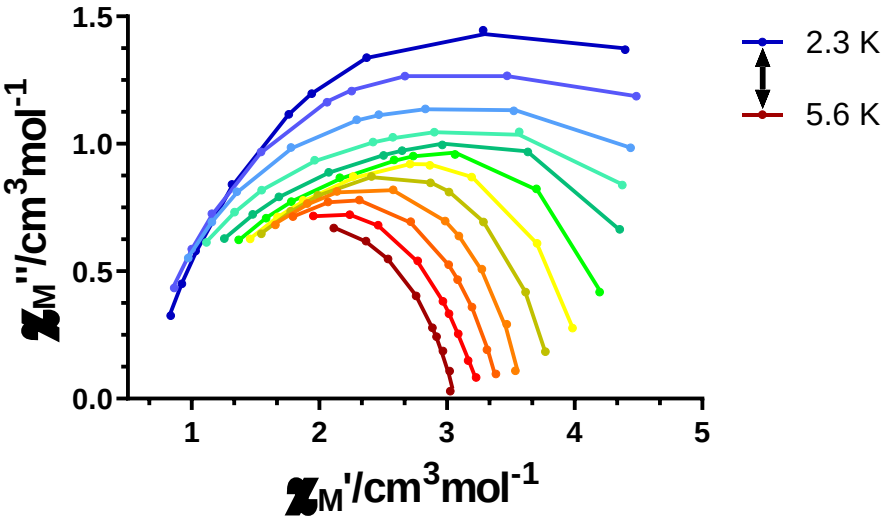

Figure A2.66.- Cole-Cole plots under 1.5 kOe field for **9**. Solid lines represent the best fit using a sum of two modified Debye functions.

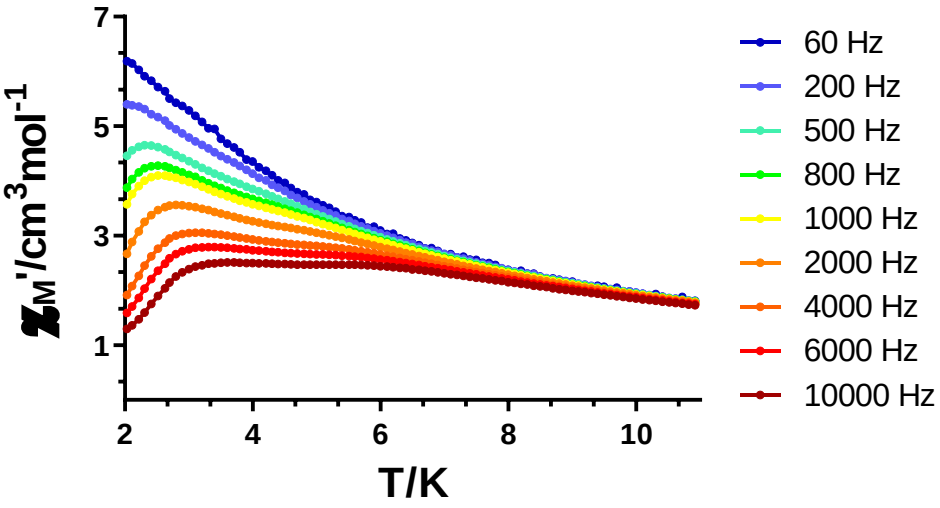

Figure A2.67.- Temperature dependence of the in phase components of the *ac* susceptibility in a *dc* applied field of 1 kOe for **10**.

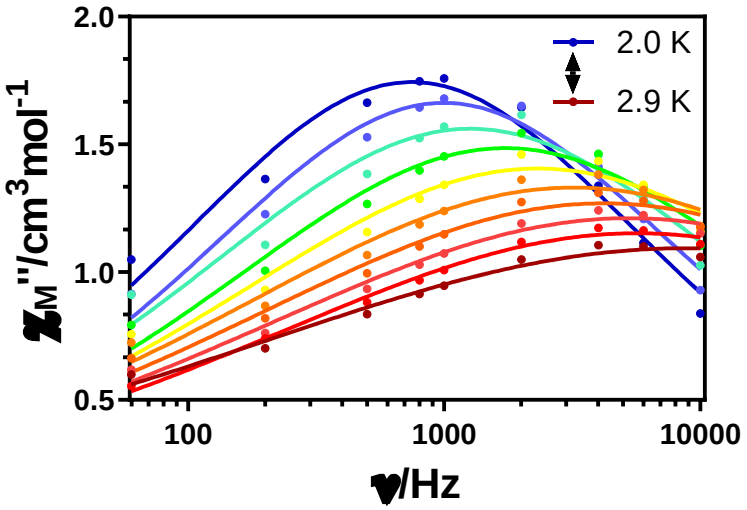

Figure A2.68.- Variable-temperature frequency dependence of the χ_M'' signal under 1 kOe applied field for **10** FR. Solid lines represent the best fitting of the experimental data to the Debye model.

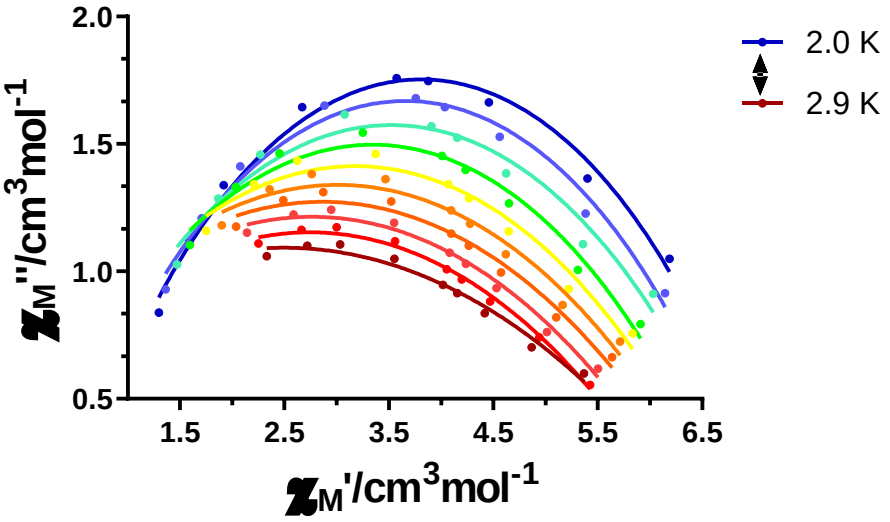

Figure A2.69.- Cole-Cole plots under 1 kOe field for **10** FR. Solid lines represent the best fit to the generalized Debye model.

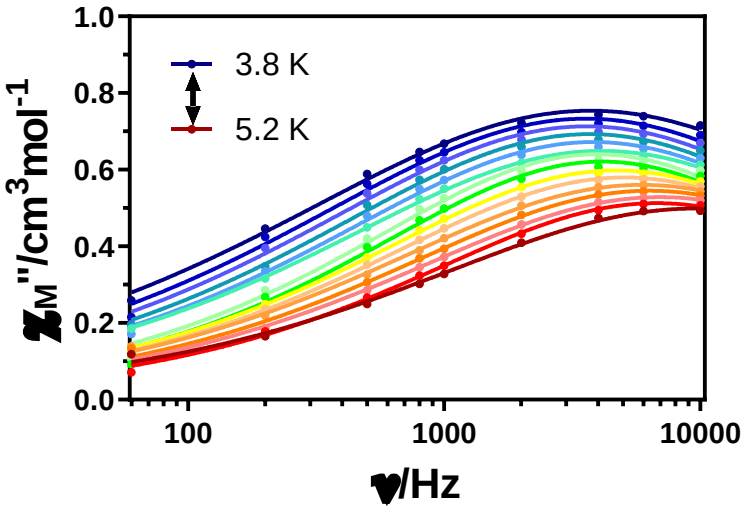

Figure A2.70.- Variable-temperature frequency dependence of the χ_M'' signal under 1 kOe applied field for **10** SR. Solid lines represent the best fitting of the experimental data to the Debye model.

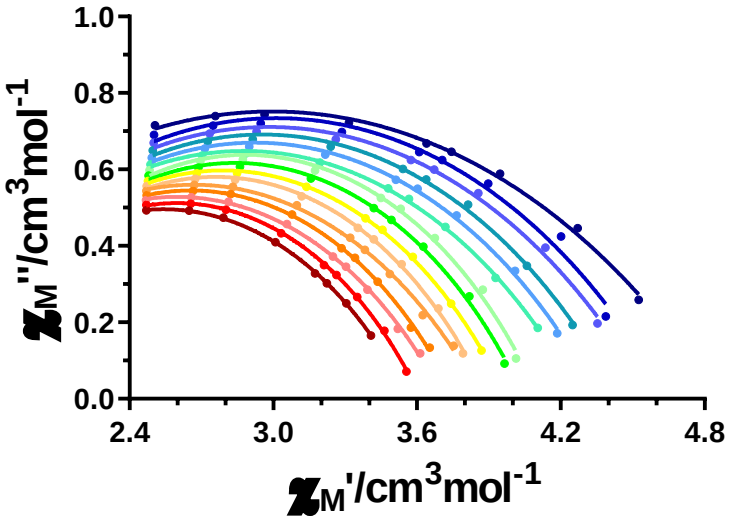

Figure A2.71.- Cole-Cole plots under 1 kOe field for **10** SR. Solid lines represent the best fit to the generalized Debye model.

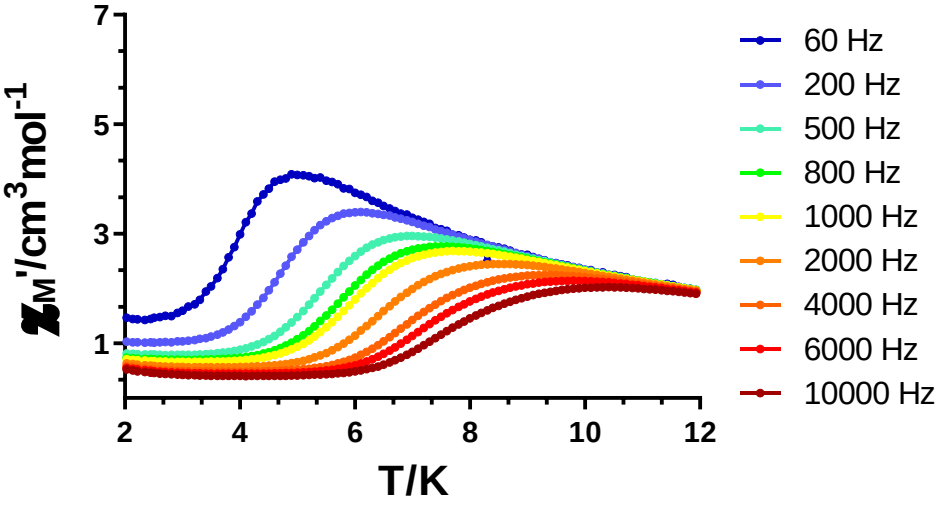

Figure A2.72.- Temperature dependence of the in phase components of the *ac* susceptibility in a *dc* applied field of 1.5 kOe for **11**.

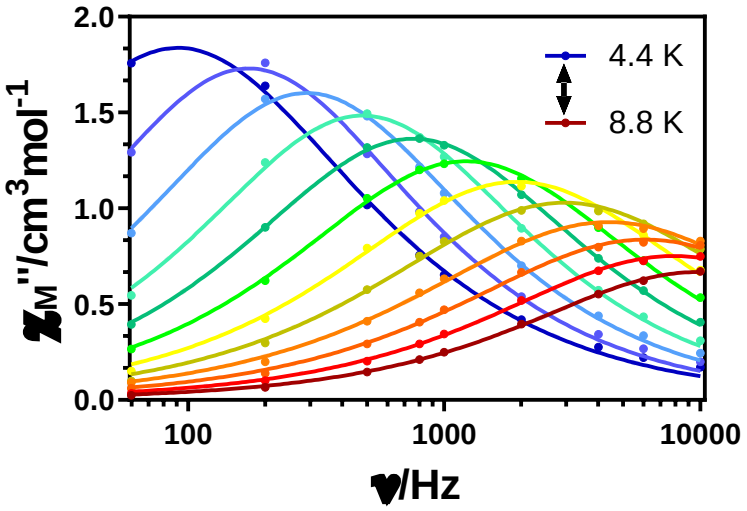

Figure A2.73.- Variable-temperature frequency dependence of the χ_M'' signal under 1.5 kOe applied field for **11**. Solid lines represent the best fitting of the experimental data to the Debye model.

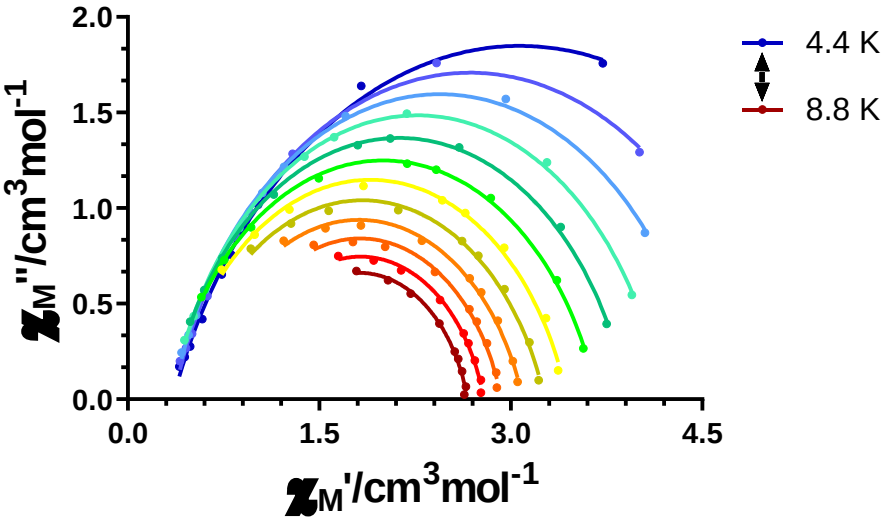

Figure A2.74.- Cole-Cole plots under 1.5 kOe field for **11**. Solid lines represent the best fit to the generalized Debye model.

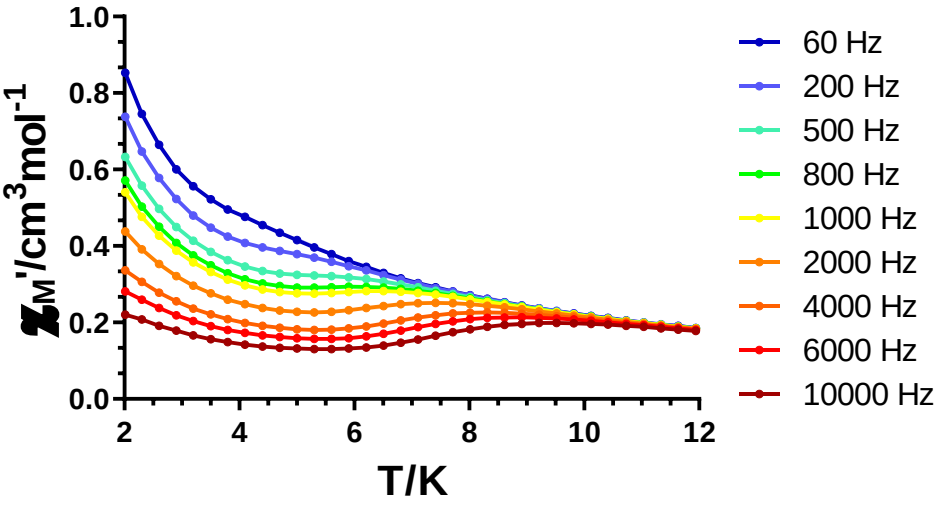

Figure A2.75.- Temperature dependence of the in phase components of the *ac* susceptibility in a zero applied *dc* field for **11**$_{DyY}$.

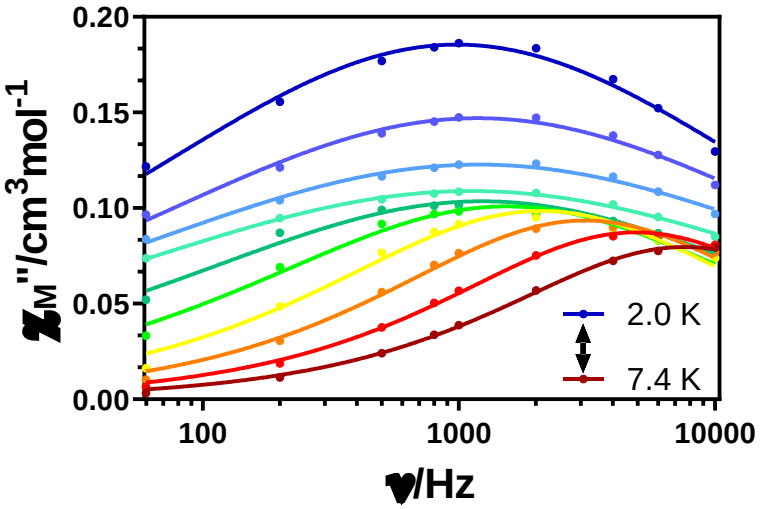

Figure A2.76.- Variable-temperature frequency dependence of the χ_M'' signal under zero applied *dc* field for **11**$_{DyY}$. Solid lines represent the best fitting of the experimental data to the Debye model.

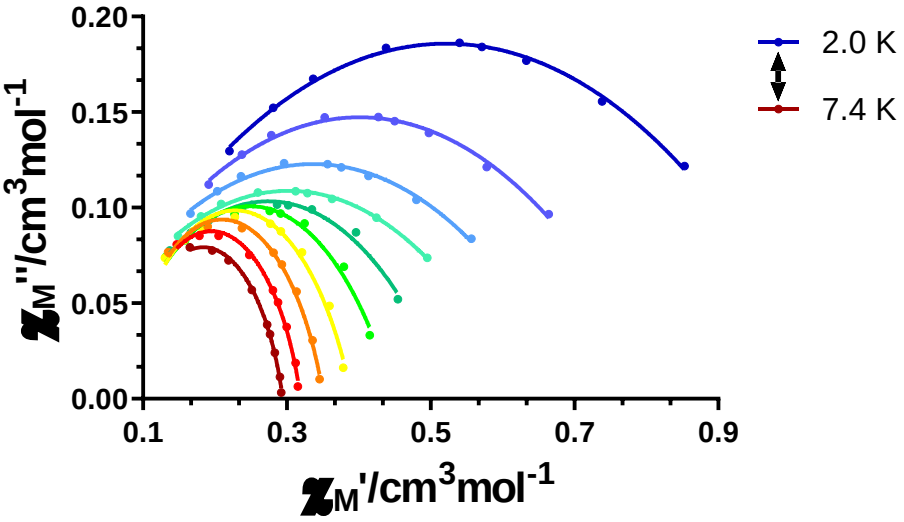

Figure A2.77.- Cole-Cole plots under zero applied *dc* field for **11**$_{DyY}$. Solid lines represent the best fit to the generalized Debye model.

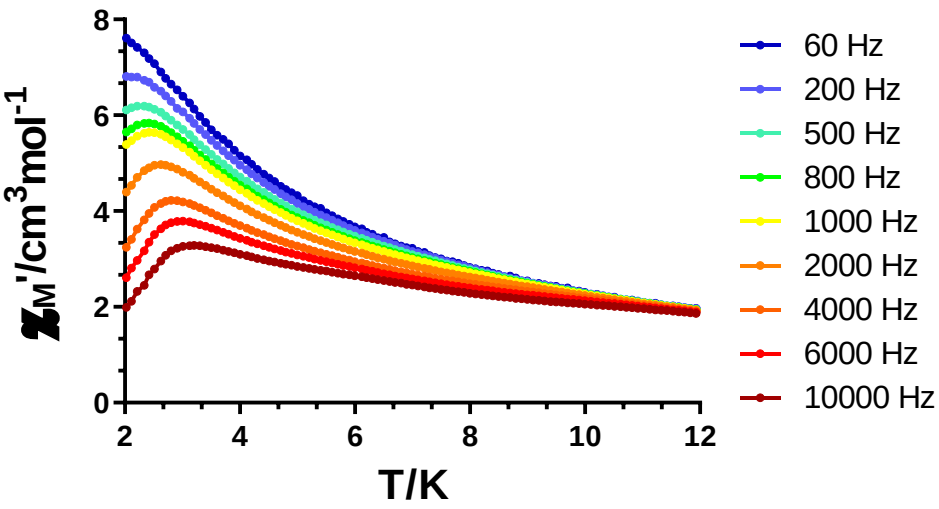

Figure A2.78.- Temperature dependence of the in phase components of the *ac* susceptibility in a *dc* applied field of 1.5 kOe for **12**.

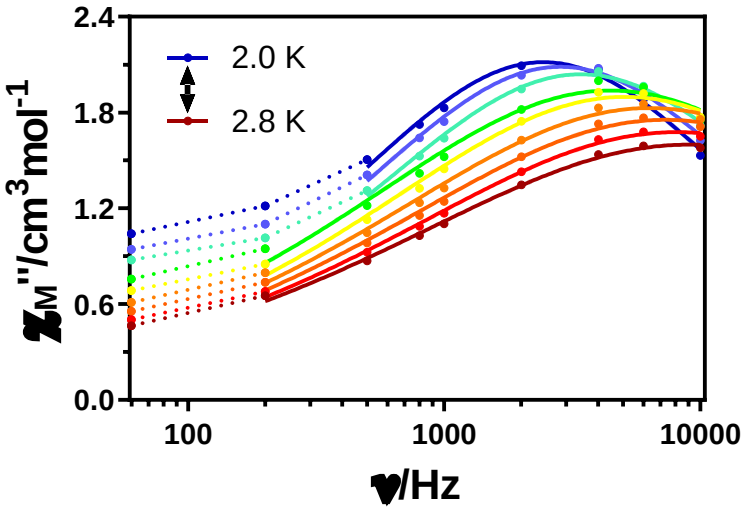

Figure A2.79.- Variable-temperature frequency dependence of the χ_M'' signal under 1.5 kOe applied field for **12**. Solid lines represent the best fitting of the experimental data to the Debye model. Dashed lines are a guide to the eye.

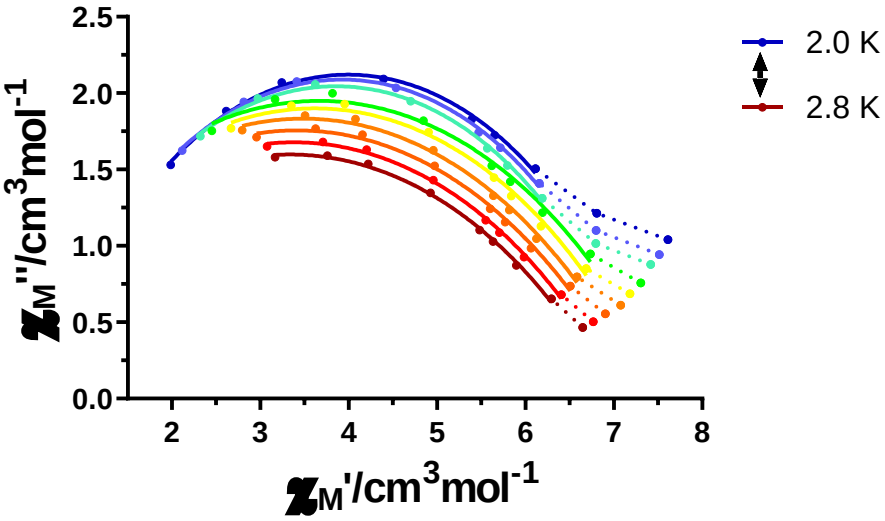

Figure A2.80.- Cole-Cole plots under 1.5 kOe field for **12**. Solid lines represent the best fit to the generalized Debye model. Dashed lines are a guide to the eye.

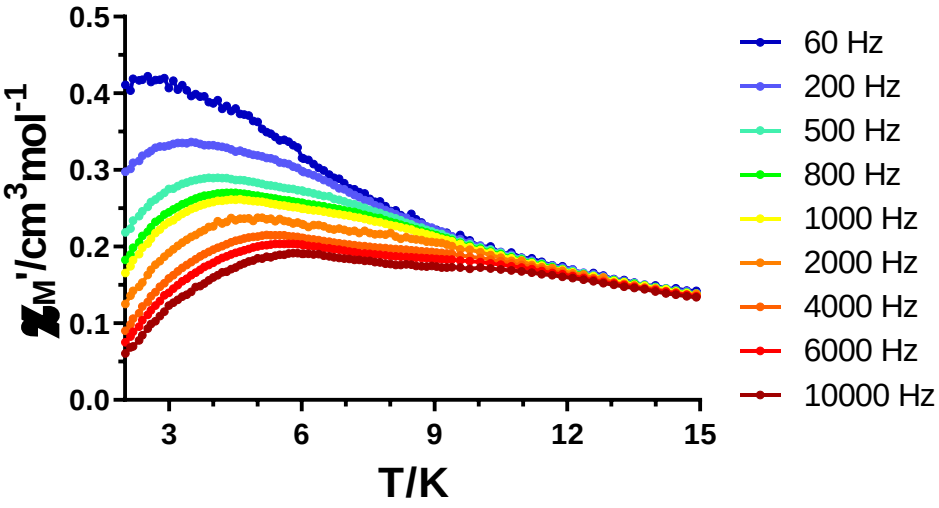

Figure A2.81.- Temperature dependence of the in phase components of the *ac* susceptibility in a *dc* applied field of 1.5 kOe for **12**$_{DyY}$.

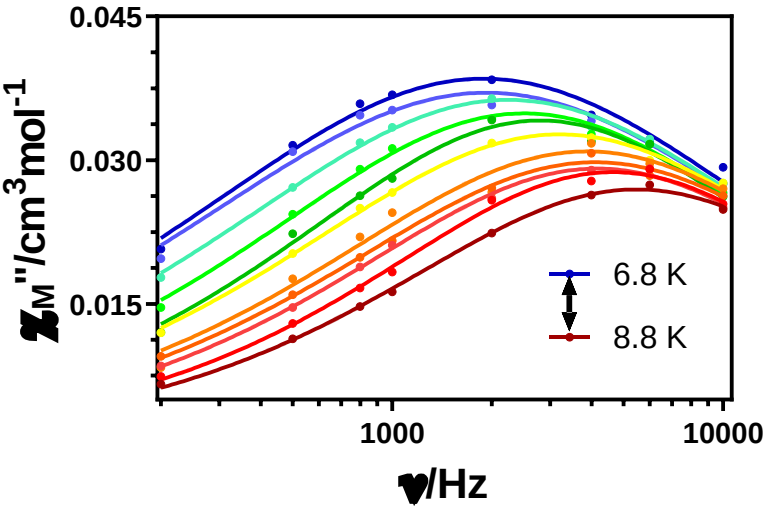

Figure A2.82.- Variable-temperature frequency dependence of the χ_M" signal under 1.5 kOe applied field for **12**$_{DyY}$. Solid lines represent the best fitting of the experimental data to the Debye model.

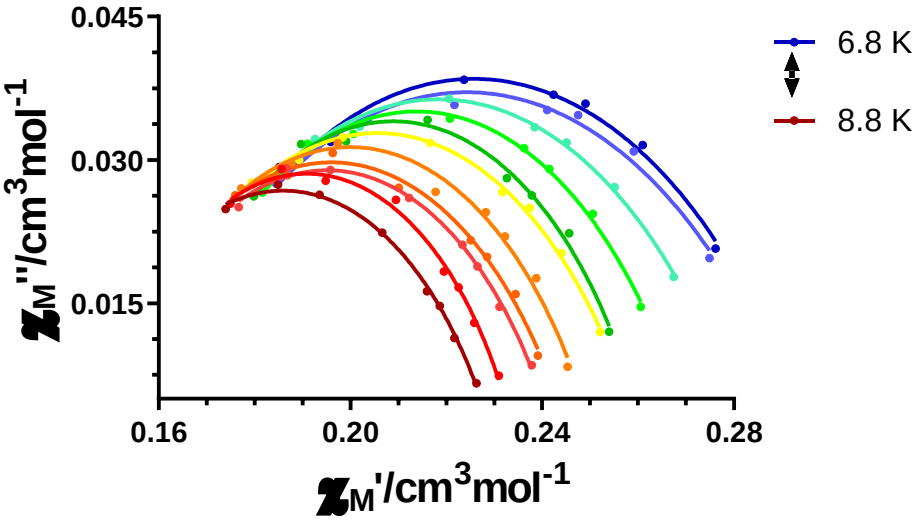

Figure A2.83.- Cole-Cole plots under 1.5 kOe field for **12**$_{DyY}$. Solid lines represent the best fit to the generalized Debye model.

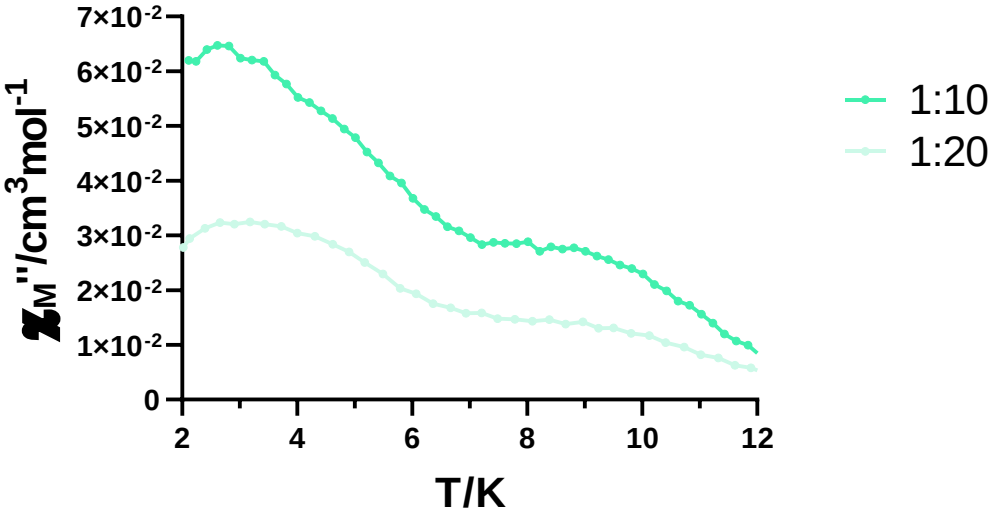

Figure A2.84.-Temperature dependence of the out-of-phase χ_M'' susceptibility signals for two diluted systems of **12** under an applied field of 1.5 kOe. An oscillating field of 3.5 Oe was used with a frequency of 10000 Hz.

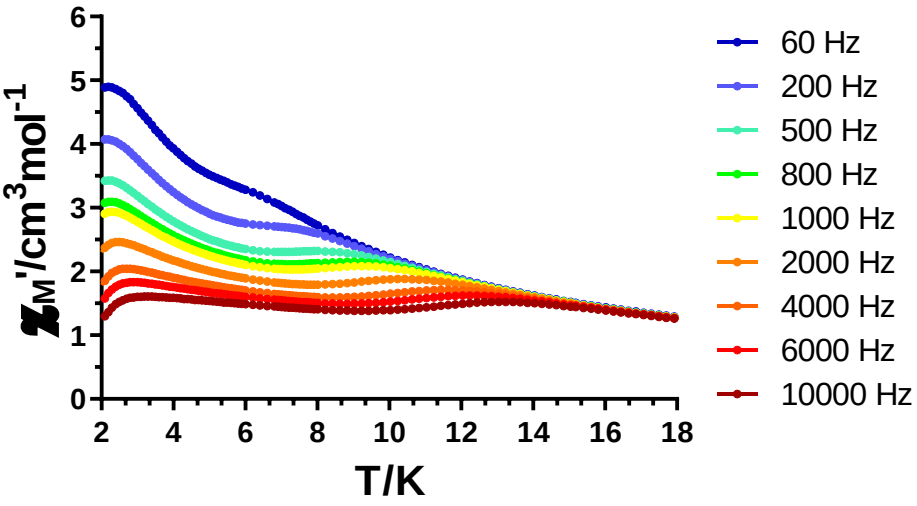

Figure A2.85.- Temperature dependence of the in phase components of the *ac* susceptibility in a *dc* applied field of 1 kOe for **13**.

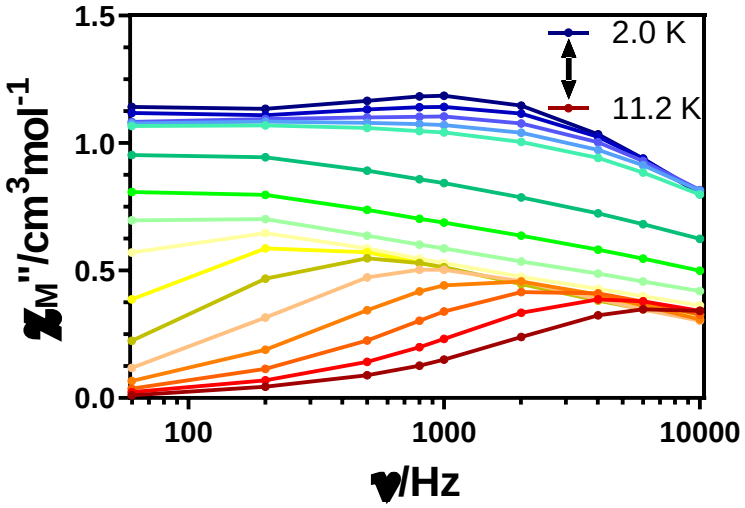

Figure A2.86.- Variable-temperature frequency dependence of the χ_M'' signal under 1 kOe applied field for **13**. Solid lines are a guide to the eye.

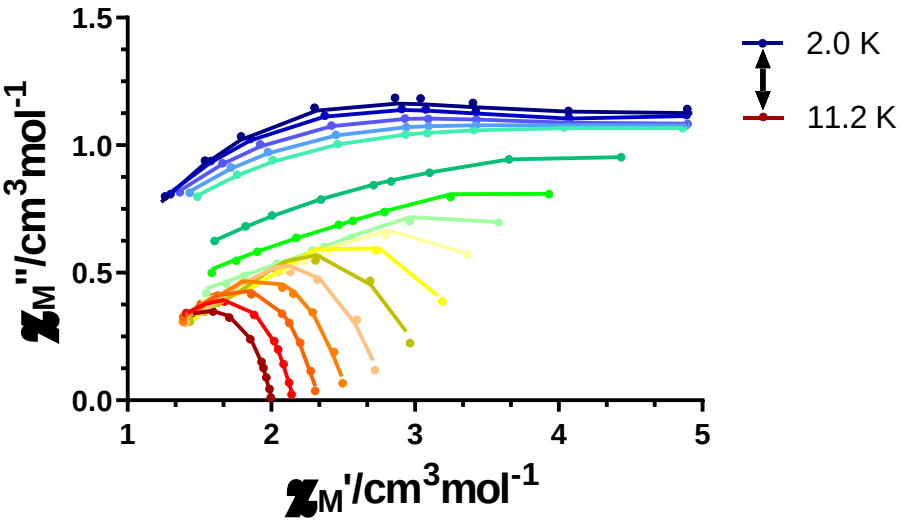

Figure A2.87.- Cole-Cole plots under 1 kOe field for **13**. Solid lines represent the best fit using a sum of two modified Debye functions.

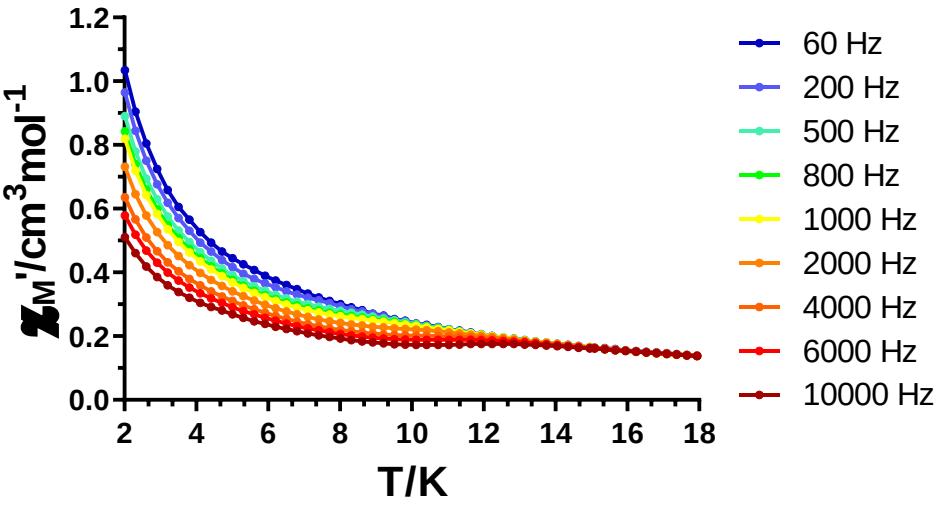

Figure A2.88.- Temperature dependence of the in phase components of the *ac* susceptibility in a zero applied *dc* field for **13**$_{DyY}$.

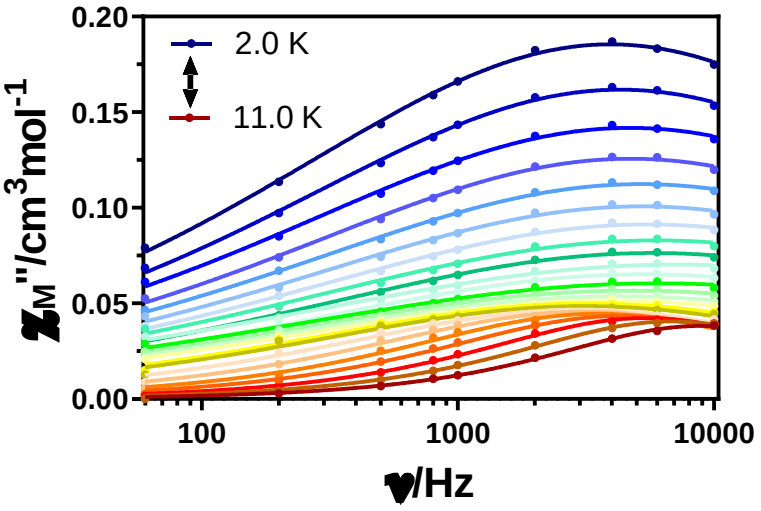

Figure A2.89.- Variable-temperature frequency dependence of the χ_M'' signal under zero applied *dc* field for **13**$_{DyY}$. Solid lines represent the best fitting of the experimental data to the Debye model.

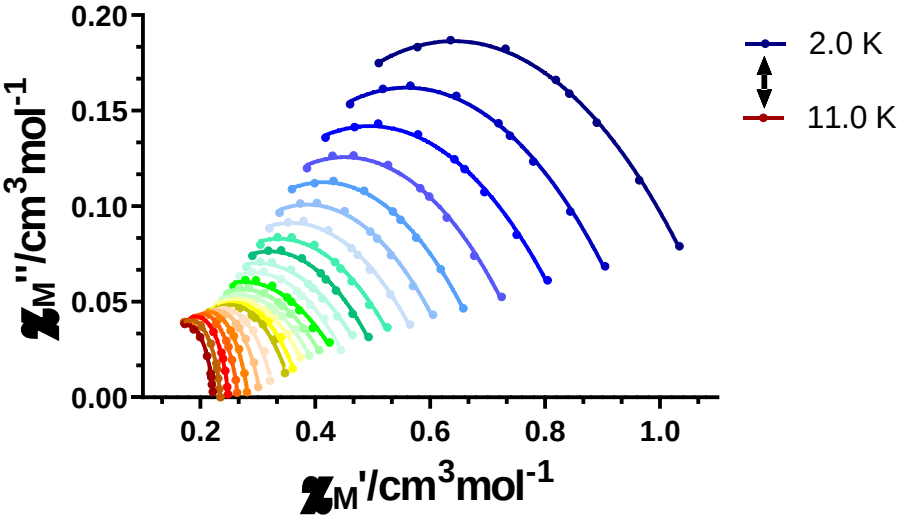

Figure A2.90.- Cole-Cole plots under zero applied *dc* field for **13**$_{DyY}$. Solid lines represent the best fit to the generalized Debye model.

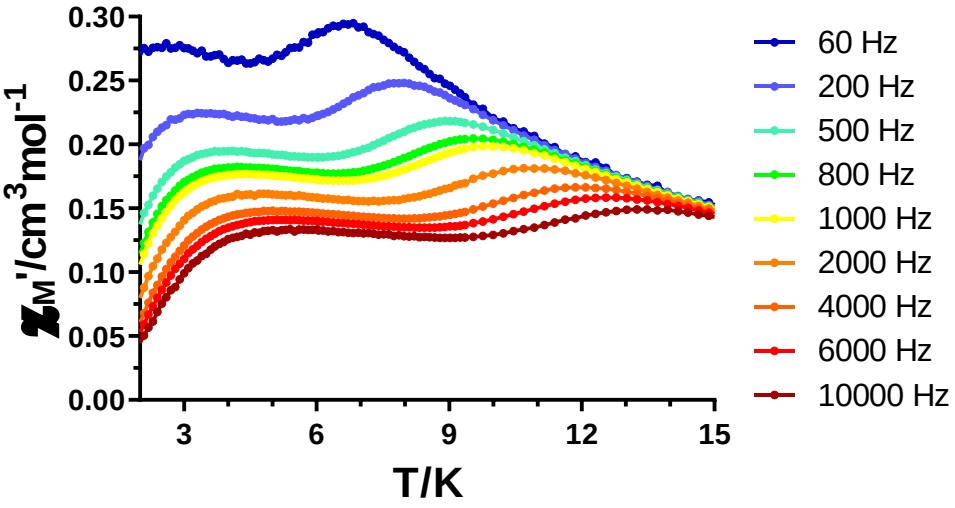

Figure A2.91.- Temperature dependence of the in phase components of the *ac* susceptibility in a *dc* applied field of 1 kOe for **13**$_{DyY}$.

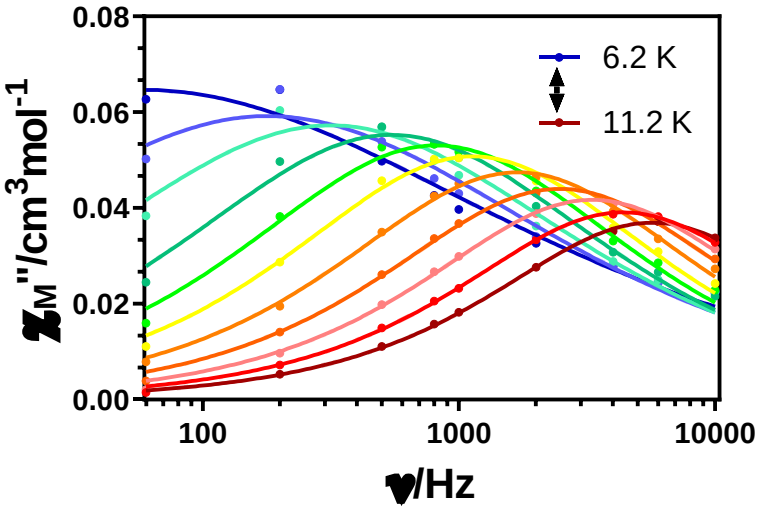

Figure A2.92.- Variable-temperature frequency dependence of the χ_M'' signal under 1 kOe applied field for **13**$_{DyY}$. Solid lines represent the best fitting of the experimental data to the Debye model.

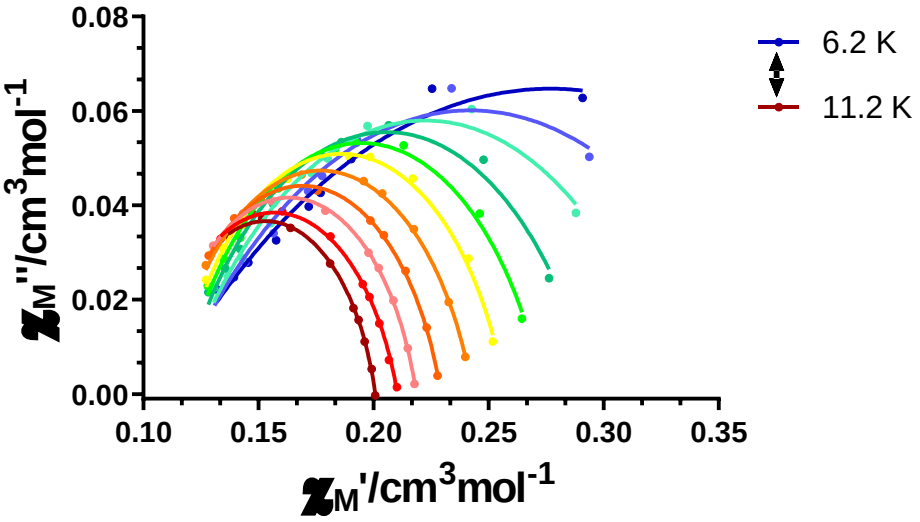

Figure A2.93.- Cole-Cole plots under 1 kOe field for **13**$_{DyY}$. Solid lines represent the best fit to the generalized Debye model.

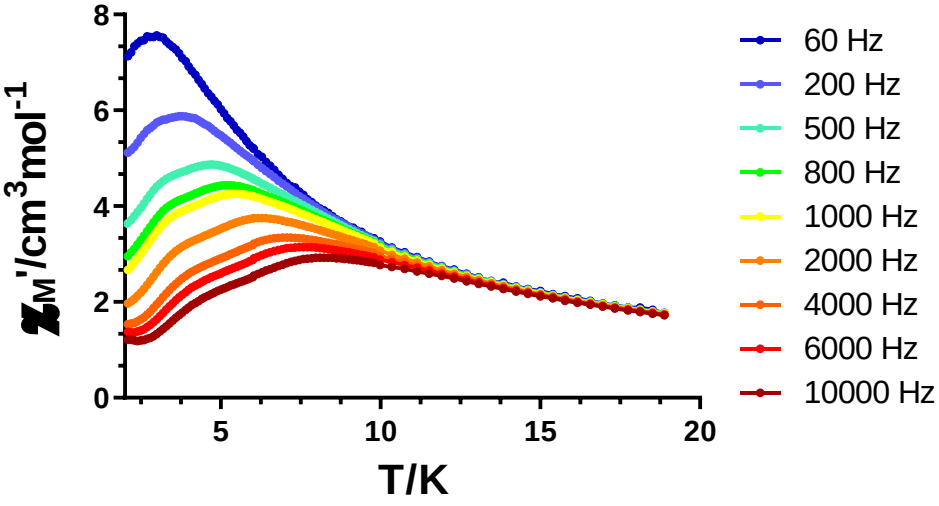

Figure A2.94.- Temperature dependence of the in phase components of the *ac* susceptibility in a *dc* applied field of 1 kOe for **14**.

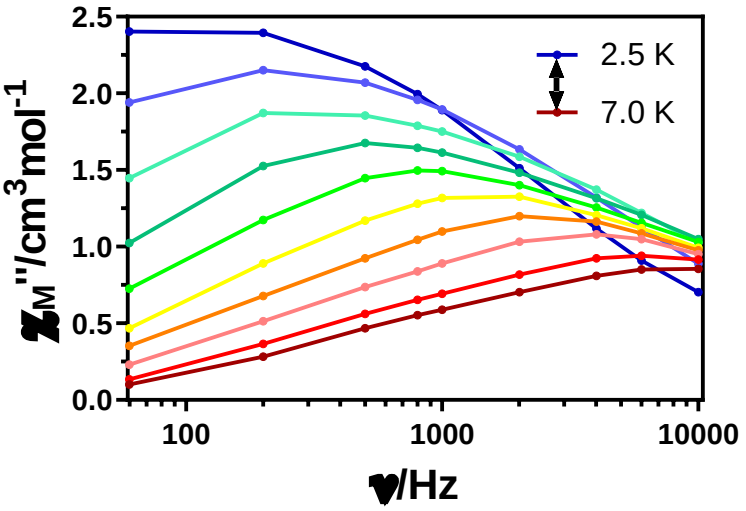

Figure A2.95.- Variable-temperature frequency dependence of the χ_M'' signal under 1 kOe applied field for **14**. Solid lines are a guide to the eye.

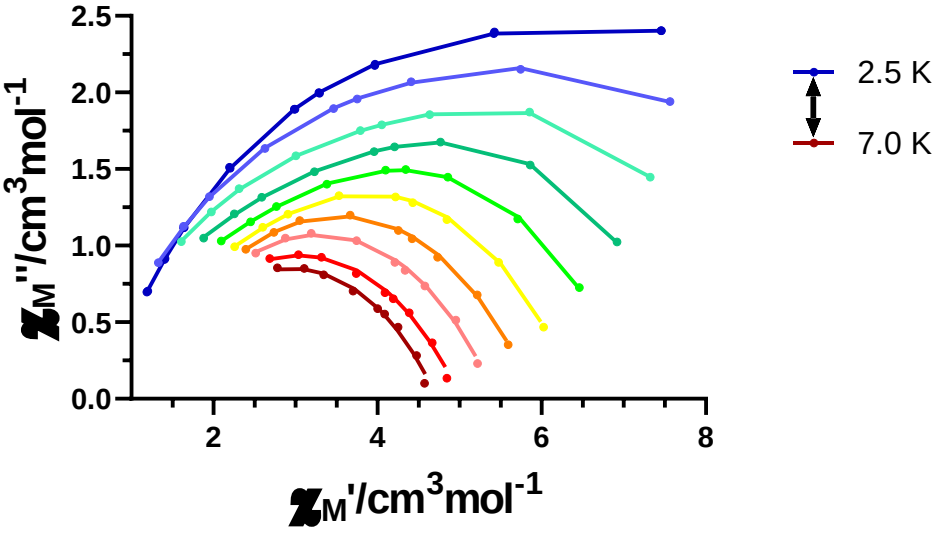

Figure A2.96.- Cole-Cole plots under 1 kOe field for **14**. Solid lines represent the best fit using a sum of two modified Debye functions.

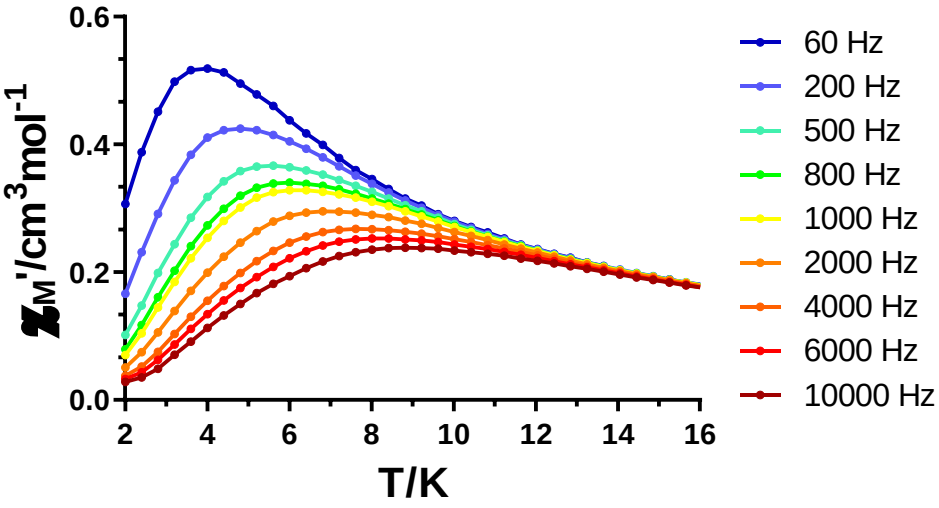

Figure A2.97.- Temperature dependence of the in phase components of the *ac* susceptibility in a *dc* applied field of 1 kOe for **14**$_{DyY}$.

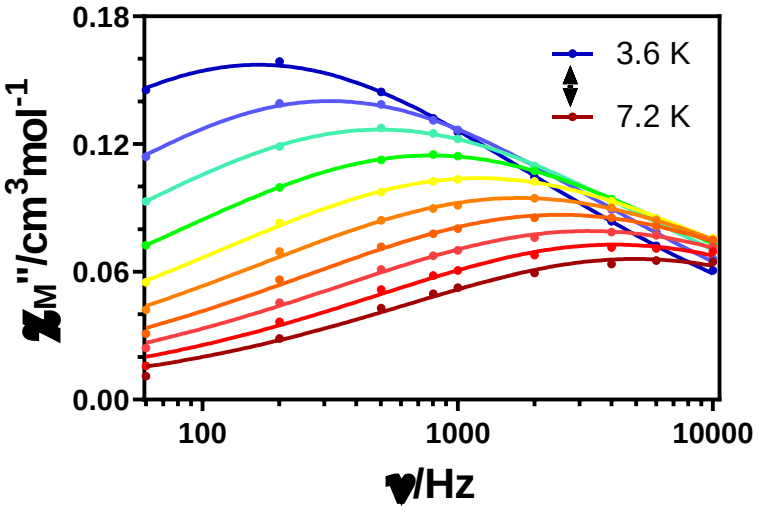

Figure A2.98.- Variable-temperature frequency dependence of the χ_M'' signal under 1 kOe applied field for **14**$_{DyY}$. Solid lines represent the best fitting of the experimental data to the Debye model.

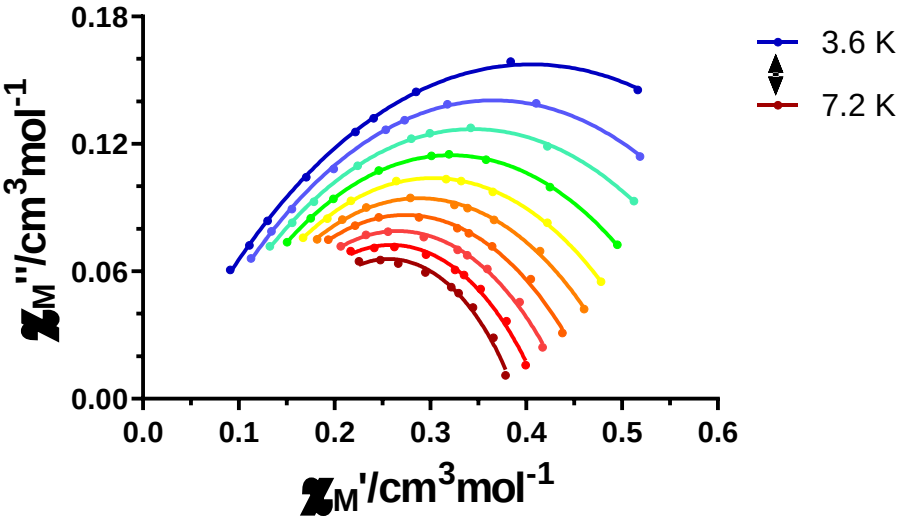

Figure A2.99.- Cole-Cole plots under 1 kOe field for **14**$_{DyY}$. Solid lines represent the best fit to the generalized Debye model.

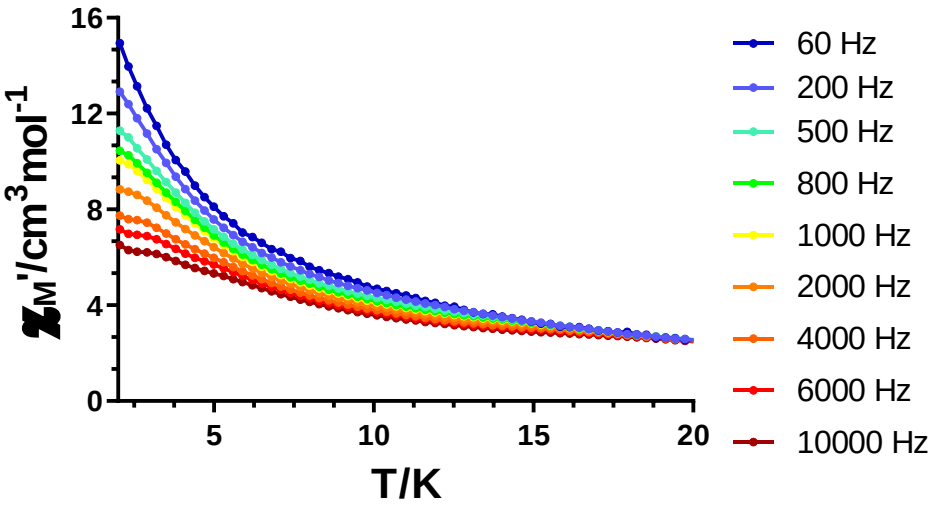

Figure A2.100.- Temperature dependence of the in phase components of the *ac* susceptibility in a *dc* applied field of 1 kOe for **15**.

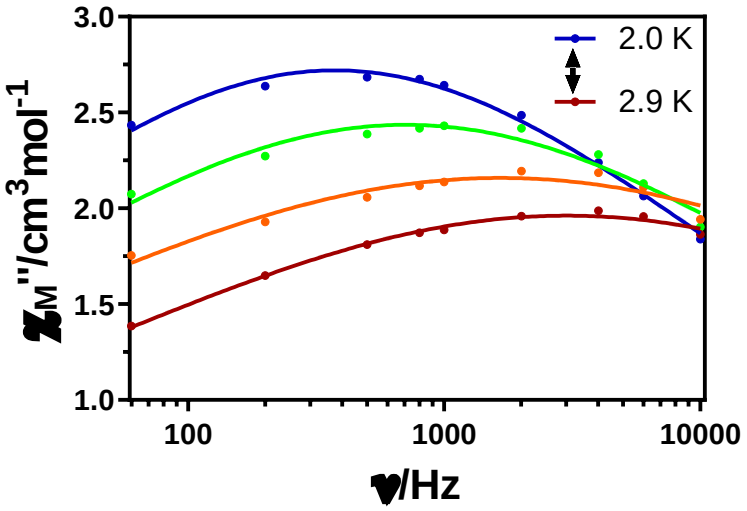

Figure A2.101.- Variable-temperature frequency dependence of the χ_M'' signal under 1 kOe applied field for **15** FR. Solid lines represent the best fitting of the experimental data to the Debye model.

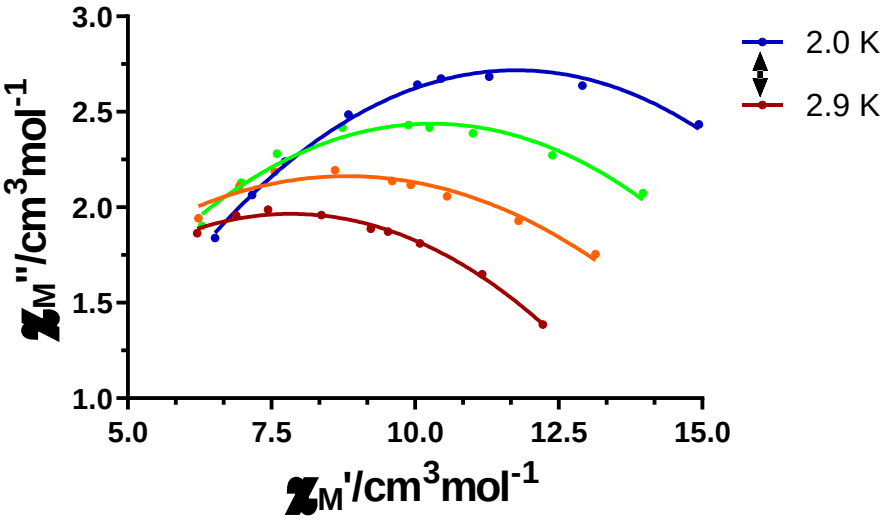

Figure A2.102.- Cole-Cole plots under 1 kOe field for **10** FR. Solid lines represent the best fit to the generalized Debye model.

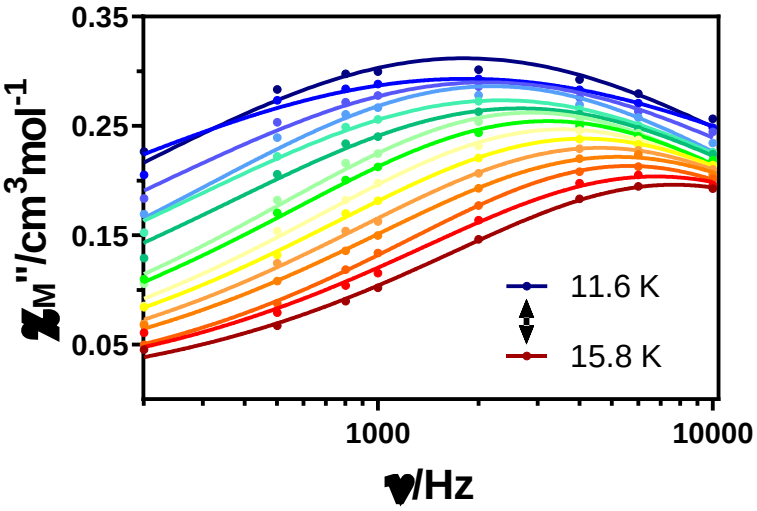

Figure A2.103.- Variable-temperature frequency dependence of the χ_M'' signal under 1 kOe applied field for **15** SR. Solid lines represent the best fitting of the experimental data to the Debye model.

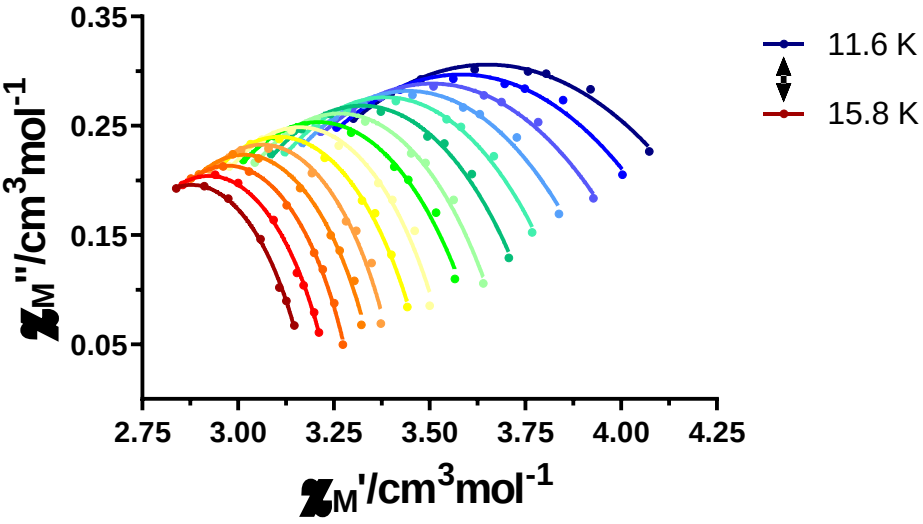

Figure A2.104.- Cole-Cole plots under 1 kOe field for **10** SR. Solid lines represent the best fit to the generalized Debye model.

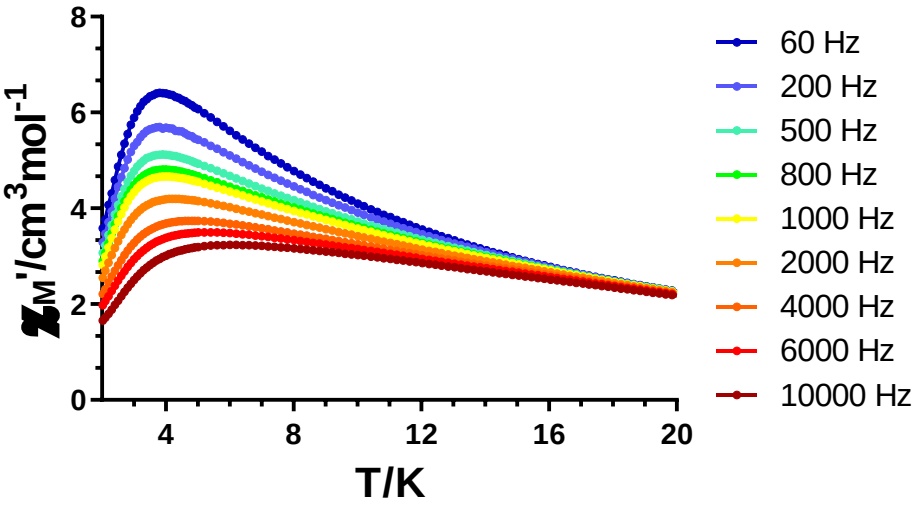

Figure A2.105.- Temperature dependence of the in phase components of the *ac* susceptibility in a *dc* applied field of 2.5 kOe for **15**.

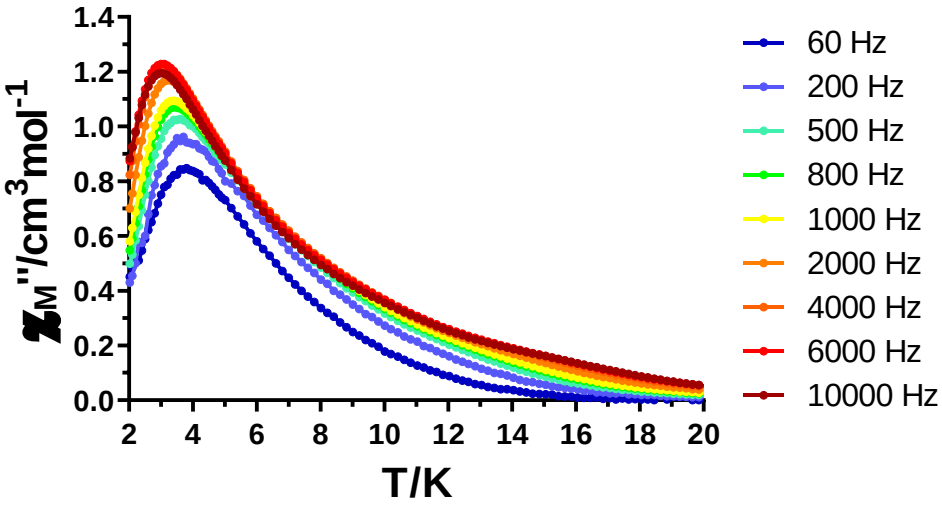

Figure A2.106.- Temperature dependence of the out-of-phase components of the *ac* susceptibility in a *dc* applied field of 2.5 kOe for **15**.

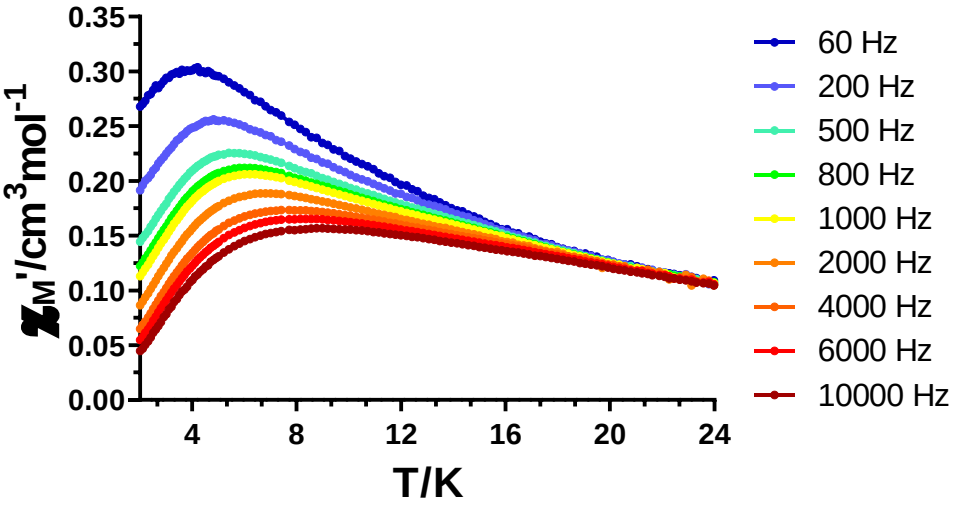

Figure A2.107.- Temperature dependence of the in phase components of the *ac* susceptibility in a *dc* applied field of 2.5 kOe for **15**$_{DyY}$.

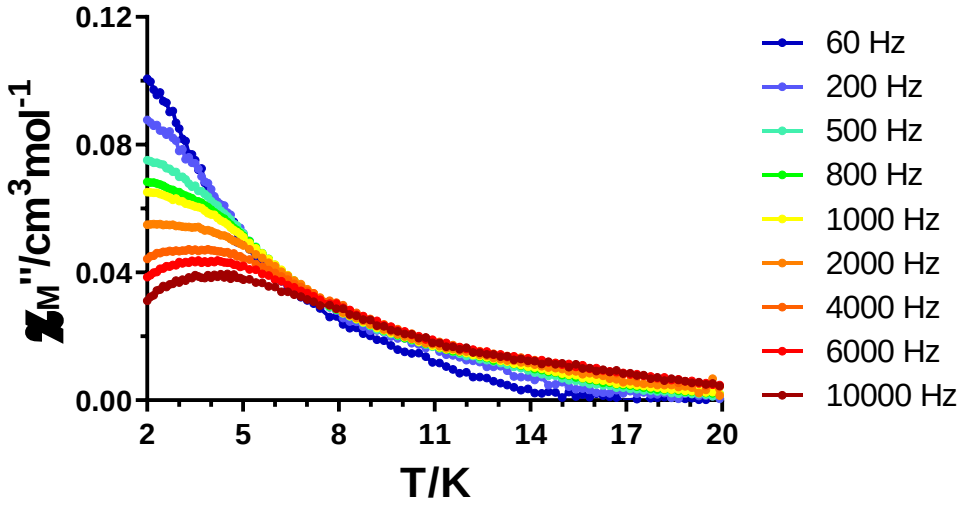

Figure A2.108.- Temperature dependence of the out-of-phase components of the *ac* susceptibility in a *dc* applied field of 2.5 kOe for **15**$_{DyY}$.

8. Magellan Figures.

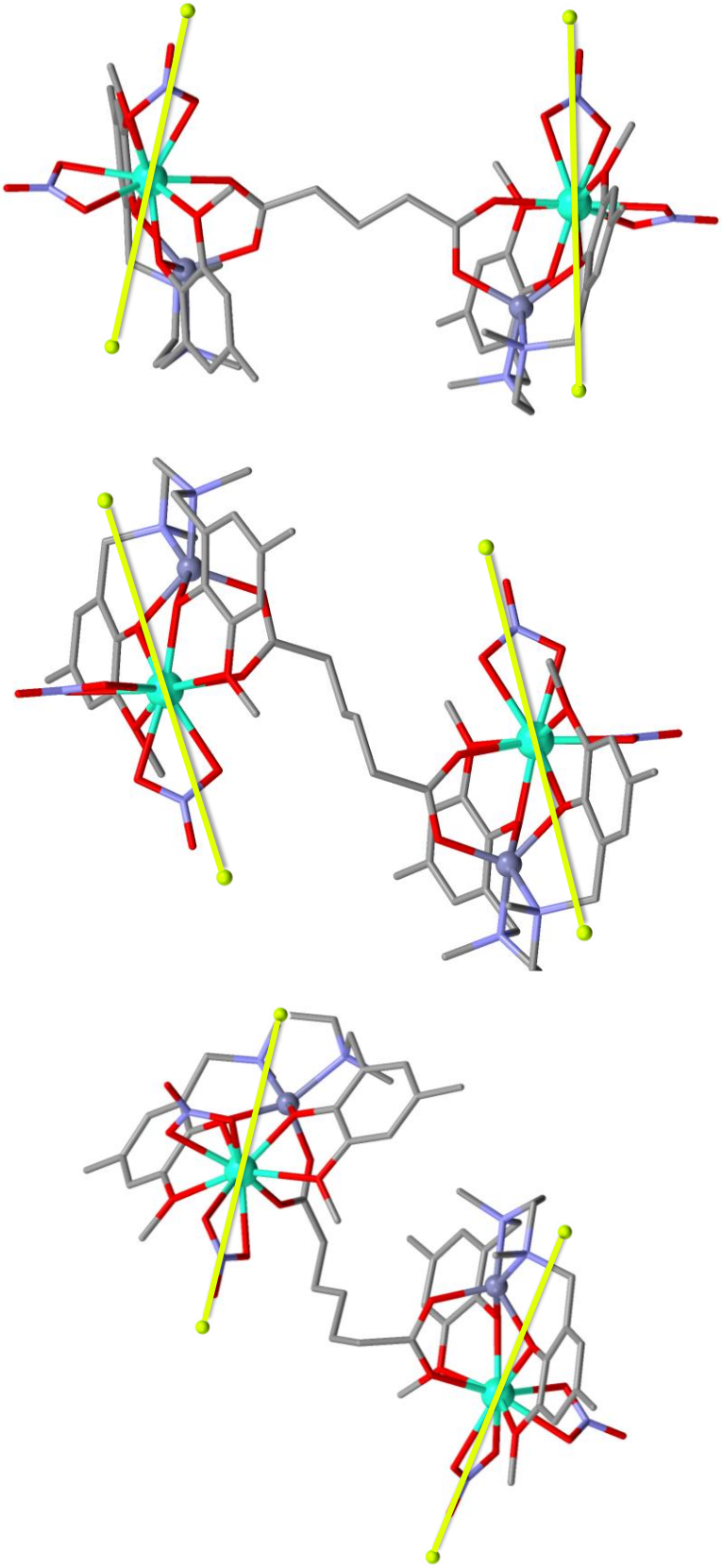

Figure A2.109.- Anisotropy axes for compounds **9** (top), **10** (middle) and **11** (bottom) obtained by Magellan software (green line).

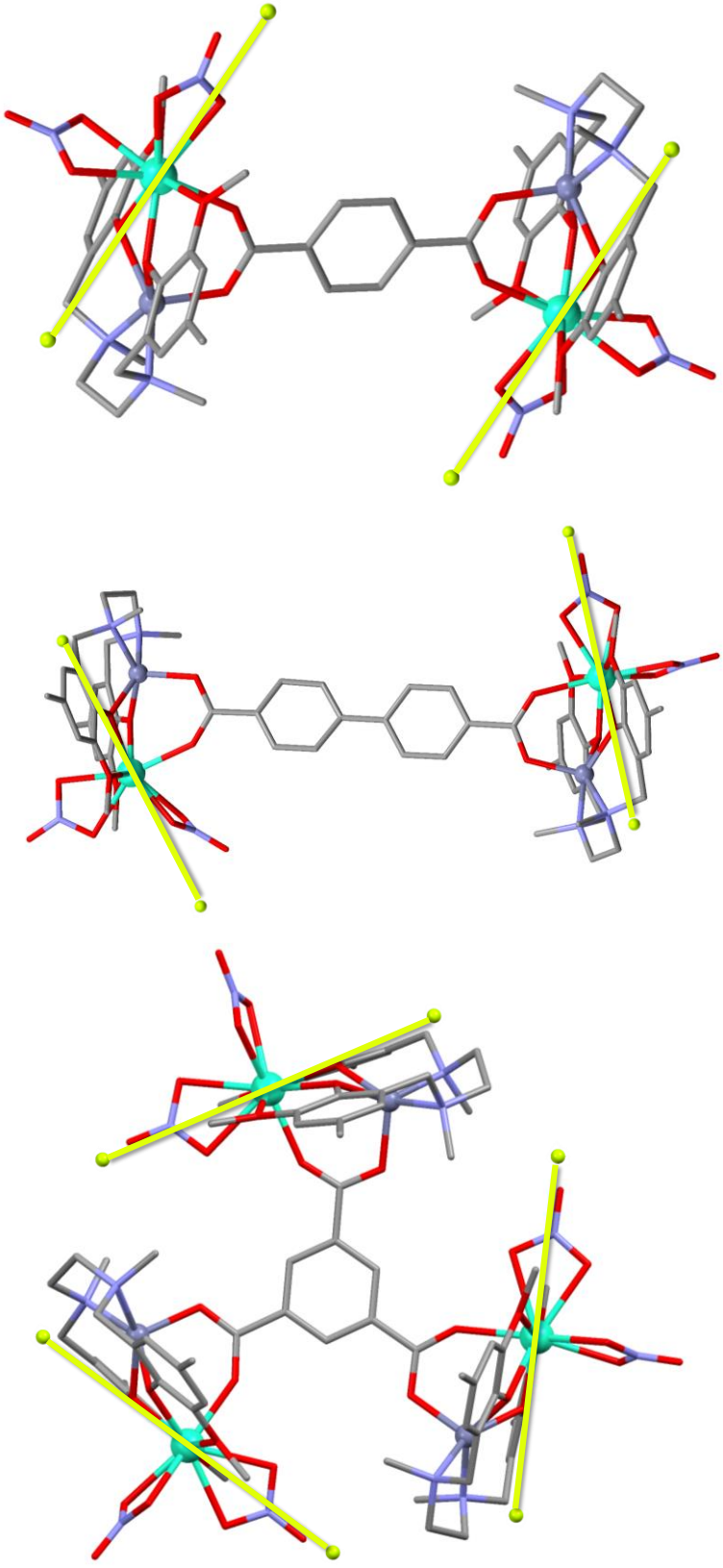

Figure A2.110.- Anisotropy axes for compounds **12** (top), **13** (middle) and **14** (bottom) obtained by Magellan software (green line).

8. Nuclear Magnetic Resonance.

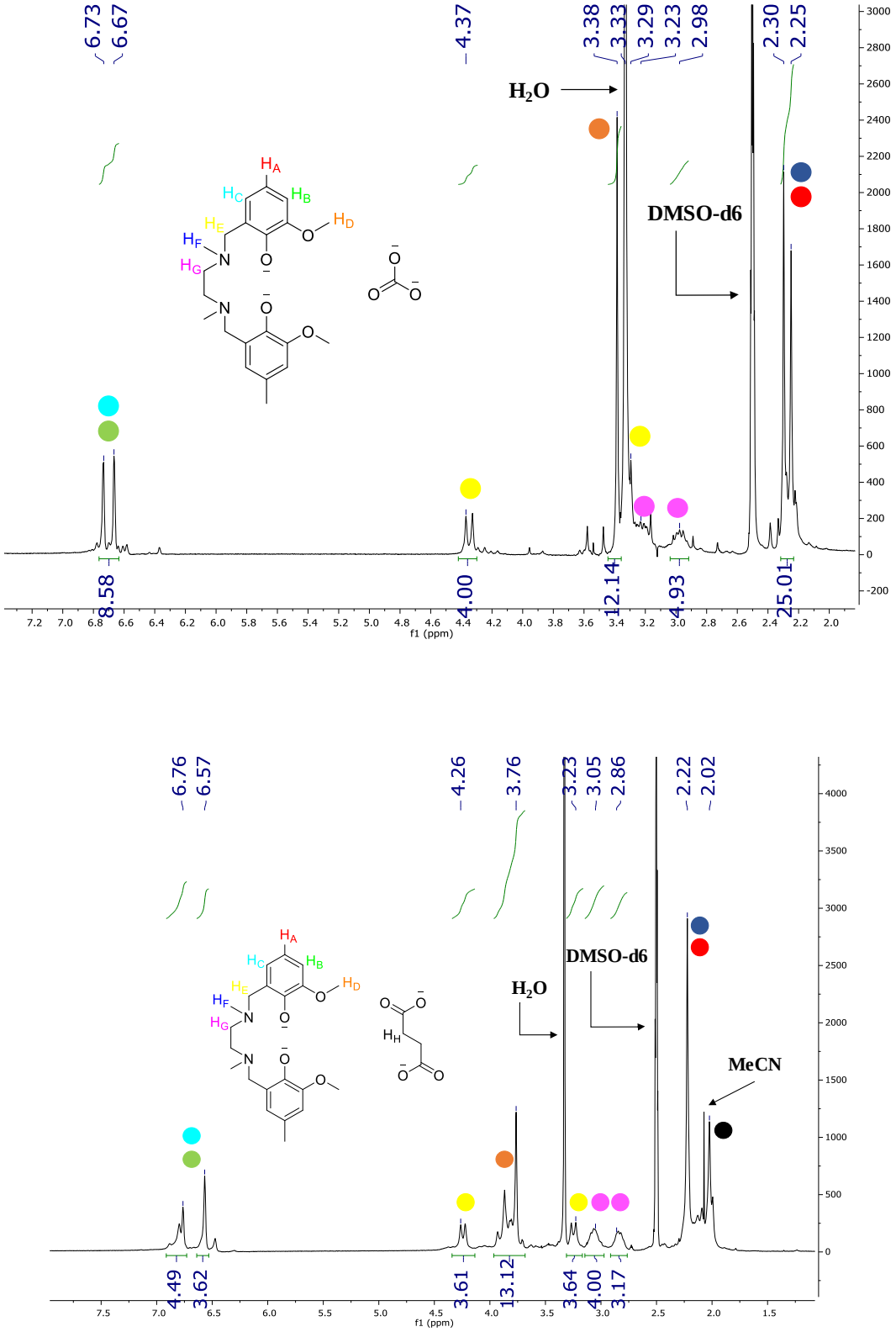

Figure A2.111.-^{1}H-NMR of **7$_Y$** (top) and **8$_Y$** (bottom) in DMSO-d^{6}.

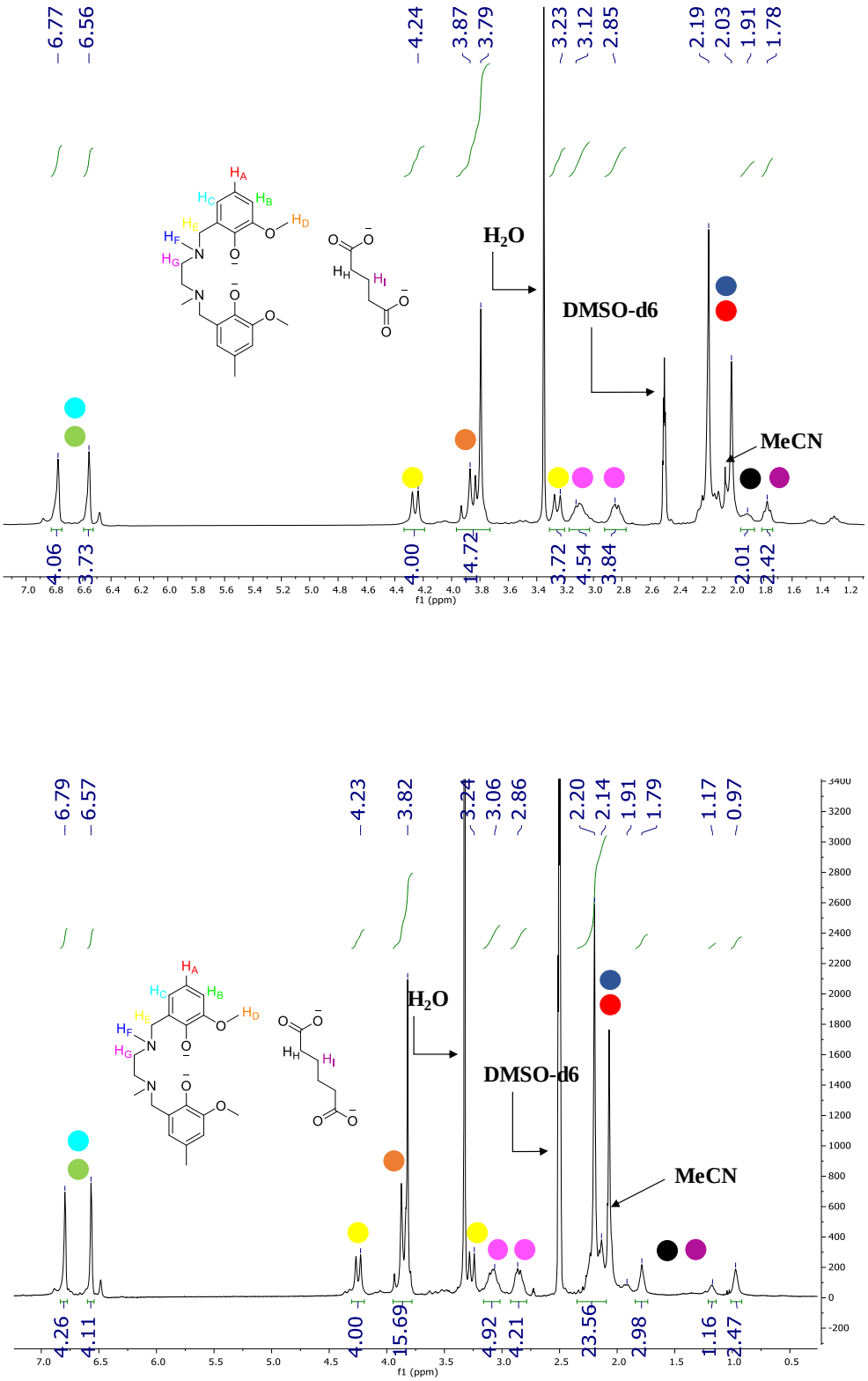

Figure A2.112.-^{1}H-NMR of **9$_{Y}$** (top) and **10$_{Y}$** (bottom) in DMSO-d^{6}.

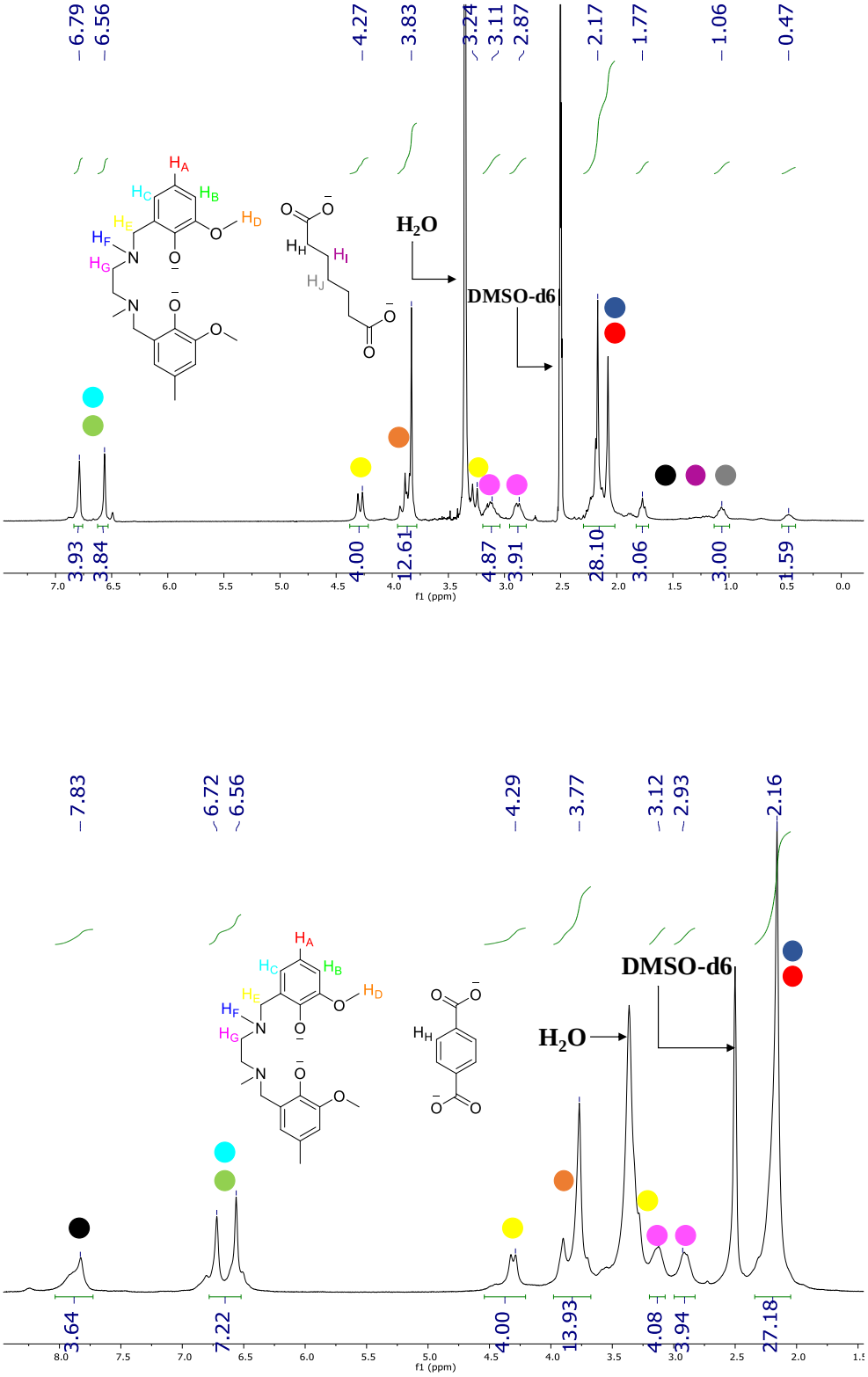

Figure A2.113.-^{1}H-NMR of **11**$_{Y}$ (top) and **12**$_{Y}$ (bottom) in DMSO-d^{6}.

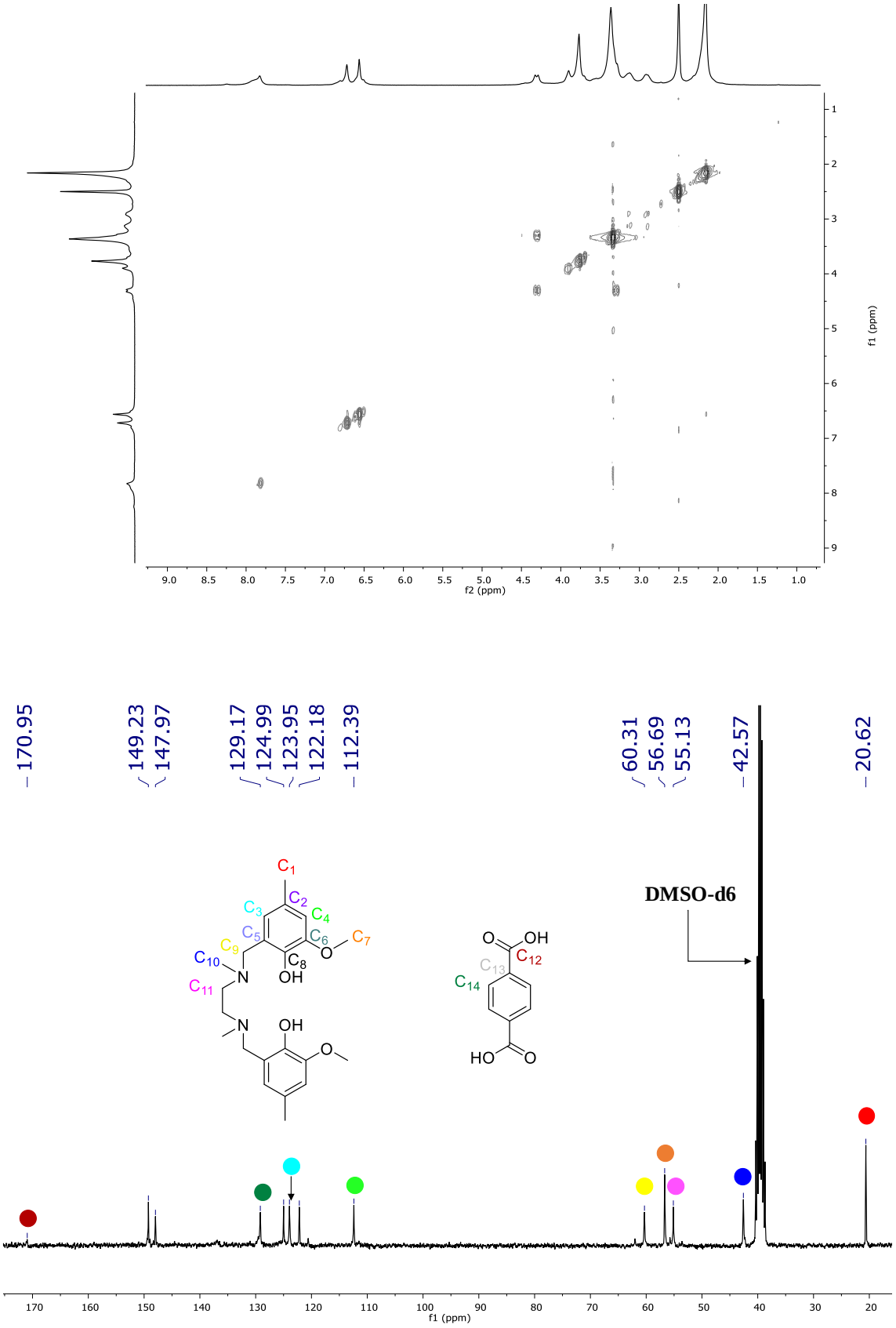

Figure A2.114.-COSY spectrum (top) and $^{13}C\{^{1}H\}$-NMR (bottom) of **12$_Y$** in DMSO-d^6.

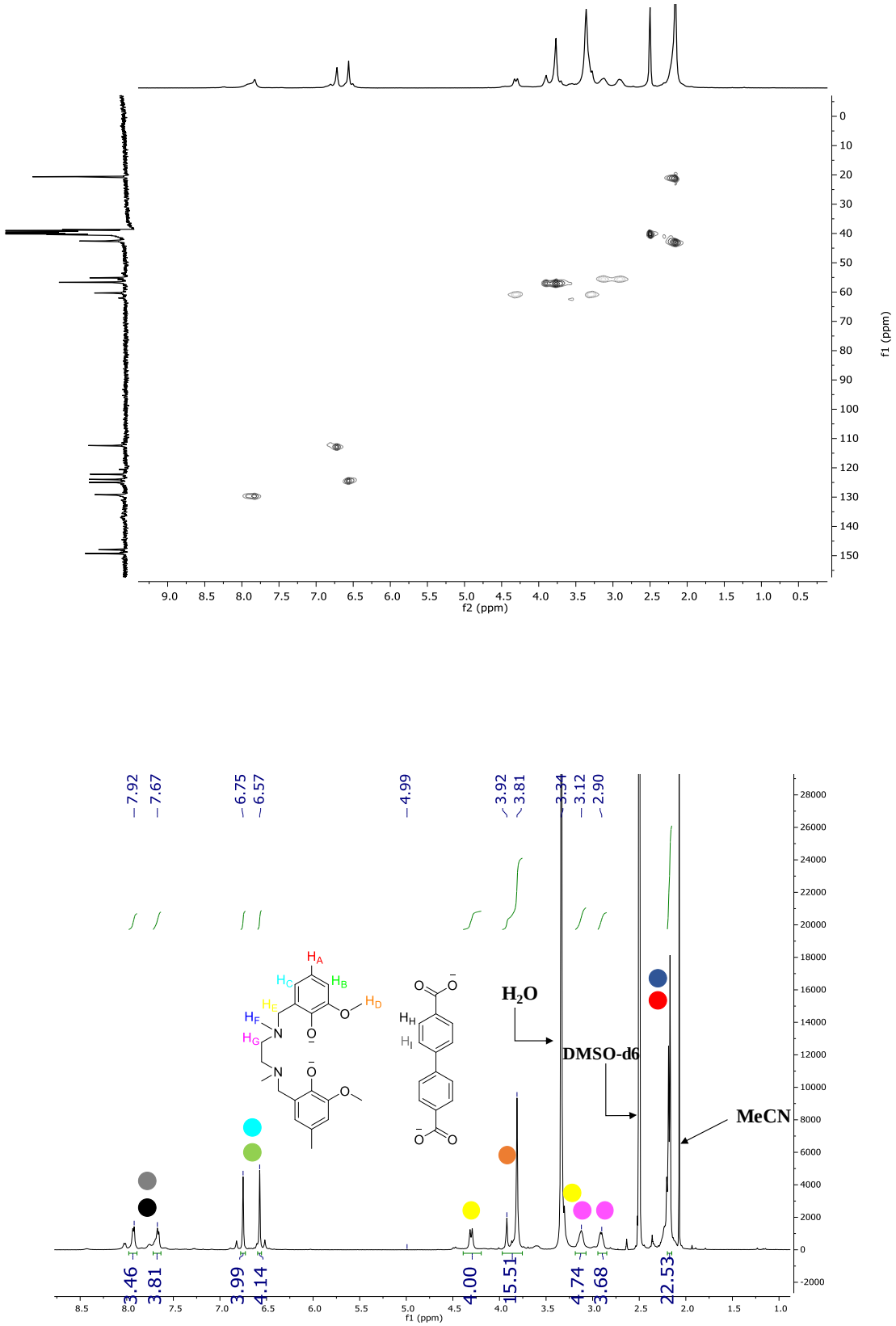

Figure A2.115.-^{1}H-^{13}C-HSQC of **12$_{Y}$** (top) and ^{1}H-NMR of **13$_{Y}$** (bottom) in DMSO-d^{6}.

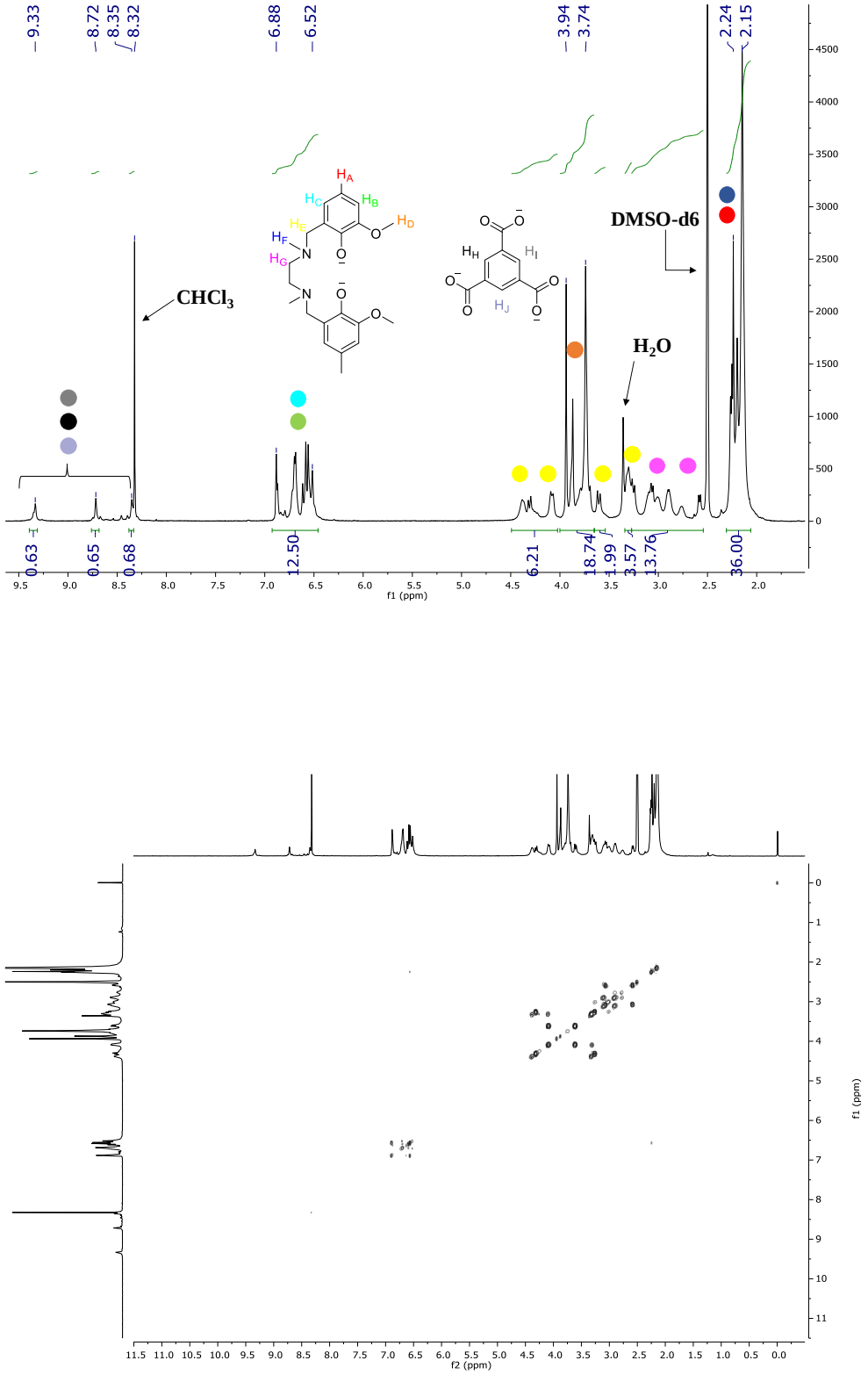

Figure A2.116.-^{1}H-NMR (top) and COSY spectrum (bottom) of **14$_{Y}$** in DMSO-d^{6}.

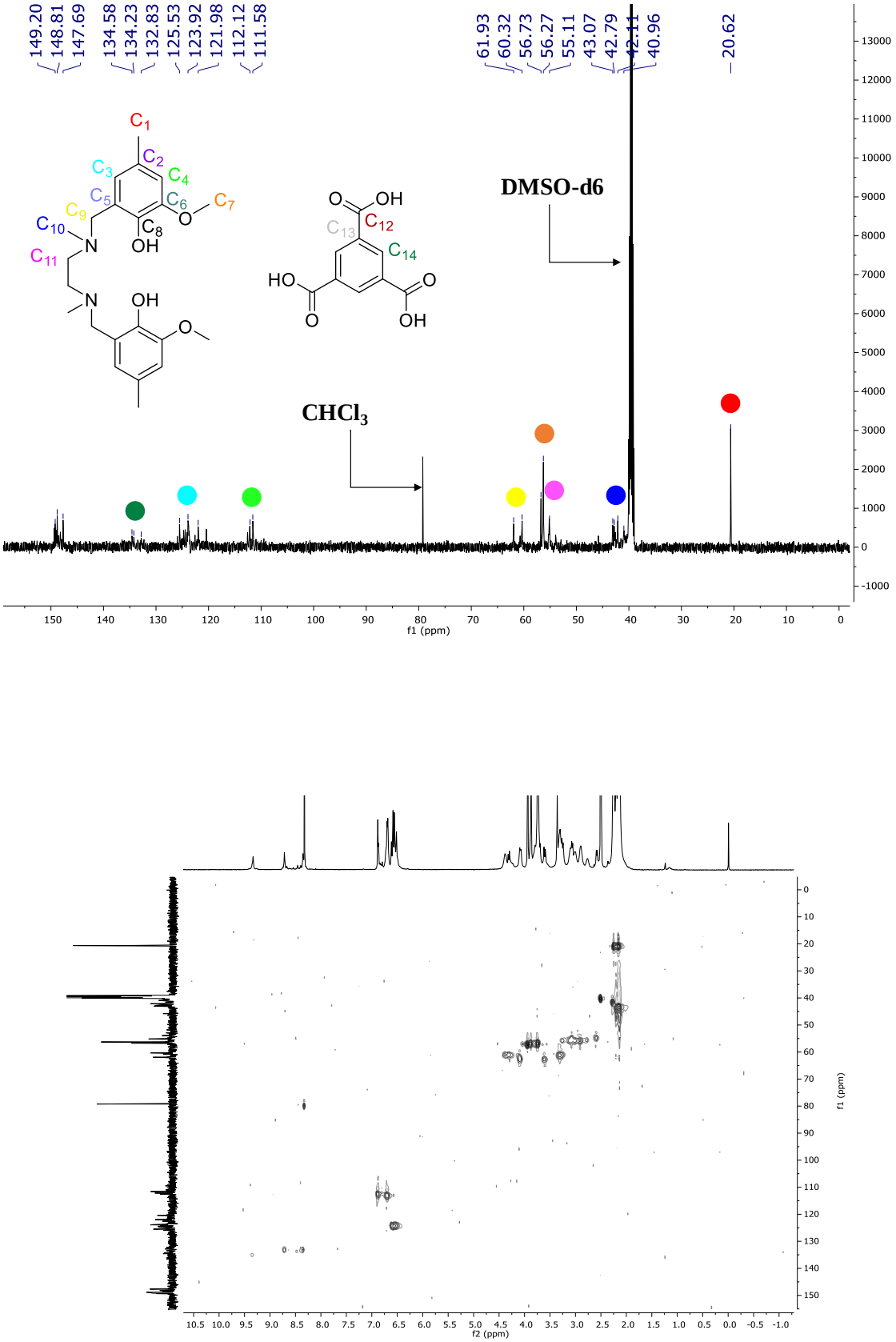

Figure A2.117.- $^{13}C\{^{1}H\}$-NMR (top) and ^{1}H-^{13}C-HSQC (bottom) of **14$_Y$** in DMSO-d^6.

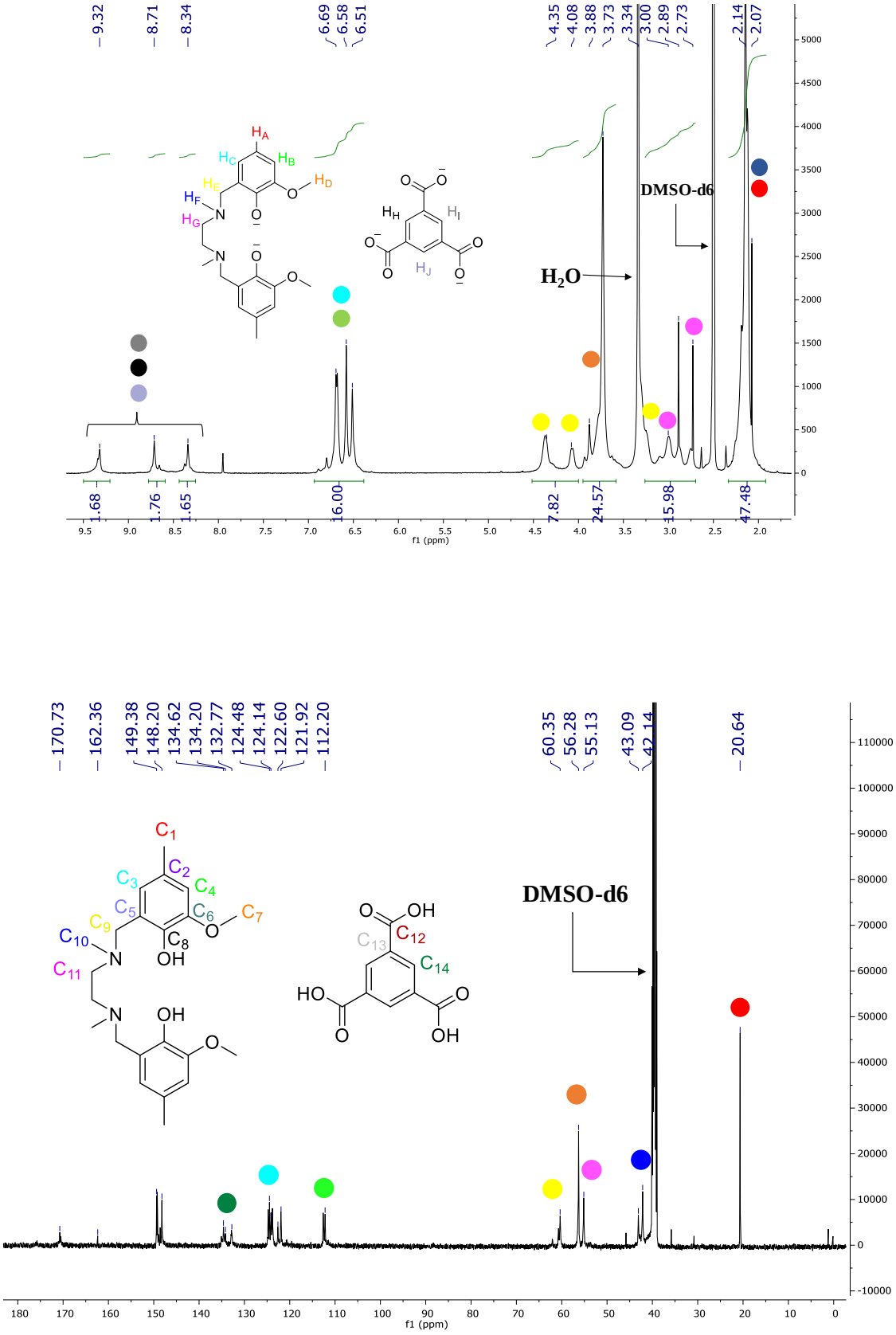

Figure A2.118.- ^{1}H-NMR (top) and ^{13}C{^{1}H}-NMR (bottom) of **15$_{Y}$** in DMSO-d^{6}.

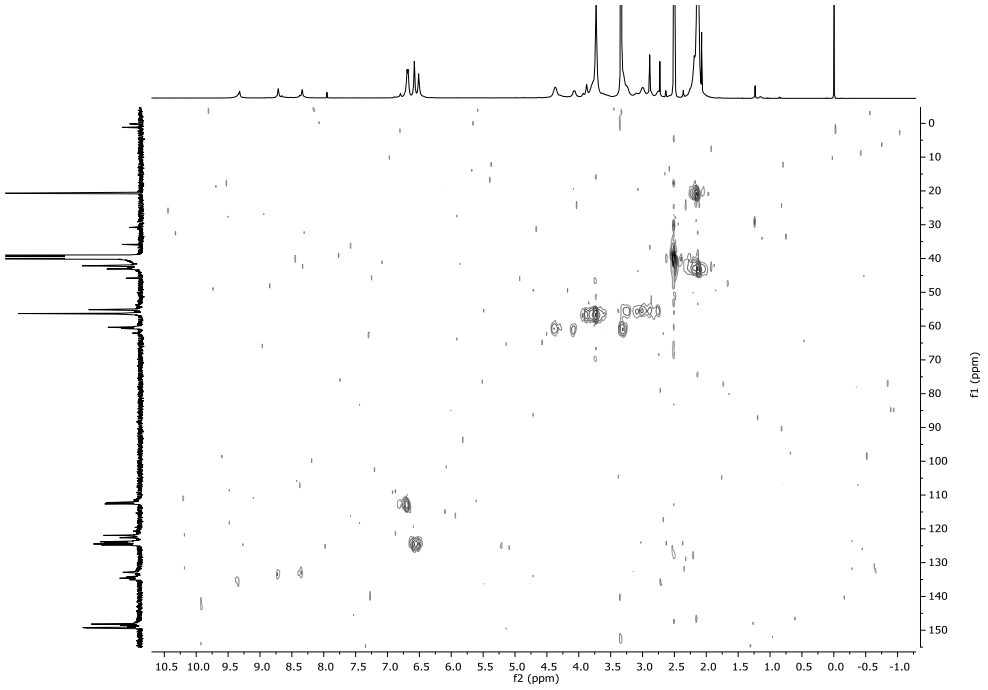

Figure A2.119.- ^{1}H-^{13}C-HSQC of **15_Y** in DMSO-d^6.

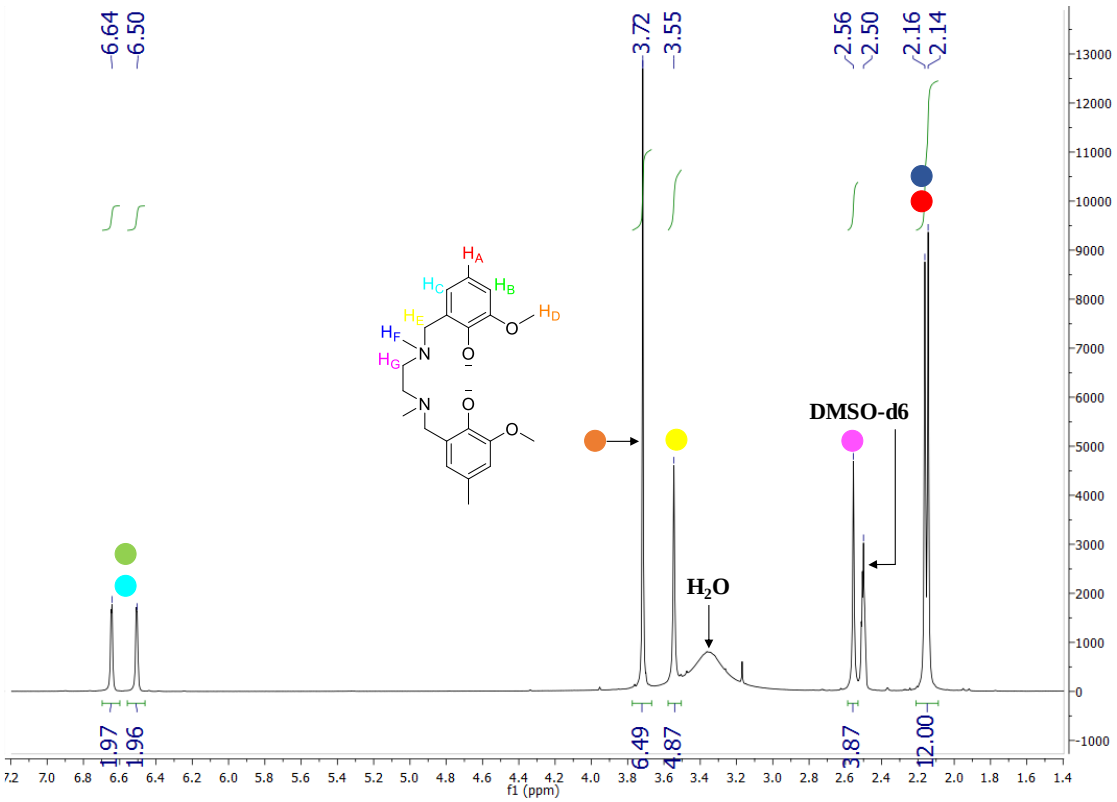

Figure A2.120.-^{1}H-NMR of H_2L^3 in DMSO-d^6.

APPENDICES

Chapter 3: *Magnetic study of multinuclear Co^{II} based and mixed heterotrinuclear $TM^{II}Ln^{III}TM^{II}$ compounds: role of intramolecular interactions to obtain zero field SMMs*

Index:

1. Elemental Analyses and Crystallographic Tables.

Table A3.1.- Yields and elemental analyses for complexes **16-25**. The formulas for **20** and **24** correspond to the phase with water and acetonitrile crystallization solvent molecules. The formulas for **19**, **21-23** and **25** are a combination of both possible phases in 50:50 molar ratios.

Complex	Yield (%)	Formula	% C calc./found	% H calc./found	% N calc./found
16	27	$C_{44}H_{64}N_4O_{10}Cl_4Co_4$	44.53/44.47	5.44/5.59	4.72/4.52
17	62	$C_{44}H_{64}N_{16}O_{10}Co_4$	43.57/43.77	5.32/5.51	18.48/18.31
18a	23	$C_{62}H_{88}N_8O_{19}Co_5$	48.23/48.33	5.74/5.60	7.26/7.49
19	68	$C_{46}H_{68}N_5O_{10.5}Cl_3Co_2Y$	47.13/46.80	5.85/5.94	5.97/5.80
20	49	$C_{46}H_{69}N_5O_{11}Cl_3Co_2Gd$	44.22/44.10	5.56/5.63	5.60/5.69
21	61	$C_{46}H_{68}N_5O_{10.5}Cl_3Co_2Tb$	44.48/44.31	5.52/5.43	5.64/5.67
22	56	$C_{46}H_{68}N_5O_{10.5}Cl_3Co_2Dy$	44.35/44.26	5.50/5.45	5.62/5.67
23	63	$C_{46}H_{68}N_5O_{10.5}Cl_3Co_2Er$	44.18/44.03	5.48/5.59	5.60/5.43
24	74	$C_{46}H_{69}N_5O_{11}Cl_3Co_2Yb$	43.66/43.78	5.50/5.35	5.53/5.46
25	62	$C_{46}H_{68}N_5O_{10.5}Cl_3Zn_2Dy$	43.89/43.60	5.44/5.41	5.56/5.63

Table A3.2.- Crystallographic data for compounds **16-19**.

Complex	**16**	**17**	**18a**	**18b**	**19**
Formula	$C_{44}H_{64}Cl_4Co_4N_4O_{10}$	$C_{44}H_{64}Co_4N_{16}O_{10}$	$C_{62}H_{88}Co_5N_8O_{19}$	$C_{60}H_{85}Co_5N_7O_{19}$	$C_{46}H_{67}Cl_3Co_2YN_5O_{10}$
M_r	1186.51	1212.83	1544.06	1503.00	1163.16
Crystal system	*trigonal*	*trigonal*	*triclinic*	*triclinic*	*orthorhombic*
Space group (no.)	*R-3* (148)	*R-3* (148)	*P*-1 (2)	*P*-1 (2)	$C222_1$ (20)
a (Å)	33.5955(19)	32.0856(5)	11.6986(12)	11.871(5)	9.5410(6)
b (Å)	33.5955(19)	32.0856(5)	12.4982(12)	15.460(5)	27.1091(16)
c (Å)	11.6721(8)	13.7672(3)	25.602(3)	19.301(5)	20.5493(11)
α (°)	90	90	95.936(3)	89.938(5)	90
β (°)	90	90	92.743(3)	85.464(5)	90
γ (°)	120	120	106.908(3)	73.751(5)	90
V (Å^3)	11408.8(15)	12274.3(5)	3550.3(6)	3389(2)	5315.0(5)
Z	9	9	2	2	4
D_c (g cm^{-3})	1.554	1.477	1.444	1.473	1.454
μ(MoK$_\alpha$) (mm^{-1})	1.554	1.263	1.216	1.272	1.908
T (K)	100	100	100	100	100
Observed reflections	4569 (2553)	5704 (4112)	17537 (7885)	17524 (13275)	5435 (5023)
R_{int}	0.0710	0.0784	0.1595	0.0740	0.0661
Parameters	304	341	874	844	316
GOF	0.736	1.059	0.992	1.067	1.026
$R_1^{a,b}$	0.0968 (0.0405)	0.1003 (0.0655)	0.2284 (0.0826)	0.0712 (0.0441)	0.0253 (0.0213)
wR_2^c	0.0645 (0.0553)	0.1983 (0.1736)	0.1690 (0.1310)	0.1143 (0.0973)	0.0485 (0.0479)
Largest difference in peak and hole (e Å^{-3})	0.403 and -0.338	2.046 and -1.076	0.685 and -1.140	0.584 and -1.087	0.316 and -0.351

[a] $R_1 = \Sigma||F_o| - |F_c||/\Sigma|F_o|$. [b] Values in parentheses for reflections with $I > 2\sigma(I)$. [c] $wR_2 = \{\Sigma[w(F_o^2 - F_c^2)^2]/\Sigma[w(F_o^2)^2]\}^{½}$

Table A3.3.- Crystallographic data for compounds **20-22** and **24-25**.

Complex	**20**	**21**	**22**	**24**	**25**
Formula	$C_{46}H_{69}Cl_3Co_2GdN_5O_{11}$	$C_{46}H_{69}Cl_3Co_2TbN_5O_{11}$	$C_{46}H_{69}Cl_3Co_2DyN_5O_{11}$	$C_{46}H_{69}Cl_3Co_2YbN_5O_{11}$	$C_{46}H_{67}Cl_3Zn_2DyN_5O_{10}$
M_r	1249.53	1251.19	1254.78	1265.32	1249.63
Crystal system	*monoclinic*	*monoclinic*	*monoclinic*	*monoclinic*	*orthorhombic*
Space group (no.)	$P2_1/c$ (14)	$P2_1/c$ (14)	$P2_1/c$ (14)	$P2_1/c$ (14)	$C222_1$ (20)
a (Å)	22.590(4)	22.5697(11)	22.499(4)	22.5379(7)	9.5438(6)
b (Å)	9.5414(16)	9.5564(5)	9.5412(14)	9.5642(3)	27.0693(19)
c (Å)	26.970(4)	26.9530(13)	26.911(4)	26.9072(10)	20.5270(11)
α (°)	90	90	90	90	90
β (°)	114.416(2)	114.336(2)	114.317(2)	114.5280(10)	90
γ (°)	90	90	90	90	90
V (Å^3)	5293.3(15)	5296.8(5)	5264.4(14)	5276.6(3)	5303.0(6)
Z	4	4	4	4	4
D_c (g cm^{-3})	1.568	1.569	1.583	1.593	1.565
μ(MoK_α) (mm^{-1})[a]	2.069	2.151	2.240	2.591	2.500
T (K)	100	100	100	100	100
Observed reflections	12489 (10681)	13743 (12982)	9452 (5413)	13646 (9706)	6910 (6468)
R_{int}	0.0430	0.0248	0.1064	0.0765	0.0554
Parameters	626	626	614	642	307
GOF	1.059	1.083	1.021	1.016	1.084
R_1[a,b]	0.0426 (0.0353)	0.0277 (0.0257)	0.1271 (0.0737)	0.0740 (0.0391)	0.0293 (0.0240)
wR_2[c]	0.0927 (0.0880)	0.0646 (0.0633)	0.2369(0.1854)	0.0829 (0.0726)	0.0509 (0.0491)
Largest difference in peak and hole (e Å^{-3})	2.475 and -0.864	1.117 and -1.341	2.020 and -4.259	1.650 and -1.200	1.173 and -1.054

[a]$R_1 = \Sigma||F_o| - |F_c||/\Sigma|F_o|$. [b]Values in parentheses for reflections with $I > 2\sigma(I)$. [c]$wR_2 = \{\Sigma[w(F_o^2 - F_c^2)^2]/\Sigma[w(F_o^2)^2]\}^{½}$

Table A3.4.- Bond lengths (Å) and angles (°) for compounds **16** and **17**.

Symmetry operations: (i) –x, -y, -z; (ii) –x+2/3, -y+1/3, -z+1/3.

Compound	**16**		**17**
Co1-O1	2.061(3)	Co1-O1	2.044(3)
Co1-O3	2.054(3)	Co1-O3	2.046(3)
Co1-N1	2.175(3)	Co1-N1	2.173(4)
Co1-N2	2.171(4)	Co1-N2	2.190(4)
Co1-Cl1(i)	2.5051(11)	Co1-N1A1(ii)	2.229(4)
Co1-Cl1	2.5149(13)	Co1-N1A1	2.230(4)
Co2-O1(i)	2.006(3)	Co2-O1	1.988(4)
Co2-O2(i)	2.218(3)	Co2-O2	2.212(4)
Co2-O3	2.016(3)	Co2-O3(ii)	1.984(3)
Co2-O4	2.389(3)	Co2-N1A1	2.252(4)
Co2-Cl1	2.5400(13)	Co2-N1A2	1.993(5)
Co2-Cl2	2.3145(13)		
Co1-O1-Co2(i)	111.67(13)	Co1-O1-Co2	108.70(16)
Co1-O3-Co2	115.76(15)	Co1-O3-Co2(ii)	107.45(16)
Co1(i)-Cl1-Co1	89.40(4)	Co1(ii)-N1A1-Co1	100.41(17)
Co1(i)-Cl1-Co2	83.66(4)	Co1(ii)-N1A1-Co2	92.95(16)
Co1-Cl1-Co2	85.98(4)	Co1-N1A1-Co2	93.94(16)
O1-Co1-O3	164.37(12)	O1-Co1-O3	167.21(14)
O1-Co1-N1	88.68(12)	O1-Co1-N1	86.51(15)
O1-Co1-N2	104.21(13)	O1-Co1-N2	104.18(15)
O1-Co1-Cl1(i)	82.21(8)	O1-Co1-N1A1(ii)	89.31(15)
O1-Co1-Cl1	88.07(9)	O1-Co1-N1A1	78.30(15)
O3-Co1-N1	100.96(12)	O3-Co1-N1	101.64(15)
O3-Co1-N2	89.46(13)	O3-Co1-N2	86.93(15)
O3-Co1-Cl1(i)	89.58(8)	O3-Co1-N1A1(ii)	79.40(15)
O3-Co1-Cl1	78.70(9)	O3-Co1-N1A1	93.63(15)
N1-Co1-N2	81.71(13)	N1-Co1-N2	81.35(16)
N1-Co1-Cl1(i)	168.22(10)	N1-Co1-N1A1(ii)	102.24(16)
N1-Co1-Cl1	96.57(10)	N1-Co1-N1A1	164.70(16)
N2-Co1-Cl1(i)	93.25(9)	N2-Co1-N1A1(ii)	166.29(16)
N2-Co1-Cl1	167.52(10)	N2-Co1-N1A1	100.49(16)
Cl1(i)-Co1-Cl1	90.60(4)	N1A1(ii)-Co1-N1A1	79.59(17)
O1(i)-Co2-O2(i)	77.45(11)	O1-Co2-O2	76.70(14)
O1(i)-Co2-O3	96.00(11)	O1-Co2-O3(ii)	97.33(15)
O1(i)-Co2-O4	151.39(11)		
O1(i)-Co2-Cl1	82.38(9)	O1-Co2-N1A1	78.95(14)
O1(i)-Co2-Cl2	114.67(9)	O1-Co2-N1A2	120.4(2)
O2(i)-Co2-O3	106.29(12)	O2-Co2-O3(ii)	109.94(14)
O2(i)-Co2-O4	81.24(10)		
O2(i)-Co2-Cl1	159.58(8)	O2-Co2-N1A1	154.61(15)
O2(i)-Co2-Cl2	91.05(9)	O2-Co2-N1A2	95.30(19)
O3-Co2-O4	71.90(11)		
O3-Co2-Cl1	78.75(9)	O3-Co2-N1A1(ii)	80.17(15)
O3-Co2-Cl2	147.61(8)	O3(ii)-Co2-N1A2	138.8(2)
O4-Co2-Cl1	118.82(8)		
O4-Co2-Cl2	84.38(8)		
Cl1-Co2-Cl2	94.54(4)	N1A1-Co2-N1A2	90.80(19)

Table A3.5.- Bond lengths (Å) and angles (°) for compounds **18a** and **18b**.

Compound	**18a**	**18b**
Co1-O1A	1.988(4)	2.0101(18)
Co1-O1C	1.994(4)	2.0018(19)
Co1-O1OH	2.020(4)	2.0272(18)
Co1-O1D	2.034(3)	2.0306(19)
Co1-O3A	2.330(3)	2.3112(19)
Co2-O1B	2.038(3)	2.0540(19)
Co2-O1OH	2.041(4)	2.0494(19)
Co2-O2B	2.337(4)	2.329(2)
Co2-O2C	2.052(4)	2.0497(19)
Co2-O2D	2.027(3)	2.050(2)
Co2-O3B	2.219(4)	2.1932(19)
Co3-O1B	2.024(4)	2.0466(18)
Co3-O1E	2.048(4)	2.0899(19)
Co3-O2E	2.431(4)	2.394(2)
Co3-O3B	1.989(3)	2.002(2)
Co3-N1B	2.258(4)	2.271(2)
Co3-N2B	2.145(4)	2.165(2)
Co4-O1F	2.043(4)	2.051(2)
Co4-O1G	2.092(4)	2.0854(19)
Co4-O1OH	2.028(4)	2.0486(19)
Co4-O2E	2.130(4)	2.1304(18)
Co4-O3A	2.128(4)	2.1176(17)
Co4-O4A	2.167(4)	2.2119(19)
Co5-O1A	2.077(3)	2.0930(19)
Co5-O2F	2.053(4)	2.063(2)
Co5-O2G	2.061(4)	2.066(2)
Co5-O3A	2.080(4)	2.0990(18)
Co5-N1A	2.181(5)	2.201(2)
Co5-N2A	2.219(5)	2.197(2)
Co1-O1OH-Co2	106.26(19)	106.65(8)
Co1-O1OH-Co4	108.54(17)	105.99(8)
Co1-O3A-Co4	94.89(13)	94.50(7)
Co1-O1A-Co5	108.24(15)	107.50(8)
Co1-O3A-Co5	96.50(14)	97.13(7)
Co2-O1B-Co3	103.67(17)	102.24(8)
Co2-O3B-Co3	98.56(15)	98.99(7)
Co2-O1OH-Co4	127.63(19)	128.73(9)
Co3-O2E-Co4	128.6(2)	133.02(9)
Co4-O3A-Co5	103.47(17)	102.99(8)

Table A3.6.- Bond lengths (Å) and angles (°) for compounds **19-21**. For compound **19**, the B fragment (and O2W) is formed by the following symmetry operation: (i) -x, y, -z+1/2.

Compound	**19**	**20**	**21**
Ln1···Co1	3.4449(4)	3.5082(5)	3.4995(3)
Ln1···Co2	-	3.4759(5)	3.4640(3)
Ln1-O1A	2.2498(18)	2.288(2)	2.2719(14)
Ln1-O1B	2.2498(18) (i)	2.2939(19)	2.2756(14)
Ln1-O1W	2.306(2)	2.348(2)	2.3352(16)
Ln1-O2A	2.6335(17)	2.652(2)	2.6655(15)
Ln1-O2B	2.6335(17) (i)	2.613(2)	2.6143(14)
Ln1-O2W	2.306(2) (i)	2.377(2)	2.3625(16)
Ln1-O3A	2.3107(17)	2.3611(19)	2.3459(14)
Ln1-O3B	2.3106(17) (i)	2.3479(19)	2.3289(13)
Co1-O1A	1.9789(18)	1.983(2)	1.9867(14)
Co1-O3A	2.1131(18)	2.108(2)	2.1047(14)
Co1-N1A	2.265(2)	2.280(2)	2.2707(17)
Co1-N2A	2.107(2)	2.099(2)	2.1007(17)
Co1-Cl1A	2.2666(9)	2.2902(9)	2.2902(6)
Co2-O1B	-	1.979(2)	1.9763(14)
Co2-O3B	-	2.133(2)	2.1368(14)
Co2-N1B	-	2.268(3)	2.2674(18)
Co2-N2B	-	2.093(2)	2.0955(17)
Co2-Cl1B	-	2.2624(9)	2.2650(6)
Co1-Ln1-Co2	163.129(15) (i)	163.339(10)	163.340(7)
Ln1-O1A-Co1	108.94(7)	110.24(9)	110.35(6)
Ln1-O3A-Co1	102.19(6)	103.28(8)	103.55(6)
Ln1-O1B-Co2	-	108.64(8)	108.91(6)
Ln1-O3B-Co2	-	101.63(8)	101.65(5)
O1A-Ln1-O3A	69.47(6)	67.76(7)	67.91(5)
O1A-Ln1-O1B	133.45(8) (i)	134.62(7)	134.26(5)
O1A-Ln1-O3B	155.52(6) (i)	154.40(7)	154.77(5)
O3A-Ln1-O1B	155.52(6) (i)	155.13(7)	155.12(5)
O3A-Ln1-O3B	89.91(9) (i)	91.64(7)	91.46(5)
O1B-Ln1-O3B	69.46(6) (i)	69.18(7)	69.44(5)
O2A-Ln1-O2B	64.53(8) (i)	64.41(6)	64.38(5)
O1W-Ln1-O2W	159.51(9) (i)	159.08(7)	159.19(5)

Table A3.7.- Bond lengths (Å) and angles (°) for compounds **22**, **24** and **25**. For compound **25**, the B fragment (and O2W) is formed by the following symmetry operation: (i) -x, y, -z+1/2.

Compound	**22**	**24**	**25**
Ln1···TM1	3.4859(15)	3.4516(5)	3.5002(4)
Ln1···TM2	3.4532(15)	3.4184(5)	-
Ln1-O1A	2.258(6)	2.221(3)	2.266(2)
Ln1-O1B	2.262(6)	2.226(2)	2.266(2) (i)
Ln1-O1W	2.322(7)	2.261(3)	2.342(3)
Ln1-O2A	2.657(7)	2.657(3)	2.629(3)
Ln1-O2B	2.585(6)	2.583(3)	2.629(3)
Ln1-O2W	2.354(7)	2.287(3)	2.342(3)
Ln1-O3A	2.335(6)	2.291(2)	2.315(2)
Ln1-O3B	2.326(6)	2.282(3)	2.315(2) (i)
TM1-O1A	1.978(6)	1.988(3)	2.002(2)
TM1-O3A	2.102(7)	2.106(3)	2.164(3)
TM1-N1A	2.271(9)	2.261(3)	2.275(3)
TM1-N2A	2.090(9)	2.098(3)	2.103(3)
TM1-Cl1A	2.290(3)	2.2945(12)	2.2291(10)
TM2-O1B	1.979(6)	1.978(3)	-
TM2-O3B	2.150(7)	2.141(3)	-
TM2-N1B	2.257(9)	2.259(3)	-
TM2-N2B	2.092(9)	2.089(3)	-
TM2-Cl1B	2.256(3)	2.2645(12)	-
TM1-Ln1-TM2	163.02(3)	163.045(13)	163.755(16) (i)
Ln1-O1A-TM1	110.6(3)	110.06(12)	110.03(11)
Ln1-O3A-TM1	103.5(3)	103.37(10)	102.71(10)
Ln1-O1B-TM2	108.9(3)	108.66(11)	-
Ln1-O3B-TM2	100.9(2)	101.19(10)	-
O1A-Ln1-O3A	67.9(2)	69.13(9)	69.19(9)
O1A-Ln1-O1B	134.6(2)	133.67(9)	133.93(13) (i)
O1A-Ln1-O3B	153.8(2)	153.98(10)	155.41(9) (i)
O3A-Ln1-O1B	154.8(2)	154.18(9)	155.41(9) (i)
O3A-Ln1-O3B	90.5(2)	89.92(9)	89.86(12) (i)
O1B-Ln1-O3B	70.1(2)	70.73(9)	69.19(9) (i)
O2A-Ln1-O2B	64.5(2)	64.49(9)	64.81(11) (i)
O1W-Ln1-O2W	159.3(2)	159.23(11)	159.96(13)

2. Continuous Shape Measurements

The nearer the value to zero, the better fits to an ideal polyhedron.

Table A3.8.- Continuous Shape Measurements for compound **16**.

HP-6 1 D6h Hexagon

PPY-6 2 C5v Pentagonal pyramid

OC-6 3 Oh Octahedron

TPR-6 4 D3h Trigonal prism

JPPY-6 5 C5v Johnson pentagonal pyramid J2

Structure [ML6]	HP-6	PPY-6	OC-6	TPR-6	JPPY-6
Co1	32.162	22.777	1.857	11.212	27.427
Co2	31.777	14.801	6.845	5.565	19.229

Table A3.9.- Continuous Shape Measurements for Co1 in compound **17**.

HP-6 1 D6h Hexagon

PPY-6 2 C5v Pentagonal pyramid

OC-6 3 Oh Octahedron

TPR-6 4 D3h Trigonal prism

JPPY-6 5 C5v Johnson pentagonal pyramid J2

Structure [ML6]	HP-6	PPY-6	OC-6	TPR-6	JPPY-6
Co1	29.814	22.307	2.044	11.878	25.757

Table A3.10.- Continuous Shape Measurements for Co2 in compound **17**.

PP-5 1 D5h Pentagon

vOC-5 2 C4v Vacant octahedron

TBPY-5 3 D3h Trigonal bipyramid

SPY-5 4 C4v Spherical square pyramid

JTBPY-5 5 D3h Johnson trigonal bipyramid J12

Structure [ML5]	PP-5	vOC-5	TBPY-5	SPY-5	JTBPY-5
Co1	28.203	7.295	2.895	5.181	3.903

Table A3.11.- Continuous Shape Measurements for Co1 in compounds **18a** and **18b**.

PP-5 1 D5h Pentagon
vOC-5 2 C4v Vacant octahedron
TBPY-5 3 D3h Trigonal bipyramid
SPY-5 4 C4v Spherical square pyramid
JTBPY-5 5 D3h Johnson trigonal bipyramid J12

Structure [ML5]	PP-5	vOC-5	TBPY-5	SPY-5	JTBPY-5
Co1 (18a)	31.576	6.333	1.940	4.243	3.111
Co1 (18b)	32.792	5.440	1.864	3.459	3.297

Table A3.12.- Continuous Shape Measurements for Co2-Co5 in compounds **18a** and **18b**.

Structure [ML6]	HP-6	PPY-6	OC-6	TPR-6	JPPY-6
Co2 (18a)	28.396	16.760	3.953	7.267	20.146
Co2 (18b)	27.927	19.287	2.655	8.725	22.683
Co3 (18a)	30.404	19.714	4.945	8.033	23.393
Co3 (18b)	30.025	19.442	5.464	7.018	22.794
Co4 (18a)	29.960	20.159	2.450	8.375	23.819
Co4 (18b)	29.718	21.053	2.053	8.935	24.903
Co5 (18a)	32.416	22.679	1.476	9.585	26.609
Co5 (18b)	32.948	22.479	1.637	9.335	26.474

Table A3.13.- Continuous Shape Measurements for Co1 (Zn1 in **25**) and Co2 in compounds **19-22** and **24-25**.

PP-5 1 D5h Pentagon
vOC-5 2 C4v Vacant octahedron
TBPY-5 3 D3h Trigonal bipyramid
SPY-5 4 C4v Spherical square pyramid
JTBPY-5 5 D3h Johnson trigonal bipyramid J12

Structure [ML5]	PP-5	vOC-5	TBPY-5	SPY-5	JTBPY-5
Co1 (19)	32.331	4.702	2.207	1.788	4.795
Co1 (20)	33.138	5.142	2.303	2.045	4.923
Co1 (21)	32.933	5.116	2.363	2.036	5.038
Co1 (22)	33.238	5.122	2.384	2.005	5.046
Co1 (24)	32.694	5.305	2.411	2.172	5.125
Zn1 (25)	32.401	4.907	2.330	1.813	4.749
Co2 (20)	32.367	4.674	2.054	1.829	4.490
Co2 (21)	32.444	4.666	2.100	1.817	4.535
Co2 (22)	32.109	4.659	2.104	1.822	4.497
Co2 (24)	32.379	4.820	2.076	1.922	4.521

Table A3.14.- Continuous Shape Measurements for Ln1 in compounds **19-22** and **24-25**.

OP-8	1 D8h	Octagon
HPY-8	2 C7v	Heptagonal pyramid
HBPY-8	3 D6h	Hexagonal bipyramid
CU-8	4 Oh	Cube
SAPR-8	5 D4d	Square antiprism
TDD-8	6 D2d	Triangular dodecahedron
JGBF-8	7 D2d	Johnson gyrobifastigium J26
JETBPY-8	8 D3h	Johnson elongated triangular bipyramid J14
JBTPR-8	9 C2v	Biaugmented trigonal prism J50
BTPR-8	10 C2v	Biaugmented trigonal prism
JSD-8	11 D2d	Snub diphenoid J84
TT-8	12 Td	Triakis tetrahedron
ETBPY-8	13 D3h	Elongated trigonal bipyramid

Structure [ML8]	OP-8	HPY-8	HBPY-8	CU-8	SAPR-8	TDD-8	JGBF-8
Y (19)	32.615	22.513	15.168	10.848	1.946	1.800	14.196
Gd (20)	33.207	21.849	14.585	10.070	1.880	2.242	14.803
Tb (21)	32.999	21.987	14.734	10.202	1.917	2.186	14.705
Dy (22)	33.133	22.130	14.694	10.090	1.847	2.162	14.597
Yb (24)	33.386	22.346	15.015	10.103	1.681	2.177	14.510
Dy (25)	32.474	22.676	15.091	10.837	2.038	1.752	14.291

Structure [ML8]	JETBPY-8	JBTPR-8	BTPR-8	JSD-8	TT-8	ETBPY-8
Y (19)	29.192	2.824	2.821	3.300	11.021	23.674
Gd (20)	29.289	3.070	2.947	4.006	10.892	23.462
Tb (21)	29.187	3.049	2.974	3.865	11.005	23.470
Dy (22)	28.931	2.975	2.886	3.792	10.896	23.783
Yb (24)	28.820	2.755	2.804	3.592	10.889	24.402
Dy (25)	29.256	2.934	2.858	3.412	11.117	23.492

3. Figures of compounds 26-27 and supramolecular structures.

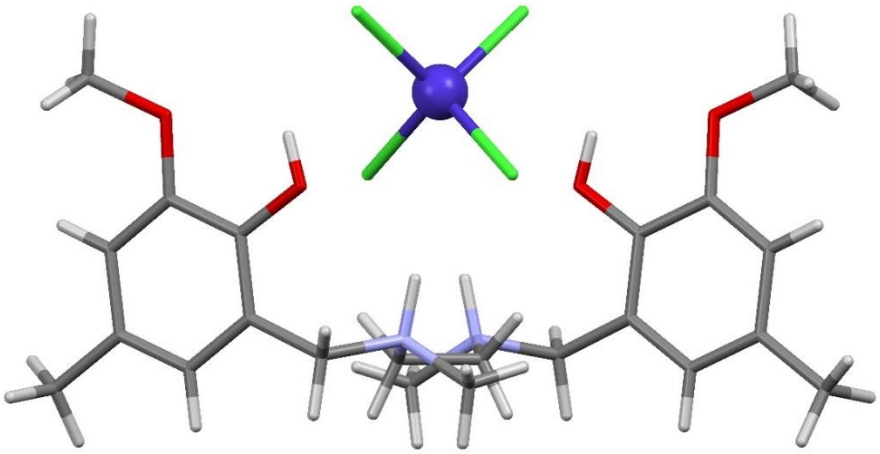

Figure A3.1.- Perspective view of the structure of **26**. Cobalt, chloride, oxygen, nitrogen, carbon and hydrogen atoms are in purple, green, red, blue, grey and white, respectively.

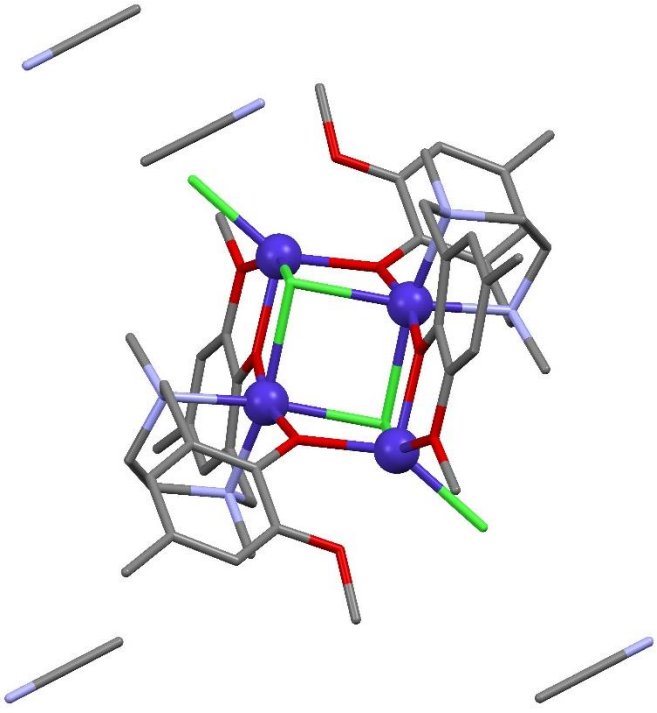

Figure A3.2.- Perspective view of the structure of **27**. Cobalt, chloride, oxygen, nitrogen and carbon atoms are in purple, green, red, blue and grey, respectively. Hydrogen atoms are omitted for the sake of clarity.

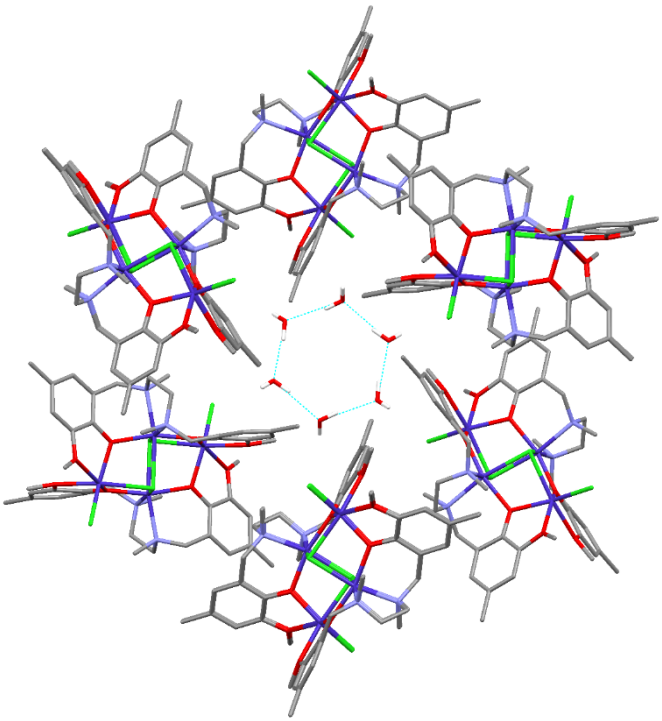

Figure A3.3.- Hexanuclear water cluster surrounded by tetranuclear units of **16**, perspective view from the *c* axis. Dashed blue lines show the hydrogen bonds between water molecules.

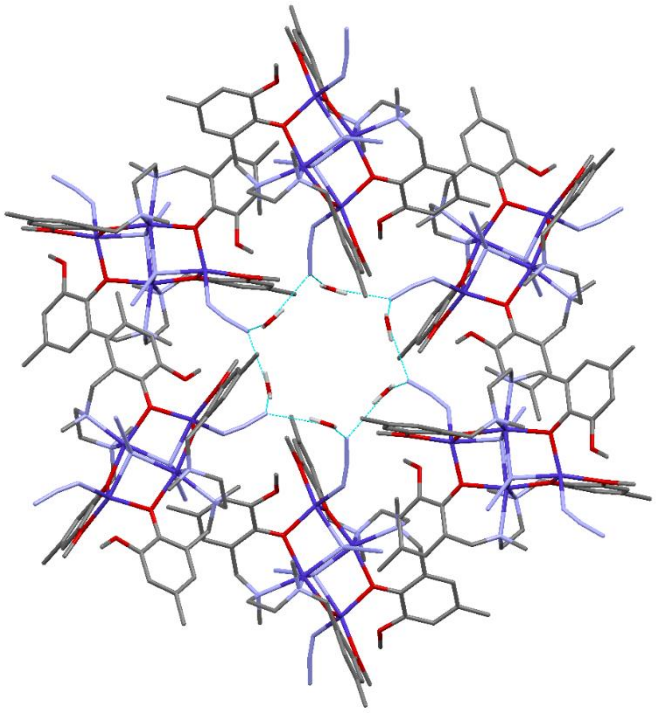

Figure A3.4.- Star shaped water cluster formed by hydrogen bonds between azide and water molecules surrounded by tetranuclear units of **17**, perspective view from the *c* axis. Dashed blue lines show the hydrogen bonds between water molecules.

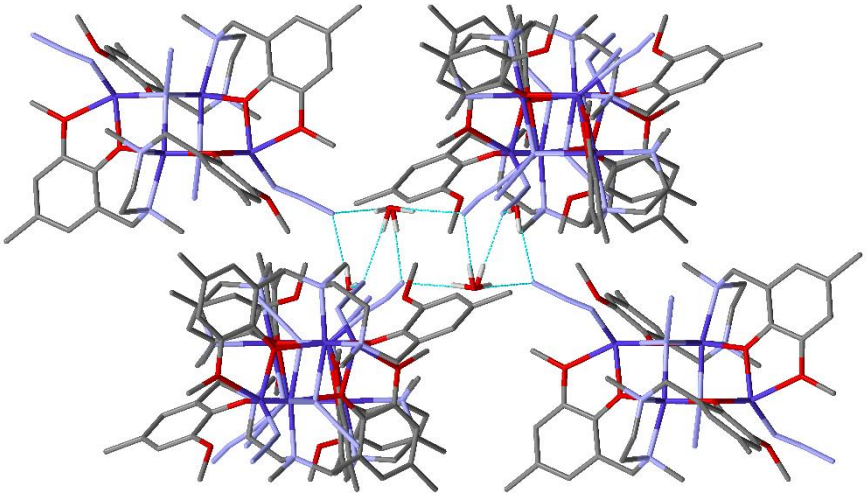

Figure A3.5.- Star shaped water cluster formed by hydrogen bonds between azide and water molecules surrounded by tetranuclear units of **17**, perspective view from the *b* axis. Dashed blue lines show the hydrogen bonds between water molecules.

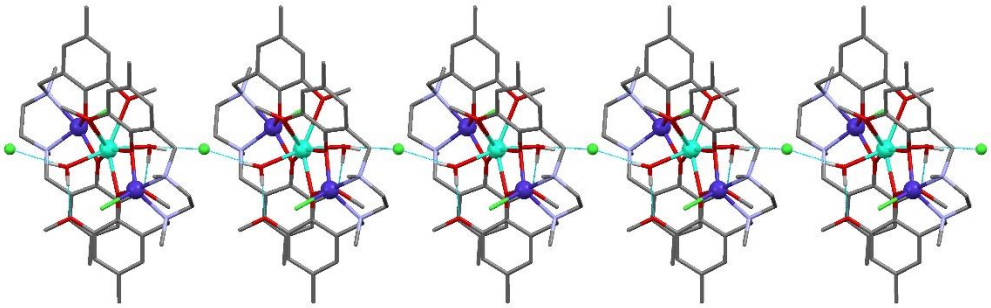

Figure A3.6.- Hydrogen bonding supramolecular structure of **22**, perspective view from the *a* axis. Dashed blue lines show the hydrogen bonds between water and chloride and water and methoxy groups.

4. Experimental XRPD.

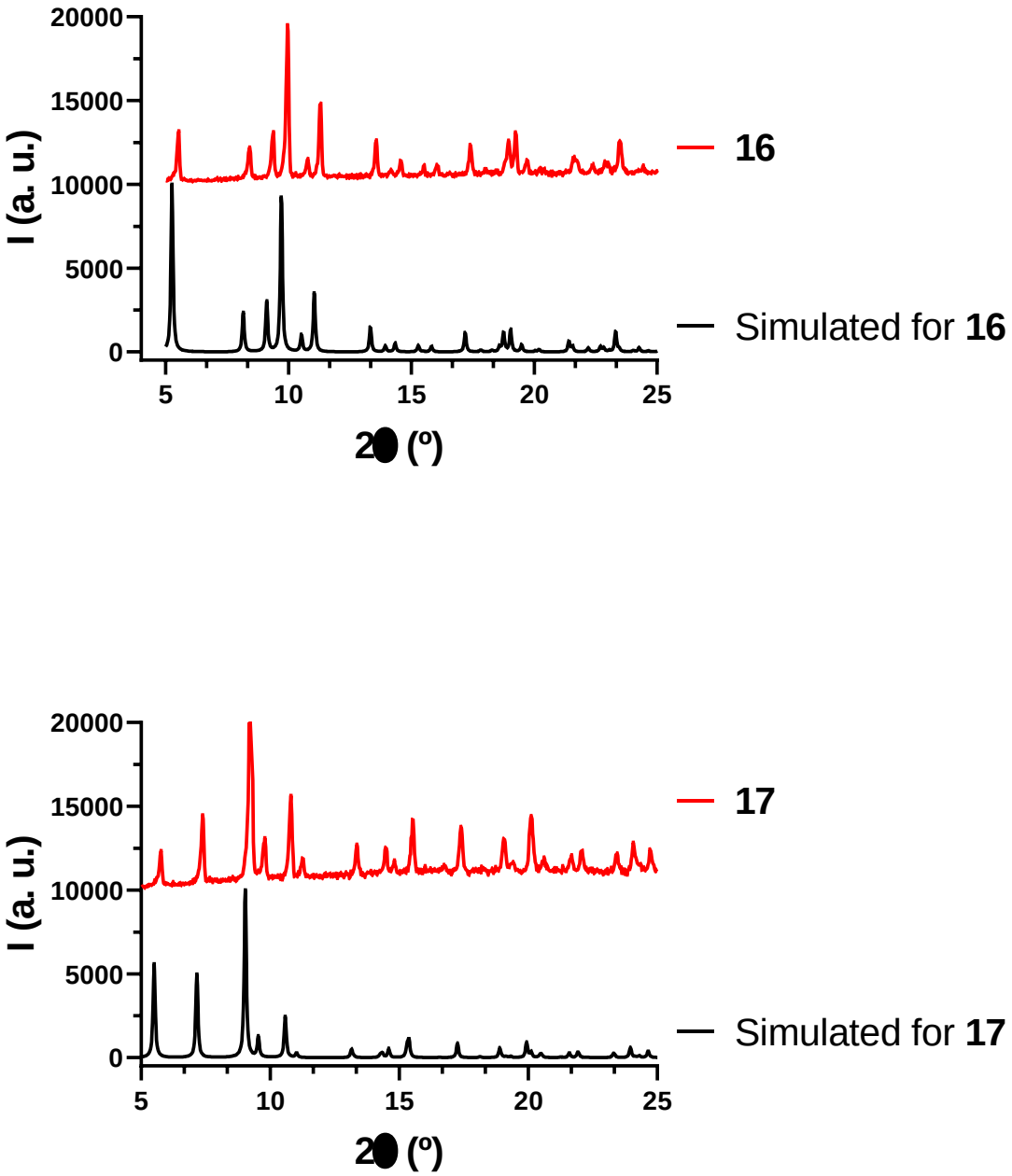

Figure A3.7.- Simulated pattern from single-crystal X-ray diffraction (black line) and experimental XRPD (red) for complexes **16** (top) and **17** (bottom).

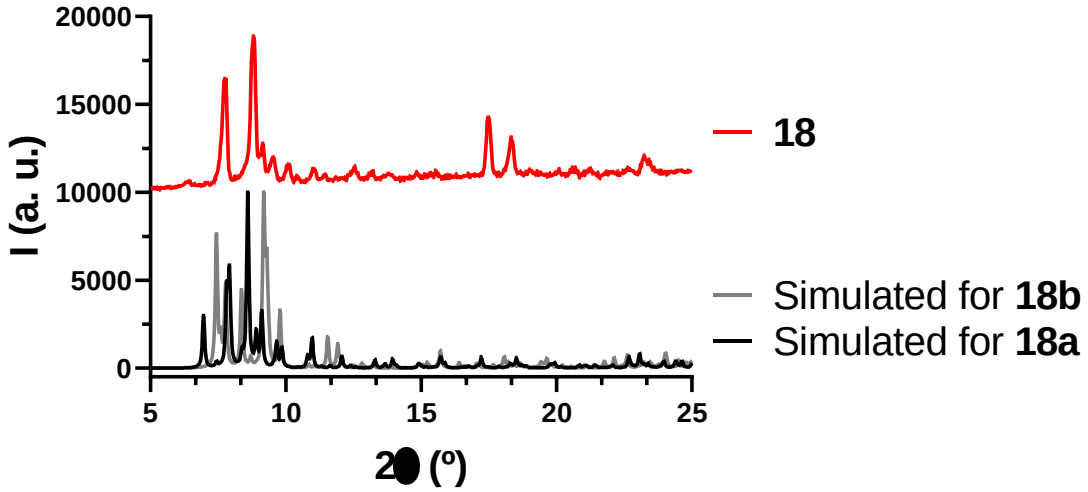

Figure A3.8.- Simulated pattern from single-crystal X-ray diffraction (black and grey lines) and experimental XRPD for complex **18** (red).

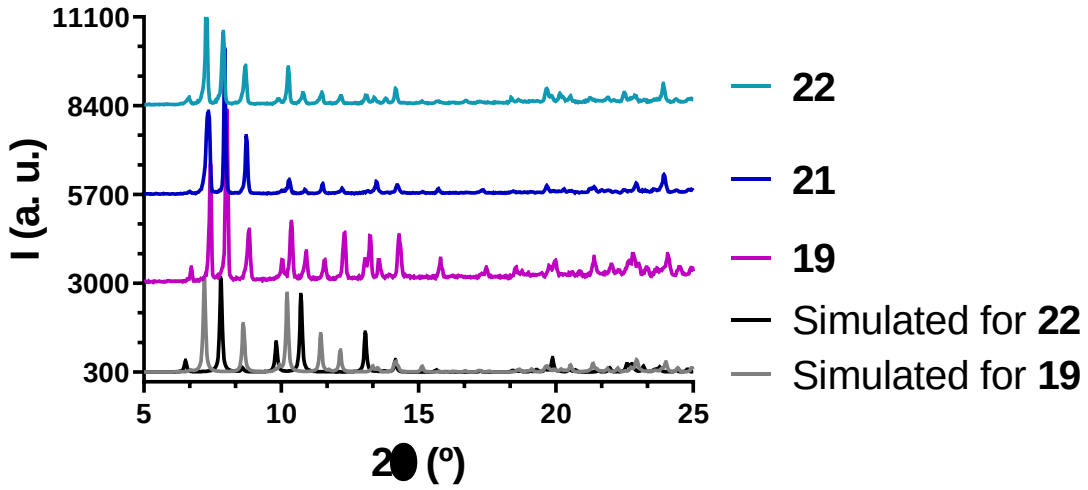

Figure A3.9.- Simulated pattern from single-crystal X-ray diffraction (black line) and experimental XRPD for complexes **19** (purple), **21** (blue) and **22** (turquoise).

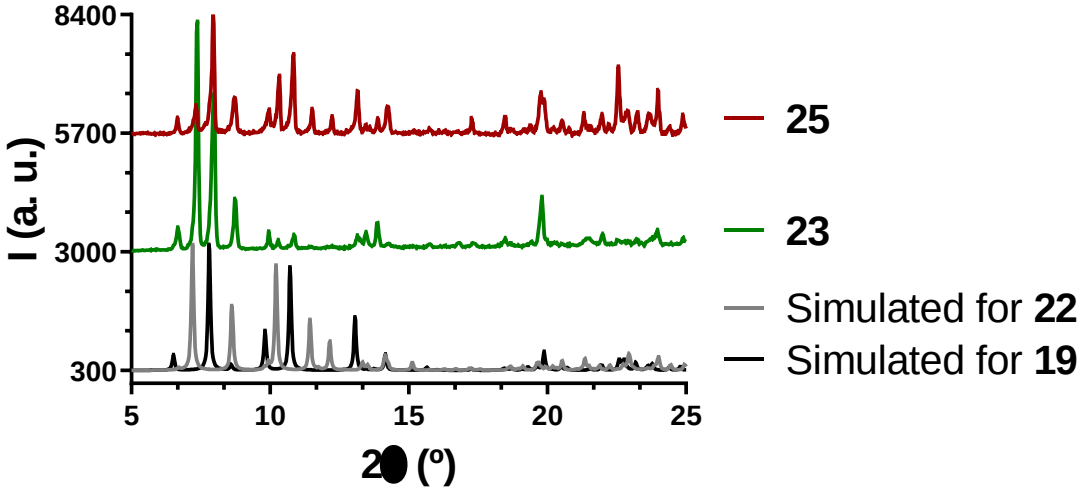

Figure A3.10.- Simulated pattern from single-crystal X-ray diffraction (black line) and experimental XRPD for complexes **23** (green) and **25** (brown).

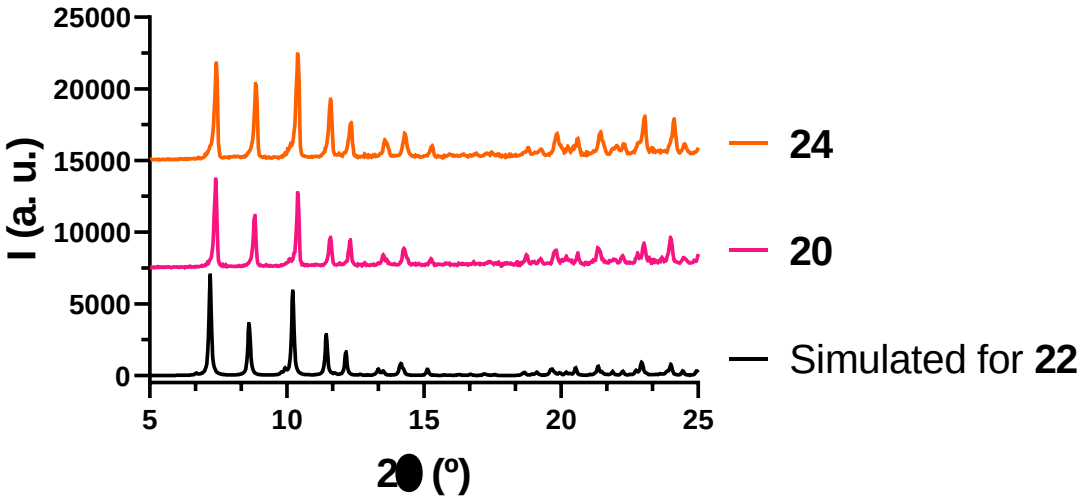

Figure A3.11.- Simulated pattern from single-crystal X-ray diffraction (black line) and experimental XRPD for complexes **20** (pink) and **24** (orange).

5. IR spectra

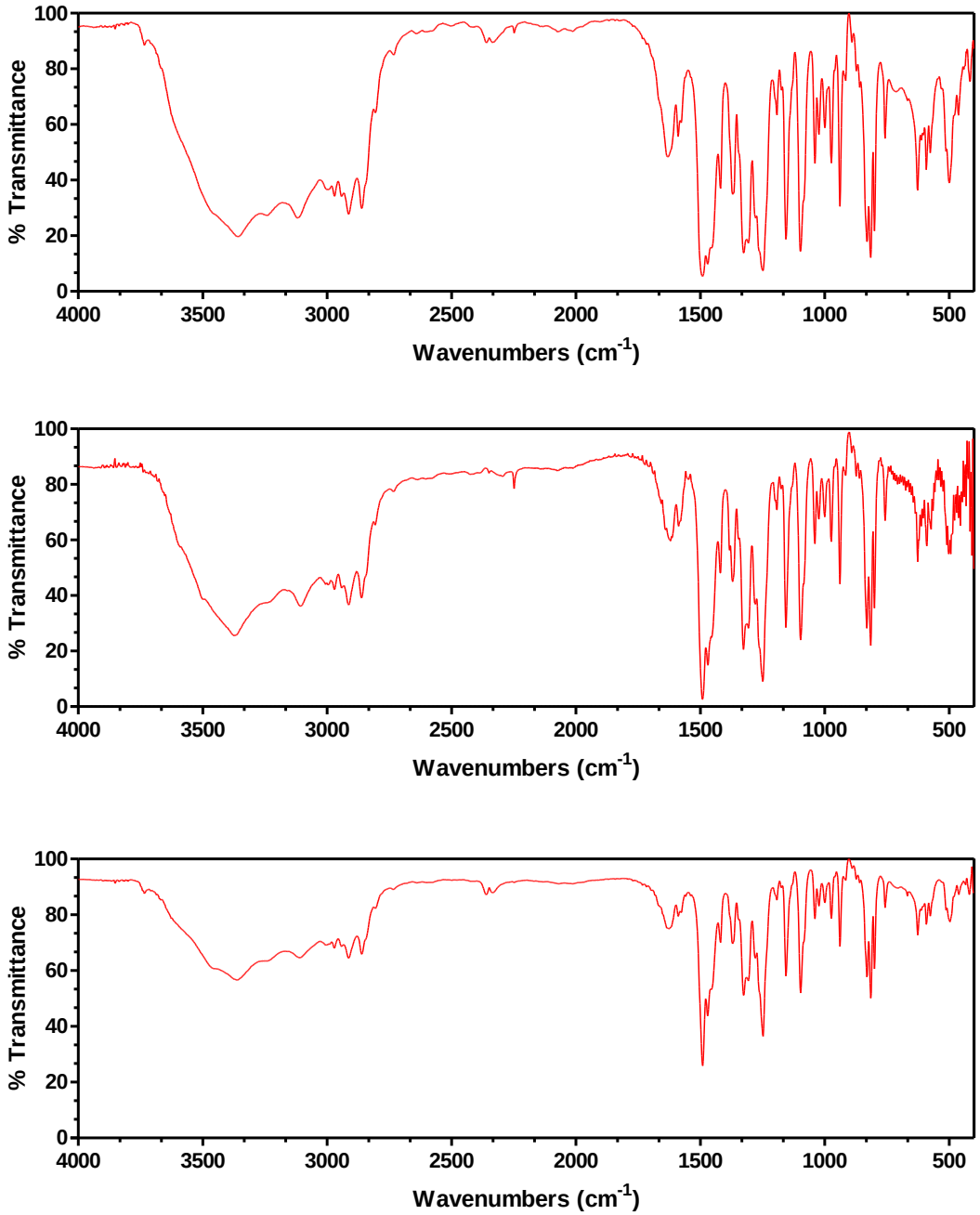

Figure A3.12.- IR spectra for compounds **19** (top), **20** (middle) and **21** (bottom).

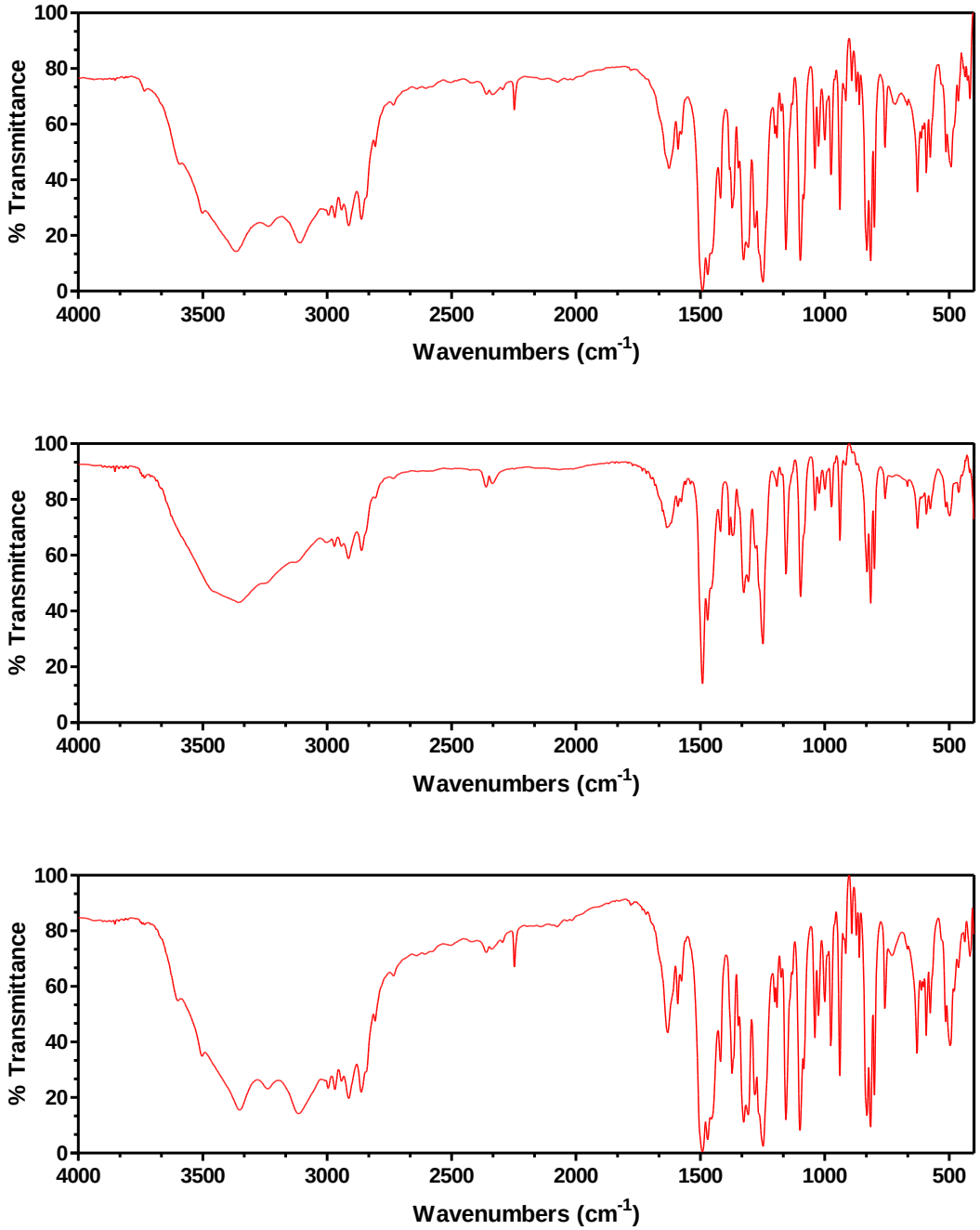

Figure A3.13.- IR spectra for compounds **22** (top), **23** (middle) and **24** (bottom).

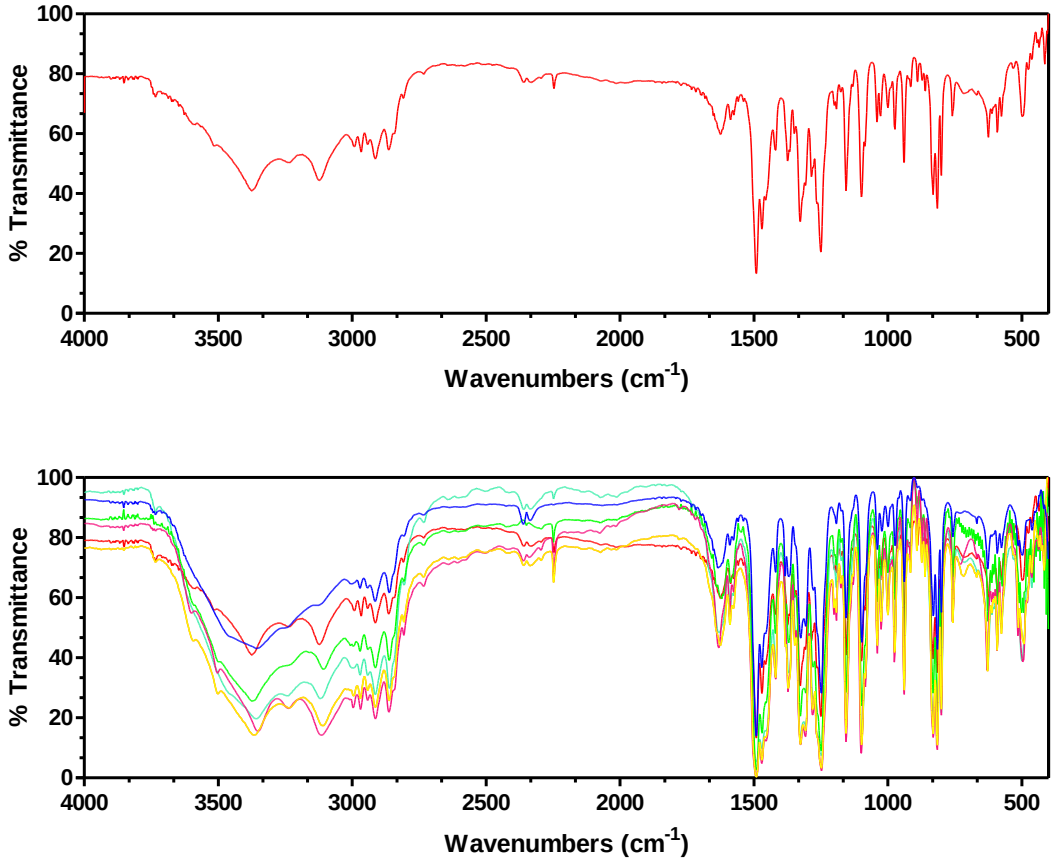

Figure A3.14.- IR spectra for compound **25** (top) and the combination of **19-25** (bottom) to prove that they all overlap.

6. Thermogravimetric Analysis.

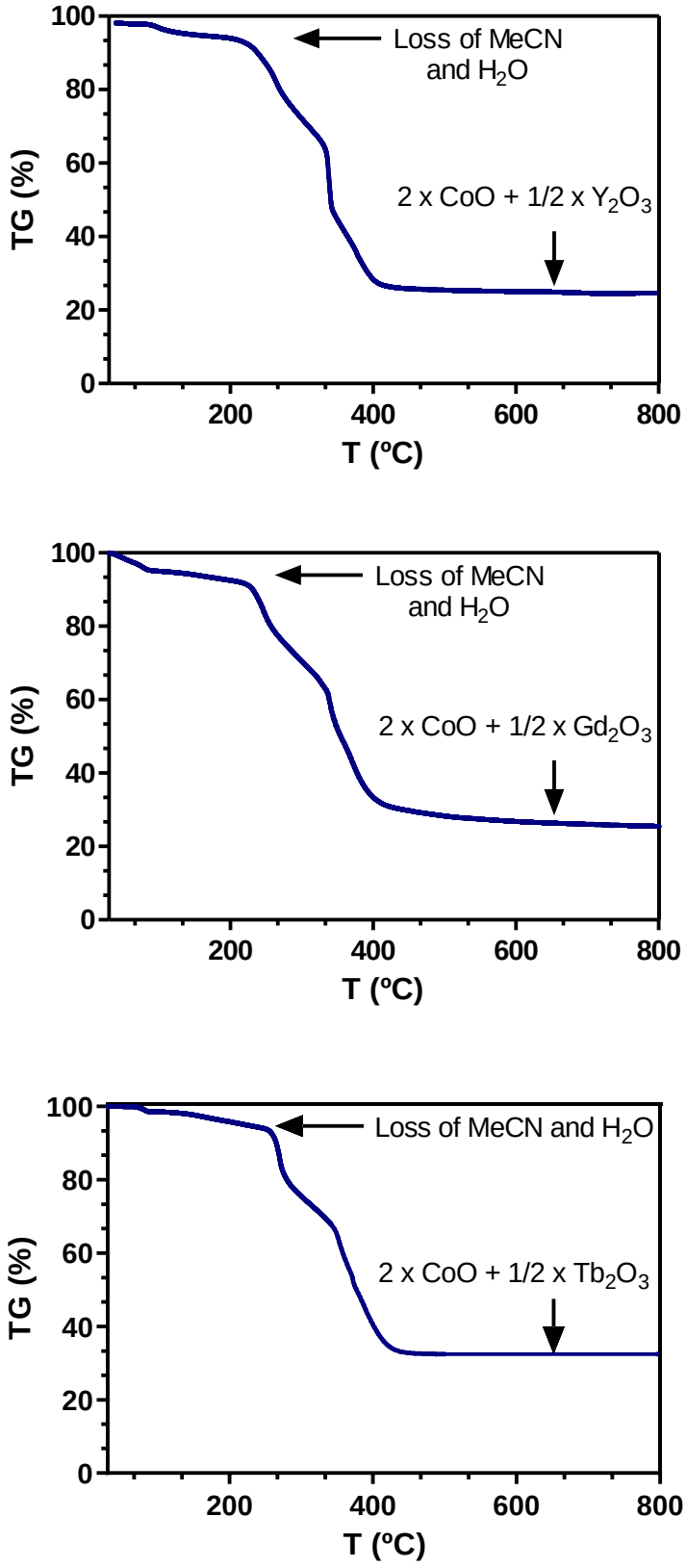

Figure A3.15.- Thermogravimetric analyses of compounds **19** (top), **20** (middle) and **21** (bottom).

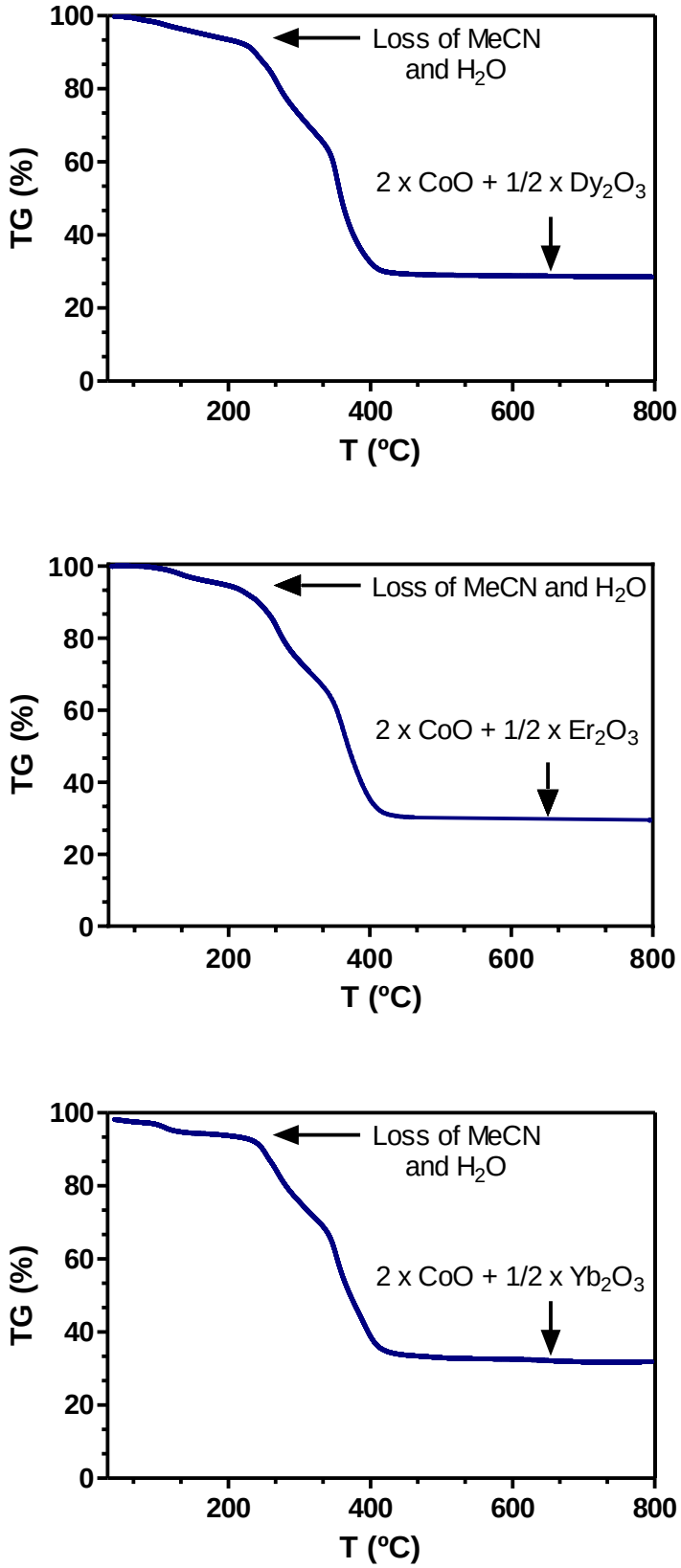

Figure A3.16.- Thermogravimetric analyses of compounds **22** (top), **23** (middle) and **24** (bottom).

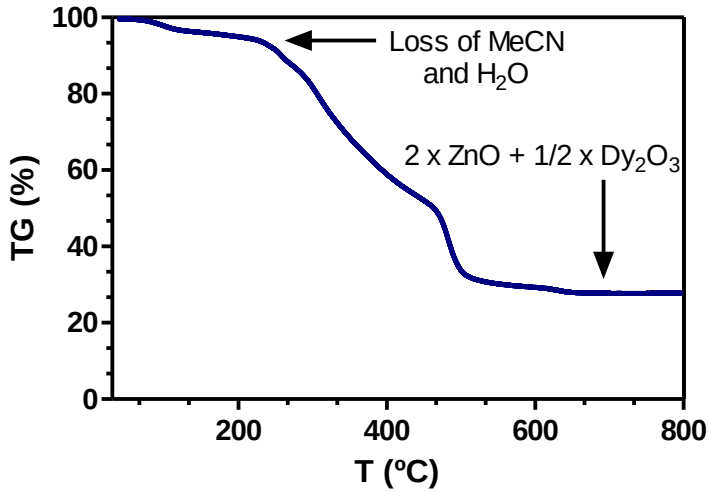

Figure A3.17.- Thermogravimetric analysis of compound **25**.

7. Magnetic measurements

Dynamic magnetic properties

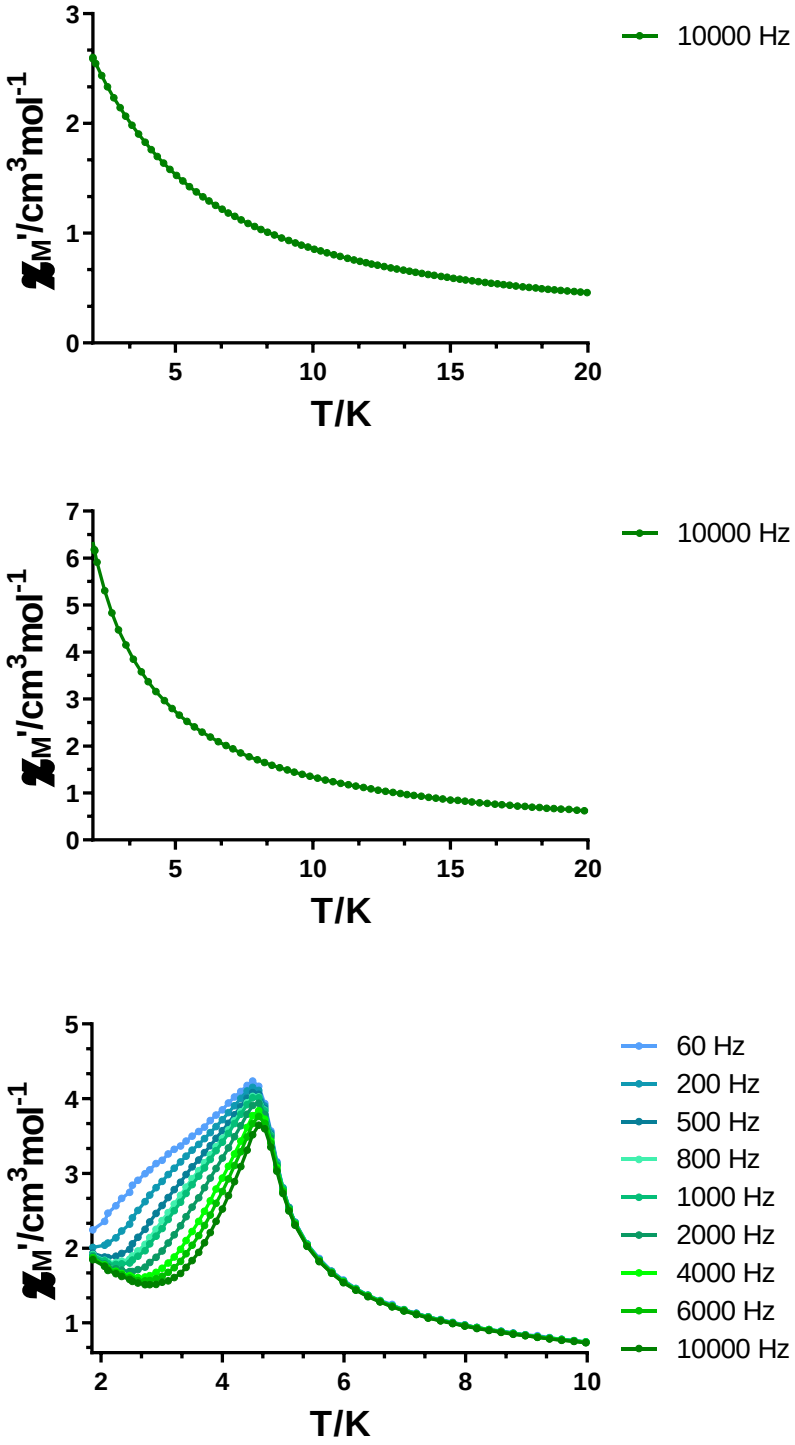

Figure A3.18.- Temperature dependence of the in phase χ_M' susceptibility signals for complexes **16** (top), **17** (middle) and **18** (bottom) under zero applied *dc* field.

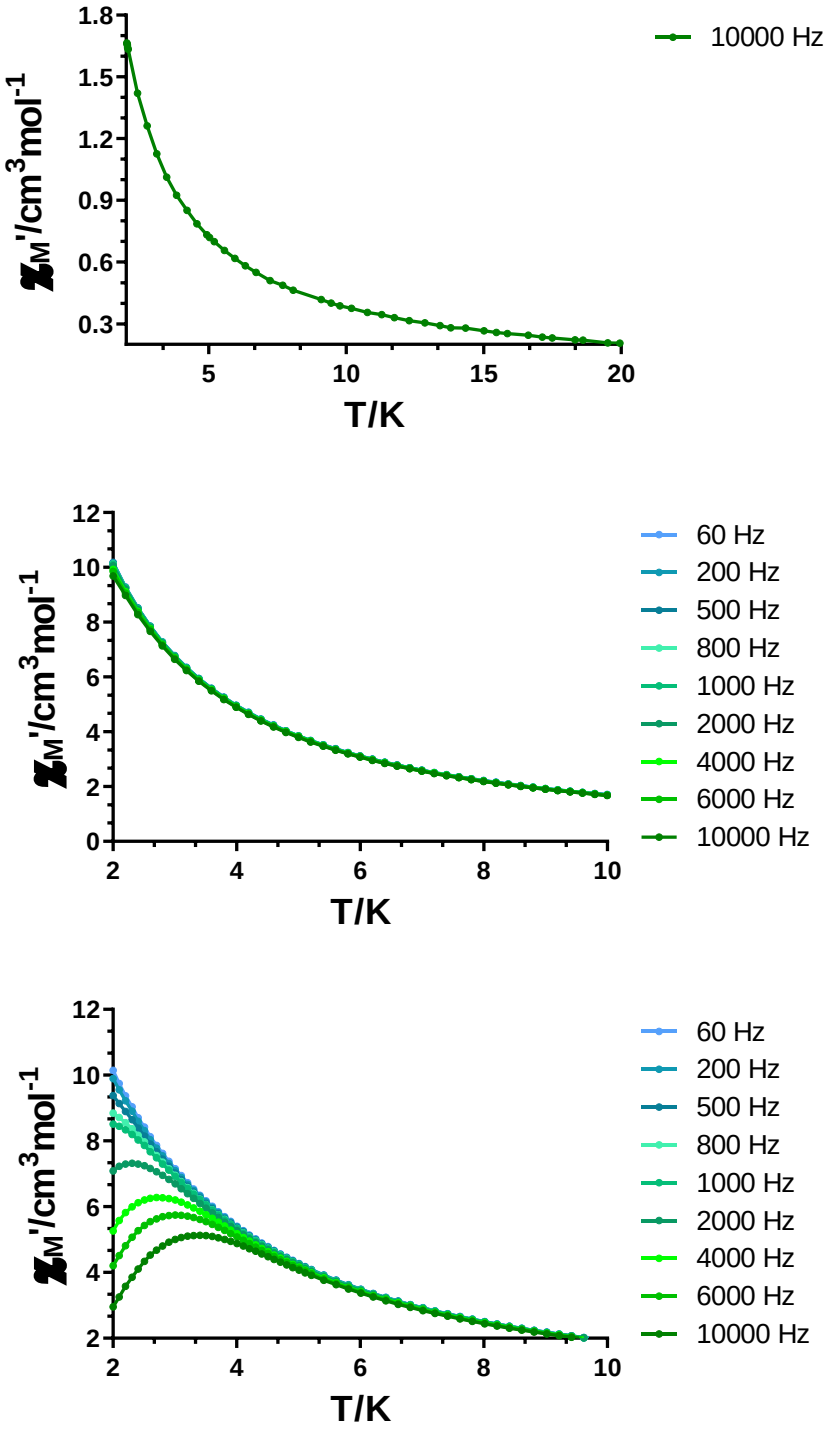

Figure A3.19.- Temperature dependence of the in phase χ_M' susceptibility signals for complexes **19** (top), **20** (middle) and **21** (bottom) under zero applied *dc* field.

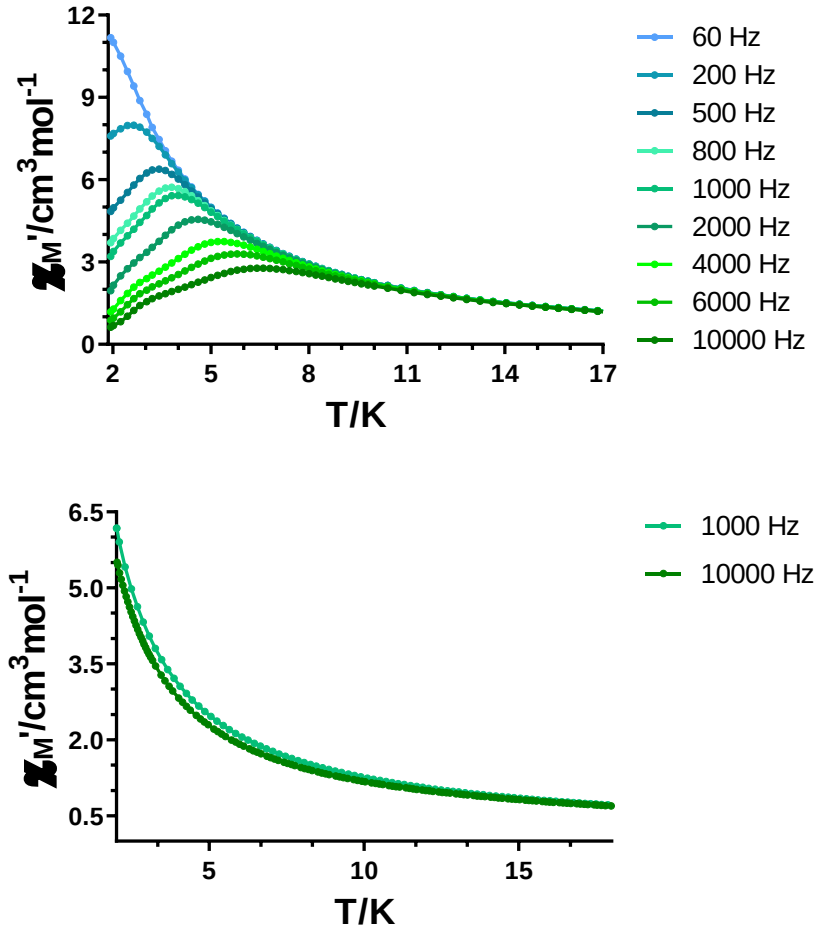

Figure A3.20.- Temperature dependence of the in phase χ_M' susceptibility signals for complexes **22** (top) and **25** (bottom) under zero applied *dc* field.

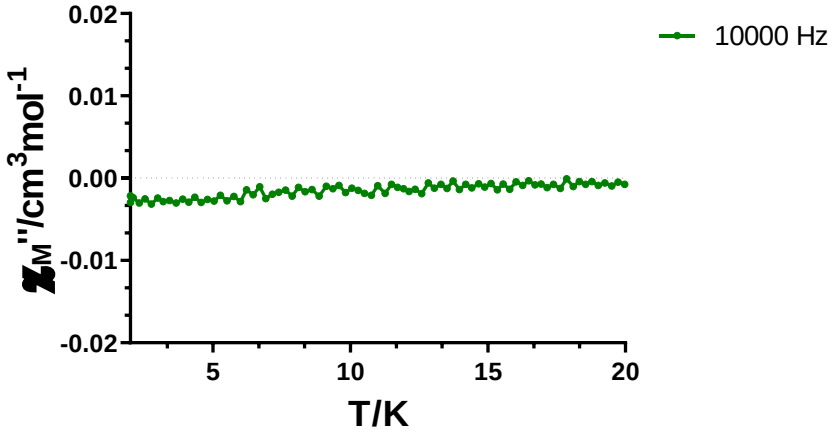

Figure A3.21.- Temperature dependence of the out-of-phase χ_M'' susceptibility signal for complex **16** under zero applied *dc* field.

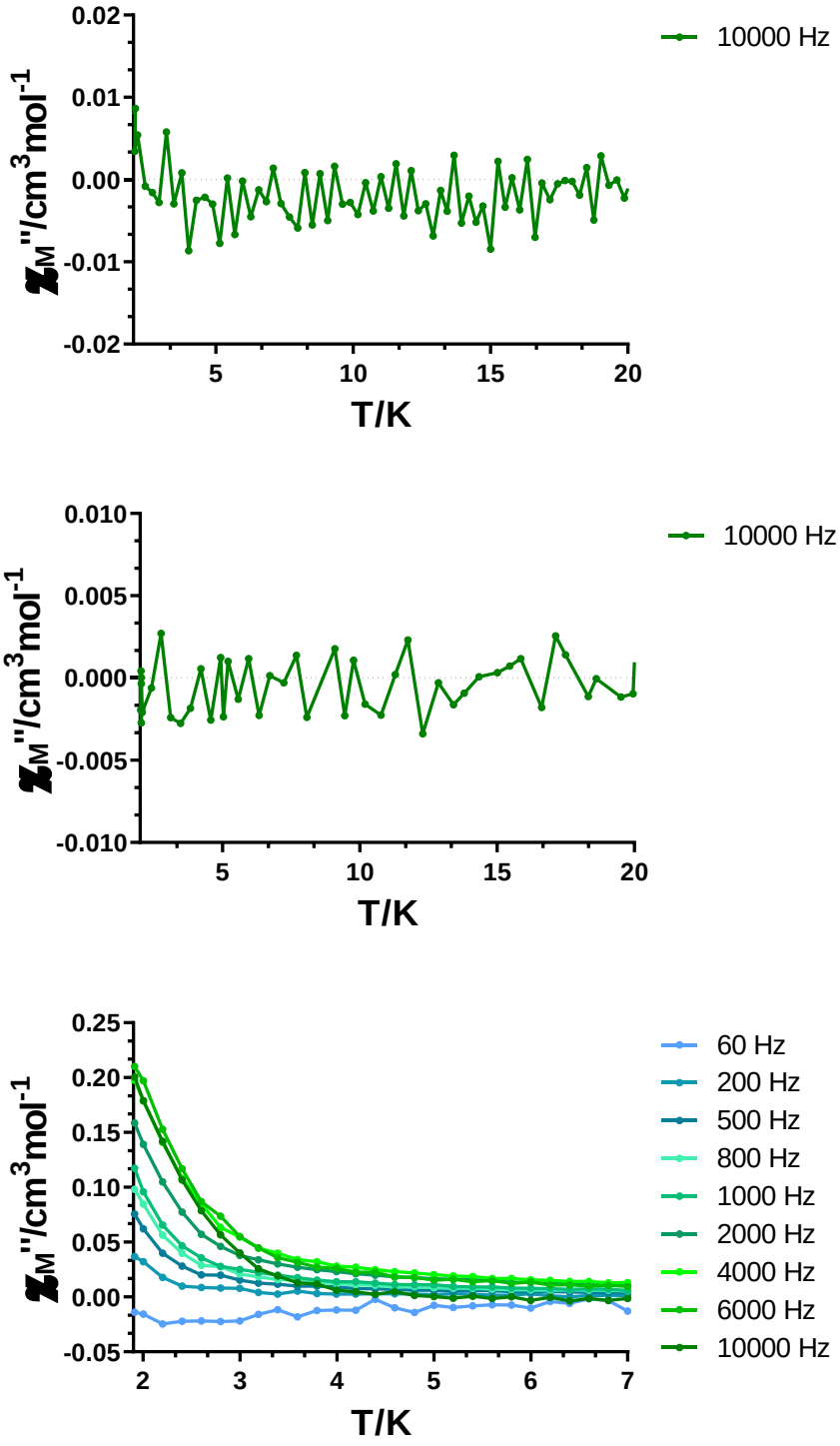

Figure A3.22.- Temperature dependence of the out-of-phase χ_M'' susceptibility signals for complexes **17** (top), **19** (middle) and **20** (bottom) under zero applied *dc* field.

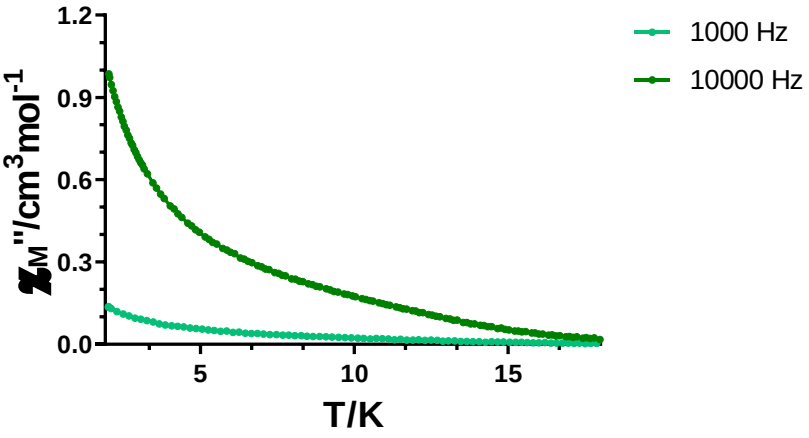

Figure A3.23.- Temperature dependence of the out-of-phase χ_M'' susceptibility signals for complex **25** under zero applied *dc* field.

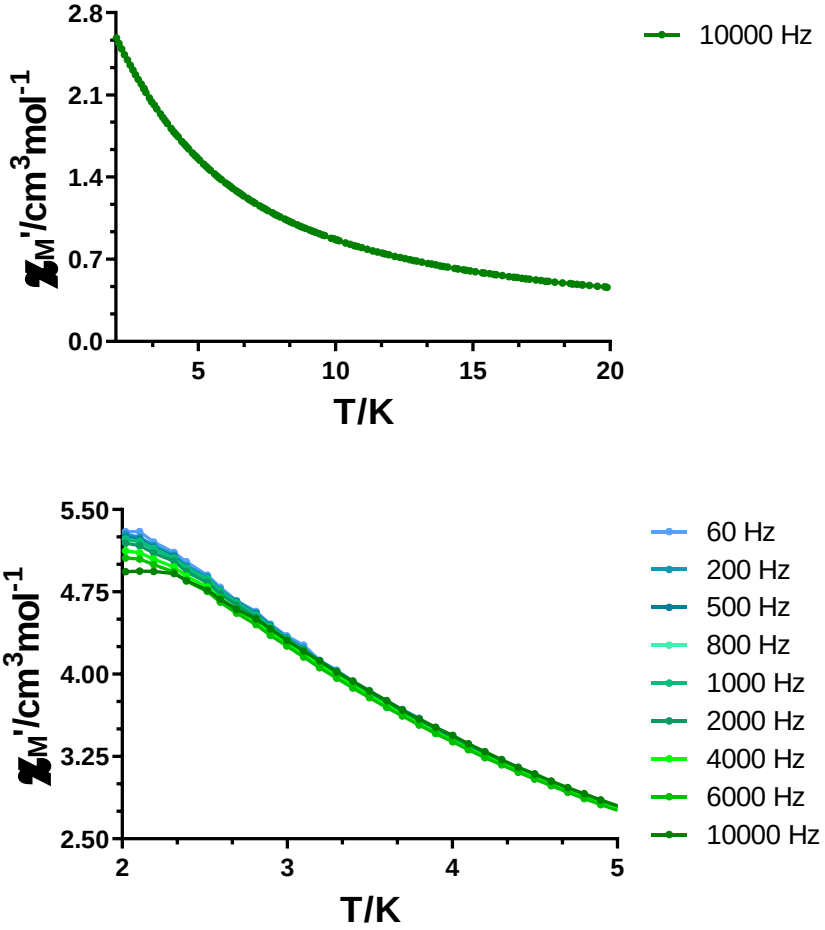

Figure A3.24.- Temperature dependence of the in phase χ_M' susceptibility signals for complexes **16** (top) and **17** (bottom) under an applied field of 1000 Oe.

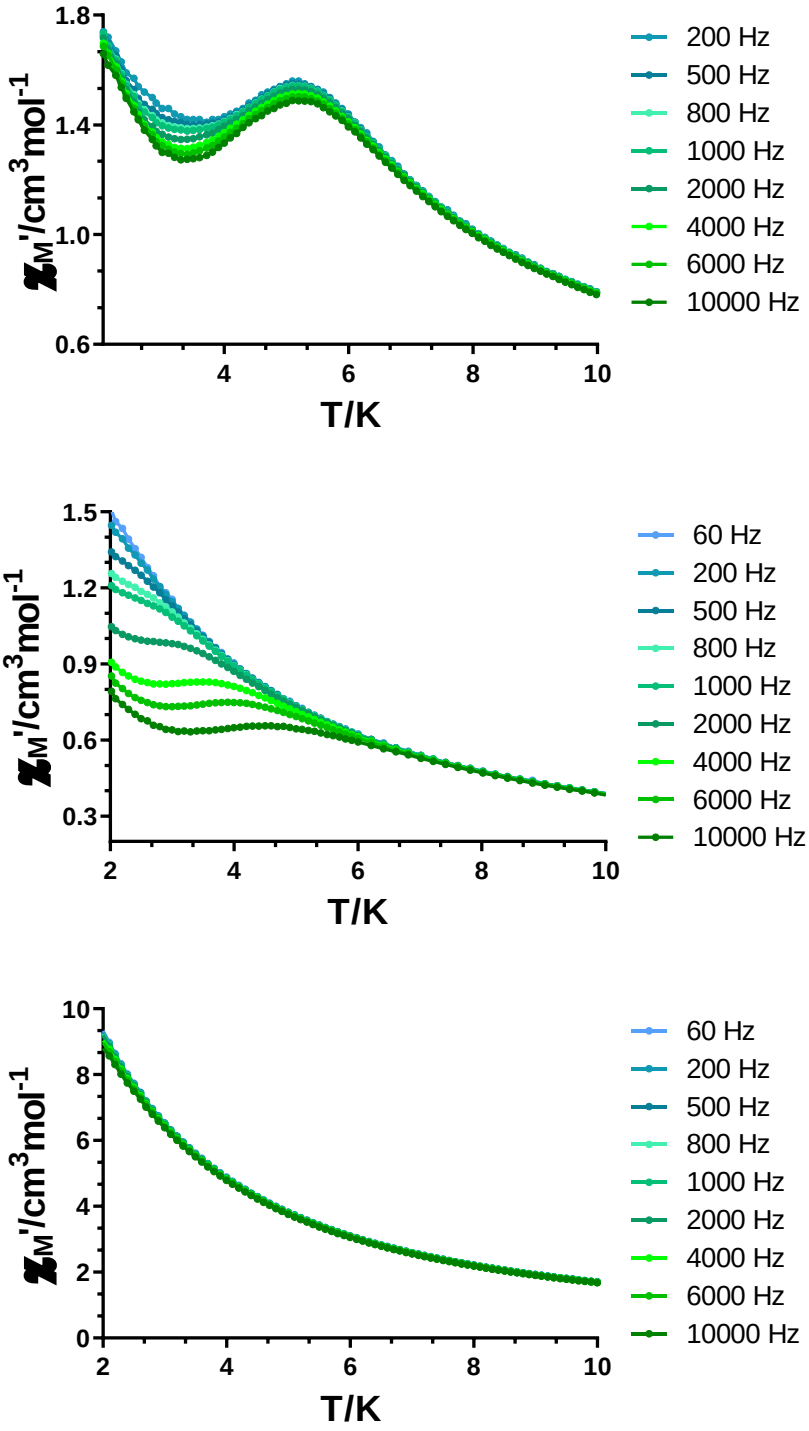

Figure A3.25.- Temperature dependence of the in phase χ_M' susceptibility signals for complexes **18** (top), **19** (middle) and **20** (bottom) under an applied field of 1000 Oe.

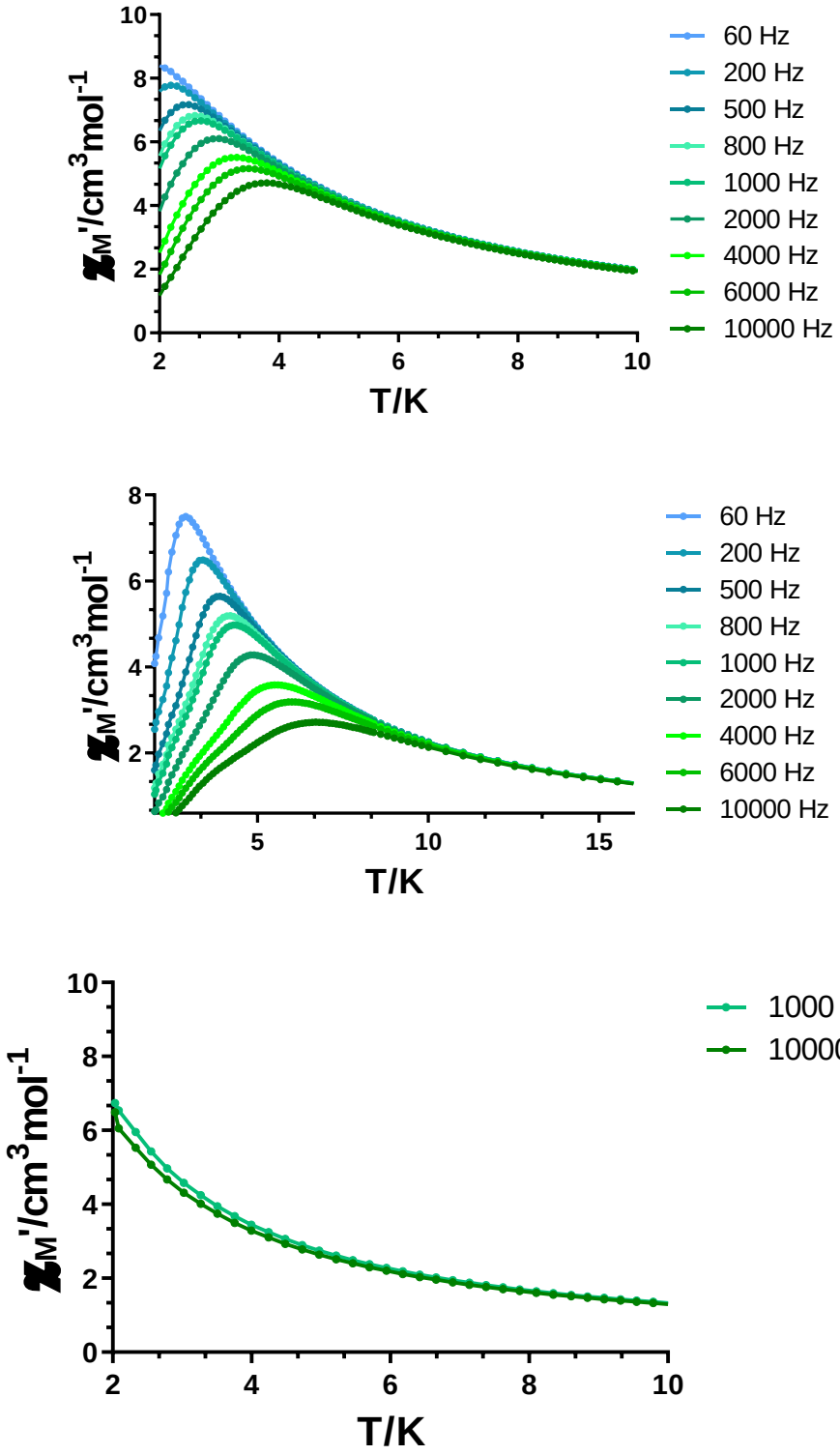

Figure A3.26.- Temperature dependence of the in phase χ_M' susceptibility signals for complexes **21** (top), **22** (middle) and **23** (bottom) under an applied field of 1000 Oe.

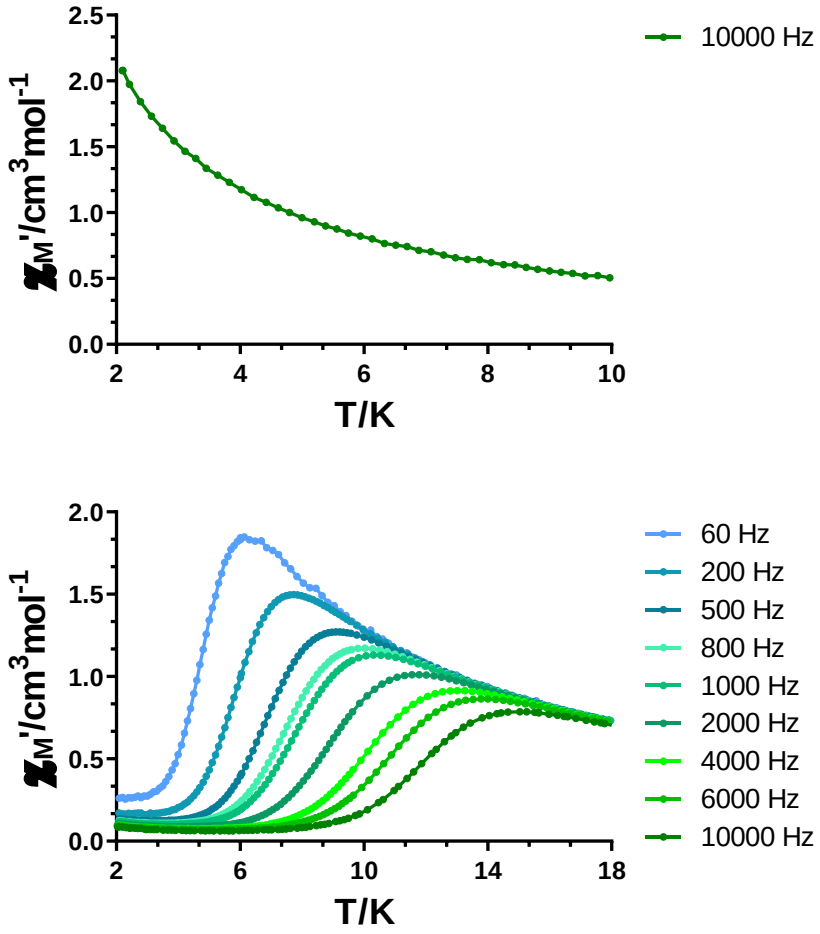

Figure A3.27.- Temperature dependence of the in phase χ_M' susceptibility signals for complexes **24** (top) and **25** (bottom) under an applied field of 1000 Oe.

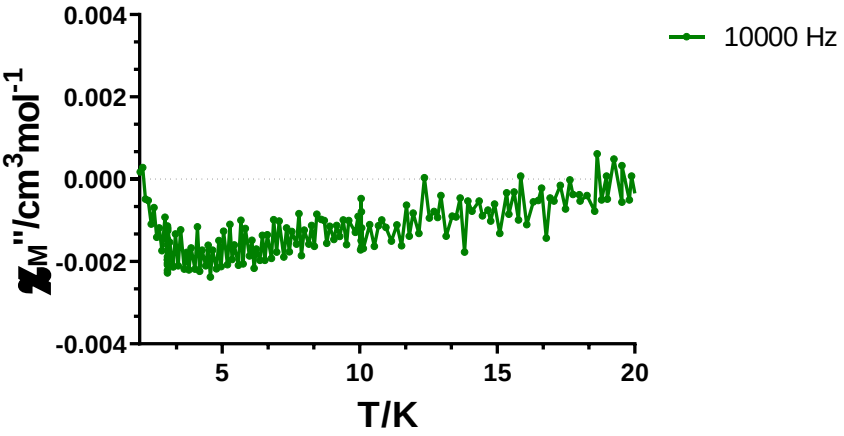

Figure A3.28.- Temperature dependence of the out-of-phase χ_M'' susceptibility signal for complex **16** under an applied field of 1000 Oe.

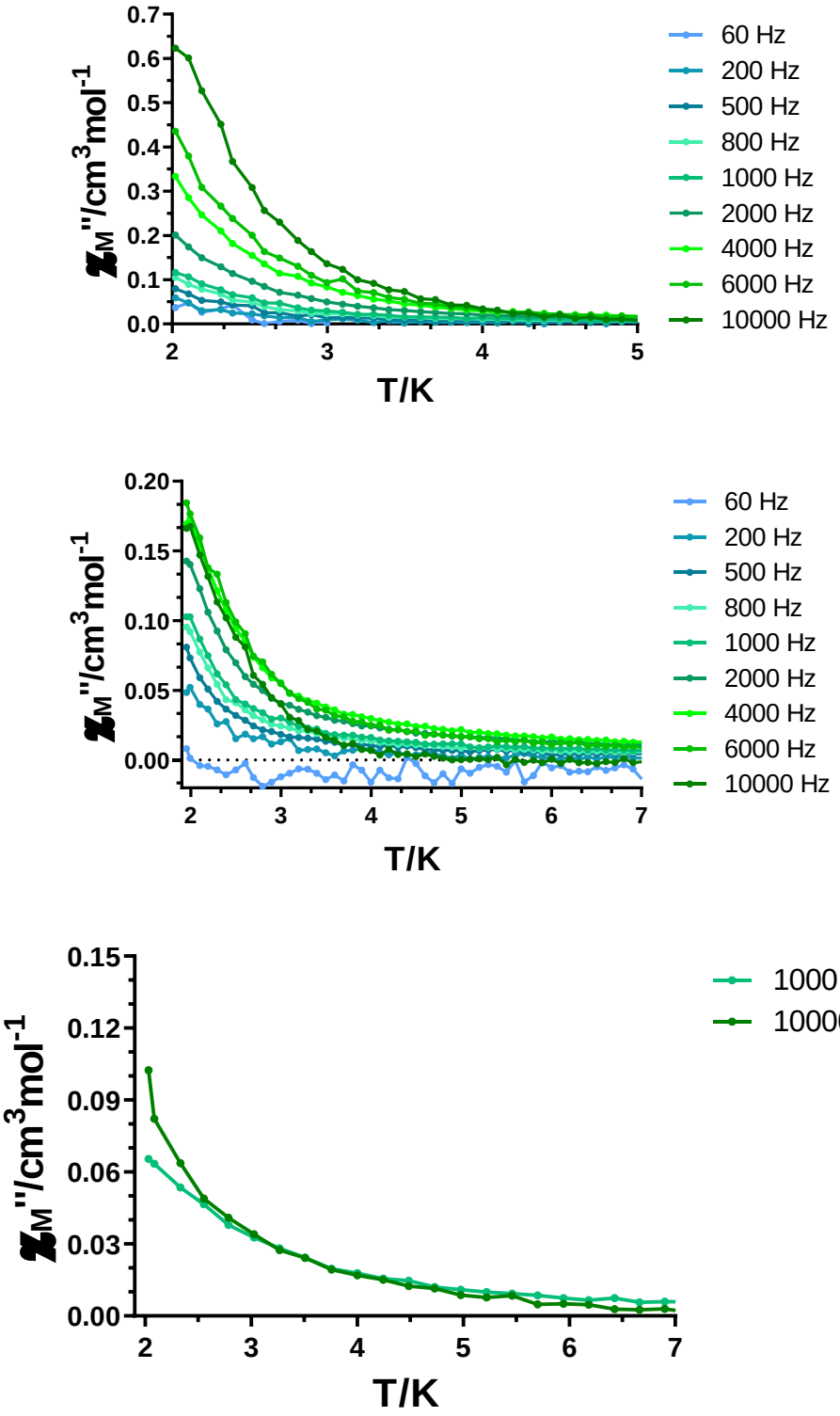

Figure A3.29.- Temperature dependence of the out-of-phase χ_M'' susceptibility signals for complexes **17** (top), **20** (middle) and **23** (bottom) under an applied field of 1000 Oe.

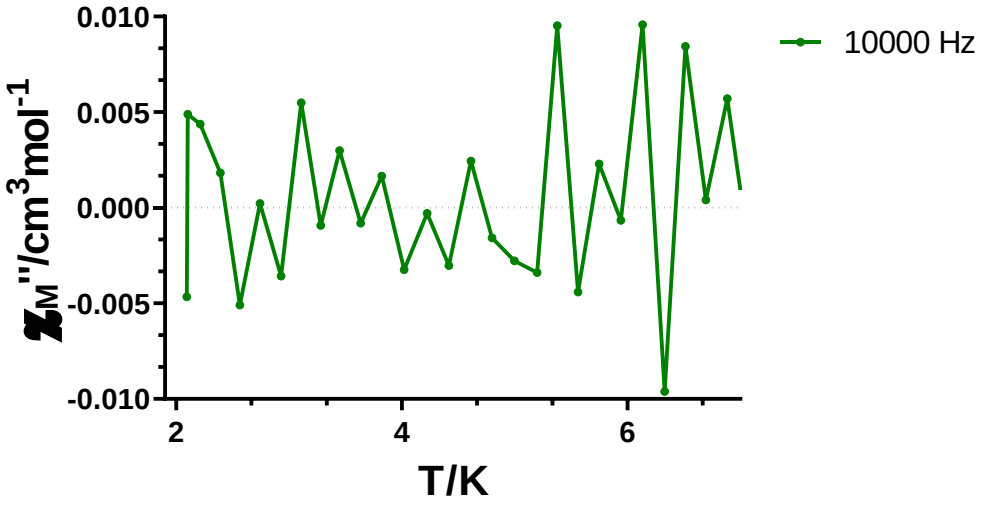

Figure A3.30.- Temperature dependence of the out-of-phase χ_M'' susceptibility signals for complex **24** under an applied field of 1000 Oe.

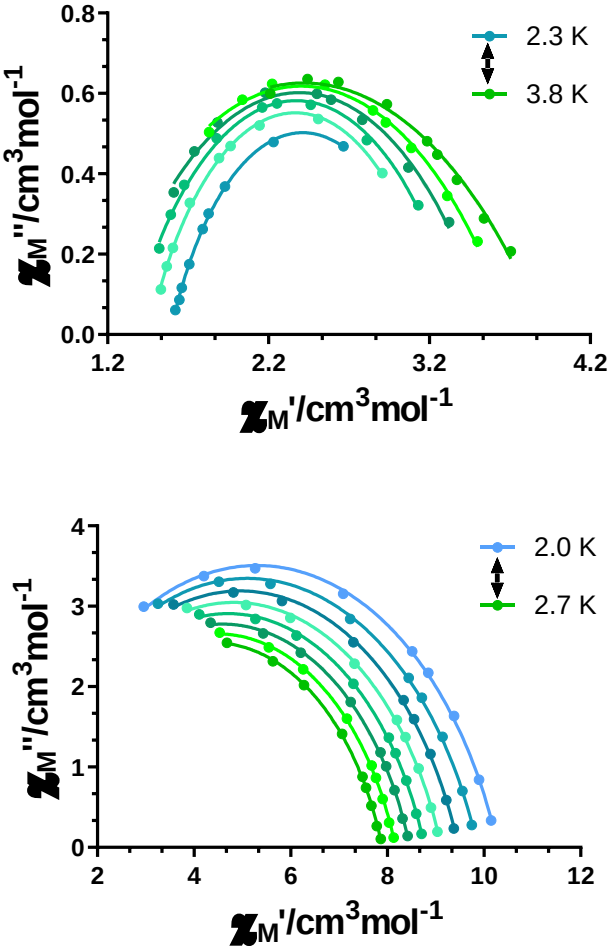

Figure A3.31.- Cole-Cole plots under zero applied *dc* field for **18** (top) and **21** (bottom). Solid lines represent the best fits to the generalized Debye model.

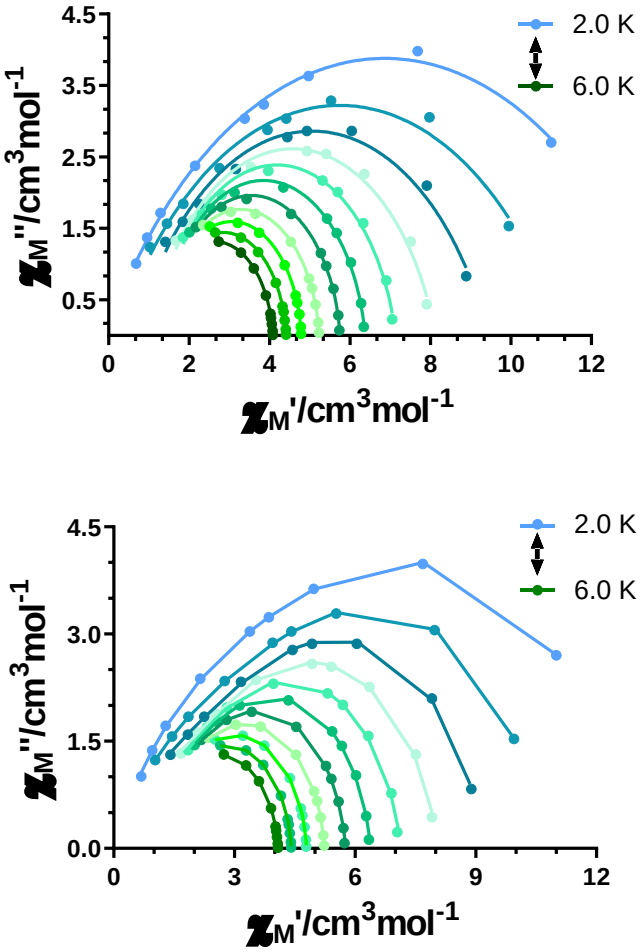

Figure A3.32.- Cole-Cole plots under zero applied *dc* field for **22**. Solid lines represent the best fits to the generalized Debye model (top) or to a sum of two modified Debye functions (bottom).

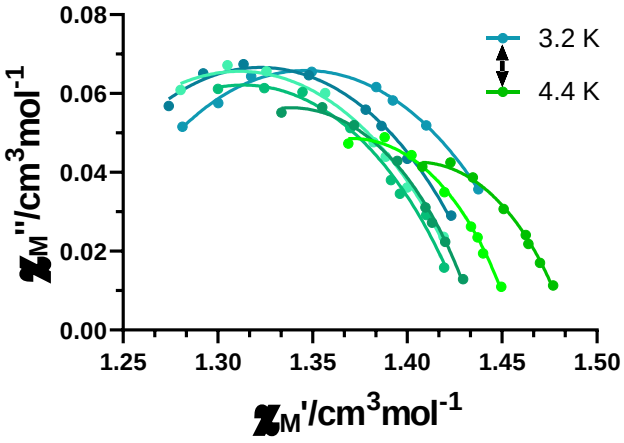

Figure A3.33. Cole-Cole plots in a *dc* applied field of 1000 Oe for **18**. Solid lines represent the best fits to the generalized Debye model.

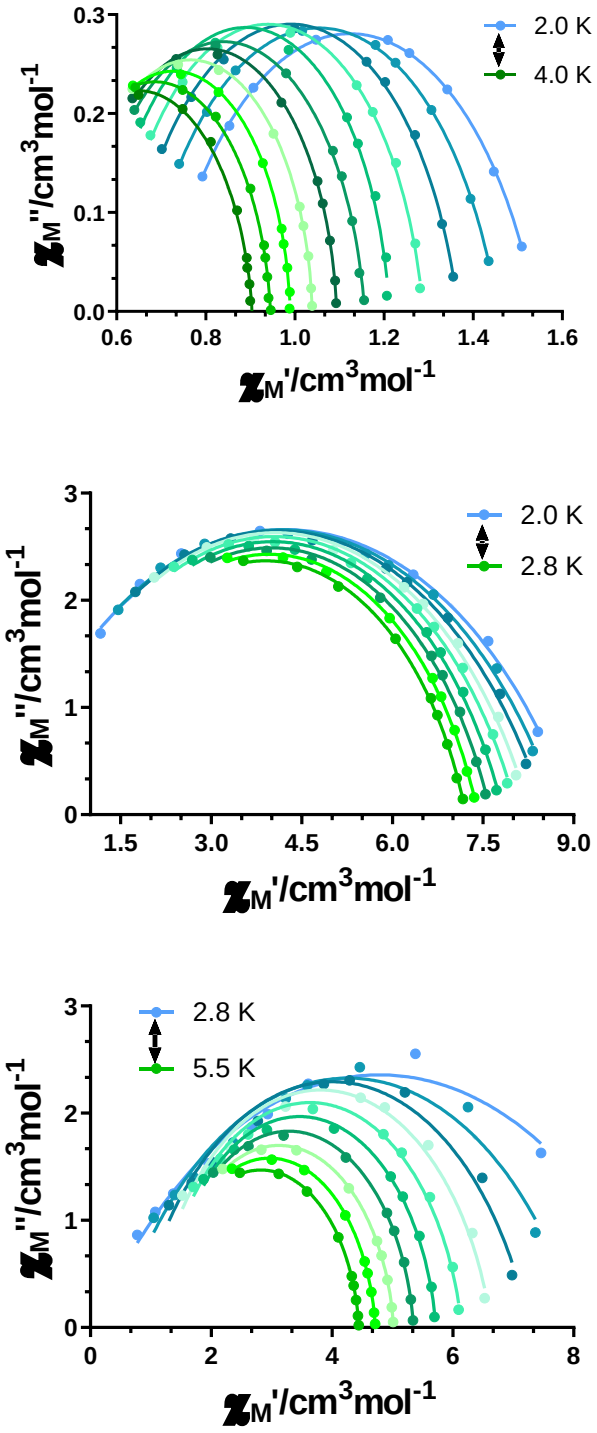

Figure A3.34. Cole-Cole plots in a *dc* applied field of 1000 Oe for **19** (top), **21** (middle) and **22** (bottom). Solid lines represent the best fits to the generalized Debye model.

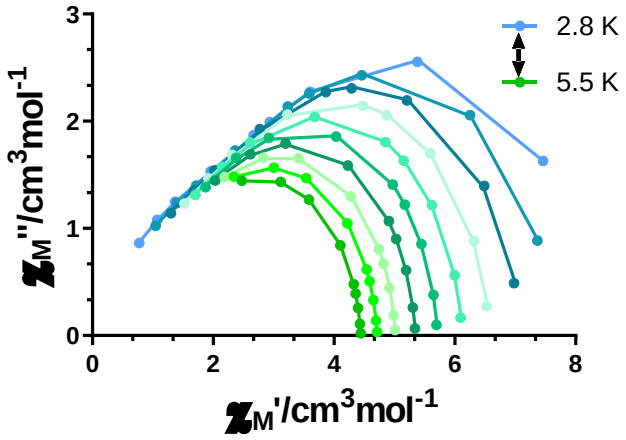

Figure A3.35. Cole-Cole plots in a *dc* applied field of 1000 Oe for **22**. Solid lines represent the best fits using a sum of two modified Debye functions.

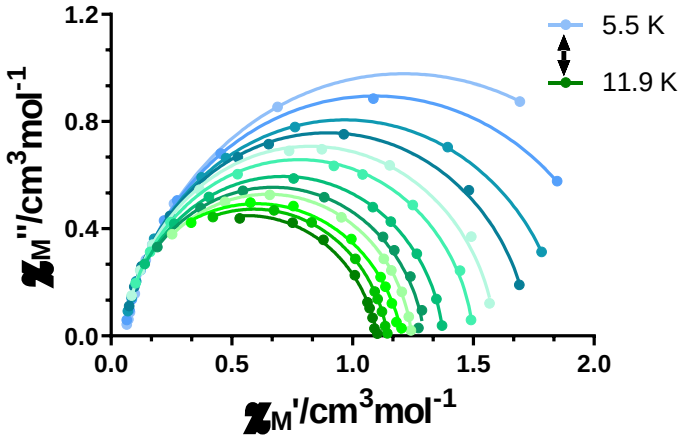

Figure A3.36. Cole-Cole plots in a *dc* applied field of 1000 Oe for **25**. Solid lines represent the best fits to the generalized Debye model.

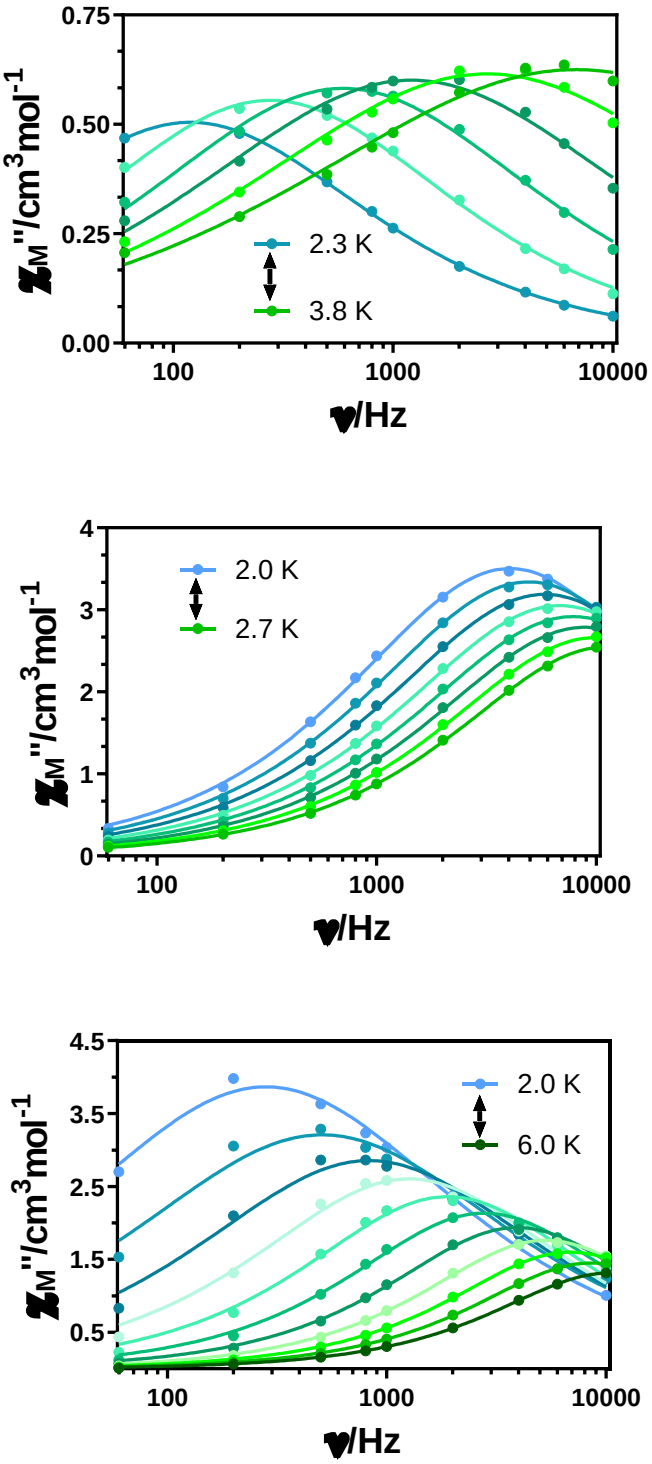

Figure A3.37. Variable-temperature frequency dependence of the χ_M'' signal under zero applied *dc* field **18** (top), **21** (middle) and **22** (bottom). Solid lines represent the best fitting of the experimental data to the Debye model.

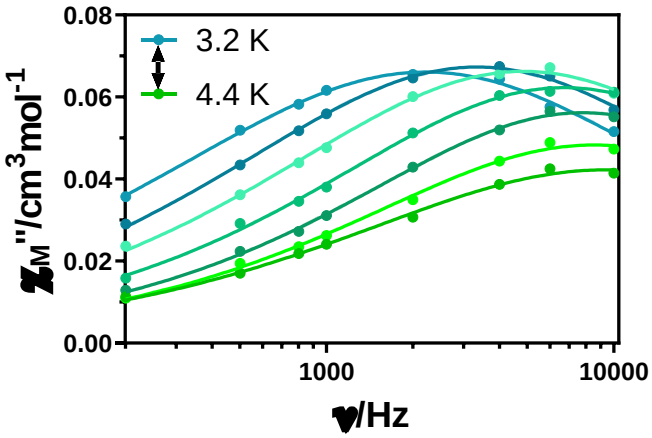

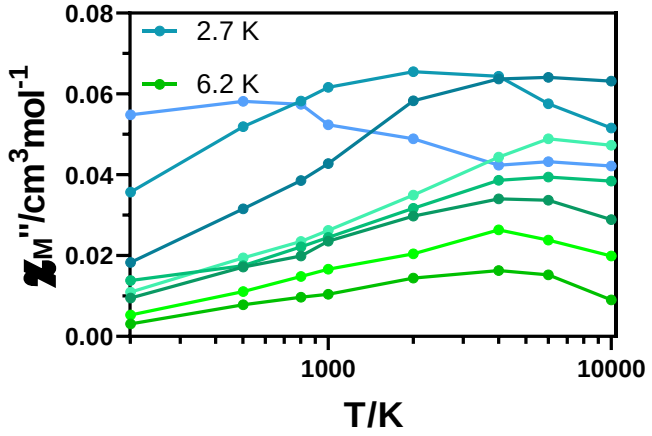

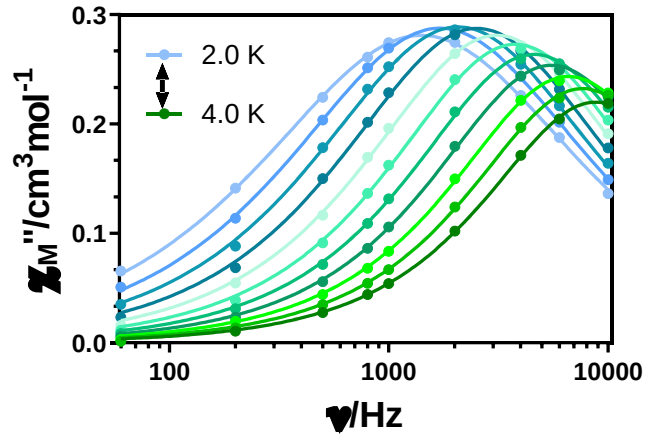

Figure A3.38. Variable-temperature frequency dependence of the χ_M'' signal under 1000 Oe applied field for **18** (top and middle) and **19** (bottom). Solid lines represent the best fitting of the experimental data to the Debye model except in the plot in the middle, where the solid lines are a guide to the eye.

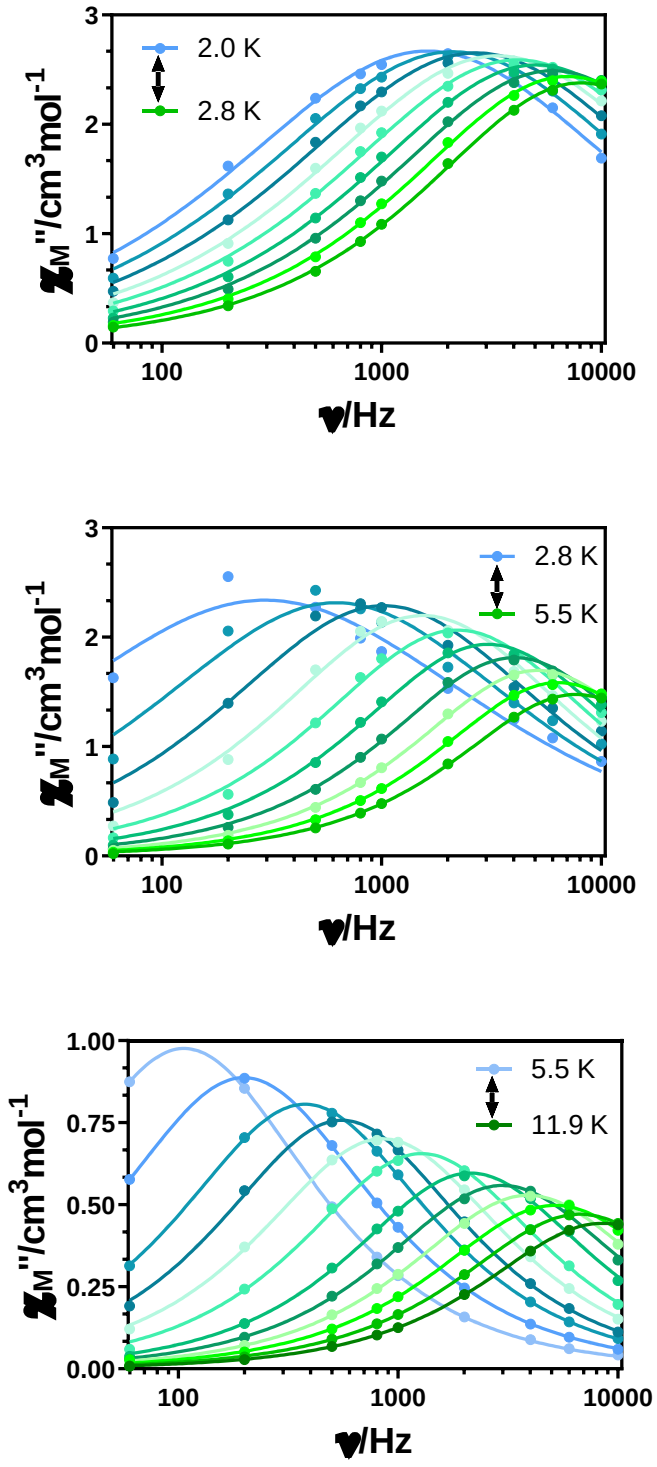

Figure A3.39. Variable-temperature frequency dependence of the χ_M'' signal under 1000 Oe applied field for **21** (top), **22** (middle) and **25** (bottom). Solid lines represent the best fitting of the experimental data to the Debye model.

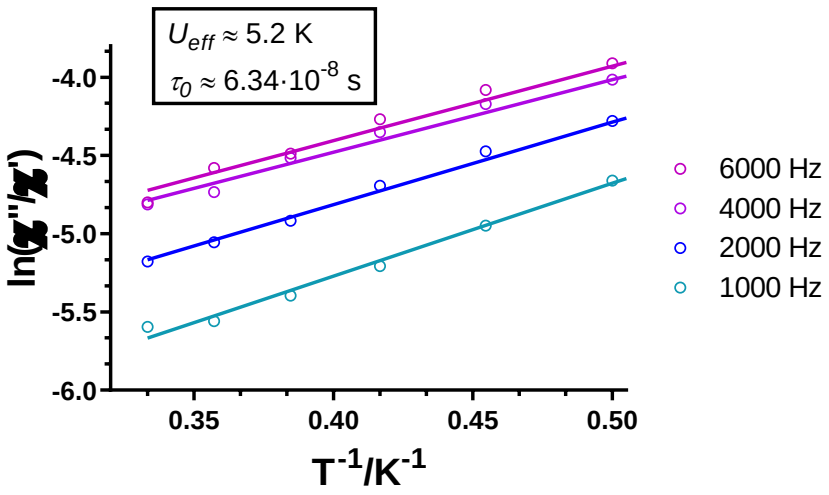

Figure A3.40.- *ln(χM''/ χM')(T^{-1})* plot of **20** under zero applied *dc* field.

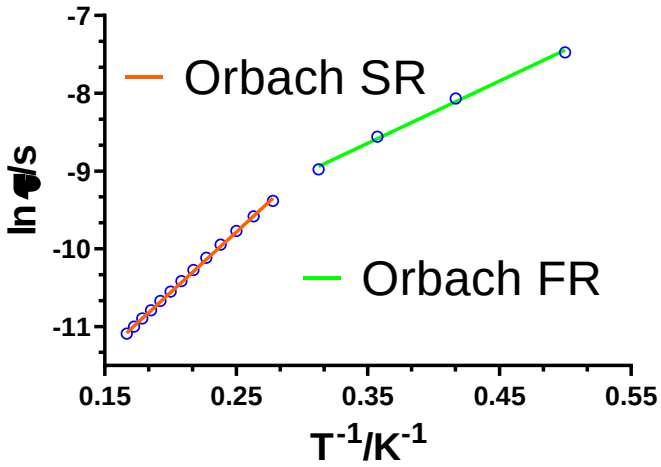

Figure A3.41.- Arrhenius plot for the relaxation times for **22** under zero *dc* field. Relaxation times were obtained considering a single process.

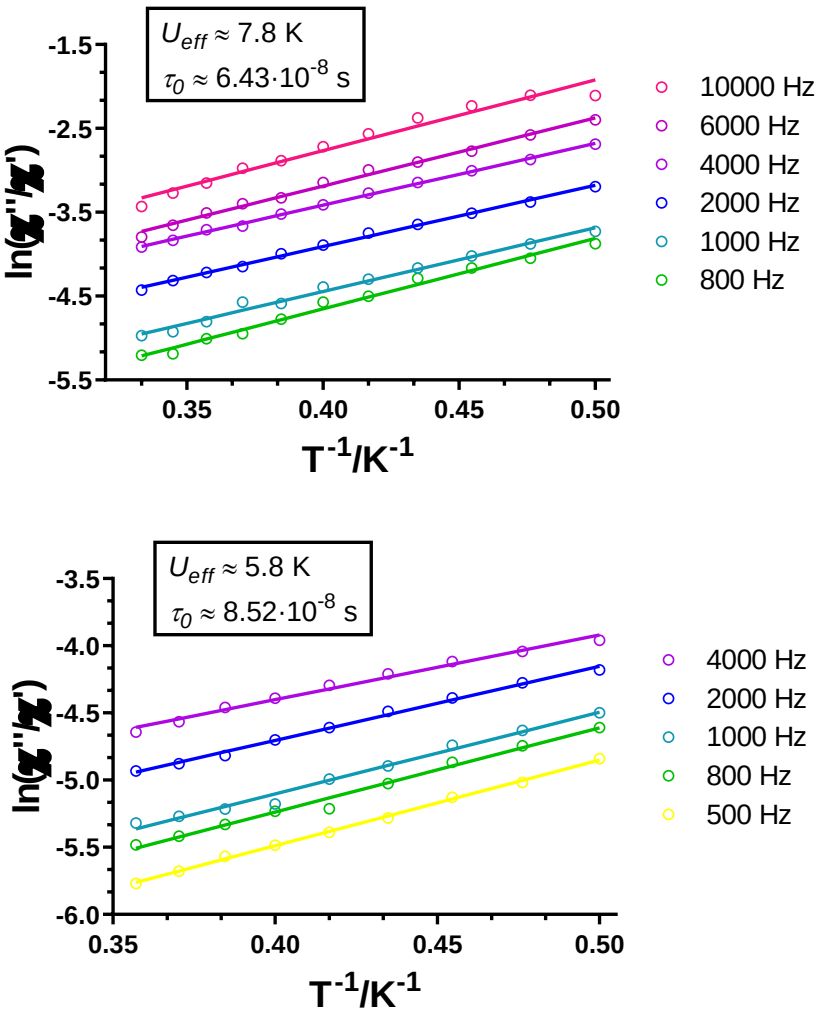

Figure A3.42.- *ln(χ_M''/ χ_M')(T^{-1})* plots of **17** (top) and **20** (bottom) under 1000 Oe applied field.

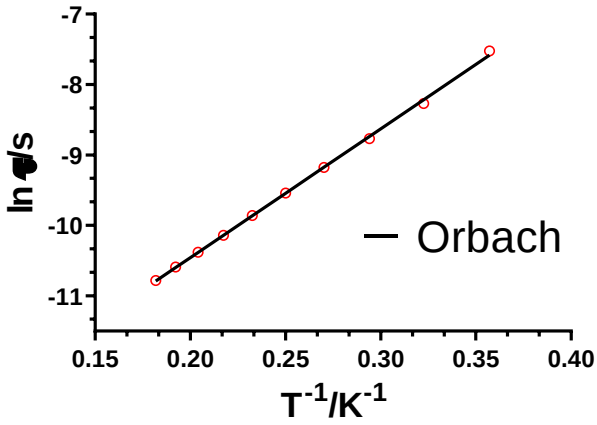

Figure A3.43.- Arrhenius plot for the relaxation times for **22** under an external *dc* field of 1000 Oe. Relaxation times were obtained considering a single process.

APPENDICES

***Chapter 4**: On the way towards 1D extended magnets: serendipitous formation of a tetranuclear $Zn^{II}_2Dy^{III}_2$ zero field SMM, an exhaustive magnetic study*

Index:

1. Elemental Analyses and Crystallographic Tables.

Table A4.1.- Yields and elemental analyses for complexes **28-37**.

Complex	Yield (%)	Formula	% C calc./found	% H calc./found	% N calc./found
28	91	$C_{46}H_{68}N_4O_{12}Cu_2$	55.46/55.69	6.88/7.05	5.62/5.31
29	31	$C_{110}H_{150}Cl_{12}N_{14}O_{48}Zn_4Y_4$	37.98/38.12	4.34/4.47	5.64/5.51
30	28	$C_{110}H_{150}Cl_{12}N_{14}O_{48}Zn_4Dy_4$	35.01/35.25	4.01/4.00	5.20/5.12
31	53	$C_{102}H_{156}N_{12}O_{40}Co_2Y_2$	49.28/49.43	6.32/6.48	6.76/6.90
32	63	$C_{102}H_{156}N_{12}O_{40}Co_2Gd_2$	46.71/46.80	6.00/6.08	6.41/6.29
33	46	$C_{102}H_{156}N_{12}O_{40}Co_2Dy_2$	46.52/46.66	5.97/6.26	6.38/6.12
34	27	$C_{102}H_{156}N_{12}O_{40}Zn_2Y_2$	49.02/49.21	6.29/6.18	6.73/6.55
35	60	$C_{102}H_{156}N_{12}O_{40}Zn_2Tb_2$	46.42/46.22	5.96/6.14	6.37/6.67
36	61	$C_{102}H_{156}N_{12}O_{40}Zn_2Dy_2$	46.30/46.35	5.94/6.03	6.35/6.27
37	54	$C_{102}H_{156}N_{12}O_{40}Zn_2Er_2$	46.13/46.02	5.92/6.01	6.33/6.40

Table A4.2.- Crystallographic data for H_4L^4 and compounds **28**, **30**, **31**, **33** and **36**.

Structure	**H_4L^4**	**28**	**30**	**31**	**33**	**36**
Formula	$C_{46}H_{64}N_4O_8$	$C_{46}H_{68}N_4O_{12}Cu_2$	$C_{110}H_{150}Cl_{12}N_{14}O_{48}Zn_4Dy_4$	$C_{102}H_{156}N_{12}O_{40}Co_2Y_2$	$C_{102}H_{156}N_{12}O_{40}Co_2Dy_2$	$C_{102}H_{156}N_{12}O_{40}Zn_2Dy_2$
M_r	801.01	996.12	3773.31	2486.06		2646.12
Crystal system	*triclinic*	*monoclinic*	*monoclinic*	*orthorhombic*	*orthorhombic*	*orthorhombic*
Space group (no.)	*P*-1 (2)	*P* 2_1/c (14)	*P* 2/c (13)	*Pba2* (32)	*Pba2* (32)	*Pba2* (32)
a (Å)	7.7203(4)	12.6992(2)	22.4610(7)	20.941(4)	20.934(2)	20.89300(10)
b (Å)	11.3727(5)	10.21400(10)	11.6306(4)	22.770(4)	22.821(2)	22.74300(10)
c (Å)	12.6080(6)	17.5302(2)	26.5609(9)	12.275(2)	12.2957(13)	12.2250(8)
α (°)	91.3198(17)	90	90	90	90	90
β (°)	103.0343(16)	100.0440(10)	97.4880(10)	90	90	90
γ (°)	100.5413(18)	90	90	90	90	90
V (Å^3)	1057.88(9)	2238.99(5)	6879.5(4)	5853.0(18)	5874.2(10)	5808.9(4)
Z	1	2	2	2	2	2
D_c (g cm^{-3})	1.257	1.478	1.822	1.411	1.489	1.513
μ(MoK_α) (mm^{-1})[d]	0.086	1.738	3.151	1.347	1.622	7.970
T (K)	100(2)	100(2)	100(2)	100(2)	100(2)	150.00(10)
Observed reflections	5476 (4032)	4638 (4422)	17844 (16076)	8597 (6271)	13908 (11122)	11050 (10714)
R_{int}	0.0667	0.0200	0.0489	0.2760	0.0774	0.0609
Parameters	266	307	796	650	735	659
GOF	1.047	1.001	1.144	1.029	1.128	1.106
R_1[a,b]	0.0852 (0.0562)	0.0380 (0.0366)	0.0424 (0.0359)	0.1255 (0.0849)	0.0985 (0.0678)	0.0403 (0.0389)
wR_2[c]	0.1347 (0.1226)	0.1029 (0.1016)	0.0774 (0.0754)	0.2089 (0.1856)	0.1714 (0.1516)	0.0904 (0.0898)
Largest difference in peak and hole (e Å^{-3})	0.400 and -0.349	0.719 and -0.574	1.522 and -1.625	2.229 and -0.757	3.298 and -2.848	0.798 and -1.557

[a] $R_1 = \Sigma||F_o| - |F_c||/\Sigma|F_o|$. [b] Values in parentheses for reflections with $I > 2\sigma(I)$. [c] $wR_2 = \{\Sigma[w(F_o^2 - F_c^2)^2]/\Sigma[w(F_o^2)^2]\}^{½}$. [d] μ(CuK_α) (mm^{-1}) in **28** and **36**.

Table A4.3.- Bond lengths (Å) and angles (°) for compounds **28** (top) and **30** (down).

Compound	**28**
Cu1-O1	1.9004(13)
Cu1-O3	1.9263(13)
Cu1-N1	2.0766(15)
Cu1-N2	2.0156(15)
O1-Cu1-O3	87.81(6)
O1-Cu1-N1	90.75(6)
O1-Cu1-N2	177.14(6)
O3-Cu1-N1	170.48(6)
O3-Cu1-N2	94.82(6)
N1-Cu1-N2	86.47(6)

Compound	**30A**		**30B**
Dy1A···Zn1A	3.3884(4)	Dy1B···Zn1B	3.4009(4)
Dy1A-O1A	2.262(2)	Dy1B-O1B	2.274(2)
Dy1A-O2A	2.563(3)	Dy1B-O2B	2.515(2)
Dy1A-O3A	2.278(2)	Dy1B-O3B	2.285(2)
Dy1A-O4A	2.547(3)	Dy1B-O4B	2.572(2)
Dy1A-O1C	2.329(3)	Dy1B-O1D	2.346(3)
Dy1A-O5A	2.466(3)	Dy1B-O5B	2.452(3)
Dy1A-O6A	2.441(3)	Dy1B-O6B	2.500(3)
Dy1A-O8A	2.449(3)	Dy1B-O8B	2.407(3)
Dy1A-O9A	2.486(3)	Dy1B-O9B	2.441(3)
Zn1A-N1A	2.143(3)	Zn1B-N1B	2.140(3)
Zn1A-N2A	2.181(3)	Zn1B-N2B	2.221(3)
Zn1A-O1A	2.064(2)	Zn1B-O1B	2.055(2)
Zn1A-O3A	2.040(3)	Zn1B-O3B	2.007(2)
Zn1A-O2C	1.977(3)	Zn1B-O2D	1.969(2)
Dy1A-O1A-Zn1A	103.01(10)	Dy1B-O1B-Zn1B	103.41(10)
Dy1A-O3A-Zn1A	103.27(10)	Dy1B-O3B-Zn1B	104.63(10)
O1A-Dy1A-O3A	65.67(9)	O1B-Dy1B-O3B	64.56(8)
O1A-Dy1A-O1C	82.05(9)	O1B-Dy1B-O1D	81.76(9)
O3A-Dy1A-O1C	82.11(9)	O3B-Dy1B-O1D	79.45(9)
O1A-Zn1A-O3A	73.72(10)	O1B-Zn1B-O3B	73.65(9)
O1A-Zn1A-O2C	100.11(11)	O1B-Zn1B-O2D	98.56(10)
O3A-Zn1A-O2C	102.79(11)	O3B-Zn1B-O2D	104.83(10)
N1A-Zn1A-N2A	85.25(12)	N1B-Zn1B-N2B	85.76(10)

Table A4.4.- Bond lengths (Å) and angles (°) for compounds **31**, **33** and **36** (TM = Co for **31**-**33** and TM = Zn for **36**; Ln = Y for **31** and Ln = Dy for **33** and **36**).

Compound	**31**	**33**	**36**
Ln1···TM1	3.345(3)	3.3545(17)	3.3611(8)
Ln1-O1	2.286(10)	2.291(9)	2.286(4)
Ln1-O2	2.550(12)	2.563(9)	2.536(5)
Ln1-O3	2.312(10)	2.322(9)	2.313(4)
Ln1-O4	2.638(11)	2.665(9)	2.653(5)
Ln1-O7	2.226(9)	2.234(8)	2.227(4)
Ln1-O8	2.698(11)	2.710(9)	2.708(5)
Ln1-O1N	2.434(11)	2.467(10)	2.456(5)
Ln1-O2N	2.506(11)	2.517(10)	2.519(4)
Ln1-O1S	2.322(10)	2.321(9)	2.320(4)
TM1-N1	2.112(15)	2.111(11)	2.101(5)
TM1-N2	2.184(14)	2.196(10)	2.190(5)
TM1-O1	2.076(10)	2.079(9)	2.083(4)
TM1-O3	1.945(11)	1.965(9)	1.995(5)
TM1-O2S	1.985(11)	1.994(9)	1.979(4)
Ln1-O1-TM1	100.0(4)	100.2(4)	100.46(17)
Ln1-O3-TM1	103.3(5)	102.6(4)	102.3(2)
O1-Ln1-O3	65.9(4)	65.8(3)	65.96(15)
O1-Ln1-O7	137.0(4)	137.3(3)	137.32(16)
O1-Ln1-O1N	83.4(4)	83.1(3)	83.69(16)
O1-Ln1-O2N	91.6(4)	92.0(3)	92.24(15)
O1-Ln1-O1S	81.2(4)	81.3(3)	81.44(15)
O3-Ln1-O7	144.1(4)	144.3(3)	143.73(15)
O3-Ln1-O1N	77.9(4)	78.1(3)	78.55(16)
O3-Ln1-O2N	127.9(4)	127.6(3)	127.66(15)
O3-Ln1-O1S	84.4(4)	84.7(3)	84.52(16)
O7-Ln1-O1N	124.3(4)	124.0(3)	123.75(15)
O7-Ln1-O2N	84.3(4)	84.2(3)	84.53(14)
O7-Ln1-O1S	75.5(4)	75.6(3)	75.29(14)
O1-TM1-O3	76.8(4)	76.5(4)	75.72(17)
O1-TM1-O2S	95.8(4)	96.3(4)	96.48(18)
O3-TM1-O2S	106.3(4)	107.1(4)	107.65(18)
N1-TM1-N2	83.5(5)	83.9(4)	84.3(2)

2. Continuous Shape Measurements.

The nearer the value to zero, the better fits to an ideal polyhedron.

Table A4.5.- Continuous Shape Measurements for the CuN_2O_2 coordination environment in **28**.

SP-4 1 D4h Square
T-4 2 Td Tetrahedron
SS-4 3 C2v Seesaw
vTBPY-4 4 C3v Vacant trigonal bipyramid

Structure [ML4]	SP-4	T-4	SS-4	v-TBPY-4
Cu1 (28)	**0.321**	29.913	16.391	31.323

Table A4.6.- Continuous Shape Measurements for the TMN_2O_3 (where TM is Zn or Co) coordination environment in compounds **30**, **31**, **33** and **36**.

PP-5 1 D5h Pentagon
vOC-5 2 C4v Vacant octahedron
TBPY-5 3 D3h Trigonal bipyramid
SPY-5 4 C4v Spherical square pyramid
JTBPY-5 5 D3h Johnson trigonal bipyramid J12

Structure [ML5]	PP-5	vOC-5	TBPY-5	SPY-5	JTBPY-5
Zn1A (30)	30.823	2.719	4.182	**0.853**	6.711
Zn1B (30)	31.431	2.883	5.082	**0.820**	7.485
Co1 (31)	29.738	1.868	4.680	**0.802**	6.475
Co1 (33)	29.733	1.975	4.720	**0.747**	6.598
Zn1 (36)	29.270	2.116	4.850	**0.724**	6.843

Table A4.7.- Continuous Shape Measurements for the LnO_9 (where Ln is Dy or Y) coordination environment in compounds **30**, **31**, **33** and **36**.

EP-9	1 D9h	Enneagon
OPY-9	2 C8v	Octagonal pyramid
HBPY-9	3 D7h	Heptagonal bipyramid
JTC-9	4 C3v	Johnson triangular cupola J3
JCCU-9	5 C4v	Capped cube J8
CCU-9	6 C4v	Spherical-relaxed capped cube
JCSAPR-9	7 C4v	Capped square antiprism J10
CSAPR-9	8 C4v	Spherical capped square antiprism
JTCTPR-9	9 D3h	Tricapped trigonal prism J51
TCTPR-9	10 D3h	Spherical tricapped trigonal prism
JTDIC-9	11 C3v	Tridiminished icosahedron J63
HH-9	12 C2v	Hula-hoop
MFF-9	13 Cs	Muffin

Structure [ML9]	EP-9	OPY-9	HBPY-9	JTC-9	JCCU-9	CCU-9	JCSAPR-9
Dy1A (30)	36.050	23.179	18.395	14.580	10.293	8.501	3.625
Dy1B (30)	36.235	23.443	17.621	14.275	9.804	8.084	3.560
Y1 (31)	33.585	22.453	16.220	16.027	8.120	7.211	3.494
Dy1 (33)	33.643	22.448	16.181	16.120	8.056	7.164	3.520
Dy1 (36)	33.637	22.257	16.216	16.204	8.183	7.223	3.641

Structure [ML9]	CSAPR-9	JTCTPR-9	TCTPR-9	JTDIC-9	HH-9	MFF-9
Dy1A (30)	**2.202**	4.802	2.825	10.230	9.817	2.322
Dy1B (30)	**2.207**	4.328	2.455	10.178	9.531	2.278
Y1 (31)	2.912	3.932	3.325	11.089	8.229	**2.564**
Dy1 (33)	2.961	4.077	3.433	11.198	8.264	**2.624**
Dy1 (36)	3.019	4.137	3.457	11.099	8.242	**2.654**

3. Figures of H_4L^4 and supramolecular structures.

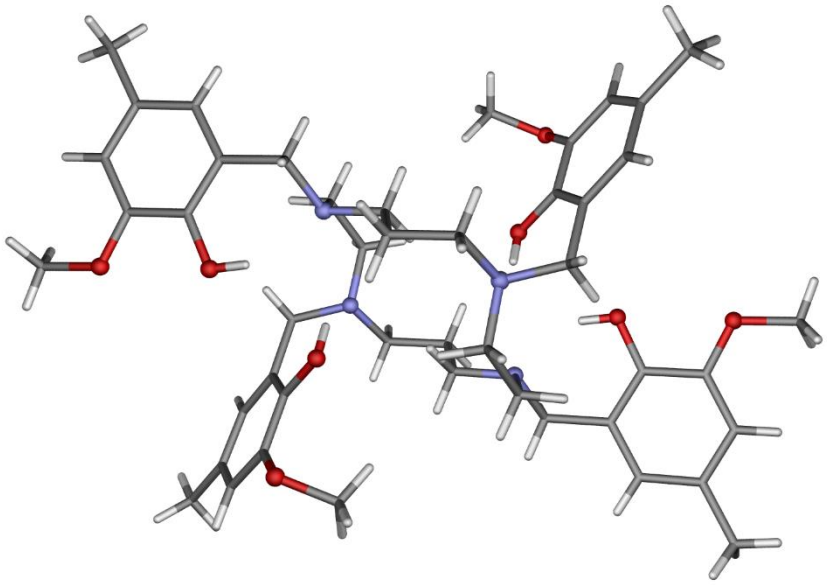

Figure A4.1.- Perspective view of the structure of H_4L^4. Oxygen, nitrogen, carbon and hydrogen are in red, blue, grey and white, respectively.

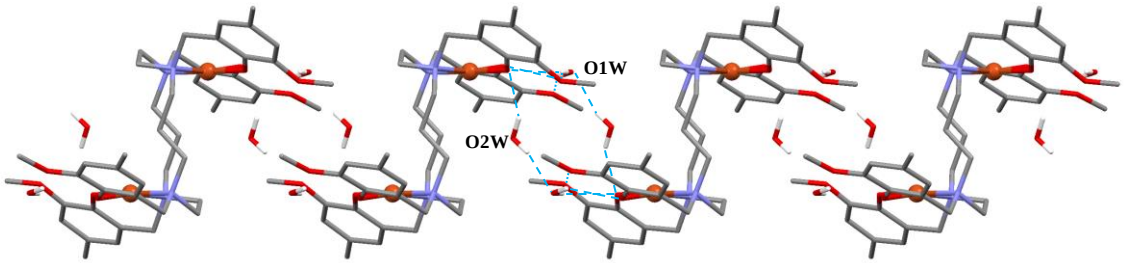

Figure A4.2.- Supramolecular arrangement of **28**, a view along the *a* axis. The individual molecules are organized in 1D by hydrogen bonds along the *b* axis.

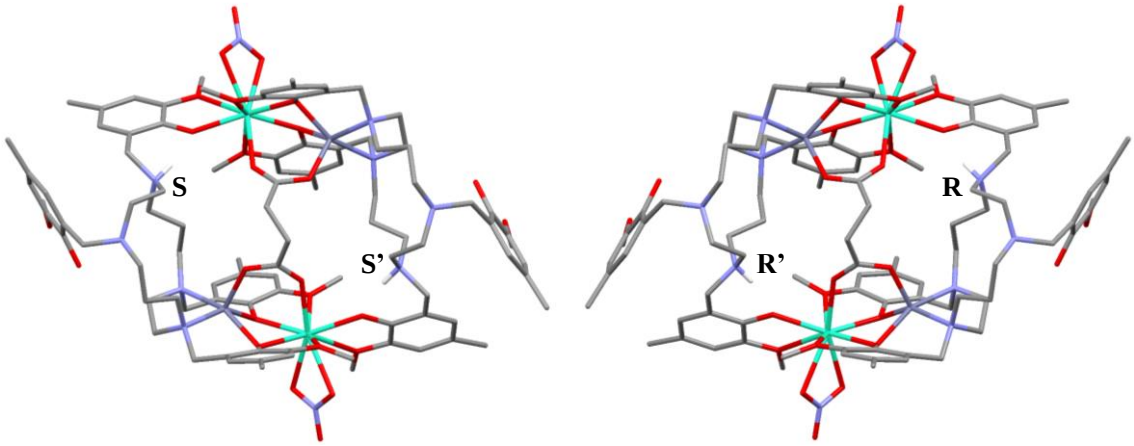

Figure A4.3.- Perspective view of the two possible enantiomers cocrystallized in **36**. All hydrogen atoms, except the ones that form the asymmetric centers have been omitted for the sake of clarity.

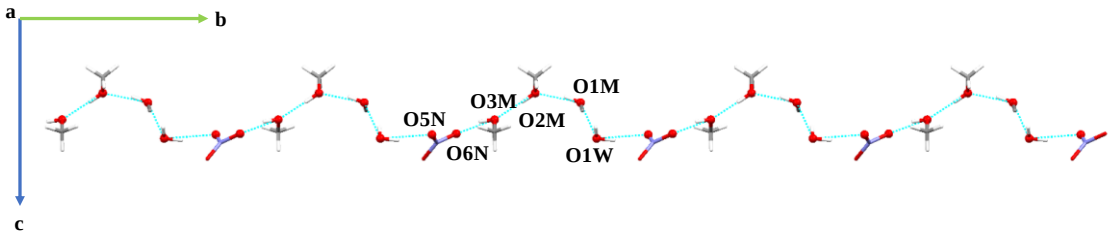

Figure A4.4.- Hydrogen bonding pattern (blue dashed lines) between counterions (NO_3^-) and solvent molecules (methanol and water) for **33** viewed along the *a* axis. Cationic molecular structures of **33** have been omitted. The methanol related to O1M does not have hydrogen atoms because of the disordered character of the C1M atom.

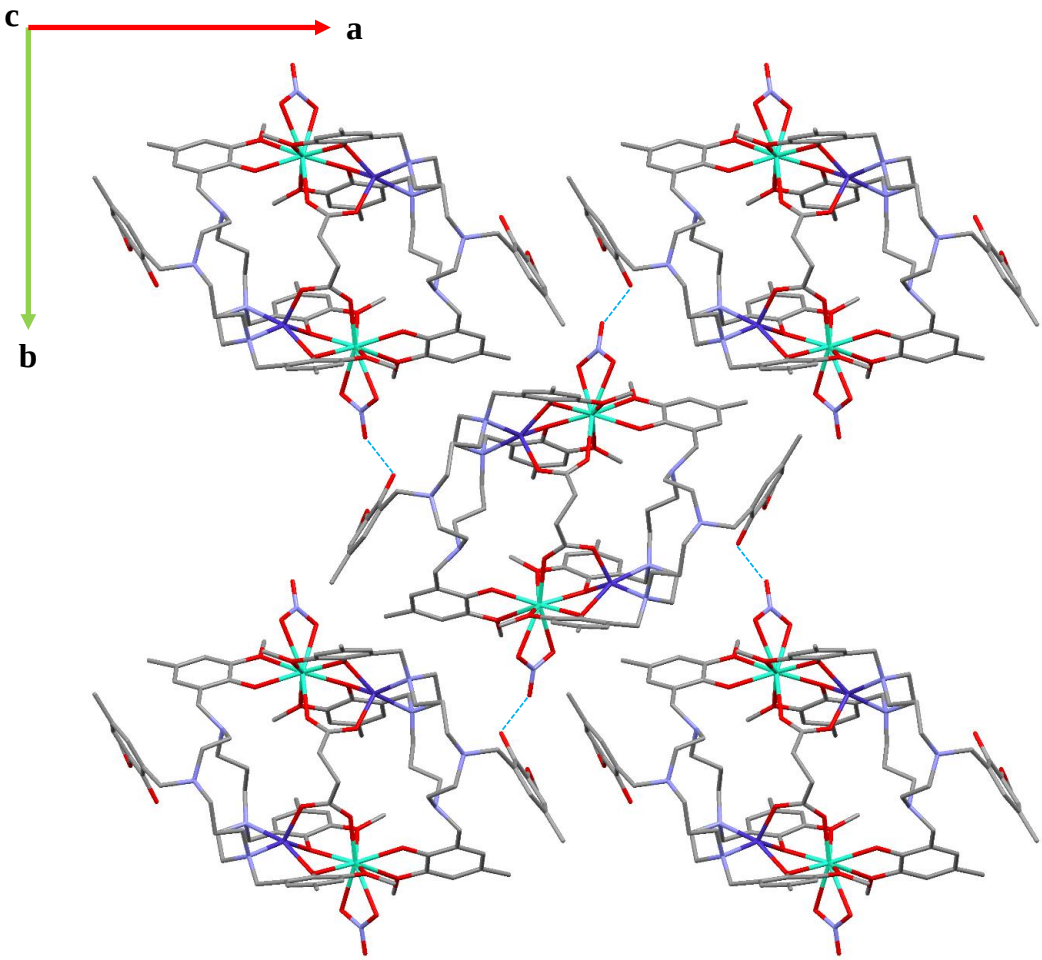

Figure A4.5.- Hydrogen bonding pattern (blue dashed lines) between cationic fragments of **33**, viewed along the *c* axis. Both possible enantiomers are visible, *R,R'* in the center and *S,S'* in the four vertices.

4. Experimental XRPD.

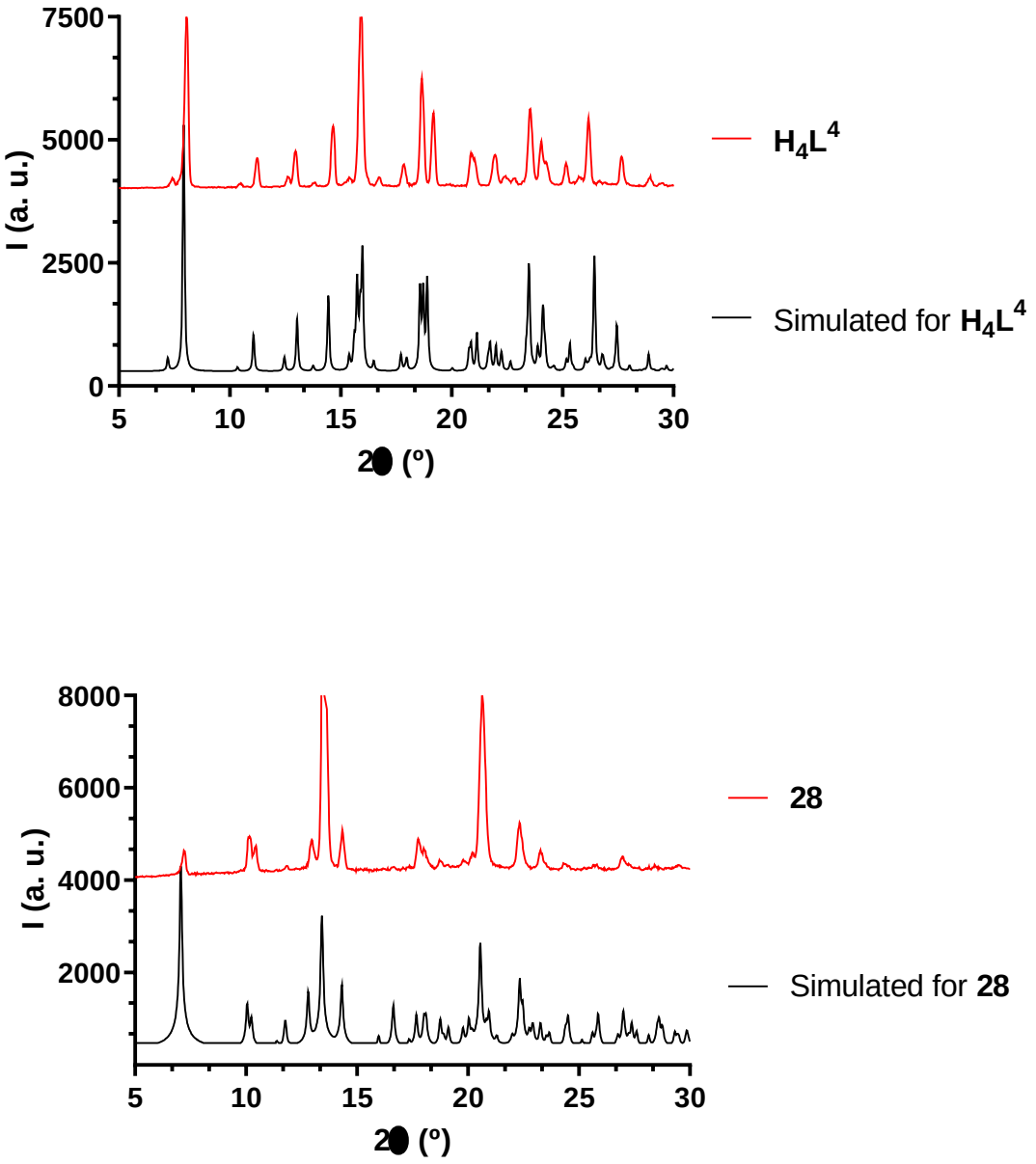

Figure A4.6.- For H_4L^4 (top) and compound **28** (bottom), simulated pattern from single-crystal X-ray diffraction (black line) and experimental XRPD (red).

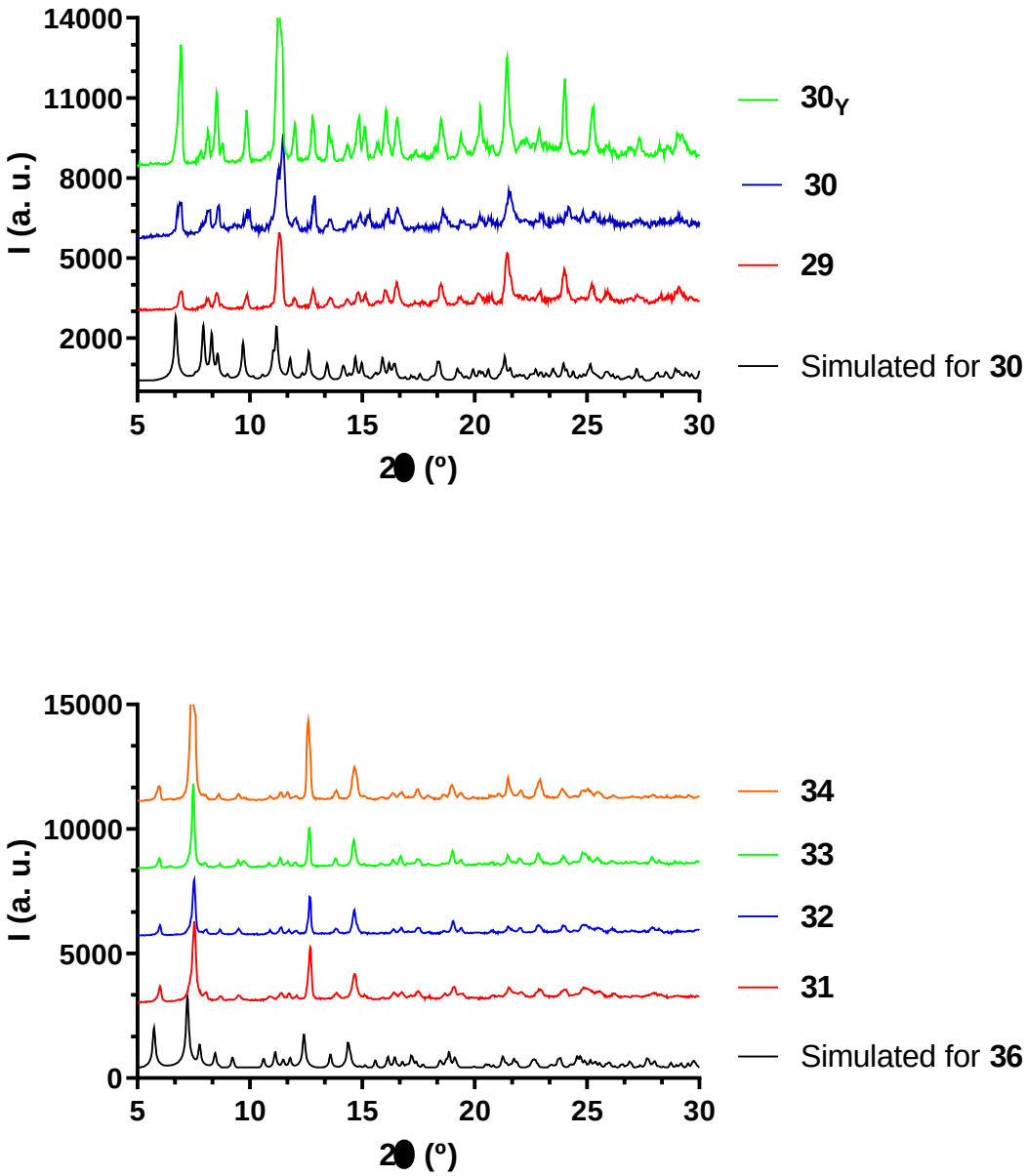

Figure A4.7.- For compounds **29**, **30**, **30**$_Y$ (top) and **31**, **32**, **33** and **36** (bottom), simulated pattern from single-crystal X-ray diffraction of **30** and **36** (black line) and experimental XRPD for **29** and **31** (red), **30** and **32** (blue), **30**$_Y$ and **33** (green) and **34** (orange).

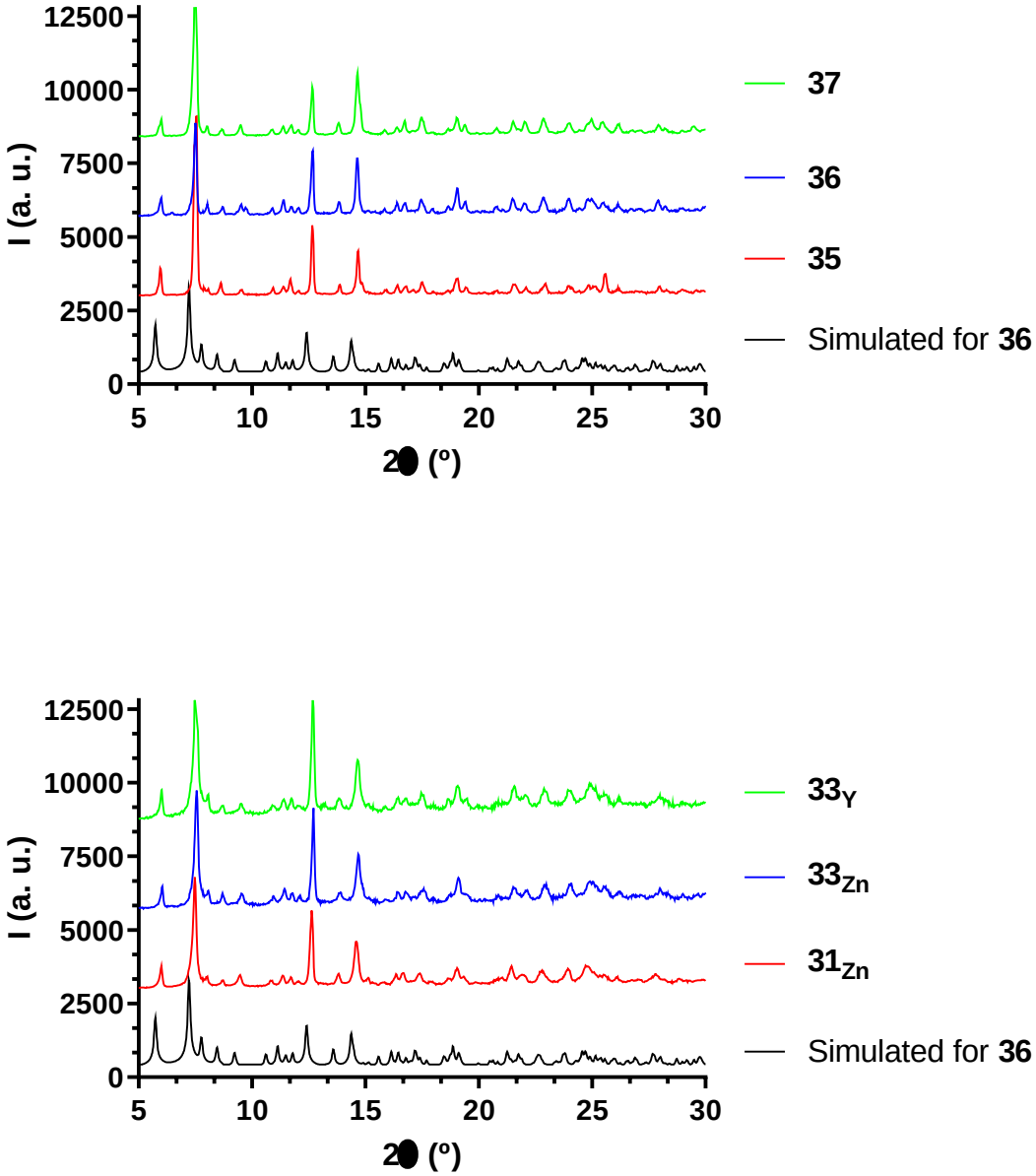

Figure A4.8.- For compounds **35**, **36**, **37** (top) and $\mathbf{31}_{Zn}$, $\mathbf{33}_{Zn}$, $\mathbf{33}_{Y}$ (bottom), simulated pattern from single-crystal X-ray diffraction of **36** (black line) and experimental XRPD for **35** and $\mathbf{31}_{Zn}$ (red), **36** and $\mathbf{33}_{Zn}$ (blue) and **37** and $\mathbf{33}_{Y}$ (green).

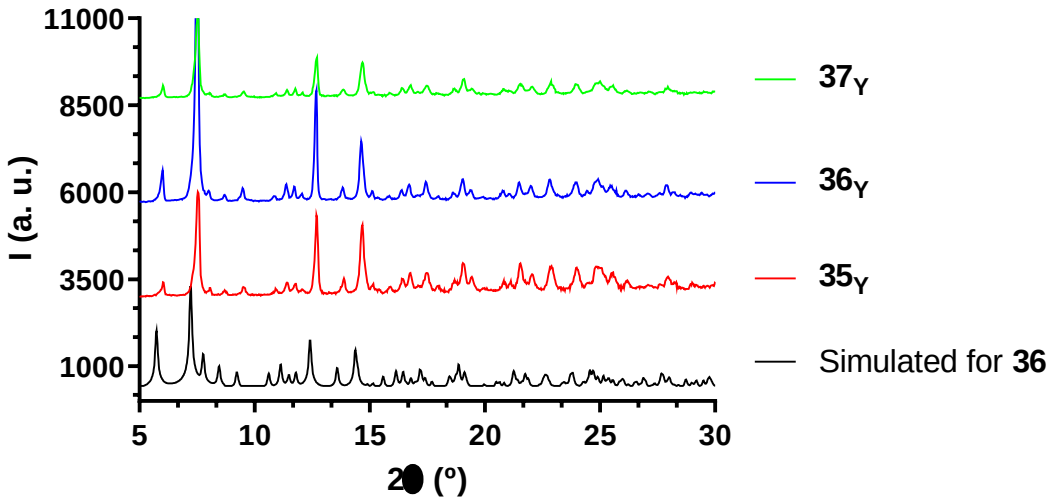

Figure A4.9.- For compounds **35**$_Y$, **36**$_Y$ and **37**$_Y$, simulated pattern from single-crystal X-ray diffraction of **36** (black line) and experimental XRPD for **35**$_Y$ (red), **36**$_Y$ (blue) and **37**$_Y$ (green).

5. Dynamic Magnetic Measurements.

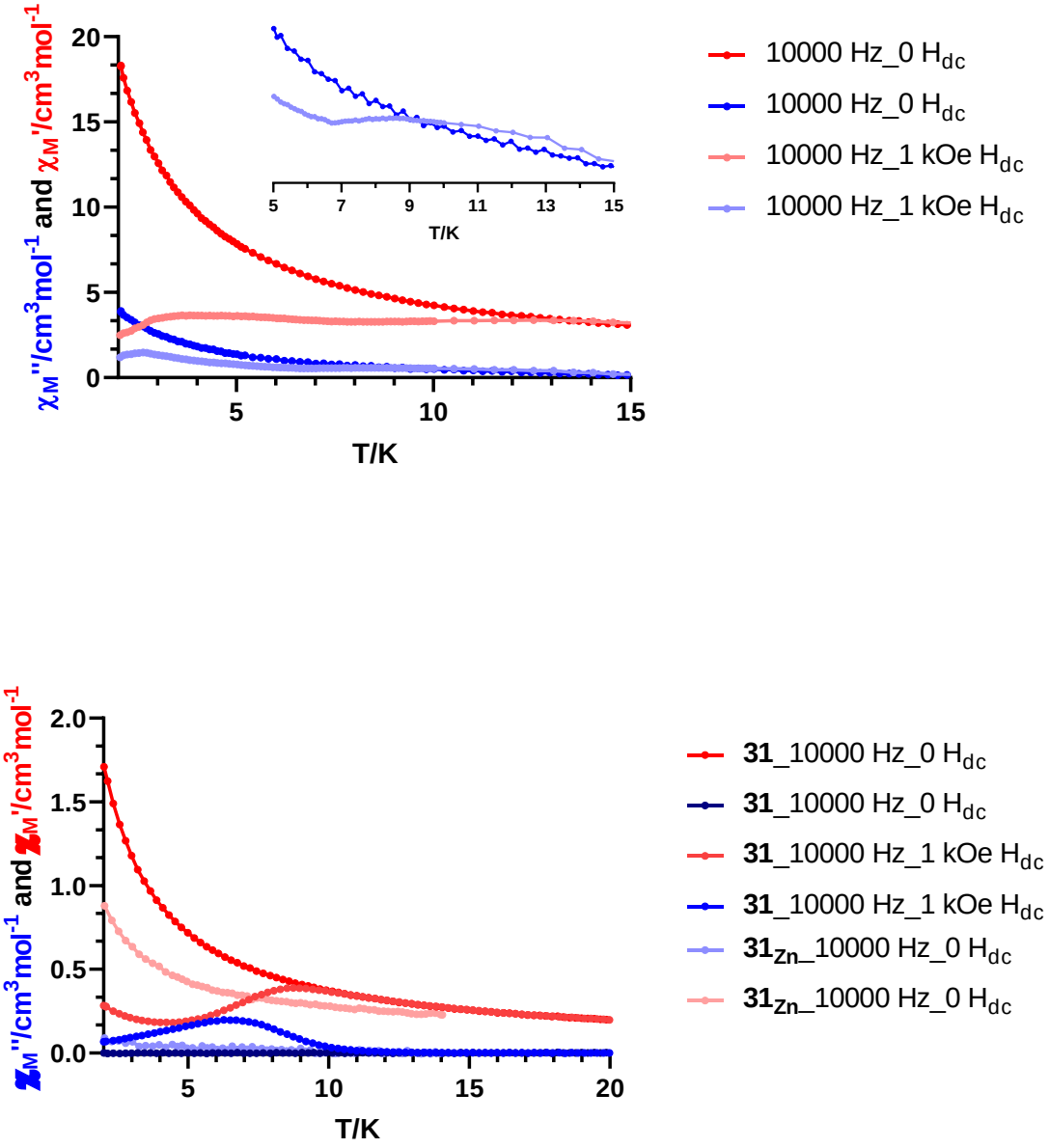

Figure A4.10.- Temperature dependence of in-phase (red) and out-of-phase (blue) components of the *ac* susceptibility in a zero (dark) and 1 kOe (light) applied *dc* field for **30** (top) and **31** (down). Data for **31$_{Zn}$** in a zero applied *dc* field is also shown (down) with light colours, which has been arbitrarily scaled.

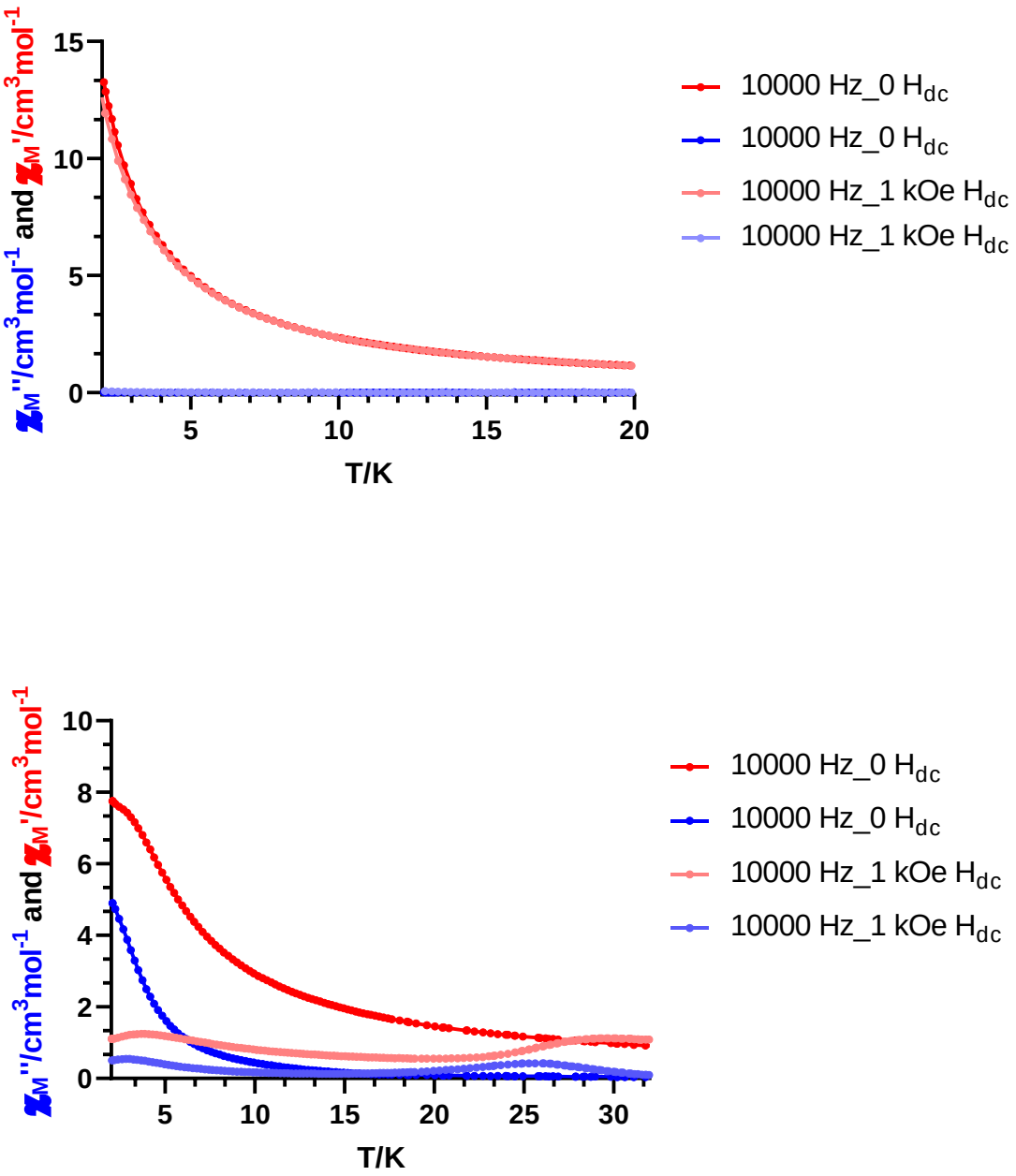

Figure A4.11.- Temperature dependence of in-phase (red) and out-of-phase (blue) components of the *ac* susceptibility in a zero (dark) and 1 kOe (light) applied *dc* field for **32** (top) and **33** (down).

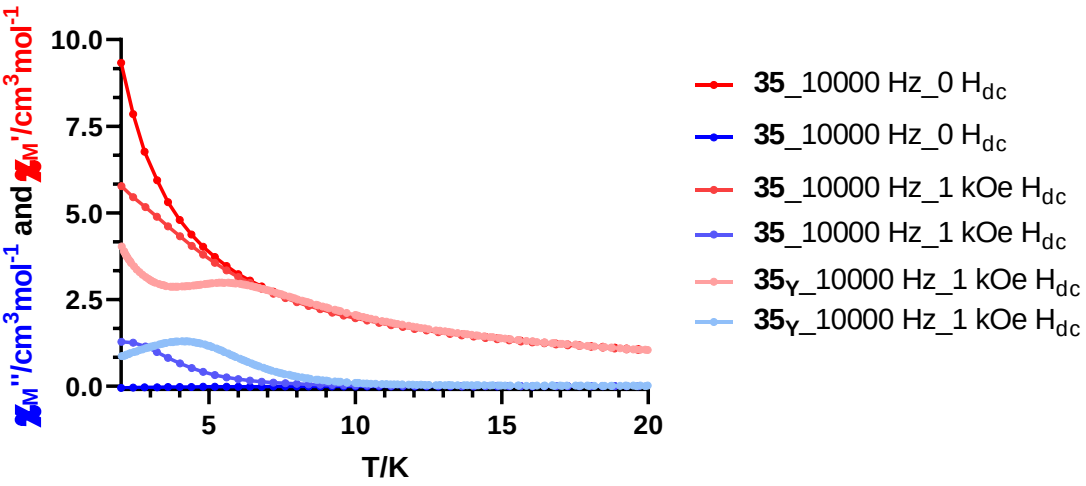

Figure A4.12.- Temperature dependence of in-phase (red) and out-of-phase (blue) components of the *ac* susceptibility in a zero (dark) and 1 kOe (light) applied *dc* field for **35-35$_Y$** (down). Susceptibility values have been arbitrarily scaled for **35$_Y$**.

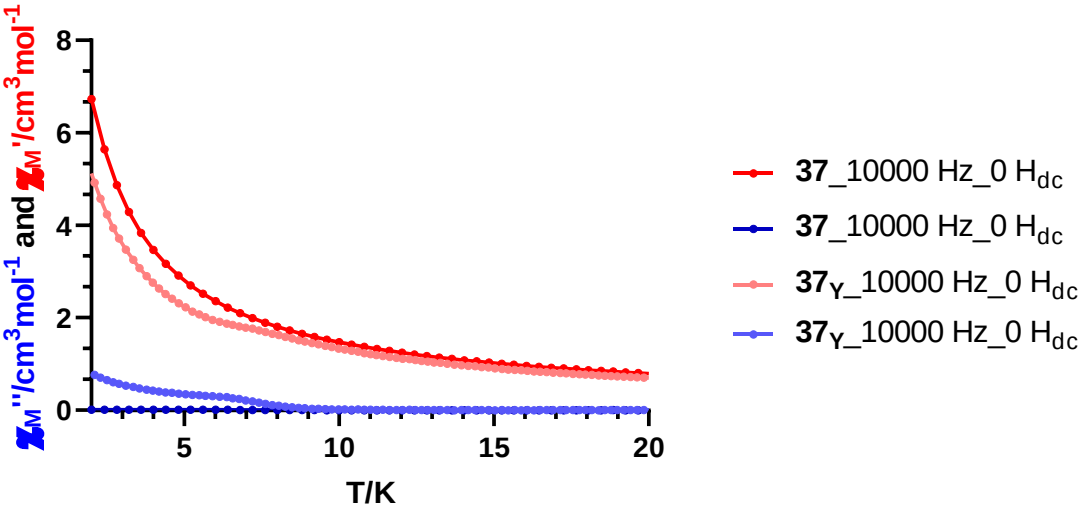

Figure A4.13.- Temperature dependence of in-phase (red) and out-of-phase (blue) components of the *ac* susceptibility in a zero applied *dc* field for **37** (dark) and **37$_Y$** (light). Susceptibility values have been arbitrarily scaled for **37$_Y$**.

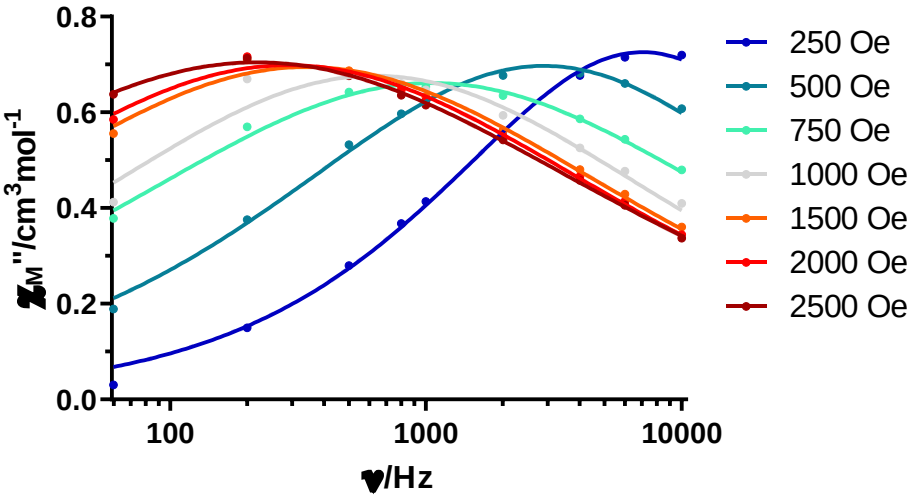

Figure A4.14.- Field dependence of the out-of-phase signal *vs* frequency at 8.0 K for **30**.

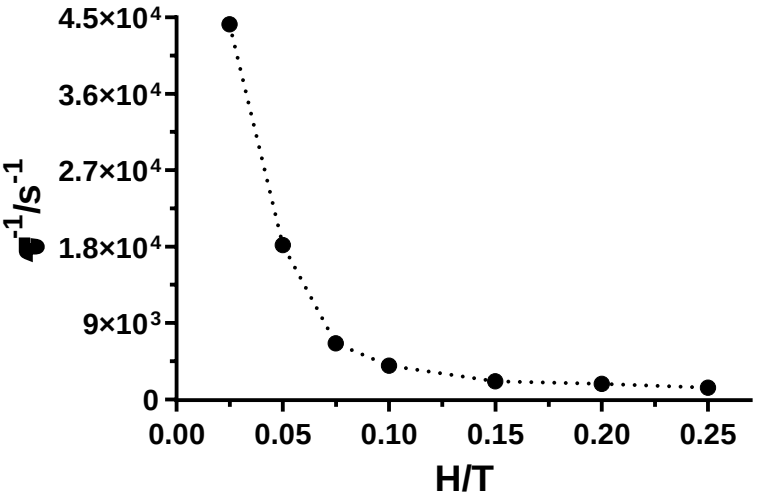

Figure A4.15.- The inverse of the relaxation times obtained at different magnetic fields at 8.0 K for **30**.

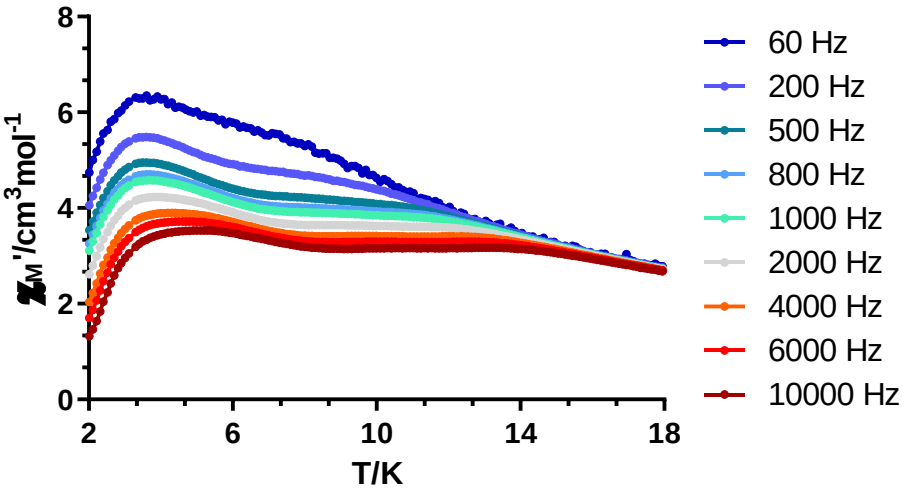

Figure A4.16.- Temperature dependence of the in phase components of the *ac* susceptibility in a *dc* applied field of 2.5 kOe for **30**.

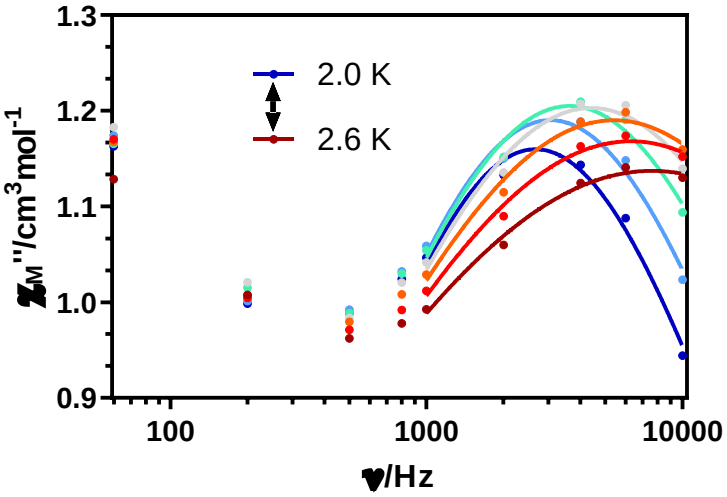

Figure A4.17.- Variable-temperature frequency dependence of the χ_M'' signal under 2.5 kOe applied field for **30**. Solid lines represent the best fitting of the experimental data to the Debye model.

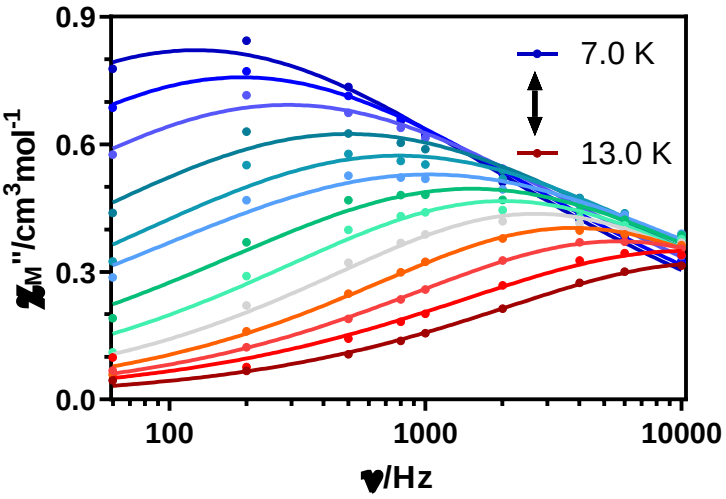

Figure A4.18.- Variable-temperature frequency dependence of the χ_M'' signal under 2.5 kOe applied field for **30**. Solid lines represent the best fitting of the experimental data to the Debye model.

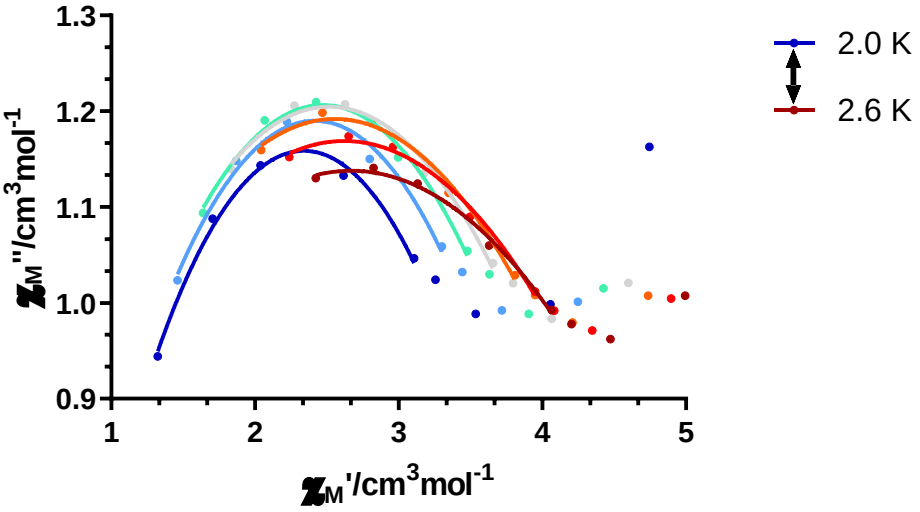

Figure A4.19.- Cole-Cole plots under 2.5 kOe field for **30**. Solid lines represent the best fit to the generalized Debye model.

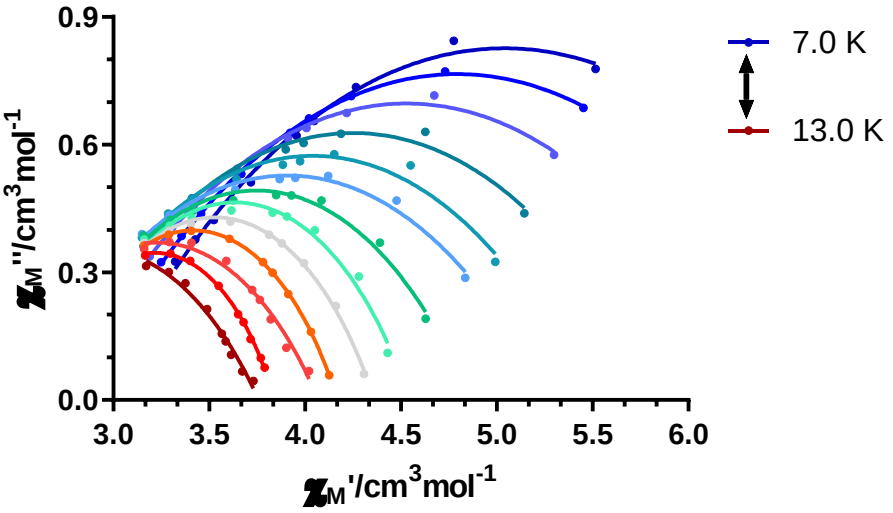

Figure A4.20.- Cole-Cole plots under 2.5 kOe field for **30**. Solid lines represent the best fit to the generalized Debye model.

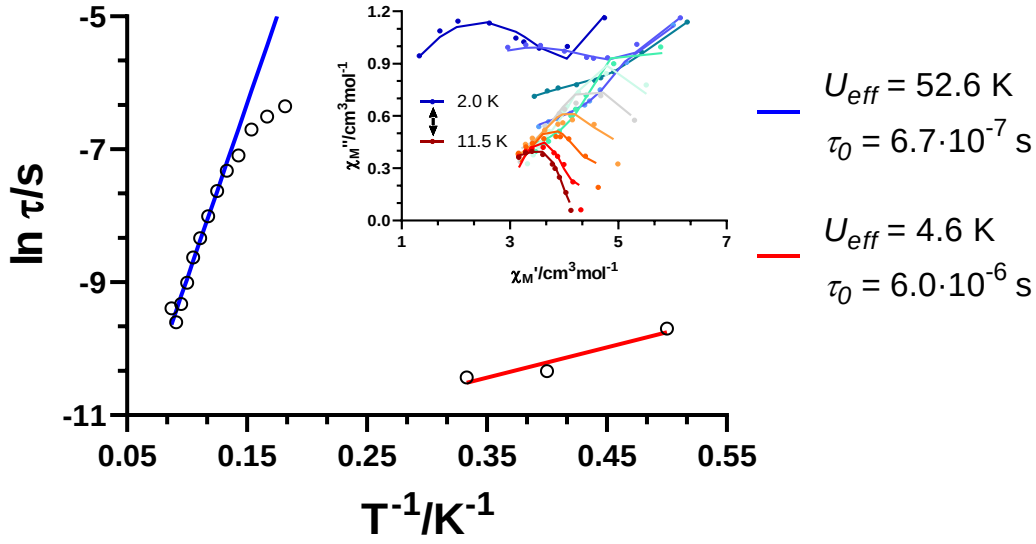

Figure A4.21.- Arrhenius plot for the relaxation times with Orbach fittings for FR and SR. Inset: Cole-Cole plots under 2.5 kOe field for **30**. Solid lines represent the best fit using a sum of two modified Debye functions.

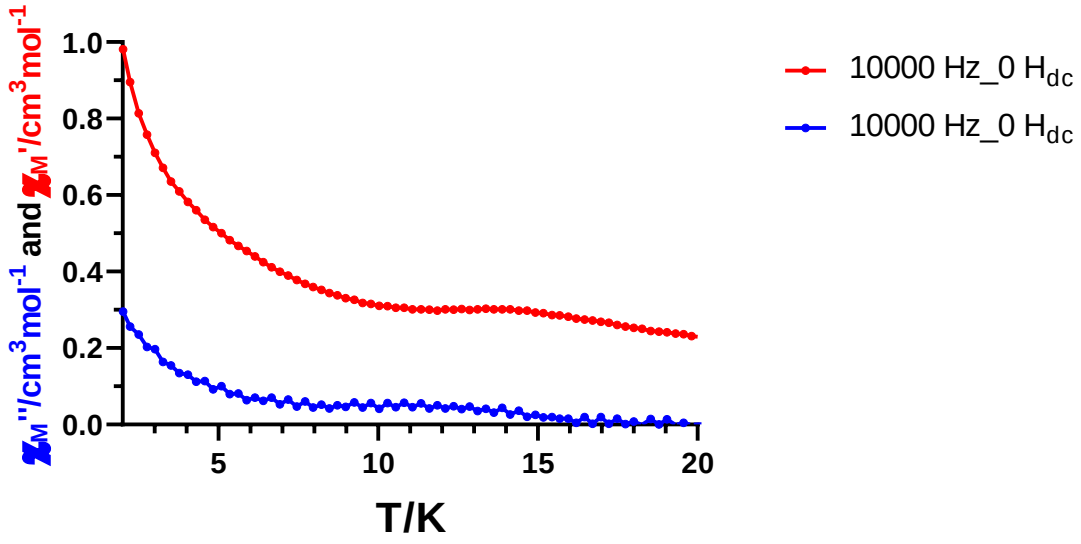

Figure A4.22.- Temperature dependence of in-phase (red) and out-of-phase (blue) components of the *ac* susceptibility in a zero applied *dc* field for **30$_Y$**.

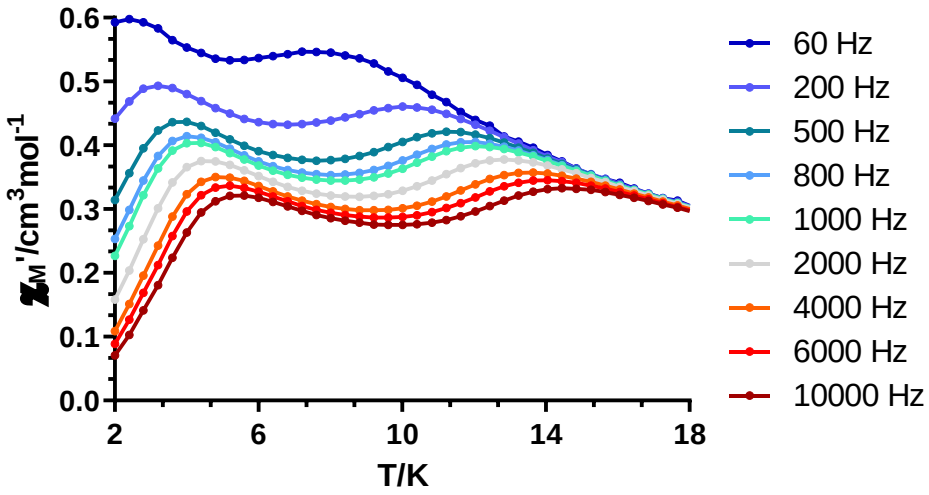

Figure A4.23.- Temperature dependence of the in phase components of the *ac* susceptibility in a *dc* applied field of 2.5 kOe for **30$_Y$**.

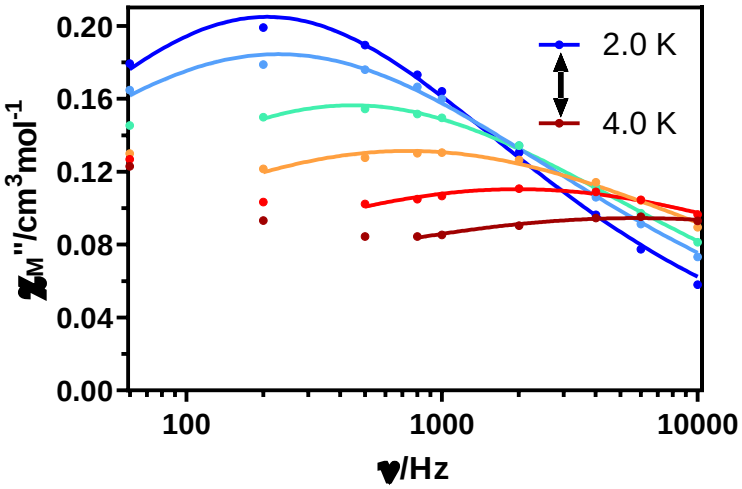

Figure A4.24.- Variable-temperature frequency dependence of the χ_M'' signal under 2.5 kOe applied field for **30$_Y$**. Solid lines represent the best fitting of the experimental data to the Debye model.

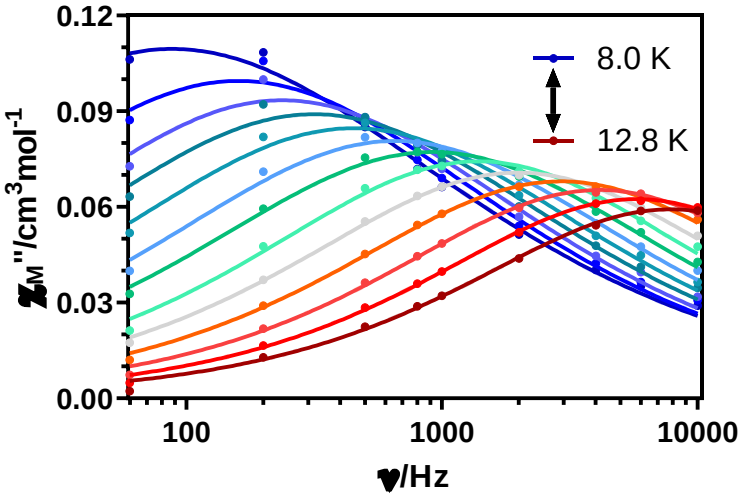

Figure A4.25.- Variable-temperature frequency dependence of the χ_M'' signal under 2.5 kOe applied field for **30$_Y$**. Solid lines represent the best fitting of the experimental data to the Debye model.

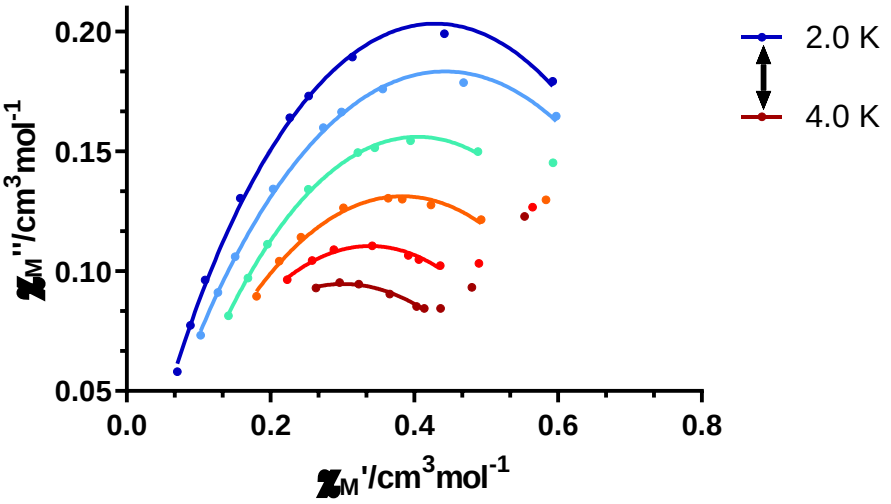

Figure A4.26.- Cole-Cole plots under 2.5 kOe field for **30$_Y$**. Solid lines represent the best fit to the generalized Debye model.

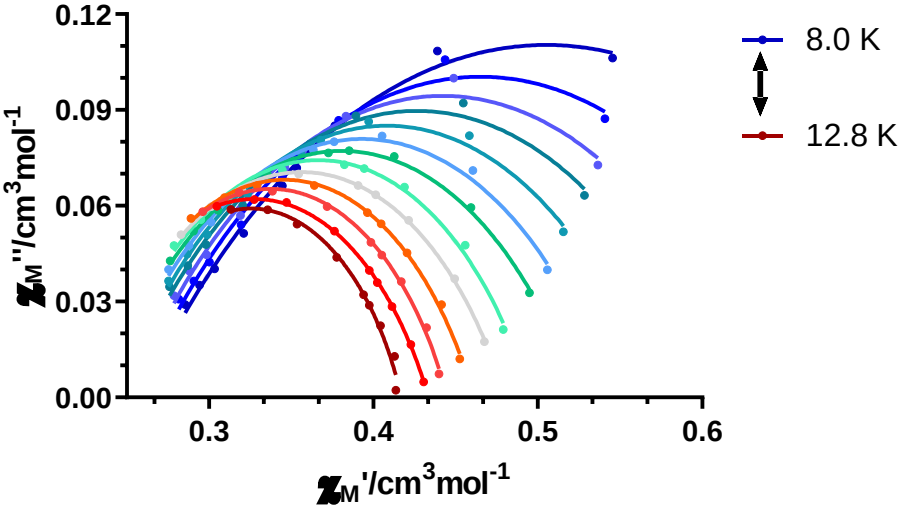

Figure A4.27.- Cole-Cole plots under 2.5 kOe field for **30$_Y$**. Solid lines represent the best fit to the generalized Debye model.

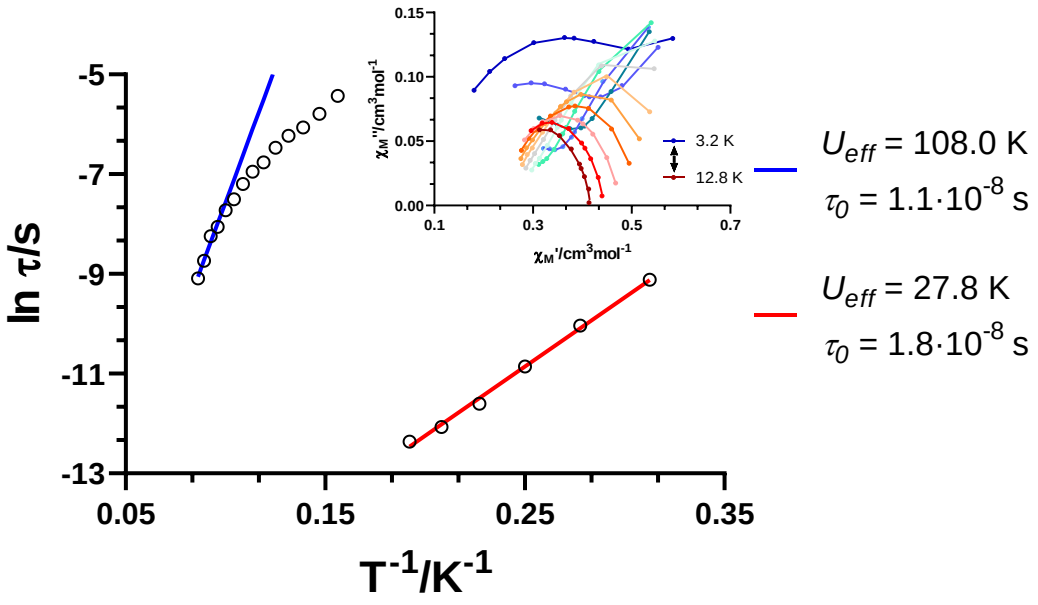

Figure A4.28.- Arrhenius plot for the relaxation times with Orbach fittings for FR and SR. Inset: Cole-Cole plots under 2.5 kOe field for **30**$_{Y}$. Solid lines represent the best fit using a sum of two modified Debye functions.

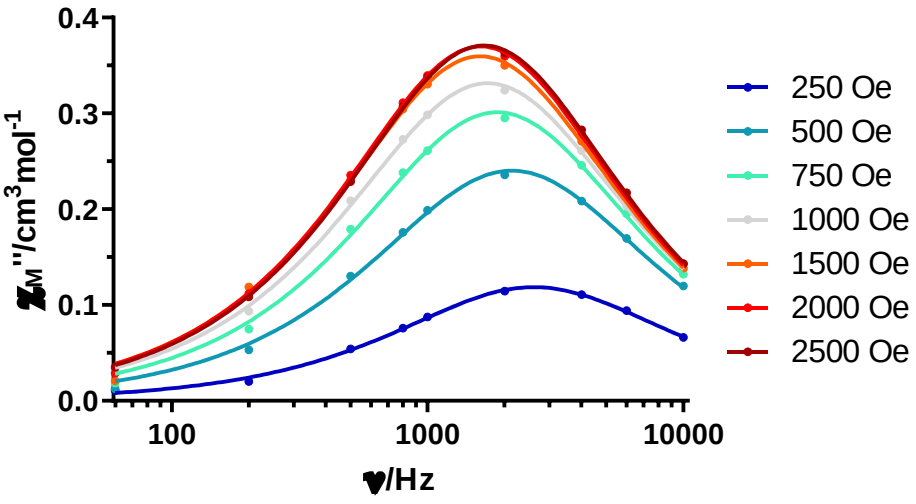

Figure A4.29.- Field dependence of the out-of-phase signal *vs* frequency at 4.0 K for **31**.

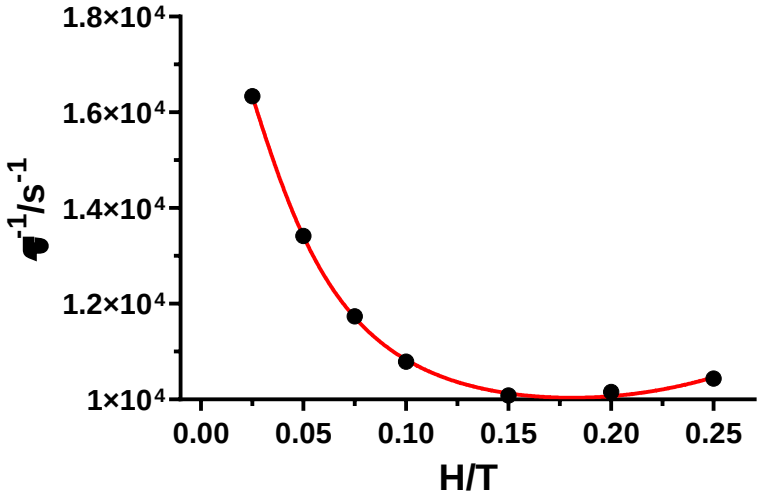

Figure A4.30.- The inverse of the relaxation times obtained at different magnetic fields at 4.0 K for **31**. The red line represents the best fit to Equation 4.2 in the main text.

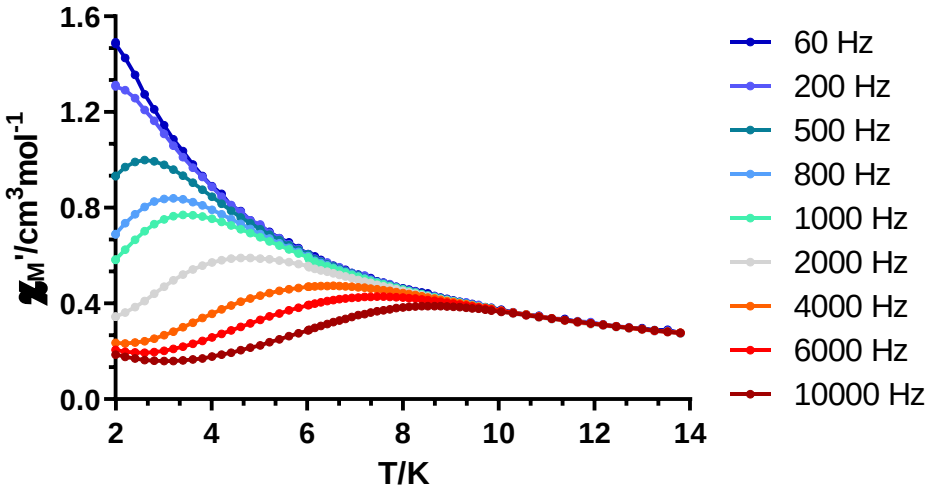

Figure A4.31.- Temperature dependence of the in phase components of the *ac* susceptibility in a *dc* applied field of 1.5 kOe for **31**.

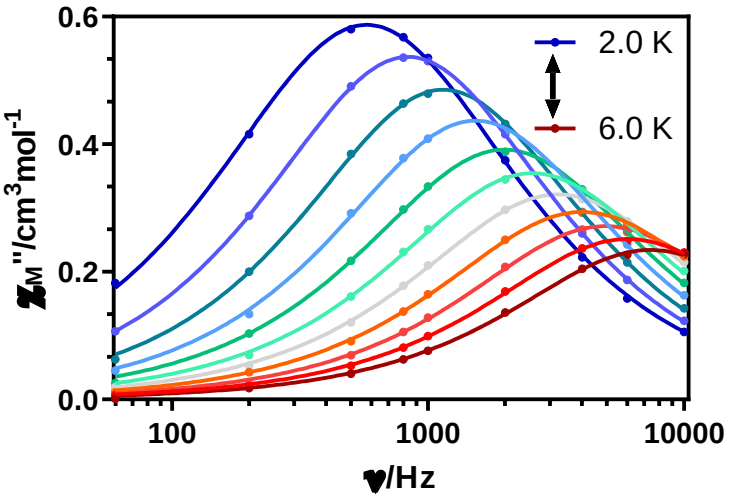

Figure A4.32.- Variable-temperature frequency dependence of the χ_M'' signal under 1.5 kOe applied field for **31**. Solid lines represent the best fitting of the experimental data to the Debye model.

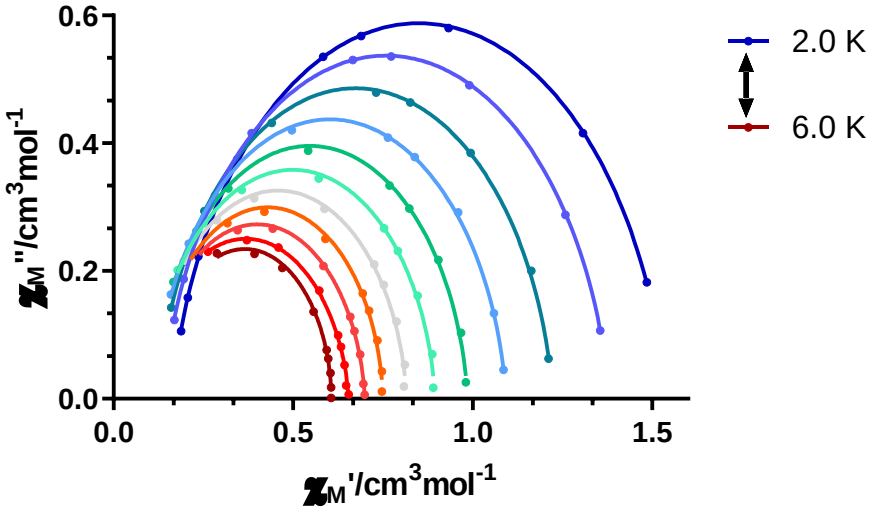

Figure A4.33.- Cole-Cole plots under 1.5 kOe field for **31**. Solid lines represent the best fit to the generalized Debye model.

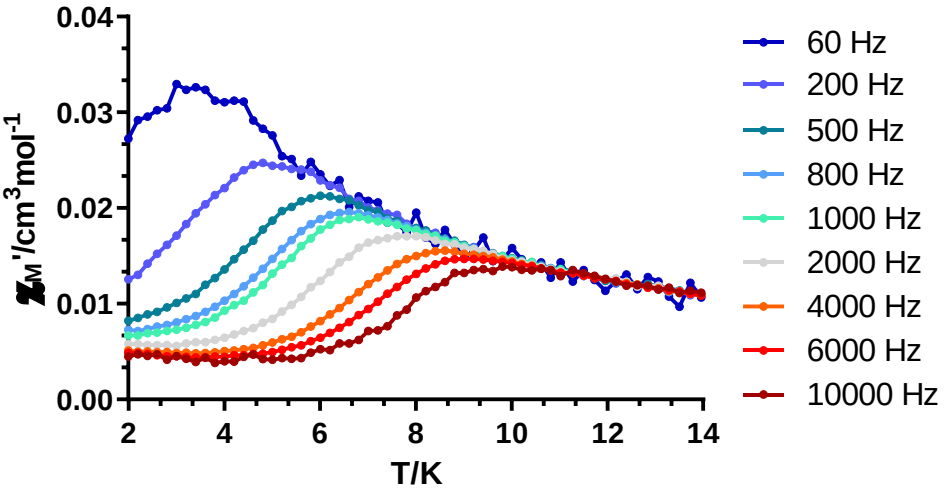

Figure A4.34.- Temperature dependence of the in phase components of the *ac* susceptibility in a *dc* applied field of 1.5 kOe for **31**$_Y$.

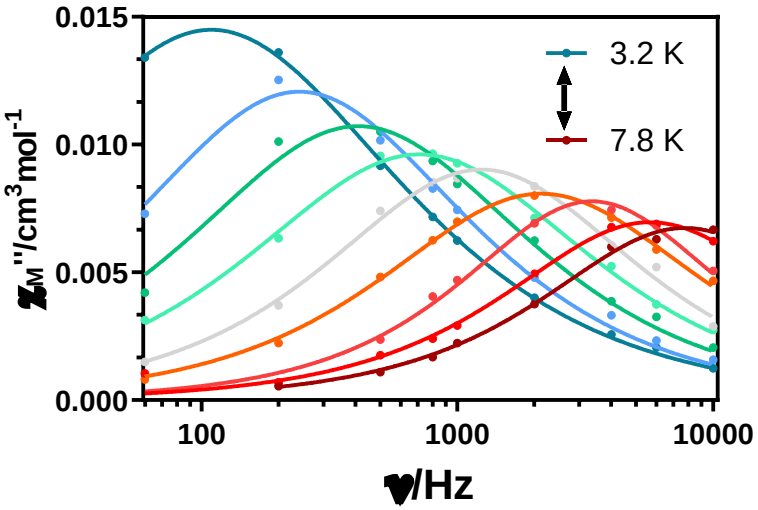

Figure A4.35.- Variable-temperature frequency dependence of the χ_M'' signal under 1.5 kOe applied field for **31**$_Y$. Solid lines represent the best fitting of the experimental data to the Debye model.

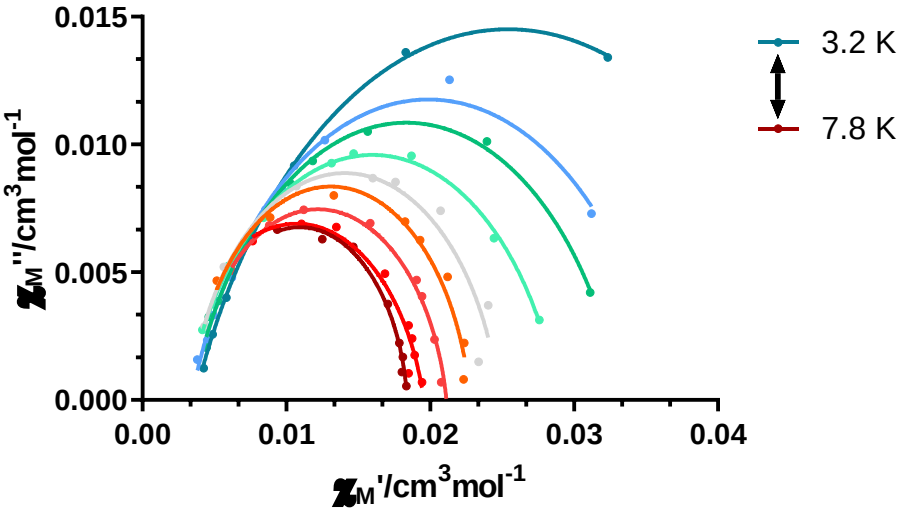

Figure A4.36.- Cole-Cole plots under 1.5 kOe field for **31**$_Y$. Solid lines represent the best fit to the generalized Debye model.

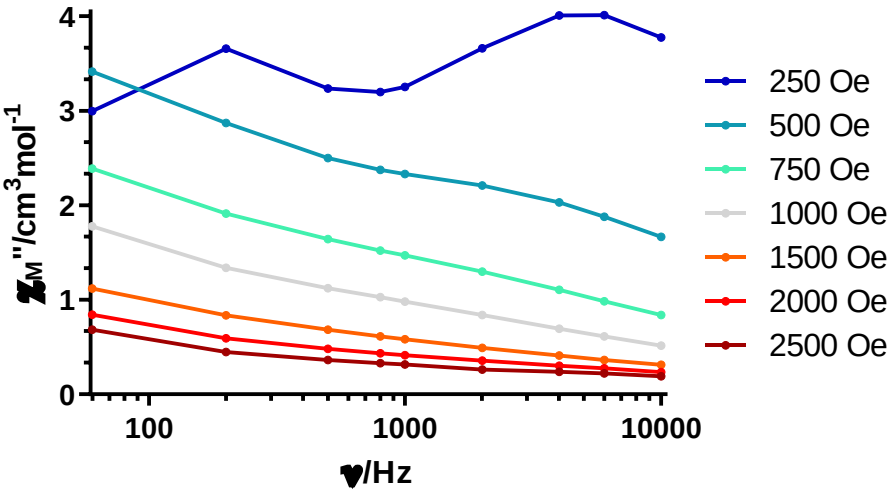

Figure A4.37.- Field dependence of the out-of-phase signal *vs* frequency at 2.0 K for **33**.

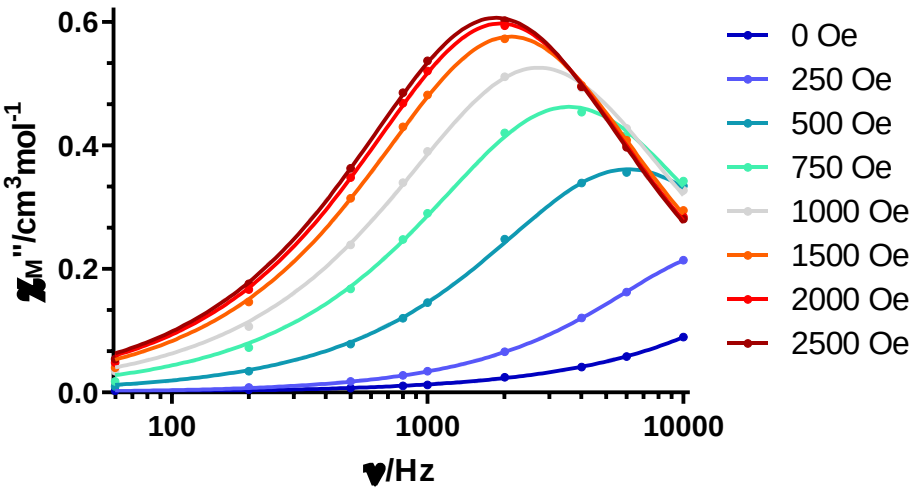

Figure A4.38.- Field dependence of the out-of-phase signal *vs* frequency at 22.6 K for **33**.

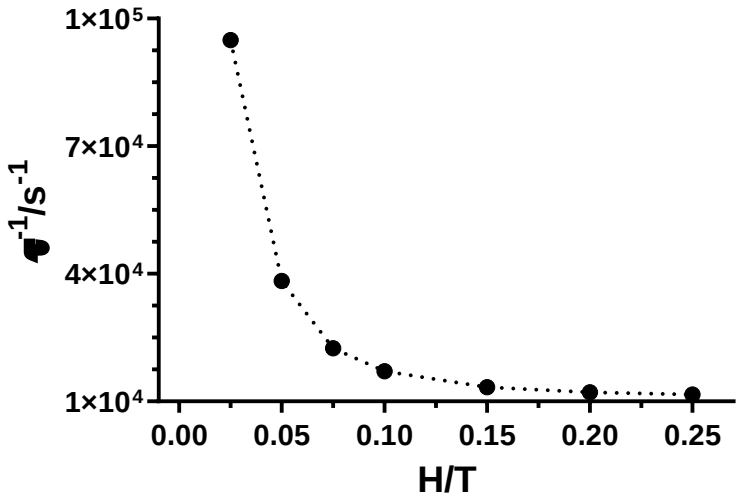

Figure A4.39.- The inverse of the relaxation times obtained at different magnetic fields at 22.6 K for **33**.

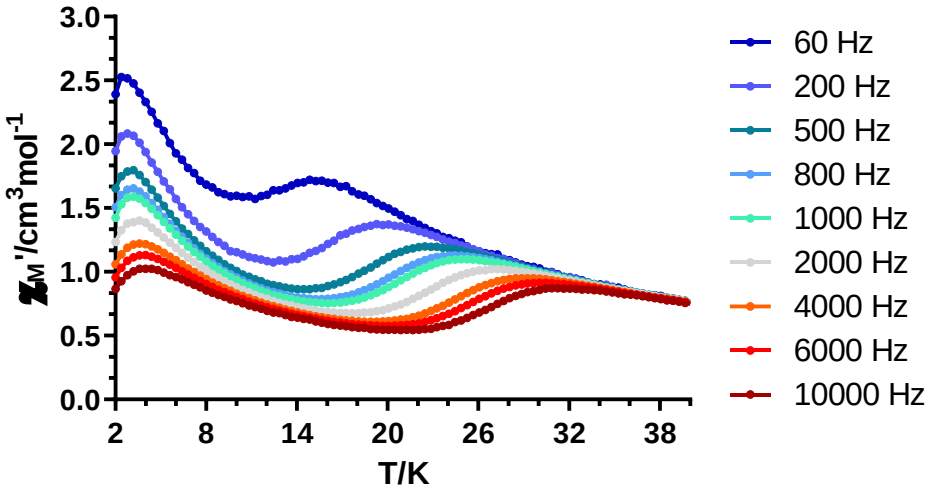

Figure A4.40.- Temperature dependence of the in phase components of the *ac* susceptibility in a *dc* applied field of 2.5 kOe for **33**.

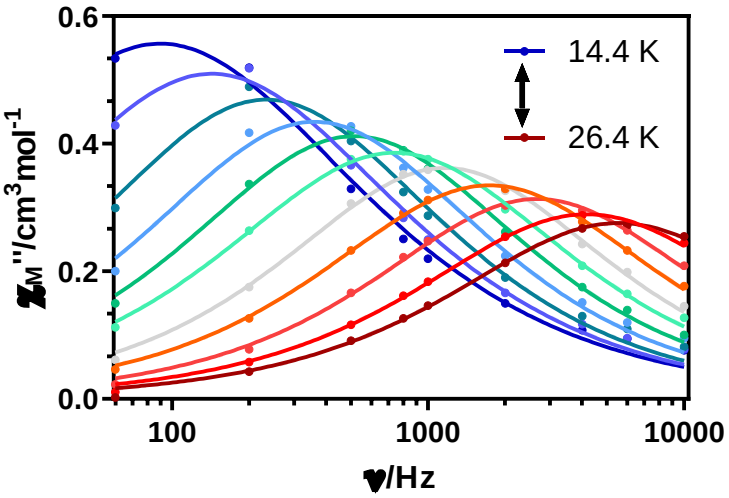

Figure A4.41.- Variable-temperature frequency dependence of the χ_M'' signal under 2.5 kOe applied field for **33**. Solid lines represent the best fitting of the experimental data to the Debye model.

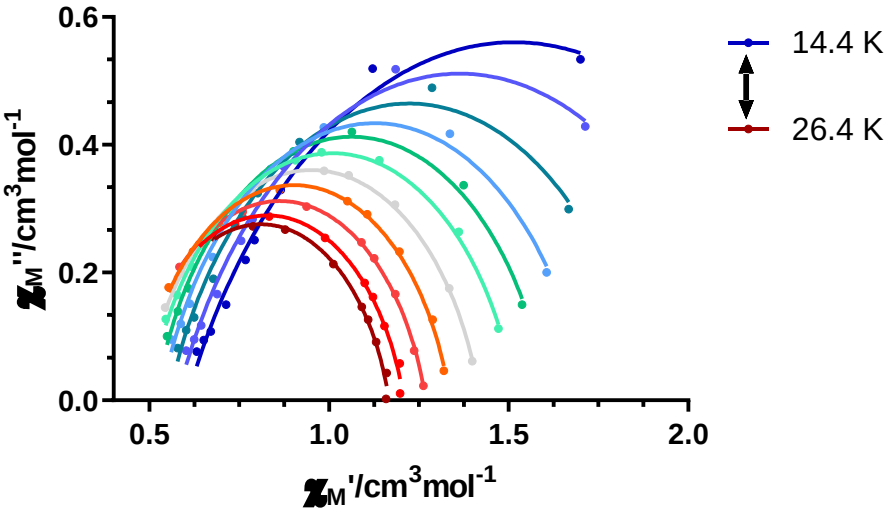

Figure A4.42.- Cole-Cole plots under 2.5 kOe field for **33**. Solid lines represent the best fit to the generalized Debye model.

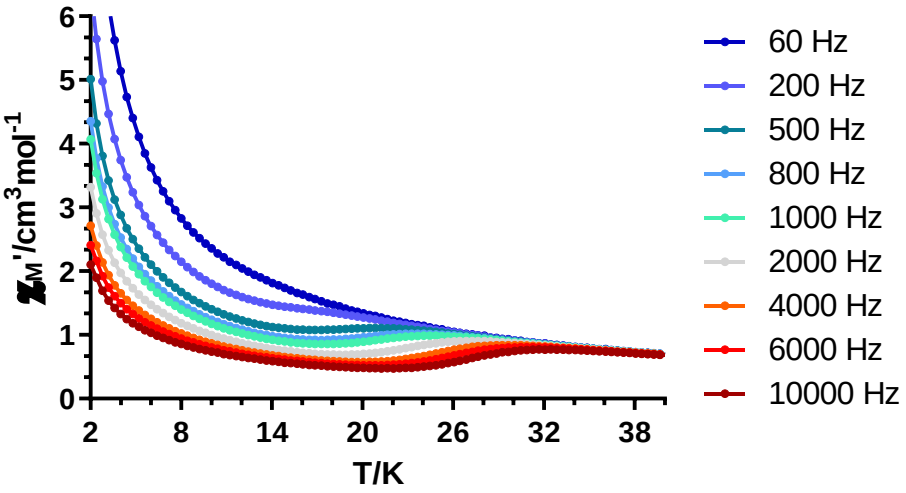

Figure A4.43.- Temperature dependence of the in phase components of the *ac* susceptibility in a zero applied field for **33$_{Zn}$**.

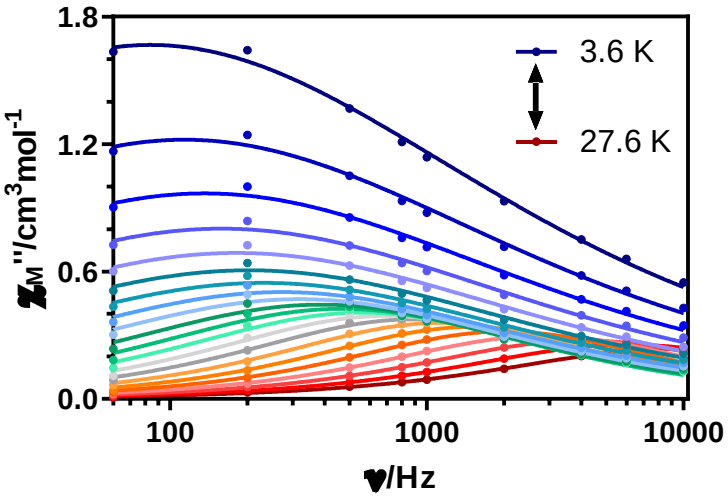

Figure A4.44.- Variable-temperature frequency dependence of the χ_M'' signal under zero applied field for **33**$_{Zn}$. Solid lines represent the best fitting of the experimental data to the Debye model.

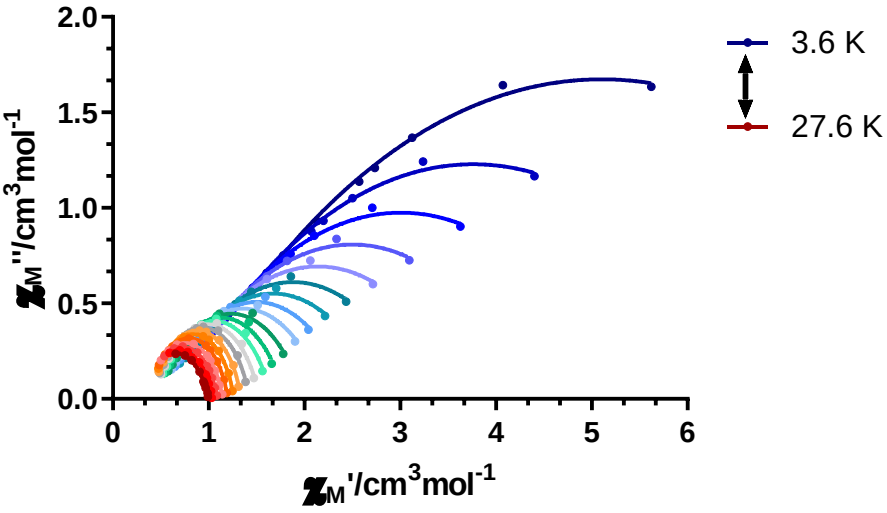

Figure A4.45.- Cole-Cole plots under zero field for **33**$_{Zn}$. Solid lines represent the best fit to the generalized Debye model.

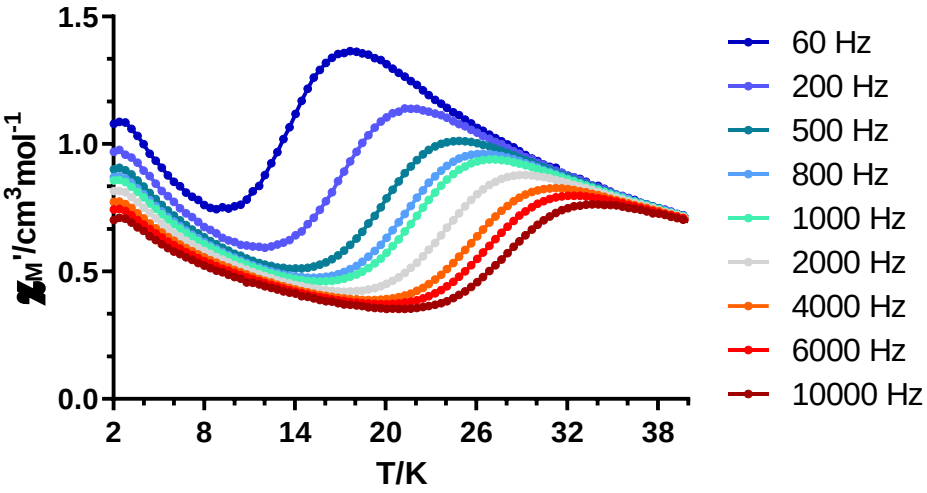

Figure A4.46.- Temperature dependence of the in phase components of the *ac* susceptibility in a *dc* applied field of 2.5 kOe for **33**$_{Zn}$.

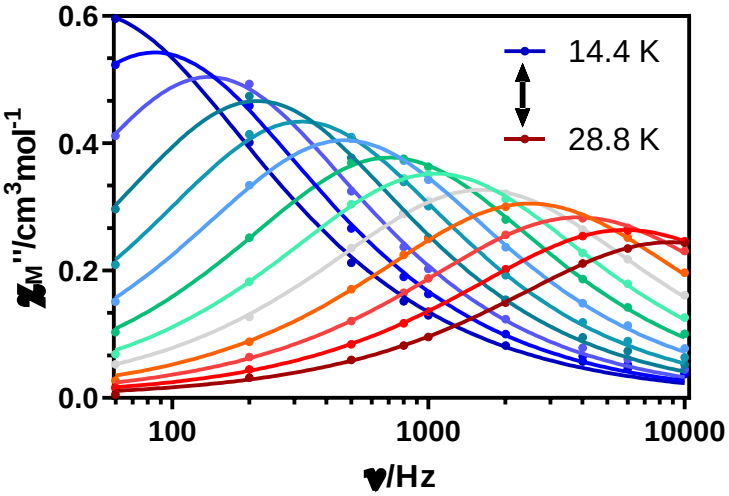

Figure A4.47.- Variable-temperature frequency dependence of the χ_M'' signal under 2.5 kOe applied field for **33**$_{Zn}$. Solid lines represent the best fitting of the experimental data to the Debye model.

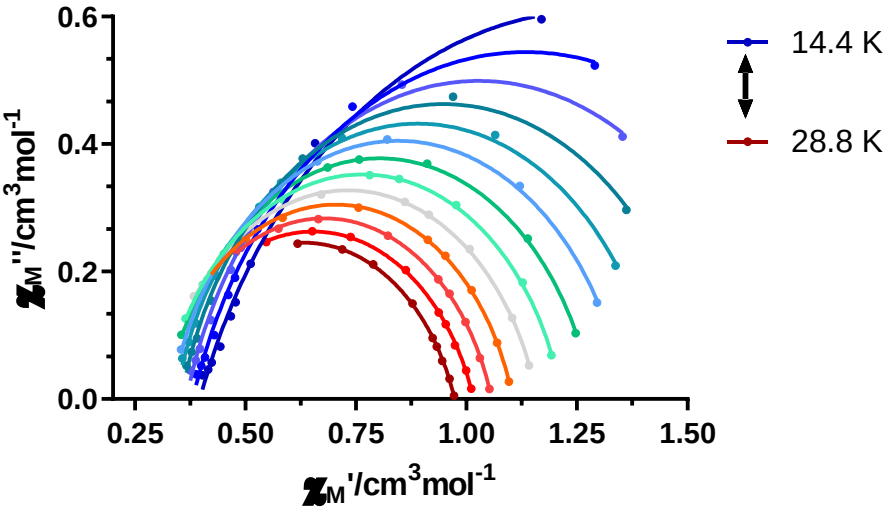

Figure A4.48.- Cole-Cole plots under 2.5 kOe field for **33$_{Zn}$**. Solid lines represent the best fit to the generalized Debye model.

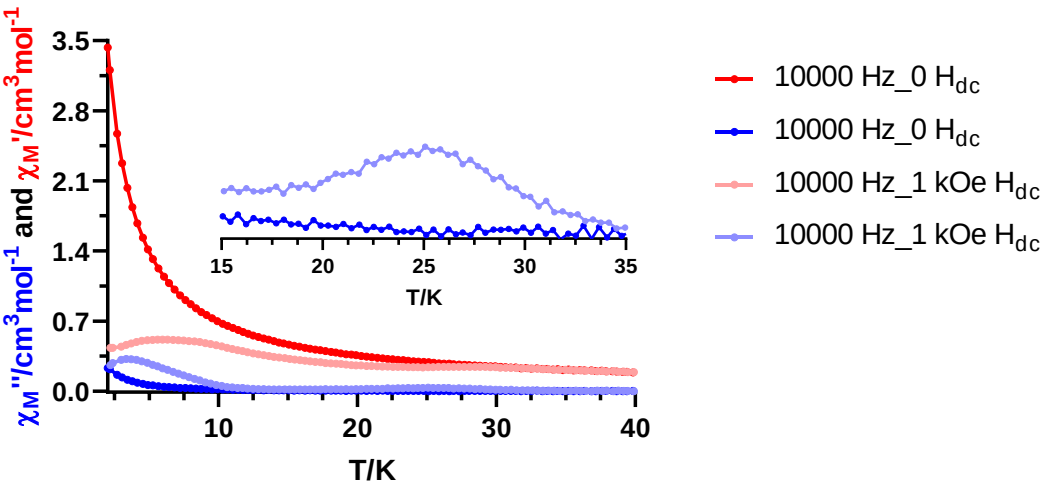

Figure A4.49.- Temperature dependence of in-phase (red) and out-of-phase (blue) components of the *ac* susceptibility in a zero (dark) and 1 kOe (light) applied *dc* field for **33$_{Y}$**.

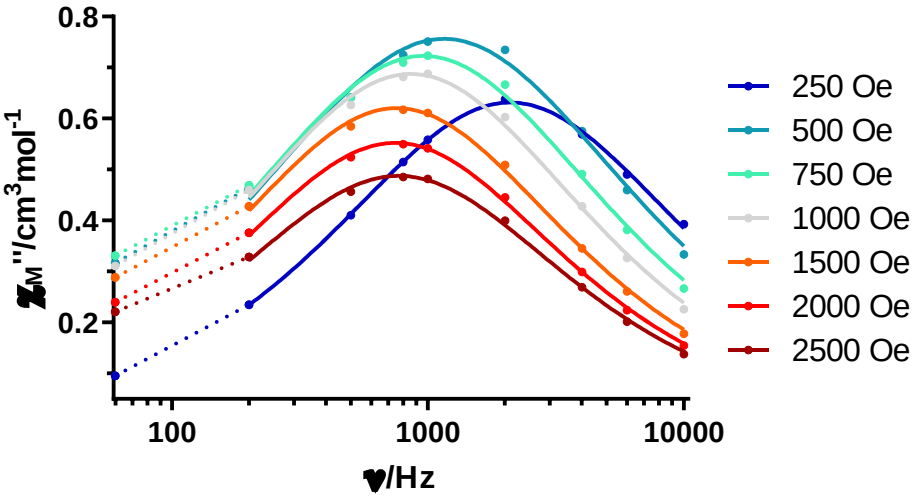

Figure A4.50.- Field dependence of the out-of-phase signal *vs* frequency at 2.0 K for **33$_Y$**. Dashed lines are a guide to the eye.

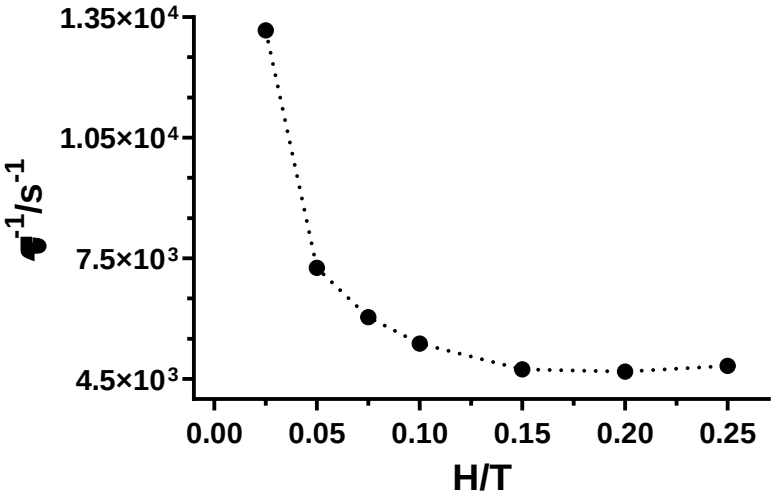

Figure A4.51.- The inverse of the relaxation times obtained at different magnetic fields at 2.0 K for **33$_Y$**.

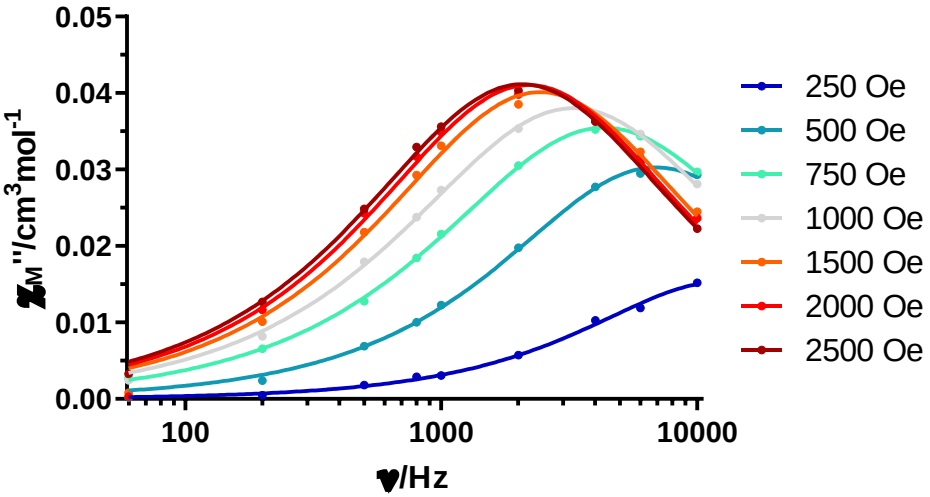

Figure A4.52.- Field dependence of the out-of-phase signal *vs* frequency at 22.6 K for **33$_Y$**.

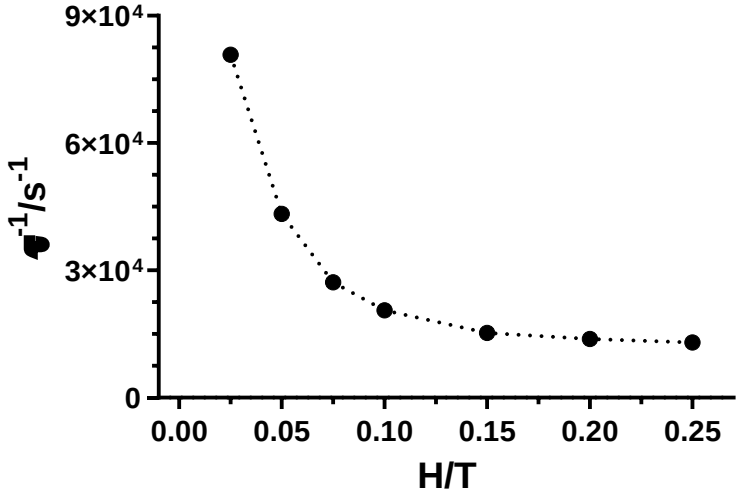

Figure A4.53.- The inverse of the relaxation times obtained at different magnetic fields at 22.6 K for **33$_Y$**.

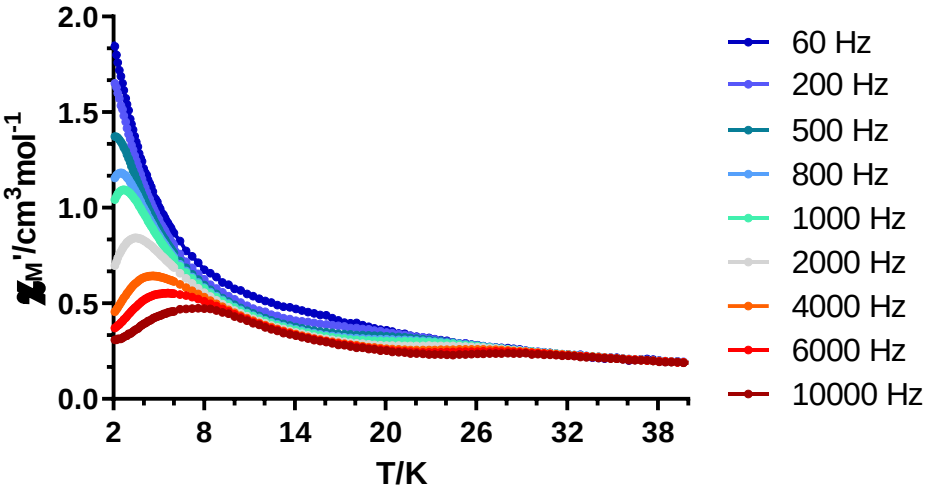

Figure A4.54.- Temperature dependence of the in phase components of the *ac* susceptibility in a *dc* applied field of 1.5 kOe for **33**$_Y$.

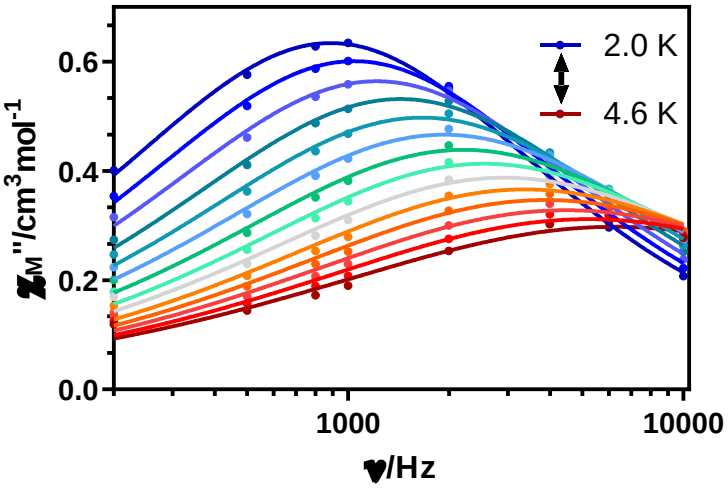

Figure A4.55.- Variable-temperature frequency dependence of the χ_M'' signal under 1.5 kOe applied field for **33**$_Y$. Solid lines represent the best fitting of the experimental data to the Debye model.

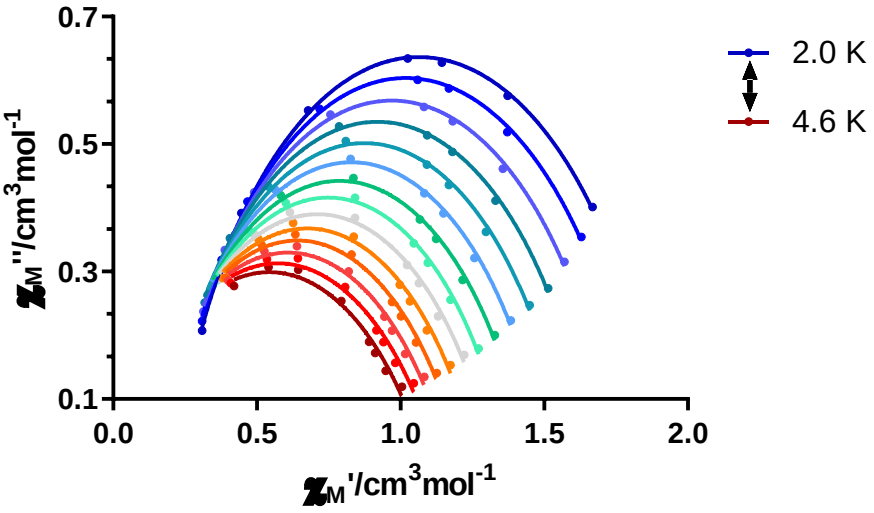

Figure A4.56.- Cole-Cole plots under 1.5 kOe field for **33**$_Y$. Solid lines represent the best fit to the generalized Debye model.

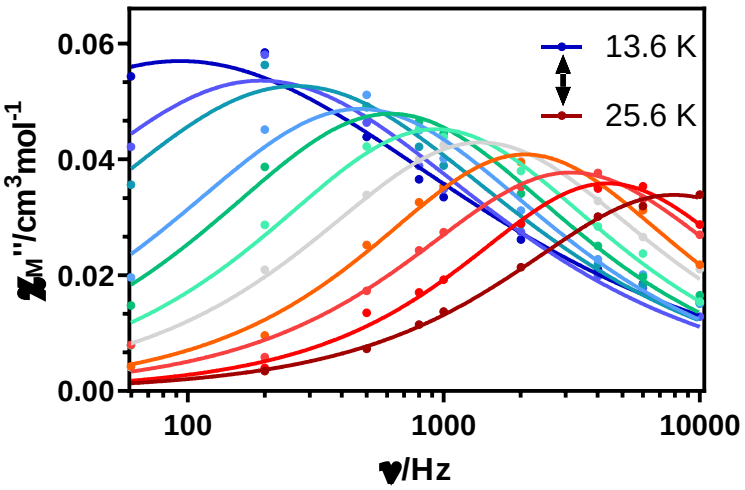

Figure A4.57.- Variable-temperature frequency dependence of the χ_M'' signal under 1.5 kOe applied field for **33**$_Y$. Solid lines represent the best fitting of the experimental data to the Debye model.

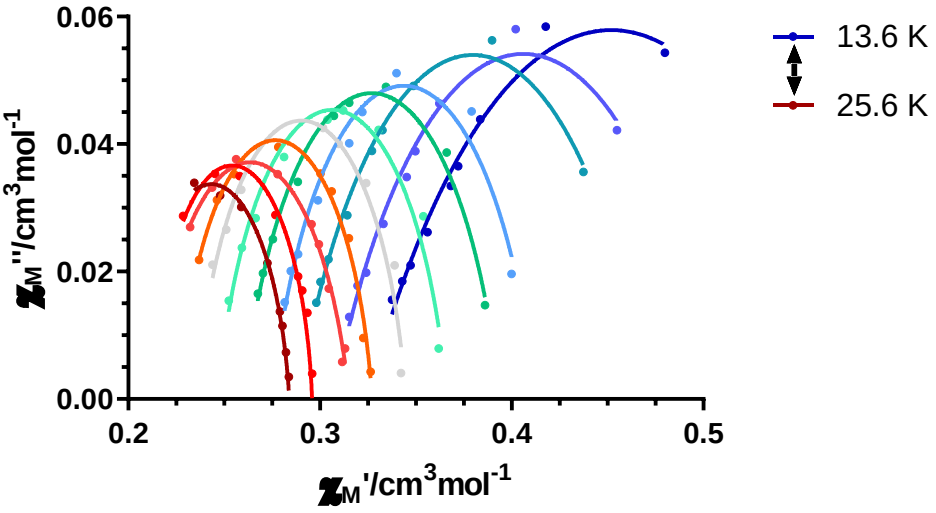

Figure A4.58.- Cole-Cole plots under 1.5 kOe field for **33**$_Y$. Solid lines represent the best fit to the generalized Debye model.

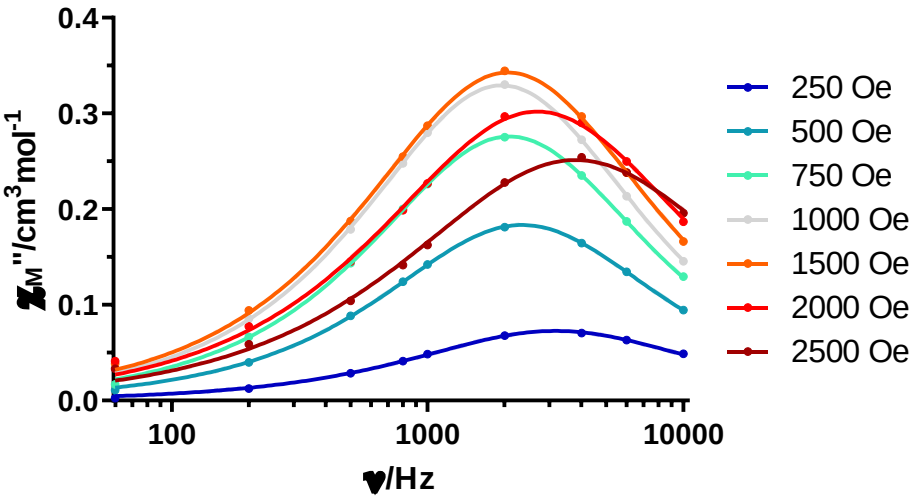

Figure A4.59.- Field dependence of the out-of-phase signal *vs* frequency at 2.0 K for **35**$_Y$.

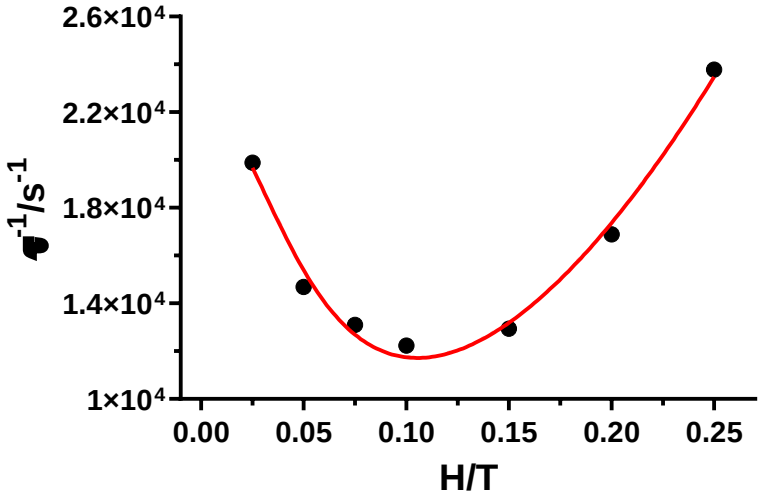

Figure A4.60.- The inverse of the relaxation times obtained at different magnetic fields at 2.0 K for **35**$_{Y}$. The red line represents the best fit to Equation 4.6 in the main text.

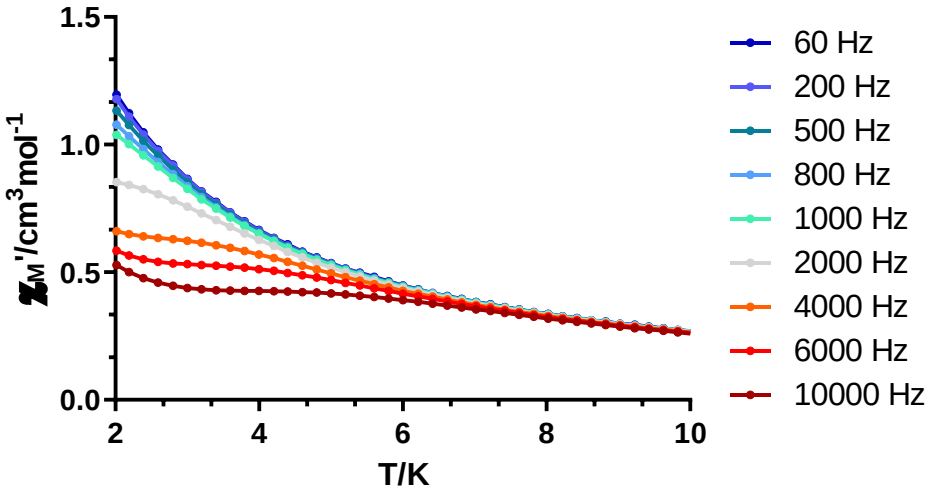

Figure A4.61.- Temperature dependence of the in phase components of the *ac* susceptibility in a *dc* applied field of 1 kOe for **35**$_{Y}$.

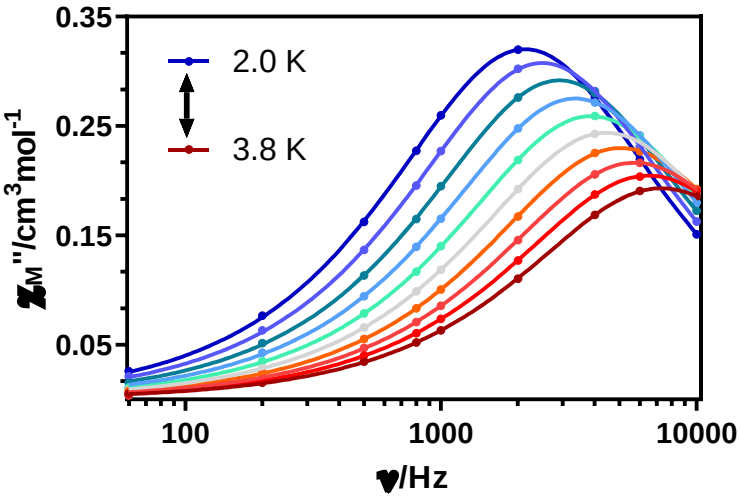

Figure A4.62.- Variable-temperature frequency dependence of the χ_M'' signal under 1 kOe applied field for **35$_Y$**. Solid lines represent the best fitting of the experimental data to the Debye model.

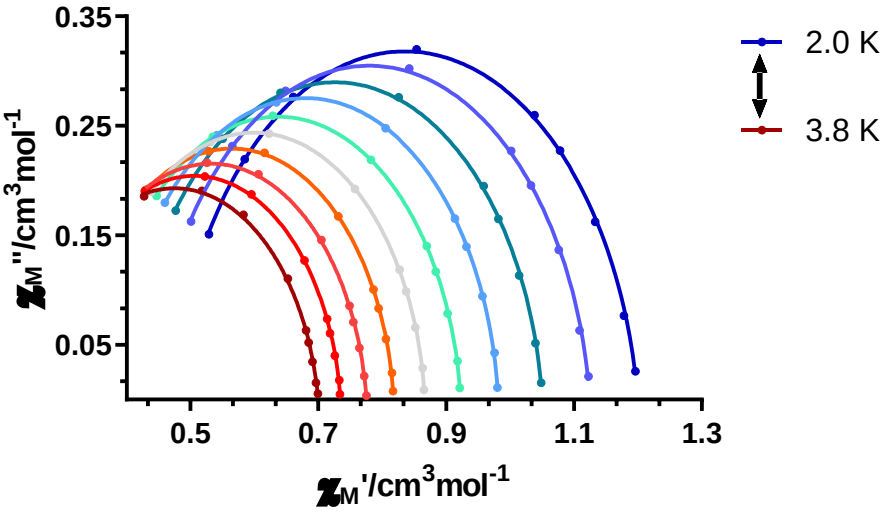

Figure A4.63.- Cole-Cole plots under 1 kOe field for **35$_Y$**. Solid lines represent the best fit to the generalized Debye model.

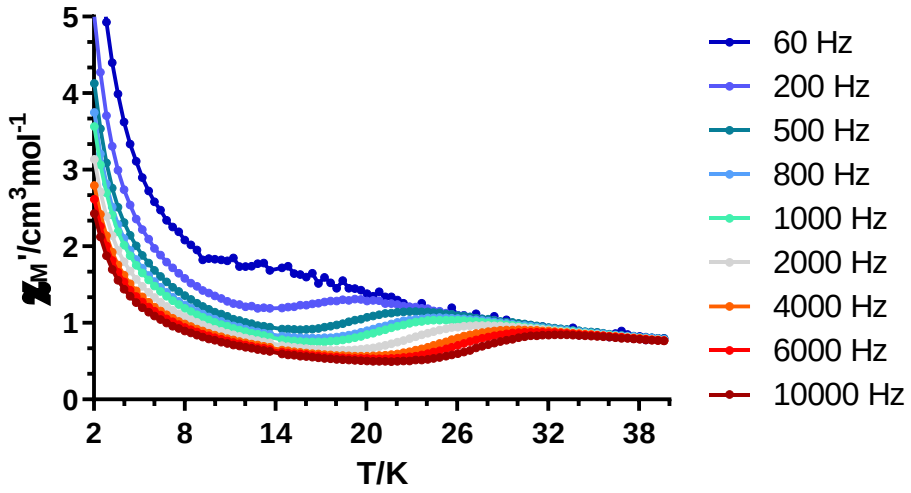

Figure A4.64.- Temperature dependence of the in phase components of the *ac* susceptibility in a zero applied field for **36**.

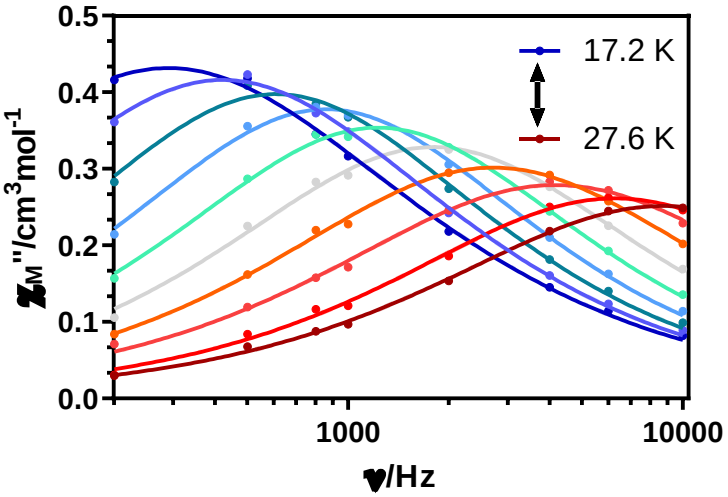

Figure A4.65.- Variable-temperature frequency dependence of the χ_M'' signal under zero applied field for **36**. Solid lines represent the best fitting of the experimental data to the Debye model.

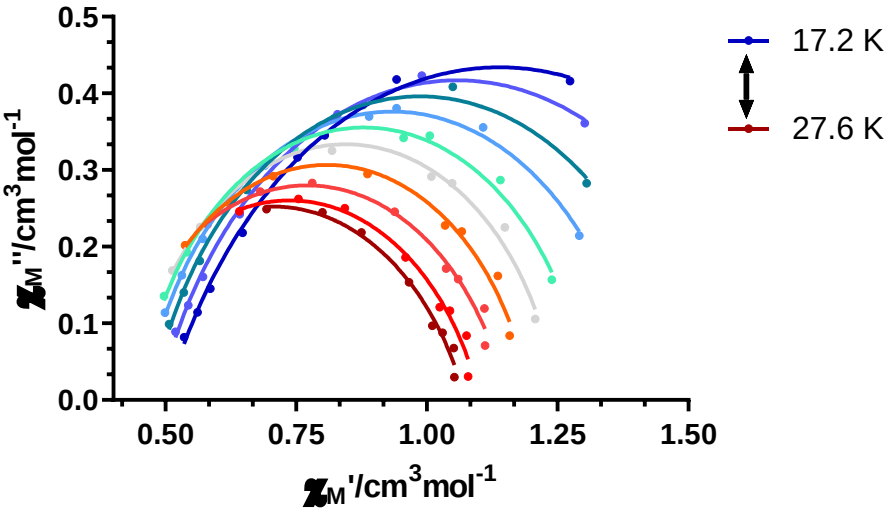

Figure A4.66.- Cole-Cole plots under zero field for **36**. Solid lines represent the best fit to the generalized Debye model.

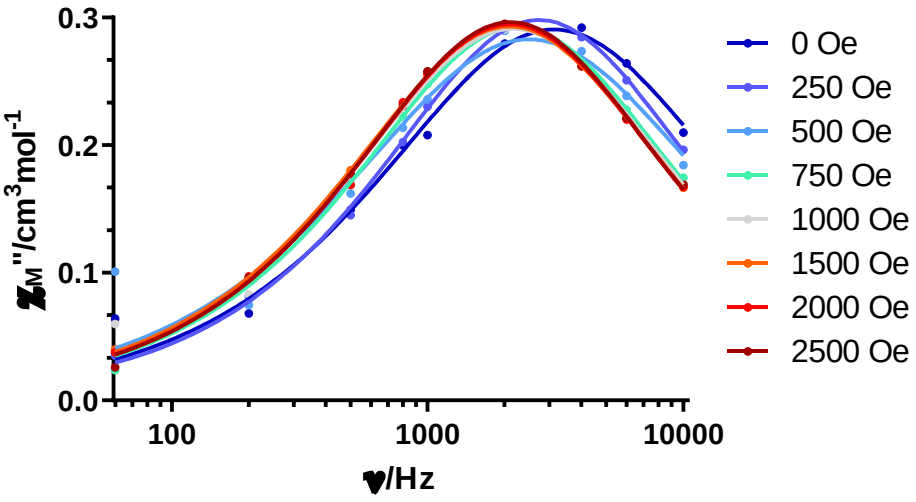

Figure A4.67.- Field dependence of the out-of-phase signal *vs* frequency at 24.8 K for **36**.

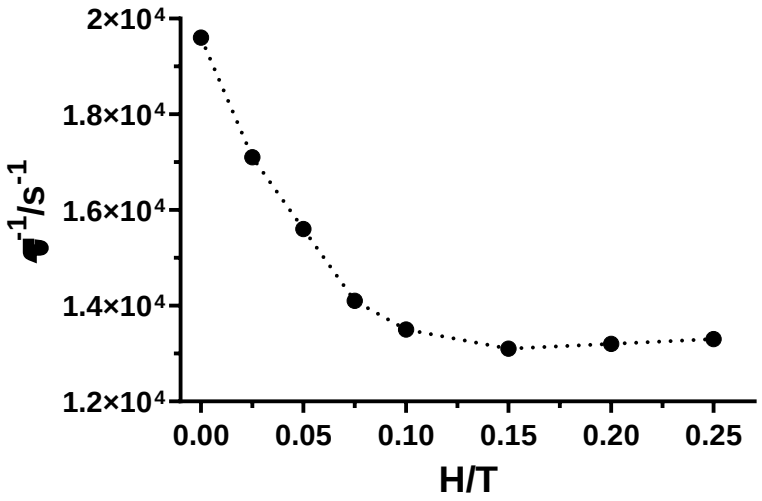

Figure A4.68.- The inverse of the relaxation times obtained at different magnetic fields at 24.8 K for **36**.

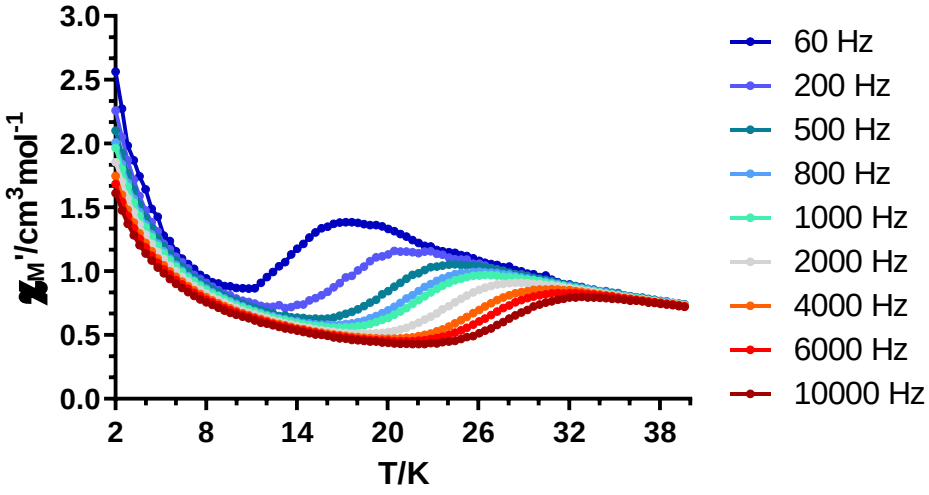

Figure A4.69.- Temperature dependence of the in phase components of the *ac* susceptibility in a *dc* applied field of 1 kOe for **36**.

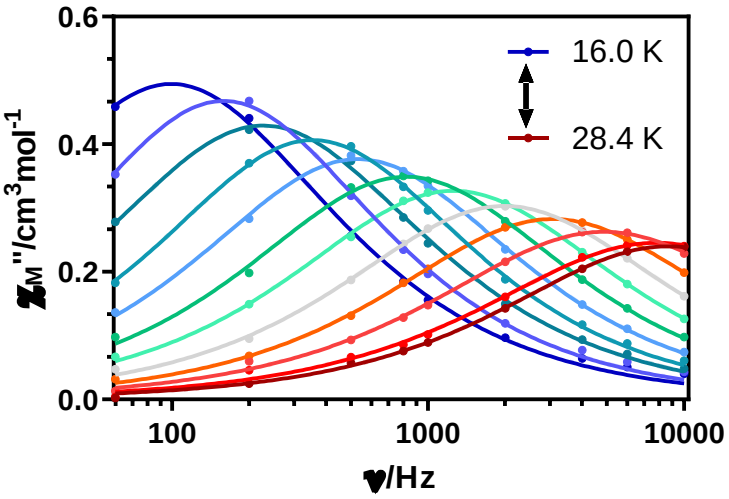

Figure A4.70.- Variable-temperature frequency dependence of the χ_M'' signal under 1 kOe applied field for **36**. Solid lines represent the best fitting of the experimental data to the Debye model.

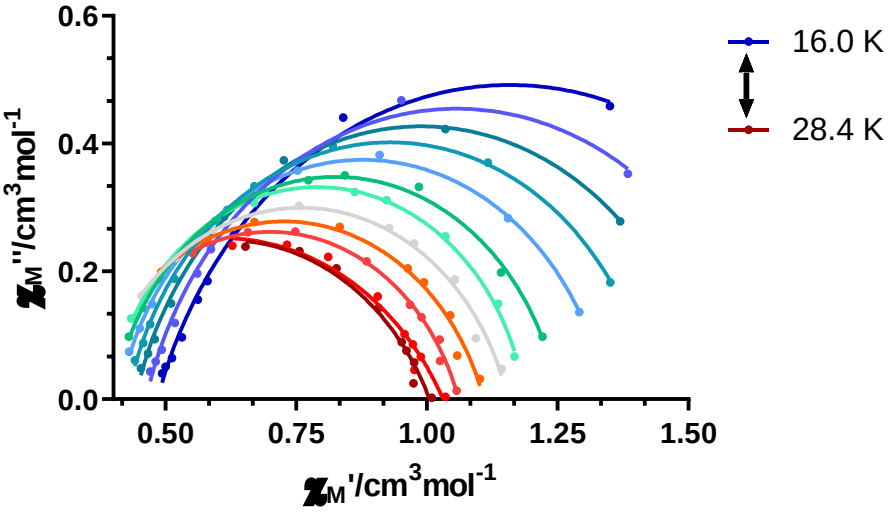

Figure A4.71.- Cole-Cole plots under 1 kOe field for **36**. Solid lines represent the best fit to the generalized Debye model.

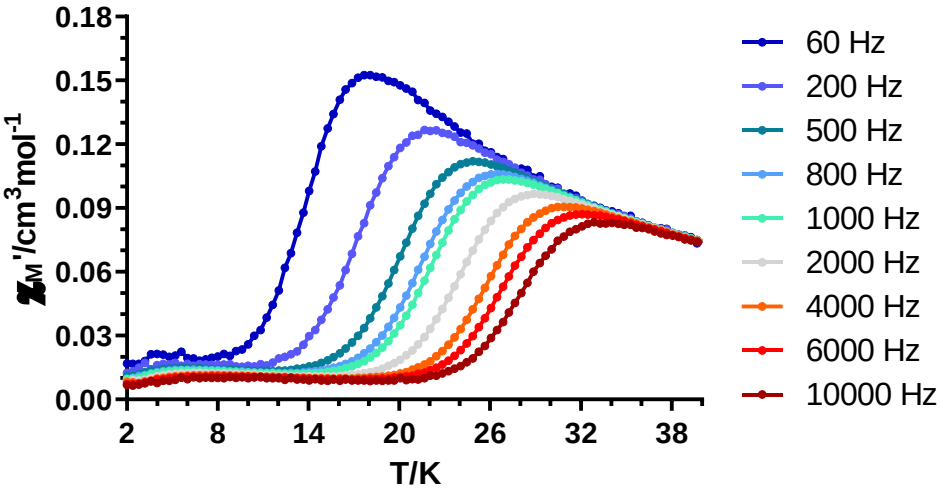

Figure A4.72.- Temperature dependence of the in phase components of the *ac* susceptibility in a *dc* applied field of 1 kOe for **36$_Y$**.

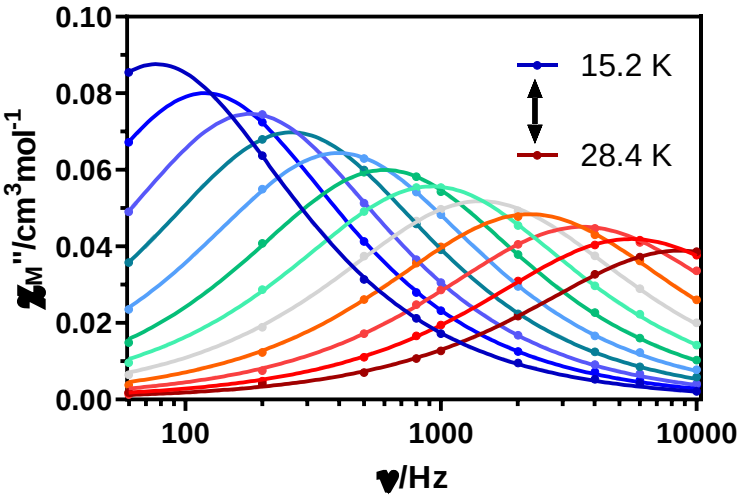

Figure A4.73.- Variable-temperature frequency dependence of the χ_M'' signal under 1 kOe applied field for **36$_Y$**. Solid lines represent the best fitting of the experimental data to the Debye model.

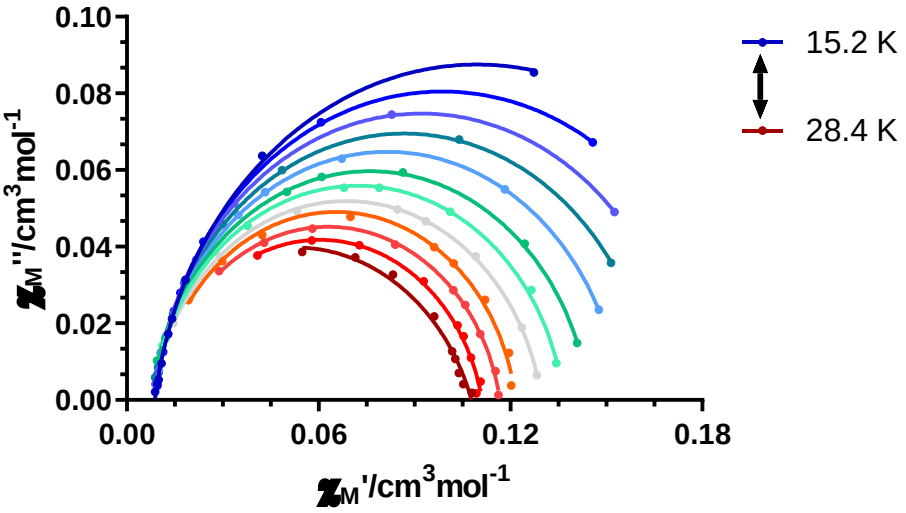

Figure A4.74.- Cole-Cole plots under 1 kOe field for **36$_Y$**. Solid lines represent the best fit to the generalized Debye model.

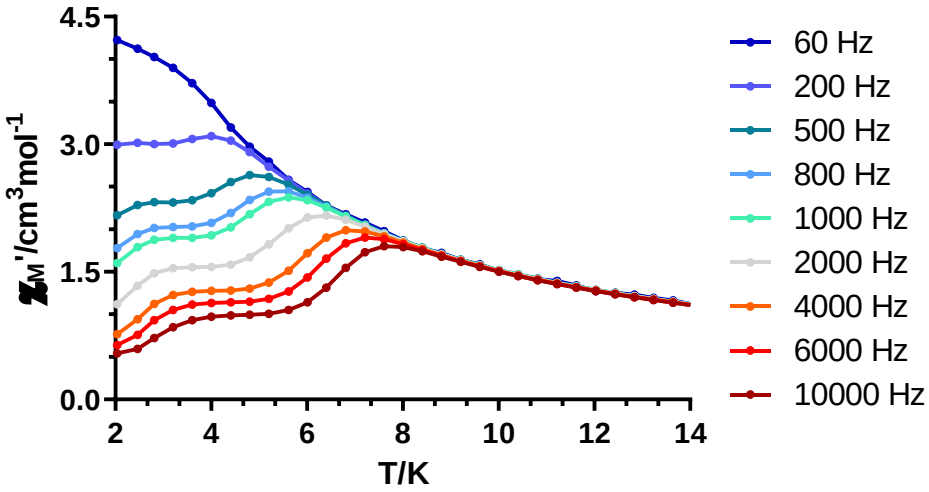

Figure A4.75.- Temperature dependence of the in phase components of the *ac* susceptibility in a *dc* applied field of 500 Oe for **37**.

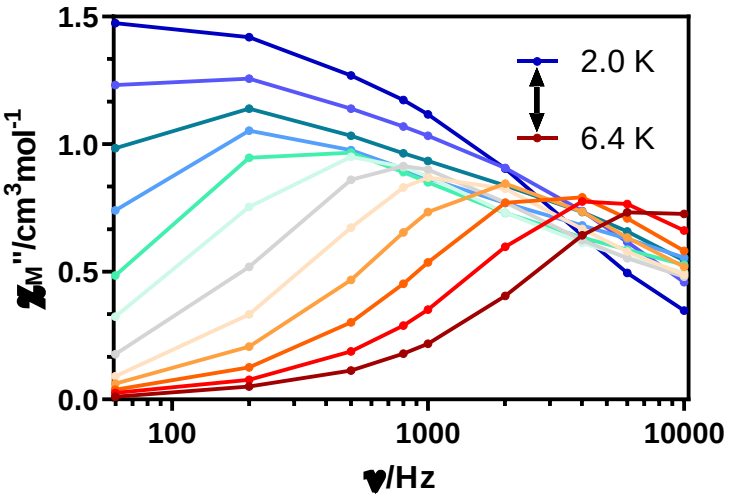

Figure A4.76.- Variable-temperature frequency dependence of the χ_M'' signal under 500 Oe applied field for **37**. Solid lines are a guide to the eye.

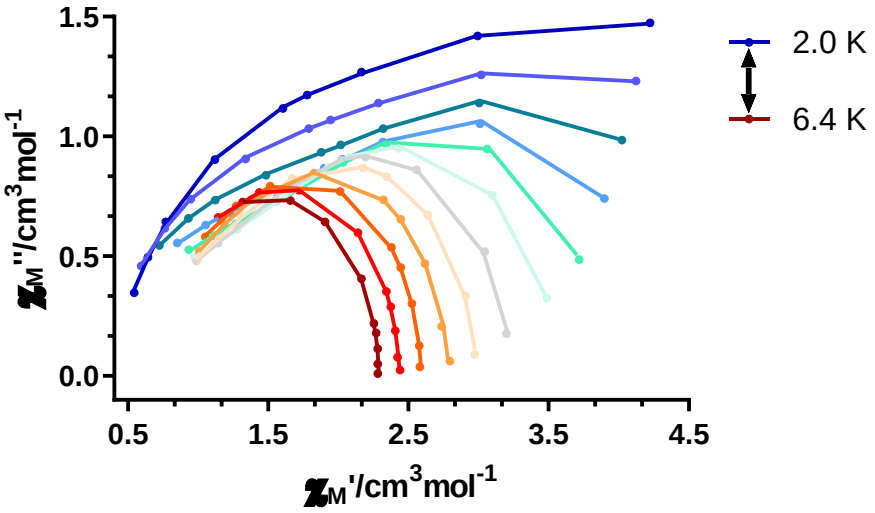

Figure A4.77.- Cole-Cole plots under 500 Oe field for **37**. Solid lines represent the best fit using a sum of two modified Debye functions.

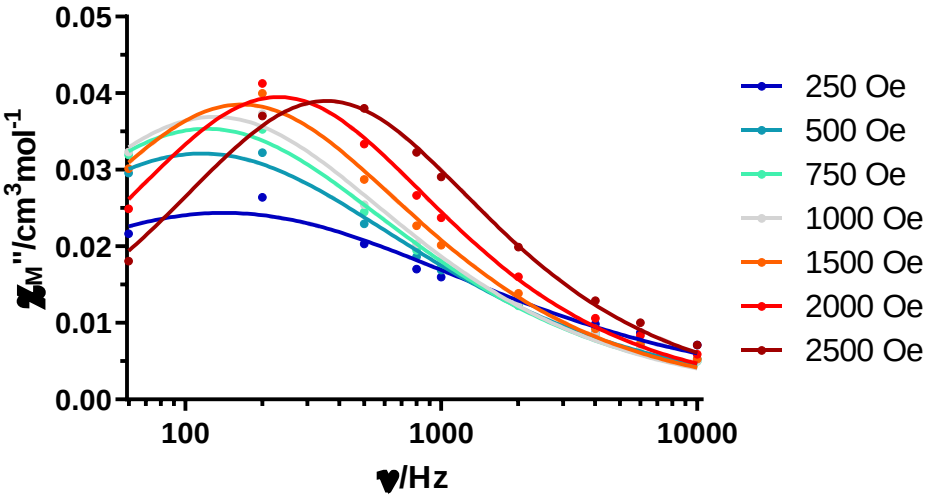

Figure A4.78.- Field dependence of the out-of-phase signal *vs* frequency at 3.6 K for **37**$_{Y}$.

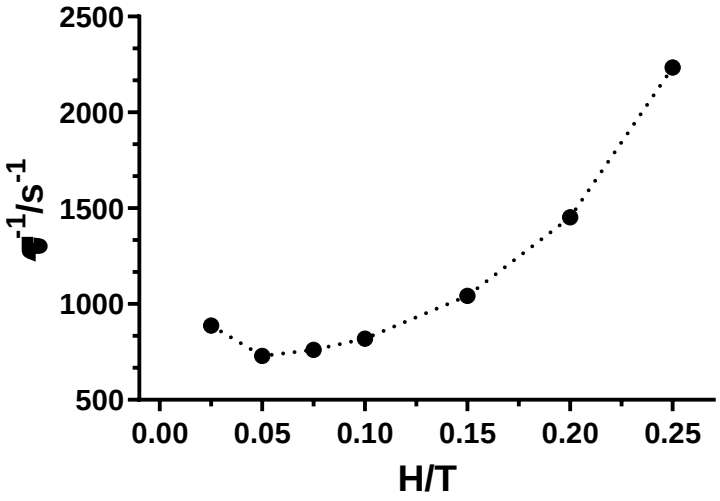

Figure A4.79.- The inverse of the relaxation times obtained at different magnetic fields at 3.6 K for **37**$_{Y}$.

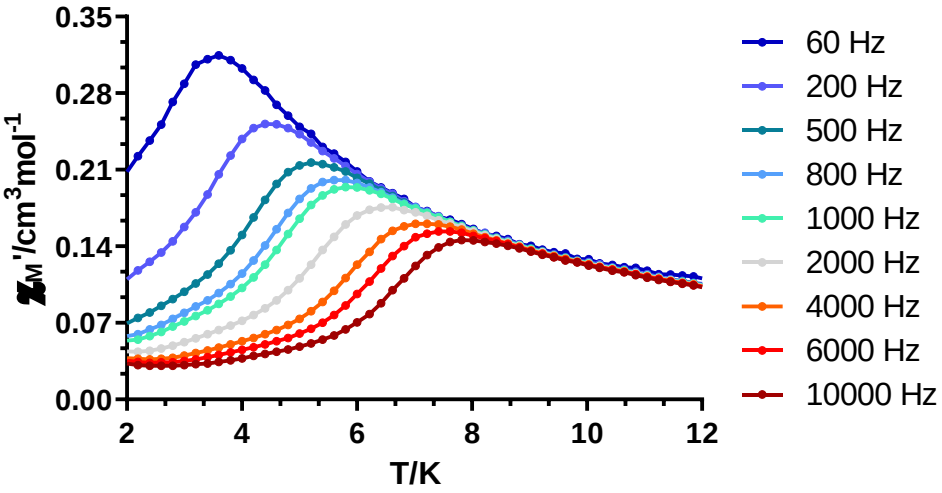

Figure A4.80.- Temperature dependence of the in phase components of the *ac* susceptibility in a *dc* applied field of 500 Oe for **37**$_Y$.

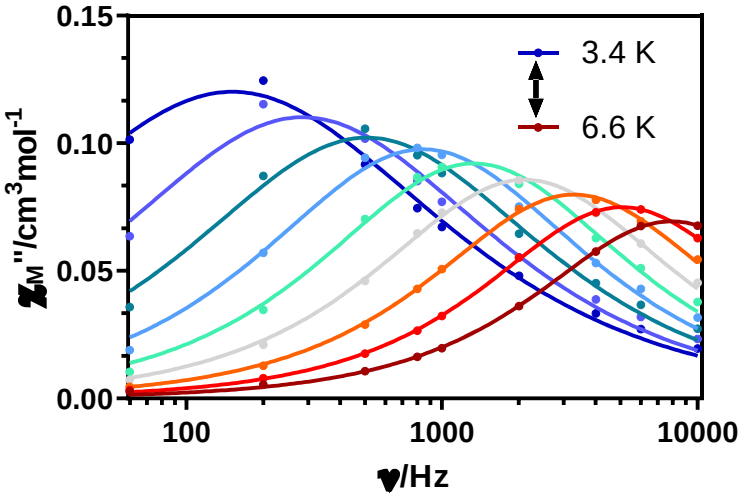

Figure A4.81.- Variable-temperature frequency dependence of the χ_M'' signal under 500 Oe applied field for **37**$_Y$. Solid lines represent the best fitting of the experimental data to the Debye model.

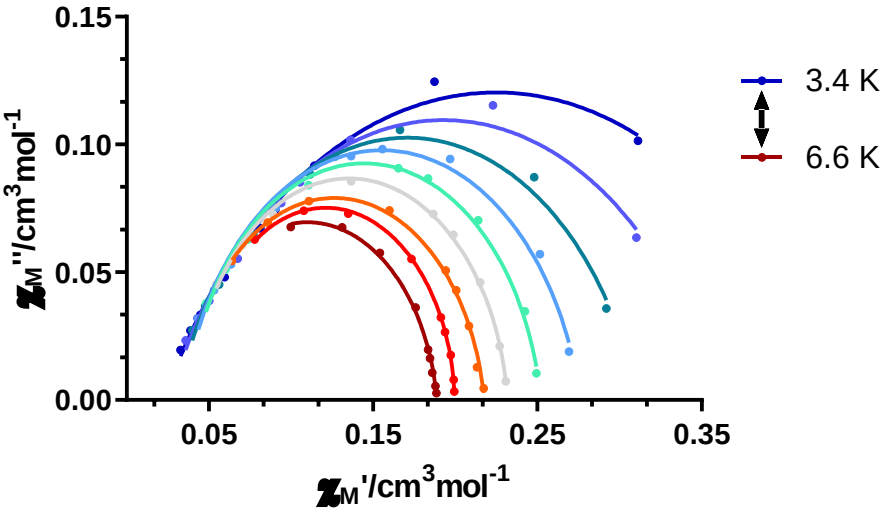

Figure A4.82.- Cole-Cole plots under 500 Oe field for **37$_Y$**. Solid lines represent the best fit to the generalized Debye model.

6. Magellan Figures.

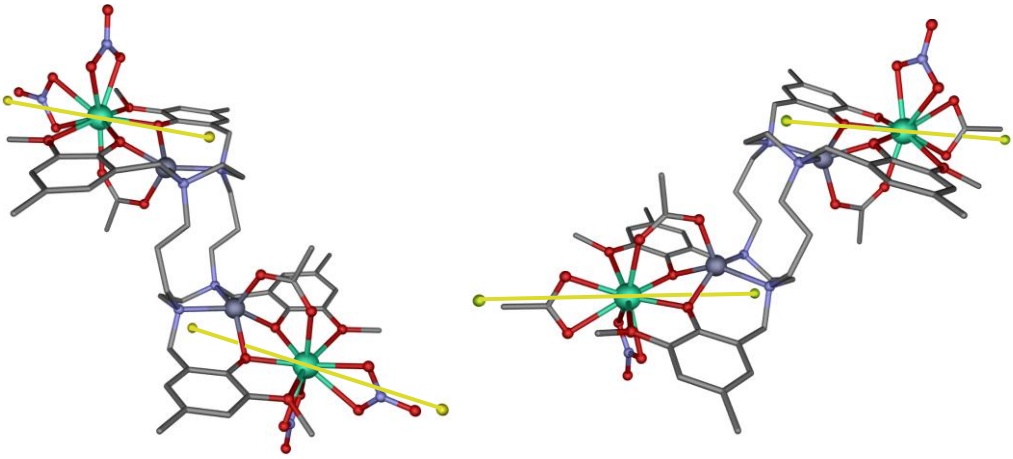

Figure A4.83.- Anisotropy axes calculated by Magellan software for **30**.

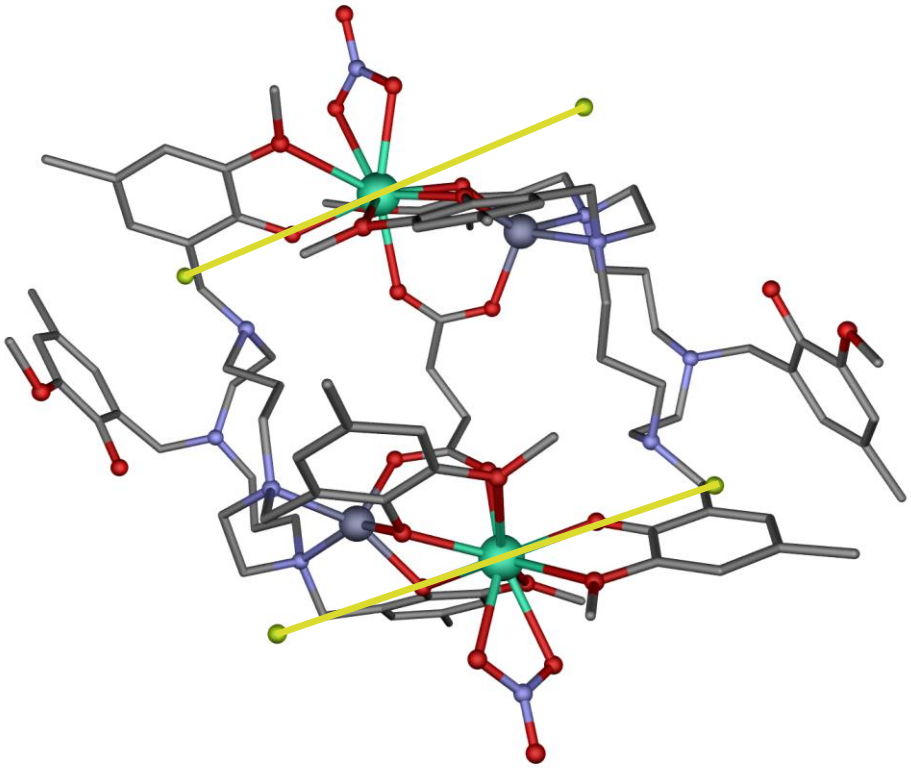

Figure A4.84.- Anisotropy axes calculated by Magellan software for **36**.

7. Pulse Magnetization Measurements.

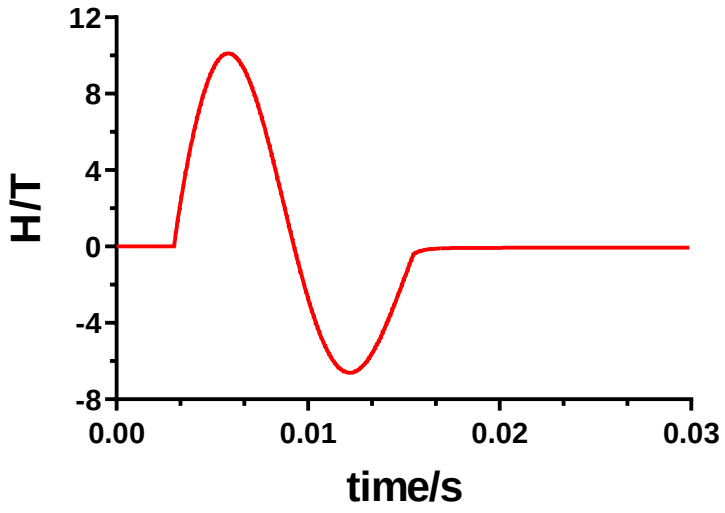

Figure A4.85.- Field-scan sequence as a function of time for a maximum field of 10.4 T.

8. ^{1}H Nuclear Magnetic Resonance.

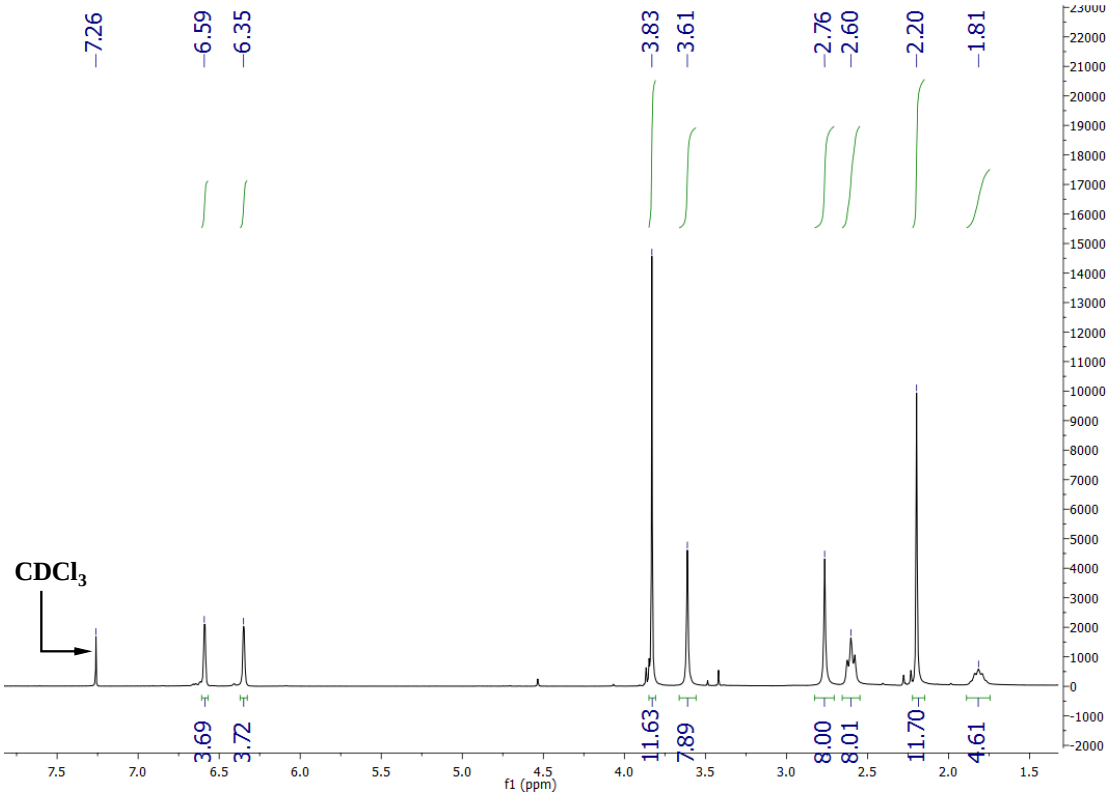

Figure A4.86.- ^{1}H NMR spectrum for H_4L^4 in $CDCl_3$.

APPENDICES

***Chapter 5**: R- and S-methylsuccinate induced enantiospecific formation of novel $Zn^{II}_2Ln^{III}_2$ based tetranuclear compounds: a study of the magnetic and photoluminescent properties*

Index:

1. Elemental Analyses and Crystallographic Tables.

Table A5.1.- Yields and elemental analyses for enantiomeric pairs of **38**, **39**, **40**, **41**, **42** and **43**, as well as **44-rac**.

Complex	Yield (%)	Formula	% C calc./found	% H calc./found	% N calc./found
38-R	75	$C_{100}H_{146}N_{12}O_{37}Zn_2Sm_2$	47.29/46.95	5.79/6.00	6.62/6.47
38-S	64	$C_{100}H_{146}N_{12}O_{37}Zn_2Sm_2$	47.29/47.02	5.79/5.91	6.62/6.72
39-R	59	$C_{100}H_{146}N_{12}O_{37}Zn_2Eu_2$	47.23/47.33	5.79/5.64	6.61/6.58
39-S	80	$C_{100}H_{146}N_{12}O_{37}Zn_2Eu_2$	47.23/47.21	5.79/6.06	6.61/6.48
40-R	63	$C_{100}H_{146}N_{12}O_{37}Zn_2Tb_2$	46.97/47.15	5.76/5.99	6.57/6.40
40-S	60	$C_{100}H_{146}N_{12}O_{37}Zn_2Tb_2$	46.97/47.00	5.76/5.70	6.57/6.41
41-R	66	$C_{100}H_{146}N_{12}O_{37}Zn_2Dy_2$	46.84/46.75	5.74/5.74	6.56/6.82
41-S	53	$C_{100}H_{146}N_{12}O_{37}Zn_2Dy_2$	46.84/46.83	5.74/5.63	6.56/6.79
42-R	67	$C_{100}H_{146}N_{12}O_{37}Zn_2Er_2$	46.67/46.66	5.72/5.81	6.53/6.49
42-S	71	$C_{100}H_{146}N_{12}O_{37}Zn_2Er_2$	46.67/46.59	5.72/5.80	6.53/6.68
43-R	49	$C_{100}H_{146}N_{12}O_{37}Zn_2Yb_2$	46.46/46.67	5.69/5.77	6.50/6.33
43-S	62	$C_{100}H_{146}N_{12}O_{37}Zn_2Yb_2$	46.46/46.42	5.69/5.31	6.50/6.84
44-rac	74	$C_{103}H_{158}N_{12}O_{40}Zn_2Dy_2$	46.50/46.20	5.99/6.03	6.32/6.55

Table A5.2.- Crystallographic data for compounds **41-R**, **41-S** and **44-rac**.

Structure	**41-R**	**41-S**	**Dy-rac**
Formula	$C_{100}H_{146}N_{12}O_{37}Zn_2Dy_2$	$C_{100}H_{146}N_{12}O_{37}Zn_2Dy_2$	$C_{103}H_{158}N_{12}O_{40}Zn_2Dy_2$
M_r	2564.05	2564.05	2660.17
Crystal system	*orthorhombic*	*orthorhombic*	*orthorhombic*
Space group (no.)	*P212121* (19)	*P212121* (19)	*Aba2* (41)
a (Å)	17.3591(2)	17.3393(8)	21.1391(2)
b (Å)	26.5713(5)	26.4047(12)	22.6084(3)
c (Å)	27.5656(4)	27.7370(10)	24.7912(5)
α (°)	90	90	90
β (°)	90	90	90
γ (°)	90	90	90
V (Å^3)	12714.7(3)	12699.1(9)	11848.2(3)
Z	4	4	4
D_c (g cm^{-3})	1.270	1.272	1.363
μ(MoK$_\alpha$) (mm^{-1})[d]	7.191	1.606	1.721
T (K)	150.3(4)	100(2)	100.00(10)
Observed reflections	25642 (17850)	9957 (8998)	12131 (10279)
R_{int}	0.1246	0.0716	0.0376
Parameters	1245	591	668
GOF	1.057	1.033	1.015
R_1[a,b]	0.1053 (0.0676)	0.0479 (0.0404)	0.0454 (0.0321)
wR_2[c]	0.1828 (0.1575)	0.0841 (0.0816)	0.0741 (0.0668)
Largest difference in peak and hole (e Å^{-3})	2.843 and -1.999	0.460 and -0.577	1.254 and -0.649

[a] $R_1 = \Sigma||F_o| - |F_c||/\Sigma|F_o|$. [b] Values in parentheses for reflections with $I > 2\sigma(I)$. [c] $wR_2 = \{\Sigma[w(F_o^2 - F_c^2)^2]/\Sigma[w(F_o^2)^2]\}^{½}$. [d] μ(CuK$_\alpha$) (mm^{-1}) in **41-R**.

Table A5.3.- Bond lengths (Å) and angles (°) for compound **41-R**. Note that when referring to fragment A O7 and O8 belong to ligand B and vice versa. OXS and OYS are O1S and O2S for fragment A and O3S and O4S for fragment B.

Compound	**41-R (A)**	**41-R (B)**
Dy1···Zn1	3.3675(17)	3.3602(18)
Dy1-O1	2.289(7)	2.294(8)
Dy1-O2	2.571(10)	2.587(9)
Dy1-O3	2.328(8)	2.337(8)
Dy1-O4	2.640(10)	2.641(11)
Dy1-O7	2.222(7)	2.234(9)
Dy1-O8	2.703(10)	2.737(10)
Dy1-O1N	2.442(11)	2.452(9)
Dy1-O2N	2.461(8)	2.478(9)
Dy1-OXS	2.353(8)	2.340(8)
Zn1-N1	2.123(10)	2.128(11)
Zn1-N2	2.189(10)	2.187(11)
Zn1-O1	2.091(8)	2.111(8)
Zn1-O3	1.960(9)	1.981(9)
Zn1-OYS	1.980(9)	1.984(8)
Dy1-O1-Zn1	100.4(3)	99.3(3)
Dy1-O3-Zn1	103.2(4)	101.9(4)
O1-Dy1-O3	65.5(3)	66.7(3)
O1-Dy1-O7	135.0(3)	139.5(3)
O1-Dy1-O1N	85.4(4)	81.9(3)
O1-Dy1-O2N	84.8(3)	83.7(3)
O1-Dy1-OXS	79.5(3)	82.4(3)
O3-Dy1-O7	144.0(3)	142.5(3)
O3-Dy1-O1N	75.2(3)	75.2(3)
O3-Dy1-O2N	122.3(3)	122.4(3)
O3-Dy1-OXS	83.2(3)	84.1(3)
O7-Dy1-O1N	127.1(3)	125.3(3)
O7-Dy1-O2N	92.0(3)	91.6(4)
O7-Dy1-OXS	74.9(3)	76.5(3)
O1-Zn1-O3	76.0(3)	76.9(3)
O1-Zn1-OYS	98.1(3)	97.0(3)
O3-Zn1-OYS	108.3(4)	106.4(4)
N1-Zn1-N2	84.8(4)	84.2(5)

Table A5.4.- Bond lengths (Å) and angles (°) for compounds **41-S** and **44-rac**. Note that when referring to fragment A O7 and O8 belong to ligand B and vice versa. OXS and OYS are O1S and O2S for fragment A and O3S and O4S for fragment B.

Compound	**41-S (A)**	**41-S (B)**	**44-rac**
Dy1···Zn1	3.3662(17)	3.3725(18)	3.3616(7)
Dy1-O1	2.302(9)	2.317(9)	2.277(4)
Dy1-O2	2.583(8)	2.576(9)	2.559(5)
Dy1-O3	2.334(9)	2.325(10)	2.306(4)
Dy1-O4	2.658(9)	2.628(9)	2.600(5)
Dy1-O7	2.237(8)	2.209(9)	2.217(3)
Dy1-O8	2.727(10)	2.769(9)	2.844(5)
Dy1-O1N	2.449(9)	2.436(10)	2.447(4)
Dy1-O2N	2.490(9)	2.448(9)	2.488(4)
Dy1-OXS	2.324(8)	2.377(8)	2.355(4)
Zn1-N1	2.075(11)	2.075(11)	2.099(5)
Zn1-N2	2.153(11)	2.192(11)	2.188(5)
Zn1-O1	2.085(8)	2.095(8)	2.099(4)
Zn1-O3	1.996(9)	1.992(9)	1.972(5)
Zn1-OYS	1.963(9)	1.985(9)	1.959(4)
Dy1-O1-Zn1	100.1(3)	99.6(4)	100.30(18)
Dy1-O3-Zn1	101.8(4)	102.5(4)	103.3(2)
O1-Dy1-O3	65.6(3)	66.4(3)	66.18(15)
O1-Dy1-O7	142.0(3)	135.6(3)	139.63(16)
O1-Dy1-O1N	80.4(3)	86.9(3)	84.14(15)
O1-Dy1-O2N	84.7(3)	86.4(3)	89.62(14)
O1-Dy1-OXS	83.2(3)	79.8(3)	80.65(14)
O3-Dy1-O7	141.5(3)	142.8(3)	143.16(14)
O3-Dy1-O1N	74.3(3)	76.3(3)	76.85(15)
O3-Dy1-O2N	122.9(3)	123.4(4)	125.95(14)
O3-Dy1-OXS	83.8(3)	84.2(3)	84.40(14)
O7-Dy1-O1N	125.8(3)	125.4(3)	122.54(14)
O7-Dy1-O2N	91.4(3)	91.4(4)	86.16(13)
O7-Dy1-OXS	76.9(3)	74.2(3)	77.74(13)
O1-Zn1-O3	75.9(3)	76.9(4)	75.77(17)
O1-Zn1-OYS	98.7(3)	98.9(4)	97.78(17)
O3-Zn1-OYS	106.3(4)	107.6(4)	105.79(17)
N1-Zn1-N2	85.1(4)	85.8(4)	85.1(2)

2. Continuous Shape Measurements.

The nearer the value to zero, the better fits to an ideal polyhedron.

Table A5.6.- Continuous Shape Measurements for the ZnN_2O_3 coordination environment in compounds **41-R**, **41-S** and **44-rac**.

PP-5 1 D5h Pentagon
vOC-5 2 C4v Vacant octahedron
TBPY-5 3 D3h Trigonal bipyramid
SPY-5 4 C4v Spherical square pyramid
JTBPY-5 5 D3h Johnson trigonal bipyramid J12

Structure [ML5]	PP-5	vOC-5	TBPY-5	SPY-5	JTBPY-5
Zn1A (41-R)	29.807	2.104	4.840	**0.657**	6.791
Zn1B (41-R)	30.095	2.008	4.629	**0.641**	6.583
Zn1A (41-S)	30.561	1.975	4.676	**0.577**	6.706
Zn1B (41-S)	30.168	1.937	4.875	**0.538**	6.769
Zn1 (44-rac)	30.505	2.040	4.756	**0.676**	6.599

Table A5.7.- Continuous Shape Measurements for the DyO_9 coordination environment in compounds **41-R**, **41-S** and **44-rac**.

EP-9	1 D9h	Enneagon
OPY-9	2 C8v	Octagonal pyramid
HBPY-9	3 D7h	Heptagonal bipyramid
JTC-9	4 C3v	Johnson triangular cupola J3
JCCU-9	5 C4v	Capped cube J8
CCU-9	6 C4v	Spherical-relaxed capped cube
JCSAPR-9	7 C4v	Capped square antiprism J10
CSAPR-9	8 C4v	Spherical capped square antiprism
JTCTPR-9	9 D3h	Tricapped trigonal prism J51
TCTPR-9	10 D3h	Spherical tricapped trigonal prism
JTDIC-9	11 C3v	Tridiminished icosahedron J63
HH-9	12 C2v	Hula-hoop
MFF-9	13 Cs	Muffin

Structure [ML9]	EP-9	OPY-9	HBPY-9	JTC-9	JCCU-9	CCU-9	JCSAPR-9
Dy1A (41-R)	33.423	22.522	16.974	15.147	7.988	7.165	3.940
Dy1B (41-R)	34.951	22.132	17.447	15.956	8.195	7.336	3.417
Dy1A (41-S)	34.970	22.489	17.299	15.924	8.487	7.554	3.451
Dy1B (41-S)	33.259	22.393	17.021	15.343	7.890	7.068	4.048
Dy1 (44-rac)	33.280	22.464	16.949	15.549	8.508	7.624	3.591

Structure [ML9]	CSAPR-9	JTCTPR-9	TCTPR-9	JTDIC-9	HH-9	MFF-9
Dy1A (41-R)	2.850	3.649	3.158	10.463	8.356	**2.842**
Dy1B (41-R)	2.861	3.536	2.759	10.786	9.520	**2.537**
Dy1A (41-S)	2.819	3.545	2.722	10.711	9.408	**2.418**
Dy1B (41-S)	3.085	3.711	3.340	10.231	8.398	**3.021**
Dy1 (44-rac)	3.011	3.500	3.206	10.589	8.977	**2.604**

3. Figures of Supramolecular Structures.

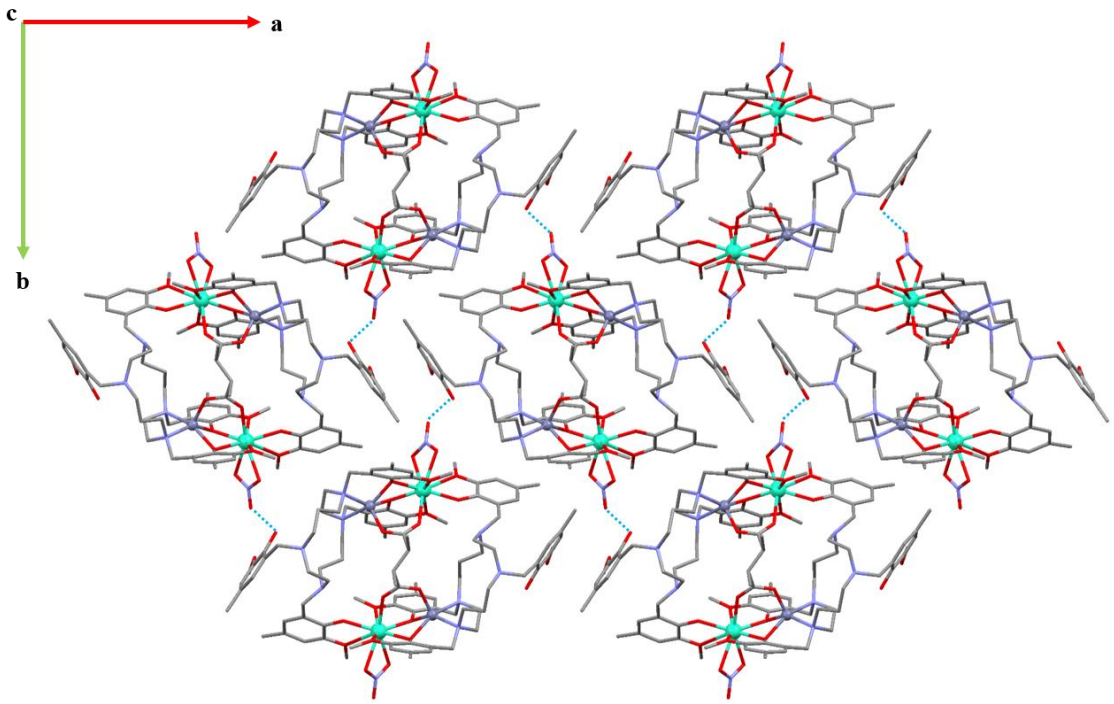

Figure A5.1.- Hydrogen bonding pattern (blue dashed lines) between cationic fragments of **44-rac**, viewed along the *c* axis. Both possible enantiomers are visible, R,S',S'' in the center and S,R',R'' up and down.

4. Experimental XRPD.

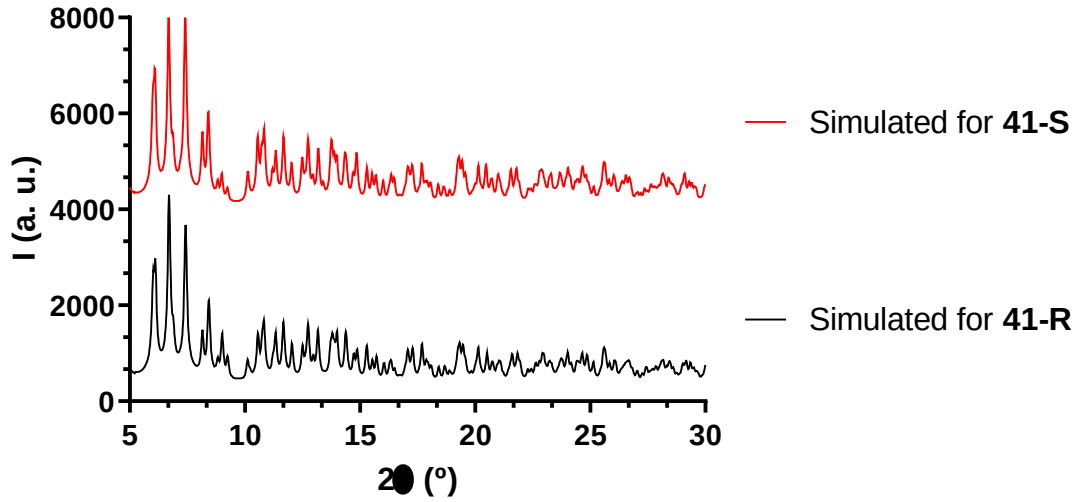

Figure A5.2.- Simulated patterns from single-crystal X-ray diffraction for **41**-R (black) and **41**-S (red).

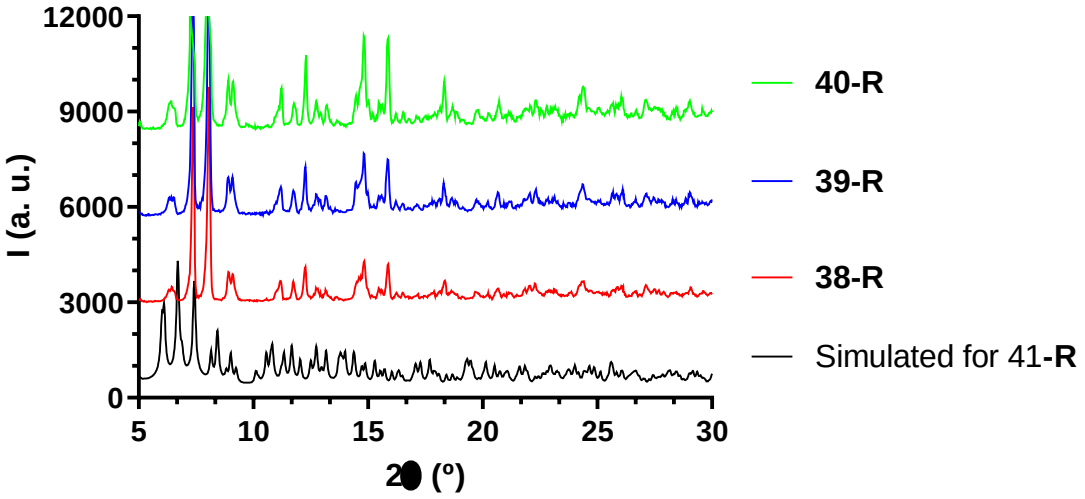

Figure A5.3.- For compounds **38-R**, **39-R** and **40-R**, simulated pattern from single-crystal X-ray diffraction of **41-R** (black line) and experimental XRPD for **38-R** (red), **39-R** (blue) and **40-R** (green).

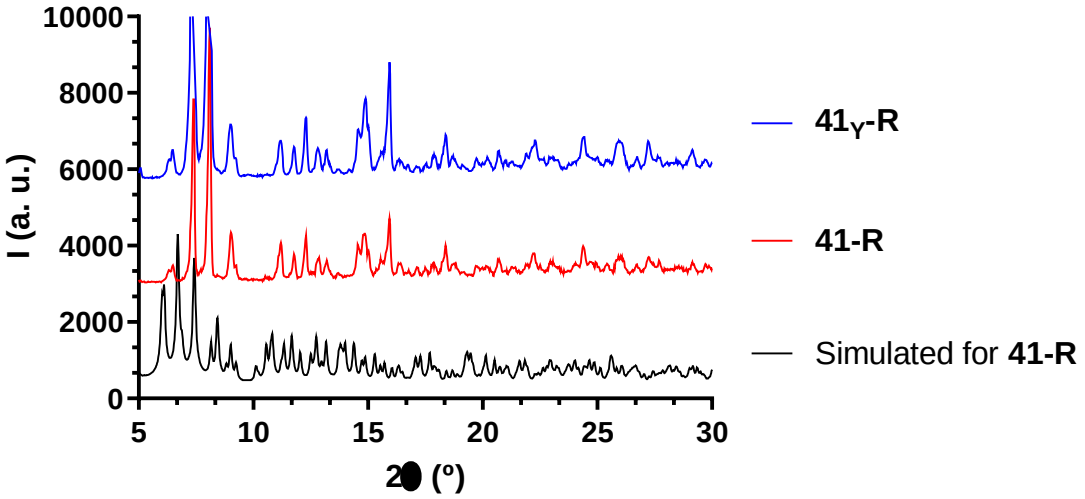

Figure A5.4.- For compounds **41-R** and **41$_Y$-R**, simulated pattern from single-crystal X-ray diffraction of **41-R** (black line) and experimental XRPD for **41-R** (red) and **41$_Y$-R** (blue).

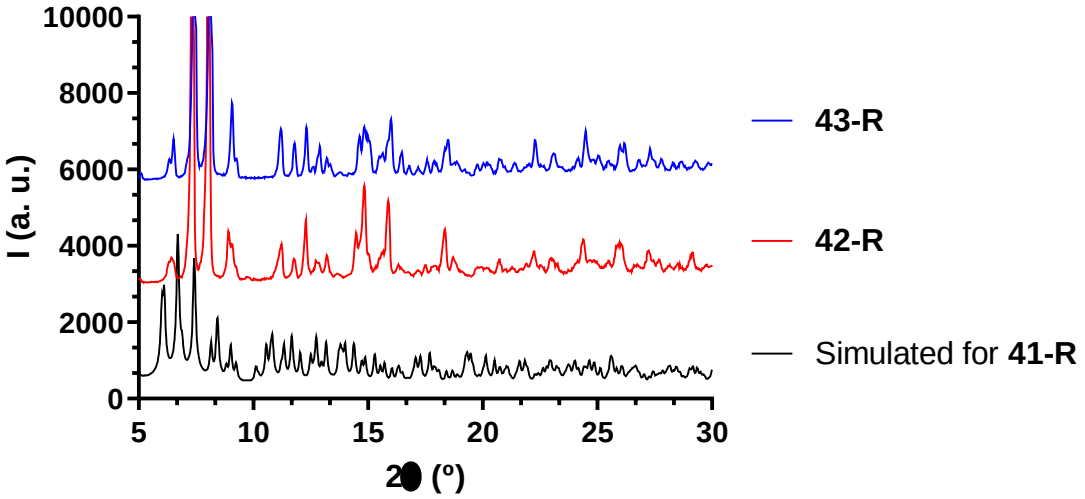

Figure A5.5.- For compounds **42-R** and **43-R**, simulated pattern from single-crystal X-ray diffraction of **41-R** (black line) and experimental XRPD for **42-R** (red) and **43-R** (blue).

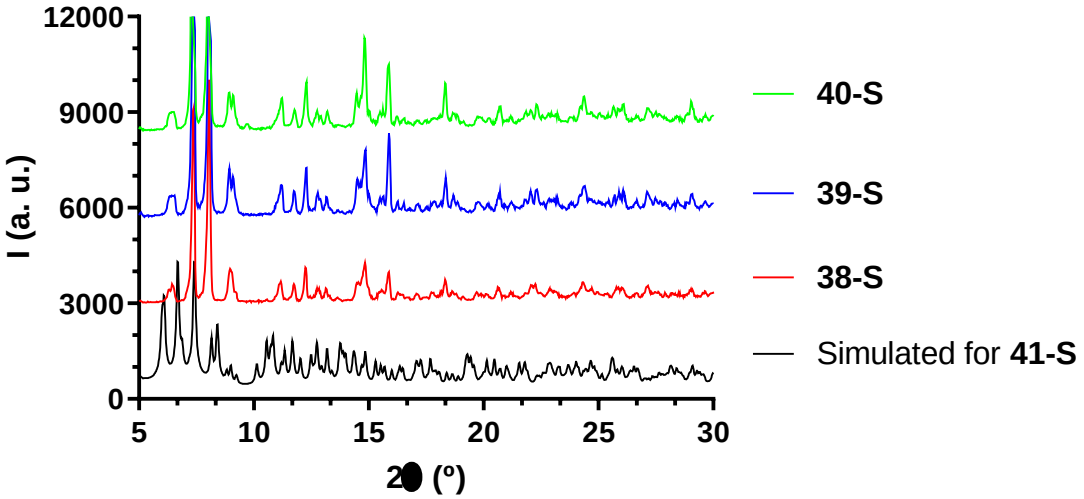

Figure A5.6.- For compounds **38-S**, **39-S** and **40-S**, simulated pattern from single-crystal X-ray diffraction of **41-S** (black line) and experimental XRPD for **38-S** (red), **39-S** (blue) and **40-S** (green).

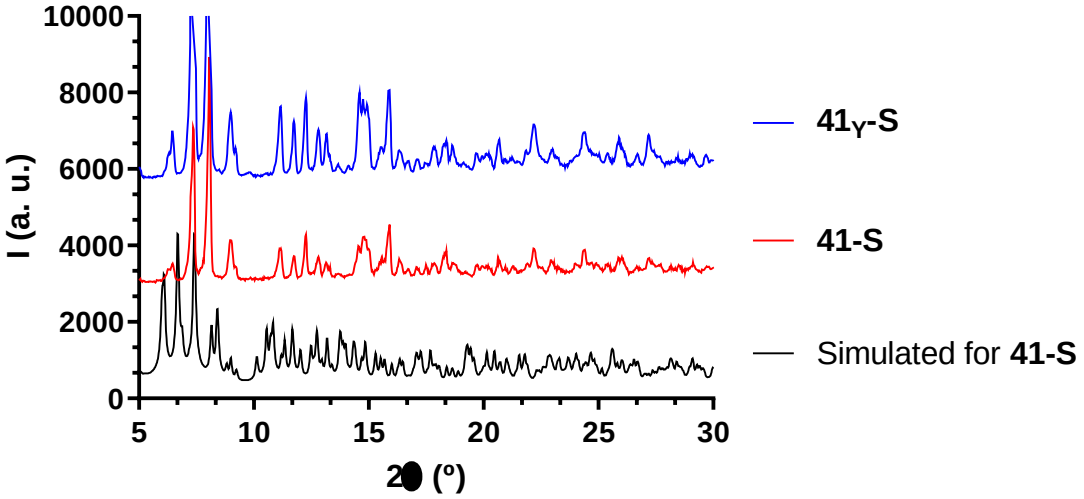

Figure A5.7.- For compounds **41-S** and **41$_Y$-S**, simulated pattern from single-crystal X-ray diffraction of **41-S** (black line) and experimental XRPD for **41-S** (red) and **41$_Y$-S** (blue).

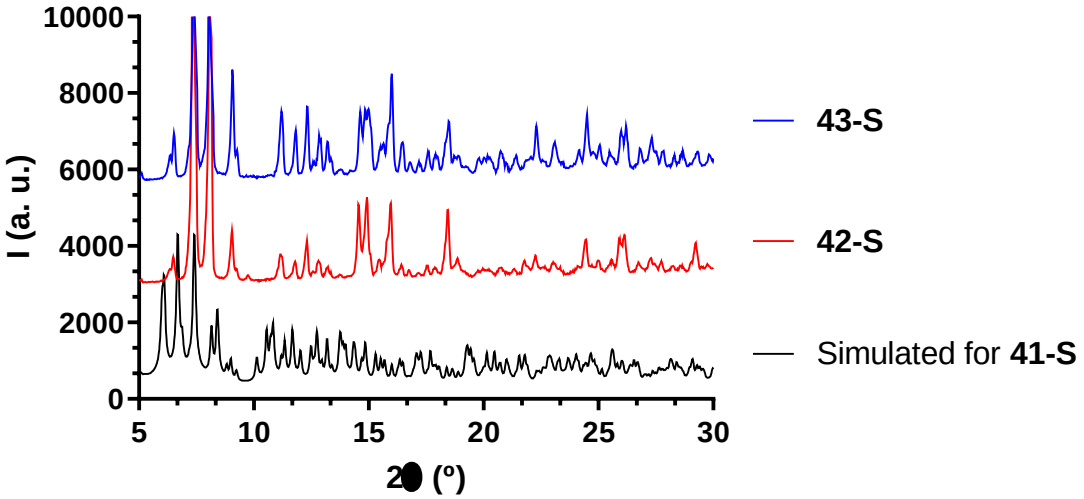

Figure A5.8.- For compounds **42-S** and **43-S**, simulated pattern from single-crystal X-ray diffraction of **41-S** (black line) and experimental XRPD for **42-S** (red) and **43-S** (blue).

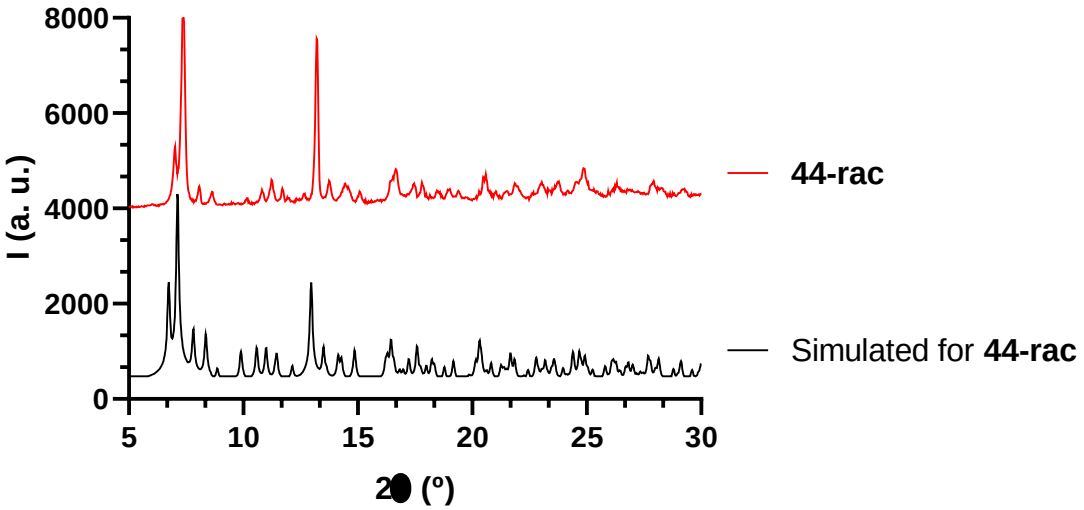

Figure A5.9.- For compound **44-rac**, simulated pattern from single-crystal X-ray diffraction of **44-rac** (black line) and experimental XRPD for **44-rac** (red).

5. Thermogravimetric Analysis.

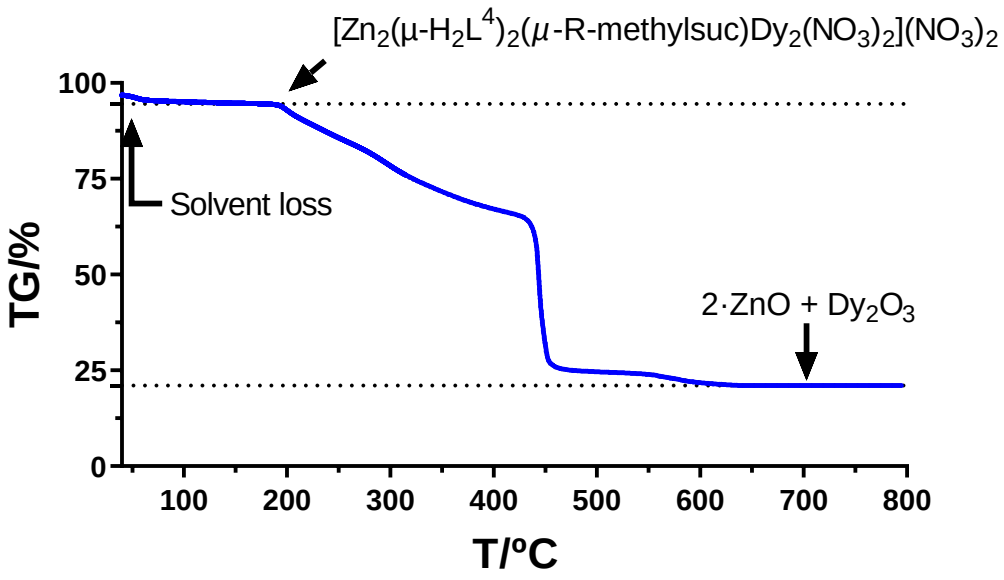

Figure A5.10.- Thermogravimetric analysis of compound **41-R**.

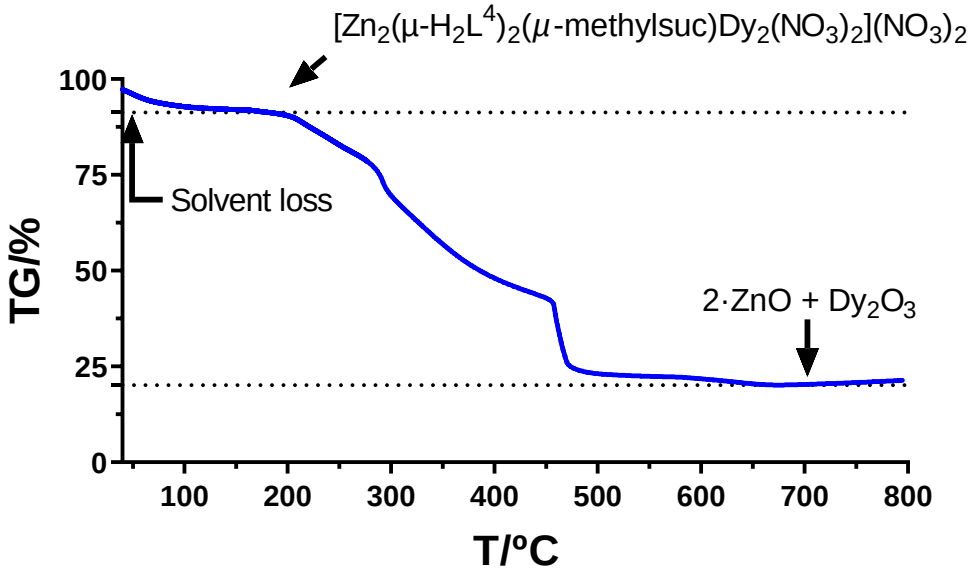

Figure A5.11.- Thermogravimetric analysis of compound **44-rac**.

6. Magnetic Measurements.

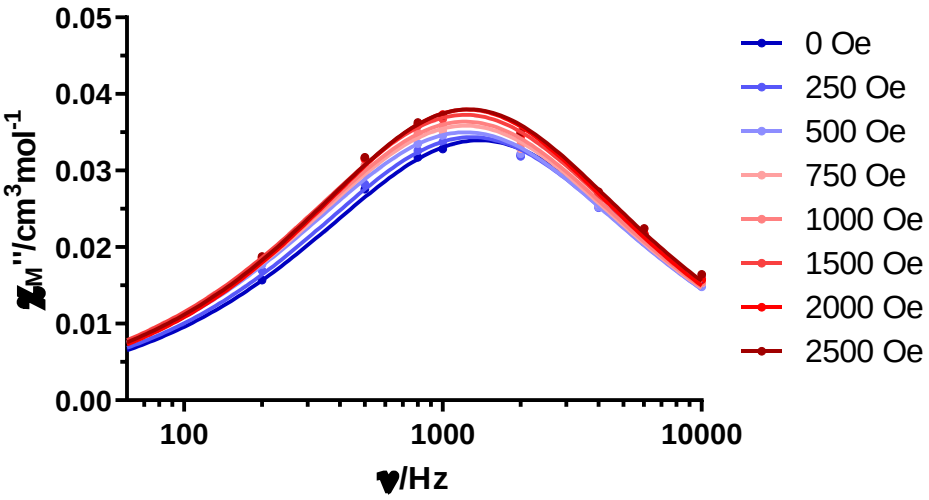

Figure A5.12.- Field dependence of the out-of-phase signal *vs* frequency at 24.8 K for **41$_Y$-R**.

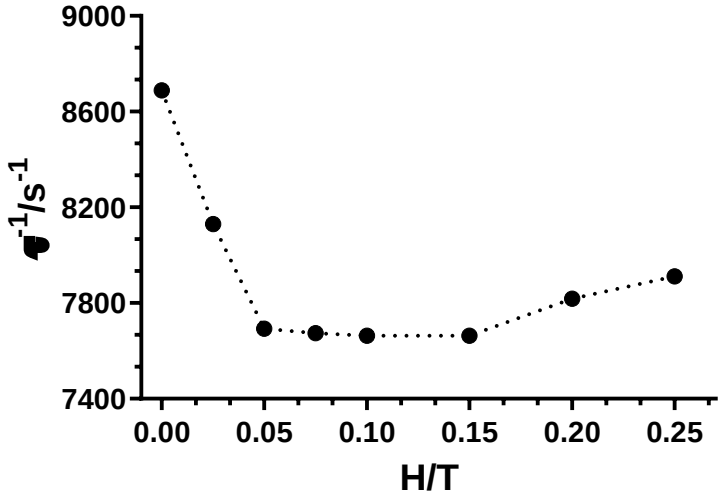

Figure A5.13.- The inverse of the relaxation times obtained at different magnetic fields at 24.8 K for **41$_Y$-R**.

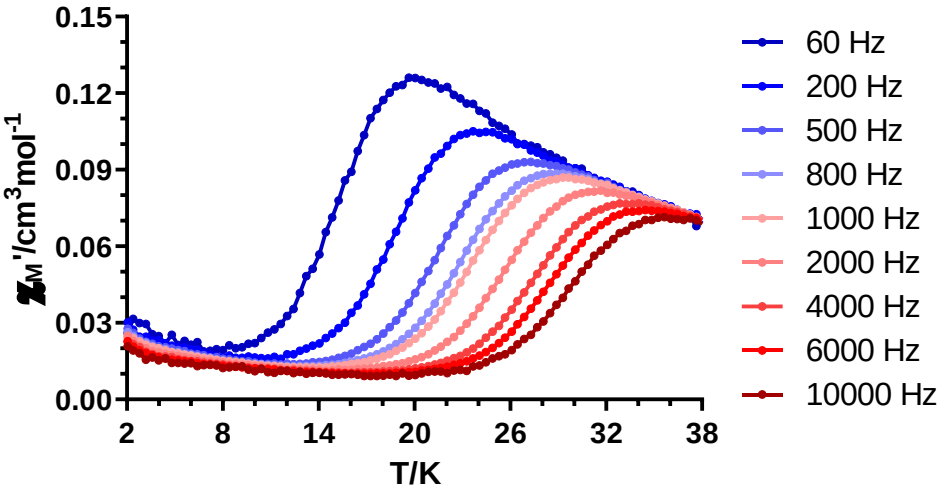

Figure A5.14.- Temperature dependence of the in phase χ_M' susceptibility signals for complex **41$_Y$-R** under an applied field of 1000 Oe.

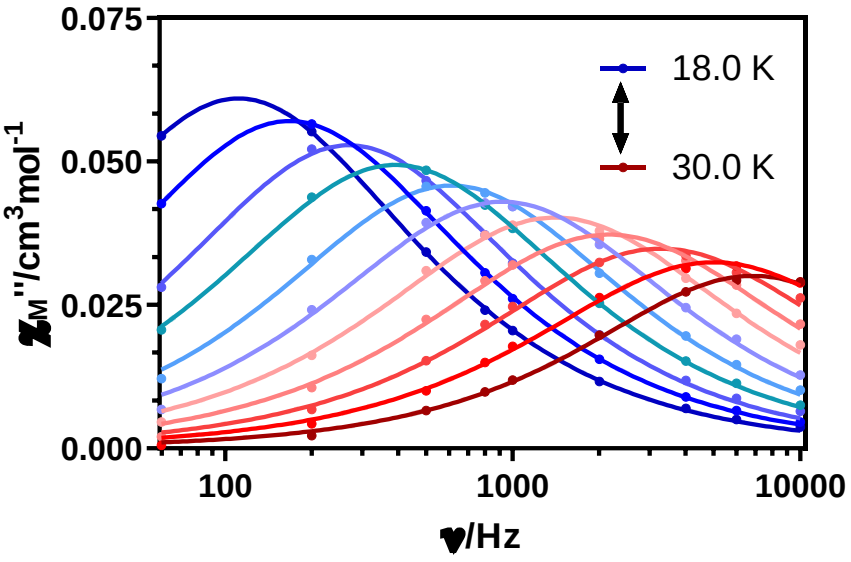

Figure A5.15.- Variable-temperature frequency dependence of the χ_M'' signal under 1 kOe applied field for **41$_Y$-R**. Solid lines represent the best fitting of the experimental data to the Debye model.

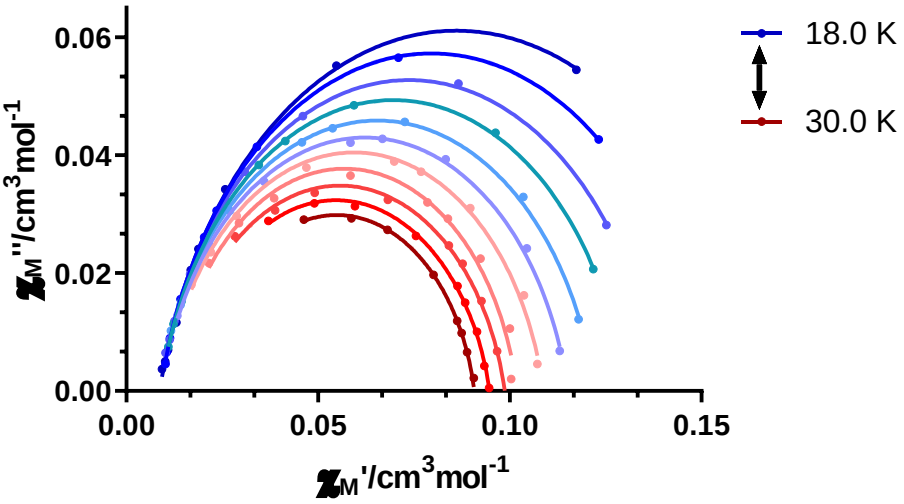

Figure A5.16.- Cole-Cole plots under 1 kOe field for **41$_Y$-R**. Solid lines represent the best fit to the generalized Debye model.

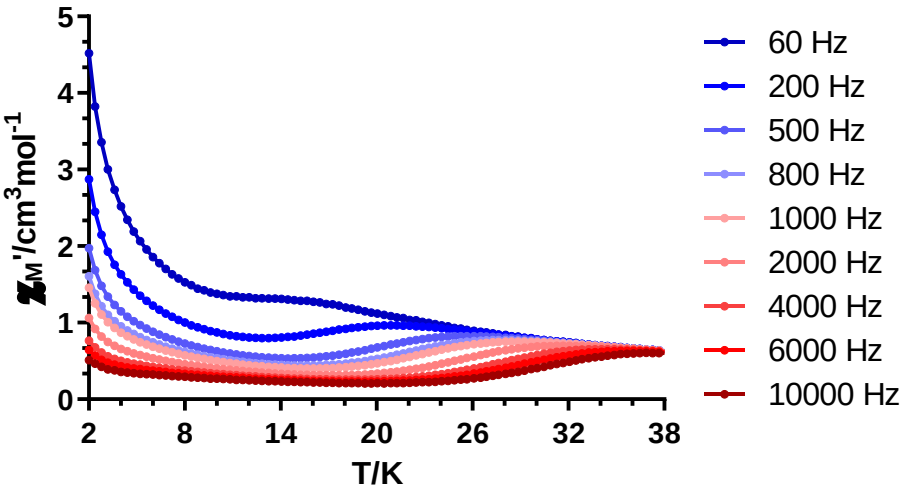

Figure A5.17.- Temperature dependence of the in phase χ_M' susceptibility signals for complex **44-rac** under zero applied *dc* field.

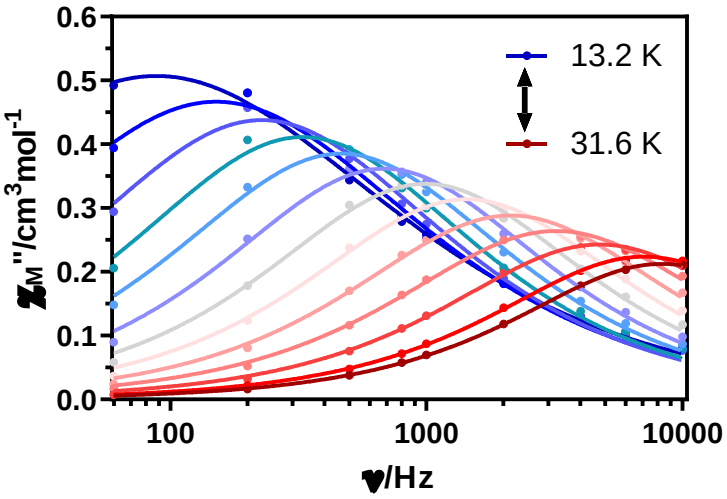

Figure A5.18.- Variable-temperature frequency dependence of the χ_M'' signal under zero applied *dc* field for **44-rac**. Solid lines represent the best fitting of the experimental data to the Debye model.

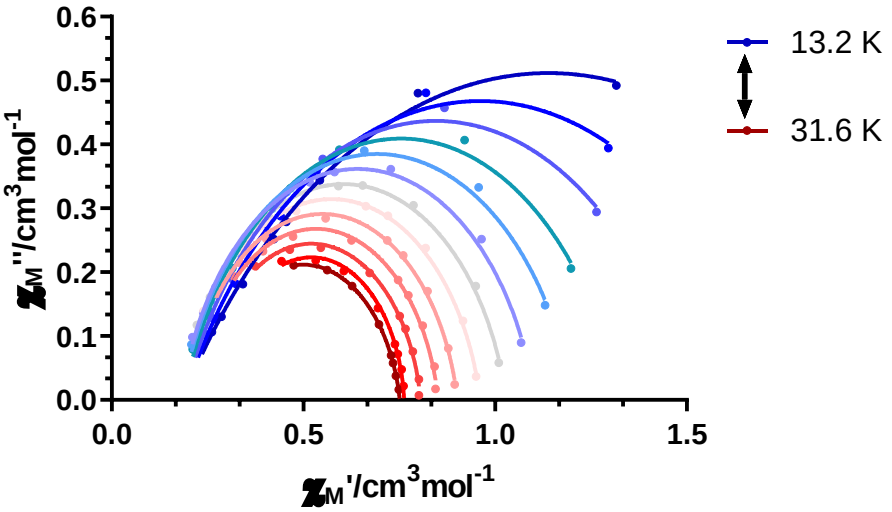

Figure A5.19.- Cole-Cole plots under zero applied *dc* field for **44-rac**. Solid lines represent the best fit to the generalized Debye model.

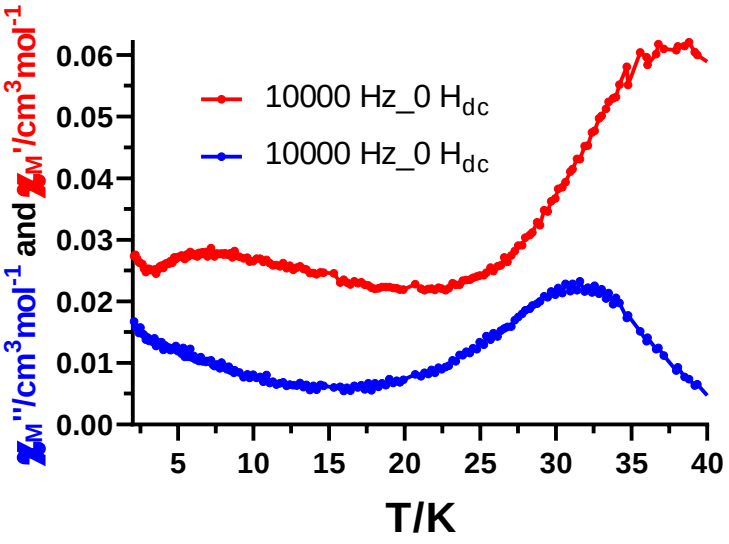

Figure A5.20.- Temperature dependence of the in phase χ_M' (red) and out-of-phase (blue) susceptibility signals for complex **44$_Y$-rac** under zero applied *dc* field.

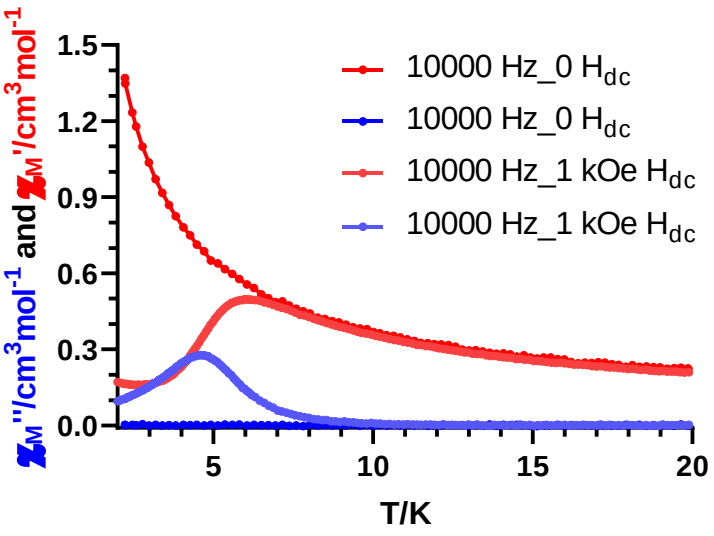

Figure A5.21.- Temperature dependence of the in phase χ_M' (red) and out-of-phase (blue) susceptibility signals for complex **43-R** under zero and 1 kOe applied *dc* field.

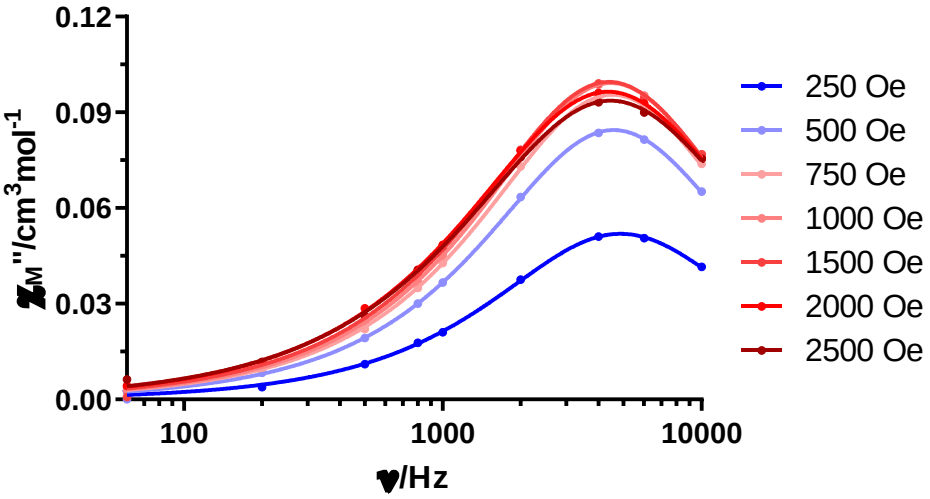

Figure A5.22.- Field dependence of the out-of-phase signal *vs* frequency at 3.8 K for **43-R**.

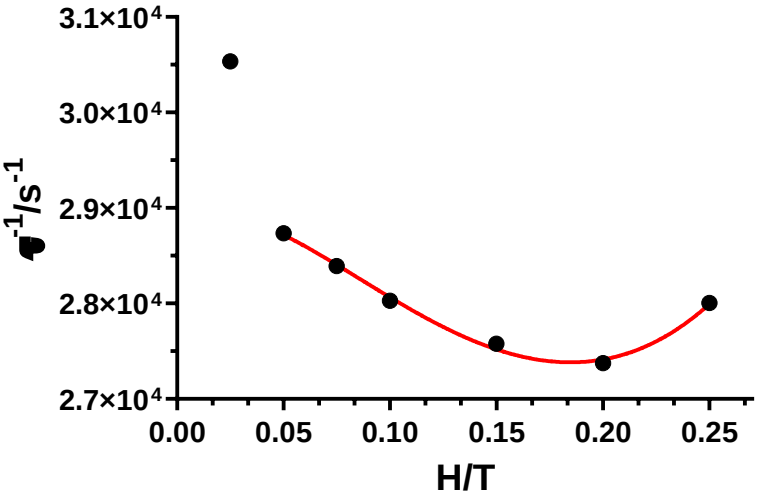

Figure A5.23.- The inverse of the relaxation times obtained at different magnetic fields at 3.8 K for **43-R**. The red line represents the best fit to Equation 5.2 in the manuscript.

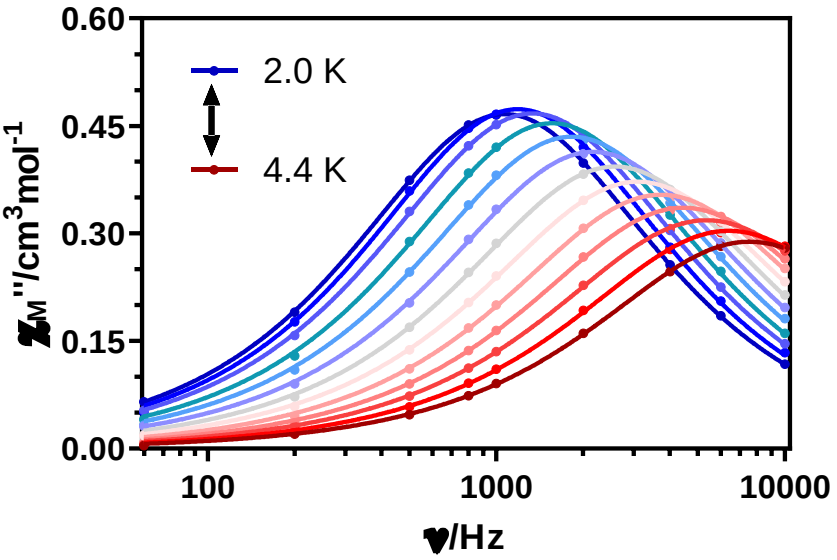

Figure A5.24.- Variable-temperature frequency dependence of the χ_M'' signal under 2 kOe applied field for **43-R**. Solid lines represent the best fitting of the experimental data to the Debye model.

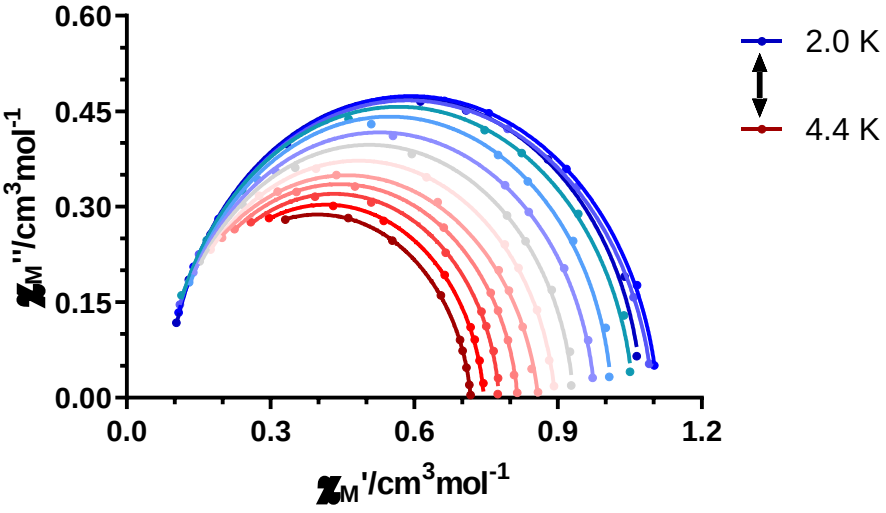

Figure A5.25.- Cole-Cole plots under 2 kOe field for **43-R**. Solid lines represent the best fit to the generalized Debye model.

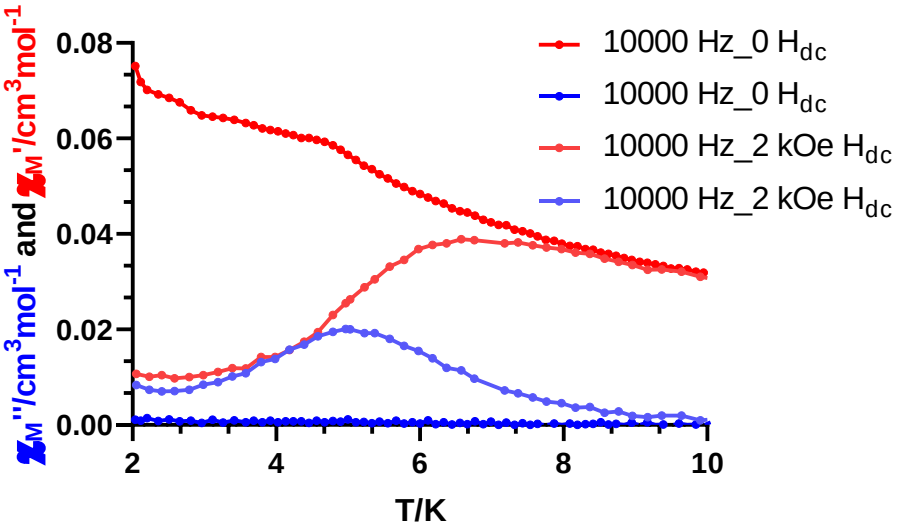

Figure A5.26.- Temperature dependence of the in phase χ_M' (red) and out-of-phase (blue) susceptibility signals for complex **43$_Y$-R** under zero and 2 kOe applied *dc* field.

7. Luminescence Properties.

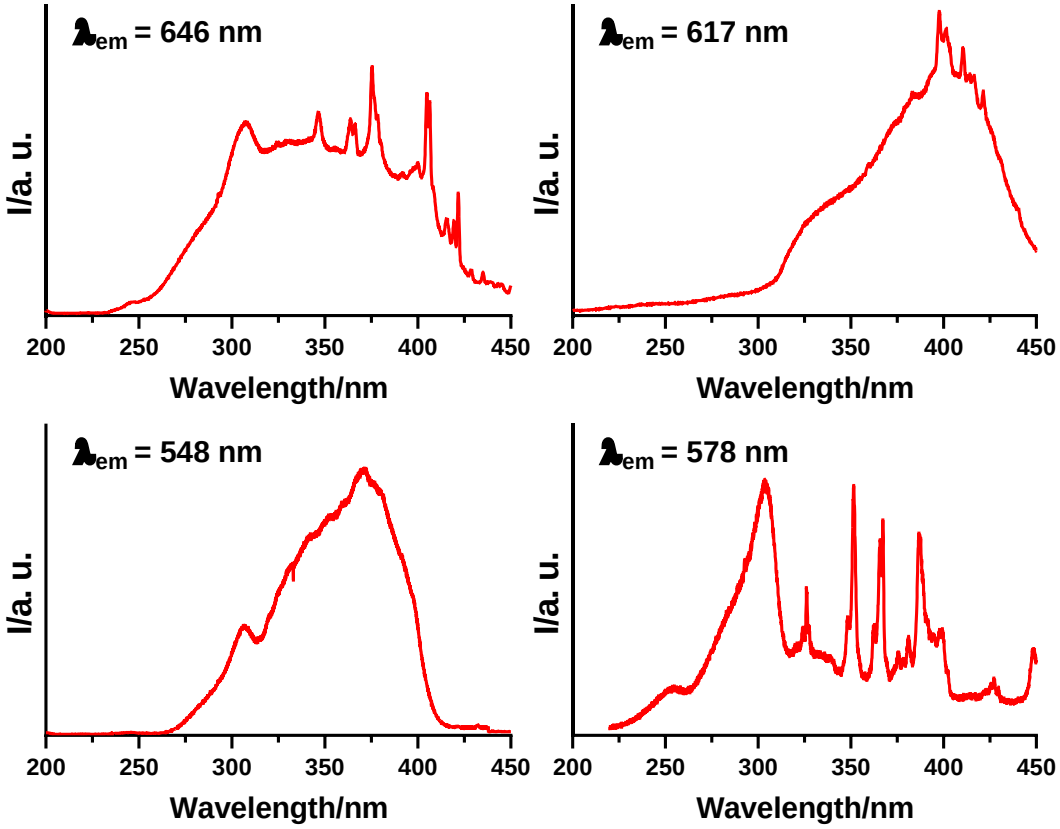

Figure A5.27.- Excitation spectra of **38-R** (top left), **39-R** (top right), **40-R** (bottom left) and **41-R** (bottom right) recorded at 15, 15, 20 and 10 K, respectively.

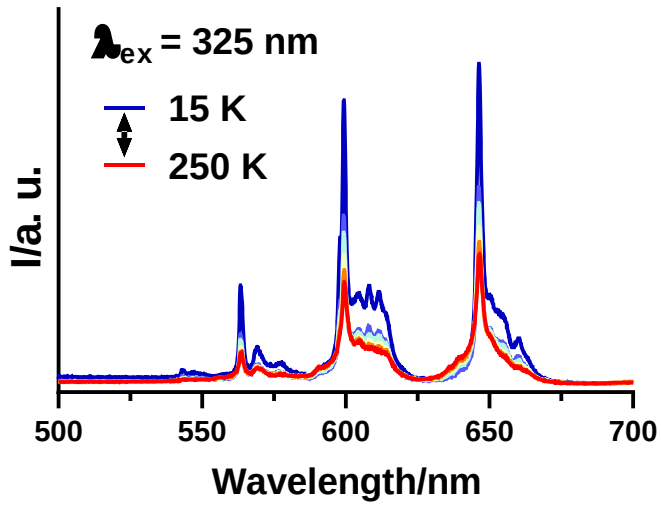

Figure A5.28.- Emission spectra at variable temperature of **38-R** excited at 325 nm.

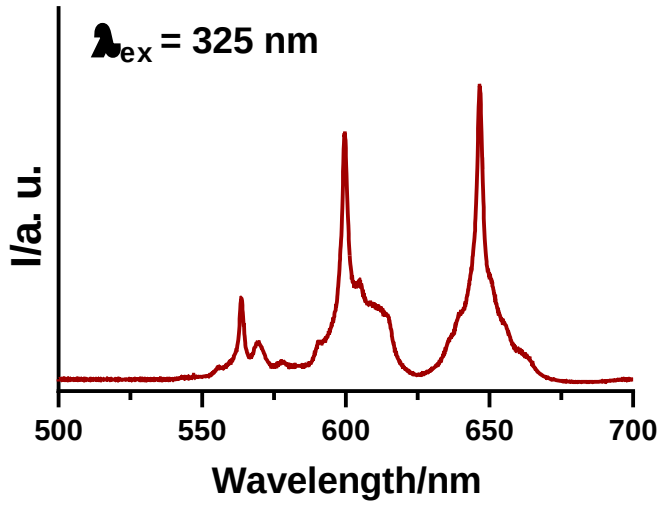

Figure A5.29.- Emission spectra at room temperature of **38-R** excited at 325 nm.

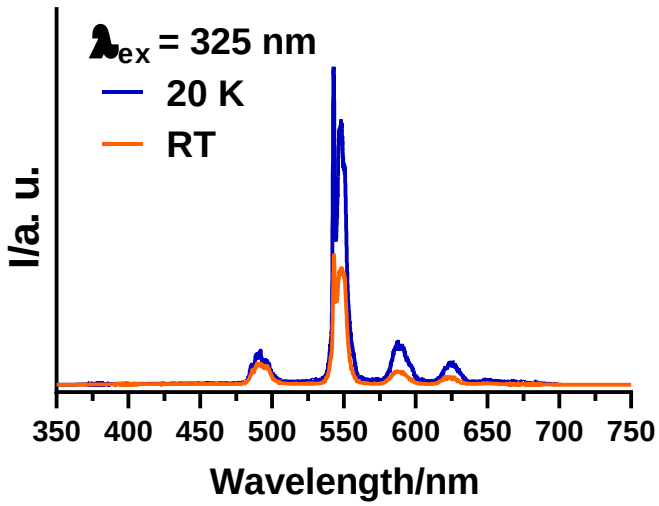

Figure A5.30.- Emission spectra at 20 K (blue) and room temperature (orange) of **40-R** excited at 325 nm.

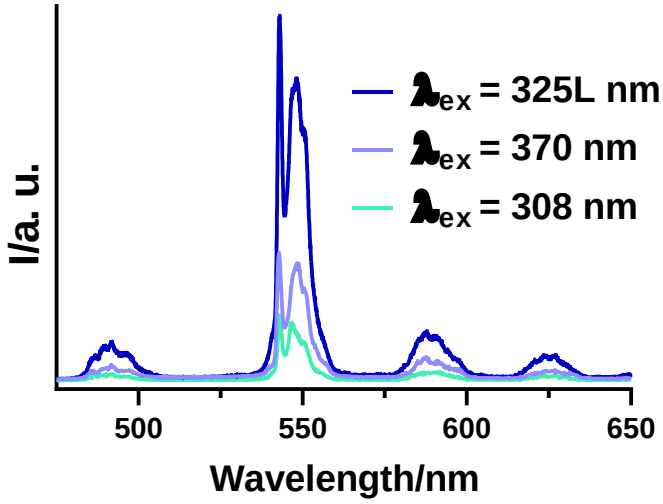

Figure A5.31.- Emission spectra at 20 K of **40-R** excited at 308 (lamp), 370 (lamp) and 325 nm (laser).

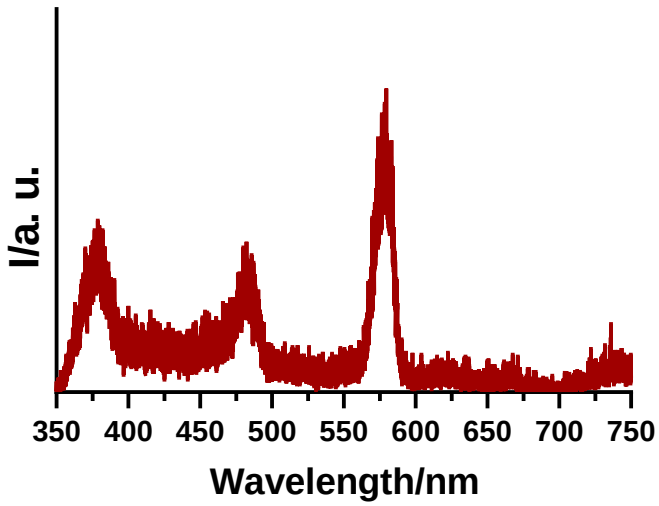

Figure A5.32.- Emission spectra at room temperature of **41-R** excited at 325 nm.

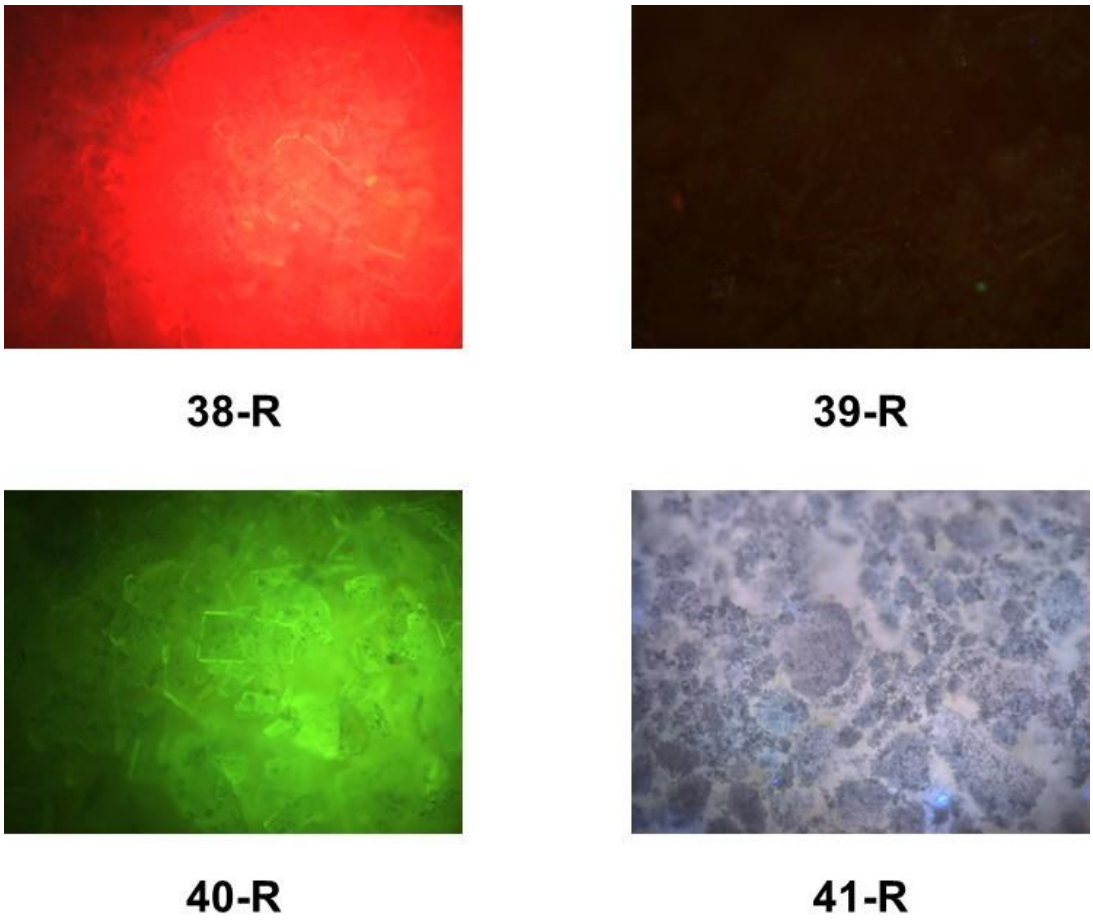

Figure A5.33.- Micro-photoluminescence images taken on polycrystalline samples at room temperature excited at 355 nm.

APPENDICES

***Chapter 6**: Modulating the SMM properties of a $Zn^{II}_2Dy^{III}_2$ based compound by rationally reducing/increasing the electron density in the equatorial plane perpendicular to the $O_{phenoxido}$-Dy-$O_{phenoxido\text{-}bridges}$ direction*

Index:

1. Crystallographic Tables.

Table A6.1.- Crystallographic data for compounds **45-47**. Note that the formula in **46** and **47** is not complete. Counterions and solvent crystallization molecules are missing.

Compound	**45**	**46**	**47**
Formula	$C_{105}H_{160}N_{12}O_{41}F_4Zn_2Dy_2$	$C_{106}H_{130}N_8O_{24}F_{12}Zn_2Dy_2$	$C_{106}H_{126}N_8O_{24}F_{16}Zn_2Dy_2$
M_r	2778.18	2583.91	2655.88
Crystal system	*monoclinic*	*triclinic*	*triclinic*
Space group (no.)	*P* 21/c (14)	*P -1* (2)	*P -1* (2)
a (Å)	13.0698(8)	19.2020(3)	17.0854(3)
b (Å)	48.732(3)	27.6848(5)	18.9558(3)
c (Å)	20.0222(12)	39.2013(8)	23.3790(5)
α (°)	90	89.466(2)	97.183(2)
β (°)	105.084(2)	78.420(2)	93.196(2)
γ (°)	90	75.048(2)	114.960(2)
V (Å^3)	12313.2(13)	19704.3(7)	6760.9(2)
Z	4	6	2
D_c (g cm^{-3})	1.499	1.307	1.305
μ(MoK_α) (mm^{-1})	1.676	1.564	1.526
T (K)	100.00(10)	100(2)	100.01(10)
Observed reflections	32009 (23397)	73436 (44480)	26742 (21524)
R_{int}	0.0878	0.0515	0.0220
Parameters	1514	4167	1468
GOF	1.127	1.026	1.029
R_1[a,b]	0.1015 (0.0645)	0.1385 (0.0859)	0.0506 (0.0363)
wR_2[c]	0.1409 (0.1299)	0.2320 (0.1947)	0.0855 (0.0787)
Largest difference in peak and hole (e Å^{-3})	1.965 and -2.619	5.853 and -3.128	1.340 and -0.967

[a]$R_1 = \Sigma||F_o| - |F_c||/\Sigma|F_o|$. [b]Values in parentheses for reflections with $I > 2\sigma(I)$. [c]$wR_2 = \{\Sigma[w(F_o^2 - F_c^2)^2]/\Sigma[w(F_o^2)^2]\}^{½}$.

Table A6.2.- Crystallographic data for compounds **48a**, **48b** and **49**. Note that a definitive structure refinement has not been still obtained for **49**.

Compound	**48a**	**48b**	**49**
Formula	$C_{107}H_{148}N_8O_{35}F_{12}S_2Zn_2Dy_2$	$C_{108}H_{156}N_8O_{38}F_{12}S_2Zn_2Dy_2$	$C_{135}H_{182}N_8O_{39}F_6S_2Zn_2Dy_2$
M_r	2854.19	2922.26	3174.74
Crystal system	*triclinic*	*monoclinic*	*triclinic*
Space group (no.)	*P -1* (2)	*C 2/c* (15)	*P -1* (2)
a (Å)	12.252(2)	35.7147(9)	16.9088(9)
b (Å)	18.4676(10)	12.1364(2)	19.4639(11)
c (Å)	30.4352(19)	32.9862(7)	23.3378(13)
α (°)	73.731(5)	90	100.267(2)
β (°)	86.145(10)	109.406(3)	95.998(2)
γ (°)	88.167(10)	90	106.595(2)
V (Å^3)	6595.3(13)	13485.5(5)	7143.9(7)
Z	2	4	2
D_c (g cm^{-3})	1.437	1.439	1.476
μ(MoK_α) (mm^{-1})	1.602	1.570	1.483
*T (*K)	100.00(10)	100.00(10)	100(2)
Observed reflections	25753 (12844)	15251 (11019)	36881 (28497)
R_{int}	0.1032	0.0640	0.0417
Parameters	1423	802	1738
GOF	1.070	1.051	1.132
$R_1^{a,b}$	0.1564 (0.0871)	0.1037 (0.0731)	0.0954 (0.0654)
wR_2^c	0.2125 (0.1928)	0.2146 (0.1903)	0.1625 (0.1364)
Largest difference in peak and hole (e Å^{-3})	4.189 and -2.259	2.384 and -1.833	4.326 and -4.218

[a]$R_1 = \Sigma||F_o| - |F_c||/\Sigma|F_o|$. [b]Values in parentheses for reflections with $I > 2\sigma(I)$. [c]$wR_2 = \{\Sigma[w(F_o^2 - F_c^2)^2]/\Sigma[w(F_o^2)^2]\}^{½}$.

Table A6.3.- Bond lengths (Å) and angles (°) for compound **45**. Note that when referring to fragment A O7 and O8 belong to ligand B and vice versa. OXS and OYS are O1S and O2S for fragment A and O3S and O4S for fragment B.

Compound	**45 (A)**	**45 (B)**
Dy1⋯Zn1	3.3832(7)	3.4021(7)
Dy1-O1	2.280(4)	2.280(4)
Dy1-O2	2.667(4)	2.584(4)
Dy1-O3	2.316(4)	2.298(4)
Dy1-O4	2.681(4)	2.625(4)
Dy1-O7	2.234(4)	2.237(4)
Dy1-O8	2.630(4)	2.689(4)
Dy1-O1N	2.447(4)	2.427(4)
Dy1-O2N	2.456(4)	2.454(4)
Dy1-OXS	2.377(4)	2.432(4)
Zn1-N1	2.097(5)	2.099(4)
Zn1-N2	2.167(5)	2.169(4)
Zn1-O1	2.075(4)	2.066(4)
Zn1-O3	1.990(4)	1.966(4)
Zn1-OYS	2.021(4)	2.007(4)
Dy1-O1-Zn1	101.83(15)	102.91(15)
Dy1-O3-Zn1	103.32(17)	105.59(17)
O1-Dy1-O3	66.22(14)	66.52(13)
O1-Dy1-O7	138.54(14)	139.06(13)
O1-Dy1-O1N	86.14(14)	80.24(14)
O1-Dy1-O2N	79.39(15)	78.01(13)
O1-Dy1-OXS	81.73(13)	79.22(13)
O3-Dy1-O7	144.16(14)	137.93(15)
O3-Dy1-O1N	127.47(14)	73.66(16)
O3-Dy1-O2N	78.33(14)	119.39(15)
O3-Dy1-OXS	83.00(14)	78.34(14)
O7-Dy1-O1N	85.56(14)	131.76(14)
O7-Dy1-O2N	124.48(14)	100.99(14)
O7-Dy1-OXS	77.94(13)	77.04(13)
O1-Zn1-O3	76.27(16)	77.00(15)
O1-Zn1-OYS	94.63(15)	96.21(15)
O3-Zn1-OYS	104.75(17)	100.92(17)
N1-Zn1-N2	84.7(2)	85.08(17)

Table A6.4.- Bond lengths (Å) and angles (°) for compound **46**. Note that when referring to fragment A O7 and O8 belong to ligand B and vice versa. OXS and OYS are O1S and O2S for fragment A and O3S and O4S for fragment B.

Compound	**46 (A)**	**46 (B)**
Dy1⋯Zn1	3.3695(12)	3.3699(10)
Dy1-O1	2.263(7)	2.276(5)
Dy1-O2	2.625(10)	2.650(6)
Dy1-O3	2.329(8)	2.321(6)
Dy1-O4	2.679(9)	2.671(6)
Dy1-O7	2.237(6)	2.243(5)
Dy1-O8	2.693(8)	2.646(6)
Dy1-O1H	2.364(8)	2.401(6)
Dy1-O2H	2.398(10)	2.419(6)
Dy1-OXS	2.387(6)	2.374(6)
Zn1-N1	2.112(8)	2.107(7)
Zn1-N2	2.184(9)	2.208(6)
Zn1-O1	2.074(8)	2.113(5)
Zn1-O3	1.975(8)	1.978(6)
Zn1-OYS	1.960(6)	1.963(5)
Dy1-O1-Zn1	101.9(4)	100.3(2)
Dy1-O3-Zn1	102.8(4)	102.9(3)
O1-Dy1-O3	68.2(3)	68.1(2)
O1-Dy1-O7	139.8(3)	139.2(2)
O1-Dy1-O1H	81.8(3)	82.6(2)
O1-Dy1-O2H	82.3(3)	78.2(2)
O1-Dy1-OXS	80.4(2)	80.82(19)
O3-Dy1-O7	133.7(3)	135.5(2)
O3-Dy1-O1H	132.0(3)	133.6(2)
O3-Dy1-O2H	67.7(3)	68.5(2)
O3-Dy1-OXS	76.7(3)	78.3(2)
O7-Dy1-O1H	93.3(3)	90.1(2)
O7-Dy1-O2H	134.2(3)	136.5(2)
O7-Dy1-OXS	75.4(2)	75.24(19)
O1-Zn1-O3	78.9(4)	78.0(2)
O1-Zn1-OYS	97.4(3)	97.5(2)
O3-Zn1-OYS	101.4(3)	105.1(2)
N1-Zn1-N2	83.8(4)	84.8(2)

Table A6.5.- Bond lengths (Å) and angles (°) for compound **46**. Note that when referring to fragment C O7 and O8 belong to ligand D and vice versa. OXS and OYS are O1S and O2S for fragment C and O3S and O4S for fragment D.

Compound	**46 (C)**	**46 (D)**
Dy1···Zn1	3.3749(11)	3.3605(12)
Dy1-O1	2.276(6)	2.283(7)
Dy1-O2	2.644(7)	2.702(8)
Dy1-O3	2.325(6)	2.325(6)
Dy1-O4	2.664(6)	2.669(7)
Dy1-O7	2.235(5)	2.241(5)
Dy1-O8	2.670(6)	2.627(7)
Dy1-O1H	2.381(7)	2.398(7)
Dy1-O2H	2.394(6)	2.425(7)
Dy1-OXS	2.403(6)	2.370(6)
Zn1-N1	2.101(7)	2.098(8)
Zn1-N2	2.171(7)	2.199(7)
Zn1-O1	2.095(6)	2.089(6)
Zn1-O3	1.974(6)	1.975(7)
Zn1-OYS	1.971(6)	1.965(6)
Dy1-O1-Zn1	101.0(2)	100.4(2)
Dy1-O3-Zn1	103.2(3)	102.5(3)
O1-Dy1-O3	68.2(2)	68.0(2)
O1-Dy1-O7	138.9(2)	138.5(3)
O1-Dy1-O1H	81.8(2)	82.6(3)
O1-Dy1-O2H	80.9(2)	78.2(3)
O1-Dy1-OXS	79.7(2)	80.1(2)
O3-Dy1-O7	135.5(2)	137.5(2)
O3-Dy1-O1H	69.8(2)	133.2(2)
O3-Dy1-O2H	132.5(2)	68.8(2)
O3-Dy1-OXS	77.8(2)	79.8(2)
O7-Dy1-O1H	133.6(2)	88.4(2)
O7-Dy1-O2H	91.4(2)	135.8(2)
O7-Dy1-OXS	76.0(2)	75.7(2)
O1-Zn1-O3	78.6(2)	78.6(3)
O1-Zn1-OYS	96.9(2)	95.7(3)
O3-Zn1-OYS	103.8(2)	105.1(3)
N1-Zn1-N2	84.7(3)	84.8(3)

Table A6.6.- Bond lengths (Å) and angles (°) for compound **46**. Note that when referring to fragment E O7 and O8 belong to ligand F and vice versa. OXS and OYS are O1S and O2S for fragment E and O3S and O4S for fragment F.

Compound	**46 (E)**	**46 (F)**
Dy1···Zn1	3.3680(10)	3.3838(13)
Dy1-O1	2.286(6)	2.310(7)
Dy1-O2	2.670(7)	2.671(7
Dy1-O3	2.315(6)	2.292(7)
Dy1-O4	2.709(6)	2.660(7)
Dy1-O7	2.238(5)	2.262(6)
Dy1-O8	2.660(7)	2.684(7)
Dy1-O1H	2.388(6)	2.383(6)
Dy1-O2H	2.432(7)	2.395(7)
Dy1-OXS	2.366(6)	2.365(6)
Zn1-N1	2.100(7)	2.121(8)
Zn1-N2	2.197(7)	2.160(8)
Zn1-O1	2.101(6)	2.095(6)
Zn1-O3	1.983(6)	1.988(7)
Zn1-OYS	1.961(6)	1.960(6)
Dy1-O1-Zn1	100.2(2)	100.2(3)
Dy1-O3-Zn1	102.9(3)	104.3(3)
O1-Dy1-O3	68.3(2)	67.0(2)
O1-Dy1-O7	139.2(2)	141.1(2)
O1-Dy1-O1H	84.8(2)	79.4(2)
O1-Dy1-O2H	77.1(2)	83.8(2)
O1-Dy1-OXS	80.9(2)	82.0(2)
O3-Dy1-O7	135.1(2)	137.0(2)
O3-Dy1-O1H	135.5(2)	71.3(2)
O3-Dy1-O2H	69.4(2)	135.6(2)
O3-Dy1-OXS	78.4(2)	78.0(2)
O7-Dy1-O1H	88.2(2)	131.9(3)
O7-Dy1-O2H	137.1(2)	86.5(2)
O7-Dy1-OXS	75.0(2)	76.9(2)
O1-Zn1-O3	78.4(2)	76.8(3)
O1-Zn1-OYS	97.6(2)	96.7(2)
O3-Zn1-OYS	103.9(2)	104.7(3)
N1-Zn1-N2	84.5(3)	84.5(3)

Table A6.7.- Bond lengths (Å) and angles (°) for compound **47**. Note that when referring to fragment A O7 and O8 belong to ligand B and vice versa. OXS and OYS are O1S and O2S for fragment A and O3S and O4S for fragment B.

Compound	**47 (A)**	**47 (B)**
Dy1···Zn1	3.3990(4)	3.4098(4)
Dy1-O1	2.270(2)	2.291(2)
Dy1-O2	2.667(3)	2.644(3)
Dy1-O3	2.316(2)	2.331(3)
Dy1-O4	2.670(2)	2.658(3)
Dy1-O7	2.238(2)	2.238(2)
Dy1-O8	2.597(3)	2.674(3)
Dy1-O1H	2.387(2)	2.358(3)
Dy1-O2H	2.416(2)	2.377(3)
Dy1-OXS	2.437(2)	2.440(2)
Zn1-N1	2.093(3)	2.103(3)
Zn1-N2	2.163(3)	2.157(3)
Zn1-O1	2.074(2)	2.068(3)
Zn1-O3	1.970(2)	1.961(2)
Zn1-OYS	2.000(2)	1.996(2)
Dy1-O1-Zn1	102.89(9)	102.81(10)
Dy1-O3-Zn1	104.65(9)	104.91(11)
O1-Dy1-O3	67.08(7)	67.13(9)
O1-Dy1-O7	138.24(9)	140.41(9)
O1-Dy1-O1H	81.78(8)	80.09(9)
O1-Dy1-O2H	78.19(9)	81.85(9)
O1-Dy1-OXS	79.39(7)	79.69(8)
O3-Dy1-O7	135.76(8)	134.27(8)
O3-Dy1-O1H	133.15(8)	70.43(9)
O3-Dy1-O2H	69.29(8)	133.89(9)
O3-Dy1-OXS	77.61(7)	75.50(8)
O7-Dy1-O1H	90.72(8)	134.34(9)
O7-Dy1-O2H	137.49(9)	91.29(9)
O7-Dy1-OXS	75.16(8)	76.80(8)
O1-Zn1-O3	77.54(9)	78.70(10)
O1-Zn1-OYS	94.58(9)	95.74(10)
O3-Zn1-OYS	102.70(9)	99.66(10)
N1-Zn1-N2	85.53(10)	84.92(12)

Table A6.8.- Bond lengths (Å) and angles (°) for compound **48**. Note that when referring to fragment A O7 and O8 belong to ligand B and vice versa. OXS and OYS are O1S and O2S for fragment A and O3S and O4S for fragment B.

Compound	**48 (A)**	**48 (B)**
Dy1···Zn1	3.3888(13)	3.3836(13)
Dy1-O1	2.316(6)	2.309(7)
Dy1-O2	2.623(7)	2.674(7)
Dy1-O3	2.314(7)	2.332(7)
Dy1-O4	2.657(7)	2.688(7)
Dy1-O7	2.247(7)	2.269(7)
Dy1-O8	2.772(7)	2.723(8)
Dy1-O1T	2.371(7)	2.373(7)
Dy1-O1M	2.412(7)	2.407(6)
Dy1-OXS	2.354(7)	2.364(6)
Zn1-N1	2.115(8)	2.112(9)
Zn1-N2	2.188(9)	2.183(8)
Zn1-O1	2.102(7)	2.097(7)
Zn1-O3	1.972(7)	1.991(7)
Zn1-OYS	1.973(7)	1.969(7)
Dy1-O1-Zn1	100.1(3)	100.2(3)
Dy1-O3-Zn1	104.2(3)	102.7(3)
O1-Dy1-O3	65.7(2)	66.5(2)
O1-Dy1-O7	139.3(2)	139.2(2)
O1-Dy1-O1T	94.5(2)	95.5(3)
O1-Dy1-O1M	85.5(2)	84.1(2)
O1-Dy1-OXS	81.2(2)	81.4(2)
O3-Dy1-O7	137.8(2)	137.3(2)
O3-Dy1-O1T	141.6(3)	142.6(2)
O3-Dy1-O1M	72.7(2)	73.7(2)
O3-Dy1-OXS	80.5(3)	81.5(2)
O7-Dy1-O1T	78.7(3)	77.9(2)
O7-Dy1-O1M	128.7(2)	129.4(2)
O7-Dy1-OXS	74.2(2)	73.3(2)
O1-Zn1-O3	76.1(3)	76.9(3)
O1-Zn1-OYS	97.5(3)	96.3(3)
O3-Zn1-OYS	107.0(3)	107.0(3)
N1-Zn1-N2	85.3(3)	85.1(3)

Table A6.9.- Bond lengths (Å) and angles (°) for compound **49**. Note that when referring to fragment A O7 and O8 belong to ligand B and vice versa. OXS and OYS are O1S and O2S for fragment A and O3S and O4S for fragment B.

Compound	**49 (A)**	**49 (B)**
Dy1···Zn1	3.4063(6)	3.4115(6)
Dy1-O1	2.320(4)	2.328(4)
Dy1-O2	2.683(4)	2.672(4)
Dy1-O3	2.358(4)	2.332(3)
Dy1-O4	2.654(4)	2.631(4)
Dy1-O7	2.279(4)	2.260(3)
Dy1-O8	2.787(4)	2.920(4)
Dy1-O1C/D	2.300(4)	2.275(4)
Dy1-O2C/D	2.300(4)	2.305(4)
Dy1-OXS	2.422(4)	2.427(4)
Zn1-N1	2.087(4)	2.102(4)
Zn1-N2	2.228(4)	2.202(4)
Zn1-O1	2.110(3)	2.104(3)
Zn1-O3	1.947(4)	1.952(4)
Zn1-OYS	1.959(4)	1.963(4)
Dy1-O1-Zn1	100.39(14)	100.53(14)
Dy1-O3-Zn1	104.19(15)	105.22(15)
O1-Dy1-O3	65.77(12)	65.87(12)
O1-Dy1-O7	136.16(13)	136.09(13)
O1-Dy1-O1C/D	92.38(13)	85.10(13)
O1-Dy1-O2C/D	85.39(13)	94.48(13)
O1-Dy1-OXS	79.85(12)	79.34(12)
O3-Dy1-O7	136.53(13)	135.70(13)
O3-Dy1-O1C/D	71.52(13)	132.08(13)
O3-Dy1-O2C/D	132.12(13)	72.91(13)
O3-Dy1-OXS	78.57(13)	77.48(12)
O7-Dy1-O1C/D	127.92(13)	91.76(13)
O7-Dy1-O2C/D	90.85(13)	126.19(13)
O7-Dy1-OXS	72.39(12)	72.67(12)
O1-Zn1-O3	77.41(14)	77.19(14)
O1-Zn1-OYS	97.76(14)	98.62(14)
O3-Zn1-OYS	107.15(16)	105.62(16)
N1-Zn1-N2	83.98(16)	84.43(16)

2. Continuous Shape Measurements.

The nearer the value to zero, the better fits to an ideal polyhedron.

Table A6.10.- Continuous Shape Measurements for the ZnN_2O_3 coordination environment in compounds **45-49**.

PP-5 1 D5h Pentagon
vOC-5 2 C4v Vacant octahedron
TBPY-5 3 D3h Trigonal bipyramid
SPY-5 4 C4v Spherical square pyramid
JTBPY-5 5 D3h Johnson trigonal bipyramid J12

Structure [ML5]	PP-5	vOC-5	TBPY-5	SPY-5	JTBPY-5
Zn1A (45)	30.883	2.069	4.102	**0.826**	6.170
Zn1B (45)	30.574	1.943	5.705	**0.624**	7.745
Zn1A (46)	30.273	1.936	5.796	**0.564**	8.156
Zn1B (46)	30.207	2.008	5.339	**0.544**	7.160
Zn1C (46)	29.802	1.916	5.709	**0.512**	7.677
Zn1D (46)	30.576	2.110	4.658	**0.623**	6.550
Zn1E (46)	30.695	1.988	5.233	**0.513**	7.127
Zn1F (46)	30.371	2.073	5.070	**0.581**	7.187
Zn1A (47)	30.658	2.035	4.934	**0.645**	6.981
Zn1B (47)	30.639	1.877	5.929	**0.596**	8.104
Zn1A (48)	29.484	2.070	5.163	**0.628**	7.084
Zn1B (48)	29.876	1.989	4.631	**0.644**	6.592
Zn1A (49)	29.785	2.036	5.014	**0.666**	6.580
Zn1B (49)	29.966	2.014	5.532	**0.572**	7.306

Table A6.11.- Continuous Shape Measurements for the DyO_9 coordination environment in compounds **45-49**. Note that we have considered a DyO_9 coordination environment also for fragment B in **49**.

EP-9	1 D9h	Enneagon
OPY-9	2 C8v	Octagonal pyramid
HBPY-9	3 D7h	Heptagonal bipyramid
JTC-9	4 C3v	Johnson triangular cupola J3
JCCU-9	5 C4v	Capped cube J8
CCU-9	6 C4v	Spherical-relaxed capped cube
JCSAPR-9	7 C4v	Capped square antiprism J10
CSAPR-9	8 C4v	Spherical capped square antiprism
JTCTPR-9	9 D3h	Tricapped trigonal prism J51
TCTPR-9	10 D3h	Spherical tricapped trigonal prism
JTDIC-9	11 C3v	Tridiminished icosahedron J63
HH-9	12 C2v	Hula-hoop
MFF-9	13 Cs	Muffin

Structure [ML9]	EP-9	OPY-9	HBPY-9	JTC-9	JCCU-9	CCU-9	JCSAPR-9	CSAPR-9	JTCTPR-9	TCTPR-9	JTDIC-9	HH-9	MFF-9
Dy1A (45)	35.418	22.342	15.827	15.669	7.227	6.578	2.809	2.466	4.069	3.142	12.606	9.313	**2.258**
Dy1B (45)	35.721	21.181	18.504	15.026	9.228	8.363	3.291	**2.002**	3.393	2.396	10.858	9.996	2.239
Dy1A (46)	32.801	22.892	19.206	14.458	9.649	8.285	2.799	**1.615**	2.281	2.348	10.820	9.451	2.197
Dy1B (46)	34.343	23.519	18.381	15.168	9.519	8.837	2.360	1.800	2.221	**1.745**	11.618	9.374	2.001
Dy1C (46)	32.933	23.186	18.463	14.037	9.555	8.666	2.954	**1.728**	2.219	2.179	11.021	9.461	2.226
Dy1D (46)	34.463	23.473	17.669	15.047	8.662	8.383	2.043	1.883	2.314	**1.850**	11.822	9.533	1.919
Dy1E (46)	34.223	23.371	17.665	15.309	9.447	8.354	2.448	2.199	2.422	**2.022**	11.523	8.651	2.053
Dy1F (46)	33.965	23.078	16.642	14.745	8.907	8.109	2.368	2.034	2.267	**1.969**	11.790	9.181	2.015
Dy1A (47)	34.725	23.212	18.064	15.228	9.020	8.633	2.187	1.930	2.364	**1.721**	11.830	9.612	1.965
Dy1B (47)	33.220	23.181	18.136	14.043	9.074	8.249	2.995	**1.871**	2.160	2.084	11.350	9.306	2.430
Dy1A (48)	31.657	22.483	15.048	13.022	8.487	7.865	2.663	2.367	2.481	2.749	11.129	8.003	**2.137**
Dy1B (48)	32.391	22.093	14.336	13.533	8.476	7.680	2.657	2.421	2.906	3.024	11.121	7.508	**2.012**
Dy1A (49)	32.203	22.968	17.610	13.670	7.767	7.351	3.297	2.215	**2.115**	2.517	10.731	9.002	2.473
Dy1B (49)	31.446	22.685	18.572	13.769	8.921	8.531	3.307	**2.207**	2.233	3.051	10.410	9.112	2.676

Table A6.12.- Continuous Shape Measurements for the DyO_8 coordination environment in compound **49** (fragment B).

OP-8	1 D8h	Octagon
HPY-8	2 C7v	Heptagonal pyramid
HBPY-8	3 D6h	Hexagonal bipyramid
CU-8	4 Oh	Cube
SAPR-8	5 D4d	Square antiprism
TDD-8	6 D2d	Triangular dodecahedron
JGBF-8	7 D2d	Johnson – Gyrobifastigium (J26)
JETBPY-8	8 D3h	Johnson – Elongated triangular bipyramid (J14)
JBTP-8	9 C2v	Johnson – Biaugmented trigonal prism (J50)
BTPR-8	10 C2v	Biaugmented trigonal prism
JSD-8	11 D2d	Snub disphenoid (J84)
TT-8	12 Td	Triakis tetrahedron
ETBPY-8	13 D3h	Elongated trigonal bipyramid (see 8)

Structure [ML8]	**OP-8**	**HPY-8**	**HBPY-8**	**CU-8**	**SAPR-8**	**TDD-8**	**JGBF-8**	**JETBPY-8**	**JBTP-8**	**BTPR-8**	**JSD-8**	**TT-8**	**ETBPY-8**
Dy1B (49)	30.496	22.132	15.135	11.424	3.865	3.808	13.005	22.467	2.369	**1.628**	4.215	12.197	22.119

3. Additional Figures.

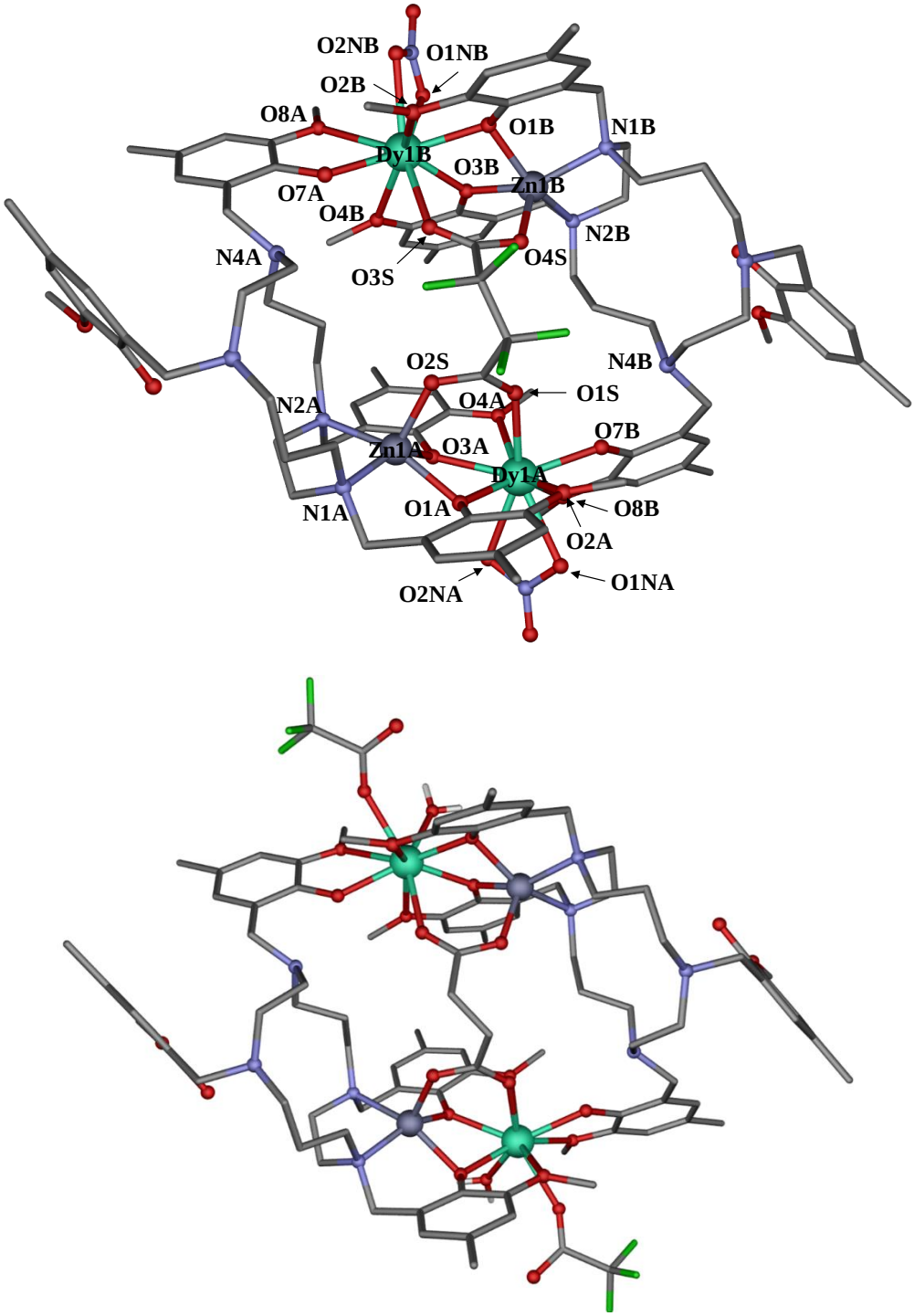

Figure A6.1.- Labelled coordination environment for Zn^{II} and Dy^{III} ions in **45** (top) and perspective view for **48b** (bottom). The rest of the structures follow the same labelling. For hfac, $CF_3CO_2^-$ and dbm "H", "T" and "C/D" letters are used respectively. In case of compound **46**, the two other independent molecules are labelled with C, D, E and F letters.

4. Experimental XRPD.

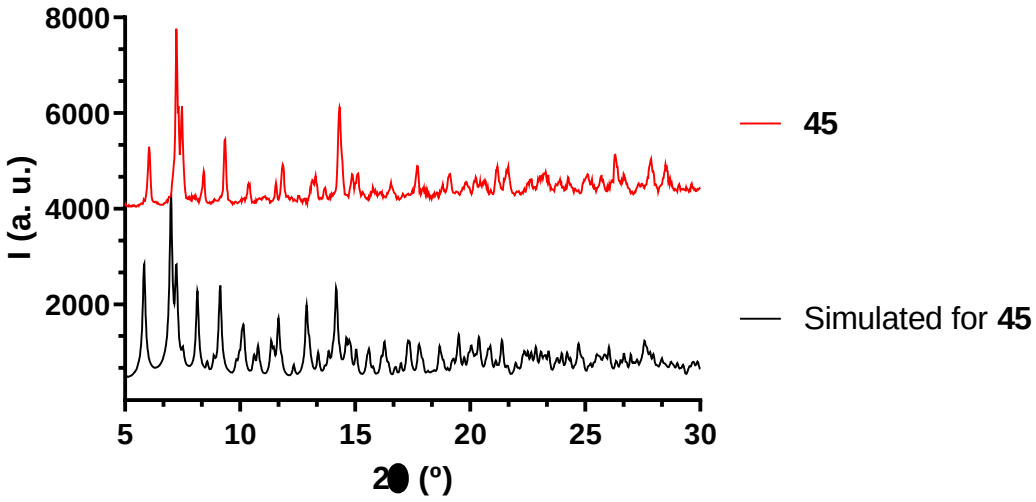

Figure A6.2.- For **45**, simulated pattern from single-crystal X-ray diffraction (black line) and experimental XRPD (red).

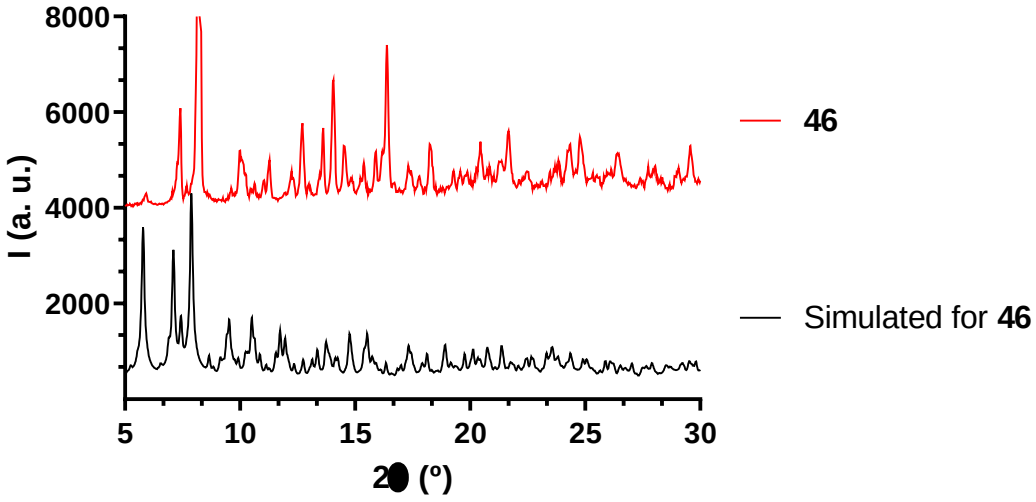

Figure A6.3.- For **46**, simulated pattern from single-crystal X-ray diffraction (black line) and experimental XRPD (red).

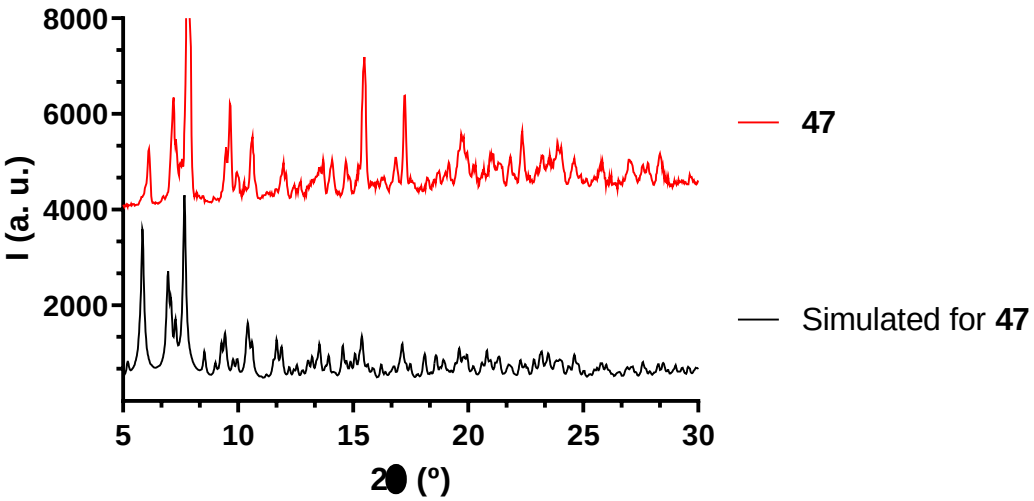

Figure A6.4.- For **47**, simulated pattern from single-crystal X-ray diffraction (black line) and experimental XRPD (red).

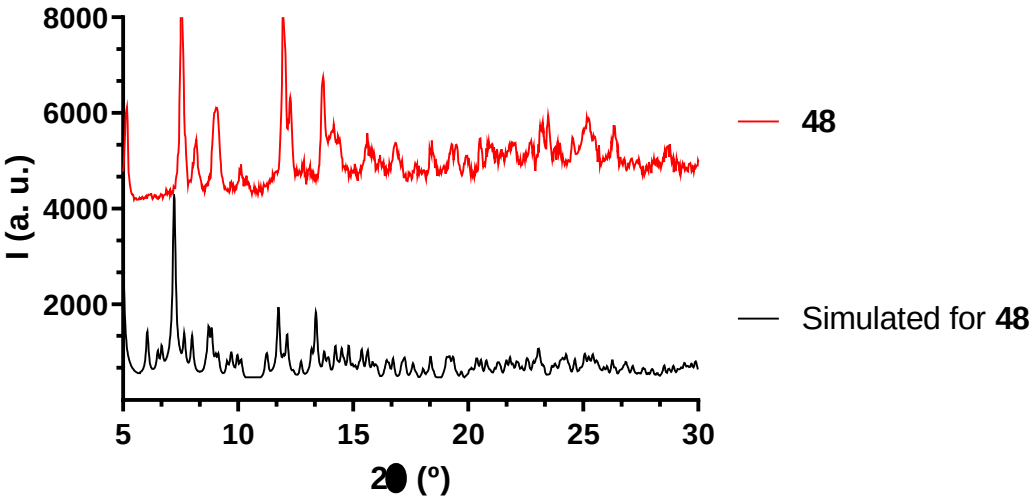

Figure A6.5.- For **48**, simulated pattern from single-crystal X-ray diffraction (black line) and experimental XRPD (red).

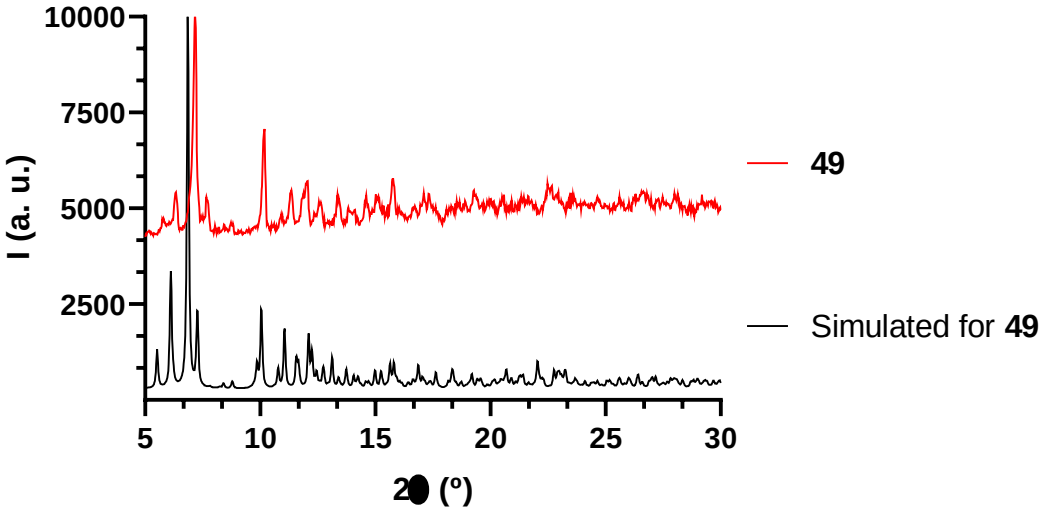

Figure A6.6.- For **49**, simulated pattern from single-crystal X-ray diffraction (black line) and experimental XRPD (red).

5. Magnetic measurements.

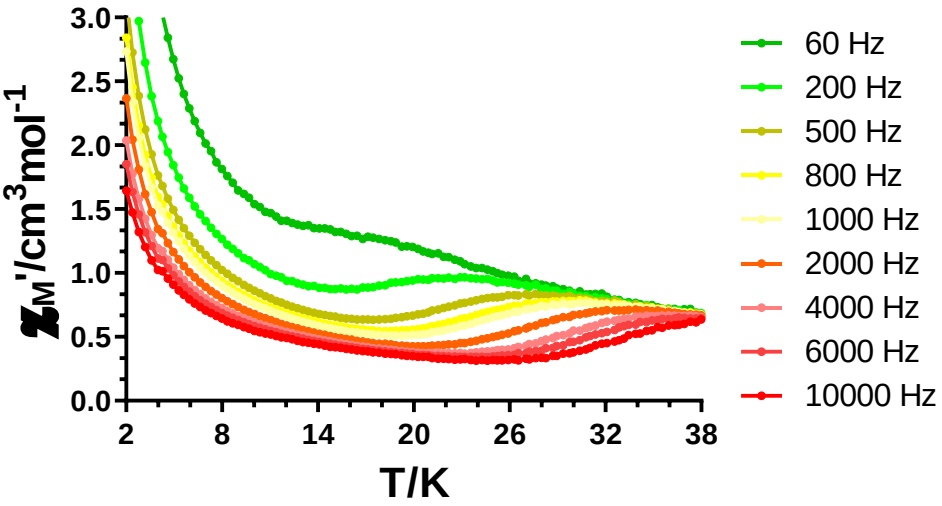

Figure A6.7.- Temperature dependence of the in phase components of the *ac* susceptibility in a zero applied field for **45**.

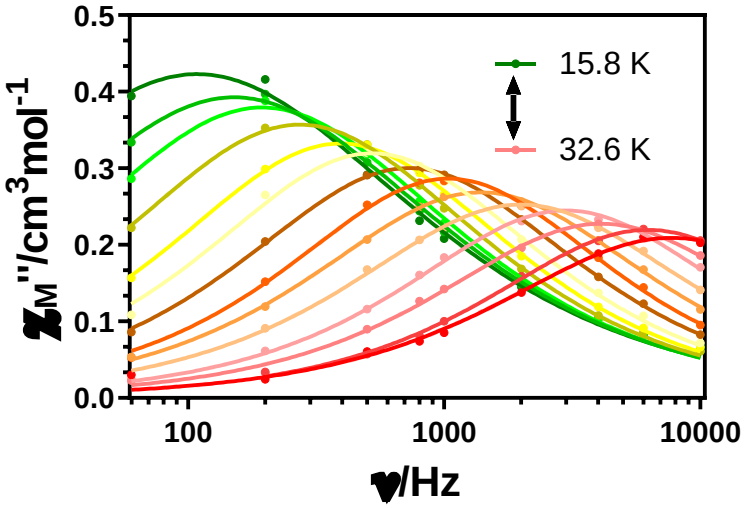

Figure A6.8.- Variable-temperature frequency dependence of the χ_M'' signal under zero applied field for **45**. Solid lines represent the best fitting of the experimental data to the Debye model.

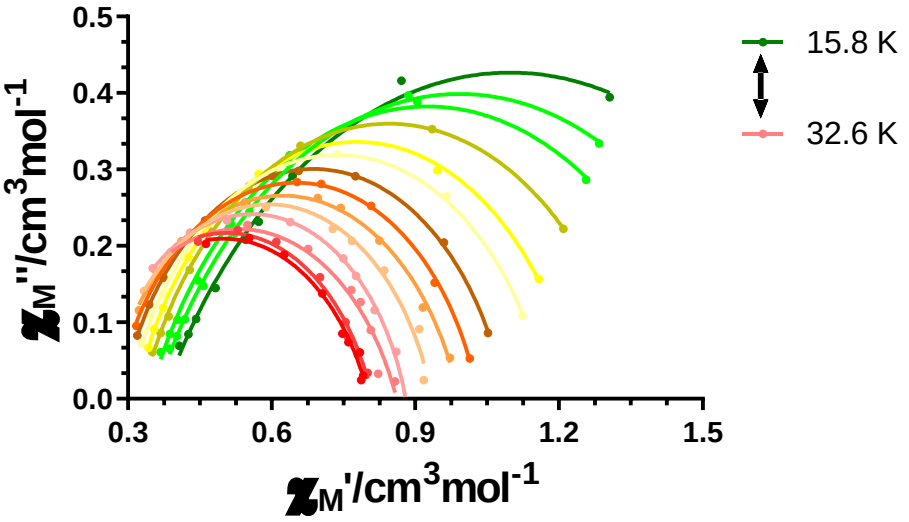

Figure A6.9.- Cole-Cole plots under zero field for **45**. Solid lines represent the best fit to the generalized Debye model.

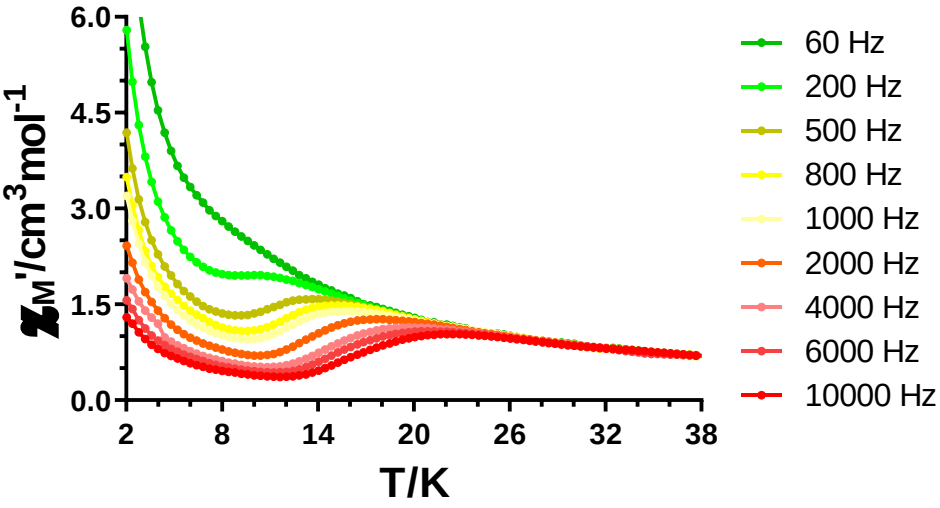

Figure A6.10.- Temperature dependence of the in phase components of the *ac* susceptibility in a zero applied field for **46**.

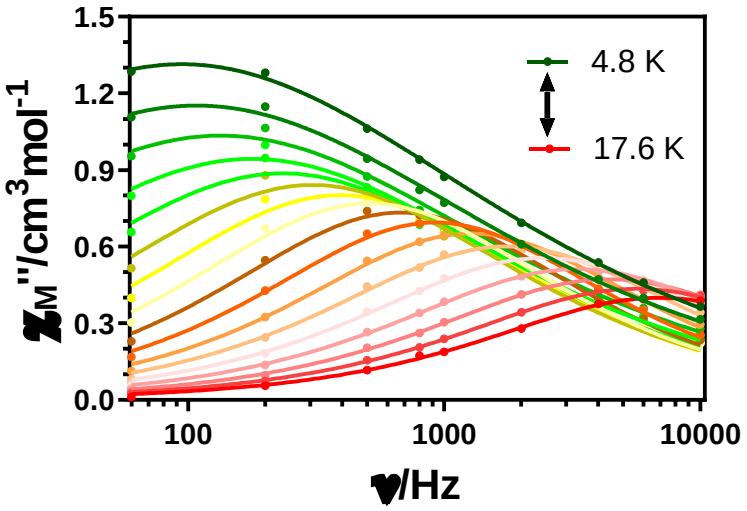

Figure A6.11.- Variable-temperature frequency dependence of the χ_M'' signal under zero applied field for **46**. Solid lines represent the best fitting of the experimental data to the Debye model.

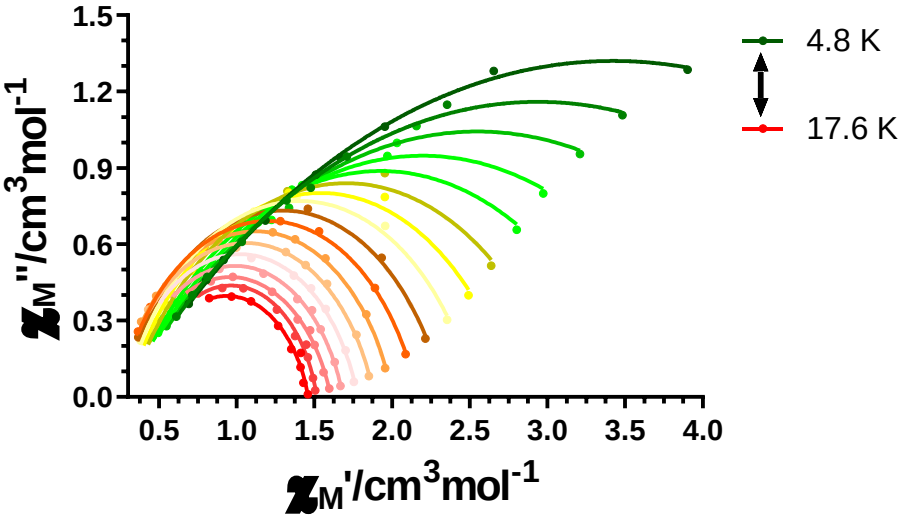

Figure A6.12.- Cole-Cole plots under zero field for **46**. Solid lines represent the best fit to the generalized Debye model.

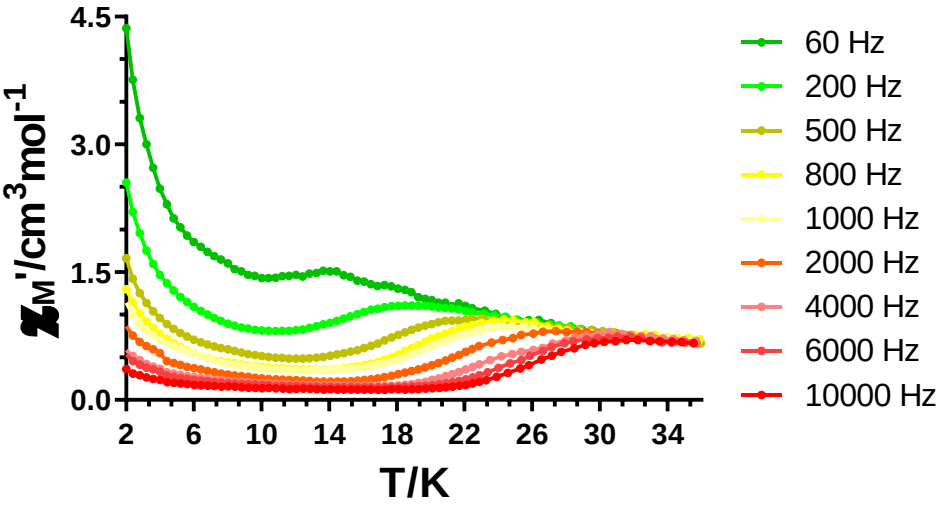

Figure A6.13.- Temperature dependence of the in phase components of the *ac* susceptibility in a zero applied field for **47**.

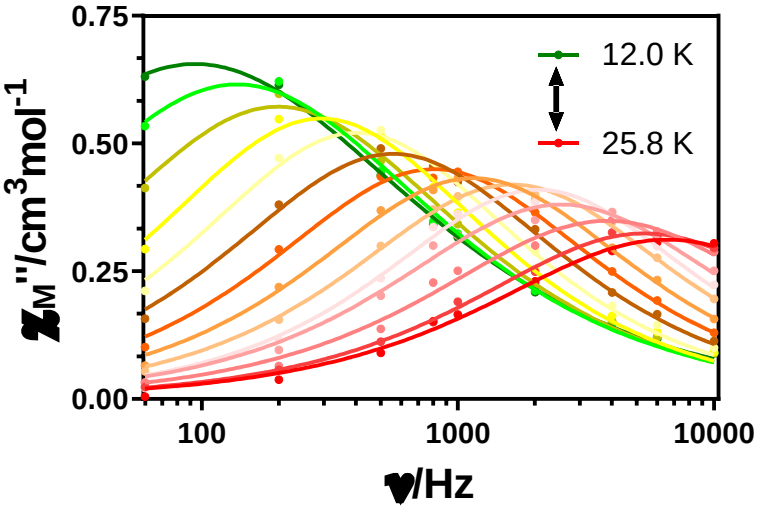

Figure A6.14.- Variable-temperature frequency dependence of the χ_M'' signal under zero applied field for **47**. Solid lines represent the best fitting of the experimental data to the Debye model.

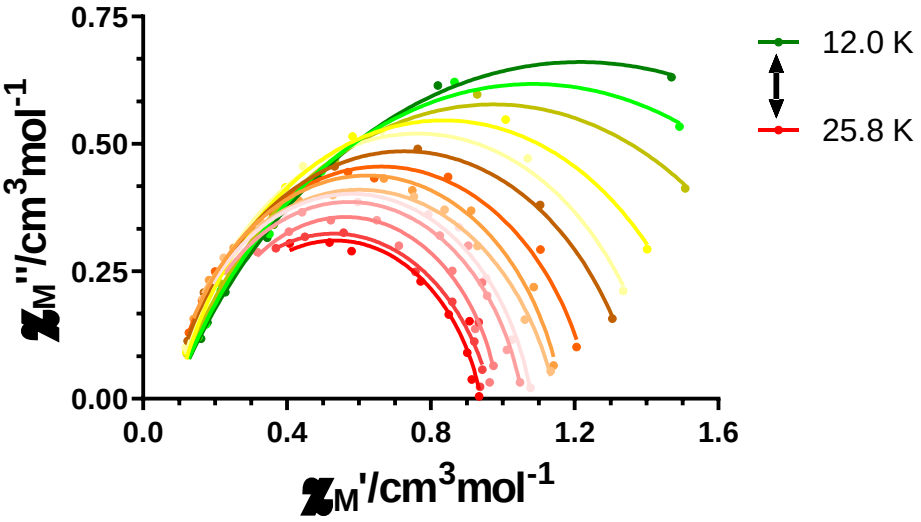

Figure A6.15.- Cole-Cole plots under zero field for **47**. Solid lines represent the best fit to the generalized Debye model.

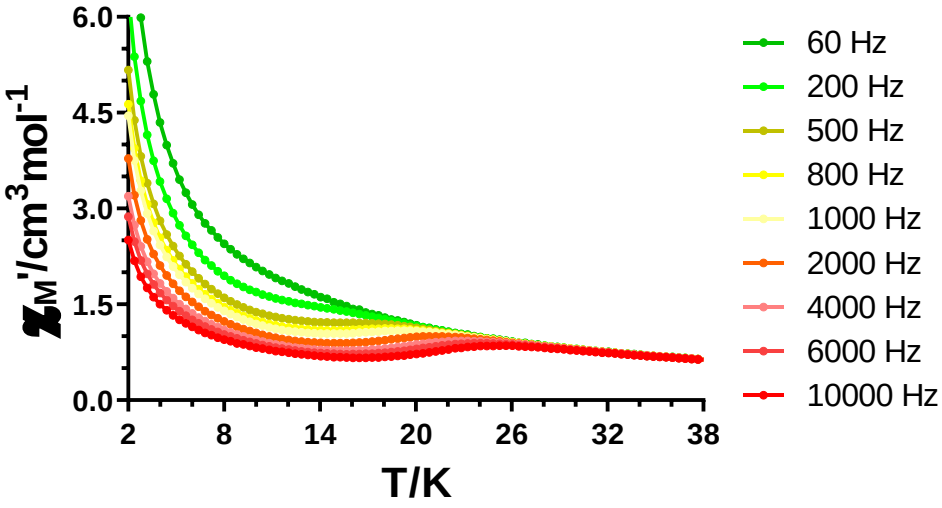

Figure A6.16.- Temperature dependence of the in phase components of the *ac* susceptibility in a zero applied field for **48**.

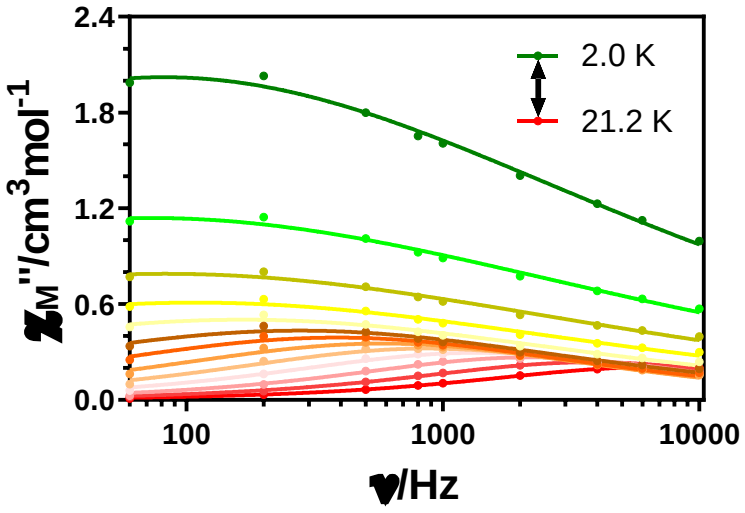

Figure A6.17.- Variable-temperature frequency dependence of the χ_M'' signal under zero applied field for **48**. Solid lines represent the best fitting of the experimental data to the Debye model.

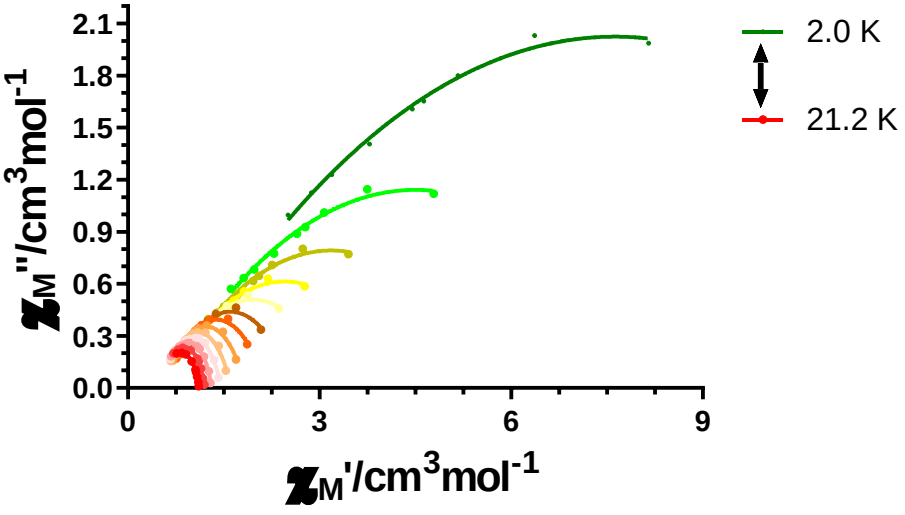

Figure A6.18.- Cole-Cole plots under zero field for **48**. Solid lines represent the best fit to the generalized Debye model.

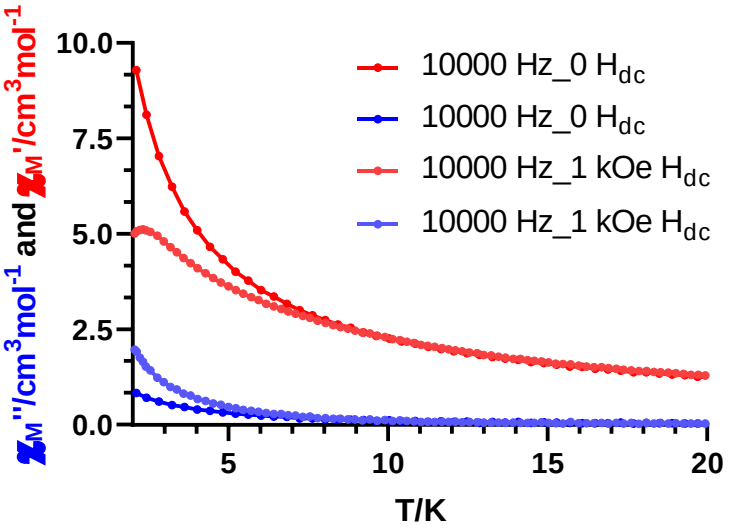

Figure A6.19.- Temperature dependence of the in phase χ_M' (red) and out-of-phase (blue) susceptibility signals for complex **49** under zero and 1 kOe applied *dc* field.

6. *Ab initio* calculations.

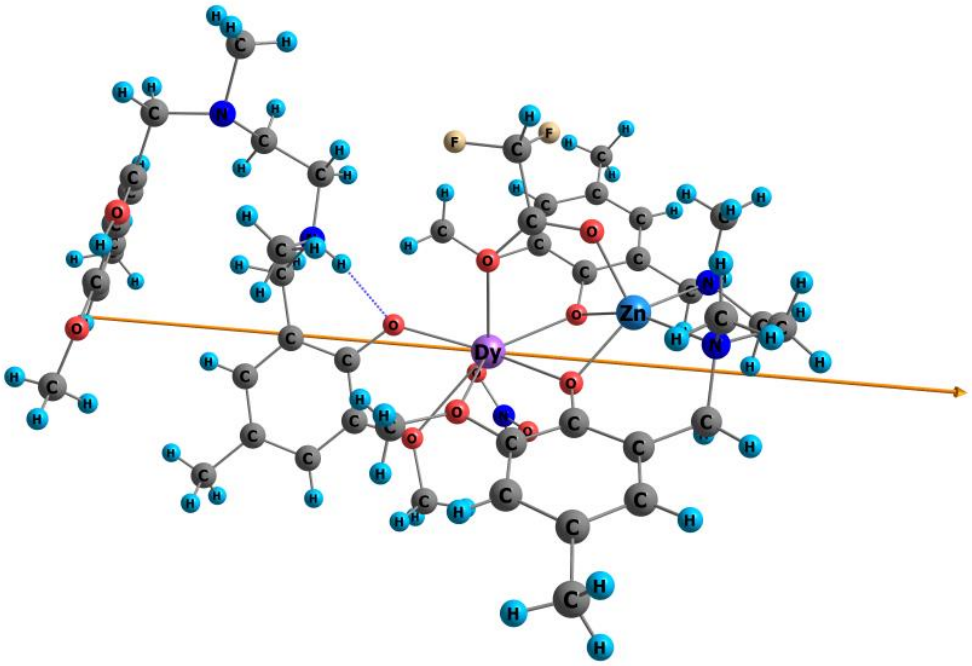

Figure A6.20.- Molecular structure of complex **45** and the easy axis orientation (orange arrow line).

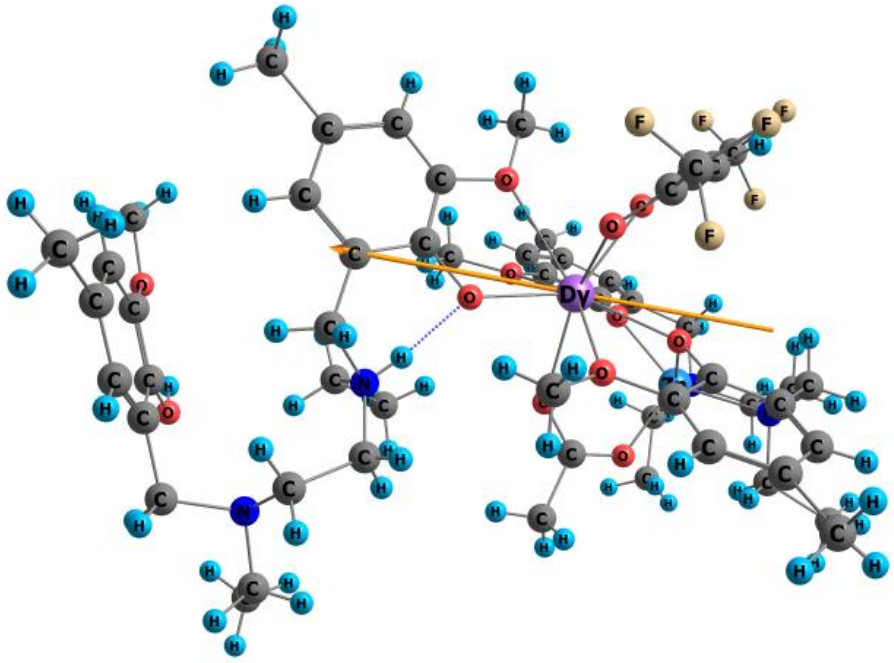

Figure A6.21.- Molecular structure of complex **46** and the easy axis orientation (orange arrow line).

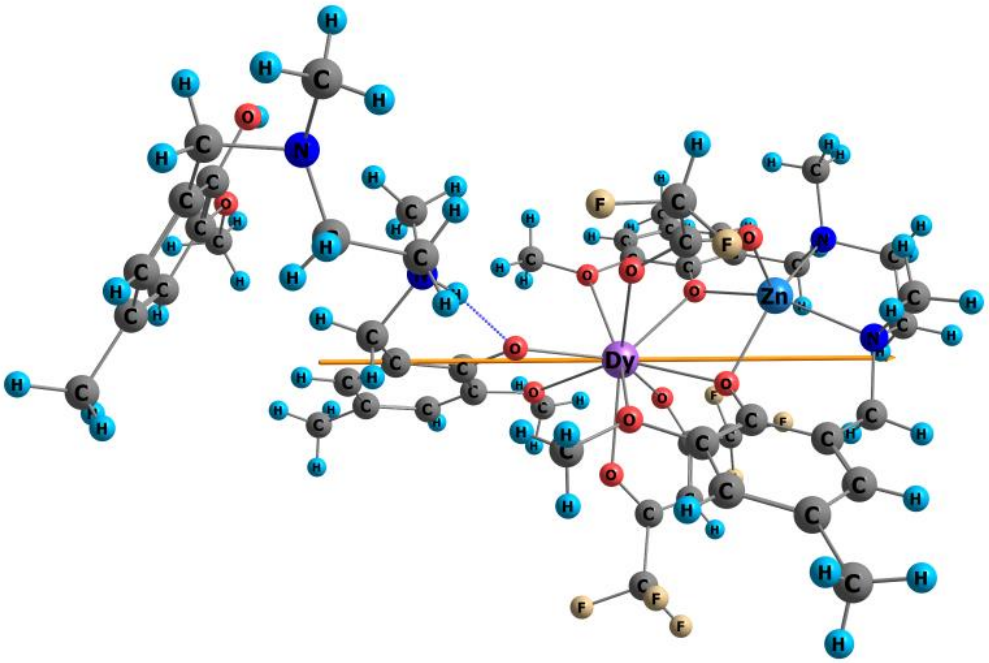

Figure A6.22.- Molecular structure of complex **47** and the easy axis orientation (orange arrow line).

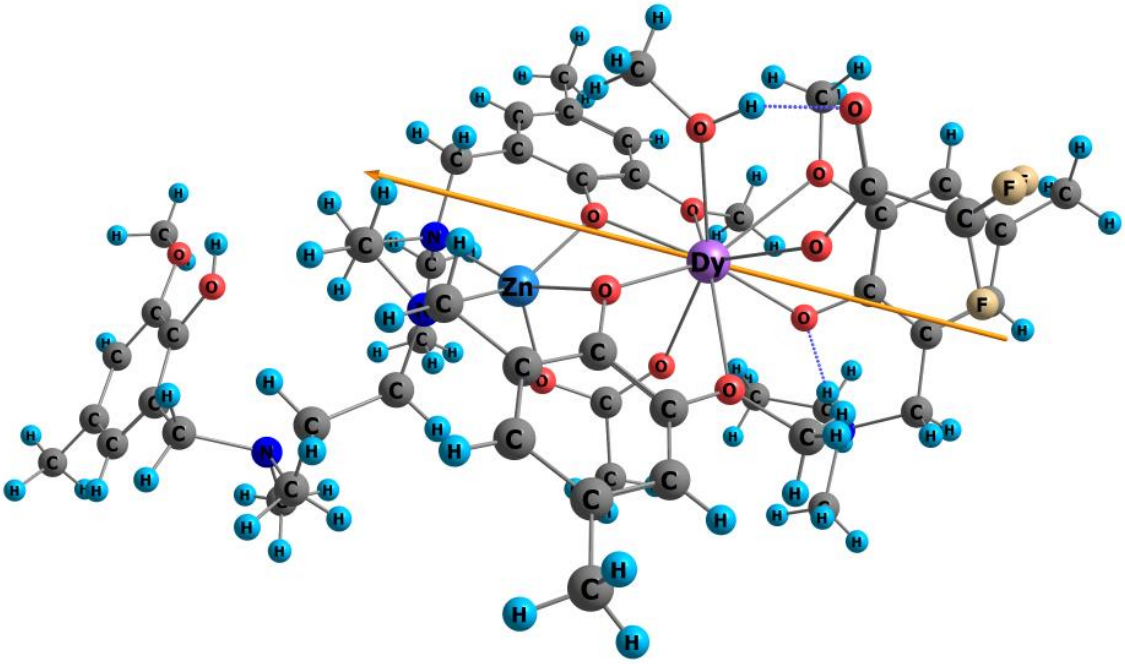

Figure A6.23.- Molecular structure of complex **48** and the easy axis orientation (orange arrow line).

Table A6.13.- The energy splitting of the ground $^6H_{15}$ multiplet**,** principal values of the *g* tensor for each Kramers' doublet and decomposition of the wavefunctions of the components of each Kramers' doublet to the wavefunctions with definite J_z (z is the easy exes for the ground Kramers doublet).

Complex	KD	E, cm^{-1}	g_x	g_y	g_z	$\|J_z\|$ (contribution in %)
45	1	0	0.0004	0.001	19.9	15/2 (99)
	2	210	0.054	0.059	17.16	13/2 (94.4)
	3	345	0.37	0.9	13.6	11/2 (71.8), 9/2 (14.5)
	4	410	3.91	4.15	12.61	3/2 (25.7), 7/2 (20.4), 9/2 (18.7), 1/2 (17.4), 5/2 (10.7)
	5	478	1.1	3.91	9.73	9/2 (38.4), 1/2 (19), 5/2 (15.4), 7/2 (12.9), 11/2 (11.1)
	6	572	1.48	2.36	13.52	7/2 (40.4), 9/2 (23.8), 5/2 (12.5)
	7	640	0.46	0.93	15.83	5/2 (41.6), 3/2 (30.9), 7/2 (18.2), 11/2 (12.3)
	8	813	0.02	0.06	19.4	1/2 (47), 3/2 (31.3), 5/2 (14.3)

Table A6.14.- The energy splitting of the ground $^6H_{15}$ multiplet**,** principal values of the *g* tensor for each Kramers' doublet and decomposition of the wavefunctions of the components of each Kramers' doublet to the wavefunctions with definite J_z (z is the easy exes for the ground Kramers doublet).

Complex	KD	E, cm^{-1}	g_x	g_y	g_z	$\|J_z\|$ (contribution in %)
46	1	0	0.008	0.012	19.85	15/2 (99.1)
	2	172	0.28	0.4	16.94	13/2 (92.7)
	3	247	2.67	5.6	13.38	11/2 (30.4), 5/2 (20), 9/2 (15.2), 7/2 (10)
	4	288	7.64	5.04	1.0	11/2 (35.4), 3/2 (20.8), 9/2 (15.1), 1/2 (12.7), 7/2 (12.1)
	5	370	1.53	2.88	10.94	9/2 (27.3), 1/2 (19.1), 11/2 (18.2), 7/2 (18), 5/2 (15.4)
	6	465	0.78	1.15	14.05	9/2 (33.1), 7/2 (22.4), 3/2 (16.5), 5/2 (10.5), 11/2 (11.2)
	7	533	0.1	0.27	16.1	5/2 (35.7), 7/2 (29.7), 3/2 (19.7)
	8	722	0.016	0.03	19.41	1/2 (42.8), 3/2 (31.5), 5/2 (17)

Table A6.15.- The energy splitting of the ground $^6H_{15}$ multiplet**,** principal values of the *g* tensor for each Kramers' doublet and decomposition of the wavefunctions of the components of each Kramers' doublet to the wavefunctions with definite J_z (z is the easy exes for the ground Kramers doublet).

Complex	KD	E, cm^{-1}	g_x	g_y	g_z	$\|J_z\|$ (contribution in %)
47	1	0	0.005	0.007	19.8	15/2 (99.2)
	2	198	0.14	0.16	17.02	13/2 (96)
	3	318	1.32	2.76	13.44	11/2 (69.7), 9/2 (12)
	4	360	8.58	6.74	3.59	9/2 (25.2), 3/2 (24.4), 1/2 (13.9), 11/2 (10.9)
	5	431	0.64	2.71	10.8	9/2 (28), 1/2 (24.5), 5/2 (18.8), 7/2 (16.6), 11/2 (10.1)
	6	519	0.51	1.41	12.33	9/2 (28.9), 3/2 (26.2), 7/2 (24.2)
	7	564	0.73	1.86	15.63	5/2 (39.3), 7/2 (30.8), 3/2 (13.7)
	8	726	0.013	0.03	19.49	1/2 (42.1), 3/2 (32.7), 5/2 (17.9)

Table A6.16.- The energy splitting of the ground $^6H_{15}$ multiplet**,** principal values of the *g* tensor for each Kramers' doublet and decomposition of the wavefunctions of the components of each Kramers' doublet to the wavefunctions with definite J_z (z is the easy exes for the ground Kramers doublet).

Complex	KD	E, cm^{-1}	g_x	g_y	g_z	$\|J_z\|$ (contribution in %)
48	1	0	0.002	0.003	19.75	15/2 (98.7)
	2	138	0.06	0.13	17.1	13/2 (85.3), 11/2 (10.6)
	3	209	1.62	2.74	13.52	11/2 (38.6), 9/2 (26.4), 5/2 (13.5)
	4	266	3.97	5.52	8.58	3/2 (24.2), 11/2 (22.2), 7/2 (18.7), 1/2 (15.2), 9/2 (10.4)
	5	345	1.24	2.58	10.74	9/2 (25.1), 1/2 (23.2), 5/2 (17.5), 7/2 (15.3), 11/2 (14.9)
	6	447	0.85	1.1	13.91	9/2 (29), 7/2 (23.9), 3/2 (17.3), 11/2 (10.8), 5/2 (10.7)
	7	520	0.24	0.37	16.13	5/2 (37.4), 7/2 (27), 3/2 (20.8)
	8	680	0.024	0.056	19.26	1/2 (46.6), 3/2 (32.5), 5/2 (14.9)

APPENDICES

***mini-Chapter I**: How does the diamagnetic ion influence the SMM behaviour?*

Index:

1. Crystallographic Table.

Table AI.I.- Crystallographic data for compound **50**.

Compound	**50**
Formula	$C_{50}H_{74}N_7O_{19}CdDy$
M_r	1352.06
Crystal system	*monoclinic*
Space group (no.)	*P* 21/c (14)
a (Å)	12.5263(14)
b (Å)	18.648(2)
c (Å)	23.599(2)
α (°)	90
β (°)	98.397(4)
γ (°)	90
V (Å^3)	5453.4(10)
Z	4
D_c (g cm^{-3})	1.647
μ(MoK$_\alpha$) (mm^{-1})	1.830
*T (*K)	100(2)
Observed reflections	14261 (9684)
R_{int}	0.1523
Parameters	713
GOF	1.014
$R_1^{a,b}$	0.1074 (0.0569)
wR_2^c	0.1415 (0.1179)
Largest difference in peak and hole (e Å^{-3})	1.905 and -2.972

[a]$R_1 = \Sigma||F_o| - |F_c||/\Sigma|F_o|$. [b]Values in parentheses for reflections with $I > 2\sigma(I)$. [c]$wR_2 = \{\Sigma[w(F_o^2 - F_c^2)^2]/\Sigma[w(F_o^2)^2]\}^{½}$

2. Hydrogen bonding pattern for 50.

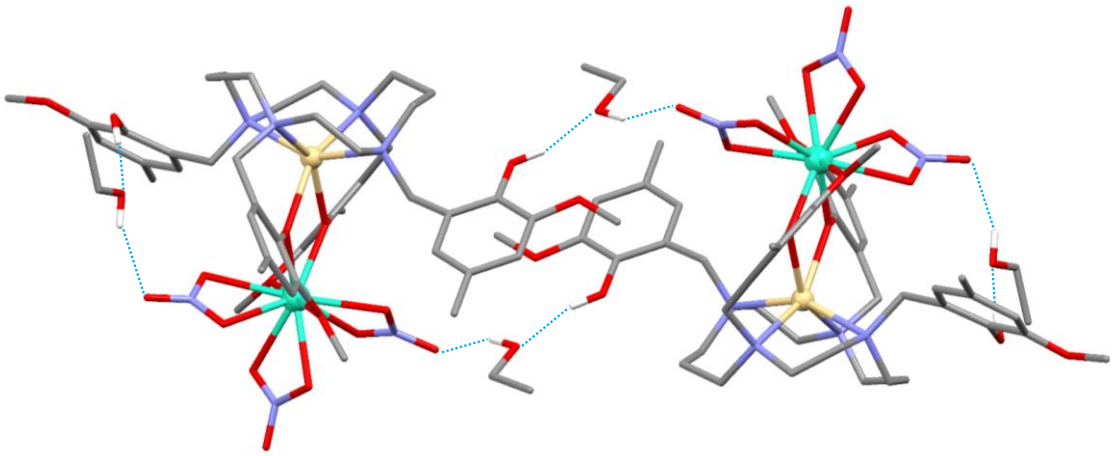

Figure AI.I.- Intermolecular hydrogen bonding pattern for compound **50**.

3. Experimental XRPD.

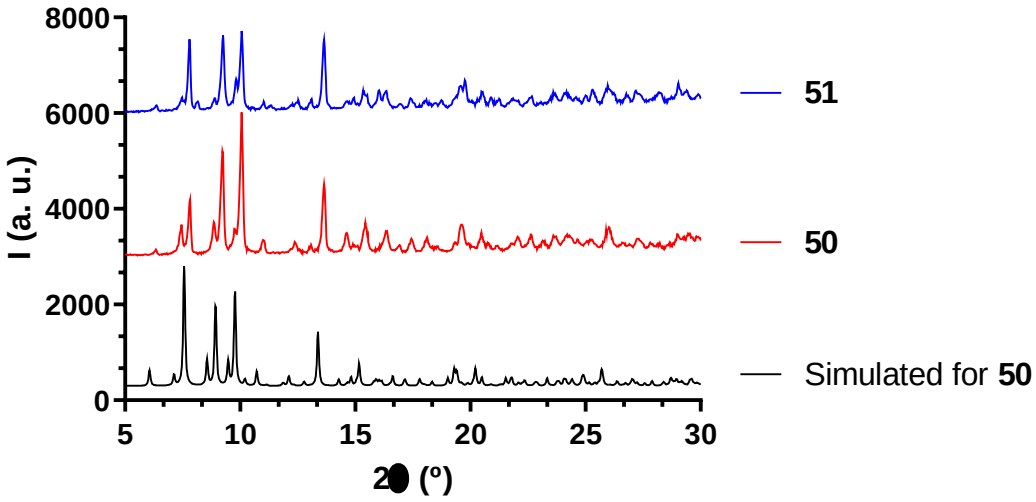

Figure AI.II.- For compounds **50** and **51**, simulated pattern from single-crystal X-ray diffraction of **50** (black line) and experimental XRPD for **50** (red) and **51** (blue).

4. Magnetic measurements.

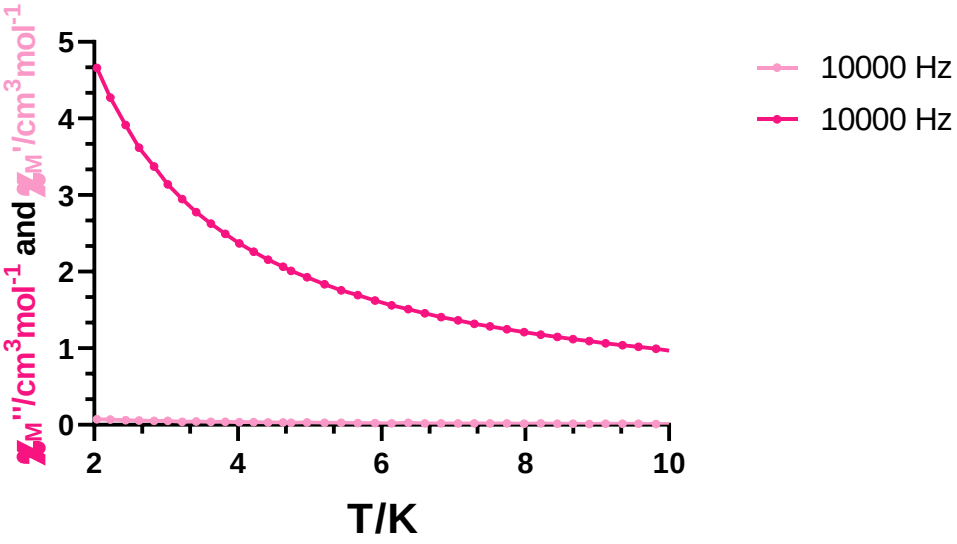

Figure AI.III.- Temperature dependence of the in phase χ_M' (pink) and out-of-phase (light pink) susceptibility signals for complex **50** under zero applied *dc* field.

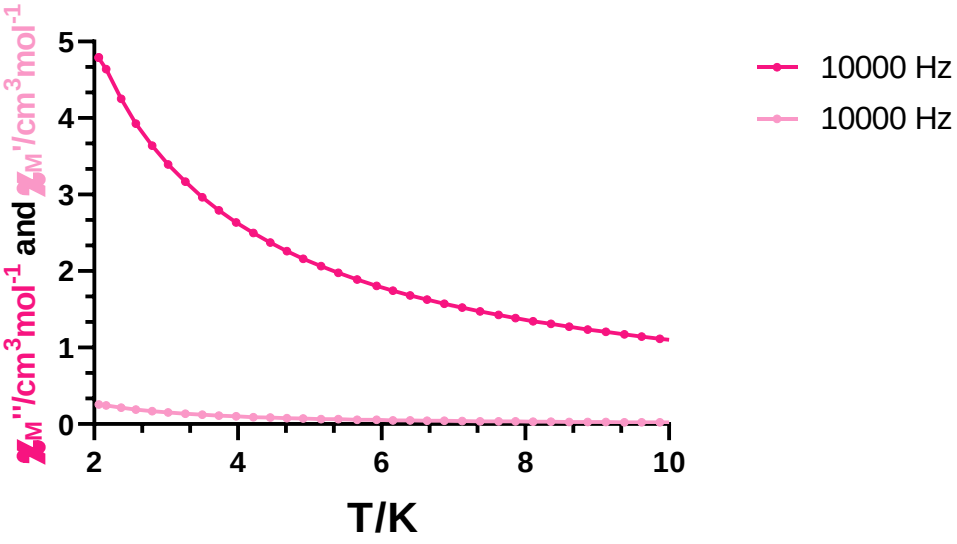

Figure AI.IV.- Temperature dependence of the in phase χ_M' (pink) and out-of-phase (light pink) susceptibility signals for complex **51** under zero applied *dc* field.

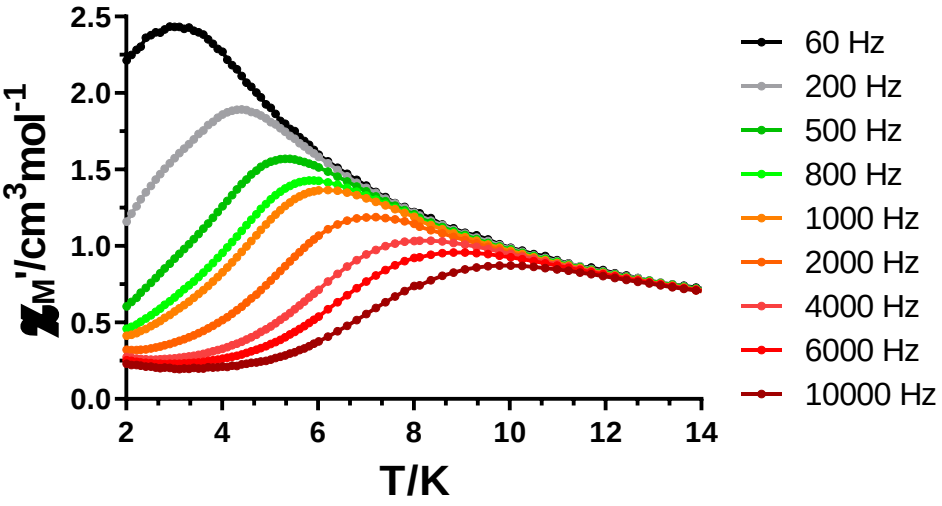

Figure AI.V.- Temperature dependence of the in phase χ_M' susceptibility signals for complex **50** under an applied field of 1000 Oe.

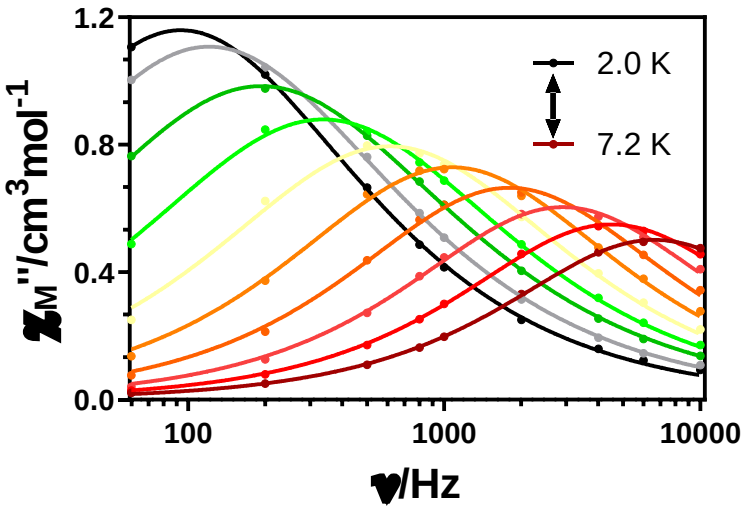

Figure AI.VI.- Variable-temperature frequency dependence of the χ_M'' signal under 1 kOe applied field for **50**. Solid lines represent the best fitting of the experimental data to the Debye model.

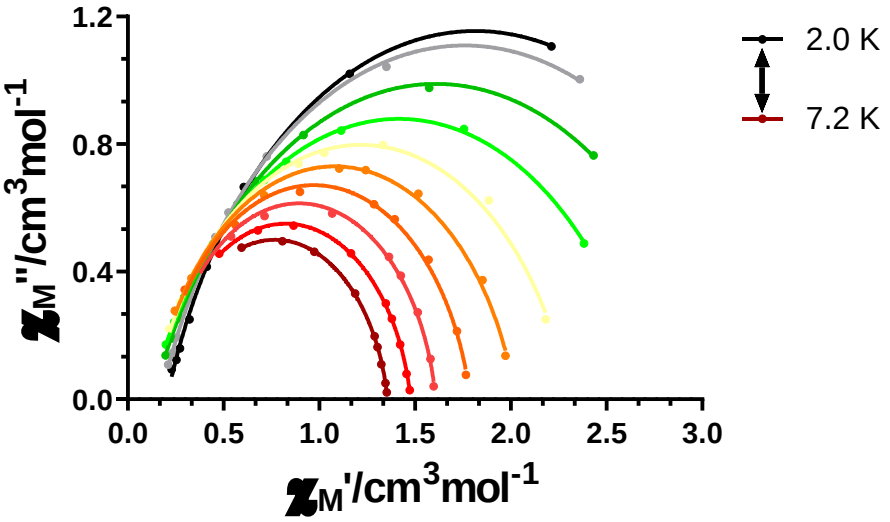

Figure AI.VII.- Cole-Cole plots under 1 kOe field for **50**. Solid lines represent the best fit to the generalized Debye model.

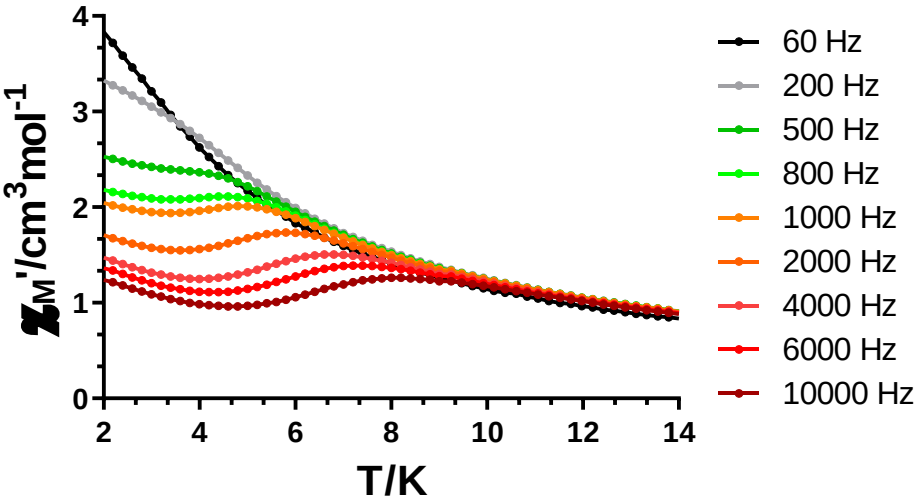

Figure AI.VIII.- Temperature dependence of the in phase χ_M' susceptibility signals for complex **51** under an applied field of 1000 Oe.

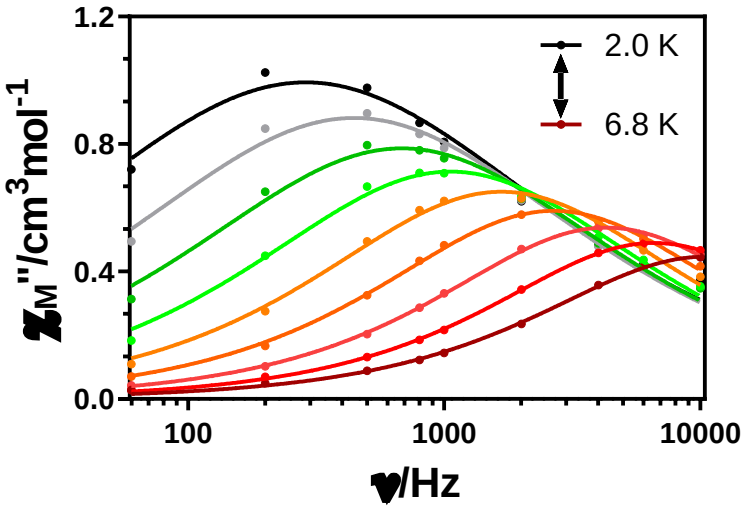

Figure AI.IX.- Variable-temperature frequency dependence of the χ_M'' signal under 1 kOe applied field for **51**. Solid lines represent the best fitting of the experimental data to the Debye model.

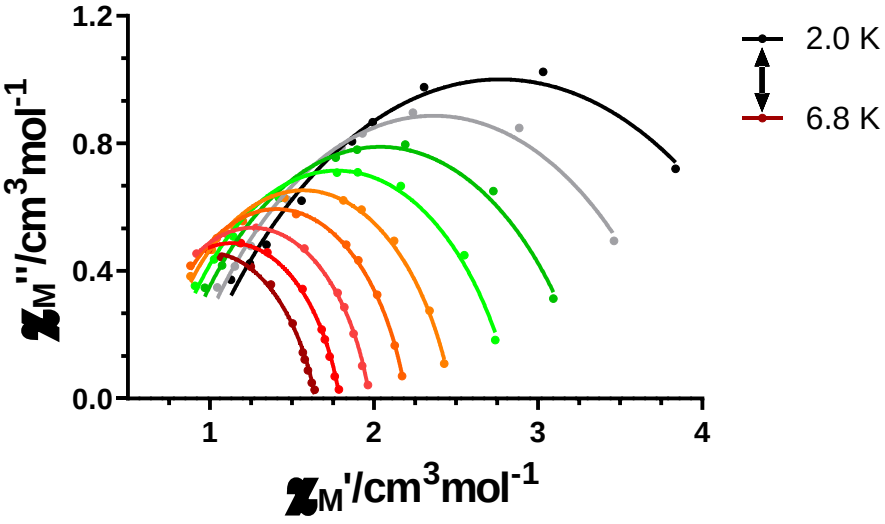

Figure AI.X.- Cole-Cole plots under 1 kOe field for **51**. Solid lines represent the best fit to the generalized Debye model.

APPENDICES

***mini-Chapter II**: Anchoring a tetranuclear $Zn^{II}_2Dy^{III}_2$ based SMM to graphene and graphene oxide surfaces*

Index:

1. Crystallographic Tables.

Table AII.I.- Crystallographic data for compound **52**.

Structure	**52**
Formula	$C_{144}H_{168}N_{10}O_{26}B_2Zn_2Dy_2$
M_r	2932.23
Crystal system	*monoclinic*
Space group (no.)	*I 2/a* (15)
a (Å)	25.7167(5)
b (Å)	16.5637(2)
c (Å)	30.9428(8)
α (°)	90
β (°)	95.107(2)
γ (°)	90
V (Å^3)	13128.2(5)
Z	4
D_c (g cm^{-3})	1.484
μ(CuK_α) (mm^{-1})	7.031
T (K)	150.00(10)
Observed reflections	13384 (8969)
R_{int}	0.0948
Parameters	842
GOF	0.877
R_1[a,b]	0.1022 (0.0620)
wR_2[c]	0.1943 (0.1622)
Largest difference in peak and hole (e Å^{-3})	1.772 and -0.766

[a]$R_1 = \Sigma||F_o| - |F_c||/\Sigma|F_o|$. [b]Values in parentheses for reflections with $I > 2\sigma(I)$. [c]$wR_2 = \{\Sigma[w(F_o^2 - F_c^2)^2]/\Sigma[w(F_o^2)^2]\}^{½}$

Table AII.II.- Bond lengths (Å) and angles (°) for compound **52**.

Compound	**52**
Dy1···Zn1	3.3581(9)
Dy1-O1	2.292(4)
Dy1-O2	2.619(4)
Dy1-O3	2.337(4)
Dy1-O4	2.606(5)
Dy1-O7	2.217(4)
Dy1-O8	2.723(5)
Dy1-O1N	2.434(6)
Dy1-O2N	2.441(6)
Dy1-O1S	2.351(5)
Zn1-N1	2.100(5)
Zn1-N2	2.235(5)
Zn1-O1	2.103(4)
Zn1-O3	1.984(4)
Zn1-O2S	1.960(5)
Dy1-O1-Zn1	99.56(17)
Dy1-O3-Zn1	101.69(17)
O1-Dy1-O3	66.94(14)
O1-Dy1-O7	137.15(16)
O1-Dy1-O1N	78.29(18)
O1-Dy1-O2N	85.42(17)
O1-Dy1-O1S	78.86(16)
O3-Dy1-O7	143.61(17)
O3-Dy1-O1N	75.81(16)
O3-Dy1-O2N	125.64(16)
O3-Dy1-O1S	84.31(16)
O7-Dy1-O1N	128.13(18)
O7-Dy1-O2N	88.03(17)
O7-Dy1-O1S	77.39(16)
O1-Zn1-O3	77.26(17)
O1-Zn1-O2S	97.51(19)
O3-Zn1-O2S	108.21(19)
N1-Zn1-N2	83.7(2)

2. Continuous Shape Measurements.

The nearer the value to zero, the better fits to an ideal polyhedron.

Table AII.III.- Continuous Shape Measurements for the ZnN_2O_3 coordination environment in compound **52**.

PP-5	1 D5h	Pentagon
vOC-5	2 C4v	Vacant octahedron
TBPY-5	3 D3h	Trigonal bipyramid
SPY-5	4 C4v	Spherical square pyramid
JTBPY-5	5 D3h	Johnson trigonal bipyramid J12

Structure [ML5]	PP-5	vOC-5	TBPY-5	SPY-5	JTBPY-5
Zn1 (52)	29.435	1.964	4.696	**0.722**	6.338

Table AII.IV.- Continuous Shape Measurements for the DyO_9 coordination environment in compound **52**.

EP-9	1 D9h	Enneagon
OPY-9	2 C8v	Octagonal pyramid
HBPY-9	3 D7h	Heptagonal bipyramid
JTC-9	4 C3v	Johnson triangular cupola J3
JCCU-9	5 C4v	Capped cube J8
CCU-9	6 C4v	Spherical-relaxed capped cube
JCSAPR-9	7 C4v	Capped square antiprism J10
CSAPR-9	8 C4v	Spherical capped square antiprism
JTCTPR-9	9 D3h	Tricapped trigonal prism J51
TCTPR-9	10 D3h	Spherical tricapped trigonal prism
JTDIC-9	11 C3v	Tridiminished icosahedron J63
HH-9	12 C2v	Hula-hoop
MFF-9	13 Cs	Muffin

Structure [ML9]	EP-9	OPY-9	HBPY-9	JTC-9	JCCU-9	CCU-9	JCSAPR-9
Dy1 (52)	35.501	23.112	17.175	15.511	7.584	6.962	2.686

Structure [ML9]	CSAPR-9	JTCTPR-9	TCTPR-9	JTDIC-9	HH-9	MFF-9
Dy1 (52)	2.376	3.666	2.932	12.153	9.457	**2.175**

3. Experimental XRPD.

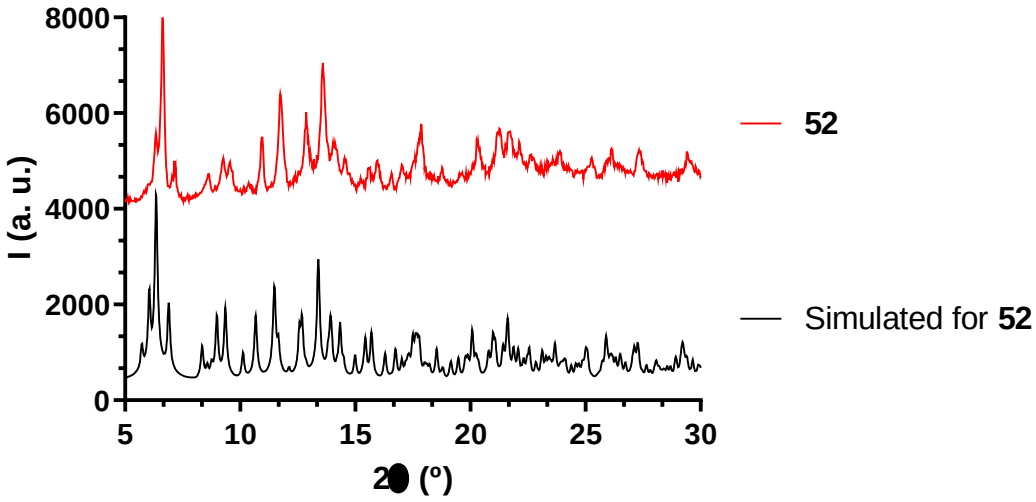

Figure AII.I.- For **52**, simulated pattern from single-crystal X-ray diffraction (black line) and experimental XRPD (red).

4. Magnetic Measurements.

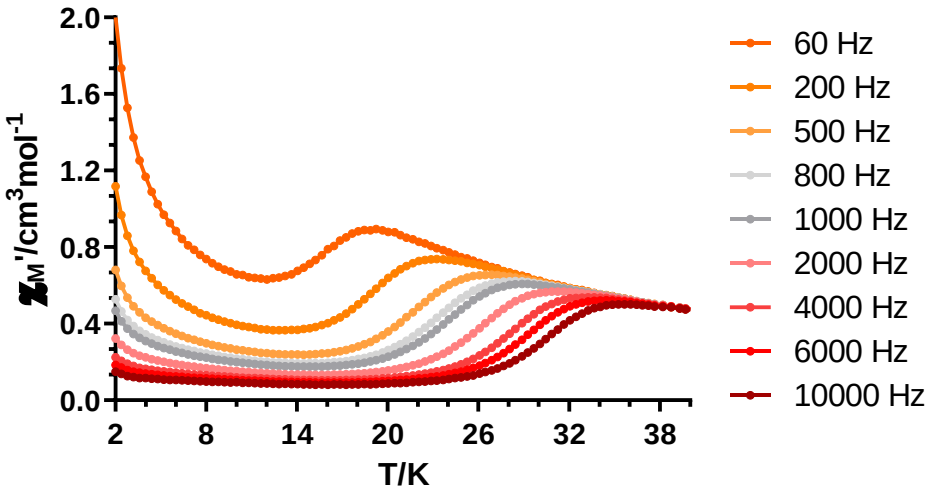

Figure AII.II.- Temperature dependence of the in phase components of the *ac* susceptibility in a zero applied field for **52**.

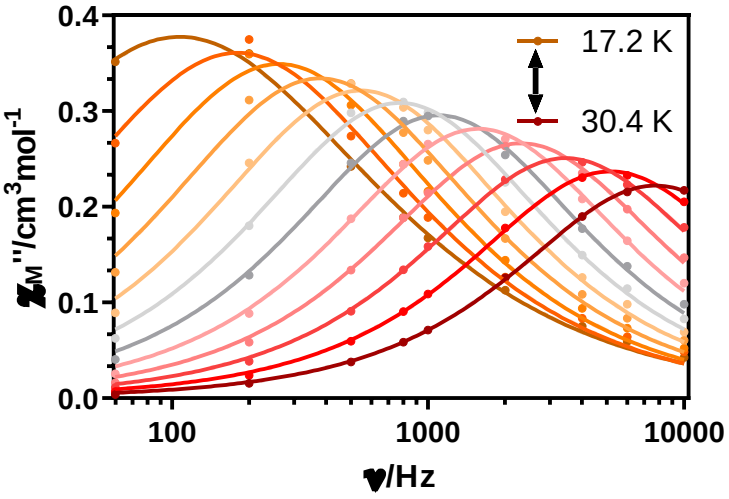

Figure AII.III.- Variable-temperature frequency dependence of the χ_M'' signal under zero applied field for **52**. Solid lines represent the best fitting of the experimental data to the Debye model.

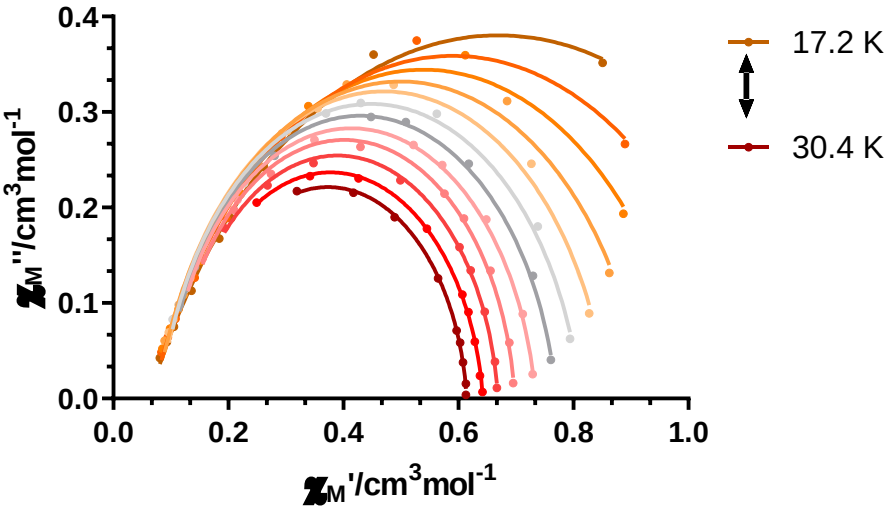

Figure AII.IV.- Cole-Cole plots under zero field for **52**. Solid lines represent the best fit to the generalized Debye model.

APPENDICES

***mini-Chapter III**: In search of Co^{II} based zero field SMMs based on tripodal ligands*

Index:

1. Crystallographic Tables.

Table AIII.I.- Crystallographic data for compounds **53** and **54**.

Structure	**53**	**54**
Formula	$C_{27}H_{28}N_3O_4Co$	$C_{52}H_{48}N_6O_6Co_3$
M_r	517.45	1029.75
Crystal system	*monoclinic*	*monoclinic*
Space group (no.)	*P* 21/c (14)	*C 2/c* (15)
a (Å)	9.1098(6)	22.2609(7)
b (Å)	14.6128(10)	10.6725(2)
c (Å)	17.6638(10)	21.4093(5)
α (°)	90	90
β (°)	100.179(2)	98.166(2)
γ (°)	90	90
V (Å^3)	2314.4(3)	5034.8(2)
Z	4	4
D_c (g cm^{-3})	1.485	1.358
μ(MoK$_\alpha$) (mm^{-1})	0.782	1.030
*T (*K)	100(2)	100.01(10)
Observed reflections	5961 (4150)	5246 (3649)
R_{int}	0.1161	0.0820
Parameters	319	305
GOF	1.045	0.950
R_1[a,b]	0.1049 (0.0642)	0.0783 (0.0477)
wR_2[c]	0.1499 (0.1327)	0.1092 (0.0965)
Largest difference in peak and hole (e Å^{-3})	0.975 and -1.057	0.454 and -0.565

[a]$R_1 = \Sigma||F_o| - |F_c||/\Sigma|F_o|$. [b]Values in parentheses for reflections with $I > 2\sigma(I)$. [c]$wR_2 = \{\Sigma[w(F_o^2 - F_c^2)^2]/\Sigma[w(F_o^2)^2]\}^{½}$

Table AIII.II.- Bond lengths (Å) and angles (°) for compounds **53** and **54**. Symmetry operation: (i) –x+1/2, -y+3/2, -z+1.

Compound	**53**	**54**		**54**
Co1-Co2		2.9088(4)		
Co1-O1A	1.902(2)	2.072(2)	Co2-O1A	2.1033(19)
Co1-O1B	1.907(2)	2.078(2)	Co2-O1B	2.096(2)
Co1-O1C	1.915(2)	2.0999(18)	Co2-O1C	2.0948(19)
Co1-N1A	1.915(3)	2.124(2)	Co2-O1A(i)	2.1033(19)
Co1-N1B	1.914(2)	2.083(3)	Co2-O1B(i)	2.096(2)
Co1-N1C	1.916(3)	2.094(3)	Co2-O1C(i)	2.0947(19)
O1A-Co1-O1B	86.81(9)	76.92(8)	O1A-Co2-O1B	75.85(8)
O1A-Co1-O1C	86.77(9)	78.27(8)	O1A-Co2-O1C	77.69(7)
O1A-Co1-N1A	93.11(10)	85.55(8)	O1A-Co2-O1A(i)	180.00(11)
O1A-Co1-N1B	178.87(10)	155.94(10)	O1A-Co2-O1B(i)	104.15(8)
O1A-Co1-N1C	90.77(10)	113.91(10)	O1A-Co2-O1C(i)	102.31(7)
O1B-Co1-O1C	87.13(9)	76.60(8)	O1B-Co2-O1C	76.33(8)
O1B-Co1-N1A	90.49(10)	116.68(9)	O1B-Co2-O1A(i)	104.15(8)
O1B-Co1-N1B	93.20(10)	86.69(10)	O1B-Co2-O1B(i)	180.0
O1B-Co1-N1C	177.55(10)	157.40(9)	O1B-Co2-O1C(i)	103.68(8)
O1C-Co1-N1A	177.62(10)	156.24(10)	O1C-Co2-O1A(i)	102.31(7)
O1C-Co1-N1B	92.10(10)	115.22(9)	O1C-Co2-O1B(i)	103.67(8)
O1C-Co1-N1C	93.05(10)	86.03(9)	O1C-Co2-O1C(i)	180.0
N1A-Co1-N1B	88.02(11)	86.27(10)	O1A(i)-Co2-O1B(i)	75.85(8)
N1A-Co1-N1C	89.32(11)	84.76(9)	O1A(i)-Co2-O1C(i)	77.69(7)
N1B-Co1-N1C	89.23(11)	87.78(11)	O1B(i)-Co2-O1C(i)	76.33(8)
			Co1-O1A-Co2	88.32(8)
			Co1-O1B-Co2	88.34(9)
			Co1-O1C-Co2	87.81(7)

2. Continuous Shape Measurements.

The nearer the value to zero, the better fits to an ideal polyhedron.

Table AIII.III.- Continuous Shape Measurements for the CoN_3O_3 (**53** and **54-Co1**) and CoO_6 (**54-Co2**) coordination environments in compounds **53** and **54**.

HP-6 1 D6h Hexagon
PPY-6 2 C5v Pentagonal pyramid
OC-6 3 Oh Octahedron
TPR-6 4 D3h Trigonal prism
JPPY-6 5 C5v Johnson pentagonal pyramid J2

Structure [ML6]	HP-6	PPY-6	OC-6	TPR-6	JPPY-6
Co1 (53)	32.299	29.165	**0.096**	15.197	32.721
Co1 (54)	32.835	19.493	5.298	**3.984**	23.388
Co2 (54)	28.810	28.851	**2.470**	14.306	31.574

3. Experimental XRPD.

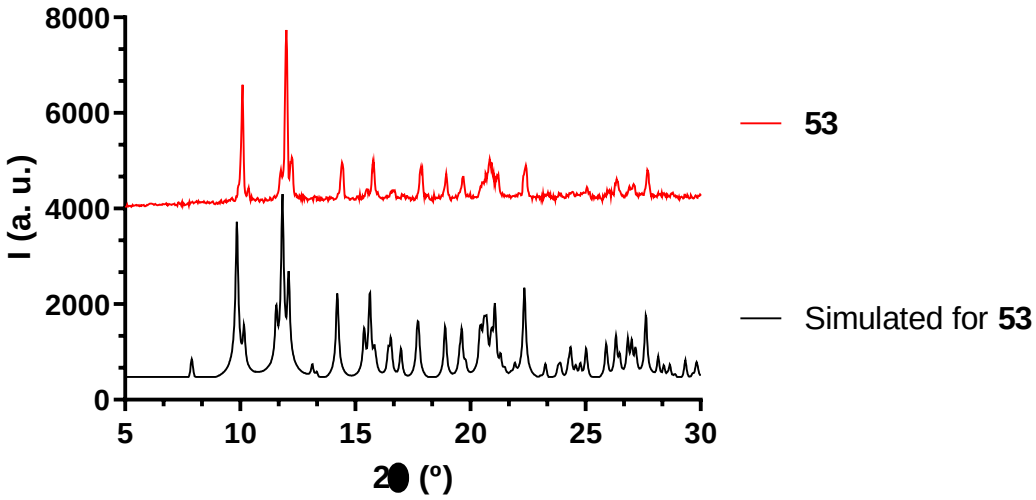

Figure AIII.I.- For **53**, simulated pattern from single-crystal X-ray diffraction (black line) and experimental XRPD (red).

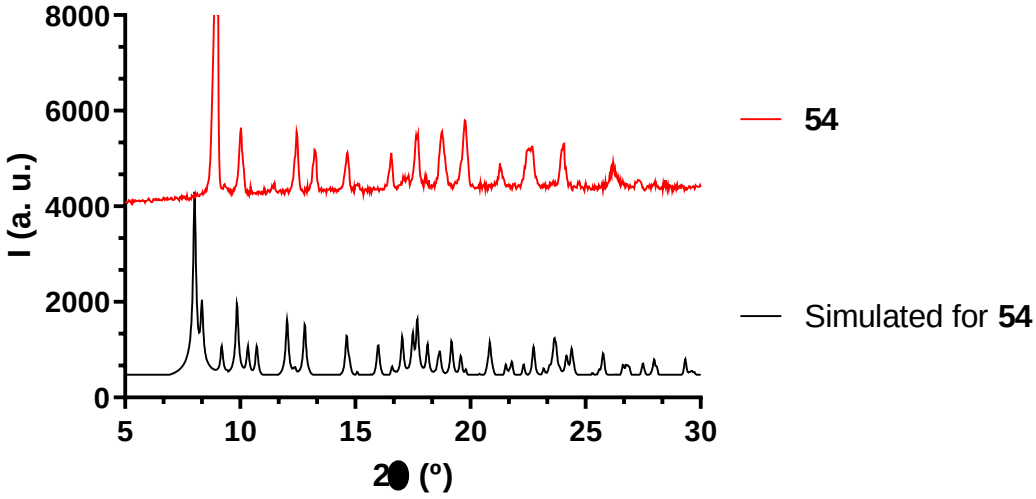

Figure AIII.II.- For **54**, simulated pattern from single-crystal X-ray diffraction (black line) and experimental XRPD (red).

4. Thermogravimetric analysis.

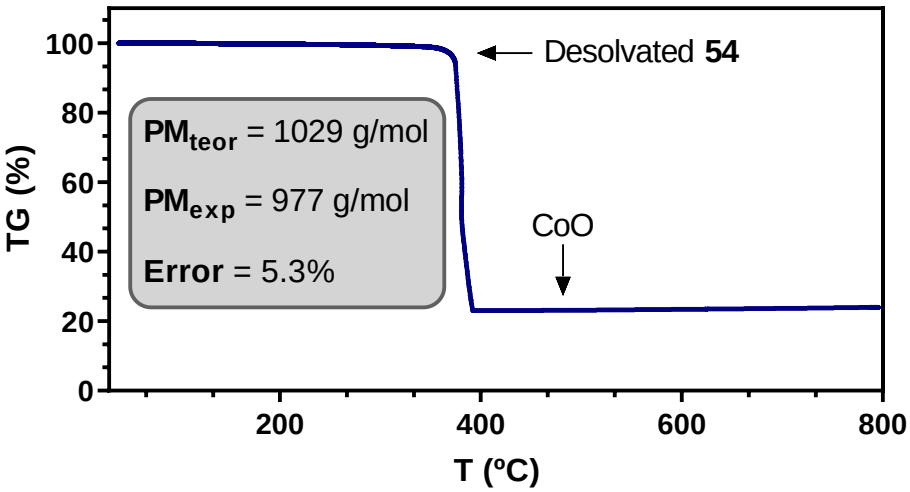

Figure AIII.III.- Thermogravimetric analysis of compound **54**.

5. ^{1}H Nuclear Magnetic Resonance.

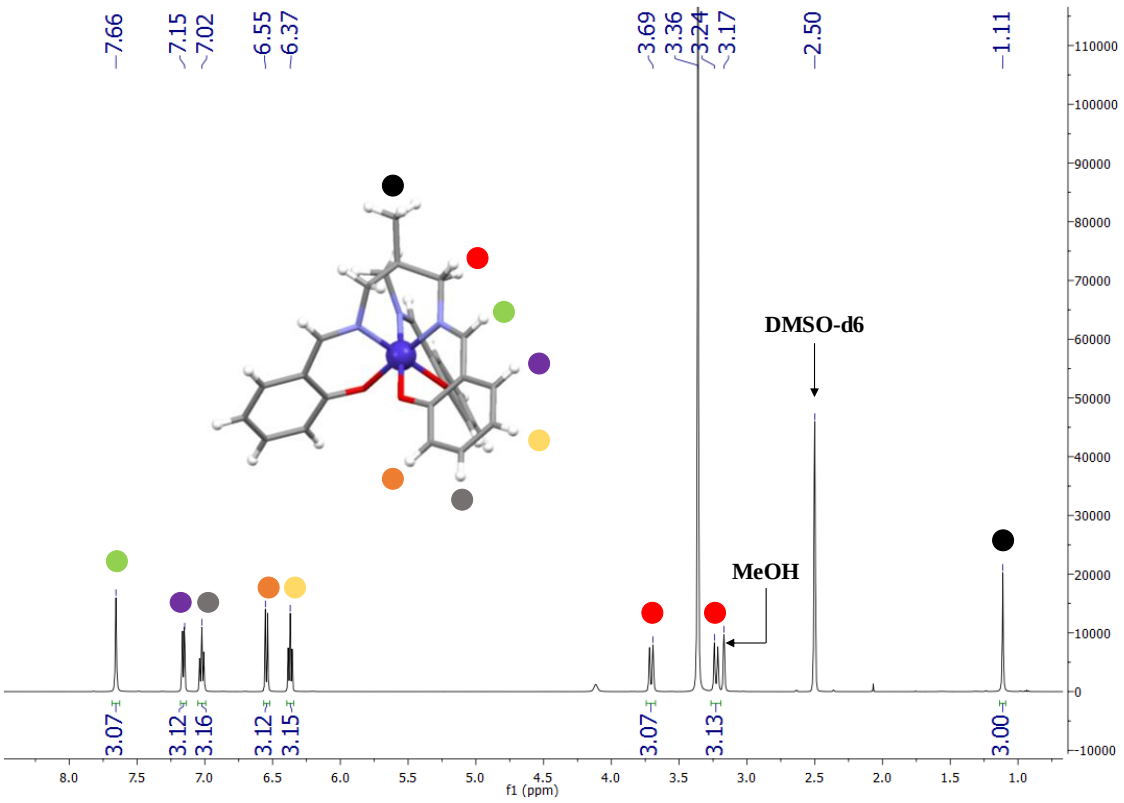

Figure AIII.IV.-^{1}H-NMR of **53** in DMSO-d^{6}.

6. Magnetic Measurements.

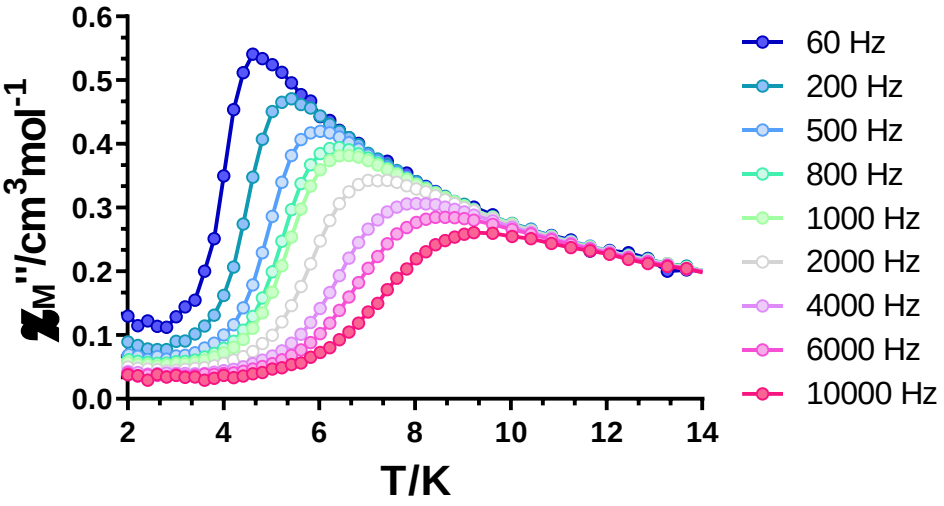

Figure AIII.V.- Temperature dependence of the in phase components of the *ac* susceptibility in a zero applied field for **54**.

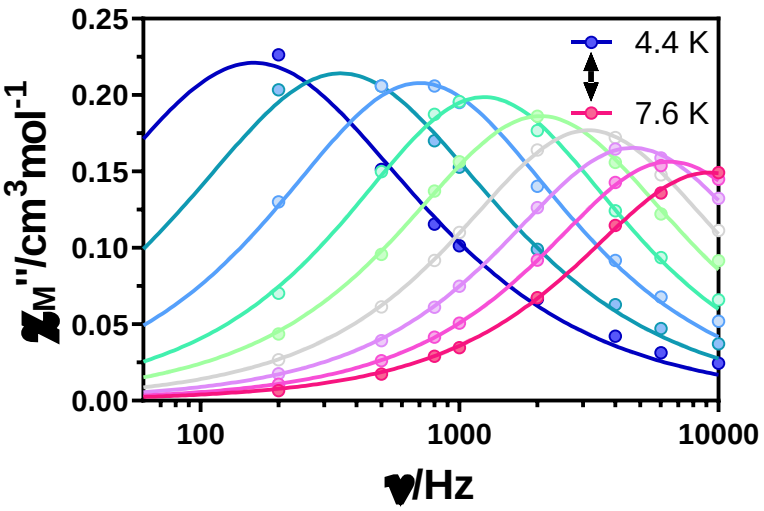

Figure AIII.VI.- Variable-temperature frequency dependence of the χ_M'' signal under zero applied field for **54**. Solid lines represent the best fitting of the experimental data to the Debye model.

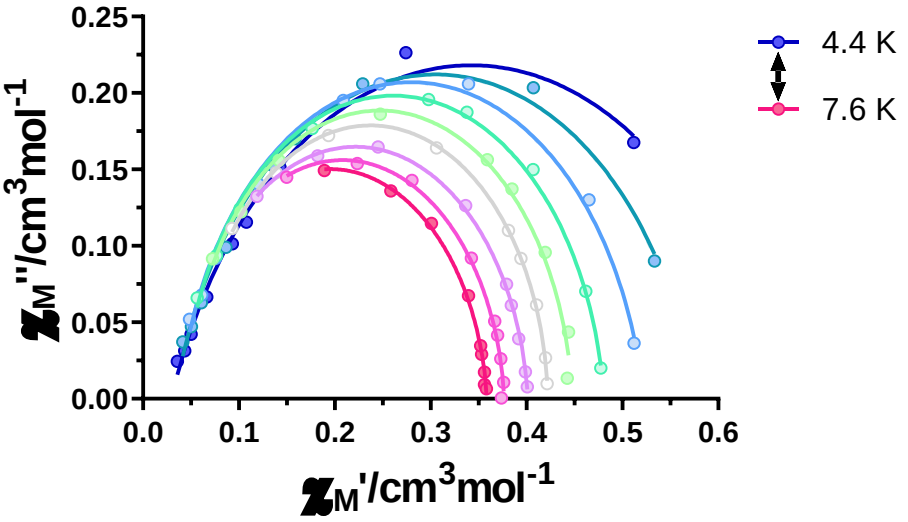

Figure AIII.VII.- Cole-Cole plots under zero field for **54**. Solid lines represent the best fit to the generalized Debye model.

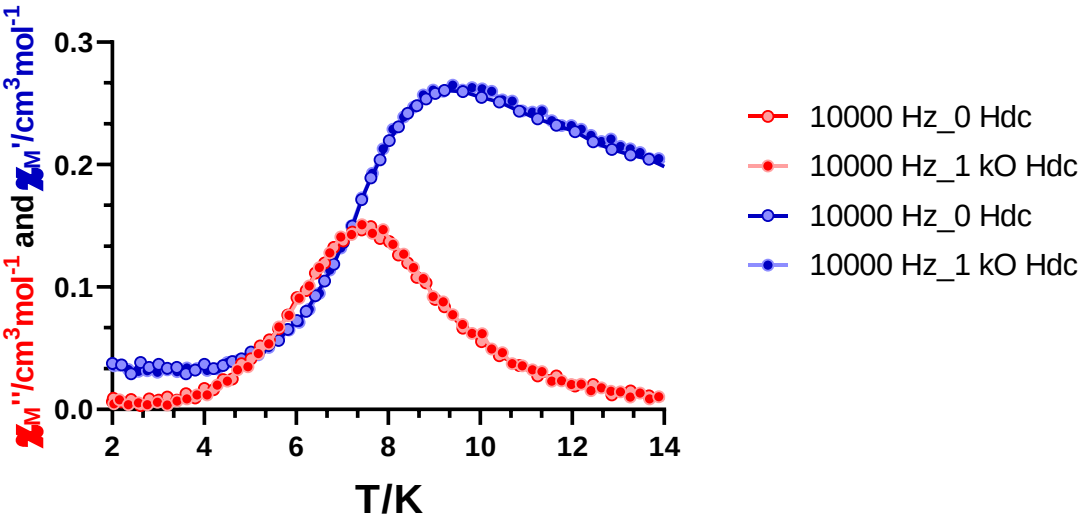

Figure AIII.VIII.- Temperature dependence of in-phase (blue) and out-of-phase (red) components of the *ac* susceptibility in a zero (light dots) and 1 kOe (dark dots) applied *dc* field for **54**.

APPENDICES

Instrumental methods

All the experimental conditions applied for the characterization methods are described in this section. Thermal analyses and infrared spectra were performed and measured at Applied Chemistry Department (UPV/EHU Gipuzkoa). Thermogravimetric analyses were performed at Polymer Science and Technology Department (UPV/EHU, Gipuzkoa). The powder and single-crystal X-ray diffraction studies and magnetic susceptibility measurements were carried out at General Research Services (SGIker) of UPV/EHU and University of Granada. Luminescence measurements were performed by Dr. Javier Cepeda at Physics Department (UPV/EHU, Bizkaia). Circularly Polarized Measurements and circular dichroism were carried out in University of Granada. Pulse magnetization measurements were measured in the University of Tohoku (Japan).

- **Elemental analyses**: The C, H and N content of all the compounds was determined in a Leco CHNS-932 microanalyzer.
- **Single Crystal X-ray diffraction:** Single crystals of suitable dimensions were used for data collection. The diffraction intensities were collected on four different diffractometers.
    - Oxford Diffraction Xcalibur diffractometer, equipped with graphite monochromated Mo Kα radiation (λ = 0.71069 Å).
    - Agilent Technologies Super-Nova diffractometer, equipped with monochromated Mo Kα radiation (λ = 0.71069 Å) and Eos CCD detector.
    - Agilent Technologies Super-Nova diffractometer, equipped with monochromated Cu Kα radiation (λ = 1.54180–4 Å) and Atlas CCD detector.
    - Bruker SMART APEX CCD diffractometer, equipped with graphitemonochromated Mo Kα (λ = 0.71073 Å) radiation.
- **Powder X-ray diffraction**: The XRPD patterns were collected on a Phillips X'PERT powder diffractometer with Cu Kα radiation (λ = 1.5418 Å) over the range $5 < 2\theta < 50°$ with a step size of 0.02° and an acquisition time of 2.5 s per step at 25 °C.

- **Magnetic measurements**: Variable-temperature magnetic susceptibility and magnetization measurements were carried out with a Quantum Design SQUID MPMS-7T device, Quantum Design SQUID MPMS XL-5 device and PPMS (Physical Property Measurement System) - Quantum Design Model 6000 magnetometer. Diamagnetic corrections were estimated from the Pascal's constants. *Alternating-current* (*ac*) susceptibility measurements were performed on the PPMS magnetometer.
- **Photoluminescence measurements**: Photoluminescence (PL) emission spectra and lifetime measurements were carried out for powdered samples from 10 K to room temperature using a close cycle helium cryostat contained in an Edinburgh Instruments FLS920 spectrometer. For the measurements an IK3552R-G HeCd continuous laser (325 nm) and a Müller-Elektronik- Optik SVX1450 Xe lamp were used as excitation sources. The lifetime measurements were performed by using a μF1 pulsed microsecond flashlamp as excitation source. Photographs were taken in a micro-photoluminescence system included in an Olympus optical microscope (Colour View III camera) illuminated with a Hg lamp.
- **Circularly polarized luminescence**: Measurements were performed on an Olis DSM172 spectrophotometer.
- **Thermogravimetric analyses**: Thermal analysis (TGA) was performed on a METTLER TOLEDO TGA/SDTA851 thermal analyzer in synthetic air (80% N_2, 20 %O_2) flux of 50 $cm^3 \cdot min^{-1}$, from room temperature to 800 °C with heating rate of 10 °C min^{-1} and a sample size of about 5 mg per run.
- **Infrared spectroscopy**: IR spectra were obtained between a wave number range of 4000-500 cm^{-1} with a Nicolet FTIR 510 spectrometer. Measurements were performed in a KBr disc.
- **Nuclear magnetic resonance spectroscopy**: RMN spectra were recorded on Bruker AVD 300 MHz spectrometer at room temperature. ^1H and $^{13}C\{^1H\}$ NMR spectra were referenced to the solvent residual signal.

eman ta zabal zazu

Universidad del País Vasco
Euskal Herriko Unibertsitatea

Kimika Aplikatua Saila/Departamento de Química Aplicada

Mannich base estekatzaileetan eta trantsizio-metal, lantanido eta 3d-4f mistoetan oinarritutako konposatuak: ikerketa magnetiko progresiboa material hobeen bila

Andoni Zabala Lekuonak aurkeztutako tesia

Euskal Herriko Unibertsitatea/Universidad del País Vasco

Zuzendariak: José Manuel Seco eta Enrique Colacio

Donostian, 2021eko maiatzean

AURKIBIDEA

SARRERA

IMAN MOLEKULARRAK: Mn12-ac MOLEKULATIK DISPROSIOZENOETARA, DENBORAN ZEHARREKO BIDAIA

i. SARRERA

Gaur egun, informazio gehiena elektronikoki gordetzen da. Duela urte gutxi batzuk arte, liburuak, oharrak, dokumentuak, argazkiak, egunkariak eta abar inprimatuta eta paperean aurki genitzakeen. Gaur egun, ordea, datu horiek guztiak digitalki gorde daitezke. Hala ere, aipatu beharra dago teknologia berri honen bilakaera hamarkada gutxitan zehar eman dela, aldaketa handi eta azkarrekin. Datuak biltzeko lehen gailuak 70eko hamarkadan kaleratu ziren, disketeak izenekoak. Tamaina handikoak izan arren, 8 hazbete inguru, ia pdf sinple bati buruzko informazioa ere ezin zuten gorde. Bost bat hamarkada geroago, gure hatz lodiak baino handiagoak ez diren USB memoriak gai dira filmak, milaka argazki eta milioika dokumentu pilatzeko. Bilakaera berebizikoa izan da.

Datu horiek guztiak gorde ahal izateko, gailuek hizkuntza bitarra erabiltzen dute: 1 eta 0 konbinazioak, *bit* informazio unitatearen adierazgarri direnak. Adibidez, disko gogorren nukleoak aleazio nanoskopikoen partikula (hamarnaka nanometro batzuez), ferro edo ferrimagnetikoz (iman portaera dute Curie tenperaturaren azpitik, T_C) osatuak daude, domeinu magnetiko indibidualak eratzen dituztenak, non bakoitzak momentu magnetiko kopuru handi bat duen. Curieren tenperaturaren, T_C-ren, azpitik nanopartikula bakoitzaren barruko momentu magnetiko guztiak lerrokatu egiten dira momentu magnetiko bat sortuz, M_S. Konposatu paramagnetikos arruntetan bezala, M_S guztiak ausaz orientatzen dira energia termikoaren ondorioz, baina une magnetikoak atomo sinple batenak baino askoz handiagoak direnez, fenomeno honi *superparamagnetismoa* deitzen zaio (i.1. irudia).

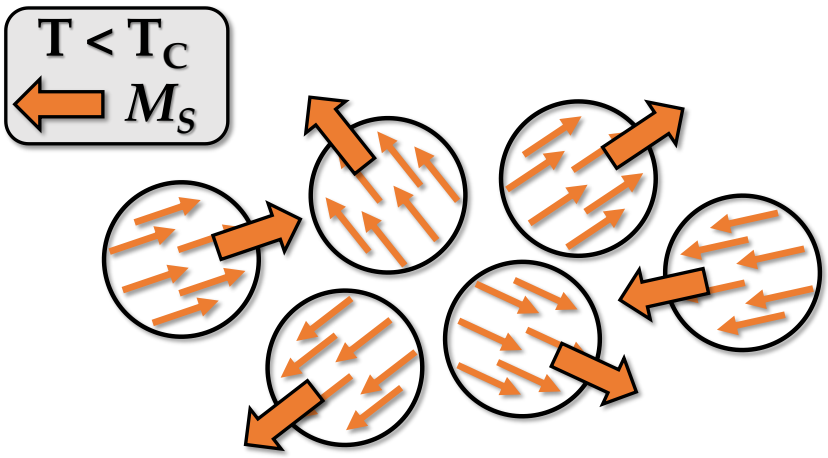

i.1. irudia. Material superparamagnetikoa.

Eremu magnetiko baten presentzian, nanopartikula hauek erraz magnetizatu daitezke norabide jakin batean (magnetizazio errazeko ardatza) anisotropia axial baten presentziaren ondorioz. Anisotropia hau faktore intrintsekoen menpe dago: ioi metaliko mota eta nanopartikulen forma, besteak beste. Eremu magnetiko bat aplikatzen denean, nanopartikulek euren momentu magnetikoak eremuarekiko paraleloki jartzeko joera dute, momentu magnetiko maximoa lortuz (M_S). Eremu magnetikoa kentzen bada (H = 0) eta sistemaren tenperatura tenperatura jakin bat baino txikiagoa bada (T_B blokeo-tenperatura), momentu magnetikoa blokeatuta egongo da norabide berean. Beraz, sistemak iman bezala jokatzen du, histeresi ziklo bat ikus daiteke eta, ondorioz, memoria efektua du. Hori energia-barrera, ΔE, baten ondorioz gertatzen da; izan ere, magnetizazioaren birbideratzea eragozten. Barrera honen balioa anisotropiaren (K) eta nanopartikularen bolumenaren (V) menpekoa da (i.2. irudia). T_B-*aren* azpitik, energia termikoa, E_T, ez da energia-barrera gainditzeko bezain handia ($E_T < \Delta E$), eta, beraz, momentu magnetikoa blokeatu egiten da. T_B-*aren* gainetik, aldiz, sistemak hesia gainditzeko energia nahikoa du ($E_T > \Delta E$) eta bi orientazioen arteko oreka lortzen da (positiboa eta negatiboa), non materialak portaera superparamagnetikoa duen eta histeresirik ikusi ezin izango den. Hala, sistema T_B-aren azpitik mantentzen bada, norabide bateko magnetizazioaren orientazioak (goruntzako orientazioak) hizkuntza bitarreko 1 zenbakiari dagokion informazioa adieraziko du, eta kontrako orientazioak (beheruntzakoak), berriz, 0 zenbakiari dagokiona. Ondorioz, nanopartikularen neurria zenbat eta txikiagoa izan, orduan eta handiagoa izango da gailuaren barruko informazio-dentsitatea.

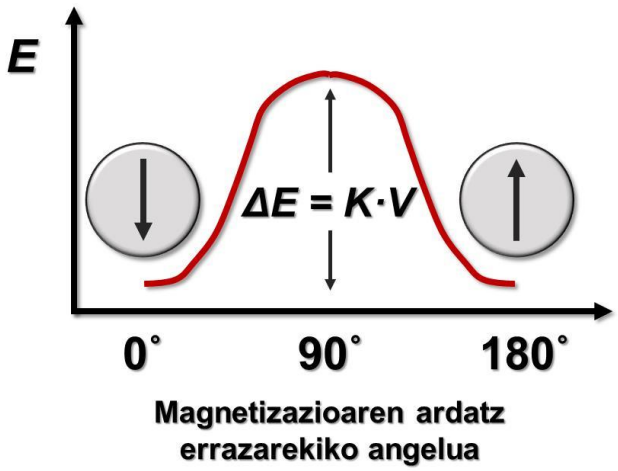

i.2. irudia. Magnetizazioaren orientazioaren energia, magnetizazio errazeko ardatza kontuan hartuta.

Hala ere, informazioa biltegiratzeko "goruntza-beheruntza" (*up-down*) estrategiak zenbait muga ditu. Adibidez, ezin da nanopartikularen tamaina nahi bezainbeste murriztu, horrek, aldi berean, anisotropiaren balioa murrizten baitu eta, beraz, energia-barreraren balioa. Izan ere, nanopartikulen tamaina kritikoa 10 nm ingurukoa da eta horren azpitik portaera histeretikoa desagertzen denez, ezin da informaziorik gorde (i.3. irudia). Gainera, lan zaila da partikulen sakabanaketa ona lortzea eta normalean tamaina eta forma desberdinak dituzten nanopartikulak lortzen dira. Horrek esan nahi du anisotropia balioak desberdinak izango direla eta baita energia-barrerak ere.

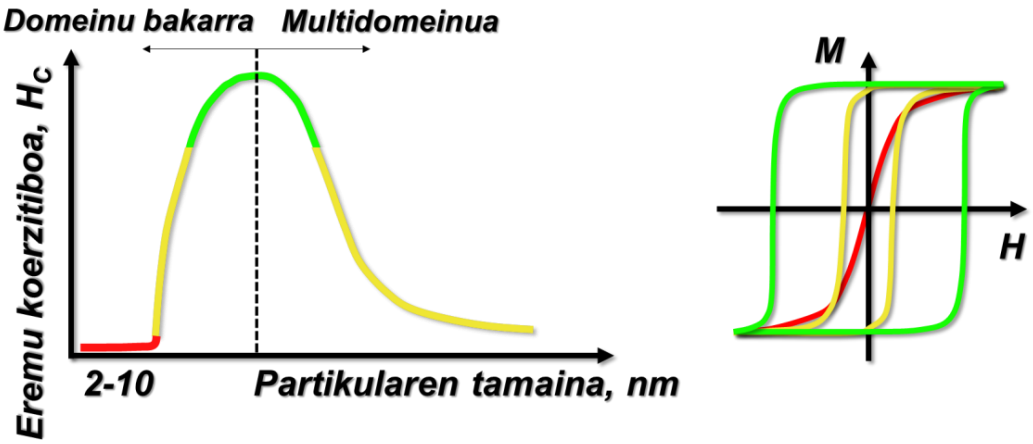

i.3. irudia. Histeresi-zikloen bilakaera partikulen tamaina kontuan hartuta.

Testuinguru honetan sortu zen lehen Iman Molekularra (*SMM, Single Molecule Magnet*). Hain zuzen, 1993. urtean Sessoli eta bere taldekideek Mn12-ac konposatua maila molekularrean informazioa gordetzeko gai zela ikusi zutenean (**i1** konposatua, i.4. irudia [1]. Honela, memoria efektua zuen entitate txikiena ehunka nanometro ingurutik angstrom gutxi batzuetara murriztu zuten.

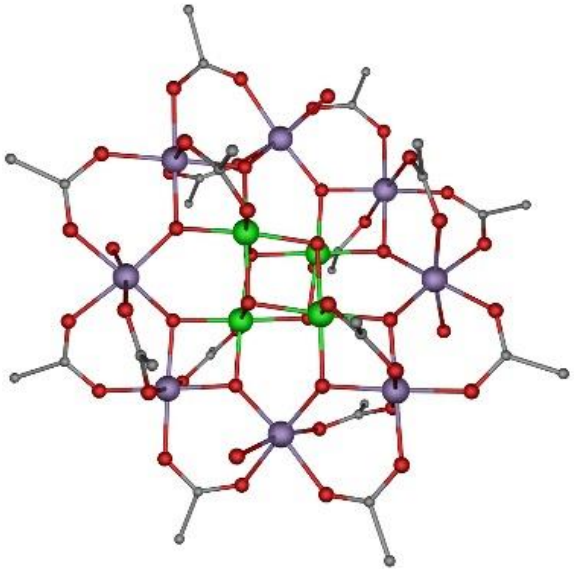

i.4. irudia. Mn12-ac egitura [1]. Kolore-kodea: Mn^{III}, Mn^{IV}, karbonoa eta oxigenoa more, berde, gris eta gorri kolorez, hurrenez hurren. Hidrogeno atomoak ez dira irudikatu argitasunaren mesedetan. [2] erreferentziatik ateratako irudia Ekaiaren baimenarekin.

i.i. Nola funtzionatzen dute Iman Molekularrek?

Izenetik ondoriozta daitekeen bezala, Mn12-ac koordinazio konposatu bat da, 12 zentro metaliko dituena: lau Mn^{IV} eta zortzi Mn^{III} ioi hain zuzen. Oxidazio egoera desberdina duten zentro metalikoen arteko interakzio antiferromagnetikoek $S = 10$ (S spina izanik) oinarrizko egoera sortzen dute, aldi berean 21 aldiz degeneratuta dagoena ($M_S = 2S + 1$). Hala ere, oinarrizko egoerako anisotropia axialaren mende dagoen zero eremuko zabaltzearen (*ZFS, Zero Field Splitting*) ondorioz, 21 aldiz degeneratutako azpimailak (M_S) honako ekuazioak adierazitako energiaren bitartez banatuta daude: $E(M_S) = M_S^2 \cdot D$, non D anisotropia axialaren parametroa den (i.5. Irudia).

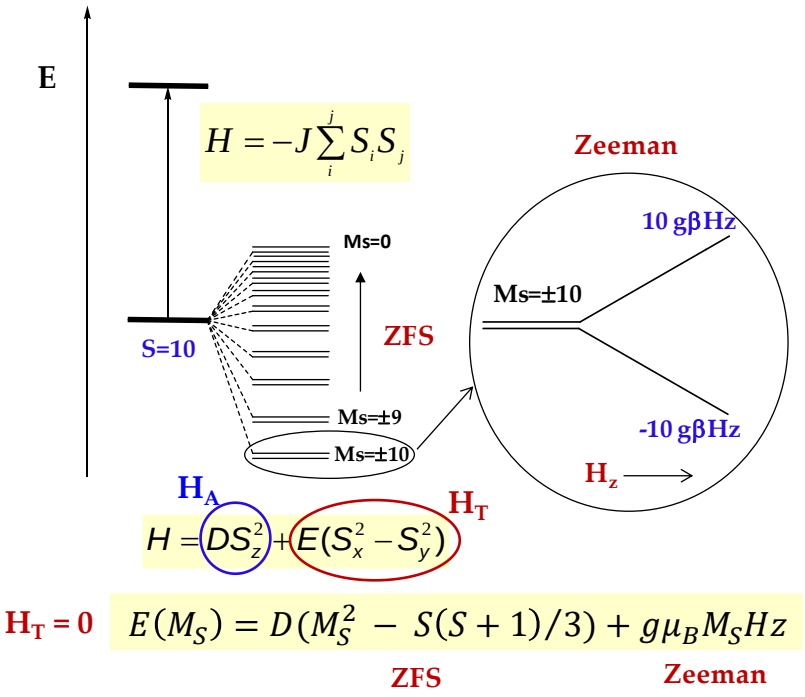

i.5. irudia. Mn12-ac molekularen energia diagrama, oinarrizko egoera (S = 10) zero eremuko banatzea (*ZFS*) definitzen duen Hamiltoniano axial eta transbertsalekin (H_A eta H_T = 0, hurrenez hurren) banatuta. Zeeman interakzioek eragindako M_S = ±10 azpimailen banatzea ere nabarmenduta dago.

D < 0 denean, energia-maila baxueneko azpimailak |M_S| balio handienekoak dira, kasu honetan M_S = ±10. Azpimaila bakoitzari lotutako magnetizazioak bere orientazio jakina du (i.6. irudia, nanopartikula superparamagnetikoen kasuan gertatzen den bezala), beraz, M_S = +10 egoerak spina goruntz izango du (edo 1 zenbakia hizkuntza bitarrean) eta M_S = -10 egoerak, ordea, spina beheruntz (edo 0). Bestalde, D > 0 denean, kontrako egoera gertatzen da. Azpimailak alderantziz orientatuta egongo lirateke, eta, beraz, oinarrizko egoera M_S = 0 izango litzateke. Egoera berezi horretan, ez dago oinarrizko egoera biegonkor bat izateko aukerarik, eta, ondorioz, sistema ez da baliagarria informazioa gordetzeko. Lehen kasura itzuliz, M_S = +10 azpimailatik M_S = -10 azpimailara (edo alderantziz) pasatzeko, sistemak energia-barrera bat gainditu behar du, U, material superparamagnetikoetan gertatzen den bezala (i.6. irudia). Barreraren balioa eszitazio-egoera altuenaren eta oinarrizko egoeraren arteko diferentzia da. Spin osoa eta erdiosoa duten sistementzat honela definitzen da: $U = S^2|D|$ eta $U = S^2 - 1/4|D|$; hurrenez hurren (S oinarrizko egoerako spinaren balioa da).

i1 konposatuaren adibidearekin jarraituz, kanpoko eremu magnetikorik ezean, M_S = ±10 azpimailek energia bera dute, berdin populatuta daude eta, beraz, sistemak ez du magnetizaziorik (i.6.irudia, ezkerrean). Norabide jakin batean intentsitate nahikoa duen kanpoko eremu magnetiko polarizatzaile bat aplikatzen denean, M_S azpimailetako bat egonkortzen da bestearekin alderatuta. Beraz, materiala magnetizatzen da, molekula guztien spinek norabide berean seinalatzen baitute (i.6. irudia, erdialdean). Eremu magnetiko polarizatzailea kentzen denean, oinarrizko egoera berriro ere bi aldiz degeneratutako egoera izatera pasatzen da, eta $E_T > U$ bada, materialak bi orientazioen arteko oreka (positiboa eta negatiboa) lortzeko joera izango du magnetizazioa galduz. Hala ere, $E_T < U$ bada ($T < T_B$ kasuan sortzen den egoera), magnetizazioa blokeatuta geratuko da eta, horregatik, *SMM*a informazioa gordetzeko gai da. Hori dela eta, erraza da ondorioztatzea zenbat eta handiagoa izan energia-barrera, orduan eta handiagoa izango dela magnetizazioari eutsi ahal izateko tenperatura. Hala ere, hori ez da beti (edo ia inoiz) horrela izaten.

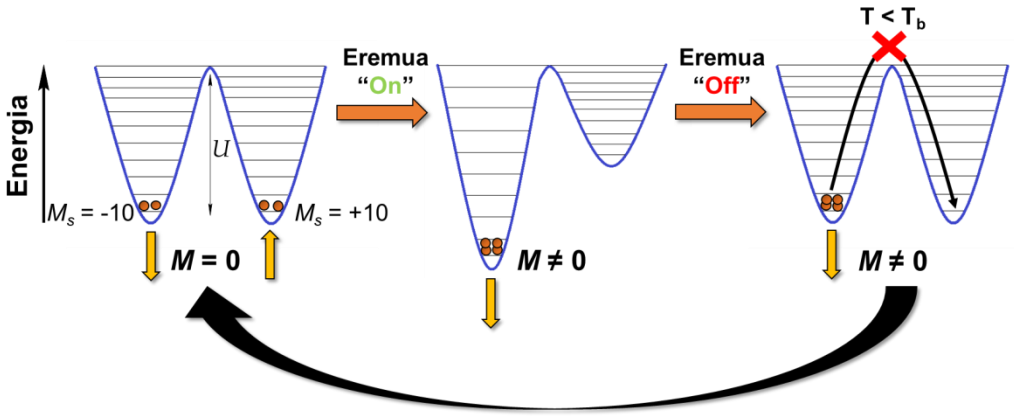

i.6. irudia. Magnetizazioaren proiekzioak (gezi laranjak) orekan kanpoko eremu magnetikorik gabe (ezkerrean), materialaren magnetizazioa kanpoko eremu baten presentziaren ondorioz (erdian) eta eremu magnetikorik gabe magnetizazioaren blokeoa $T < T_B$ denean (eskuinean). [2] erreferentziatik moldatuta Ekaiaren baimenarekin.

i.ii. Erlaxazio-prozesuak

Magnetizazioaren birorientazioa edo erlaxazioa egoera kitzikatu guztietatik pasatuz eta energia-barrera gainditzuz bakarrik gertatuko balitz, $U \sim 298$ K (~ 207 cm^{-1}) bat duen edozein material baliagarria izango litzateke informazioa biltegiratzeko gailu batean inplementatzeko. Aipatutako gailuaren tenperatura 298 K-etik behera mantentzeak

magnetizazioa ez galtzea ziurtatuko luke eta, ondorioz, memoria efektua izango luke. Hala ere, material hauen izaera kuantikoaren ondorioz, erlaxazio mekanismoak askotarikoak, konplexuak eta faktore askorekiko oso sentikorrak dira, hala nola, tenperaturarekiko, eremu magnetikoarekiko, eta interakzio hiperfin (spin elektroniko eta nuklearren arteko interakzioak) nahiz molekulartekoekiko sentikorrak.

*SMM*etan ematen diren erlaxazio-prozesu ohikoenak spin-fonoi akoplamenduaren bidez gertatzen direnak (Orbach, Raman eta prozesu zuzena) edo materialen izaera kuantikoaren ondorioz gertatzen direnak dira (magnetizazioaren tunel kuantikoa, *QTM*, eta termikoki lagundutako tunel kuantikoa, *TA-QTM*) [3]. Orbachek eta Ramanek bi fonoi inplikatzen dituzte, prozesu zuzenak, berriz, bakarra.

Orbach erlaxazio ideala sistemak barrera osoa gainditzen duenean izango litzateke. Sistemak sare kristalinotik energia zehatzeko fonoiak absorbatuko lituzke (($\hbar/2\pi$)/ω_1), oinarrizko egoeratik (M_S = ±S) azpimaila eszitatu altuenera (M_S = *0*) salto eginez. Eszitazio-egoera honetatik oinarrizko egoerako edozein M_S = ±S egoerara erlaxatuko litzateke sistema fonoi berriak askatuz (($\hbar/2\pi$)/ω_2, i.7. irudia, goian ezkerrean). Nabarmentzekoa da irudian hasierako eta amaierako egoeren energiak interakzio dipolarrek edo hiperfinek eragindako barne-eremuengatik banatuta daudela. Horrela, absorbatutako fonoiaren eta askatutako fonoiaren arteko energia-diferentzia oinarrizko egoerako ±M_S azpimailen arteko diferentziari dagokio. Nolanahi ere, normalean Orbach prozesua ez da egoera kitzikatu altuenetik pasatzen, kitzikatutako lehen edo bigarren egoeratik baizik (sistemaren axialitatearen arabera, i.7. irudia, behean eskuinean). Prozesu hau gertatzeko behar den fonoien energia handia dela eta, tenperatura altuenetan ematen da mekanismo mota hau.

Orbach prozesuarekin lotutako baldintza energetikoak ez daude Raman prozesuarentzat, mekanismo hau fonoien dispertsio inelastikoak bultzatzen baitu. Molekulak fonoi bat absorbatzen du (($\hbar/2\pi$)/ω_3), kitzikatutako egoera birtual batera iristen da eta beste fonoi bat igortzen du (($\hbar/2\pi$)/ω_4) (i.7. irudia, goian eskuinean). Berriz ere, bi fonoien arteko energia diferentzia oinarrizko egoerako ±M_S azpimailen arteko energia diferentziari dagokio. Bien bitartean, prozesu zuzenean fonoi bakar batek hartzen du parte sistemak fonoia igorri (($\hbar/2\pi$)/ω_5). Fonoiaren energia oinarrizko egoerako ±M_S azpimailen arteko energia-diferentziari dagokio (i.7. irudia, behean ezkerrean).

Mekanismo horiek guztiek energia behar dute (laguntza termikoa), baina *QTM*rentzat desberdina da (*QTM, Quantum Tunneling of the Magnetization*). Prozesu hau oinarrizko egoerako ±M_S azpimailen artean gertatzen da eta ohiko erlaxazio mekanismoa izan ohi

da tenperatura baxuetan, nagusiki oinarrizko egoera baitago populatuta (i.7. irudia, behean eskuinean). Dena den, magnetizazioaren erlaxazioa prozesu ezberdinen konbinazio bitartez eman daiteke, non kitzikatutako egoerak fonoien absortzio bidez populatzen diren eta, ondoren, *QTM* gerta daitekeen energia bereko (baina zeinu ezberdineko) M_S egoeren artean, azkenik oinarrizko egoerara erlaxatuz. Mekanismo konbinatu hau termikoki lagundutako tunel kuantiko bezala ezagutzen da, *TA-QTM* (*Thermally Assisted-QTM*, i.7. irudia, behean eskuinean). Nabarmendu beharra dago *QTM*k eta prozesu zuzenak normalean tenperatura baxuetan jarduten dutela, Orbachek altuenetan eta *TA-QTM*ek tartekoetan. Raman mekanismoa, aldiz, tenperatura maila osoan ager daiteke. Horien guztien artean, *QTM* eta *TA-QTM* magnetizazioaren erlaxazioaren prozesuan bidezidor bezala kontsideratzen dira, sistemak energia-barrera gainditu gabe galtzen baitu magnetizazioa. Beraz, *U* barreraren balioa murriztea eragiten dute eta energia-barrera efektiboaz hitz egin daiteke, U_{eff}. Horrek, aldi berean, blokeo-tenperaturaren balioan eta erlaxazio-denboran (τ) eragiten du.

QTM deuseztatzeko estrategiarik ohikoenak hauek dira: *(i)* laginak magnetikoki diluitzea *SMM*a analogo diamagnetikoekin batera kokristalizatuz (normalean Zn^{II} ioiekin trantsizio-metalekin lan egiten denean eta Y^{III} edo La^{III} ioiekin lantanidoak erabiltzen direnean), honek *QTM*a bultzatzen duten molekulen arteko interakzioak saihestuko baititu, edo *(ii)* kanpoko eremu magnetiko bat aplikatzea $M_S = \pm S$ (edo $M_J = \pm J$, lantanidoak direnean) azpimailen arteko degenerazioa apurtzen duena. Nabarmendu behar da *QTM* gehiago ematen dela spin balio osoa duten sistemetan ez-osoa dutenetan baino (Kramers ioiak) Van Vlecken ezeztapen printzipioaren ondorioz [4]. Printzipio honen arabera, saretik sortzen diren fonoiek ezingo dute *QTM* edo erlaxazio zuzenik eragin Kramers ioietan kanpoko eremurik ez dagoen kasuetan. Zoritxarrez, interakzio hiperfinek eta eremu magnetiko transbertsalek (molekulen arteko interakzioek sortuak) Kramersen dobleteak banatzen dituzte magnetizazioaren erlaxaziorako kanal berriak sortuz *QTM* eta prozesu zuzenentzat. Hala ere, aurrerago eztabaidatuko den moduan, lantanidoak erabiltzen direnean, maizago erabiltzen da Dy^{III} ioia Tb^{III} ioia baino, Kramers eta ez-Kramers ioiak baitira, hurrenez hurren. Gainera, ez-Kramers ioietan oinarritzen diren konposatuek berezkoa dute *QTM* mekanismoa kanpoko eremurik ez dagoen kasuetan. Laburbilduz, eremu magnetiko transbertsalek eta berezko tunel bidezidorrek zehazten dute erlaxatzeko oinarrizko mekanismoa *SMM* propietateak dituzten konplexu metalikoetan.

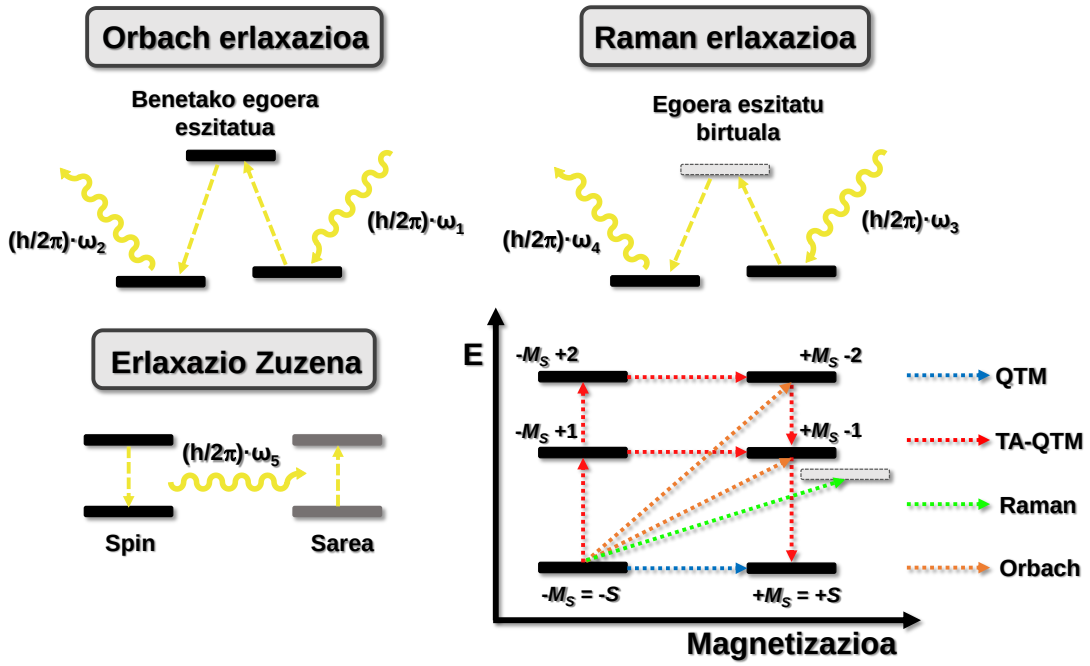

i.7. irudia. Orbach (goian ezkerrean), Raman (goian eskuinean) eta prozesu zuzenaren (behean ezkerrean) erlaxazio-mekanismoen irudikapen eskematikoa. Hainbat erlaxazio-mekanismoren konbinazioa, *QTM* eta *TA-QTM* barne.

i.iii. SMM portaera detektatzea

Material batek magnetizazioaren erlaxazio motela duen ala ez detektatzeko bi teknika nagusi erabili ohi dira. Lehenengoa, eta gehien erabiltzen dena, suszeptibilitate magnetikoaren neurketak egitea da, fasean (χ_M') eta fasez kanpo (χ_M''), eremu magnetiko alterno (*ac*) bat erabiliz. Horrelako neurketak 2 K eta 300 K artean egin ohi dira (normalean tenperatura baxuagoekin nahikoa den arren) korronte alternoaren frekuentzia aldatuz (i.8a. irudia). Irudian erakutsitako adibidean, 20 K-etera eta 60 Hz-ko frekuentziarekin, materialak ez du $\chi_M''(T)$ seinalerik erakusten. Horrek esan nahi du tenperatura horretan materialak eremu magnetiko alternoaren norantza aldaketak jarraitzeko energia nahikoa duela. Hori dela eta, momentu magnetikoak eremu magnetikoaren norantza-aldaketak erraz jarraitzen ditu, denbora guztian fasean (χ_M') egonda. Tenperatura 12 K-etik behera jaisten denean, fasez kanpoko seinalea (χ_M'') handitzen hasten da. Une honetan, materialak energia gutxiago du, eta molekula batzuen momentu magnetikoa ez da gai eremu magnetiko alternoaren aldaketak jarraitzeko (bere anisotropia axialagatik eta, beraz, U_{eff}-rengatik). Bestela esanda, spin batzuk desfasean geratzen dira eta, ondorioz, seinalea agertzen da fasez kanpo. Korronte alternoaren frekuentzia handitzean, adibidez 10000 Hz-tara, eremu

magnetikoaren norantza aldaketak askoz azkarrago gertatzen direnez, seinalea tenperatura handiagoan detektatzen da. Ondorioz, $\chi_M''(T)$ grafikoetan maximoak detektatzeak esan nahi du sistemak magnetizazioaren erlaxazio motela eta *SMM* portaera erakusten dituela. Aipagarria da maximoak agertzen diren tenperaturaren azpitik seinaleak berriz ere igotzeko joera duela erakutsitako adibidean, efektu hori *QTM* prozesuaren adierazgarri da. Efektu berbera $\chi_M''(\upsilon)$ grafikoetan detektatu daiteke (i.8b. irudia), maximoen posizioa aldatzen ez denean tenperaturan aldaketarekin (kasu honetan ez da halakorik ikusten tenperatura baxuagoetako kurbak beharko liratekeelako).

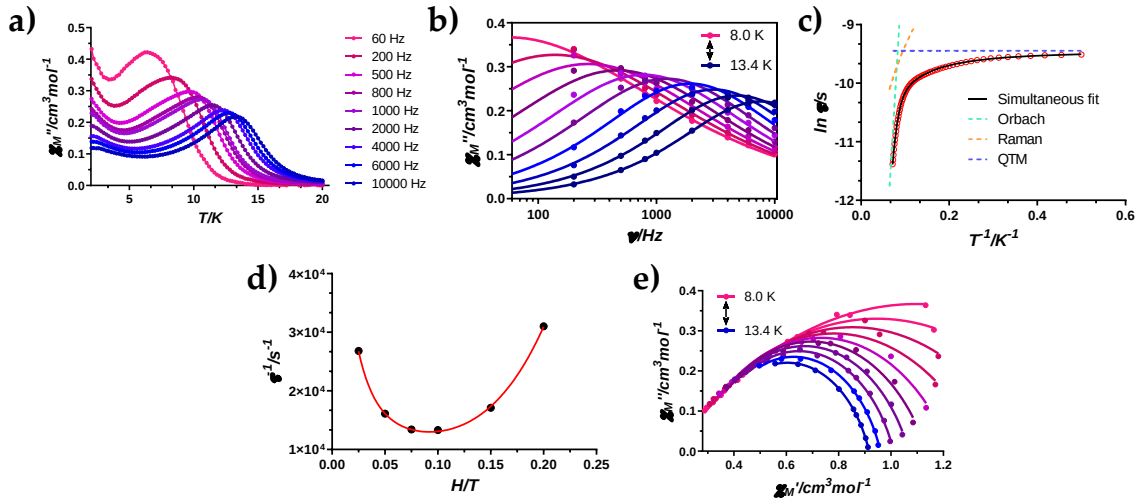

i.8. irudia. Dy^{III} ioian oinarritutako *SMM* batentzat: a) fasez kanpoko suszeptibilitate magnetikoaren (χ_M'') tenperaturarekiko mendekotasuna, hainbat frekuentziatan; b) χ_M''-ren frekuentziarekiko mendekotasuna, hainbat tenperaturatan; c) erlaxazio-denboren doitzea Orbach, Raman eta *QTM* prozesuak kontutan hartuz; d) eremu magnetiko desberdinetan lortutako erlaxazio-denboren alderantzizkoa, tenperatura finkoan; e). Cole-Cole grafika.

Molekularen magnetizazioa eremu magnetikoaren norantza aldaketa jarraitzeko gai ez izatea anisotropia magnetikoarekin lotuta dago, spin proiekzio bakoitzak bere energia propioa baitu. Erlaxazio-denbora eta korronte alternoaren periodoa bat datozenean, maximo bat agertzen da $\chi_M''(T)$ grafiketan frekuentzia desberdinetan edo $\chi_M''(\upsilon)$ grafiketan tenperatura desberdinetan (i.8a eta i.8b irudiak). Bi grafiko moten artean, $\chi_M''(\upsilon)$ motakoak Debyeren eredura doitu daitezke Casimir-Du Preren ekuazioarekin [5]. Aztertutako frekuentzia-tartean maximoa erakusten duten tenperatura desberdinetako

kurbak (8,0-13,4 K, i.8b irudia) aipatutako eredura doitzen dira, eta horrek erlaxazio-denborak ateratzea ahalbidetzen du tenperatura bakoitzerako. Erlaxazio mekanismoa soilik Orbach motakoa denean, erlaxazio-denborak Arrheniusen lege linealari jarraitzen dio (i.1. ekuazioa) eta doiketak zuzenean ematen du energia-barrera efektiboaren balioa (U_{eff}). Hala ere, hori gutxitan gertatzen da eta magnetizazioaren erlaxazioa hainbat mekanismoren bidez gertatzen da. Kasu horietan, beharrezkoa da ekuazioan beste prozesuak deskribatzen dituzten doikuntza-parametro berriak sartzea, i.2. ekuazioan ikus daitekeen bezala (τ_{QTM}^{-1} = *QTM*; BT^n = Raman eta *AT* = zuzena). i.8c irudiak erlaxazio-denboren doikuntza erakusten du, Orbach, Raman eta *QTM* prozesuen aldi bereko presentzia kontuan hartuta. Lerro etenek aurreko baieztapena berresten dute, prozesu horiek tenperatura baxuetan (*QTM*), tartekoetan (Raman) eta altuetan (Orbach) jarduten dutela adierazten duena.

$$\tau^{-1} = \tau_0^{-1} exp(-U_{eff}/k_B T) \qquad \text{(i.1)}$$

$$\tau^{-1} = \tau_{QTM}^{-1} + AT + BT^n + \tau_0^{-1} exp(-U_{eff}/k_B T) \qquad \text{(i.2)}$$

Erlaxazio-denborak aurreko adibidean bezala zenbait mekanismora egokitu ohi diren arren, batzuetan, ekuazioan prozesu gehiegi sartzen direnean, gainparametrizazio-egoera gisa har daiteke. Ereduan hainbat mekanismo sartzeak doikuntza hobea eman liezaguke, baina mekanismo bakoitzerako lortutako balioek ziurrenik esanahi fisikoa galduko dute. Egoera hori gainditzeko, esperimentu gehigarriak egin daitezke. Tenperatura jakin batean eremuak erlaxazio-denboretan duen eragina aztertuta, i.8d irudian erakusten den bezala. Ikus daitekeenez, erlaxazio-denborak handiagoak dira, eta erlaxazio-prozesuak motelagoak, kanpoko eremu magnetikoaren balioa handitu ahala. Hau 0,1 T arte gertatzen da, non erlaxazio-prozesua maximora moteltzen den ziuraski *QTM* blokeatzearen ondorioz. Haren gainetik, erlaxazio-denborak azkarragoak izaten hasten dira berriro, eta hori, ziur asko, zuzeneko prozesu bat bultzatzearen ondorioz sortzen da. Horrela, kurba hau i.3. ekuaziora doi daiteke, *QTM* eta prozesu zuzenen eremuaren mendekotasuna azaltzen duena:

$$\tau^{-1} = AH^4T + B_1/(1+B_2H^2) + C \qquad \text{(i.3)}$$

Lehen terminoa prozesu zuzenari dagokio, horrek azaltzen du eremu altuetara zergatik nagusitzen den (H^4-ren mende dago, *H* eremua izanik). Bigarren terminoak *QTM* deskribatzen du, eta termino konstanteak, *C* terminoak, eremuarekiko independienteak diren erlaxazio prozesuak. Beraz, erlaxazio-denboren eremuarekiko mendekotasunaren azterketak erlaxazio-mekanismoei buruzko informazio gehigarria

eman diezaguke. Horrela, doikuntzak mekanismo zuzenari eta *QTM*ari dagozkien parametroen balioa eman diezaguke eta horiek, aldi berean, i.2. ekuazioan finka daitezke gainparametrizazio-egoera saihestuz. Horri esker, parametro fidagarriagoak lortuko ditugu erlaxazio-mekanismo bakoitzerako.

Arrheniusen grafikoan (i.8c irudia) linealtasunik ez dagoenez, garbi dago prozesu ugari ari direla martxan, baina Cole-Coleren grafikoek (i.8e irudia) frogatu dezakete hori. Grafiko horietan, χ_M'' vs χ_M' kurbek zirkuluerdiak erakusten dituzte tenperatura bakoitzerako, eta Debyeren eredu orokorrera egokitu daitezke [6]. Doikuntzak α balioak ematen ditu 1 eta 0 artean, non $\alpha = 0$ erlaxazio-mekanismo bakarra den; aldiz, 1 baliotik zenbat eta gertuago, handiagoa da aldi berean jarduten duten erlaxazio-bideen kopurua. Aipatzekoa da literaturan ohikoa dela $\chi_M''(T)$ grafikoetan bi maximo multzo erakusten dituzten materialak aurkitzea (horrek, aldi berean, maximoen bi multzo egotea eragiten du $\chi_M''(\upsilon)$ grafikoetan, eta bi zirkuluerdien batura Cole-Cole grafikoetan) [7–9]. Hau termikoki aktibatutako Orbach prozesu biren presentziarekin lotzen da. Honen jatorria ez dago beti argi, baina hainbat arrazoi aurkeztu izan dira eta kasu batetik bestera arrazoia alda daiteke. Egitura berean kristalografikoki independenteak diren bi konposaturen presentzia arrazoi bat izan liteke [10], nahiz eta ioi paramagnetiko bakarrak bi maximo multzo eman ditzakeen [11]. Kasu horietan, termikoki aktibatutako bi prozesuren presentzia maila anitzeko sistematik eratorritako zuzeneko prozesuei (kanpoko eremu magnetiko baten presentziak sortuak) edo molekulen arteko interakzioei egotzi zaie [12,13]. Nolanahi ere, kasu berezi horietan datuak tratatu ahal izateko, aldatutako bi Debye funtzio erabil daitezke prozesu indibidual bakoitzerako erlaxazio-denborak lortuz. Hori erraz egin daiteke Chilton eta kolaboratzaileek berriki garatutako CCFIT softwarearekin [14].

Sistema batek *SMM* gisa jokatzen duen ala ez zehazteko bigarren teknika da magnetizazioaren eremuarekiko mendekotasuna neurtzea tenperatura desberdinetan. Konposatua *SMM* bat denean, histeresi ziklo irekiak ikusten dira (i.9. irudia). Hertsiki esanda, hori da *SMM* baten ezaugarririk garrantzitsuena bere potentziala ebaluatzeko. Hurrengo ataletan deskribatuko den bezala, literaturan U_{eff} altuak (> 350 cm^{-1}) dituzten *SMM*en kantitate handi bat deskribatu den arren, horietako gehienek ez dute irekia den histeresi-ziklo argirik erakusten edo oso tenperatura baxuetan erakutsi ohi dituzte, 2 K inguruan (i.9a irudia). Egoera ideal batean i.9b irudiako zikloa esperoko genuke giro tenperaturan, eremu magnetikorik gabe ere magnetizazio guztia mantentzen duena. Gaur egun, 80 K arteko histeresi ziklo irekiak deskribatu dira (ikus beherago) eta hori

urrats handitzat hartu da alor honetan, tenperatura hori nitrogeno likidoarena baino handiagoa baita.

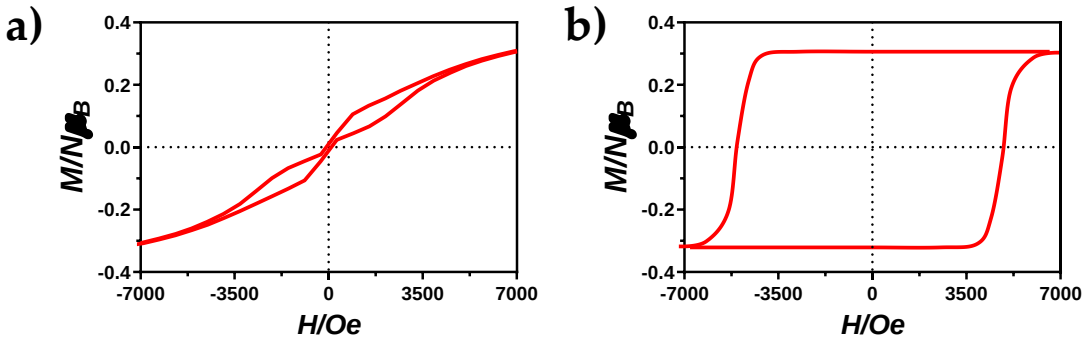

i.9. irudia. a) QTMak eragindako histeresi-ziklo arrunta 2 K-etan. b) Histeresi-ziklo ideala giro tenperaturan.

Korronte alternoarekin egindako neurketek ez bezala, azken teknika honek *SMM*en ezaugarri den parametro oso garrantzitsu bat definitzea ahalbidetzen du, blokeo-tenperatura (T_B). Bere definiziorik ohikoenaren arabera, histeresi-ziklo irekia ikus daitekeen tenperaturarik altuenak definitzen du T_B. Hala ere, tenperatura hau, neurri handi batean, eremu magnetikoaren ekorketa-abiaduraren araberakoa da. Hori dela eta, blokeo-tenperaturaren balioa erabiliz *SMM* ezberdinak alderatzen direnean, derrigorrezkoa da histeresi-zikloak baldintza esperimental berdinetan erregistratu zirela ziurtatzea. Bestalde, T_B zehazteko beste irizpide batzuk ere badaude: (i) tenperatura non τ = 100 s edo (ii) *FC* (*Field Cooled*) eta *ZFC* (*Zero-Field Cooled*) suszeptibilitate magnetiko kurbak bereizten diren tenperatura.

ii. HASIERA: KLUSTER METALIKOEN AROA

Mn12-ac molekularen aurkikuntza gertaera garrantzitsua izan zen materialen zientzian, zehazki magnetismo molekularraren alorrean. Izan ere, trantsizio-metalen klusterretan oinarritutako *SMM*ek funtzionatzeko behar duten tenperatura (normalean 5 K-etik beherakoa) nitrogeno likidoaren tenperaturaren gainetik igoko balitz, datuak biltegiratzeko gailuetan erabili ahal izango lirateke potentziala izugarri areagotuz. Sistema horien lan-tenperatura baxuaren handicapa gainditzen saiatzeko, kontuan izan behar da magnetizazioaren birorientazioa eragozten duen energia barrera, aldi berean, spinaren eta anisotropiaren mende dagoela:

$$U = S^2 \cdot |D|;\ S = osoa \qquad \text{(i.4)}$$

$$U = (S^2 - ¼) \cdot |D|;\ S = erdiosoa \qquad \text{(i.5)}$$

Spinaren mendekotasun koadratikoari erreparatuz, energia-barrera hobetzeko modurik logiko eta errazena eta, beraz, blokeo-tenperatura, oinarrizko egoeraren spin balioa handitzea litzateke. Horretarako, ferromagnetikoki akoplatutako nukleartasun handiko sistemak sintetizatu ziren. Horien artean, Mn^{III} ioia zutenak hautagai egokiak ziren *SMM* portaera erakusteko bi arrazoirengatik: (i) spin altuko konfigurazioan parekatu gabeko 4 elektroi ditu eta hori positiboa da *S*-ren balio osoa handitzeko eta (ii) eremu kristalino oktaedriko batean (ohikoena ioi metaliko honentzat), Mn^{III} ioia Jahn-Teller distortsioaren mende dago, horrek oinarrizko egoerako zero eremuko zabaltzea (*ZFS*) eta aldi bereko anisotropia axiala dakar, *D* parametroak definitua. Gainera, urte horietan zehar ikerketa teoriko eta esperimental ugari egin ziren korrelazio magneto-estruktural berriak aurkitzeko helburuarekin. Modu horretan, kimikariek ioi metalikoen arteko interakzio ferromagnetikoak zituzten trantsizio-metalen kluster berriak diseinatu eta sintetizatu ahal izan zituzten [15–20]. Aipatzekoa da kasu batzuetan azida estekatzaile laguntzaile gisa erabili zela, *end-on* moduan koordinatuta interakzio ferromagnetikoak eragin ditzakeelako [21,22]. Gainera, ohiko sintesi metodoez gain (presio atmosferikora eta disolbatzailearen irakite-puntura mugatutako erreakzioak), ikerketa talde batzuk teknika solbotermikoak ustiatzen hasi ziren, konplexu polinuklearrak lortzea ahalbidetu zutenak [23]. Aipatutako estrategia sintetiko horiei esker, spin eta nukleartasun handiko sistema asko prestatu ahal izan ziren, Mn^{III} ioiak ez ezik, beste trantsizio-metal batzuk ere erabiliz. Sistema polinuklear horien adibide dira Mn_9Mo_6 (**i2**), Fe_{19} (**i3**), Mn_{19} (**i4**) eta Mn_{25} (**i5**) konposatuak [24–27]. Nabarmentzekoa da **i4** konposatuak, benetan $Mn^{II}_7Mn^{III}_{12}$ konplexua denak, S = 83/2 spin balio errekorra lortu zuela (i.10. irudia). Hala eta guztiz ere, koordinazio konposatu guzti hauentzat aurkitutako oinarrizko egoerako *S* balioa handia zen arren, U_{eff} eta T_B balioei zegokionez Mn12-ac konposatuarenak baino pobreagoak ziren. Zehazki, **i4** konposatuak anisotropia mespretxagarria du eta U_{eff} = 4 cm^{-1}.

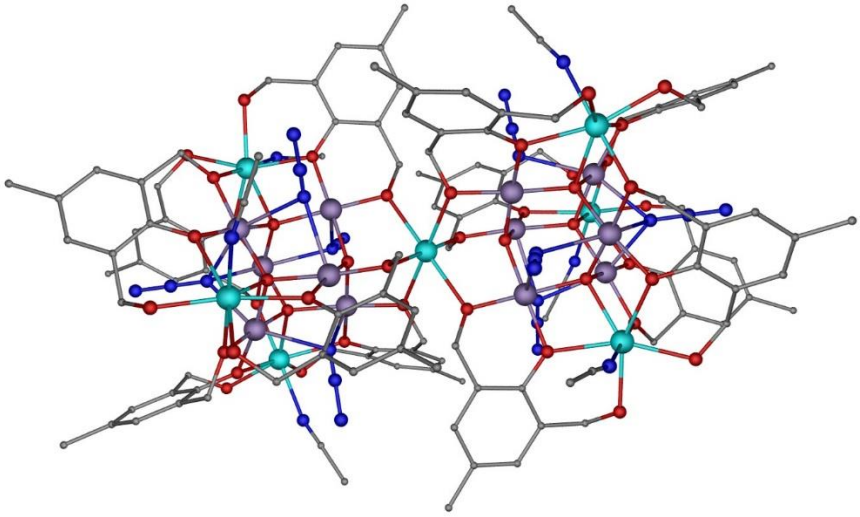

i.10 irudia. i4 konposatuaren ikuspegia. Kolore-kodea: Mn^{II}, Mn^{III}, karbonoa, nitrogenoa eta oxigenoa urdin argi, more, gris, urdin ilun eta gorri kolorez, hurrenez hurren. Hidrogeno atomoak ez dira irudikatu argitasunaren mesedetan. [26] erreferentziako kristal-egituratik abiatuta sortutako irudia.

Denborak aurrera egin ahala, arazoa gero eta nabarmenagoa zen. Sisteman ioi paramagnetiko ugari sartzeak anisotropiaren balioa murrizten zuela ikusi zen. Zenbait ikerketak frogatu dute anisotropiaren balio globala sentikorra dela zentro metaliko bakoitzaren Jahn-Teller ardatzaren orientazioarekiko, eta anisotropiaren balio osoa murriztu egiten dela Jahn-Teller ardatzak kolinealak ez direnean. Beraz, klusterrean ioi metaliko asko sartzen direnean normala da *D*-ren azken balioa txikiagoa izatea [28]. Gainera, zenbait adierazpen matematiko proposatu dira kluster baten erabateko anisotropia kalkulatzeko. Hala nola, ioi bakoitzaren Jahn-Teller ardatzak erabateko anisotropia ardatzarekiko (α) duen angelua kontuan hartuta [29]. Horretaz gain, Neesek eta egilekideek egindako azterketa teorikoek frogatu zuten $D \propto 1/S^2$ dela eta, beraz, $U_{eff} = DS^2$ formularen hurbilketa on batean, energia-barrera *S*-rekiko independentea dela [30].

Emaitza horiek guztiek aro berri bat eragin dute azkenaldian *SMM*entzat, non nukleartasun txikiagoko koordinazioko konposatuek, baina anisotropia magnetiko handiagokoek, garrantzi handiagoa hartu duten.

Aniosotropia magnetikoaren balio oso altuak lortzeko nagusiki bi aukera daude: (i) trantsizio-metaletan oinarritutako koordinazio mononuklearrak diseinatzea ioi indibidualak anisotropia nabarmena edukiz eta (ii) ioi lantanidoak dituzten koordinazioko

konposatuak erabiltzea, berriz ere ioi indibidualen anisotropia sustatuz (Gd^{III} ioia izan ezik, isotropikoa baita). Lehen kasuan, koordinazio-zenbaki baxuko konplexuek eremu kristalino ahulak sortzen dituzte, momentu angeluar orbital altuak, spin-orbita akoplamendua eta, beraz, anisotropia magnetiko handia. Bigarren kasuan, ordea, anisotropia magnetiko handia espina-orbita akoplamendu indartsuaren eta kristal-eremuaren ekintza konbinatuen emaitza da. Gainera, geometriak funtsezko eginkizuna betetzen du *SMM*en portaera determinatzeko.

iii. TRANTSIZIO-METALETAN OINARRITUTAKO KOORDINAZIO-ZENBAKI BAXUKO IOI BAKARREKO IMANAK (*SIMs*, *SINGLE ION MAGNETS*)

Konposatuen *S* balioa nabarmen handitzeko ideia nolabait alde batera utzi eta anisotropia balioa handitzeko estrategia indartu zen. Lantanidoen balentzia-elektroiak ez bezala, non 4f orbitalak atomoaren barruan askoz babestugo dauden estekatzaileen eraginetik (ikusi aurrerago), lehen lerroko trantsizio-metaletan 3d orbitalek askoz gehiago sumatzen dute estekatzaileen eragina. Beraz, estekatzaileek eragindako kristal-eremuak, kasu batzuetan (ioi metalikoaren eta simetriaren arabera), momentu angeluar orbitala erraz deusezta dezake, ondorioz, lehen mailako spin-orbita akoplamendua (*SOC, Spin-Orbit Coupling*) deuseztatuz [31]. Baieztapen horrek esan nahi du anisotropia magnetikoa eragiten duen *SOC*a sarritan bigarren mailako *SOC*tik sortzen dela, oinarrizko eta egoera kitzikatuen spin-orbita nahasketatik [32,33]. Hala ere, lehen mailako spina-orbita akoplamendua mantendu daiteke estekatzaileen diseinu arrazional baten bidez koordinazio zenbaki baxuak lortuz. Azken urteotan koordinazio-zenbaki baxuko *SIM* portaera duten koordinazio konposatu ugari deskribatu badira ere [34–38], hemen propietate onenak dituztenak soilik aurkeztuko ditugu, geometria lineala dutenak eta Kramers ioi metalikoak dauzkatenak.

Gogoeta horietan oinarrituta eta $S = 2$ duten Fe^{II} sistema linealentzat ikusitako emaitza interesgarrien ondoren, zeinak eremu eraginpeko *SMM* portaera erakusten zuten [39–43], Longen taldeak erabaki zuen pauso bat gehiago ematen saiatzea: kanpo eremu magnetiko baten beharrik izan gabe energia-barrera altuko *SIM*ak sortzen saiatzea trantsizio-metalekin. Horretarako, Kramersen teoremaz baliatu ziren Fe^{I} ioiaz osatutako koordinazio konposatu lineal bat aztertuz, $S = 3/2$ duena. i.11. irudian agertzen da konposatua eta honako formula orokorra du: $[K(crypt\text{-}222)][Fe(C(SiMe_3)_3)_2]$ (**i6**) [44]. *Ab initio* kalkuluetan oinarrituz, koordinazio-zenbaki eta oxidazio egoera baxuen konbinaketak estekatzaile-eremu oso ahula sortzen duela frogatu zuten, momentu

angeluar orbitala mantenduz eta konposatuaren erabateko anisotropia areagotuz. Horrek oinarrizko ^{4}E egoera lau Kramers dobletetan (KD) banatzea dakar, M_J zenbaki kuantikoek hobeto deskribatuta M_J = ±7/2, ±5/2, ±3/2 eta ±1/2 balioekin. Gainera, oinarrizko egoeraren eta lehen egoera kitzikatuaren artean kalkulatutako energia diferentzia handia zen, *SMM* potentziala adierazten zuena.

Hain zuzen, kanpo eremu magnetiko gabe egindako *ac* neurketek erakutsi zuten konposatu honen *SMM* portaera esperimentalki kalkulatutako U_{eff} = 226(4) cm^{-1} balioarekin. Energia-barrera efektiboaren balio hori oinarrizko egoeraren (M_J = ±7/2) eta kitzikatutako lehen egoeraren (M_J = ±5/2) artean kalkulatutako energia-diferentziarekiko gertu dago; horrek adierazten du erlaxazioa, ziurrenik, kitzikatutako lehen egoera horretatik gertatzen dela. Erlaxazio-denborek Arrheniusen legeari jarraitzen dioten arren 20-29 K-eko tenperatura-tartean, τ balioak nabarmen desbideratzen dira linealtasunetik 20 K-etik behera, tenperatura baxuenetan *QTM* mekanismoak jarduten duela adieraziz.

Hasieran aipatu den bezala, blokeo-tenperatura (T_B) zehazteko beste modu bat da *FC/ZFC* neurketak egitea. Izan ere, blokeo magnetikoa ematen bada, $\chi_M T$ kurbek desberdinak izan behar dute neurketa eremu magnetiko baten presentzian edo gabezian egiten denean. Horrela, **i6** konposatuaren kasuan, 4,5 K-etan ikusi zen kurba bien dibergentzia. Honek, aldi berean, histeresi-zikloak ikus zitezkeela iradokitzen zuenez, 1,8-6,5 K-eko tenperatura-tartean neurtu ziren zikloak, tximeleta formako ziklo irekiak agerraraziz. Horrelako formek *QTM*ren presentzia esanguratsua adierazten dute. Efektu honen jatorria ezagutzeko asmoz, neurketa magnetiko berdinak egin zituzten **i6** konposatuaren disoluzio izoztuetarako, jakina baita molekula arteko interakzio dipolarrek *QTM* eragiten dutela. Hala ere, datuak, oro har, material mikrokristalinorako bildutakoekin alderatu ahal izan ziren, tunel kuantikoaren jatorri molekularra baieztatuz. Gauzak horrela, efektu kuantiko hau C-Fe-C loturek disoluzioan zein egoera solidoan jasan ditzaketen distortsio geometrikoei egotzi zieten (jakina, gutxiago egoera solidoan) eta baita Renner-Teller aktibitate bibronikoari ere [43].

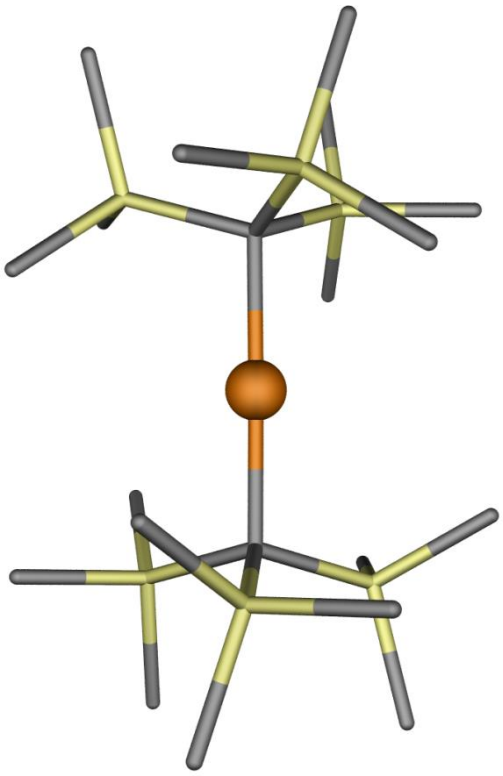

i.11. irudia. i6 konposatuaren zati anionikoaren ikuspegia. Kolore-kodea: burdina, karbonoa eta silizioa laranja, gris eta hori kolorez, hurrenez hurren. Hidrogeno atomoak ez dira irudikatu argitasunaren mesedetan. [44] erreferentziako kristal-egituratik abiatuta sortutako irudia.

Erakutsitako adibideaz gain, beste ikerlari batzuek burdin, kobalto edo nikel ioietan oinarritutako konposatu lineal homoleptikoei buruzko informazioa ere eman zuten, baina guztiek ez zuten hain errendimendu ona izan *QTM* indartsuago baten ondorioz [35,38,45–47]. Aipatu berri bezala, akoplamendu bibronikoek tunel-efektu azkarra eragin dezakete eta hori aipatutako adibideetan agertzen diren metal-estekatzaile lotura luzeen distortsio dinamikoaren ondorio argia da. Arazo hauek gainditzeko, Atanasov, Neese eta kolaboratzaileek lotura kimikoaren papera, akoplamendu bibronikoarena eta anisotropia magnetikoarena kontuan hartzen dituen lan teoriko bat argitaratu zuten *SMM* portaera erakusten duten Fe^{II} konplexu linealetan oinarrituz [43]. Ondorio nagusi gisa, izaera kobalente altuagoko metal-estekatzaile loturek akoplamendu bibronikoa ekidin dezaketela proposatu zuten, aldi berean anisotropia balioa sustatuz.

Kobalentzia-izaera areagotzeko bilaketan, Gao eta lankideek Co^{II} ioian oinarritutako hiru konposaturen sintesi eta propietate magnetikoei buruzko informazioa argitaratu

zuten [(NHC)CoNDmp] formula orokorrarekin, non Dmp = 2,6-dimesitifenil eta NHC karbeno N-heteroziklikiko estekatzaile desberdinak diren, i.12. irudian adierazten den bezala [48]. Aipatzekoa da **i7** konposatuaren sintesia, egitura eta erreaktibitatea aldez aurretik deskribatuak zeudela [49]. Co^{II} ioian oinarritutako imido konposatu hauek estekatzaileen antolamendu ia lineala erakutsi zuten, $Co\text{-}N_{imido}$ lotura-distantzia oso motzekin (1,691(6) Å, lotura-ordena bikoitzari dagokiona).

Lehen mailako *SCO* mantendu izanaren lehen froga argia jada identifikatu zen *dc* datuetan oinarrituta. Giro tenperaturan neurtutako $\chi_M T$ balio altuak (3,86, 3,72 eta 3,74 $emu \cdot K \cdot mol^{-1}$, **i7**, **i8** eta **i9** konposatuentzat, hurrenez hurren) estekatzaileek eragindako eremu ahularen isla ziren eta momentu angeluar orbitala deuseztatu gabea zegoela adierazten zen. Gainera, **i9** konposatuarentzat 3,5 K-etan erorketa malkartsu bat identifikatu zen (i.12c irudia), momentu magnetikoen blokeoa adierazten zuena eta histeresi zikloak neurtuz egiaztatu zena. Korronte alternoarekin (*ac*) egindako neurketek erakutsi zuten hiru konplexuek *SIM* portaera zutela kanpo *dc* eremu magnetikorik aplikatu gabe. Aipatzekoa da, halaber, $\chi_M''(\upsilon)$ grafiketan maximoak 50 K-etaraino detektatu zirela 10000 Hz-ko frekuentzia-mugan. Datuen tratamendutik 413 cm^{-1}-eko energia-barrera efektiboa determinatu zen, ordura arte 3d-tan oinarritutako *SMM* batentzako lortutako altuena.

Portaera bikain hori azaltzeko eta korrelazio magneto-estrukturalak egiteko, azterketa teoriko sakonak egin zituzten. Co=N lotura-distantzia laburretik espero zen bezala, lotura-luzera hori modifikatuz simulatutako aldaketek ondorio nabarmenak eragin zituzten. Hain zuzen, oinarrizko egoeren eta egoera kitzikatuen arteko desberdintasun energetikoak eta baita sistemaren axialtasuna ere, erabat modulatzen ziren lotura pixka bat luzatu edo laburtze hutsarekin, konplexuen erabateko anisotropia magnetikoaren balioan betetzen zuen papera berretsiz. Azkenik, Co^{II} ioian oinarritutako *SMM* eredu mononuklear sinplea aintzat hartzea baztertu ez zuten arren, proposatu zuten sistemen anisotropia magnetiko handia $[CoN]^+$ nukleotik zetorrela, zeinak Kramers doblete bat izango lukeen oinarrizko egoeran $M_J = \pm 7/2$ balioarekin eta Co-N akoplamendu handi batekin. Eredu horrek nolabait azal lezake *QTM*ren deuseztapen efektiboa sistema hauetan.

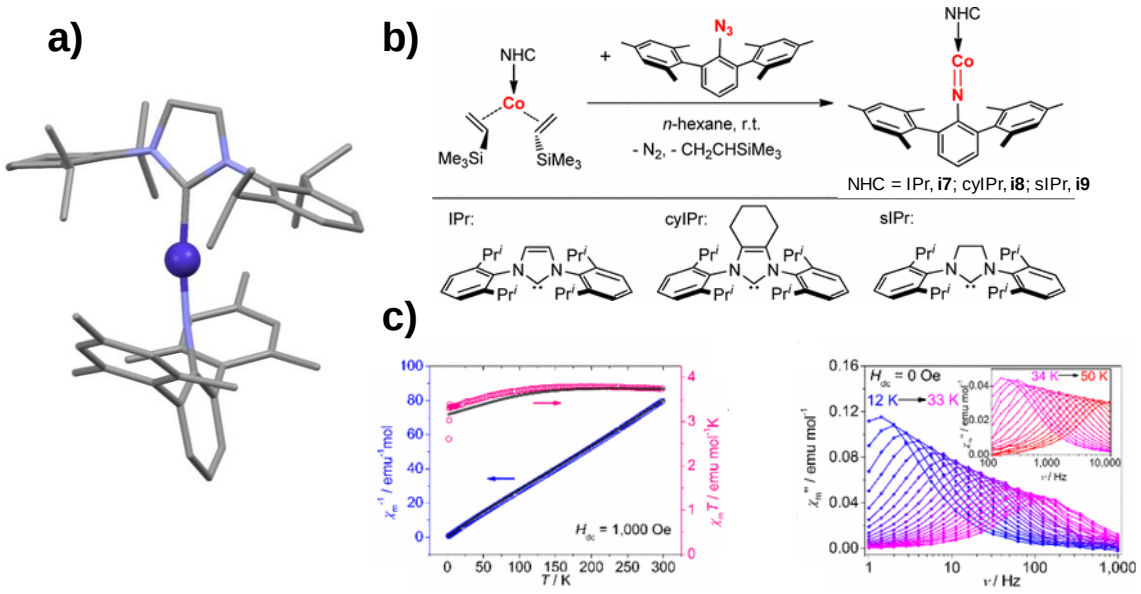

i.12. irudia. a) **i7** konposatuaren ikuspegia. Kolore-kodea: Co^{II}, karbonoa eta nitrogenoa more, gris eta urdin kolorez, hurrenez hurren. Hidrogeno atomoak ez dira irudikatu argitasunaren mesedetan. b) Konposatuen lorpenearako ibilbide sintetikoa eta NHC estekatzaileen izendapena. c) $\chi_M T$ eta χ_M^{-1} balioen tenperaturarekiko mendekotasuna 2-300 K tenperatura tartean (ezkerrean) eta χ_M''-ren frekuentziarekiko mendekotasuna **i9** konposatuarentzat (eskuinean). **i7** molekularen ikuspegia [49] erreferentziako egitura kristalinotik abiatuta sortu da. Ibilbide sintetikoaren eskema eta propietate magnetikoen irudia [48] erreferentziaren baimenarekin egokitu da. Copyright 2017 American Chemical Society.

Azkenik, Long eta lankideek **i10** (i.13. irudia) molekula deskribatu zuten $[Co(C(SiMe_2ONaph)_3)_2]$ (Naph = naftalenoa) formula orokorrarekin [50]. Konposatu horretara heltzeko arrazoia $[Co(C(SiMe_3)_3)_2]$ sistema hipotetikoan oinarritutako kalkuluak izan ziren, izan ere, L = 3 oinarrizko egoera aurreikusten zitzaion Aufbauen araua beteko ez lukeelako 3d orbitalak elektroiez betetzerako garaian [51]. Honek, nolabait, lantanidoen portaera imitatuko luke momentu angeluar orbital maximoa lortuz eta, beraz, anisotropia magnetiko oso handia. Hala ere, bazekiten teorikoki planteatutako konposatua lortzea zaila izango zela, estekatzaile alkilikoak dituzten trantsizio-metalen koordinazio-konplexu linealak $[M(C(SiMe_3)_3)_2]^{0/1-}$ formularekin baino ez baitziren ezagutzen: M = Fe^{II} [52], Fe^{I} [53], Mn^{II} [54] eta Mn^{I} [55] izanik. Co^{II} ioiarentzat, aldiz, aurretik aipatutakoak bezalako beste sistema batzuk deskribatu dira, baina baita

$[OCoO]^-$ anioiak apatitazko kanal batean txertatuta [56] eta Co^{II} ioi indibidualak MgO gainazaletan ere [57].

Planteatutako konposatu lineala lortu aurretik erronka sintetiko asko izan zituzten, hala nola, karbanioien izaera bereziki erreduzitzailea, C-Co-C angelu itxiak beste estekatzaile batzuekin probatzean eta sistema dinuklearren eraketa, besteak beste. Azkenean, dena den, estekatzaileetan -ONaph taldeak sartzean konposatu lineal desiratua kristalizatu zuten. Egituraren azterketari erreparatuz, -C-H···π interakzio intramolekularrak garrantzitsuak izan zitezkeela ondorioztatu zuten konposatuaren egonkortzean.

Aurretik egindako kalkuluetatik espero zen bezala, **i10** sistemarentzak eginiko analisi teorikoak iradokitzen zuten $^4\Phi$ oinarrizko egoerak d orbitalen betetzea ez-Aufbau motakoa izango zuela, $(d_{x^2-y^2}, d_{xy})^3(d_{xz}, d_{yz})^3(d_{z^2})^1$ emanez. Estekatzaile-eremua hain zen ahula, non spin altuko egoera maximizatu bat lortu baitzen. Ondorioz, gaur egun trantsizio-metal batean oinarritutako *SIM*entzat errekorra den U_{eff} = 450 cm^{-1} balioa kalkulatu zen. Energia-barrera efektiboaren balioak M_J = ±9/2 oinarrizko egoera eta M_J = ±7/2 lehen egoera kitzikatuaren arteko energia-diferentzia adierazten du, kalkulu teorikoetatik, infragorri urrunaren espektroskopiatik (*FIR, far-infrared*) eta *ac* neurketetatik ondorioztatu zena.

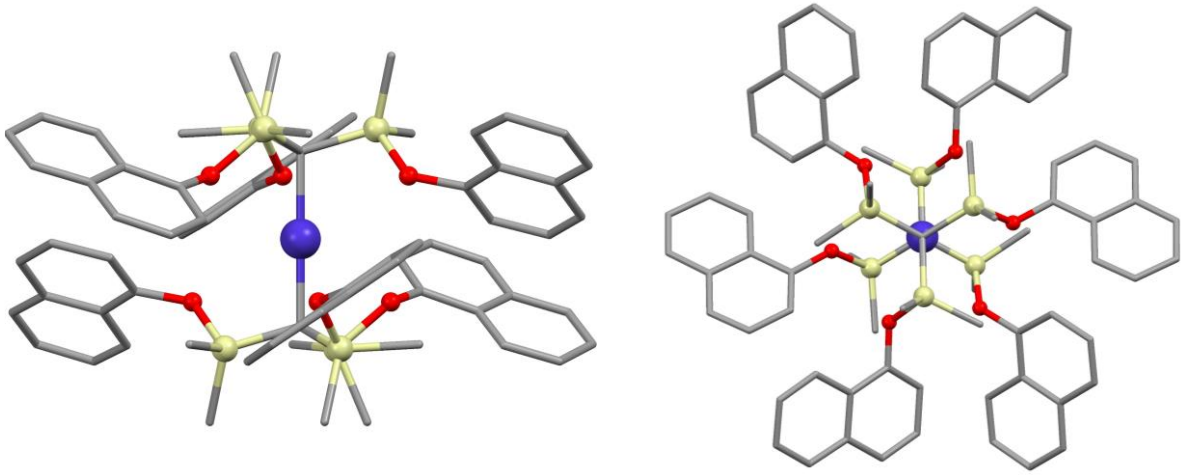

i.13. irudia. i10 konposatuaren ikuspegia (ezkerrean). Egitura molekularra *c* ardatz kristalografikoan zehar (eskuinean). Kolore-kodea: Co^{II}, karbonoa, oxigenoa eta silizioa more, gris, gorri eta hori kolorez, hurrenez hurren. [50] erreferentziako kristal-egituratik abiatuta sortutako irudia.

iv. LANTANIDOEN AROA

Lantanidoetan oinarritutako *SMM*en berri Ishikawak eta kolaboratzaileek eman zuten lehen aldiz 2003an [58]. Sandwich motako koordinazio konposatuak ziren, aurretik Koikeren taldeak deskribatuak, non bi ftalozianina deribatuk Ln^{III} ioiak inguratzen dituzten (**i11**, i.14. irudia) [59]. Lantanidoen artean, Tb^{III} (**i12**) eta Dy^{III} (**i13**) analogoek 230 eta 28 cm^{-1}-ko energia-barrerak erakutsi zituzten, hurrenez hurren. Gertaera honek baieztatu zuen zentro metaliko bakar bat nahikoa izan zitekeela energia-barrera altuko *SMM*ak diseinatzeko.

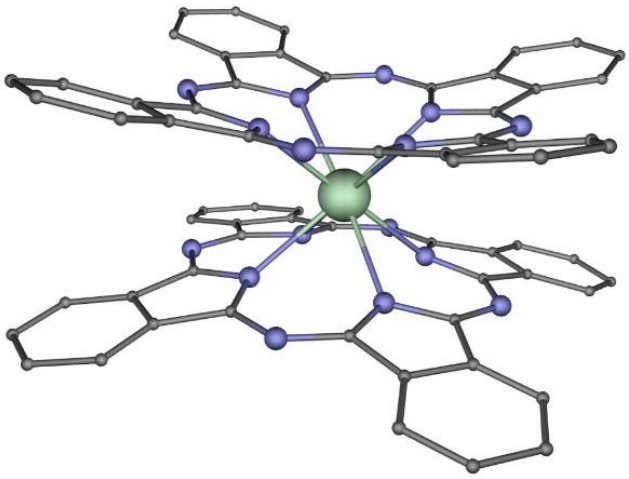

i.14. irudia. Koikeren taldeak deskribatutako sandwich motako **i11** konposatuaren ikuspegia. Kolore-kodea: Nd^{III}, karbonoa eta nitrogenoa berde, urdin eta gris kolorez, hurrenez hurren. Hidrogeno atomoak ez dira irudikatu argitasunaren mesedetan.

Trantsizioko-metalen aldean, lantanidoen abantaila da, lehen esan bezala, 4f orbitalak oso babestuta daudela atomoaren barruan, erabat okupatutako $5s^2$ eta $5p^6$ orbitalak baitaude kanpoalderago. Honek, estekatzaileen atomo emaileen eta ion lantanidoaren arteko interakzioa ia guztiz elektrostatikoa izatea dakar eta, ondorioz, spin-orbita akoplamendua (anisotropia magnetikoaren kausa nagusia) ez da trantsizio-metaletan bezain erraz deuseztatzen. Horrek esan nahi du, printzipioz, anisotropiaren balioa normalean handiagoa izango dela lantanidoentzat trantsizio-metalez osatutako konplexuentzat baino; beraz, teorian, propietate hobeak dituzten *SMM*ak lortzea espero daiteke. Hala ere, aurrerago aipatzen den bezala, trantsizio-metalentzat hain ohikoak ez diren desabantaila batzuk ere badituzte.

Spin-orbita akoplamendu indartsuaren ondorioz, lantanido ioi gehienentzat spina ez da momentu angeluarraren iturri bakarra. Beraz, propietate magnetikoak deskribatzean, spin-orbita akoplamenduaren terminoak (*J* zenbaki kuantikoak definitzen dituenak) eta estekatziale-eremuak sortutako banatzea kontuan hartu behar dira. Horrela, azpimailak M_J bidez deskribatzen dira lantanidoetan M_s zenbaki kuantikoen bidez deskribatu beharrean. Esanahia batetik bestera ezberdina bada ere, interpretazioa antzekoa da. Izan ere, *SMM*ak diseinatzen direnean, oinarrizko egoerak ondo definitutako oinarrizko egoera izan behar du, ahalik eta M_J balio absolutu handienarekin. Hori oinarrizko egoeraren anisotropia axiala denean lortzen da (trantsizio-metaletan $D < 0$ izango litzatekeena). Gainera, M_J eta $M_J \pm 1$ egoeren arteko energia-diferentzia ahalik eta altuena izatea komeni da U_{eff} parametroaren balio altuak lortzeko. Honek, aldi berean, estekatzaileen diseinu arrazionala eskatzen du.

Diseinu arrazional horretarako, Rinehartek eta Longek oso jarraibide erabilgarriak eta kontzeptualki ulerterrazak proposatu zituzten [60]. Lantanido seriearen barruan, bakoitzak bere ezaugarriak ditu. Adibidez, nahiz eta gehienek spin-orbita akoplamendu nabarmena izan, Gd^{III} ioia erabat isotropikoa da. Beraz, lantanido ioen artean elektroi desparekatu gehien dituen arren (horrek, printzipioz, *S* balio handia ekarriko luke oinarrizko egoeran), *SMM*ak diseinatzeko duen potentziala nulua da. Dentsitate elektroniko anisotropikoa duten ioien artean bi multzo nagusi bereiz daitezke (i.15. irudia): oblatu motako ioiak (esferoide kamutsa: Tb^{III} eta Dy^{III}, besteak beste) eta prolatu motakoak (esferoide luzango: Er^{III} eta Yb^{III}, besteak beste).

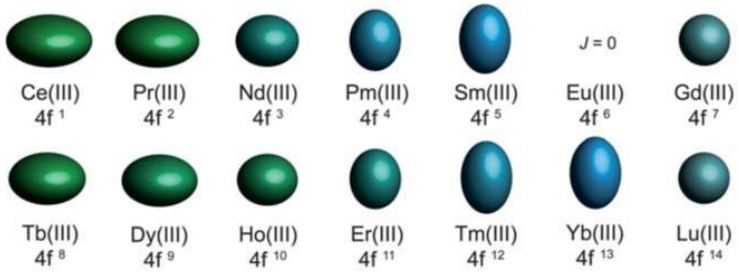

i.15. irudia. Ln^{III} ioien 4f geruzako elektroi-dentsitatearen distribuzioa. [60] erreferentziatik baimenarekin erreproduzitua. Copyright 2011 The Royal Society of Chemistry.

Lantanido ioi bakoitzerako elektroi-dentsitatearen forma nolakoa den ezagutze hutsak estekatzaile-eremu espezifikoaren diseinu arrazional eraginkorragoa ahalbidetzen du, anisotropia magnetiko axial handia lortzeko (oinarrizko egoerak M_J-ren baliorik handiena izan dezan). Horrela, oblatu motako ioien kasuan, dentsitate elektroniko handieneko estekatzaileak posizio axialetan koordinatu beharko lirateke (i.16. irudia, goian). Antolamendu horrek aldaratze elektroniko txikiagoa eragingo du ioi lantanidoaren elektroi-dentsitate oblatuaren eta estekatzaileen atomo emaileen artean M_J balio altuko oinarrizko egoera egonkortuz. Egoera honetan, anisotropia ardatza, elektroi-dentsitate oblatuarekiko perpendikularra dena, Ln-X distantzia laburrena duen atomo elektronegatiboenak definitua egongo da (X atomo emailea izanik). Azpimarratu behar da ekuatore-posizioetan atomo emailerik koordinata ez badago, elektroi-dentsitatea planoan zehar hedatuko dela, anisotropia axiala indartuz. Aitzitik, atomo emaileak ekuatore-posizioetan koordinatzen badira, esfera elektronikoa isotropikoagoa bihurtuko da, *SMM* izateko potentziala galduz (i.16. irudia, behean).

Prolatu motako ioien kasuan, dentsitate elektroniko handieneko estekatzaileen atomo emaileak ekuatore-posizioetan koordinatu behar dira anisotropia axiala lortzeko. Antolamendu honetan, lantanido ioiaren elektroi-dentsitate prolatuaren eta atomo estekatzaileen elektroien arteko aldaratze elektronikoa txikiagoa da. Kasu honetan, ardatz anisotropikoa, elektroi-dentsitate prolatuarekiko paraleloa dena, estekatzaileen atomo emaileak dauden planoarekiko perpendikularki dago. Posizio axialetan atomo emailerik ez badago, ioi metalikoaren elektroi-dentsitatea norabide axialean zehar heda daiteke, anisotropia axial handiagoa sortuz. Aldiz, posizio axialetan estekatzaileak koordinatzen badira, banaketa isotropikoagoa eragiten da eta, beraz, anisotropia gutxitu egiten da (i.16. irudia, behean).

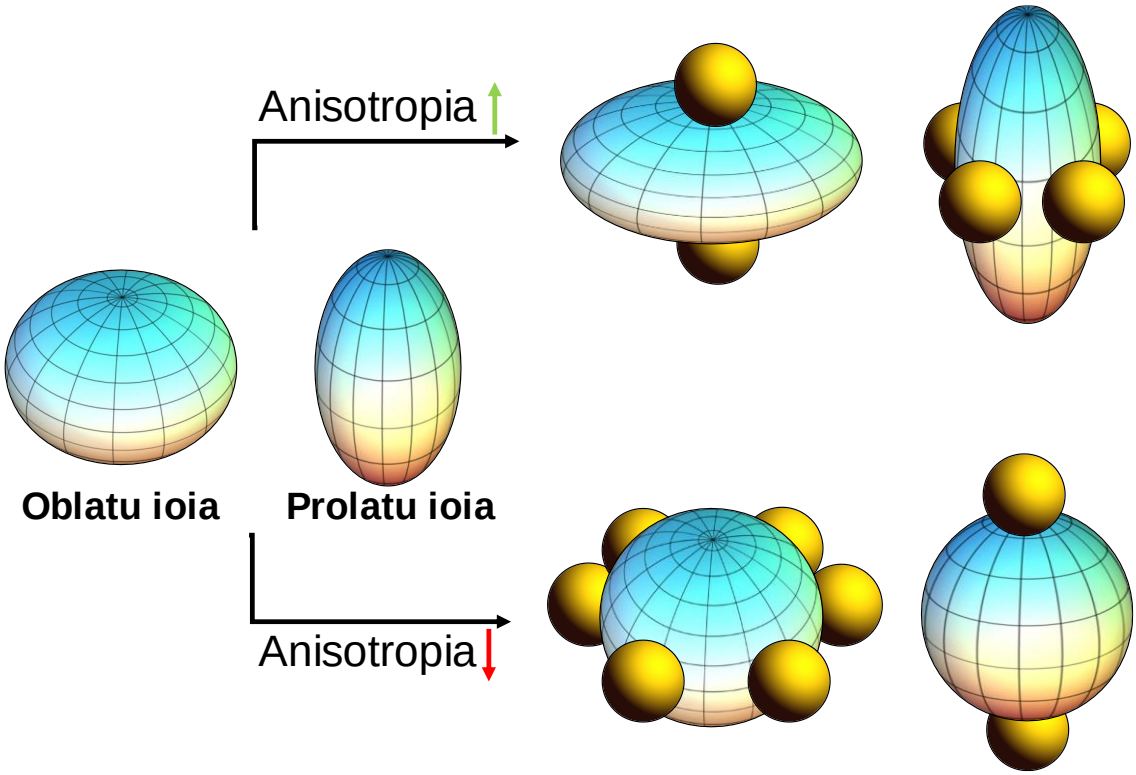

i.16. irudia. Nola aldatu oblatu eta prolatu motako ioien anisotropia.

Teoriak erraza dirudien arren, lantanidoen erradio ioniko handia oztopo bihurtzen da. Izan ere, estekatzaileak ez direnean espezifikoki diseinatzen geometria jakin bat lortzeko, oso ohikoa da koordinazio-zenbaki altuak lortzea (> 8). Hala ere, inpaktu handiko bi ikerketa erakusten dira hemen, Rinehartek eta Longek proposatutako jarraibideek anisotropia magnetikoa hobetzeko bidea erakusten dutela frogatzen dutenak.

2013an, Murugesuren taldeak Dy^{III} sistema dinuklear batean oinarritutako sei sistema antzeko, baina berriren propietate magnetikoak aztertu zituen. Ezberdintasun nagusia estekatzaile sekundarioen elektroi emaile izaera zen (lan honetan horietako hiru baino ez dira deskribatzen) [61]. Horretarako, aurretik aztertutako **i14** konposatu dinuklearra (i.17. irudia, ezkerrean) hartu zuten oinarri gisa [62,63]. Egitura orokorrari eutsiz, plano ekuatorialeko nitratoen ordez (fenoxido talde batek ematen dio axialitatea sistemari), azetilazetonatoa, *acac*, (**i15**, i.17. irudia, goian) edo hexafluoroazetiletonatoa, *hfac* (**i16**, i.17. irudia, behean) bezalako beste estekatzaile sekundario batzuk erabili zituzten, nitratoa baino elektroi-emaile hobea eta txarragoa diren taldeak, hurrenez hurren.

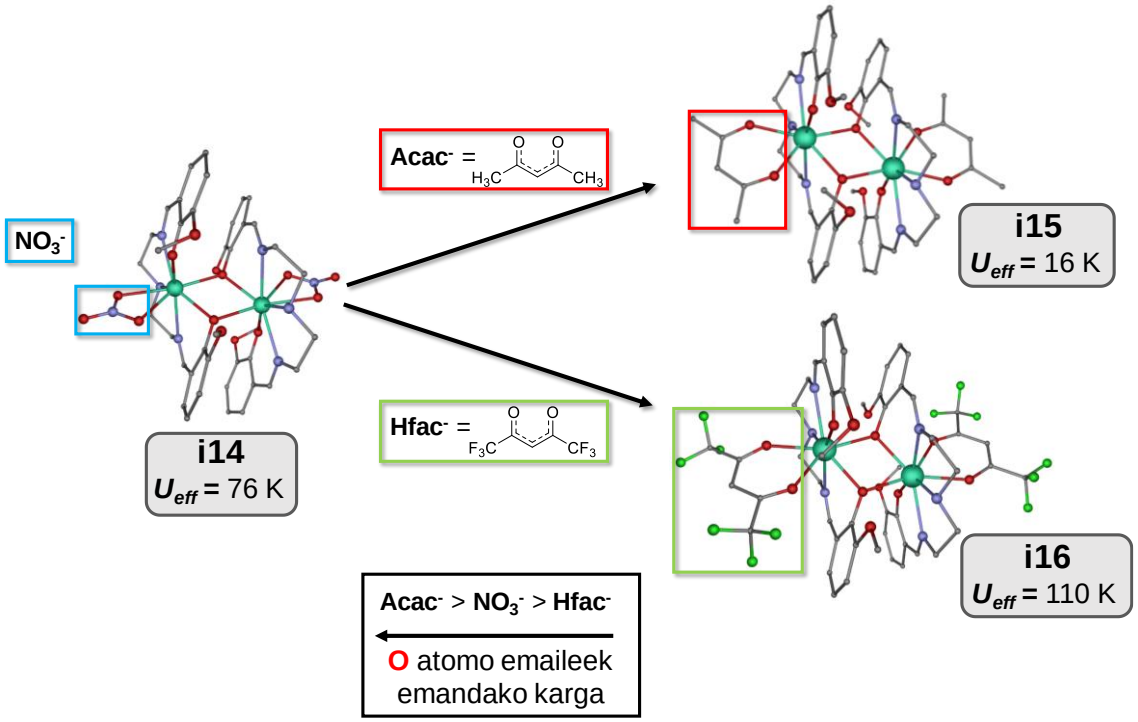

i.17. irudia. i14 erreferentziazko konposatua (ezkerrean), *acac* kelatoekin osatutako konposatua (**i15**, goian eskuinean) eta *hfac* kelatoekin osatutakoa (**i16**, behean eskuinean). Lauki beltza: kelatoen ordena lantanido ioiari ematen dioten kargaren arabera; *ab initio* kalkuluetan oinarrituta. Kolore-kodea: Dy^{III}, karbonoa, nitrogenoa, oxigenoa eta fluorra turkesa, gris, urdin, gorri eta berde kolorez, hurrenez hurren. Hidrogeno atomoak ez dira irudikatu argitasunaren mesedetan. [61,62] erreferentzietako kristal-egituretatik sortutako irudia.

i15 konposatuarentzat, nitratoak azetilazetonato kelatoagatik aldatzeak, Dy-O_{kel} distantziak laburtzea eragiten du, atomo emaileen karga handiagoaren ondorioz. Honela, plano ekuatorialean estekatzaile-eremua nabarmenagoa egiten da. Hau *ac* propietate magnetiko dinamikoak neurtuz eta erlaxazio-denborak Arrheniusen legera doituz egiaztatu zen. Doikuntzak 52,8 eta 11,1 cm^{-1} U_{eff} balioak eman zituen **i14** eta **i15**-entzeko, hurrenez hurren. *acac* estekatzaileak *hfac* homologoekin ordezkatzean **i16** lortzeko, oxigeno atomoak emaile ahulagoak bihurtzen dira, baita nitratoaren oxigeno atomoak baino ahulago ere (hori *ab initio* kalkuluen bidez egiaztatu zen). Honela, Dy-O_{kel} lotura-distantziak handiagoak bihurtzen dira, plano ekuatorialeko elektroi-dentsitatea murrizten da eta U_{eff} balioa 76,4 cm^{-1}-raino igotzen da.

Ioi lantanido prolatuak dituzten *SMM*en artean, Er^{III} ioian oinarritutakoak dira ohikoenak. Tangen taldeak argitaratutako ikerketa batean, bi sistema alderatu zituzten

ondoko formula orokorrarekin: $Ln[N(SiMe_3)_2]_3$, non Ln^{III} = Dy^{III} (**i17**) eta Er^{III} (**i18**). Bi ioi horien elektroi-hodeiaren distribuzioa aurkakoa denez, kristal eremuak alderantzizko efektuak eragiten ditu, **i.18.** irudian erakusten den bezala. Kramers dobleteen (KD) ordena aurkako da bi konposatuen. Oinarrizko egoerako KD M_J = ± 1/2 da **i17**-rako; **i18**-rako, berriz, M_J = ± 15/2 KDa da egonkorrena. Emaitza horiek bat datoz Rinehartek eta Longek proposatutako ereduarekin. Plano ekuatorialeko kristal-eremu indartsu batek aldarapen elektronikoak murrizten ditu Er^{III} bezalako ioi prolatuetan M_J-ren balio altueneko azpimailak egonkortuz oinarrizko egoeran (axialki, anisotropikoa den oinarrizko egoera). Aurretik aipatu bezala, *SMM* portaera behatzeko baldintza garrantzitsuenetako bat M_J egoerak balio absolutu altuenekin egonkortzea da oinarrizko egoeran (axialki anisotropikoa den KDa, alegia). Beraz, zentzuzkoa dirudi **i18** konposatuak 84,8 cm^{-1}-eko magnetizazioaren inbertsiorako energia-barrera izatea, **i17** konposatuak magnetizazioaren erlaxazio motela erakusten ez duen bitartean.

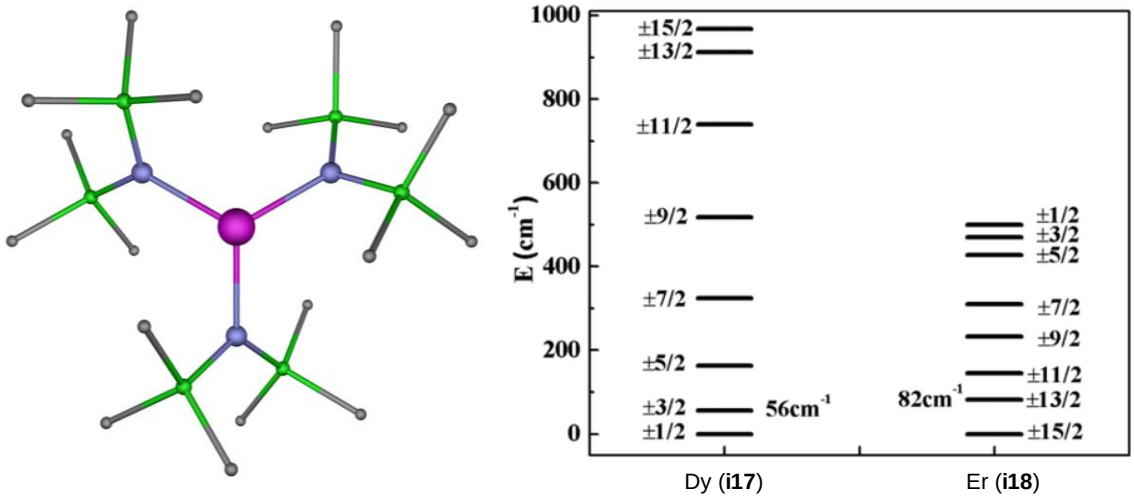

i.18. irudia. i18 konposatuaren egitura (ezkerrean) eta Kramers dobleteen energia-diagrama **i17** eta **i18** sistementzat (eskuinean). Kolore-kodea: Er^{III}, karbonoa, nitrogenoa eta silizioa arrosa, gris, urdin eta berde kolorez, hurrenez hurren. Hidrogeno atomoak ez dira irudikatu argitasunaren mesedetan. **i18** konposatuaren irudia CCDCtik deskargatutako kristal-egituratik (YIBRUW) abiatuta sortu da. Energia diagrama [64] erreferentziaren baimenarekin egokitu da. Copyright 2014 American Chemical Society.

Deskribatutako oblatu-prolatu ereduan oinarrituta, gure ikerketa-taldeak ere ekarpen garrantzitsuak egin zituen *SMM*en arloan. Adibidez, $Zn^{II}Dy^{III}Zn^{II}$ sistema trinuklearra, **i19**, Mannich base motako estekatzailea erabiliz prestatu zen [65]. Aurkezten duen estekatzaileen antolamendu mota hau oinarrizko egoeran M_J baliorik altuenak

egonkortzeko eraginkorra dela frogatu zen (oinarrizko egoera axiala lortuz), izan ere, lau fenoxido motako oxigenoak (sistema horretan elektroi-dentsitate handiena dutenak) bikoteka kokatuta daude Dy^{III} ioiaren kontrako aldeetan (i.19. irudia). Gainera, Zn^{II} ioi diamagnetikoak egituran sartzeak hainbat onura izan ditzake. Alde batetik, Zn^{II} ioia ez da paramagnetikoa, eta jakina da zentro metaliko paramagnetikoek zeharkako eremu magnetikoak sortzen dituztela, *QTM* bidez magnetizazioaren erlaxazio azkarra ahalbidetzen dutenak [66]. Bestalde, Rajaraman eta kolaboratzaileek jakinarazi zuten, fenoxido zubiak dituzten sistemetarako, ioi diamagnetikoak sartzeak kargaren polarizazio handiagoa eragin dezakeela fenoxido taldeetan, horrela, energia-diferentzia handiagoa sortuz oinarrizko egoeraren eta egoera kitzikatuen artean [67].

i19 konposatuak DyO_8 koordinazio-ingurunea du, antiprisma karratu gisa deskriba daitekeena (SHAPE softwarearekin kalkulatua [68]). *QTM*ren presentzia nabarmena bada ere $\chi_M''(T)$ grafiketan (i.19c irudia), kanpo eremu magnetikorik aplikatu gabe *SMM* portaera erakusten du. Izan ere, oinarrizko egoera $M_J = \pm 15/2$ ia purua da, anisotropia axial nabarmenarekin eta zeharkako osagai mespretxagarriekin (CASSCF+RASSI metodo bidez kalkulatuta). Anisotropia axial handia duen oblatu ioi batentzat espero den bezala, momentu magnetikoaren norantza fenoxido oxigeno elektronegatiboetara bideratuta dago, gutxi gorabehera, bi Dy-O distantziarik laburrenekiko ia paralelo kokatuta.

i19 molekulako estekatzaile-eremuaren egokitasuna are gehiago berresteko, estekatzaileek eragindako eta Dy^{III} ioian proiektatutako potentzial elektrostatikoaren mapak kalkulatu ziren. Oinarrizko egoerako beta elektroien dentsitatea aldaratze elektroniko txikieneko zonaldean kokatzen zela egiaztatu zen. Honekiko perpendikular, aldiz, momentu magnetikoa elektroi-dentsitate handieneko fenoxido oxigenoetara orientatua zegoela frogatu zen. Azkenik, kontzeptu-proba gisa, Er^{III} analogo isoestrukturala ere aztertu zen (**i20**). Espero bezala, estekatzaile-eremua aproposa da M_J balio altuak egonkortzeko oinarrizko egoeran ioi oblatuentzat, baina ez zen horrela izan Er^{III} ioi prolatuarentzat. Horrela, **i20** konposatuak magnetizazioaren erlaxazio mantsoa erakusten bazuen ere, kanpo eremu magnetikoaren beharra dago propietate hori ikusteko. Gainera, kalkulatutako energia-barrera oso baxua zen.

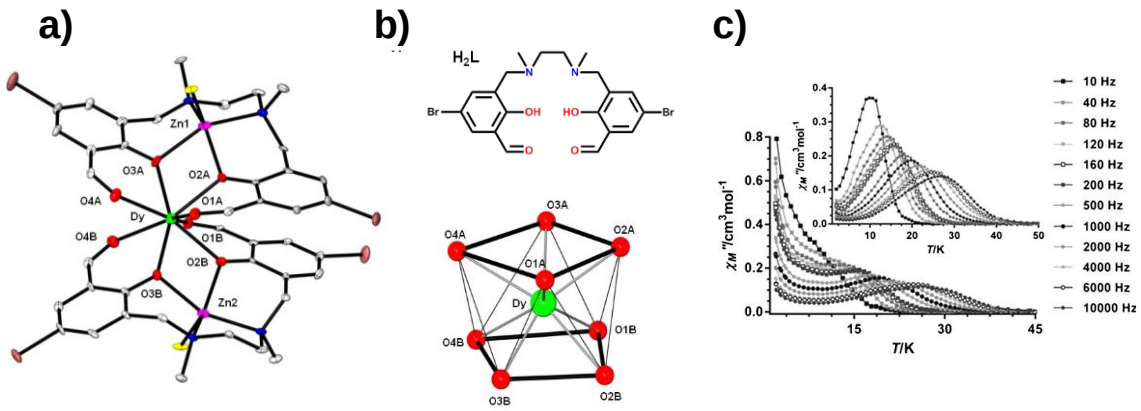

i.19. irudia. a) **i19** konposatuaren egitura kationikoaren ikuspegia. b) Mannich base motako estekatzailea (goian) eta DyO_8 koordinazio-ingurunea (behean). c) $\chi_M''(T)$ grafikak kanpo eremu magnetikorik gabe eta H_{dc} = 1000 Oe-ko kanpo eremuarekin (barruko grafika). Kolore-kodea: Dy^{III}, Zn^{II}, karbonoa, oxigenoa, nitrogenoa, bromoa eta kloroa berde, arrosa, gris, gorri, urdin, marroi eta hori kolorez, hurrenez hurren. Hidrogeno atomoak eta kontraioiak ez dira irudikatu argitasunaren mesedetan. [65] erreferentziako kristal-egituratik abiatuta sortutako irudia. Propietate magnetikoak baimenarekin erreproduzitu dira. Copyright 2014 John Wiley and Sons.

Esan bezala, ahalegin handiak egin dira lantanidoetan oinarritutako *SMM*ak sintetizatu eta haien propietate magnetikoak ulertzeko. Izan ere, oblatu-prolatu ereduari jarraitutako estrategia arrazionalak aukera eman die ikertzaileei korrelazio magneto-estruktural berriak proposatu eta estekatzaile-eremuak aldatu ahal izateko. Horren adibide argiak dira geometria bipiramide pentagonaleko (*PB*, *pentagonal bipyramid*) konposatuak. Oro har, sistema hauek oxigeno atomo emaile indartsuak dituzte posizio axialetan, adibidez: fenoxido taldeak, fosfina oxidoak edo siloxidoak. Aldiz, posizio ekuatorialetan disolbatzaile molekulak (tetrahidrofuranoa edo piridina, adibidez) edo koordinazio ahulagoa duten estekatzaileak izan ohi dituzte.

Talde honen barruan, adibidez, $[Dy(O^tBu)_2(py)_5][BPh]_4$ (**i21**, O^tBu = tert-butoxidoa, py = piridina) [69], [Dy(bbpen)Br] (**i22**, H_2bbpen = N,N′-bis(2-hidroxibenzil)-N,N′-bis(2-metipiridil)etilenediamina) [70] eta $[Dy(Cy_3PO)_2(H_2O)_5]Br_3\cdot2(Cy_3PO)\cdot2H_2O\cdot2EtOH$ (**i23**, Cy_3PO = triziklohexil fosfina oxidoa) [71] aurkitzen dira. Sistema hauetan guztietan, axialitatea posizio apikaletan kokatutako oxigeno atomo emaile indartsuek ematen dute, plano ekuatoriala elektroi emaile ahulagoak diren atomoek betetzen duten bitartean. Hauek, aldi berean, lotura-distantzia luzeagoak erakutsi ohi dituzte. Konposatu

hauentzat kalkulaturiko energia-barrera efektiboek 1815 K, 1025 K eta 543 K-eko balioa dute **i21**, **i22** eta **23i** sistementzat, hurrenez hurren. Gainera, nahiz eta normalean Orbach erlaxazio-bidea lehen egoera kitzikatuaren bidez gertatzen den (*TA-QTM* bezala hobeto deskriba daitekeena), konposatu hauetan egoera kitzikatu altuagoetatik ematen da erlaxazio mekanismoa estekatzaileen diseinu egokia dela eta. Azkenik, propietate interesgarriak izateaz gain, airean egonkorrak diren konposatuak diseinatzearen eta sintetizatzearen garrantzia aipatu behar da. Aipatutako azken hiru konposatuetatik energia-barrera altuena duena (**i21**) airearekiko sentikorra da. Egoera honek zaildu egiten du etorkizun hurbilean sistema gailu batean erabili ahal izatea. Ildo horretan, airean egonkorrak diren eta energia-barrera efektibo handiak dituzten beste konposatu batzuen berri ere eman da, *PB* geometriarekin edo F^- bezalako talde elektronegatiboak erabiliz [72–75].

Pensta liteke deskribatutako energia-barrera altuko azken sistema horiek hautagai idealak direla informazioa biltegiratzeko gailuetan inplementatzeko. Hala ere, lantanidoetan oinarritutako *SMM* gehienek desabantaila komun eta garrantzitsu bati egin behar diote aurre: blokeo tenperatura baxuei. **i21** konposatuak, adibidez, "soilik" 14 K-eko T_B balioa du (*FC/ZFC* esperimentu bidez definitua), nagusiki *QTM* mekanismo bidez erlaxatzen delako sistema kanpo eremurik ez dagoenean. Hori da ikertzaileek gaur egun duten arazorik handienetako bat, blokeo-tenperatura handiko *SMM*ak lortzeko.

v. *QTM*: EKIDIN BEHARREKO FENOMENOA

Testuan zehar aipatu den bezala, oro har, errazagoa da *SMM* propietateak dituen koordinazio konposatu bat sintetizatzea lantanidoak erabiltzen direnean. Gainera, energia-barrera efektiboak altuagoak izan ohi dira trantsizio-metalen ioietan oinarritutako *SMM*etarako baino. Dena den, *QTM* oso indartsua izaten da kanpo eremu magnetikoa kentzen denean eta, honek, kanpo eremurik magnetikorik ez dagoenean magnetizaziorik ez geratzea dakar. Hori arazo handia da materialak etorkizuneko gailu batean erabiltzeko. Beraz, *QTM* efektuaren jatorria asko aztertu da azken urteotan eta pixkanaka nola deuseztatu ikasten ari gara.

Tongen taldeak, adibidez, koordinazio-esferaren geometriak *QTM*rengan duen eragina aztertu zuen [76]. Horretarako, $Zn^{II}Dy^{III}Zn^{II}$ motako bi sistema trinuklear oso antzeko ikertu zituzten, non haien arteko ezberdintasun nagusia plano ekuatorialeko metanol molekula baten presentzia/gabezia zen (i.20. irudia). **i24** konposatuak metanol molekula bat du plano ekuatorialean. Horrela, lantanido ioiaren inguruko geometria *PB*

motakoa da. **i25** konposatuak, ordea, metanolik ez duenez koordinazio oktaedrikoa du lantanido ioiak. **i24** sistemako metanolaren oxigeno atomoa izan ezik, Dy^{III} ioiaren inguruko oxigeno atomo emaile guztiak fenoxido motakoak diren arren, estekatzaile-eremua optimotzat har liteke Rinehartek eta Longek iradokitako ereduari erreferentzia eginez. Izan ere, *PB* geometriaren barruan, posizio axialetako oxigeno atomoek plano ekuatorialekoek baino lotura distantzia nabarmen laburragoak erakusten dituzte. Konposatuak oso antzekoak diren arren, eta kristal-eremua axialki definitua dagoela esan daitekeen arren, **i24** konposatuak U_{eff} = 305 ± 3 cm^{-1}-eko balioa erakusten du, **i25** konposatuak, aldiz, ez du fasez kanpoko seinalerik erakusten $\chi_M''(T)$ grafiketan *QTM* azkarraren ondorioz (kanpoko eremu magnetiko optimo batekin deuseztatzea lortzen dute *QTM* efektua). Portaera hori arrazionalizatzeko, *ab initio* kalkuluak erabili zituzten. Ikerketa horretatik ondorioztatu zuten, lehen aipatu bezala, *PB* geometria hautagai ezin hobea dela *SMM* portaera behatzeko. Geometria oktaedriko batek, ordea, tunel-efektua jasateko joera du. Aipatu behar da geometriak ez direla inoiz idealak izaten, eta horrek ondorio kaltegarriak dakartza *SMM* portaerarako (izan ere, geometria distortsioek *QTM*ren mesedetan parte hartezen dute). Honi dagokionez, **i24** konposatuan *SMM* portaera ez da espero bezain ona. **i25** sistemaren kasuan, berriz, geometria ideala ez bada ere, kanpo eremu magnetiko bat aplikatuz magnetizazioaren erlaxazio mantsoa beha daiteke.

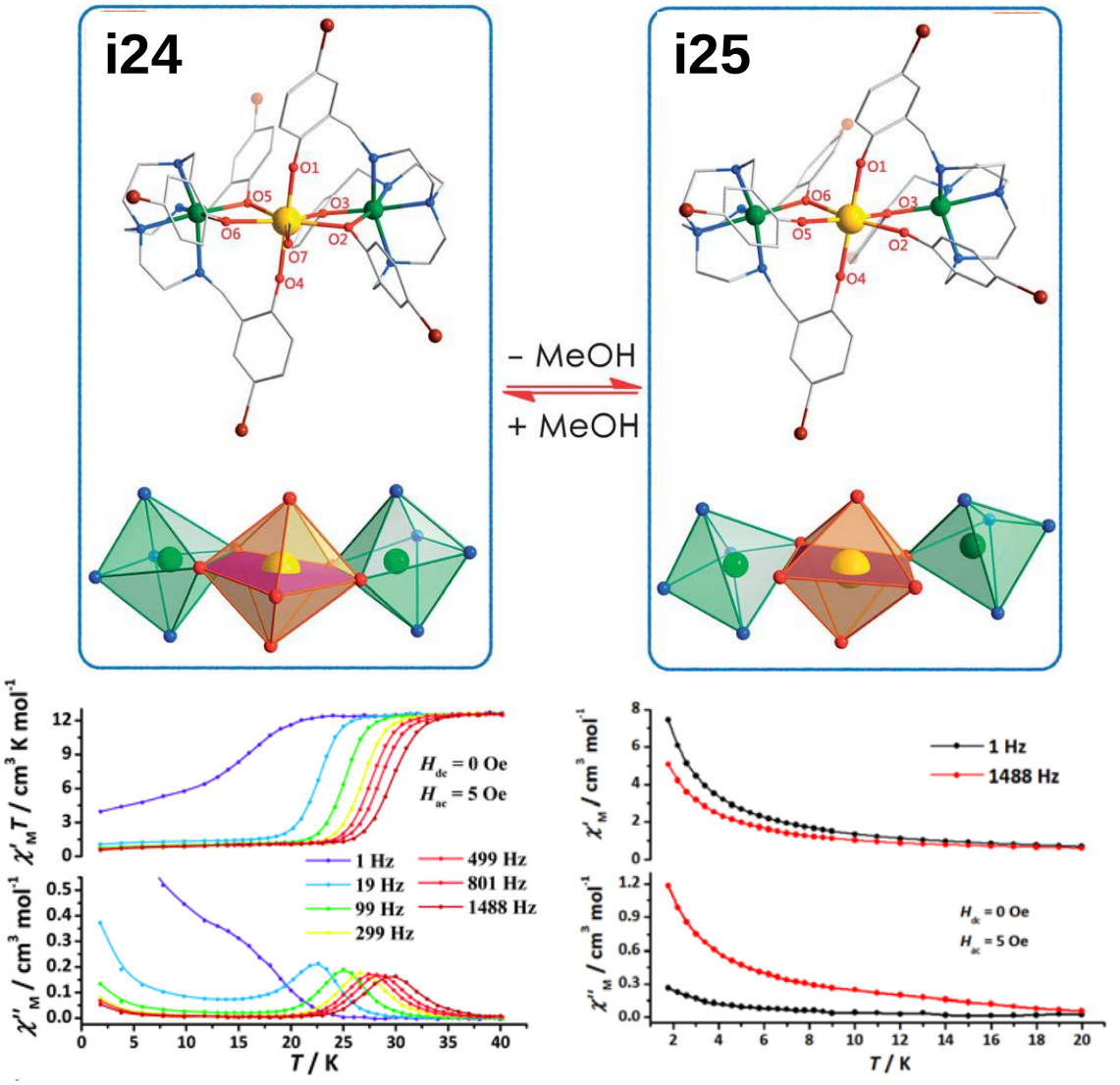

i.20. irudia. i24 eta **i25** konplexuen egitura, dagozkien koordinazio-poliedroekin Zn^{II} eta Dy^{III} ioietarako (goian). Kolore-kodea: Zn^{II}, Dy^{III}, karbonoa, nitrogenoa, oxigenoa eta bromoa berde, hori, gris, urdin, gorri eta marroi kolorez, hurrenez hurren. Hidrogeno atomoak ez dira irudikatu argitasunaren mesedetan. [76] erreferentziaren baimenarekin egokitua. Copyright 2013 The Royal Society of Chemistry.

Lantanidoetan oinarritutako errendimendu altuko *SIM*ak lortzerako garaian simetriak betetzen duen funtsezko eginkizuna ikusita, Tongen taldeak duela gutxi ikerketa kualitatibo bat egin zuen, karga-eredu eraginkor batean oinarrituta. Ikerketa honek frogatu zuen simetria-talde jakin batzuek, hala nola, Cn ($n \geq 7$), S_8/D_{4d}, C_{5h}/D_{5h} eta S_{12}/D_{6d} taldeek, zeharkako kristal-eremuaren parametroak minimizatu ahal izango lituzketela eta, beraz, *QTM* [77]. Aipatzekoa da simetria hauetako bat bera ere ez dagoela 32 talde puntual kristalografikoen artean eta, beraz, ezinezkoa izango litzatekeela konplexu

kristalinoetan halako geometria perfektuak lortzea. Hala eta guztiz ere, lehen adierazitako simetrietatik ahalik eta hurbilen dagoen simetria lortzen saiatzea bideragarria litzateke. Tongen taldeak lortutako ondorio kualitatibo horiek babesten dituzte, adibidez, **i21-i23** konposatuentzat behatutako emaitza esperimentalek. Zehaztea komeni da zeharkako kristal-eremuaren parametroak, eta ondorioz *QTM*, minimizatzeko oinarrizko egoerako $\pm M_J$ dobletearen anisotropia magnetikoaren ardatzak simetria ardatz nagusiarekin bat etorri behar duela. Hau gertatzen denean, lehen egoera kitzikatuari eta oinarrizko egoerari dagozkion anisotropia ardatzak paraleloak izaten dira, eta magnetizazioaren erlaxazioa ez da gertatzen lehen egoera kitzikatuaren bidez. Aldiz, energetikoki altuago dauden egoera kitzikatuetatik gertatzen da erlaxazioa, U_{eff} balio altuagoak emanez. Hori gertatzen da, oro har, Dy^{III} ioian oinarritutako errendimendu altuko *SMM*ekin. Adibidez, **i21** konposatuan, lehen hiru maila kitzikatuen anisotropia ardatzak ia paraleloak dira oinarrizko egoerarenarekin eta, beraz, erlaxazio magnetikoa altuago kokatuta dauden egoera kitzikatuetaik gertatzen da. Azpimarratu behar da, halaber, karga-dentsitatearen banaketa lantanido ioiaren inguruan aldatzea funtsezkoagoa dela simetria zehazteko garaian geometria molekularra baino.

QTM fenomenoa ekiditeko beste funtsezko alderdi bat, ahal den neurrian, molekulen arteko interakzio ahulak saihestea da. Berebiziko garrantzia du molekula indibidualak egitura kristalinoaren barruan ondo isolatuta edukitzeak, aldameneko ioi paramagnetikoen artean interakzioa magnetikorik egon ez dadin. Izan ere, interakzio horiek *QTM* laguntzen duten zeharkako eremu magnetikoak eragin ditzakete. Asko erabiltzen den estrategia molekulen arteko hidrogeno loturak osatzeko gai ez diren estekatzaileak diseinatzearena da. Modu horretan, molekulak isolatuta egoten dira kristal-egituraren barruan [78]. Hala ere, metodo hau ez da beti eraginkorra. Lehen begiratuan molekula indibidualak distantzia handi batez bananduta egon daitezkeen arren, interakzio dipolar ahulak ager daitezke. Beste estrategia sintetiko bat zentro paramagnetikoak matrize diamagnetiko baten barruan diluitzea izan liteke. Horretarako, diluitu nahi den *SMM*ak ioi diamagnetiko batekin kristalizatutako homologo isoestrukturala izan behar du. Adibidez, lantanidoak erabiltzen direnean, Y^{III} ioia erabili ohi da, Dy^{III} eta Er^{III} metal ioen antzeko erradio ionikoa baitu (La^{III} ere diamagnetikoa da, baina bere erradio ionikoa handiagoa da eta ez da hain ohikoa). Homologo paramagnetiko eta diamagnetikoak edukita, elkarrekin kristalizatzen dira proportzio desberdinetan, neurri batean behintzat, molekulen arteko interakzio dipolarrak ekidituz. Estrategia hori dagoeneko erabili zuten Ishikawa eta kolaboratzaileek lantanidoetan oinarritutako lehen *SMM*ak aurkitu zituztenean. Gaur egun, beste ikerketa taldeetara asko zabaldu den estrategia da [79–82]..

Ziurrenik ez molekulen arteko interakzio dipolarren maila berean, baina elektroien eta nukleo aktiboen arteko interakzio hiperfinak ezabatzeak ere badu bere garrantzia tunel-efektua murrizteko garaian. Zentzu honetan, Cador eta kolaboratzaileek aplikatu zuten estrategia hau lehen aldiz $[Dy(tta)_3(L)]\cdot C_6H_{14}$ (**i26**, i.21. irudia) konposatu mononuklearrean (tta^- = 2-tenoiltrifluoroazetonato eta L = 4,5-bis(propiltio)-tetrafulvaleno-2-(2-piridil)-benzimidazol metil-2-piridina) [83]. Ikerketa honen helburua molekula indibidualen portaera magnetikoa hobetzea zen, diluzio magnetikoaren estrategiak ingurunea optimizatzeko balio baitu, ez molekula berarena portaera. Horretarako, **i26** koordinazio-konposatua Dy^{III} ioi naturalarekin sintetizatu zuten lehendabizi, nagusiki zazpi isotopo ezberdinetatik lauren nahasketa bat dena: ^{161}Dy (%18,9) eta ^{163}Dy (%24,9), non I = 5/2 eta espin nuklearrik gabeko ^{162}Dy (%25,5) eta ^{164}Dy (%28,2). Ondoren, sistema berak eraiki zituzten ^{161}Dy (I = 5/2) eta ^{164}Dy (I = 0) ioiekin isotopikoki aberasteko, hemendik aurrera **i^{161}26** eta **i^{164}26** deituak. Aberastutako bi konposatuek frekuentziaren menpeko suszeptibilitate seinaleak erakusten dituzte fasez kanpo 14 K-etik behera (kanpo eremu magnetikorik aplikatu gabe), baina alde nabarmenak dituzte. Maximoak $\chi_M''(\upsilon)$ grafiketan askoz ere frekuentzia baxuagoetara desplazatuak daude **i^{164}26** materialarentzako. Nahiz eta termikoki aktibatutako prozesuari dagozkion τ_0 eta U_{eff} balioak antzekoak diren bi sistementzat, tenperatura baxuetako erlaxazio-denborak ia hamar aldiz mantsoagoak dira nukleo ez-aktiboa duen konposatuarentzat. Erlaxazio-denboren moteltzea interakzio hiperfinen gabeziari dagokiola egiaztatzeko, neurketak errepikatu zituzten kanpo eremu magnetiko batekin *QTM* deuseztatzeko. Ateratako erlaxazio-denborak sistema guztientzat berdinak zirenez, argi eta garbi geratzen da aberaste isotopikoak tenperaturarekiko independenteak diren erlaxazio-denboretan eragiten duela.

Erlaxazio denboren moteltzea, bestalde, histeresi-ziklo neurketen bidez baieztatu zen (i.21. irudia, eskuinean). **i26** konposatuak tximeleta forma tipikoa erakusten du. Bestaldetik, isotopikoki aberastutako **i^{164}26** analogoan zikloaren irekiera nabarmenagoa da zero eremuan, akoplamendu hiperfinak ekiditeak *SMM*aren propietateak nolabait hobetzen dituela frogatuz. Hala eta guztiz ere, aurkikuntza hori tentuz hartu behar da; izan ere, hainbat estrategia konbinatuta ere (hala nola, aberaste isotopikoa) *QTM*ak bere horretan jarraitzen du. Lan honi lotuta, Chiltonek eta kolaboratzaileek azterketa sakon bat egin zuten eremu eta tenperaturaren mendeko erlaxazio denboren inguran energia-barrera altuko *SMM* batean oinarrituz [84]. Lan horretan, diluzio magnetikoaren eta aberastasun isotopikoaren estrategiak tenperatura baxuetan portaera magnetikoa aldatzeko eraginkorrak direla baieztatzen duten arren, jarraitu beharreko bidea,

ziurrenik, egitura molekularraren ingeniaritzan datzala diote, kristal-eremuaren efektuen bidez lortuko baita benetan tunel kuantikoa saihestea.

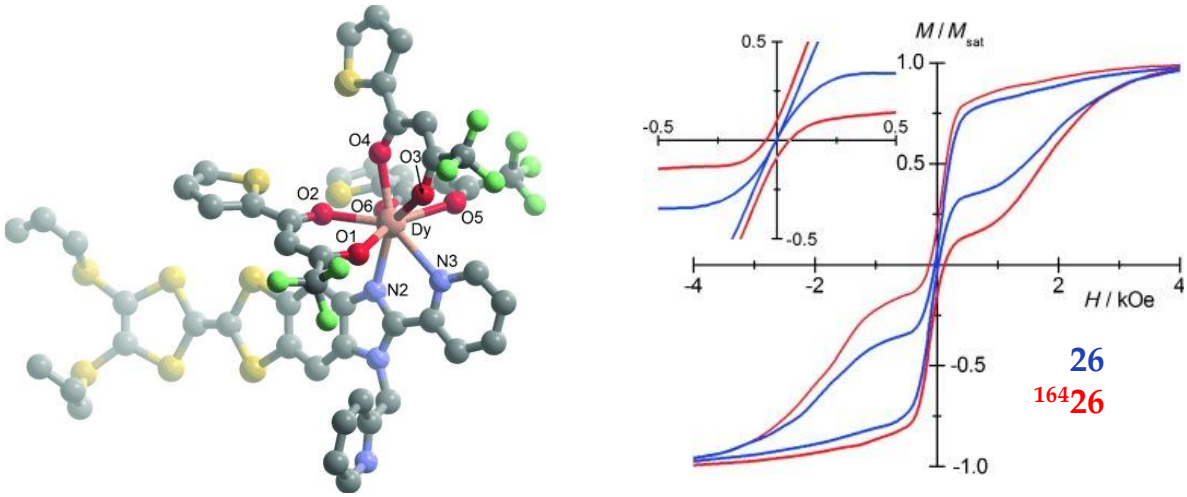

i.21. irudia. i26 konplexuaren egitura (ezkerrean). Histeresi-zikloak 0,46 K-etan **i26** eta **i^{164}26** konposatuentzako (eskuinean). Kolore-kodea: Dy^{III}, karbonoa, nitrogenoa, oxigenoa, sufrea eta fluorra arrosa, gris, urdin, gorri, hori eta berde kolorez, hurrenez hurren. Hidrogeno atomoak eta disolbatzaile molekulak ez dira irudikatu argitasunaren mesedetan. [83] erreferentziaren baimenarekin erreproduzitua. Copyright 2015 John Wiley and Sons.

Aurreko estrategiaren guztiz kontrakoa, nahikoa sendoak diren ioien arteko interakzio magnetikoak bilatzea da, metal-metal interakzioak sendoak direnean *QTM* efektua deuseztatu baitaiteke. Langleyen taldeak argitaratutako lana da, esate baterako, estrategia berri honen erakusgarri garbia. Lan honetan, tximeleta itxurako bi konplexuren arteko alderaketaren berri eman zuten: $Co_2^{III}Dy_2^{III}$ (**i27**) eta $Cr_2^{III}Dy_2^{III}$ (**i28**) sistemena (i.22. irudia) [85]. Lehenengoarentzat, Co^{III} ioiak espin baxuko egoeran daudenez, diamagnetikoak dira. Hortaz, propietate magnetikoak Dy^{III} ioietatik bakarrik datoz. Bigarrenarentzat, Cr^{III} eta Dy^{III} ioi paramagnetikoen arteko interakzio magnetikoek, berriz, garrantzi handia dute. Bi konposatuen energia-barrera konparagarria den arren, **i27** konposatua portaera kuantiko puru batera igarotzen da 2,5 K-tik behera. Aldiz, **i28** konposatuak 3,5 K-etaraino histeresi-zikloa irekiak erakusten ditu 2,8 T-rainoko (1,8 K-etan) eremu hertsagarriarekin. Portaera desberdin honen jatorriari buruz ikertzeko asmotan, *ab initio* kalkuluak egin zituzten. Horien arabera, truke-interakzio bidez akoplatutako sistemarako (**i28**), tunel-efektua efektiboki deuseztatuta dago bai oinarrizko egoeran eta baita lehenengo egoera kitzikatuetan ere. Horren ondorio garbia

dira neurtutako histeresi-ziklo irekiak. Ikerketa honek truke-interakzio magnetikoek erlaxazio-prozesuetan duten eragina erakusten du.

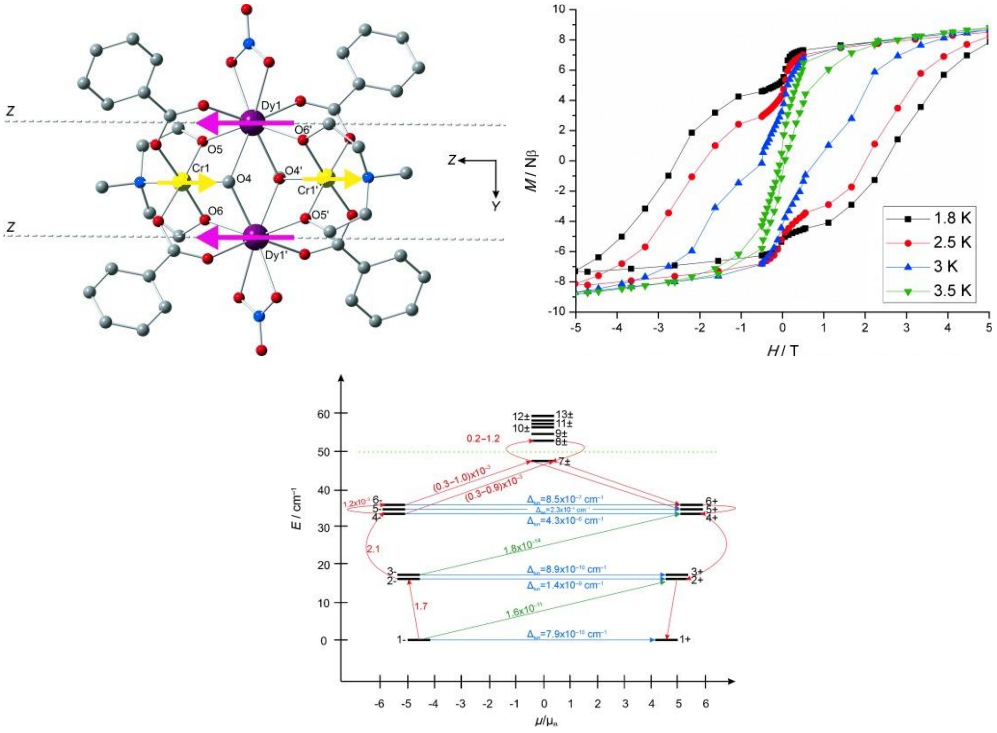

i.22. irudia. i28 konplexuaren egitura. Lerro etenak Dy^{III} ioien ardatz magnetiko nagusiei dagozkie. Geziek oinarrizko egoerako truke-dobletearen momentu magnetikoen orientazioa erakusten dute. Kolore-kodea: Cr^{III}, Dy^{III}, karbonoa, nitrogenoa eta oxigenoa hori, more, gris, urdin eta gorri kolorez, hurrenez hurren. Hidrogeno atomoak ez dira irudikatu argitasunaren mesedetan (goian ezkerrean). Tenperatura baxuan neurtutako histeresi-zikloak (goian eskuinean). Truke-interakzioz sortutako energia-diagrama. [85] erreferentziaren baimenarekin erreproduzitua. Copyright 2013 John Wiley and Sons.

Rajaramanen taldeak ere azterketa sakonak egin izan ditu 3d-4f sistema mistoei dagokionez. 2017an argitaratutako artikulu batean, antzeko lau sistema oktanuklear alderatu zituzten, non egitura orokorra mantentzen zuten, baina metalen arteko zubiak eta/edo 3d ioi metalikoak aldatzen zituzten [86]. **i29** eta **i30** konposatuek $Co_4^{III}Dy_4^{III}$ nukleoak dituzte, desberdintasun nagusia metalen arteko OH^- (**i29**) edo F^- (**i30**) zubiak izanik. **i31** eta **i32** konposatuek, ordea, bi ioi paramagnetiko mota dituzte $Cr_4^{III}Dy_4^{III}$ eta F^- (**i31**) edo N_3^- (**i32**) zubiekin(i.23. irudia). **i31** eta **i32** konposatuak aldez aurretik deskribatuak izan ziren [87,88]. Hasieran, 3d ioi metalikoaren efektua alde batera utzita, F^- zubiek oinarrizko egoeraren eta lehen egoera kitzikatuaren arteko energia-diferentzia

handiagoa ematen dutela ikusi zuten. Nahiz eta biek (**i29** eta **i30**) M_J = ±15/2 duten oinarrizko egoera eta M_J = ±1/2 lehen egoera kitzikatua, fluoruroaren elektroi-dentsitate handiagoak bi azpimailen arteko banaketa handiagoa ziurtatzen du. Beraz, **i29** konposatua ez da *SMM* bat, baina **i30** bai *QTM* prozesu nabariarekin. Bigarren ioi paramagnetiko mota bat duten egituretara pasatzean, **i32** konposatuak **i30** konposatuarekin alderatuta hobetutako bi ezaugarri erakusten ditu. Energia-barrera altuagoa eta *QTM* murriztua. Gainera, Cr^{III} ioiak eta F^- zubiak konbinatuz, emaitzarik onenak lortu ziren **i31** konposatuarentzat U_{eff} handienarekin eta *QTM*ren deuseztatzearekin. Emiatzen fidagarritasuna indartzeko, kasu honetan ere, *ab initio* kalkuluak egin zituzten. Molekula barneko truke-interakzioak kontuan hartu gabe, **i31** konposatuak tunel-efektua izan beharko luke oinarrizko egoeran, **i30** baino are markatuagoa gainera. Hori esperimentuek erakutsi zutenaren kontrakoa da. Beraz, Cr···Dy eta Dy···Dy truke-interakzioak kontuan hartu zituzten kalkuluetan. Kasu horretan, egiaztatu zuten Cr^{III} eta Dy^{III} ioi paramagnetikoen arteko truke-interakzioek funtsezko eginkizuna dutela **i30** konposatuan agertzen diren tenperatura baxuko erlaxazio-kanalak deuseztatzeko.

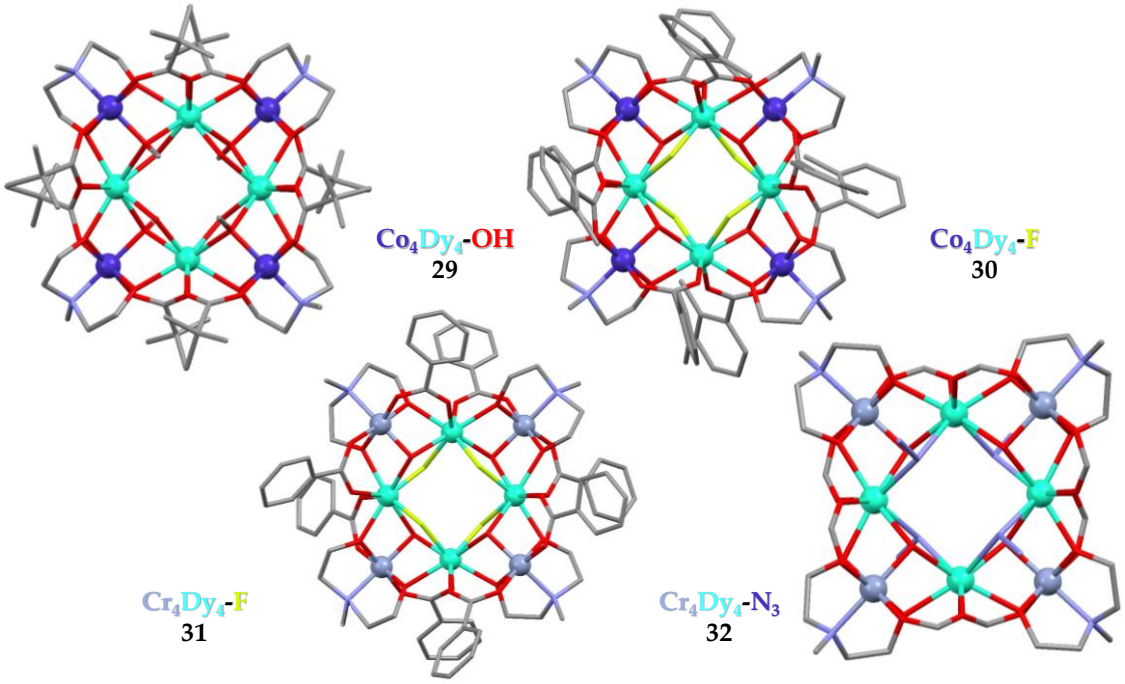

i.23. irudia. i29- i32 konplexuen egitura. Kolore-kodea: Co^{III}, Cr^{III}, Dy^{III}, karbonoa, nitrogenoa, oxigenoa eta fluorra more, gris argi, turkesa, gris, urdin, gorri eta berde kolorez, hurrenez hurren. Hidrogeno atomoak, disolbatzaile molekulak eta zati kristalografikoki desordenatuak ez dira irudikatui argitasunaren mesedetan. [86–88] erreferentzietako kristal-egituretatik sortutako irudia.

Aipatutako adibideek Cr^{III} ioien presentzia inplikatzen duten arren, beste 3d metal batzuk ere erabili izan dira, hala nola, Mn^{II}, Fe^{II} eta Co^{II} ioiak [89–92]. Horiez gain, Rajaraman eta kolaboratzaileek [93] aurretik deskribatutako Ni_3Dy (**i33**) konposatu tetranuklear baten [94] ikerketa teorikoa ere egin zuten (i.24. irudia). Ahula bada ere, konposatuak kanpo eremu magnetiko baten beharrik gabe *SMM* portaera du. **i25** konposaturako frogatu den bezala, koordinazio-ingurune oktaedrikoak ez dira egokienak errendimendu handiko *SMM*ak diseinatzeko. Beraz, ez da harrigarria **i33** konposatuan estekatzaile-eremua ez izatea gai M_J = ±15/2 azpimaila oinarrizko egoeratzat egonkortzeko. Are gehiago, oinarrizko egoeraren eta lehen egoera kitzikatuaren arteko energia-diferentzia oso txikia izango litzateke kalkulu teorikoen arabera.

Izan ere, konposatu honen oinarrizko egoera Ising motakoa (axiala) izatetik urrun dago eta nagusiki M_J = ±13/2 azpimailak osatzen badu ere oinarrizko egoera, hiru uhin-funtzio desberdinen konbinazioak deskribatzen du ondoen. Bestalde, *g* tentsoreen balioek adierazten badute ere oinarrizko egoera axiala dela, zeharkako osagaiak ezin dira gutxietsi. Azken batean, kalkuluen arabera, konposatuak *QTM* erakutsiko beharko luke eta ez litzateke *SMM*a izateko hautagaia. Hala ere, beste behin ere, truke-interakzioz akoplatutako sisteman oinarritutako kalkuluek *QTM* partzialki ezabatua dagoela iradokitzen dute, *SMM* portaera ahalbidetzen duten Ni···Dy interakzio nahikoa indartsuen ondorioz. Ikusitako adibideetan 3d-4f metalen konbinaketa estrategia positibotzat azaldu bada ere, konposatu mistoetan 3d ioi paramagnetikoak sartzea ez da beti efektiboa. Horrelako konposatuetan erlaxazio-bideak oso konplexuak izan ohi dira eta egitura barneko desberdintasun txikiek ezartzen dute muga askotan, non 3d ioi paramagnetiko/diamagnetiko batek *SMM* portaera hobetzen/okertzen duen [95].

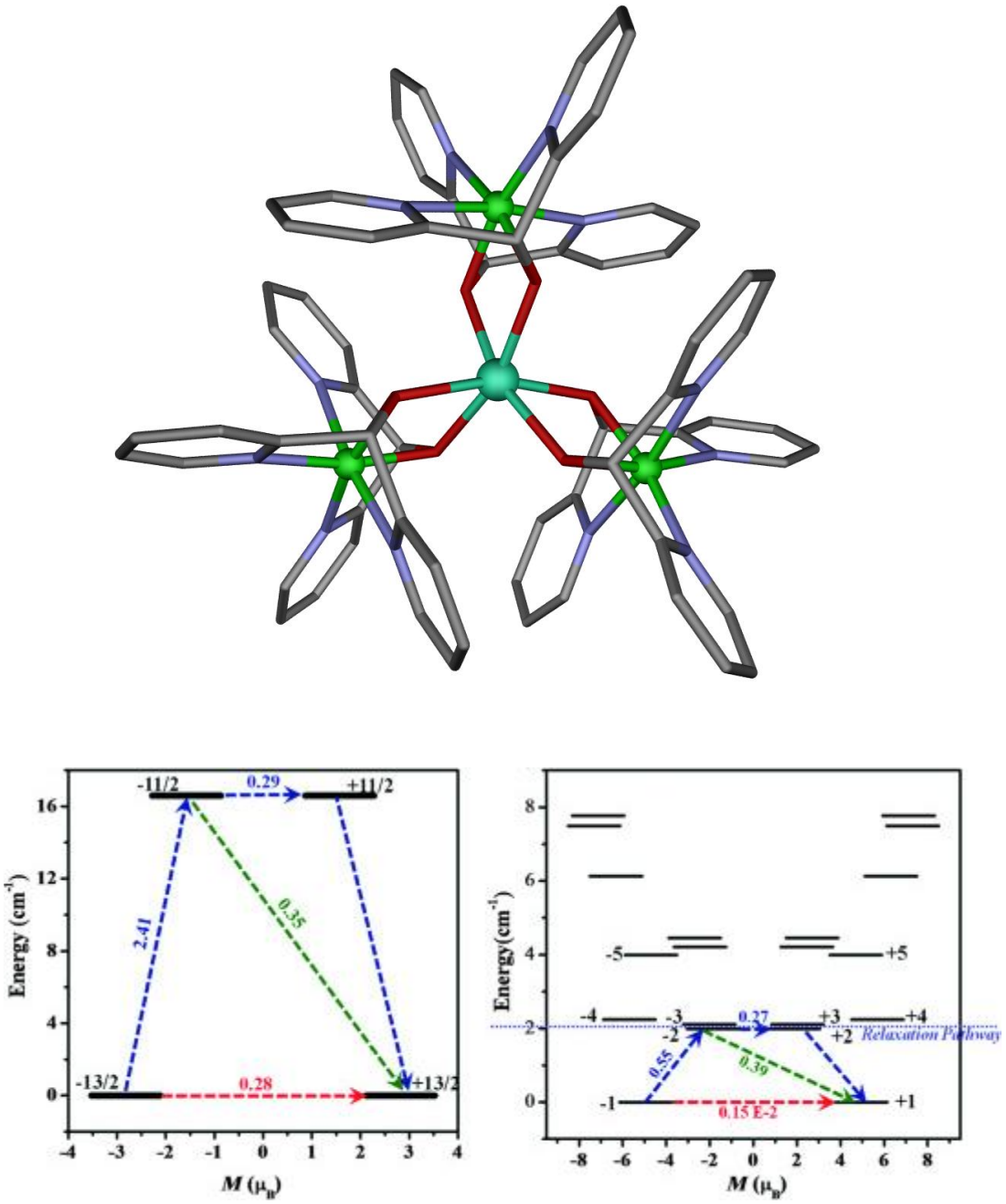

i.24. irudia. i33 konposatuaren egitura. Kolore-kodea: Ni^{II}, Dy^{III}, karbonoa, nitrogenoa eta oxigeno berde, turkesa, gris, urdin eta gorri kolorez, hurrenez hurren. Hidrogeno atomoak eta kontraioiak ez dira irudikatu argitasunaren mesedetan (goian). Ab initio bidez kalkulatutako energia diagramak truke-interakzioak kontuan hartuta (eskuinean) edo hartu gabe (ezkerrean). Egituraren irudia [94] erreferentziako kristal-egituratik abiatuta sortu da. Energia diagramak [93] erreferentziaren baimenarekin erreproduzituta. Copyright 2016 John Wiley and Sons.

Hainbat zubi-taldek edo heteroatomok truke-interakzio desberdinak eragin ditzakete, bai izaerari dagokionez (ferro edo antiferromagnetikoa), bai indarrari dagokionez. Hala ere, 4f balentzia elektroiak $5s^2$ eta $5p^6$ elektroiez "babestuta" daudenez, metal-estekatzaile interakzioak elektrostatikoak izaten dira eta, beraz, heteroatomo batek bi Ln^{III} ioien arteko zubi lana egiten duenean, truke-interakzio ahulak eman ohi dira. Beraz, Ln^{III} nukleo anitzeko sistementzat, *SMM* portaera ioi bakar baten portaerarekin zuzenean lotuta egon daiteke eta, askotan, interakzio ahulek zeharkako eremuak sortu besterik ez dute egiten erlaxazio azkarragoaren mesedetan. Metalen eta estekatzaileen arteko elkarrekintza sendoagoak lortzeko etorkizun handiko estrategia bat estekatzaile paramagnetikoak edo, beste hitz batzuetan, erradikalak erabiltzea da.

Erradikalen elektroiek duten izaera difusoari esker, lantanidoen orbitalak zeharkatzeko gai dira. Modu honetan, estekatzaile diamagnetikoekin lortu ezin diren metal-estekatzaile truke-interakzio bereziki sendoak sortzen dira. Horren adibide argiak dira N_2^{3-} formuladun zubia duten konposatu dinuklearrak: [K(18-crown-6)][{[$(Me_3Si)_2N$]$_2$(THF)Ln}$_2$(μ-η^2: η^2-N_2)], non Ln = Gd^{III} (**i34**) eta Dy^{III} (**i35**) konposatuak (i.25. irudia) [96]. Truke-interakzio bortitza berehala frogatu zen $\chi_M T$ kurbei erreparatuz. Izan ere, giro-tenperaturaren azpitik ikusitako igoera nabarmena metal-estekatzaile arteko interakzio antiferromagnetikoen ondorioa da. Gainera, **i34** konposatuarentzat neurtutako 300 K-etako $\chi_M T$ balioa dagoeneko espero zena baino baxuagoa zen aipatutako interakzio sendoak direla eta (interakzionatzen ez duten bi S = 7/2 Gd^{III} ioi eta S = 1/2 N_2^{3-} unitate erradikal bat kontuan hartuz). Datu esperimentaletatik J = -27 cm^{-1}-eko truke-interakzio konstate handia kalkulatu zuten, Gd^{III} sistemetarako aurkitu ohi direnak baino nabarmen altuagoa, normalean 3 cm^{-1} baino baxuagoak izaten dira [97]. Interakzio handia N_2^{3-} erradikalaren izaera difusotik sortzen dela egiaztatzeko, erradikal izaerarik ez duen N_2^{2-} zubiekin egindako analogoak ere aztertu ziren (Gd^{III} (**i36**) eta Dy^{III} (**i37**). Nahiz eta $\chi_M T$ kurben behaketa nahikoa izan aldaketa sumatzeko, **i36** konposatuaren datuak tratatutakoan truke-interakzio konstante askoz baxuagoa lortu zuten, J = -0,49 cm^{-1} balioduna. Aipatzekoa da analogo erradikal eta ez-erradikalen kristal egiturak ez direla guztiz berdinak (zenbait desberdintasun ikus daitezke lotura-luzera nahiz angeluetan), baina sistema konparagarriak direla onartzen da.

Gd^{III} ioian spin-orbita akoplamendurik ez dagoenez, egokia da *dc* datuak tratatu eta truke-interakzio konstantearen balioa erraz lortzeko. Hala ere, bere izaera isotropikoa dela eta, ez da hautagai ona *SMM*ak diseinatzeko. Dy^{III} ioi metalikoan oinarritutako **i35** konposatuak, aldiz, kanpo eremurik aplikatu gabe *SMM* portaera erakusten du bere izaera anisotropikoaren ondorioz. Lortutako 123 cm^{-1}-eko U_{eff} balioa Dy^{III} ioian

oinarritutako beste *SMM* batzuekin aldera badaiteke ere, tenperatura baxuko portaera ez da ohikoa sistema honentzat. Antzeko energia-barrera efektiboak dituzten beste konposatu batzuek [98] ez dute portaera lineala tenperatura baxuan Arrheniusen grafikoetan. Portaera hori argi eta garbi lotuta dago energia-barrera zeharkatzen duten lasterbideekin. **i35** konposatuak portaera lineal argia erakusten du aztertutako tenperatura tarte osoan Orbach mekanismo puru baten ezaugarria izanik. Gainera, N_2^{2-} zubia duen **i37** analogoak 18 cm^{-1}-eko barrera apala du, tenperatura baxuan teneperaturarekiko independenteak diren erlaxazio-denborak erakutsiz (tunel-efektuaren adierazgarri garbia). **i35** ez bezala, molekula barneko metalen arteko interakzioak ahulak direnean, magnetizazioaren erlaxazio motela *SIM* portaerarekin hobeto deskriba daiteke *SMM* portaerarekin baino, erlaxazioak ioi indibidualean izaten baitu jatorria. Azkenik, **i35** sistemaren *SMM* portaera 8,3 K arteko histeresi-zikloak eremu hertsagarri handiekin neurtuz egiaztatu zen.

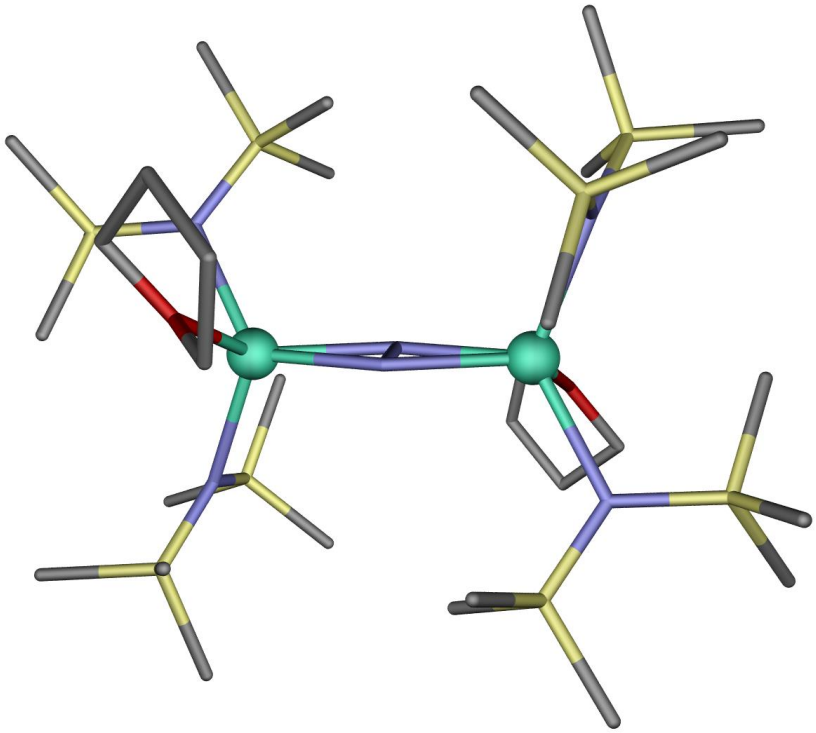

i.25. irudia. i34 konposatuko [{[$(Me_3Si)_2N$]$_2$(THF)Gd}$_2$(μ-η^2: η^2-N_2)] anioiaren egitura. Kolore-kodea: Gd^{III}, karbonoa, nitrogenoa, silizioa eta oxigenoa turkesa, gris, urdin, hori eta gorri kolorez, hurrenez hurren. Hidrogeno atomoak eta kontraioiak ez dira irudikatu argitasunaren mesedetan. [96] erreferentziako kristal-egituratik abiatuta sortutako irudia.

Gd^{III} eta Dy^{III} ioiekin lortutako emaitzen ondoren, Longen taldeak N_2^{3-} zubidun sistemak esploratzen jarraitu zuen. Lehenik eta behin, egitura mantenduz, Tb^{III} ioiean oinarritutako **i38** konposatua deskribatu zuen emaitza hobeak lortuz. Hain zuzen, 14 K-eko blokeo-tenperatura altua neurtu zuten sistema honentzat [99]. Honen ondoren, ziklopentadieno sandwich konposatuentzat lortutako emaitza bikainetan oinarrituz (ondoren eztabaidatuak), aipatutako sandwich sistemetan berriz ere N_2^{3-} erradikala sartzea lortu zuten Dy^{III} eta Tb^{III} ioietan oinarritutako sistema dinuklearrak ikertzeko [100].

Besteak beste, ondoko formula orokorra duten lau konposatu berriren sintesi, karakterizazio eta propietate magnetikoei buruzko informazioa eman zuten: [K(crypt-222)(THF)][$(Cp^{Me4H}_2Ln(THF))_2(\mu-N^{\cdot}_2)$] Ln^{III} = Tb^{III} (**i39**) eta Dy^{III} (**i40**), eta [K(crypt-222)][$(Cp^{Me4H}_2Ln)_2(\mu-N^{\cdot}_2)$] Ln^{III} = Tb^{III} (**i41**) eta Dy^{III} (**i42**), non crypt-222 = 2,2,2-kriptand eta Cp^{Me4H} = tetrametilziklopentadieniloa (i.26 irudia) Egiturari dagokionez, bi egituren arteko desberdintasun nagusia lantanido ioietara koordinatutako THF molekula baten presentzia/gabezia da. Lotutako THF molekula erraz ateratzen da koordinazio-esferatik konposatua 2-metiltetrahidrofuranoan disolbatuta. Nahiz eta lau materialak *SMM* portaera erakutsi kanpo eremu magnetikorik gabe, alde nabarmenak daude haien artean. Neurketa dinamikoetatik (*ac*) ateratako erlaxazio-denborek Arrheniusen legea jarraitzen dute tenperatura tarte osoan **i40** sistemarentzako izan ezik, *QTM* portaera nagusitzen baita tenperatura baxuenetan. Histeresi zikloetan ere nabarmendu zen efektua, 2 K-etan neurketa eginda ere ez baitzen eremu hertsigarri nabarmenik deteketatu. Hala ere, THF molekulak koordinazio-esferatik kentzeak **i40** sistemaren portaera magnetikoa nabarmen hobetzen du eta histeresi-ziklo irekiak detektatu ahal izan ziren 8 K-etaraino **i42** konposatuan. Kontuan izanik **i39** Tb^{III} analogoak jada 15 K-etarainoko ziklo irekiak erakusten zituela, THF deuseztatu ondoren **i41** konplexuarentzat hobekuntza handia aurreikusten zen. Hain zuzen, 30 K-etaraino neurtu ahal izan ziren histeresi-ziklo irekiak eta 20 K-eko blokeo-tenperatura determinatu zuten τ = 100 s kriterioa erabiliz. Beraz, ikerketa hauek guztiek argi utzi zuten erradikalen erabilera estrategia egokia izan daitekeela errendimendu altuko *SMM*ak diseinatzeko.

i.26. irudia. i39 eta **i41** konposatuen egitura anionikoa. Kolore-kodea: Tb^{III}, karbonoa, nitrogenoa eta oxigenoa turkesa, gris, urdin eta gorri kolorez, hurrenez hurren. Hidrogeno atomoak eta kontraioiak ez dira irudikatu argitasunaren mesedetan. [100] erreferentziako kristal-egituretatik sortutako irudia.

Hurrengo atalean eztabaidatuko den bezala, gaur egungo *state of the art* Dy^{III} ioian oinarritutako *SIM*ek osatzen dute. Hala ere, oraindik beharrezkoa da anisotropia altua mantentzen duten nukleo anitzeko sistemak aztertzea. Rineharten taldeak $[Er(COT)]^{+}$ (COT^{2-} = ziklooktatetraenida anioia) ioia erabili zuen lau konposatu berri sintetizatzeko: mononuklear bat (**i43**) eta hiru sistema dinuklear (**i44-i46**) eraikitzeko [101]. COT^{2-} estekatzailea aukeratu zuten jakina delako aproposa dela Er^{III} ioiaren momentu-magnetiko handieneko egoerak egonkortzeko oinarrizko egoeran (M_J = ±15/2). Gainera, jakina da anisotropia ardatzak Er-$COT_{zentroide}$ ardatzarekin egiten duela bat. Koordinazio esferak I^- ioiekin eta koordinazio ahula duten fosfinekin osatu ziren (i.27. irudia). Sistema dinuklearren artean, I^- ioiek metalen arteko zubi lana egiten dute eta fosfinak, aldiz, anisotropia ardatzen arteko angeluak aldatzen dituzte. Interesgarria da aipatzea fosfinak koordinazio ahula sortzeko erabili zirela, horrela, ez baitute Er-$COT_{zentroide}$ loturan oinarritutako anisotropia ardatzaren norabidea aldatuko. Lau konposatu horien azterketatik ondorio interesgarriak atera ziren. Alde batetik, **i44-i46** konplexuek **i43** sistemak baino 100 cm^{-1} inguru gehiagoko energia-barrera efektiboak dituzte. Hala ere, 2 K-etan neurtutako histeresi-zikloek ez dute portaera bera erakusten (i.27. irudia). **i43** eta **i44** konposatuek tximeleta itxurako zikloak erakusten dituzte, *QTM*ren eragina handia izanik. Aitzitik, **i45** eta **i46** konposatuek, Er-COT zentroideen arteko angelu handiagoak erakusten dituztenek, histeresi-ziklo irekiak erakusten dituzte eremu magnetikoaren gabezian ere *QTM*ren desagerpena dela eta. Horrela, ikerketa honek nukleo anitzeko sistemetan anisotropia ardatzak lerrokatzearen garrantzia azpimarratzen du (aurretik trantsizio-metalen klusterrentzat frogatu zen bezala). Gainera, 2 K-etako erlaxazio-denborak sei magnitude-ordena inguru handitzen dira **i43**

sistematik **i46** konposatura nukleartasuna areagotzearen nahiz magnetizazioaren ardatzen lerrokatzearen garrantzia berretsiz.

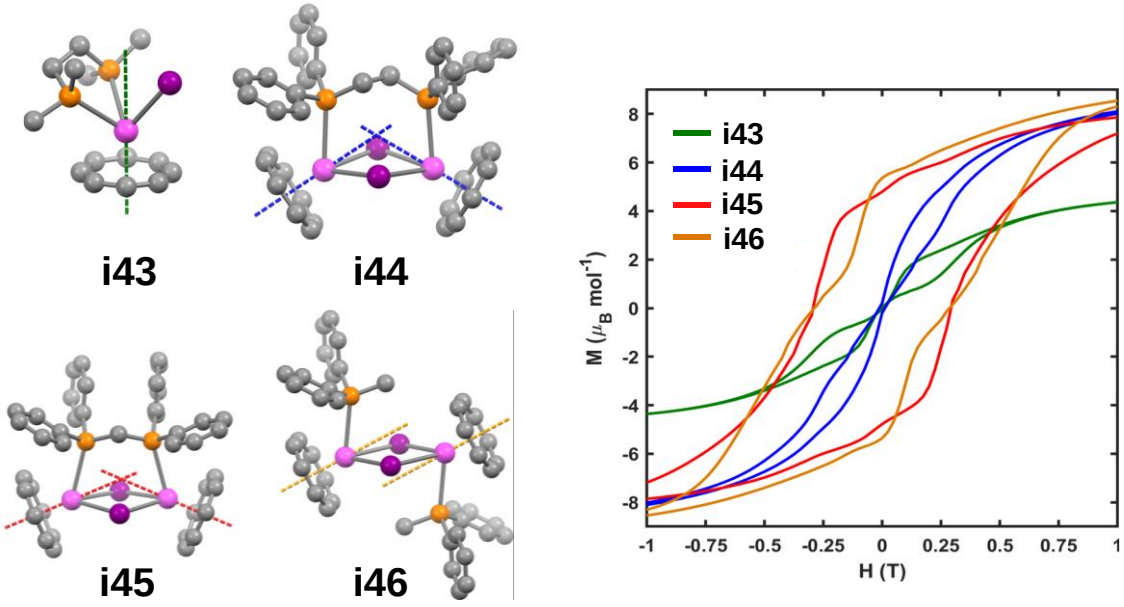

i.27. irudia. i43-i46 konplexuen egitura, Er-$COT_{zentroide}$ bektoreen norabideekin batera (ezkerrean). Histeresi-zikloak 2 K-etan (eskuinean). Kolore-kodea: Er^{III}, karbonoa, fosforoa eta ioduroa arrosa, gris, laranja eta more kolorez, hurrenez hurren. Hidrogeno atomoak ez dira irudikatu argitasunaren mesedetan. [101] erreferentziaren baimenarekin egokitua. Copyright 2019 American Chemical Society.

vi. *STATE OF THE ART*: DISPROSIO-METALOZENOAK

Artikuluan zehar eztabaidatzen den bezala, azken hamarkadetan hainbat *SMM* deskribatu dira, magnetizazioaren birorientazioa blokeatzeko energia-barrera altuak dituztenak. Blokeo-tenperaturak, aldiz, ez dira erritmo berean hobetu barrera-energetikoa zeharkatzen duten bidezidorrak direla eta. Dena den, gaur egungo *state of the art* osatzen duten disprosiozenoak joera orokorretik kanpo daude, energia-barrera altuez gain blokeo-tenperatura altuak erakustera heldu direlako (nitrogeno likidoaren gainetik dagoeneko). COT ligandoak Er^{III} ioientzat egokiak diren bezala, Cp deribatuek (Cp = ziklopentadienilo anioia) Dy^{III} ioi oblatuan oinarritutako sistemen iraultza eragin dute. Jada Rineharten eta Longen diseinu printzipioetatik $[DyCp_2]^+$ sandwich konposatuak (plano ekuatorialean estekatzailerik gabe) hautagai potentzialtzat hartzen ziren, baina Ln^{III} ioien erradio ioniko handiek euren sintesia zailtzen zuten. Hala ere, Millsen eta Layfielden taldeek ia aldi berean eman zuten Cp^{ttt} (Cp^{ttt} = {$C_5H_2{}^tBu_3$-1,2,4}

eta ^{t}Bu = $C(CH_3)_3$) (**i47**, i.28. irudia) estekatzailean oinarritutako disprosozeno konposatu baten berri [102,103]: $[Dy(Cp^{ttt})_2][B(C_6F_5)_4]$. Kristal-egiturari erreparatuz, 152,56(7)˚-ko Cp-Dy-Cp angelu zabala eta Dy-$Cp_{centroid}$ distantzia nahiko motzak ditu, 2,316(3) Å [102]. Ezaugarri horietan oinarrituz, argi zegoen *SMM* portaera edukitzeko potentzial handiko sistema zela. Esperotako portaeraren isla gisa, sistemak histeresi-ziklo irekiak aurkezten ditu 60 K-etik behera (22 Oe/s-ko ekorketa-abiadurarekin neurtuta), nahiz 2 K-etan dagoeneko *QTM* efektua ikus daitekeen eremu magnetikorik gabeko puntuan. *FC/ZFC* neurketen bidez berretsi zuten T_B-ren balioa, bi kurben banatzea 61 K-etan ematen baita.

Erlaxazio magnetikoaren mekanismoa aztertzeko *ab initio* kalkuluak egin zituzten. Bitxia bada ere, Cp^{ttt} estekatzaileetan C-H bibraziotik eratorritako spin-fonoi akoplamendua garrantzitsua zela frogatu zuten oinarrizko ±15/2 egoeratik lehen ±13/2 egoera kitzikatura trantsizioa sustatzeko. Horrela, talde funtzional horren ordezkapenak disprosio-metalozenoaren portaera hobetu beharko lukeela adierazi zuten. Bestalde, konposatu honen portaera bereziki ona ioiaren inguruko estekatzaile-eremu ezohikoari egotzi zitzaion, Cp^{ttt} estekatzaile zurrunek ez baitituzte ahalbidetzen energia-barrera bidezidor bidez zeharkatzeko beharrezko bibrazioak. Izan ere, konposatu honentzat kalkulaturiko U_{eff} = 1223 cm^{-1} altua bada ere, aurretik deskribatutako konposatu gehiago ere badira energia-barrera balio antzekoekin, esate baterako: $[Dy(O^{t}Bu)_2(py)_5][BPh]_4$ (**i 21**) [69]. Blokeo-tenperatura, ordea, askoz handiagoa da **i47** konplexuarentzat. Bi sistemak alderatuz, lehenengoak atomo emaile indibidualak ditu lehen kordinazio-esferan eta, horregatik, metal-estekatzaile flexibilitate handiagoa du. Flexibilitate horrek nahi gabeko bibrazioak sor ditzakela uste da.

Lortutako emaitza bikainen argitan, 2018an berriz ere Layfielden taldeak beste pauso bat eman zuen disprosiozeno berri bat deskribatuz [104]. Horretarako, **i47** sistemaren ikerketatik ateratako ondorioez baliatu ziren estekatzaile aproposagoak diseinatzeko: (i) Dy-Cp lotura-distantzia laburragoak behar dira, (ii) Cp-Dy-Cp angelu zabalagoak eta (iii) C-H loturarik eza. Hala ere, asmo hauek betetzeko konpromiso batera heldu behar zuten, tamaina handiko estekatzaileek angelu zabalak eman ditzaketen arren, horrek aldi berean lotura distantziak handituko lituzke. Baldintza horiek kontuan izanik, **i48**. molekula (i.28. irudia) sintetizatzea lortu zuten honako formularekin: $[(\eta^5\text{-Cp*})Dy(\eta^5\text{-}Cp^{iPr5})][B(C_6F_5)_4]$, non Cp* = pentametilziklopentadienilo anioia eta Cp^{iPr5} = pentaisopropilziklopentadienilo anioia. Estekatzaileen diseinu arrazionalaren ondorioz, kristal-egituratik Dy-Cp* eta Dy-Cp^{iPr5} distantziak, batez beste, 0,026 Å laburragoak zirela ondorioztatu zuten **i47**-rekin alderatuta. Gainera, Cp*-Dy-Cp^{iPr5} angelu zabalagoak

lortu zituzten (162,507(1)˚), linealtasunetik oso gertu. Datu horiek kontuan hartuta, lehen begiratuan kristal-eremuak egokiagoa zirudien eta, ondorioz, propietate hobeak espero ziren sistema berri honentzat.

Hain zuzen, 25 Oe/s-ko ekorketa-abiadura erabiliz, 80 K-era arte neurtu zituzten histeresi-ziklo irekiak, hau da, dagoeneko nitrogeno likidoaren gainetik dagoen tenperatura arte. Blokeo-tenperatura hori *FC/ZFC* neurketen bidez ere ziurtatu zen. Neurketa horietan bi kurben banaketa 78 K-etara neurtu zen (i.28. irudia, behean ezkerrean). Sistemaren axialitatea *ab initio* kalkuluen bidez baieztatu zen oinarrizko egoera erabat axiala zela determinatuz. Hori bat dator 2 K-etan neurtutako histeresi-zikloarekin. **i47** *SMM*aren kasuan QTMari lotutako jauzia detektatu bazen ere, **i48** konposatuarentzat ez zuten halakorik neurtu tuenl efektuaren deuseztatzen totalagatik. Azkenik, C-H talde funtzionalen ordez isopropiloak eta metiloak erabili zirela kontuan hartuta, oinarrizko egoeratik lehen egoera kitzikaturako jauzia eragiten duen bibrazioa Cp* estekatzailearen planoz kanpoko bibrazioa dela proposatu zuten.

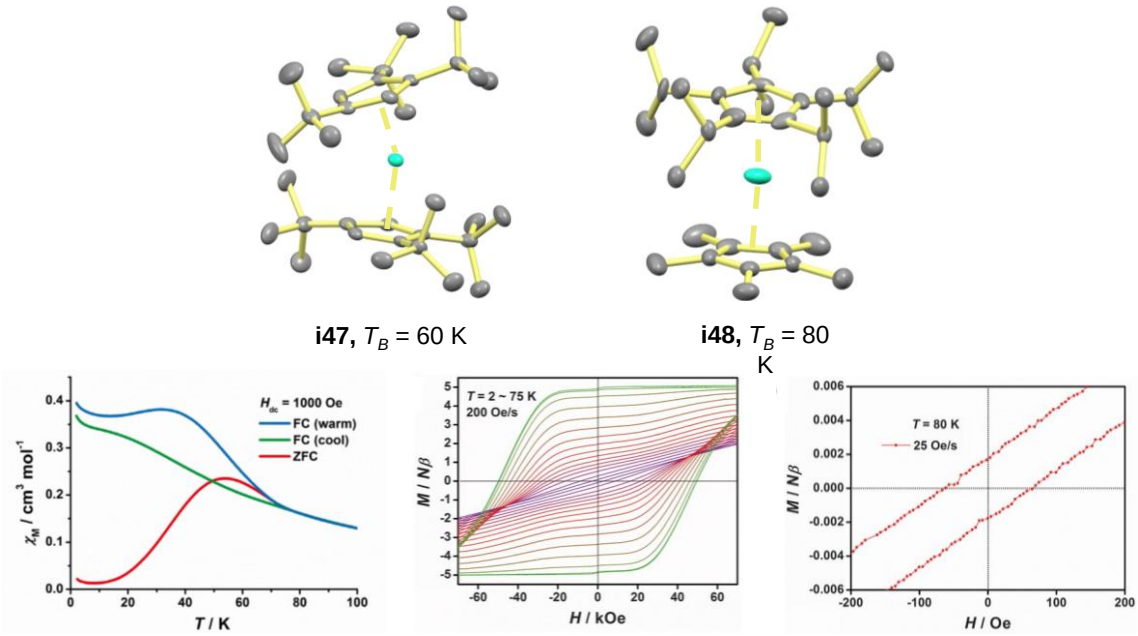

i47, T_B = 60 K **i48,** T_B = 80 K

i.28. irudia. i47 eta **i48** konplexuen egitura kationikoak (goian). FC/ZFC neurketak (behean ezkerrean), 2-75 K tenperatura-tartean neurtutako histeresi-zikloak (behean erdian) eta 80 K-etan neurtutakoa (behean eskuinean). Kolore-kodea: Dy^{III} eta karbonoa turkesa eta gris kolorez, hurrenez hurren. Hidrogeno atomoak eta kontraioiak ez dira irudikatu argitasunaren mesedetan. [102,104] erreferentzietako kristal-egituretatik abiatuta sortutako irudiak. Datu magnetikoak [104] erreferentziaren baimenarekin erreproduzitu dira. Copyright 2018 The American Association for the Advancement of Science.

Azken metalozeno honen aurkikuntzarekin batera, Harveyek eta egilekideek sandwich motako beste lau Dy^{III} konposatu deskribatu zituzten (i.29. irudia) formula orokor honekin: $[Dy(Cp^{iPr4R})_2][B(C_6F_5)_4]$ (R = H (**i49**), Me (**i50**), Et (**i51**), iPr (**i52**)] [105]. Hauek ere **i47** molekularentzat lortutako emaitzetan oinarritu zirenez, nagusiki Dy-Cp distantzia, Cp-Dy-Cp angelua eta ioi metalikoaren inguruko bibrazioak aldatzea zen beraien helburua, ondoren korrelazio magneto-estruktural berriak egin ahal izateko. Aurkitutako egitura-parametroak koherenteak dira erabili zituzten ordezkatzaileekin. Ziklopentadienilo estekatzile handienek lotura-distantzia luzeagoak eragiten dituzten, baina baita angelu zabalagoak ere (i.28. irudia). Ondorioz, Cp eraztunean aldaketa txiki bat sartzeak ioi metalikoaren inguruan estekatzaile-eremua aldatzen duela erakusten du, ziur aski magnetizazioaren erlaxazio-dinamika aldatuz. Horren lehen ebidentzia *FC/ZFC* neurketen bidez ikusi zen, 28-65 K-eko tarte zabalean topatu baitziren kurben banatzeak. Neurketa dinamikoetatik, bestalde, ondorengo U_{eff} balioak kalkulatu zituzten **i49**, **i50**, **i51**eta **i52** imanentzat: 1285, 1468, 1380 eta 1334 cm^{-1}, hurrenez hurren. Portaera hori arrazionalizatu ahal izateko, korrelazio magneto-estrukturaletan oinarritu ziren. Lau konposatuen artean, **i49** sistemak erakusten du Cp-Dy-Cp eta, ondorioz, energia-barrera baxuena. Angeluen linealtasuna handitu egiten da Cp estekatzailean bosgarren posizioan ordezkatzaile handiagoak sartzean (**i50**-**i52**). Hala ere, horien artean lotura-angelua jada faktore erabakigarria ez dela eta Dy-Cp lotura-distantzia jokoan sartzen dela teorizatzen dute. Beraz, U_{eff}-ren balioa **i52** molekulatik **i50** molekulara handitzen da Dy-Cp lotura distantzia murriztu ahala. Behatutako joeraren erakusle, **i50** konposatuak aurkezten ditu histeresi-ziklo irekiak tenperatura altuenean. Ondorio orokor gisa, Cp-Dy-Cp angelu zabalen eta Dy-Cp lotura-distantzia laburren arteko konpromisoa aurkitzeko gai diren estekatzaileak direla hurrengo helburua aldarrikatzen dute, nahiz eta funtsezkoa den spin-fonoi akoplamenduari buruzko ezagutza sakonagoa izatea. Izan ere 100 segundoko blokeo-tenperaturak Raman bidea jokoan sartzen den puntuan agertzen dira. Orbachen erlaxazioari dagokionez, bibrazio molekularren eragina ebalua daitekeen arren, energia-barrera zeharkatzen duten beste mekanismo batzuetarako ereduak behar beharrezkoak dira.

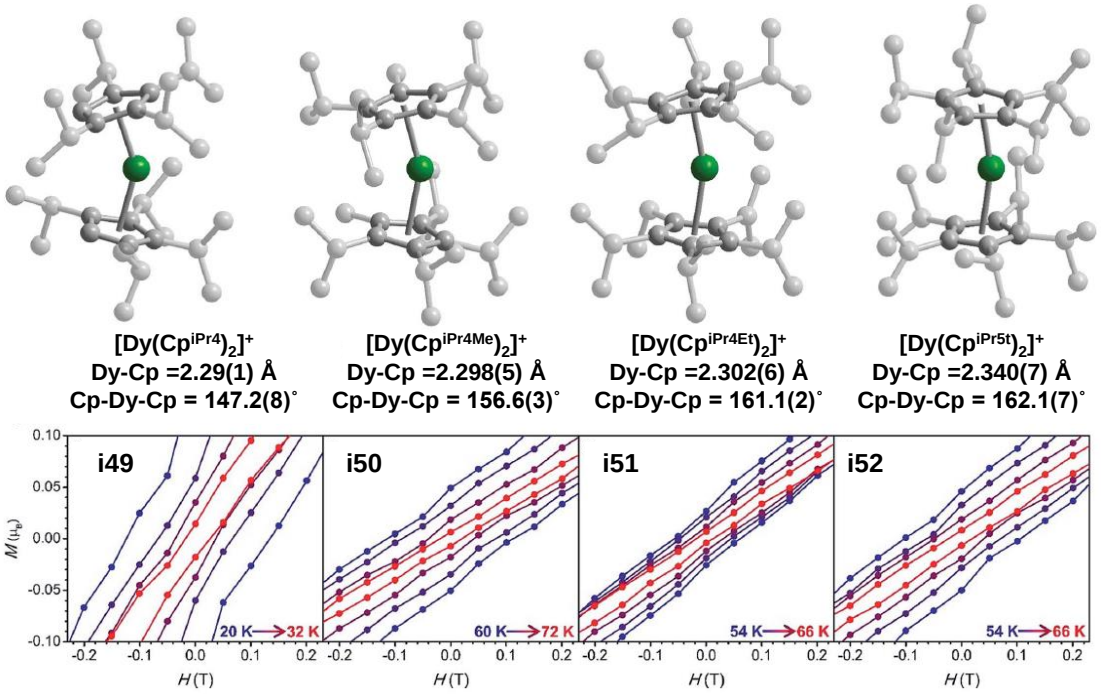

i.29. irudia. i49-i52 konplexuen egitura kationikoak. Kolore-kodea: Dy^{III} eta karbonoa berde eta gris kolorez, hurrenez hurren. Hidrogeno atomoak, kontraioiak eta posizio desordena ez dira irudikatu argitasunaren mesedetan (goian). Histeresi-zikloak zero kanpo eremutik gertu eta tenperatura altuetan (31 (4) Oe/s-ko ekorketa-abiadura H < 2 T denean) (behean). [105] – Published by The Royal Society of Chemistry.

Metalozeno guzti hauentzat lortutako emaitza apartak ikusita, azken urteetan hainbat egitura berri deskribatu dira. Adibidez, Evans eta kolboratzaileek beste sandwich egitura baten berri eman zuten, non ligandoen izaera kimikoa aldatu zuten karbono atomo bat fosforo batekin aldatuz disprosio bis-monofosfolilo konposatu batean [106]. Sistema berri honek histeresi magnetikoa erakusten du 48 K-eraino. Mengi eta egilekideek, bestalde, truke-interakzio bidez akoplatutako sistema dinuklearrak aztertu zituzten zubiak aldatuz (CH_3^-, Cl^-, Br^- eta I^-) [107]. Gainera, isokarboniloarekin lotutako koordinazio polimero ere aztertu dira [108], baita sistema dinuklearrak ere, zeinetan fulvalenoa plataforma gisa erabili den Cp eraztunen ordez [109]. Ikerketa guzti hauek agerian uzten dute sistema berri hauek *SMM*en eremua irauli dutela eta interesa duen irakurlea aipatutako literatura gehigarria irakurtzera gonbidatzen da [110–113].

vii. *AB INITIO* KALKULUAK: TRESNA EGOKIAK JAKINTZA HOBE BATERAKO ETA ESTEKATZAILEEN DISEINU HOBETURAKO

Ab initio kalkuluak gero eta gehiago erabiltzen dira SMMen alorrean. Izan ere, datu esperimentalak interpretatzen laguntzen dute, baina baita emaitzak aurresaten ere. Gainera, honek, aldi berean, estekatzaileen diseinua hobetzea ahalbidetzen du. Alor honetan, autore jakin batzuen lana bereziki azpimarratzekoa da software batzuen erabileran oinarriak finkatu baitituzte: ORCA [114] eta MOLCAS [115]. Alde batetik, Frank Neesek garatu zuen lehenengoa eta oso erabilia eta efektiboa da *g* eta *ZFS* parametroen kalkulurako, baita d orbitalen banatzea kalkulatzeko ere AILF teoriaren bitartez (*Ab Initio Ligand Field theory*, [51]). Beste aldetik, Liviu F. Chibotaruren eta Liviu Ungurren ekarpena ere bereziki azpimarragarria da MOLCAS softwarearekin lantanidoetan oinarritutako *SMM*en egitura elektronikoari eta propietate magnetikoen interpretazioari buruz egindako lan teorikoagatik. Gainera, SINGLE_ANISO eta POLY_ANISO programak sortu dituzte konposatu polinuklearrei buruzko informazioa lortzeko MOLCAS softwarean inplementatuta. Lantanido *SMM*entzat baliagarria bada ere, softwareak trantsizio-metalekin lan egiteko ere balio du. Aipatutako autoreez gain, magnetismo molekularrean lanean dabiltzan ikerlari gehiagoren lanak ere merezi du aipua, besteak beste, Gopalan Rajaraman [116], Eliseo Ruiz [117], Nicholas F. Chilton [118], Roberta Sessoli [119] eta Alessandro Soncini [120]. Soncinik, adibidez, duela gutxi garatu *ab initio* kodigo berry bat lantanidoen egitura elektronikoa eta propietate magnetikoak kalkulatzeko (CERES, *Computational Emulator of Rare Earth Systems*, [120]). Atal txiki honetan, azken urteetan garatutako punta-puntako ikerketa batzuk bildu ditugu kalkulu teorikoen inguruan.

Chiltonen taldeak, adibidez, oso berriki argitaratu dute ikerketa teoriko bat, non erlaxazio-denborak aurresaten dituzten *ab initio* metodoetan oinarrituta [118]. Lan honetan, metodo hobe batzuen bitartez teorikoki kalkulatu dituzte **i47**, **i48** eta **i49** sandwich konposatuen erlaxazio-denborak, zeinak lan horretan kontuan hartutako *SMM* erdibidekoa, onena eta txarrena diren, hurrenez hurren. Azken biak aztertuz, beren ustez magnetizazioaren erlaxazio denboretan eragin nagusia duen faktorea kristal-eremuak eragindako azpimailen energia banatze desberdina da. Hain zuzen, **i48** molekulak energia diferentzi handiagoa duenez oinarrizko egoeraren eta kitzikatuen artean, **i49** *SMM*ak baino portaera magnetiko hobea du. **i47** eta **i48** konparatzerakoan, hasierako usteen arabera, propietateen hobekuntza C-H talde funtzionalen ordezkatzeak eragindakoa zen, horiek baitziren oinarrizko egoera eta lehen eszitatuaren arteko jauziaren erantzule. Aldiz, ikerlan berri honen esanetan, spin-fonoi akoplamendu

pobreagoa eta azpimailen arteko energia-diferentzia handiagoa dira **i48** *SMM*aren propietate hobetuen erantzule, vaina azken faktorea izanik mugatzailea. Aurkikuntza berri honez gain, beste konposatu-modelo batzuk ere ikertu dituzte: $[Dy(C_5R_5)_2]^+$ eta $[Dy(C_4R_4)_2]^-$. Ondorio nagusienetakoa da, ziur aski, sandwich motako disprosio-metalozenoek topea jo dutela U_{eff} balioez hitz egiterakoan (2100 K inguru). Hortaz, orain laldu beharreko alorra spin-fonoi akoplamendua dela diote. Izan ere, ikertutako modelo batzuk **i48** sistemaren antzeko energia-barrerak izatea espero bada ere, kalkulatutako erlaxazio-denborak askoz ere motelagoak dira. Haien ustez, bibrazio jakin batzuk saihestea da erlaxazioa moteltzeko giltza, edo bibrazio horiek mailen arteko trantsizioak emateko gai ez izatea.

Ikerketa teorikoak oso baliagarriak izan dira begien bistako erantzunik ez duten beste galdera batzuk ere erantzuteko. Egia da Rinehartek eta Longek proposatutako diseinu printzipioek emaitza paregabeak eman dituztela, baina zergatik gertatu da hori Dy^{III} ioiekin baina ez Er^{III} ioiekin? Estekatzaileak posizio axialetan jarri beharrean plano ekuatorialean jartzea ez al da bada nahikoa? *Ab initio* metodoetan oinarritutako ikerketak oso baliagarriak dira galdera hauei erantzuteko.

Galdera horiei erantzuteko asmoz, Lu eta egilekideek [121] posizio ekuatorialen hiru estekatzaile koordinatuta dituzten hiru sistema aztertu zituzten: **i18** ($Er[N(SiMe_3)_2]_3$), **i53** ($Er(dbpc)_3$; dbpc = tris(2,6-di-*tert*-butil-*p*-cresola)) eta **i54** ($Er(btmsm)_3$; btmsm = tris(bis(trimetilsilil)metil)), azken biak Yamashitaren taldeak lehenago deskribatuak izanik [122]. Irudian erakutsitako (i.30. irudia) hiru sistementzat teorikoki kalkulatutako axialitatea espero zena baino baxuagoa zela ondorioztatu zuten. Izan ere, lehenengo Kramers doblete kitzikatuarentzat kalkulatutako $g_{x,y}$ balioak zerotik urrun zeuden. Horrela, zeharkako parametro horiek dira seguruenik lehen egoera kitzikatuan *QTM* ahalbidetzen dutenak eta, beraz, U_{eff} parametroaren balioa oinarrizko egoera eta lehen kitzikatuaren energia-diferentziara mugatzen da. Horretaz gain, beste ikerketa teoriko bat gauzatu zuten θ angeluen (Er-L lotura bektorearen eta anisotropia ardatzaren arteko angelua, i.30. irudia) eta Er-L lotura-distantzien balioak aldatuz. Alde batetik, U_{eff} balio altuenak θ = 90º kasurako kalkulatu ziren eta, bestetik, Er-L distantzia luzatu ahala oinarrizko egoeraren eta lehen kitzikatuaren arteko energia diferentzia murrizten zela ikusi zuten. Er-L lotura-distantziak laburtzeak, ordea, kontrako efektua ematen zuela ere determinatu zuten, izan ere, laburtze horrek zeharkako parametroak handitzen zituen ($g_{x,y}$ altuagoak) M_J azpimailetan. Ondorio orokor gisa, uste dute Er^{III} ioietan oinarritutako *SMM*ek kostata lortuko dituztela inoiz Dy^{III} ioietan oinarritutako imanek bezain propietate onak.

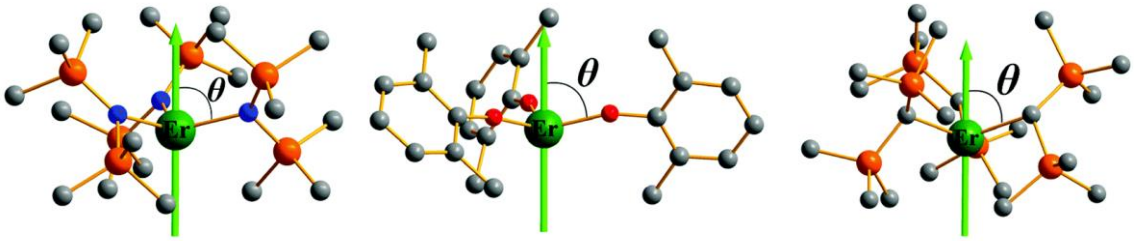

i18 **i53** **i54**

i.30. irudia. i18-i52 konplexuen egitura. Gezi berdeek ardatz anisotropikoen orientazioa erakusten dute oinarrizko KDarentzat. Kolore-kodea: Er^{III}, karbonoa, nitrogenoa, silizioa eta oxigenoa berde, gris, urdin, laranja eta gorri kolorez, hurrenez hurren. Hidrogeno atomoak eta tert-butilo taldeak ez dira irudikatu argitasunaren mesedetan. [121] erreferentziaren baimenarekin erreproduzitua. Copyright 2020 The Royal Society of Chemistry.

Duela gutxi argitaratutako beste ikerketa interesgarri bat Zhang eta egilekideek egindakoa da [123]. Ab initio kalkuluak egin zituzten [LnO] sistementzat, Dy^{II} ioia izanik kasu honetan. Komentatu behar da aurretik ikerketa antzekoa ere egin zela $[DyO]^{+}$ unitateentzat [124]. Gainera, etorkizuneko gailuei begira iman molekularrak gainazaletan txertatzeak duen garrantzia kontuan izanik (ikusi hurrengo atala), boro nitruro sistema hexagonalean (h-BN) absorbatutako [DyO] unitatearen propietateak ere ikertu zituzten. Haien esanetan, ikerketaren ondorio nagusiak bi dira. Lehenik eta behin eta aurretik aipatu bezala, badirudi Dy^{III} metalozenoek muga jo dute energia-barreraren balioari dagokionez eta ez dirudi hobetu ahal izango denik. Hein batean, oso zaila delako koordinazio-zenbaki baxuko konposatuak sortzea lantanidoak erabiltzen direnean. Hori dela eta, [LnO] sistemak erabiltzea aukera erakargarria izan daiteke *SMM* hobeak lortzeko bidean. [DyO] unitatearen izaera kobalente altua eta Dy-O lotura-distantzia laburren ondorioz, energia-diagrama 2500 cm^{-1}-eraino zabaltzen da oinarrizko egoeratik hasi eta azken maila kitzikaturaino (kontuan hartu kasu honetan J = 8 dela). Ondorioz, potentzial handiko hautagaitzat har daiteke neurketa esperimentalak gauzatzeko. Azkenik, [DyO] unitatea teorikoki h-BN gainazalean horizontalki absorbatuko balitz ere, kalkulu teorikoen arabera izaera axiala mantenduko luke oraindik 2000 cm^{-1}-eraino zabalduz energia-diagrama.

Azken urteotan beste ikerketa asko garatu dira bibrazio molekularrek eta kristal-sareko bibrazioek erlaxazio prozesuan nola eragin dezaketen jakiteko. Esate baterako,

Irländer eta Schanckek erakutsi zuten fonoien tunel kuantikoa gertatzen bideak ireki ditzaketela berez degeneratuak diren egoeren artean [125]. Haien ustetan horrelako ikerketak funtsezkoak dira, magnetizazioaren erlaxazioa ahalbidetzen duten bibrazioak identifikatzeko balio baitute eta, ondorioz, estekatzaile berrien diseinua errazten dute.

Atal honetako azken adibide gisa Aravenaren lan interesgarri bat aipatu nahi genuke [126]. Lehenik eta behin, azpimarratzen du zein garrantzitsua den *ab initio* kalkuluak egitea, oso erabilgarriak baitira esperimentalki lortutako emaitzak hobeto ulertzeko. Kontua da, normalki metodo hauek kasu bakoitzerako espezifikoak izaten direla eta orokorragoak izan daitezkeen ereduak edukitzea oso interesgarria litzateke. Hori dela eta, Aravenak lan honetan metodo berri eta orokor bat proposatzen du tunel-efektuaren parametroa (τ_{QTM}) eta energia-barrera kalkulatzeko. Metodoa erabili ahal izateko, molekularen orientazioa kristal-egituran, oinarrizko egoera eta kitzikatuen energiak eta *g* balioak behar dira. Eredu berri honen eraginkortasuna balioztatzeko aurretik deskribatutako 18 *SMM* erabiltzen ditu (15 Dy^{III} ioian eta 3 Er^{III} ioian oinarrituak) argitaratutako emaitzak eta berak lortutakoak alderatzeko.

viii. SMMETAN OINARRITUTAKO MATERIAL HIBRIDOAK ETORKIZUNEKO APLIKAZIOEI BEGIRA

Azken hamarkadetan *SMM* kopuru izugarria argitaratu da. Horietako gehienentzat, propietate magnetikoak forma polikristalinoan aztertu dira. Hala ere, etorkizuneko dispositibo bat garatzeko eta irakurketarako/idazketarako, sistema horiek gainazaletan txertatzea behar beharrezkoa da haien propietate magnetikoak mantentzen diren bitartean. Azken baldintza hori, dena den, handicap handia izan liteke gainazal-molekula interakzioen ondorioz [127–130]. Gainera, sistema hibridoetan molekulen antolamendu ordenatua eta dentsitate handia izatea beharrezkoa da. Orain arte material hibridoen adibide ugari deskribatu diren arren, hemen adibide batzuk baino ez ditugu deskribatuko.

Aukera desberdinen artean [131,132], koordinazio-polimero metal-organikoak (*MOF, Metal Organic Framework*) erabiltzea aukera erakargarria izan liteke. Izan ere, sistema horietako batzuek egokiak izan daitezke poroetan molekulak garraiatzeko. Aldez aurretik sistema hibrido horietako batzuen berri eman bada ere [133,134], arazoa poro-tamaina espezifikoak eta talde funtzionalak diseinatzerakoan sortu ohi da, poroak molekulak bertan egonkortzeko egokia izan behar baitu eta, aldi berean, molekula asko barneratzeko ahalmena nahi izaten da. Chenek eta kolaboratzaileek berriki egindako ikerketa batean, *MOF* mesoporoso bat sintetizatu zuten La^{III} ioian oinarrituta, 2 nm-ko

poro-diametroa erakusten zuen estekatzaile labur eta zurrunekin [135]. Tamaina hori egokia da barnean Mn12-ac molekulak sartzeko (i.30. irudia). *MOF*aren lagin kolorgeak Mn12-ac disoluzio aseetan murgiltzean, kristalak marroi bihurtzen dira molekulak poroetan sartu direla adieraziz. Material polikristalinoari egindako X-izpi neurketek erakutsi zuten 3D sarea osorik mantentzen dela. Bestalde, Mn12-ac molekulak poroetan sartzen direla egiaztatzeko N_2 adsortzio-isotermak erabili ziren, baita BET gainazalaren neurketak ere. Diseinatutako sistemak molekula dentsitate altua barneratzeko ezaugarri egokiak zituela ondorioztatu zuten. Alde batetik, *MOF*ak berak poroen zentrora bideratuta dituen –OH taldeek Mn12-ac molekularen azetatoekin sortzen ditu hidrogeno-zubiak (ikusi i.31. irudiko lerro gorri etenak). Bestetik, materialaren malgutasuna funtsezkoa da, *MOF*aren eta *SMM*en arteko interakzioek poroen uzkurdura ekartzen baitute edukiera hobetzen. EDX, ICP-MS eta ^{1}H-NMR tekniketan oinarrituta, mol bakoitzeko %40,15-eko karga-ahalmen errekorra kalkulatu zuten. Azkenik, sistema hibridoaren propietate magnetikoak neurtuz, iman propietateak ondo mantentzen zirela frogatu zuten, maximoak ikusi baitzituzten $\chi_M''(T)$ grafiketan eta histeresi-zikloak irekiak 2 K-etan.

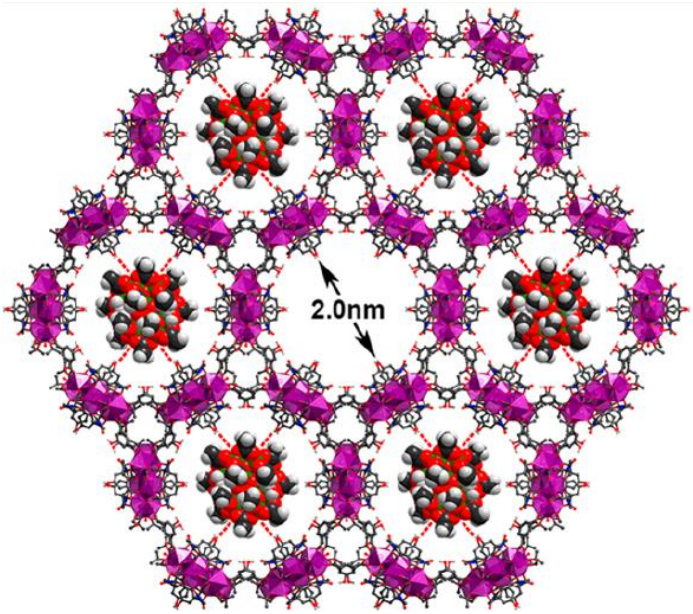

i.31. irudia. *MOF*aren egitura kristalinoa Mn12-ac molekulak poroetan daudelarik. [135] erreferentziaren baimenarekin erreproduzitua. Copyright 2019 American Chemical Society.

Aurreko adibidean eta aurreko azterlanetan ikusi den bezala, poroetan zenbat *SMM* sartzen den jakiteko zeharkako metodoak erabili ohi dira. Hala ere, duela pare bat urtera

arte ez da metodo zuzenik erabili molekulak poroen barruan sartuta daudela ikusteko. Aulakh eta egilekideek izan dira honetan aitzindari. Horretarako, lehenik *SMM@MOF* konposatu bat sintetizatu zuten, Mn12-ac molekulak eta Zr^{IV} ioian oinarritutako NU-1000 *MOF*a erabiliz [136]. **Mn12-ac@NU-1000** deitu zuten sistema hibridoa [137]. Bereizmen handiko transmisioko mikroskopia elektronikoa (*HRTEM, High-Resolution Transmission Electron Microscopy*) erabiliz, *SMM*ak *MOF*aren poroetan sartu zirela frogatzeko gai izan ziren zalantzarik gabe. i.32. irudian agertzen den bezala, [001] norabidean ateratako irudian 2 nm inguruko tamaina duten partikula diskretuak ikusten dira poro hexagonaletan. Partikula tamaina hau bat dator Mn12-ac molekularen dimentsioekin (1,6 nm). Esposizio-denbora luzeen ondorioz partikula horiek *MOF*aren deskonposiziotik sor zitezkeela baztertzeko, beste irudi batzuk hartu ziren NU-1000 *MOF* hutsarentzat. Behatutako partikulak Mn12-ac molekulei zegozkiela frogatu zuten.

Ikerketarekin amaitzeko, konposatu hibridoaren propietate magnetikoak aztertu zituzten. Magnetizazioaren erlaxazioa zertxobait aldatzen bazen ere Mn12-ac molekula hutsarekiko, *SMM* portaera mantentzen zela ikusi zuten. Egileek lana konposatuaren film mehe baten sintesi eta karakterizaziora hedatu zuten, etorkizuneko gailuetan ezartzeko hurrengo urratsa izango litzatekeena.

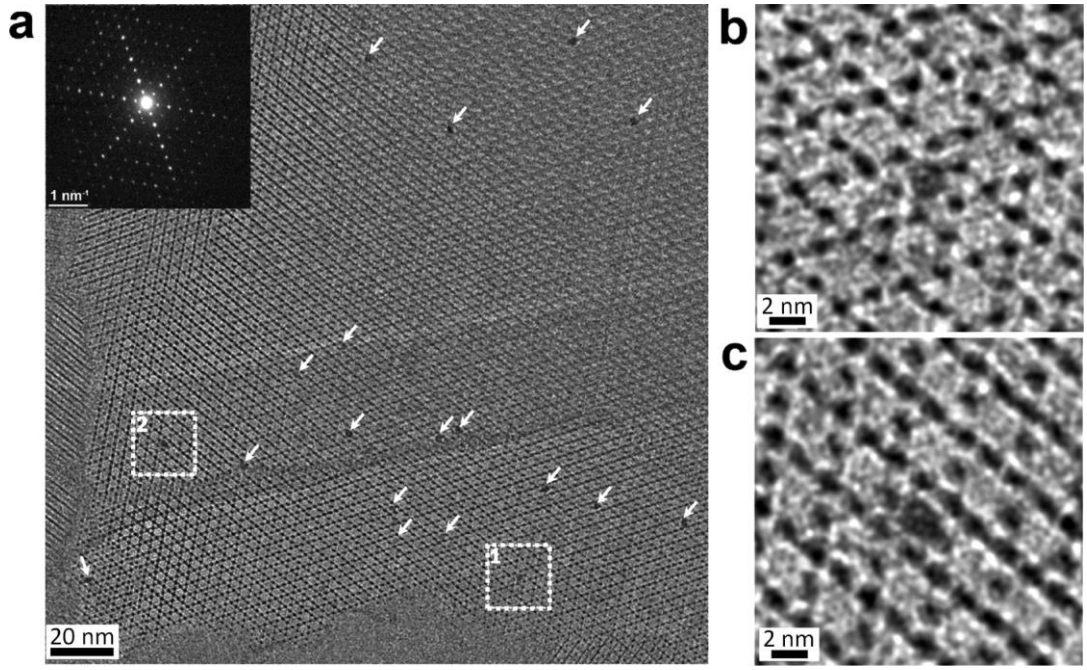

i.32. irudia. Mn12-ac@NU-1000 egitura *HRTEM* bidez karakterizatuta. a) *HRTEM* irudia eta **Mn12-ac@NU-1000** sistemaren elektroien difrakzio-patroia (lauki beltza), NU-1000ren [001] ardatzean neurtua. Geziek adierazten dute Mn12-ac molekulak non topatu diren. b) eta c) 1 eta 2 eremuetan nabarmendutako eremuen irudi handituak, hurrenez hurren. Mn12-ac klusterrak NU-1000ren kanal hexagonaletan bikainki kapsulatuta daudela ikusten da. Irudiak Gaussian iragazki bat erabiliz prozesatu ziren seinale-zarata erlazioa hobetzeko. [137] erreferentziaren baimenarekin erreproduzitua. Copyright 2019 American Chemical Society.

Aurreko bi adibide horietan *SMM*ak arrakastaz sartu ziren *MOF* diamagnetikoetan. Kasu horietan, koordinazio-polimero metal-organikoak plataforma soila dira iman molekularrak era ordenatuan antolatzeko propietate dinamikoak mantenduz. Beste ikuspegi interesgarria magnetikoki aktiboak diren *MOF*en eta *SMM*en arteko konbinazioa izan liteke. Mon eta egilekideek [138], sistema hibrido berean, eremu magnetikoz induzitutako *SMM* bat konbinatu zuten 15 K-etik behera irismen luzeko ordenamendu magnetikoa erakusten duen Mn^{II} eta Cu^{II} ioietan oinarritutako 3D *MOF* batekin. Hain zuzen, $[Mn^{III}(TPP)(H_2O)_2]ClO_4$ (TPP = 5,10,15,20-tetrafenilporfirina) *SMM*a [139,140] eta $Na_4\{Mn_4[Cu_2(Me_3mpba)_2]_3\}\cdot 60H_2O$ (Me_3mpba^4 = N,N'-2,4,6-trimetil-1,3-fenilenbis(oxamatoa)) *MOF*a [141]. *SMM*a *MOF*aren barruan prozedura post-sintetiko baten bidez sartu zen, monokristaletik monokristalerako prozesu baten bidez **MnTPP@1** hibridoa lortuz. Interesgarriena da bai *MOF*aren eta bai *SMM*ren propietate magnetikoek aldaketak jasan zituztela. Alde batetik, korronte alternoarekin egindako neurketek

frekuentziarekiko independenteak ziren χ_M'' seinaleak azaleratu zituzten 20 K inguruan, alegia, 3D sistema originalak baino 5 K gehiagotan detektatu zen irismen luzeko antolamendu magnetikoa. Erlaxazio magnetikoari dagokionez, sistema hibridoak frekuentziaren mendeko χ_M'' seinalea erakutsi zuen kanpo eremu magnetikorik gabe. Honek, zalantzarik gabe erakusten du *MOF* ferrimagnetikoaren barruan sortzen diren barne eremu magnetikoak gai direla *QTM* desaktibatu eta SMM propietateak hobetzeko. Dena den, proposatutakoa benetan frogatzeko asmoz, 3D konposatu isoestrukturala ere sintetizatu zuten Mn^{II} ioi paramagnetikoa Mg^{II} diamagnetikoarekin ordezkatuz $Mg_2\{Mg_4[Cu_2(Me_3mpba)_2]_3\}\cdot 45H_2O$ lortzeko [142]. 3D *MOF* diamagnetikoa eta *SMM*a konbinatuz **MnTPP@2** sistema hibridoa lortu zuten. Aurretik iradokitako hipotesia berretsiz, ez zen χ_M'' seinalerik ikusi kanpo eremu magnetikorik aplikatu gabe *QTM*ren desaktibazio prozesuan barne eremuek zuten garrantzia azpimarratuz.

Informazioaren irakurketa/idazketa prozesuetarako funtsezko beste baldintza molekulen ardatz anisotropikoa gainazalarekiko perpendikularki orientatzea da. Horretarako, sistema hibrido asko deskribatu dira, non *SMM*ak gainazal bidimentsionaletan txertatu diren. Adibidez, Dreiser eta kolaboratzaileek Ru(0001) eta Ir(111) monokristaletan hazi zituzten grafeno (G) desakoplamendu-geruzei lotutako Er(trensal) (H_3trensal = 2,2′,2″-tris- (salizilideneimino)-trietilamina) *SMM*ak [143]. Ondoren konparaketak egin ahal izateko, Ru(0001) hutsean (desakoplamendu-geruzarik gabe) hazitako Er(trensal) molekulak ere ikertu zituzten. Horrela, hiru sistema hibrido prestatu ziren: **Er(trensal)/G/Ru(0001)**, **Er(trensal)/G/Ir(111)** eta **Er(trensal)/Ru(0001)**. Lehenengo bien kasuan, tunel-efektuko mikroskopio irudiek (*STM, Scanning Tunneling Microscope*) erakutsi zuten gainazalari lotutako Er(trensal) molekulen gelaxka-unitatearen alboko tamaina eredu-sistemaren (Er(trensal) hutsa) gelaxka-unitatearenarekin aldera zitekeela. Hortaz, material hibridoetan antzeko paketatzea ematen dela ondorioztatu zuten. Aldiz, Ru(0001) hutsean hazitako molekulek ez zuten antolamendu garbirik erakutsi. Konparaketa honek molekulen eta gainazal metalikoen artean G desakoplamendu-geruza jartzearen garrantzia azpimarratzen du.

G geruza duten eta ez duenaren arteko paketatze portaera ezberdina tenperatura baxuko X izpien dikroismo zirkular magnetikoaren (*XMCD, X-ray Magnetic Circular Dichroism*) datuetatik lortutako *M(H)* kurbetan isladatu zen. Teknika hau une magnetikoak gai da izpi-sortaren norabidean momentu magnetikoaren proiekzioa kalkulatzeko. Horrela, gainazal jakin batean molekula guztiek orientazio bera badute, sistema horien guztien ardatz anisotropikoek ere norabide bera izango dute. Beraz, izpi-sorta gainazalarekiko perpendikularki edo angelu txikiago batekin erabiltzen bada,

momentu magnetikoaren balioa ere desberdina izango da. Aldiz, molekulek ez badute antolamendu jakin bat gainazalaren gainean, izpi-sortaren angeluarekiko erantzuna berbera izango da. Neurtutako hiru sistemen kasuan, G desakoplamendu-geruza duten sistema hibridoen eta Ru(0001) hutsaren arteko aldea nabarmena da (i.33. irudia). G geruza duten bi sistema hibridoen kasuan, Er^{III} ioiak proiektatutako momentu magnetikoa askoz indartsuagoa da eremu magnetikoa gainazalarekiko perpendikularra denean (datuak beltzez) angelu txikiagoarekin neurtutakoa denean baino (datuak gorriz). Horrek esan nahi duena da, molekulen ardatz magnetiko anisotropikoak G azalerarekiko perpendikularki orientatuta daudela, *STM* datuekin adostasunean. Aldiz, Ru(0001) hutsean hazitako Er(trensal) molekulen kasuan, ez zen inolako angelu-menpekotasunik ikusi. Ondorioz, azken kasu honetan molekulak ordena jakin batean antolatuta ez daudela ziurtatzen da, berriz ere *STM* datuekin adostasunean. Lan honetaz gain, Marocchi eta kolaboratzaileek eginikoak bezalako beste ikerketek berresten dute *SMM* eta azalera metalikoaren artean grafeno desakoplamendu-geruza jartzeak duen garrantzia [144]. Molekulen orientazioan eta ordenamenduan izan dezakeen eraginaz gain, azken ikerketa lan honetan grafeno geruzak berebiziko garrantzia izan zuen *SMM*aren oinarrizko izaera mantentzeko. $TbPc_2$ sandwich konposatu ezagunak G/Ni(111) geruzan txertatu zituzten, baina G erabili ezean, ftalozianinaren erradikal izaera suntsitzen zela ikusi zuten.

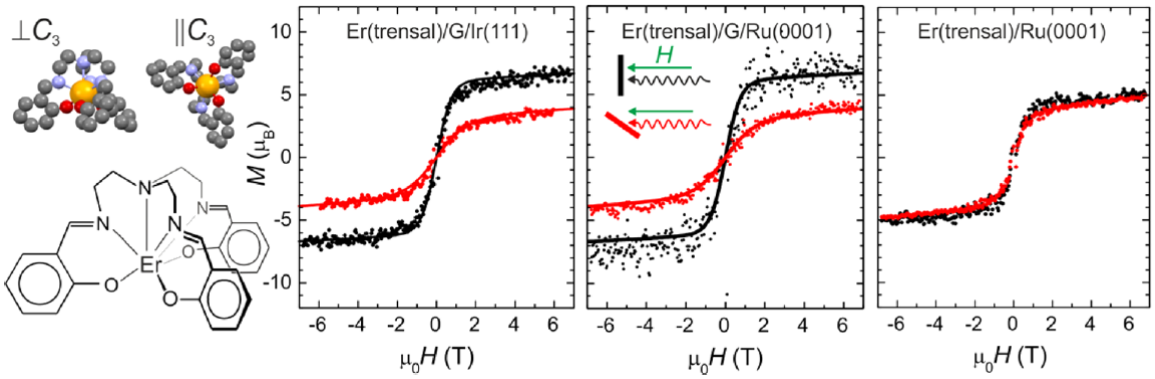

i.33. irudia. Er (trensal) molekularen egiturazko ikuspegiak eta eskema (ezkerrean). 3 K-etan eginiko *XMCD* neurketetatik ateratako Er^{III} *M(H)* kurbak gainazalarekiko perpendikularki ($\theta = 0^{o}$) eta angelu txikiagoan ($\theta = 65^{o}$). [143] erreferentziatik erreproduzitua. *ACS Author Choice*.

*SMM*ak txertatzeko beste material interesgarri bat karbono-nanohodia (*CNT, Carbon Nanotube*) da. Datuak biltegiratzeko, espintronika egiteko edo informazio kuantikoa

prozesatzeko, funtsezkoa da materialaren kontrol elektrikoa edukitzea [145,146]. *CNT*ak eroale elektriko bikainak direnez [147], *CNT-SMM* hibridoak interes handikoak dira. Gainera, euren egonkortasun kimiko eta termikoa dela eta, fabrikaziorako ere hautagai aproposak dira [148]. *CNT*ekin aurretik ere aztertu izan dira material hibridoak, hala nola, urrezko nanopartikulekin edo magnetikoekin, proteinekin, entzimekin edo molekula luminiszenteekin [149–154].

CNT-SMM hibridoen garapenerako, Boganiren taldeak **i55** konposatua diseinatu eta sintetizatu zuen ondorengo formula orokorrarekin: $[Fe_4(L)_2(dpm)_6]$, non Hdpm = dipivaloilmetano eta H_3L = 2-hidroximetil-2-(4-(pireno-1-il)butoxi) metilpropano-1,3-diola [155]. Nabarmendu behar da Fe^{III} ioian oinarritutako beste egitura tetranuklear antzeko asko ere aztertu direla urrea edo grafenoa oinarri duten gainazaletan txertatzeko [156–158]. Kasu honetarako H_3L apropos diseinatu zen, alboko kateetan pireno taldeak baititu (*CNT*arekin $\pi\cdots\pi$ interakzioak emateko egokiak). Sistema hibridoa sortu aurretik **i55** konposatuak *SMM* propietateak dituela frogatu zuten 1 K azpitik histeresi-ziklo irekiak neurtuz. Ondoren, *CNT*ak **i55** konplexuaren disoluzioetan murgilduz, sistema hibridoak sintetizatzea lortu zuten. *CNT* eta *SMM*en artean loturak sortzen zirela egiaztatzeko *AFM* (*Atomic Force Microscopy*) teknika erabili zen. Taldeak erabilitako pirenoen estrategiari esker, *SMM*ak *CNT*en kanpoko azaleran lotuta zeudela ikusi zuten. Aurrerapauso handia izan bazen ere, agian, ikuspegi interesgarriagoa litzateke *SMM*ak karbono-nanohodiaren barruan kapsulatzea, honela ingurunetik babestuta geratuko bailirateke eta erlaxazioa errazten duten prozesuak errazago ekidin ahal izango lirateke, funtsezkoa informazioa prozesatzeko [159].

Ideia horren adibide garbia da Gimenez-Lópezek eta kolaboratzaileek egindako ikerketa, Mn12-ac molekulak kapsulatu baitzituzten *CNT*en barruan [160]. Lehenik eta behin, Mn12-ac molekularen tamaina kontuan hartuta, eta molekulen eta *CNT*en artean beharrezkoa den gutxieneko 0,3 nm-ko Van der Waals bereizketa kontuan hartuta [148], horma anitzeko karbono-nanohodiak (*MWNT, MultiWalled carbon nanotube*) erabili ziren. Kasu espezifiko honetarako 6,5±1,8 nm-ko barne-diametroko *GMWNT*a (*graphitized MWNT*) erabili zen. **Mn12-ac@GMWNT** hibridoa (i.34. irudia) *TEM* bidez karakterizatuz, SMM molekulak nonohodien barruan zeudela ondorioztatu zuten eta ez hodien kanpoan beste hainbat lanetan ikusi den bezala [155,161,162]. Gainera, *PXRD* eta *TG* esperimentuak egin zituzten molekulek nonohodien barnealdearekin kanpoaldearekin baino interakzio sendoagoak sortzen dituztela ikusteko. **Mn12-ac@GMWNT** material hibridoaren $\chi_M''(T)$ grafikoek jatorrizko portaeraren mantentzea erakutsi zuten. Hala ere, grafiko horietan bi maximo-multzo desberdinen agertzea Jahn-

Teller ardatz batean distortsio bati lotuta dagoela adierazi zuten, erlaxazio-prozesu azkarrago bat ahalbidetzen duena. Histeresi-zikloek *QTM*ren eragin nabarmenagoa erakutsi zuten material hibridoan zeharkako anisotropia handiagoaren ondorioz, kalkulatutako energia-barrera txikiagoarekin bat datorrena. Dena den, nanohodien barruan *SMM*ak sartuta dituzten material hibrido hauek etorkizunera begira duten potentziala azaleratu dute.

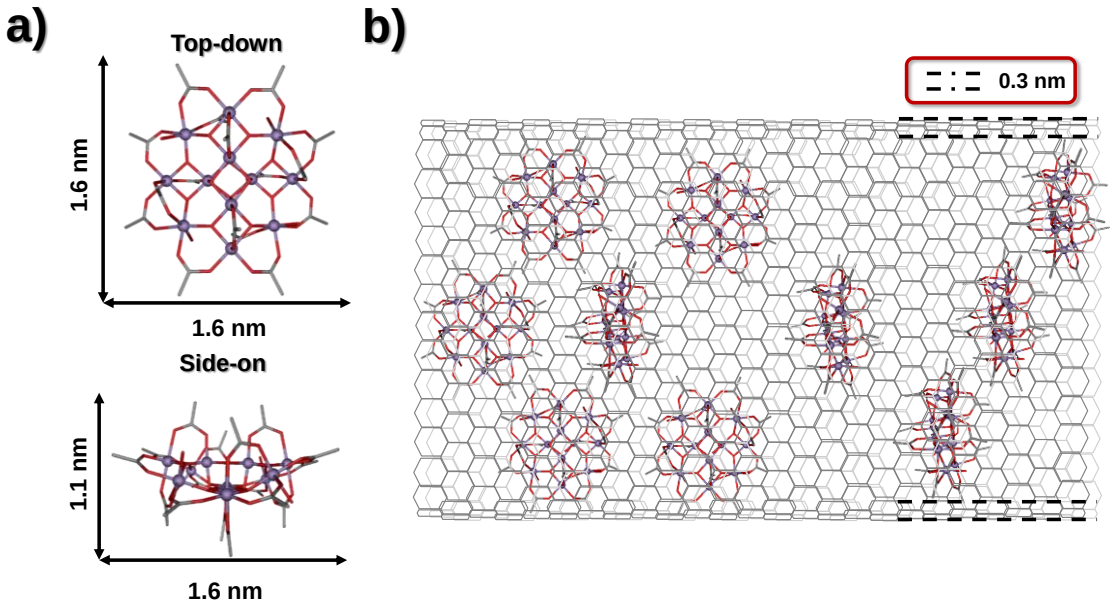

i.34. irudia. a) Mn12-ac molekularen egitura eta neurriak. b) GMWNT nanohodia barruan SMMekin. Irudi eskematikoa jatorrizko lanean [160] oinarritzen da.

Atal honi amaiera emateko, nabarmendu nahi genuke kalkulu teorikoak sistema hibridoetan egiteak duen garrantzia. Arazo handienetakoa da (normalean) sistema hauek ez dutela kristal-egiturarik atomo bakoitzaren posizio zehatza definitzen duena. Hori dela eta, korrelazio magneto-estrukturalak proposatzea zailagoa bilakatzen da. Testuinguru honetan, 2015ean Sessoli, Totti eta egilekideek *AIMD* (*Ab Initio Molecular Dynamics*) metodoa erabili zuten molekula baten egituraren bilakaera aztertzeko gainazal batean txertatu ahala [119]. Modu honetan, gai izan ziren propietate magnetikoen aldaketak aurresateko material polikristalinotik hibridora pasatzerakoan. Ondorio interesgarri bezala, eurek ikertutako sisteman garrantzi handiagoa zuen egiturak jasandako berrantolaketak gainazalarekiko interakzioek baino amaierako propietate magnetikoetan.

ix. *SMM* MULTIFUNTZIONALAK

Oso ohikoa da bibliografian funtzionalitate anitzak dituzten *SMM*ak aurkitzea, eta hori oso interesgarria da horien batura sinergikoa denean. Aristoteles filosofoaren hitzetan, sistema beraren funtzionaltasun ugaritasuna justifikatzen da *"osotasuna zatien batura baino hobea denean"*. Ln-*SMM*en sinergiarik ohikoena propietate magnetikoak eta luminiszenteak konbinatzen direnean ematen da. Aurretik aipatu bezala, Ln^{III} ioietako spin-orbita akoplamendua ondo babestutako 4f balentzia elektroietatik sortzen da. Aldi berean, 4f elektroiek koordinazio-inguruneareki ko duten sentsibilitate baxua dela eta, aldaketa txikiak ematen dira Ln^{III} bakoitzaren energia-mailen espektroan eta, beraz, absortzio- eta emisio-bandak oso estuak dira, kolore oso puruak sortuz. Emisio-banda bakoitza, beraz, ioi motaren aztarna ere bada. Lantanido seriean zehar, emisio-bandak ikusgai espektroan (Tm^{III}, Tb^{III}, Dy^{III}, Eu^{III} eta Sm^{III}; i.35a irudia) nahiz infragorri hurbilean (Yb^{III}, Nd^{III} eta Er^{III}; i.35a irudia) ikus daitezke.

Gainditu beharreko arazo nagusia distira gutxiko emisioena da, izan ere, Laporteren arauak 4f-4f trantsizio elektronikoak debekatzen ditu. Gainera, Ln^{III} ioia zuzenean kitzikatzea ez da estrategia eraginkorra, absortzio-koefiziente txikiak baititu (ε). Arazoari aurre egiteko modu eraginkorra ioia matrize organiko batean sartzea izan daiteke, luminiszentzia sentsibilizatzeko. Horretarako, absortzio-banda zabalak dituzten estekatzaile organikoak hautatu ohi dira (talde aromatikoak edo lotura insaturatu konjugatuak dituztenak, adibidez) antena efektua deiturikoa lortzeko. Efektu horren eraginkortasuna, beste faktore batzuen artean, estekatzailearen triplete-egoera baxuenaren (T_1, i.35b irudia) posizioaren araberakoa da Ln^{III} ioiaren emisio-egoerarekiko. Kitzikapen-argia erabiliz, estekatzailea egoera singletera (S_n) kitzikatzen da eta hortik fluoreszentzia emanez erlaxatu daiteke edo T_1 egoera hirukoitzera erlaxatu daiteke. Aldi berean, T_1 maila honetatik bi gauza gerta daitezke (i) estekatzailea hasierako egoerara erlaxatu daiteke fosforeszentzia emanez edo (ii) estekatzailearen T_1 mailaren eta Ln^{III} ioiaren emisio-mailaren arteko energia-diferentzia maila optimoan badago, energia transferentzia gerta daiteke Ln^{III} ioi metalikoaren emisioa sentsibilizatuz (i.35b irudia). Energia-diferentzia maila optimoak lehenago deskribatuak izan dira ioi mota bakoitzarentzat [163]. Hala ere, sentsibilizazio-prozesuaren ondoren, erlaxazioa bide ez-erradiatiboen bidez ere gerta daiteke emisioaren etekin kuantikoa (Φ) murriztuz. Sakonki azalduko ez dugun arren, prozesu ez-erradiatiboak, alde batetik, Ln^{III} ioiaren arabera gertatzen dira (ioi bakoitzak bere probabilitatea du prozesu ez-erradiatiboak emateko), baina, bestetik, kanpoko faktoreek bultza ditzakete. Emisio-egoeraren eta azpian dagoen lehen energia-mailaren arteko energia-diferentzia zenbat eta txikiagoa

izan, orduan eta handiagoa izango da erlaxazio-prozesu ez-erradiatiboak gertatzeko probabilitatea (hori da Tb^{III} konposatuek igorpen distiratsuagoa izatearen arrazoietako bat Dy^{III} ioian oinarritutako konposatuek baino). Gainera, emisioa oztopatzen duten talde funtzionalen artean, jakina da O-H, N-H eta C-H talde osziladoreek nahi ez diren prozesu ez-erradiatiboak bultzatzen dituztela. Beraz, oso garrantzitsua da talde funtzional horiek ahalik eta gehien urruntzea emisioa emango duten ioietatik [164,165]. Atal honetan ezaugarri garrantzitsuenetako batzuk bakarrik eztabaidatuko direnez, Ln-*SMM* luminiszenteetan interesa duen irakurlea aipatutako beste lanak irakurtzera gonbidatzen da [166–169].

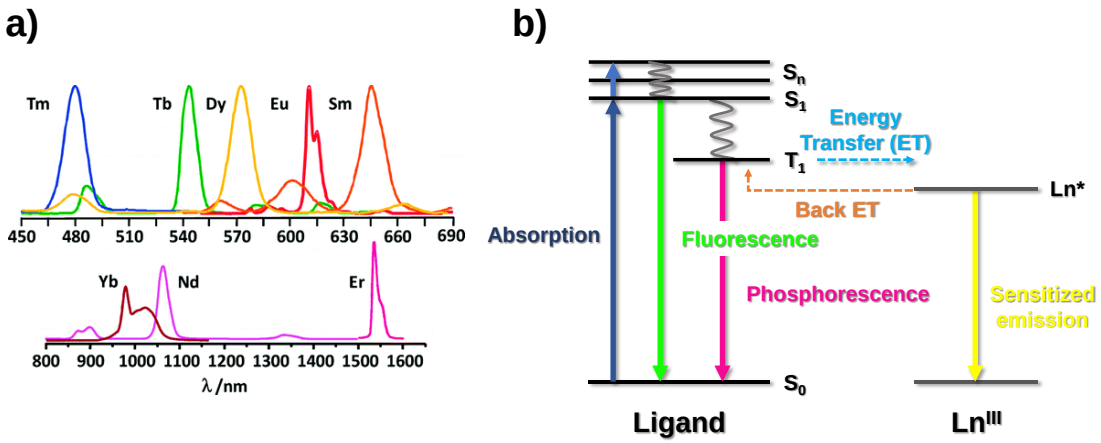

34. Irudia. a) Tris-β-diketonato konposatuen emisio espektroak. b) Jablonskyren diagrama sinplifikatua. [170] erreferentziaren baimenarekin erreproduzitua. Copyright 2010 American Chemical Society. Jatorrizko datuak hemen aurki daitezke [171].

Propietate magnetikoak eta fotoluminiszenteak konbinatzearen abantaila interesgarrietako bat da, behin molekulak gainazal batean daudenean, horien emisioa posizioa egiaztatzeko eta materialean duten kontzentrazioa kuantifikatzeko erabil daitekeela. Aipatzekoa da, emisio distiratsuak garatzeko, ingurune asimetrikoak onuragarriagoak direla oso simetrikoekin alderatuta. Hori, nolabait, ez da bateragarria propietate magnetikoen hobekuntzarekin; izan ere, esan bezala, ezaugarri asimetrikoek erlaxazio-denbora azkarragoak eragiten dituzten zeharkako eremu magnetikoak eman diezazkiekete sistemei, energia-barrera zeharkatzen duten bidezidorrak sortuz. Beraz, material bifuntzionalak diseinatzerakoan konpromiso bat bilatu behar da simetria eta asimetriaren artean.

Propietate luminiszenteen beste alderdi interesgarri bat M_J azpimailen energia-diagramari buruzko informazioa lortzea da. Normalean, *SMM*ak lehen M_J egoera kitzikatutik erlaxatzen dira (edo egoera kitzikatu altuagoetatik sistema oso axiala den kasuetan) eta oinarrizko egoeraren eta egoera kitzikatu horren arteko energia-diferentzia *ab initio* metodo konputazionalen bidez kalkulatu ohi da. Kontua da, lantanidoen emisio "lerro" estuak benetan multipleteak direla eta M_J azpimailen energia-banaketa eman diezagukete [172–175]. Ln^{III} ioia egoera elektroniko kitzikatutik erlaxatzen denean, erlaxazioa M_J azpimaila guztietara gertatzen da aipatutako multipletea emanez. Beraz, erlaxazio bakoitzari dagokion posizioaren arabera, estatuen banaketa energetikoa kalkula liteke (i.36. irudia). Hala ere, luminiszentzia espektro batetik informazio hori lortzea ez da dirudien bezain erraza. Multipleteak ez dira soilik M_J emisio-egoera baxuenaren eta oinarrizko egoeran dauden M_J ezberdinen arteko trantsizioz osatzen (trantsizio hauei zero-fonoi bandak deitzen zaie), banda beroak eta alboko banda bibronikoak ere multipletearen barnean egon ohi dira interpretazioa zailduz. Banda beroak emisio-egoeran altuago dauden M_J egoeren eta oinarrizko egoerako M_J azpimailen arteko trantsizioei dagozkie; alboko banda bibronikoak, berriz, elektroi-fonoi akoplamenduaren ondorio dira. Dena den, espektroen kalitatea hobetzeko eta ikusi nahi ez diren bandak saihesteko, neurketak tenperatura baxuetan egitea izan daiteke irtenbidea.

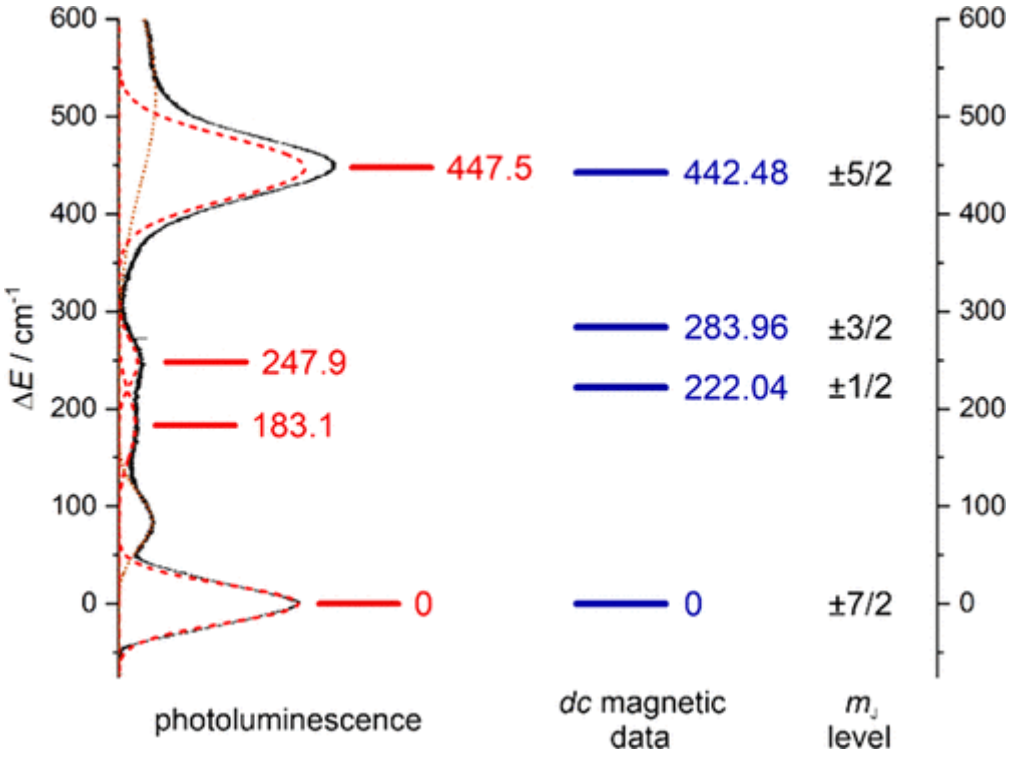

i.36. irudia. Yb^{III} konposatu baten energia-mailen diagrama erakusten da adibide gisa. $^2F_{7/2}$ multipletearen kristal-eremuaren banatzea 6 K-eko emisio-espektroan (ezkerrean) eta *dc* datu magnetikoen tratamenduan (eskuinean) oinarrituta. [176] erreferentziaren baimenarekin erreproduzitua. Copyright 2020 American Chemical Society.

Propietate magnetiko eta luminiszenteen arteko beste sinergia luminiszentzian oinarritutako termometriarekin lotuta dago. Sarrera osoan zehar argitu den bezala, tenperatura funtsezko faktorea da sistemen portaera magnetikoa zehazteko. Tenperatura jakin batetik behera, *SMM*ak informazioa biltzeko gai dira eta, horren gainetik, memoria efektua galtzen da. Hori dela eta, sistemaren barruko tenperaturaren kontrola funtsezkoa da. Molekula indibidualen tenperaturaz ari garenez, kontaktu-termometro konbentzionalak jada ez dira aukera bideragarria. Termometro hauek ordezkatzeko aukera erakargarri bat Ln^{III} ioien emisio-espektroetan ikus daitezkeen aldaketa termikoak aprobetxatzea da. Tenperaturaren arabera, espektroen profila nabarmen alda daiteke eta, beraz, emisio seinalearen mendekotasun termikoa kontakturik gabeko termometro zehatz bezala erabil daiteke [176–180]. Nolanahi ere, sistema bakar batean bi ezaugarri horiek (*SMM* portaera eta tenperaturarekiko mendekoa den emisioa) konbinatzeko honakoa hartu behar da kontuan: *SMM*ak

informazio-gordailu gisa lan egin dezakeen tenperatura-tartean eduki behar du tenperaturarekiko mendekoa den emisioa. Horrela, tenperatura zehaztu ahal izango da sistemak funtzionatzen duen tenperatura-tartean.

Fotoluminiszentziarekin lotuta, indarra hartzen diharduen beste propietatea luminiszentzia zirkularki polarizatua (*CPL*, *Circularly Polarized Luminescence*) da, ezkerrera/eskuinera emititutako argi zirkularki polarizatua eskuinera/ezkerrera emititutakoa baino sendoagoa denean detekta daitekeena. *SMM* eta *CPL* propietateen konbinazioa liluragarria da; izan ere, *SMM*ak bezala (ikus hurrengo atala), propietate kiroptiko hau erakusten duten sistemak hautagai onak izan daitezke gailu espintronikoetarako [181] eta informazioa gordetzeko [182] beste aplikazio batzuen artean [183,184]. *CPL*a konposatu kiralek eragiten badute ere, disolbatzailea [185] edo kontraioia [186] bezalako osagai akiralen eragina funtsezkoa izan daiteke azken emaitzan [187]. Efektua kuantifikatzeko g_{lum} luminiszentzia-disimetria faktorea honako ekuazio honen bidez kalkulatzen da (-2 eta +2 arteko balioa lortzen da):

$$g_{lum} = \frac{I_L - I_R}{{}^1\!/_2\,(I_L + I_R)} = \frac{\Delta I}{I} \qquad \text{(i.6)}$$

I_L eta I_R parametroek emisio zirkularraren intentsitate polarizatua adierazten dute, ezkerrera eta eskuinera, hurrenez hurren. Molekula organikoentzat edo trantsizio-metaletan oinarritutako koordinazio-konposatuentzat g_{lum} -balio txikiak (≤0,2) aurkitu izan diren bitartean [188–193], Ln^{III} ioien f-f trantsizioen izaerak efektu honetarako hautagai potentzial bihurtzen ditu, g_{lum} = 1,45 bezain balio altuak erakutsiz [194]. Adibide gisa, i.37. irudian bi $Zn^{II}Dy^{III}$ konposatu kiralen emaitzak erakusten dira (**i56-Λ** eta **i56-Δ**), Sutter eta egilekideek deskribatuak [195]. 12 K-etik behera magnetizazioaren erlaxazio motela erakusteaz gain, 0,04 eta 0,18 bitarteko eta -0,04 eta -0,16 bitarteko g_{lum} balioak kalkulatu zituzten **i56-Λ** eta **i56-Δ** konposatuentzat, hurrenez hurren (25 K-etan galtzen da *CPL* propietatea). Jakinik *CPL*a eremu magnetikoek eragindakoa ere izan daitekeela (aplikatutakoa edo intrintsekoa) [196], $Zn^{II}Eu^{III}$ analogoen *CPL*a ere aztertu zuten. Bitxia bada ere, bi polarizazio zirkularren emisioa berdin-berdin mantendu zen 5 K arte zero inguruko g_{lum} balioak lortuz. Beraz, molekula kasu konkretu horretan egituran oinarritutako *CPL*a oso ahula zela frogatu zuten.

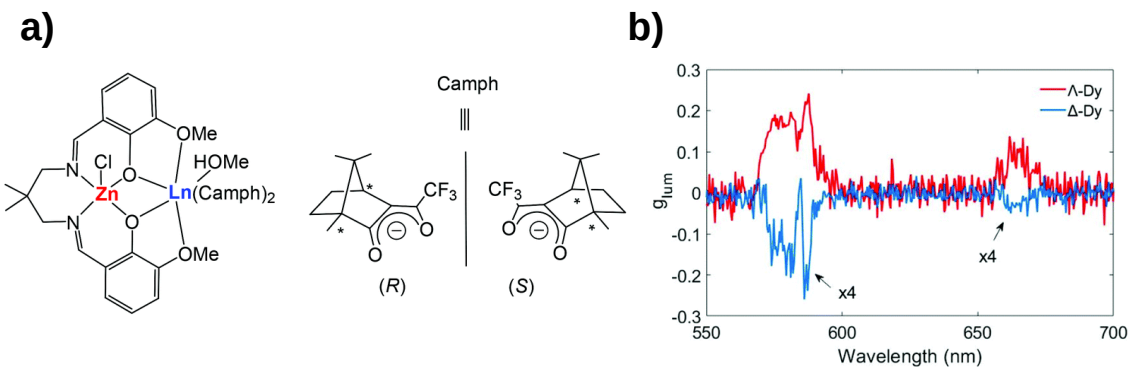

i.37. irudia. a) $Zn^{II}Ln^{III}$ konposatuen eskema. b) **56-Λ** eta **56-Δ** konposatuentzat *CPL* g_{lum} disimetria-faktorea uhin-luzeraren baitan eta 5 K-etan. [195] erreferentziaren baimenarekin erreproduzitua. Copyright 2020 the Partner Organisations.

Egitura molekularrean kiraltasuna sartzen denean, kristal-egitura ez-zentrosimetrikoak sor daitezke hamar talde puntual polarretako bati lotutako talde espaziala hartuz: C_1, C_S, C_2, C_{2V}, C_3, C_{3V}, C_4, C_{4V}, C_6 eta C_{6V}. Material hauek ferroelektrizitatea eman dezakete [197]. Material ferroelektrikoak berezko polarizazio elektrikoa erakusten duten materialak dira. Propietate magnetiko eta luminiszenteekin sinergian, funtzionalitate horiek guztiak dituzten materialak helburu oso erakargarritzat hartzen dira, informazio gordailu edo sentsore multifuntzionalak izan daitezkeelako [198,199]. Hala ere, funtzionalitate horiek guztiak bateratzeko behar diren baldintza ugariek (anisotropia sustatzeko estekatzaile eremu egokiak, emisio intentsoak lortzeko ioiaren sentsibilizazio ona eta talde espazial zehatz bateko kristalizazioa, besteak beste) deskribatutako adibide gutxi egotea dakarte [200–203]. Bestalde, izan ditzaketen aplikazioei begira, material ferroelektriko guztiak aldi berean piezoelektrikoak eta piroelektrikoak dira, eta bigarren harmonikoen sorrera ere badute (*SHG, Second Harmonic Generation*). Perovskitek ez bezala, material molekularretan askoz errazago sar daitezke aldaketak estekatzaileak eraldatuz propietateak aldatzeko. Gainera, dentsitate ere txikiagoa dute perovskitek baino. Horregatik, alternatiba erakargarriak dira propietate hauek ere aztertzeko.

Atal honetarako azken funtzionalitate gisa, propietate elektriko gehigarriak dituzten *SMM*ak ere aztertu dira. Adibidez, disolbatzaile polar protikoak erabiltzen direnean (hala nola alkoholak edo ura) eta sulfatoa, perkloratoa edo nitratoa bezalako kontraioiak, ardatz batean zehar luzatzen diren hidrogeno-lotura sareak lor daitezke. Kasu horietan, materialak protoi-eroankortasuna erakutsi dezake [176,204]. Bestalde, *SMM* portaera

eroankortasun elektrikoarekin konbinatzea ere oso interesgarria izan daiteke. Hori garatzeko, bi osagaiko estrategia erabili izan da normalean, non egitura kationiko edo anioniko hedatuek eroale elektriko gisa jokatzen duten, kontraioiak izanik magnetizazioaren erlaxazio motela erakusten dutenak [205,206].

x. *SMM*EN APLIKAZIO GEHIGARRIAK

Oro har, testu osoan zehar emandako ikuspegiak *SMM*ak informazio-gordailu gisa erabiltzeko proposamena aldarrikatzen du. Dena den, gaur egungo gizarteak informazio-gordailu berrien beharra ez ezik, prozesadoreena ere badu. Lehen helbururako hautagai paregabeak dira SMMak, izan ere, 1-2 nm inguruko diametroa dutela kalkulatzen badugu, 30 Tbit/cm^2 ingurko informazio-dentsitateaz ariko ginake hitz egiten. Konparazio gisa, 2015ean Seagate etxeak 0.21 Tbit/cm^2 informazio-dentsitatea izan zezakeen gailua merkaturatu zuen. Informazioaren prozesaketa azkarrago baten beharrak, bestalde, konputazio kuantikoaren eremura garamatza [207]. Bit tradizionalek informazio bitarra “bakarrik” gorde dezaketen bitartean, *qubit*ek (*quantum bits*) bi balio gorde ditzakete aldi berean jatorri kuantikoa dutelako. Testuinguru honetan, *SMM*ak fisika klasikoaren eta kuantikoaren artean kokatzen direnez, konputazio kuantikorako ere hautagai aproposak izan daitezke. Shor eta Groveren lan baten arabera, konputagailu kuantiko baten efikazia edozein konputagailu klasikorena baino altuagoa da [208,209]. Honen harira, Groveren algoritmoa *SMM*ekin bat etor litekeela egiaztatua izan da [210].

Baita ere, gailuen tamaina txikitze aldera, SMMak beste aplikazio batzuetan ere erabiltzeko aukera mahai gainean dago, esate baterako: spintronikan [145], elektronikan [211] edo magneto-optikan [212]. Aplikazio hauen inguruko fisika dagoeneko dexente jorratu da azken urteotan, baina testu honen markoan sartzen ez deez, interesa duen irakurlea aipatutako lanak irakurtzera gonbidatzen da.

xi. ETORKIZUNERA BEGIRA

Mundu mailan martxan dagoen miniaturizazio joerak, informazio-gordailuena barne, zientzialariak lehen *SMM*a aurkitzera bultzatu zuen: Mn12-ac, magnetismo molekularraren arloan mugarria. Landutako atal guztietan zehar ikusi da nola aldatu diren iman molekularrak sintetizatzeko estrategiak urteotan: spin altuko eta nuklearitate handiko kluster metalikoetatik hasi eta nuklearitate baxuko sistema anisotropikoetaraino.

Dy^{III} metalozenoen azken aurkikuntza berritzaileek, nolabait, jarraitu beharreko bidea erakutsi dute handicapik handienetako bat gainditu baita: blokeo-tenperaturak nitrogeno likidoaren tenperatura-muga gainditzea. Dy^{III} ioiaren inguruko kristal-eremu bereziak *QTM* eragiten duten bibrazio-modu kaltegarriak mugatzen ditu. Horrela, U_{eff} parametroen balioak ez badira ere aurretik ikusiak baino altuagoak, energia-barrera zeharkatzen duten lasterbideak ematen ez direnez T_B balioak hobetu dira. Sistema berri hauen aurkikuntzak komunitate zientifikoan korrelazio magneto-estruktural berriak sortzea ahalbidetu du, estekatzaile berrien diseinua erraztuz. Testuinguru honetan, Zhengen taldeak [213] aurretik deskribatutako iman molekular baten portaera hobetzea lortu du ($[Dy(O^tBu)_2(py)_5][BPh]_4$, **i21**) lortu du blokeo-tenperaturari dagokionez. Fenilo taldea duen alkoxido bat aukeratu zuten **i57** konposatua prestatzeko: $[Dy(L)_2(py)_5][BPh_4]$ (HL = (S)-(-)-1-feniletanola). Estrategia honen helburua molekula barneko nahiz molekularteko interakzioak ahalbidetzea zen kristal-egitura zurrundu eta *QTM* desagerrarazteko. Espero bezala, parametro kristalografikoak (lotura-distantziak eta angeluak) konparagarriak dira **i21** eta **i57** sistemetan. Desberdintasun gisa, bigarrenak molekula barneko C-H$\cdots\pi$ interakzioak ditu plano ekuatorialeko piridinen eta posizio axialeko fenilo taldeen artean (i.38a irudia). Gainera, molekularteko C-H$\cdots\pi$ eta $\pi\cdots\pi$ interakzioak ere badaude egituran (i.38b irudia). DFT (*Density Functional Theory*) kalkuluen arabera, interakzioak nahikoa indartsuak beharko lukete izan molekularen zurruntasuna areagotzeko. Histeresi-zikloak neurtzerakoan, **i57** konposatuak **i21** sistemak baino tenperatura altuagoan erakusten zituela ziklo irekiak ikusi zuten. Gainera, zero eremuko tunel efektua txikiagoa zela ikusi zuten lehenarentzat. Kontuan hartuta ab initio bidez kalkulatutako energia-diagrama oso antzekoa dela bi konposatuentzat, egileen esanetan zurruntasunak eragindako bibrazioen gutxiagotzea da propietate hobetuen arrazoia. Ateratako ondorioa indartzeko, esan behar da Ortu eta egilekideek lehenago enpirikoki frogatu zutela QTM eta malgutasun molekularra erlazionatuak daudela [214].

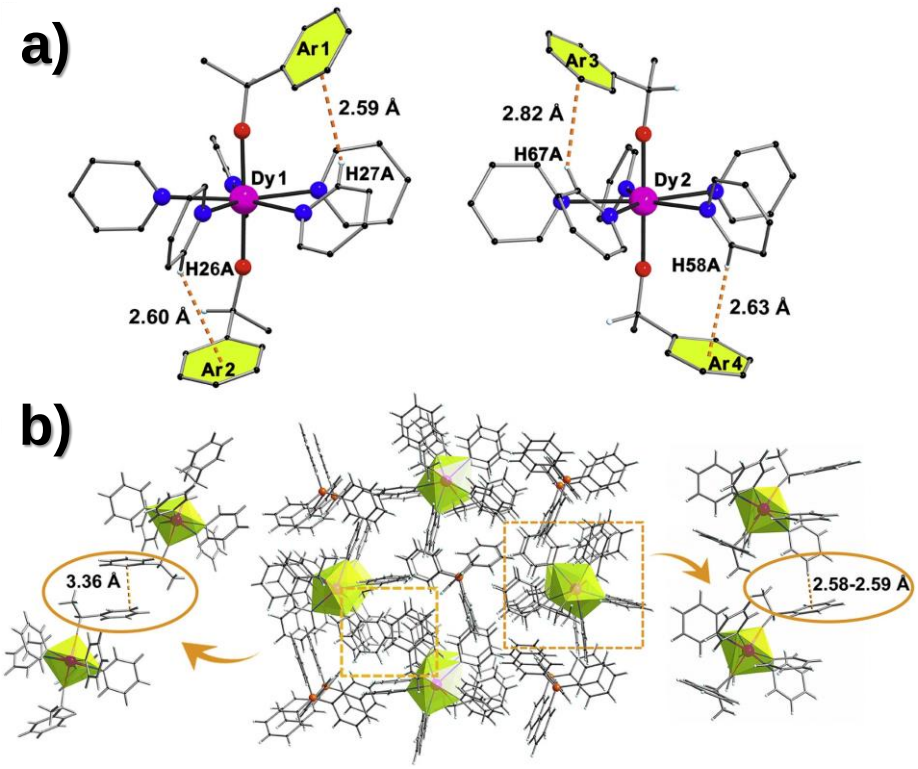

i.38. irudia. a) **i57** konposatuaren egitura eta molekula barneko C-H···π interakzioak. b) Molekularteko C-H···π eta π···π interakzioak. [213] erreferentziaren baimenarekin erreproduzitua.

Hala ere, esan bezala, oso garrantzitsua da oinarri teoriko berriak lantzea T_B parametroaren balioa mugatzen duten spin-fonoi interakzioak eta energia-barrera zeharkatzen duten bidezidorrak hobeto ulertzeko. zehazten duten hesiaren azpiko lasterbideak sakon ulertzeko. Izan ere, nahiz eta interakzio horien eragina ebalua dezakegun Orbach prozesuari dagokionez, ikusi da blokeo-tenperaturak Raman mekanismoaren eragin handia duela [215]. Chiltonen taldeak egindako lan baten arabera, badirudi erlazio zuzena egon daitekeela T_B balioaren eta Raman erlaxazioa hasten den puntuaren (τ_{switch}) artean (lan horretarako errendimendu altuko SMM batzuk aukeratu zituzten, U_{eff} > 600 K zutenak) [216]. Kontuan hartu lan horretan erabilitako T_B balioak *FC/ZFC* neurketetatik lortuak direla. $log_{10}(T_B)$ *vs* $log_{10}(\tau_{switch})$ irudikatuz, korrelazio lineal argia ikusi zuten. Honek, esan bezala, aditzera ematen du erlazio zuzen bat egon daitekeela T_B balioen eta Raman prozesua gailentzen den puntuaren artean. Ondorio zuzen gisa, erlaxazio-mekanismo hau hobeto ulertzeko beharraz hitz egiten dute egileek estekatzaile-eremuak hobeto diseinatzeko helburuarekin.

Lantanidoetan oinarritutako azken konposatu talde interesgarria klusterfulerenoena da. Oso ikerketa lan interesgarriak egin izan dira Ln^{III} ioiak fulerenoen barruan sartuz [217–219]. Punta-puntako disprosio-metalozenoen aldean aire eta tenperaturarekiko egonkortasun hobea erakusten dute sistema hauek. Gainera, fulereno barnean lor daitezkeen Ln-X (X = N^{3-}, S^{2-} or O^{2-}) lotura distantzia laburrek anisotropia altuak nahiz truke-interakzio indartsuak eragin ditzakete. Interesa duen irakurleari aipatutako artikuluak irakurtzea proposatzeaz gain, azken urteotan sistema hauek gainazaletan txertatzeko egin diren aurrerapausoei buruzko berrikuntzak [220–222] nahiz kalkulo teorikoenak [116] proposatzen zaizkio.

Orokorrean, badirudi lantanidoen erabilera bide oparoa dela. Gainera, sistema bakar batean funtzionalitate ugari konbinatzeko aukera eskaintzen dute bide berriak eta aplikazio sinergikoak zabalduz. Hala ere, honek ez du esan nahi trantsizio-metalak alde batera utzi direnik. Esate baterako, oso berriki anisotropia magnetiko handia eta truke-interakzio indartsuak konbinatu dira trantsizio-metal kluster batean. Berezitasun gisa, hori lortzeko ibilbidea guztiz berria izan da, metal-metal interakzio zuzenak erabili baitira.

Longen taldeak konposatu tetranuklear isoestrukturalak sintetizatu zituen ondorengo formularekin: $M_4(NP^tBu_3)_4 \cdot n\text{-}C_6H_{14}$ (M^I = Ni^I (**i58**) or Cu^I (**i59**); ^{t}Bu = tert-butiloa [200]. Horretarako, aldez aurretik deskribatutako prozedura bat [201] eta mesitilkobre(I) konposatuaren protonolisiaren erabili zituzten, hurrenez hurren (i.39. irudia, ezkerrean). Gainera, espezie oxidatuak ere aztertu zituzten: $[M_4(NP^tBu_3)_4][B(C_6F_5)_4]$ ($M^{I/II}$ = $Ni^{I/II}$ (**i60**) edo $Cu^{I/II}$ (**i61**). **i58** klusterrean Ni^I ioiak plano berean kokatzen dira, N-Ni-N angelu ia linealak erakutsiz (174,4 (6)º, batez beste), anisotropia magnetikoa hobetzeko eraginkorra dena. Gainera, Ni-Ni batez besteko distantziak 2,3631(1) Å-ekoak dira, metal-metal interakzioen tartean [225]. Elektroi baten oxidazioaren ondoren, **i60** molekulan Ni-N lotura distantzia guztiak txikitzen direnez, ezinezkoa da esatea metal ioi jakin bat oxidatu dela. Honek, aldi berean, metal-metal lotura izaera baieztatzen du elektroien deslokalizazioagatik (esperimentu elektrokimiko gehiago ere egin ziren, baita korronte zuzeneko (*dc*) neurketa magnetikoak ere hipotesi hau baieztatzeko).

Ardatz errazeko eta plano errazeko anisotropia magnetikoa kalkulatu zen **i58** eta **i60** klusterrentzat, hurrenez hurren, *D* balio altu samarrekin (**i58**: *D* = -1,93 eta -1,74 cm^{-1}, neurketa magnetikoetatik eta *EPR*tik abiatuta kalkulatuak, hurrenez hurren; **i60**: *D* = +7,95 eta +9,2 cm^{-1}, teknika berdinekin). Hala ere, **i58** konposatuak, ardatz errazekoak, ez zuen inolako magnetizazioaren erlaxazio motelik erakutsi, ziuraski, oinarrizko egoeraren eta lehen egoera kitzikatuaren arteko energia-diferentzia txikiaren ondorioz. Literaturan frogatu den bezala [226,227], *D* > 0 duten Kramers ioiek *SMM* portaera

erakutsi dezakete kanpoko eremu magnetikopean, beraz, **i60** aztertu zuten. Kanpo eremu magnetikorik gabe ez zen fasez kanpoko seinalerik detektatu, baina bai 400 Oe-ko kanpo eremu txiki batekin. 1,85-2,05 K-eko tenperatura aztertuz 16,53 cm^{-1}-eko energia-barrera kalkulatu zuten. Halaber, erlaxazio-denboren doikuntzak iradoki zuen Orbachen zela eraginkorra aztertutako tenperatura-tartean, aurretik deskribatutako $D > 0$ duten *SMM*ekin gertatzen ez den bezala [228]. Oraindik ere interesgarriago, *ac* neurketak disoluzio izoztu batean errepikatutakoan, kanpo eremu magnetikorik aplikatu gabe **i60** molekulak magnetizazioaren erlaxazio motela erakutsi zuen. Beraz, molekularteko interakzioek *QTM* eragiten zutela ondorioztatu zuten. Orain arte, hauxe da $D > 0$ duen eta kanpo eremurik gabe *SMM* portaera duen lehen adibidea. Azkenik, **i61** konposatuak ere erlaxazio motela zuela neurtu zuten kanpo eremu magnetikopean. Erlaxazioa azaltzeko Raman eta prozesu zuzena erabiltzen dira, ez baitago egoera magnetiko kitzikaturik $S = 1/2$ sistema batentzat. Zalantzarik gabe, metal-metal truke-interakzio zuzeneko kluster mota berri hauek *SMM*ak diseinatzeko bide berria ireki dute. Oinarri hauekin, Co^{II} [229] edo $Fe^{I/II}$ [230] sistemen berri eman da berriki (adibidez, ikusi i.39. irudia).

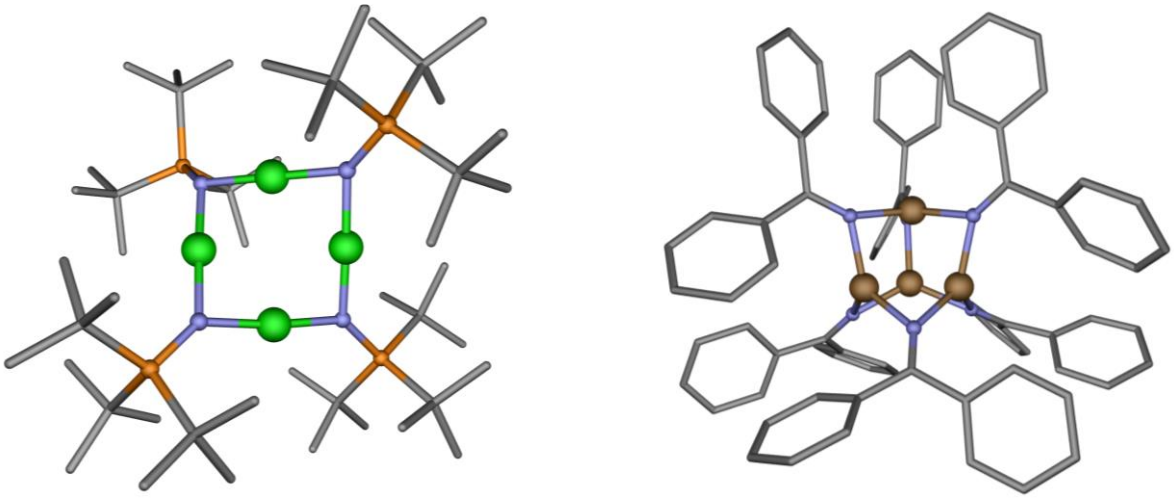

i.39. irudia. **i58** (ezkerrean) eta Fe ioian (eskuinean) oinarritutako konposatuen ikuspegia. Kolore-kodea: Ni^{II}, Fe^{I}/Fe^{II}, karbonoa, nitrogenoa eta fosforoa berde, marroi, gris, urdin eta laranja kolorez, hurrenez hurren. Hidrogeno atomoak, kontraioiak eta disolbatzaile molekulak ez dira irudikatu argitasunaren mesedetan. [223] and [230] erreferentzietako kristal-egituretatik abiatuta sortutako irudia.

Nuklearitate handiko konposatuek ere oraindik interes handia pizten dute. Esate baterako, Abbasi eta egilekideek duela gutxi deskribatu zuten oxidazio egoera mistoko Mn_{31} egitura bat ondorengo formula orokorrarekin: $[Mn_{31}O_{24}(OH)_2(OMe)_{24}(O_2CPh)_{16}(rac\text{-}mpm)_2]$ (**i62**), non mpmH = *α*-metil-2-piridin-metanola [231]. Kristal-egituraren barruan $\{Mn^{II}_2Mn^{III}_{28}Mn^{IV}\}$ ioiak aurkitu zituzten, non Mn^{III} ioi gehienen Jahn-Teller ardatzak elkarrekiko paraleloak ziren. Honek, agian, $D \neq 0$ adierazi zezakeen. Hain zuzen, magnetizazioaren erlaxazio motela detektatu zuten konposatuarentzak 58 K-eko energia-barrerarekin eta histeresi-zikloekin 5 K-etik behera. Barreraren balioa altutzat har daiteke 3d metaletan oinarritutako *SMM*a dela kontuan hartuta [232,233]. Interesgarriena da, hala ere, **i62** klusterraren tamaina konparagarria dela nanopartikula magnetikoekin, baina 0,5 K azpitik fenomeno kuantikoak jasaten ditu. Hortaz, halako sistemak egokiak izan daitezke *SMM* eta nanopartikula magnetikoen muga ikertzeko.

Nahiz eta inpaktua edo etorkizuneko perspektibak ez diren hain oparoak, ioi metaliko isotropikoetan oinarritutako *SMM*ek ere beren lekua dute arlo honetan. Esate baterako, Mn^{II} [234], Fe^{III} [235] edo Gd^{III} [236–240] ioiak dituzten konplexuen berri eman da, erlaxazio magnetiko motela erakusten dutenak kanpoko eremu magnetikopean. Bestalde, aktinidoen erabilera ere aztertzen ari dira [241,242]. Azken hauek, spin-orbita akoplamendu indartsuagoa erakusten dute eta, ondorioz, anisotropia magnetiko handiagoa erakutsi dezakete. Seriearen barruan, bereziki U^{III} ioian oinarritutako konposatuak deskribatu dira [243–245], nahiz eta beste oxidazio egoera batzuetako uranio konposatuak eta Np^{III} ioian oinarritutako ere aztertu diren [246].

Amaitzeko, *SMM*en alorra oraindik ere gaztetzat har daiteke, Mn12-ac aurkitu zenetik hiru hamarkada baino ez baitira igaro. Urte hauetan guztietan elkarlanean aritu dira kimikari sintetiko eta konputazionalak estrategia sintetiko berriak eta ezagutza teorikoak konbinatuz. Elkarlan horren fruitua da gero eta hobeto ulertzea magnetizazioaren erlaxazio motela nola ematen den eta nola mantsotu daitekeen. Horregatik, bi eremu horiek uztartzearen garrantzia azpimarratu nahi da. Kimikari sintetikoek konposatuak ia *à la carte* diseinatzeko eta sintetizatzeko gaitasuna erakutsi dute, baina kimikari teorikoek eta fisikariek funtsezko eginkizuna egin dute *SMM*en atzean dauden fenomeno kuantikoen azalpenean.

xii. HELBURUAK

Oro har, lan honetan lortu nahi diren helburuak honakoak dira:

1. Dy^{III} eta Er^{III} ioietan oinarritutako konposatu mononuklearrak sintetizatu Mannich estetekatzaile berrekin (eta dagoeneko deskribatutakoekin) propietate magnetiko dinamikoak aztertzeko.

2. Aurretik eginiko ikerketan oinarrituta (*CrystEngComm*, 2017, **19**, 256), azetato zubiak dikarboxilato eta trikarboxilato ezberdinez ordezkatu $Zn^{II}Dy^{III}$ entitateak luzatzeko. Koordinazio-ingurunea mantenduz, aldaketa txikiek propietateetan nola eragiten duten ikusi. Gainera, horien propietate luminiszenteak ikertu, erabilitako zubi desberdinek emisio propietateetan eragina izan baitezakete.

3. Co^{II} ioian oinarritutako konposatu polinuklearrak sintetizatu zubi estekatzaileak aldatuz. Horrela, estekatzaile mota ezberdinek eragindako truke-interakzioen izaera nola aldatzen den ikertu ahal izango da.

4. 3d eta 4f ioi paramagnetikoak konbinatu sistema berean eta propietate magnetikoak aztertu. Aurretik ikusi izan den bezala, truke-interakzio bidez akoplatutako sistemek propietate hobeak erakutsi ditzakete *QTM* desaktibatzearen ondorioz. Konposatu horien analogoak prestatu ioi paramagnetiko mota bakarrarekin (bestea diamagnetikoa). Bi sistema moten arteko desberdintasunak ebaluatu.

5. Mannich estekatzaile berriak sintetizatu eta lantanidoetan oinarritutako konposatu berriak sintetizatu energia-barrera altuagoak lortzen saiatuz. Korrelazio magneto-estrukturalak bilatu propietateak hobetzeko helburuarekin.

6. Beste lantanido batzuen propieta luminiszenteak ikertu, esate baterako: Sm^{III}, Eu^{III}, Tb^{III} edo Yb^{III}. Ikuskorrean nahiz infragorrian eman dezakete emisioa ioi hauek.

7. Energia-barrera altuko konposaturen bat gainazal batean depositatzen saiatu. Konposatu polikristalinoen eta hibridoen arteko propietate magnetikoak aztertu.

xiii. ERREFERENTZIAK

R. Sessoli, D. Gatteschi, A. Caneschi, M.A. Novak, Magnetic bistability in a metal-ion cluster, Nature. 365 (1993) 141–143. https://doi.org/10.1038/365141a0.

[2] A. Zabala-Lekuona, Iman Molekularrak: Informazio unitate txikienaren bila, Ekaia. 35 (2019) 85–99. https://doi.org/0.1387/ekaia.19692.

[3] A. Abragam, B. Bleaney, Electron Paramagnetic Resonance of Transition Ions, Clarendon Press Oxford, UK,. (1970) 925.

[4] J.H. Van Vleck, Paramagnetic relaxation times for titanium and chrome alum, Phys. Rev. 57 (1940) 426–447. https://doi.org/10.1103/PhysRev.57.426.

[5] H.B.G. Casimir, D. Bijl, F.K. Du Pré, Measurememts on paramagnetic relaxation in chromium potassium alum, Physica. 8 (1941) 449–460. https://doi.org/10.1016/S0031-8914(41)90066-6.

[6] K.S. Cole, R.H. Cole, Dispersion and absorption in dielectrics I. Alternating current characteristics, J. Chem. Phys. 9 (1941) 341–351. https://doi.org/10.1063/1.1750906.

[7] I.F. Díaz-Ortega, J.M. Herrera, D. Aravena, E. Ruiz, T. Gupta, G. Rajaraman, H. Nojiri, E. Colacio, Designing a Dy2 Single-Molecule Magnet with Two Well-Differentiated Relaxation Processes by Using a Nonsymmetric Bis-bidentate Bipyrimidine- N-Oxide Ligand: A Comparison with Mononuclear Counterparts, Inorg. Chem. 57 (2018) 6362–6375. https://doi.org/10.1021/acs.inorgchem.8b00427.

[8] L. Zhang , J. Jung, P. Zhang, M. Guo, L. Zhao, J. Tang, B. Le Guennic, Site-Resolved Two-Step Relaxation Process in an Asymmetric Dy $_2$ Single-Molecule Magnet, Chem. - A Eur. J. 22 (2016) 1392–1398. https://doi.org/10.1002/chem.201503422.

[9] E. Echenique-Errandonea, A. Zabala-Lekuona, J. Cepeda, A. Rodríguez-Diéguez, J.M. Seco, I. Oyarzabal, E. Colacio, Effect of the change of the ancillary carboxylate bridging ligand on the SMM and luminescence properties of a series of carboxylate-diphenoxido triply bridged dinuclear ZnLn and tetranuclear Zn 2 Ln 2 complexes (Ln = Dy, Er), Dalton Trans. 48 (2019) 190–201. https://doi.org/10.1039/c8dt03800g.

[10] C. Shi, R. Nie, X. Yao, S. Fan, G. An, Y. Dong, G. Li, Asymmetry-unit-dominated double slow-relaxation modes of 2,6-dimethyl-3,5-heptanedione dysprosium SMMs, RSC Adv. 7 (2017) 49701–49709. https://doi.org/10.1039/c7ra09711e.

[11] J. Ruiz, A.J. Mota, A. Rodríguez-Diéguez, S. Titos, J.M. Herrera, E. Ruiz, E. Cremades, J.P. Costes, E. Colacio, Field and dilution effects on the slow relaxation of a luminescent DyO9 low-symmetry single-ion magnet, Chem. Commun. 48 (2012) 7916–7918. https://doi.org/10.1039/c2cc32518g.

[12] B. Liu, B. Wang, Z. Wang, S. Gao, Static field induced magnetic relaxations in dinuclear lanthanide compounds of [phen 2Ln 2(HCOO) 4(HCOO) 2-2x (NO 3) 2x] (1, Ln = Gd and x = 0.52; 2, Ln = Er and x = 0.90; Phen = 1,10-phenanthroline), Sci. China Chem. 55 (2012) 926–933. https://doi.org/10.1007/s11426-012-4599-5.

[13] A. Arauzo, A. Lazarescu, S. Shova, E. Bartolomé, R. Cases, J. Luzón, J. Bartolomé, C. Turta, Structural and magnetic properties of some lanthanide (Ln = Eu(iii), Gd(iii) and Nd(iii)) cyanoacetate polymers: Field-induced slow magnetic relaxation in the Gd and Nd substitutions, Dalton Trans. 43 (2014) 12342–12356. https://doi.org/10.1039/c4dt01104j.

[14] D. Reta, N.F. Chilton, Uncertainty estimates for magnetic relaxation times and magnetic relaxation parameters, Phys. Chem. Chem. Phys. 21 (2019) 23567–23575. https://doi.org/10.1039/c9cp04301b.

[15] O. Kahn, Molecular magnetism, VCH, Weinheim, Germany, 1993.

[16] T. Glaser, H. Theil, I. Liratzis, T. Weyhermüller, E. Bill, Ferromagnetic coupling by orthogonal magnetic orbitals in a heterodinuclear CuIIVIV=O complex and in a homodinuclear Cu IICuII complex, Inorg. Chem. 45 (2006) 4889–4891. https://doi.org/10.1021/ic0606328.

[17] T. Glaser, M. Gerenkamp, R. Fröhlich, Targeted Synthesis of Ferromagnetically Coupled Complexes with Modified 1,3,5-Trihydroxybenzene Ligands, Angew. Chem. Int. Ed. 41 (2002) 3823–3825. https://doi.org/10.1002/1521-3773(20021018)41:20<3823::AID-ANIE3823>3.0.CO;2-I.

[18] T. Glaser, T. Beissel, E. Bill, T. Weyhermüller, V. Schünemann, W. Meyer-Klaucke, A.X. Trautwein, K. Wieghardt, Electronic structure of linear thiophenolate-bridged heterotrinuclear complexes [LFeMFeL](n+) (M = Cr, Co, Fe; n = 1-3): Localized vs delocalized models, J. Am. Chem. Soc. 121 (1999) 2193–2208. https://doi.org/10.1021/ja982898m.

[19] C. Beghidja, G. Rogez, J. Kortus, M. Wesolek, R. Welter, Very strong ferromagnetic interaction in a new binuclear μ-methoxo-bridged Mn(III) complex: Synthesis, crystal structure, magnetic properties, and DFT calculations, J. Am. Chem. Soc. 128 (2006) 3140–3141. https://doi.org/10.1021/ja0575023.

[20] A. Ferguson, J. Lawrence, A. Parkin, J. Sanchez-Benitez, K. V. Kamenev, E.K. Brechin, W. Wernsdorfer, S. Hill, M. Murrie, Synthesis and characterisation of a Ni4 single-molecule magnet with S4 symmetry, J. Chem. Soc. Dalt. Trans. (2008) 6409–6414. https://doi.org/10.1039/b807447j.

[21] G.S. Papaefstathiou, A. Escuer, C.P. Raptopoulou, A. Terzis, S.P. Perlepes, R. Vicente, Defective Double-Cubane, Tetranuclear Manganese(II) and Cobalt(II) Complexes with Simultaneous μ1,1-Azido and μ-O Bridges, Eur. J. Inorg. Chem. 2001 (2001) 1567–1574. https://doi.org/10.1002/1099-0682(200106)2001:6<1567::aid-ejic1567>3.0.co;2-7.

[22] G.S. Papaefstathiou, A. Escuer, R. Vicente, M. Font-Bardia, X. Solans, S.P. Perlepes, Reactivity in polynuclear transition metal chemistry as a means to obtain high-spin molecules: Substitution of μ4-OH− by η1,μ4-N3− increases nine times the ground-state S value of a nonanuclear nickel(II) cage, Chem. Commun. 1 (2001) 2414–2415. https://doi.org/10.1039/b106472j.

[23] D.M. Low, L.F. Jones, A. Bell, E.K. Brechin, T. Mallah, E. Rivière, S.J. Teat, E.J.L. McInnes, Solvothermal synthesis of a tetradecametallic FeIII cluster, Angew. Chem. Int. Ed. 42 (2003) 3781–3784. https://doi.org/10.1002/anie.200351865.

[24] J. Larionova, M. Gross, M. Pilkington, H. Andres, H. Stoeckli-Evans, H.U. Güdel, S. Decurtins, High-spin molecules: A novel cyano-bridged Mn9/(II)Mo6/(V) molecular cluster with a S = 51/2 ground state and ferromagnetic intercluster ordering at low temperatures, Angew. Chem. Int. Ed. 39 (2000) 1605–1609. https://doi.org/10.1002/(SICI)1521-3773(20000502)39:9<1605::AID-ANIE1605>3.0.CO;2-5.

[25] M. Affronte, J.C. Lasjaunias, W. Wernsdorfer, R. Sessoli, D. Gatteschi, S.L. Heath, A. Fort, A. Rettori, Magnetic ordering in a high-spin Fe19 molecular nanomagnet, Phys. Rev. B. 66 (2002) 644081–644087. https://doi.org/10.1103/PhysRevB.66.064408.

[26] A.M. Ako, I.J. Hewitt, V. Mereacre, R. Clérac, W. Wernsdorfer, C.E. Anson, A.K. Powell, A ferromagnetically coupled Mn19 aggregate with a record S = 83/2 ground spin state, Angew. Chem. Int. Ed. 45 (2006) 4926–4929. https://doi.org/10.1002/anie.200601467.

[27] M. Murugesu, M. Habrych, W. Wernsdorfer, K.A. Abboud, G. Christou, Single-Molecule Magnets: A Mn25 Complex with a Record S = 51/2 Spin for a Molecular Species, J. Am. Chem. Soc. 126 (2004) 4766–4767. https://doi.org/10.1021/ja0316824.

[28] J. Cirera, E. Ruiz, S. Alvarez, F. Neese, J. Kortus, How to build molecules with large magnetic anisotropy, Chem. - A Eur. J. 15 (2009) 4078–4087. https://doi.org/10.1002/chem.200801608.

[29] A. Sieber, R. Bircher, O. Waldmann, G. Carver, G. Chaboussant, H. Mutka, H.-U. Güdel, Effect of Pressure on the Magnetic Anisotropy in the Single-Molecule Magnet Mn12-Acetate: An Inelastic Neutron Scattering Study, Angew. Chem. Int. Ed. 44 (2005) 4239–4242. https://doi.org/10.1002/anie.200500171.

[30] F. Neese, D. a Pantazis, What is not required to make a single molecule magnet., Faraday Discuss. 148 (2011) 229–238; discussion 299-314. https://doi.org/10.1039/c005256f.

[31] P.P. Power, Stable two-coordinate, open-shell (d 1-d 9) transition metal complexes, Chem. Rev. 112 (2012) 3482–3507. https://doi.org/10.1021/cr2004647.

[32] R. Ruamps, L.J. Batchelor, R. Maurice, N. Gogoi, P. Jiménez-Lozano, N. Guihéry, C. Degraaf, A.L. Barra, J.P. Sutter, T. Mallah, Origin of the magnetic anisotropy in heptacoordinate NiII and CoII complexes, Chem. - A Eur. J. 19 (2013) 950–956. https://doi.org/10.1002/chem.201202492.

[33] Y. Rechkemmer, F.D. Breitgoff, M. Van Der Meer, M. Atanasov, M. Hakl, M. Orlita, P. Neugebauer, F. Neese, B. Sarkar, J. Van Slageren, A four-coordinate cobalt(II) single-ion magnet with coercivity and a very high energy barrier, Nat. Commun. 7 (2016) 10467. https://doi.org/10.1038/ncomms10467.

[34] J.M. Frost, K.L.M. Harriman, M. Murugesu, The rise of 3-d single-ion magnets in molecular magnetism: Towards materials from molecules?, Chem. Sci. 7 (2016) 2470–2491. https://doi.org/10.1039/c5sc03224e.

[35] S. Gómez-Coca, D. Aravena, R. Morales, E. Ruiz, Large magnetic anisotropy in mononuclear metal complexes, Coord. Chem. Rev. 289–290 (2015) 379–392. https://doi.org/10.1016/j.ccr.2015.01.021.

[36] M. Feng, M.L. Tong, Single Ion Magnets from 3d to 5f: Developments and Strategies, Chem. - A Eur. J. 24 (2018) 7574–7594. https://doi.org/10.1002/chem.201705761.

[37] S. Tripathi, A. Dey, M. Shanmugam, R.S. Narayanan, V. Chandrasekhar, Cobalt(II) complexes as single-ion magnets, in: Top. Organomet. Chem., Springer, 2019: pp. 35–75. https://doi.org/10.1007/3418_2018_8.

[38] G.A. Craig, M. Murrie, 3d single-ion magnets, Chem. Soc. Rev. 44 (2015) 2135–2147. https://doi.org/10.1039/c4cs00439f.

[39] W.M. Reiff, A.M. LaPointe, E.H. Witten, Virtual free ion magnetism and the absence of Jahn-Teller distortion in a linear two-coordinate complex of high-spin iron(II), J. Am. Chem. Soc. 126 (2004) 10206–10207. https://doi.org/10.1021/ja030632w.

[40] W.M. Reiff, C.E. Schulz, M.H. Whangbo, J.I. Seo, Y.S. Lee, G.R. Potratz, C.W. Spicer, G.S. Girolami, Consequences of a linear two-coordinate geometry for the orbital magnetism and Jahn-Teller distortion behavior of the high spin iron(II) complex Fe[N(t-Bu)2]2, J. Am. Chem. Soc. 131 (2009) 404–405. https://doi.org/10.1021/ja806660f.

[41] W.A. Merrill, T.A. Stich, M. Brynda, G.J. Yeagle, J.C. Fettinger, R. De Hont, W.M. Reiff, C.E. Schulz, R.D. Britt, P.P. Power, Direct spectroscopic observation of large quenching of first-order orbital angular momentum with bending in monomeric, two-coordinate Fe(II) primary amido complexes and the profound magnetic effects of the absence of Jahnand- and Renner-Teller distortions in rigorously linear coordination, J. Am. Chem. Soc. 131 (2009) 12693–12702. https://doi.org/10.1021/ja903439t.

[42] J.M. Zadrozny, M. Atanasov, A.M. Bryan, C.Y. Lin, B.D. Rekken, P.P. Power, F. Neese, J.R. Long, Slow magnetization dynamics in a series of two-coordinate iron(ii) complexes, Chem. Sci. 4 (2013) 125–138. https://doi.org/10.1039/c2sc20801f.

[43] M. Atanasov, J.M. Zadrozny, J.R. Long, F. Neese, A theoretical analysis of chemical bonding, vibronic coupling, and magnetic anisotropy in linear iron(ii) complexes with single-molecule magnet behavior, Chem. Sci. 4 (2013) 139–156. https://doi.org/10.1039/c2sc21394j.

[44] J.M. Zadrozny, D.J. Xiao, M. Atanasov, G.J. Long, F. Grandjean, F. Neese, J.R. Long, Magnetic blocking in a linear iron(I) complex, Nat. Chem. 5 (2013) 577–581. https://doi.org/10.1038/nchem.1630.

[45] M. Dey, N. Gogoi, Geometry-mediated enhancement of single-ion anisotropy: A route to single-molecule magnets with a high blocking temperature, Angew. Chem. Int. Ed. 52 (2013) 12780–12782. https://doi.org/10.1002/anie.201304982.

[46] J.M. Frost, K.L.M. Harriman, M. Murugesu, The rise of 3-d single-ion magnets in molecular magnetism: towards materials from molecules?, Chem. Sci. 7 (2016) 2470–2491. https://doi.org/10.1039/C5SC03224E.

[47] Y.S. Meng, Z. Mo, B.W. Wang, Y.Q. Zhang, L. Deng, S. Gao, Observation of the single-ion magnet behavior of d8 ions on two-coordinate Co(i)-NHC complexes, Chem. Sci. 6 (2015) 7156–7162. https://doi.org/10.1039/c5sc02611c.

[48] X.N. Yao, J.Z. Du, Y.Q. Zhang, X.B. Leng, M.W. Yang, S. Da Jiang, Z.X. Wang, Z.W. Ouyang, L. Deng, B.W. Wang, S. Gao, Two-coordinate Co(II) imido complexes as outstanding single-molecule magnets, J. Am. Chem. Soc. 139 (2017) 373–380. https://doi.org/10.1021/jacs.6b11043.

[49] J. Du, L. Wang, M. Xie, L. Deng, A Two-Coordinate Cobalt(II) Imido Complex with NHC Ligation: Synthesis, Structure, and Reactivity, Angew. Chem. Int. Ed. 54 (2015) 12640–12644. https://doi.org/10.1002/anie.201505937.

[50] P.C. Bunting, M. Atanasov, E. Damgaard-Møller, M. Perfetti, I. Crassee, M. Orlita, J. Overgaard, J. Van Slageren, F. Neese, J.R. Long, A linear cobalt(II) complex with maximal orbital angular momentum from a non-Aufbau ground state, Science. 362 (2018) 3719. https://doi.org/10.1126/science.aat7319.

[51] M. Atanasov, D. Aravena, E. Suturina, E. Bill, D. Maganas, F. Neese, First principles approach to the electronic structure, magnetic anisotropy and spin relaxation in mononuclear 3d-transition metal single molecule magnets, Coord. Chem. Rev. 289–290 (2015) 177–214. https://doi.org/10.1016/j.ccr.2014.10.015.

[52] T. Viefhaus, W. Schwarz, K. Hübler, K. Locke, J. Weidlein, Das unterschiedliche Reaktionsverhalten von basefreiem Tris(trimethylsilyl)methyl-Lithium gegenüber den Trihalogeniden der Erdmetalle und des Eisens, Zeitschrift Fur Anorg. Und Allg. Chemie. 627 (2001) 715–725. https://doi.org/10.1002/1521-3749(200104)627:4<715::aid-zaac715>3.0.co;2-0.

[53] J.M. Zadrozny, D.J. Xiao, M. Atanasov, G.J. Long, F. Grandjean, F. Neese, J.R. Long, Magnetic blocking in a linear iron(I) complex, Nat. Chem. 5 (2013) 577–581. https://doi.org/10.1038/nchem.1630.

[54] N.H. Buttrus, C. Eaborn, P.B. Hitchcock, J.D. Smith, A.C. Sullivan, Preparation and crystal structure of a two-co-ordinate manganese compound, bis[tris(trimethyl)silylmethyl]manganese, J. Chem. Soc. Chem. Commun. (1985) 1380–1381. https://doi.org/10.1039/c39850001380.

[55] C.Y. Lin, J.C. Fettinger, N.F. Chilton, A. Formanuik, F. Grandjean, G.J. Long, P.P. Power, Salts of the two-coordinate homoleptic manganese(i) dialkyl anion [Mn{C(SiMe3)3}2]- with quenched orbital magnetism, Chem. Commun. 51 (2015) 13275–13278. https://doi.org/10.1039/c5cc05166e.

[56] P.E. Kazin, M.A. Zykin, L.A. Trusov, A.A. Eliseev, O. V. Magdysyuk, R.E. Dinnebier, R.K. Kremer, C. Felser, M. Jansen, A Co-based single-molecule magnet confined in a barium phosphate apatite matrix with a high energy barrier for magnetization relaxation, Chem. Commun. 53 (2017) 5416–5419. https://doi.org/10.1039/c7cc02453c.

[57] I.G. Rau, S. Baumann, S. Rusponi, F. Donati, S. Stepanow, L. Gragnaniello, J. Dreiser, C. Piamonteze, F. Nolting, S. Gangopadhyay, O.R. Albertini, R.M. Macfarlane, C.P. Lutz, B.A. Jones, P. Gambardella, A.J. Heinrich, H. Brune, Reaching the magnetic anisotropy limit of a 3d metal atom, Science. 344 (2014) 988–992. https://doi.org/10.1126/science.1252841.

[58] N. Ishikawa, M. Sugita, T. Ishikawa, S.Y. Koshihara, Y. Kaizu, Lanthanide double-decker complexes functioning as magnets at the single-molecular level, J. Am. Chem. Soc. 125 (2003) 8694–8695. https://doi.org/10.1021/ja029629n.

[59] N. Koike, H. Uekusa, Y. Ohashi, C. Harnoode, F. Kitamura, T. Ohsaka, K. Tokuda, Relationship between the Skew Angle and Interplanar Distance in Four Bis(phthalocyaninato)lanthanide(III)

Tetrabutylammonium Salts ([NBu4n][LnIIIPc2]; Ln = Nd, Gd, Ho, Lu), Inorg. Chem. 35 (1996) 5798–5804. https://doi.org/10.1021/ic960158d.

[60] J. Rinehart, J. Long, Exploiting single-ion anisotropy in the design of f-element single-molecule magnets, Chem. Sci. 2 (2011) 2078–2085. https://doi.org/10.1039/c1sc00513h.

[61] F. Habib, G. Brunet, V. Vieru, I. Korobkov, L.F. Chibotaru, M. Murugesu, Significant enhancement of energy barriers in dinuclear dysprosium single-molecule magnets through electron-withdrawing effects, J. Am. Chem. Soc. 135 (2013) 13242–13245. https://doi.org/10.1021/ja404846s.

[62] J. Long, F. Habib, P.H. Lin, I. Korobkov, G. Enright, L. Ungur, W. Wernsdorfer, L.F. Chibotaru, M. Murugesu, Single-molecule magnet behavior for an antiferromagnetically superexchange-coupled dinuclear dysprosium(III) complex, J. Am. Chem. Soc. 133 (2011) 5319–5328. https://doi.org/10.1021/ja109706y.

[63] F. Habib, P.H. Lin, J. Long, I. Korobkov, W. Wernsdorfer, M. Murugesu, The use of magnetic dilution to elucidate the slow magnetic relaxation effects of a Dy2 single-molecule magnet, J. Am. Chem. Soc. 133 (2011) 8830–8833. https://doi.org/10.1021/ja2017009.

[64] P. Zhang, L. Zhang, C. Wang, S. Xue, S.Y. Lin, J. Tang, Equatorially coordinated lanthanide single ion magnets, J. Am. Chem. Soc. 136 (2014) 4484–4487. https://doi.org/10.1021/ja500793x.

[65] I. Oyarzabal, J. Ruiz, J.M. Seco, M. Evangelisti, A. Cam??n, E. Ruiz, D. Aravena, E. Colacio, Rational electrostatic design of easy-axis magnetic anisotropy in a ZnII-DyIII-ZnII single-molecule magnet with a high energy barrier, Chem. - A Eur. J. 20 (2014) 14262–14269. https://doi.org/10.1002/chem.201403670.

[66] L. Ungur, M. Thewissen, J.P. Costes, W. Wernsdorfer, L.F. Chibotaru, Interplay of strongly anisotropic metal ions in magnetic blocking of complexes, Inorg. Chem. 52 (2013) 6328–6337. https://doi.org/10.1021/ic302568x.

[67] A. Upadhyay, S.K. Singh, C. Das, R. Mondol, S.K. Langley, K.S. Murray, G. Rajaraman, M. Shanmugam, Enhancing the effective energy barrier of a Dy(iii) SMM using a bridged diamagnetic Zn(ii) ion., Chem. Commun. 50 (2014) 8838–41. https://doi.org/10.1039/c4cc02094d.

[68] M. Llunell, D. Casanova, J. Cirera, J.M. Bofill, P. Alemany, S. Alvarez, M. Pinsky, D. Avnir, SHAPE, (2005).

[69] Y.S. Ding, N.F. Chilton, R.E.P. Winpenny, Y.Z. Zheng, On Approaching the Limit of Molecular Magnetic Anisotropy: A Near-Perfect Pentagonal Bipyramidal Dysprosium(III) Single-Molecule Magnet, Angew. Chem. Int. Ed. 55 (2016) 16071–16074. https://doi.org/10.1002/anie.201609685.

[70] J. Liu, Y.C. Chen, J.L. Liu, V. Vieru, L. Ungur, J.H. Jia, L.F. Chibotaru, Y. Lan, W. Wernsdorfer, S. Gao, X.M. Chen, M.L. Tong, A Stable Pentagonal Bipyramidal Dy(III) Single-Ion Magnet with a Record Magnetization Reversal Barrier over 1000 K, J. Am. Chem. Soc. 138 (2016) 5441–5450. https://doi.org/10.1021/jacs.6b02638.

[71] Y.C. Chen, J.L. Liu, L. Ungur, J. Liu, Q.W. Li, L.F. Wang, Z.P. Ni, L.F. Chibotaru, X.M. Chen, M.L. Tong, Symmetry-Supported Magnetic Blocking at 20 K in Pentagonal Bipyramidal Dy(III) Single-Ion Magnets, J. Am. Chem. Soc. 138 (2016) 2829–2837. https://doi.org/10.1021/jacs.5b13584.

[72] S.K. Gupta, T. Rajeshkumar, G. Rajaraman, R. Murugavel, An air-stable Dy(III) single-ion magnet with high anisotropy barrier and blocking temperature, Chem. Sci. 7 (2016) 5181–5191. https://doi.org/10.1039/c6sc00279j.

[73] Z. Jiang, L. Sun, Q. Yang, B. Yin, H. Ke, J. Han, Q. Wei, G. Xie, S. Chen, Excess axial electrostatic repulsion as a criterion for pentagonal bipyramidal DyIII single-ion magnets with high: U eff and T B, J. Mater. Chem. C. 6 (2018) 4273–4280. https://doi.org/10.1039/c8tc00353j.

[74] A.B. Canaj, S. Dey, C. Wilson, O. Céspedes, G. Rajaraman, M. Murrie, Engineering macrocyclic high performance pentagonal bipyramidal Dy(iii) single-ion magnets, Chem. Commun. 56 (2020) 12037–12040. https://doi.org/10.1039/d0cc04559d.

[75] L. Norel, L.E. Darago, B. Le Guennic, K. Chakarawet, M.I. Gonzalez, J.H. Olshansky, S. Rigaut, J.R. Long, A Terminal Fluoride Ligand Generates Axial Magnetic Anisotropy in Dysprosium Complexes, Angew. Chem. Int. Ed. 57 (2018) 1933–1938. https://doi.org/10.1002/anie.201712139.

[76] J. Liu, Y. Chen, Y. Zheng, W. Lin, L. Ungur, W. Wernsdorfer, L. Chibotaru, M. Tong, Switching the anisotropy barrier of a single-ion magnet by symmetry change from quasi-D5h to quasi-Oh, Chem. Sci. 4 (2013) 3310. https://doi.org/10.1039/c3sc50843a.

[77] J.L. Liu, Y.C. Chen, M.L. Tong, Symmetry strategies for high performance lanthanide-based single-molecule magnets, Chem. Soc. Rev. 47 (2018) 2431–2453. https://doi.org/10.1039/c7cs00266a.

[78] E. Colacio, J. Ruiz-Sanchez, F.J. White, E.K. Brechin, Strategy for the rational design of asymmetric triply bridged dinuclear 3d-4f single-molecule magnets, Inorg. Chem. 50 (2011) 7268–7273. https://doi.org/10.1021/ic2008599.

[79] S. Titos-Padilla, J. Ruiz, J.M. Herrera, E.K. Brechin, W. Wersndorfer, F. Lloret, E. Colacio, Dilution-triggered SMM behavior under zero field in a luminescent Zn 2Dy2 tetranuclear complex incorporating carbonato-bridging ligands derived from atmospheric CO2 fixation, Inorg. Chem. 52 (2013) 9620–9626. https://doi.org/10.1021/ic401378k.

[80] T. Han, M.J. Giansiracusa, Z. Li, Y. Ding, N.F. Chilton, R.E.P. Winpenny, Y. Zheng, Exchange-Biasing in a Dinuclear Dysprosium(III) Single-Molecule Magnet with a Large Energy Barrier for Magnetisation Reversal, Chem. – A Eur. J. 26 (2020) 6773–6777. https://doi.org/10.1002/chem.202000719.

[81] R.J. Blagg, L. Ungur, F. Tuna, J. Speak, P. Comar, D. Collison, W. Wernsdorfer, E.J.L. McInnes, L.F. Chibotaru, R.E.P. Winpenny, Magnetic relaxation pathways in lanthanide single-molecule magnets., Nat. Chem. 5 (2013) 673–678. https://doi.org/10.1038/nchem.1707.

[82] K.R. Meihaus, J.D. Rinehart, J.R. Long, Dilution-Induced Slow Magnetic Relaxation and Anomalous Hysteresis in Trigonal Prismatic Dysprosium(III) and Uranium(III) Complexes, Inorg. Chem. 50 (2011) 8484–8489. https://doi.org/10.1021/ic201078r.

[83] F. Pointillart, K. Bernot, S. Golhen, B. Le Guennic, T. Guizouarn, L. Ouahab, O. Cador, Magnetic memory in an isotopically enriched and magnetically isolated mononuclear dysprosium complex, Angew. Chem. Int. Ed. 54 (2015) 1504–1507. https://doi.org/10.1002/anie.201409887.

[84] Y.S. Ding, K.X. Yu, D. Reta, F. Ortu, R.E.P. Winpenny, Y.Z. Zheng, N.F. Chilton, Field- and temperature-dependent quantum tunnelling of the magnetisation in a large barrier single-molecule magnet, Nat. Commun. 9 (2018) 3134. https://doi.org/10.1038/s41467-018-05587-6.

[85] S.K. Langley, D.P. Wielechowski, V. Vieru, N.F. Chilton, B. Moubaraki, B.F. Abrahams, L.F. Chibotaru, K.S. Murray, A {CrIII2DyIII2} single-molecule magnet: Enhancing the blocking temperature through 3d magnetic exchange, Angew. Chem. Int. Ed. 52 (2013) 12014–12019. https://doi.org/10.1002/anie.201306329.

[86] K.R. Vignesh, S.K. Langley, K.S. Murray, G. Rajaraman, Quenching the Quantum Tunneling of Magnetization in Heterometallic Octanuclear {TM $^{III}_{4}$ Dy $^{III}_{4}$ } (TM=Co and Cr) Single-Molecule Magnets by Modification of the Bridging Ligands and Enhancing the Magnetic Exchange Coupling, Chem. - A Eur. J. 23 (2017) 1654–1666. https://doi.org/10.1002/chem.201604835.

[87] S.K. Langley, C.M. Forsyth, B. Moubaraki, K.S. Murray, A fluoride bridged {CrIII4DyIII4} single molecule magnet, Dalton Trans. 44 (2014) 912–915. https://doi.org/10.1039/c4dt03100h.

[88] J. Rinck, G. Novitchi, W. Van Den Heuvel, L. Ungur, Y. Lan, W. Wernsdorfer, C.E. Anson, L.F. Chibotaru, A.K. Powell, An octanuclear [Cr^{III}4DyIII4] 3d-4f single-molecule magnet, Angew. Chem. Int. Ed. 49 (2010) 7583–7587. https://doi.org/10.1002/anie.201002690.

[89] X.L. Li, F.Y. Min, C. Wang, S.Y. Lin, Z. Liu, J. Tang, Utilizing 3d-4f magnetic interaction to slow the magnetic relaxation of heterometallic complexes, Inorg. Chem. 54 (2015) 4337–4344. https://doi.org/10.1021/acs.inorgchem.5b00019.

[90] J.L. Liu, J.Y. Wu, Y.C. Chen, V. Mereacre, A.K. Powell, L. Ungur, L.F. Chibotaru, X.M. Chen, M.L. Tong, A Heterometallic FeII-DyIII Single-Molecule Magnet with a Record Anisotropy Barrier, Angew. Chem. Int. Ed. 53 (2014) 12966–12970. https://doi.org/10.1002/anie.201407799.

[91] M. Hołyńska, D. Premužić, I.R. Jeon, W. Wernsdorfer, R. Clérac, S. Dehnen, [MnIII6O3Ln2] single-molecule magnets: Increasing the energy barrier above 100 K, Chem. - A Eur. J. 17 (2011) 9605–9610. https://doi.org/10.1002/chem.201101807.

[92] K.C. Mondal, A. Sundt, Y. Lan, G.E. Kostakis, O. Waldmann, L. Ungur, L.F. Chibotaru, C.E. Anson, A.K. Powell, Coexistence of distinct single-ion and exchange-based mechanisms for blocking of magnetization in a Co II2Dy III2 single-molecule magnet, Angew. Chem. Int. Ed. 51 (2012) 7550–7554. https://doi.org/10.1002/anie.201201478.

[93] S.K. Singh, M.F. Beg, G. Rajaraman, Role of Magnetic Exchange Interactions in the Magnetization Relaxation of {3d-4f} Single-Molecule Magnets: A Theoretical Perspective, Chem. - A Eur. J. 22 (2016) 672–680. https://doi.org/10.1002/chem.201503102.

[94] C.G. Efthymiou, T.C. Stamatatos, C. Papatriantafyllopoulou, A.J. Tasiopoulos, W. Wernsdorfer, S.P. Perlepes, G. Christou, Nickel/lanthanide single-molecule magnets: {Ni3Ln} “stars” with a ligand derived from the metal-promoted reduction of di-2-pyridyl ketone under solvothermal conditions, Inorg. Chem. 49 (2010) 9737–9739. https://doi.org/10.1021/ic101504c.

[95] T. Gupta, M.F. Beg, G. Rajaraman, Role of Single-Ion Anisotropy and Magnetic Exchange Interactions in Suppressing Zero-Field Tunnelling in {3d-4f} Single Molecule Magnets, Inorg. Chem. 55 (2016) 11201–11215. https://doi.org/10.1021/acs.inorgchem.6b01831.

[96] J.D. Rinehart, M. Fang, W.J. Evans, J.R. Long, Strong exchange and magnetic blocking in N_2^{3-}-radical-bridged lanthanide complexes., Nat. Chem. 3 (2011) 538–42.

https://doi.org/10.1038/nchem.1063.

[97] C. Benelli, D. Gatteschi, Magnetism of lanthanides in molecular materials with transition-metal ions and organic radicals, Chem. Rev. 102 (2002) 2369–2387. https://doi.org/10.1021/cr010303r.

[98] Y.N. Guo, G.F. Xu, P. Gamez, L. Zhao, S.Y. Lin, R. Deng, J. Tang, H.J. Zhang, Two-step relaxation in a linear tetranuclear dysprosium(III) aggregate showing single-molecule magnet behavior, J. Am. Chem. Soc. 132 (2010) 8538–8539. https://doi.org/10.1021/ja103018m.

[99] J.D. Rinehart, M. Fang, W.J. Evans, J.R. Long, A N23- radical-bridged terbium complex exhibiting magnetic hysteresis at 14 K, J. Am. Chem. Soc. 133 (2011) 14236–14239. https://doi.org/10.1021/ja206286h.

[100] S. Demir, M.I. Gonzalez, L.E. Darago, W.J. Evans, J.R. Long, Giant coercivity and high magnetic blocking temperatures for N23- radical-bridged dilanthanide complexes upon ligand dissociation, Nat. Commun. 8 (2017) 2144. https://doi.org/10.1038/s41467-017-01553-w.

[101] J.D. Hilgar, M.G. Bernbeck, J.D. Rinehart, Million-fold Relaxation Time Enhancement across a Series of Phosphino-Supported Erbium Single-Molecule Magnets, J. Am. Chem. Soc. 141 (2019) 1913–1917. https://doi.org/10.1021/jacs.8b13514.

[102] C.A.P. Goodwin, F. Ortu, D. Reta, N.F. Chilton, D.P. Mills, Molecular magnetic hysteresis at 60 kelvin in dysprosocenium, Nature. 548 (2017) 439–442. https://doi.org/10.1038/nature23447.

[103] F.S. Guo, B.M. Day, Y.C. Chen, M.L. Tong, A. Mansikkamäki, R.A. Layfield, A Dysprosium Metallocene Single-Molecule Magnet Functioning at the Axial Limit, Angew. Chem. Int. Ed. 56 (2017) 11445–11449. https://doi.org/10.1002/anie.201705426.

[104] F.S. Guo, B.M. Day, Y.C. Chen, M.L. Tong, A. Mansikkamäki, R.A. Layfield, Magnetic hysteresis up to 80 kelvin in a dysprosium metallocene single-molecule magnet, Science. 362 (2018) 1400–1403. https://doi.org/10.1126/science.aav0652.

[105] K.R. McClain, C.A. Gould, K. Chakarawet, S.J. Teat, T.J. Groshens, J.R. Long, B.G. Harvey, High-temperature magnetic blocking and magneto-structural correlations in a series of dysprosium(III) metallocenium single-molecule magnets, Chem. Sci. 9 (2018) 8492–8503. https://doi.org/10.1039/C8SC03907K.

[106] P. Evans, D. Reta, G.F.S. Whitehead, N.F. Chilton, D.P. Mills, Bis-monophospholyl dysprosium cation showing magnetic hysteresis at 48 K, J. Am. Chem. Soc. 141 (2020) 19935–19940. https://doi.org/10.1021/jacs.9b11515.

[107] Y. Meng, J. Xiong, M. Yang, Y. Qiao, Z. Zhong, H. Sun, J. Han, T. Liu, B. Wang, S. Gao, Experimental Determination of Magnetic Anisotropy in Exchange-Bias Dysprosium Metallocene Single-Molecule Magnets, Angew. Chem. Int. Ed. 59 (2020) 13037–13043. https://doi.org/10.1002/anie.202004537.

[108] R. Collins, M.J. Heras Ojea, A. Mansikkamäki, J. Tang, R.A. Layfield, Carbonyl Back-Bonding Influencing the Rate of Quantum Tunnelling in a Dysprosium Metallocene Single-Molecule Magnet, Inorg. Chem. 59 (2020) 642–647. https://doi.org/10.1021/acs.inorgchem.9b02895.

[109] M. He, F.S. Guo, J. Tang, A. Mansikkamäki, R.A. Layfield, Fulvalene as a platform for the synthesis of a dimetallic dysprosocenium single-molecule magnet, Chem. Sci. 11 (2020) 5745–5752. https://doi.org/10.1039/d0sc02033h.

[110] B.M. Day, F.S. Guo, R.A. Layfield, Cyclopentadienyl Ligands in Lanthanide Single-Molecule Magnets: One Ring to Rule Them All?, Acc. Chem. Res. 51 (2018) 1880–1889. https://doi.org/10.1021/acs.accounts.8b00270.

[111] T. Pugh, N.F. Chilton, R.A. Layfield, A Low-Symmetry Dysprosium Metallocene Single-Molecule Magnet with a High Anisotropy Barrier, Angew. Chem. Int. Ed. 55 (2016) 11082–11085. https://doi.org/10.1002/anie.201604346.

[112] P. Evans, D. Reta, C.A.P. Goodwin, F. Ortu, N.F. Chilton, D.P. Mills, A double-dysprosocenium single-molecule magnet bound together with neutral ligands, Chem. Commun. 56 (2020) 5677–5680. https://doi.org/10.1039/c9cc08945d.

[113] D. Errulat, B. Gabidullin, A. Mansikkamäki, M. Murugesu, Two heads are better than one: Improving magnetic relaxation in the dysprosium metallocene DyCp2*BPh4 upon dimerization by use of an exceptionally weakly-coordinating anion, Chem. Commun. 56 (2020) 5937–5940. https://doi.org/10.1039/d0cc01980a.

[114] F. Neese, The ORCA program system, WIREs Comput. Mol. Sci. 2 (2012) 73–78. https://doi.org/10.1002/wcms.81.

[115] F. Aquilante, J. Autschbach, R.K. Carlson, L.F. Chibotaru, M.G. Delcey, L. De Vico, I. Fdez. Galván, N. Ferré, L.M. Frutos, L. Gagliardi, M. Garavelli, A. Giussani, C.E. Hoyer, G. Li Manni, H. Lischka, D. Ma, P.Å. Malmqvist, T. Müller, A. Nenov, M. Olivucci, T.B. Pedersen, D. Peng, F. Plasser, B.

Pritchard, M. Reiher, I. Rivalta, I. Schapiro, J. Segarra-Martí, M. Stenrup, D.G. Truhlar, L. Ungur, A. Valentini, S. Vancoillie, V. Veryazov, V.P. Vysotskiy, O. Weingart, F. Zapata, R. Lindh, <scp>Molcas</scp> 8: New capabilities for multiconfigurational quantum chemical calculations across the periodic table, J. Comput. Chem. 37 (2016) 506–541. https://doi.org/10.1002/jcc.24221.

[116] A. Swain, A. Sarkar, G. Rajaraman, Role of Ab Initio Calculations in the Design and Development of Organometallic Lanthanide-Based Single-Molecule Magnets, Chem. – An Asian J. 14 (2019) 4056–4073. https://doi.org/10.1002/asia.201900828.

[117] D. Aravena, E. Ruiz, Shedding light on the single-molecule magnet behavior of mononuclear DyIII complexes, Inorg. Chem. 52 (2013) 13770–13778. https://doi.org/10.1021/ic402367c.

[118] D. Reta, J.G.C. Kragskow, N.F. Chilton, Ab Initio Prediction of High-Temperature Magnetic Relaxation Rates in Single-Molecule Magnets, J. Am. Chem. Soc. (2021) jacs.1c01410. https://doi.org/10.1021/jacs.1c01410.

[119] A. Lunghi, M. Iannuzzi, R. Sessoli, F. Totti, Single molecule magnets grafted on gold: magnetic properties from ab initio molecular dynamics †, J. Mater. Chem. C. 7294 (2015) 7294. https://doi.org/10.1039/c5tc00394f.

[120] S. Calvello, M. Piccardo, S.V. Rao, A. Soncini, CERES: An ab initio code dedicated to the calculation of the electronic structure and magnetic properties of lanthanide complexes, J. Comput. Chem. 39 (2018) 328–337. https://doi.org/10.1002/jcc.25113.

[121] F. Lu, M.M. Ding, J.X. Li, B.L. Wang, Y.Q. Zhang, Why lanthanide ErIIISIMs cannot possess huge energy barriers: A theoretical investigation, Dalton Trans. 49 (2020) 14576–14583. https://doi.org/10.1039/d0dt02868a.

[122] H. Zhang, R. Nakanishi, K. Katoh, B.K. Breedlove, Y. Kitagawa, M. Yamashita, Low coordinated mononuclear erbium(III) single-molecule magnets with C3v symmetry: A method for altering single-molecule magnet properties by incorporating hard and soft donors, Dalton Trans. 47 (2018) 302–305. https://doi.org/10.1039/c7dt04053a.

[123] W. Zhang, A. Muhtadi, N. Iwahara, L. Ungur, L.F. Chibotaru, Magnetic Anisotropy in Divalent Lanthanide Compounds, Angew. Chem. Int. Ed. 59 (2020) 12720–12724. https://doi.org/10.1002/anie.202003399.

[124] L. Ungur, L.F. Chibotaru, Magnetic anisotropy in the excited states of low symmetry lanthanide complexes, Phys. Chem. Chem. Phys. 13 (2011) 20086–20090. https://doi.org/10.1039/c1cp22689d.

[125] K. Irländer, J. Schnack, Spin-phonon interaction induces tunnel splitting in single-molecule magnets, Phys. Rev. B. 102 (2020) 054407. https://doi.org/10.1103/PhysRevB.102.054407.

[126] D. Aravena, Ab Initio Prediction of Tunneling Relaxation Times and Effective Demagnetization Barriers in Kramers Lanthanide Single-Molecule Magnets, J. Phys. Chem. Lett. 9 (2018) 5327–5333. https://doi.org/10.1021/acs.jpclett.8b02359.

[127] L. Bogani, L. Cavigli, M. Gurioli, R.L. Novak, M. Mannini, A. Caneschi, F. Pineider, R. Sessoli, M. Clemente-León, E. Coronado, A. Cornia, D. Gatteschi, Magneto-Optical Investigations of Nanostructured Materials Based on Single-Molecule Magnets Monitor Strong Environmental Effects, Adv. Mater. 19 (2007) 3906–3911. https://doi.org/10.1002/adma.200700594.

[128] Z. Salman, K.H. Chow, R.I. Miller, A. Morello, T.J. Parolin, M.D. Hossain, T.A. Keeler, C.D.P. Levy, W.A. MacFarlane, G.D. Morris, H. Saadaoui, D. Wang, R. Sessoli, G.G. Condorelli, R.F. Kiefl, Local magnetic properties of a monolayer of Mn12 single molecule magnets, Nano Lett. 7 (2007) 1551–1555. https://doi.org/10.1021/nl070366a.

[129] F. Moro, R. Biagi, V. Corradini, M. Evangelisti, A. Gambardella, V. De Renzi, U. Del Pennino, E. Coronado, A. Forment-Aliaga, F.M. Romero, Electronic and magnetic properties of Mn 12 molecular magnets on sulfonate and carboxylic acid prefunctionalized gold surfaces, J. Phys. Chem. C. 116 (2012) 14936–14942. https://doi.org/10.1021/jp3031896.

[130] C. Wäckerlin, F. Donati, A. Singha, R. Baltic, S. Rusponi, K. Diller, F. Patthey, M. Pivetta, Y. Lan, S. Klyatskaya, M. Ruben, H. Brune, J. Dreiser, Giant Hysteresis of Single-Molecule Magnets Adsorbed on a Nonmagnetic Insulator, Adv. Mater. 28 (2016) 5195–5199. https://doi.org/10.1002/adma.201506305.

[131] D. Aulakh, H.K. Bilan, M. Wriedt, Porous substrates as platforms for the nanostructuring of molecular magnets, CrystEngComm. 20 (2018) 1011–1030. https://doi.org/10.1039/c7ce01978e.

[132] E. Coronado, Molecular magnetism: from chemical design to spin control in molecules, materials and devices, Nat. Rev. Mater. 5 (2020) 87–104. https://doi.org/10.1038/s41578-019-0146-8.

[133] D. Aulakh, J.B. Pyser, X. Zhang, A.A. Yakovenko, K.R. Dunbar, M. Wriedt, Metal-Organic Frameworks as Platforms for the Controlled Nanostructuring of Single-Molecule Magnets, J. Am.

Chem. Soc. 137 (2015) 9254–9257. https://doi.org/10.1021/jacs.5b06002.

[134] D. Aulakh, H. Xie, Z. Shen, A. Harley, X. Zhang, A.A. Yakovenko, K.R. Dunbar, M. Wriedt, Systematic Investigation of Controlled Nanostructuring of Mn12 Single-Molecule Magnets Templated by Metal-Organic Frameworks, Inorg. Chem. 56 (2017) 6965–6972. https://doi.org/10.1021/acs.inorgchem.7b00514.

[135] H.-J. Chen, X.-Y. Zheng, Y.-R. Zhao, D.-Q. Yuan, X.-J. Kong, L.-S. Long, L.-S. Zheng, A Record-Breaking Loading Capacity for Single-Molecule Magnet Mn 12 Clusters Achieved in a Mesoporous Ln-MOF , ACS Appl. Electron. Mater. 1 (2019) 804–809. https://doi.org/10.1021/acsaelm.9b00088.

[136] T.C. Wang, N.A. Vermeulen, I.S. Kim, A.B.F. Martinson, J. Fraser Stoddart, J.T. Hupp, O.K. Farha, Scalable synthesis and post-modification of a mesoporous metal-organic framework called NU-1000, Nat. Protoc. 11 (2016) 149–162. https://doi.org/10.1038/nprot.2016.001.

[137] D. Aulakh, L. Liu, J.R. Varghese, H. Xie, T. Islamoglu, K. Duell, C.W. Kung, C.E. Hsiung, Y. Zhang, R.J. Drout, O.K. Farha, K.R. Dunbar, Y. Han, M. Wriedt, Direct Imaging of Isolated Single-Molecule Magnets in Metal-Organic Frameworks, J. Am. Chem. Soc. 141 (2019) 2997–3005. https://doi.org/10.1021/jacs.8b11374.

[138] M. Mon, A. Pascual-Álvarez, T. Grancha, J. Cano, J. Ferrando-Soria, F. Lloret, J. Gascon, J. Pasán, D. Armentano, E. Pardo, Solid-State Molecular Nanomagnet Inclusion into a Magnetic Metal-Organic Framework: Interplay of the Magnetic Properties, Chem. - A Eur. J. 22 (2016) 441–441. https://doi.org/10.1002/chem.201504827.

[139] B.J. Kennedy, K.S. Murray, Magnetic Properties and Zero-Field Splitting in High-Spin Manganese(III) Complexes. 2. Axially Ligated Manganese(HI) Porphyrin Complexes, Inorg. Chem. 24 (1985) 1557–1560. https://doi.org/10.1021/ic00204a030.

[140] M.M. Williamson, C.L. Hill, Molecular Stereochemistry of Aquamanganese(III) Porphyrins. Demonstrable Effect of π-Arene-Porphyrin Interaction on the Metal Coordination Environment in a Metalloporphyrin, Inorg. Chem. 26 (1987) 4155–4160. https://doi.org/10.1021/ic00272a005.

[141] J. Ferrando-Soria, P. Serra-Crespo, M. De Lange, J. Gascon, F. Kapteijn, M. Julve, J. Cano, F. Lloret, J. Pasán, C. Ruiz-Pérez, Y. Journaux, E. Pardo, Selective gas and vapor sorption and magnetic sensing by an isoreticular mixed-metal-organic framework, J. Am. Chem. Soc. 134 (2012) 15301–15304. https://doi.org/10.1021/ja3045822.

[142] T. Grancha, J. Ferrando-Soria, H.-C. Zhou, J. Gascon, B. Seoane, J. Pasán, O. Fabelo, M. Julve, E. Pardo, Postsynthetic Improvement of the Physical Properties in a Metal-Organic Framework through a Single Crystal to Single Crystal Transmetallation, Angew. Chem. Int. Ed. 54 (2015) 6521–6525. https://doi.org/10.1002/anie.201501691.

[143] J. Dreiser, G.E. Pacchioni, F. Donati, L. Gragnaniello, A. Cavallin, K.S. Pedersen, J. Bendix, B. Delley, M. Pivetta, S. Rusponi, H. Brune, Out-of-Plane Alignment of Er(trensal) Easy Magnetization Axes Using Graphene, ACS Nano. 10 (2016) 2887–2892. https://doi.org/10.1021/acsnano.5b08178.

[144] S. Marocchi, A. Candini, D. Klar, W. Van Den Heuvel, H. Huang, F. Troiani, V. Corradini, R. Biagi, V. De Renzi, S. Klyatskaya, K. Kummer, N.B. Brookes, M. Ruben, H. Wende, U. Del Pennino, A. Soncini, M. Affronte, V. Bellini, Relay-Like Exchange Mechanism through a Spin Radical between TbPc2 Molecules and Graphene/Ni(111) Substrates, ACS Nano. 10 (2016) 9353–9360. https://doi.org/10.1021/acsnano.6b04107.

[145] L. Bogani, W. Wernsdorfer, Molecular spintronics using single-molecule magnets, Nat. Mater. 7 (2008) 179–186. https://doi.org/10.1038/nmat2133.

[146] M. Trif, F. Troiani, D. Stepanenko, D. Loss, Spin-electric coupling in molecular magnets, Phys. Rev. Lett. 101 (2008) 217201. https://doi.org/10.1103/PhysRevLett.101.217201.

[147] A. Saywell, G. Magnano, C.J. Satterley, L.M.A. Perdigão, A.J. Britton, N. Taleb, M. Del Carmen Giménez-López, N.R. Champness, J.N. O'Shea, P.H. Beton, Self-assembled aggregates formed by single-molecule magnets on a gold surface, Nat. Commun. 1 (2010) 75. https://doi.org/10.1038/ncomms1075.

[148] T.W. Chamberlain, M.C. Giménez-López, A.N. Khlobystov, Carbon Nanotubes and Related Structures: Synthesis, Characterization, Functionalization, and Applications, Wiley-VCH, 2010. https://www.wiley.com/en-ar/Carbon+Nanotubes+and+Related+Structures%3A+Synthesis%2C+Characterization%2C+Functionalization%2C+and+Applications-p-9783527324064 (accessed January 28, 2021).

[149] K. Jiang, A. Eitan, L.S. Schadler, P.M. Ajayan, R.W. Siegel, N. Grobert, M. Mayne, M. Reyes-Reyes, H. Terrones, M. Terrones, Selective attachment of gold nanoparticles to nitrogen-doped carbon nanotubes, Nano Lett. 3 (2003) 275–277. https://doi.org/10.1021/nl025914t.

[150] V. Georgakilas, D. Gournis, V. Tzitzios, L. Pasquato, D.M. Guldi, M. Prato, Decorating carbon

nanotubes with metal or semiconductor nanoparticles, J. Mater. Chem. 17 (2007) 2679–2694. https://doi.org/10.1039/b700857k.

[151] Y.B. Zhang, M. Kanungo, A.J. Ho, P. Freimuth, D. Van Der Lelie, M. Chen, S.M. Khamis, S.S. Datta, A.T.C. Johnson, J.A. Misewich, S.S. Wong, Functionalized carbon nanotubes for detecting viral proteins, Nano Lett. 7 (2007) 3086–3091. https://doi.org/10.1021/nl071572l.

[152] K. Besteman, J.O. Lee, F.G.M. Wiertz, H.A. Heering, C. Dekker, Enzyme-coated carbon nanotubes as single-molecule biosensors, Nano Lett. 3 (2003) 727–730. https://doi.org/10.1021/nl034139u.

[153] S. Banerjee, T. Hemraj-Benny, S.S. Wong, Covalent Surface Chemistry of Single-Walled Carbon Nanotubes, Adv. Mater. 17 (2005) 17–29. https://doi.org/10.1002/adma.200401340.

[154] J. Kong, N.R. Franklin, C. Zhou, M.G. Chapline, S. Peng, K. Cho, H. Dai, Nanotube molecular wires as chemical sensors, Science. 287 (2000) 622–625. https://doi.org/10.1126/science.287.5453.622.

[155] L. Bogani, C. Danieli, E. Biavardi, N. Bendiab, A.-L. Barra, E. Dalcanale, W. Wernsdorfer, A. Cornia, Single-Molecule-Magnet Carbon-Nanotube Hybrids, Angew. Chem. Int. Ed. 48 (2009) 746–750. https://doi.org/10.1002/anie.200804967.

[156] L. Malavolti, V. Lanzilotto, S. Ninova, L. Poggini, I. Cimatti, B. Cortigiani, L. Margheriti, D. Chiappe, E. Otero, P. Sainctavit, F. Totti, A. Cornia, M. Mannini, R. Sessoli, Magnetic bistability in a submonolayer of sublimated Fe4 single-molecule magnets, Nano Lett. 15 (2015) 535–541. https://doi.org/10.1021/nl503925h.

[157] L. Gragnaniello, F. Paschke, P. Erler, P. Schmitt, N. Barth, S. Simon, H. Brune, S. Rusponi, M. Fonin, Uniaxial 2D Superlattice of Fe4 Molecular Magnets on Graphene, Nano Lett. 17 (2017) 7177–7182. https://doi.org/10.1021/acs.nanolett.6b05105.

[158] C. Cervetti, A. Rettori, M.G. Pini, A. Cornia, A. Repollés, F. Luis, M. Dressel, S. Rauschenbach, K. Kern, M. Burghard, L. Bogani, The classical and quantum dynamics of molecular spins on graphene, Nat. Mater. 15 (2016) 164–168. https://doi.org/10.1038/nmat4490.

[159] S.C. Benjamin, A. Ardavan, G.A.D. Briggs, D.A. Britz, D. Gunlycke, J. Jefferson, M.A.G. Jones, D.F. Leigh, B.W. Lovett, A.N. Khlobystov, S.A. Lyon, J.J.L. Morton, K. Porfyrakis, M.R. Sambrook, A.M. Tyryshkin, Towards a fullerene-based quantum computer, J. Phys. Condens. Matter. 18 (2006) S867. https://doi.org/10.1088/0953-8984/18/21/S12.

[160] M. Del Carmen Giménez-López, F. Moro, A. La Torre, C.J. Gómez-García, P.D. Brown, J. Van Slageren, A.N. Khlobystov, Encapsulation of single-molecule magnets in carbon nanotubes, Nat. Commun. 2 (2011) 407. https://doi.org/10.1038/ncomms1415.

[161] S. Kyatskaya, J.R.G. Mascarós, L. Bogani, F. Hennrich, M. Kappes, W. Wernsdorfer, M. Ruben, Anchoring of rare-earth-based single-molecule magnets on single-walled carbon nanotubes, J. Am. Chem. Soc. 131 (2009) 15143–15151. https://doi.org/10.1021/ja906165e.

[162] A. Giusti, G. Charron, S. Mazerat, J.-D. Compain, P. Mialane, A. Dolbecq, E. Rivière, W. Wernsdorfer, R. Ngo Biboum, B. Keita, L. Nadjo, A. Filoramo, J.-P. Bourgoin, T. Mallah, Magnetic Bistability of Individual Single-Molecule Magnets Grafted on Single-Wall Carbon Nanotubes, Angew. Chem. Int. Ed. 48 (2009) 4949–4952. https://doi.org/10.1002/anie.200901806.

[163] J.C.G. Bünzli, On the design of highly luminescent lanthanide complexes, Coord. Chem. Rev. 293–294 (2015) 19–47. https://doi.org/10.1016/j.ccr.2014.10.013.

[164] M.J. Weber, Radiative and multiphonon relaxation of rare-earth ions in Y2O3, Phys. Rev. 171 (1968) 283–291. https://doi.org/10.1103/PhysRev.171.283.

[165] C.P. Montgomery, D. Parker, L. Lamarque, Effective and efficient sensitisation of terbium luminescence at 355 nm with cell permeable pyrazoyl-1-azaxanthone macrocyclic complexes, Chem. Commun. (2007) 3841–3843. https://doi.org/10.1039/b709805g.

[166] J. Long, Y. Guari, R.A.S. Ferreira, L.D. Carlos, J. Larionova, Recent advances in luminescent lanthanide based Single-Molecule Magnets, Coord. Chem. Rev. 363 (2018) 57–70. https://doi.org/10.1016/j.ccr.2018.02.019.

[167] J.H. Jia, Q.W. Li, Y.C. Chen, J.L. Liu, M.L. Tong, Luminescent single-molecule magnets based on lanthanides: Design strategies, recent advances and magneto-luminescent studies, Coord. Chem. Rev. 378 (2019) 365–381. https://doi.org/10.1016/j.ccr.2017.11.012.

[168] J. Long, Luminescent Schiff-Base Lanthanide Single-Molecule Magnets: The Association Between Optical and Magnetic Properties, Front. Chem. 7 (2019) 63. https://doi.org/10.3389/fchem.2019.00063.

[169] F. Pointillart, O. Cador, B. Le Guennic, L. Ouahab, Uncommon lanthanide ions in purely 4f Single Molecule Magnets, Coord. Chem. Rev. 346 (2017) 150–175. https://doi.org/10.1016/j.ccr.2016.12.017.

[170] J.C.G. Bünzli, Lanthanide luminescence for biomedical analyses and imaging, Chem. Rev. 110

(2010) 2729–2755. https://doi.org/10.1021/cr900362e.

[171] S. V. Eliseeva, M. Ryazanov, F. Gumy, S.I. Troyanov, L.S. Lepnev, J.-C.G. Bünzli, N.P. Kuzmina, Dimeric Complexes of Lanthanide(III) Hexafluoroacetylacetonates with4-CyanopyridineN-Oxide: Synthesis, Crystal Structure, Magnetic and Photoluminescent Properties, Eur. J. Inorg. Chem. (2006) 4809–4820. https://doi.org/10.1002/ejic.200600673.

[172] D. Errulat, R. Marin, D.A. Gálico, K.L.M. Harriman, A. Pialat, B. Gabidullin, F. Iikawa, O.D.D. Couto, J.O. Moilanen, E. Hemmer, F.A. Sigoli, M. Murugesu, A Luminescent Thermometer Exhibiting Slow Relaxation of the Magnetization: Toward Self-Monitored Building Blocks for Next-Generation Optomagnetic Devices, ACS Cent. Sci. 5 (2019) 1187–1198. https://doi.org/10.1021/acscentsci.9b00288.

[173] F. Pointillart, J. Jung, R. Berraud-Pache, B. Le Guennic, V. Dorcet, S. Golhen, O. Cador, O. Maury, Y. Guyot, S. Decurtins, S.X. Liu, L. Ouahab, Luminescence and single-molecule magnet behavior in lanthanide complexes involving a tetrathiafulvalene-fused dipyridophenazine ligand, Inorg. Chem. 54 (2015) 5384–5397. https://doi.org/10.1021/acs.inorgchem.5b00441.

[174] F. Pointillart, B. Le Guennic, S. Golhen, O. Cador, O. Maury, L. Ouahab, A redox-active luminescent ytterbium based single molecule magnet, Chem. Commun. 49 (2013) 615–617. https://doi.org/10.1039/c2cc37635k.

[175] G. Brunet, R. Marin, M.J. Monk, U. Resch-Genger, D.A. Gálico, F.A. Sigoli, E.A. Suturina, E. Hemmer, M. Murugesu, Exploring the dual functionality of an ytterbium complex for luminescence thermometry and slow magnetic relaxation, Chem. Sci. 10 (2019) 6799–6808. https://doi.org/10.1039/c9sc00343f.

[176] J. Wang, J.J. Zakrzewski, M. Heczko, M. Zychowicz, K. Nakagawa, K. Nakabayashi, B. Sieklucka, S. Chorazy, S.I. Ohkoshi, Proton Conductive Luminescent Thermometer Based on Near-Infrared Emissive {YbCo2} Molecular Nanomagnets, J. Am. Chem. Soc. 142 (2020) 3970–3979. https://doi.org/10.1021/jacs.9b13147.

[177] J. Wang, J.J. Zakrzewski, M. Zychowicz, V. Vieru, L.F. Chibotaru, K. Nakabayashi, S. Chorazy, S. Ohkoshi, Holmium(iii) molecular nanomagnets for optical thermometry exploring the luminescence re-absorption effect , Chem. Sci. 12 (2021) 730–741. https://doi.org/10.1039/d0sc04871b.

[178] A.A. Kitos, D.A. Gálico, R. Castañeda, J.S. Ovens, M. Murugesu, J.L. Brusso, Stark Sublevel-Based Thermometry with Tb(III) and Dy(III) Complexes Cosensitized via the 2-Amidinopyridine Ligand, Inorg. Chem. 59 (2020) 11061–11070. https://doi.org/10.1021/acs.inorgchem.0c01534.

[179] M. Fondo, J. Corredoira-Vázquez, A.M. García-Deibe, J. Sanmartín-Matalobos, M. Amoza, A.M.P. Botas, R.A.S. Ferreira, L.D. Carlos, E. Colacio, Field-induced slow magnetic relaxation and luminescence thermometry in a mononuclear ytterbium complex, Inorg. Chem. Front. 7 (2020) 3019–3029. https://doi.org/10.1039/d0qi00637h.

[180] R. Marin, G. Brunet, M. Murugesu, Shining New Light on Multifunctional Lanthanide Single-Molecule Magnets, Angew. Chem. Int. Ed. 60 (2021) 1728–1746. https://doi.org/10.1002/anie.201910299.

[181] R. Farshchi, M. Ramsteiner, J. Herfort, A. Tahraoui, H.T. Grahn, Optical communication of spin information between light emitting diodes, Appl. Phys. Lett. 98 (2011) 162508. https://doi.org/10.1063/1.3582917.

[182] J.F. Sherson, H. Krauter, R.K. Olsson, B. Julsgaard, K. Hammerer, I. Cirac, E.S. Polzik, Quantum teleportation between light and matter, Nature. 443 (2006) 557–560. https://doi.org/10.1038/nature05136.

[183] M.C. Heffern, L.M. Matosziuk, T.J. Meade, Lanthanide probes for bioresponsive imaging, Chem. Rev. 114 (2014) 4496–4539. https://doi.org/10.1021/cr400477t.

[184] M. Schadt, Liquid crystal materials and liquid crystal displays, Annu. Rev. Mater. Sci. 27 (1997) 305–379. https://doi.org/10.1146/annurev.matsci.27.1.305.

[185] M. Leonzio, M. Bettinelli, L. Arrico, M. Monari, L. Di Bari, F. Piccinelli, Circularly Polarized Luminescence from an Eu(III) Complex Based on 2-Thenoyltrifluoroacetyl-acetonate and a Tetradentate Chiral Ligand, Inorg. Chem. 57 (2018) 10257–10264. https://doi.org/10.1021/acs.inorgchem.8b01480.

[186] L. Arrico, C. De Rosa, L. Di Bari, A. Melchior, F. Piccinelli, Effect of the Counterion on Circularly Polarized Luminescence of Europium(III) and Samarium(III) Complexes, Inorg. Chem. 59 (2020) 5050–5062. https://doi.org/10.1021/acs.inorgchem.0c00280.

[187] S. Wada, Y. Kitagawa, T. Nakanishi, M. Gon, K. Tanaka, K. Fushimi, Y. Chujo, Y. Hasegawa, Electronic chirality inversion of lanthanide complex induced by achiral molecules, Sci. Rep. 8 (2018) 16395. https://doi.org/10.1038/s41598-018-34790-0.

[188] K. Dhbaibi, L. Favereau, J. Crassous, Enantioenriched Helicenes and Helicenoids Containing Main-

Group Elements (B, Si, N, P), Chem. Rev. 119 (2019) 8846–8953. https://doi.org/10.1021/acs.chemrev.9b00033.

[189] Z.P. Yan, K. Liao, H.B. Han, J. Su, Y.X. Zheng, J.L. Zuo, Chiral iridium(III) complexes with four-membered Ir-S-P-S chelating rings for high-performance circularly polarized OLEDs, Chem. Commun. 55 (2019) 8215–8218. https://doi.org/10.1039/c9cc03915e.

[190] G. Park, H. Kim, H. Yang, K.R. Park, I. Song, J.H. Oh, C. Kim, Y. You, Amplified circularly polarized phosphorescence from co-assemblies of platinum(ii) complexes, Chem. Sci. 10 (2019) 1294–1301. https://doi.org/10.1039/c8sc04509g.

[191] R. Aoki, R. Toyoda, J.F. Kögel, R. Sakamoto, J. Kumar, Y. Kitagawa, K. Harano, T. Kawai, H. Nishihara, Bis(dipyrrinato)zinc(II) Complex Chiroptical Wires: Exfoliation into Single Strands and Intensification of Circularly Polarized Luminescence, J. Am. Chem. Soc. 139 (2017) 16024–16027. https://doi.org/10.1021/jacs.7b07077.

[192] J.R. Jiménez, B. Doistau, C.M. Cruz, C. Besnard, J.M. Cuerva, A.G. Campaña, C. Piguet, Chiral Molecular Ruby [Cr(dqp)2]3+ with Long-Lived Circularly Polarized Luminescence, J. Am. Chem. Soc. 141 (2019) 13244–13252. https://doi.org/10.1021/jacs.9b06524.

[193] M. Deng, N.F.M. Mukthar, N.D. Schley, G. Ung, Yellow Circularly Polarized Luminescence from C_1-Symmetrical Copper(I) Complexes, Angew. Chem. Int. Ed. 59 (2020) 1228–1231. https://doi.org/10.1002/anie.201913672.

[194] J. Kumar, B. Marydasan, T. Nakashima, T. Kawai, J. Yuasa, Chiral supramolecular polymerization leading to eye differentiable circular polarization in luminescence, Chem. Commun. 52 (2016) 9885–9888. https://doi.org/10.1039/c6cc05022k.

[195] B. El Rez, J. Liu, V. Béreau, C. Duhayon, Y. Horino, T. Suzuki, L. Coolen, J.P. Sutter, Concomitant emergence of circularly polarized luminescence and single-molecule magnet behavior in chiral-at-metal Dy complex, Inorg. Chem. Front. 7 (2020) 4527–4534. https://doi.org/10.1039/d0qi00919a.

[196] J.P. Riehl, F.S. Richardson, Circularly Polarized Luminescence Spectroscopy, Chem. Rev. 86 (1986) 1–16. https://doi.org/10.1021/cr00071a001.

[197] W. Zhang, H.Y. Ye, R.G. Xiong, Metal-organic coordination compounds for potential ferroelectrics, Coord. Chem. Rev. 253 (2009) 2980–2997. https://doi.org/10.1016/j.ccr.2009.02.028.

[198] M. Gajek, M. Bibes, S. Fusil, K. Bouzehouane, J. Fontcuberta, A. Barthélémy, A. Fert, Tunnel junctions with multiferroic barriers, Nat. Mater. 6 (2007) 296–302. https://doi.org/10.1038/nmat1860.

[199] J.F. Scott, Multiferroic memories, Nat. Mater. 6 (2007) 256–257. https://doi.org/10.1038/nmat1868.

[200] P.H. Guo, Y. Meng, Y.C. Chen, Q.W. Li, B.Y. Wang, J.D. Leng, D.H. Bao, J.H. Jia, M.L. Tong, A zigzag DyIII4 cluster exhibiting single-molecule magnet, ferroelectric and white-light emitting properties, J. Mater. Chem. C. 2 (2014) 8858–8864. https://doi.org/10.1039/c4tc01275e.

[201] X.L. Li, C.L. Chen, H.P. Xiao, A.L. Wang, C.M. Liu, X. Zheng, L.J. Gao, X.G. Yang, S.M. Fang, Luminescent, magnetic and ferroelectric properties of noncentrosymmetric chain-like complexes composed of nine-coordinate lanthanide ions, Dalton Trans. 42 (2013) 15317–15325. https://doi.org/10.1039/c3dt51743h.

[202] P.-H. Guo, J.-L. Liu, J.-H. Jia, J. Wang, F.-S. Guo, Y.-C. Chen, W.-Q. Lin, J.-D. Leng, D.-H. Bao, X.-D. Zhang, J.-H. Luo, M.-L. Tong, Multifunctional Dy^{III}_4 Cluster Exhibiting White-Emitting, Ferroelectric and Single-Molecule Magnet Behavior, Chem. - A Eur. J. 19 (2013) 8769–8773. https://doi.org/10.1002/chem.201300299.

[203] J. Long, J. Rouquette, J.-M. Thibaud, R.A.S. Ferreira, L.D. Carlos, B. Donnadieu, V. Vieru, L.F. Chibotaru, L. Konczewicz, J. Haines, Y. Guari, J. Larionova, A High-Temperature Molecular Ferroelectric Zn/Dy Complex Exhibiting Single-Ion-Magnet Behavior and Lanthanide Luminescence, Angew. Chemie. 127 (2015) 2264–2268. https://doi.org/10.1002/ange.201410523.

[204] S.D. Zhu, J.J. Hu, L. Dong, H.R. Wen, S.J. Liu, Y.B. Lu, C.M. Liu, Multifunctional Zn(ii)-Yb(iii) complex enantiomers showing second-harmonic generation, near-infrared luminescence, single-molecule magnet behaviour and proton conduction, J. Mater. Chem. C. 8 (2020) 16032–16041. https://doi.org/10.1039/d0tc03687k.

[205] G. Cosquer, Y. Shen, M. Almeida, M. Yamashita, Conducting single-molecule magnet materials, Dalton Trans. 47 (2018) 7616–7627. https://doi.org/10.1039/c8dt01015c.

[206] N.D. Kushch, L.I. Buravov, P.P. Kushch, G. V. Shilov, H. Yamochi, M. Ishikawa, A. Otsuka, A.A. Shakin, O. V. Maximova, O.S. Volkova, A.N. Vasiliev, E.B. Yagubskii, Multifunctional Compound Combining Conductivity and Single-Molecule Magnetism in the Same Temperature Range, Inorg. Chem. 57 (2018) 2386–2389. https://doi.org/10.1021/acs.inorgchem.7b03152.

[207] J.A. Jones, Fast Searches with Nuclear Magnetic Resonance Computers, Science. 280 (1998) 229–229. https://doi.org/10.1126/science.280.5361.229.

[208] P.W. Shor, Algorithms for quantum computation: discrete logarithms and factoring, in: Institute of Electrical and Electronics Engineers (IEEE), Santa Fe, NM, USA, 1994: pp. 124–134. https://doi.org/10.1109/sfcs.1994.365700.

[209] L.K. Grover, Quantum computers can search arbitrarily large databases by a single query, Phys. Rev. Lett. 79 (1997) 4709–4712. https://doi.org/10.1103/PhysRevLett.79.4709.

[210] M.N. Leuenberger, D. Loss, Quantum computing in molecular magnets, Nature. 410 (2001) 789–793. https://doi.org/10.1038/35071024.

[211] C. Joachim, J.K. Gimzewski, A. Aviram, Electronics using hybrid-molecular and mono-molecular devices, Nature. 408 (2000) 541–548. https://doi.org/10.1038/35046000.

[212] M. Affronte, Molecular nanomagnets for information technologies, J. Mater. Chem. 19 (2009) 1731–1737. https://doi.org/10.1039/b809251f.

[213] K.X. Yu, J.G.C. Kragskow, Y.S. Ding, Y.Q. Zhai, D. Reta, N.F. Chilton, Y.Z. Zheng, Enhancing Magnetic Hysteresis in Single-Molecule Magnets by Ligand Functionalization, Chem. 6 (2020) 1777–1793. https://doi.org/10.1016/j.chempr.2020.04.024.

[214] F. Ortu, D. Reta, Y.S. Ding, C.A.P. Goodwin, M.P. Gregson, E.J.L. McInnes, R.E.P. Winpenny, Y.Z. Zheng, S.T. Liddle, D.P. Mills, N.F. Chilton, Studies of hysteresis and quantum tunnelling of the magnetisation in dysprosium(iii) single molecule magnets, Dalton Trans. 48 (2019) 8541–8545. https://doi.org/10.1039/c9dt01655d.

[215] A. Chiesa, F. Cugini, R. Hussain, E. MacAluso, G. Allodi, E. Garlatti, M. Giansiracusa, C.A.P. Goodwin, F. Ortu, D. Reta, J.M. Skelton, T. Guidi, P. Santini, M. Solzi, R. De Renzi, D.P. Mills, N.F. Chilton, S. Carretta, Understanding magnetic relaxation in single-ion magnets with high blocking temperature, Phys. Rev. B. 101 (2020) 174402. https://doi.org/10.1103/PhysRevB.101.174402.

[216] R.E.P. Winpenny, N.F. Chilton, M. Giansiracusa, D. Collison, A. Kostopoulos, Correlating Blocking Temperatures with Relaxation Mechanisms in Monometallic Single-Molecule Magnets with High Energy Barriers (Ueff > 600 K), Chem. Commun. (2019). https://doi.org/10.1039/C9CC02421B.

[217] G. Velkos, W. Yang, Y.R. Yao, S.M. Sudarkova, X. Liu, B. Büchner, S.M. Avdoshenko, N. Chen, A.A. Popov, Shape-adaptive single-molecule magnetism and hysteresis up to 14 K in oxide clusterfullerenes Dy2O@C72 and Dy2O@C74 with fused pentagon pairs and flexible Dy-(μ2-O)-Dy angle, Chem. Sci. 11 (2020) 4766–4772. https://doi.org/10.1039/d0sc00624f.

[218] F. Liu, S. Wang, C.-L. Gao, Q. Deng, X. Zhu, A. Kostanyan, R. Westerström, F. Jin, S.-Y. Xie, A.A. Popov, T. Greber, S. Yang, Mononuclear Clusterfullerene Single-Molecule Magnet Containing Strained Fused-Pentagons Stabilized by a Nearly Linear Metal Cyanide Cluster, Angew. Chem. Int. Ed. 56 (2017) 1830–1834. https://doi.org/10.1002/anie.201611345.

[219] F. Liu, C.L. Gao, Q. Deng, X. Zhu, A. Kostanyan, R. Westerström, S. Wang, Y.Z. Tan, J. Tao, S.Y. Xie, A.A. Popov, T. Greber, S. Yang, Triangular Monometallic Cyanide Cluster Entrapped in Carbon Cage with Geometry-Dependent Molecular Magnetism, J. Am. Chem. Soc. 138 (2016) 14764–14771. https://doi.org/10.1021/jacs.6b09329.

[220] L. Spree, A.A. Popov, Recent advances in single molecule magnetism of dysprosium-metallofullerenes, Dalton Trans. 48 (2019) 2861–2871. https://doi.org/10.1039/c8dt05153d.

[221] D.S. Krylov, F. Liu, A. Brandenburg, L. Spree, V. Bon, S. Kaskel, A.U.B. Wolter, B. Büchner, S.M. Avdoshenko, A.A. Popov, Magnetization relaxation in the single-ion magnet DySc2N@C80: Quantum tunneling, magnetic dilution, and unconventional temperature dependence, Phys. Chem. Chem. Phys. 20 (2018) 11656–11672. https://doi.org/10.1039/c8cp01608a.

[222] C.H. Chen, D.S. Krylov, S.M. Avdoshenko, F. Liu, L. Spree, R. Westerström, C. Bulbucan, M. Studniarek, J. Dreiser, A.U.B. Wolter, B. Büchner, A.A. Popov, Magnetic hysteresis in self-assembled monolayers of Dy-fullerene single molecule magnets on gold, Nanoscale. 10 (2018) 11287–11292. https://doi.org/10.1039/c8nr00511g.

[223] K. Chakarawet, M. Atanasov, J. Marbey, P.C. Bunting, F. Neese, S. Hill, J.R. Long, Strong electronic and magnetic coupling in M4(M = Ni, Cu) clusters via direct orbital interactions between low-coordinate metal centers, J. Am. Chem. Soc. 142 (2020) 19161–19169. https://doi.org/10.1021/jacs.0c08460.

[224] J. Camacho-Bunquin, M.J. Ferguson, J.M. Stryker, Hydrocarbon-soluble nanocatalysts with no bulk phase: Coplanar, two-coordinate arrays of the base metals, J. Am. Chem. Soc. 135 (2013) 5537–5540. https://doi.org/10.1021/ja401579x.

[225] P. Pyykkö, M. Atsumi, Molecular Single-Bond Covalent Radii for Elements 1-118, Chem. - A Eur. J. 15 (2009) 186–197. https://doi.org/10.1002/chem.200800987.

[226] M.A. Palacios, J. Nehrkorn, E.A. Suturina, E. Ruiz, S. Gómez-Coca, K. Holldack, A. Schnegg, J. Krzystek, J.M. Moreno, E. Colacio, Analysis of Magnetic Anisotropy and the Role of Magnetic

Dilution in Triggering Single-Molecule Magnet (SMM) Behavior in a Family of Co ^{II} Y ^{III} Dinuclear Complexes with Easy-Plane Anisotropy, Chem. - A Eur. J. 23 (2017) 11649–11661. https://doi.org/10.1002/chem.201702099.

[227] A.K. Mondal, A. Mondal, B. Dey, S. Konar, Influence of the Coordination Environment on Easy-Plane Magnetic Anisotropy of Pentagonal Bipyramidal Cobalt(II) Complexes, Inorg. Chem. 57 (2018) 9999–10008. https://doi.org/10.1021/acs.inorgchem.8b01162.

[228] J.M. Zadrozny, J. Liu, N.A. Piro, C.J. Chang, S. Hill, J.R. Long, Slow magnetic relaxation in a pseudotetrahedral cobalt(ii) complex with easy-plane anisotropy, Chem. Commun. 48 (2012) 3927–3929. https://doi.org/10.1039/c2cc16430b.

[229] K. Chakarawet, P.C. Bunting, J.R. Long, Large Anisotropy Barrier in a Tetranuclear Single-Molecule Magnet Featuring Low-Coordinate Cobalt Centers, J. Am. Chem. Soc. 140 (2018) 2058–2061. https://doi.org/10.1021/jacs.7b13394.

[230] A.W. Cook, J.D. Bocarsly, R.A. Lewis, A.J. Touchton, S. Morochnik, T.W. Hayton, An iron ketimide single-molecule magnet [Fe4(NCPh2)6] with suppressed through-barrier relaxation, Chem. Sci. 11 (2020) 4753–4757. https://doi.org/10.1039/d0sc01578d.

[231] P. Abbasi, K. Quinn, D.I. Alexandropoulos, M. Damjanović, W. Wernsdorfer, A. Escuer, J. Mayans, M. Pilkington, T.C. Stamatatos, Transition Metal Single-Molecule Magnets: A {Mn31} Nanosized Cluster with a Large Energy Barrier of ~60 K and Magnetic Hysteresis at ~5 K, J. Am. Chem. Soc. 139 (2017) 15644–15647. https://doi.org/10.1021/jacs.7b10130.

[232] N.E. Chakov, S.C. Lee, A.G. Harter, P.L. Kuhns, A.P. Reyes, S.O. Hill, N.S. Dalal, W. Wernsdorfer, K.A. Abboud, G. Christou, The properties of the [Mn12O12(O2CR) 16(H2O)4] single-molecule magnets in truly axial symmetry: [Mn12O12(O2CCH 2Br)16(H2O)4]·4CH 2Cl2, J. Am. Chem. Soc. 128 (2006) 6975–6989. https://doi.org/10.1021/ja060796n.

[233] C.J. Milios, A. Vinslava, W. Wernsdorfer, S. Moggach, S. Parsons, S.P. Perlepes, G. Christou, E.K. Brechin, A record anisotropy barrier for a single-molecule magnet, J. Am. Chem. Soc. 129 (2007) 2754–2755. https://doi.org/10.1021/ja068961m.

[234] K. Uchida, G. Cosquer, K. Sugisaki, H. Matsuoka, K. Sato, B.K. Breedlove, M. Yamashita, Isostructural M(II) complexes (M = Mn, Fe, Co) with field-induced slow magnetic relaxation for Mn and Co complexes, Dalton Trans. 48 (2019) 12023–12030. https://doi.org/10.1039/c8dt02150c.

[235] C. Rajnák, J. Titiš, J. Moncoľ, F. Renz, R. Boča, Slow magnetic relaxation in a high-spin pentacoordinate Fe(iii) complex, Chem. Commun. 55 (2019) 13868–13871. https://doi.org/10.1039/c9cc06610a.

[236] G. Handzlik, M. Magott, M. Arczyński, A.M. Sheveleva, F. Tuna, M. Sarewicz, A. Osyczka, M. Rams, V. Vieru, L.F. Chibotaru, D. Pinkowicz, Magnetization Dynamics and Coherent Spin Manipulation of a Propeller Gd(III) Complex with the Smallest Helicene Ligand, J. Phys. Chem. Lett. 11 (2020) 1508–1515. https://doi.org/10.1021/acs.jpclett.9b03275.

[237] M.J. Martínez-Pérez, S. Cardona-Serra, C. Schlegel, F. Moro, P.J. Alonso, H. Prima-García, J.M. Clemente-Juan, M. Evangelisti, A. Gaita-Ariño, J. Sesé, J. Van Slageren, E. Coronado, F. Luis, Gd-based single-ion magnets with tunable magnetic anisotropy: Molecular design of spin qubits, Phys. Rev. Lett. 108 (2012) 247213. https://doi.org/10.1103/PhysRevLett.108.247213.

[238] R.J. Holmberg, L.T.A. Ho, L. Ungur, I. Korobkov, L.F. Chibotaru, M. Murugesu, Observation of unusual slow-relaxation of the magnetisation in a Gd-EDTA chelate, Dalton Trans. 44 (2015) 20321–20325. https://doi.org/10.1039/c5dt04072h.

[239] D.C. Izuogu, T. Yoshida, H. Zhang, G. Cosquer, K. Katoh, S. Ogata, M. Hasegawa, H. Nojiri, M. Damjanović, W. Wernsdorfer, T. Uruga, T. Ina, B.K. Breedlove, M. Yamashita, Slow Magnetic Relaxation in a Palladium–Gadolinium Complex Induced by Electron Density Donation from the Palladium Ion, Chem. – A Eur. J. 24 (2018) 9285–9294. https://doi.org/10.1002/chem.201800699.

[240] J. Mayans, A. Escuer, Correlating the axial Zero Field Splitting with the slow magnetic relaxation in Gd III SIMs , Chem. Commun. 57 (2021) 721–724. https://doi.org/10.1039/d0cc07474h.

[241] S.T. Liddle, J. van Slageren, Actinide Single-Molecule Magnets, in: Lanthanides Actinides Mol. Magn., Wiley-VCH Verlag GmbH & Co. KGaA, Weinheim, Germany, 2015: pp. 315–340. https://doi.org/10.1002/9783527673476.ch10.

[242] S.K. Singh, C.J. Cramer, L. Gagliardi, Correlating Electronic Structure and Magnetic Anisotropy in Actinide Complexes [An(COT)2], AnIII/IV = U, Np, and Pu, Inorg. Chem. 59 (2020) 6815–6825. https://doi.org/10.1021/acs.inorgchem.0c00105.

[243] J.T. Coutinho, M. Perfetti, J.J. Baldoví, M.A. Antunes, P.P. Hallmen, H. Bamberger, I. Crassee, M. Orlita, M. Almeida, J. van Slageren, L.C.J. Pereira, Spectroscopic Determination of the Electronic Structure of a Uranium Single-Ion Magnet, Chem. - A Eur. J. 25 (2019) 1758–1766.

https://doi.org/10.1002/chem.201805090.

[244] K.R. Meihaus, S.G. Minasian, W.W. Lukens, S.A. Kozimor, D.K. Shuh, T. Tyliszczak, J.R. Long, Influence of pyrazolate vs N -heterocyclic carbene ligands on the slow magnetic relaxation of homoleptic trischelate lanthanide(III) and uranium(III) complexes, J. Am. Chem. Soc. 136 (2014) 6056–6058. https://doi.org/10.1021/ja501569t.

[245] J.J. Le Roy, S.I. Gorelsky, I. Korobkov, M. Murugesu, Slow magnetic relaxation in uranium(III) and neodymium(III) cyclooctatetraenyl complexes, Organometallics. 34 (2015) 1415–1418. https://doi.org/10.1021/om501214c.

[246] N. Magnani, C. Apostolidis, A. Morgenstern, E. Colineau, J.-C. Griveau, H. Bolvin , O. Walter, R. Caciuffo, Magnetic Memory Effect in a Transuranic Mononuclear Complex, Angew. Chem. Int. Ed. 50 (2011) 1696–1698. https://doi.org/10.1002/anie.201006619.

1. KAPITULUA

Ln^{III} (Dy eta Er) IOIETAN, 5-BROMOSALIZILALDEHIDOAN ETA AMINA LINEALETAN OINARRITUTAKO MANNICH-BASE ESTEKATZAILEEKIN SORTUTAKO KONPOSATU MONONUKLEARREN IKERKETA ESPERIMENTALA: *SMM* PORTAERA AZALTZEKO KORRELAZIO MAGNETO-ESTRUKTURALAK

1.1. SARRERA

Sarrera orokorrean aipatu den bezala, lantanidoen inguruko koordinazio-inguruneak eragin erabakigarria du Kramers dobleteen azken energia-banaketan (Kramers ioiak erabiltzen direnean) eta erlaxatzeko mekanismoetan. Izan ere, geometria eta atomo emaile berak dituzten koordinazio-konposatuek propietate magnetiko erabat desberdinak erakuts ditzakete, distantzia, angelu edo atomo emaileen karga aldatzerakoan. Horrek esan nahi du korrelazio magneto-estrukturalak oso garrantzitsuak direla propietate magnetiko kontrolatuak dituzten *SMM*ak era arrazionalean diseinatzeko.

Nahiz eta azken urteetan ahalegin handiak egin diren norabide honetan, erradio ioniko handiaren eta lantanidoen koordinazio-zenbaki altuaren ondorioz, hainbat koordinazio-ingurune lor daitezke. Aipatu bezala, sistema bereziak sintetizatu izan dira, adibidez bipiramide pentagonalak, zeinetan posizio axialak nahiz plano ekuatorialak aldatzeko aukera dagoen [1]. Hala ere, kapitulu honetan erabiltzen diren estekatzaile motak erabiltzen direnean (1.1. irudia), zaila da konposatuen azken geometria iragartzea. Ikerketa honetarako, N,N',N''-trimetil-N, N''-bis (2-hidroxi-3-formil-5-bromo-bentzil) dietilentriamina eta N,N'-dimetil- N,N''-bis (2-hidroxi-3-formil-5-bromo-bentzil) etilendiamina estekatzaileak erabili dira, hemendik aurrera H_2L^1 eta H_2L^2 izendatuak.

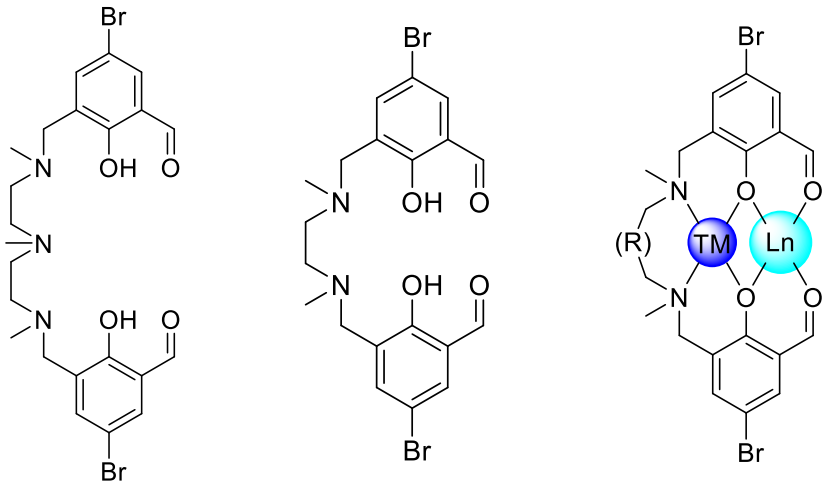

H_2L^1 H_2L^2

1.1. irudia.- H_2L^1 eta H_2L^2 estekatzaileen egitura, baita trantsizio-metal baten (TM) eta lantanido baten (Ln) irudikapena ere, barneko eta kanpoko posizioetan, hurrenez hurren. R = $(CH_2)_2NCH_3$ eta R = ezer ez H_2L^1 eta H_2L^2 estekatzaileen kasuan, hurrenez hurren.

Mannich-base estekatzaileak bereziki egokiak dira trantsizio-metalak barruko “poltsikoan” (N_2O_2) eta lantanidoak kanpokoan (O_4) egonkortzeko. Dena den, kapitulu honetan soilik kanpokoa erabili da lantanido bat sartzeko. Gainera, emaile izaera desberdina duten atomoak erabiltzeak aukera ematen du estekatzaile-eremu anisotropikoak sortzeko. Estekatzaile-eremu anisotropiko horiek amaierako propietate magnetikoak definitzen dituzte. Gure kasuan, protoirik gabeko fenol taldeek elektroi-dentsitate handia eta lotura-distantzia laburrak eskainiko dizkiote sistemari. Aldiz, aldehidoek lotura-distantzia luzeagoak erakutsiko dituzte eta ez dute zehaztuko ardatz anisotropikoen norabidea. Amina albo-katearen luzera aldatzea (diamina edo triamina) ere oso interesgarria izan daiteke, honek estekatzaileari malgutasun handiagoa edo txikiagoa ematen baitio eta, horrela, atomo emaileek koordinazio esferako posizio ezberdinak hartuko dituzte eta geometria aldakorrak sortuko dira.

Kapitulu hau, gure taldeko kide batzuek aldez aurretik egindako lanaren jarraipen gisa proposatu da [2]. Lan horretan, antzeko estekatzaile batekin Dy^{III} ioian oinarritutako *SMM* (kanpo eremu magnetikoak eragindakoa) mononuklear bat aztertu zuten. Kasu horretan, H_2L^1 estekatzaileak dituen aldehidoen ordez, metoxi taldeak erabili ziren (1.2. irudia). Lortutako emaitza interesgarriek bultzatuta, zenbait aldaera dituzten estekatzaileak hautatu dira azterlan honetarako.

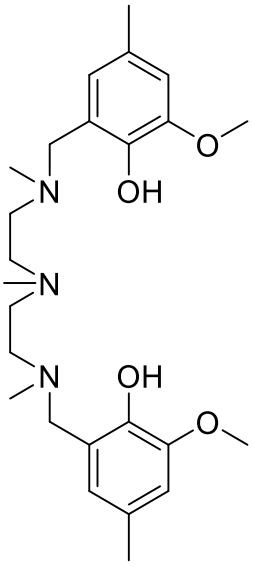

Irudia 1.2.- Aurreko ikerketa batean erabilitako estekatzailearen egitura.

Gainera, kontuan izanik simetria baxuko sistema-mota hauetarako ez dela erraza aurreikustea ea estekatzaileen posizioa egokia izango den oinarrizko egoeran momentu

magnetiko altuko egoerak egonkortzeko oblatu edo prolatu ioietan, oso interesgarria da bi motak erabiltzea sistema isoestrukturalak aztertzeko.

Horrela, kapitulu honek H_2L^1 eta H_2L^2 molekuletan oinarritutako Dy^{III} eta Er^{III} konplexuen hiru bikoteen sintesia, egituraren karakterizazioa eta propietate magnetikoak jasotzen ditu. Ioi hauek bi arrazoirengatik aukeratu dira: (i) biak Kramers motako ioiak dira eta, beraz, nahi ez den *QTM* fenomenoa jasateko probabilitate txikiagoa dute, eta (ii) aurkako elektroi-dentsitate forma dute, oblatu eta prolatu formakoak izanik.

1.2. ESTEKATZAILEEN PRESTAKETA

1.2.1. H_2L^1: N,N',N''-trimetil-N,N''-bis(2-hidroxi-3-formil-5-bromo-bentzil) dietilentriamina

N,N',N'''-trimetildietilentriamina (1,45 g, 10 mmol), 5-bromosalizilaldehidoa (4,02 g, 20 mmol) eta %37 formaldehido akuosoa (1,62 g, 20 mmol) etanoletan nahasten dira eta disoluzioa 48 orduz errefluxuan irabiatuz mantentzen da. Lortutako disoluzio marroia giro-tenperaturan hoztu ondoren, disolbatzailea hutsune bidez kentzen da olio marroi ilun bat lortuz. Estekatzailearen erabilera errazteko, produktua azetonitriloan diluitu eta %100eko errendimendua kontuan hartuz 0,072 M-eko disoluzioa prestatzen da.

^{1}H-EMN (300 MHz, $CDCl_3$, ppm, A1.55. irudia): 10,25 (s, 2H, formil-*H*), 7,73 (d, 2H, aril-*H*), 7,33 (d, 2H, aril-*H*), 3,67 (s, 4H, aril-CH_2N), 2,60 (m, 8H, NCH_2CH_2N), 2,30 (s, 6H, NCH_3), 2,26 (s, 3H, NCH_3).

1.2.2. H_2L^2: N,N'-dimetil-N,N'-bis(2-hidroxi-3-formil-5-bromo-bentzil) etilendiamina

Aurretik deskribatutako prozedurak erabiliz sintetizatua [3].

1.3. KONPLEXUEN PRESTAKETA

1.3.1. $[Ln(H_2L^1)(NO_3)_3]$ (Ln^{III} = Dy (1), Er (2))

1,7 mL H_2L^1 (0,125 mmol) 7 ml azetonitrilotan diluitzen da eta jarraian dagokion $Ln(NO_3)_3{\cdot}xH_2O$ (0,125 mmol) gehitzen da. Disoluzioa 30 minutuz irabiatu eta, iragazi ondoren, giro-tenperaturan uzten da kristalizatzen. Egun gutxiren buruan, X-izpi bidez

aztertzeko kalitatea duten kristalak lortzen dira, iragazi, azetonitriloz garbitu eta lehortzen direnak. Bi produktu horiek kristalizazio disolbatzaile molekularik gabe lortzen ditugun arren, normalean bi azetonitrilo molekulekin batera kristalizatzen dute (**8-MeCN** eta **9-MeCN**). Kristalizazio molekulak galdu egiten dira material polikristalinoa lortzeko birrintzen direnean. Material osagarrian daude taula kristalografikoak. . Etekinak eta analisi elementalen emaitzak A1.1. taulan daude.

1.3.2. $[Ln(H_2L^1)(H_2O)(NO_3)_2]\cdot 0{,}75Br\cdot 0{,}25NO_3\cdot CH_3CN\cdot 0{,}5CH_3OH$ (Ln^{III} = Dy (3), Er (4))

Azetonitrilo eta metanol nahasketa batean (1:1 proportzioan) 1,7 mL H_2L^1 (0,125 mmol) diluitu ondoren, 14,9 mg potasio bromuroa (0,125 mmol) eta 0,125 mmol dagokion $Ln(NO_3)_3\cdot xH_2O$ gehitzen zaizkio. 30 minutuz irabiatu ondoren disoluzio horia lortzen da, giro-tenperaturan uzten dena. Egun gutxiren buruan, X izpi bidez aztertzeko kalitatea duten kristalak lortzen dira. Iragazi, azetonitriloz eta metanolez garbitu eta lehortu egiten dira. Etekinak eta analisi elementalen emaitzak A1.1. taulan daude.

1.3.3. $[Ln(H_2L^2)(NO_3)_3)]\cdot CH_3CN$ (Ln^{III} = Dy (5), Er (6))

Lehenik eta behin, 0,125 mmol $Ln(NO_3)_3\cdot xH_2O$ azetonitriloan disolbatu eta ondoren, 62,5 mg H_2L^2 (0,125 mmol) gehitzen dira. Hasieran disoluzio hori bat lortzen da, baina segundo gutxiren buruan hauspeakin asko agertzen da. Prezipitatua iragazi, azetonitriloz garbitu eta lehortzen da. Ama-urak giro-tenperaturan mantenduz, X izpi bidez aztertzeko kalitatea duten kristalak lortzen dira. Etekinak eta analisi elementalen emaitzak A1.1. taulan daude.

1.3.4. Magnetikoki diluitutako 1_Y-6_Y konposatuen prestaketa

Magnetikoki diluitutako deribatuak, diluitu gabeko konposatuentzat deskribatutako prozedura berari jarraituz sintetizatzen dira, baina Ln:Y 1:10 erlazio molarra erabiliz.

1.4. EMAITZAK ESPERIMENTALAK

$Ln(NO_3)_3\cdot xH_2O$ eta H_2L^1 estekatzailearen arteko erreakzioak, azetonitriloan, kristal hori prismatikoen eraketa dakar, $[Ln(H_2L^1)(NO_3)_3]$ (Ln^{III} = Dy (**1**), Er (**2**)) edo $[Ln(H_2L^1)(NO_3)_3]\cdot 2CH_3CN$ (Ln^{III} = Dy (**8-MeCN**), Er (**9-MeCN**)) formula orokorrekin. Azetonitrilo molekulak dituzten egituren irudiak material osagarrian daude. Nolanahi ere, analisi elementalen emaitzek eta material polikristalinoaren X izpien difraktogramek argi

uzten dute **8-MeCN** eta **9-MeCN** produktuek disolbatzaile molekulak galtzen dituztela eta **1** eta **2** sortzen direla. $Ln(NO_3)_3 \cdot xH_2O$, KBr eta H_2L^1 erreaktiboen erreakzioak, 1:1 proportzioa duen metanol eta azetonitrilo nahastean, ondorengo bi konplexu ioniko mononuklearren sorrera ematen du $[Ln(H_2L^1)(H_2O)(NO_3)_2] \cdot 0{,}75Br \cdot 0{,}25NO_3 \cdot CH_3CN \cdot 0{,}5CH_3OH$ (Ln^{III} = Dy (**3**), Er (**4**)).

$Ln(NO_3)_3 \cdot xH_2O$ eta H_2L^2 estekatzailearen arteko erreakzioak, azetonitriloan, solido hori bat ematen du ondoko formula honekin: $[Ln(H_2L^2)(NO_3)_3)] \cdot CH_3CN$ (Ln^{III} = Dy (**5**), Er (**6**)). Ama-urak giro-tenperaturan utziz, X izpien difrakziorako egokiak diren kristal gutxi batzuk lortzen dira.

1.4.1. 1, 3-6 eta 1-MeCN - 10-MeCN konposatuen kristal-egiturak

Dy^{III} eta Er^{III} konposatuen izaera isoestrukturala dela eta, Dy^{III} analogoen egituraren deskripzioa egingo da, nahiz eta, Er^{III} ioian oinarritutako konposatuen berezitasunak ere aipatuko diren. Aukeratutako lotura-distantziak eta lehen aipatutako egitura guztietarako datu kristalografikoak A1.2-A1.8. tauletan jaso dira. **1** konposatuaren kristal-egitura 1.3. irudian agertzen da, *P-1* talde espazial triklinikoan monomero diskretu gisa kristalizatzen duena.

Aurrez azaldutako eta antzeko konplexuetan [2] gertatzen den bezala, fenoxido taldeen koordinazioa protoi fenolikoak talde bentzilaminoetara migratzearen ondorioz sortzen da, fenolato-amonio forma zwitterionikoa hartuz. DyO_9 ioi lantanidoaren koordinazio-ingurunea bi aldehido, bi nitrato hortz biko eta nitrato hortz bakar baten koordinazioaren bidez osatzen da. Zein poliedro motara doitzen den ikusteko SHAPE softwarea erabili zen [4]. Lortutako emaitzak A1.9. taulan ikus daitezke, baina ondorio orokor gisa, ioiaren inguruko poliedroa oso distortsionatua dagoela esan daiteke.

Dy-O lotura laburrenak fenoxido taldeeekin osatuak dira, Dy-O2 eta Dy-O3 lotura-distantziek 2,234(5) Å eta 2,310(5) Å-eko balioa dute. Aldehidoekiko eta nitratoekiko lotura-luzerak luzeagoak dira, 2,401(5)-2,410(5) Å eta 2,398(5)-2,519(5) Å tarteetan daude, hurrenez hurren. Molekula barneko hidrogeno-loturek aurretik aipatu den forma zwitterionikoa egonkortzen dute. N1 · · · O2, N3 · · · O3 eta N3 · · · · O7N distantziek 2,828, 2,742 eta 2,977 Å-eko balioa dute. Dy · · · Dy molekularteko distantziarik laburrena 8,448 Åekoa da.

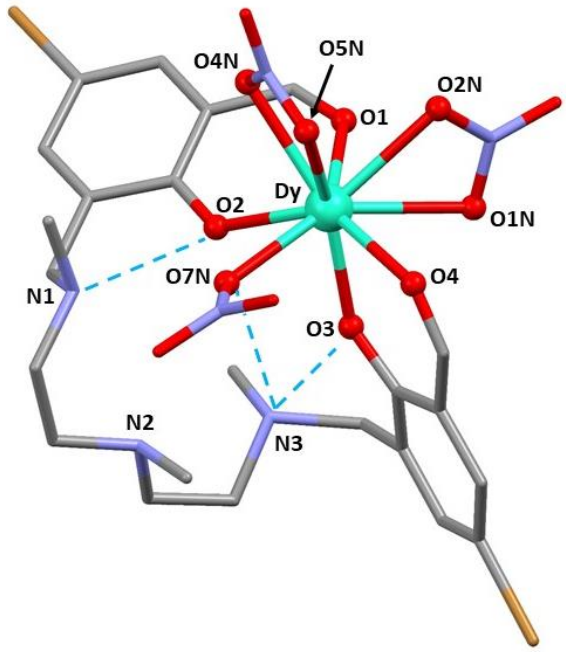

1.3. irudia.- 1 konplexuaren ikuspegia. Kolore-kodea: disprosio, bromo, nitrogeno, oxigeno eta karbono atomoak turkesa, marroi, urdin argi, gorri eta gris kolorez daude, hurrenez hurren. Hidrogeno atomoak ez dira irudikatu argitasunaren mesedetan.

Atal esperimentalean aipatu bezala, normalean **1** eta **2** konposatu mononuklearrek bi azetonitrilo molekula gehigarrirekin kristalizatzen dute, **8-MeCN** eta **9-MeCN** emanez. Hala ere, horien lagin polikristalinoak **1** eta **2** konposatuen isoestrukturalak dira, kristalizazio-molekularik gabe. Joera hau frogatzeko, hainbat kristal neurtu ziren lantanido seriean zehar eta beti disolbatzaile molekulak zituzten analogoak lortzen zirela ikusi zen. Zehazki, ondorengo Ln^{III} ioien egiturak neurtu ziren: Ce, Pr, Nd, Sm, Eu, Gd, Tb, Dy, Er $Dy_{0,1}Y_{0,9}$ eta Y (**1-MeCN**-tik (Ce) **9-MeCN**-ra (Er), **8_Y-MeCN** ($Dy_{0,1}Y_{0,9}$) eta **10-MeCN** (Y) izenekin). Ikerketa horren bidez, ama-uretan espezie egonkorrenak azetonitrilo kristalizazio-molekulak dituztenak direla erakutsi da eta mortairuan birrindu ondoren disolbatzaile lurrunkorrak nola edo hala galtzen dituztela. Disolbatzaile molekulen galtzea azetonitriloek kristal-egituraren barruan sortzen dituzten molekularteko elkarrekintza ahul edo nuluen bidez azal daiteke. Izan ere, bi kristalizazio-molekuletatik bakar batek erakusten ditu interakzio ahulak H_2L^1 estekatzailearen bromo batekin. Azetonitriloaren eta bromoaren arteko distantzia laburtu egiten da konposatuaren gelaxka-unitatearen bolumena murriztu ahala (1.4. irudia), eta hori, aldi berean, erabilitako ioiarekin lotuta dago.

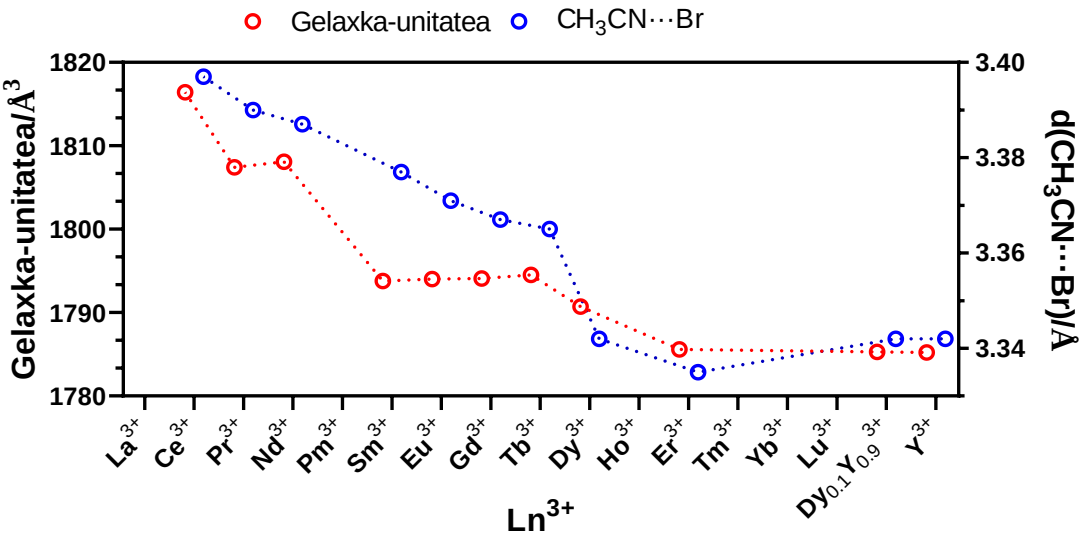

Irudia 1.4.- Gelaxka-unitatearen bolumena vs erabilitako ioia (ezkerreko *y* ardatza, gorria) eta d ($CH_3CN \cdot \cdot Br$) vs erabilitako ioia (eskuineko *y* ardatza, urdina).

Beste alderdi interesgarri bat nitratoen portaera eta ioi metaliko bakoitzaren inguruko koordinazio-zenbakia da. Aztertutako ioi handienentzat, Ce^{III} eta Nd^{III}, koordinazio-zenbakia 10 da eta hiru nitratoak kelato moduan koordinatzen dira. Bitartean, Sm^{III} eta Eu^{III} ioiek zehaztugabeko koordinazio-zenbakia erakusten dute. Izan ere, lehenengoarentzat, nitratoetako bat % 50eko desordenarekin errefinatu zen, non nitratoaren erdiak kelato gisa jarduten duen, eta beste erdiak hortzbakar gisa (1.5. irudia). **5-MeCN** konposatuan, aldiz, nitrato berak hortzbakar izaera nabarmena du, %85 hortzbakar gisa errefinatu baitzen eta %15 kelato gisa. **6-MeCN** molekulatik aurrera, gainerakoek 9 koordinazio-zenbakia dute, bi kelato nitratorekin eta hortzbakarreko batekin.

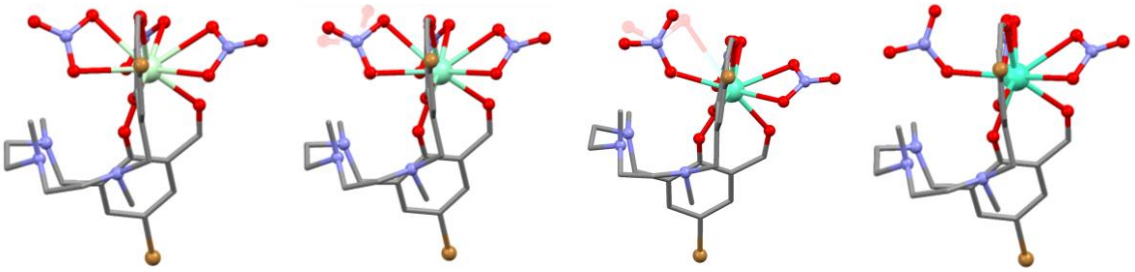

3-MeCN (Nd) **4-MeCN (Sm)** **5-MeCN (Eu)** **6-MeCN (Gd)**

1.5. irudia.- Ioien inguruko koordinazio-zenbaki aldaketa. Mugako bi kasuak **(3-MeCN** eta **6-MeCN)** eta tartekoak **(4-MeCN** eta **5-MeCN)** agertzen dira. Kristalizazio-disolbatzaile molekulak ez dira irudikatu argitasunaren mesedetan.

Ln-O distantziei dagokienez, **1** eta **2** konposatuen joera bera da, non lotura-distantziarik laburrenak Ln-$O_{phenoxo}$ motakoak diren. Aldiz, Ln-$O_{karbonilo}$ eta Ln-O_{NO3} distantziak askoz luzeagoak dira (1.6. irudia). Lantanidoen erradio ionikoak txikiagoak direnean, lotura-distantziak ere txikiagoak dira, espero bezala. Kelatoekin alderatuta, ikusten da hortzbakarreko nitratoek lotura distantzia askoz laburragoak dituztela (Ln-$O_{karbonilo}$ tartean), eta hori ere aurreikus zitekeen. Hala ere, interesgarria da tarteko konposatuen portaera nabarmentzea. **4-MeCN** sistemarentzat, hortzbakarreko nitratoak distantzia handiagoa erakusten du karboniloekin alderatuta, eta hori 50:50 errefinamendu proportzioaren bidez azal daiteke. Izan ere, lotura-distantzia nolabait luzatu eta hortzbakar/kelato arteko batez besteko balioa hartzen du. **5-MeCN** molekulatik aurrera, ordea, hortzbakarreko nitratoek beti karboniloek baino distantzia laburragoa erakusten dute. Azkenik, Y^{III} analogoak (**10-MeCN**) Dy^{III} eta Er^{III} analogoen antzeko egitura-parametroak erakusten ditu, diluzio magnetikoa egiteko hautagai aproposa dela erakutsiz.

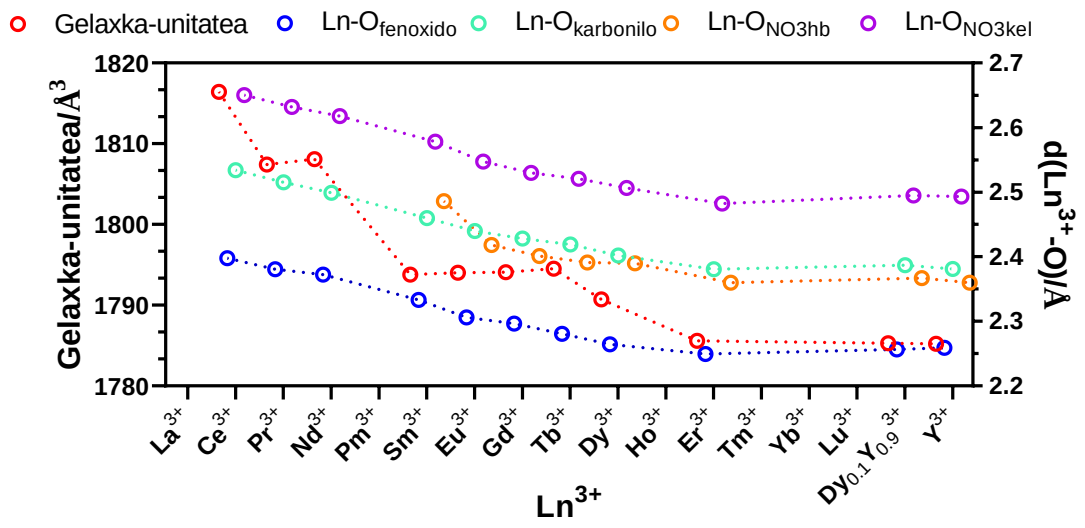

1.6. irudia.- Gelaxka-unitatearen bolumena vs erabilitako ioia (ezkerreko *y* ardatza, gorria) eta neurtutako batez besteko Ln-O distantzia vs erabilitako ioia (eskuineko *y* ardatza; urdina, turkesa, laranja eta morea).

3 konplexuak *P-1* talde espazial triklinikoan kristalizatzen du. $[Dy(H_2L^1)(H_2O)(NO_3)_2]^+$ zati kationikoari dagokion egitura 1.7. irudian azaltzen da. Kasu honetan ere Dy^{III} ioiak 9ko koordinazio-zenbakia du, hala ere, hortzbakarreko nitrato anioia ur molekula batez ordezkatu da. Konposatuaren karga positiboa anioi egitura konplexu batek neutralizatzen du. Izan ere, bromuro erdia aurkitu da posizio batean eta gainerako karga erdia *xyz* koordenatu berdinak dituzten beste nitrato laurden eta bromuro laurden batekin orekatuta dago (A1.1. irudia). DyO_9 koordinazio-esfera berriz ere distortsio-maila altukoa dela frogatu da (2,008 SHAPE balioa erakusten baitu gutxienez poliedro jakin baterako, A1.9. taula). **4** Er^{III} analogoaren kasuan, lantanidoaren erradio ionikoa apur bat txikiagoa denez, nitratoetako bat hortzbakarreko gisa koordinatzen da ErO_8 koordinazio-ingurunea sortuz. Kasu horretan, koordinazio-esfera dodekaedro triangeluarrari nahiko ondo egokitzen zaio. Dy-$O_{fenoxido}$ lotura-distantziak 2,284(3) Å eta 2,238(3) Å-ekoak dira, Dy-O2 eta Dy-O3, hurrenez hurren. Berriro ere, gainerako Dy-O lotura-distantzia guztiak luzeagoak dira, 2,368(4)-2,746(5) Å tartean. N1etik O2ra eta N1Nra, eta baita N3tik O3ra agertzen diren hidrogeno-loturek forma zwitterionikoa egonkortzen dute, 2,733 Å, 2,947 Å eta 2,777 Å-eko lotura-luzerak aurkezten dituzte, hurrenez hurren. Gainera, koordinatuta dagoen ur molekulak beste bi hidrogeno-lotura sortzen ditu ondoko molekulekin. Lehenengoa metanol disolbatzaile molekularekin (O1W ⋯ O1M) eta bigarrena bromuro erdi independentearen kontraioiarekin, zein, aldi berean, beste unitate kationiko batekin dagoen lotua (A1.12. irudia). Entitate kationiko mononuklearrak

elkarrengandik isolatuta daude, molekularteko Dy ⋯ Dy distantzia laburrena 9,324 Å-ekoa izanik.

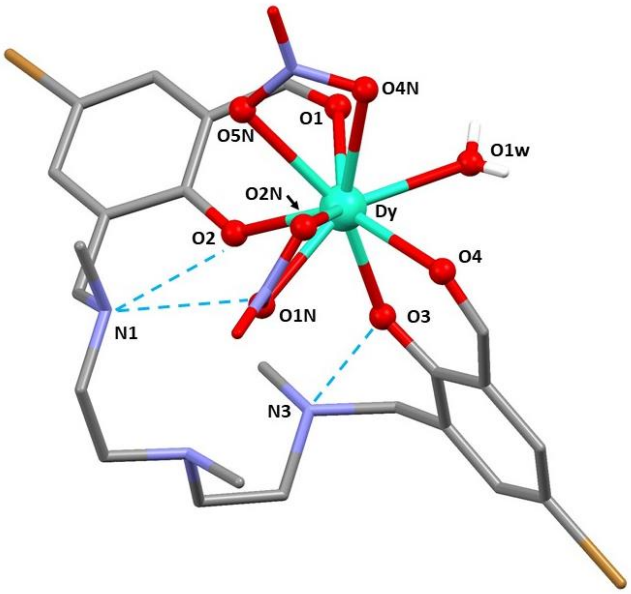

1.7. irudia.- 3 konplexuaren ikuspegia. Kolore-kodea: disprosioa, bromoa, nitrogenoa, oxigenoa, karbonoa eta hidrogeno atomoak turkesa, marroi, urdin argi, gorri, gris eta zuri kolorez, hurrenez hurren. Estekatzaileko hidrogeno atomoak, disolbatzaile molekulak eta kontraioiak ez dira irudikatu argitasunaren mesedetan.

1.8 irudian agertzen den konplexua, **5**, mononuklearra da eta *P 2₁/c* talde espazial monoklinikoan kristalizatzen du. **1** konplexuari gertatzen zaion bezala, distortsionatutako *muffin* itxurako DyO_9 koordinazio-ingurunea bi fenoxido, bi aldehido, bi nitrato hortz biko eta hortzbakarreko nitrato anioi batek osatzen dute. Dy-O2 eta Dy-O3 lotura-luzerak 2,2795(18) Å eta 2,2459(17) Å-ekoak dira, gainerako loturak baino motzagoak (2,3994(19)-2,5329(19) Å tartean daude besteak). Nitrogeno zwitterioniko bakoitzak bi hidrogeno lotura sortzen ditu, bata fenoxido talde hurbilenarekin eta bestea O7N oxigeno atomoarekin, N1 ⋯ O2, N1 ⋯ O7N, N2 ⋯ O3 eta N2 ⋯ O7N distantziak 2,755 Å, 2,955 Å, 2,759 Å eta 3,041 Å-ekoak dira, hurrenez hurren. Molekularteko Dy ⋯ Dy distantzia laburrena 9,004 Å-ekoa da.

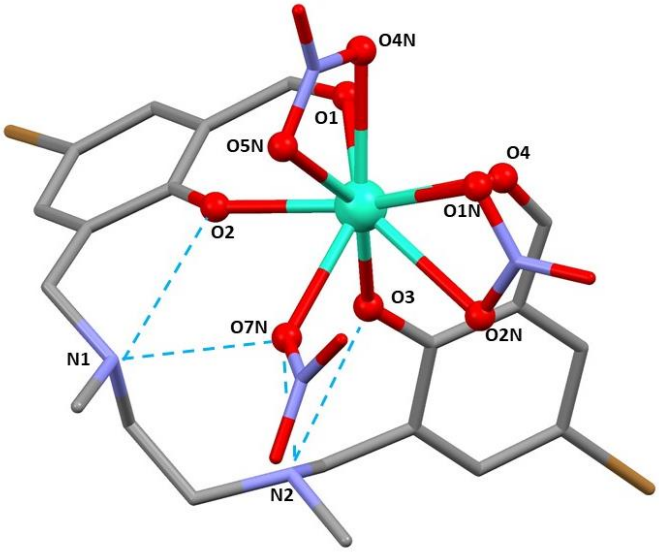

1.8. irudia.- 5 konplexuaren ikuspegia. Kolore-kodea: disprosioa, bromoa, nitrogenoa, oxigenoa eta karbonoa turkesa, marroi, urdin argi, gorri eta gris kolorez, hurrenez hurren. Hidrogeno atomoak eta disolbatzaile molekulak ez dira irudikatu argitasunaren mesedetan.

1.4.2. 1-6 konplexuen propietate magnetiko estatikoak

Suszeptibilitate magnetikoaren tenperaturarekiko mendekotasuna **1-6** konposatuen lagin polikristalinoetarako neurtu da, 2-300 K tenperatura tartean 0,1 T-ko kanpo eremu magnetikoa erabiliz (1.9. irudia). Giro tenperaturan neurtutako $\chi_M T$ balioak 14,24 (**1**), 11,88 (**2**), 14,20 (**3**), 11,60 (**4**), 14,24 (**5**) eta 11,65 (**6**) $cm^3 \cdot mol^{-1} \cdot K$ bat datoz Dy^{III} (14,17 $cm^3 \cdot mol^{-1} \cdot K$; $^6H_{15/2}$, eta g = 4/3) eta Er^{III} (11,48 $cm^3 \cdot mol^{-1} \cdot K$; $^4I_{15/2}$, eta g = 6/5) ioientzat teorikoki kalkulatutakoekin. Orokorrean, kasu guztietan ikus daiteke tenperatura jaistean $\chi_M T$ balioa ere jaisten dela; gainera, jaitsiera horiek nabarmenagoak dira tenperatura baxuenetan Portaera hau bat dator Stark azpimailen despopulazioarekin eta nahiko ohikoa da Dy^{III} eta Er^{III} ioietan oinarritutako *SMM*etan. 2-7 K tenperatura tartean neurtutako magnetizazio-kurbak (irudien barruan) ez dira saturaziora heltzen eta ez dira gainezargarriak. Ezaugarri hauek anisotropia magnetikoa adierazi dezakete.

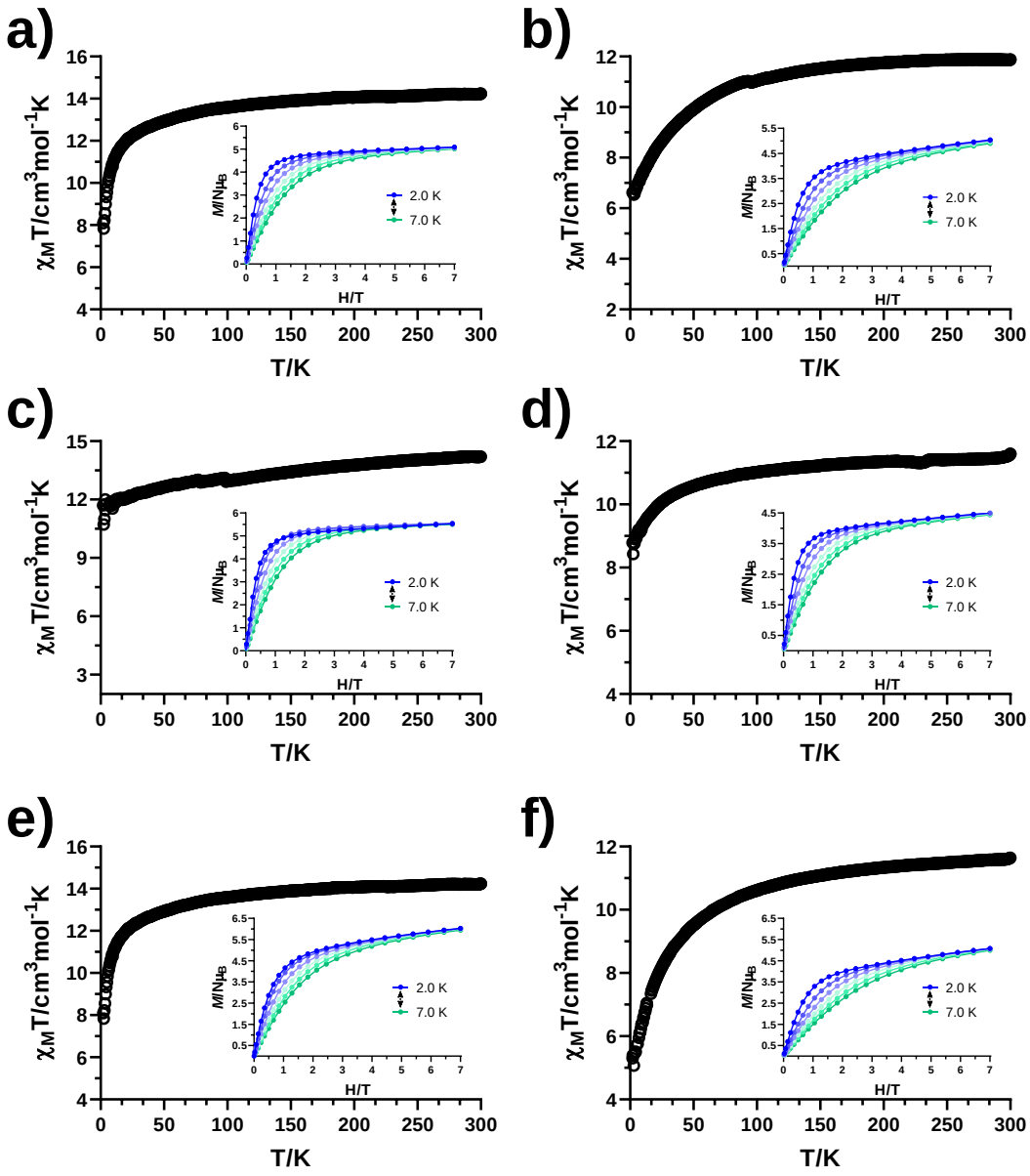

1.9. irudia.- $\chi_M T$ balioaren tenperaturarekiko mendekotasuna 1000 Oe-eko eremu magnetikoa erabiliz **1-6** konplexuentzat (a)-tik f)-ra, hurrenez hurren). Grafiko txikia: 2-7 K tenperatura tartean neurtutako magnetizazio kurbak. Marra etenek ez dute esanahi fisikorik.

1.4.3. 1-6 konposatuen propietate magnetiko dinamikoak

Konplexuek *SMM* portaera duten ala ez zehazteko, korronte alternoko (*ac*) suszeptibilitate magnetikoaren neurketak egin dira tenperaturarekiko eta frekuentziarekiko mendekotasuna ikusteko. **1**-**6** konposatuen lagin polikristalinoetan eta

3,5 Oe-ko oszilazio eremuarekin egin dira neurketak. Kanpo eremu magnetikorik aplikatu gabe, soilik **1** konposatuak erakusten du maximoa suszeptibitilatearen fasez kanpoko osagaian (χ_M''), neurtutako frekuentzia altuenean (10000 Hz; A1.9-1.11. irudiak). Disprosioan oinarritutako beste bi konposatuek (**3** eta **5**) seinalea aurkezten dute χ_M'' osagaian, baina 2,0 K-etik gorako maximorik izan gabe.

Er^{III} homologoek ez dute seinalerik erakusten fasez kanpoko osagaian. Seinale edo maximo eza tunel-efektuaren ondorio izan liteke eta *SMM* portaera ezkutatzen du. Hori dela eta, atal honetan aurrerago eztabaidatuko denez, kanpo eremu magnetikoa erabiltzeak eta diluzio magnetikoaren estrategia erabiltzeak eragindako efektua ere aztertu da. Kontuan hartu atal honen amaieran 1.1. taulan lortutako parametro guztien balioak laburbiltzen direla.

Esan bezala, **1** konposatuak *SMM* portaera du kanpo eremu magnetikorik aplikatu gabe ere. Halako baldintzetan, ordea, frekuentzia guztietan agertzen diren maximoak ez daude oso definituta, QTM efektuarekin nahasita baitaude. Efektu hori maximoen azpitik agertzen diren eta infinitura doazen seinaleek baieztatzen dute (1.10. irudia, ezkerrean). Hori χ_M''(υ) kurbetan ere islatzen da, non maximoen posizioa ia ez den aldatzen tenperatura baxueneko eremuan (A1.16. irudia). Azken kurba horiek Debyeren modelora doituz, erlaxazio-denborak (τ) kalkulatu dira tenperatura bakoitzerako. $\ln\tau$ vs T^{-1} irudikatuz, ikus daiteke tenperatura altuetan linealtasuna mantentzen dela, ondoren kurbadura dagoela tarteko tenperaturetan eta, azkenik, tenperaturarekiko independentea den erlaxazio argia ikusten da tenperatura baxuetan (*QTM* eremua; 1.10. irudia, barruan). Horrek guztiak argi eta garbi iradokitzen du erlaxazio magnetikoan hainbat mekanismok hartzen dutela parte, Cole-Cole grafikoetatik ateratako α balio altuekin adostasunean (0,33(2,0 K)-0,11(14,0 K)). Horrela, erlaxazio-denborak *QTM*, Raman eta Orbach prozesuak aldi berean kontuan hartzen dituen ekuazioari egokitu daitezke:

$$\tau^{-1} = \tau_{QTM}^{-1} + BT^{n} + \tau_0^{-1}exp(-U_{eff}/k_BT) \qquad \textit{1.1. ekuazioa}$$

Doiketak honako parametro multzoa ematen du: τ_{QTM} = 7,9·10^{-5} s, B = 234,4 s^{-1}K$^{-1,696}$, n = 1,696, τ_0 =2,4·10^{-9} s eta U_{eff} = 125,2 K. Kramers ioi baterako n = 9-ko balioa espero da [5], nahiz eta 1-6 arteko balioak ere zentzuzkotzat jotzen diren [6].

QTM osotasunean (edo gutxienez hein batean) deuseztatzeko helburuarekin, neurketak 1 kOe-etako kanpoko eremu magnetiko optimo batekin errepikatu ziren (eremu magnetiko optimoa aukeratzeko datuak A1.18 eta A1.19. irudietan). Kasu

honetan, 14,0 K-etik beherako maximoak askoz hobeto daude definituta *QTM* blokeatu izanaren ondorioz (1.10. irudia, eskuinean). Hala ere, tenperaturarik baxuenetan dauden seinaleak nabarmenak dira oraindik eta horrek adierazten du tunel-efektua oraindik ere martxan dagoela. $\chi_M''(\upsilon)$ eta Cole-Cole grafikoak 8,0-13,4 K tenperatura-tartean aztertu dira, non erlaxazio-mekanismoen banaketa nahiko altua espero den (α balioak 0,52(8,0 K)-0,22 (13,4 K) tartean). Erlaxazio-denborek, ordea, joera lineal ia perfektua erakusten dute aztertutako tenperatura-eremuan eta, beraz, Arrheniusen legera egokitu dira τ_0 eta U_{eff} parametroentzat $2{,}4 \cdot 10^{-8}$ s eta 93,5 K balioak emanez. 8,0 K-etan lortutako α balio altuak, seguruenik, adierazten du tenperatura honen azpitik hainbat aldibereko mekanismok hartzen dutela parte. Hori bat dator kanpo eremurik gabe egindako neurketan Raman prozesuaren eragina nagusitzen den tenperatura tartearekin. Kasu horretan, ordea, Raman prozesuaren eragina 8,0 K-etik bera ikusiko litzateke, baina $\chi_M''(\upsilon)$ kurbetan maximoak ikusi ahal izateko frekuentzia balio txikiagotara egin beharko litzateke neurketa, hots, tresnaren frekuentzia mugaren azpitik (A1.21. irudia).

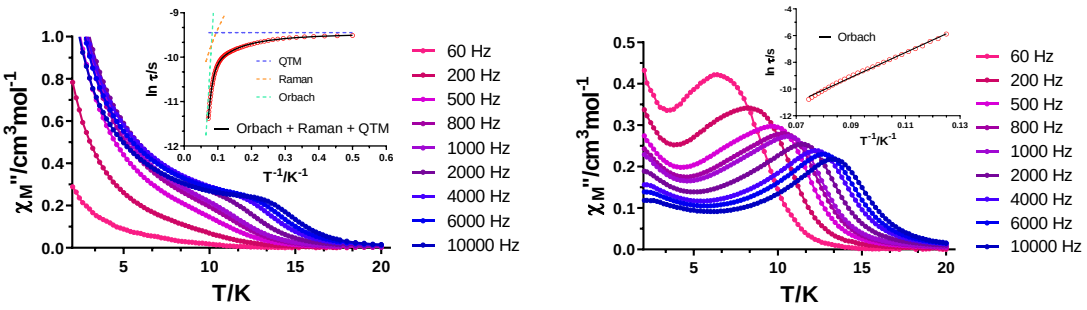

1.10. irudia.- 1 konposatuentzat, fasez kanpoko suszeptibilitatearen tenperaturarekiko mendekotasuna hainbat frekuentziatan kanpoko eremu magnetikorik aplikatu gabe (ezkerrean) eta 1 kOe-etako kanpoko eremu magnetikopean (eskuinean). Grafika txikia: Arrheniusen grafikoa erlaxazio-denboretarako Orbach + Raman + *QTM* prozesuak (ezkerrean) eta Orbach prozesua (eskuinean) kontuan hartuz. Lerro etenek mekanismo bakoitzaren ekarpen indibiduala erakusten dute.

2 konposatuak fasez kanpoko seinalea erakusten du 1 kOe-etako kanpoko eremu magnetikopean eta 500 Hz-tako frekuentziarekin, baina maximorik gabe (A1.12. irudia). Beraz, kanpoko eremua optimizatzeko neurketak 2,0 K-etan egin dira. A1.23. irudian ikus daitekeen bezala, erlaxazioa motelagoa bihurtzen da kanpoko eremua handitzen den heinean (maximoak frekuentzia baxuagoetara mugitzen dira), baina 1000 Oe-etatik gora maximoak berriz ere frekuentzia altuagoetara mugitzen dira. Efektu hori prozesu

zuzen baten agerpenarekin lotuta dago [7]. Kanpoko eremu magnetiko desberdinetara neurtutako $\chi_M''(\upsilon)$ kurbak Debyeren modelo orokortuari doitzen zaizkio erlaxazio-denbora motelenak 1000 Oe-etara lortuz (A1.24. irudia). Aipatzekoa da 2500 Oe-etara neurtutako kurba ezin izan dela frekuentzia guztietako datuekin doitu, izan ere, frekuentzia baxuenetan bigarren maximo baten agerpena iragar zitekeen. Bestalde, $\tau^{-1}(H)$ grafika hurrengo ekuaziora doitu da, non lehen bi terminoak eremu magnetikoaren menpeko *QTM* eta prozesu zuzena ordezkatzen dituzten, hurrenez hurren. Azken terminoak, berriz, eremu magnetikoarekiko independenteak diren prozesuak ordezkatzen ditu.

$$\tau^{-1} = \frac{B_1}{1+B_2 \cdot H^2} + AH^4T + k \quad \textit{1.2. ekuazioa}$$

Doikuntzarik onenak B_1 = 41990 s^{-1}, B_2 = 2436 T^{-2}, A = 6,36·10^6 $s^{-1}T^{-4}K^{-1}$ eta k = 10146 s^{-1} ematen ditu. k–ren balio handiak adierazten du 2,0 K-eko tenperaturan ere eremuarekiko independenteak diren erlaxazio-mekanismoek parte hartzen dutela, hala nola Raman edo Orbach mekanismoak. Tenperaturaren eta frekuentziaren mendeko suszeptibilitate neurketa osoa egin da ondoren 1 kOe-eko kanpo eremu magnetikopean fasez kanpoko osagaian maximo multzoa detektatuz 3,5 K-etik behera (1.11. irudia). Datuen tratamendua 2,0-3,5 K tenperatura tartean eginez lortu dira erlaxazio-denborak eta α balioak. Azkenekoen arabera, erlaxazio-prozesuen banaketa estua da (prozesu gutxi), baina kurbadura leun bat identifika daiteke Arrheniusen grafikan tenperatura baxuenetan (1.11. irudia, grafika txikia). Horrela, 1.2. ekuaziotik lortutako parametroak erabiliz, ondorengo 1.3. ekuazioan aurretik lortutako balioak finkatu dira aldagaiak izan ez daitezen: τ_{QTM}^{-1} = 1656 s^{-1} eta AH^4 = 636,4 $s^{-1}K^{-1}$. Modu honetan, lehen eta bigarren terminoak finkatuta daude (*QTM* eta prozesu zuzenari dagozkienak) eta Orbach mekanismoa bakarrik da aldagaia:

$$\tau^{-1} = \tau_{QTM}^{-1} + AH^4T + \tau_0^{-1}exp(-U_{eff}/k_BT) \qquad \textit{1.3. ekuazioa}$$

Doikuntzak τ_0 = 5,0·10^{-7} eta U_{eff} = 12,8 K balioak ematen ditu. Erabilitako estrategiari esker, erlaxazio-denborak deskribatzen dituen ekuazioan aldagai aske gehiegi sartzea ekiditen da, zentzu fisikoa galtzeko arriskua murriztuz. Hala ere, doikuntzan argi dago erlaxazio-bide nagusia Orbach mekanismoa dela; zuzeneko mekanismoak eta *QTM*ak, berriz, eragin txikia dute erlaxazio-prozesuan (1.11. irudia, grafika txikia). Hori nahiko ados dago α balioekin, nagusia den prozesu bakarra adierazten baitute.

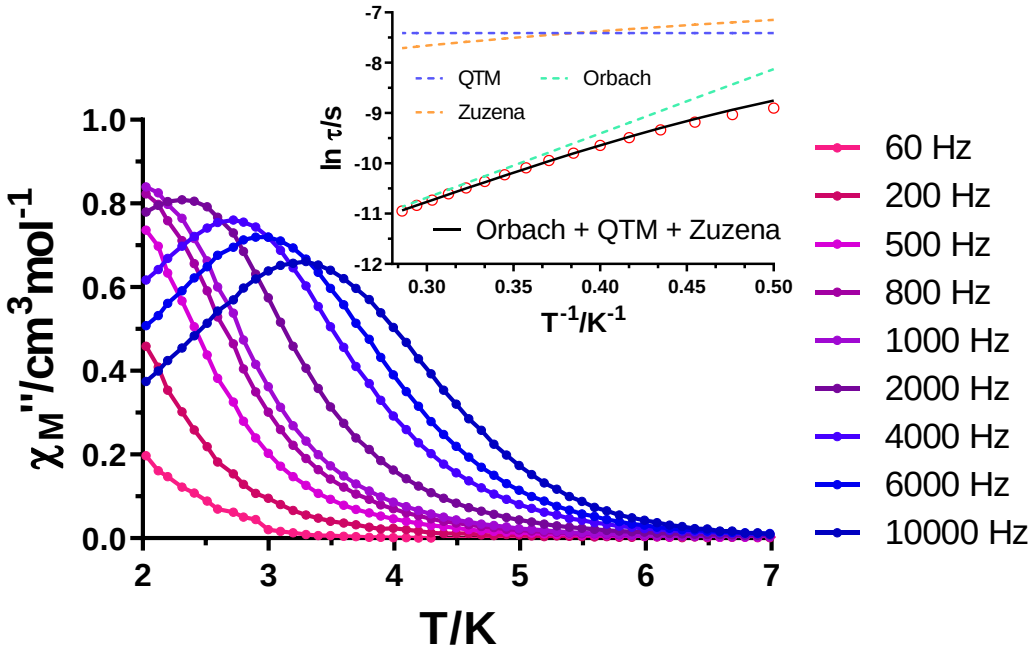

1.11. irudia.- 2 konposatuentzat, fasez kanpoko suszeptibilitatearen tenperaturarekiko mendekotasuna hainbat frekuentziatan 1 kOe-etako kanpoko eremu magnetikopean. Grafika txikia: Arrheniusen grafikoa erlaxazio-denboretarako Orbach + *QTM* + zuzena prozesuak kontuan hartuz. Lerro etenek mekanismo bakoitzaren ekarpen indibiduala erakusten dute.

Disprosioan oinarritutako **3** konposatuak ondo definitutako maximoa du 6 K inguruan 1 kOe-etako kanpo eremupean eta 500 Hz-tako frekuentzian (A1.13. irudia). 5,0 K-etan eremua optimizatzeko egindako neurketek *dc* optimoa 1,5 kOe-etakoa dela erakusten dute (A1.28-A1.29. irudiak); beraz, neurketa osoa errepikatu da baldintza horietan (1.12. irudia). Erlaxazio-denborek portaera lineala erakusten dute tenperatura altuenetan, baina kurbadura ikus daiteke tenperatura jaitsi ahala. Bi eremu bereiztu horiek bat datoz Cole-Cole grafikoetatik lortutako α balioekin (0,34 (5,0 K) – 0,32 (9,9 K)). Dena den, tenperatura-tarte osoko datuak ezin izan dira hainbat prozesu kontuan hartzen dituen ekuazio batetara doitu. Hori dela eta, tenperatura altueneko puntuak Arrheniusen ekuaziora doitu dira ondoko parametro balioak lortuz: $\tau_0 = 1{,}4 \cdot 10^{-8}$ s eta $U_{eff} = 68{,}8$ K.

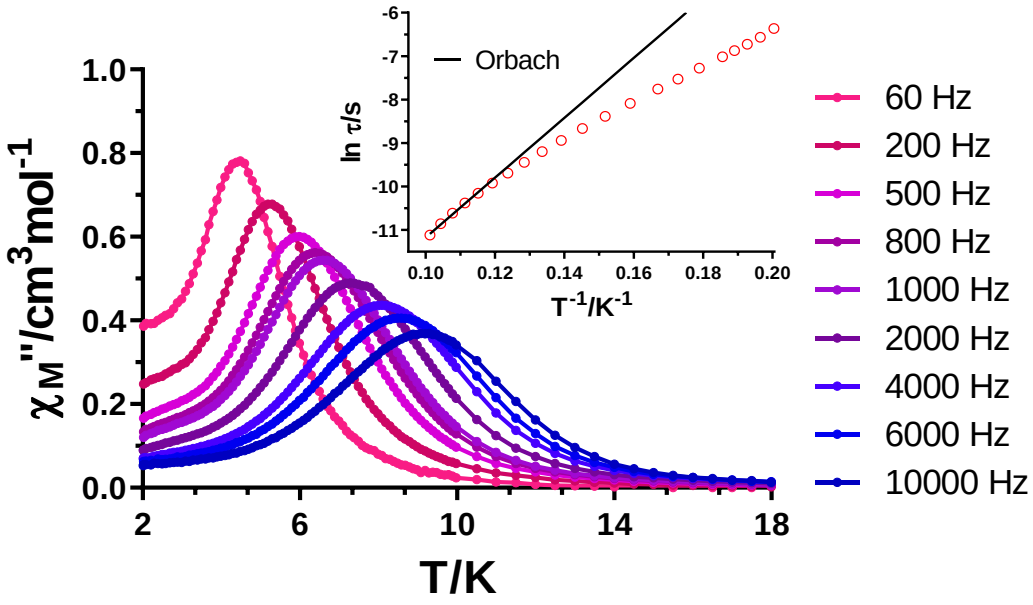

1.12. irudia.- 3 konposatuentzat, fasez kanpoko suszeptibilitatearen tenperaturarekiko mendekotasuna hainbat frekuentziatan 1,5 kOe-etako kanpoko eremu magnetikopean. Grafika txikia: Arrheniusen grafikoa erlaxazio-denboretarako Orbach mekanismoa kontuan hartuz.

Kontuan hartuta **4** konplexuaren *SMM* propietate eskasak (2,0 K-etan eta 1 kOe-etako kanpoko eremu magnetikoarekin ez du maximorik erakusten fasez kanpo, A1.13. irudia), energia-barreraren balioaren hurbilketa bat lortzeko, neurketa aipatutako eremu magnetiko arbitrario baten pean egin da. 1.13. irudian ikusten den bezala, χ_M'' seinaleak frekuentziarekiko menpekotasun nabarmena erakusten dute, baina ez dago maximo argirik 2,0 K-etatik gora. Horren ondorioz, erlaxazio-denborak ezin dira $\chi_M''(\upsilon)$ kurbak doituz lortu. Horri aurre egiteko, $\chi''_M/\chi'_M = 2\pi\upsilon\tau$ hurbilketa egiten da eta Orbach erlaxazio-prozesu bakarra dagoela onartuta, ondoko ekuazioa planteatzen da:

$$ln(\chi_M''/\chi_M') = ln(2\pi\upsilon\tau_0) + E_a/k_BT \qquad 1.4.\ ekuazioa$$

Datuak hainbat frekuentziatara doituz (1.13. irudia, grafika txikia), energia-barrera efektiboaren eta τ_0 balioen gutxi gorabeherako balioak lortzen dira, 6,2 K eta $1{,}2\cdot10^{-6}$ s, hurrenez hurren.

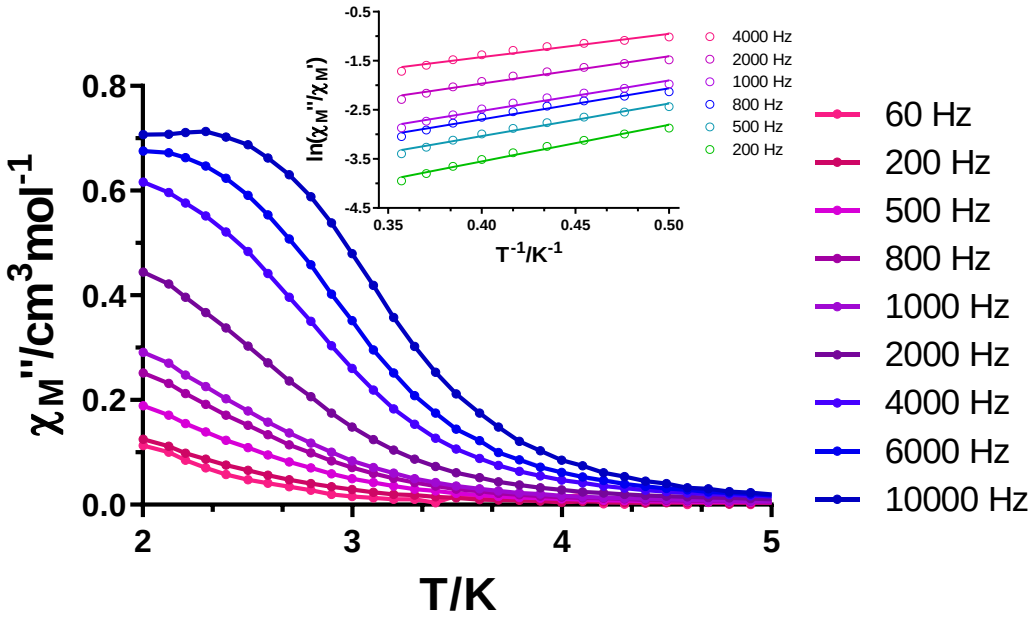

1.13. irudia.- 4 konposatuentzat, fasez kanpoko suszeptibilitatearen tenperaturarekiko mendekotasuna hainbat frekuentziatan 1 kOe-etako kanpoko eremu magnetikopean. Grafika txikia: Datuen doikuntza hurrengo ekuazioaren bidez $ln(\chi_M''/\chi_M') = ln(2\pi\upsilon\tau_0) + E_a/k_BT$.

H_2L^2 estekatzailean oinarritutako **5** konposatuak erakusten ditu *SMM* propietate ahulenak. 1 kOe-etako kanpoko eremu magnetikopean ere, frekuentziaren mendeko seinale bat ikus daitekeen arren, maximoak tresnaren behe-tenperatura mugatik kanpo daude, ziur aski **4** konposatuaren maximoak baino ere beherago (A1.14. irudia). Honek energia-barrera efektiboaren balio mespretxagarria iradokitzen du; beraz, ez da analisi gehigarririk egin konposatu honentzat.

6 konposaturako, 2,0 K-etan egindako eremuaren mendeko neurketek **2** konposatuaren antzeko portaera erakusten dute (A1.37-A1.38. irudiak). Kasu honetan, ordea, frekuentzia txikienetan bigarren maximoa eremu baxuagoetan agertzen hasten da (1000 Oe, A1.37. irudia). Neurketa horietatik eremu optimoa 500 Oe-etakoa dela erabaki da, non maximo bakarra lortzen den erlaxazio-denborarik motelenarekin. Tenperaturaren mendeko fasez kanpoko suszeptibilitate magnetikoak 2,5 K azpitik erakusten ditu maximoak hiru frekuentzia altuenetan. Gainerako frekuentzietarako tresnaren mugaren azpitik daude maximoak (1.14. irudia). 2,0-2,5 K tenperatura-tarterako kalkulatutako erlaxazio-denborek joera lineala dute. Hori dela eta, Arrheniusen

legea erabiliz doiketa egin eta 14,6 K-eko balioa duen energia-barrera efektiboa lortu da, baita τ_0 = 3,3·10^{-8} s balioa ere. Gainera, Cole-Cole grafikoek α balio nahiko baxuak ematen dituzte 0,15-0,13 tartean (2,0-2,5 K). Horrek erlaxazio-mekanismoen banaketa estua iradokitzen du.

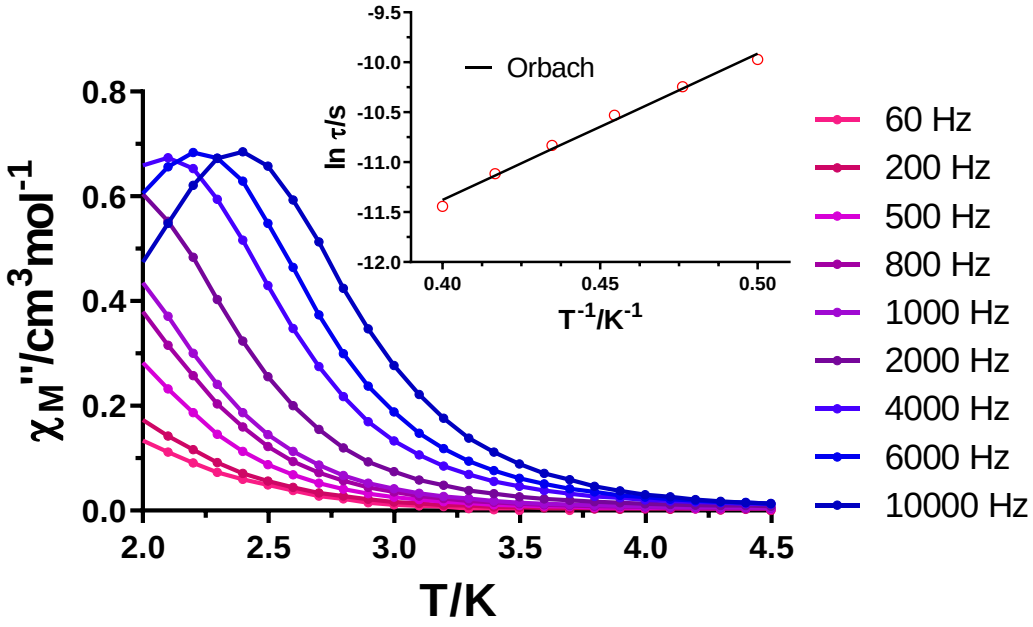

1.14. irudia.- 6 konposatuentzat, fasez kanpoko suszeptibilitatearen tenperaturarekiko mendekotasuna hainbat frekuentziatan 500 Oe-etako kanpoko eremu magnetikopean. Grafika txikia: Arrheniusen grafikoa erlaxazio-denboretarako Orbach mekanismoa kontuan hartuz.

Behin lagin puruen propietate magnetikoak aztertu ondoren bai kanpoko eremu magnetikorik gabe eta baita eremu magnetiko optikoekin, konposatu guztien analogo diluituak sintetizatu dira Ln:Y 1:10 erlazio molarra erabiliz. Horrela, molekula arteko interakzio dipolarretatik sor daitekeen *QTM* deuseztatzea espero da. Kanpoko eremu magnetikorik aplikatu gabe, Er^{III} analogo bakar batek ere ez du maximoa erakusten fasez kanpoko seinalean, nahiz eta **2**$_Y$ eta **4**$_Y$ kasuetan seinale ahulak ageri diren (A1.9-A1.10 irudiak). Aldiz, **1**$_Y$ konposatuak hobeto definitutako maximoa erakusten du *QTM* partzialki deuseztatu izanaren ondorioz (A1.9. irudia). **3**$_Y$ konposatuak 10 K-etik behera maximoa erakusten du orain. Horrek iradokitzen du molekulen arteko interakzioek konplexu honen *SMM* portaera ezkutatzen zutela kanpoko eremu magnetiko baten faltan (A1.10. irudia).

Dena dela, bi kasuetan, maximoaren azpiko isats luzeak desaktibatu gabeko *QTM* efektuaren adierazle dira. Horrek esan nahi du, konplexu horientzat simetria baxuko koordinazio-inguruneak zeharkako osagarriak sortzen dituztela eta molekulei tunel erlaxazio-mekanismoa ahalbidetzen die. Dy^{III} ioian oinarritutako azken konposatuaren kasuan, $\mathbf{5_Y}$, ez da alde nabarmenik ikusi diluitzerakoan (A1.11. irudia). *QTM* desaktibatzeko bi teknikak konbinatzean (diluzio diamagnetikoa + kanpo eremu magnetikoa, A1.12-A1.14), isatsa erabat desagertzen da $\mathbf{1_Y}$ konposatuan, gainontzeko konposatuentzat alde nabarmenik nabaritzen ez den bitartean. Kontuan izan behar da **3** konposatuarentzat *QTM* dagoeneko deuseztatua zegoela kanpoko eremu magnetiko baten aplikazioagatik, eta, beraz, ez dela **3** eta $\mathbf{3_Y}$ arteko alderik nabaritu eremuarekin neurketa egitean. Er^{III} homologoentzat, aldiz, alde nabarmenena $\mathbf{4_Y}$-rako ikusi da, non maximoaren desplazamendu argia ikusten den tenperatura altuagoetan. (A1.13. irudia).

$\mathbf{1_Y}$ diluituaren kasuan, kanpoko eremu magnetikorik gabe lortutako erlaxazio-denborek tenperaturarik altuenetarako joera lineala erakusten dute; gainerako tenperatura-tarteetan, berriz, kurbadura ikusten da (1.15. irudia, ezkerreko grafika txikia). **1** konposatuan ez bezala, ezin izan dira datuak tenperatura baxuenetaraino doitu, 7,0 K-etik behera neurtutako frekuentzia-tartean maximoak ez direlako ikusten (A1.43. irudia). Beraz, nahiz eta kurbadura lautada batera iritsiko den *QTM*ri dagozkion tenperatura baxuenetan, kasu honetan Raman eta Orbach prozesuak bakarrik hartu dira kontuan doikuntza egiteko:

$$\tau^{-1} = BT^n + \tau_0^{-1} exp(-U_{eff}/k_BT) \qquad \textit{1.5. ekuazioa}$$

Doikuntza onena honako parametro multzo honek ahalbidetzen du: n = 4,408, B = 0,19 $s^{-1}K^{-4,408}$, τ_0 = $5{,}7 \cdot 10^{-10}$ s eta U_{eff} = 147,0 K. Datuen kurbaduraz gain, Cole-Cole grafikoetatik lortutako α balioek ere erlaxazio-bideen banaketa nahiko zabala adierazten dute (0,54 (7,0 K) - 0,15 (13,4 K)). Kanpoko eremu magnetiko optimoa $\mathbf{1_Y}$ konposatuari aplikatzean, maximoen azpiko isats luzeak erabat desagertzen dira, diluzioaren eta eremu magnetikoaren estrategiak *QTM* modu eraginkorrean ezabatzeko gai direla adieraziz. Kasu honetan, erlaxazio denborak, Orbach prozesu bakarrera egokitu dira Arrheniusen legeari jarraituz. Lortutako energia-barrera eta τ_0 balioak 111,5 K eta $6{,}7 \cdot 10^{-9}$ s dira.

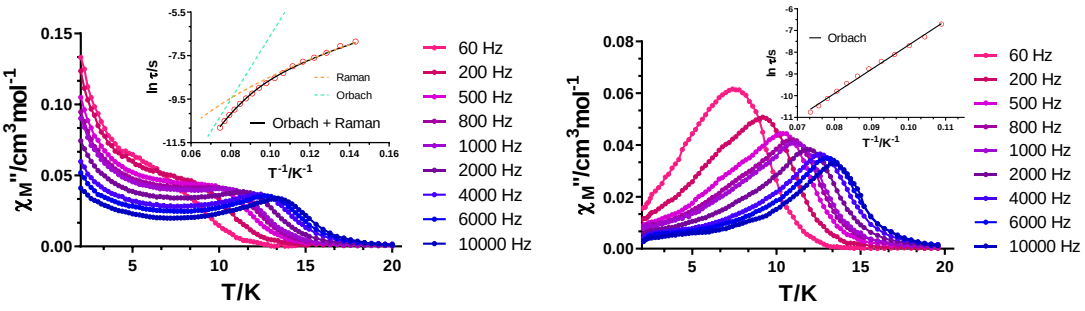

1.15. irudia.- 1$_Y$ konposatuentzat, fasez kanpoko suszeptibilitatearen tenperaturarekiko mendekotasuna hainbat frekuentziatan kanpoko eremu magnetikorik aplikatu gabe (ezkerrean) eta 1 kOe-etako kanpoko eremu magnetikopean (eskuinean). Grafika txikia: Arrheniusen grafikoa erlaxazio-denboretarako Orbach + Raman prozesuak (ezkerrean) eta Orbach prozesua (eskuinean) kontuan hartuz. Lerro etenek mekanismo bakoitzaren ekarpen indibiduala erakusten dute.

3$_Y$ konposatuan molekulen arteko interakzioak saihestean, ikusi da konposatu horrek *SMM* portaera duela kanpoko *dc* eremurik aplikatu gabe ere. 2,0-10,8 K-eko tenperatura-tartean erlaxazio-denboren banaketak tenperatura altuenetarako eremu lineala erakusten du, kurbadura tarteko tenperaturetan eta, azkenik, *QTM*ri dagokion tenperaturarekiko independentea den eremua tenperatura baxuenetan. Erlaxazio-mekanismo anitzen batura ondo islatzen da α balioetan, ez baitira 0,35 baliotik behera jaisten. Doikuntza fidagarri bat lortzeko, datuak Orbach, Raman eta *QTM* mekanismoak kontuan hartzen dituen ekuaziora doitu dira (1.1. ekuazioa erabiliz). Dena den, τ_{QTM}^{-1} parametroari 992 s^{-1}-eko balioa finkatu zaio 2,0 K-etan lortutako erlaxazio-denboraren alderantzizkoa dena. Izan ere, tenperatura horretan, ziur asko, *QTM* izango da prozesu nagusi. Balio hori finkatu gabe ezinezkoa zen zentzu fisikoa duten parametroak lortzea hiru prozesuak kontuan hartuz. Doikuntzak, azkenean, ondoko parametroak ematen ditu: B = 2,8 $s^{-1}K^{-3,743}$, n = 3,743, τ_0 =3,1·10^{-8} s and U_{eff} = 77,2 K. **3** eta **3$_Y$** konposatuek portaera bera erakusten dutenez kanpo eremu magnetiko batenpean (A1.13. irudia), ez da neurketa gehiagorik egin.

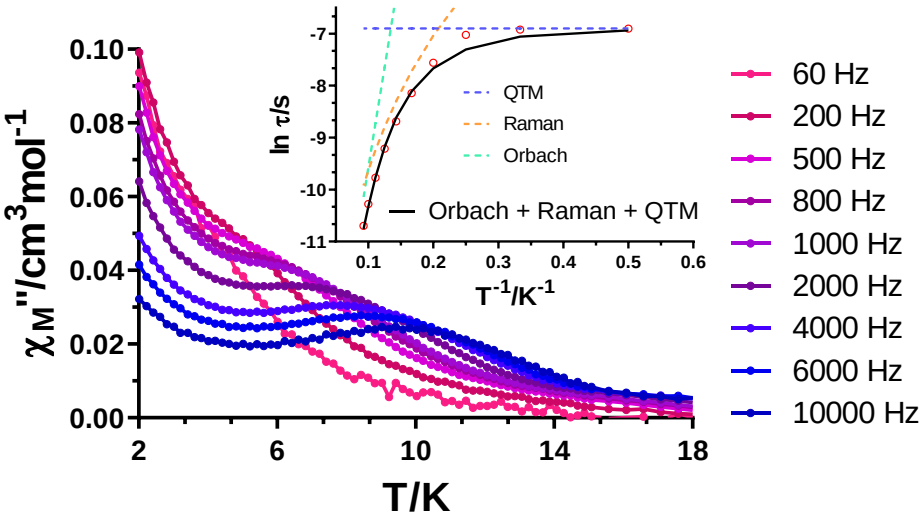

1.16. irudia.- 3$_Y$ konposatuentzat, fasez kanpoko suszeptibilitatearen tenperaturarekiko mendekotasuna hainbat frekuentziatan kanpoko eremu magnetikorik gabe. Grafika txikia: Arrheniusen grafikoa erlaxazio-denboretarako Orbach + Raman + *QTM* prozesuak kontuan hartuz. Lerro etenek mekanismo bakoitzaren ekarpen indibiduala erakusten dute.

4$_Y$ konposatuak, **4** molekularekin alderatuz gero, ondo definitutako maximoak erakusten ditu 3 K azpitik kanpo eremu magnetikoa aplikatzean (1.17. irudia). Erlaxazio-denborak $\chi_M''(\upsilon)$ kurbak 2,0-3,2 K tenperatura-tartean aztertuz lortu dira. Kurbadurak eta α (0,30 (2,0 K) -0,16 (3,2 K) balio altu samarrek adierazten dute aldibereko erlaxazio-mekanismoak daudela. Datuak 1.6. ekuaziora doitzen dira ondoen, Orbach eta prozesu zuzena kontuan hartuz:

$$\tau^{-1} = AH^4T + \tau_0^{-1}exp(-U_{eff}/k_BT) \qquad 1.6.\ ekuazioa$$

Parametro multzo hau lortu da: AH^4 = 1966 s^{-1}, τ_0 = 8,5·10^{-8} s eta U_{eff} = 17,8 K.

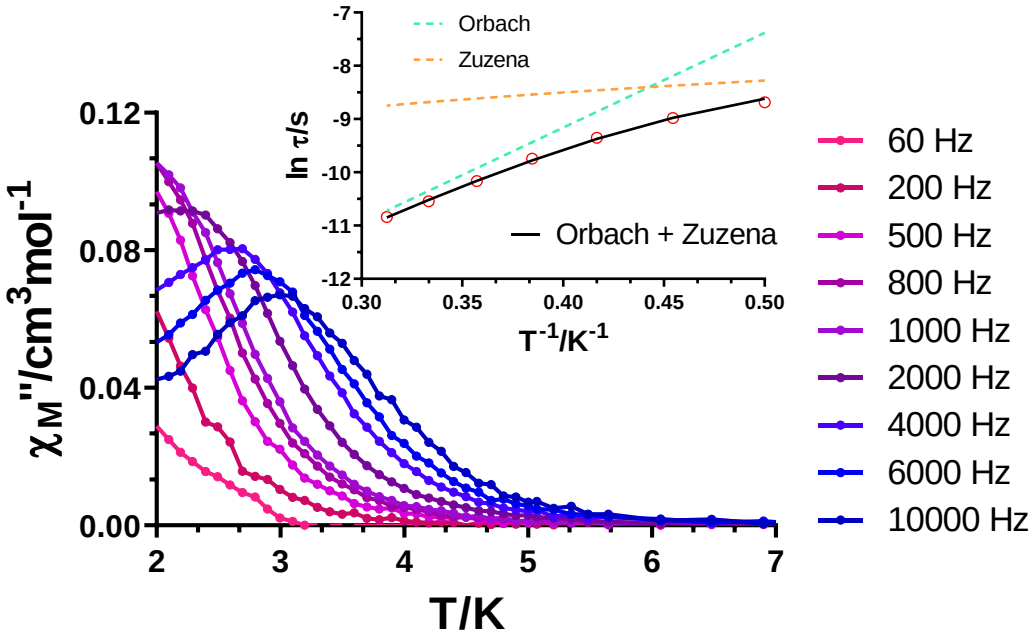

1.17. irudia.- $\mathbf{4_Y}$ konposatuentzat, fasez kanpoko suszeptibilitatearen tenperaturarekiko mendekotasuna hainbat frekuentziatan 1 kOe-etako kanpoko eremu magnetikopean. Grafika txikia: Arrheniusen grafikoa erlaxazio-denboretarako Orbach + Zuzena prozesuak kontuan hartuz. Lerro etenek mekanismo bakoitzaren ekarpen indibiduala erakusten dute.

1.1. taula.- U_{eff}, τ_0, B, n, τ_{QTM} eta A parametroentzako lortutako balioak **1**, $\mathbf{1_Y}$, **2**, **3**, $\mathbf{3_Y}$, **4**, $\mathbf{4_Y}$ eta **6** konposatuentzat.

	***dc* eremua**	**Orbach**		**Raman**		**QTM**	**Direct**
Konp.	Oe	U_{eff} (K)	τ_0 (s)	B ($s^{-1}K^{-n}$)	n	τ_{QTM} (s)	A ($s^{-1}T^{-4}$ K^{-1})
1	0	125,2	$2{,}4\cdot10^{-9}$	234,4	1,7	$7{,}9\cdot10^{-5}$	
	1000	93,5	$2{,}4\cdot10^{-8}$				
$\mathbf{1_Y}$	0	147,0	$5{,}7\cdot10^{-10}$	0,19	4,4		
	1000	111,5	$6{,}7\cdot10^{-9}$				
2	1000	12,8	$5{,}0\cdot10^{-7}$			$6{,}0\cdot10^{-4}$	$6{,}4\cdot10^{6}$
3	1500	68,8	$1{,}4\cdot10^{-8}$				
$\mathbf{3_Y}$	0	77,2	$3{,}1\cdot10^{-8}$	2,8	3,7	$1{,}0\cdot10^{-3}$	
4	1000	6,2	$1{,}2\cdot10^{-6}$				
$\mathbf{4_Y}$	1000	17,8	$8{,}5\cdot10^{-8}$				$2{,}0\cdot10^{7}$
6	500	14,6	$3{,}3\cdot10^{-8}$				

1.4.4. Korrelazio magneto-estrukturalak

Berebiziko garrantzia du korrelazio magneto-estrukturalak lortzeak, propietate magnetiko dinamikoetan eragin handiena duten parametroak zeintzuk diren ulertzeko eta, horrela, sistemen kristal-eremua hobetzeko balio baitute. Hori oraintsu egin da errendimendu handiko *SMM*etarako, simetria lineal eta $D5_h$ mota dutenentzako bereziki [1,8,9]. Aipatutako sistema horietan koordinazio-ingurunea oso zehaztuta dago eta, ondorioz, estekatzaile-eremuan egiten diren aldaketek sortutako eragina erraz detektatzen da normalean. Hau da, aldaketak oso espezifikoak izan ohi dira eta aldaketa konkretu horri lotu ahal izaten zaio eragindako ondorioa. Adibidez, sistema bipiramide pentagonal batean (non plano ekuatoriala THF molekulez osatuta dagoen) baieztapen orokor gisa, posizio axialean dauden eta lotura-distantziarik motzenak sortzen dituzten atomo elektronegatiboenek emango diote axialitatea sistemari. Ondorioz, plano ekuatorialean sortutako estekatzaile-eremua zenbat eta ahulagoa izan eta, aldi berean, axialetakoa zenbat eta sendoagoa izan, energia-barrera ere handiagoa izango da. Simetria baxuko sistementzat, ordea, halako ondorio zuzenak lortzea zailagoa izan liteke.

Magellan programa informatikoarekin lortutako emaitzen arabera [10], hiru Dy^{III} konposatuetan Dy-$O_{fenoxido}$ lotura laburrenak, Dy-O_{FM} izenekoak, bideratzen dute ardatz anisotropikoaren (An_{ard}) norabidea. Dy-$O_{fenoxido}$ luzeena Dy-O_{FL} deitzen da 1.2. taulan (ikusi 1.18. irudia **1** konposatuarentzat eta A1.54. irudia **3** eta **5** konposatuentzat). Hau esperotako ezaugarria da, atomo emaile guztien artean fenoxidoek baitute karga negatibo handiena eta lotura-distantziarik laburrenak sortzen dituzte. Sarrera orokorrean ikusi den bezala, anisotropia-ardatzak Dy^{III} ioiaren elektroi-hodei oblatuarekiko perpendikularki kokatuta daudela kontuan hartuta, parametro erabakigarrienak honako hauek direla uste dugu: Dy-$O_{fenoxido}$ distantziak, Dy-O distantziak nitrato hortzbakarrarekiko (edo ur-molekularekiko **3** molekulan) eta An_{ard}-Dy-O angeluak oxigeno atomoak aipatutakoak izanik. Angelu horiek α (An_{ard}-Dy-O_{PM}), β (An_{ard}-Dy-O_{PL}) eta γ (An_{ard}-Dy-$O_{NO3/1U}$) bezala definitu ditugu (1.2. taula eta 1.18. irudia). Hortzbakarreko nitrato ioia sartu dugu nitrato guztien artean lotura-distantziarik laburrenak erakusten dituelako.

Alde batetik, **1** eta **3** konplexuek Dy-O_{FM} lotura-distantziarik laburrenak erakusten dituzte, nahiz eta **5** konposatuak Dy-O_{FL} lotura distantzia pixka bat laburragoa duen. Hori ikusita, α eta β angeluak aztertzea erabaki da. Idealki, balio altueneko M_J azpimaila oinarrizko egoeran egonkortzeko, lotura-luzera laburrena erakusten duten karga negatibo altueneko oxigeno atomoek kontrako posizioetan egon behar lukete. Hau ez

da konposatu bakar baten kasua. Are gehiago, fenoxido atomoak euren artean ortogonalak izatetik gertuago daude, oinarrizko egoera axiala lortzeko kaltegarria litzatekeena. Gauzak horrela, *α* eta β angeluak zenbat eta txikiagoak izan, axialitatea orduan eta handiagoa izango dela pentsatzen dugu, izan ere, bi fenoxido taldeak esferoidearen egotetik gertuago daudela esan nahiko baitu (1.18c irudia). Hori kontuan hartuta, α eta β angelu txikienak **1** konposaturako kalkulatu dira, hau da, kanpoko eremu magnetikorik gabe *SMM* portaera erakusten duen konposatu bakarrarentzako eta energia-barrera efektibo handiena duenarentzako. Bestalde, **3** eta **5** konposatuek α eta β balio ia berdinak dituzte, α txikiagoa izanik **5** molekularako eta β **3** konposaturako. Arrazoi horrengatik erabaki dugu hortzbakarreko nitratoari edo ur-molekulari lotutako parametroak aztertzea. Azken heteroatomo hauek angelu zabalagoak erakusten dituzte anisotropia ardatzarekiko, γ, eta, hortaz, estekatzaile hauek plano ekuatorialean daudela interpreta daiteke. Ezberdintasuna da, **3** molekularen kasuan posizio ekuatorial hau ur-molekula neutro eta ez hain emailea den batek betetzen duela, eta **5** konposatuaren kasuan, aldiz, negatiboki kargatutako (eta lotura-luzera laburragoko, beste nitratoekin alderatuz) nitrato oxigeno atomo batek. Ondorioz, γ angeluetan eta Dy-O distantzietan (hortzbakarreko nitratora edo ur molekulara) egon daitezkeen desberdintasunek azaldu dezakete, agian, **3** eta **5** konposatuen arteko *SMM* portaera desberdintasuna.

1.2. taula- 1, **3** eta **5** sistementzat: aukeratutako Dy-O lotura-luzerak eta angelu esanguratsuak kalkulatutako anisotropia ardatzarekiko.

	Dy-O_{FM} (Å)	**Dy-O_{FL} (Å)**	**Dy-$O_{NO3/1U}$ (Å)**	**α (º)**	**β (º)**	**γ (º)**
1	2,234(5)	2,310(5)	2,397(5)	18,32	56,92	77,04
3	2,238(3)	2,284(3)	2,368(4)	18,22	60,49	94,06
5	2,2459(17)	2,2795(18)	2,3994(19)	17,68	61,82	67,35

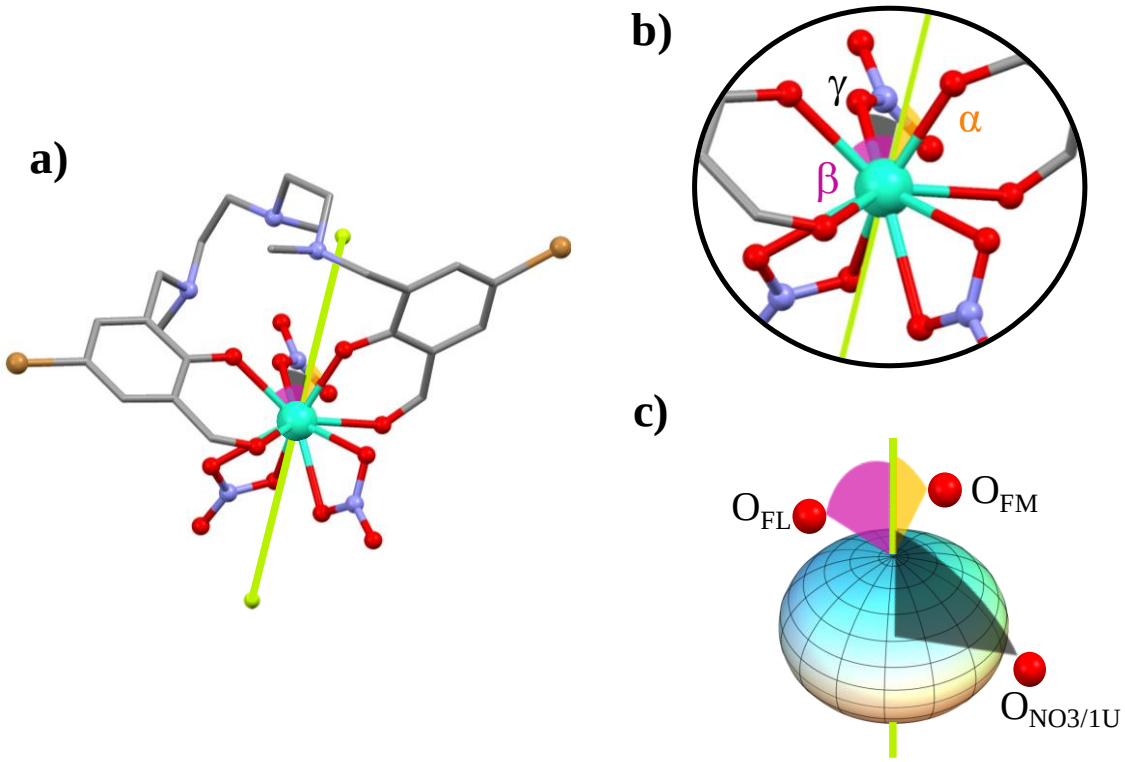

1.18. irudia.- a) Magellan softwarearekin lortutako **1**. konposatuaren anisotropia-ardatza (lerro berdea); b) Dy^{III} ioian oinarritutako konposatuen propietate magnetiko dinamikoetan eragina dezaketen angeluak: **α**: An_{ard}-Dy-O_{FM}; **β**: An_{ard}-Dy-O_{FL}; **γ**: An_{ard}-Dy-O_{NO3}; c) Dy^{III} ioiaren inguruan iradokitako elektroien banaketa eta eragin handiena duten atomo emaileen posizioa.

Hau guztia proposatuta, merezi du aipatzea iradokitako korrelazio horiek tentuz hartu behar direla kontuan. Hain koordinazio-zenbaki altua duten sistemetan, aldagaien eta angeluen/distantzien aldaketa arinen batura biderkatu egiten da. Horiek guztiek eragin propioa izango dute propietate magnetiko dinamiko orokorretan, baina eragin handiena dutenak ebaluatzen saiatu gara.

2, **4** eta **6** konposatuen kasuan, Er^{III} ioiek zehazki kontrako dentsitate elektronikoaren banaketa dute, prolatua. Kasu horietan, momentu magnetiko altueneko egoerak egonkortzeko oinarrizko egoeran, estekatzaileek kristal-eremu sendoa sortu behar dute plano ekuatorialean. **1**, **3** eta **5**-erako frogatu den bezala, estekatzaile-eremua ez da ez axiala ez ekuatoriala. Hala ere, pentsa genezake batentzat egokia dena bestearentzat okerragoa izango dela. Beraz, **2** konposatuarentzat *SMM* portaera ahulena ikusi izana eta **6** molekularentzat, berriz, hoberena, zentzuzko ondorioa izan daiteke.

1.5. ONDORIOAK

H_2L^1 eta H_2L^2 estekatzaileek Dy^{III} (oblatu) eta Er^{III} (prolatu) ioietan oinarritutako hiru sistema mononuklear pare berri sintetizatzeko aukera eman digute. Koordinazio-inguruneak simetria baxukoak izan arren, oso antzekoak dira hiru sistemetan. Propietate magnetiko dinamikoak, ordea, oso ezberdinak dira. Soilik **1** konposatuak du kanpoko eremu magnetikorik aplikatu gabe *SMM* portaera. Definitu gabeko geometria arrazoi nagusia izan liteke magnetizazioaren tunel efektua ahalbidetzeko. Ondorioz, kanpoko eremu magnetikoak beharrezkoak izan dira beste konposatuetan magnetizazioaren erlaxazio motela detektatu ahal izateko.

Lehen begiratuan sistema mononuklearrak egitura kristalinoan ondo isolatuta daudela ematen duen arren (ioien artean 8 Å-etik gora daude kasu guztietan), magnetikoki diluitutako konposatuen azterketa garrantzitsua izan da, molekulen arteko interakzioek *QTM* ahalbidetzen duten zeharkako eremu magnetikoen sorreran paper garrantzitsua dutela frogatu baita. Izan ere, tunel-efektua partzialki murriztu da $\mathbf{1_Y}$ eta $\mathbf{3_Y}$ konposatuetan eta maximoak neurtu dira fasez kanpoko osagaian kanpoko eremu magnetikorik gabeko neurketan. Bestalde, maximoak tenperatura altuagoetara mugitu dira $\mathbf{4_Y}$ konposatuan.

Aztertutako sistemetarako ez da erraza korrelazio magneto-estrukturalak aurkitzea, estekatzaile-eremu axialak edo ekuatorialak ez baitaude ondo zehaztuta. Hala ere, kapitulu honetan, propietate magnetikoetan eragiten duten faktore nagusiak identifikatzen saiatu gara. Espero bezala, fenoxido oxigeno atomoei dagozkien lotura-distantziarik laburrenek definitzen dituzte anisotropia magnetikoaren ardatzak Dy^{III} konposatuentzat (Magellan softwareak kalkulatutakoak). Hortik haratago, definitutako α, β eta γ angeluek eta fenoxido edo hortzbakarreko nitrato (edo ur-molekula) atomoekiko distantzien diferentziek emaitza esperimentalak azaltzea ahalbidetu digute. Azkenik, Dy^{III} eta Er^{III} ioien arteko kontrako dentsitate-elektronikoa kontuan hartuta, alderantzikatutako propietate magnetiko dinamikoek zentzua izan dezaketela proposatu dugu.

1.6. ERREFERENTZIAK

[1] Y. Ding, T. Han, Y. Zhai, D. Reta, N.F. Chilton, R.E.P. Winpenny, Y. Zheng, A Study of Magnetic Relaxation in Dysprosium(III) Single-Molecule Magnets, Chem. – A Eur. J. 26 (2020) 5893–5902. https://doi.org/10.1002/chem.202000646.

[2] J. Ruiz, A.J. Mota, A. Rodríguez-Diéguez, S. Titos, J.M. Herrera, E. Ruiz, E. Cremades, J.P. Costes,

E. Colacio, Field and dilution effects on the slow relaxation of a luminescent DyO9 low-symmetry single-ion magnet., Chem. Commun. 48 (2012) 7916–8. https://doi.org/10.1039/c2cc32518g.

[3] M. Yonemura, Y. Matsumura, M. Ohba, H. Okawa, D.E. Fenton, Template synthesis of phenol-based heterodinucleating macrocycles with dissimilar N(amine)2O2 and N(imine)2O2 metal-binding sites, Chem. Lett. (1996) 601–602. https://doi.org/10.1246/cl.1996.601.

[4] M. Llunell, D. Casanova, J. Cirera, J.M. Bofill, P. Alemany, S. Alvarez, M. Pinsky, D. Avnir, SHAPE, (2005).

[5] A. Abragam, B. Bleaney, Electron Paramagnetic Resonance of Transition Ions, Clarendon Press Oxford, UK,. (1970) 925.

[6] K.N. Shrivastava, Theory of Spin–Lattice Relaxation, Phys. Status Solidi. 117 (1983) 437–458. https://doi.org/10.1002/pssb.2221170202.

[7] S. Roy, I. Oyarzabal, J. Vallejo, J. Cano, E. Colacio, A. Bauza, A. Frontera, A.M. Kirillov, M.G.B. Drew, S. Das, Two Polymorphic Forms of a Six-Coordinate Mononuclear Cobalt(II) Complex with Easy-Plane Anisotropy: Structural Features, Theoretical Calculations, and Field-Induced Slow Relaxation of the Magnetization, Inorg. Chem. 55 (2016) 8502–8513. https://doi.org/10.1021/acs.inorgchem.6b01087.

[8] K.R. McClain, C.A. Gould, K. Chakarawet, S.J. Teat, T.J. Groshens, J.R. Long, B.G. Harvey, High-temperature magnetic blocking and magneto-structural correlations in a series of dysprosium(III) metallocenium single-molecule magnets, Chem. Sci. 9 (2018) 8492–8503. https://doi.org/10.1039/C8SC03907K.

[9] H. Wu, M. Li, B. Yin, Z. Xia, H. Ke, Q. Wei, G. Xie, S. Chen, S. Gao, Fine-Tuning the type of equatorial donor atom in pentagonal bipyramidal Dy(iii) complexes to enhance single-molecule magnet properties, Dalton Trans. 48 (2019) 16384–16394. https://doi.org/10.1039/c9dt03292d.

[10] N.F. Chilton, D. Collison, E.J.L. McInnes, R.E.P. Winpenny, A. Soncini, An electrostatic model for the determination of magnetic anisotropy in dysprosium complexes, Nat. Commun. 4 (2013) 1–7. https://doi.org/10.1038/ncomms3551.

2. KAPITULUA

$Zn^{II}Dy^{III}$ ENTITATE DINUKLEARREN LUZATZEA DI- ETA TRIKARBOXILATOAK ERABILIZ: AZTERKETA MAGNETIKO SAKONA

2.1. SARRERA

Tesi honen bigarren kapitulua gure aurreko ikerketaren jarraipen zuzena da [1], non difenoxido eta azetato zubi hirukoitza duten hamabi $Zn^{II}Ln^{III}$ sistema dinuklearren propietate magnetiko eta luminiszenteak aztertu genituen. Horien artean, $Zn^{II}Dy^{III}$ ioietan oinarritutako homologoak erakutsi zituen propietate magnetikoak interesgarrienak eta, beraz, ikerketa sakonago baterako hautatu dira.

Mn12-ac aurkitu ondoren, propietate magnetikoak hobetzeko hasierako joera molekulen spin balio totala handitzea izan zen (sarrera orokorrean aipatzen den bezala, *U* definitzen da S^2IDI edo S^2IDI bezala, spin osoentzako eta erdiosoentzako, hurrenez hurren). Hala ere, ikuspegi honek ez zuen espero zen arrakasta izan, spin altuko sistemak aurkitu ziren arren, lan zaila baitzen anisotropia mantentzea. Ikusi denez, trantsizio-metalen nahiz lantanidoen kasuan, anisotropia-ardatzak lerrokatzeak ondorio positiboak izan ditzake erlaxazio magnetiko propietateetan [2,3]. Beraz, molekula baten barruan zentro metaliko paramagnetikoen anisotropia-ardatzak lerrokatzeak eragin gehigarria izan lezake, *D* balio handiagoak eta, beraz, energia-barrera handiagoak sortuz.

Murugesuren taldeak ikuspegi hau erabili zuen Dy^{III} ioian oinarritutako helikato/mesokato konplexu dinuklearrentzat [4]. Ikerketa honetan, Schiff motako hiru estekatzaile erabili zituzten, non koordinazio-inguruneak mantentzen zituzten, baina zubi lana egiten zuten taldeak aldatzen zituzten helikato/mesokatato konplexuak lortzeko. Honen helburua, Dy^{III} ioiaren koordinazio-ingurunea ahalik eta antzekoen mantentzea zen, Kramers dobleteen energia-banaketa bera izateko, baina anisotropia-ardatzen orientazioak aldatuz. Estrategia horrek korrelazio magneto-estruktural oso interesgarriak azaleratu ditzake, anisotropia-ardatzen arteko angeluen aldaketekin lotutako ezaugarri estrukturalak propietate magnetiko desberdinekin zuzenean lotuta egon baitaitezke. Aipatu bezala, estekatzailea aldatuz hiru sistema dinuklear lortu zituzten, non ardatz anisotropoen arteko angeluak aldatzen ziren. Hala ere, zoritxarrez, ezin izan zituzten argi eta garbi ezarri angelu-diferentzia eta propietate magnetikoen arteko korrelazio magneto-estrukturalak. Hain zuzen ere, ondorioztatu zuten behatutako propietate magnetiko desberdinak ioi metalikoen koordinazio-ingurune desberdinekin lotuta zeudela, alde txikiak aurkitu baitziren batetik bestera.

Berrikiago, beste konposatu mononuklear eta polinuklear batzuk aztertu dira, tris(pirazolil) borato eta oligo(β-diketonato) estekatzaileetan oinarrituak [5]. Sistema

polinuklearrek, mononuklearrek ez bezala, kanpoko eremu magnetikorik aplikatu gabe SMM portaera dutela detektatu badute ere, beste behin, ez dago korrelazio argirik ardatz anisotropikoen orientazio eta propietate magnetiko dinamikoen artean. Propieate magnetikoez gain, Tb^{III} eta Eu^{III} ioietan oinarritutako konplexuen luminiszentzia propietateak aztertu dituzte. Ondorio orokor gisa, propietate magnetikoak zein luminiszenteak konbinatu eta hobetzeko, zentzuzkoena sistema mononuklearretan zentratzea dela diote, nahiz molekula barneko Ln···Ln distantzia luzeak dituzten sistema dinuklearrak ere interesgarriak izan daitezkeen.

Zhao eta egilekideek $Zn^{II}Dy^{III}$ unitatean oinarritutako sistema dinuklearrentzako antzeko lan bat argitaratu berri dute, zeinean entitate dinuklearrak sistema tetraknuklearretara luzatzea lortu duten [6]. Eredu gisa erabiltzen duten konposatuko Zn^{II} ioiak piramide karratuko koordinazio-ingurunea du, non posizio axialean piridina estekatzaile bat duen. Estekatzaile hori zubi lana egin dezakeen beste batez aldatuz (adibidez, 4,4'-bipiridina), helburu sistema tetranuklearra sintetizatzea lortu dute. Beste behin, estekatzaile aldaketak Dy^{III} ioiaren koordinazio-ingurunean aldaketxa txikiak sortzen ditu eta, ziur aski, aldaketa horiek dira propietate magnetikoen hobekuntzaren arrazoia.

Aurreko lan horietan oinarrituta, antzeko estrategia proposatzen da gure $Zn^{II}Dy^{III}$ ereduari egokitzeko (2.1. irudia). Helburua, azetato zubia karbonato edo beste di- eta trikarboxilato batzuekin ordezkatzea da (2.1. irudia). Espero da karbonato zubiak Dy-Dy molekula barneko distantziarik laburrenak sortzea, aurretik antzeko beste konposatu batzuetan ikusi den bezala [7]. Bitartean, luzera desberdineko azido karboxiliko alifatikoak erabiliz, luzatutako entitate dinuklearrek tolestura desberdinak izango dituzte eta, beraz, anisotropia-ardatzen orientazioan aldaketak izango dituzte. Azido tereftalikoa edo bifenil-4,4'-dikarboxilikoa bezalako estekatzaileekin konposatu linealak osatzea espero da. Azido trimesikoak, bestalde, helize moduko egiturak sor ditzakela pentsatzen da, Powellek eta kolaboratzaileek argitaratutakoak bezala [8]. Gainera, estekatzaile alifatiko edo aromatiko desberdinak erabiltzeak talde horiek lantanidoan zentratutako emisioari eragiten dioten ala ez aztertzea ahalbidetzen digu, balizko propietate luminiszente interesgarriak sortuz.

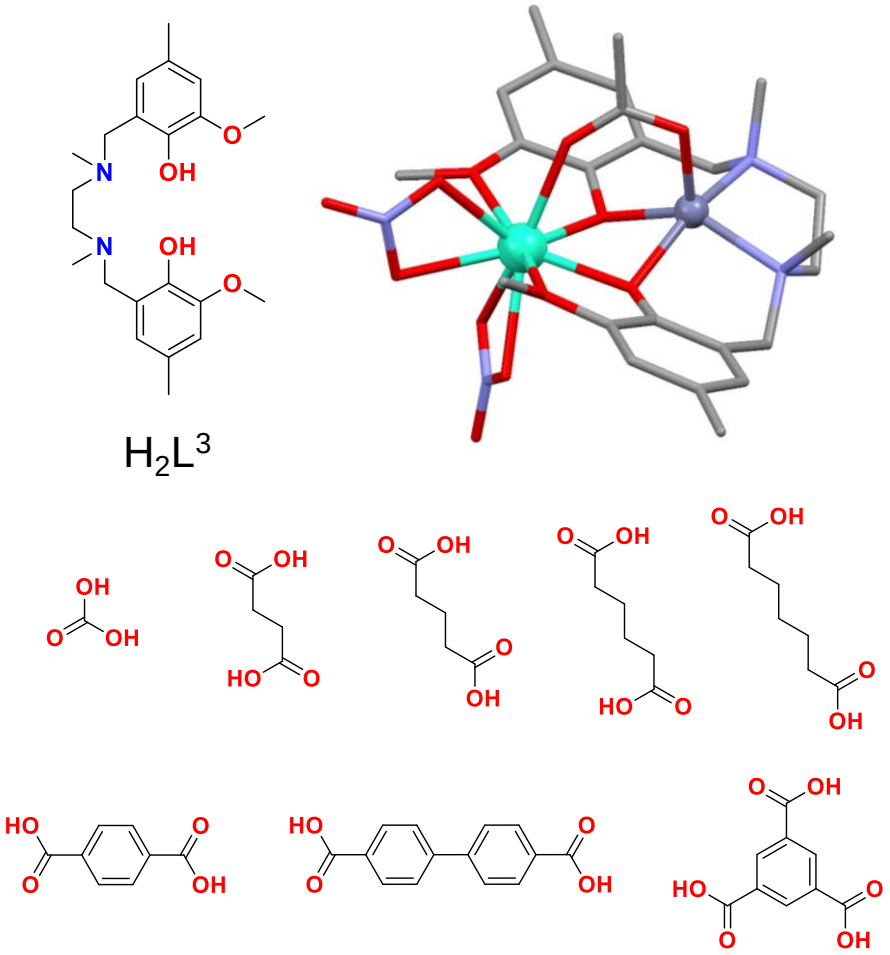

2.1 irudia.- Azterketa honetan erabilitako estekatzailearen egitura (goian ezkerrean), aurrez deskribatutako ZnDy konplexuaren ikuspegia, (goian eskuinean) eta kapitulu honetarako erabilitako zubiak. Disprosioa, zinka, nitrogenoa, oxigenoa eta karbonoa turkesa, gris ilun, urdin argi, gorri eta gris kolorez, hurrenez hurren. Hidrogeno atomoak eta disolbatzaile molekulak ez dira irudikatu argitasunaren mesedetan.

Beraz, kapitulu honek karboxilato talde desberdinez luzatutako eta $Zn^{II}Dy^{III}$ unitatean oinarritutako bederatzi konposatu polinuklear berriren sintesia, karakterizazioa eta azterketa magnetikoa deskribatzen ditu. Guztientzat magnetikoki diluitutako homologoak ere aztertu dira. Amaitzeko, behatutako propietate magnetikoak hobeto ulertzeko helburuarekin, korrelazio magneto-estrukturalak proposatu dira.

2.2. ESTEKATZAILEAREN SINTESIA

2.2.1. H_2L^3: N,N′-dimetil-N,N′-bis-2-hidroxi-3-metoxi-5-metilbenzil)-etilendiamina

Aurretik deskribatutako prozedurak erabiliz sintetizatua [9].

2.3. KONPLEXUEN PRESTAKETA

2.3.1. {(μ-CO_3)$_2$[Zn(μ-L^3)Dy(NO_3)$_2$]$_2$} (7)

H_2L^3 estekatzailea (48,0 mg, 0,125 mmol), $Zn(NO_3)_2 \cdot 6H_2O$ (37,2 mg, 0,125 mmol) eta $Dy(NO_3)_3 \cdot 5H_2O$ (54,8 mg, 0,125 mmol) 7 mL etanol absolututan disolbatzen dira etengabe irabiatuz. Honi trietilamina (0,034 ml, 0,250 mmol) eta Na_2CO_3 (13,2 mg, 0,125 mmol) gehitzen zaizkio, hurrenez hurren, eta nahastea 70 °C-tan mantentzen da 4 orduz. Lortutako hauts zuria iragazi, etanol absolutuz garbitu eta lehortzen uzten da. Ama-urak giro tenperaturan utzi eta egun gutxiren buruan kalitate oneko kristalak lortzen dira. Etekinak eta analisi elementalen emaitzak A2.1. taulan daude.

2.3.2. {(μ-L')[Zn(μ-L^3)Dy(NO_3)$_2$]$_2$}·nMeCN (L' = sukzinatoa, n = 2 (8); L' = glutaratoa, n = 0 (9), L' = adipatoa, n = 0.5 (10); L' = pimelatoa, n = 0 (11))

H_2L^3 estekatzailea (48,0 mg, 0,125 mmol) eta $Zn(NO_3)_2 \cdot 6H_2O$ (37,2 mg, 0,125 mmol) 8 mL azetonitrilotan disolbatzen dira. Jarraian, azido dikarboxilikoa (0,0625 mmol) eta trietilamina (0,051 ml, 0,375 mmol) dituen 2 mL-ko disoluzioa gehitzen da. Ondoren $Dy(NO_3)_3 \cdot 5H_2O$ (54,8 mg, 0,125 mmol) gehitzen da etengabe irabiatuz. Disolbatu gabeko partikulak ezabatzeko disoluzioa iragazi eta giro-tenperaturan uzten da. Egun gutxiren buruan, X-izpien difrakziorako egokiak diren kristalak lortzen dira. Etekinak eta analisi elementalen emaitzak A2.1. taulan daude.

2.3.3. {(μ-L')[Zn(μ-L^3)Dy(NO_3)$_2$]$_2$} (L' = tereftalatoa (12))

H_2L^3 estekatzailea (48,0 mg, 0,125 mmol) eta $Zn(NO_3)_2 \cdot 6H_2O$ (37,2 mg, 0,125 mmol) 16 mL azetonitrilotan disolbatzen dira eta disoluzioa 78 ºC-tan berotzen da. Ondoren bi disoluzio gehitzen dira jarraian, lehenengoa azido tereftalikoarena (10,4 mg, 0,0625 mmol) eta trietilaminarena (0,051 mL, 0,375 mmol) 2 mL azetonitrilotan eta bigarrena $Dy(NO_3)_3$-$5H_2O$ (54,8 mg, 0,125 mmol) 2 mL azetonitrilotan; biak tantaz tanta gehituta.

Disprosio disoluzioa gehitzean prezipitatu zuri bat sortzen da. Hala ere, berehala birdisolbatzen da. Une horretan, erreakzioa giro-tenperaturan dagoen ontzi batera iragazi eta tenperatura alde horren ondorioz, produktua kristalizatzen hasten da segundo gutxitan. Etekinak eta analisi elementalen emaitzak A2.1. taulan daude.

2.3.4. {(μ-L')[Zn(μ-L^3)Dy(NO_3)$_2$]$_2$}·2MeCN (L' = bifenil-4,4'-dikarboxilatoa (13))

12 konposatua sintetizatzeko prozedura bera erabili da, baina azido tereftalikoa erabili beharrean azido bifenil-4,4'-dikarboxilikoa erabiliz (15,1 mg, 0,0625 mmol) eta azetonitriloaren ordez azetonitrilo:metanol (1:1) nahasketa: Lehen kristalak minutu gutxitan hasten dira agertzen. Etekinak eta analisi elementalen emaitzak A2.1. taulan daude.

2.3.5. {(μ-L')[Zn(μ-L^3)Dy(NO_3)$_2$]$_3$}·$CHCl_3$·1.5·MeOH (L' = trimesatoa (14))

15 konposatua azpiprodukturik gisa ez eratzeko, beharrezkoa da azido trimesikoaren kantitate azpiestekiometrikoak erabiltzea. H_2L^3 estekatzailea (48,0 mg, 0,125 mmol), $Zn(NO_3)_2·6H_2O$ (37,2 mg, 0,125 mmol) eta $Dy(NO_3)_3·5H_2O$ (54,8 mg, 0,125 mmol) kloroformo, azetonitrilo eta metanol 1:1:1 nahasketaren 9 mL-tan disolbatzen dira. 10 minutuz irabiatu ondoren, azido trimesiko disoluzioa gehitzen da (2,63 mg, 0,0125 mmol) trietilaminarekin (0,039 mL, 0,288 mmol) 2 mL metanoletan. Disoluzioa 15 minutuz irabiatzen da, iragazi eta giro-tenperaturan pausatzen utzi. Egun gutxiren buruan, kalitate oneko kristalak lortzen dira. Etekinak eta analisi elementalen emaitzak A2.1. taulan daude.

2.3.6. {(μ-L')$_2$[Zn(μ-L^3)Dy(NO_3)$_2$]$_2$[Zn(μ-L^3)Dy(NO_3)]$_2$} (L' = trimesatoa (15))

H_2L^3 estekatzailea (48.0 mg, 0.125 mmol), $Zn(NO_3)_2·6H_2O$ (37.2 mg, 0.125 mmol) eta $Dy(NO_3)_3·5H_2O$ (54.8 mg, 0.125 mmol) kloroformo, azetonitrilo eta metanol 1:1:1 nahasketaren 9 mL-tan disolbatzen dira. 10 minutuz irabiatu ondoren, azido trimesiko disoluzioa gehitzen da (13,2 mg, 0,0625 mmol) trietilaminarekin (0,039 mL, 0,288 mmol) 2 mL metanoletan. Karboxilatoa gehitzean disoluzio uher bat lortzen da, berehala iragazi eta ama-urak giro-tenperaturan mantentzen dira. Egun gutxiren buruan, kalitate oneko kristalak lortzen dira. Etekinak eta analisi elementalen emaitzak A2.1. taulan daude.

2.3.7. 7_{Y}-15_{Y}, 7_{Gd}, 14_{Gd} eta magnetikoki diluitutako 7_{DyY}-15_{DyY} konposatuen sintesia

7_{Y}-15_{Y} deribatu diamagnetikoak, **7_{Gd}** eta **14_{Gd}** isotropikoak eta **7_{DyY}-15_{DyY}** magnetikoki magnetikoki diluitutako konplexuak **7-15** sistementzat deskribatutako prozedura berei jarraituz sintetizatu dira. **7_{DyY}-13_{DyY}** konplexuetarako erabilitako Dy:Y erlazio molarra 1:10 izan da, aldiz **14_{DyY}-15_{DyY}** kasuetarako, 1:15 eta 1:20 erlazioak erabili dira, hurrenez hurren, diluzio magnetiko eraginkorra ziurtatzeko.

2.4. EMAITZA ESPERIMENTALAK

H_2L^3 estekatzaileak bi koordinazio gune ditu, N_2O_2 barneko gunea, trantsizio-metalak koordinatzeko egokiagoa dena, eta O_4 kanpokoa, metal ioi gogorragoentzat egokia dena, adibidez, lantanidoak. Aurretik deskribatutako ikerketan oinarrituz [1], zeinean $Zn^{II}Ln^{III}$ unitatean oinarritutako konplexu dinuklear multzo esanguratsua sintetizatzea lortu genuen, kapitulu honetan entitate dinuklearrak luzatzea lortu dugu azetato zubiaren ordez karbonatoa, dikarboxilato desberdin ugari eta trikarboxilato zubi bat jarriz. Horrela, zazpi konposatu tetranuklear eta hexanuklear eta oktanuklear bana sintetizatzea lortu da.

Kasu guztietan, X-izpien difrakzio bidezko analisirako kristal egokiak lortu dira. Hala ere, gelaxka-unitatean oinarritutako eta esperimentalki lortutako difraktogramak ez datoz beti bat (A2.2-A2.6. irudiak). Gure ustez, egitura barruan kristalizazio-molekula nahiko lurrunkorrak galdu direlako gertatzen da hau eta, ondorioz, kristal-egiturak berrantolaketa jasaten du. Antolaketa berri hori **8**-**12** eta **15** konposatuen kasuan gertatzen da. Gure hipotesia egiaztatzeko, konposatu guztietarako materialen karakterizazio alternatiboa egin da (nahiz eta **7** eta **13**-**14** konposatuak puruak izan, difrkatograma esperimentalen bidez frogatuta). Lehenik eta behin, egiaztatu dugu berrantolaketa **7_{Y}-15_{Y}** analogo diamagnetikoentzat ere gertatzen dela eta, beraz, bi sistema motek patroi bera dutela (A2.2-A2.6. irudiak). Bigarrenik, Y^{III} analogoetarako analisi termograbimetrikoak egin dira materialen hasierako pisu molekularra zehazteko (A2.16-A2-18. irudiak). Hirugarrenik, konposatu diamagnetiko guztiak (**7_{Y}-15_{Y}**) EMN bidez karakterizatu dira (A2.111-A2.119. irudiak). Beraz, **7_{Y}-15_{Y}** konposatuek kristal-egituran lortutako estruktura mantentzen dutela jakinda, haien difraktogramak **7-15** konposatuen difraktogramekiko berdinak izateak gure hipotesia berretsi du. Azkenik, X-izpien difrakzioa neurtu zaie ama-uretako kristalei lagin polikristalinoa balira bezala

(A2.8-A2.10. irudiak). Azken esperimentu honek egiaztatu du konposatuek eraldaketak jasaten dituztela lehortutakoan, baina ezin hobeto egokitzen direla simulatutako ereduetara ama-uretan daudenean. Gainera, **7-15** konposatuen IG (infragorri) espektroak ere neurtu dira. Konposatu guztien bandak aurretik deskribatutako azetato zubia duen $Zn^{II}Dy^{III}$ konposatuaren antzekoak dira (**0** konposatua bezala izendatu da, A2.12-A2-15. irudiak). Analisi elementalek ere disolbatzaile galeraren hipotesia berresten dute. Beraz, garrantzitsua da esatea, taula kristalografikoetan agertzen diren formula eta atal esperimentalean agertzen diren formula batzuek ez dutela bat egiten. Adibidez, **9** konplexuaren kristal-egiturak bi azetonitrilo molekula ditu, baina ikertutako hautsak bat bera ere ez. Argitasunaren mesedetan, nomenklatura bera erabiltzea erabaki dugu nahiz zehazki konposatu berdinak ez izan.

2.4.1. X izpien hauts-difrakzioaren bidezko analisia 7-15, 7_Y-15_Y eta 7_{DyY}-15_{DyY} konplexuentzako

Azetonitriloa, metanola edo kloroformoa bezalako disolbatzaileak erabiltzeak arazo batzuk eragin ditzake, kasu honetan gertatu den bezala. Irakite-puntu baxu samarrak eta egituraren barruan interakzio handirik ez izateak izan litezke lurruntzearen arrazoia, eta, beraz, kristal-egituren berrantolaketen arrazoia (disolbatzaile molekulen galera lehenengo kapituluan ere ikusi da). Fenomeno honen lehen froga egitura batzuek (**7**, **8**, **12** eta **15**) *squeeze* errutina behar zutela izan daiteke, disolbatzaile molekulek ezaugarri desordenatuak eta ongi definitu gabeko okupazioak erakusten baitzituzten. Beraz, karakterizazio alternatiboa **7_Y-15_Y** analogo diamagnetikoen X izpien hauts-difrakazioarekin hasi zen. Helburua zera zen, hasieran fase berri hauek zeri zegozkien ez genekien arren, analogo diamagnetikoak erabat karakterizatzeko gai izango bagina kristal-egituratik lortutako estrukturak mantentzen direla ondorioztatuz, Dy^{III} ioian oinarritutako materialek ere mantentzen dutela ondorioztatuko genuke. Beraz, beste teknika batzuen laguntza ere baliatuz, X izpien difraktograma berriak disolbatzaile gabeko molekulenak direla ondorioztatuko genuke.

A2.2-A2.6. irudietan erakusten den bezala, fase-eraldaketak detektatu diren konposatuen kasuan (**8**-**12** eta **15**), Dy^{III} eta Y^{III} ioietan oinarritutako konposatuen difraktogramak ezin hobeto datoz bat euren artean, egitura kristalinoaren fase bera direla baieztatuz (**8_Y** konposatua salbuespena da, nahiz eta **8** eta **8_{DyY}** ezin hobeto egokitzen diren). Gainera, magnetikoki diluitutako **7_{DyY}-15_{DyY}** sistemen difraktogramak ere irudi beretan erakusten dira izaera isoestrukturala frogatzeko.

Azkenik, difrakzioa ama-uretan sortutako kristaletarako ere neurtu da. Horri esker, materialak aztertu ahal izan ditugu kristalizazio-molekulen galera izan aurretik. A2.8-A2.10. irudietan erakusten den bezala, baldintza hauetan lortutako difraktogramak ondo egokitzen dira simulatutako patroietara eta behin lehortutakoan ondo egokitzen dira lehen deskribatutako difraktogrametara.

2.4.2. 7_Y-15_Y konplexuen analisi termograbimetrikoa

Analogo paramagnetiko eta diamagnetikoen izaera isoestrukturala baieztatu ondoren, **7_Y-15_Y** analogoen analisi termikoa egin da. Esperimentu honek informazio oso baliotsua ematen du: (i) kristalizazio-molekulak egituran mantentzen diren kasuetan, horien galera 200 ºC-tik behera ikusten da eta (ii) kasu guztietan (**8**-rentzat izan ezik, ZnO eta Dy_2O_3 hondarrak lortzen dira) sortutako hondakina ZnO eta Y_2O_3 oxidoei dagokiela kontuan hartuta (A2.11. irudia), hasierako produktuen pisu molekularra kalkulatzen da esperotakoarekin bat datorrela ikusiz.

7_Y, **13_Y** eta **14_Y** konposatuen X izpien difraktogramak ezin hobeto doitzen dira simulatutako ereduei. Hortik ondorioztatzen da analisi termograbimetrikoak bat etorri behar duela kristal-egituran ikusten denarekin. Hain zuzen, **7_Y** konposatuak ez du disolbatzaile galera nabarmenik erakusten 200 ºC-tik behera, disolbatzailerik gabeko egiturarekin bat datorrena. **13_Y** eta **14_Y** konposatuek, aldiz, aipatutako tenperaturaren azpitik masa galera argiak ematen dituzte bi azetonitrilo molekula eta kloroformo bat gehi metanolezko 1,5 molekula galerari egotziak, hurrenez hurren.

8 molekularen kristal-egitura *squeeze* errutina erabiliz errefinatzen da, partzialki lurrundutako disolbatzaile molekulen ondorio izan litekeena. Izan ere, analisi termograbimetrikoak masa galera argia ematen du bi azetonitrilo molekula galerari dagokiona. **9** konposatuak bi azetonitrilo molekula ditu kristal egituran; aldiz, **9_Y** konposatuaren portaera termikoak argi adierazten du ez dagoela disolbatzaile molekularik bertan, eta horrek berrantolaketa justifikatzen du. **10** konposatuaren egiturak ere bi MeCN molekula ditu, baina soilik 0,5 MeCN molekulen askapenarekin lotutako galera txikia ikus daiteke **10_Y** analogoarentzat. **11** tetranuklearrak izan behar lukeen azetonitrilo molekula ez da ageri **11_Y** molekularako. Azkenik, **12** eta **15** konposatuen kristal-egiturak *squeeze* errutinaren bidez errefinatu dira. Metodo hori erabili behar izanak azal dezake zergatik ez den ikusten masa galerarik analogo diamagnetikoentzat.

Konposatuen pisu molekularrak kalkulatzeko eta alderatzeko, bi ikuspegi desberdin erabili dira. Alde batetik, bagenekienez **7_Y**, **13_Y** eta **14_Y** molekula puruak zirela, jakinik hondar-portzentajea ZnO eta Y_2O_3 oxidoen baturari dagokiola, materialaren %100ari dagokion pisu molekularra kalkulatzen da (2.1. taula). Aldiz, berrantolaketa jasaten duten konposatuen kasuan, ordokiei dagokien pisu molekularra kalkulatu da (batzuetan %100ari dagokiona izanik, baina beste batzuetan lehen masa galera ondoren dagoen ordokiari) ondoren disolbatzaile molekularik gabeko formula molekularren pisu molekularrarekin alderatzeko. Masa galera aurkezten duten konposatuen kasuan, masa galera hori disolbatzaile kantitatea kalkulatzeko erabiltzen da. Azkenik, esperimentalki kalkulatutako balioen eta balio teorikoen arteko errorea honako ekuazio honen bidez kalkulatzen da:

$$Errorea\ (\%) = (pm_{teor.} - pm_{esp.}) \cdot 100 / pm_{esp.} \qquad 2.1.\ ekuazioa$$

2.1. taula.- Pisu molekularren datuak (pm), kalkulatutako errorea eta kristal-egituratik (KE) eta analisi termograbimetrikotik (TG) lortutako disolbatzaile molekulen balioa.

	$pm_{teor.}$ (g/mol)	$pm_{exp.}$ (g/mol)	Errorea (%)	Disolb. (KE)	Disolb. (TG)
7_Y	1325,6	1260,4	5,2	-	-
8	1592,8	1572,5	1,2	-	2 MeCN
9_Y	1459,7	1418,1	2,9	2 MeCN	-
10_Y	1473,7	1390,1	6,0	2 MeCN	0,5 MeCN
11_Y	1487,7	1421,8	4,6	MeCN	-
12_Y	1493,7	1405,0	6,3	-	-
13_Y	1651,9	1538,3	7,2	2 MeCN	2 MeCN
14_Y	2368,9	2297,4	3,2	$CHCl_3$, 1,5 MeOH	$CHCl_3$, 1,5 MeOH
15_Y	2949,3	2899,8	1,7	-	-

Errore batzuk nolabait altuak izan daitezkeen arren (> %5), kasu guztietan balio esperimental baxuagoak lortu izanak errore negatibo hori tresnarekiko berezkoa izan litekeela esan nahi dezake. Aldi berean, honek, benetako pm-en balioak handiagoak direla iradokitzen du eta, beraz, errorea txikiagoa izango litzateke.

2.4.3. Erresonantzia Magnetiko Nuklearra 7_Y-15_Y konplexuentzat

Uste dugun arren X izpien hauts-difrakzioan eta analisi termograbimetrikoak oinarritutako ikerketak egitura kristalino berrantolatuei buruzko gure hipotesia ziurtatzen duela, Y^{III} ioian oinarritutako konposatu diamagnetikoek EMN bidez aztertzeko aukera ematen dute. Konposatu guztiak hobeto disolbatzen dira DMSOn (dimetil sulfoxidoa) eta, beraz, esperimentuak DMSO-d^6 disolbatzaile deuteratuan egin dira.

A2.111-A2.118 irudietan ^{1}H-EMN espektro guztiak erakusten dira, non estekatzaile nagusiari eta di- edo trikarboxilatoei dagozkien protoi guztiak kolore desberdinen arabera esleitzen diren. Konposatu batzuentzat (**12_Y**, **14_Y** eta **15_Y**) COSY, ^{13}C{^{1}H} eta ^{1}H-^{13}C-HSQC esperimentu gehigarriak egin dira, seinale-esleipen konplexuago baten ondorioz. Aipatzekoa da, lotura-distantzia handiagoak direla eta (ikusi hurrengo atala), metoxi taldeak disoluzioan nolabait labilak direla uste dugula. Seinale bakarra eman beharko lukete, baina seinale ugari lortzen dira konposatu guztientzat. Seinale guztiak metoxi talde berekoak eta, beraz, karbono atomo berekoak direla egiaztatzeko HSQC esperimentuak egin dira.

Interesgarria da aipatzea metileno taldeetako protoi geminalak (arrosa eta hori kolorez adieraziak) ppm balio desberdinetan agertzen direla. Honek adierazten du disoluzioan egiturak mantentzen direla. Protoi hauek diastereotopikoak dira [10] eta kristal egituran ingurune elektroniko desberdina jasaten dute. Hain zuzen, estekatzaile hutsaren seinaleak singletea ematen du (A2.120. irudia) protoi mota hauentzat interkonbertsio probabilitatea dela eta.

2.4.4. 7-15 konplexuen kristal-egiturak

Bederatzi konplexuetan, oinarrizko unitatea entitate dinuklear batean datza, $[ZnDyL(NO_3)]^{2+}$. **7** konposatuan, lau hortzeko bi karbonato anioik bi oinarrizko unitate konektatzen dituzte (2.2. irudia). **8**-**14** konposatuek hortz biko nitrato anioi gehigarri bat dute funtsezko unitatean (2.3.-2.4. irudiak) eta dikarboxilato batek (trikarboxilatoa **14**

sistemaren kasuan) estekatzaile-zubi gisa jarduten du, koordinazio-konposatu tetranuklearrak eratuz (hexanuklearra **14**-ren kasuan). Azkenik, **15** konposatuak oinarrizko bi sistema ditu: $[ZnDyL(NO_3)]^{2+}$ eta $[ZnDyL(NO_3)_2]^{+}$, bakoitzetik bi (2.5. irudia). Lotura-distantzia eta angelu garrantzitsuenak, baita konplexuen datu kristalografikoak ere A2.2.-A2.7. tauletan ageri dira.

Monokristalen X izpien analisien arabera, **7**, **11** eta **15** konposatuek *P-1* talde espazial triklinikoan kristalizatzen dute; **8**, **10**, **12** eta **13** molekulek *P 2₁/c* monoklinikoan; **9** sistemak *C 2/c* monoklinikoan eta, azkenik, **14** konplexuak *R-3* talde espazial trigonalean. **7**, **9**, **12**, **14** eta **15** kristal-egituren unitate asimetrikoaren barruan, Zn^{II} bakar bat eta Dy^{III} bakar bat ageri dira; **8**, **10**, **11**, **13** eta **15** egituretan kristalografikoki independenteak diren Zn^{II} eta Dy^{III} zentro metalikoen bi pare ageri diren bitartean. Zn^{II} ioiek, barneko gunean, ondo definitutako (1 baino balio txikiagoak, A2.8. taula) ZnN_2O_3 koordinazio esfera erakusten dute, piramide karratu gisa deskribatua (SHAPE softwarearen [11] bidez kalkulatua). Kasu guztietan, bi nitrogeno eta bi oxigeo atomo protonatu gabeko L^{2-} estekatzaileari dagozkio, piramidearen oinarria osatzen duten amina eta fenoxido taldeak direlarik. Geratzen den oxigeno axiala $Zn^{II}Dy^{III}$ ioiak konektatzen dituen karbonatotik dator **7** konposatuan eta karboxilikoetatik **8**-**15** molekulen kasuan.

DyO_9 koordinazio-ingurunea poliedro ideal batetik asko urruntzen da kasu guztietan. Hala ere, ioi guztietan estekatzaile-eremua ahalik eta antzekoena mantentzeko helburu nagusia arrakastaz betea izan da. Izan ere, guztiak deskriba daitezke hiru poliedro desberdinen nahasketa gisa (A2.9. taula).

Aipatu bezala, **7** tetranuklearrak bi unitate dinuklear $[ZnDyL(NO_3)]^{2+}$ ditu bi karbonato anioiz lotuta. DyO_9 ingurunea L^{2-} estekatzaileari dagozkion lau oxigeno atomok, karbonato zubiei dagozkien hiru oxigeno atomok eta nitrato kelato bati dagozkion bi oxigeno atomok osatzen dute. Lotura-distantziak hirutan sailka daitezke; laburrak Dy-$O_{fenoxido}$ (2,288(9) - 2,319(9) Å), tartekoak Dy-$O_{karbonato}$ (2,347(9) – 2,395(8) Å) eta luzeak Dy-O_{metoxi} edo Dy-O_{NO3} (2,431(9) - 2,555(9) Å). Molekula barneko Dy1⋯Dy1 (*i: 1-x, -y, 2-z*) distantzia 4,039(1) Å-ekoa da eta Dy1-$O_{karbonato}$-Dy1(i) angelua 116,9(3)º-koa da.

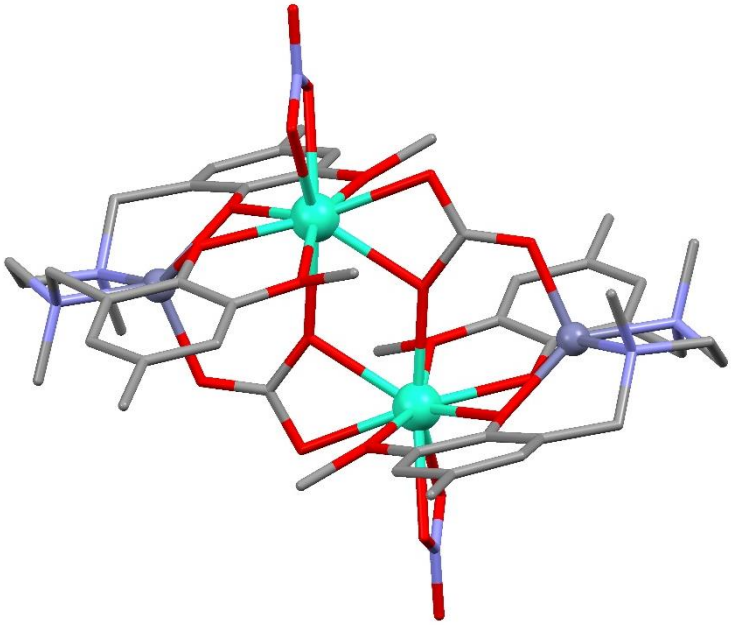

2.2. irudia.- 7 konposatuaren ikuspegia. Kolore-kodea: disprosio, zink, nitrogeno, oxigeno eta karbono atomoak turkesa, gris ilun, urdin argi, gorri eta gris kolorez, hurrenez hurren. Hidrogeno atomoak ez dira irudikatu argitasunaren mesedetan.

8-**13** konposatu tetranuklearrek oinarrizko bi $[ZnDyL(NO_3)_2]^+$ entitate dituzte sukzinato, glutarato, adipato, pimelato, tereftalato eta bifenil-4,4'-dikarboxilato zubiek konektatuta, hurrenez hurren. Beraz, DyO_9 esfera, estekatzaileari dagozkion lau oxigeno atomorekin, bi nitrato kelatoren lau oxigeno atomorekin eta karboxilato zubiaren oxigeno batekin osatzen da kasu guztietan. Oinarrizko unitate bakoitzean, Dy-$O_{fenoxido}$ lotura da beti laburrena, baina Dy-$O_{karboxilato}$ loturarekin batera taldekatu daitezke laburrenak bezala (2,242(3) – 2,3296(14) Å tartean). Dy-O_{NO3} lotura-distantziek tarteko balioak erakusten dituzte (2,417(5) – 2,560(5) Å), Dy-O_{metoxi} loturak, berriz, luzeenak dira (2,5016(15) – 2,612(3) Å). Molekula barneko Dy···Dy distantziek ez dute joera zehatzik jarraitzen zubi alifatikoen kasuan, katearen luzera handitzen bada ere, tolestura desberdinak lortzen direlako. Hala, distantzia hauek neurtu dira: 9,377 (2), 11,616 (3), 9,5908 (8) eta 9,7774 (8), **8**-**11** molekuletarako, hurrenez hurren. Molekula barneko Dy···Dy distantzia luzeenak **12** eta **13** sistemen kasuan agertzen dira, 11,823(2) Å eta 15,811(2) Å, hurrenez hurren.

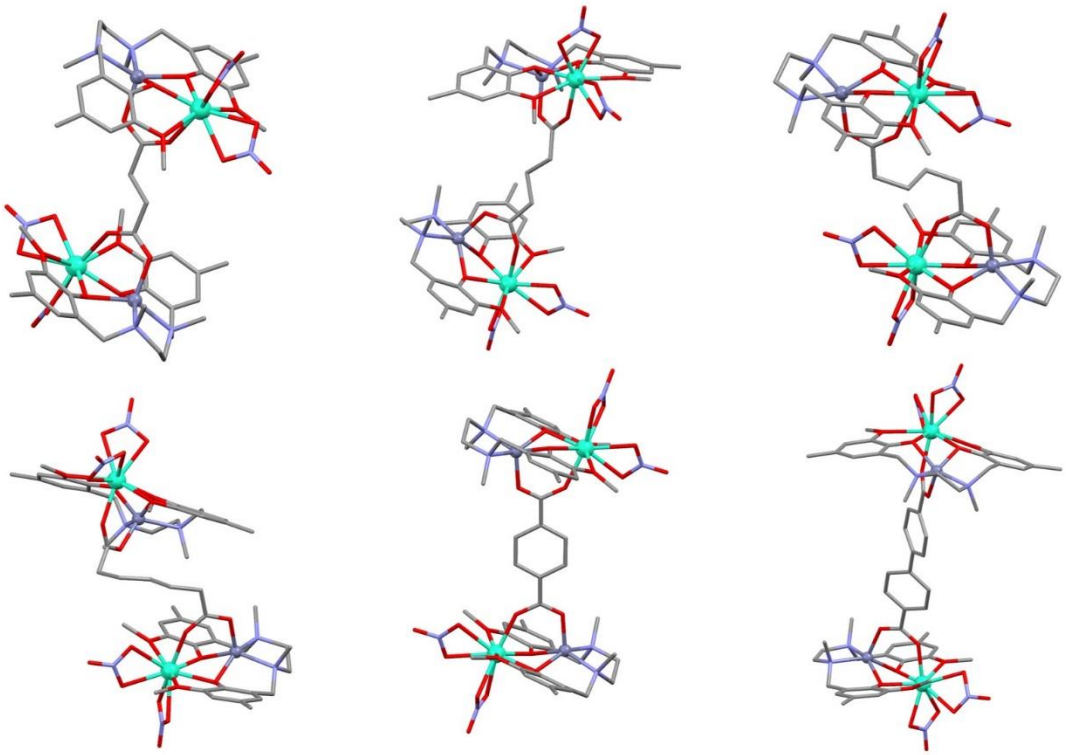

2.3. irudia.- 8-13 konposatuen ikuspegia. Kolore-kodea: disprosio, zink, nitrogeno, oxigeno eta karbono atomoak turkesa, gris ilun, urdin argi, gorri eta gris kolorez, hurrenez hurren. Hidrogeno atomoak eta disolbatzaile molekulak ez dira irudikatu argitasunaren mesedetan.

Dikarboxilatoen ordez trimesato trikarboxilatoa erabiltzen denean, **14** eta **15** konposatu hexanuklear eta oktanuklearra lortzen dira, hurrenez hurren. Bat edo beste lortzeko estekiometriarekin jokatzen da. Koordinazio-inguruneari dagokionez, DyO_9 koordinazio-esferak, **14** konposatuan, **8**-**13** sistemetako joera bera jarraitzen du (Dy^{III} esfera desberdin bakarra dago C_3 simetria ardatza dela eta). Dy-$O_{fenoxido/karboxilato}$ lotura-distantzia dira laburrenak (2,2764(17) – 2,3122(17) Å), Dy-O_{NO3} tartekoak (2,4372(19) – 2,4858(19) Å) eta Dy-O_{metoxi} motakoak dira luzeenak (2,510(2)-2,5724(18) Å). Egituraren barruan, kloroformo-kristalizazio molekula batek funtsezko eginkizuna betetzen du molekularen tolesturan (A2.1. irudia). Disolbatzaile molekula trimesatoaren eraztun aromatikoarekiko C-H$\cdots\pi$ molekularteko interakzio bidez (H$\cdots$Erazt.$_{zentroide}$ distantzia 2,401 Å-ekoa da) eta Cl$\cdots\pi$ interakzio bidez egonkortzen da. Horrela, trimesatoaren eraztunaren alde bietan sortzen diren barrunbeek ez dute tamaina bera, txikiagoa delarik kloroformo molekula duena (A2.1. irudia). Estekatzaile nagusien eraztunen zentroideen arteko distantzia 8.726 Å-ekoa da kloroformo molekula dagoen barrunbean. Bestalde,

beste barrunbeko eraztunen zentroideen arteko distantzia 10.881 Å-ekoa da. Honek frogatzen du haloformoak egitura tolesten duela eta, ondorioz, entitate dinuklearrak euren artean paraleloak ez izatera behartzen ditu. Molekula barneko Dy···Dy distantziak 10,123 Å-ekoak dira.

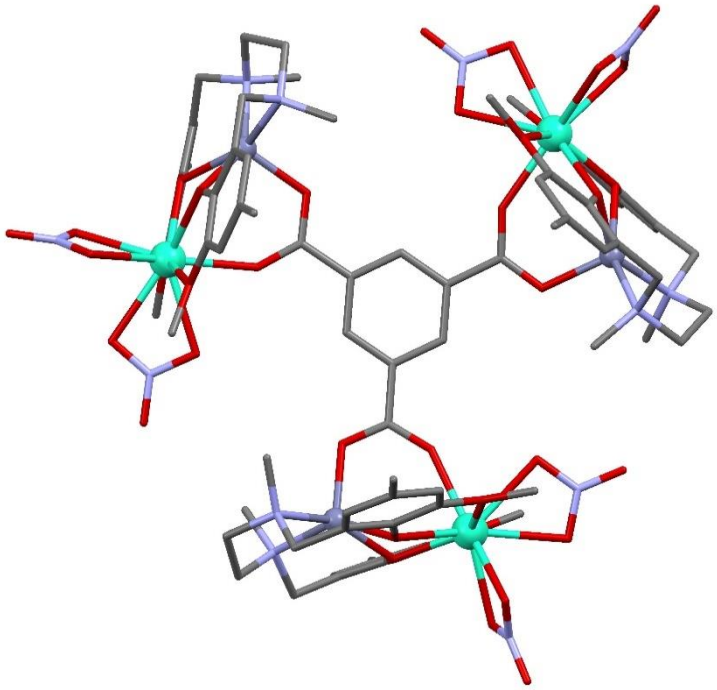

2.4. irudia.- 14 konposatuaren egitura. Kolore-kodea: disprosio, zink, nitrogeno, oxigeno eta karbono atomoak turkesa, gris ilun, urdin argi, gorri eta gris kolorez, hurrenez hurren. Hidrogeno atomoak eta disolbatzaile molekulak ez dira irudikatu argitasunaren mesedetan..

15 konposatua erreakzio-ingurunean azido trimesiko kontzentrazioa handitzean lortzen da. Aipatu bezala, oinarrizko bi unitate mota ditu: $[ZnDyL(NO_3)_2]^+$ eta $[ZnDyL(NO_3)]^{2+}$, bakoitzetik bi. Horiek, bi trimesato zubirekin daude lotuta, lehen motakoak unitate terminalak izanik eta, bigarrenak, molekula barnekoak. Posizio terminalean dauden unitate dinuklearrek **14** konplexuaren atomoen kokapen bera erakusten dute. Aitzitik, barneko gunean daudenek karboxilato kelato talde bat dute Dy^{III} ioira koordinatua nitrato baten ordez. Hala ere, atomoen antolamenduak berdina izaten jarraitzen du. Lotura-distantzien joera ia konstante mantentzen da, $Dy\text{-}O_{fenoxido/karboxilato}$ lotura laburrak (2,235(9) - 2,302(8) Å), $Dy\text{-}O_{NO3}$ tartekoak (2,433(9) - 2,496(9) Å) eta $Dy\text{-}O_{metoxi}$ lotura luzeak (2,496(10) - 2,644(10) Å) neurtu dira. Hala ere, karboxilato kelato taldeen lotura-distantziak apur bat ezberdinak dira: Dy1B-O6TR laburtzat har baitaiteke

(2,345(9) Å) eta Dy1B-O5TR, berriz, luzetzat (2,612(8) Å). Molekularen barruan, bi trimesato zubiak, bi entitate dinuklear terminalak eta barne sistema dinuklearrak paraleloak dira euren artean. Minimoa den arren, 0,157 Å-eko tartea dago bi trimesato eraztunek sortutako planoen artean. Lau DyIII ioiak, bestalde, guztiz planokideak dira (2.5. irudia, eskuinean). Amaitzeko, molekula barneko Dy1A···Dy1B, Dy1A···Dy1B(iv: 1-x, 1-y, -z) eta Dy1A···Dy1A(iv) distantziak 9,968(1), 11,041(1), 8,218(1) and 19,364(2) Å-ekoak dira, hurrenez hurren.

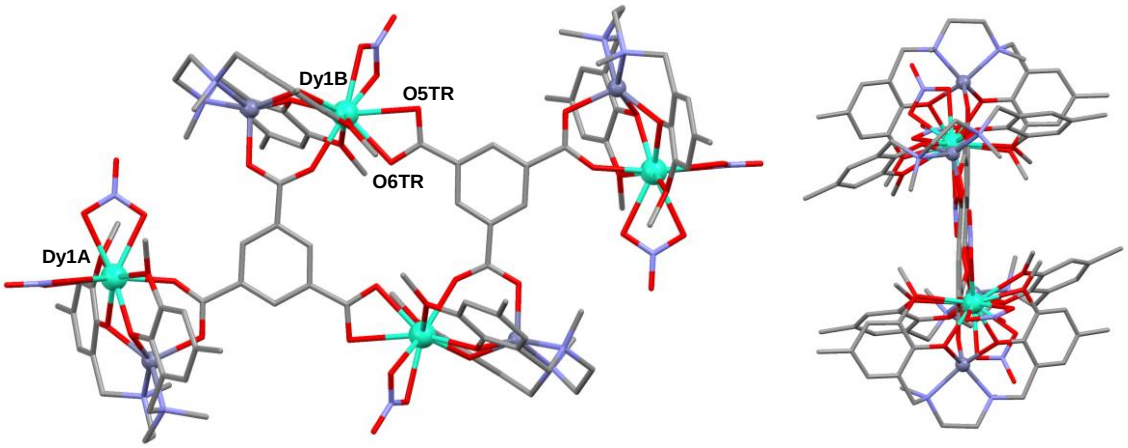

2.5. irudia- 15. konposatuaren bi ikuspegi. Kolore-kodea: disprosio, zink, nitrogeno, oxigeno eta karbono atomoak turkesa, gris ilun, urdin argi, gorri eta gris kolorez, hurrenez hurren. Hidrogeno atomoak ez dira irudikatu argitasunaren mesedetan.

2.4.5. 7-15, 7_{Gd} eta 14_{Gd} konplexuen propietate magnetiko estatikoak

Suszeptibilitate magnetikoaren tenperaturarekiko mendekotasuna **7-15**, $\mathbf{7_{Gd}}$ eta $\mathbf{14_{Gd}}$ konposatuen lagin polikristalinoetarako neurtu zen, 2-300 K tenperatura tartean 0,1 T-ko kanpo eremu magnetikoa erabiliz (2.6., 2.7. eta A2.19. irudiak). Giro-tenperaturan, **7** konposatuarentzat neurtutako 28,54 $cm^3 \cdot mol^{-1} \cdot K$-eko $\chi_M T$ balioa bat dator interakzionatzen ez duten bi Dy^{III} ioientzat espero den balioarekin (14,17 $cm^3 \cdot mol^{-1} \cdot K$; $^6H_{15/2}$, and g = 4/3). Tenperatura jaitsi ahala, $\chi_M T$ ere jaisten doa Stark azpimailen despopulazioa dela eta 20,54 $cm^3 \cdot mol^{-1} \cdot K$-eko baliora heldu arte 2,0 K-etan. 2-7 K tenperatura tartean neurtutako magnetizazio kurbak (grafika txikia) ez dira saturaziora heltzen eta ez dira gainezargarriak, anisotropiaren eragina izan daitekeena.

$\chi_M T$ balioaren jaitsiera truke-interakzio antiferromagnetikoen ondorio ere izan daitekeenez, horiek eztertzeko helburuarekin, $\mathbf{7_{Gd}}$ konposatuaren propietateak aztertu

dira. Giro-tenperaturako 15,68 $cm^3 \cdot mol^{-1} \cdot K$ balioa esperotakotik oso hurbil dago bi Gd^{III} ioientzat (7,88 $cm^3 \cdot mol^{-1} \cdot K$; $^8S_{7/2}$, and $g = 2$). Balio hau ia konstante mantentzen da 300-10 K tenperatura tartean igotzen hasi aurretik 2,0 K-etako 18,55 $cm^3 \cdot mol^{-1} \cdot K$ balio maximoa lortu aurretik. Azken igoera hau molekula barneko truke-interakzio ferromagnetiko ahulek eragindakoa da. $\chi_M T(T)$ kurba ondoko eredu sinplera doitu da PHI softwarea erabiliz [12]:

$$\hat{H} = -J\hat{S}1 \cdot \hat{S}2 \quad 2.2. ekuazioa$$

Doiketak J = 0,015 cm^{-1}-eko balioa ematen du g = 1,99 balioarekin truke-interakzio ferromagnetiko-ahularen presentzia frogatuz. 2,0 K-etan neurtutako magnetizazio kurbak igoera zorrotza erakusten du 2 T-ra heldu arte, ondoren igoera lineala erakutsiz 13,63 μ_B-ra heldu arte. Balio hau bi Gd^{III} ioi indibiduali dagokion 14,0 μ_B-ra ondo egokitzen da. Izan ere, 2,0 K-etako kurba ondo erreproduzitzen du Brillouin funtzioak bi Gd^{III} ioi isolaturentzeko interakzio ahulen presentzia frogatuz.

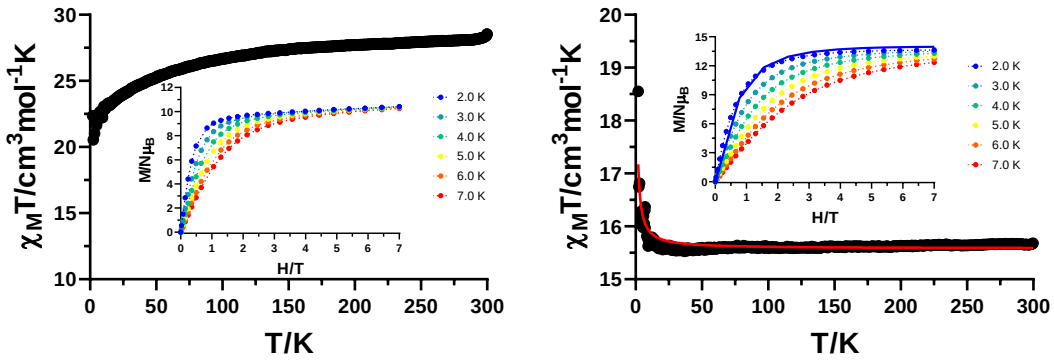

2.6. irudia- $\chi_M T$ balioaren tenperaturarekiko mendekotasuna 1000 Oe-ko eremu magnetikoa erabiliz **7** (ezkerrean) eta $\mathbf{7_{Gd}}$ (eskuinean) konplexuentzat. Grafiko txikia: 2-7 K tenperatura tartean neurtutako magnetizazio kurbak. Marra jarraiak Brillouin funtzioa irudikatzen du.

8-15 konposatuentzat honako $\chi_M T$ balioak neurtu dira giro-tenperaturan: 28.47, 27.97, 28.53, 28.52, 28.20, 28.30, 42.66 and 57.29 $cm^3 \cdot mol^{-1} \cdot K$. Balio horiek esperotako tartean sartzen dira bi (**8-13**), hiru (**14**) eta lau (**15**) interakzionatzen ez duten Dy^{III} ioietarako (2.7. irudia). **7** konplexuan ez bezala, ioi paramagnetikoen artean zubi zuzenik ez dagoenez, giro-tenperaturatik 2,0 K-etaraino ematen den jaitsiera jarraia Stark azpimailen despopulazioagatik gertatzen dela esan dezakegu. Kasu hauetan ere, magnetizazio kurbak ez dira saturazio balioetara heltzen eta ez dira gainezargarriak,

hortaz, anisotropia magnetikoaren presentzia adierazi dezakete. Dena den, **14**$_{Gd}$ konposatuaren propietate magnetiko estatikoak ere aztertu ditugu. Sistema triangular honetan Dy^{III} ioien anisotropia-ardatzek duten orientazioa (eztabaida beherago, A2.110. irudia) egokia izan daiteke momentu toroidalak behatzeko [13–15]. Hala ere, egia da halakorik ikusi ahal izateko truke-interakzioek nahiko indartsuak izan behar dutela. Espero zen bezala eta A2.19. irudian ikus daitekeen bezala, ez da interakziorik antzematen ioi metalikoen artean.

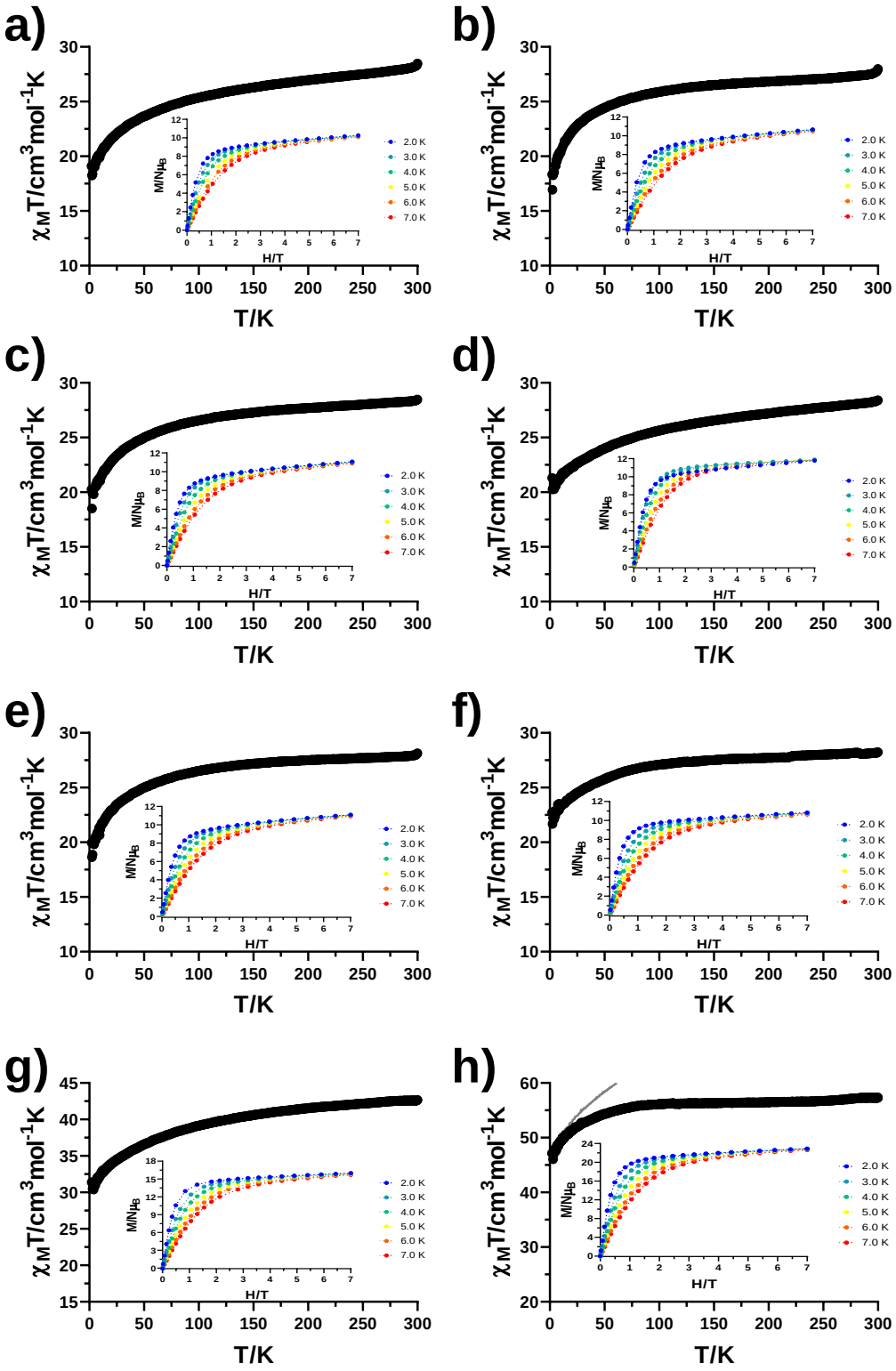

2.7. irudia.- $\chi_M T$ balioaren tenperaturarekiko mendekotasuna 1000 Oe-ko eremu magnetikoa erabiliz **8-15** konplexuentzat (a)-tik h)-ra, hurrenez hurren). Grafiko txikia: 2-7 K tenperatura tartean neurtutako magnetizazio kurbak. Marra etenek ez dute esanahi fisikorik.

2.4.6. 7-15 konposatuen propietate magnetiko dinamikoak

Bederatzi konposatuen propietate magnetiko dinamikoak egiaztatzeko *ac* korronte alternoko neurketak egin dira, bai kanpoko eremu magnetikorik aplikatu gabe eta baita 1 kOe-eko eremu aplikatuarekin ere, bi kasuetan 3,5 Oe-eko eremu oszilatzailearekin. Hau **7-15** konposatu puru eta $\mathbf{7_{DyY}}$-$\mathbf{15_{DyY}}$ dilituentzako egin da frekuentzia altuenean (10000 Hz). Modu honetan, *SMM* propietateen ebaluaketa azkarra egiten da (A2.21.A2.30. irudiak). Gauza jakina da Dy^{III} ioian oinarritutako konposatuek kristal-eremu axial zorrotzik gabe, sarritan ez dutela maximorik erakusten fasez kanpoko suszeptibilitate osagaian (χ''_M) *dc* kanpoko eremu magnetikorik aplikatu gabe *QTM* indartsuaren ondorioz. Gainera, molekula barruko edo molekularteko interakzio ahulek tunel efektua ahalbidetzen laguntzen duten zeharkako eremuak sor ditzakete, erlaxazio magnetiko motela ezkutatuz. Bi egoera horiek gainditzeko, M_J egoeren degenerazioa apurtzen duen kanpoko eremu magnetikoa erabil daiteke, *QTM* erabat edo partzialki ezabatuz, edo zentro paramagnetikoak matrize diamagnetiko batean diluitu daitezke (Y^{III} kasu honetan). Beraz, aurreanalisi honek ikuspegi orokor bat ematen digu, teknika horien eraginkortasunaz beste neurketa batzuk egin aurretik.

Kanpoko eremu magnetikorik aplikatu ezean, konposatu puruetako batek ere ez du maximorik erakusten fasez kanpoko osagaian. Hala ere, alde batetik, diluitutako $\mathbf{7_{DyY}}$, $\mathbf{11_{DyY}}$ eta $\mathbf{13_{DyY}}$ konposatuek nahiko ondo definitutako maximoak ematen dituzte 9 K, 7,5 K eta 11 K-en azpitik, hurrenez hurren. Konposatu hauetan, molekula barneko nahiz molekularteko interakzio dipolarrak (gogoratu $\mathbf{7_{Gd}}$ konposatuarentzat kalkulatutako truke-interakzioaren balioa ia arbuiagarria zela) ezabatzeak partzialki desaktibatzen du QTM efektua kanpoko eremu magnetikorik gabe *SMM* propietatea bistaratuz. Bestalde, $\mathbf{8_{DyY}}$ eta $\mathbf{9_{DyY}}$ konposatuek 5 K-etik behera ondo definitu gabeko maximoak dituzte. Kasu hauetan guztietan, maximoen azpitik agertzen diren seinale handiak *QTM* desaktibatu gabearen adierazle dira. Neurketak 1000 Oe-eko kanpoko eremu magnetiko arbitrario baten pean errepikatzean, konposatu guztiek maximo bat erakusten dute, gutxienez, $\chi''_M(T)$ grafikan, agerian utziz eremuak eragindako *SMM* portaera. Baldintza horietan desberdintasun nabarmen batzuk ikus daitezke konposatu diluitu eta puruen artean. **7** tetranuklearraren kasuan, kanpoko eremu magnetikoaren eta diluzio diamagnetikoaren arteko konbinazioak nahi ez den *QTM* efektuaren erabateko ezabatzea dakar. Sukzinato zubidun **8** molekularen kasuan, *QTM* arrakastaz ezabatzen da kanpoko eremu bat aplikatuz, baina analogo diluituak hobeto definitutako maximoa erakusten du, aldi berean, maximoa tenperatura altuagotara desplazatuz. **9** konplexuak bi maximo erakusten ditu, diluitzerakoan bere horretan mantentzen direnak. Adipato zubia duten

konposatuentzat ez da **10** eta **10$_{DyY}$** arteko alde nabarmenik ikusten, baina tenperatura-aldaketa positibo txiki bat gertatzen da tenperatura baxuko maximoarentzat eta tenperatura altuagoko sorbaldarentzat. Kanpoko eremurik aplikatu gabe **11$_{DyY}$**-rako ikusten den maximoa ondo definitzen da **11** eta **11$_{DyY}$** sistementzat kanpoko eremua aplikatzean (tunel-efektua desaktibatuz). **12$_{DyY}$** analogo diluituak emaitza interesgarriak erakusten ditu, izan ere maximo/sorbalda gehigarria agertzen da 9 K-etik behera **12** puruan agertzen ez dena. **13$_{DyY}$** kasuan, kanpoko eremu magnetikorik gabeko neurketan ikusitako maximoaz gain, maximo gehigarri bat ikus daiteke tenperatura baxuan, konposatu puruarentzat ere agertzen dena. **14** konposatuak gainjarritako maximoak ditu 5 K inguruan, **14$_{DyY}$** konposatuak, berriz, maximo zabal bakarra erakusten du. Azkenik, **15** eta **15$_{DyY}$** oktanuklearrek antzeko portaera erakusten dute. Tenperatura baxuenen ongi definitutako maximoa dute eta 15 K inguruan sorbalda itxurako seinalea detektatzen da. Hori guztia kontuan hartuta, kanpoko eremu magnetikoa optimizatzeko, **9**, **11** eta **15** laginak erabili dira puruen kasuan, eta **7$_{DyY}$**-**8$_{DyY}$**, **10$_{DyY}$** eta **12$_{DyY}$**-**14$_{DyY}$** diluituenean. Gainera, frekuentzia eta tenperaturarekiko mendekotasuna aztertu da **7$_{DyY}$**, **11$_{DyY}$** eta **13$_{DyY}$** sistementzat kanpoko eremu magnetikorik aplikatu gabe.

1,5 kOe-eko kanpoko eremu magnetiko optimopean, **7** konposatuak 10 K-etik gora ondo definitutako maximo multzoa erakusten du, maximo horien azpitik desaktibatu gabeko *QTM* nabarmena izanik (2.8. irudia, goian). Erlaxazio-denborak eta α balioak $\chi''_M(\upsilon)$ eta $\chi''_M(\chi'_M)$ kurbak Debyeren eredu orokorrera doituz lortu dira 5,0-10,5 K-eko tenperatura-tartean (A2.50.-A2.51. irudiak). α balio altuek (0,48 (5,0 K) - 0,29 (10,5 K)) eta Arrheniusen grafikoan erlaxazio-denboren kurbadurak erlaxazio-prozesuen banaketa zabala adierazten dute. Hala ere, tenperatura altueneko zati lineala, non Orbach mekanismoak eragiten duen batez ere, Arrheniusen legera egokitzen da 65,7 K-eko energia-barrera efektiboa eta $\tau_0 = 2{,}9\cdot10^{-8}$ s-ko balioa lortuz (konplexu guztientzat lortutako balioak 2.2. taulan agertzen dira). Dena den, datuak tenperatura tarte osoan aldibereko Orbach eta Raman prozesuak kontuan hartzen dituen ekuaziora doitu daitezke, α balioekin adostasunean:

$$\tau^{-1} = BT^n + \tau_0^{-1}exp(-U_{eff}/k_BT) \qquad \text{2.3. ekuazioa}$$

Doikuntzak ondorengo parametroak ematen ditu: $B = 1{,}8\ s^{-1}K^{-4{,}192}$, $n = 4{,}192$, $\tau_0 = 3{,}1\cdot10^{-9}$ s eta $U_{eff} = 96{,}5$ K. Kramers ioientzat n = 9 espero bada ere,1-6 arteko balioak ere zentzuzkotzat har daitezke fonoi optikoen eta akustikoen presentzia kontuan hartzean [16]. **7$_{DyY}$** analogo diluituak *SMM* portaera erakusten du kanpoko eremu magnetikorik aplikatu gabe, 8,5 K-etik beherako maximoak erakutsiz. Honek, *dc* propietate magnetikoetatik ateratako ondorioekin batera, adierazten du SMM portaera

ioi indibidualetatik eratorria dela. $\mathbf{7_{DyY}}$ konposatuarentzat erabilitako 1:10 diluzio magnetikoarekin, zentro paramagnetikoek behar bezain urrun egon behar dute, eta 2.8. irudian bistaratutako *ac* maximoak, beraz, DyY unitatean oinarritutako molekularenak dira. Konposatu diluituak kanpoko eremuaren beharrik gabe *SMM* portaera edukitzea adierazgarria da. **7** puruan molekula barneko edo molekularteko interakzioek *QTM* ahalbidetzen duten zeharkako eremuak sortzen dituztela adierazten du. Definizio handirik gabeko maximoak eta tenperatura baxuko isats luzeek desaktibatu gabeko tunel-efektua adierazle dute. Aztertutako tenperatura tartean lortutako α balio handiek (0,59 (2,0 K) - 0,28 (9,2 K)) eta erlaxazio-denboren kurbadurak ondo adierazten dute erlaxazio-bide desberdinek hartzen dutela parte magnetizazioaren erlaxazioan. Tenperatura altuenetan agertzen den zati linealak Arrheniusen legeari jarraitzen dio eta doikuntzak U_{eff} = 43,0 K eta τ_0 = $1{,}6\cdot10^{-7}$ s balioak ematen ditu. Tenperatura-tarte osoa kontuan hartuz gero, ordea, datuen doikuntza onena *QTM* eta Orbach prozesuak elkartzen dituen ondoko ekuazioak ematen du:

$$\tau^{-1} = \tau_{QTM}^{-1} + \tau_0^{-1}exp(-U_{eff}/k_BT) \qquad \textit{2.4. ekuazioa}$$

Honako balio hauek lortu dira τ_{QTM}, τ_0 eta U_{eff} parametroentzako: $1{,}4\cdot10^{-4}$ s, $1{,}4\cdot10^{-7}$ s eta 45,9 K, hurrenez hurren. Neurketa 1,5 kOe-eko eremu optimo baten pean egitean, aurretik desaktibatu gabe geratutako tunela erabat deuseztatzen da. Hala ere, lehenago detektatu gabeko bigarren maximo multzo bat ikus daiteke frekuentzia altuetan. Kasu berezi honetarako, erlaxazio-denborak eta α balioak batera lortzen dira $\chi''_M(\chi'_M)$ kurbak CCFIT softwarearekin [17] doituz. Arrheniusen grafikoan zati linealak lortu dira bai erlaxazio azkarrerako (*FR, Fast Relaxation*) bai erlaxazio motelerako (*SR, Slow Relaxation*). Doikuntzak 52,3 K-eko U_{eff} eta τ_0 = $10\cdot10^{-8}$ s balioak ematen ditu *FR*-rako eta 102,2 K-eko U_{eff} eta τ_0 = $4{,}7\cdot10^{-9}$ s balioak *SR*-rako. Aipatzekoa da, halaber, *QTM*ren desaktibazioa α parametro txikiagoetan ere islatzen dela (0,29 (7,8 K) - 0,37 (11,8 K) *FR* eta 0,12 (7,8 K) - 0,08 (11,8 K) *SR*). *FR*-ko joera kontrajarria (balioak handitu egiten dira tenperatura igo ahala) bi prozesuen nahasketaren bidez azal daiteke, tarteko tenperaturetan bi mekanismoek erlaxatzen laguntzen baitute; tenperatura baxuagoetan eta altuagoetan, aldiz, horietako bakar batek bakarrik jarduten du.

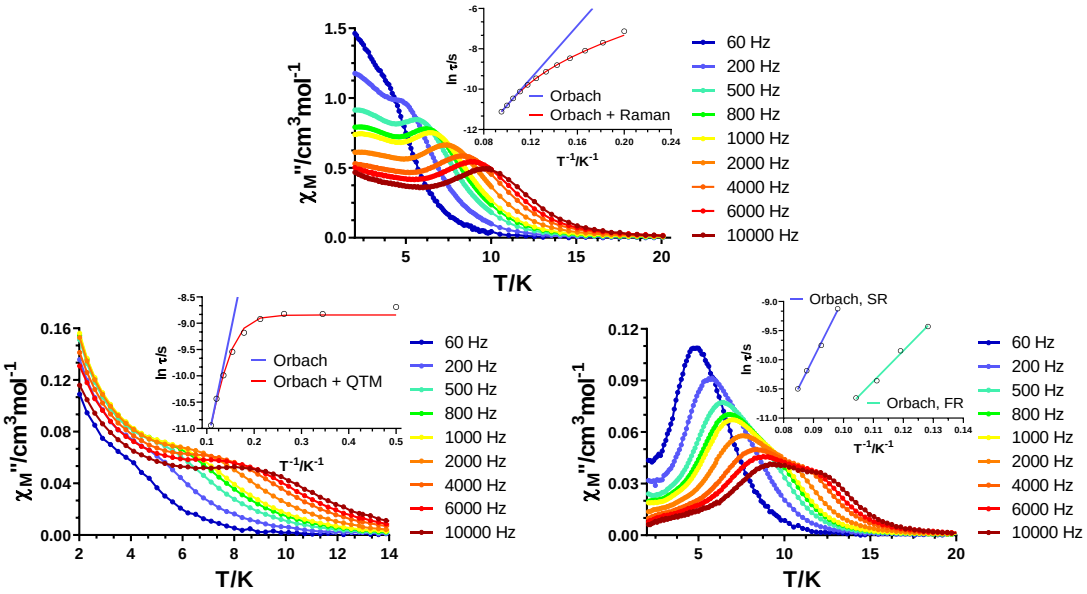

2.8. irudia.- Fasez kanpoko suszeptibilitatearen tenperaturarekiko mendekotasuna hainbat frekuentziatan 1,5 kOe-etako kanpo eremu magnetikopean (goian) **7** konposatuarentzat eta kanpoko eremu magnetikorik aplikatu gabe (behean ezkerrean) eta 1,5 kOe-etako kanpoko eremu magnetikopean (behean eskuinean) $\mathbf{7_{DyY}}$ diluituarentzat. Grafiko txikia: Arrheniusen grafikoa erlaxazio-denboretarako Orbach mekanismoa kontuan hartuz (lerro urdin eta turkesak) eta hainbat prozesu bateratuz (lerro gorriak).

8 konposatuarentzat 750 Oe-eko eremu optimoan egindako neurketek seinale zabalak erakusten dituzte fasez kanpoko osagaian (2.9. irudia). Hori gainjarritako bi maximoren ondorio izan daitekeen arren, datuak Debyeren eredu bakar baten bidez ebaluatu dira, ezin izan baitira bi prozesu bereizi ez Cole-Cole ez $\chi''_M(\upsilon)$ grafikoetan. Tenperatura altuenetako erlaxazio-denborak Arrheniusen legera egokitu dira, U_{eff} = 35,5 K eta $\tau_0 = 6{,}6\cdot10^{-8}$ s balioak lortuz. $\mathbf{8_{DyY}}$ analogo diluituarentzat neurketa bera egitean, maximoak askoz hobeto definitzen dira. Horrek adierazten du molekularteko edo barneko interakzio dipolarrek erlaxazioaren portaera dinamikan eragina dutela. Datuak Arrheniusen legera doituz, energia-barrera efektibo altuxeagoa lortu da 50,9 K-eko balioarekin eta $\tau_0 = 3{,}3\cdot10^{-10}$ s balioarekin. Hainbat erlaxazio mekanismo bateratuz doikuntzak egiten ere saiatu gara, baina ez dugu zentzuzko doikuntzarik lortzerik izan.

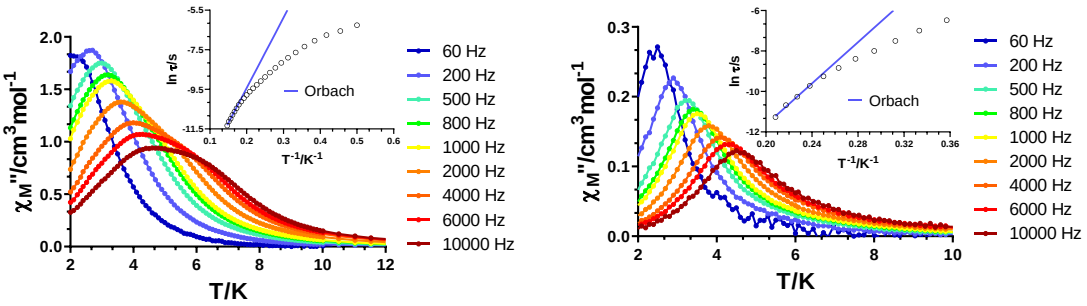

2.9. irudia.- Fasez kanpoko suszeptibilitatearen tenperaturarekiko mendekotasuna hainbat frekuentziatan 750 Oe-etako kanpo eremu magnetikopean **8** (ezkerrean) eta $\mathbf{8_{DyY}}$ (eskuinean) konposatuentzat. Grafiko txikia: Arrheniusen grafikoa erlaxazio-denboretarako Orbach mekanismoa kontuan hartuz.

9 konposatuaren kasuan, lagin hutsa bakarrik aztertzen da, analogo diluituarentzat ez baita alde nabarmenik ikusi. 1,5 kOe-eko eremu magnetikopean $\chi''_M(T)$ kurbek ondo bereizitako bi maximo multzo erakusten dituzte, bata *FR*ri lotua 2,2-3,2 K-eko tartean eta bestea *SR*ri 3,2-5,2 K-eko tartean (2.10. irudia). Beraz, datuak berriz ere CCFITen softwarearekin aztertu dira eta hortik prozeu bakoitzarentzat erlaxazio-denborak lortuz. 2,3-2,9 K eta 3,0-5,6 K tenperatura-tarteetako erlaxazio-denborek mendekotasun lineala erakusten dute *FR* eta *SR* prozesuentzat. Datuen doikuntzak ondorengo parametroak ematen ditu U_{eff} eta τ_0 balioentzat: 15,9 K eta $4{,}5\cdot10^{-7}$ s *FR*rentzat eta 32,0 K with $8{,}0\cdot10^{-8}$ s *SR*rentzat. Datuen baliotasuna frogatzeko, $ln(1/(2\cdot\pi\cdot\upsilon))$ *vs* T^{-1} ere irudikatu da maximo bakoitzaren posizioa kontuan hartuz. Doikuntza alternatibo honek 19,5 K eta $6.6\cdot10^{-8}$ s eta 39,9 K eta $7{,}7\cdot10^{-9}$ s balioak ematen ditu U_{eff} eta τ_0 parametroentzat FR eta SR prozesuentzat, hurrenez hurren. CCFIT softwarearekin lortutako datuen antzekoak izanik, fidagarritasuna frogatzen da.

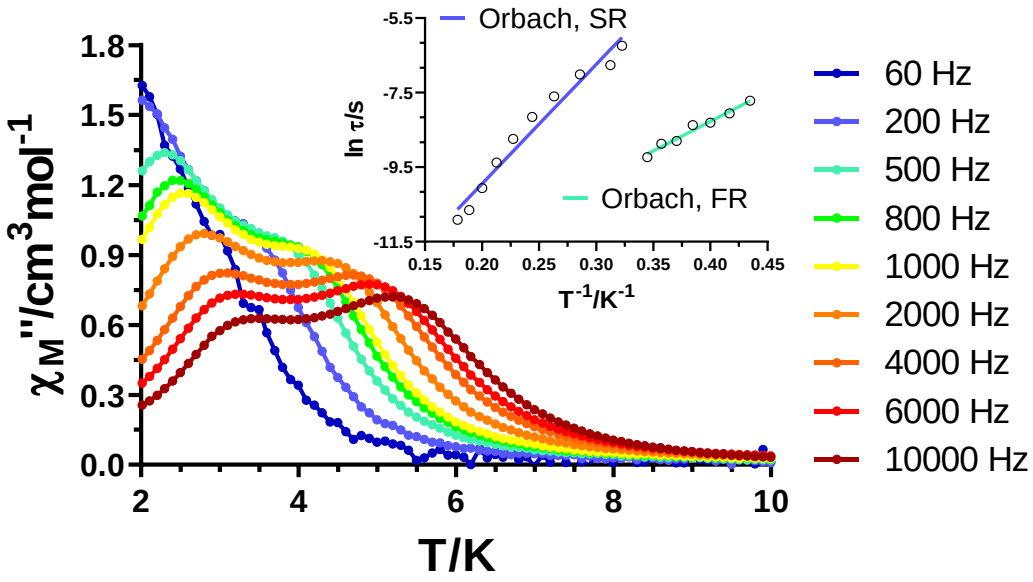

2.10. irudia.- 9 konposatuarentzat, fasez kanpoko suszeptibilitatearen tenperaturarekiko mendekotasuna hainbat frekuentziatan 1,5 kOe-etako kanpo eremu magnetikopean. Grafiko txikia: Arrheniusen grafikoa erlaxazio-denboretarako Orbach mekanismoa kontuan hartuz.

10 konposatua ere diluitu gabe aztertzen da, diluitzean ez baita alde nabarmenik ikusi. Agerikoa ez bada ere, $\chi''_M(T)$ grafiketan bi prozesu bereiz daitezke: lehenengoa 2,0-2,5 K artean eta bigarrena 5,0 K-etik behera. Hala ere, datuak aztertzeko, $\mathbf{7}_{DyY}$ eta **9** konposatuetarako erabili ez den estrategia baliatu da. Kasu honetan, 2,0-2,9 K eta 3,8-5,2 K arteko $\chi''_M(\upsilon)$ kurbak modu independentean doitu ahal izan dira, *FR* eta *SR* prozesuen erlaxazio-denborak lortzeko, hurrenez hurren (A2.68. eta A2.70. irudiak). Lehenengoarentzat, kurba guztiek frekuentziarekiko desplazamendu argia erakusten dute tenperatura igo ahala, tenperaturaren mendeko Orbach mekanismoa islatuz. Bigarrenarentzat, aldiz, frekuentziarekiko desplazamendu ia nulua ikusten da tenperatura baxuenetarako, *QTM*ri egotz dakiokeena. Tenperatura altuenetan eragin hori desagertu egiten zaien (A2.70. irudia). Horrela, erlaxazio-denborek hartzen duten forma ez da harritzekoa. *FR*ak tenperatura-tarte osoan zati erabat lineala erakusten du, *SR*ak tenperatura baxuenetan tenperaturarekiko independentea den portaera erakusten duen bitartean. Dena den, egia da tenperaturarekiko independentea den zonaldea FRren seinale intentsoagoak eragindakoa ere izan daitekeela. Zati linealak Arrheniusen

legera doituz U_{eff} eta τ_0 balioak lortu dira: 15,6 K eta $9{,}6\cdot10^{-8}$ s (*FR*) eta 24,2 K eta $1{,}8\cdot10^{-7}$ s (*SR*) balioekin.

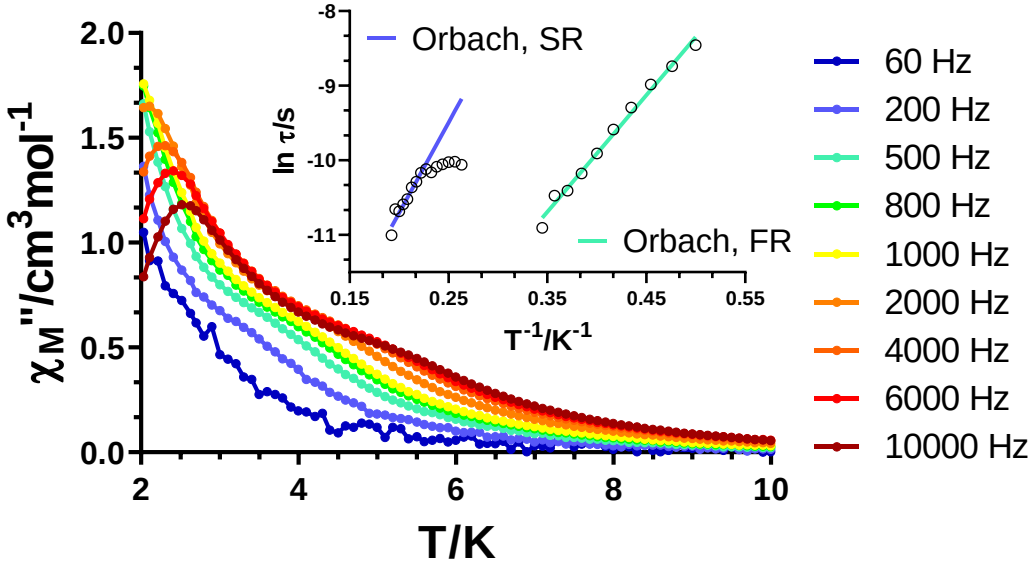

2.11. irudia.- 10 konposatuarentzat, fasez kanpoko suszeptibilitatearen tenperaturarekiko mendekotasuna hainbat frekuentziatan 1 kOe-etako kanpo eremu magnetikopean. Grafiko txikia: Arrheniusen grafikoa erlaxazio-denboretarako Orbach mekanismoa kontuan hartuz.

Aipatu bezala, **11** konposatuarentzat 1,5 kOe-eko kanpoko eremu magnetiko optimoa aplikatzea nahikoa izan da *QTM* guztiz ezabatzeko eta eremuak eragindako *SMM* portaera bistaratzeko (2.12. irudia). Gainera, sistema matrize diamagnetikoan diluitzeak ez du hobekuntza esanguratsurik ekartzen. 3,9-7,8 K-eko tenperatura tartean ongi definitutako maximo multzoa hautematen da, desaktibatu gabeko *QTM* efekturik gabe. Arrheniusen irudikapenak joera lineala erakusten du erlaxazio-denboretarako tenperatura-tarte osoan eta horrek Orbach mekanismo bakarra iradokitzen du. Azken hori bat dator kalkulatutako α balio baxu xamarrekin (0,24 (4,4 K) - 0,15 (8,8 K)). Doikuntzak U_{eff} = 42,3 K eta $\tau_0 = 1{,}5\cdot10^{-7}$ s balioak ematen ditu. $\mathbf{11}_{\mathbf{DyY}}$ diluituak, hein batean, $\mathbf{7}_{\mathbf{DyY}}$ materialaren antzeko portaera du. Dy^{III} ioi paramagnetikoen artean zubi motzik ez dagoen arren, diluzio magnetikoaren bidez molekula barneko eta molekularteko interakzioak ezabatzeak, $\mathbf{11}_{\mathbf{DyY}}$ konposatuan aplikatutako kanpoko eremu magnetikorik gabe *SMM* portaera azaleratzea eragiten du (2.12. irudia, eskuinean).

Maximoen posizioek bere horretan jarraitzen dute, baina tenperatura baxuetan desaktibatu gabeko *QTM* detektatzen da. Erlaxazio-denboren doikuntza linealak U_{eff} = 34,2 K eta τ_0 = 2,1·10^{-7} s balioak ematen ditu, lagin puruaren termikoki aktibatutako zonarekin bat datozenak. Cole-Cole grafikoetatik ateratako α balioak eta erlaxazio-denboren distribuzioa bat datoz hainbat erlaxazio-mekanismorekin, QTM barne. Hortaz, tenperatura-tarte osoko datuak 2.4. ekuaziora doitzen dira ondoko parametro balioak lortuz: τ_{QTM} = 1,4·10^{-4} s, τ_0 = 5,9·10^{-8} s and U_{eff} = 44,6 K. Bi neurketa hauek erakusten duten bezala, kanpoko eremu magnetikoa aplikatzea diluzio magnetikoa baino estrategia eraginkorragoa da tunel-efektua deuseztatzeko. **11$_{DyY}$** konposatua kanpoko eremu magnetikopean neurtzean, ez dira **11** puruarentzat ikusitako propietateak hobetzen. Ondorioz, ez da jarraitzen ikerketarekin.

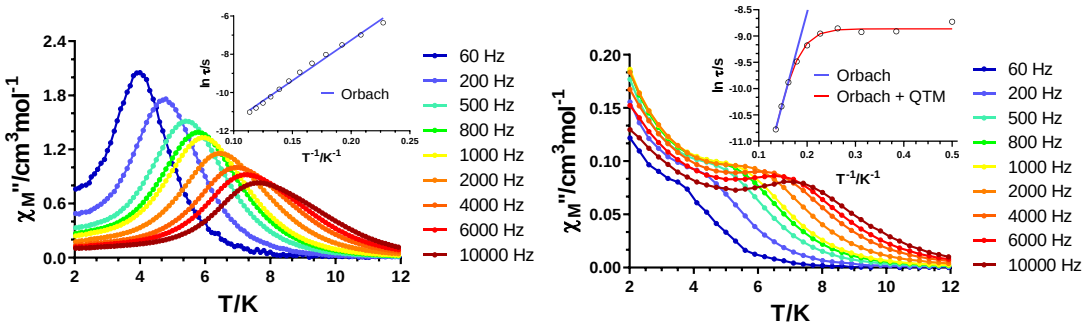

2.12. irudia.- Fasez kanpoko suszeptibilitatearen tenperaturarekiko mendekotasuna hainbat frekuentziatan 1,5 kOe-etako kanpo eremu magnetikopean (ezkerrean) **11** konposatuarentzat eta kanpoko eremu magnetikorik aplikatu gabe (eskuinean) **11$_{DyY}$** diluituarentzat. Grafiko txikia: Arrheniusen grafikoa erlaxazio-denboretarako Orbach mekanismoa kontuan hartuz (lerro urdinak) eta hainbat prozesu bateratuz (lerro gorria).

Kanpoko eremu magnetiko optimo baten pean, 1,5 kOe, **12** konposatuak fasez kanpoko osagaian 2,5 K-etik beherako maximoak erakusten ditu (*FR*), ia detektatu ezin den sorbalda gehigarri batekin tenperatura altuagoetan (*SR*, 2.13. irudia, ezkerrean). Hala ere, Cole-Cole eta $\chi''_M(\upsilon)$ grafikoetan bigarren maximo multzoaren eragina argi eta garbi ikus daiteke. Izan ere, bi kasuetan, *SR* prozesuari dagozkion puntuak ikus daitezke frekuentzia txikiko eskualdean (60-200 Hz). Horrek Debyeren eredura eginiko doikuntzan eragina izan dezakeenez, ez dira kontuan hartzen (A2.79.-A2.80. irudiak). Espero bezala, α balioak 2 K-etik (0,30) 2,8 K-era (0,48) handitzen dira, bigarren erlaxazio-prozesu baten agerpenarekin bat etorriz. Erlaxazio-denborek, ordea,

linealtasuna erakusten dute aztertutako tenperatura-tartean eta, ondorioz, Arrheniusen legera egokitu dira: U_{eff} = 9,6 K eta $\tau_0 = 5{,}5 \cdot 10^{-7}$ s.

Baldintza berberetan, **12**$_{DyY}$ lagin diluituak maximoen lehen multzo bat erakusten du ia posizio berean, baina **12** puruan dagoen sorbalda hobeto definituta agertzen da kasu honetan (2.13. irudia, eskuinean). Tenperatura baxuko datuen izaera dela eta, ezin izan dira $\chi''_M(\upsilon)$ kurbak modu fidagarrian doitu, baina maximoen posizioetan oinarrituz, **12** konposatuarentzat ateratako energia-barrera efektibo antzekoa espero da ($\tau = 1/2\pi\upsilon_{max}$ hurbilketa kontuan hartuz, U_{eff} eta τ_0 parametroek 8 K eta $1 \cdot 10^{-6}$ s-ko gutxi gorabeherako balioak dituzte). Aldiz, tenperatura altuko erregimena (*SR*rekin lotutakoa) 6,8-8,8 K-eko tenperatura-tartean aztertzen da. Tenperatura baxuko $\chi''_M(\upsilon)$ kurben zabalera (A2.82. irudia) bi prozesuen nahasketa partzialaren adierazle izan litezke, α balio altuekin bat etorriko litzatekeena (0,36 6,8 K-etan). Tenperatura-tarte osoko erlaxazio-denboren portaera lineala ikusita, datuak Arrheniusen legera doitu dira U_{eff} = 36,4 K eta $\tau_0 = 4{,}6 \cdot 10^{-7}$ s lortuz. Ustez 1:10 erlazio molarreko diluzioak Dy^{III} ioi paramagnetikoak behar bezala isolatzeko nahikoa izan beharko lukeen arren, diluzio handiago bat probatu da 1:20 erlazio molarrarekin *SR* hobeto defini zitekeen ala ez ikusteko. A2.84. irudian erakusten den bezala, ez da alde nabarmenik ikusten bi diluzioen artean.

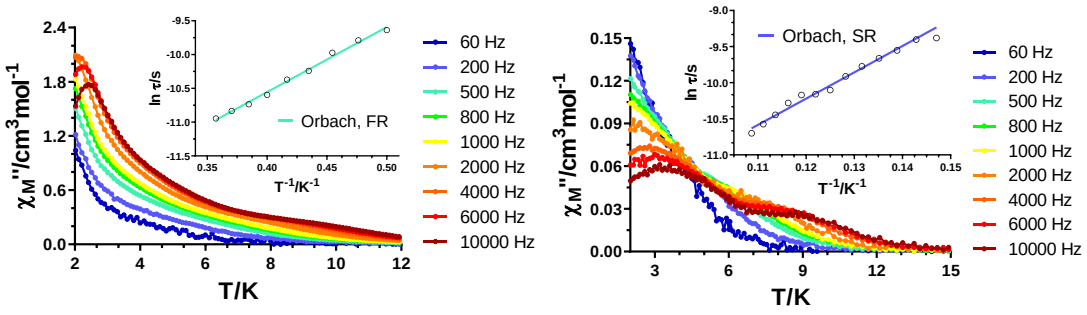

2.13. irudia.- Fasez kanpoko suszeptibilitatearen tenperaturarekiko mendekotasuna hainbat frekuentziatan 1,5 kOe-etako kanpo eremu magnetikopean **12** (ezkerrean) eta **12**$_{DyY}$ (eskuinean) konposatuentzat. Grafiko txikia: Arrheniusen grafikoa erlaxazio-denboretarako Orbach mekanismoa kontuan hartuz.

1 kOe-eko kanpoko eremu magnetiko optimopean egindako neurketek agerian utzi dute eremuak eragindako *SMM* portaera **13** sistemarentzat. Hain zuzen, maximo zabalak erakusten ditu 11 K-etik behera eta estuagoak 2,4 K-etik behera (2.14. irudia, goian). Lehen begiratuan tenperatura-tarteari dagokionez bi maximo multzoak ondo

bananduta badaude ere, tenperatura baxuenetan $\chi''_M(\upsilon)$ kurbek bi erlaxazio-prozesuen konbinazioa erakusten dute (A2.86. irudia). *FR*ari dagokion maximoa 1000 Hz ingurukoa da. Kurbaduraren formak, bestalde *SR*ari dagokiona instrumentuaren frekuentzia mugatik oso behera dagoela iradokitzen du. Hori dela eta, **10** konposatuaren datuak tratatzeko erabilitako estrategia ez da bideragarria kasu honetarako. Beraz, datuak CCFIT softwarearekin aztertu dira 2,0-11,2 K-eko tenperatura-tartean. *FR* prozesuari dagozkion erlaxazio-denborak, 2,0-2,4 K tartekoak, Arrheniusen legera egokitu dira eta U_{eff} eta τ_0 parametroak lortu dira: 4,4 K eta $7{,}5\cdot10^{-6}$ s, hurrenez hurren. *SR*ren kasuan, tenperatura altuenetako erlaxazio-denborek zati lineal argia erakusten dute, erlaxazio-mekanismo bakarra proposatuz eta α balioekin bat eginez (≈ 0). Tarteko tenperaturetako kurbadura eta tenperaturarekiko independentea den erregimen baterako joera *FR* prozesuarekin nahasteagatik ematen dela pentsa daiteke. Srri dagokion Orbach prozesurako parametro hauek lortu dira: 51,0 K eta $3{,}6\cdot10^{-7}$ s U_{eff} -rentzat eta τ_0-rentzat, hurrenez hurren.

Aurretik aipatu bezala, $\mathbf{13_{DyY}}$ konposatu diluituak *SMM* portaera du kanpoko eremurik aplikatu gabe. **13** konposatuarentzat tenperatura altuko tartean detektatutako maximoak ikus daitezke kasu honetan (2.14. irudia, behean ezkerrean). $\chi''_M(T)$ grafikoak maximoen multzo bakarra erakusten badu ere, $\chi''_M(\upsilon)$ kurbak oso baliagarriak dira kasu honetarako (A2.89. irudia). 2,0 K-etan, maximoa argi eta garbi 4000 Hz-tara agertzen da eta tenperaturarekiko mendekotasun oso txikia erakusten du, ekipoaren frekuentzia-muga altuenera (10000 Hz) 4,7 K-etan iritsiz (hamargarren kurba, kolore urdin argia A2.89. irudian). Hori bat dator erlaxazio-denbora azkarrenekin 2.14. irudiko grafika txikian, behean ezkerrean. Hala ere, tenperatura horretatik gora, maximoa frekuentzia-tarte baxuagoetara mugitzen da (4000 Hz-tik behera) eta tenperaturarekiko mendekotasun argia erakusten du tenperatura altuetarako. Gure ustez, portaera hori bi erlaxazio-prozesuren presentziarekin lotuta dago, kanpoko eremu baten presentzian analogo puruarekin gertatzen den bezala. Horrela, tenperatura-tarte osoan (2,0-11,0 K) lortutako erlaxazio-denborak bi Orbach prozesu indibidualetara doitu dira. *FR* eta *SR*-ren kasuan, Arrheniusen doikuntzak ondoko U_{eff} eta τ_0 balioak ematen ditu: 1,5 K eta $1{,}9\cdot10^{-5}$ s, eta 43,8 K eta $3{,}4\cdot10^{-7}$ s, hurrenez hurren. Aztertutako tenperatura-tarte osoko $\chi''_M(\upsilon)$ kurbek dutenez maximoa, horietatik lortutako erlaxazio-denbora guztiek dute zentzu fisikoa. Beraz, mekanismo batetik besterako prozesu aldaketa ikusteko irudikatu egin dira denak.

Neurketa kanpoko eremu magnetiko optimopean egiteak bi ondorio ditu $\mathbf{13_{DyY}}$ diluituarentzat. Alde batetik, **13** puruarentzat tenperatura baxuetan ikus zitezkeen

maximoak berriz agertzen dira eta, bestetik, tenperatura altuagoetan ikus zitezkeen maximoak askoz hobeto definituta daude *QTM* ezabatzearen ondorioz (2.14. irudia, behean eskuinean). Tenperatura baxuko erlaxazioarekin lotutako maximoen posizioa ia aldatzen ez bada ere, horien izaera aldatu egin da eta ezin izan dira $\chi''_M(\upsilon)$ kurbak doitu erlaxazio-denborak lortzeko. Hala ere, **12$_{DyY}$** sistemarentzat erabilitako hurbilketa kontuan hartuta, erlaxazio-parametroen nondik norakoa lortzen da: $U_{eff} \approx 19$ K eta $\tau_0 \approx 6 \cdot 10^{-8}$ s. Tenperatura altuko eremuari dagokionez, erlaxazio-denborek 6,2-11,2 K-eko tenperatura-tartean zati lineala erakusten dute. Horrela, Arrheniusen legea erabiliz U_{eff} = 60,2 K eta $\tau_0 = 1{,}3 \cdot 10^{-7}$ s parametroen balioak lortzen dira Orbach prozesurako. Tenperatura baxuenetan lortutako α balio handiak (0,54, 6,2 K-etan) tenperatura baxuagoko *FR* erlaxazioaren eraginagatik izan daitezke; tenperatura altuetan, aldiz, askoz balio txikiagoak lortzen dira (0,16 11,2 k-etan) Orbach mekanismo bakar batekin adostasunean.

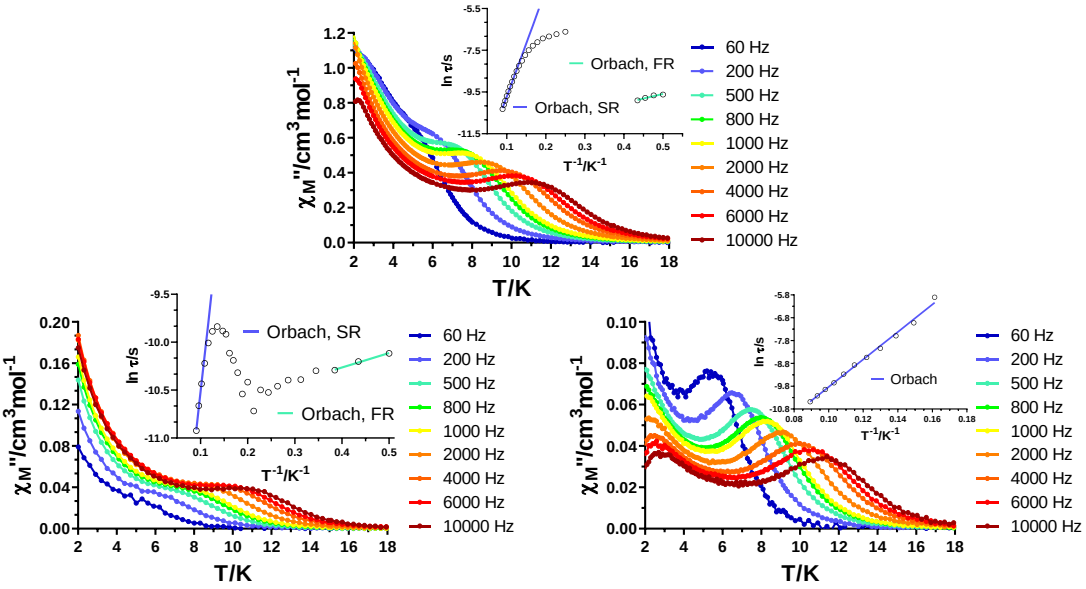

2.14. irudia.- Fasez kanpoko suszeptibilitatearen tenperaturarekiko mendekotasuna hainbat frekuentziatan 1 kOe-etako kanpo eremu magnetikopean (goian) **13** konposatuarentzat eta kanpoko eremu magnetikorik aplikatu gabe (behean ezkerrean) eta 1 kOe-etako kanpoko eremu magnetikopean (behean eskuinean) **13$_{DyY}$** diluituarentzat. Grafiko txikia: Arrheniusen grafikoa erlaxazio-denboretarako Orbach mekanismoa kontuan hartuz (lerro urdin eta turkesak).

14 konposatuak suszeptibilitate-osagaietan gainjarritako maximoak erakusten ditu, fasean eta fasez kanpo, 1 kOe-etako kanpoko eremu magnetiko baten pean (2.15. eta A2.94. irudiak). Horrela, bi Debyeren modelo aldatu eta CCFIT softwarearekin aztertzen dira $\chi''_M(\chi'_M)$ datuak. *FR* eta *SR* prozesuetarako lortutako erlaxazio-denborek Arrheniusen legeari jarraitzen diote ondoko U_{eff} eta τ_0 balioak emanez: 13,2 K eta $1{,}9\cdot10^{-6}$ s *FR*rentzat eta 31,5 K eta $2{,}3\cdot10^{-7}$ s *SR*rentzat. Tenperatura-tarte osoan lortutako α balio altuak (0,36 (2,5 K)-0,40 (3,5 K) FR; (0,23 (4,0 K)-0,43 (7,0 K) SR) bat datoz bi prozesuak erabat gainezarriak egotearekin. **14_{DyY}** konposatu diluituak maximo zabalak ditu tenperatura-tarte berean, bi mekanismo gainezarriren ondorio izan daitekeena. Hala ere, datuak Debyeren funtzio bakar baten bidez aztertu dira, ez baitago bi maximo multzo daudenaren seinale argirik, ezta $\chi''_M(\chi'_M)$ edo $\chi''_M(\upsilon)$ grafikoetan ere. α balioak altuak dira aztertutako tenperatura-tarte osoan (0,51 (3,6 K)-0,39 (7,2 K)), gainezarrita egon daitezkeen bi prozesuren hipotesiarekin bat eginez. Erlaxazio-denborek Arrheniusen legeari jarraitzen diote tenperatura-tarte osoan, 23,9 K-eko energia-barrera balioa eta $\tau_0 = 1{,}2\cdot10^{-6}$ s emanez. Balio horiek konparagarriak dira diluitu gabeko laginean *FR* eta *SR* prozesuetarako lortutako parametroen batez bestekoekin.

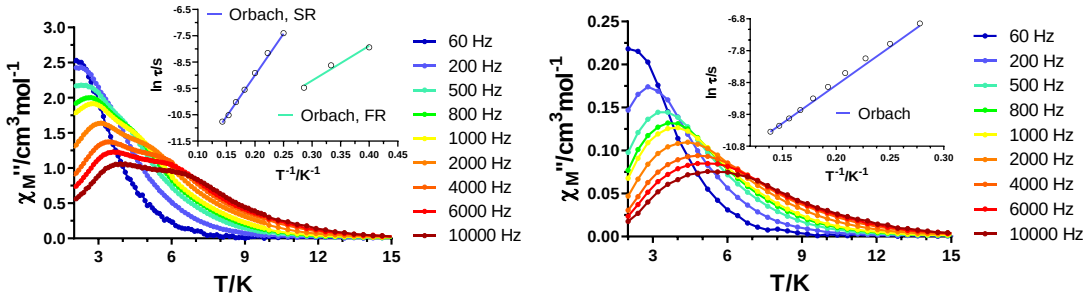

2.15. irudia.- Fasez kanpoko suszeptibilitatearen tenperaturarekiko mendekotasuna hainbat frekuentziatan 1 kOe-etako kanpo eremu magnetikopean **14** (ezkerrean) eta **14_{DyY}** (eskuinean) konposatuentzat. Grafiko txikia: Arrheniusen grafikoa erlaxazio-denboretarako Orbach mekanismoa kontuan hartuz (lerro urdin eta turkesak).

15 konposatuarentzat, 1 kOe-etako eremu magnetiko arbitrariopean egindako neurketak (2.16. irudia) bi maximo multzo erakusten ditu $\chi''_M(T)$ grafikoan, lehena 3,0 K azpitik eta bigarrena 16,0 K azpitik (azken multzo hau ez hain definitua). *FR* prozesuarentzako erlaxazio-denborak $\chi''_M(\upsilon)$ kurbak 3,0 K azpitik aztertuz lortu dira. Ageri den bezala, portaera lineala aurkezten dute eta Arrheniusen legera doitu dira U_{eff} = 13,6 K eta $\tau_0 = 5{,}2\cdot10^{-7}$ s lortuz. Bereziki α balio altuak lortzen diren arren (0.63 (2.0 K)

- 0.69 (2.9 K)), datuen linealtasunak eta lortutako puntu kantitate urriak ez du ahalbidetzen prozesu gehiagoren presentzia kontuan hartzea. Bestalde, SR mekanismo independeteki aztertu da 11,6-15,8 K tenperatura tartean. Tenperatura altuetako erlaxazio-denborak, beste behin, Arrheniusen legera doitzen dira energia-barrera efektiboaren eta τ_0 parametroaren ondoko balioak lortuz: 106,1 K eta $2{,}5\cdot10^{-8}$ s. Kanpoko eremu magnetikoa optimizatzeko helburuarekin, hein batean erlaxazio motelenari dagozkion maximoak hobeto definitzeko, erlaxazio-denboren eremuarekiko mendekotasuna ikertu da 12,5 K-etan (A2.47.-A2.48. irudiak). Ikerketa honetatik, 2,5 kOe-etako kanpo eremu magnetikoa dela optimoa ondorioztatzen da. Hala ere, neurketa eremu honen pean egindakoan, ez da esperotako emaitza lortu. A2.106. irudian ikus daitekeen bezala, tenperatura baxuenetako maximoak nolabait tenperatura altuagoetara lerratzen dira, baina ez dago frekuentziarekiko mendekotasun logikorik. Gainera, tenperatura altutako maximo multzoa lehen baino gutxiago definitzen da orain. Badaezpada, kasu honetan ere diluzioa ikertu dugu, baina nuklearitate handiagoa dela eta, zuzenean 1:20 erlazio molarra erabili dugu **15_{DyY}** sisteman metal paramagnetikoak elkarrengandik erabat urruntzeko asmoz. Dena den, beste behin ere, emaitza ez da esperotakoa izan. A2.108. irudian ageri den bezala, orain tenperatura baxuko maximoak frekuentziarekiko mendekotasuna dute, baina izaeragatik ezin dira $\chi''_M(\upsilon)$ kurbak doitu. Bestalde, tenperatura altuetan ez da maximorik ageri, edo ia detektaezinak dira. Izan daiteke diluzio estrategia ez dela hain eraginkorra sistema polinuklearrak erabiltzen direnean, izan ere, nahasketak (Dy_4, Dy_3Y, Dy_2Y_2 edo DyY_3) izateko probabilitatea handitu egiten da eta ez da hain erraza esatea ioiak ondo banatuta daudela. Hori kontuan izanik, zaila da lortutako emaitzei interpretazio zuzena ematea.

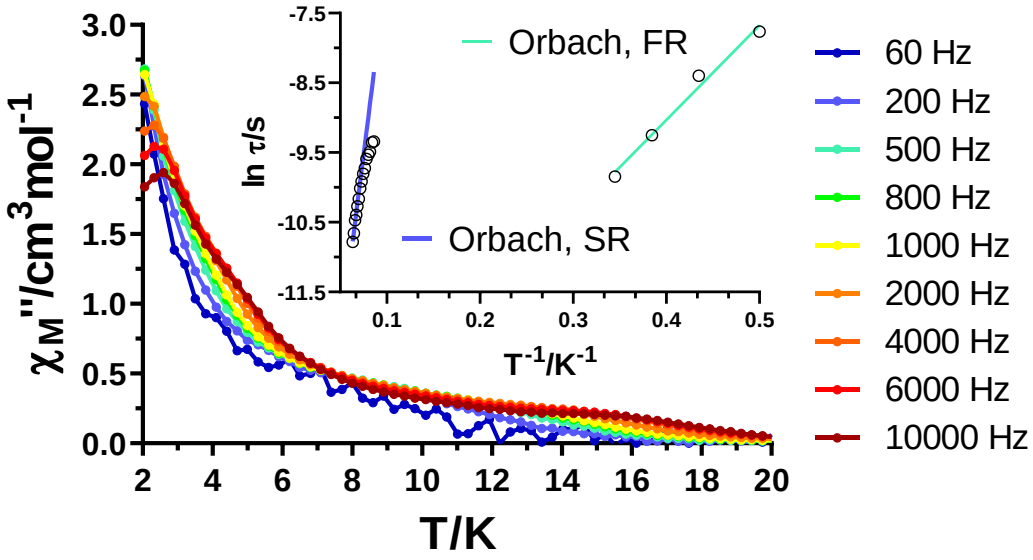

2.16. irudia.- 15 konposatuarentzat, fasez kanpoko suszeptibilitatearen tenperaturarekiko mendekotasuna hainbat frekuentziatan 1 kOe-etako kanpo eremu magnetikopean. Grafiko txikia: Arrheniusen grafikoa erlaxazio-denboretarako Orbach mekanismoa kontuan hartuz.

2.2. taula.- U_{eff}, τ_0, B, n, eta τ_{QTM} parametroentzako lortutako balioak **7-15** eta analogo diluituentzat.

	***dc* erem.**	**Orbach**		**Prozesuen konbinaketa**				
				Orbach		**Raman**		**QTM**
Konp.	kOe	U_{eff} (K)	τ_0 (s)	U_{eff} (K)	τ_0 (s)	B ($s^{-1}K^{-n}$)	n	τ_{QTM} (s)
7	1.5	65.7	$2.9\cdot10^{-8}$	96.5	$3.1\cdot10^{-9}$	1.8	4.2	
7_{DyY}	0	43.0	$1.6\cdot10^{-7}$	45.9	$1.4\cdot10^{-7}$			$1.4\cdot10^{-4}$
		52.3 (*FR*)	$10.0\cdot10^{-8}$					
7_{DyY}	1.5	102.2 (SR)	$4.7\cdot10^{-9}$					
8	0.75	35.5	$6.6\cdot10^{-8}$					
8_{DyY}	0.75	50.9	$3.3\cdot10^{-10}$					
9	1.5	15.9 (*FR*)	$4.5\cdot10^{-7}$					
		32.0 (*SR*)	$8.0\cdot10^{-8}$					
10	1	15.6	$9.6\cdot10^{-8}$					
		24.2	$1.8\cdot10^{-7}$					
11	1.5	42.3	$1.5\cdot10^{-7}$					
11_{DyY}	0	34.2	$2.1\cdot10^{-7}$	44.6	$5.9\cdot10^{-8}$			$1.4\cdot10^{-4}$
12	1.5	9.6 (*FR*)	$5.5\cdot10^{-7}$					
12_{DyY}	1.5	~8 (*FR*)	$\sim1\cdot10^{-6}$					
		36.4 (*SR*)	$4.6\cdot10^{-7}$					
13	1	4.4 (*FR*)	$7.5\cdot10^{-6}$					
		51.0 (*SR*)	$3.6\cdot10^{-7}$					
13_{DyY}	0	1.5 (*FR*)	$1.9\cdot10^{-5}$					
		43.8 (*SR*)	$3.4\cdot10^{-7}$					
13_{DyY}	1	~19 (*FR*)	$\sim6\cdot10^{-8}$					
		60.2 (*SR*)	$1.3\cdot10^{-7}$					
14	1	13.2 (*FR*)	$1.9\cdot10^{-6}$					
		31.5 (*SR*)	$2.3\cdot10^{-7}$					
14_{DyY}	1	23.9	$1.2\cdot10^{-6}$					
15	1	13.6 (*FR*)	$5.2\cdot10^{-7}$					
		106.1 (SR)	$2.5\cdot10^{-8}$					

2.4.7. Korrelazio magneto-estrukturalak

Proiektu honi hasiera eman zitzaionean, helburu nagusia Dy^{III} ioien koordinazio-ingurunea (ia) aldaketarik mantentzea zen aurretik deskribatutako $Zn^{II}Dy^{III}$ konposatuarekiko. Hori egin eta zubi lana egiten duten karboxilatoak aldatzea zen helburua, zubi malguago edo zurrunagoak erabiliz. Azken urtetako lan batzuetan ikusi den bezala, lantanidoaren inguruan eman daitezkeen bibrazioek magnetizazioaren erlaxazio prozesu azkarrak ahalbidetu ditzakete. Ikerketa horien arabera, konposatu zurrunek potentzial altuagoa dute *SMM* portaera hobea erakusteko [18]. Gure iritziz, proposatutako lehen baldintza bete dugu CShM balioek erakutsi bezala kristal-egituren deskribapenean. Bestalde, kristal-eremua berdin mantentzeak, aldi berean, esan nahiko

luke M_J azpimailek energia-banaketa antzekoa erakutsiko dutela eta anisotropia-ardatzek orientazio antzekoa. Gaur egun kalkulu teorikoen emaitzen zain bagaude ere, nolabaiteko hurbilketa bat gauzatu dugu Magellan softwarea erabiliz ardatz anisotropikoen orientazioa determinatzeko [19].2.17. irudian hiru konposatu adierazgarri erakusten dira kalkulatutako anisotropia-ardatzekin batera (gainontzekoak A2.109-A2.110. irudietan aurki daitezke). Hiru hauek aukeratu ditugu (i) **7** konposatua bakarra delako CO_3^{2-} kelatoak dituena, (ii) **8** konposatua bi nitrato kelato dituzten konposatuena adierazgarria da eta (iii) **15** da konplexu bakarra karboxilato kelatoa duena. Ikus daitekeen bezala, anisotropia-ardatzak konposatu guztietan Dy-$O_{fenoxido}$ loturek baldintzatuta daude, beste posizioetan dagoena dagoela. Hori dela eta, ardatzak bi fenoxidoen tartetik eta, ondorioz, kontrako aldean dauden kelatoen tartetik (CO_3^{2-} **7** konposatuarentzat, NO_3^- **8**-rentzat eta NO_3^-/karboxilato **15** oktanuklearrarentzat) pasatzen dira.

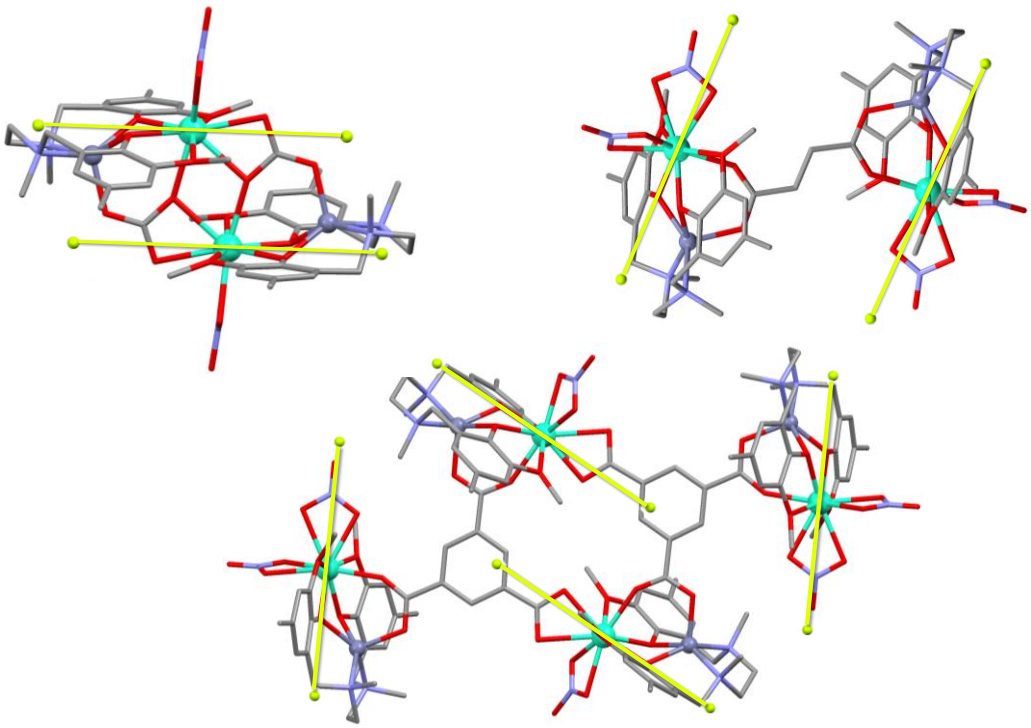

2.17. irudia.- Magellan bidez kalkulatutako anisotropia-ardatzak (lerro berdeak) **7** (goian ezkerrean), **8** (goian eskuinean) eta **15** (behean) konposatuentzat.

Zoritxarrez, gure ustez ezin dugu korrelaziorik egin molekulen zurruntasuna eta propietate magnetiko dinamikoen artean. Egia da $\mathbf{7}_{DyY}$ eta $\mathbf{13}_{DyY}$ konposatuak zurrunak direla eta SMM portaera dutela kanpoko eremu magnetikorik aplikatu gabe, baina $\mathbf{12}_{DyY}$,

14$_{DyY}$ eta **15**$_{DyY}$ ere sar daitezke talde horretan eta ez dute halako propietate onik erakusten. Gainera, **11**$_{DyY}$ konposatuak malgua den pimelato zubia du eta, horrek ere, *SMM* portaera du eremu magnetikorik aplikatu gabe. Beraz, zurruntasunaren hipotesia baztertzera behartuak gaude.

Dena den, kapitulu honetan eta **30** konposatuarentzat (ikusi 4. kapitulua) lortutako emaitzak ikusita, eta baita literaturan ikusitakoaren arabera ere [20,21], **7**$_{DyY}$ eta **15** konposatuen energia-barrera altuak azal ditzakegula uste dugu. Besteekin alderatuta, bi konposatu horiek U_{eff} nabarmen altuagoak dituzte kanpoko eremu magnetiko baten presentzian, 100 K-eko balioak gaindituz. Kontuan izanik fenoxido taldeak direla anisotropia-ardatzen orientazioa definitzko erantzule nagusiak, M_J = ±15/2 oinarrizko egoeraren hodei-elektroniko oblatua 2.18. irudian bezala egotea espero daiteke. Fenoxido oxigeno atomoak hodeiaren alde batean egongo lirateke, bestean, berriz, CO_3^{2-}, NO_3^- edo RCO_2 taldeak. Hortaz, karbonato nahiz karboxilato taldeek (nitratoen aldean) karga negatibo handiagoa emango dutenez, hobeto egonkortuko dute M_J = ±15/2 azpimaila oinarrizko egoeran egoera eszitatuarekiko energia-diferentzia altuagoarekin. Ondorioz, U_{eff} balio altuagoa zentzuzkoa izan daiteke. Gauzak horrela badira, esan genezake **15** konposatuan agertzen den *SR* prozesua Dy1B ioiari dagokiola, honek baitu karboxilato kelatoa fenoxidoen beste aldean.

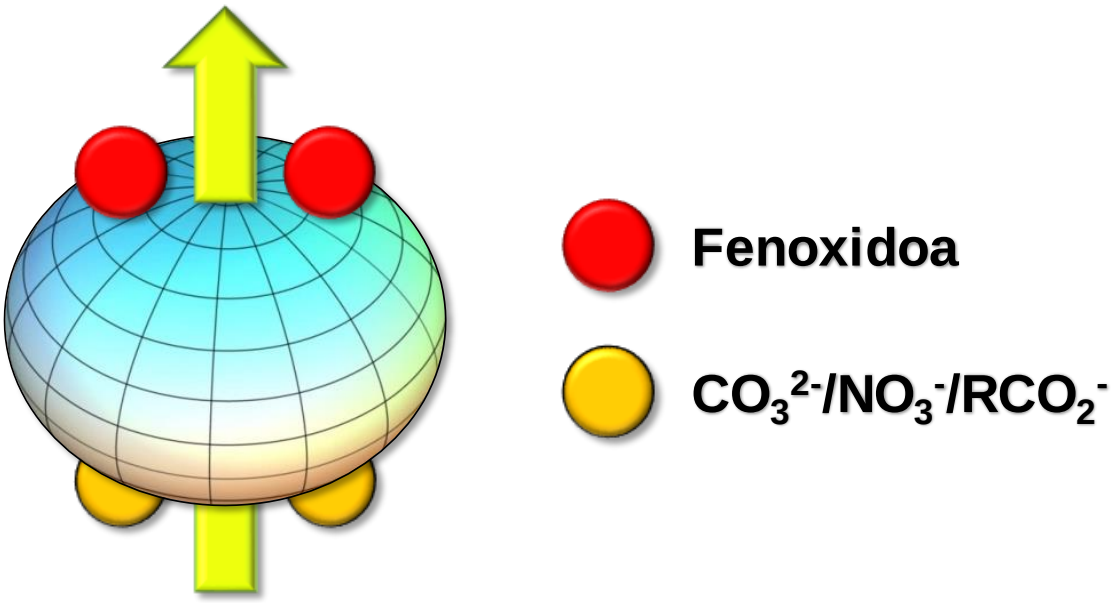

2.18. irudia.- Dy^{III} ioiarentzat M_J = ±15/2 azpimaila oblatuaren elektroi-hodeiaren banaketa. Anisotropia-ardatza hodeiarekiko perpendikularra da. Borobil gorri eta laranjek fenoxido eta karbonato/nitrato/karboxilato taldeen posizioak irudikatzen dituzten, hurrenez hurren.

Esandakoaz gain, korrelazio gehiago egitea zaila dela pentsatzen dugu. Koordinazio-zenbakia hain altua den sistemetan lotura-distantzia nahiz angeluetan ematen diren aldaketa txikiek eragin handia izan dezakete, baina, aldi berean, zailak izan daitezke detektatzeko. Bestalde, uste dugu ezin dugula halako ikerketa sakonik egin kristal-egiturako parametroetan oinarrituta, izan ere, konposatu gehienek egituraren berrantolaketa jasaten dute disolbatzaile molekulen galeragatik.

2.5. ONDORIOAK

Arrakasta izan dugu aurretik deskribatutako $Zn^{II}Dy^{III}$ sistemako egitura luzatzen azetatoa ordezkatu eta karbonatoa eta karboxilato desberdinak erabiliz. Hain zuzen, 9 sistema polinuklear berri deskribatu ahal izan ditugu kapitulu honetan. Guztien kristal-egiturak lortu baditugu ere, gehienek disolbatzaile molekula galerei loturiko berrantolaketa jasaten dute. Hipotesi hau frogatu ahal izan da $Zn^{II}Y^{III}$ analogoen karakterizazio alternatiboa eginez.

Diluziorik egin gabe, konposatu bakar batek ere ez du *SMM* propietatea erakusten kanpoko eremu magnetikorik aplikatu ezean. Eremua aplikatzean, berriz, konposatu guztiek erakusten dituzten maximoak fasez kanpoko osagaian *QTM* guztiz edo partzialki desaktibatuz. Sistema diluituei dagokionez, $\mathbf{7_{DyY}}$, $\mathbf{11_{DyY}}$ eta $\mathbf{13_{DyY}}$ materialek *SMM* portaera erakutsi dute kanpoko eremu magnetikorik gabe. $\mathbf{7_{Gd}}$ konposatuarentzat eginiko dc neurketek lantanido arteko truke-interakzioa ia arbuiagarria dela ondorioztatzeko balio izan dute. Honek azaldu dezake zergatik den $\mathbf{7_{DyY}}$ molekularen portaera **7** analogo puruarena baino hobea. Ziur aski, truke-interakzio ahulek zeharkako eremu magnetikoak sortzen dituzte *QTM* ahalbidetuz. $\mathbf{11_{DyY}}$ eta $\mathbf{13_{DyY}}$ konplexuen kasuan, berriz, interakzio dipolarrak ekiditeak ere *QTM* desaktibatzea eragin du.

Lortutako emaitzetan oinarrituz, molekulen zurruntasunean oinarritutako korrelazio magneto-estrukturalak egiteko aukera baztertu dugu. Dena den, $\mathbf{7_{DyY}}$ eta **15** konposatuen energia-barrera altuak (100 K-en gainetik) azaltzeko gai izan gara Kristal-eremu egokiago batean oinarrituz. Magellan softwarearekin eginiko kalkuluen arabera, anisotropia-ardatzak Dy-$O_{fenoxido}$ loturen menpekoak dira. Beraz, zenbat eta dentsitate elektroniko altuagoa fenoxidoen kontrako aldean, orduan eta energia-diferentzia handiagoa oinarrizko egoeraren eta lehen eszitatuaren artean U_{eff} balio altuagoa emanez. Ikertutako sistema guztien artean, soilik **7** eta **15** konposatuko Dy1B ioiak dira nitrato kelatoa ez dutenak. Horren ordez, karbonatoa eta karboxilatoa dituzten, hurrenez

hurren. Talde hauek elektroi dentsitate handiagoa ematea espero da nitratoen aldean eta, ondorioz, energia-barrera handiagoak sortzen dituzte.

2.6. ERREFERENTZIAK

[1] A. Zabala-Lekuona, J. Cepeda, I. Oyarzabal, A. Rodríguez-Diéguez, J.A. García, J.M. Seco, E. Colacio, Rational design of triple-bridged dinuclear ZnIILnIII-based complexes: a structural, magnetic and luminescence study, CrystEngComm. 19 (2017) 256–264. https://doi.org/10.1039/c6ce02240e.

[2] R. Sessoli, D. Gatteschi, H.L. Tsai, D.N. Hendrickson, A.R. Schake, S. Wang, J.B. Vincent, G. Christou, K. Folting, High-Spin Molecules: [Mn12O12(O2CR)16(H2O)4], J. Am. Chem. Soc. 115 (1993) 1804–1816. https://doi.org/10.1021/ja00058a027.

[3] J.D. Hilgar, M.G. Bernbeck, J.D. Rinehart, Million-fold Relaxation Time Enhancement across a Series of Phosphino-Supported Erbium Single-Molecule Magnets, J. Am. Chem. Soc. 141 (2019) 1913–1917. https://doi.org/10.1021/jacs.8b13514.

[4] F. Habib, J. Long, P.H. Lin, I. Korobkov, L. Ungur, W. Wernsdorfer, L.F. Chibotaru, M. Murugesu, Supramolecular architectures for controlling slow magnetic relaxation in field-induced single-molecule magnets, Chem. Sci. 3 (2012) 2158–2164. https://doi.org/10.1039/c2sc01029a.

[5] E.A. Mikhalyova, M. Zeller, J.P. Jasinski, R.J. Butcher, L.M. Carrella, A.E. Sedykh, K.S. Gavrilenko, S.S. Smola, M. Frasso, S.C. Cazorla, K. Perera, A. Shi, H.G. Ranjbar, C. Smith, A. Deac, Y. Liu, S.M. McGee, V.P. Dotsenko, M.U. Kumke, K. Müller-Buschbaum, E. Rentschler, A.W. Addison, V. V. Pavlishchuk, Combination of single-molecule magnet behaviour and luminescence properties in a new series of lanthanide complexes with tris(pyrazolyl)borate and oligo(β-diketonate) ligands, Dalton Trans. 49 (2020) 7774–7789. https://doi.org/10.1039/d0dt00600a.

[6] Z.Y. Zhao, H.H. Xu, P. Chen, Y.X. Li, Y. Sui, W. Bin Sun, Optimization and expansion of the Schiff base [Zn-Dy] unit to enhance the performance of single molecule magnetic materials, J. Mater. Chem. C. 8 (2020) 4843–4850. https://doi.org/10.1039/d0tc00207k.

[7] S. Titos-Padilla, J. Ruiz, J.M. Herrera, E.K. Brechin, W. Wersndorfer, F. Lloret, E. Colacio, Dilution-triggered SMM behavior under zero field in a luminescent Zn 2Dy2 tetranuclear complex incorporating carbonato-bridging ligands derived from atmospheric CO2 fixation, Inorg. Chem. 52 (2013) 9620–9626. https://doi.org/10.1021/ic401378k.

[8] G. Novitchi, W. Wernsdorfer, L.F. Chibotaru, J.-P. Costes, C.E. Anson, A.K. Powell, Supramolecular “Double-Propeller” Dimers of Hexanuclear CuII/LnIII Complexes: A {Cu3Dy3}2 Single-Molecule Magnet, Angew. Chem. Int. Ed. 48 (2009) 1614–1619. https://doi.org/10.1002/anie.200805176.

[9] S.H. Kim, J. Lee, D.J. Kim, J.H. Moon, S. Yoon, H.J. Oh, Y. Do, Y.S. Ko, J.H. Yim, Y. Kim, Titanium complexes containing new dianionic tetradentate [ONNO]-type ligands with benzyl substituents on bridging nitrogen atoms: Syntheses, X-ray structures, and catalytic activities in ring opening polymerization of lactide, J. Organomet. Chem. 694 (2009) 3409–3417. https://doi.org/10.1016/j.jorganchem.2009.06.037.

[10] D. Brackemeyer, C. Schulte To Brinke, F. Roelfes, F.E. Hahn, Regioselective C8-metalation of N-phosphine tethered adenine derivatives via C8-H activation, Dalton Trans. 46 (2017) 4510–4513. https://doi.org/10.1039/c7dt00682a.

[11] M. Llunell, D. Casanova, J. Cirera, J.M. Bofill, P. Alemany, S. Alvarez, M. Pinsky, D. Avnir, SHAPE, (2005).

[12] N.F. Chilton, R.P. Anderson, L.D. Turner, A. Soncini, K.S. Murray, PHI: A powerful new program for the analysis of anisotropic monomeric and exchange-coupled polynuclear *d* - and *f* -block complexes, J. Comput. Chem. 34 (2013) 1164–1175. https://doi.org/10.1002/jcc.23234.

[13] X.L. Li, J. Tang, Recent developments in single-molecule toroics, Dalton Trans. 48 (2019) 15358–15370. https://doi.org/10.1039/c9dt02113b.

[14] Z.H. Zhu, X.F. Ma, H.L. Wang, H.H. Zou, K.Q. Mo, Y.Q. Zhang, Q.Z. Yang, B. Li, F.P. Liang, A triangular Dy3 single-molecule toroic with high inversion energy barrier: Magnetic properties and multiple-step assembly mechanism, Inorg. Chem. Front. 5 (2018) 3155–3162. https://doi.org/10.1039/c8qi01069b.

[15] S.K. Langley, K.R. Vignesh, B. Moubaraki, G. Rajaraman, K.S. Murray, Oblate versus Prolate Electron Density of Lanthanide Ions: A Design Criterion for Engineering Toroidal Moments? A Case Study on {Ln $^{III}_{6}$ } (Ln=Tb, Dy, Ho and Er) Wheels, Chem. – A Eur. J. 25 (2019) 4156–4165. https://doi.org/10.1002/chem.201805765.

[16] K.N. Shrivastava, Theory of Spin–Lattice Relaxation, Phys. Status Solidi. 117 (1983) 437–458. https://doi.org/10.1002/pssb.2221170202.

[17] D. Reta, N.F. Chilton, Uncertainty estimates for magnetic relaxation times and magnetic relaxation parameters, Phys. Chem. Chem. Phys. 21 (2019) 23567–23575.

https://doi.org/10.1039/c9cp04301b.
[18] K.X. Yu, J.G.C. Kragskow, Y.S. Ding, Y.Q. Zhai, D. Reta, N.F. Chilton, Y.Z. Zheng, Enhancing Magnetic Hysteresis in Single-Molecule Magnets by Ligand Functionalization, Chem. 6 (2020) 1777–1793. https://doi.org/10.1016/j.chempr.2020.04.024.
[19] N.F. Chilton, D. Collison, E.J.L. McInnes, R.E.P. Winpenny, A. Soncini, An electrostatic model for the determination of magnetic anisotropy in dysprosium complexes, Nat. Commun. 4 (2013) 1–7. https://doi.org/10.1038/ncomms3551.
[20] F. Habib, G. Brunet, V. Vieru, I. Korobkov, L.F. Chibotaru, M. Murugesu, Significant enhancement of energy barriers in dinuclear dysprosium single-molecule magnets through electron-withdrawing effects, J. Am. Chem. Soc. 135 (2013) 13242–13245. https://doi.org/10.1021/ja404846s.
[21] J. Rinehart, J. Long, Exploiting single-ion anisotropy in the design of f-element single-molecule magnets, Chem. Sci. 2 (2011) 2078–2085. https://doi.org/10.1039/c1sc00513h.

3. KAPITULUA

Co^{II} IOIAN OINARRITUTAKO KONPOSATU POLINUKLEARREN ETA $TM^{II}Ln^{III}TM^{II}$ KONPOSATU TRINUKLEAR MISTOEN IKERKETA MAGNETIKOA: MOLEKULA BARNEKO INTERAKZIOEN GARRANTZIA *SMM* PORTAERA AZALERATZEKO

3.1. SARRERA

Sarrera orokorrean aipatu den bezala, nahiz eta azken urteotan *SMM*ak diseinatzeko joera 4f ioietan oinarritutako koordinazio-zenbaki txikiko konplexu mononuklearretara mugitu den, badirudi kluster magnetiko polinuklearren azterketak interes handikoa izaten jarraitzen duela. Lehen adibideek Mn^{III} zuten, Jahn-Tellerren distortsioek emandako anisotropia negatiboagatik, baina Co^{II} ioia ere (anisotropia altukoa izanik) potentzial handiko hautagaia da *SMM* polinuklearrak sortzeko. Konplexu homometalikoetan pentsatzen denean, egoera kitzikatuetatik ondo banatuta dagoen spin altuko oinarrizko egoera lortzeko estrategia mota bat 90º inguruko metal-zubi-metal angeluak ezartzen dituzten estekatzaileak erabiltzea izan liteke. Honek, zentro metalikoen arteko interakzio ferromagnetikoak (F) errazten ditu, $\{Ni_4O_4\}$ nukleoak dituzten kubanoetan [1,2] edo partekatutako aurpegia duten $\{Ni_4O_6\}$ dikubano akastunetan gertatzen den bezala [3]. Gainera, F interakzioak sustatzeko helburu nagusi hau aipatutako egiturak azida estekatzaileekin konbinatuz bete liteke, *end-on* (EO) koordinazio moduan F akoplamendua transferitzeko joera baitute [4–6].

Hala ere, 4f elementuak erabiltzean, estrategia aldatu egin behar da. 4f elektroi geruza $5s^2$ eta $5p^6$ kanpoko orbital beteek babesten dute eta, beraz, lantanidoen konposatu polinuklear gehienek molekula barneko truke-interakzio magnetiko oso ahul edo nulua erakusten dute [7]. Beraz, magnetizazioaren inbertsioa eragozten duten energia-barrera balio altuak lortzea posible bada ere, tenperatura baxuan energia barrera zeharkatzen duen tunel-efektu azkarra eman ohi da. Hori dela eta, askotan histeresi-zikloek ez dute irekierarik ematen zero eremu inguruan edo ez da SMM portaera detektatzen *ac* neurketak egitean. Aurretik aipatu den bezala, *QTM* desaktiba daiteke eremu magnetiko bat aplikatuz, lagina matrize diamagnetiko batean diluituz, estekatzaile arruntak (diamagnetikoak) erradikalekin ordezkatuz, etab. Azken aukera honek ikuspegi arrakastatsua dirudien arren, espezie horien manipulazioa eta isolamendua zailagoa da.

Beraz, 4f sistemetan 3d elementuak sartzea izan liteke beste aukera bat, zentro metalikoen arteko truke-interakzioak ahalbidetzeko. Adibidez, K. S. Murray eta egilekideek 2014an tximeleta itxurako konposatu bat argitaratu zuten $[Co^{III}_2Dy^{III}_2]$ nukleoarekin [8]. SMM portaera bazuen ere, 2,2 K-etik behera tunel-efektua nagusitzen zen sistema honetan. Urte bat lehenago, berriz, $[Cr^{III}_2Dy^{III}_2]$ nukleoko analogoa deskribatu zuten, Cr^{III} paramagnetiko ioiak zituena Co^{III} diamagnetikoen ordez.

Konposatu horrek propietate magnetiko hobeak zituen. Energia-barreraren balioa ia berdina bazen ere, histeresi-ziklo irekiak erakusten zituen 3,5 K-etaraino [9].

Testuinguru honetan, aipatutako estrategietako batzuk konbinatu ditugu hamar konplexu berri lortuz *N,N'*-dimetil-*N,N'*-bis(2-hidroxi-3-metoxi-5-metilbentzil) etilendiamina (H_2L^3) estekatzailearekin. Alde batetik, Co^{II} ioian oinarritutako bi konposatu tetranuklear sintetizatu ditugu (dikubano akastunak), truke-interakzioa aldatzen duten estekatzaile desberdinak erabiliz. Gainera, kasualitatez lortutako konposatu pentanuklear bat ere deskribatu dugu, kanpoko eremu magnetikorik gabe *SMM* propietateak dituena. Bestalde, 3d-4f-3d motako sei sistema heterotrinuklear misto aztertu dira, truke-interakzioek *QTM*ren deuseztatzean edo aktibazioan duten eragina aztertzeko. Horretarako, sei konposatuetatik lautan bi ioi paramagnetiko konbinatu ditugu (Co^{II} eta Ln^{III} ioi ezberdinak), beste bitan, aldiz, Co^{II} edo Dy^{III} bakarrik da paramagnetikoa (Y^{III} edo Zn^{II} diamagnetikoak erabili dira 4f eta 3d ioi gisa kasu horietan). Oro har, konposatu guztien sintesia, karakterizazio kimikoa, X izpien bidezko egitura-deskribapena eta propietate magnetikoei buruzko informazioa ematen da kapitulu honetan.

3.2. KONPLEXUEN PRESTAKETA

3.2.1. $[Co_4(\mu\text{-}L^3)_2(\mu\text{-}Cl)_2Cl_2]\cdot 2H_2O$ (16)

H_2L^3 estekatzailearen 5 mL-ko MeCN disoluzio bati (48 mg, 0,125 mmol), beste $CoCl_2\cdot 6H_2O$ disoluzio bat gehitzen zaio (59,5 mg, 0,250 mmol) etengabe, baina poliki irabiatuz. Gehikuntza amaitu ondoren, disoluzio urdina giro-tenperaturan pausatzen uzten da. Egun gutxiren buruan, kristal prismatiko urdin argiak, more/urdinak eta moreak (azken hauetatik gutxi edo alerik ez) lortzen dira. Lehenengoak $H_4L^3[CoCl_4]$ monomero ioniko bati dagozkio (**26** konposatua, A3.1. irudia), bigarrenak nahi den produktuari eta azkenak ia berdina den koordinazio-konposatu bati (**27** konposatua, A3.2. irudia). Desberdintasuna, **16** klusterrean dauden bi ur molekulen ordez lau azetonitrilo kristalizazio-molekula dituela da. Monomeroa kentzeko, ama-urak kendu eta ura gehitzen da produktu ionikoa disolbatuz. Ondoren, solido more/urdina iragazi, urez garbitu eta lehortzen da. Etekinak eta analisi elementalen emaitzak A3.1. taulan daude.

3.2.2. $[Co_4(\mu\text{-}L)_2(\mu\text{-}N_3)_2(N_3)_2]\cdot 2H_2O$ (17)

H_2L^3 (69 mg, 0,18 mmol) eta $Co(NO_3)_2\cdot 6H_2O$ (104,8 mg, 0,36 mmol) dituen MeCN disoluzio more bati (8 mL-tan) tantaz tanta gehitzen zaio NaN_3 (23,4 mg, 0,36 mmol) disoluzioa 2 mL azetonitrilotan (hiru H_2O tanta erabiltzen dira gatza hobeto disolbatzeko). Prezipitatu urdin bat lortzen da berehala. Erreakzioa 10 minutuz irabiatu, produktua iragazi, azetonitriloarekin garbitu eta lehortzen da. Ama-uretatik kolore moreko kristalak lortzen dira X izpien difrakziorako. Etekinak eta analisi elementalen emaitzak A3.1. taulan daude.

3.2.3. $[Co_5(\mu\text{-}L^3)_2(\mu\text{-}OAc)_5(\mu\text{-}OH)]\cdot n$MeCN (n = 4 (18a); n = 3 (18b)

H_2L^3 (48 mg, 0,125 mmol) MeCN disoluzio bati (5 mL-tan), ur destilatu tanta bat eta trietilamina (0,085 mL, 0,625 mmol) gehitzen zaizkio, hurrenez hurren. Ondoren, $Co(OAc)_2\cdot 4H_2O$ (78 mg, 0,312 mmol) solidoa gehitzen zaio. Disolbatzen eta erreakzionatzen laguntzeko, intentsitate handiz irabiatzeaz gain, ultrasoinuak erabiltzen dira kolore moreko disoluzio bat lortuz. Erreakzioa 1,5 orduz irabiatu eta giro-tenperaturan pausatzen da. Egun gutxiren buruan, kolore moreko kristalak lortzen dira. Iragazi, azetonitriloz garbitu eta lehortzen dira. Etekinak eta analisi elementalen emaitzak A3.1. taulan daude.

3.2.4. $[LnTM_2(\mu\text{-}L^3)_2(H_2O)_2Cl_2]Cl\cdot nH_2O\cdot$MeCN (TM = Co^{II}, Ln^{III} = Y (19), Gd (20), Tb (21), Dy (22), Er (23) eta Yb (24); TM = Zn^{II}, Ln^{III} = Dy (25); n = 0 19 eta 25-entzat, n = 1 20-22 eta 24-rentzat; n = definitu gabe 23-rentzat)

H_2L^3 (48 mg, 0,125 mmol) estekatzailearen MeCN disoluzio bati (4 mL-tan) trietilamina (0,034 mL, 0,25 mmol) eta ur tanta destilatu bat gehitzen dira, hurrenez hurren etengabe irabiatuz. Jarraian, tantaka gehitzen da dagokion $TMCl_2\cdot nH_2O$ (0,125 mmol) eta $Ln(NO_3)_2\cdot nH_2O$ (0,0625 mmol) dituen disoluzioa 1 mL azetonitrilotan disoluzio morea emanez. Disoluzioa giro-tenperaturan pausatzen da eta egun gutxiren buruan kalitate oneko kristal moreak lortzen dira. Kasu batzuetan, konplexu trinuklearrek **16** konposatuarekin batera kristalizatzen dute, beraz, bereizi egin behar dira. Etekinak eta analisi elementalen emaitzak A3.1. taulan daude.

3.3. EMAITZA ESPERIMENTALAK

Lehen begiratuan, H_2L^3 estekatzailea aurretik deskribatutako beste Schiff baseen antzekoa bada ere [10], Mannich baseek duten malgutasun gehigarriak ohiko sistema linealez gain [11], ohiz kanpoko egiturak lortzea ahalbidetu du, **18a** eta **18b** kasu (kontuan hartu Schiff baseek ere konposatu mota ugari eman ditzaketela [12]). Gainera, bi guneetan trantsizio-metalak koordinatzeko aukera edukita [13], Co^{II} ioi paramagnetikoan oinarritutako hiru koordinazio-konposatu berri sintetizatu ahal izan ditugu (**16**, **18a** eta **18b**) eta aurrez deskribatutako azida-zubidun konposatuaren sintesia errepikatu dugu (**17**) [14]. Kobaltoan oinarritutako konposatu homonuklearrez gain, 3d-4f-3d konposatu misto heterotrinuklearrak lortu dira. **16-22**, **24** eta **25** konposatuen datu kristalografikoak, lotura-luzerak eta angeluak A3.2.-A3.7. tauletan laburbildu dira.

Konplexuen sintesiaren atalean adierazi den bezala, konposatu trinuklearrek bi fase desberdinetan kristalizatzen dira, non batek ur eta azetonitrilo kristalizazio-molekula bana duen eta besteak azetonitriloa bakarrik. Honetaz berriki jabetu gara, izan ere, hasiera batean kristalizatutako **20-22** eta **24** konposatuek kristal-egitura bera erakusten dute. Hala ere, konturatu ginen hautsean eginiko X izpi difrakzio esperimentuetan konposatu gehienek (**19**, **21**, **22**, **23** eta **25**) difrakzio seinale gehigarriak erakusten zituztela (A3.9.-A3.10. irudiak). Hasiera batean, difrakzio gehigarriak simetria-galera partzial batekin lotu genituen (disolbatzaile lurrunketaren ondorioz eman daitekeena); izan ere, difrakzioen posizioak bat datoz, nolabait, absentzia sistematikoekin. **20** eta **24** konposatuen difrakzio espektroak simulatutakoekin guztiz bat etortzeak (A3.11. irudia), erradio ionikoarekin zerikusia izan zezakeen edozein hipotesi baztertzea eragin zuen (Gd^{III} eta Yb^{III} ioiek, aztertutako lantanidoen artean, erradio ionikorik handiena eta txikiena baitute, hurrenez hurren). Beraz, ausazko efektutzat hartuta, konposatu trinuklear guztien portaera termikoa aztertzea erabaki genuen.

Esperimentuak aire sintetikoan egitean, hondakinak oxido metalikoak izatea espero da (**19-24** konposatuentzat CoO eta Ln_2O_3, eta **25** sistemarentzat ZnO eta Dy_2O_3). Horrela, teknika honek hasierako produktuen pisu molekularrak sistema trinuklearrei dagozkiela baieztatzea ahalbidetu du (A3.15.-A3.17. irudiak).

Difrakzio gehigarriak dituzten konposatu guztiak TM_2Ln sistema trinuklear puruak direla baieztatu da **19** eta **25** konposatuen kristal-egiturak neurtu direnean. Fase berri honek ez du kristalizazio-ur molekularik eta aurretik aipatutako difrakzio gehigarrien erantzule da. A3.9.-A3.10. irudiek argi eta garbi erakusten dute aztertutako konposatu gehienak bi faseen nahasketa direla.

3.3.1. 16-22, 24 eta 25 konposatuen kristal-egiturak

H_2L^3 eta $CoCl_2 \cdot 6H_2O$ erreaktiboen arteko erreakzioak, 1:1 erlazio molarrean eta azetonitrilotan, hiru produktu kristalino ezberdinen sorrera ahalbidetzen du (ikusi konplexuen sintesia eta A3.1.-A3.2. irudiak), baina soilik **16** konposatua aztertu da. Konplexuaren egitura kristalinoak $[Co_4(\mu\text{-}L^3)_2(\mu\text{-}Cl)_2Cl_2] \cdot 2H_2O$ formula orokorra du eta 3.1. irudian erakusten da. *R-3* talde espazialean kristalizatzen du. Konposatu tetranuklear zentrosimetriko honek lau Co^{II} ioi ditu, protonatu gabeko bi estekatzaile (L^{2-}), zubi hirukoitza egiten duten bi kloruro anioi, bi kloruro anioi terminal eta bi kristalizazio-ur molekula. Aurretik deskribatutako konposatu planoetan ez bezala, non L^{2-} estekatzailearen eraztun aromatikoak ia planokideak diren, estekatzaileak tolestu egiten dira eraztun aromatikoek osatutako planoen artean ia angelu perpendikularra sortzeko (83,40º). Horrela, L^{2-} bakoitza hiru ioi metalikora koordinatzen da, bi erpin falta dituen aurpegi partekatuko dikubano distortsionatua sortuz. Partekatutako aurpegia zentrosimetrikoak diren Co1 eta Co1(i) ioiek eta bi kloruro zubik osatzen dute (ikusi taula kristalografikoak simetria-eragiketetarako).

Protonatu gabeko estekatzaileak heteroatomo guztiak erabiltzen ditu Co^{II} ioietara koordinatzeko. Nitrogeno eta kloruro zubiak *cis* posizioan daude Co1 eta Co1(i) ioien $CoN_2O_2Cl_2$ ingurune oktaedriko distortsionatuetan. Fenoxido zubiek *trans* posizioak betetzen dituzte. Bestalde, Co2 eta Co2(i) ioi metalikoen CoO_4Cl_2 koordinazio-inguruneak prisma trigonalaren eta poliedro oktaedrikoen artean daude (SHAPE softwarearen [15] bidez kalkulatuak, 5,565 eta 6,845 balioak, hurrenez hurren; A3.8. taula), non bi oxigeno atomo fenoxido zubiak diren, beste biak metoxi taldeetakoak (estekatzaile banatakoak) eta, azkenik, bi kloruro atomo, bat zubi hirukoitza eta bestea terminala.

Co-heteroatomo lotura-distantziak 2,006(3)-2,515(13) Å tartean daude, non distantziarik laburrenak $Co\text{-}O_{fenoxido}$ loturei dagozkien, eta luzeenak $Co\text{-}Cl_{zubi}$ motakoei. Lotura-luzera guztiak izaeraren arabera multzokatu daitezke (antzeko distantziak sortuz), $Co\text{-}O_{metoxi}$ loturak motzagoak (2,218(3) Å) edo luzeagoak (2,389(3) Å) izan daitezke. Co-X-Co (X = Cl edo $O_{fenoxido}$) zubien angeluak askoz ere zorrotzagoak dira zubia kloruroa denean (83,66(4)º edo 89,40(4)º) oxigenoa izan beharrean (111,67(13) edo 115,76(15) °). Beraz, dikubanoaren aurpegi partekatua ia karratu perfektua da, baina beste aurpegiak askoz ere distortsionatuagoak daude. $Co1\text{-}(\mu\text{-}Cl_2)\text{-}Co1(i)$ zatia planokidea da, baina Co1-μ-fenoxido/μ-kloruro-Co2 zatiak ez. Hain zuzen, 3,47 eta

10,78º-ko bisagra angeluak ematen dituzte. Co1···Co2 eta Co1···Co2(i) arteko distantziak 3,447 eta 3,365 Å-ekoak dira, hurrenez hurren.

Azkenik, aipatu behar da egitura kristalinoa hidrogeno-loturen sare supramolekular batek egonkortzen duela, ur-molekulek kluster hexanuklearra eratzen dute (*c* ardatzean ikus daiteke). 119,42º-ko O1W···O1W···O1W angeluak dituen hexagono ia perfektua sortzen da 2,866 Å-eko O1W···O1W hidrogeno-loturekin (A3.3. irudia). Hori izan liteke produktu nagusiak azetonitrilo kristalizazio molekulak izan beharrean ur-molekulak izatearen arrazoia, erreakzioa ur gehigarririk gehitu gabe gauzatzen bada ere.

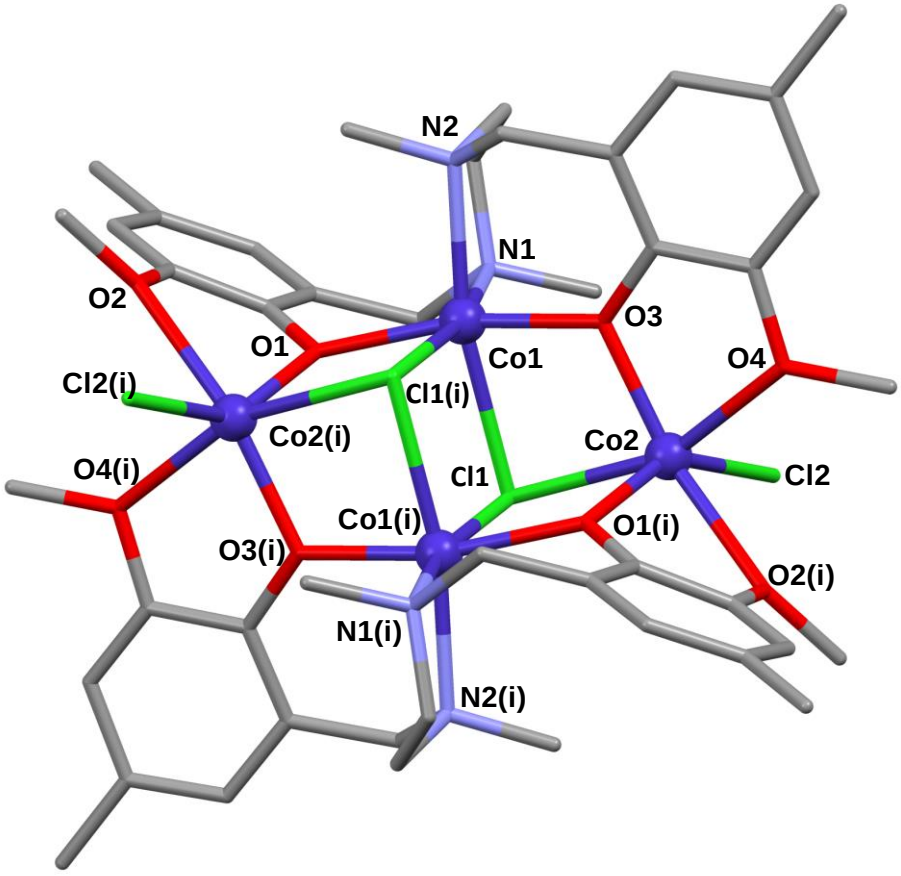

3.1. irudia.- 16 konplexuaren ikuspegia. Kolore-kodea: kobalto, kloruro, nitrogeno, oxigeno eta karbono atomoak more, berde, urdin argi, gorri eta gris kolorez, hurrenez hurren. Hidrogeno atomoak eta disolbatzaile molekulak ez dira irudikatu argitasunaren mesedetan.

H_2L^3, NaN_3 eta $Co(NO_3)_2{\cdot}6H_2O$ erreaktiboen arteko erreakzioak 1:2:2 erlazio molarrean azetonitrilotan **17** konplexuaren sorrera dakar ondoko formula orokorrarekin: $[Co_4(\mu\text{-}L)_2(\mu\text{-}N_3)_2(N_3)_2]{\cdot}2H_2O$. Konplexuak *R-3* talde espazialean kristalizatzen du eta

bere egitura 3.2. irudian agertzen da. **16** konposatuaren oso antzeko egitura erakusten badu ere, kasu honetan $\mu_{1,1,1}$-azida zubi hirukoitzek eta azida terminalek ordezkatzen dituzte kloruroak. Kristalografikoki erlazionatutako Co1 eta Co1(ii) ioiek CoN_4O_2 ingurune oktaedrikoak dituzte, apur bat distortsionatuak (A3.9. taula), non fenoxidoak *trans* posizioetan kokatuta dauden. Bestalde, Co2 eta Co2(ii) ioiek CoN_2O_3 koordinazio-ingurunea dute. Kasu honetan, SHAPE balioek ez dute poliedro jakin baterako doikuntza argirik ematen. Zerotik gertuen dauden balioak 2,895 eta 3,903 dira bipiramide trigonalarentzat eta Johnson bipiramide trigonalarentzat, hurrenez hurren (A3.10. taula).

Aurreko **16** konplexu tetranuklearrarekin alderatuta, Co-heteroatomo distantziak tarte estuago batean daude, non lotura laburrenak Co-$O_{fenoxido}$ (1,984(3)-2,046(3) Å) eta Co2-$N_{azidaterminala}$ (1,993(5) Å) diren. Gainerako Co-N_{amina} eta Co-$N_{azidazubia}$ lotura-distantziak tarte zabalagoan daude (2,173(4) eta 2,252(4) Å, hurrenez hurren). Aurreko konplexuan gertatzen denaren antzera, hemen ere Co1-X-Co2 (X = N_{azida} edo $O_{fenoxido}$) zubien angeluak zorrotzagoak dira zubia azida denean (92,95(16)-93,94(16)º; fenoxidoa denean 107,45(16)-108,70(16)º). Hala ere, partekatutako aurpegiak geometria karratua galtzen du Co1-N_{azida}-Co1(ii) angelu handiagoa emanez (100,41(17)º). Co-(μ-azida)-Co(ii) zatia planokidea da eta, Co1 eta Co2 ioiak μ-fenoxido/μ-azida bidez lotutako zatiak planokide izatetik gertu daude: 3,90 eta 1,97º-ko bisagra angeluak sortzen dituzte. Azkenik, molekula barneko Co^{II} arteko distantziak 3,249 eta 3,427 Å bitartean daude.

Molekulen arteko antolamenduari dagokionez, **16** konposatuarekin gertatzen den bezala, ordenamendu supramolekularra ikusten da. Kasu honetan, ur-molekulaz osatutako kluster hexanuklearraren ordez izar itxurako klusterra sortzen da, non sei ur molekulek hidrogeno-loturak sortzen dituzten azida terminalekin (A3.4. irudia). Azpimarratu behar da kasu honetan ur-molekulak ez direla planokideak. A3.5. irudian *b* ardatzean zehar ikus daitekeen bezala, ur-molekulak entitate tetranuklearrekin sigi-sagan lotuta daude.

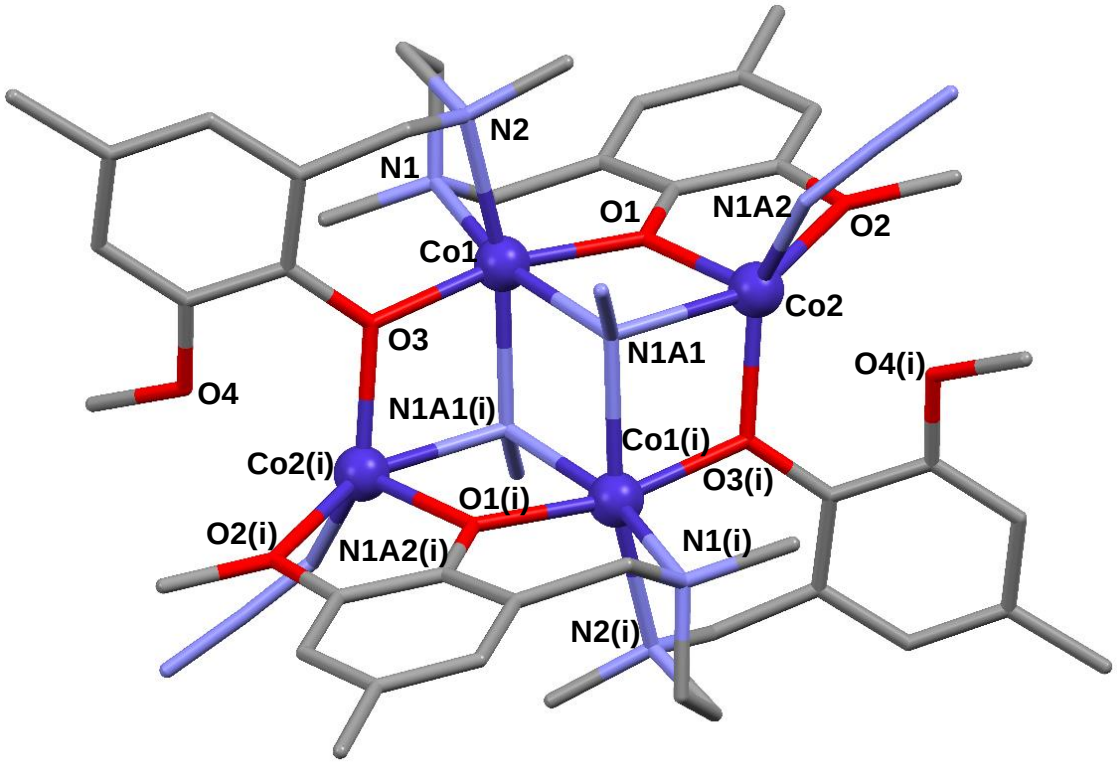

3.2. irudia.- 17. konposatuaren ikuspegia. Kolore-kodea: kobalto, nitrogeno, oxigeno eta karbono atomoak more, urdin argi, gorri eta gris kolorez, hurrenez hurren. Hidrogeno atomoak eta disolbatzaile molekulak ez dira irudikatu argitasunaren mesedetan.

H_2L^3, $Co(OAc)_2{\cdot}4H_2O$ eta Et_3N erreaktiboen arteko erreakzioak, 2:5:10 erlazio molarrean eta azetonitrilotan, **18** konposatu pentanuklear berdinaren bi fase desberdin ematen ditu. Desberdintasun nagusia azetonitrilo kristalizazio molekula kopurua da (lau eta hiru molekula **18a** eta **18b** faseetan, hurrenez hurren). Desberdintasuna arbuiagarria izanik, **18a** fasearen kristal-egitura baino ez da deskribatuko. Egitura 3.3. irudian aurkezten da $[Co_5(\mu\text{-}L)_2(\mu\text{-}OAc)_5(\mu\text{-}OH)]{\cdot}4MeCN$ formula orokorrarekin. Konplexu honek *P-1* talde espazialean kristalizatzen du. Egituraren konplexutasunak eta heteroatomoentzat dauden koordinazio-moduen aniztasunak agerian uzten du Mannich motako H_2L^3 estekatzaileak duen malgutasuna ohiz kanpoko konposatuak sintetizatzeko. Bost Co^{II} katioiren hamar karga positiboak protonatu gabeko bi estekatzaileekin (L^{2-}), lau azetato zubi hortz biko eta hiru hortzeko bat eta OH^- zubi hirukoitz batekin orekatzen dira. Co^{II} ioien arteko antzekotasunak ez dira nabarmenak, baina Co1 da 5 koordinazio-zenbakia duen bakarra, gainerakoek sei koordinazio-zenbakia dute. Co1 zentroaren SHAPE analisiaren arabera, kobalto ioiak geometria

bipiramide trigonala du (Co^{II} ioi guztien SHAPE balioak A3.11.-A3.12. tauletan daude). Bipiramidearen oinarria Co1-Co2 elkartzen dituen azetato oxigeno atomo batek (O1C), egituraren erdian dagoen Co1-Co2-Co4 elkartzen dituen OH^- taldeak eta Co1-Co5 elkartzen dituen fenoxido oxigeno (O1A) atomo batek osatzen dute. Gainerako bi erpinak Co1-Co2 zubiko beste azetato (O1D) batenak eta Co1-Co4-Co5 lotzen dituen fenoxido zubi batenak (O3A) dira. Co2 ioiarentzat CoO_6 koordinazio-ingurunea oktaedrikoa da (nabarmen distortsionatuagoa **18a** fasean **18b** fasean baino). Co2-aren oktaedroak Co1-aren ingurunearekin antzekotasunak ditu, baina O2B oxigeno atomoa da oktaedro distortsionatua osatzen duena (Co1 ioiaren kasuan, O2A metoxi taldea urrunegi dago eta ez dago zentro metalikoari lotuta). Sei oxigeno-atomoetatik bost zubiak dira. Horietako bi *cis* posizioan dauden eta Co2-Co1 lotzen dituzten azetatoei dagozkie (O2C eta O2D); hurrengo biak *cis* posizioan eta plano ekuatoriala osatuz Co2-Co3 lotzen dituzten fenoxidoei dagozkie (O1B eta O3B), eta azken oxigeno zubia (O1OH), O2B metoxi oxigenorako *trans* dagoena, Co1-Co2-Co4 lotzen dituen zubi hirukoitzaren OH^- taldeari dagokio. Co3 eta Co5 atomoen CoN_2O4 ingurunea oktaedriko distortsionatua da. Bi kasuetan, nitrogeno atomoek eta fenoxido oxigeno zubiek, elkarrekiko *cis* posizioa dute. Hala ere, Co3 ioiaren kasuan, gainerako bi posizioak hiru hortzeko azetato kelato batek osatzen ditu (Co3 eta Co4 lotzen dituen azetatoa). Aldiz, Co5 zentroaren koordinazio-ingurunea Co5-Co4 lotzen dituzten bi azetato desberdinen oxigeno atomoek osatzen dute (O2G eta O2F). Aipatu behar da Co3 ioiak aurkezten duen distortsio maila oso altua dela eta prisma trigonal gisa ere deskriba daitekeela. Azkenik, Co4 zentroa Co5 ioiaren aldera mugituta dago, bi azetato taldek eta fenoxido oxigeno atomo batek bi ioi metalikoen arteko zubi lana egiten baitute (3,304(1) eta 4,11(1) Å-eko distantzia dago Co4···Co5 eta Co4···Co3 artean, hurrenez hurren). Azken hiru posizioak metoxi oxigeno atomo bati (O4A), hiru hortzeko OH^- taldeari eta hiru hortzeko azetato zubiaren oxigeno bati (O2E) dagozkio.

OH^- taldea egituraren erdian egonkortzen da O4B metoxi taldearen oxigeno atomoarekin hidrogeno-lotura bat sortuz. Co-heteroatomo lotura-distantzia laburrenak oxigenoa inplikatzen dutenak dira, baina oso tarte zabalean aurki daitezke (1,988(4) eta 2,338(4) Å-eko tartean). Bestalde, Co-N lotura-distantziak 2,146(4)-2,258(4) Å tartean daude. Co-X-Co (X = $O_{fenoxido}$ edo OH^-) zubi-angeluek balio tarte handia erakusten dute, zorrotzagoetatik (94,87(13)º) zabalagoetaraino (127,64(19)º). Azkenik, ioi metalikoen arteko distantziarik laburrena 3,194 Å-ekoa da (Co2···Co3) eta luzeena 7,216 Å-ekoa (Co5···Co3).

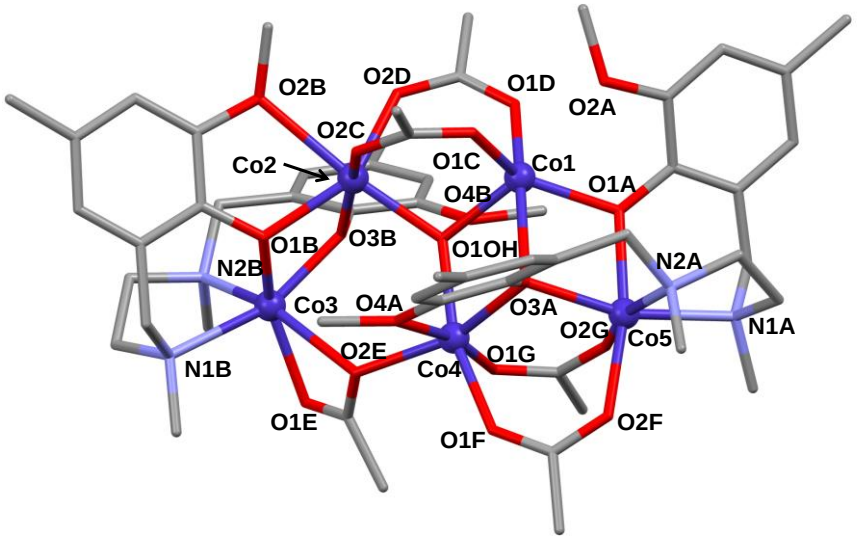

3.3. irudia.- 18a konposatuaren ikuspegia. Kolore-kodea: kobalto, nitrogeno, oxigeno eta karbono atomoak more, urdin argi, gorri eta gris kolorez, hurrenez hurren. Hidrogeno atomoak eta disolbatzaile molekulak ez dira irudikatu argitasunaren mesedetan.

19-25 konplexuak, H_2L^3, Et_3N, $TMCl_2{\cdot}nH_2O$ eta $Ln(NO_3)_2{\cdot}nH_2O$ erreakzionaraziz sintetizatuak, bi polimorfotan kristalizatzen dute: *P2₁/c* (**20-22** eta **24**) talde espazial monoklinikoan edo *C222₁* talde espazial ortorronbikoan (**19** eta **25**). Lehenengoak molekula oso bat du unitate asimetrikoaren barruan eta bigarrenak, aldiz, molekula erdia. Nukleo trinuklearra, ordea, berdin mantentzen da bi polimorfo posibleetan, desberdintasun nagusia ur-molekula baten presentzia/gabezia izanik. Adibide gisa, 3.4. irudian **22** konposatuaren egitura ematen da, ondoko formula orokorra duena: $[DyCo_2(\mu\text{-}L^3)_2(H_2O)_2Cl_2]Cl{\cdot}H_2O{\cdot}MeCN$. Konplexua $[DyCo_2(\mu\text{-}L^3)_2(H_2O)_2Cl_2]^+$ unitate kationiko batez, Cl^- anioi batez eta ur eta azetonitrilo kristalizazioko molekula banaz osatua dago. Entitate trinuklear kationikoaren barruan, bi $[CoCl(L^3)]^-$ unitate $[Dy(H_2O)_2]^{3+}$ unitate zentralari koordinatzen dira bakoitzak bi fenoxido zubi eta metoxi talde bakarra erabiliz,

Horrela, lau fenoxido taldek, bi metoxik eta bi ur molekulek osatzen dute lantanido ioiaren DyO_8 koordinazio-poliedroa. Dy-O1 lotura laburrenak eta Dy-O3 edo Dy-OW tarteko loturak 2,258(6)-2,354(7) Å tartean daude; $Dy\text{-}O_{metoxi}$ luzeenak, berriz, 2,585(6)-2,657(7) Å tartean. Koordinazio esfera SHAPE softwarearekin aztertu zen (A3.14. taula) zortzi erpineko poliedro ideal batekiko distortsio maila ikusteko. Analisiaren arabera, 1,847 SHAPE balioa duen antiprisma karratuak deskribatzen du ondoen poliedroa.

Edonola ere, antiprisma karratuaren eta dodekaedro triangeluarraren poliedroek antzeko SHAPE balioak erakusten dituzte konplexu guztietan. Co^{II} ioiek, aldiz, CoO_2N_2Cl koordinazio-ingurunea erakusten dute, non Co-$O_{fenoxido}$, Co-N eta Co-Cl distantziak 1,978(6)-2,150(7), 2,090(9)-2,271(9) eta 2,29 (3)-2,256(3) Å-eko tarteetan dauden, hurrenez hurren. SHAPE balioen arabera, bi Co^{II} ioiek distortsionatutako piramide karratua dute. Nitrogeno eta oxigeno atomoak oinarri karratuaren erpinetan daude eta posizio axiala kloruro ioiak hartzen du. Co^{II} eta Dy^{III} zentro paramagnetikoen molekula barneko distantziak 3,4859(15) eta 3,4532(15) Å-ekoak dira eta hiru ioiek osatutako angelua linealtasunetik gertu dago: 163,02(3)º. Molekula barneko Co···Co distantzia 6,863(2) Å-ekoa da. Fenoxido zubiek 100,9(2)-110,6(3)º-ko Co-O-Dy angeluak osatzen dituzte. $[Dy(H_2O)_2]^{3+}$ unitatean kontrako posizioan dauden ur-molekulek hidrogeno-loturak osatzen dituzte kloruro kontraioiekin (O1W···Cl2 eta O2W···Cl2) *b* ardatzean zehar kateak osatuz (A3.6. irudia). Molekula barnean hidrogeno lotura gehigarri bat ematen dute koordinatu gabeko metoxi taldearekin (O1W···O4B eta O2W···O4A). Gainera, kristalizazio-ur molekula hidrogeno lotura gehigarriek egonkortzen dute: O1S···Cl1A eta O1S···O2W. Kontuan izan azken hauek ez direla agertzen **19** eta **25** konposatuetan. Azkenik, molekularteko Co···Co eta Dy···Dy distantziarik laburrenak 7,924 eta 9,541 Å-ekoak dira. Beraz, erabat isolatutzat jo daitezke.

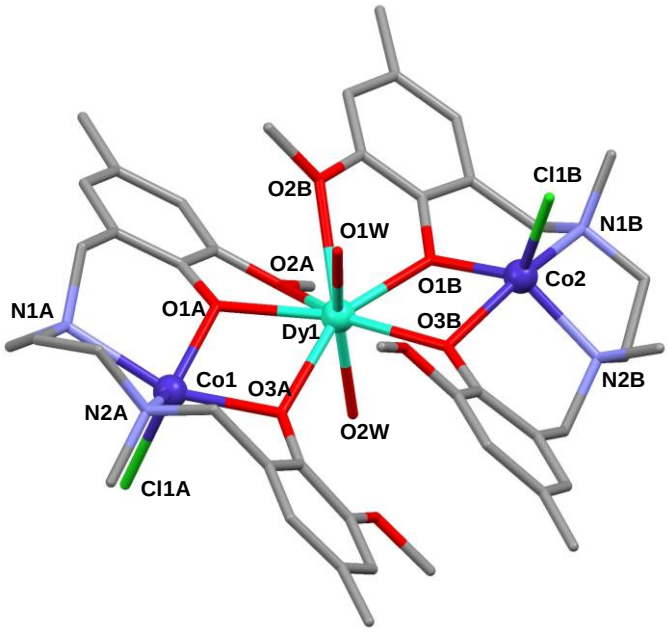

3.4. irudia.- 22 konplexuaren ikuspegia. Kolore-kodea: kobalto, disprosio, nitrogeno, oxigenoaren eta karbono atomoak more, turkesa, urdin argi, gorri eta gris kolorez, hurrenez hurren. Hidrogeno atomoak, kontraioiak eta disolbatzaile molekulak ez dira irudikatu argitasunaren mesedetan.

3.3.2. 16-25 konplexuen propietate magnetiko estatikoak

Suszeptibilitate magnetikoaren tenperaturarekiko mendekotasuna **16-25** konposatuen lagin polikristalinoetarako neurtu da, 2-300 K tenperatura tartean 0,1 T-ko kanpo eremu magnetikoa erabiliz.

Giro-tenperaturan, **16** konplexuak erakusten duen 12,56 $cm^3 \cdot mol^{-1} \cdot K$-eko $\chi_M T$ balioa spinaren balioa (7,50 cm3$\cdot mol^{-1} \cdot K$) baino handiagoa da S = 3/2 eta g = 2,0 (3.5. irudia, ezkerrean) duten lau Co^{II} ioi isolaturentzat. Hau da, momentu angeluar orbitala duela adierazten du. Era berean, **17** konposatuarentzat 11,46 $cm^3 \cdot mol^{-1} \cdot K$-eko balioa neurtu da giro-tenperaturan (3.5. irudia, eskuinean). Hala ere, tenperatura jaistean, portaera nabarmen aldatzen da batetik bestera. Lehenengoaren kasuan, $\chi_M T$ balioa ia konstante mantentzen da giro-tenperaturatik 75 K-eraino, non nabarmenago erortzen hasten den 5,97 $cm^3 \cdot mol^{-1} \cdot K$-eko gutxieneko baliora heldu arte 2 K-etan. Jaitsiera hori spin-orbita akoplamenduaren eraginagatik nahiz molekula barneko interakzio antiferromagnetikoengatik eman daiteke. Bigarrenaren kasuan, tenperatura giro-tenperaturatik 26,0 K-eraino jaisten den heinean, $\chi_M T$ balioa etengabe handitzen da 13,61 $cm^3 \cdot mol^{-1} \cdot K$ balioraino. Ondoren, igoera zorrotzagoa gertatzen da 15,60 $cm^3 \cdot mol^{-1} \cdot K$-eko balio maximoa lortuz 7,0 K-etan. Honen azpitik, bat-bateko jaitsiera ematen da 14,41 $cm^3 \cdot mol^{-1} \cdot K$-eko baliora 2,5 K-etan. Hasierako eta amaierako igoera handiek iradokitzen dute molekula barneko truke-interakzioak ferromagnetikoak direla. Azken jaitsiera, berriz, molekulen arteko interakzio antiferromagnetikoek eta antzeko klusterretarako behatutako kontribuzio anisotropikoak (D) eman dezakete [16–18]. Bi konplexuek egitura bera dutela kontuan hartuta, truke-interakziorako bi bide posiblerekin (J_1 eta J_2 3.5. irudian), suszeptibilitate datuak doitzen saiatu gara PHI softwarearekin [19] eta aurretik erabilitako eredu Hamiltondar sinple batekin [14]. Zoritxarrez, ez gara gai izan doikuntza on bat lortzeko. Zailtasuna hainbat faktoreri lotuta dagoela uste dugu: (i) spin-orbita akoplamendua, (ii) bi truke-interakzio bide desberdinen presentzia, (iii) bi koordinazio-ingurune desberdin eta (iv) molekularteko interakzio posibleak, besteak beste. Dena den, azpimarratzekoa da estekatzaileak klorurotik azidara aldatzean interakzioaren izaera guztiz aldatzen dela, antiferromagnetiko izatetik ferromagnetiko izatera pasatzen baita.

Tenperatura desberdinetan neurtutako *M(H)* kurbak (3.5. irudia, grafika txikiak) ez dira gainezartzen eta ez dira saturaziora heltzen eremu altuenean ere (7 T). Honetan oinarrituz, sistemek anisotropia magnetikoa izan dezaketela ondorioztatzen da. Aipatzekoa da, **16** konposatuaren kasuan magnetizazioa mantsoago gertatzen dela **17** konplexuaren kasuan baino. Hori bat dator lehenak erakusten duen portaera

antiferromagnetikoarekin eta bigarrenaren portaera ferromagnetikoarekin. 2 K-etan neurtutako magnetizazio balioak 7 T-tan 9,23 eta 8,3 $N_{\mu B}$ dira, hurrenez hurren. Balio horiek bat datoz teorikoki kalkulatutako 8,6 $N_{\mu B}$ balioarekin isolatutako Co^{II} oktaedriko ioientzat ($S_{eraginkorra}$ = 1/2 eta g = 4/3).

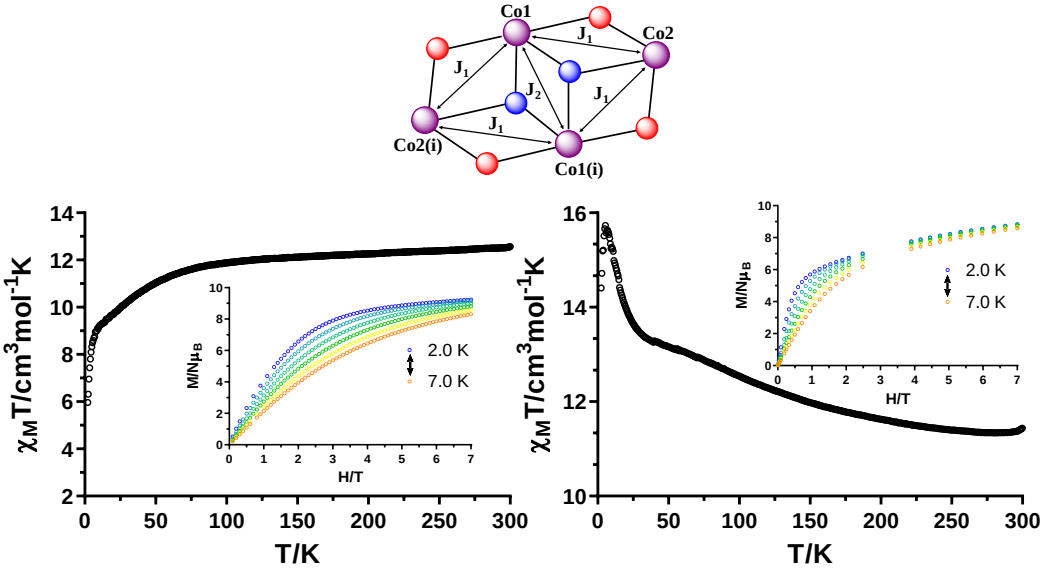

3.5. irudia.- $\chi_M T$ balioaren tenperaturarekiko mendekotasuna 1000 Oe-eko eremu magnetikoa erabiliz **16** (ezkerrean) eta **17** (eskuinean) konplexuentzat. Grafiko txikia: 2-7 K tenperatura tartean neurtutako magnetizazio kurbak. Marra etenek ez dute esanahi fisikorik. Goian: truke magnetikoko bideak **16** eta **17** konposatuetan, non bola gorriek oxigeno atomoak irudikatzen dituzten eta urdinek kloruro edo azida N atomoak.

Giro-tenperaturan, **18** konposatuarentzat neurtutako 18,36 $cm^3 \cdot mol^{-1} \cdot K$-eko $\chi_M T$ balioa spina bakarrik kontuan hartuta baino handiagoa da momentu angeluar orbitalaren presentzia dela eta. Tenperatura jaistean, $\chi_M T$ balioak behera egiten du pixkanaka 8,83 $cm^3 \cdot mol^{-1} \cdot K$-eko gutxieneko baliora iritsi arte 10 K-etan. Jarraian, igoera handia detektatzen da 13,24 $cm^3 \cdot mol^{-1} \cdot K$-era iritsiz 4 K-etan. Azkenik, 9,08 $cm^3 \cdot mol^{-1} \cdot K$-eko baliora jaisten da 2 K-etan. Hasierako pixkanakako jaitsierak eta magnetizazio-kurben gainezarpen ezak adierazten dute sistemak anisotropia magnetikoa izan dezakeela (3.6. irudia). Ondoren datorren bat-bateko gorakadak agerian uzten ditu ioien arteko molekula barneko interakzio ferromagnetikoak. Azken jaitsiera, berriz, zero eremuko zabaltzearen edo/eta molekula arteko interakzio antiferromagnetikoen ondorio izan daiteke.

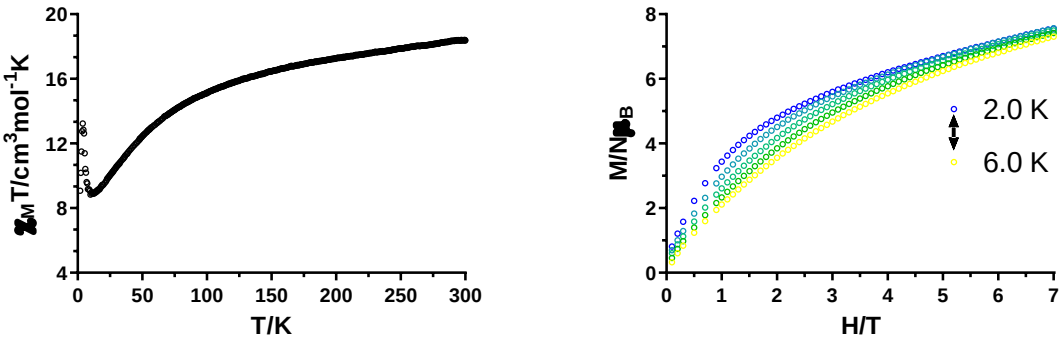

3.6. irudia.- $\chi_M T$ balioaren tenperaturarekiko mendekotasuna 1000 Oe-eko eremu magnetikoa erabiliz (ezkerrean) eta 2-6 K tenperatura tartean neurtutako magnetizazio kurbak (eskuinean) **18** konplexuentzat.

19-25 konposatuen kasuan, tenperaturaren mendeko suszeptibilitate-datuak 3.7. irudian erakusten dira. Giro-tenperaturan neurtutako $\chi_M T$ balioak ondokoak dira **19-24** konposatuentzat, hurrenez hurren: 6,24, 14,24, 25,27, 20,33, 17,71 eta 9,74 $cm^3 \cdot mol^{-1} \cdot K$. Guztiak dira bi Co^{II} ioien eta Ln^{III} ioi batentzat espero direnak baino handiagoak, ziur aski, Co^{II} ioien momentu angeluar orbitalaren ondorioz. Aldiz, 13,43 $cm^3 \cdot mol^{-1} \cdot K$-eko balioa **25** konposatuarentzat 14,17 $cm^3 \cdot mol^{-1} \cdot K$-eko balio teorikoa baino pixka bat txikiagoa da ioi isolatu baterako (Dy^{III}, $^6H_{15/2}$, S = 5/2, L = 5, eta g = 4/3). Dena den, espero den tartearen barruan sartzen da [20]. Tenperatura jaitsi ahala, portaera desberdinak detektatzen dira hainbat konplexutarako. **19** molekularen kasuan, $\chi_M T$ produktua pixkanaka txikitzen da tenperatura hoztean, nahiz eta malda aldaketa nabaritzen den 50 K-etik behera. 3,80 $cm^3 \cdot mol^{-1} \cdot K$-eko balioa lortzen da 2 K-etan. Portaera hori batez ere Co^{II} ioien spin-orbita akoplamenduaren ondorioz ematen da, sistema trinuklearrak teorian ondo isolatuta baitaude kristal-egituraren deskribapenean aipatu den bezala. **20-24** konposatuen kasuan beste efektu batzuk ere ikus daitezke; bai lantanido ioiek edo baita Co^{II} eta Ln^{III} ioien arteko truke-interakzioek eragindakoak ere (Co···Co molekula barneko distantziak handiegiak direla uste dugu haien arteko interakzioak kontuan hartzeko). **20** konposatuaren kasuan, $4f^7$ konfigurazioa duen Gd^{III} ioiak izaera isotropikoa izatea espero da eta, beraz, $\chi_M T$ produktuaren pixkanakako igoera (19,04 $cm^3 \cdot mol^{-1} \cdot K$-eko gehieneko balioa lortzen duena 2,5 K-etan) molekula barneko truke-interakzio ferromagnetikoei lotzen da. **21, 22 eta23** konposatuek Tb^{III}, Dy^{III} eta Er^{III} ioiak dituzte, hurrenez hurren. Kasu horietan, tenperaturarekiko mendekotasuna nabarmenagoa da. Pixkanaka, $\chi_M T$ balioa jaitsiz doa giro-tenperaturatik 50 K, 28 K eta 9 K-era **21**, **22** eta **23** sistementzat tenperatura baxuenetan balio maximora heldu

aurretik (21,62, 18,74 eta 13,64 $cm^3 \cdot mol^{-1} \cdot K$). Kasu hauetan, $\chi_M T$ vs T kurben forma Ln^{III} ioien presentziak determinatzen dute. Pixkanakako jaitsiera oinarrizko egoerako M_J azpimailen despopulazio termikotik sortzen da. Tenperatura baxueneko maximoak, aldiz, CoGdCo analogoan dagoeneko detektatu diren truke-interakzio ferromagnetikoen ondorio dira. Maximoak posizio antzekoetan ematen direnez, truke-interakzioen antzeko balioa espero da denentzat. **21** eta **22** konposatuetan maximoen azpitik beherakada txiki bat ikusten da, molekularteko interakzio antiferromagnetiko ahulen adierazle izan daitekeena. **24** konposatuak, aldiz, pixkanaka behera egiten du tenperatura-tarte osoan 5,28 $cm^3 \cdot mol^{-1} \cdot K$-era heldu arte 2 K-etan. Beherakada Stark azpimailen despopulazioari dagokio. Kasu honetan, ez da molekula barneko interakzio ferromagnetikoen zeinurik ikusi. Azkenik, **25** konposatuak $\chi_M T$ produktuarekiko ohiko mendekotasun termikoa erakusten du tenperatura-tarte osoan jaitsiera mailakatua emanez 11,61 $cm^3 \cdot mol^{-1}$ K-eko baliora heldu arte 2 K-etan.

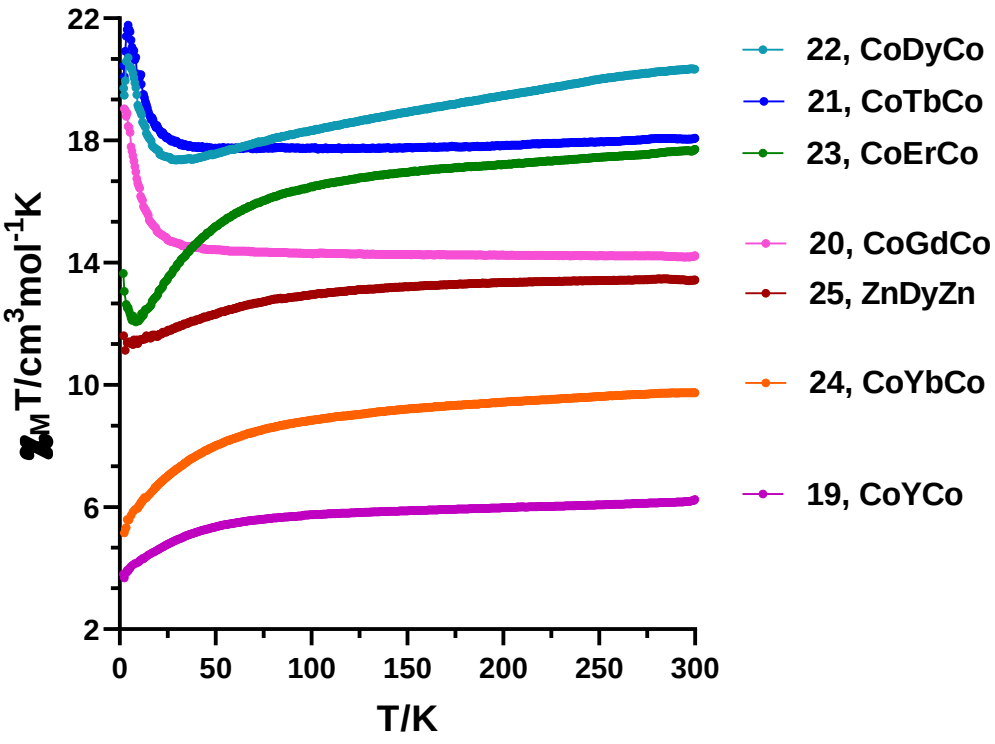

3.7. irudia.- $\chi_M T$ balioaren tenperaturarekiko mendekotasuna 1000 Oe-eko eremu magnetikoa erabiliz **19-25** konplexuentzat.

19-25 konposatuentzat 2 K-etan neurtutako magnetizazio kurbek ez dute espero den saturazio balioa erakusten neurtutako eremu magnetiko altuenean (7 T). Hain zuzen,

honako balio maximoak erakusten dituzte: 4,75, 11,59, 9,59, 8,52, 9,45, 7,32 eta 5,23 $N_{\mu B}$, hurrenez hurren (3.8. irudia). Balio hauek, Co^{II} eta Ln^{III} (**19-24**) eta Dy^{III} (**25**) ioientzako kalkulatutako balioetatik urrun daude, hauek izanik balio teorikoak: 6, 13, 15, 16, 15, 10 eta 10 $N_{\mu B}$, hurrenez hurren (*g* = 2 eta *S* = 3/2 Co^{II} ioiarentzat eta dagokion *g* eta *J* lantanidoentzat). Portaera hau anisotropia magnetikoaren adierazle garbia dela uste dugu. Izan ere, **19** konposatuaren magnetizazio balioa bi kobalto anisotropikorentzat espero den ~4.3 $N_{\mu B}$ baliotik gertu dago. **20** konposatuaren kasuan, lortutako balioa bat dator bi Co^{II} anisotropiko eta Gd^{III} isotropiko batentzat espero denarekin. Amaitzeko, beste konposatu guztietarako espero den magnetizazio balioa (bi Co^{II} anisotropiko eta Ln^{III} ioia kontuan hartuz) beti da esperimentalki kalkulatutakoa baino altuagoa Ln^{III} ioien izaera anisotropikoarekin bat eginez.

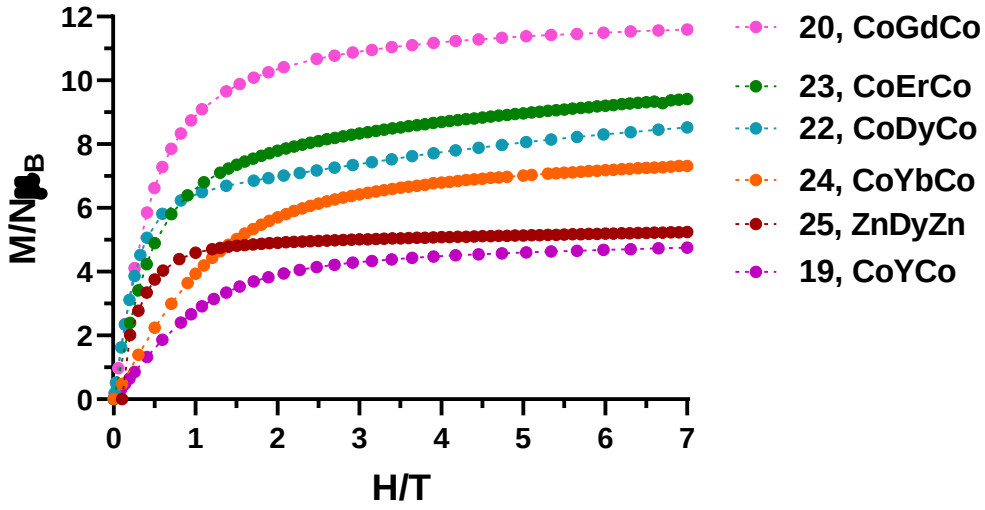

3.8. irudia.- Magnetizazioaren eremuarekiko mendekotasuna 2 K-etan **19-25** konposatuentzat.

3.3.3. 16-25 konposatuen propietate magnetiko dinamikoak

Propietate magnetiko dinamikoei dagokienez, korronte alternoko (*ac*) neurketak egin ziren kanpoko eremu magnetikorik gabe ia konplexu guztientzat (**23** eta **24** konposatuak baztertu ziren, kanpoko eremu magnetiko pean lehenak frekuentziarekiko mendekotasun ahula erakusten baitu fasez kanpoko osagaian, A3.29. irudia, eta, bigarrenak, ezta seinalerik ere, A3.30. irudia). Baldintza hauetan, soilik **18** eta **22** konplexuek erakusten dituzte frekuentziarekiko mendekotasuna duten maximoak 5 K-etik behera χ_M'' osagaian (3.9. eta 3.12. irudiak). **21** konposatuak maximo bakar bat erakusten du 10000 Hz-tan, ekipoaren tenperatura mugan (3.12. irudia). **20** eta **25**

konposatuek frekuentziarekiko mendekotasun ahula erakusten dute eta, **16**, **17** eta **19** konposatuek, aldiz, ez dute seinalerik erakusten fasez kanpo (A3.21.-A3.23. irudiak). Hala ere, *SMM* gehienetan ikusten den bezala, *QTM* azkarrak magnetizazioaren erlaxazio mantsoa ezkuta dezake. Aipatu behar da efektu hau debekatuta dagoela Kramers dobleteentzat, baina interakzio dipolarrek nahiz kobalto ioiaren spin nuklearrarekin eman daitekeen interakzioak ahalbidetu dezakete [21]. Tunel efektua deuseztatzeko, neurketa guztiak errepikatu dira 1000 Oe-eko kanpoko eremu magnetiko arbitrariopean. Kanpoko eremu magnetiko hau aukeratu da *QTM* erabat edo partzialki desaktiba dezakelako, baina eremuaren mendeko mekanismo zuzena indartu gabe (Co^{II} ioientzat nahiko ohikoa den prozesua [22,23]). Baldintza berri hauetan, **17**, **20** eta **23** konposatuek frekuentziarekiko mendekotasun ahuleko seinaleak erakusten dituzte (A3.29. irudia). **18**, **19**, **21** eta **22** sistemek, bestalde, maximo argiak erakusten dituzte 5 K-etik behera fasez kanpoko osagaian (3.9., 3.11. eta 3.12. irudiak). Azkenik, **25** konplexuak erakusten du alderik nabarmenena 12 K-etik beherako maximoekin (3.13. irudia). Beraz, kanpoko eremu magnetikorik gabe egindako neurketetan tunel-efektua prozesu garrantzitsua dela frogatu da, baina kanpoko eremu magnetikoa erabiliz desaktibatzen da konposatu gehienentzat (gutxienez hein batean).

16 konposatuan ez bezala, azida zubiek eragindako truke-interakzio magnetiko ferromagnetikoa eta kanpoko eremuaren aplikazioa nahikoa dira **17** konposatuan magnetizazioaren erlaxazio motela emateko. Dena den, *QTM* guztiz ezabatu ez izanak maximoak ezin detektatzea eragiten du eta, ondorioz, ez du ahalbidetzen $\chi_M''(\upsilon)$ kurben doikuntza energia-barrera efektiboaren balioa (U_{eff}) lortzeko. Hala ere, erlaxazio-prozesu bakarra dagoela suposatuz, Debyeren eredua honela erabil daiteke:

$$ln(\chi_M''/\chi_M') = ln(2\pi\upsilon\tau_0) + E_a/k_BT \qquad \textit{3.1. ekuazioa}$$

Hurbilketa honek U_{eff} eta τ_0 parametroen ondoko balioak ematen ditu: 7,8 K eta $6{,}43\cdot10^{-8}$ s, hurrenez hurren (A3.42. irudia).

Kristal-egituraren deskribapenean aipatu den bezala, **18a**/**18b** konposatuak lau zentro oktaedriko distortsionatu eta bipiramide trigonal bat ditu. Lehenengoentzat, anisotropia positibo edo plano errazekoa espero izaten da ($D > 0$) [24–26]; azken geometria-motarentzat, berriz, plano errazekoa nahiz ardatz errazekoa ($D < 0$) deskribatu izan dira [27]. $D > 0$ egoera orokorra izanez gero, magnetizazioaren erlaxazio motela detektatzeko kanpoko eremu magnetiko baten beharra espero daiteke, anisotropia positiboa duten Kramers ioiek hori eskatzen baitute. Dakigunaren arabera, $Ni^{I/II}$ ioi mistoetan oinarritutako kluster tetranuklearra da $D > 0$ duen eta kanpoko eremu

magnetikorik gabe SMM portaera azaltzen duen sistema bakarra [28]. Hala ere, **18** konposatuak maximo nabarmenak erakusten ditu kanpo *dc* eremurik gabe 2,3-4 K-eko tenperatura-tartean $\chi_M''(T)$ grafikoan (3.9. irudia, ezkerrean). Maximoen zabalera handia bi maximo multzoen batuketaren bidez azal daiteke, frekuentzia baxuetan nabarmenagoa dena (60-500 HZ). Baldintza hauetan ematen den erlaxazio magnetiko motela arrazoi hauen bidez azal liteke: (i) *D* balio negatibo baten bidez, zeina Co1 bipiramide trigonalak edo Co2 eta Co3 distortsionatuek ematen dezaketen (azken horiek prisma trigonal distortsionatu gisa ere deskriba daitezke), (b) kobalto ioien artean ematen den truke-interakzio indartsuen bidez edo (c) bi efektuen baturaren bidez. Hain zuzen, bada kobaltoan oinarritutako konposatu heptanuklear baten beste adibide bat, bi zentro bipiramide trigonal eta bost zentro oktaedriko dituena, zeinak frekuentziaren mendeko χ_M'' seinaleak erakusten dituen 4 K-en azpitik eremu magnetikorik aplikatu gabe [29].

Maximo ia gainjarrien presentzia termikoki aktibatutako bi prozesuren ondorioa izan daiteke, energia-barrera balio oso antzekoak izango lituzketenak. 2,3-3,8 K tenperatura-tartean aztertutako Cole-Cole grafikoetatik lortutako α balioek zentzua ematen diote esandakoari (A3.31. irudia), erlaxazio-prozesuen banaketa zabala adierazten baitute (0,30-0,50). Hala ere, ezin izan dira bereizi bi prozesu desberdinei dagozkien zirkuluerdi independenteak. Frekuentzia bakoitzerako fasez kanpoko suszeptibilitatearen tenperaturarekiko mendekotasuna Debye eredu orokortuari doitu zaio, tenperatura bakoitzerako erlaxazio-denborak lortzeko (A3.37. irudia). Erlaxazio-denboren linealtasuna ikusita, datuak Arrheniusen ekuaziora egokitu dira energia-barrera efektiborako 23,8 K-eko balioa eta τ_0 parametroarentzat $6{,}52\text{-}10^{-8}$ s-ko balioa lortuz.

1000 Oe-eko kanpoko eremu magnetiko arbitrarioa aplikatzeak ustekabeko emaitzak sortzen ditu. Alde batetik, 3.9. irudian (eskuinean) ikusten den bezala, χ_M'' osagaiak normalki *QTM*ri lotzen diren seinaleak ematen ditu maximoen azpitik. Kasu honetan, ordea, ziur aski seinale hauek eremuak aktibatutako prozesu zuzen bati lotutakoak dira (ikusi eztabaida beherago). Bestalde, bi maximo multzoak orain hobeto definituta agertzen dira, lehena 4 K azpitik eta bigarrena 5 K azpitik. Dena den, datuen izaera dela eta $\chi_M''(\upsilon)$ kurbak 3,2-4,4 K tenperatura tartean soilik aztertu ahal izan ditugu, lehen maximo multzoari dagokion tartea kontutan hartuz (A3.38. irudia). A3.38. irudian (erdian) ikus daitekeen bezala, tenperatura altuagoetan maximoaren posizioa nolabait egonkor mantentzen da eta, beraz, bertatik lortutako erlaxazio-denborak ez datoz bat *SMM* portaerarekin. Ez gaude ziur bigarren maximo multzo honen jatorriari buruz, baina seinale zaratatsuaren eta definizio gutxiko maximoen izaera dela eta, zaila da datuak ondo interpretatzea. Ondorioz, 3,2-4,4 K tenperatura-tartean aztertu ditugu datuak eta,

berriz ere, Arrheniusen legera doitu ditugu datuak honako parametro balioak lortuz: U_{eff} = 17,3 K eta τ_0 = 2,92-10^{-7} s. Cole-Cole grafikoetatik lortutako α parametroek balio altuak ematen dituzte bai 3,2 K-etan (0,38) eta baita 4,4 K-etan ere (0,37), tenperatura baxuetako prozesu zuzenarekin eta tenperatura altuetako bigarren maximo multzoarekin adostasunean. *Dc* suszeptibilitate magnetiko neurketa gehiago egiteko asmoa dugu eremu magnetiko desberdinekin irismen luzeko ordenamendu baten hipotesia baztertzeko.

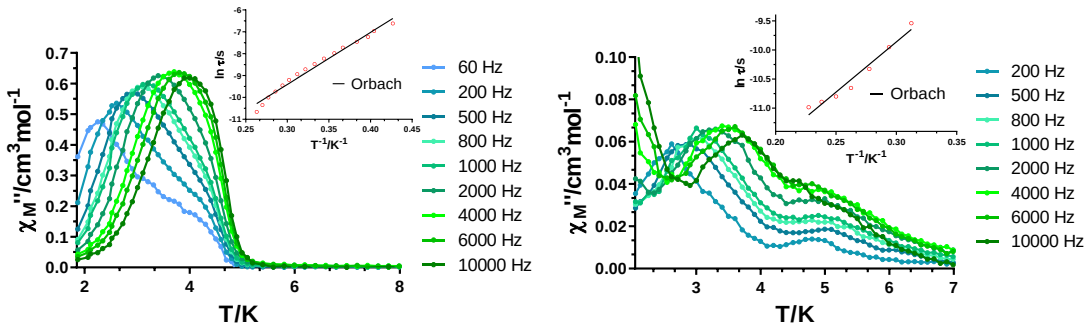

3.9. irudia.- 18 konposatuentzat, fasez kanpoko suszeptibilitatearen tenperaturarekiko mendekotasuna frekuentzia desberdinetan kanpoko eremu magnetikorik aplikatu gabe (ezkerrean) eta 1 kOe-etako kanpoko eremu magnetikopean (eskuinean). Grafika txikia: Arrheniusen grafikoa erlaxazio-denboretarako Orbach prozesua kontuan hartuz.

Eremu magnetikoaren presentziak/gabeziak eragindako emaitzak ikusita, erlaxazio-denboren eremuarekiko mendekotasuna aztertu dugu 3,2 K-eko tenperatura finkoan, 3.10. irudian azaltzen den bezala. Erlaxazio-denbora motelenak kanpoko eremurik aplikatzen ez denean lortzen dira. Gainera, eremu magnetikoaren intentsitatea handitu ahala, erlaxazio-denborak gero eta azkarragoak bilakatzen dira, prozesu zuzen baten agerpena berretsiz (kontuan hartu prozesu zuzena honela definitzen dela: $\tau^{-1} = AH^4T$). Magnetizazioaren erlaxazio motela nondik eratorria den jakiteko estrategia ona diluzio magnetikoa egitea litzateke. Izan ere, modu horretan molekula barneko Co···Co truke-interakzioak ekidingo lirateke. Hortaz, jakin ahal izango genuke ea SMM portaera ioi indibidualetatik datorren, edo truke-interakzio magnetiko indartsuengatik ematen den. Zoritxarrez, orain arte ez gara gai izan Zn^{II} analogo diamagnetikoa sintetizatzeko.

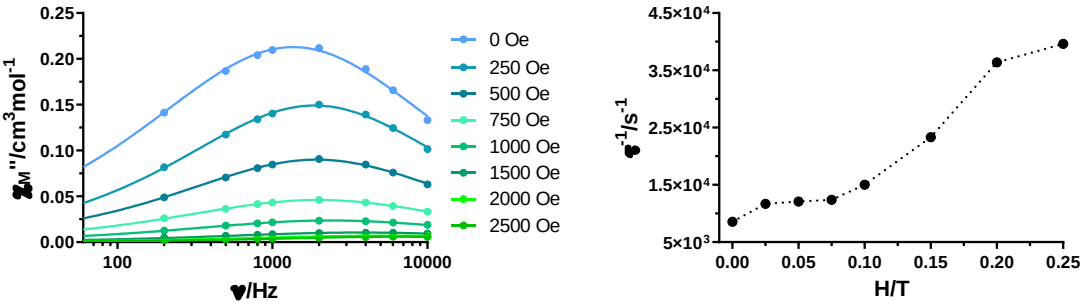

3.10. irudia- Fasez kanpoko suszeptibilitate osagaiaren frekuentziarekiko mendekotasuna kanpoko eremu desberdinetan eta 3,2 K-eko tenperaturan (ezkerrean). Eremu magnetiko desberdinetan lortutako erlaxazio-denboren alderantzizkoa eremu magnetikoaren aurrean (eskuinean).

Konposatu heterotrinuklearrei dagokienez, lehenik eta behin estekatzailearen diseinu arrazionala nabarmendu nahiko genuke. Colaciok eta kolaboratzaileek, aurretik $Co^{II}Y^{III}$ ioietan oinarritutako konposatu baten berri eman zuten antzeko estekatzailearekin, baina hiru aminako albo kate luzeago batekin [25]. Kasu horretan, estekatzailearen barneko gunean kokatzen da kobalto ioia koordinazio-ingurune oktaedrikoa erakutsiz (koordinazio-ingurunea bi ioien arteko zubi lana egiten duen azetatoak osatzen du). Lehen aipatu bezala, ingurune mota horrek normalean *D* balio positiboak sortzen ditu, aipatutako artikuluan berresten den bezala. Gure kasuan, gure helburu nagusia zen triamina bat erabili beharrean diamina bat erabiltzea bosteko koordinazio-zenbakia sortzeko. Ideia hau aurretik gure taldean deskribatutako $Zn^{II}Dy^{III}Zn^{II}$ sistementzako lortutakoa ikusita sortzen da, non Zn^{II} ioiek piramide karratu geometria duten [30]. Bost koordinazio-zenbakidun Co^{II} konposatuentzat, Cui eta kolaboratzaileek egindako lan batean jasotzen dira bipiramide trigonal edo piramide karratu geometrietarako lortutako emaitza asko [31]. Lan horren arabera, bi geometria hauetarako *D* balio positiboak zein negatiboak espero daitezke. Interesgarria da ikustea bipiramide trigonalek SMM portaera eman dezaketela kanpoko eremu magnetikorik gabe [32]. Gure kasuan, **19**. konposatuko Co^{II} zentroak hobeto deskribatzen dira piramide karratuko geometria batekin, baina 0,46 balioa duen Addison τ^5 parametroak [33] bi geometria posibleen nahasketa adierazten du (τ^5 zero da piramide karratu ideal batentzat, 1 balioak konfigurazio bipiramide trigonal ideala irudikatzen duen bitartean). Beraz, **19** konposatua *SMM* izateko hautagaia da.

Hala ere, **19** konposatu trinuklearrak ez du χ_M'' seinalerik erakutsi kanpoko eremu magnetikorik aplikatu gabe, ziur aski *QTM* (A3.22. irudia) azkarraren ondorioz. 1000 Oe-eko kanpoko eremu magnetiko bat aplikatzean, frekuentziaren mendeko maximo argiak agertzen dira 4 K-etik behera *SMM* portaera adieraziz (3.11. irudia). Nahiz eta Cole-Cole diagrametatik 2,0-4,0 K tenperatura-tartean lortutako α balioek erlaxazio-prozesuen banaketa nahiko estua dela adierazten duten (0,24(2,0 K) eta 0,08(4,0 K)), tenperatura baxuetako balio altuagoek eta $\chi_M'(T)$ (A3.25. irudia) grafikan maximoen azpitik dauden seinaleek oraindik *QTM* efektuaren edo prozesu zuzen baten presentzia adierazi dezakete. Kontuan izanik *D* parametroaren zeinu eta magnitudeari buruzko informazio gehiagorik ez dugula (ezin izan ditugu **19** eta **20** konposatuen dc datuak doitu D parametroen balioak lortzeko), $\chi_M''(\upsilon)$ kurbetatik lortutako erlaxazio-denborak ondoko ekuazioetara doitu dira:

$$\tau^{-1} = \tau_{QTM}^{-1} + \tau_0^{-1} \exp(-U_{eff}/k_BT) \qquad \textit{3.2. ekuazioa}$$

$$\tau^{-1} = AT + BT^n \qquad \textit{3.3. ekuazioa}$$

3.2. ekuazioak aldibereko *QTM* eta Orbach prozesuak hartzen ditu kontuan (3.11. irudia, lerro grisa). Doikuntza honek τ_{QTM}, U_{eff} eta τ_0 parametroentzako ondoko balioak ematen ditu, $1{,}42\cdot10^{-4}$ s, 12,7 K eta $8{,}51\cdot10^{-7}$ s, hurrenez hurren. 3.3. ekuazioak, bestalde, aldibereko prozesu zuzena eta Raman mekanismoa hartzen ditu kontuan (lerro urdin iluna). Doikuntzak *A*, *B* eta *n* parametroentzako ondoko balioak ematen ditu, 2319 $s^{-1}K^{-1}$, 322,3 $s^{-1}K^{-3.61}$ eta 3,61, hurrenez hurren. Bi doikuntzetarako lortutako parametroek zentzudunak ematen dute. *Ab initio* kalkuluen zain gaudenez, eskura ditugunean erlaxazio prozesuari buruzko iritzi landuagoa emateko gai izango gara.

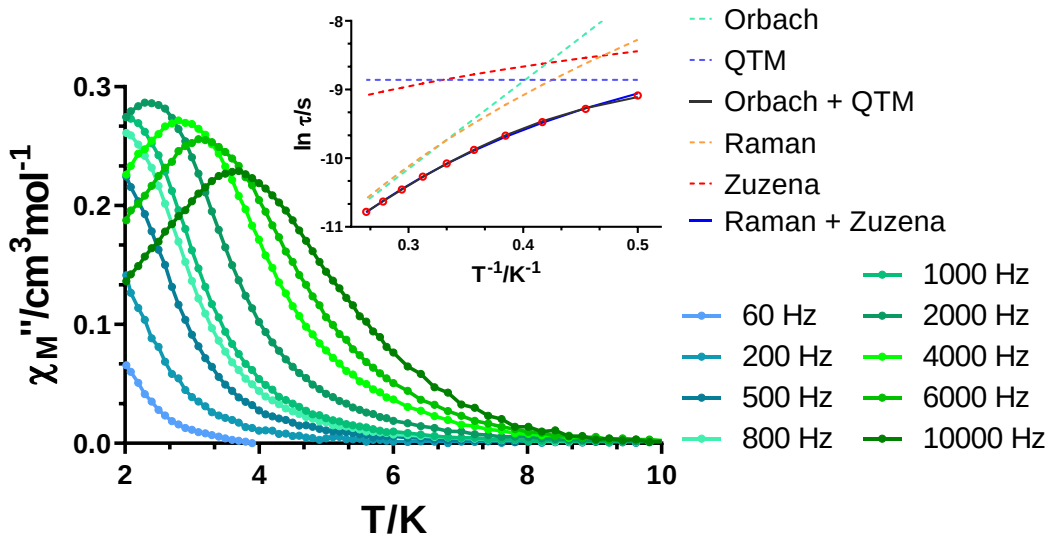

3.11. irudia.- 19 konposatuentzat, fasez kanpoko suszeptibilitatearen tenperaturarekiko mendekotasuna hainbat frekuentziatan 1 kOe-etako kanpoko eremu magnetikopean. Grafika txikia: Arrheniusen grafikoa erlaxazio-denboretarako Orbach + QTM nahiz Raman + Zuzena prozesuak kontuan hartuz. Lerro etenek mekanismo bakoitzaren ekarpen indibiduala erakusten dute.

Co_2Ln unitateetan oinarritutako konposatuei dagokienez (Ln ioi paramagnetikoa izanik), azken urteotan antzeko hainbat sistema aztertu diren arren [34,35], oraindik ez dago argi *SMM* portaera hobetzeko estrategiarik onena zein den. Ungurrek eta egilekideek [34] eginiko ikerketa lanean, kanpoko eremu magnetikorik gabe *SMM* portaera duten konplexuak sintetizatzeko estrategia onena Co^{II} ioien anisotropia Gd^{III} ioiaren spin altuarekin konbinatzea zela ondorioztatu zuten. Hala ere, beste ikerketa batzuek frogatu dute ezinezkoa dela estrategia hori CoLn sistema guztietara orokortzea. Beste sistema batzuetan ikusi den bezala, $Co^{II}Dy^{III}$ (edo $Co^{II}Tb^{III}$) analogoak ere izan ditzakete propietate interesgarriak, Dy^{III} anisotropikoa 3d ioi anisotropikoekin arrakastaz konbina daitekeela frogatuz [36–38].

Halaber, oso jakina da 4f ioiaren inguruko koordinazio-esferak duen garrantzia $\pm M_J$ balio altueneko azpimailak oinarrizko egoeran egonkortzeko (aldi berean garrantzitsua dena errendimendu altuko *SMM*ak diseinatzeko). Gure kasuan, lantanido ioiaren inguruko antiprisma karratua/dodekaedro triangeluarra magnitude altuko $\pm M_J$ azpimailak egonkortzeko baliagarria izatea espero da oblatu formako ioietan. Hori espero dugu aurretik taldean ikusitako emaitzetan oinarrituta [30]. Izan ere, kasu hartan gertatzen den

bezala, gure konposatu trinuklearretan karga negatiboa duten fenoxido taldeak kontrako aldeetan daude kokatuta Dy-O lotura laburrenak sortuz. Gainontzeko posizioak, berriz, atomo emaile neutroek betetzen dituzte. Beraz, estekatzaile-eremua potentzialki egokia da $\pm M_J$ egoerarik altuenak oinarrizko egoeran egonkortzeko ioi oblatuetan. Hipotesi hori frogatzeko, bi konposatu heterotrinuklear pare aztertu dira: oblatu motakoak (**21**, Tb^{III} eta **22**, Dy^{III}) eta prolatu motakoak (**23**, Er^{III} eta **24**, Yb^{III}). Gainera, Gd^{III} ioi isotropikoa duen $Co^{II}Gd^{III}Co^{II}$ (**20**) homologoa ere aztertu da.

Kanpoko eremu magnetikorik aplikatu ezean, soilik **21** eta **22** konposatuek erakusten dituzte maximoak suszeptibilitatearen fasez kanpoko osagaian (3.12. irudia). **21** konposatuaren kasuan, 2,0-2,7 K tartean lortutako α balioek erlaxazio-prozesuen banaketa nahiko zabala adierazten dute (0,22 (2,0 K)-0,20 (2,7 K)). Dena den, $\chi_M''(\upsilon)$ grafikoetatik lortutako erlaxazio-denborek linealtasuna erakusten dutenez (3.12. irudia, grafika txikia), Arrheniusen ekuaziora egokitu dira Orbach prozesua soilik kontuan hartuta eta doikuntzak U_{eff} = 7,7 K eta $\tau_0 = 8{,}27 \cdot 10^{-7}$ s parametro balioak ematen ditu. **22** konposatuaren kasuan, $\chi_M''(T)$ grafikoetan bi maximo multzo identifika daitezke 2000 Hz-tik gora, baina oro har tenperatura tarte osoan gainjartzen dira (3.12. irudia, goian eskuinean). Honek iradokitzen du, magnetizazioaren erlaxazio motela energia-barrera antzeko bi prozesuren bitartez ematen dela. Beraz, erlaxazio azkar eta moteletarako parametro independenteak lortzeko (*FR* eta *SR*), $\chi_M''(\chi_M')$ datuak CCFIT softwarearekin [39] doitu dira, tenperatura bakoitzerako prozesu bakoitzari dagokion erlaxazio-denbora lortuz. Arrheniusen grafikak eraiki dira bi prozesuetarako antzeko energia-barrera efektiboak eta τ_0 balioak lortuz: 13,0 K eta $3{,}19 \cdot 10^{-7}$ s *FR* prozesuarentzat eta 16,7 K eta $1{,}08 \cdot 10^{-6}$ s *SR* prozesuarentzat. Nolanahi ere, konposatu espezifiko honen kasuan, gutxi gorabehera ondo bereizita dauden bi maximo multzo desberdin ikusten badira ere $\chi_M''(T)$ grafikoetan, $\chi_M''(\upsilon)$ eta Cole-Cole grafikoak soilik kontuan hartuz gero, termikoki aktibatutako prozesu bakar batek jarduten duela esango genuke (ikusi A3.32. eta A3.37. irudiak). Beraz, datuak Debye eredu orokorrera ere doitu ditugu 2,0-6,0 K tenperatura-tartean α balioak eta erlaxazio-denborak lortzeko (prozesu bakarra kontuan hartuta). Alde batetik, 2,0 K-etan lortutako α = 0,35 balio altuak bi prozesu gainjarrien egoera ondo azaltzen du. Bestalde, 6,0 K-etan lortutako α = 0,06 balio askoz baxuagoa prozesu bakar bati lotua legoke, izan ere, *FR* prozesuak ez du jarduten tenperatura horietan eta soilik SRren eragina ikusten da. Erlaxazio-denborekin eraikitako Arrheniusen grafikoak ondo ebatzitako bi erregimen erakusten ditu (A3.41. irudia), bata 2,0-3,2 K tartean eta bestea 3,6-6,0 K tartean, $\chi_M''(T)$ grafikoan ikusten denarekin bateragarria. Datuak Orbach mekanismoetara doituz, ondoko U_{eff} eta τ_0 balioak lortzen dira: 8,0 K eta $1{,}08 \cdot 10^{-5}$ s eta 15,5 K eta $1{,}17 \cdot 10^{-6}$s *FR* eta *SR* prozesuentzako, hurrenez hurren.

Bi maximoen presentzia bi zentro metaliko anisotropikoen presentziagatik azal daiteke [40], baina aurretik aipatutako *dc* propietate magnetikoak eta **25** konposatuarentzako antzemandako portaera erabat ezberdina kontuan hartuta (ikusi aurrerago), gure ustez arrazoia beste bat da. Kasu batzuetan, Dy^{III} zentro anisotropiko bakar batek ere erlaxazio prozesu ugari erakuts ditzake [41]. Bi konposatuentzat neurketak 1000 Oe-eko kanpoko *dc* eremu magnetiko batekin errepikatzean, bi konposatuen maximoak tenperatura altuagoetara mugitzen dira (3.12. irudia, behean), *QTM*ren presentzia gutxienez partzialki desaktibatzen dela adieraziz. Bi kasuetan, energia-barreren balioak zertxobait hobetzen dira. Arrheniusen doikuntzek honako parametroak ematen dituzte energia-barrera efektibo eta τ_0 parametroentzat (azkenak parentesi artean): 11,3 K ($3{,}50\cdot10^{-7}$ s), 13,6 K ($4{,}76\cdot10^{-7}$ s) eta 20,0 K ($6{,}72\cdot10^{-7}$ s) **21**, **22** *FR* eta **22** *SR* prozesuentzat, hurrenez hurren. Kanpoko eremu magnetikorik gabeko egindako neurketan erabilitako estrategia bera erabiltzen saiatu gara **22** konposaturako, baina Arrheniusen doikuntzak erregimen lineal bakarra erakusten du tenperatura-tarte osoan (A3.43. irudia).

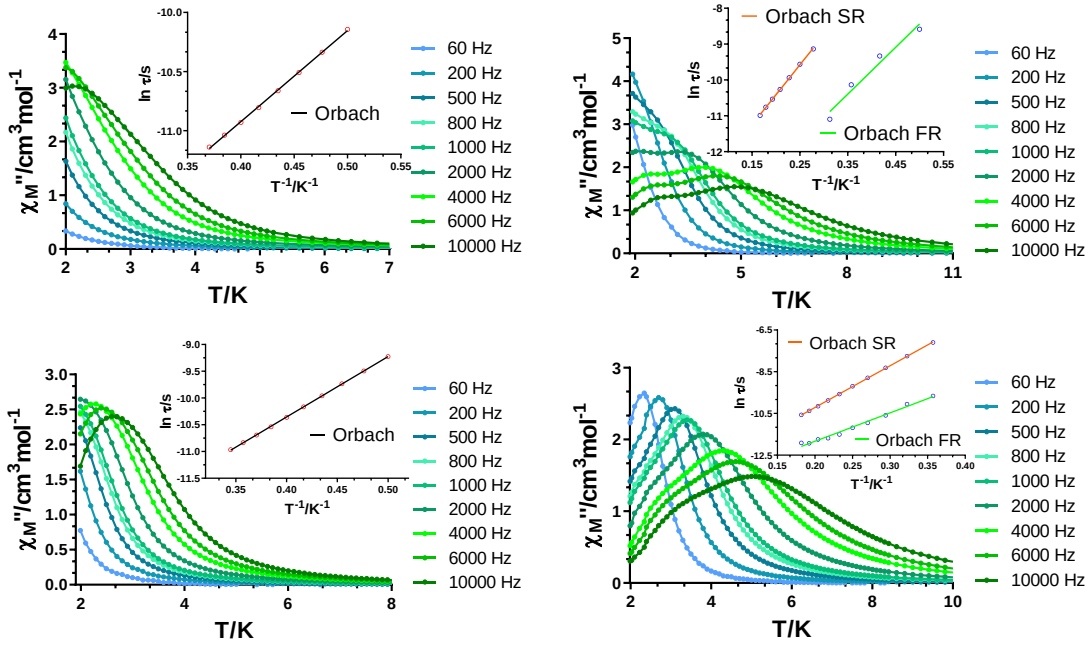

3.12. irudia.- Fasez kanpoko suszeptibilitatearen tenperaturarekiko mendekotasuna hainbat frekuentziatan kanpoko eremu magnetikorik aplikatu gabe **21** (goian ezkerrean) eta **22** (goian eskuinean) konposatuentzat eta 1 kOe-etako kanpoko eremu magnetikopean **21** (behean ezkerrean) eta **22** (behean eskuinean) konposatuentzat. Grafika txikia: Arrheniusen grafikoa erlaxazio-denboretarako Orbach prozesua kontuan hartuz.

Beste $Co^{II}Ln^{III}Co^{II}$ konposatu heterotrinuklearretara itzuliz, non Ln^{III} ioia isotropikoa (Gd^{III}, **20**) edo prolatua (Er^{III}, **23** eta Yb^{III}, **24**) den, soilik **20** konposatuak erakusten du frekuentziarekiko mendekotasuna $\chi_M''(T)$ seinaleetan, nahiz eta ez den maximorik ikusi ekipoaren tenperatura-mugatik gora (A3.22. irudia). *QTM*ren balizko efektua ezabatzeko, hiru konposatuak 1000 Oe-eko kanpoko *dc* eremu magnetikopean neurtu dira. **20** konposatuaren portaera antzekoa da, frekuentziarekiko eta tenperaturarekiko mendekotasuna ikusten da, baina maximorik gabe (A3.29. irudia). **23** konposatuak ere halako portaera erakusten du (A3.29. irudia), baina **24** konposatuak ez du seinalerik erakusten (A3.30. irudia). Alde batetik, emaitza hauek erakusten dute gure kasuan 3d ioi metaliko anisotropikoen eta spin altuko 4f ioi isotropikoen konbinazioa ez dela *SMM*ak sintetizatzeko eredurik eraginkorrena. Bestalde, badirudi lantanido ioiaren inguruko geometria antiprisma karratua egokia dela Tb^{III} eta Dy^{III} bezalako ioi oblatuen M_J azpimaila altuak oinarrizko egoeran egonkortzeko, baina ez ioi prolatuetarako. **17** konposatuaren kasuan bezala, **22** konposatuaren datuak Debyeren eredura egokitu dira $ln(\chi_M''/\chi_M') = ln(2\pi\upsilon\tau_0) + E_a/k_BT$ ekuazioa erabiliz. Doikuntzak energia-barrera efektiboaren eta τ_0 balioen ondoko balioak eman ditu: 5,2 K ($6{,}34\cdot10^{-8}$ s) eta 5,8 K ($8{,}52\cdot10^{-8}$ s) kanpoko eremurik aplikatu gabe eta 1000 Oe-eko eremuarekin, hurrenez hurren (A3.40. eta A3.42. irudiak).

Azkenik, **25** konposatuaren propietate dinamikoak aztertu dira zentro paramagnetikoen arteko molekula barruko truke-interakzioak ezabatzeak magnetizazioaren erlaxazio motela hobetzen edo okertzen duen aztertzeko. Neurketa kanpoko eremu magnetikorik gabe egiterakoan, $\chi_M''(T)$ grafikoan frekuentziarekiko eta tenperaturarekiko mendeko seinaleak detektatu dira, baina maximorik gabe (A3.23. irudia). Aurreko kasuetan bezala, lagina berriz neurtu da 1000 Oe-eko kanpoko eremu batekin *QTM* ezabatzeko. Kasu honetan, ondo definitutako maximoak lortu dira 12,0 K-etik behera frekuentzia guztietarako (3.13. irudia). Gainera, χ_M'' seinaleek zerora jotzen dute maximoen azpitik, *QTM* prozesua ondo desaktibatu dela baieztatuz. Cole-Cole grafikoek, 5,5-11,9 K tenperatura-tartean, erlaxazio-prozesuen banaketa nahiko estua iradokitzen dute (0,10 (5,5 K) eta 0,11 (11,9 K). Hala ere, erlaxazio-denborak irudikatzean, tenperatura altuko zati linealaz gain, kurbadura nabarmena ikusten da erdiko tenperatura-tartean eta baxuan. Horrek erlaxazio-prozesu anitzen presentzia iradokitzen du. Beraz, erlaxazio-denborak honako ekuazio honetara egokitu dira:

$$\tau^{-1} = BT^n + \tau_0^{-1}exp(-U_{eff}/k_BT) \qquad \textit{3.4. ekuazioa}$$

Ekuazio honek aldibereko Raman eta Orbach erlaxazio mekanismoak hartzen ditu kontuan, hurrenez hurren. Doikuntza onenak B = 0,1 $s^{-1}K^{-5,23}$; n = 5,23; τ_0 = 5,14·10^{-9} s eta U_{eff} = 115,6 K. balioak eman ditu. Raman prozesuaren n parametroari dagokionez, 9 balioa espero da Kramers ioietarako [42], baina azpimailen egituraren arabera, 1 eta 6 arteko balioak ere ontzat eman daitezke [43]. 3.13. irudiko grafika txikian erakusten den bezala, U_{eff} parametroaren balioa gainestimazio bat izan liteke, Orbach mekanismoaren ekarpenak ez baititu zehazki tenperatura altuenetarako erlaxazio-denborak ordezkatzen eta, aldiz, Raman prozesuak, ia erabat deskribatzen du tarte osoa. Beste doikuntza bat egiten ere saiatu gara, Raman mekanismoa bakarrik kontuan hartuta, baina ez da hain ondo egokitzen tenperatura baxueneko erlaxazio-denboretara. Beraz, kalkulu teorikoek lagunduko dute esaten ea 115,6 K-eko energia-barrera oinarrizko egoeraren eta (ziur aski) lehen egoera kitzikatuaren arteko energia-diferentziari dagokion, edo erlaxazioa egoera birtual baten bidez gertatzen den.

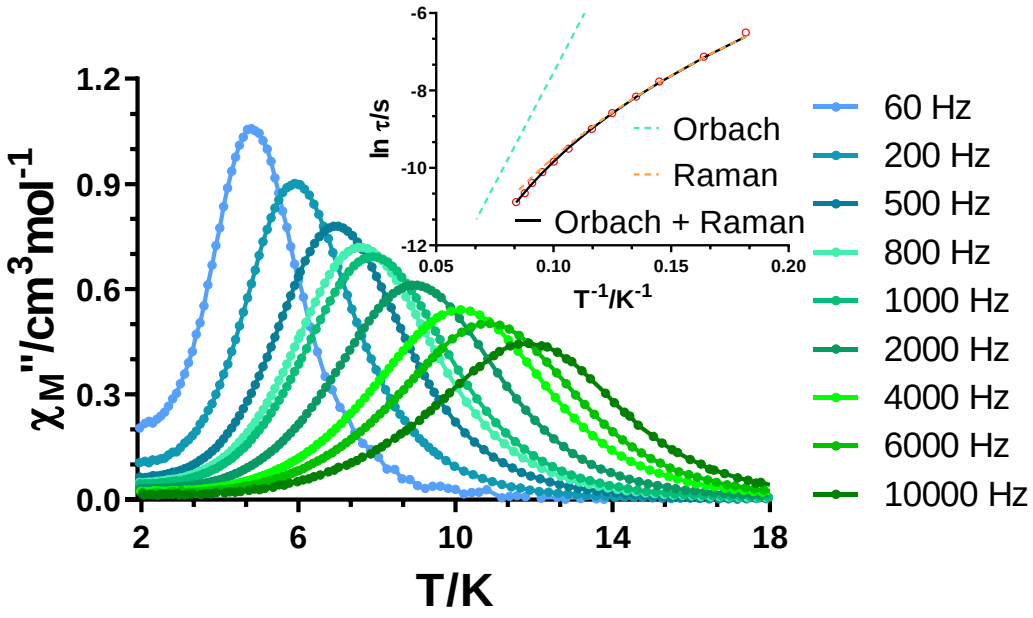

3.13. irudia.- 25 konposatuentzat, fasez kanpoko suszeptibilitatearen tenperaturarekiko mendekotasuna hainbat frekuentziatan 1 kOe-etako kanpoko eremu magnetikopean. Grafika txikia: Arrheniusen grafikoa erlaxazio-denboretarako Orbach + Raman prozesuak kontuan hartuz. Lerro etenek mekanismo bakoitzaren ekarpen indibiduala erakusten dute.

Azterketa sakon honek erakusten du, lehenik eta behin, diseinatutako estekatzaileak ±M_J altuko azpimaila magnetikoak egonkortzen dituela oblatu motako ioietarako, eta,

beraz, egokia dela Tb^{III} eta Dy^{III} ioietarako. Bigarrenik, molekula barneko truke-interakzio magnetikoek magnetizazioaren tunel-efektu azkarra moteltzen dute, horrela, *SMM* portaera azaleratuz **21** eta **22** konposatuetan kanpoko eremu magnetikorik aplikatu gabe ere. Interakzio hauek ekiditean Co^{II} ioi paramagnetikoak Zn^{II} ioi diamagnetikoekin ordezkatuz, **25**. konposatuak *SMM* portaera galtzen du eremu magnetikorik gabe *QTM* azkarra dela eta. Hau aldez aurretik ikusi izan da truke-interakzio bidez akoplatutako 3d-4f sistemetan [9]. Askotan, ioi lantanidoen 4f elektroiek interakzio oso txikia izaten dute beste ioi metaliko batzuekin eta *SMM* portaera ioi indibidualari lotua egoten da. Gainera, elkarrekintza hauek ahulak direnean zeharkako eremu magnetikoak sor ditzakete eta *QTM* are nabarmenagoa izan daiteke. Hala ere, hori ez da beti horrela izaten eta *SMM* portaera truke-interakzio akoplamenduaren ondorioz sortzen den beste sistema asko jakinarazi dira. Hirugarrenik, gure taldeak deskribatutako $Zn^{II}Dy^{III}Zn^{II}$ sistemarekin alderatuta, badirudi gure kasuan Dy^{III} ioiaren inguruko koordinazio-ingurunea distortsionatuagoa dagoela, eta horrek azaltzen du *SMM* portaerarik ez izatea kanpoko eremu magnetikorik gabe. Hala ere, **25** konposatuarentzat kalkulatutako 115,6 K-eko U_{eff} altua ikusita, **22** konposatuarena baino askoz altuagoa izanik, azken honentzat truke-interakzio bidez sortutako energia-diagrama hartu behar da kontuan.

3.4. ONDORIOAK

Laburbilduz, Co^{II} ioian oinarritutako hiru konposatu homonuklear eta zazpi 3d-4f-3d konposatu misto sintetizatu dira N,N′-dimetil-N,N′-bis(2-hidroxi-3-metoxi-5-metilbentzil)-etilendiamina (H_2L^3) estekatzailean oinarrituta. **16** konposatuko kloruro zubien ordez *end-on* eran koordinatutako azida taldeak sartzean **17** konplexuan, molekula barneko interakzio ferromagnetikoak eragiten dira. Azken honen eremuaren eraginpean SMM portaera ahula du U_{eff} eta τ_0 gutxi gorabeherako honako balioekin: 7,8 K eta $6{,}43 \cdot 10^{-8}$ s. **18** konposatuaren kasua oraindik ez dago argi. Co^{II} ioietan oinarritutako eremu aplikaturik gabeko *SMM* bat izatea interesgarria da, baina egituraren konplexutasunaren, zentro metaliko guztien geometria distortsionatuen eta nukleartasun handiaren ondorioz, ezin dugu irmoki baieztatu magnetizazioaren erlaxazio mantsoa nondik sortzen den.

Aztertutako lehen konposatu trinuklearrak, **19** konplexuak, ioi paramagnetiko mota bakarra du, Co^{II} ioia. Konposatu pentakoordinatua genuen helburu $D < 0$ balioak erakuts ditzaketelako. Hala ere, *SMM* portaera ikusi ahal izateko, kanpoko eremu magnetikoa aplikatu behar izan dugu. 4f ioi paramagnetikoak dituzten 3d-4f-3d konposatuei

dagokienez, **20-22** konposatuek soilik erakutsi dute *SMM* portaera eremu magnetikoaren gabezian. **20** konposatuarentzat frekuentziarekiko mendeko seinaleak lortu dira, baina maximoak ekipoaren tenperatura mugaren azpitik daude eta energia-barreraren balio hurbildua baino ezin izan da lortu. Kanpoko eremu magnetikoa aplikatzean ez da desberdintasunik aurkitu, U_{eff} parametroaren oso balio txikia iradokitzen duena. **21** eta **22** konposatuek 2 eta 5 K-etik beherako maximoak dituzte, hurrenez hurren, eremurik gabe. 1000 Oe-eko kanpoko eremua aplikatzean maximoak tenperatura altuagoetara lerratzen dira, *QTM* guztiz/partzialki desaktibatzearen ondorioz. Baldintza horietan, U_{eff} balioak 7,7 K-etik 11,3 K-era areagotzen dira **21** sistemarentzat eta 13,0 K-etik (*FR*) edo 16,7 K-etik (*SR*)-tik 13,6 K-era (*FR*) edo 20,0 K-era (*SR*) **22** konposatuan. **23** eta **24** konposatuek ez dute apenas *SMM* portaerarik erakusten. Oblatu eta prolatu motako ioien arteko konparaketa honek estekatzailearen diseinua lehenengoentzat egokiagoa dela ondorioztatzea ahalbidetzen du. Azkenik, **25** konposatuak 115,6 K-eko energia-barrera efektiboa du *dc* eremu magnetikoa aplikatzean. Emaitza horietatik ondorioztatzen dugu (i) Co-Ln molekula barneko truke-interakzioak tunel-efektua desaktibatzeko hainako / gaitasuna indartsuak direla eta (ii) **22** konposatuaren erlaxazio magnetiko geldoak ez duela ioi bakarrean jatorria, truke-interakzio sisteman baizik.

3.5.- ERREFERENTZIAK

[1] E.C. Yang, W. Wernsdorfer, L.N. Zakharov, Y. Karaki, A. Yamaguchi, R.M. Isidro, G. Di Lu, S.A. Wilson, A.L. Rheingold, H. Ishimoto, D.N. Hendrickson, Fast magnetization tunneling in tetranickel(II) single-molecule magnets, Inorg. Chem. 45 (2006) 529–546. https://doi.org/10.1021/ic050093r.

[2] A. Ferguson, J. Lawrence, A. Parkin, J. Sanchez-Benitez, K. V. Kamenev, E.K. Brechin, W. Wernsdorfer, S. Hill, M. Murrie, Synthesis and characterisation of a Ni4 single-molecule magnet with S4 symmetry, J. Chem. Soc. Dalt. Trans. (2008) 6409–6414. https://doi.org/10.1039/b807447j.

[3] I. Oyarzabal, J. Ruiz, A.J. Mota, A. Rodríguez-Diéguez, J.M. Seco, E. Colacio, An experimental and theoretical magneto-structural study of polynuclear NiII complexes assembled from a versatile bis(salicylaldehyde)diamine polytopic ligand, Dalton Trans. 44 (2015) 6825–6838. https://doi.org/10.1039/c5dt00356c.

[4] T.C. Stamatatos, K.A. Abboud, W. Wernsdorfer, G. Christou, {Mn 6} n single-chain magnet bearing azides and di-2-pyridylketone-derived ligands, Inorg. Chem. 48 (2009) 807–809. https://doi.org/10.1021/ic8020645.

[5] A. Escuer, G. Aromí, Azide as a Bridging Ligand and Magnetic Coupler in Transition Metal Clusters, Eur. J. Inorg. Chem. 2006 (2006) 4721–4736. https://doi.org/10.1002/ejic.200600552.

[6] S. Schmidt, D. Prodius, V. Mereacre, A.K. Powell, G.E. Kostakis, Unprecedented chemical transformation: Crystallographic evidence for 1,1,2,2-tetrahydroxyethane captured within an Fe6Dy3 single molecule magnet, Chem. Commun. 49 (2013) 1696–1698. https://doi.org/10.1039/c2cc38006d.

[7] J.D. Rinehart, M. Fang, W.J. Evans, J.R. Long, Strong exchange and magnetic blocking in N_2^{3-}-radical-bridged lanthanide complexes., Nat. Chem. 3 (2011) 538–42. https://doi.org/10.1038/nchem.1063.

[8] S.K. Langley, L. Ungur, N.F. Chilton, B. Moubaraki, L.F. Chibotaru, K.S. Murray, Single-molecule magnetism in a family of {CoII2DyIII2} butterfly complexes: Effects of ligand replacement on the dynamics of magnetic relaxation, Inorg. Chem. 53 (2014) 4303–4315.

https://doi.org/10.1021/ic4029645.

[9] S.K. Langley, D.P. Wielechowski, V. Vieru, N.F. Chilton, B. Moubaraki, B.F. Abrahams, L.F. Chibotaru, K.S. Murray, A {CrIII2DyIII2} single-molecule magnet: Enhancing the blocking temperature through 3d magnetic exchange, Angew. Chem. Int. Ed. 52 (2013) 12014–12019. https://doi.org/10.1002/anie.201306329.

[10] A. Vráblová, M. Tomás, L.R. Falvello, Ľ. Dlháň, J. Titiš, J. Černák, R. Boča, Slow magnetic relaxation in Ni-Ln (Ln = Ce, Gd, Dy) dinuclear complexes, Dalton Trans. 48 (2019) 13943–13952. https://doi.org/10.1039/c9dt02122a.

[11] A. Zabala-Lekuona, J. Cepeda, I. Oyarzabal, A. Rodríguez-Diéguez, J.A. García, J.M. Seco, E. Colacio, Rational design of triple-bridged dinuclear ZnIILnIII-based complexes: a structural, magnetic and luminescence study, CrystEngComm. 19 (2017) 256–264. https://doi.org/10.1039/c6ce02240e.

[12] M. Andruh, The exceptionally rich coordination chemistry generated by Schiff-base ligands derived from o-vanillin, Dalton Trans. 44 (2015) 16633–16653. https://doi.org/10.1039/c5dt02661j.

[13] L. Botana, J. Ruiz, A.J. Mota, A. Rodríguez-Diéguez, J.M. Seco, I. Oyarzabal, E. Colacio, Anion controlled structural and magnetic diversity in unusual mixed-bridged polynuclear NiII complexes with a versatile bis(2-methoxy phenol)diamine hexadentate ligand. An experimental and theoretical magneto-structural study, Dalton Trans. 43 (2014) 13509–13524. https://doi.org/10.1039/c4dt01253d.

[14] A. Das, S. Goswami, A. Ghosh, Rare azido and hydroxido bridged tetranuclear Co(ii) complexes of a polynucleating Mannich base ligand with a defect dicubane core: structures, magnetism and phenoxazinone synthase like activity, New J. Chem. 42 (2018) 19377–19389. https://doi.org/10.1039/c8nj04750b.

[15] M. Llunell, D. Casanova, J. Cirera, J.M. Bofill, P. Alemany, S. Alvarez, M. Pinsky, D. Avnir, SHAPE, (2005).

[16] P. King, R. Clérac, W. Wernsdorfer, C.E. Anson, A.K. Powell, Synthesis and magnetism of oxygen-bridged tetranuclear defect dicubane Co(II) and Ni(II) clusters, Dalton Trans. (2004) 2670–2676. https://doi.org/10.1039/b405881j.

[17] J.M. Clemente-Juan, E. Coronado, Magnetic clusters from polyoxometalate complexes, Coord. Chem. Rev. 193–195 (1999) 361–394. https://doi.org/10.1016/S0010-8545(99)00170-8.

[18] H. Andres, J.M. Clemente-Juan, M. Aebersold, H.U. Güdel, E. Coronado, H. Büttner, G. Kearly, J. Melero, R. Burriel, Magnetic excitations in polyoxometalate clusters observed by inelastic neutron scattering: Evidence for anisotropic ferromagnetic exchange interactions in the tetrameric cobalt(II) cluster [Co4(H2O)2(PW9O34)2]10-. Comparison with the magnetic and specific heat properties, J. Am. Chem. Soc. 121 (1999) 10028–10034. https://doi.org/10.1021/ja990198r.

[19] N.F. Chilton, R.P. Anderson, L.D. Turner, A. Soncini, K.S. Murray, PHI: A powerful new program for the analysis of anisotropic monomeric and exchange-coupled polynuclear d- and f-block complexes, J. Comput. Chem. 34 (2013) 1164–1175. https://doi.org/10.1002/jcc.23234.

[20] L. Norel, L.E. Darago, B. Le Guennic, K. Chakarawet, M.I. Gonzalez, J.H. Olshansky, S. Rigaut, J.R. Long, A Terminal Fluoride Ligand Generates Axial Magnetic Anisotropy in Dysprosium Complexes, Angew. Chem. Int. Ed. 57 (2018) 1933–1938. https://doi.org/10.1002/anie.201712139.

[21] S. Vaidya, S. Tewary, S.K. Singh, S.K. Langley, K.S. Murray, Y. Lan, W. Wernsdorfer, G. Rajaraman, M. Shanmugam, What Controls the Sign and Magnitude of Magnetic Anisotropy in Tetrahedral Cobalt(II) Single-Ion Magnets?, Inorg. Chem. 55 (2016) 9564–9578. https://doi.org/10.1021/acs.inorgchem.6b01073.

[22] S. Roy, I. Oyarzabal, J. Vallejo, J. Cano, E. Colacio, A. Bauza, A. Frontera, A.M. Kirillov, M.G.B. Drew, S. Das, Two Polymorphic Forms of a Six-Coordinate Mononuclear Cobalt(II) Complex with Easy-Plane Anisotropy: Structural Features, Theoretical Calculations, and Field-Induced Slow Relaxation of the Magnetization, Inorg. Chem. 55 (2016) 8502–8513. https://doi.org/10.1021/acs.inorgchem.6b01087.

[23] O. Pajuelo-Corral, A. Zabala-Lekuona, E. San Sebastian, A. Rodríguez-Diéguez, J.A. García, L. Lezama, E. Colacio, J.M. Seco, J. Cepeda, Modulating Magnetic and Photoluminescence Properties in 2-Aminonicotinate-Based Bifunctional Coordination Polymers by Merging 3d Metal Ions, Chem. – A Eur. J. 26 (2020) 13484–13498. https://doi.org/10.1002/chem.202002755.

[24] R. Herchel, L. Váhovská, I. Potočňák, Z. Trávníček, Slow magnetic relaxation in octahedral cobalt(II) field-induced single-ion magnet with positive axial and large rhombic anisotropy, Inorg. Chem. 53 (2014) 5896–5898. https://doi.org/10.1021/ic500916u.

[25] E. Colacio, J. Ruiz, E. Ruiz, E. Cremades, J. Krzystek, S. Carretta, J. Cano, T. Guidi, W. Wernsdorfer, E.K. Brechin, Slow Magnetic Relaxation in a Co ^{II} -Y ^{III} Single-Ion Magnet with Positive Axial Zero-Field Splitting, Angew. Chem. Int. Ed. 52 (2013) 9130–9134. https://doi.org/10.1002/anie.201304386.

[26] Y.F. Deng, M.K. Singh, D. Gan, T. Xiao, Y. Wang, S. Liu, Z. Wang, Z. Ouyang, Y.Z. Zhang, K.R. Dunbar, Probing the Axial Distortion Effect on the Magnetic Anisotropy of Octahedral Co(II) Complexes, Inorg. Chem. 59 (2020) 7622–7630. https://doi.org/10.1021/acs.inorgchem.0c00531.

[27] A. Świtlicka, B. Machura, J. Cano, F. Lloret, M. Julve, A Study of the Lack of Slow Magnetic Relaxation in Mononuclear Trigonal Bipyramidal Cobalt(II) Complexes, ChemistrySelect. 6 (2021) 576–582. https://doi.org/10.1002/slct.202100061.

[28] K. Chakarawet, M. Atanasov, J. Marbey, P.C. Bunting, F. Neese, S. Hill, J.R. Long, Strong electronic and magnetic coupling in M4(M = Ni, Cu) clusters via direct orbital interactions between low-coordinate metal centers, J. Am. Chem. Soc. 142 (2020) 19161–19169. https://doi.org/10.1021/jacs.0c08460.

[29] E.C. Yang, Z.Y. Liu, L. Zhang, N. Yang, X.J. Zhao, Magnetism behaviours dominated by the interplay of magnetic anisotropy and exchange coupling in local Co II 7 discs, Dalton Trans. 45 (2016) 8134–8141. https://doi.org/10.1039/c6dt00010j.

[30] I. Oyarzabal, J. Ruiz, J.M. Seco, M. Evangelisti, A. Cam??n, E. Ruiz, D. Aravena, E. Colacio, Rational electrostatic design of easy-axis magnetic anisotropy in a ZnII-DyIII-ZnII single-molecule magnet with a high energy barrier, Chem. - A Eur. J. 20 (2014) 14262–14269. https://doi.org/10.1002/chem.201403670.

[31] H.H. Cui, M.M. Ding, X. Du Zhang, W. Lv, Y.Q. Zhang, X.T. Chen, Z. Wang, Z.W. Ouyang, Z.L. Xue, Magnetic anisotropy in square pyramidal cobalt(ii) complexes supported by a tetraazo macrocyclic ligand, Dalton Trans. 49 (2020) 14837–14846. https://doi.org/10.1039/d0dt01954b.

[32] A. Packová, J. Miklovič, R. Boča, Manifold relaxation processes in a mononuclear Co(II) single-molecule magnet, Polyhedron. 102 (2015) 88–93. https://doi.org/10.1016/j.poly.2015.08.002.

[33] A.W. Addison, T.N. Rao, J. Reedijk, J. Van Rijn, G.C. Verschoor, Synthesis, structure, and spectroscopic properties of copper(II) compounds containing nitrogen-sulphur donor ligands; the crystal and molecular structure of aqua[1,7-bis(N-methylbenzimidazol-2′;-yl)-2,6-dithiaheptane]copper(II) perchlorate, J. Chem. Soc. Dalt. Trans. (1984) 1349–1356. https://doi.org/10.1039/DT9840001349.

[34] L. Ungur, M. Thewissen, J.P. Costes, W. Wernsdorfer, L.F. Chibotaru, Interplay of strongly anisotropic metal ions in magnetic blocking of complexes, Inorg. Chem. 52 (2013) 6328–6337. https://doi.org/10.1021/ic302568x.

[35] Q.W. Xie, S.Q. Wu, W.B. Shi, C.M. Liu, A.L. Cui, H.Z. Kou, Heterodinuclear MII-LnIII single molecule magnets constructed from exchange-coupled single ion magnets, Dalton Trans. 43 (2014) 11309–11316. https://doi.org/10.1039/c4dt00740a.

[36] M. Towatari, K. Nishi, T. Fujinami, N. Matsumoto, Y. Sunatsuki, M. Kojima, N. Mochida, T. Ishida, N. Re, J. Mrozinski, Syntheses, structures, and magnetic properties of acetato- and diphenolato-bridged 3d-4f binuclear complexes [M(3-MeOsaltn)(MeOH) x(ac)Ln(hfac)2](M = ZnII, CuII,NiII,CoII;Ln = LaIII,GdIII, TbIII, DyIII; 3-MeOsaltn = N,N-Bis(3-methoxy-2-oxybenzylidene)-1,3-propanediaminato; Ac = Acetato; Hfac = Hexafluoroacetylacetonato; X = 0 or 1), Inorg. Chem. 52 (2013) 6160–6178. https://doi.org/10.1021/ic400594u.

[37] X.Q. Zhao, J. Wang, D.X. Bao, S. Xiang, Y.J. Liu, Y.C. Li, The ferromagnetic [Ln2Co6] heterometallic complexes, Dalton Trans. 46 (2017) 2196–2203. https://doi.org/10.1039/c6dt04375e.

[38] S. Chen, V. Mereacre, Z. Zhao, W. Zhang, Z. He, Synthesis, structures and magnetic properties of linear {Co II 2 Ln III 2 } coordination clusters, New J. Chem. 42 (2018) 1284–1289. https://doi.org/10.1039/c7nj04022a.

[39] D. Reta, N.F. Chilton, Uncertainty estimates for magnetic relaxation times and magnetic relaxation parameters, Phys. Chem. Chem. Phys. 21 (2019) 23567–23575. https://doi.org/10.1039/c9cp04301b.

[40] L. Zhang , J. Jung, P. Zhang, M. Guo, L. Zhao, J. Tang, B. Le Guennic, Site-Resolved Two-Step Relaxation Process in an Asymmetric Dy $_2$ Single-Molecule Magnet, Chem. - A Eur. J. 22 (2016) 1392–1398. https://doi.org/10.1002/chem.201503422.

[41] J. Ruiz, A.J. Mota, A. Rodríguez-Diéguez, S. Titos, J.M. Herrera, E. Ruiz, E. Cremades, J.P. Costes, E. Colacio, Field and dilution effects on the slow relaxation of a luminescent DyO9 low-symmetry single-ion magnet., Chem. Commun. 48 (2012) 7916–8. https://doi.org/10.1039/c2cc32518g.

[42] A. Abragam, B. Bleaney, Electron Paramagnetic Resonance of Transition Ions, Clarendon Press Oxford, UK,. (1970) 925.

[43] K.N. Shrivastava, Theory of Spin–Lattice Relaxation, Phys. Status Solidi. 117 (1983) 437–458. https://doi.org/10.1002/pssb.2221170202.